UNIVERSITAT DE BARCELONA

Síntesis de compuestos bioactivos: Ligandos de los receptores imidazolínicos I_2 e inhibidores de la enzima PEPCK

Sergio Rodríguez Arévalo

UNIVERSITAT DE BARCELONA

FACULTAT DE FARMÀCIA I CIÈNCIES DE L'ALIMENTACIÓ

LABORATORI DE QUÍMICA FARMACÈUTICA
DEPARTAMENT DE FARMACOLOGIA, TOXICOLOGIA I QUÍMICA TERAPÈUTICA

SÍNTESIS DE COMPUESTOS BIOACTIVOS: LIGANDOS DE LOS RECEPTORES IMIDAZOLÍNICOS I_2 E INHIBIDORES DE LA ENZIMA PEPCK

SERGIO RODRÍGUEZ ARÉVALO
2021

UNIVERSITAT DE BARCELONA

FACULTAT DE FARMÀCIA I CIÈNCIES DE L'ALIMENTACIÓ

PROGRAMA DE DOCTORAT DE QUÍMICA ORGÀNICA

SÍNTESIS DE COMPUESTOS BIOACTIVOS: LIGANDOS DE LOS RECEPTORES IMIDAZÓLICOS I_2 E INHIBIDORES DE LA ENZIMA PEPCK

Memòria presentada per Sergio Rodríguez Arévalo per optar al títol de doctor per la Universitat de Barcelona

Directora i tutora:	Codirector:	Doctorand:
CPISR-1 C MARIA CARMEN ESCOLANO MIRON Firmado digitalmente por CPISR-1 C MARIA CARMEN ESCOLANO MIRON Fecha: 2021.09.06 21:07:45 +02'00'	CPISR-1 C SANTIAGO VAZQUEZ CRUZ Firmado digitalmente por CPISR-1 C SANTIAGO VAZQUEZ CRUZ Fecha: 2021.09.06 21:08:16 +02'00'	
Prof. Carmen Escolano Mirón	Prof. Santiago Vázquez Cruz	Sergio Rodríguez Arévalo

Barcelona, 2021

El trabajo experimental recogido en esta memoria se ha realizado en el Laboratorio de la Unidad de Química Farmacéutica de la Facultad de Farmacia y Ciencias de la Alimentación de la Universidad de Barcelona y el último año en el Departamento de Química Biológica del Instituto de Química Avanzada de Catalunya (IQAC-CSIC), bajo la dirección de la Prof. Carmen Escolano Mirón y el Prof. Santiago Vázquez Cruz.

Esta Tesis Doctoral ha sido posible gracias a la concesión de una Beca Predoctoral "d'ajuts destinats a universitats, centres de recerca i fundacions hospitalàries per a la contractació de personal investigador novell (2018FI_B_00227) de l'Agència de Gestió d'Ajuts Universitaris i de Recerca (AGAUR)", a la cual quiero expresar mi gratitud.

El presente trabajo ha sido financiado por el Ministerio de Ciencia, Innovación y Universidades, Agencia Estatal de Investigación (proyectos BQU2015-66030-R, SAF2016-77703-C2-1-R y PID2019-107991RB-I00), la Generalitat de Catalunya (proyecto 2017SGR106) y la Fundación "la Caixa" (proyecto CI18-00002).

Agradecimientos

Sabiendo que, con toda probabilidad, me olvidaría de incluir a alguien en estos agradacimientos, voy a generalizar.

Quisiera agradecer a toda la gente (y equipos de laboratorio) que han colaborado en que sea posible la realización de esta Tesis Doctoral. En especial, me gustaría hacer una mención a mi directora de Tesis, Carmen Escolano, que me ha guiado y acompañado durante estos largos años de trabajo. Sin ella, el camino hubiese sido mucho más duro.

Gracias a todos por el apoyo moral, físico, económico y emocional entregado.

Índice

Prólogo ***11***

Difusión de resultados ***13***

Capítulo 1. Introducción ***17***

1.1. Química de los isocianuros 18

1.2. Receptores imidazolínicos 25

1.3. Enzima Fosfoenolpiruvato carboxiquinasa mitocondrial (PEPCK-M) 35

1.4. *Transient Receptor Potential Cation Channel M8* (TRPM8) y candidato clínico AR-15512 40

1.5. Estructura de la memoria y objetivos 43

Capítulo 2. Bicyclic α-Iminophosphonates as High Affinity Imidazoline I_2 Receptor Ligands for Alzheimer's Disease ***49***

2.1. *Journal of Medicinal Chemistry* 2020, *63*, 3610-3633 49

2.2. Resultados no publicados 225

Capítulo 3. Benzofuranyl-2-imidazoles as Imidazoline I_2 Receptor Ligands for Alzheimer's Disease ***235***

3.1. *European Journal Medicinal Chemistry* 2021, *222*, 113540 235

3.2. Resultados no publicados 311

Capítulo 4. The first consecutive multicomponent reaction leading diastereoselectively to bis(2-imidazolin-4-yl)phosphonates ***325***

4.1. Introducción 327

4.2. Objetivo 329

4.3. Discusión de los resultados 330

4.3.1. Búsqueda de las condiciones de reacción óptimas 330

4.3.2. Estudio de la reacción con diferentes diaminas alifáticas 333

4.3.3. Estudio de la reacción con diferentes diaminas bencílicas 335

4.3.4. Estudio de la reacción con diferentes diaminas impedidas estéricamente o dianilina. 336

4.3.5. Estudio de la reacción con diamina asimétrica 337

4.3.6. Estudio de la reacción con triamina alifática 338

4.3.7. Estudio de la reacción con diferentes carbonilos 339

4.3.8. Determinación de la diastereoselectividad de la reacción para la formación de 1a..... 340

4.3.9. cMCR utilizando isocianoacetato de metilo 342

4.3.10. Propuesta del mecanismo de reacción 344

4.3.11. Estudio farmacológico 345
4.4. Conclusiones 347
Capítulo 5. Pharmacology and preclinical validation of a novel anticancer compound targeting PEPCK-M 413
5.1. *Biomedicine & Pharmacotherapy* 2020, *121*, 109601 413
5.2. Resultados no publicados 439
Capítulo 6. Synthesis, Characterization and HPLC Analysis of the (1S,2S,5R)-Diastereomer and the Enantiomer of the Clinical Candidate AR-15512 449
6.1. *Molecules* 2021, *26*, 906 449
Conclusiones 495
Anexo: Otras publicaciones 497
A1. *British Journal of Pharmacology 2021, 178, 3017-3033* 499
A2. *GeroScience* 2021, *43*, 965-983 517
A3. *Pharmaceutics 2020, 12, 475* 537
A4. *Cells 2020, 9, 18* 557
A5. *Neurotherapeutics 2019, 16, 416-431* 573

Prólogo

La presente Tesis Doctoral ha sido realizada en la Unidad de Química Farmacéutica de la Facultad de Farmacia y Ciencias de la Alimentación de la Universidad de Barcelona (UB) y el último año en el Departamento de Química Biológica del Instituto de Química Avanzada de Catalunya (IQAC-CSIC).

Esta Tesis Doctoral se presenta como Compendio de Publicaciones. De acuerdo con la normativa vigente, la memoria incluye un apartado de introducción general donde se discute la temática y se comentan los objetivos marcados al inicio del proyecto junto a un resumen global de los resultados obtenidos (*Capítulo 1*), una discusión de parte del trabajo llevado a cabo mediante las copias completas de los artículos publicados (*Capítulos 2, 3, 5 y 6*), un capítulo que recoge la memoria de un proyecto aún no publicado (*Capítulo 4*) y, finalmente las conclusiones extraídas a partir de toda la investigación realizada.

La presente Tesis Doctoral se ha dividido en 6 capítulos:

El *Capítulo 1* consiste en una introducción haciendo un repaso a los antecedentes del grupo y la importancia de los isocianometilfosfonatos en el ámbito de la química sintética. También se describen brevemente las diferentes dianas terapéuticas con las que interaccionan los compuestos sintetizados. Adicionalmente, en este capítulo inicial se discute la organización de la memoria y se introducen los objetivos de cada uno de los estudios realizados, en su mayoría publicados en revistas internacionales de reconocido prestigio.

En el *Capítulo 2* se incluye la publicación *Bicyclic α-iminophosphonates as high affinity imidazoline I_2 receptor ligands for Alzheimer's disease* (Abás, S.; Rodríguez-Arévalo, S.; Bagán, A.; Griñán-Ferré, C.; Vasilopoulou, F.; Brocos-Mosquera, I.; Muruguza, C.; Pérez, B.; Molins, E.; Luque, F.J.; Pérez-Lozano, P.; de Jonghe, S.; Daelemans, D.; Naesens, L.; Brea, J.; Loza, M.I.; Hernández-Hernández, E.; García-Sevilla, J.A.; García-Fuster, M.J.; Radan, M.; Djikic, T.; Nikolic, K.; Pallàs, M.; Callado, L.F.; Escolano, C. *J. Med. Chem.* **2020**, *63*, 3610-3633). El trabajo realizado para cumplir los objetivos fijados en este apartado dio lugar a resultados que no se incluyeron en la publicación pero que quedan recogidos en el apartado 2.2 de este capítulo.

En el *Capítulo 3* se adjunta el artículo titulado *Benzofuranyl-2-imidazoles as imidazoline I_2 receptor ligands for Alzheimer's disease* (Rodríguez-Arévalo, S.; Bagán, A.; Griñán-Ferré, C.; Vasilopoulou, F.; Pallàs, M.; Brocos-Mosquera, I.; Callado, L.F.; Loza, M.I.;

Martínez, A.L.; Brea, J.; Pérez, B.; Molins, E.; de Jonghe, S.; Daelemans, D.; Radan, M.; Djikic, T.; Nikolic, K.; Hernández-Hernández, E.; García-Fuster, M.J.; García-Sevilla, J.A.; Escolano, C. *Eur. J. Med. Chem.* **2021**, *222*, 113540). Los estudios realizados para cumplir los objetivos fijados en este capítulo dieron lugar a resultados que no se incluyeron en la publicación pero que quedan recogidos en el apartado 3.2 de este capítulo.

El *Capítulo 4*, titulado *The first consecutive multicomponent reaction leading diastereoselectively to bis(2-imidazolin-4-yl)phosphonates,* contiene la memoria (introducción, objetivos, discusión de resultados y conclusiones) del proyecto de investigación en el cual se describe la síntesis diastereoselectiva de bis(2-imidazolin-4-il)fosfonatos mediante reacciones multicomponente consecutivas.

En el *Capítulo 5* se adjunta el artículo *Pharmacology and preclinical validation of a novel anticancer compound targeting PEPCK-M* (Aragó, M.; Moreno-Felici, J.; Abás, S.; Rodríguez-Arévalo, S.; Hyrossova, P.; Figueras, A.; Viñals, F.; Pérez, B.; Loza, M.I.; Brea, J.; Latorre, P.; Carrodeguas, J.A.; García-Rovés, P.M.; Galdeano, C.; Ginex, T.; Luque, F.J.; Escolano, C.; Perales, J.C. *Biomed. Pharmacother.* **2020**, *121*, 109601). El trabajo realizado para cumplir los objetivos fijados en este apartado dio lugar a resultados que no se incluyeron en la publicación pero que quedan recogidos en el apartado 5.2 de este capítulo.

El *Capítulo 6* contiene los resultados derivados de un proyecto de servicio gestionado a través de la Fundació Bosch i Gimpera (UB) con la empresa Avizorex Pharma S.L. Los resultados de este trabajo se recogen en el artículo *Synthesis, characterization and HPLC analysis of the (1S,2S,5R)-diastereomer and the enantiomer of the clinical candidate AR-15512* (Rodríguez-Arévalo, S.; Pujol, E.; Abás, S.; Galdeano, C.; Escolano, C.; Vázquez, S. *Molecules* **2021**, *26*, 906).

Por último, la memoria contiene un apartado con las conclusiones y un anexo en el que se incluyen las publicaciones relativas al estudio de la actividad farmacológica de los compuestos sintetizados durante esta Tesis Doctoral.

Difusión de resultados

Publicaciones

1. **Benzofuranyl-2-imidazoles as Imidazoline I_2 Receptor Ligands for Alzheimer's Disease.** Rodríguez-Arévalo, S.; Bagán, A.; Griñán-Ferré, C.; Vasilopoulou, F.; Pallàs, M.; Brocos-Mosquera, I.; Callado, L.F.; Loza, M.I.; Martínez, A.L.; Brea, J.; Pérez, B.; Molins, E.; de Jonghe, S.; Daelemans, D.; Radan, M.; Djikic, T.; Nikolic, K.; Hernández-Hernández, E.; García-Fuster, M.J.; García-Sevilla, J.A.; Escolano, C. *Eur. J. Med. Chem.* **2021**, *222*, 113540.

2. **Disease-modifying treatment with I_2 imidazoline receptor ligand LSL60101 in an Alzheimer's disease mouse model: A Comparative study with donepezil**. Vasilopoulou, F.; Rodríguez-Arévalo, S.; Bagán, A.; Escolano, C.; Griñán-Ferré, C.; Pallàs, M. *Br. J. Pharmacol*. **2021**, 178, 3017-3033.

3. **Synthesis, Characterization and HPLC Analysis of the (1*S*,2*S*,5*R*)-Diastereomer and the Enantiomer of the Clinical Candidate AR-15512.** Rodríguez-Arévalo, S.; Pujol, E.; Abás, S.; Galdeano, C.; Escolano, C.; Vázquez, S. *Molecules* **2021**, *26*, 906.

4. **I_2 imidazoline receptor modulation protects aged SAMP8 mice against cognitive decline by suppressing the calcineurin pathway**. Vasilopoulou, F.; Griñán-Ferré, C.; Rodríguez-Arévalo, S.; Bagán, A.; Abás, S.; Escolano, C.; Pallàs, M. *GeroScience* **2021**, *43*, 965-983.

5. **Amelioration of BPSD-Like Phenotype and Cognitive Decline in SAMP8 Mice Model Accompanied by Molecular Changes after Treatment with I_2-Imidazoline Receptor Ligand MCR5.** Vasilopoulou, F.; Bagán, A.; Rodríguez-Arévalo, S.; Escolano, C.; Griñán-Ferré, C.; Pallàs, M. *Pharmaceutics* **2020**,*12*, 475.

6. **Bicyclic α-Iminophosphonates as High Affinity Imidazoline I_2 Receptor Ligands for Alzheimer's Disease.** Abás, S.; Rodríguez-Arévalo, S.; Bagán, A.; Griñán-Ferré, C.; Vasilopoulou, F.; Brocos-Mosquera, I.; Muruguza, C.; Pérez, B.; Molins, E.; Luque, F.J.; Pérez-Lozano, P.; de Jonghe, S.; Daelemans, D.; Naesens, L.; Brea, J.; Loza, M.I.; Hernández-Hernández, E.; García-Sevilla, J.A.; García-Fuster, M.J.; Radan, M.; Djikic, T.; Nikolic, K.; Pallàs, M.; Callado, L.F.; Escolano, C. *J. Med. Chem.* **2020**, *63,* 3610-3633.

7. **Phosphoenolpyruvate from Glycolysis and PEPCK Regulate Cancer Cell Fate by Altering Cytosolic Ca^{2+}.** Moreno-Felici, J.; Hyrossova, P.; Aragó, M.; Rodríguez-Arévalo, S.; García-Rovés, P.M.; Escolano, C.; Perales, J.C. *Cells* **2020**, *9*, 18.

8. **Pharmacology and preclinical validation of a novel anticancer compound targeting PEPCK-M.** Aragó, M.; Moreno-Felici, J.; Abás, S.; Rodríguez-Arévalo, S.; Hyrossova, P.; Figueras, A.; Viñals, F.; Pérez, B.; Loza, M.I.; Brea, J.; Latorre, P.; Carrodeguas, J.A.; García-Rovés, P.M.; Galdeano, C.; Ginex, T.; Luque, F.J.; Escolano, C.; Perales, J.C. *Biomed. Pharmacother.* **2020**, *121*, 109601.

9. **Study of the behavioral and cognitive improvement induced by novel imidazoline I_2 receptor ligands in SAMP8 mice model.** Griñán-Ferré, C.; Vasilopoulou, F.; Abás, S.; Rodríguez-Arévalo, S.; Bagán, A.; Sureda, F.X.; Pérez, B.; Callado, L.F.; García-Sevilla, J.A.; García-Fuster, J.; Escolano, C.; Pallàs, M. *Neurotherapeutics* **2019**, *16*, 416-431.

10. **Neuroprotective Effects of a Structurally New Family of High Affinity Imidazoline I_2 Receptor Ligand.** Abás, S.; Erdozain, A.M.; Keller, B.; Rodríguez-Arévalo, S.; Callado, L.F.; García-Sevilla, J.A.; Escolano, C. *ACS Chem. Neurosci*. **2017**, *8*, 737-742.

Otras publicaciones

E-book Pharmaceutical Industry: A World of Opportunities. Ed. E. García and C. Escolano, **2021**, University of Barcelona. Available at https://university.galenicum.com/Inicio.html

Publicaciones derivadas de congresos

1. Escolano, C.; Abás, S.; Rodríguez-Arévalo, S.; Bagán, A.; Griñán-Ferré, C.; Vasilopoulou, F.; Pallàs, M.; Pérez-Lozano, P.; Brocos-Mosquera, I.; Muguruza, C.; Callado, L.F.; Pérez, B.; M.; Brea, J.M.; Loza, M.I.; Hernández-Hernández, E.; García-Sevilla, J.A.; García-Fuster, M.J.; Radan, M.; Nikolic, K.; Djikic, T.; Díaz, C.; Pérez del Palacio, J.; Ramos, C.; Vicente, F.; Molins, E. A bicyclic α-iminophosphonate improves cognitive decline in 5xFAD murine model of neurodegeneration. *The FASEB journal*, 14 May **2021**, *35*, supplement 1.

2. Bagán, A.; Abás, S.; Rodríguez-Arévalo, S.; Rodríguez-Arévalo, G.; Vasilopoulou, F.; Griñán-Ferré, C.; Pallàs, M.; Pérez-Lozano, P.; Radan, M.; Djikic, T.; Nikolic, K.;

Escolano, C. (2-Imidazolin-4-yl)phosphonates: Green Chemistry and Biology Walk Together. *Proceedings*, **2019**, *22*, 97.

3. Rodríguez-Arévalo, S.; Abás, S.; Aragó, M.; Moreno-Felici, J.; Hyrossova, P.; Perales, J.C.; Galdeano, C.; Ginex, T.; Luque, F.J.; Escolano, C. Biological Evaluation of a Mitochondrial Phosphoenolpyruvate Carboxykinase Inhibitor. *Proceedings*, **2019**, *22*, 95.

4. Piticchio, S.G.; Martínez-Cartró, M.; Scaffidi, S.; Rodríguez-Arévalo, S.; Bagán, A.; Sánchez-Arfelis, A.; Escolano, C.; Galdeano, C.; Barril, X. Hydrophobic Waters in Bromodomains. *Proceedings*, **2019**, *22*, 80.

5. Aragó, M.; Rodríguez-Arévalo, S.; Hyrossova, P.; Moreno-Felici, J.; Abás, S.; Figueras, A.; Pérez, B.; Viñals, F.; Escolano, C.; Perales, J.C. Dibenzylxanthines as PEPCK-M Inhibitors for Cancer Therapy. *Proceedings*, **2019**, *22*, 79.

6. Escolano, C.; Griñán-Ferré, C.; Vasilopoulou, F.; Abás, S.; Rodríguez-Arévalo, S.; Bagán, A.; Pérez, B.; Callado, L.F.; García-Sevilla, J.A.; García-Fuster, J.; Pallàs, M.; Brea, J.M.; Loza, M.I. A New Family of Imidazoline I_2 Receptor Ligands Improves Behavior and Cognition in SAMP8 Mice. *The FASEB journal*, 1 April **2019**, *33*, supplement 1.

7. Escolano, C.; Abás, S.; Rodríguez-Arévalo, S.; Bagán, A.; Pallàs, M.; Griñán-Ferré, C.; Vasilopoulou, F.; Callado, L. F.; García-Sevilla, J.; García-Fuster, J.; Sureda, F.X.; Pérez, B. Novel Imidazoline I_2 Receptor Ligands for Alzheimer's Desease. *The FASEB journal*, 20 April **2018,** *32*, supplement 1.

Capítulo 1. Introducción

La presente Tesis Doctoral se enmarca en el campo de la Química Médica (o Química Farmacéutica). Esta área de investigación tiene como finalidad desarrollar nuevas estrategias terapéuticas mediante el diseño y la preparación de nuevos compuestos para su posterior evaluación farmacológica, con el objetivo final de establecer relaciones entre la estructura-actividad que contribuya al desarrollo de nuevos fármacos.

Los investigadores que trabajan en este campo establecen colaboraciones con profesionales de otras disciplinas, formando equipos multidisciplinares. Para los profesionales que trabajan en el campo de la Química Médica es esencial tener conocimientos de química orgánica, pero también de otras materias relacionadas como farmacología, bioquímica, biofarmacia, entre otras, para tener una mayor comprensión e interpretación de los resultados y de los complejos problemas que conlleva la interacción de los fármacos con el entorno biológico.

Por esta razón, a lo largo de esta Tesis Doctoral he trabajado en colaboración con grupos de investigación de diversos ámbitos, que han realizado la evaluación farmacológica, toxicológica, determinación del mecanismo de acción, etc. de los compuestos diseñados y sintetizados.

En los diferentes apartados en los que se divide esta introducción, se contextualiza el proyecto realizado incluyendo una explicación de la importancia del grupo funcional isocianuro en la química de síntesis y los precedentes en el grupo de investigación que han dado lugar a la propuesta de mi proyecto de Tesis. También se incluyen las explicaciones relativas a la diana terapéutica, los receptores imidazólicos I_2 (I_2-IR) que se fijaron como objetivo de los nuevos compuestos sintetizados y las estrategias y resultados tanto sintéticos como farmacológicos que han permitido llevar a término los proyectos planteados con éxito.

Seguidamente, se comenta el trabajo de síntesis de un inhibidor de la isoforma mitocondrial de la enzima fosfoenolpiruvato carboxiquinasa (PEPCK-M) y los resultados biológicos de su estudio *in vitro* y, después *in vivo* en un modelo murino de cáncer.

Finalmente, se presenta el trabajo de servicio dado a la empresa Avizorex Pharma S.L. preparando un diastereoisómero y el enantiómero del agonista del *Transient receptor potential melastatin member 8* (TRPM8), **AR-15512** que se encuentra en fases clínicas.

1.1. Química de los isocianuros

Dada la gran demanda de productos con finalidades biomédicas, la síntesis de compuestos con potenciales actividades biológicas supone un reto para la investigación en Química Médica. Dentro de los grupos funcionales con relevancia en el desarrollo de nuevos compuestos bioactivos destacan los isocianuros, también conocidos como isonitrilos.[1] Este grupo funcional con estructura carbenoide puede interaccionar tanto con nucleófilos como con electrófilos, gracias a la ambivalencia del átomo de carbono, lo que permite que reaccionen con una amplia gama de reactivos permitiendo el acceso a productos heterocíclicos nitrogenados como pirroles, índoles y quinolinas,[2] convirtiéndolo en un grupo funcional privilegiado en síntesis orgánica.

Entre los derivados de isocianuros, destacan los isocianoacetatos, ampliamente utilizados en Química Orgánica, Inorgánica y de Coordinación, Polimérica y Médica. Además, se usan como reactivos en la síntesis de moléculas bioactivas y de productos naturales.[3] Los isocianoacetatos pueden estar implicados en una gran variedad de transformaciones que incluyen: adiciones asimétricas a aldehídos, nitroalquenos, iminas y azodicarboxilatos, además de la adición enantioselectiva a nitroolefinas.[4]

El grupo funcional isocianoacetato dispone de un elevado potencial sintético, ya que posee una posición reactiva adicional respecto al grupo isocianuro gracias a la presencia del grupo éster, que convierte en ácido el protón situado en la posición alfa del isocianuro, siendo ésta susceptible de reaccionar con electrófilos (Figura 1.1).[5]

---

[1] (a) Dömling, A.; Ugi, I. *Angew. Chem. Int. Ed*. **2000**, *29*, 3168-3210; (b) Sadjadi, S.; Heravi, M.M. *Tetrahedron* **2011**, *67*, 2702-2752; (c) Bhat, S.I. *ChemistrySelect* **2020**, *5*, 8040-8080.

[2] (a) Mironov, M.A*. In Isocyanide Chemistry: Applications in Synthesis and Material Science*; Nenajdenko, V., Ed.; Wiley-VCH Verlag GmbH: Weinheim, **2012**, 35-73; (b) Bon, R.S.; van Vliet, B.; Sprenkels, N.E.; Schmitz, R.F.; de Kanter, F.J.J.; Stevens, C.V.; Swart, M.; Bickelhaupt, M.; Groen, M.B.; Orru, R.V.A. *J. Org. Chem*. **2005**, *70*, 3542-3552; (c) Dömling, A. *Chem. Rev.* **2006**, *106*, 17-89.

[3] (a) Hoppe, I.; Schöllkopf, U. *Liebigs Ann. Chem.* **1984**, *1984*, 600-607; (b) Zhang, X.; Evanno, L.; Poupon, E. *Eur. J. Org. Chem.* **2020**, *2020*, 1919-1929; (b) Massarotti, A.; Brunelli, F.; Aprile, S.; Giustiniano, M.; Tron, G.C. *Chem. Rev*. **2021**, *121*, 10742-10788.

[4] (a) Guo, C.; Xue, M.-X.; Zhu, M.-K.; Gong, L.-Z. *Angew. Chem. Int. Ed*. **2008**, *47*, 3414-3417; (b) Sladojevich, F.; Trabocchi, A.; Guarna, A.; Dixon, D. J. *J. Am. Chem. Soc.* **2011**, *133*, 1710-1713; (c) Zhang, Z.-W.; Lu, G.; Chen, M.-M.; Lin, N.; Li, Y.-B.; Hayashi, T.; Chan, A.S.C. *Tetrahedron: Asymmetry* **2010**, *21*, 1715-1721; (d) Monge, D.; Jensen, K.L.; Marín, I.; Jørgensen, K.A. *Org. Lett.* **2011**, *13*, 328-331.

[5] (a) Ugi, I.; Betz, W.; Fetzer, U.; Offermann, K. *Chem. Ber.* **1961**, *94*, 2814-2816; (b) Zhu, J. *Eur. J. Org. Chem.* **2003**, *7*, 1133-1144; (c) Gulevich, A.V.; Zhdanko, A.G.; Orru, R.V.A.; Nenajdenko, V.G. *Chem. Rev.* **2010**, *110*, 5235-5331; (d) Bode, M.L.; Gravestock, D.; Rousseau, A.L. *Org. Prep. Proced. Int.* **2016**, *48*, 89-221; (e) Massarotti, A.; Novellino, E.; Tron, G.T.; Zhu, J. *Chem. Soc. Rev.* **2017**, *46*, 1295-1357.

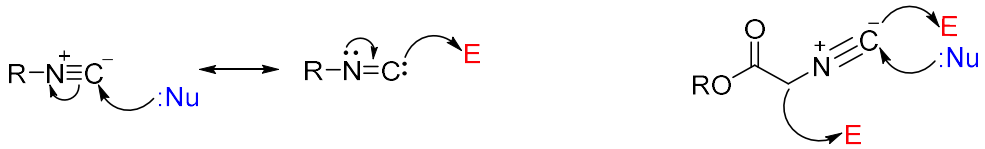

Figura 1.1. Perfil de reactividad de isocianuros e isocianoacetatos.

En los últimos años, el grupo de investigación de la Prof. Carmen Escolano ha trabajado en la obtención de heterociclos, con especial interés en la síntesis de anillos nitrogenados de cinco átomos, mediante reacciones que implican el uso de isocianoacetatos. Los heterociclos de cinco miembros, como pirrolinas, imidazolinas e imidazoles están presentes en productos naturales y otros compuestos de interés biológico.[6]

En este contexto, aunque se han desarrollado numerosos métodos para la preparación de pirrolinas (dihidropirroles), la mayor parte de estos se centran en la obtención de 3-pirrolinas.[7] Por lo tanto, el estudio de nuevos procedimientos para acceder a 1 y 2-pirrolinas es de interés.[8]

El Prof. Grigg y colaboradores publicaron en la revista *Tetrahedron* en 1999 la reacción de isocianoacetato de metilo y aceptores de Michael para dar lugar a 1- y 2-pirrolinas.[9] Inspirados por este artículo, en nuestro grupo de investigación se realizaron estudios para acceder a 2-pirrolinas enantiopuras y nuevas estructuras que contuviesen 1-pirrolinas.

Así, en el contexto de la Tesis Doctoral del Dr. Carlos Arróniz se desarrolló la primera reacción de cicloadición formal [3+2] asimétrica de isocianoacetatos diversamente sustituidos y cetonas α,β-insaturadas mediante una cascada multicatalítica cooperativa promovida por el alcaloide de tipo chincona cupreína (base de Brønsted) y nitrato de plata (ácido de Lewis) para acceder a 2,3-dihidropirrolinas sustituidas enantioenriquecidas (e.e. 16-90%).[10] Una de las 2,3-dihidropirrolinas preparadas

[6] (a) Herzon, S.B.; Myers, A.G. *J. Am. Chem. Soc.* **2005**, *127*, 5342-5344; (b) Arai, S.; Nakajima, M.; Nishida, A. *Angew. Chem. Int. Ed.* **2014**, *53*, 5569-5572; (c) Domagala, A.; Jarosz, T.; Lapkowski, M. *Eur. J. Med. Chem.* **2015**, *100*, 176-187.

[7] (a) Green, M.P.; Prodger, J.C.; Sherlock, A.E.; Hayes, C.J. *Org. Lett.* **2001**, *3*, 3377-3379; (b) Tran, G.; Meier, R.; Harris, L.; Browne, D.L.; Ley, S.V. *J. Org. Chem.* **2012**, *77*, 11071-11078; (c) Flores-Constante, G.; Sánchez-Chávez, A.I.; Polindara-García, L.A. *Eur. J. Org. Chem*. **2018**, *33*, 4586-4591.

[8] (a) Wender, P.A.; Strand, D. *J. Am. Chem. Soc.* **2009**, *131*, 7528-7529; (b) Schlegel, M.; Schneider, C. *Org. Lett*. **2018**, *20*, 3119-3123; (c) El-Sepelgy, O.; Brzozowska, A.; Sklyaruk, J.; Jang, Y. K.; Zubar, V.; Rueping, M. *Org. Lett.* **2018**, *20*, 696-699.

[9] Grigg, R.; Lansdell, M.I.; Thornton-Pett, M. *Tetrahedron* **1999**, *55*, 2025-2044.

[10] Arróniz, C.; Gil-González, A.; Semak, V.; Escolano, C.; Bosch, J.; Amat, M. *Eur. J. Org. Chem.* **2011**, 3755-3760.

permitió acceder a un intermedio tricíclico dilactámico clave en la preparación de compuestos con actividad antitumoral con estructura de pirrolobenzodiazepina (PBD) (Esquema 1.1).[11]

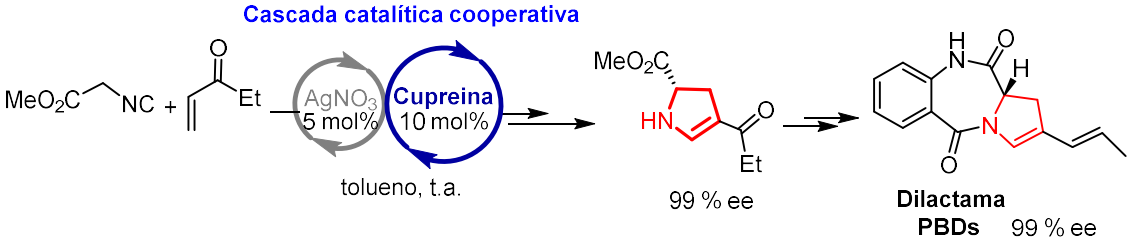

Esquema 1.1. Síntesis de un intermedio 2-pirrolina clave y acceso al núcleo de PBDs.

En el mismo artículo de 1999,[9] el Prof. Grigg describió la reacción del isocianoacetato de metilo con *N*-fenilmaleimida catalizada por acetato de plata en acetonitrilo dando como resultado una mezcla 2:1 de los diastereómeros de las 1-pirrolinas bicíclicas **A** (H1-H3a *trans*) y **B** (H1-H3a *cis*) correspondientes.[12]

También, en la Tesis del Dr. Carlos Arróniz se describió la reacción de cicloadición [3+2] análoga sustituyendo el isocianoacetato de metilo por su homólogo fosforado, el isocianometilfosfonato de dietilo (PhosMic) y maleimidas diversamente sustituidas en el átomo de nitrógeno (Esquema 1.2). Esta reacción transcurrió con buenos rendimientos y excelente diastereoselectividad, generándose únicamente uno de los dos posibles diastereómeros. En concreto, se formaron las 1-pirrolinas bicíclicas con un grupo fosfonato en la posición α de la imina que poseían una relación *trans* entre los hidrógenos de las posiciones cabeza de puente (H3a y H6a) y el hidrógeno que se encuentra en el carbono que soporta el éster fosfónico (H1). La configuración relativa de los tres nuevos estereocentros generados se asignó inequívocamente por análisis de cristalografía de rayos X tras obtener un monocristal de uno de los derivados (R=Ph) (Esquema 1.2.).[13]

[11] Abás, S.; Arróniz, C.; Molins, E.; Escolano, C. *Tetrahedron* **2018**, *74*, 867-871.
[12] Carretero y colaboradores reportaron una versión enantioselectiva de esta reacción utilizando reactivos relacionados mediante la catálisis con complejos de oro. Padilla, S.; Adrio, J.; Carretero, J.C. *J. Org. Chem.* **2012**, *77* (8), 4161-4166.
[13] Arróniz, C.; Molina, J.; Abás, S.; Molins, E.; Campanera, J.M.; Luque, F.J.; Escolano, C. *Org. Biomol. Chem*. **2013**, *11*, 1640-1649.

Trabajo del profesor Grigg

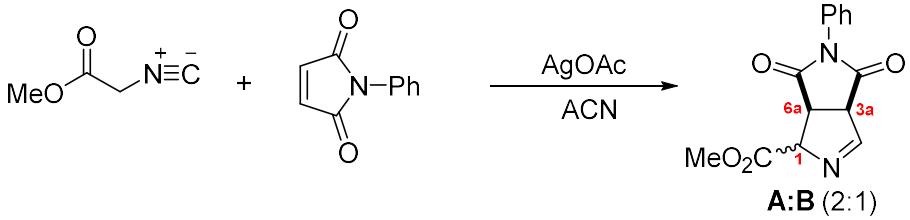

Antecedentes del grupo

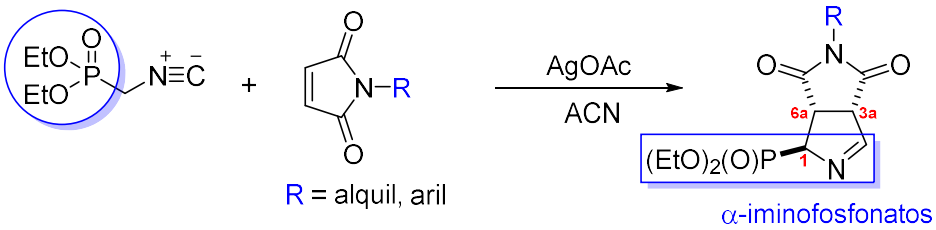

Esquema 1.2. Reacción de cicloadición [3+2] entre isocianoacetatos e isocianofosfonatos y maleimidas.

Los α-iminofosfonatos bicíclicos preparados ofrecen un elevado número de posibilidades sintéticas debido a que poseen en su estructura numerosos grupos funcionales. Por ejemplo, la reducción mediante hidrogenación catalítica del grupo funcional α-iminofosfonato condujo a α-aminofosfonatos bicíclicos.[13] En la literatura se encuentran descritos compuestos que poseen en su estructura un grupo α-aminofosfonato, que han mostrado actividad antitumoral, antibiótica, etc.[14] Este grupo funcional se considera bioisóstero de un α-aminoéster y de interés en la química de peptidomiméticos. Las propiedades biológicas de los compuestos que poseen ésteres fosfónicos se asocia a la estructura tetraédrica de dicho grupo funcional. Esta geometría es la responsable de su actividad como análogos del estado de transición como, por ejemplo, ocurre en la hidrólisis enzimática peptídica. De hecho, está descrito en diversos estudios, que derivados de ácido α-aminofosfónico actúan como inhibidores de numerosas enzimas implicadas en el metabolismo endógeno peptídico.[15]

[14] (a) Kafarski, P.; Lejczak, B. *Curr. Med. Chem.*: *Anti-Cancer Agents,* **2001**, *1*, 301-312; (b) Wuggening, F.; Schweifer, A.; Mereiter, K.; Hammerschmidt, F. *Eur. J. Org. Chem*. **2011**, *10*, 1870-1879; (c) Shen, G.H.; Hong, J.H. *Carbohydr. Res.* **2018**, *463*, 47-106; (d) Skoreński, M.; Milewska, A.; Pyrć, K.; Sieńczyk, M.; Oleksyszyn, J. *J Enzyme Inhib. Med. Chem.* **2019**, *34* (1), 8-14; (e) López-Francés, A.; Del Corte, X.; Martínez de Marigorta, E.; Palacios, F.; Vicario, J. *Molecules* **2021**, *26*, 1654.

[15] (a) Aminophosponic and Aminophosphinic Acids*: Chemistry and Biological Activity*; Kukhar, V.P., Hudson, H.R., Eds; John Wiley & Sons; Chichester, UK, **2000**; (b) Orsini, F.; Sello, G.; Sisti, M. *Curr. Med. Chem.* **2010**, *17*, 264-289; (c) Viveros-Ceballos, J.L.; Ordóñez, M.; Sayago, F.J.; Cativiela, C. *Molecules* **2016**, *21*, 1141; (d) Viveros-Ceballos, J.L.; Matías-Valdez, L.A.; Sayago, F.J.; Cativiela, C.; Ordóñez, M. *Amino Acids* **2021**, *53*, 451-459.

La transformación de los α-aminofosfonatos bicíclicos obtenidos en sistemas monocíclicos conduciría a compuestos con estructura de fosfoprolina, análogos de la prolina. Este estudio se está llevando a cabo en la actualidad en el contexto de la Tesis Doctoral de la Sra. Andrea Bagán (Esquema 1.3).[16]

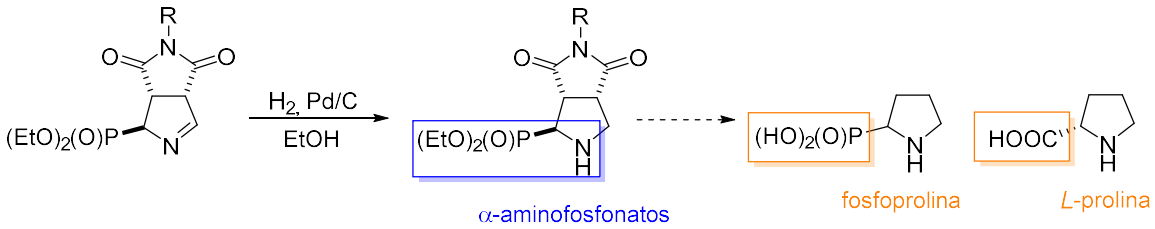

Esquema 1.3. Reacción de reducción de α-iminofosfonatos a α-aminofosfonatos. Transformación en fosfoprolina.

Posteriormente, en la Tesis Doctoral de la Dra. Sònia Abás, con el objetivo de buscar nuevas aplicaciones sintéticas para el reactivo PhosMic se estudió su papel en la síntesis de heterociclos nitrogenados mediante reacciones multicomponente (MCR).[17]

Las MCR se caracterizan por ser procesos *one-pot* eficientes que, a partir de al menos tres reactivos de partida, originan un único producto final con una elevada economía de átomo, ya que incorpora todos los átomos de los precursores. Estos procesos se caracterizan por exhibir un índice de formación de enlaces muy alto. Las MCR son ampliamente utilizadas en Química Médica para la obtención de moléculas bioactivas[18] dado que su alto índice de formación de enlaces permite acceder a una gran diversidad de compuestos altamente funcionalizados en un solo paso, mediante procesos que cumplen los criterios de una síntesis "ideal".[19] Las MCR que implican isocianuros se conocen como IMCRs (*isocyanide-base multicomponent reactions*) e incluyen

[16] (a) Baylis, E.K.; Campbell, C.D.; Dingwall, J.G. *J. Chem. Soc. Perkin Trans.* **1984**, *1*, 2845-2853; (b) Moone, K.; Laureyn, I.; Stevens, C.V. *Chem. Rev*. **2004**, *104*, 6177-6215; (c) Qian, R.; Kuliszewska, E.; Macoratti, E.; Hammerschimidt, F. *Eur. J. Org. Chem*. **2017**, *32*, 4836-4845.

[17] (a) Wu, J.; Cao, S. *Curr. Org. Chem.* **2009**, *13*, 1791-1804; (b) Tobisu, M.; Chatani, N. *Chem. Lett*. **2011**, *40*, 330-340; (c) Ibarra, I.A.; Islas-Jácome, A.; González-Zamora, E. *Org. Biomol. Chem*. **2018**, *16*, 1402-1418.

[18] (a) Dömling, A.; Wang, W.; Wang, K. *Chem. Rev.* **2012**, *112*, 3083-3135; (b) Pedrola, M.; Jorba, M.; Jardas, E.; Jardi, F.; Ghashghaei, O.; Viñas, M.; Lavilla, R. *Front. Chem*. **2019**, *7*, 475; (c) Graebin, C.S.; Ribeiro, F.V.; Rogério, K.R.; Kümmerle, A.E. *Curr. Org. Synth.* **2019**, *16*, 855-899; (d) Insuasty, D.; Castillo, J.; Becerra, D.; Rojas, H.; Abonia, R. *Molecules*, **2020**, *25*, 505.

[19] (a) Bienaymé, H.; Hulme, C.; Oddon, G.; Schmitt, P. *Chem.-Eur. J.* **2000**, *6*, 3321-3329; (b) Wender, P.A.; Miller, B.L. *Nature* **2009**, *460*, 197-201; (c) Gaich, T.; Baran, P.S. *J. Org. Chem.* **2010**, *75*, 4657-4673; (d) Ruijter, E.; Scheffelaar, R.; Orru, R.V.A. *Angew. Chem. Int. Ed.* **2011**, *50*, 6234-6246; (e) Cioc, R.C.; Ruijter, E.; Orru, R.V.A. *Green Chem.* **2014**, *16*, 2958-2975.

reacciones conocidas como las de Passerini y Ugi, que dan lugar a moléculas lineales, heterocíclicas y macrocíclicas de interés.[20]

Inspirados en el trabajo desarrollado por el Prof. Orru para la síntesis de 2-imidazolinas diversamente sustituidas mediante una MCR eficiente, empleando isocianoacetatos, un compuesto carbonílico y una amina,[21,2b] nuestro grupo describió la primera IMCR asistida por microondas que implicaba el reactivo PhosMic. Utilizando diversas aminas primarias y compuestos carbonílicos se pudieron describir numerosos compuestos con estructura general de (2-imidazolin-4-il)fosfonato.[22] (Esquema 1.4).

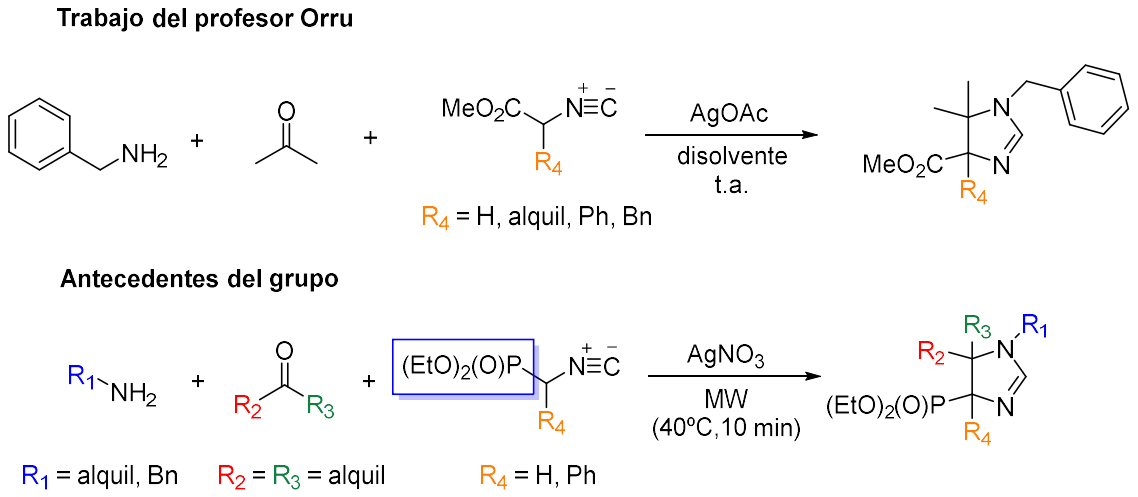

Esquema 1.4. MCR descritas por el Prof. Orru y por nuestro grupo.

Las 2-imidazolinas constituyen una estructura heterocíclica importante que puede reconocerse en productos naturales, compuestos de coordinación de interés y compuestos orgánicos bioactivos.[23] En particular, algunos compuestos que contienen en su estructura una 2-imidazolina pueden modular los receptores α_2-adrenérgicos (α_2-AR), y a menudo muestran una alta afinidad por los receptores imidazolínicos (IR).[24]

[20] (a) Janvier, P.; Bois-Choussy, M.; Bienaymé, H.; Zhu, J. *Angew. Chem. Int. Ed*. **2003**, *42*, 811-814; (b) Sadjadi, S.; Heravi, M.M.; Nazari, N. *RSC Adv*. **2016**, *6*, 53203-53272; (c) Biesen, L.; Müller, T.J.J. *Adv. Synth. Catal*. **2021**, *363*, 980-1006.

[21] (a) Bon, R.S.; Hong, C.; Bouma, M.J.; Schmitz, R.F.; De Kanter, F.J.J.; Lutz, M.; Spek, A.L.; Orru, R.V.A. *Org. Lett.* **2003**, *5*, 3759-3762; (b) Orru, R.V.A.; De Greef, M. *Synthesis* **2003**, *10*, 1471-1499; (c) Elders, N.; Schmitz, R.F.; De Kanter, F.J.J.; Ruijter, E.; Groen, M.B.; Orru, R.V.A. *J. Org. Chem.* **2007**, *72*, 6135-6142; (d) Elders, N.; Ruijter, E.; de Kanter, F.J.J.; Groen, M.B.; Orru, R.V.A. *Chem.-Eur. J.* **2008**, *14*, 4961-4973.

[22] Abás, S.; Estarellas, C.; Luque, F.J.; Escolano, C. *Tetrahedron* **2015**, *71*, 2872-2881.

[23] (a) Weiss, M.E.; Fisher, D.F.; Xin, Z.Q.; Jautza, S.; Schweizer, W.B.; Peters, R. *Angew. Chem. Int. Ed.* **2006**, *45*, 5694-5699; (b) Bon, R.S.; de Kanter, F.J.J.; Lutz, M.; Spek, A.L.; Jahnke, J.C.; Hahn, F.E.; Orru, R.V.A. *Organometallics* **2007**, *26*, 3639-3650; (c) Murai, K.; Fukushima, S.; Nakamura, A.; Shimura, M.; Fujioka, H. *Tetrahedron* **2011**, *67*, 4862-4868.

[24] (a) Bousquet, P.; Feldman, J.; Schwartz, J.J. *Pharmacol. Exp. Ther.* **1984**, *230*, 232-236; (b) Heemskerk, F.M.; Dontenwill, M.; Greney, H.; Vonthron, C.; Bousquet, P. *J. Neurochem.* **1998**, *71*, 2193-2202; (c) Gentili, F.; Bousquet, P.; Brasili, L.; Dontenwill, M.; Feldman, J.; Ghelfi, F.; Giannella, M.; Piergentili, A.; Quaglia, W.; Pigini, M. *J. Med. Chem.* **2003**, *46*, 2169-2176.

Estos últimos receptores se describen en el siguiente apartado de manera más detallada y constituyen una diana terapéutica de interés en el grupo de investigación y en esta Tesis.

Considerando el interés del grupo en el desarrollo de reacciones que involucren isocianometilfosfonatos respectando las recomendaciones de la química sostenible, se propuso explorar el uso de MCR consecutivas (cMCR) para la formación en nuevos sistemas imidazolínicos más complejos que los descritos previamente por nosotros. Las cMCR son reacciones que emplean una combinación de dos o más MCR generando, como mínimo, seis enlaces covalentes mediante la presencia de reactivos de partida bifuncionales o multifuncionales, utilizados después de una primera MCR para una segunda MCR.[25]

La cMCR que nos propusimos implicaba la reacción *one-pot* de tres componentes: isocianuros α-sustituidos, en especial isocianometilfosfonatos, cetonas y diaminas diversamente sustituidas para la formación de bis(2-imidazolin-4-il)fosfonatos (Esquema 1.5).

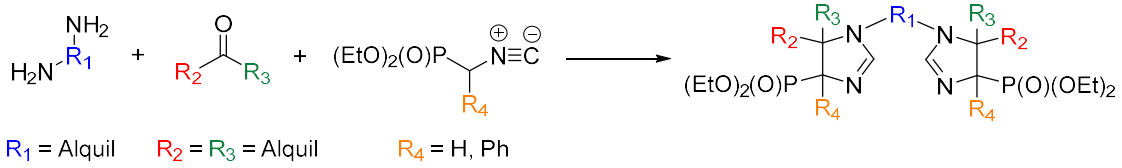

Esquema 1.5. cMCR propuesta para la obtención de bis(2-imidazolin-4-il)fosfonatos.

Este estudio se presenta en el *Capítulo 4* de la presente Tesis Doctoral, dando lugar a la primera cMCR que emplea isocianuros fosforados y la consecuente obtención de compuestos con núcleo de bismidazolina.

[25] Ghashghaei, O.; Seghetti, F.; Lavilla, R. Beilstein *J. Org. Chem*. **2019**, *15*, 521–534.

1.2. Receptores imidazolínicos

Los receptores imidazolínicos (IR) se definen como lugares de unión no adrenérgicos y se dividen en tres subtipos, denominados I_1-IR, I_2-IR e I_3-IR, en función de la afinidad que presentan por radioligandos específicos como la [^{3}H]-clonidina o [^{3}H]-idazoxan. Los IR se encuentran distribuidos en diferentes órganos y se relacionan con una amplia variedad de funciones fisiológicas (Figura 1.2).[26]

Figura 1.2. Diferentes tipos de IR, localización y e implicación en procesos fisiológicos.

Hasta la fecha, los I_1-IR son los más conocidos y han dado lugar a fármacos antihipertensivos aprobados en clínica como la moxomidina o la rilmenidina.[27] Por otro lado, los I_3-IR son los más desconocidos y se relacionan con la regulación de secreción de insulina por parte de las células β-pancreáticas.[28] Los I_2-IR no se han descrito desde el punto de vista estructural, pero se conoce su implicación en determinados procesos fisiológicos gracias a su interacción con ligandos I_2-IR bien caracterizados. En los humanos, los I_2-IR se localizan de manera considerable en el sistema nervioso central (SNC, especialmente en la glía), plaquetas, hígado, adipocitos y, en menor cantidad, en el riñón.[29] A través de estudios de distribución celular, se ha descubierto que los I_2-IR se encuentran principalmente en la membrana externa de las mitocondrias de astrocitos presentes en tejidos periféricos y centrales. La desregulación de los niveles de I_2-IR implica trastornos del SNC como depresión, tumores gliales, dolor y enfermedades como el Parkinson o Huntington.[30] Asimismo, está publicado que estos receptores se

[26] (a) Li, J.X.; Zhang, Y. *Eur. J. Pharmacol.* **2011**, *658*, 49-56; (b) Lowry, J.A.; Brown, J.T. *Clin. Toxicol*. **2014**, *52*, 454-469; (c) Li, J.X. *Pharmacol. Ther.* **2017**, *178*, 48-56; (d) Bousquet, P.; Hudson, A.; García-Sevilla, J.A.; Li, J.-X. *Pharmacol. Rev.* **2020**, *72*, 50-79.

[27] (a) Ernsberger, P.; Graves, M.E.; Graff, L.M.; Zakieh, N.; Nguyen, P.; Collins, L.A.; Westbrooks, K.L.; Johnson, G.G. *Ann. N. Y. Acad. Sci.* **1995**, *763*, 22-42; (b) Reid, J.L. *Am. J. Hypertens*. **2000**, *13*, 106-111.

[28] Chan, S.L.; Brown, C.A.; Scarpello, K.E.; Morgan, N.G. *Br. J. Pharmacol.* **1994**, *112*, 1065-1070.

[29] (a) Tesson, F.; Limon, I.; Parini. A. *Eur. J. Pharmacol.* **1992**, *219*, 335-338; (b)Tesson, F.; Limon-Boulez, I.; Urban, P.; Puype, M.; Vandekerckhove, J.; Coupry, I.; Parini, A. *J. Biol. Chem.* **1995**, *270*, 9856-9861; (c) Callado, L.F.; Martín-Gómez, J.I.; Ruiz, J.; Garibi, J.M.; Meana, J.J. *J. Neurol. Neurosurg. Psychiatry* **2004**, *75*, 785-787.

[30] (a) Meana, J.J.; Barturen, F.; Martín, I.; García-Sevilla, J. A. *Biol. Psychiatry* **1993**, *34*, 498−501; (b) Martín-Gómez, J.I.; Ruíz, J.; Callado, L.F.; Garibi, J.M.; Aguinaco, L.; Barturen, F.; Meana, J.J. *NeuroReport* **1996**, *7*,

encuentran incrementados en el cerebro de pacientes que han sufrido la enfermedad de Alzheimer (AD).[31]

La implicación de los I_2-IR en múltiples patologías y procesos fisiológicos de elevada prevalencia, como las enfermedades neurodegenerativas y dolor, apoya la necesidad de realizar estudios en profundidad sobre ellos y descubrir nuevos ligandos que presenten elevada afinidad. Es importante resaltar que la mayoría de los compuestos descritos como ligandos de I_2-IR presentan el problema de ser también afines por α_2-AR. Por esta razón, el hallazgo de nuevos compuestos con una elevada afinidad y selectividad por I_2-IR es crucial para caracterizar los I_2-IR farmacológicamente.[32]

La importancia de estos receptores en clínica queda avalada por **CR4056**, que se encuentra en Fase Clínica II y está descrito como el *first-in-class I_2-IR ligand* con actividad analgésica para osteoartritis y dolor odontológico y por el radioligando **[^{11}C]-BU99008**, que está en Fase Clínica I para el diagnóstico de PET en pacientes que sufren AD.[33]

Los ligandos descubiertos hasta la fecha se clasificaron en un artículo de revisión de la Prof. Isabel Rozas y colaboradores en cuatro familias químicas: imidazolinas, 2-aminoimidazolinas, guanidinas y carbolinas.[34] Destacan las imidazolinas como las más selectivas y, aunque hay alguna excepción como **LSL60101** y **CR4056** que se presentan como imidazoles, gran parte de los ligandos I_2-IR conocidos (**idazoxan**, **tracizolina**, **2-BFI, BU224, BU99008**) son estructuras con un núcleo de imidazolina con sustituyentes en la posición 2, generalmente heterocíclicos (Figura 1.3).

1393-1396; (c) Reynolds, G.P.; Boulton, R.M.; Pearson, S.J.; Hudson, A.L.; Nutt, D.J. *Eur. J. Pharmacol.* **1996**, *301*, 19-21; (d) García- Sevilla, J.; Escribá, P.V.; Sastre, M.; Walzer, C.; Busquets, X.; Jaquet, G.; Reis, D.J.; Guimón, J. *Arch. Gen. Psychiatry.* **1996**, *53*, 803-810; (e) Gargalidis-Moudanos, C.; Pizzinat, N.; Javoy-Agid, F.; Remaury, A.; Parini, A. *Neurochem. Int*. **1997**, *30*, 31−36.

[31] (a) Ruíz, J.; Martín, I.; Callado, L.F.; Meana, J.J.; Barturen, F.; García-Sevilla, J.A. *Neurosci. Lett.* **1993**, *160*, 109-112; (b) García-Sevilla, J.A.; Escribá, P.V.; Walzer, C.; Bouras, C.; Guimón, J. *Neurosci. Lett*. **1998**, *247*, 95-98.

[32] (a) Regunathan, S.; Feinstein, D.L.; Reis, D.J. *Ann. N.Y. Acad. Sci*. **1999**, *881*, 410-419; (b) Smith, K.L.; Jessop, D.S.; Finn, D.P. *Stress* **2009**, *12*, 97-114.

[33] (a) Comi, E.; Lanza, M.; Ferrari, F.; Mauri, V.; Caselli, G.; Rovati, L.C. *J. Pain Res*. **2017**, *10*, 1033-1043; (b) Tyacke, R.J.; Myers, J.F.M.; Venkataraman, A.V.; Mick, I.; Turton, S.; Passchier, J.; Husbands, S.M.; Rabiner, E.A.; Gunn, R.N.; Murphy, P.S.; Parker, C.A.; Nutt, D.J.J. *Nucl. Med.* **2018**, *59*, 1597-1602; (c) Wilson, H.; Dervenoulas, G.; Pagano, G.; Tyacke, R.J.; Polychronis, S.; Myers, J.; Gunn, R.N.; Rabiner, E.A.; Nutt, D.J.J.; Politis, M. *Brain* **2019**, *142*, 3116-3124; (d) Rovati, L.C.; Brambilla, N.; Blicharski, T.; Connell, J.; Vitalini, C.; Bonazzi, A.; Giacovelli, G.; Girolami, F.; D'Amato, M. *Osteoarthritis and Cartilage* **2020**, *28*, 22-28.

[34] (a) Dardonville, C.; Rozas, I.; Callado, L.F.; Meana, J. J. *Bioorg. Med. Chem*. **2002**, *10*, 1525-1533; (b) Dardonville, C.; Rozas, I. *Med. Res. Rev.* **2004**, *24*, 639-661.

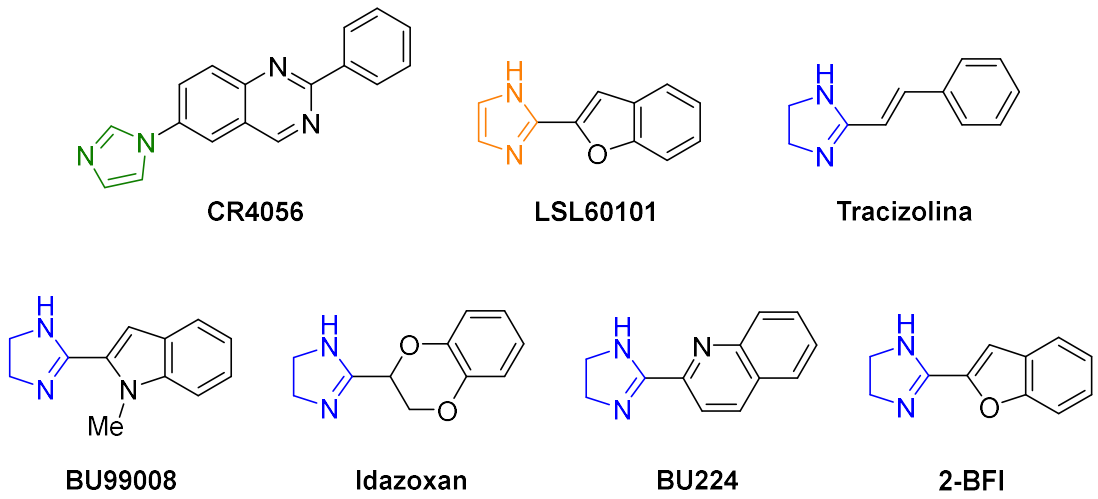

Figura 1.3. Estructura de los ligandos I_2-IR más representativos.

Hasta 2016, todos los ligandos I_2-IR sintetizados que contenían un núcleo de 2-imidazolina presentaban sustituyentes únicamente en la posición 2. Con el fin de explorar ligandos I_2-IR con nuevas estructuras imidazolínicas, el grupo de investigación de la Prof. Carmen Escolano describió una familia de compuestos con núcleo de (2-imidazolin-4-il)fosfonato diversamente sustituidos utilizando las IMCR descritas anteriormente en el grupo.[18] Esta nueva familia, a diferencia de los ligandos I_2-IR conocidos, presenta distintos sustituyentes en las posiciones 1, 4 y 5, mientras que la posición 2 no está sustituida (Figura 1.4A), es decir, un patrón de sustitución completamente diferente al de los ligandos I_2-IR conocidos. La actividad como ligandos I_2-IR de esta nueva familia fue evaluada por el Prof. Luis F. Callado de la Universidad del País Vasco (UPV), mediante estudios competitivos de unión con el radioligando selectivo de I_2-IR, [^{3}H]-2-(benzofuran-2-il)-2-imidazolina ([^{3}H]-2-BFI) y el radioligando selectivo de α_2-AR, 2-metoxiidazoxan ([^{3}H]-RX821002). Los estudios se realizaron en membranas de la corteza frontal humana *post-mortem*, un área del cerebro que muestra una densidad importante de I_2-IR y α_2-AR. Los compuestos sintetizados resultaron ser altamente afines y selectivos para I_2-IR frente a los α_2-AR. Dos compuestos representativos, **MCR5** y **MCR9** (Figura 1.4B), presentaban excelentes valores de afinidad, expresados en pK_i, por los I_2-IR, 9.42 y 8.85, y una selectividad I_2/α_2 de 457 y 1862, respectivamente, mejorando los valores del estándar **idazoxan** (pK_i 7.41 y sin selectividad I_2/α_2). Dichos compuestos, que difieren entre sí únicamente en la presencia de un éster fosfónico (**MCR5**) o un éster metílico (**MCR9**), se evaluaron *in vivo* para determinar algunas de sus propiedades farmacológicas resultando inducir hipotermia y neuroprotección en los animales tratados. Los resultados se recogieron en la Tesis de la Dra. Sònia Abás y en una publicación en la revista *ACS Chemical Neuroscience* de la que soy coautor por mi aportación realizada diseñando, sintetizando y caracterizando

varios de los compuestos ensayados en el periodo en el que realicé la asignatura del grado de farmacia trabajo dirigido y prácticas de verano.[35]

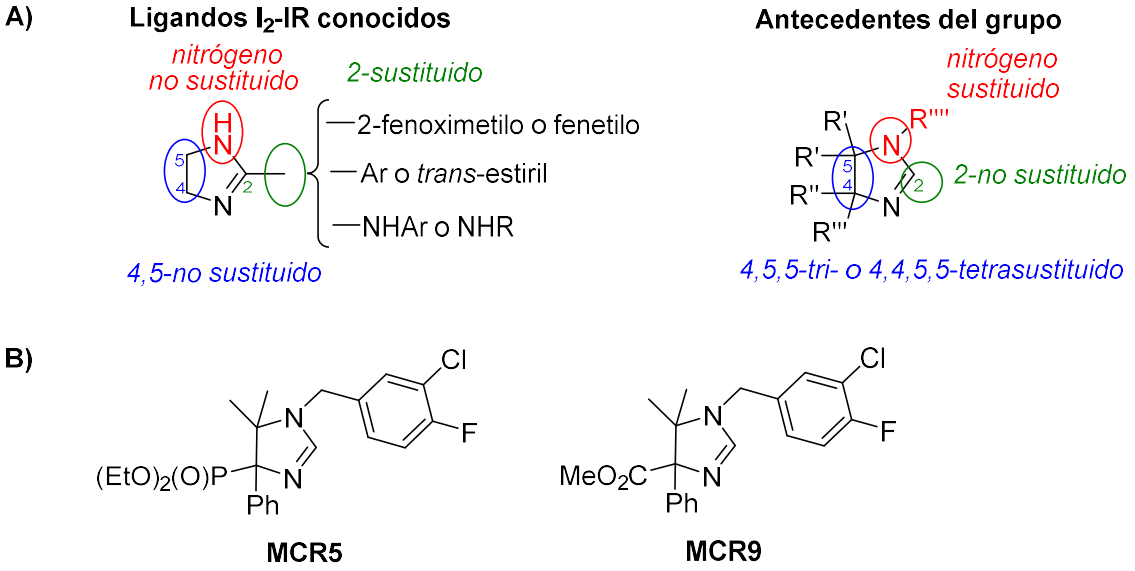

Figura 1.4. **A)** Estructura de los ligandos I_2-IR conocidos y (2-imidazolin-4-il)fosfonatos descritos como ligandos I_2-IR. **B)** Estructura de los ligandos I_2-IR **MCR5** y **MCR9**.[35]

Dados los buenos resultados preliminares encontrados con **MCR5** o **MCR9** el grupo de la Prof. Mercè Pallàs de nuestro departamento, diseñó y llevó a cabo un completo estudio farmacológico en el modelo murino de neurodegeneración *Senescence-Accelerated Mouse-Prone 8* (SAMP8). El resultado obtenido fue una mejora en el deterioro cognitivo y de los biomarcadores relacionados con neurodegeneración de los animales tratados vía oral con **MCR5** o **MCR9**.

Este fue el primer ejemplo publicado de un estudio *in vivo* que proponía los I_2-IR como una diana terapéutica prometedora para el tratamiento del deterioro cognitivo asociado a enfermedades neurodegenerativas.[36]

Siguiendo con el mismo modelo animal, SAMP8, la Prof. Pallàs llevó a cabo un estudio para evaluar la implicación del ligando de I_2-IR **MCR5** en la mejora de los síntomas fisiológicos y de comportamiento asociados a la demencia, como conductas depresivas o ansiedad, junto al deterioro de la memoria. La administración oral de **MCR5** redujo el comportamiento depresivo y la ansiedad, produciendo una mejora cognitiva en los

[35] Abás, S.; Erdozain, A.M.; Keller, B.; Rodríguez-Arévalo, S.; Callado, L.F.; García-Sevilla, J.A.; Escolano, C. *ACS Chem. Neurosci*. **2017**, *8*, 737-742.
[36] Griñán-Ferré, C.; Vasilopoulou, F.; Abás, S.; Rodríguez-Arévalo, S.; Bagán, A.; Sureda, F.X.; Pérez, B.; Callado, L.F.; García-Sevilla, J.A.; García-Fuster, M.J.; Escolano, C.; Pallàs, M. *Neurotherapeutics* **2019**, *16*, 416-431.

animales tratados.[37] Los resultados farmacológicos de estos dos estudios *in vivo* se publicaron en las revistas *Neurotherapeutics*[36] y *Pharmaceutics*,[37] respectivamente.

En el contexto de la presente Tesis Doctoral, dado el interés en desarrollar nuevos ligandos I_2-IR para el tratamiento de enfermedades neurodegenerativas, se propuso ampliar el arsenal sintético de ligandos incluyendo compuestos de diferente naturaleza estructural: α-iminofosfonatos bicíclicos y benzofuranil-2-imidazoles derivados del ligando I_2-IR conocido **LSL60101** (Figura 1.3). El diseño, síntesis y evaluación farmacológica de estas dos familias de compuestos se recoge en las publicaciones incluidas de los *Capítulos 2* y *3*, respectivamente (Figura 1.5).

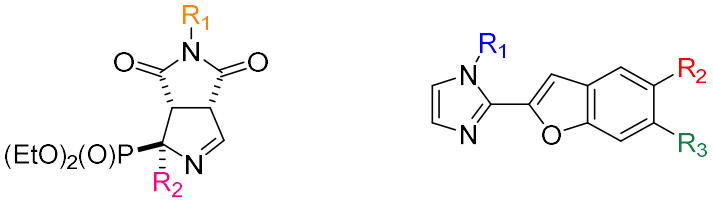

α-Iminofosfonatos bicíclicos **Benzofuranil-2-imidazoles**

Figura 1.5. Estructura de los ligandos I_2-IR descritos en los *Capítulos 2* y *3*.

En primer lugar, teniendo en cuenta la estructura del compuesto **MCR5** que contiene un grupo α-feniliminofosfonato y con el objetivo de sintetizar nuevas estructuras que contuvieran ese grupo funcional, decidimos aprovechar la experiencia en el acceso a α-iminofosfonato bicíclicos[13] y los sintetizamos modificados en la posición α con un amplio abanico de *N*-maleimidas sustituidas (Esquema 1.6), ampliando así el número de compuestos de esta familia de biciclos. La reacción de cicloadición [3+2] entre derivados de PhosMic α-sustituidos y maleimidas cursó con buenos rendimientos y una excelente diastereoselectividad, obteniendo en todos los casos únicamente uno de los dos posibles diastereómeros, de manera análoga a como había trascurrido la reacción en el caso de utilizar PhosMic (Esquema 1.2).[13] La configuración relativa fue confirmada inequívocamente por análisis cristalográfico de rayos X de varios miembros de la familia, indicando una relación *trans* entre los hidrógenos cabeza de puente y el sustituyente en el α que se encuentra en el carbono que soporta el grupo fosfonato. La resolución de los cristales se realizó por el Prof. Elies Molins en el Institut de Ciència de Materials de Barcelona (CSIC). El Prof. F. Javier Luque de nuestra facultad propuso un modelo teórico que justificaba la estereoquímica y diastereoselectividad observada.

[37] Vasilopoulou, F.; Bagán, A.; Rodríguez-Arévalo, S.; Escolano, C.; Griñán-Ferré, C.; Pallàs, M. *Pharmaceutics* **2020**, *12*, 475.

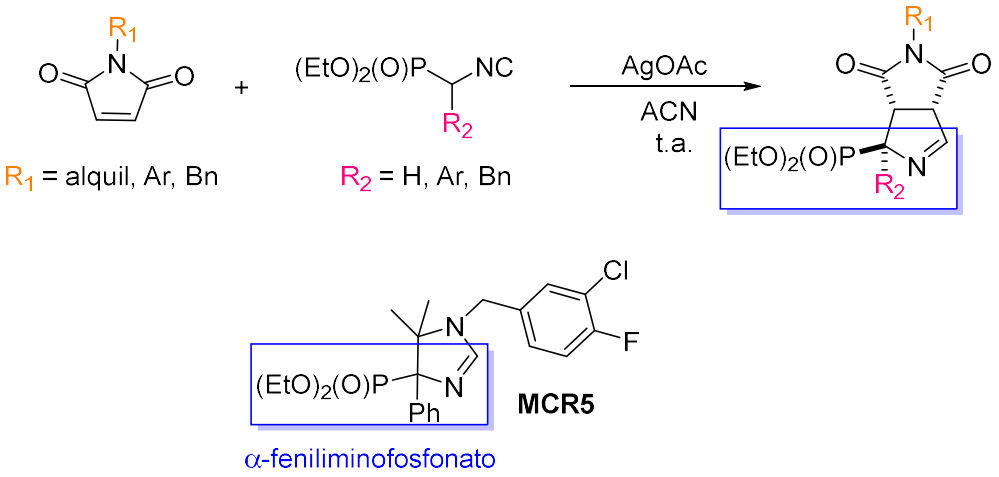

Esquema 1.6. Reacción de cicloadición [3+2] entre isocianometilfosfonatos y maleimidas y estructura de **MCR5**. Se indica el grupo funcional común de α-iminofosfonato sustituido.

Un total de 36 α-iminofosfonatos bicíclicos diversamente sustituidos en el nitrógeno de la maleimida o en la posición α del PhosMic se sintetizaroncon rendimientos de medios a altos. Teniendo en cuenta la localización de I_2-IR en el SNC, la capacidad para cruzar la barrera hematoencefálica (BHE) es un requisito esencial para desarrollar ligandos I_2-IR eficaces con posibles aplicaciones terapéuticas en el campo de la neuroprotección. Por esta razón, la permeabilidad *in vitro* de los nuevos compuestos se determinó utilizando el ensayo de permeación con membrana artificial en paralelo para BHE (PAMPA-BBB) por la Dra. Belén Pérez de la Universidad Autónoma de Barcelona (UAB). Todos los compuestos resultaron situarse por encima del umbral establecido para una óptima permeabilidad de la BHE, considerándose adecuados para proseguir en los estudios. Seguidamente, su actividad como ligandos I_2-IR se evaluó por el Prof. Luis F. Callado (UPV), presentando algunos de ellos, una alta afinidad y selectividad para I_2-IR frente a los α_2-AR, constituyendo la primera familia de ligandos de estos receptores que no conteníannúcleos de imidazolina o imidazol en su estructura.

Cabe destacar que la originalidad estructural de la familia de α-iminofosfonatos bicíclicos, su actividad destacada como ligandos de los I_2-IR y los resultados de mejora cognitiva producidos en el modelo murino 5xFAD, permitió su protección intelectual (WO2019121853A1) gestionado por la Fundación Bosch i Gimpera (UB).[38] Además, el

[38] Escolano, C.; Pallàs, M.; Griñán-Ferré, C.; Abás, S.; Callado, L.F.; García-Sevilla, J.A. *Synthetic I_2 Imidazoline Receptor Ligands for Prevention or Treatment of Human Brain Disorders*. WO 2019/121853 A1, 27 Junio, **2019**.

proyecto recibió financiación para su valorización dentro del programa *CaixaImpulse* 2018.

En segundo lugar, el compuesto conocido como ligando I_2-IR **LSL60101**,[39] sirvió de cabeza de serie para preparar una bateria de productos en los que se habían introducido sustituyentes en el fenilo del núcleo de benzofurano y sobre el sistema imidazólico. La ruta de sintética empleada, aunque requirió múltiples etapas, fue eficiente y económica (rendimientos globales cercanos al 60%) utilizando como productos de partida los correspondientes benzofuranil-2-carboxilatos comerciales (Esquema 1.7). Los nuevos compuestos se evaluaron como ligandos I_2-IR, pero en este caso, aunque presentaban buenos valores de afinidad para I_2-IR y selectividad frente a los α_2-AR, resultaron ser menos activos que **LSL60101**. También se evaluó la capacidad de atravesar la BHE de los compuestos preparados, resultando ser adecuados, excepto en el caso de los derivados fenólicos R^1 o R^2 = OH, para proseguir los estudios *in vivo*.

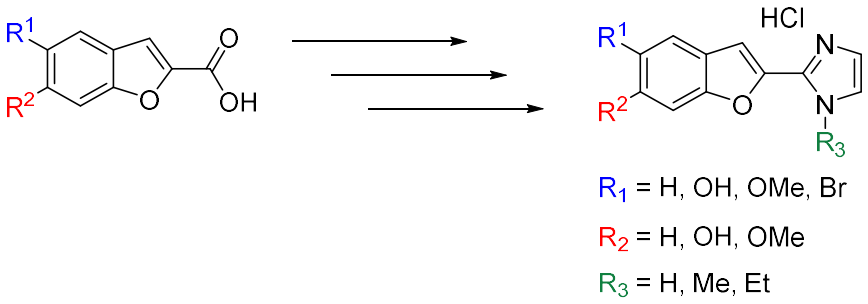

Esquema 1.7. Estructura de los benzofuranil-2-imidazoles sintetizados.

Debido a la falta de descripción de los I_2-IR, para realizar mejoras estructurales en las dos nuevas familias sintetizadas de α-iminofosfonatos bicíclicos y benzofuranil-2-imidazoles, se llevaron a cabo estudios de 3D-QSAR por el grupo de investigación la Dra. Katalina Nikolic de la Universidad de Belgrado. Estos estudios, además de sugerir cambios estructurales que podrían mejorar el perfil de los compuestos preparados, permitieron determinar el farmacóforo de las dos familias. El mismo grupo de Belgrado realizó estudios de ADMET *in silico* para determinar si los compuestos presentaban algún parámetro que pudiese comprometer su desarrollo posterior.

[39] (a) Alemany, R.; Olmos, G.; Escribá, P.V.; Menargues, A.; Obach, R.; García-Sevilla, J.A. *Eur. J. Pharmacol*. **1995**, *280*, 205-210; (b) Casanovas, A.; Olmos, G.; Ribera, J.; Boronat, M.A.; Esquerda, J.E.; García-Sevilla, J.A. *Br. J. Pharmacol.* **2000**, *130*, 1767-1776; (c) Hernández-Hernández, E.; García-Sevilla, J.A.; García-Fuster, M.J. *Pharmacol Rep.* **2021**, *73*, 288-295.

Los nuevos compuestos se sometieron a estudios de citotoxicidad en diferentes líneas celulares, en el grupo del Prof. Steven de Jonghe en el Rega Institute, resultando ser seguros para posteriores estudios *in vitro* e *in vivo*.

Los datos recogidos permitieron seleccionar el α-iminofosfonato bicíclico **B06** y el benzofuranil-2-imidazol **LSL60101** (Figura 1.6), los cuales presentan valores de afinidad por los I_2-IR expresados en pK_i de 8.56 y 6.67 y una selectividad I_2/α_2 195 y 3090, respectivamente. Ambos compuestos se sometieron a estudios de ADMET *in vitro* por el grupo de los Profs. M. Isabel Loza y José Brea de la Universidad de Santiago de Compostela (USC) como son la estabilidad microsomal, la inhibición de citocromos, la citotoxicidad, unión a proteínas plasmáticas, solubilidad, etc. Además, del compuesto **B06** se realizó un panel de unión a 44 receptores para descartar posibles *off-targets* que pudiesen comprometer la seguridad del compuesto.

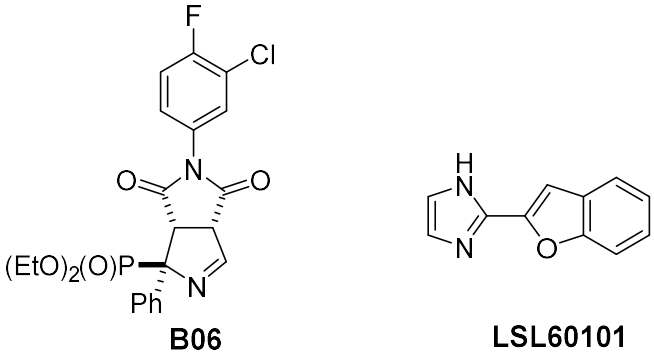

Figura 1.6. Estructura de los ligandos I_2-IR **B06** y **LSL60101**.

Seguidamente, se realizaron estudios *in vivo* evaluando el efecto hipotérmico de **B06** en ratas y de **LSL60101** en ratón. La hipotermia se ha relacionado con una acción neuroprotectora y beneficiosa en múltiples enfermedades como por ejemplo en la isquemia cerebral.[40] Además, se observó una reducción de la proteína apoptótica FADD en el hipocampo indicando un papel neuroprotector de los compuestos administrados.[41] Estos estudios fueron realizados por la Dra. M. Julia García-Fuster de la Universidad de las Islas Baleares (UIB).

De manera análoga a los estudios *in vivo* previos del grupo que validaban los ligandos I_2-IR para el tratamiento de enfermedades neurodegenerativas, los nuevos compuestos **B06** y **LSL60101**, se evaluaron en un modelo murino de enfermedad de Alzheimer,

[40] (a) Thorn, D.A.; An, X.; Zhang, Y.; Pigini, M.; Li, J. *Br. J. Pharmacol.* **2012**, *166*, 1936-1945; (b) Hernández-Hernández, E.; García-Fuster, M.J. *Naunyn-Schmiedeberg's Arch. Pharmacol*. **2021**, *394*, 989-996.
[41] (a) Hernández-Hernández, E.; Miralles, A.; Esteban, S.; García-Fuster, M.J. *Neurobiol. Aging* **2018**, *71*, 115-126; (b) Hernández-Hernández, E.; Miralles, A.; Esteban, S.; García-Fuster, M.J. *J. Psychopharmacol.* **2018**, *32*, 248-255.

5xFAD, por el grupo de investigación de la Prof. M. Pallàs. Se llevaron a cabo estudios de comportamiento como, por ejemplo, *Novel Object Recognition* (NORT) y *Open Field Test* (OFT) que mostraron una mejora en las capacidades cognitivas de aprendizaje y memoria a corto y largo plazo en los animales tratados respecto al grupo control.

Los resultados sintéticos y farmacológicos preliminares de ambas familias, α-iminofosfonatos bicíclicos y benzofuranil-2-imidazoles derivados de **LSL60101**, han dado lugar dos publicaciones en revistas de alto impacto en el campo de la Química Médica, *Journal of Medicinal Chemistry*[42] y *European Journal of Medicinal Chemistry*,[43] respectivamente, que representan las dos publicaciones más relevantes de la presente Tesis Doctoral. Estas publicaciones se incluyen como copias completas en los *Capítulos 2 y 3*, respectivamente.

Debido a la mejora cognitiva encontrada en los dos estudios preliminares llevados a cabo con los animales de experimentación tratados con **B06** por un lado y **LSL60101** por otro, el grupo de la Prof. M. Pallàs realizó ensayos *in vivo* completos en los dos modelos murinos uno de neurodegeneración, SAMP8 y, otro específico de enfermedad de Alzheimer, 5xFAD. Los animales tratados mostraron mejoras cognitivas y de marcadores de estrés oxidativo y neuroinflamación. Además, en los ratones 5xFAD tratados con terapia combinada de **LSL60101** y donepezilo (el *gold standard* para el tratamiento de AD que actúa inhibiendo la enzima acetilcolinesterasa) se observó un efecto sinérgico provocando una mayor eficacia y mejora de determinados marcadores a nivel molecular.

En conjunto, estos trabajos apoyan el potencial de los ligandos I_2-IR como posibles agentes terapéuticos en el tratamiento de enfermedades neurodegenerativas y de los síntomas derivados de las mismas.

Los resultados farmacológicos de los ensayos *in vivo* se publicaron en revistas de alto impacto a nivel farmacológico, *GeroScience*[44] que recoge el estudio *in vivo* con el

[42] El compuesto **B06** es **9d** en el artículo: Abás, S.; Rodríguez-Arévalo, S.; Bagán, A.; Griñán-Ferré, C.; Vasilopoulou, F.; Brocos-Mosquera, I.; Muruguza, C.; Pérez, B.; Molins, E.; Luque, F.J.; Pérez-Lozano, P.; de Jonghe, S.; Daelemans, D.; Naesens, L.; Brea, J.; Loza, M.I.; Hernández-Hernández, E.; García-Sevilla, J.A.; García-Fuster, M.J.; Radan, M.; Djikic, T.; Nikolic, K.; Pallàs, M.; Callado, L.F.; Escolano, C. *J. Med. Chem.* **2020**, *63*, 3610-3633.

[43] Rodríguez-Arévalo, S.; Bagán, A.; Griñán-Ferré, C.; Vasilopoulou, F.; Pallàs, M.; Brocos-Mosquera, I.; Callado, L.F.; Loza, M.I.; Martínez, A.L.; Brea, J.; Pérez, B.; Molins, E.; de Jonghe, S.; Daelemans, D.; Radan, M.; Djikic, T.; Nikolic, K.; Hernández-Hernández, E.; García-Fuster, M.J.; García-Sevilla, J.A.; Escolano, C. *Eur. J. Med. Chem.* **2021**, *222*, 113540.

[44] Vasilopoulou, F.; Griñán-Ferré, C.; Rodríguez-Arévalo, S.; Bagán, A.; Abás, S.; Escolano, C.; Pallàs, M. *GeroScience* **2021**, *43*, 965-983.

ligando I_2-IR **B06** y *British Journal of Pharmacology*, que incluye el estudio *in vivo* con el ligando I_2-IR **LSL60101**.[45]

[45] Vasilopoulou, F.; Rodríguez-Arévalo, S.; Bagán, A.; Escolano, C.; Griñán-Ferré, C.; Pallàs, M. *Br. J. Pharmacol*. **2021**, 178, 3017-3033.

1.3. Enzima Fosfoenolpiruvato carboxiquinasa mitocondrial (PEPCK-M)

El control de la producción de glucosa es uno de los aspectos clave en una terapia antidiabética. La gluconeogénesis mantiene los niveles de glucosa en sangre durante los períodos de ayuno, pero en pacientes diabéticos contribuye a la hiperglucemia. Una de las múltiples etapas existentes en la gluconeogénesis consiste en la conversión del oxalacetato (OAA) a fosfonoenolpiruvato (PEP) y está catalizada por la enzima fosfoenolpiruvato carboxiquinasa (PEPCK) que utiliza un nucleósido trifosfato (GTP) como donador del grupo fosforilo (Esquema 1.8).[46]

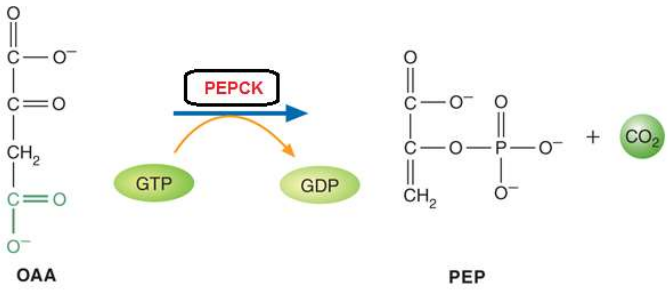

Esquema 1.8. Etapa de conversión del OAA a PEP en la gluoconeogénesis mediante la enzima PEPCK.

Se conoce que la PEPCK es una enzima esencial para la homeostasis de la glucosa gracias a un estudio *in vivo* realizado en animales transgénicos en los que se sobreexpresó la PEPCK, dando como resultado la presencia de hiperglucemia en ayunas y disminución de la tolerancia a la glucosa.[47] Por tanto, se podría esperar que inhibiendo la actividad de la PEPCK disminuyera el nivel de glucosa en ayuno en pacientes diabéticos.

La PEPCK está formada por dos isoenzimas localizadas en el citosol, PEPCK-C, o en la mitocondria, PEPCK-M, codificadas por distintos genes nucleares, PCK1 y la PCK2, respectivamente. La proteína humana está compuesta por 622 (PEPCK-C) y 640 (PEPCK-M) aminoácidos y ambas, comparten un 69% de identidad y un 83% de similitud en su secuencia.[48] Curiosamente, ambas isoenzimas se expresan y regulan procesos fisiológicos diferentes. Por una parte, la PEPCK-C regula el control hormonal y está restringida a tejidos gluconeogénicos y gliceroneogénicos (hígado, intestino

[46] (a) Nordlie, R.C.; Lardy, H.A. *J. Biol. Chem*. **1963**, *238*, 2259-2263; (b) Chang, H.C.; Lane, M.D. *J. Biol. Chem*. **1966**, *241*, 2413-2420; (c) Hanson, R.W.; Garber, A.J. *Am. J. Clin. Nutr*. **1972**, *25*, 1010-1021.
[47] Rosella, G.; Zajac, D.J.; Baker, L.; Kaczmarczyk, S.J.; Andrikopoulos, S.; Adams, T.E.; Proietto, J. *Mol. Endocrinol*. **1995**, *9*, 1396-1404.
[48] Stark, R.; Kibbey, R.G. *Biochim Biophys Acta*. **2014**, *1840*, 1313-1330.

delgado, corteza renal y tejido adiposo) y, responde a insulina, glucagón y dexametasona. Por el contrario, la PEPCK-M no se regula por señales hormonales y se encuentra ampliamente expresada en tejidos no gluconeogénicos (células T y B, células β pancreáticas, neuronas y células de tejidos no diferenciadas como células madre embrionarias y tumores).[49]

El papel dominante de la PEPCK-C hepática en el desequilibrio de la homeostasis de la glucosa en pacientes obesos y diabéticos, ha justificado el desarrollo durante años de compuestos inhibidores de esta enzima, incluidos los que son análogos estructurales de OAA, o el ácido 3-mercaptopicolínico (**3-MPA**), aunque todos ellos han resultado tener una IC_{50} en el orden micromolar.[50] En 2007, el Prof. Foley y colaboradores describieron una serie de inhibidores GTP competitivos de la PEPCK-C, con núcleo de 3-alquil-1,8-dibencilxantina, **iPEPCK-1**, IC_{50} = 0.069 μM e **iPEPCK-2**, IC_{50} = 0.029 μM), con mejor IC_{50} que 3-MPA, 20 μM. (Figura 1.7).[51]

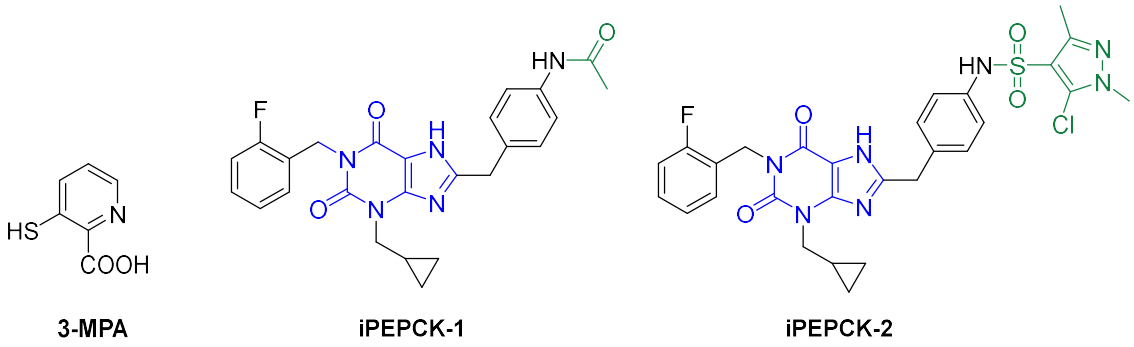

Figura 1.7 Estructura de inhibidores de PEPCK-C.

En estudios realizados con muestras de tumores humanos (mama, colon y pulmón) se observó que el gen PCK2 que codifica la PEPCK-M, se expresaba en niveles suficientemente altos para que desempeñase un papel metabólico notable. Por lo tanto, la PEPCK-M podría tener un papel relevante en la formación de células cancerosas, especialmente bajo limitación de nutrientes u otras condiciones de estrés. Así, el

[49] (a) Stark, R.; Pasquel, F.; Turcu, A.; Pongratz, R.L.; Roden, M.; Cline, G.W.; Shulman, G.I.; Kibbey, R.G. *J. Biol. Chem*. **2009**, *284*, 26578-26590; (b) Méndez-Lucas, A.; Duarte, J.A.G.; Sunny, N.E.; Satapati, S.; He, T.; Fu, X.; Bermúdez, J.; Burgess, S.C.; Perales, J.C. *J. Hepatol*. **2013**, *59*, 105-113; (c) Méndez-Lucas, A.; Hyroššová, P.; Novellasdemunt, L.; Viñals, F.; Perales, J.C. *J. Biol. Chem*. **2014**, *289*, 22090-22102; (d) Semakova, J.; Hyroššová, P.; Méndez-Lucas, A.; Cutz, E.; Bermudez, J.; Burgess, S.; Alcántara, S.; Perales, J.C. *J. Physiol. Biochem.* **2017**, *73*, 89-98.

[50] (a) Stiffin, R.M.; Sullivan, S.M.; Carlson, G.M.; Holyoak, T. *Biochemistry* **2008**, *47*, 2099-2109; (b) Balan, M.D.; Mcleod, M.J.; Lotosky, W.R.; Ghaly, M.; Holyoak, T. *Biochemistry* **2015**, *54*, 5878-5887.

[51] (a) Foley, L.H.; Wang, P.; Dunten, P.; Ramsey, G.; Gubler, M.-L.; Wertheimer, S.J. *Bioorg. Med. Chem. Lett*. **2003**, *13*, 3607-3610; (b) Foley, L.H.; Wang, P.; Dunten, P.; Ramsey, G.; Gubler, M.-L; Wertheimer, S. J. *Bioorg. Med. Chem. Lett.* **2003**, *13*, 3871-3874; (c) Pietranico, S.L.; Foley, L.H.; Huby, N.; Yun, W.; Dunten, P.; Vermeulen, J.; Wang, P.; Toth, K.; Ramsey, G.; Gubler, M.-L.; Wertheimer, S.J. *Bioorg. Med. Chem. Lett.* **2007**, *17*, 3835-3839.

desarrollo de inhibidores de la PEPCK-M ha suscitado interés como potencial terapia anticancerosa.[52]

En el contexto de esta Tesis Doctoral, en un proyecto de colaboración con el Prof. J. Carlos Perales de la Facultad de Medicina de la UB, se sintetizaron compuestos que fueran capaces de inhibir la PEPCK-M con el objetivo de determinar, en un modelo murino adecuado, su utilidad como agentes antitumorales. Para ello, se accedió a los compuestos descritos anteriormente por el Prof. Foley como los inhibidores de la PEPCK-C más potentes que se conocían, **iPEPCK-1** e **iPEPCK-2**, a partir de 6-aminouracilo, mediante numerosas etapas de síntesis e intermedios como los representados en el Esquema 1.9 y evaluar si presentaban actividad inhibitoria frente a la isoforma mitocondrial (PEPCK-M).

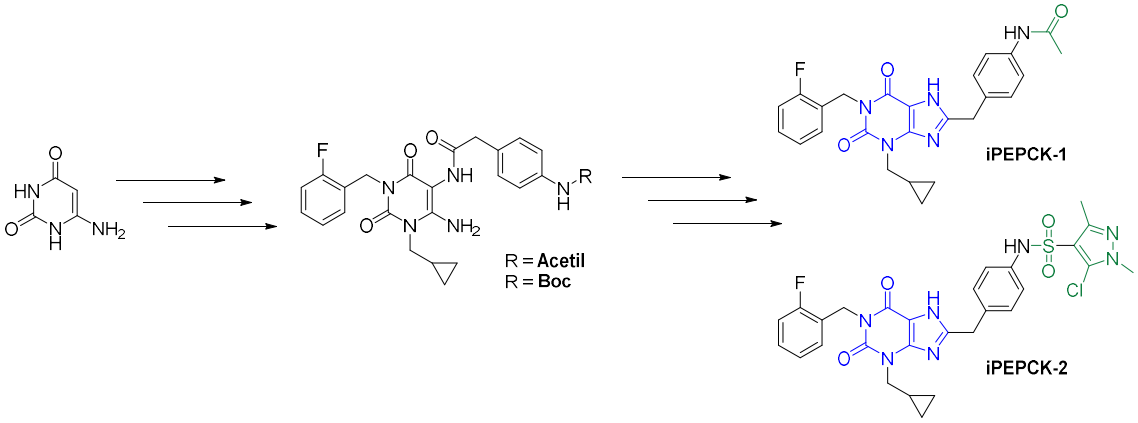

Esquema 1.9. Esquema de síntesis y estructura de **iPECK-1** e **iPECK-2**.

Ambos compuestos inhibían con éxito tanto la PEPCK-C como la PEPCK-M, mostrando una potencial similar sobre ambas isoformas y valores de actividad del orden de magnitud submicromolar (Tabla 1.1).

Tabla 1.1. Valores de IC_{50} (μM) de los compuestos sintetizados (**iPEPCK-1** e l**PEPCK-2**) y de referencia (**3-MPA**) frente a PEPCK-M y PEPCK-C recombinante humana.

Compuesto	PEPCK-C	PEPCK-M
3-MPA	10.097	17.402
iPEPCK-1	0.232	0.451
iPEPCK-2	0.061	0.117

[52] (a) Leithner, K.; Hrzenjak, A.; Trötzmüller, M.; Moustafa, T.; Köfeler, H.C.; Wohlkoenig, C.; Stacher, E.; Lindenmann, J.; Harris, A.L.; Olschewski, A.; Olschewski, H.; *Oncogene* **2015**, *34*, 1044-1050; (b) Chu, P.-Y.; Jiang, S.-S.; Shan, Y.-S.; Hung, W.-C.; Chen, M.-H.; Lin, H.-Y.; Chen, Y.-L.; Tsai, H.-J.; Chen, L.-Y. *Oncotarget* **2017**, *8*, 103613-103625; (c) Grasmann, G.; Smolle, E.; Olschewski, H.; Leithner, K. *Biochim. Biophys. Acta - Rev. Cancer* **2019**, *1872*, 24-36.

A continuación, se realizaron estudios preliminares *in vitro* de ADME del mejor inhibidor **iPEPCK-2**, en el grupo de los Profs. M. I. Loza y J. Brea de la USC determinando que el compuesto era seguro para avanzar con los ensayos *in vivo*.

Finalmente, se estudió *in vivo* la evolución del crecimiento de tumores implantados en tejido subcutáneo en ratones inmunodeprimidos que posteriormente fueron tratados con **iPEPCK-2**. Los tumores procedían de carcinomas humanos de colon (SW-480) y de células embrionarias del hígado (HEK-293). En ambas líneas celulares se expresa únicamente el gen PCK2 presente en la PEPCK-M, y no PCK1. Los resultados demuestran en ambos modelos *xenografts* una reducción tanto del volumen como el peso de los tumores en ratones tratados con **iPEPCK-2** en comparación con los tratados con el vehículo (5% DMSO:H_2O), así como la ausencia de cualquier signo de toxicidad inducida por el tratamiento (Figura 1.8).

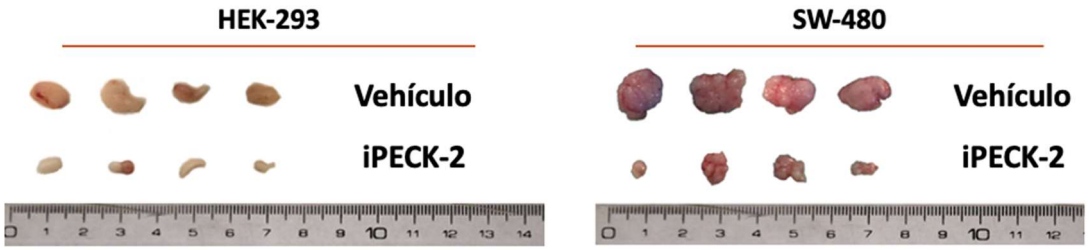

Figura 1.8. Representación de la disminución del volumen de los tumores en dos líneas celulares tratadas con el vehículo e **iPECK-2**.

Los resultados biológicos obtenidos se publicaron en la revista *Biomedicine & Pharmacotherapy*.[53] En el *Capítulo 5* se adjunta una copia completa de dicha publicación. Las observaciones reportadas en el artículo sugieren que la inhibición de la PEPCK-M podría tener un interés terapéutico en cáncer, validando PEPCK-M como una diana novedosa para la terapia cancerígena.

Adicionalmente, también se realizó un estudio en el grupo del Prof. J. C. Perales para determinar el mecanismo de acción de los inhibidores sintetizados y para ello evaluó la alteración del calcio citosólico por inhibición de la PEPCK-M y su implicación en cáncer. Como se ha comentado anteriormente, la PEPCK es la enzima que cataliza la reacción de paso del OAA a PEP en la gluconeogénesis. Asimismo, la formación de PEP inhibe *Sarco/Endoplasmic Reticulum* Ca^{2+}*/ATPase* (SERCA).[54] SERCA es un transportador

[53] Aragó, M.; Moreno-Felici, J.; Abás, S.; Rodríguez-Arévalo, S.; Hyrossova, P.; Figueras, A.; Viñals, F.; Pérez, B.; Loza, M.I.; Brea, J.; Latorre, P.; Carrodeguas, J.A.; García-Rovés, P.M.; Galdeano, C.; Ginex, T.; Luque, F.J.; Escolano, C.; Perales, J.C. *Biomed. Pharmacother.* **2020**, *121*, 109601.

[54] (a) Wiel, C.; Lallet-Daher, H.; Gitenay, D.; Gras, B.; Le Calvé, B.; Augert, A.; Ferrand, M.; Prevarskaya, N.; Simonnet, H.; Vindrieux, D. *Nat. Commun.* **2014**, *5*, 3792; (b) Monteith, G.R.; Prevarskaya, N.; Roberts-

que conduce el calcio citosólico al retículo endoplasmático. Éste, al ser un mensajero secundario, tiene diversas funciones, por lo tanto, la inhibición de SERCA por la formación de PEP provoca un aumento en el calcio intracelular. Una mayor presencia de calcio conduce, entre otros efectos, a la activación del oncogén c-Myc, responsable de regular el metabolismo celular e intensificar la supervivencia de células tumorales.[55]

Este estudio demostró que **iPEPCK-2**, baja los niveles de PEP, vuelve a activar SERCA y, finalmente disminuye el calcio citosólico disponible para activar c-Myc. Este trabajo se publicó en la revista científica *Cells*[56] y se adjunta en el anexo de la presente Tesis Doctoral.

En ambos artículos he contribuido realizando el diseño, preparación y abastecimiento de los productos en las cantidades requeridas para los estudios pertinentes *in vitro* e *in vivo*.

Thomson, S.J. *Nat. Rev. Cancer* **2017**, *17*, 367-380; (c) Xu, M.; Seas, A.; Kiyani, M.; Ji, K.S.Y.; Bell, H.N. *Cell Biosci.* **2018**, *8*, 25.

[55] (a) Wang, R.; Dillon, C.P.; Shi, L.Z.; Milasta, S.; Carter, R.; Finkelstein, D.; McCormick, L.L.; Fitzgerald, P.; Chi, H.; Munger, J. *Immunity* **2011**, *35*, 871-882; (b) Ho, P.-C.; Bihuniak, J.D.; Macintyre, A.N.; Staron, M.; Liu, X.; Amezquita, R.; Tsui, Y.-C.; Cui, G.; Micevic, G.; Perales, J.C. *Cell* **2015**, *162*, 1217-1228; (c) Gu, Y.; Zhang, J.; Ma, X.; Kim, B.; Wang, H.; Li, J.; Pan, Y.; Xu, Y.; Ding, L.; Yang, L. *Cancer Cell* **2017**, *32*, 115-128.

[56] Moreno-Felici, J.; Hyrossova, P.; Aragó, M.; Rodríguez-Arévalo, S.; García-Rovés, P.M.; Escolano, C.; Perales, J.C. *Cells* **2020**, *9*, 18.

1.4. *Transient Receptor Potential Cation Channel M8* (TRPM8) y candidato clínico AR-15512

La superfamilia de los receptores *Transient Receptor Potential Cation Channel* (TRP) están constituidos por proteínas transmembrana que forman canales iónicos. Estos receptores están ampliamente presentes en todos los mamíferos y se localizan en una gran cantidad de tejidos desde el sistema nervioso hasta células epiteliales.[57] Asimismo, la mayoría de estos canales poseen una permeabilidad no selectiva a cationes monovalentes (Na^+, K^+) y al Ca^{2+}, ligeramente mayor para éste que para los monovalentes. Estos canales se activan por estímulos mecánicos, químicos, físicos y por ligandos endógenos o exógenos.[58] Las funciones fisiológicas que desempeñan estos receptores son esencialmente sensoriales, como la percepción de la temperatura, el tacto, los olores y el sabor, el dolor, así como la regulación del tono vascular, la fertilidad masculina y la tumorogénesis, entre otras.[59]

Algunos miembros de la superfamilia de TRP responden con distintos umbrales de activación a estímulos térmicos, desde temperaturas frías nocivas (<15 ºC) a calor extremo (>45 ºC). Este subgrupo se denomina TRP térmicos (o termosensores) e incluyen a: TRPV1-4, TRPM3, TRPM8 y TRPA1.[60] Asimismo, estos canales pueden detectar estímulos químicos derivados de moléculas endógenas o sustancias externas activando las neuronas sensoriales y generando sensaciones térmicas y/o dolor agudo. Los TRPV1-4 reconocen temperaturas intermedias y altas (25-50 ºC, aproximadamente) experimentando la sensación de ardor del picante. En cambio, los TRPM8 y TRPA1 participan en la percepción de temperaturas frías (<15-23 ºC), ocasionando la sensación fría del mentol. Por ello, la disfunción de estos canales causada por alguna patología puede provocar, por ejemplo, hiperalgesia térmica o alodinia. Por lo tanto, dada la implicación de estos receptores en procesos fisiológicos y patológicos, los TRP térmicos son considerados potenciales dianas terapéuticas para el desarrollo de nuevos fármacos.

---

[57] (a) Watson, H.R.; Hems, R.; Rowsell, D.G.; Spring, D.J. *J. Soc. Cosmet. Chem.* **1978**, *29*, 185-200; (b) Clapham, D.E.; Runnels, L.W.; Strubing, C. *Nat. Rev. Neurosci.* **2001**, *2*, 387-396.

[58] (a) Nilius, B.; Owsianik, G.; Voets, T.; Peters, J.A. *Physiol. Rev.* **2007**, *87*, 165-217; (b) Vriens, J.; Nilius, B.; Venneken, R. *Curr. Neuropharmacol*. **2008**, *6*, 79-96; (c) Liu, Z.; Wu, H.; Wei, Z.; Wang, X.; Shen, P.; Chen, W.; Lu, Y. *J. Cancer. Res. Clin. Oncol.* **2016**, *142*, 1871-1881.

[59] (a) Nilius, B.; Owsianik, G. *Genome Biol.* **2011**, *12*, 218-229; (b) Brederson, J.D.; Kym, P.R.; Szallasi, A. *Eur. J. Pharmacol*. **2013**, *716*, 61-76.

[60] (a) Minke, B.; Cook, B. *Physiol. Rev*. **2002**, *82*, 429-472; (b) Stuckya, C.L.; Dubinb, A.E.; Jeskec, N.A.; Malind, S.A.; McKemy, D.D.; Story, G.M. *Brain. Res. Rev*. **2009**, *60*, 2-23.

Entre los TRP térmicos, el TRPM8 es uno de los más estudiados, ya que su distribución por múltiples órganos y tejidos provoca una elevada implicación en varias funciones fisiológicas como la proliferación celular, reacciones inflamatorias, efectos inmunomoduladores, entre otros, generando trastornos que van desde el prurito, ojo seco o tos crónica hasta cáncer o migraña. El TRPM8 es un canal catiónico no selectivo, permeable a calcio, voltaje dependiente y activado por temperatura frías inocuas (12-23 ºC). Estas bajas temperaturas pueden ser causadas por compuestos refrigerantes naturales (mentol) y sintéticos (icilina) que evocan sensaciones de frescor. El mentol es el producto natural más potente como activador de TRPM8, ocasionando sensación de frío al ser aplicado. Las propiedades analgésicas y antipruríticas del mentol se deben a la activación de estos canales que a su vez desensibilizan neuronas sensoriales, impidiendo así la transmisión de otros estímulos.[61]

Además de la icilina, existen otros productos sintéticos agonistas del TRPM8. Uno de ellos, **AR-15512** (también AVX-012 o WS-12) (Figura 1.9) es un compuesto bioactivo con efectos refrescantes similares al mentol que, actualmente, se encuentra en fase clínica 2b como solución oftálmica para el tratamiento de ojo seco, un trastorno crónico altamente prevalente, considerado una necesidad médica no cubierta. El TRPM8 está involucrado en la producción de lágrimas y el parpadeo, por ello, al ser estimulado reduce el malestar ocular en pacientes que padecen de ojo seco.[62]

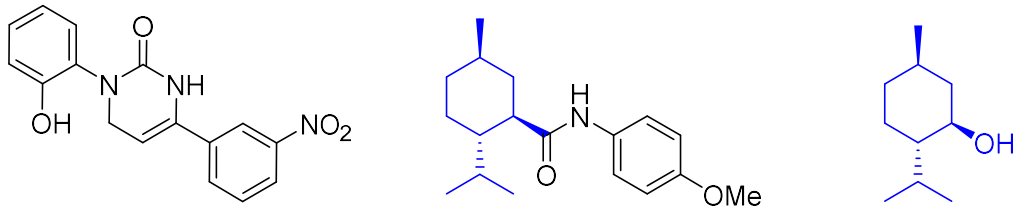

Icilina **AR-15512** **(-)-Mentol**

Figura 1.9. Estructura de los agonistas de TRPM8 icilina, **AR-15512** y (-)-mentol.

AR-15512, a diferencia de la icilina, posee una estructura similar al mentol. Este compuesto se desarrolló por Avizorex Pharma S. L. (Barcelona), una empresa farmacéutica oftálmica española que trabaja en el descubrimiento de nuevas terapias

[61] (a) McKemy, D.D.; Neuhausser, W.M.; Julius, D. *Nature* **2002**, *416*, 52-58; (b) Gonzalez-Muniz, R.; Angeles Bonache, M.; Martin-Escura, C.; Gomez-Monterrey, I. *Int. J. Mol. Sci*. **2019**, *20*, 2618; (c) Yin, Y.; Le, S.C.; Hsu, A.L.; Borgnia, M.J.; Yang, H.; Lee, S.-Y. *Science* **2019**, *363*, 945; (d) Liu, Y.; Mikrani, R.; He, Y.; Baig, M.M.F.; Abbas, M.; Naveed, M.; Tang, M.; Zhang, Q.; Li, C.; Zhou, X. *Eur. J. Pharmacol.* **2020**, *882*, 173312.

[62] (a) Belmonte, C.; Gallar, J.; Ferrer, A.; Fernandez, A.; Viana, F. *Pharmaceutical Composition for the Treatment of Dry Eye.* WO2012/032209 A2, 15 Marzo, **2012**; (b) Clayton, J.A. *N. Engl. J. Med*. **2018**, *378*, 2212-2223; (c) O'Neil, E.C.; Henderson, M.; Massaro-Giordano, M.; Bunya, V.Y. *Curr. Opin. Ophthalmol*. **2019**, *30*, 166-178.

para abordar el síndrome del ojo seco. Avizorex Pharma se integró desde 2019 en Aerie Pharmaceuticals (Durham, USA).

Para proseguir con la documentación demandada por las autoridades sanitarias, Avizorex Pharma tenía que demostrar que el compuesto **AR-15512** no contenía como impureza el diastereoisómero (***neo*-AR-15512**) o su enantiómero (***ent*-AR-15512**). Para ello se sintetizaron ambos compuestos y se desarrolló un método de HPLC para su análisis y poder descartar así su presencia en muestras de **AR-15512** (Figura 1.10).

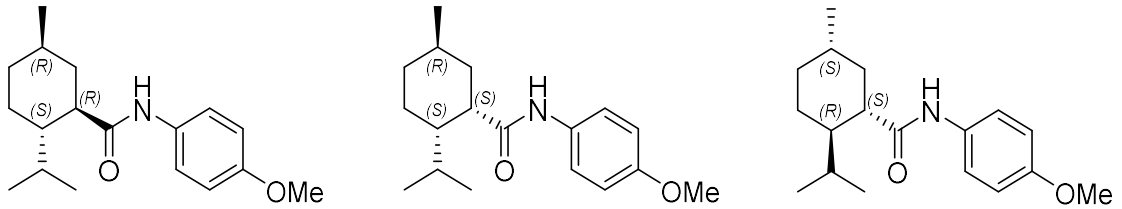

AR-15512 ***neo*-AR-15512** ***ent*-AR-15512**

Figura 1.10. Estructura de **AR-15512** y de dos estereoisómeros.

Los resultados obtenidos han sido recientemente publicados en la revista *Molecules* (Special Issue: "Active Pharmaceutical Ingredient (API): Synthetic Strategies and Characterization"),[63] la cual se incluye como copia completa en el *Capítulo 6*.

[63] Rodríguez-Arévalo, S.; Pujol, E.; Abás, S.; Galdeano, C.; Escolano, C.; Vázquez, S. *Molecules* **2021**, *26*, 906.

1.5. Estructura de la memoria y objetivos

La presente Tesis Doctoral está redactada a modo de Compendio de Publicaciones y la memoria está dividida en diferentes apartados:

1. Introducción general: Incluye los antecedentes y explicación del contenido temático, así como los objetivos y resumen de cada capítulo (*Capítulo 1*).

2. Capítulos:

   2.1. Cuatro capítulos donde se recogen las copias completas de las publicaciones y su material suplementario correspondiente. Tres de ellos, contienen apartados adicionales con resultados no publicados (*Capítulos 2, 3 y 5*).

   2.2. Un capítulo que recoge la memoria del trabajo realizado y su material suplementario correspondiente (*Capítulo 4*).

3. Conclusiones: Incluye las conclusiones generales de cada capítulo.

4. Anexos: Incluyen una serie de publicaciones derivadas del estudio de la actividad farmacológica de los compuestos sintetizados descritos en los capítulos recogidos en esta Tesis Doctoral de las cuales soy coautor.

El objetivo general de la presente Tesis Doctoral es la síntesis de compuestos orgánicos heterocíclicos de diversa naturaleza y su evaluación biológica, y la síntesis de estereoisómeros de un compuesto en fase clínica. En concreto los tres objetivos generales son:

1. Síntesis de ligandos I_2-IR de elevada afinidad y selectividad y su evaluación farmacológica en modelos murinos de neurodegeneración. Exploración de isocianometilfosfonatos en reacciones multicomponentes consecutivas.

2. Síntesis de inhibidores de la enzima PEPCK-M y su evaluación biológica en un modelo *in vivo* como antitumorales.

3. Proyecto de servicio con industria farmacéutica: síntesis de estereoisómeros del compuesto en fase clínica 2b, **AR-15512**.

Para una mayor compresión de la memoria no se ha redactado siguiendo el orden cronológico de realización de los trabajos, sino que se presenta ordenada por proyectos.

Los compuestos sintetizados y los resultados de su evaluación biológica son de gran relevancia en el campo científico, ya que han dado lugar a numerosas publicaciones y participaciones en congresos internacionales que, han contribuido a la difusión de conocimiento científico.

En el primer proyecto, recogido en los *Capítulos 2* y *3*, los esfuerzos se han centrado en el diseño y síntesis de compuestos con núcleo de α-iminofosfonato bicíclico y benzofuranil-2-imidazol, respectivamente, que actúan como ligandos de I_2-IR con elevada afinidad y selectividad. Asimismo, dada la experiencia previa del grupo con el uso del PhosMic, en el *Capítulo 4*, se presenta la síntesis de bis(2-imidazolin-4-il)fosfonatos mediante reacciones multicomponentes consecutivas. Seguidamente, en el *Capítulo 5*, se describe un proyecto en el que se han diseñado y sintetizado heterociclos complejos con potencial actividad antitumoral inhibiendo la enzima PEPCK-M. Por último, en el *Capítulo 6*, se describe un proyecto de servicio con la industria farmacéutica donde se sintetizan un diastereómero y un enantiómero del candidato clínico **AR-15512** (Esquema 1.10).

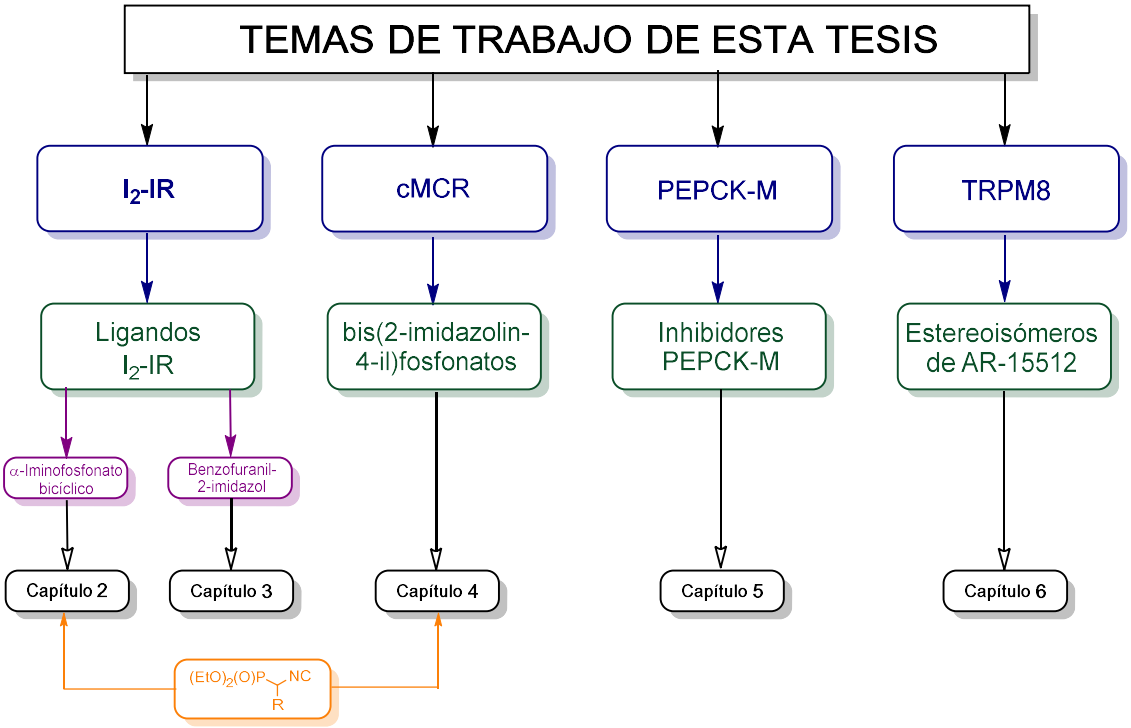

Esquema 1.10. Estructuració de la memoria.

A continuación, se describen brevemente cada uno de los diferentes capítulos de la presente Tesis Doctoral.

Capítulo 2. Bicyclic α-Iminophosphonates as High Affinity Imidazoline I_2 Receptor Ligands for Alzheimer's Disease

Como extensión de los estudios de la reacción de cicloadición [3+2] llevados a cabo en nuestro grupo de investigación,[22] se propuso la aplicación de esta metodología para la síntesis diastereoselectiva de una batería de compuestos con núcleo de α-iminofosfonato bicíclicos por reacción entre derivados del PhosMic, en especial los que contienen un fenilo en alfa del grupo isocianuro y, maleimidas diversamente sustituidas. Se estudió el perfil farmacológico de estos productos y resultaron tener una elevada afinidad y selectividad para los I_2-IR, sin presentar afinidad relevante por α_2-AR e I_1-IR en tejido de cerebro humano. Estos compuestos representan la primera familia de ligandos de los I_2-IR que no contienen el anillo de imidazol o imidazolina. Seguidamente, se realizaron estudios *in silico*, *in vitro* e *in vivo* de seguridad y metabolismo para descartar posibles riesgos biológicos de la familia, destacando el compuesto **B06**. El tratamiento agudo en ratones con **B06** disminuyó la FADD proapoptótica del hipocampo, un marcador clave en las acciones neuroprotectoras. Los estudios *in vivo* en un modelo murino de enfermedad de Alzheimer, 5xFAD, revelaron efectos beneficiosos en comportamiento y cognición. En resumen, la modulación de los I_2-IR por el α-iminofosfonato bicíclico **B06** puede representar una nueva opción terapéutica para el tratamiento de la AD (Figura 1.11).

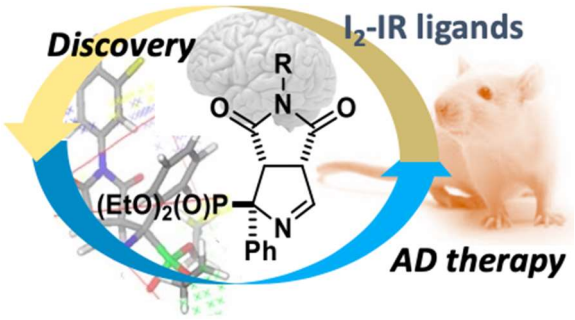

Figura 1.11. Figura representativa de este capítulo.

Capítulo 3. Benzofuranyl-2-imidazoles as Imidazoline I_2 Receptor Ligands for Alzheimer's Disease

El objetivo de este capítulo es la síntesis y evaluación farmacológica como ligandos I_2-IR de una serie de benzofuranil-2-imidazoles sustituidos. Seguidamente, los resultados del estudio de 3D-QSAR y ADMET *in silico* e *in vitro*, sumado al perfil farmacocinético óptimo del compuesto **LSL60101**, abrieron la puerta a los estudios *in vivo*. El tratamiento de ratones con **LSL60101** bajó la temperatura corporal y el contenido de la proteína

FADD proapoptótica en hipocampo. Asimismo, **LSL60101** dio lugar a una disminución de los biomarcadores de estrés oxidativo en el modelo murino 5xFAD. Todos estos resultados determinaron que **LSL60101,** con estructura de benzofuranil-2-imidazol, es un compuesto de interés como posible opción terapéutica para el tratamiento de AD (Figura 1.12).

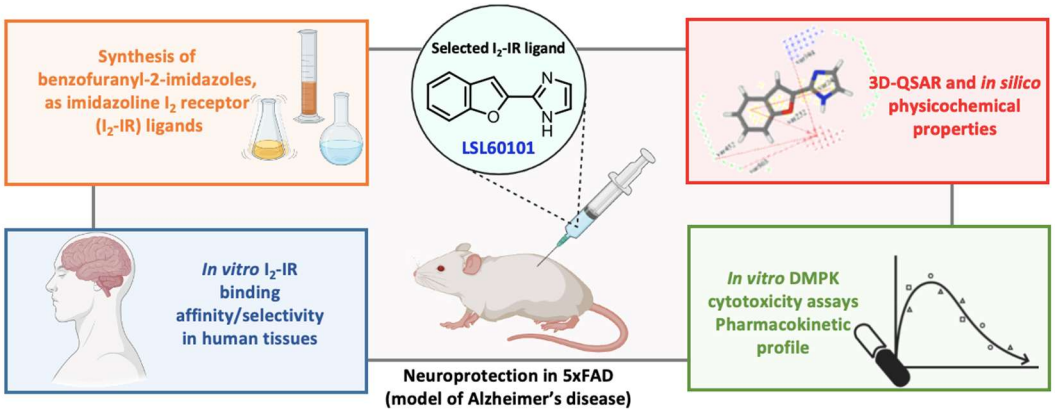

Figura 1.12. Figura representativa de este capítulo.

Capítulo 4. The first consecutive multicomponent reaction leading diastereoselectively to bis(2-imidazolin-4-yl)phosphonates (Manuscrito en preparación)

En el grupo habíamos descrito MCR que permitieron acceder a una familia de (2-imidazolin-4-il)fosfonatos.[22] Con estos precedentes nos propusimos aumentar la complejidad estructural de los compuestos a obtener, mediante el estudio de reacciones MCR consecutivas (cMCR). Estos productos contendrían dos unidades de (2-imidazolin-4-il)fosfonato y por lo tanto, como interés paralelo al proyecto se podría considerar su evaluación farmacológica, ya que serían moléculas resultantes de la duplicación molecular de compuestos que habían resultado de interés farmacológico como por ejemplo **MCR5** (Figura 1.13). Se llevaron a cabo diversas reacciones utilizando como reactivos diaminas, compuestos carbonílicos y PhosMic y derivados y se obtuvieron resultados sintéticos satisfactorios. El análisis cristalográfico de rayos X de uno de los compuestos preparados permitió determinar su estereoquímica relativa.

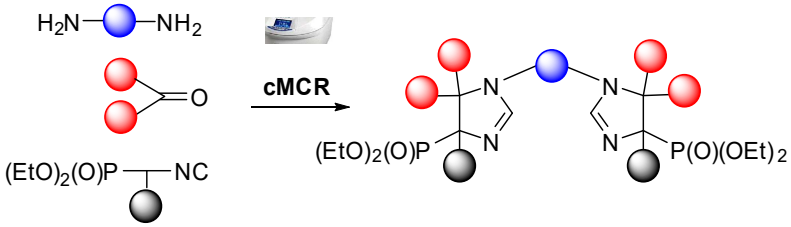

Figura 1.13. Figura representativa de este capítulo.

Capítulo 5. Pharmacology and preclinical validation of a novel anticancer compound targeting PEPCK-M

En este proyecto se sintetizaron inhibidores de la enzima PEPCK-C, con núcleo de 3-alquil-1,8-dibencilxantina, descritos por el Prof. Foley. Se evaluaron como inhibidores de la enzima PEPCK-M, en base a la similitud que existe entre ambas isoenzimas, resultando una IC_{50} del orden submicromolar que permitió, tras determinar un ADME *in vitro* preliminar y su perfil farmacológico, su estudio en un modelo *in vivo* como antitumorales. Asimismo, el *target engagement* se confirmó por el ensayo de *Cellular Thermal Shift Assay* (CETSA). Así, se demostró que el tratamiento de líneas celulares de carcinoma de colon y mama con **iPEPCK-2** inhibe la proliferación celular y disminuye la supervivencia celular en un entorno pobre en nutrientes. Finalmente, la administración diaria de **iPEPCK-2** en ratones con xenoinjerto subcutáneos redujo con éxito el crecimiento tumoral en comparación con el vehículo, sin pérdida de peso o cualquier signo de aparente toxicidad inducida por el tratamiento (Figura 1.14). Por lo tanto, se concluye que los compuestos sintetizados como inhibidores de la PEPCK-M presentan una actividad antitumoral relevante, remarcando el posible papel de este mecanismo de acción novedoso en la terapia cancerígena.

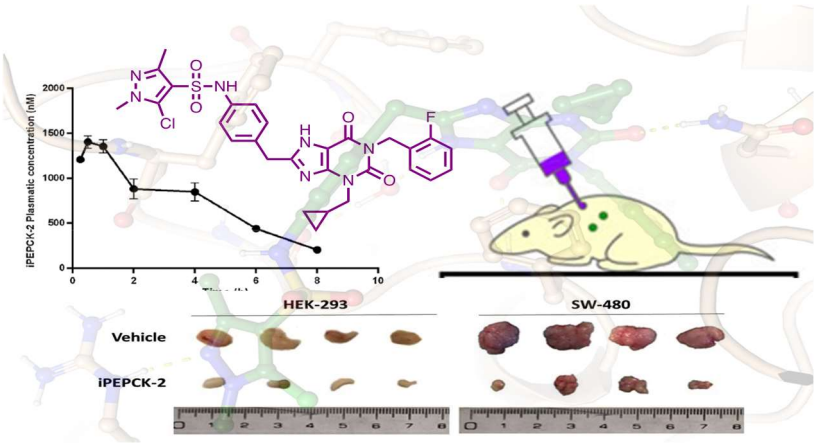

Figura 1.14. Figura representativa de este capítulo.

Capítulo 6. Synthesis, Characterization and HPLC Analysis of the (1S,2S,5R)-Diastereomer and the Enantiomer of the Clinical Candidate AR-15512.

Este último capítulo recoge los resultados de un proyecto de servicio con la empresa Avizorex Pharma S.L. donde se nos encargó la síntesis y caracterización completa de dos estereoisómeros de **AR-15512**, un agonista del TRPM8 en fase clínica 2b como solución oftálmica para el tratamiento del ojo seco. Este compuesto bioactivo con actividad refrigerante similar al mentol tiene tres centros estereogénicos con

configuración absoluta 1*R*, 2*S*, 5*R*. El proyecto implicaba la síntesis y caracterización de su diastereómero en *C*-1 (1*S*, 2*S*, 5*R*). Por otro lado, se sintetizó el enantiómero 1*S*, 2*R*, 5*S* de **AR-15512** para descartar su presencia en el producto final. Asimismo, la configuración absoluta del diastereómero (1*S*, 2*S*, 5*R*) se determinó inequívocamente por análisis cristalográfico de rayos X. Además, se proporcionaron dos métodos analíticos de HPLC diseñados y desarrollados para identificar ambos estereoisómeros y diferenciarlos del candidato clínico **AR-15512** (Figura 1.15).

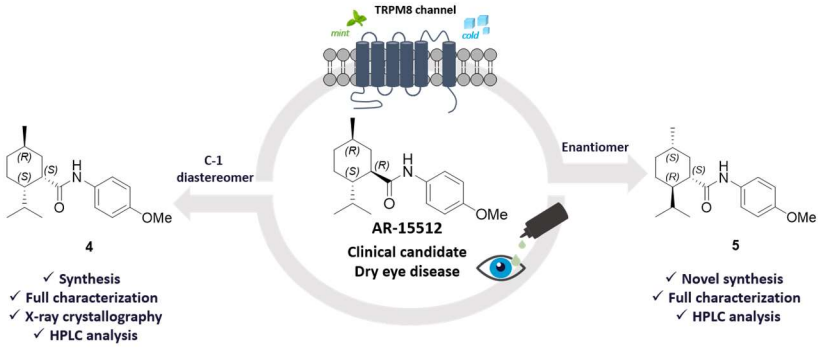

Figura 1.15. Figura representativa de este capítulo.

Capítulo 2. ***Bicyclic α-Iminophosphonates as High Affinity Imidazoline I_2 Receptor Ligands for Alzheimer's Disease***

2.1. *Journal of Medicinal Chemistry* 2020, *63*, 3610-3633

Bicyclic α-Iminophosphonates as High Affinity Imidazoline I_2 Receptor Ligands for Alzheimer's Disease

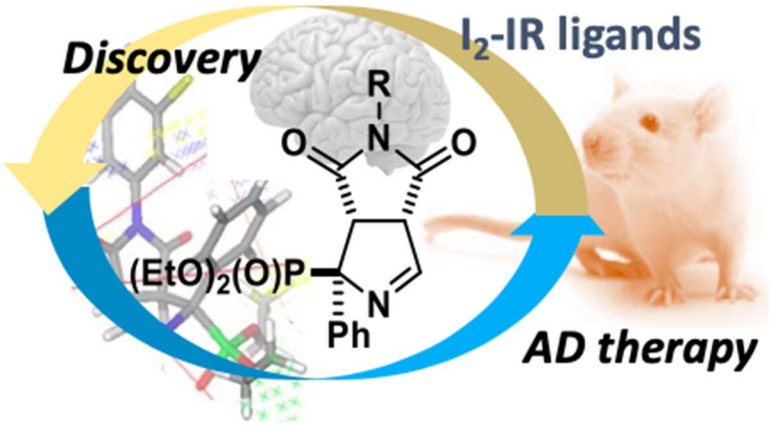

Journal of Medicinal Chemistry

pubs.acs.org/jmc Article

Bicyclic α-Iminophosphonates as High Affinity Imidazoline I_2 Receptor Ligands for Alzheimer's Disease

Sònia Abás,▲ Sergio Rodríguez-Arévalo,▲ Andrea Bagán, Christian Griñán-Ferré, Foteini Vasilopoulou, Iria Brocos-Mosquera, Carolina Muguruza, Belén Pérez, Elies Molins, F. Javier Luque, Pilar Pérez-Lozano, Steven de Jonghe, Dirk Daelemans, Lieve Naesens, José Brea, M. Isabel Loza, Elena Hernández-Hernández, Jesús A. García-Sevilla, M. Julia García-Fuster, Milica Radan, Teodora Djikic, Katarina Nikolic, Mercè Pallàs, Luis F. Callado, and Carmen Escolano*

Cite This: J. Med. Chem. 2020, 63, 3610−3633 Read Online

ACCESS | Metrics & More | Article Recommendations | Supporting Information

ABSTRACT: Imidazoline I_2 receptors (I_2-IR), widely distributed in the CNS and altered in patients that suffer from neurodegenerative disorders, are orphans from a structural point of view, and new I_2-IR ligands are urgently required for improving their pharmacological characterization. We report the synthesis and three-dimensional quantitative structure−activity relationship (3D-QSAR) studies of a new family of bicyclic α-iminophosphonates endowed with relevant affinities for human brain I_2-IR. Acute treatment in mice with a selected compound significantly decreased Fas-associated protein with death domain (FADD) in the hippocampus, a key signaling mediator of neuroprotective actions. Additionally, *in vivo* studies in the familial Alzheimer's disease 5xFAD murine model revealed beneficial effects in behavior and cognition. These results are supported by changes in molecular pathways related to cognitive decline and Alzheimer's disease. Therefore, bicyclic α-iminophosphonates are tools that may open new therapeutic avenues for I_2-IR, particularly for unmet neurodegenerative conditions.

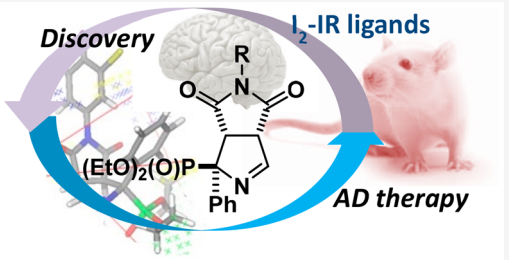

INTRODUCTION

The imidazoline receptors (IRs) (nonadrenergic receptors for imidazolines)[1] have attracted the attention of the scientific community during decades building a body of knowledge that place them as relevant biological targets.[2,3] IRs are classified in I_1-, I_2-, and I_3-types depending on the specific radiolabeled ligands that recognize their binding sites. These receptors are situated in different locations and are involved in different physiological functions.[4] I_1-, I_2-, and I_3-IRs have been unequally studied. Pharmacologically, I_1-IRs are well characterized and understood, leading to the clinically approved antihypertensive drugs moxonodine[5] and rilmenidine.[6] The most unknown are I_3-IRs, identified in pancreatic β-cells and involved in insulin secretion.[7] Regarding I_2-IRs, although structurally undescribed, a considerable understanding has been achieved on these heterogeneous receptors by using well-characterized I_2-IR ligands.[8] I_2-IRs are widely distributed in the brain and, at the molecular level, are located in the outer membrane of mitochondria. Selective I_2-IR ligands have proven that I_2-IRs are involved in analgesia,[9] inflammation,[10] and a plethora of human brain disorders.[11] Dysregulation of the levels of I_2-IRs is a hallmark in illnesses such as glial tumors,[12,13] Huntington's disease,[14] Parkinson's disease,[15] and depression,[16,17] among others. In particular, I_2-IRs are reported to be increased in the brains of patients that suffered from Alzheimer's disease (AD).[18,19] Recently, two I_2-IR ligands, CR4056 (**1**) and [^{13}C]BU99008 (**2**), have been progressed to clinical trials. CR4056 (**1**),[20,21] described as the first-in-class I_2-IR ligand embodying analgesic properties, is in clinical phase II studies for osteoarthritis and postoperative dental pain, and [^{13}C]BU99008 (**2**)[22,23] is in early clinical phase I for PET diagnosis for patients that suffer from AD.

The implication of I_2-IRs in many physiological and pathological processes emphasizes their pharmacological relevance, and the deserve in-depth studies. Since the structural data for I_2-IRs remains unknown, the discovery of better and more selective I_2-IR ligands is crucial to build a comprehensive understanding of the pharmacological implications of I_2-IR.

Although there are a few exceptions, LSL60101 (**3**) and most notably the clinical candidate CR4056 (**1**), the vast majority of known I_2-IR ligands (idazoxan, **4**; tracizoline, **5**, and 2-BFI, **6**) are 2-substituted 2-imidazolines without further decoration in the 1-, 4-, and 5-positions (Figure 1).[24]

Received: December 14, 2019
Published: March 9, 2020

https://dx.doi.org/10.1021/acs.jmedchem.9b02080
J. Med. Chem. 2020, 63, 3610−3633

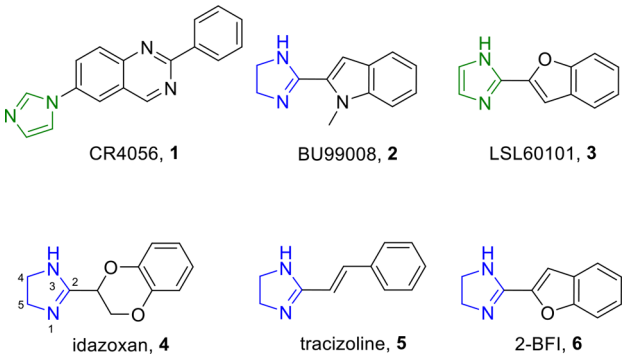

Figure 1. Representative I_2-IR ligands.

In order to explore new imidazoline-based I_2-IR ligands moving out of the comfort zone offered by the rather structurally homogeneous I_2-IR ligands reported so far (Figure 1), we have recently disclosed a family of (2-imidazolin-4-yl)phosphonates.[25,26] The putative therapeutic relevance of a member of this new family of I_2-IR ligands, MCR5 (**7**), was validated in a murine model of neurodegeneration, the senescence accelerated mouse-prone 8 (SAMP8).[27] An improvement in the cognitive decline and related biomarkers was found when MCR5 (**7**) was orally administered to the animals. This study was the first *in vivo* evidence that reinforced I_2-IRs as a promising target for the treatment of cognitive impairment associated with multiple neurodegenerative diseases.[27]

Separately, we had reported that the diastereoselective [3 + 2] cycloaddition of diethyl isocyanomethylphosphonate with 10 diversely substituted maleimides in acetonitrile under AgOAc catalysis furnished a series of bicycles of general structure **Ia** (Scheme 1a).[28] The presence within this series of compounds of an α-iminophosphonate unit, also featured in the above-mentioned (2-imidazolin-4-yl)phosphonates, prompted us to evaluate whether these bicyclo derivatives would also behave as I_2-IR ligands. We indeed found that two of these 10 already reported compounds, **8a** and **8c** (Scheme 1b), displayed an affinity for the I_2-IRs similar to that of idazoxan, **4** (see below). These promising results encouraged us to resume our research with this family of bicyclic α-iminophosphonates with the twofold aim of further exploring the scope of the aforementioned [3 + 2] cycloaddition reaction and of establishing their structure−activity relationships (SARs) as I_2-IR ligands.

Herein, we explore the synthetic scope of the [3 + 2] cycloaddition reaction of α-substituted PhosMic derivatives and diversely substituted maleimides. Particular attention was given to derivatives including a phenyl substituent in the α-position of the phosphonate leading to general structures **9** depicted as **Ib** in the Scheme 1a, in order to resemble the structure of MCR5, **7** (Scheme 1c). We also assessed the pharmacological profile and selectivity of a wide range of bicyclic α-iminophosphonates through competition binding studies against the selective I_2-IR radioligand [^{3}H]2-[(2-benzofuranyl)-2-imidazoline] ([^{3}H]2-BFI).[29] Selectivity versus two related targets, the I_1-IR and the α_2-adrenergic receptor (α_2-AR), was evaluated through competition studies using the selective radioligands [^{3}H]clonidine and [^{3}H]RX821002 (2-methoxyidazoxan), respectively. Complementarily, we performed 3D-QSAR studies. Compound **9d** (named also B06), endowed with outstanding I_2-IR affinity and excellent selectivity index regarding I_1-IR and α_2-AR, was selected for further studies. We first compared the affinity for the human I_2-IR of **9d** with those of the standards shown in Figure 1. Additionally, the affinity for I_2-IR from different species was considered for idazoxan (**4**) and **9d**. Next, we performed preliminary drug metabolism and pharmacokinetics (DMPK) studies for **9d**, including chemical stability, parallel artificial membrane permeability assay (PAMPA)−blood−brain barrier (BBB) permeability assay, solubility, cytotoxicity, microsomal stability, cytochromes inhibition, and safety. Finally, we characterized its *in vivo* neuroprotective effects in the 5xFAD murine model of AD.

RESULTS AND DISCUSSION

Chemistry. *Synthesis and Structural Characterization.* Considering the previously described compounds **8a** and **8c** as promising starting points for designing potent I_2-IR ligands, we resolved to prepare bicyclic compounds functionally close to MCR5 (**7**) by including an α-phenyliminophosphonate moiety in their structure. To this end, we decided to increase the

Scheme 1. (a) General Structure of Bicyclic α-Iminophosphonates Ia (Previously Reported) and Ib (Reported Herein),[a] (b) Chemical Structures of 8a and 8c, and (c) Chemical Structure of MCR5 (7)

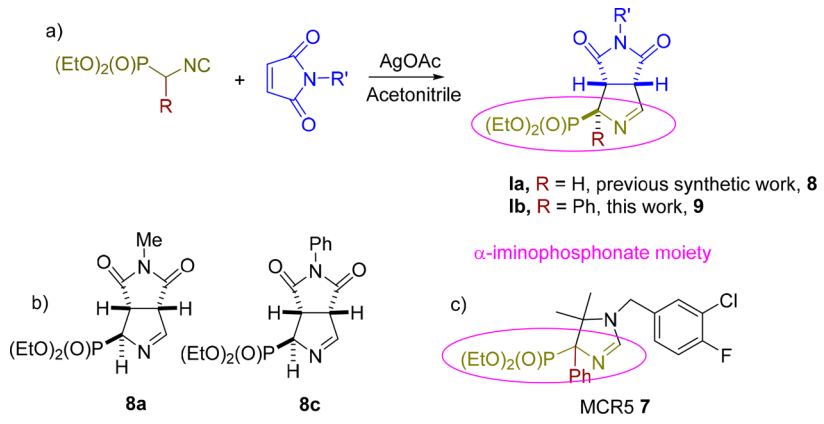

[a]Reagents and conditions: *N*-substituted maleimide derivative (1.5 mmol), PhosMic (1 mmol), AgOAc (0.06 mmol), acetonitrile, room temperature, overnight.

https://dx.doi.org/10.1021/acs.jmedchem.9b02080
J. Med. Chem. 2020, 63, 3610−3633

scope of the original [3 + 2] cycloaddition by using diversely α-substituted PhosMic derivatives (Figure 2).

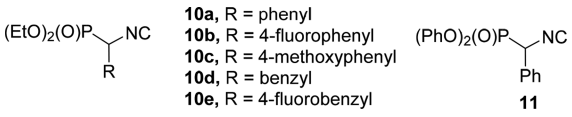

Figure 2. α-Substituted PhosMic derivatives used in this work.

The preparation of the α-substituted PhosMic derivatives was performed adapting previously described procedures (for references and experimental procedures, see Supporting Information). Briefly, the four phenylisocyanomethylphosphonates **10a**, **10b**, **10c**, and **11** were prepared by conversion of the required (α-aminophenyl)phosphonate derivative to the corresponding formamide followed by dehydration with phosphorus oxychloride. While diethyl (α-aminophenyl)-phosphonate is a commercially available compound, the other three precursors were synthesized according to published procedures. A different approach was followed for the α-benzylisocyano derivatives **10d** and **10e**. Alkylation of commercially available PhosMic with either benzylbromide or 4-fluorobenzylbromide, using potassium *tert*-butoxide furnished diethyl benzylisocyanomethylphosphonate **10d** and diethyl 4-fluorobenzylisocyanomethylphosphonate **10e**, respectively.

The maleimides used in the cycloaddition reaction were commercially available or were prepared following previously described procedures.

Gratifyingly, although the targeted compounds feature increased steric hindrance in the α-phosphonate position, our previously optimized set of conditions for the [3 + 2] cycloaddition reaction of maleimides with PhosMic also worked for the current set of α-substituted PhosMic derivatives.[28] In this way, 36 new bicycloderivatives (Schemes 2 and 3) having a quaternary stereocenter, were synthesized in medium to high yields (Experimental Section). The products were purified by column chromatography, and when they were solids, analytical samples were obtained by recrystallization. For the sake of clarity in the section I_2-IR Binding Activity and Structure−Activity Relationships, the new α-substituted bicycles, depicted in Schemes 2 and 3, were ordered and numbered attending to the SAR discussion.

Scheme 2. General Procedure for the Synthesis of Bicyclic α-Iminophosphonates[a]

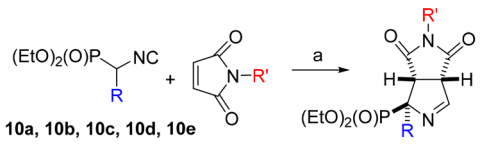

R'-	R- = H-	Ph-	4-FPh-	4-MeOPh-	$PhCH_2$-	$4FPhCH_2$-
Me	**8a**	**9a**				
cyclohexyl	**8b**	**9b**				
Ph	**8c**	**9c**	**12c**	**13c**	**14c**	**15c**
3-Cl,4-FPh	**8d**	**9d**	**12d**	**13d**		
4-MeOPh	**8e**	**9e**				

[a]Compounds prepared in previous work (R = H)[28] and compounds prepared in this work (R = Ph, 4FPh, 4-MeOPh, $PhCH_2$, $4FPhCH_2$). Reagents and conditions: (a) *N*-substituted maleimide derivative (1.5 mmol), α-substituted PhosMic (**10a**, **10b**, **10c**, **10d**, **10e**, 1 mmol), AgOAc (0.06 mmol), acetonitrile, room temperature, overnight.

Scheme 3. Second Round of Compounds Synthesized, Featuring Modified *N*-Maleimide Substituents Inspired by Compounds 9a and 9b, R′ = Alkyl, and 9c and 9d, R′ = Aryl[a]

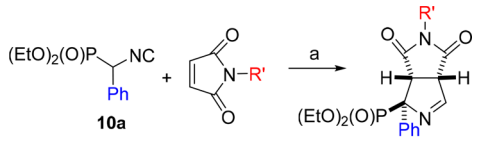

R'- = alkyl, 9a 9b

9f, ethyl
9g, propyl
9h, *t*-butyl
9i, (1-adamantyl)methyl-

9j, $PhCH_2$-
9k, $PhCH_2CH_2$-
9l, $4\text{-}FPhCH_2CH_2$-
9m, $Ph(CH_2)_2CH$-

R'- = aryl, 9c 9d

9n, $4\text{-}CF_3Ph$-
9o, $3\text{-}CF_3Ph$-
9p, 4-FPh-
9q, 4-ClPh-
9r, 2-ClPh-
9s, 3-ClPh-
9t, 4-BrPh-
9u, 3,5-diClPh-
9v, 3,4-diClPh-
9w, 2,4,6-triClPh-
9x, $3\text{-}NO_2Ph$-
9y, $3\text{-}NO_2,6\text{-}CH_3Ph$-

9z, 4-PhPh-
9aa, $4\text{-}CH_3Ph$-
9ab, 4-PhOPh-

9ac, 1-naphthyl
9ad, 2-Cl,3-pyridyl

[a]Reagents and conditions: (a) *N*-alkyl- or *N*-aryl-substituted maleimide derivative (1.5 mmol), α-PhenylPhosMic (**10a**, 1 mmol), AgOAc (0.06 mmol), acetonitrile, room temperature, overnight.

Analogously to our previous work,[28] all the [3 + 2] cycloaddition reactions occurred in a diastereoselective manner, and only one of the two possible diastereoisomers was formed. The relative configuration of the three stereocenters in the new compounds was unambiguously confirmed by X-ray crystallographic analysis for five examples, and the stereochemistry of the other compounds was assigned by comparison of their ^1H and ^{13}C NMR spectra (Tables S12 and S13).

As previously noted, the [3 + 2] cycloaddition reaction between α-substituted PhosMic derivatives and diversely substituted maleimides was completely diastereoselective, only one of the two possible diastereoisomers was observed. Iminophosphonates **9b**, **9c**, **9d**, **9v**, and **9ab** were recrystallized as monocrystals from ethyl acetate. Their relative configuration was unambiguously confirmed by X-ray crystallographic analysis, indicating a *trans* relationship between the hydrogen atoms on the bridged positions and the substituent at the α phosphonate carbon atom (Figure 3).

Finally, the origin of the diastereoselective [3 + 2] cycloaddition was investigated by quantum mechanical (QM) calculations that were performed for the addition of *N*-methylmaleimide to α-phenylPhosMic (in this latter case, the ethyl groups were replaced by methyl in order to reduce the cost of QM computations). In addition, a silver cation bound to acetonitrile was introduced to account for the catalytic effect on the chemical reaction. Reactants, transition states, and products for the *cis* and *trans* [3 + 2] cycloadditions were determined from geometry optimizations at the B3LYP/6-31+G(d) (LANL2DZ for silver) level, and the nature of the

https://dx.doi.org/10.1021/acs.jmedchem.9b02080
J. Med. Chem. 2020, 63, 3610−3633

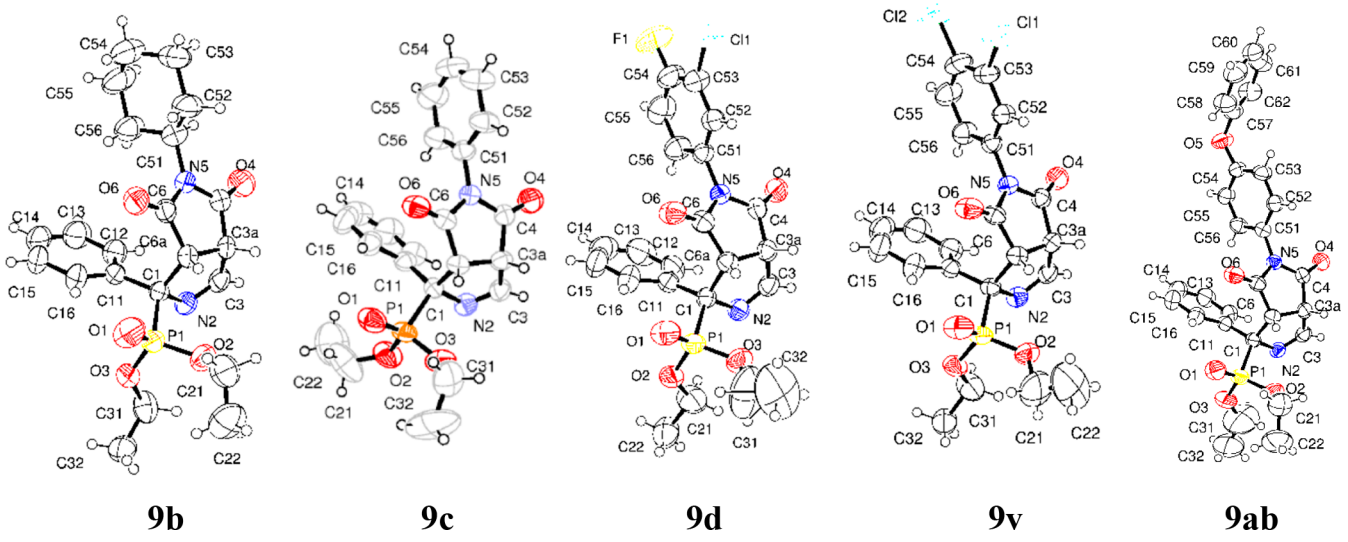

Figure 3. X-ray structures of **9b**, **9c**, **9d**, **9v**, and **9ab**.

stationary points was verified from the analysis of the vibrational frequencies. The geometries of the transition states point out that the cycloaddition occurs via an asynchronous concerted process as the length of the bond that is formed by carbon atom 3a is shorter than the bond formed by carbon atom 6a by 0.51 and 0.23 Å in the *cis* and *trans* addition, respectively (Figure 4). Moreover, a significant deviation from

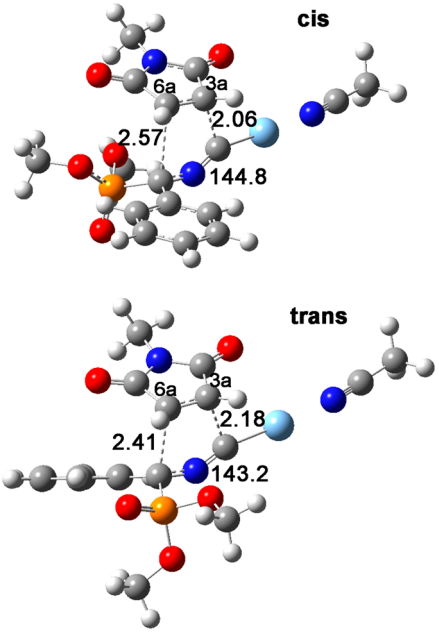

Figure 4. Representation of the transition states for the *cis* and *trans* [3 + 2] cycloaddition between *N*-methylmaleimide and *α*-phenyl-PhosMic (ethyl groups substituted by methyl) located from B3LYP calculations (C···C distances in Å; C−N−C angle in deg).

linearity is observed in the isocyano group, as the C−N−C angle is close to 144° in the two transition states. The results also point out that the transition state leading to the *trans* addition was more stable by 2.3 kcal mol^{-1} relative to the *cis* cycloaddition (Table S1), presumably due to the destabilizing electrostatic interactions between the oxygen atoms of the phosphonate and maleimide moieties. The preferred stability of the *trans* transition state was further checked by geometry optimizations performed for the *cis* and *trans* cycloadditions with the MN15L density functional, leading to a free energy difference of 1.2 kcal mol^{-1} favoring the *trans* cycloaddition. The contribution due to the solvation effects in acetonitrile was determined by means of continuum solvation calculations (see Experimental Section). The results (Table S1) reveal that solvation leads to a slight destabilization of the transition state relative to the reactants. Nevertheless, this effect cancels out for the *cis* and *trans* addition, which can be understood from the similar structural features of the two transition states. Overall, these results justify the preferential formation of the diastereoselective compound originating from the *trans* cycloaddition (Figure 4).

I_2-IR Binding Activity and Structure−Activity Relationships. The pharmacological activity of the compounds depicted in Schemes 2 and 3 was evaluated through competition binding studies against the selective I_2-IR radioligand [^{3}H]2-BFI and the selective α_2-AR radioligand [^{3}H]RX821002. The studies were performed in membranes from post-mortem human frontal cortex, a brain area that shows an important density of I_2-IR and α_2-AR.[30] Idazoxan (**4**), a compound with well-established affinity for I_2-IR (pK_i = 7.27 ± 0.07) and α_2-AR (pK_i = 7.51 ± 0.07), was used as reference. The inhibition constant (K_i) for each compound was obtained and is expressed as the corresponding pK_i (Table 1). The selectivity for these two receptors was expressed by the I_2-IR/α_2-AR index, calculated as the antilogarithm of the ratio between pK_i value for I_2-IR and pK_i value for α_2-AR (Table 1). Competition experiments against [^{3}H]2-BFI were monophasic for most of the compounds (for a few exceptions, see below).

Among the set of 10 bicycles of general structure **Ia** (Scheme 1a) already reported,[28] five representative compounds, **8a**, **8b**, **8c**, **8d**, and **8e**, were selected for evaluation as potential I_2-IR ligands considering the substitution in the *N*-maleimide by an alkyl (**8a**), cycloalkyl (**8b**), unsubstituted phenyl (**8c**), electron withdrawing-disubstituted phenyl (**8d**), and electron donating-substituted phenyl (**8e**) groups.

Pleasantly, **8a** and **8c** displayed pK_i I_2 affinity of 6.79 and 7.73, respectively, in the range of that of idazoxan (**4**) (7.41). However, no promising results were found for **8b**, **8d**, and **8e** (Table 1). As a first structural approximation, we turned our

https://dx.doi.org/10.1021/acs.jmedchem.9b02080
J. Med. Chem. 2020, 63, 3610−3633

Table 1. I_2-IR and α_2-AR Binding Affinities (pK_i) of Five Previously Reported Compounds 8[28] and New Compounds

Compound General structure	R-	R'-	pKi [a][3H]-2-BFI, I_2 one site [b][3H]-2-BFI, I_2 two sites H/L; High affinity site %	pKi [3H]-RX821002, α_2	[a]Selectivity I_2/α_2
Idazoxan			7.41 ± 0.63	8.35 ± 0.16	-
8a	H	Me	6.79 ± 0.51	9.49 ± 0.18	5
8b	H	cyclohexyl	5.74 ± 0.51	5.02 ± 0.58	-
8c	H	Ph	7.73 ± 0.19	8.49 ± 0.36	-
8d	H	3-Cl,4-FPh	<3	10.27 ± 0.32	-
8e	H	4-MeOPh	5.11 ± 0.13	6.14 ± 0.85	
9a	Ph	Me	7.97 ± 0.55	5.93 ± 0.41	110
9b	Ph	cyclohexyl	9.74 ± 0.29	9.01 ± 0.51	5
9c	Ph	Ph	10.28 ± 0.37	10.38 ± 0.22	1
9d	Ph	3-Cl,4-FPh	8.56 ± 0.32 8.61 ± 0.28/ 4.29 ± 0.20; 37 ± 4	6.27 ± 0.56	195 219
9e	Ph	4-MeOPh	6.65 ± 1.27	4.59 ± 0.22	115
12c	4-FPh	Ph	<3	6.77 ± 0.64	-
12d	4-FPh	3-Cl,4-FPh	7.55 ± 0.32	3.38 ± 0.33	14791
13c	4-MeOPh	Ph	3.39 ± 0.62	3.85 ± 0.31	-
13d	4-MeOPh	3-Cl,4-FPh	7.87 ± 0.40	<3	74131
14c	CH_2Ph	Ph	6.59 ± 0.77	3.94 ± 0.16	447
15c	4-FCH_2Ph	Ph	5.35 ± 0.35	7.20 ± 1.02	-
9f	Ph	Et	8.37 ± 0.27 8.95 ± 0.36/ 5.86 ± 0.66; 62 ± 11	5.85 ± 0.53	331 1259
9g	Ph	propyl	4.02 ± 0.41	±	-
9h	Ph	*t*-butyl	7.35 ± 0.43	6.77 ± 0.66	3
9i	Ph	(1-adamantyl)methyl	7.01 ± 0.76	4.31 ± 0.29	501
9j	Ph	$PhCH_2$	5.26 ± 0.22	8.11 ± 0.28	-
9k	Ph	$PhCH_2CH_2$	6.35±0.38	3.77 ± 0.09	380
9l	Ph	4-$FPhCH_2CH_2$	<3	5.65 ± 0.39	-
9m	Ph	$Ph(CH_2)_2CH_2$	3.84 ± 0.31 6.87 ± 0.81/ 3.20 ± 0.99; 22 ± 2	3.44 ± 0.28	2 2691
9n	Ph	4-CF_3Ph	<3	4.73 ± 0.60	-
9o	Ph	3-CF_3Ph	<3	±	-
9p	Ph	4-FPh	<3	5.34 ± 0.35	-
9q	Ph	4-ClPh	<3	±	-
9r	Ph	2-ClPh	5.09 ± 0.16 7.53 ± 0.66/ 4.74 ± 0.23; 25 ± 7	6.15 ± 0.44	- 24
9s	Ph	3-ClPh	<3	±	-
9t	Ph	4-BrPh	<3	±	-
9u	Ph	3,5-diClPh	5.81 ± 0.37	6.22 ± 0.26	-
9v	Ph	3,4-diClPh	<3	±	-
9w	Ph	2,4,6-triClPh	<3	5.16 ± 0.19	-
9x	Ph	3-NO_2Ph	6.81 ± 0.27	10.18 ± 0.41	-
9y	Ph	3-NO_2,6-CH_3Ph	<3	±	-
9z	Ph	4-PhPh	7.90 ± 0.46	5.12 ± 0.14	602
9aa	Ph	4-CH_3Ph	5.44 ± 0.16	±	-
9ab	Ph	4-PhOPh	6.96 ± 0.30	5.43 ± 0.21	34
9ac	Ph	1-naphthyl	3.11 ± 0.7	<3	-
9ad	Ph	2-Cl,3-pyridyl	7.96 ± 0.41	<3	91201

[a]Selectivity I_2-IR/α_2-AR expressed as the antilog (pK_i I_2-IR − pK_i α_2-AR). [b]The best fit of the data for **9d**, **9f**, **9m**, and **9r** was to a two-site binding model of binding with high pK_i (pK_{iH}) and low pK_i (pK_{iL}) affinities for both binding sites, respectively.

attention to compounds bearing a quaternary center in the α-position by including a phenyl group. In this manner, the new compounds would resemble the α-phenyliminophosphonate moiety of MCR5, **7** (in pink color in Scheme 1a,c). In order to maintain the homology with the first series of evaluated compounds (Scheme 2, R = H), analogous maleimide derivatives were considered to give access to compounds **9a**, **9b**, **9c**, **9d**, and **9e** (Scheme 2, R = phenyl). Indeed, this change was highly positive for the whole series, increasing the pK_i I_2 affinity for all the phenyl-substituted derivatives compared to their unsubstituted congeners, with the added benefit, in three cases (**9a**, **9d**, and **9e**), of an enhanced I_2-IR/α_2-AR selectivity ratio up to 195. A remarkable benefit in the I_2-IR affinity, pK_i I_2 9.74 (K_i = 0.18 nM), was observed in *N*-cyclohexyl derived **9b**, 4-fold improvement compared with analogous **8b**, with an I_2-IR/α_2-AR selectivity of 5. The rise in the affinity was also conserved in compounds bearing an *N*-arylimide substitution. In particular, the presence of an *N*-phenyl group **9c** led to an outstanding activity binding pK_i I_2 10.28 (K_i = 52.48 pM) but not I_2-IR/α_2-AR selectivity. Gratifyingly, introduction of halogen atoms (3-chloro-4-fluoro) in the *N*-phenyl ring of **9c** giving congener **9d** kept a nice affinity, with a pK_i I_2 8.56. Of note, **9d** fitted significantly better to a two-site binding model, with a high pK_i I_2 8.61 (K_{iH} = 2.45 nM) and a low pK_i I_2 4.29 (K_{iL} = 51.2 μM), with the high-affinity site representing a calculated 37% of the specific binding of [^{3}H]2-BFI at 2 nM concentration.

The enhancement, in terms of both affinity and selectivity, observed when moving from the α-unsubstituted to the α-substituted phosphonates prompted us to briefly consider additional variations. The introduction in the α-phosphonate position of *p*-fluorophenyl (**12c**) or *p*-methoxyphenyl (**13c**), benzyl (**14c**), and *p*-fluorobenzyl (**15c**) groups was highly deleterious for the affinity (pK_i I_2 = 6.59 for **14c** and pK_i I_2 < 3 up to 5.35 for **12c**, **13c**, and **15c**, respectively). However, for the *p*-substituted phenyl derivatives, the further introduction of halogen atoms (3-chloro-4-fluoro) in the *N*-phenyl ring (compounds **12d** and **13d**) nicely restored the affinity (pK_i I_2 7.55 for **12d** and pK_i I_2 7.87 for **13d**). Additionally, due to the lack of binding of **12d** and **13d** to α_2-AR, their I_2-IR/α_2-AR selectivity was outstanding, 14791 and 74131, respectively.

Taking into account the aforementioned results for a second round of compounds, the general structure depicted in Scheme 3 was conserved, featuring the unsubstituted phenyl group in the α-position of the phosphonate and modifying the substituents in the maleimide. New compounds were classified in two groups taking into consideration whether an alkyl or an aryl substituent was introduced in the *N*-maleimide.

Inspired by **9a** and **9b**, compounds bearing alkyl substituents with different lengths, **9f** and **9g**, ramified alkyl, **9h**, and polycycloalkane, **9i**, were prepared. From **9a**, the elongation of the *N*-alkyl chain, from methyl to ethyl, led to **9f**, with an increase in the affinity to pK_i I_2 = 8.37 (K_i = 4.3 nM) and in the I_2-IR/α_2-AR selectivity to 331, while the *n*-propyl derivative, **9g**, demonstrated much lower affinity, pK_i I_2 = 4.02. For **9f**, the best fit was a two-site model of binding with a high pK_i I_2 = 8.95 and a low pK_i I_2 = 5.86; high affinity site occupancy is 62%. Further increase of the size of the *N*-alkyl substituent to a *tert*-butyl, **9h**, or an adamantylmethyl, **9i**, did not improve the affinity. Taking together the affinity values for **9a**, **9b**, **9f**, **9g**, **9h**

https://dx.doi.org/10.1021/acs.jmedchem.9b02080
J. Med. Chem. 2020, 63, 3610−3633

and **9i**, it seems that small and large substituents are compatible with good affinity values but that conformational freedom, as in **9g**, is deleterious.

Compounds **9j**, **9k**, **9l**, and **9m**, with *N*-benzyl, *N*-phenethyl, *N*-4-fluorophenethyl, and *N*-phenylpropyl substituents, respectively, were accessed to increase the examples in the SAR study. However, their affinities revealed a remarkable decrease in the biological properties, leading to pK_i I_2 = 5.26, 6.35, <3, and 3.84 values, respectively.

Taking into account that **9c** displayed an outstanding affinity for I_2-IR but lacked selectivity over α_2-AR, further R′ = aryl derivatives were explored. As we knew that **9d** (pK_i I_2 = 8.56, I_2-IR/α_2-AR = 195) was endowed with excellent affinity and remarkable selectivity, we mainly focused on electron withdrawing groups (**9n**, **9o**, **9p**, **9q**, **9r**, **9s**, **9t**, **9u**, **9v**, **9w**, **9x**, and **9y**), although a few electron donating substituents were briefly examined (**9z**, **9aa**, and **9ab**). Overall, neither these new phenyl derivatives nor the *N*-naphthyl derivative **9ac** outperformed the excellent affinity of **9c** (Table 1), although **9z** (pK_i I_2 = 7.90) had an improved I_2-IR/α_2-AR ratio of 602. Finally, **9ad** with an *N*-(2-chloro-3-pyridyl) substituent gave a pK_i I_2 = 7.96, in the range of standard idazoxan (**4**), but it offered as an outstanding advantage a null affinity for α_2-AR, leading to an I_2-IR/α_2-AR selectivity of 91201.

Selectivity for I_2-IR versus I_1-IR. After evaluating the affinity of the indicated compounds for α_2-AR, we assessed the affinity of some representative compounds for I_1-IR. To this end, I_1-IR binding site assays were conducted in membranes obtained from the rat kidney using moxonidine, a known I_1-IR selective compound, as reference. The results are summarized in Table 2, and only **8e** deserves a mention with a pK_i I_1 8.09.

Table 2. I_1-IR Potencies (pIC_{50}) of Representative Compounds

compound	pIC_{50}, [^{3}H]-clonidine
moxonidine	8.45 ± 0.85
8a	5.13 ± 0.44
8b	5.14 ± 0.54
8c	5.47 ± 0.31
8d	<3
8e	8.09 ± 0.34
9a	6.19 ± 0.27
9b	7.54 ± 0.79
9c	6.74 ± 0.74
9d	3.04 ± 0.45
9e	3.22 ± 0.67
14c	5.12 ± 0.85
9j	5.87 ± 0.19
9k	7.98 ± 0.31
9x	5.26 ± 0.43
9z	7.19 ± 0.33

Gratifyingly, the values for the rest of the assessed compounds led to the conclusion that there was not a significant interaction with I_1-IR, highlighting the I_2-IR selective behavior of this family of ligands.

Overall, considering its excellent I_2-IR affinity (K_i = 2.8 nM) and the remarkable selectivity versus α_2-AR (K_i = 53 μM) and I_1-IR (K_i = 912 μM), we identified **9d** as the most promising compound for performing further studies.

Comparison of I_2-IR Human Receptor Binding Affinities (pK_i) of 9d and Other Ligands and across Species. A problem typically encountered when working with I_2-IR ligands is that the binding experiments reported in the bibliography have been performed in a variety of non-human species and using tissues from different anatomical parts (e.g., kidney, whole brain, cortex). Another factor of potential discrepancies is that different radioligands have been used. Overall, this makes difficult the comparison among studies. For this reason and in order to better place **9d** as a new I_2-IR ligand, unprecedented experiments of displacement of [^{3}H]2-BFI[31] in samples from post-mortem human brains were performed with clinical candidates [^{13}C]BU99008 (**2**)[32] and CR4056 (**1**)[33] and the widely used I_2-IR ligands tracizoline (**5**), LSL60101 (**3**), and 2-BFI (**6**) (Table 3).

As previously observed with **9d**, the affinity data found for BU99008 (**2**) and CR4056 (**1**) fit best to a two-site model of binding. In particular, BU99008 (**2**) showed a pK_{iH} I_2 = 6.89 (K_{iH} = 128 nM) and pK_{iL} I_2 = 3.82 (K_{iL} = 151 μM), and a good I_2-IR/α_2-AR selectivity ratio of 331. CR4056 (**1**) showed a pK_{iH} I_2 = 7.72 (K_{iH} = 19.0 nM) and pK_{iL} I_2 = 5.45 (K_{iL} = 3.5 μM) with an excellent I_2-IR/α_2-AR selectivity of 117490. The percentage of occupancy for the high affinity site was different for BU99008 (**2**) (51%) compared with CR4056 (**1**) (29%). Other well-established I_2-IR ligands, tracizoline (**5**), LSL60101 (**3**), and 2-BFI (**6**) also resulted in clearly biphasic curves. Tracizoline (**5**) displayed a pK_{iH} I_2 = 8.48 (K_{iH} = 3.3 nM) and pK_{iL} I_2 = 6.48 with an excellent I_2-IR/α_2-AR selectivity of 14125. 2-BFI (**6**) had a pK_{iH} I_2 = 9.87 (K_{iH} = 0.13 nM) and pK_{iL} I_2 = 7.94, with a good I_2-IR/α_2-AR selectivity of 1698, and LSL60101 (**3**) a pK_{iH} I_2 = 9.03 (K_{iH} = 0.9 nM) and pK_{iL} I_2 = 5.25 (K_{iL} = 5.6 μM), with a good I_2-IR/α_2-AR selectivity of 7244. The high-affinity site represented 38%, 21%, and 49% occupancy for tracizoline (**5**), 2-BFI (**6**), and LSL60101 (**3**), respectively (Table 3). Previous studies have reported [^{3}H]2-BFI identifying two binding sites in rabbit,[34] rat,[35,36] and human brain.[31] It remains unclear whether these two sites observed represent distinct receptors or interconvertible conformational states of the I_2-IR. For tracizoline (**5**), a single binding site of pK_i I_2 = 8.72, similar to the affinity described for human tissues, was described in the rabbit kidney membranes.[37] In the rat cerebral cortex, LSL60101 (**3**) shows lower affinity than in human tissues, with a K_{iH} = 350 nM and K_{iL} = 116 μM.[38]

Therefore, compounds BU99008 (**2**), tracizoline (**5**), and 2-BFI (**6**), which have a nonsubstituted 2-(imidazolin-2-yl) group, CR4056 (**1**) and LSL60101 (**3**), which feature an imidazole ring, and the structurally dissimilar **9d** have similar affinity profiles to I_2-IR in human brain.

Of note, the ability of BU99008 (**2**) to displace [^{3}H]2-BFI from I_2-IR in rat brain was fit to a two-site model of binding, with a K_{iH} = 1.4 ± 0.6 nM and K_{iL} = 238.6 ± 63.3 nM and with a percentage fraction of high occupancy of 58% ± 7%. That is, an enhanced affinity by 100 times in rat brain compared with human brain, the % of occupancy being similar in the high site. Regarding selectivity, a good I_2-IR/α_2-AR ratio of 909 was reported in rat, 4.5 times higher than that found in human. Of note, the opposite trend was found for CR4056 (**1**): the inhibition recorded in rat whole-brain for [^{3}H]2-BFI binding was IC_{50} of 596 ± 76 nM, with an improved affinity of 19 nM shown in human brain.[39] Therefore, significant differences between species occur within the two I_2-IR ligands in clinical trials, BU99008 (**2**) and CR4056 (**1**).

In an attempt to incorporate additional data regarding the differences in I_2-IR binding affinities between species, idazoxan

https://dx.doi.org/10.1021/acs.jmedchem.9b02080
J. Med. Chem. 2020, 63, 3610−3633

Table 3. I_2-IR and α_2-AR Binding Affinities (pK_i) of BU99008 2, CR4056 1, Tracizoline 5, LSL60101 3, and 9d in Post-mortem Human Brain Cortical Membranes

	[^{3}H]-2-BFI I_2 pK_i, two sites				
compound	high-affinity	low-affinity	high-affinity site (%)	[^{3}H]-RX821002 α_2 pK_i	selectivity I_2-IR/α_2-AR for [^{3}H]-2-BFI (high-affinity site)
BU99008, **2**	6.89 ± 0.21	3.82 ± 0.30	51 ± 6	4.37 ± 0.17	331
CR4056, **1**	7.72 ± 0.31	5.45 ± 0.15	29 ± 6	2.65 ± 1.24	117490
tracizoline, **5**	8.48 ± 0.51	6.48 ± 0.32	38 ± 13	4.33 ± 0.22	14125
2-BFI, **6**	9.87 ± 0.33	7.94 ± 0.11	21 ± 5	6.64 ± 0.38	1698
LSL60101, **3**	9.03 ± 0.21	5.25 ± 0.24	49 ± 4	5.17 ± 1.32	7244
9d	8.61 ± 0.28	4.29 ± 0.20	37 ± 4	6.27 ± 0.56	219

Table 4. I_2-IR Binding Affinities (pK_i) of Idazoxan 4 and 9d in the Brain Cortex of Different Species

	human		rat	mice
idazoxan, **4**	7.74 ± 0.10		7.17 ± 0.11	5.68 ± 0.31
9d	8.61 ± 0.28	4.29 ± 0.20	6.92 ± 0.35	6.41 ± 0.39

(**4**) and **9d** were investigated (Table 4). In our hands, idazoxan (**4**) gave similar results in human frontal cortex, pK_i 7.74, as compared to rat brain cortex, pK_i 7.17, and had considerably less affinity in mouse brain cortical membranes, pK_i 5.68. Importantly, differences for **9d** were found not only among species but also in its binding characteristics. As previously mentioned, the binding to I_2-IR in human frontal cortex displayed a biphasic curve, whereas a monophasic one was observed in rat and mouse brain cortex with affinity values of pK_i 6.92 and 6.41, respectively.

Finally, in order to verify if the high affinity site observed for **9d** in competition experiments against [^{3}H]2-BFI corresponded to the I_2-IR, we performed additional experiments in the presence of MCR5 (**7**), a high-affinity I_2-IR selective compound previously reported by our group.[25] Interestingly, in the presence of MCR5 (**7**) (10^{-5} M), the **9d** competition curve against [^{3}H]2-BFI became monophasic (pK_i = 6.96 ± 0.46), and the high-affinity site recognized by **9d** was completely blocked. These results confirm that the high affinity site bound by **9d** is the I_2-IR.

3D-QSAR Study. 3D-QSAR studies were performed to rationalize the differences in activity and gain insights for improved bicyclic α-iminophosphonate-based I_2-IR ligands. 3D-QSAR models were created using Pentacle program,[40] which calculates GRIND descriptors (GRIND and GRIND2) from molecular interaction fields, and were evaluated by internal and external validation parameters (Tables S2 and S3). The data set included structurally diverse bicyclic α-iminophosphonates (Schemes 2 and 3) with a wide range of binding activity on I_2-IR (pK_i I_2 = 3.11−10.28) and α_2-AR (pK_i α_2 = 3.38−10.27) ensuring the good quality and applicability of the 3D-QSAR models. Additionally, we added four I_2-IR standard ligands (tracizoline, **5**; idazoxan, **4**; BU99008, **2**; LSL60101, **3**) in both data sets to compare and validate our results. Created 3D-QSAR models were used to analyze statistically significant variables that describe distance between chemical groups in the examined compounds. These variables are presented as interactions between two same (e.g., DRY−DRY) or different (e.g., DRY−TIP) MIF probes in PLS coefficient plots (Figures S1 and S2).

Describing the most significant GRIND variables with positive and negative influence on I_2-IR and α_2-AR binding activity gave us the deeper insight into crucial interactions for enhancing activity and selectivity on I_2-IR against α_2-AR. Based on comprehensive 3D-QSAR analysis presented in Supporting Information, we can conclude that the presence of two steric hot spots (var183, TIP−TIP), such as halogen atoms (3-chloro-4-fluoro) in the *N*-phenyl ring at the distance range 6.00−6.40 Å, may be crucial for enhancing I_2-IR binding activity and selectivity. The highest values are calculated for compounds **13d** and **12d**, which possess high selectivity toward I_2-IR (Figure 5B). Likewise, var19 (DRY−DRY, 7.60−8.00 Å) implies that introduction of hydrophobic regions such as phenyl ring in the *N*-maleimide group may be crucial for establishing favorable van der Waals interactions with aromatic amino acids of the active pocket of I_2-IR (Figure 5A,B). Comparing to compounds that possess *N*-alkyl substituents instead of *N*-phenyl, such as **8a** or **9a**, we can conclude that introduction of this aromatic ring positively correlates with I_2-IR binding activity. Contrarily, the α_2-AR model pointed out a negative DRY−DRY variable (var25, 10.00−10.40 Å), which suggests that introduction of a phenyl substituent in the α-phosphonate position negatively correlates with α_2-AR activity. This is in agreement with experimental findings, which show that α-substituted ligands possess higher affinity and selectivity toward I_2-IR (**8a**, **8c**, **8d**, and **8e**). Additionally, analysis of negative variables var200 (TIP−TIP, 12.80−13.20 Å), var314 (DRY−N1, 13.60−14.00 Å), and var377 (DRY−TIP, 16.40−16.80 Å) emphasizes that introduction of bulkier substituents in the *N*-maleimide group unfavorably affects the fit in the binding site of I_2-IR and may decrease the potency of I_2 ligands (Figure 6A,B). The highest values of these variables are pronounced in compounds **9z**, **9m**, **9k**, **9j**, **9ab**, and **9ac**.

***In Silico* Analysis of Physicochemical and Pharmacokinetic Parameters.** *In silico* analysis of key parameters is one of the most important steps in drug discovery processes.[41] Thus, ADMET Predictor software 9.5,[42] and SwissADME web tool[43] were used to foresee ADMET and physicochemical properties on the most potent bicyclic α-iminophosphonate I_2-IR ligands (pK_i > 7) and four standards. The obtained results are presented in the Supporting Information (Tables S4 and S5) including solubility and lipophilicity, BBB-penetration, elimination rate, and interactions with targets. Note that introduction of aromatic rings increases log *P* values and affinity for albumin, while it decreases the water solubility (**9d**, **9z**, **12d**, and **13d**). Based on results obtained from different computational methods, we can conclude that all examined compounds possess good water solubility and lipophilicity. Furthermore, calculated values of topological polar surface area (TPSA) descriptor revealed acceptable polarity of all

https://dx.doi.org/10.1021/acs.jmedchem.9b02080
J. Med. Chem. 2020, 63, 3610−3633

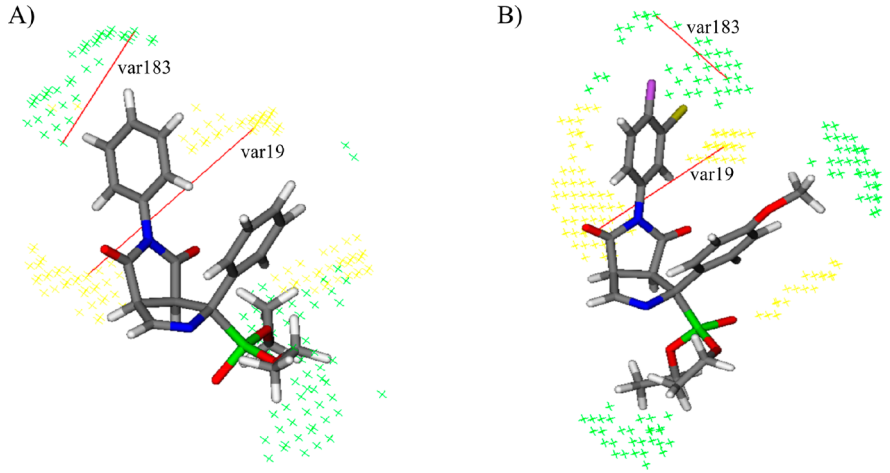

Figure 5. Representation of positive (in red) interactions of **9c** (A) and **13d** (B) in I_2-IR 3D-QSAR model. The steric hot spots (TIP) are presented in green and hydrophobic regions (DRY) in yellow.

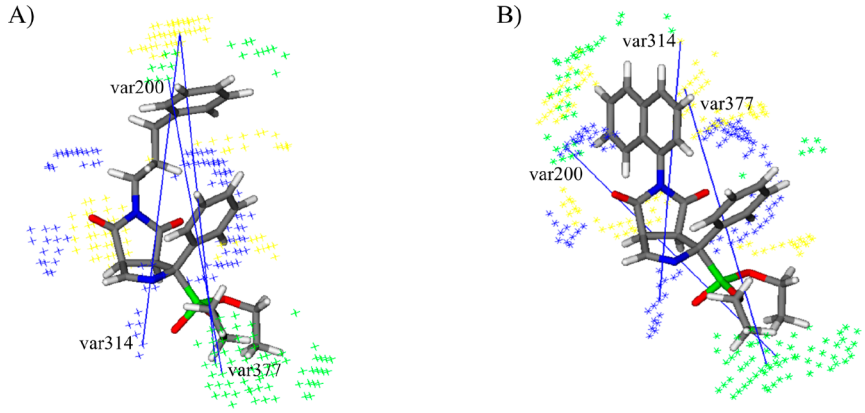

Figure 6. Representation of negative (in blue) interactions of **9m** (A) and **9ac** (B) in I_2-IR 3D-QSAR model. The steric hot spots (TIP) are presented in green, hydrophobic regions (DRY) in yellow, and H-bond acceptor regions (N1) in blue.

molecules. The Lipinski's Rule of 5 was used to describe drug-likeness properties of compounds based on physicochemical analysis (M log $P \leq 4.15$; MW ≤ 500; N or O ≤ 10; OH or NH ≤ 5). Because of the slightly higher molecular weight, **9z** and **13d** violated only one rule. Analysis of pharmacokinetic parameters shows that all compounds possess high BBB permeation. Compared to standards, bicyclic α-iminophosphonates have lower percentage of unbound drug in plasma. Also, they are estimated to have lower metabolic CYP risk compared to idazoxan. Only three compounds, **9z**, **12d**, and **13d** were identified as P-gp inhibitors. Performed calculations also show that bicyclic α-iminophosphonates possess lower toxicity risk, while compound **13d** had no predicted toxicity.

The theoretical effort paved the way to continue with crucial *in vitro* experiments (drug-like) due to the lack of warnings that had stopped the progress of this family of α-iminophosphonates as I_2-IR ligands.

BBB Permeation Assay. Considering the localization of I_2-IR in the CNS, a good ability to cross the BBB is an essential requirement for developing effective I_2-IR ligands with potential therapeutic applications in the neuroprotective field. For this reason, the *in vitro* permeability (P_e) of all the novel compounds was determined by using the PAMPA−BBB permeability assay (Table S6). In particular, our representative compound **9d** had a P_e value of $(9.7 \pm 0.7) \times 10^{-6}$ cm s^{-1}, well above the threshold established for high BBB permeation ($P_e >$ 5.198×10^{-6} cm s^{-1}). Thus, compounds were considered suitable to envisage further *in vitro* and *in vivo* studies oriented to in-depth pharmacological profiling of the new family of I_2-IR ligands.

Cytotoxicity. All the synthesized compounds were devoid of cytotoxicity in human embryonic lung fibroblast cell cultures (highest concentration tested, 100 μM). Further evaluation of eight selected compounds, including the outstanding I_2-IR ligands **9d**, **9b**, and **9c** and representative compounds **8d**, **9e**, **8b**, **9x**, and **9j** was performed in different mammalian cell lines, such as HeLa (human cervix carcinoma), Vero (African green monkey kidney), MDCK (Mandin-Darby canine kidney), and MT4 (human T-lymphocyte). Serial compound dilutions were added to semiconfluent cell cultures, and after 3−5 days incubation at 37 °C, cytotoxicity was estimated by microscopic inspection of cell morphology and by colorimetric cell viability assays. None of the compounds produced any cytotoxicity at 100 μM, the highest concentration tested. Additionally, the cytotoxicity of **9d** was tested in MRC-5 (human embryonic lung fibroblast) cells ($CC_{50} >$ 100 μM).

ADME−DMPK Profiling of 9d. In order to further progress **9d** to *in vivo* assays with the confidence that the *in silico* studies offered (see above), we evaluated its physicochemical properties, such as solubility and chemical stability, microsomal stability, cytochromes inhibition, hERG inhibition, and plasma protein binding.

https://dx.doi.org/10.1021/acs.jmedchem.9b02080
J. Med. Chem. 2020, 63, 3610−3633

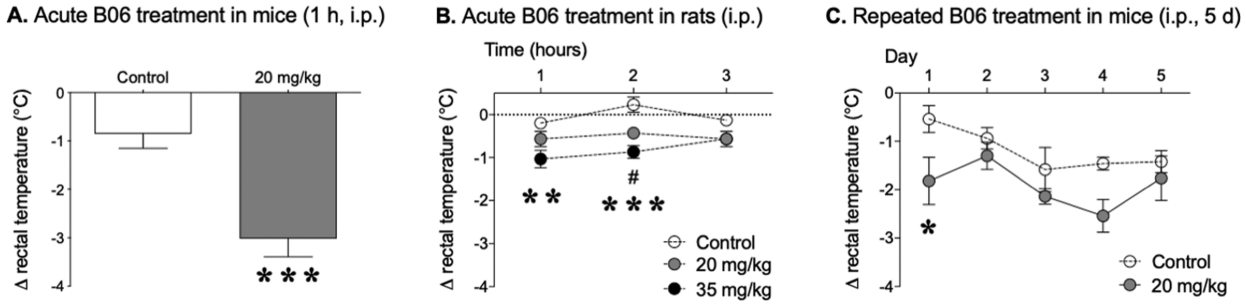

Figure 7. Hypothermic effects of **9d** (B06) in rodents. (A) Acute effect of **9d** (20 mg/kg, ip) in mice. Columns are means ± SEM of the difference (Δ, 1 h minus basal value) in body temperature (°C) for each treatment group. ***$p < 0.001$ vs control group (Student's *t*-test). (B) Acute effect of **9d** (20 or 35 mg/kg, ip) in rats. Columns are means ± SEM of the difference (Δ, 1, 2, or 3 h minus basal value) in body temperature (°C) for each treatment group. #$p < 0.05$ for dose of 20 mg/kg and **$p < 0.01$ and ***$p < 0.001$ for dose of 35 mg/kg vs control group (repeated measures ANOVA followed by Sidak's comparison test). (C) Repeated (5 days) effect of **9d** (20 mg/kg, ip) in mice. Circles are means ± SEM of the daily difference (Δ, 1 h minus basal value) in body temperature (°C) for each treatment group. *$p < 0.05$ vs control group (repeated measures ANOVA followed by Sidak's comparison test).

The solubility of **9d** was determined in several media. An excellent solubility of 92 μM was found in 1% DMSO and 99% PBS buffer. Additional solvents, methanol, acetonitrile, and water, were also evaluated with good solubility.[44] To evaluate the stability of **9d**, forced degradation studies were performed under various stress conditions for a period of 9 weeks, with HPLC and ^{1}H NMR monitoring every week.[45] Particularly, **9d** was subjected to the effect of daylight with temperatures between 0 and 23 °C and a relative humidity of 25−85%, to the effect of high temperature (thermal stability at 75 °C), and to the continuous light of a 100 W (230 V) bulb. Analysis by HPLC showed that the compound was completely stable under all the aforementioned conditions. Overall, these studies confirmed that **9d** is sufficiently stable to undertake further experiments.

Selected compound **9d** was further studied *in vitro* for ascertaining their microsomal stability, CYP inhibition, and protein plasma binding. The microsomal stability was assessed in three species (human, mouse, and rat), considering that the affinity and selectivity studies were performed in human samples, the cognition studies were envisaged in mice, and the hypothermia evaluation was planned in mice and rats (see below). Compound **9d** showed good microsomal stability (Table S7) and inhibited neither cytochromes [CYP1A2, CYP2C9, CYP2C19, CYP3A4 (BFC and DBF), and CYP2D6] nor hERG. Plasma protein binding was measured in mice and human species (Table S8) with a slight difference that should be taken into consideration if **9d** progress through additional preclinical studies.

Receptor Characterization Panel. In a Lead Profiling Screen (Eurofins)[46] of 44 potential off targets, **9d** showed a clean ancillary pharmacology (Table S9). Only one target, the cholecystokinin type A receptor (CCK_A), was inhibited more than 50% at the tested concentration of 10 μM. CCK receptors belong to the G-protein-coupled receptor superfamily and are involved in a range of biological actions mediated by two distinct receptor types, CCK_A (present in gastrointestinal tract and discrete regions of the brain) and CCK_B (present in the CNS).[47] Compound **9d** exhibited an IC_{50} of 5.94 μM upon CCK_A and an IC_{50} > 10 μM for CCK_B. Taking into account the relative high IC_{50} of **9d** for CCK_A and the lack of significant interaction with the other off targets evaluated, we conclude that **9d** shows a very selective profile.

Hypothermic Effects of 9d. It is known that I_2-IR ligands such as idazoxan (**4**) or 2-(4,5-dihydroimidazol-2-yl)quinoline (BU224) induce hypothermia in rats.[48,49] We have also found hypothermic effects with compound MCR5 (**7**) in mice.[25,27]

In the same line, acute **9d** (20 mg/kg) exposure induced hypothermia in adult CD1 mice as observed by reductions of core body temperature (ranging from −1.8 to −3.0 °C) measured 1 h postinjection (Figure 7A,C, day 1). To test for differences between species, a pilot study was performed in adult rats, which showed that acute **9d** (20 and 35 mg/kg) treatment induced moderate drops in temperature (−0.4 to −1.0 °C) as measured 1 and 2 h postinjection (Figure 7B). Repeated administration of **9d** (20 mg/kg, 5 days) in mice revealed the induction of tolerance to the acute hypothermic effect of this drug from day 2 of treatment (Figure 7C), effects previously observed for other I_2-IR compounds.[25,27]

Of note, hypothermia is well established as having a neuroprotective effect in cerebral ischemia and even mild temperature drops cause significant neuroprotection.[50] Also, hypothermia has been clinically used to improve the neurological outcome under various pathological conditions, including stroke and traumatic brain injury.[51,52] Thus, the hypothermic effects showed by **9d** might be a relevant feature that could mediate neuroprotection.

Effects of Acute and Repeated Treatments with 9d on Hippocampal FADD Protein Content in Mice. FADD multifunctional protein is an adaptor of cell death receptors that can also mediate antiapoptotic or neuroprotective actions in rodents.[25,53,54] Acute treatment with **9d** significantly decreased (−30%) the content of FADD protein in the hippocampus when compared to vehicle-treated mice (Figure 8, left panel). Following repeated (5 days) administration, no effects were observed on FADD modulation (Figure 8, right panel). The significant decrease in hippocampal pro-apopototic FADD following acute **9d** treatment suggests that this compound might be mediating some of its neuroplastic or neuroprotective actions through the regulation of this key brain marker, similarly with other I_2-IR compounds.[25]

5xFAD *in Vivo* Behavioral Studies on Selected Compound 9d. Recently, we reported the first *in vivo* study that validates I_2-IR as a target for cognitive impairment using a mouse model of age-related cognitive decline and late-onset AD, the SAMP8, a murine model that displays a phenotype of accelerated aging.[27] To further support the effect of I_2-IR

https://dx.doi.org/10.1021/acs.jmedchem.9b02080
J. Med. Chem. 2020, 63, 3610−3633

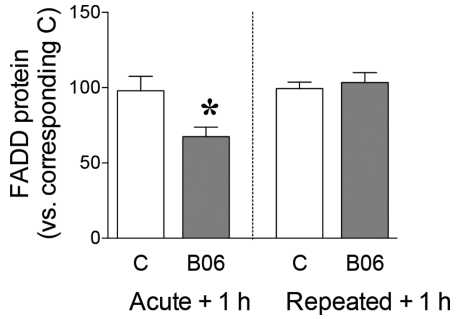

Figure 8. Effects of acute (20 mg/kg, ip) and repeated (20 mg/kg, ip, 5 days) treatments with **9d** (B06) on the contents of FADD protein in the hippocampus of mice. Columns are means ± SEM of FADD in **9d**- and vehicle-treated groups. *p < 0.05 vs control group (Student's t-test).

ligands as a putative treatment for neurodegenerative diseases, herein we evaluate **9d** in the 5xFAD, a well-established murine model of early on-set AD.[55]

Because one of the signs of AD is memory loss (cognitive decline), the effect of orally administered **9d** (5 (mg/kg)/day for 28 days) on cognitive performance was evaluated in the novel object recognition test (NORT). The NORT is a widely used behavioral task to assess visual recognition memory.[56] This brain activity relies on the hippocampus and involves the cortex to remember and recognize new and old objects. The NORT is based on an animal's innate preference for novelty. The task consists of three parts: a habituation phase; a training phase, where mice are presented with two identical objects; and a trial phase, in which following an interval time (2 or 24 h) memory was assessed by presenting the mice with a trained object and a novel one. Mice with cognitive ability preserved preferentially explore the novel object in the different time exposition studied. After a 2 h acquisition trial, one of the familiar objects was replaced with a novel object, and the time spent investigating each of the objects was recorded, and the discrimination index (DI) was calculated as the percentage of novel object interaction time relative to total interaction time during the retention trial. As expected, untreated 5xFAD did not exhibit differences between exploration times for the familiar and novel objects (DI close to 0), indicating deterioration or loss of memory for the familiar object. As shown in Figure 9A, the oral administration of **9d** to 5xFAD enhanced recognition memory at short-term, reaching DI values of WT mice (Figure 9A). Of note, 24 h after the retention trial, **9d** treated 5xFAD mice, explored the novel object for a longer time, obtaining a higher DI, indicative of preserved memory for the familiar object presented during the acquisition trial (Figure 9B). These results suggest that compound **9d** enhanced recognition memory during the NORT in 5xFAD mice.

Effects of Selected Compound 9d in 5xFAD Hippocampus: Neuroinflammation and Oxidative Stress Parameters. Inflammation is an omnipresent sign in neurodegeneration and can act as a propagation method for the deleterious effects for the characteristic event in AD.[57] Oxidative stress (OS) is another key risk factor that can promote ignition of degenerative processes.[58] The reduction in the memory impairment of the **9d** treated animals prompted us to determine indicators of brain neuroinflammation and OS by comparison of WT and 5xFAD mice (vehicle and **9d** treated). 5xFAD mice had higher gene expression of *Cxcl10* (C-X-C motif chemokine 10) and *Tnf-α* (tumor necrosis factor α) compared to WT mice (Figure 10A) that decreased after treatment of 5xFAD mice with **9d** (5 (mg/kg)/day). Of note, it has been reported that TNF-α contributes to amyloidogenesis via β-secretase regulation, apart from being involved in AD-related brain neuroinflammation.[59] In fact, when amyloid precursor protein (APP) processing was studied in treated 5xFAD mice, an increase in sAPPα, correlating with a significant decrease in sAPPβ protein levels, was determined compared with untreated mice (Figure 10B).

In reference to OS, 5xFAD mice showed no changes in gene expression for *iNOS* (inducible nitric oxide synthase, a pro-oxidant key driver)[60] and *Hmox1* (an enzyme implicated in antioxidant defense) (Figure 10A).[61] Those results correlated with published results in 5xFAD mice, and in agreement, **9d** treatment did not modify either *iNOS* or *Hmox1* (Figure 10A). Nonetheless, total levels of hydrogen peroxide (H_2O_2), although not significant, were higher in 5xFAD than in the WT and were reduced after **9d** treatment (Figure 10C). The increase of OS, without increases in *iNOS* expression, was also described in 5xFAD mice; concretely the increase in 4-HNE (4-hydroxy-2-nonenal), a protein derivative obtained when reactive species of oxygen, ROS (such as H_2O_2), increase, is significant in 6-month-old 5xFAD mice compared to WT mice.[62] All the evaluated parameters are consistent with a mild reduction in the oxidative environment in treated 5xFAD mice.

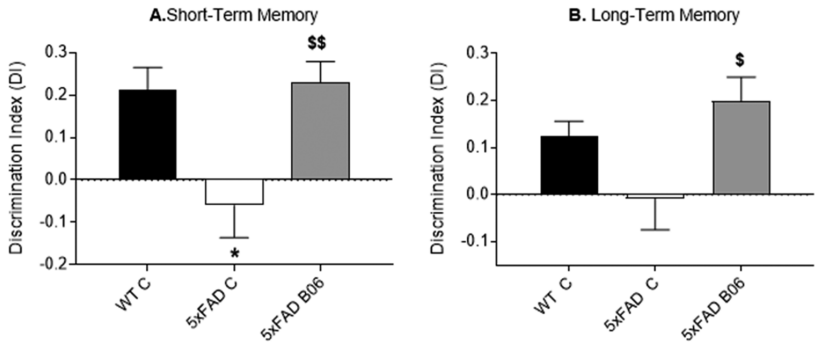

Figure 9. DI of NORT in 6-month-old (WT C, n = 12), 5xFAD (C, n = 14) control mice and 5xFAD mice after treatment with **9d** (B06) at 5 mg/kg for 4 weeks (n = 25). Summary from (A) Short-Term Memory and (B) Long-Term Memory. Values represented are mean ± standard error of the mean (SEM). One-way ANOVA followed by (Tukey post hoc test); P-value: *p < 0.05 vs WT-Control, $^{\$}p$ < 0.05; $^{\$\$}p$ < 0.01 vs 5xFAD-Control.

https://dx.doi.org/10.1021/acs.jmedchem.9b02080
J. Med. Chem. 2020, 63, 3610−3633

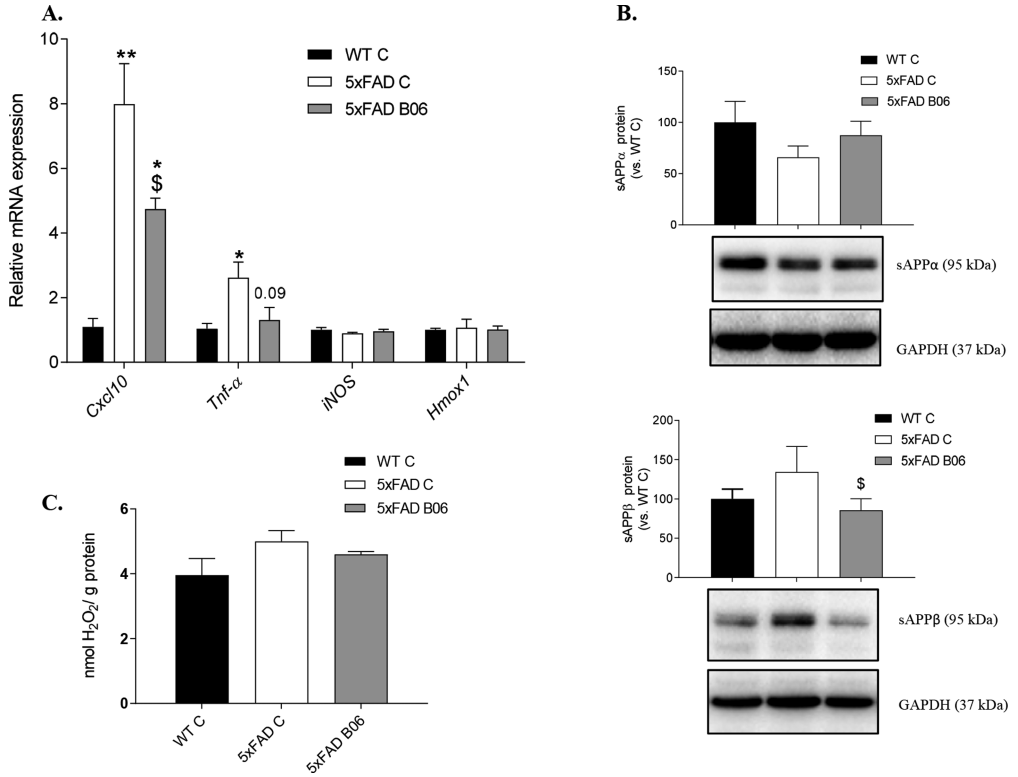

Figure 10. (A) Gene expression of inflammatory markers, *Cxcl10* and *Tnf-α*, and OS markers, *iNOS* and *Hmox1* (n = 4 for each group). (B) H_2O_2 concentration (n = 10 for each group) and (C) representative Western blot and bar chart sAPPα and sAPPβ (n = 4–6 for each group) in the hippocampus of 6-month-old female WT, 5xFAD Control mice, and 5xFAD mice after treatment with **9d** (B06) at 5 mg/kg for 4 weeks. Bars represent mean ± standard error of the mean (SEM).

CONCLUSIONS

To sum up, we have explored the scope of diastereoselective [3 + 2] cycloaddition reaction of α-substituted-PhosMic derivatives with diversely substituted maleimides leading to a family of bicyclic α-iminophosphonates. A combination of X-ray crystallographic analyses and NMR studies allowed a full stereochemical characterization, and theoretical calculations provided a basis to justify the excellent diastereoselectivity observed. The pharmacological profiling of the new compounds led to the identification of high affinity and selective I_2-IR ligands devoid of α_2-AR and I_1-IR affinities. 3D-QSAR study revealed key structural parameters for the design of future promising structures, and theoretical DMPK and physicochemical parameters were calculated in order to rule out warnings to continue the medicinal chemistry program. DMPK and cytotoxicity assays and a safety panel were carried out for the selected compound **9d**. Taking in account the improvement in the cognitive impairment in a 5xFAD model treated with **9d**, modulation of I_2-IR can be proposed as a new therapeutic strategy for AD treatment.

EXPERIMENTAL SECTION

Chemistry. *General Information.* Reagents, solvents, and starting products were acquired from commercial sources. The term "concentration" refers to vacuum evaporation using a Büchi rotavapor. When indicated, the reaction products were purified by flash chromatography on silica gel (35–70 μm) with the indicated solvent system. The melting points were measured in a MFB 59510M Gallenkamp instruments. IR spectra were performed in a spectrophotometer, Nicolet Avantar 320 FTR-IR or Spectrum Two FT-IR, and only noteworthy IR absorptions (cm^{-1}) are listed. NMR spectra were recorded in $CDCl_3$ at 400 MHz (^1H) and 100.6 MHz (^{13}C), and 162 MHz (^{31}P). Chemical shifts are reported in δ values downfield from TMS or relative to residual chloroform (7.26 ppm, 77.0 ppm) as an internal standard. Data are reported in the following manner: chemical shift, multiplicity, coupling constant (J) in hertz (Hz), integrated intensity, and assignment (when possible). Multiplicities are reported using the following abbreviations: s, singlet; d, doublet; dd, doublet of doublets; ddd, double doublet of doublets; dq, double quadrupet; t, triplet; qu, quintet; m, multiplet; br s, broad signal; app, apparent. Assignments and stereochemical determinations are given only when they are derived from definitive two-dimensional NMR experiments (g-HSQC–COSY). The accurate mass analyses were carried out using a LC/MSD-TOF spectrophotometer. The elemental analyses were carried out in a Flash 1112 series Thermofinnigan elemental microanalyzer (A5) to determine C, H, and N. HPLC-MS (Agilent 1260 Infinity II) analysis was conducted on a Poroshell 120 EC-C15 (4.6 mm × 50 mm, 2.7 μm) at 40 °C with mobile phase A (H_2O + 0.05% formic acid) and B (ACN + 0.05% formic acid) using a gradient elution and flow rate 0.6 mL/min. The DAD detector was set at 254 nm, the injection volume was 5 μL, and oven temperature was 40 °C. All tested compounds possess a purity of at least 95%.

General Procedure for the [3 + 2] Cycloaddition Reaction. To a solution of silver acetate (0.06–0.1 mmol) and maleimide (1.0–1.5 mmol) in acetonitrile was added diethyl α-methylisocyanomethylphosphonate, diethyl α-phenylisocyanomethylphosphonate, diphenyl α-phenylisocyanomethylphosphonate, diethyl α-(4-fluorophenyl)-isocyanomethylphosphonate, diethyl α-(4-methoxyphenyl)-isocyanomethylphosphonate, or diethyl α-benzylisocyanomethylphosphonate (1.0 mmol). The reaction mixture was stirred at room temperature overnight and concentrated, and the resulting residue was purified by column chromatography to afford pure products.

*Diethyl (1RS,3aSR,6aSR)-5-Methyl-4,6-dioxo-1-phenyl-1,3a,4,5,6,6a-hexahydropyrrolo[3,4-c]pyrrole-1-phosphonate (**9a**).* Following the general procedure, AgOAc (13 mg, 0.08 mmol), *N*-methylmaleimide (133 mg, 1.2 mmol), acetonitrile (6 mL), and diethyl α-phenylisocyanomethylphosphonate (202 mg, 0.8 mmol)

https://dx.doi.org/10.1021/acs.jmedchem.9b02080
J. Med. Chem. 2020, 63, 3610–3633

gave **9a** (184 mg, 64%) as a yellowish oil, after column chromatography (EtOAc/hexane 95:5). IR (NaCl) 3472, 2981, 1709, 1432, 1281, 1248, 1051, 967 cm^{-1}. ^1H NMR (400 MHz, $CDCl_3$, HETCOR) δ 1.15 (t, J = 7.0 Hz, 3H, CH_2CH_3), 1.27 (t, J = 7.0 Hz, 3H, CH_2CH_3), 2.70 (s, 3H, NCH_3), 3.83 (m, 1H, CH_2CH_3), 4.01−4.18 (m, 4H, H-6a and CH_2CH_3), 4.34 (ddd, J = 8.5, 4.0, 1.0 Hz, 1H, H-3a), 7.29−7.37 (m, 3H, ArH), 7.68−7.70 (m, 2H, ArH), 7.95 (dd, J = 5.5, 1.0 Hz, 1H, H-3). ^{13}C NMR (100.6 MHz) δ 16.1 (d, J = 5.0 Hz, CH_2CH_3), 16.2 (d, J = 5.0 Hz, CH_2CH_3), 25.0 (NCH_3), 47.7 (d, J = 2.0 Hz, C-6a), 60.5 (C-3a), 63.4 (d, J = 7.0 Hz, CH_2CH_3), 64.6 (d, J = 7.0 Hz, CH_2CH_3), 85.6 (d, J = 154.0 Hz, C-1), 127.6 (d, J = 2.0 Hz, 2CHAr), 128.4 (d, J = 2.5 Hz, CHAr), 128.5 (d, J = 6.0 Hz, 2CHAr), 133.2 (d, J = 4.5 Hz, C-*ipso*), 162.5 (d, J = 11.5 Hz, C-3), 172.1 (d, J = 5.5 Hz, CO), 172.5 (d, J = 14.0 Hz, CO). MS-EI m/z 364 M^+ (36), 255 (31), 227 (73), 199 (23), 170 (41), 143 (21), 142 (100), 115 (58). HRMS $C_{17}H_{22}N_2O_5P$ $[M + H]^+$ 365.1262; found, 365.1261. Purity 97.0% (t_R = 3.89 min).

*Diethyl (1RS,3aSR,6aSR)-5-Cyclohexyl-4,6-dioxo-1-phenyl-1,3a,4,5,6,6a-hexahydropyrrolo[3,4-c]pyrrole-1-phosphonate (**9b**).* Following the general procedure, AgOAc (15 mg, 0.09 mmol), *N*-cyclohexylmaleimide (403 mg, 2.3 mmol), acetonitrile (12 mL), and diethyl α-phenylisocyanomethylphosphonate (380 mg, 1.5 mmol) gave **9b** (494 mg, 76%) as a white solid, after column chromatography (EtOAc). Mp 128−132 °C (EtOAc). IR (NaCl) 3467, 2934, 2858, 1705, 1370, 1249, 1191, 1025, 971, 755 cm^{-1}. ^1H NMR (400 MHz, $CDCl_3$, HETCOR) δ 1.06−1.13 (m, 3H, CH_2cycl), 1.16 (t, J = 7.0 Hz, 3H, CH_2CH_3), 1.21 (m, 1H, CH_2cycl), 1.25 (t, J = 7.0 Hz, 3H, CH_2CH_3), 1.51−1.54 (m, 2H, CH_2cycl), 1.57−1.69 (m, 3H, CH_2cycl), 1.85 (m, 1H, CH_2cycl), 3.60 (m, 1H, CHcycl), 3.90 (m, 1H, CH_2CH_3), 4.03 (dd, J = 18.5, 8.5 Hz, 1H, H-6a), 4.06−4.18 (m, 3H, CH_2CH_3), 4.25 (ddd, J = 8.5, 3.0, 1.5 Hz, 1H, H-3a), 7.29−7.35 (m, 3H, ArH), 7.61−7.63 (m, 2H, ArH), 8.00 (dd, J = 5.0, 1.5 Hz, 1H, H-3). ^{13}C NMR (100.6 MHz) δ 16.1 (d, J = 5.5 Hz, CH_2CH_3), 16.2 (d, J = 5.5 Hz, CH_2CH_3), 24.7 (CH_2cycl), 25.6 ($2CH_2$cycl), 27.8 (CH_2cycl), 28.6 (CH_2cycl), 47.5 (d, J = 2.5 Hz, C-6a), 51.9 (CHcycl), 59.9 (C-3a), 63.3 (d, J = 7.5 Hz, CH_2CH_3), 64.6 (d, J = 7.5 Hz, CH_2CH_3), 85.7 (d, J = 156.0 Hz, C-1), 127.7 (d, J = 1.6 Hz, 2CHAr), 128.2 (CHAr), 128.3 (CHAr), 128.4 (CHAr), 133.6 (d, J = 4.0 Hz, C-*ipso*), 162.8 (d, J = 12.0 Hz, C-3), 172.1 (d, J = 5.5 Hz, CO), 172.5 (d, J = 12.0 Hz, CO). MS-EI m/z 432 M^+ (60), 323 (30), 295 (95), 223 (12), 170 (78), 142 (100), 115 (35), 81 (15). HRMS $C_{22}H_{30}N_2O_5P$ $[M + H]^+$ 433.1892; found, 433.1887. Anal. Calcd for $C_{22}H_{30}N_2O_5P$: C, 61.10%; H, 6.76%; N, 6.48%. Found: C, 61.42%; H, 6.81%; N, 6.47%.

*Diethyl (1RS,3aSR,6aSR)-4,6-Dioxo-1,5-diphenyl-1,3a,4,5,6,6a-hexahydropyrrolo[3,4-c]pyrrole-1-phosphonate (**9c**).* Following the general procedure, AgOAc (4 mg, 0.02 mmol), *N*-phenylmaleimide (104 mg, 0.6 mmol), acetonitrile (3 mL), and diethyl α-phenylisocyanomethylphosphonate (101 mg, 0.4 mmol) gave **9c** (108 mg, 64%) as a white solid, after column chromatography (EtOAc). Mp 158−160 °C (EtOAc). IR (NaCl) 3479, 2969, 1713, 1496, 1390, 1239, 1021, 969 cm^{-1}. ^1H NMR (400 MHz, $CDCl_3$, HETCOR) δ 1.10 (t, J = 7.0 Hz, 3H, CH_2CH_3), 1.19 (t, J = 7.0 Hz, 3H, CH_2CH_3), 3.85 (m, 1H, CH_2CH_3), 3.99−4.14 (m, 3H, CH_2CH_3), 4.17 (dd, J = 18.5, 9.0 Hz, 1H, H-6a), 4.40 (ddd, J = 8.5, 3.0, 1.6 Hz, 1H, H-3a), 6.62−6.65 (m, 2H, ArH), 7.15−7.30 (m, 6H, ArH), 7.61−7.63 (m, 2H, ArH), 7.97 (dd, J = 4.5, 1.6 Hz, 1H, H-3). ^{13}C NMR (100.6 MHz) δ 16.2 (d, J = 4.0 Hz, CH_2CH_3), 16.3 (d, J = 4.0 Hz, CH_2CH_3), 48.2 (d, J = 2.0 Hz, C-6a), 60.2 (C-3a), 63.4 (d, J = 7.0 Hz, CH_2CH_3), 64.6 (d, J = 7.0 Hz, CH_2CH_3), 86.2 (d, J = 157.0 Hz, C-1), 126.0 (2CHAr), 127.9 (CHAr), 128.0 (CHAr), 128.4 (d, J = 6.0 Hz, CHAr), 128.5 (CHAr), 128.6 (CHAr), 128.7 (CHAr), 129.0 (2CHAr), 131.1 (C-*ipso*), 133.5 (d, J = 4.0 Hz, C-*ipso*), 162.5 (d, J = 12.0 Hz, C-3), 170.9 (d, J = 5.5 Hz, CO), 171.6 (d, J = 11.5 Hz, CO). MS-EI m/z 426 M^+ (43), 317 (20), 289 (47), 244 (11), 170 (43), 142 (100), 115 (43), 81 (11). HRMS $C_{22}H_{24}N_2O_5P$ $[M + H]^+$ 427.1418; found, 427.1417. Anal. Calcd for $C_{22}H_{23}N_2O_5P$: C, 61.97%; H, 5.44%; N, 6.57%. Found: C, 62.18%; H, 5.36%; N, 6.43%.

*Diethyl (1RS,3aSR,6aSR)-5-(3-Chloro-4-fluorophenyl)-4,6-dioxo-1-phenyl-1,3a,4,5,6,6a-hexahydropyrrolo[3,4-c]pyrrole-1-phosphonate (**9d**).* Following the general procedure, AgOAc (8 mg, 0.05 mmol), *N*-(3-chloro-4-fluorophenyl)maleimide (250 mg, 1.1 mmol), acetonitrile (6 mL), and diethyl α-phenylisocyanomethylphosphonate (187 mg, 0.7 mmol) gave **9d** (189 mg, 54%) as a white needles, after column chromatography (EtOAc). Mp 185−186 °C (EtOAc). IR (NaCl) 3437, 2956, 1718, 1499, 1256, 1050, 980 cm^{-1}. ^1H NMR (400 MHz, $CDCl_3$, HETCOR) δ 1.20 (t, J = 7.0 Hz, 3H, CH_2CH_3), 1.28 (t, J = 7.0 Hz, 3H, CH_2CH_3), 3.95 (m, 1H, CH_2CH_3), 4.09−4.20 (m, 3H, CH_2CH_3), 4.25 (dd, J = 18.0, 8.0 Hz, 1H, H-6a), 4.47 (m, 1H, H-3a), 6.63 (ddd, J = 9.0, 4.0, 3.0 Hz, 1H, ArH), 6.72 (dd, J = 6.5, 2.5 Hz, 1H, ArH), 7.05 (t, J = 8.5 Hz, 1H, ArH), 7.35−7.39 (m, 3H, ArH), 7.67 (m, J = 5.0 Hz, 2H, ArH), 8.05 (d, J = 4.5 Hz, 1H, H-3). ^{13}C NMR (100.6 MHz) δ 16.3 (t, J = 5.5 Hz, $2CH_2CH_3$), 48.5 (C-6a), 60.1 (C-3a), 63.7 (d, J = 7.0 Hz, CH_2CH_3), 64.8 (d, J = 7.0 Hz, CH_2CH_3), 86.2 (d, J = 156.0 Hz, C-1), 116.8 (d, J = 22.5 Hz, CHAr), 121.5 (d, J = 19.5 Hz, C-*ipso*), 126.1 (d, J = 8.0 Hz, CHAr), 127.4 (d, J = 4.0 Hz, C-*ipso*), 128.1 (2CHAr), 128.3 (d, J = 5.5 Hz, 2CHAr), 128.6 (CHAr), 128.8 (CHAr), 133.5 (d, J = 3.0 Hz, C-*ipso*), 157.7 (d, J = 251.0 Hz, C-*ipso*), 162.0 (d, J = 12.5 Hz, C-3), 170.6 (d, J = 5.5 Hz, CO), 171.3 (d, J = 11.0 Hz, CO). ^{31}P NMR (162 MHz) δ 19.71. MS-EI m/z 478 M^+ (2), 341 (12), 281 (41), 207 (100), 191 (11), 147 (14), 73 (31). HRMS $C_{22}H_{22}ClFN_2O_5P$ $[M + H]^+$ 479.0935; found, 479.0933. Anal. Calcd for $C_{22}H_{21}ClFN_2O_5P$: C, 55.18%; H, 4.42%; N, 5.85%. Found: C, 55.28%; H, 4.49%; N, 5.56%.

*Diethyl (1RS,3aSR,6aSR)-5-(4-Methoxyphenyl)-4,6-dioxo-1-phenyl-1,3a,4,5,6,6a-hexahydropyrrolo[3,4-c]pyrrole-1-phosphonate (**9e**).* Following the general procedure, AgOAc (4 mg, 0.02 mmol), *N*-(4-methoxyphenyl)maleimide (122 mg, 0.6 mmol), acetonitrile (3 mL), and diethyl α-phenylisocyanomethylphosphonate (102 mg, 0.4 mmol) gave **9e** (119 mg, 65%) as a white solid, after column chromatography (EtOAc). Mp 167 °C (EtOAc). IR (NaCl) 3477, 2981, 2930, 1715, 1513, 1384, 1251, 1024, 970, 755 cm^{-1}. ^1H NMR (400 MHz, $CDCl_3$, HETCOR) δ 1.18 (t, J = 7.0 Hz, 3H, CH_2CH_3), 1.28 (t, J = 7.0 Hz, 3H, CH_2CH_3), 3.73 (s, 3H, OCH_3), 3.92 (m, 1H, CH_2CH_3), 4.09−4.19 (m, 3H, CH_2CH_3), 4.25 (dd, J = 18.0, 8.5 Hz, 1H, H-6a), 4.45 (ddd, J = 8.5, 3.0, 1.5 Hz, 1H, H-3a), 6.60−6.64 (m, 2H, ArH), 6.77−6.81 (m, 2H, ArH), 7.30−7.39 (m, 3H, ArH), 7.68−7.70 (m, 2H, ArH), 8.04 (dd, J = 5.0, 1.5 Hz, 1H, H-3). ^{13}C NMR (100.6 MHz) δ 16.2 (d, J = 3.5 Hz, CH_2CH_3), 16.3 (d, J = 3.5 Hz, CH_2CH_3), 48.1 (d, J = 2.0 Hz, C-6a), 55.4 (OCH_3), 60.1 (C-3a), 63.5 (d, J = 7.5 Hz, CH_2CH_3), 64.6 (d, J = 7.5 Hz, CH_2CH_3), 86.2 (d, J = 157.5 Hz, C-1), 114.3 (2CHAr), 123.6 (C-*ipso*), 127.2 (2CHAr), 127.9 (2CHAr), 128.3 (CHAr), 128.4 (CHAr), 128.5 (CHAr), 133.5 (d, J = 4.0 Hz, C-*ipso*), 159.5 (C-*ipso*), 162.4 (d, J = 12.0 Hz, C-3), 171.1 (d, J = 5.0 Hz, CO), 171.8 (d, J = 11.5 Hz, CO). HRMS $C_{23}H_{26}N_2O_6P$ $[M + H]^+$ 457.1519; found, 457.1523. Anal. Calcd for $C_{23}H_{25}N_2O_6P$: C, 60.52%; H, 5.52%; N, 6.14%. Found: C, 60.71%; H, 5.75%; N, 5.98%.

*Diethyl (1RS,3aSR,6aSR)-1-(4-Fluorophenyl)-4,6-dioxo-5-phenyl-1,3a,4,5,6,6a-hexahydropyrrolo[3,4-c]pyrrole-1-phosphonate (**12c**).* Following the general procedure, AgOAc (10 mg, 0.06 mmol), *N*-phenylmaleimide (156 mg, 0.9 mmol), acetonitrile (4 mL), and diethyl α-(4-fluorophenyl)isocyanomethylphosphonate (164 mg, 0.6 mmol) gave **12c** (159 mg, 60%) as a white solid, after column chromatography (EtOAc/hexane 4:1). Mp 191−193 °C (EtOAc). IR (ATR) 3491, 2991, 2909, 1775, 1718, 1598, 1506, 1377, 1242, 1189, 1016, 982, 742, 598 cm^{-1}. ^1H NMR (400 MHz, $CDCl_3$, HETCOR) δ 1.20 (t, J = 7.0 Hz, 3H, CH_2CH_3), 1.29 (t, J = 7.0 Hz, 3H, CH_2CH_3), 3.93 (m, 1H, CH_2CH_3), 4.08−4.19 (m, 3H, CH_2CH_3), 4.25 (dd, J = 18.0, 8.5 Hz, 1H, H-6a), 4.49 (dq, J = 8.5, 1.5 Hz, 1H, H-3a), 6.79−6.81 (m, 2H, ArH), 7.03−7.08 (m, 2H, ArH), 7.29−7.35 (m, 3H, ArH), 7.70−7.73 (m, 2H, ArH), 8.04 (dd, J = 5.0, 1.5 Hz, 1H, H-3). ^{13}C NMR (100.6 MHz) δ 16.4 (d, J = 5.5 Hz, CH_2CH_3), 16.5 (d, J = 5.0 Hz, CH_2CH_3), 48.1 (d, J = 3.0 Hz, C-6a), 60.5 (C-3a), 63.8 (d, J = 8.0 Hz, CH_2CH_3), 64.9 (d, J = 8.0 Hz, CH_2CH_3), 85.9 (d, J = 156.0 Hz, C-1), 114.9 (d, J = 2.0 Hz, CHAr), 115.1 (d, J = 2.0 Hz, CHAr), 126.2 (2CHAr), 129.0 (CHAr), 129.3 (2CHAr), 129.4 (dd, J = 4.0, 3.5 Hz, C-ipso), 130.6 (d, J = 6.0 Hz, CHAr), 130.7 (d, J = 6.0 Hz, CHAr), 131.1 (C-*ipso*), 162.8 (d, J = 12.0 H, C-3), 162.9 (dd, J = 246.0, 2.5 Hz, C-*ipso*), 171.0 (d, J = 6.0 Hz, CO), 171.8 (d, J = 12.0

https://dx.doi.org/10.1021/acs.jmedchem.9b02080
J. Med. Chem. 2020, 63, 3610−3633

Hz, CO). HRMS $C_{22}H_{23}FN_2O_5P$ $[M + H]^+$ 445.1323; found, 445.1324. Anal. Calcd for $C_{22}H_{22}FN_2O_5P$: C, 59.46%; H, 4.99%; N, 6.30%. Found: C, 59.90%; H, 5.13%; N, 6.20%.

*Diethyl (1RS,3aSR,6aSR)-5-(3-Chloro-4-fluorophenyl)-1-(4-fluorophenyl)-4,6-dioxo-1,3a,4,5,6,6a-hexahydropyrrolo[3,4-c]pyrrole-1-phosphonate (**12d**).* Following the general procedure, AgOAc (7 mg, 0.04 mmol), *N*-(3-chloro-4-fluorophenyl)maleimide (135 mg, 0.6 mmol), acetonitrile (3 mL), and diethyl α-(4-fluorophenyl)-isocyanomethylphosphonate (108 mg, 0.4 mmol) gave **12d** (124 mg, 62%) as a white solid, after column chromatography (EtOAc). Mp 179−181 °C (EtOAc). IR (ATR) 3483, 2962, 2903, 1719, 1504, 1236, 1051, 1012, 978, 739, 593 cm^{-1}. ^1H NMR (400 MHz, $CDCl_3$, HETCOR) δ 1.20 (t, *J* = 7.0 Hz, 3H, CH_2CH_3), 1.28 (t, *J* = 7.0 Hz, 3H, CH_2CH_3), 3.94 (m, 1H, CH_2CH_3), 4.08−4.19 (m, 3H, CH_2CH_3), 4.25 (dd, *J* = 18.0, 8.5 Hz, 1H, H-6a), 4.49 (ddd, *J* = 8.5, 3.0, 1.5 Hz, 1H, H-3a), 6.71 (m, 1H, ArH), 6.87 (dd, *J* = 6.5, 2.5 Hz, 1H, ArH), 7.04−7.09 (m, 3H, ArH), 7.68−7.71 (m, 2H, ArH), 8.02 (dd, *J* = 5.0, 1.5 Hz, 1H, H-3). ^{13}C NMR (100.6 MHz) δ 16.4 (d, *J* = 5.5 Hz, CH_2CH_3), 16.5 (d, *J* = 5.5 Hz, CH_2CH_3), 48.2 (d, *J* = 3.0 Hz, C-6a), 60.3 (C-3a), 63.9 (d, *J* = 7.0 Hz, CH_2CH_3), 64.9 (d, *J* = 8.0 Hz, CH_2CH_3), 86.0 (d, *J* = 156.0 Hz, C-1), 115.1 (dd, *J* = 21.0, 2.0 Hz, 2CHAr), 117.1 (d, *J* = 22.0 Hz, CHAr), 121.8 (d, *J* = 19.0 Hz, C-*ipso*), 126.1 (CHAr), 127.4 (d, *J* = 3.0 Hz, C-*ipso*), 128.7 (CHAr), 129.2 (dd, *J* = 4.0, 3.0 Hz, C-*ipso*), 130.6 (dd, *J* = 7.0, 2.0 Hz, 2CHAr), 157.9 (d, *J* = 251.0 Hz, C-*ipso*), 162.4 (d, *J* = 12.0 Hz, C-3), 163.0 (d, *J* = 249.5, 3.0 Hz, C-*ipso*), 170.5 (d, *J* = 5.0 Hz, CO), 171.5 (d, *J* = 13.0 Hz, CO). HRMS $C_{22}H_{21}ClF_2N_2O_5P$ $[M + H]^+$ 497.0839; found, 497.0840. Anal. Calcd for $C_{22}H_{20}ClF_2N_2O_5P$: C, 53.19%; H, 4.06%; N, 5.64%. Found: C, 53.45%; H, 4.24%; N, 5.46%.

*Diethyl (1RS,3aSR,6aSR)-1-(4-Methoxyphenyl)-4,6-dioxo-5-phenyl-1,3a,4,5,6,6a-hexahydropyrrolo[3,4-c]pyrrole-1-phosphonate (**13c**).* Following the general procedure, AgOAc (8 mg, 0.05 mmol), *N*-phenylmaleimide (138 mg, 0.8 mmol), acetonitrile (4 mL), and diethyl α-(4-methoxyphenyl)isocyanomethylphosphonate (142 mg, 0.5 mmol) gave **13c** (155 mg, 69%) as a white solid, after column chromatography (EtOAc/hexane 4:1). Mp 184−186 °C (EtOAc). IR (ATR) 3481, 2986, 2914, 1785, 1713, 1607, 1511, 1386, 1247, 1189, 1021, 737, 694, 598 cm^{-1}. ^1H NMR (400 MHz, $CDCl_3$, HETCOR) δ 1.20 (t, *J* = 7.0 Hz, 3H, CH_2CH_3), 1.28 (t, *J* = 7.0 Hz, 3H, CH_2CH_3), 3.79 (s, 3H, OCH_3), 3.92 (m, 1H, CH_2CH_3), 4.08−4.18 (m, 3H, CH_2CH_3), 4.23 (dd, *J* = 18.0, 8.5 Hz, 1H, H-6a), 4.46 (ddd, *J* = 8.5, 3.0, 1.5 Hz, 1H, H-3a), 6.76−6.78 (m, 2H, ArH), 6.88 (d, *J* = 9.0 Hz, 2H, ArH), 7.27−7.32 (m, 3H, ArH), 7.60−7.63 (m, 2H, ArH), 8.02 (dd, *J* = 5.5, 1.5 Hz, 1H, H-3). ^{13}C NMR (100.6 MHz) δ 16.4 (d, *J* = 5.0 Hz, $2CH_2CH_3$), 48.3 (d, *J* = 3.0 Hz, C-6a), 55.3 (OCH_3), 60.3 (C-3a), 63.5 (d, *J* = 8.0 Hz, CH_2CH_3), 64.8 (d, *J* = 8.0 Hz, CH_2CH_3), 86.0 (d, *J* = 157.0 Hz, C-1), 113.4 (d, *J* = 2.0 Hz, 2CHAr), 125.5 (d, *J* = 4.0 Hz, C-*ipso*), 126.3 (2CHAr), 128.8 (CHAr), 129.2 (2CHAr), 129.9 (d, *J* = 6.0 Hz, 2CHAr), 131.2 (C-*ipso*), 159.7 (d, *J* = 2.0 Hz, C-*ipso*), 162.3 (d, *J* = 12.0 Hz, C-3), 171.2 (d, *J* = 6.0 Hz, CO), 171.9 (d, *J* = 12.0 Hz, CO). HRMS $C_{23}H_{26}N_2O_6P$ $[M + H]^+$ 457.1523; found, 457.1520. Anal. Calcd For $C_{23}H_{25}N_2O_6P$: C, 60.52%; H, 5.52%; N, 6.14%. Found: C, 60.85%; H, 5.51%; N, 5.94%.

*Diethyl (1RS,3aSR,6aSR)-5-(3-Chloro-4-fluorophenyl)-1-(4-methoxyphenyl)-4,6-dioxo-1,3a,4,5,6,6a-hexahydropyrrolo[3,4-c]pyrrole-1-phosphonate (**13d**).* Following the general procedure, AgOAc (8 mg, 0.05 mmol), *N*-(3-chloro-4-fluorophenyl)maleimide (181 mg, 0.8 mmol), acetonitrile (4 mL) and diethyl α-(4-methoxyphenyl)isocyanomethylphosphonate (142 mg, 0.5 mmol) gave **13d** (170 mg, 67%) as a white solid, after column chromatography (EtOAc). Mp 227−228 °C (EtOAc). IR (ATR) 3481, 2986, 2905, 1771, 1718, 1612, 1497, 1386, 1237, 1184, 1026, 968, 752, 656 cm^{-1}. ^1H NMR (400 MHz, $CDCl_3$, HETCOR) δ 1.21 (t, *J* = 7.0 Hz, 3H, CH_2CH_3), 1.28 (t, *J* = 7.0 Hz, 3H, CH_2CH_3), 3.81 (s, 3H, OCH_3), 3.94 (m, 1H, CH_2CH_3), 4.09−4.18 (m, 3H, CH_2CH_3), 4.22 (dd, *J* = 18.0, 8.5 Hz, 1H, H-6a), 4.46 (ddd, *J* = 8.5, 3.0, 1.5 Hz, 1H, H-3a), 6.69−6.73 (m, 2H, ArH), 6.89 (d, *J* = 9.0 Hz, 2H, ArH), 7.07 (m, 1H, ArH), 7.59 (d, *J* = 7.5 Hz, 2H, ArH), 8.02 (dd, *J* = 5.0, 1.5 Hz, 1H, H-3). ^{13}C NMR (100.6 MHz) δ 16.4 (d, *J* = 5.0 Hz, CH_2CH_3), 16.5 (d, *J* = 5.0 Hz, CH_2CH_3), 48.6 (d, *J* = 3.0 Hz, C-6a), 55.3 (OCH_3), 60.1 (C-3a), 63.7 (d, *J* = 8.0 Hz, CH_2CH_3), 64.8 (d, *J* = 7.0 Hz, CH_2CH_3), 86.0 (d, *J* = 158.0 Hz, C-1), 113.5 (d, *J* = 1.0 Hz, 2CHAr), 117.0 (d, *J* = 22.0 Hz, CHAr), 121.7 (d, *J* = 19.0 Hz, C-*ipso*), 125.3 (d, *J* = 4.0 Hz, C-*ipso*), 126.2 (d, *J* = 8.0 Hz, CHAr), 127.5 (d, *J* = 4.0 Hz, C-*ipso*), 128.7 (CHAr), 129.8 (d, *J* = 6.0 Hz, 2CHAr), 157.9 (d, *J* = 250.0 Hz, C-*ipso*), 159.9 (d, *J* = 2.0 Hz, C-*ipso*), 161.8 (d, *J* = 13.0 Hz, C-3), 170.7 (d, *J* = 5.0 Hz, CO), 171.6 (d, *J* = 11.0 Hz, CO). HRMS $C_{23}H_{24}ClFN_2O_6P$ $[M + H]^+$ 509.1039; found, 509.1037. Anal. Calcd for $C_{23}H_{23}ClFN_2O_6P$: C, 54.29%; H, 4.56%; N, 5.51%. Found: C, 54.66%; H, 4.63%; N, 5.36%.

*Diethyl (1RS,3aSR,6aSR)-1-Benzyl-4,6-dioxo-5-phenyl-1,3a,4,5,6,6a-hexahydropyrrolo[3,4-c]pyrrole-1-phosphonate (**14c**).* Following the general procedure, AgOAc (8 mg, 0.05 mmol), *N*-phenylmaleimide (139 mg, 0.8 mmol), acetonitrile (6 mL), and diethyl α-benzylisocyanomethylphosphonate (213 mg, 0.8 mmol) gave **14c** (32 mg, 9%) as a yellowish oil, after column chromatography (EtOAc/hexane 1:1). IR (ATR) 3738, 2926, 2843, 1730, 1492, 1385, 1220, 1181, 1059, 1020, 782, 700 cm^{-1}. ^1H NMR (400 MHz, $CDCl_3$, HETCOR) δ 1.29 (t, *J* = 7.0 Hz, 3H, CH_2CH_3), 1.40 (t, *J* = 7.0 Hz, 3H, CH_2CH_3), 3.29 (dd, *J* = 15.0, 12.5 Hz, 1H, CH_2-Ar), 3.86 (dd, *J* = 15.0, 9.5 Hz, 1H, CH_2-Ar), 3.97 (dd, *J* = 19.0, 9.0 Hz, 1H, H-6a), 4.11−4.26 (m, 4H, CH_2CH_3), 4.39 (dq, *J* = 9.0, 1.5 Hz, 1H, H-3a), 6.73−6.75 (m, 2H, ArH), 7.10−7.12 (m, 3H, ArH), 7.21−7.23 (m, 2H, ArH), 7.33−7.36 (m, 3H, ArH), 7.82 (dd, *J* = 5.0, 1.5 Hz, 1H, H-3). ^{13}C NMR (100.6 MHz) δ 16.3 (d, *J* = 6.0 Hz, CH_2CH_3), 16.5 (d, *J* = 6.0 Hz, CH_2CH_3), 36.8 (d, *J* = 2.0 Hz, CH_2−Ar), 45.9 (d, *J* = 3.0 Hz, C-6a), 59.9 (C-3a), 63.4 (d, *J* = 7.0 Hz, CH_2CH_3), 64.0 (d, *J* = 6.0 Hz, CH_2CH_3), 83.7 (d, *J* = 158.0 Hz, C-1), 126.5 (2CHAr), 126.7 (CHAr), 127.8 (2CHAr), 128.7 (CHAr), 128.8 (2CHAr), 131.0 (C-*ipso*), 131.8 (2CHAr), 134.9 (d, *J* = 12.0 Hz, C-*ipso*), 161.3 (d, *J* = 13.0 Hz, C-3), 171.1 (d, *J* = 6.0 Hz, CO), 173.1 (d, *J* = 8.0 Hz, CO). HRMS $C_{23}H_{26}N_2O_5P$ $[M + H]^+$ 441.1574; found, 441.1580. Additional column chromatography led to sample for testing. Purity 95.7% (t_R = 4.50 min).

*Diethyl (1RS,3aSR,6aSR)-1-(4-Fluorobenzyl)-4,6-dioxo-5-phenyl-1,3a,4,5,6,6a-hexahydropyrrolo[3,4-c]pyrrole-1-phosphonate (**15c**).* Following the general procedure, AgOAc (12 mg, 0.07 mmol), *N*-phenylmaleimide (121 mg, 0.7 mmol), acetonitrile (5 mL) and diethyl α-(4-fluorobenzyl)isocyanomethylphosphonate (200 mg, 0.7 mmol) gave **15c** (67 mg, 21%) as an oil, after column chromatography (EtOAc). IR (ATR) 3471, 2924, 2853, 1780, 1711, 1509, 1378, 1221, 1049, 1017, 968, 691 cm^{-1}. ^1H NMR (400 MHz, $CDCl_3$, HETCOR) δ 1.30 (td, *J* = 7.0, 0.5 Hz, 3H, CH_2CH_3), 1.40 (td, *J* = 7.0, 0.5 Hz, 3H, CH_2CH_3), 3.25 (dd, *J* = 14.5, 12.5 Hz, 1H, CH_2-Ar), 3.81 (dd, *J* = 14.5, 9.0 Hz, 1H, CH_2-Ar), 3.96 (dd, *J* = 19.0, 9.5 Hz, 1H, H-6a), 4.11−4.27 (m, 4H, CH_2CH_3), 4.39 (ddd, *J* = 9.5, 3.5, 1.5 Hz, 1H, H-3a), 6.76−6.82 (m, 3H, ArH), 7.14−7.19 (m, 2H, ArH), 7.33−7.47 (m, 4H, ArH), 7.82 (dd, *J* = 5.0, 1.5 Hz, 1H, H-3). ^{13}C NMR (100.6 MHz) δ 16.3 (d, *J* = 6.0 Hz, CH_2CH_3), 16.5 (d, *J* = 5.5 Hz, CH_2CH_3), 36.0 (CH_2Ar), 45.9 (d, *J* = 2.5 Hz, C-6a), 59.9 (C-3a), 63.4 (d, *J* = 7.5 Hz, CH_2CH_3), 64.4 (d, *J* = 7.0 Hz, CH_2CH_3), 83.7 (d, *J* = 159.5 Hz, C-1), 114.5 (d, *J* = 2.0 Hz, 2CHAr), 126.3 (2CHAr), 128.9 (CHAr), 129.0 (2CHAr), 130.5 (d, *J* = 12.5. Hz, C-*ipso*), 130.9 (C-*ipso*), 133.4 (d, *J* = 8.0 Hz, 2CHAr), 161.5 (d, *J* = 12.5 Hz, C-3), 161.8 (d, *J* = 245.5 Hz, C-*ipso*), 171.0 (d, *J* = 6.0 Hz, CO), 173.2 (d, *J* = 12.5 Hz, CO). HRMS $C_{23}H_{25}FN_2O_5P$ $[M + H]^+$ 459.1480; found, 459.1483. Purity 96.4% (t_R = 4.56 min).

*Diethyl (1RS,3aSR,6aSR)-5-Ethyl-4,6-dioxo-1-phenyl-1,3a,4,5,6,6a-hexahydropyrrolo[3,4-c]pyrrole-1-phosphonate (**9f**).* Following the general procedure, AgOAc (11 mg, 0.07 mmol), *N*-ethylmaleimide (213 mg, 1.7 mmol), acetonitrile (8 mL), and diethyl α-phenylisocyanomethylphosphonate (279 mg, 1.1 mmol) gave **9f** (130 mg, 31%) as a yellowish oil, after column chromatography (EtOAc). IR (ATR) 3476, 2981, 2929, 1780, 1698, 1626, 1396, 1251, 1055, 1026, 968, 766 cm^{-1}. ^1H NMR (400 MHz, $CDCl_3$, HETCOR) δ 0.75 (t, *J* = 7.0 Hz, 3H, NCH_2CH_3), 1.15 (t, *J* = 7.0 Hz, 3H, CH_2CH_3), 1.25 (t, *J* = 7.0 Hz, 3H, CH_2CH_3), 3.21−3.27 (m, 2H, NCH_2CH_3), 3.88 (m, 1H, CH_2CH_3), 4.06−4.15 (m, 4H, CH_2CH_3 and H-6a), 4.29 (ddd, *J* = 8.5, 3.5, 1.5 Hz, 1H, H-3a), 7.31−7.34 (m, 3H, ArH), 7.65 (dbr, *J* = 11.6 Hz, 2H, ArH), 7.96 (dd, *J* = 5.0, 1.5 Hz,

https://dx.doi.org/10.1021/acs.jmedchem.9b02080
J. Med. Chem. 2020, 63, 3610−3633

1H, H-3). ^{13}C NMR (100.6 MHz) δ 12.6 (NCH_2CH_3), 16.4 (d, J = 5.5 Hz, CH_2CH_3), 16.4 (d, J = 5.5 Hz, CH_2CH_3), 34.0 (NCH_2CH_3), 47.9 (d, J = 2.0 Hz, C-6a), 60.5 (C-3a), 63.6 (d, J = 8.0 Hz, CH_2CH_3), 64.8 (d, J = 8.0 Hz, CH_2CH_3), 85.8 (d, J = 155.0 Hz, C-1), 127.9 (d, J = 1.0 Hz, 2CHAr), 128.6 (d, J = 2.0 Hz, 2CHAr), 128.6 (CHAr), 133.6 (d, J = 4.0 Hz, C-*ipso*), 162.7 (d, J = 12.0 Hz, C-3), 171.0 (d, J = 6.0 Hz, CO), 172.5 (d, J = 12.0 Hz, CO). HRMS $C_{18}H_{24}N_2O_5P$ [M + H]$^+$ 379.1417; found, 379.1418. Additional column chromatography led to sample for testing. Purity 95.5% (t_R = 4.06 min).

*Diethyl (1RS,3aSR,6aSR)-4,6-Dioxo-1-phenyl-5-propyl-1,3a,4,5,6,6a-hexahydropyrrolo[3,4-c]pyrrole-1-phosphonate (**9g**).* Following the general procedure, AgOAc (8 mg, 0.05 mmol), *N*-propylmaleimide (200 mg, 1.4 mmol), acetonitrile (7 mL), and diethyl α-phenylisocyanomethylphosphonate (228 mg, 0.9 mmol) gave **9g** (314 mg, 89%) as a yellowish oil, after column chromatography (EtOAc/hexane 1:1 to 3:2). IR (ATR) 3464, 2976, 2928, 1719, 1631, 1451, 1402, 1202, 1056, 1027, 963, 705, 583 cm^{-1}. ^{1}H NMR (400 MHz, $CDCl_3$, HETCOR) δ 0.59 (t, J = 7.0 Hz, 3H, $CH_2CH_2CH_3$), 1.13−1.19 (m, 2H, $CH_2CH_2CH_3$), 1.14 (t, J = 7.0 Hz, 3H, CH_2CH_3), 1.25 (t, J = 7.0 Hz, 3H, CH_2CH_3), 3.16 (m, 2H, $CH_2CH_2CH_3$), 3.85 (m, 1H, CH_2CH_3), 4.02−4.14 (m, 4H, CH_2CH_3 and H-6a), 4.30 (ddd, J = 8.5, 3.5, 1.5 Hz, 1H, H-3a), 7.29−7.34 (m, 3H, ArH), 7.65 (br d, J = 8.0 Hz, 2H, ArH), 7.95 (dd, J = 5.0, 1.5 Hz, 1H, H-3). ^{13}C NMR (100.6 MHz) δ 11.0 ($CH_2CH_2CH_3$), 16.3 (d, J = 4.0 Hz, CH_2CH_3), 16.4 (d, J = 6.0 Hz, CH_2CH_3), 20.7 ($CH_2CH_2CH_3$), 40.6 ($CH_2CH_2CH_3$), 47.8 (d, J = 3.0 Hz, C-6a), 60.5 (C-3a), 63.5 (d, J = 7.0 Hz, CH_2CH_3), 64.7 (d, J = 7.0 Hz, CH_2CH_3), 85.9 (d, J = 154.0 Hz, C-1), 127.8 (d, J = 2.0 Hz, 2CHAr), 128.5 (d, J = 3.0 Hz, CHAr), 128.6 (d, J = 6.0 Hz, 2CHAr), 133.5 (d, J = 4.0 Hz, C-*ipso*), 162.8 (d, J = 12.0 Hz, C-3), 172.2 (d, J = 6.0 Hz, CO), 172.7 (d, J = 12.0 Hz, CO). HRMS $C_{19}H_{26}N_2O_5P$ [M + H]$^+$ 393.1574; found, 393.1572. Additional column chromatography led to sample for testing. Purity 95.6% (t_R = 4.24 min).

*Diethyl (1RS,3aSR,6aSR)-5-(tert-Butyl)-4,6-dioxo-1-phenyl-1,3a,4,5,6,6a-hexahydropyrrolo[3,4-c]pyrrole-1-phosphonate (**9h**).* Following the general procedure, AgOAc (9 mg, 0.05 mmol), *N*-*tert*-butylmaleimide (215 mg, 1.4 mmol), acetonitrile (7 mL), and diethyl α-phenylisocyanomethylphosphonate (229 mg, 0.9 mmol) gave **9h** (202 mg, 55%) as a yellowish oil, after column chromatography (EtOAc). IR (ATR) 3454, 2981, 2923, 1777, 1709, 1348, 1265, 1241, 1173, 1061, 973, 744, 710, 588 cm^{-1}. ^{1}H NMR (400 MHz, $CDCl_3$, HETCOR) δ 1.13 [s, 9H, $C(CH_3)_3$], 1.17 (t, J = 7.0 Hz, 3H, CH_2CH_3), 1.24 (t, J = 7.0 Hz, 3H, CH_2CH_3), 3.88−3.95 (m, 2H, CH_2CH_3 and H-6a), 4.07−4.15 (m, 4H, CH_2CH_3 and H-3a), 7.28−7.33 (m, 3H, ArH), 7.59 (dbr, J = 8.0 Hz, 2H, ArH), 7.93 (dd, J = 5.0, 1.5 Hz, 1H, H-3). ^{13}C NMR (100.6 MHz) δ 16.4 (d, J = 6.0 Hz, CH_2CH_3), 16.4 (d, J = 6.0 Hz, CH_2CH_3), 27.7 ($C(CH_3)_3$), 48.1 (d, J = 2.0 Hz, C-6a), 58.6 [$C(CH_3)_3$], 60.2 (C-3a), 63.5 (d, J = 8.0 Hz, CH_2CH_3), 64.6 (d, J = 8.0 Hz, CH_2CH_3), 86.6 (d, J = 158.0 Hz, C-1), 127.9 (d, J = 2.0 Hz, 2CHAr), 128.4 (d, J = 2.0 Hz, CHAr), 128.5 (d, J = 6.0 Hz, 2CHAr), 134.1 (d, J = 4.0 Hz, C-*ipso*), 163.3 (d, J = 12.0 Hz, C-3), 172.6 (d, J = 5.0 Hz, CO), 173.6 (d, J = 10.0 Hz, CO). HRMS $C_{20}H_{28}N_2O_5P$ [M + H]$^+$ 407.1730; found, 407.1733. Additional column chromatography led to sample for testing. Purity 98.3% (t_R = 4.46 min).

*Diethyl (1RS,3aSR,6aSR)-5-(Adamantan-1-yl)methyl)-4,6-dioxo-1-phenyl-1,3a,4,5,6,6a-hexahydropyrrolo[3,4-c]pyrrole-1-phosphonate (**9i**).* Following the general procedure, AgOAc (12 mg, 0.07 mmol), *N*-(adamantan-1-methylphenyl)maleimide (270 mg, 1.1 mmol), acetonitrile (5 mL), and diethyl α-phenylisocyanomethylphosphonate (177 mg, 0.7 mmol) gave **9i** (220 mg, 63%) as a white solid, after column chromatography (EtOAc/hexane 7:3). Mp 107−108 °C (EtOAc). IR (ATR) 3469, 2908, 2850, 1714, 1446, 1392, 1226, 1158, 1012, 978, 758, 700, 573 cm^{-1}. ^{1}H NMR (400 MHz, $CDCl_3$, HETCOR) δ 0.95 (dd, J = 52.0, 12.0 Hz, 6H, $3CH_2$), 1.12 (t, J = 7.0 Hz, 3H, CH_2CH_3), 1.25 (t, J = 7.0 Hz, 3H, CH_2CH_3), 1.47 (dd, J = 53.0, 12.0 Hz, 6H, $3CH_2$), 1.72 (s, 3H, 3CH), 2.95 (s, 2H, NCH_2), 3.81 (m, 1H, CH_2CH_3), 3.99−3.15 (m, 3H, CH_2CH_3), 4.11 (dd, J = 19.0, 8.5 Hz, 1H, H-6a), 4.29 (ddd, J = 8.5, 3.0, 1.0 Hz, 1H, H-3a), 7.25−7.33 (m, 3H, ArH), 7.72 (d, J = 7.0 Hz, 2H, ArH), 7.95 (dd, J = 5.0, 1.0 Hz, 1H, H-3). ^{13}C NMR (100.6 MHz) δ 16.3 (d, J = 5.5 Hz, CH_2CH_3), 16.4 (d, J = 6.0 Hz, CH_2CH_3), 28.1 (3CH), 34.9 (C), 36.5 ($3CH_2$), 40.0 ($3CH_2$), 47.7 (d, J = 2.0 Hz, C-6a), 50.2 (NCH_2), 60.6 (C-3a), 63.6 (d, J = 7.5 Hz, CH_2CH_3), 64.7 (d, J = 7.5 Hz, CH_2CH_3), 86.0 (d, J = 155.0 Hz, C-1), 127.8 (d, J = 2.0 Hz, 2CHAr), 128.5 (d, J = 3.0 Hz, CHAr), 129.0 (d, J = 4.5 Hz, 2CHAr), 133.5 (d, J = 5.0 Hz, C-*ipso*), 162.6 (d, J = 12.0 Hz, C-3), 172.7 (d, J = 5.0 Hz, CO), 173.2 (d, J = 13.0 Hz, CO); HRMS $C_{27}H_{36}N_2O_5P$ [M + H]$^+$ 499.2356; found, 499.2359. Purity 97.8% (t_R= 5.27 min).

*Diethyl (1RS,3aSR,6aSR)-5-Benzyl-4,6-dioxo-1-phenyl-1,3a,4,5,6,6a-hexahydropyrrolo[3,4-c]pyrrole-1-phosphonate (**9j**).* Following the general procedure, AgOAc (4 mg, 0.02 mmol), *N*-benzylmaleimide (112 mg, 0.6 mmol), acetonitrile (3 mL), and diethyl α-phenylisocyanomethylphosphonate (101 mg, 0.4 mmol) gave **9j** (139 mg, 79%) as a yellowish oil, after column chromatography (EtOAc/hexane 9:1). IR (NaCl) 3472, 3068, 2984, 1778, 1698, 1632, 1495, 1249, 1172, 1021, 750, 615 cm^{-1}. ^{1}H NMR (400 MHz, $CDCl_3$, HETCOR) δ 1.14 (t, J = 7.0 Hz, 3H, CH_2CH_3), 1.25 (t, J = 7.0 Hz, 3H CH_2CH_3), 3.86 (m, 1H, CH_2CH_3), 4.00−4.18 (m, 4H, CH_2CH_3 and H-6a), 4.33 (ddd, J = 8.5, 3.5, 1.5 Hz, 1H, H-3a), 4.36 (dd, J = 53.5, 14.5 Hz, 2H, CH_2Ar), 6.94−6.96 (m, 2H, ArH), 7.14−7.22 (m, 3H, ArH), 7.23−7.30 (m, 3H, ArH), 7.61−7.63 (m, 2H, ArH), 7.92 (dd, J = 5.0, 1.5 Hz, 1H, H-3). ^{13}C NMR (100.6 MHz) δ 16.1 (d, J = 5.0 Hz, CH_2CH_3), 16.2 (d, J = 5.0 Hz, CH_2CH_3), 42.4 (CH_2Ar), 47.8 (d, J = 2.0 Hz, C-6a), 60.4 (C-3a), 63.4 (d, J = 7.5 Hz, CH_2CH_3), 64.6 (d, J = 7.5 Hz, CH_2CH_3), 85.7 (d, J = 155.0 Hz, C-1), 127.7 (d, J = 1.0 Hz, 2CHAr), 127.8 (CHAr), 128.3 (br s, 4CHAr), 128.4 (CHAr), 128.5 (2CHAr), 133.2 (d, J = 4.0 Hz, C-*ipso*), 135.0 (C-*ipso*), 162.3 (d, J = 11.5 Hz, C-3), 171.6 (d, J = 5.5 Hz, CO), 172.2 (d, J = 13.5 Hz, CO). HRMS $C_{23}H_{25}N_2O_5P$ [M + H]$^+$ 441.1574; found, 441.1579. Additional column chromatography led to sample for testing. Purity 95.4% (t_R = 4.43 min).

*Diethyl (1RS,3aSR,6aSR)-4,6-Dioxo-5-phenethyl-1-phenyl-1,3a,4,5,6,6a-hexahydropyrrolo[3,4-c]pyrrole-1-phosphonate (**9k**).* Following the general procedure, AgOAc (7 mg, 0.04 mmol), *N*-phenethylmaleimide (200 mg, 1.0 mmol), acetonitrile (5 mL), and diethyl α-phenylisocyanomethylphosphonate (170 mg, 0.7 mmol) gave **9k** (110 mg, 36%) as an oil, after column chromatography (EtOAc/hexane 1:1). IR (NaCl) 3468, 3027, 2981, 1709, 1627, 1394, 1250, 1162, 1052, 1025, 968, 792, 750 cm^{-1}. ^{1}H NMR (400 MHz, $CDCl_3$, HETCOR) δ 1.14 (t, J = 7.0 Hz, 3H, CH_2CH_3), 1.25 (t, J = 7.0 Hz, 3H, CH_2CH_3), 2.40−2.53 (m, 2H, CH_2), 3.46 (t, J = 7.5 Hz, 2H, CH_2), 3.83 (m, 1H, CH_2CH_3), 3.99−4.16 (m, 4H, CH_2CH_3 and H-6a), 4.24 (ddd, J = 8.5, 4.0, 1.0 Hz, 1H, H-3a), 6.97−6.99 (m, 2H, ArH), 7.16−7.25 (m, 3H, ArH), 7.30−7.38 (m, 3H, ArH), 7.68−7.70 (m, 2H, ArH), 7.85 (dd, J = 5.0, 1.0 Hz, 1H, H-3). ^{13}C NMR (100.6 MHz) δ 16.1 (d, J = 4.0 Hz, CH_2CH_3), 16.2 (d, J = 4.5 Hz, CH_2CH_3), 33.0 (CH_2), 39.9 (CH_2), 47.5 (d, J = 2.5 Hz, C-6a), 60.2 (C-3a), 63.4 (d, J = 7.5 Hz, CH_2CH_3), 64.6 (d, J = 7.5 Hz, CH_2CH_3), 126.6 (CHAr), 127.6 (CHAr), 127.7 (CHAr), 128.4 (d, J = 2.5 Hz, CHAr), 128.5 (2CHAr), 128.6 (CHAr), 128.7 (CHAr), 128.8 (2CHAr), 133.2 (d, J = 4.5 Hz, C-*ipso*), 137.1 (C-*ipso*), 162.6 (d, J = 11.5 Hz, C-3), 171.6 (d, J = 5.5 Hz, CO), 172.3 (d, J = 13.5 Hz, CO). HMRS $C_{24}H_{28}N_2O_5P$ [M + H]$^+$ 455.1730; found, 455.1731. Additional column chromatography led to sample for testing. Purity 98.0% (t_R = 4.54 min).

*Diethyl (1RS,3aSR,6aSR)-5-(4-Fluorophenethyl)-4,6-dioxo-1-phenyl-1,3a,4,5,6,6a-hexahydropyrrolo[3,4-c]pyrrole-1-phosphonate (**9l**).* Following the general procedure, AgOAc (8 mg, 0.05 mmol), *N*-(4-fluorophenethyl)maleimide (263 mg, 1.2 mmol), acetonitrile (6 mL), and diethyl α-phenylisocyanomethylphosphonate (202 mg, 0.8 mmol) gave **9l** (201 mg, 53%) as a white solid, after column chromatography (EtOAc). Mp 94−95 °C (EtOAc). IR (NaCl) 3466, 3050, 2976, 1779, 1702, 1632, 1507, 1257, 1153, 1013, 763, 583 cm^{-1}. ^{1}H NMR (400 MHz, $CDCl_3$, HETCOR) δ 1.23 (t, J = 7.0 Hz, 3H, CH_2CH_3), 1.25 (t, J = 7.0 Hz, 3H, CH_2CH_3), 2.40−2.52 (m, 2H, CH_2), 3.41−3.46 (m, 2H, CH_2), 3.80 (m, 1H, CH_2CH_3), 3.97−4.15 (m, 4H, CH_2CH_3 and H-6a), 4.24 (ddd, J = 8.0, 4.0, 1.5 Hz, 1H, H-3a), 6.86−6.92 (m, 4H, ArH), 7.31−7.37 (m, 3H, ArH), 7.67 (m, 2H, ArH), 7.83 (dd, J = 5.5, 1.5 Hz, 1H, H-3). ^{13}C NMR (100.6 MHz) δ

https://dx.doi.org/10.1021/acs.jmedchem.9b02080
J. Med. Chem. 2020, 63, 3610−3633

16.1 (d, J = 5.0 Hz, CH_2CH_3), 16.2 (d, J = 5.0 Hz, CH_2CH_3), 32.1 (CH_2), 39.9 (CH_2), 47.5 (d, J = 2.0 Hz, C-6a), 60.3 (C-3a), 63.4 (d, J = 7.0 Hz, CH_2CH_3), 64.6 (d, J = 7.0 Hz, CH_2CH_3), 85.7 (d, J = 153.0 Hz, C-1), 115.3 (d, J = 2.0 Hz, 2CHAr), 127.6 (d, J = 2.0 Hz, 2CHAr), 128.4 (d, J = 3.0 Hz, CHAr), 128.6 (d, J = 6.0 Hz, 2CHAr), 130.1 (d, J = 8.0 Hz, 2CHAr), 132.7 (d, J = 3.0 Hz, C-*ipso*), 133.1 (d, J = 5.0 Hz, C-*ipso*), 160.4 (d, J = 244.5 Hz, C-*ipso*), 162.5 (d, J = 12.0 Hz, C-3), 171.6 (d, J = 6.0 Hz, CO), 172.3 (d, J = 14.0 Hz, CO). HRMS $C_{24}H_{27}FN_2O_5P$ $[M + H]^+$ 473.1636; found, 473.1640. Anal. Calcd for $C_{24}H_{26}FN_2O_5P$: C, 61.01%; H, 5.55%; N, 5.93%. Found: C, 61.14%; H, 5.74%; N, 5.83%.

*Diethyl (1RS,3aSR,6aSR)-5-(2,3-Dihydro-1H-inden-2-yl)-4,6-dioxo-1-phenyl-1,3a,4,5,6,6a-hexahydropyrrolo[3,4-c]pyrrole-1-phosphonate (**9m**).* Following the general procedure, AgOAc (7 mg, 0.04 mmol), *N*-(2,3-dihydro-1*H*-inden-2-yl)maleimide (126 mg, 0.6 mmol), acetonitrile (3 mL), and diethyl α-phenylisocyanomethylphosphonate (100 mg, 0.4 mmol) gave **9m** (158 mg, 85%) as a beige solid, after column chromatography (EtOAc). Mp 124−126 °C (EtOAc). IR (ATR) 3457, 2986, 2943, 2866, 1766, 1698, 1623, 1377, 1252, 1170, 1055, 1021, 790, 704, 574 cm^{-1}. ^1H NMR (400 MHz, $CDCl_3$, HETCOR) δ 1.18 (t, J = 7.0 Hz, 3H, CH_2CH_3), 1.26 (t, J = 7.0 Hz, 3H, CH_2CH_3), 2.69 (dd, J = 15.0, 9.0 Hz, 1H, CH_2), 2.75 (dd, J = 15.0, 9.0 Hz, 1H, CH_2), 2.77 (dd, J = 15.0, 9.0 Hz, 1H, CH_2), 3.23 (dd, J = 15.0, 9.0 Hz, 1H, CH_2), 3.92 (m, 1H, CH_2CH_3), 4.08−4.17 (m, 4H, CH_2CH_3 and H-6a), 4.31 (ddd, J = 9.0, 3.0, 1.5 Hz, 1H, H-3a), 4.62 (qu, J = 9,2 Hz, 1H, CH), 7.09 (m, 1 H, ArH), 7.07−7.11 (m, 3H, ArH), 7.32−7.37 (m, 3H, ArH), 7.64 (br d, J = 7.5 Hz, 2H, ArH), 8.00 (dd, J = 5.0, 1.5 Hz, 1H, H-3). ^{13}C NMR (100.6 MHz) δ 16.4 (d, J = 2.0 Hz, CH_2CH_3), 16.5 (d, J = 3.0 Hz, CH_2CH_3), 34.6 (CH_2), 35.1 (CH_2), 48.0 (d, J = 2.0 Hz, C-6a), 50.8 (CH), 60.2 (C-3a), 63.6 (d, J = 7.0 Hz, CH_2CH_3), 64.7 (d, J = 8.0 Hz, CH_2CH_3), 86.1 (d, J = 157.0 Hz, C-1), 124.4 (d, J = 2.0 Hz, 2CHAr), 126.8 (d, J = 2.0 Hz, 2CHAr), 128.0 (d, J = 1.0 Hz, 2CHAr), 128.5 (d, J = 8.0 Hz, 2CHAr), 128.6 (CHAr), 133.7 (C-*ipso*), 133.8 (C-*ipso*), 140.5 (d, J = 9.0 Hz, C-*ipso*), 162.7 (d, J = 12.0 Hz, C-3), 172.1 (d, J = 5.0 Hz, CO), 172.7 (d, J = 12.0 Hz, CO). HRMS $C_{25}H_{28}N_2O_5P$ $[M + H]^+$ 467.1730; found, 467.1728. Anal. Calcd for $C_{25}H_{27}N_2O_5P$: C, 64.37%; H, 5.83%; N, 6.01%. Found: C,64.55%; H,6.11%; N,5.76%.

*Diethyl (1RS,3aSR,6aSR)-4,6-Dioxo-1-phenyl-5-[4-(trifluoromethyl)phenyl]-1,3a,4,5,6,6a-hexahydropyrrolo[3,4-c]pyrrole-1-phosphonate (**9n**).* Following the general procedure, AgOAc (4 mg, 0.03 mmol), *N*-(4-trifluoromethylphenyl)maleimide (144 mg, 0.6 mmol), acetonitrile (3 mL), and diethyl α-phenylisocyanomethylphosphonate (101 mg, 0.4 mmol) gave **9n** (133 mg, 67%) as a white solid, after column chromatography (EtOAc). Mp 184−185 °C (EtOAc). IR (NaCl) 3492, 3050, 2984, 1723, 1616, 1378, 1326, 1249, 1170, 1067, 758, 580 cm^{-1}. ^1H NMR (400 MHz, $CDCl_3$, HETCOR) δ 1.19 (t, J = 7.0 Hz, 3H, CH_2CH_3), 1.28 (t, J = 7.0 Hz, 3H, CH_2CH_3), 3.95 (m, 1H, CH_2CH_3), 4.10−4.20 (m, 3H, CH_2CH_3), 4.28 (dd, J = 18.0, 9.0, 1H, H-6a), 4.51 (ddd, J = 8.5, 3.0, 1.5 Hz, 1H, H-3a), 6.85−6.87 (m, 2H, ArH), 7.34−7.38 (m, 3H, ArH), 7.54−7.56 (m, 2H, ArH), 7.67−7.69 (m, 2H, ArH), 8.05 (dd, J = 5.0, 1.5 Hz, 1H, H-3). ^{13}C NMR (100.6 MHz) δ 16.2 (d, J = 5.0 Hz, CH_2CH_3), 16.3 (d, J = 5.0 Hz, CH_2CH_3), 48.3 (d, J = 3.0 Hz, C-6a), 60.1 (C-3a), 63.6 (d, J = 7.0 Hz, CH_2CH_3), 64.7 (d, J = 7.0 Hz, CH_2CH_3), 86.3 (d, J = 157.0 Hz, C-1), 123.5 (q, J = 272.5 Hz, CF_3), 126.0 (q, J = 4.0 Hz, 2CHAr), 126.3 (2CHAr), 128.0 (d, J = 1.0 Hz, 2CHAr), 128.4 (d, J = 6.0 Hz, 2CHAr), 128.7 (d, J = 2.0 Hz, CHAr), 137.5 (q, J = 33.0 Hz, CCF_3), 133.4 (d, J = 4.0 Hz, C-*ipso*), 134.1 (d, J = 1.5 Hz, C-*ipso*), 162.0 (d, J = 13.0 Hz, C-3), 170.4 (d, J = 5.0 Hz, CO), 171.2 (d, J = 12.0 Hz, CO). HRMS $C_{23}H_{23}F_3N_2O_5P$ $[M + H]^+$ 495.1291; found, 495.1288. Anal. Calcd for $C_{23}H_{22}F_3N_2O_5P$: C, 55.88%; H, 4.49%; N, 5.67%. Found: C, 56.04%; H, 4.71%; N, 5.56%.

*Diethyl (1RS,3aSR,6aSR)-4,6-Dioxo-1-phenyl-5-[3-(trifluoromethyl)phenyl]-1,3a,4,5,6,6a-hexahydropyrrolo[3,4-c]pyrrole-1-phosphonate (**9o**).* Following the general procedure, AgOAc (10 mg, 0.06 mmol), *N*-(3-trifluoromethylphenyl)maleimide (362 mg, 1.5 mmol), acetonitrile (8 mL), and diethyl α-phenylisocyanomethylphosphonate (253 mg, 1.0 mmol) gave **9o** (218 mg, 44%) as a white solid, after column chromatography (EtOAc). Mp 179−180 °C (EtOAc). IR (ATR) 3483, 3084, 2957, 2036, 1719, 1446, 1382, 1329, 1168, 1027, 978, 739, 573 cm^{-1}. ^1H NMR (400 MHz, $CDCl_3$, HETCOR) δ 1.21 (t, J = 7.0 Hz, 3H, CH_2CH_3), 1.28 (t, J = 7.0 Hz, 3H, CH_2CH_3), 3.98 (m, 1H, CH_2CH_3), 4.11−4.20 (m, 3H, CH_2CH_3), 4.27 (dd, J = 18.0, 9.0 Hz, 1H, H-6a), 4.50 (ddd, J = 9.0, 2.5, 1.5 Hz, 1H, H-3a), 6.86 (s, 1H, ArH), 6.96 (d, J = 9.5 Hz, 1H, ArH), 7.36−7.39 (m, 3H, ArH), 7.42 (t, 7.5 Hz, 1H, ArH), 7.53 (d, J = 8.0 Hz, 1H, ArH), 7.67 (br d, J = 7.0 Hz, 2H, ArH), 8.06 (dd, J = 5.0, 1.5 Hz, 1H, H-3). ^{13}C NMR (100.6 MHz) δ 16.4 (d, J = 5.5 Hz, CH_2CH_3), 16.4 (d, J = 5.5 Hz, CH_2CH_3), 48.6 (d, J = 2.0 Hz, C-6a), 60.2 (C-3a), 63.8 (d, J = 7.5 Hz, CH_2CH_3), 64.9 (d, J = 7.5 Hz, CH_2CH_3), 86.4 (d, J = 158.0 Hz, C-1), 123.3 (q, J = 4.0 Hz, CHAr), 123.4 (q, J = 272.5 Hz, CF_3), 125.6 (q, J = 4.0 Hz, CHAr), 128.2 (d, J = 2.0 Hz, 2CHAr), 128.5 (d, J = 6.0 Hz, 2CHAr), 128.9 (d, J = 2.0 Hz, CHAr), 129.5 (d, J = 1.0 Hz, CHAr), 129.7 (CHAr), 131.6 (q, J = 33.5 Hz, CCF_3), 131.7 (C-*ipso*), 133.5 (d, J = 4.0 Hz, C-*ipso*), 162.1 (d, J = 12.0 Hz, C-3), 170.6 (d, J = 5.0 Hz, CO), 171.5 (d, J = 11.0 Hz, CO). HRMS $C_{23}H_{23}F_3N_2O_5P$ $[M + H]^+$ 495.1291; found, 495.1287. Anal. Calcd for $C_{23}H_{22}F_3N_2O_5P$: C, 55.88%; H, 4.49%; N, 5.67%. Found: C, 56.00%; H, 4.63%; N, 5.46%.

*Diethyl (1RS,3aSR,6aSR)-5-(4-Fluorophenyl)-4,6-dioxo-1-phenyl-1,3a,4,5,6,6a-hexahydropyrrolo[3,4-c]pyrrole-1-phosphonate (**9p**).* Following the general procedure, AgOAc (7 mg, 0.04 mmol), *N*-(4-fluorophenyl)maleimide (211 mg, 1.1 mmol), acetonitrile (5 mL), and diethyl α-phenylisocyanomethylphosphonate (177 mg, 0.7 mmol) gave 9p (198 mg, 64%) as a white solid, after column chromatography (EtOAc). Mp 200−201 °C (EtOAc). IR (NaCl) 3481, 3061, 2980, 1787, 1717, 1511, 1385, 1245, 1017, 969, 700, 583 cm^{-1}. ^1H NMR (400 MHz, $CDCl_3$, HETCOR) δ 1.19 (t, J = 7.5 Hz, 3H, CH_2CH_3), 1.28 (t, J = 7.5 Hz, 3H, CH_2CH_3), 3.93 (m, 1H, CH_2CH_3), 4.10−4.20 (m, 3H, CH_2CH_3), 4.26 (dd, J = 18.0, 9.0, 1H, H-6a), 4.48 (ddd, J = 8.5, 3.0, 1.5 Hz, 1H, H-3a), 6.67−6.72 (m, 2H, ArH), 6.96−7.00 (m, 2H, ArH), 7.33−7.39 (m, 3H, ArH), 7.68−7.70 (m, 2H, ArH), 8.05 (dd, J = 5.0, 1.5 Hz, 1H, H-3). ^{13}C NMR (100.6 MHz) δ 16.2 (d, J = 4.0 Hz, CH_2CH_3), 16.3 (d, J = 4.0 Hz, CH_2CH_3), 48.2 (d, J = 3.0 Hz, C-6a), 60.1 (C-3a), 63.6 (d, J = 8.0 Hz, CH_2CH_3), 63.7 (d, J = 7.0 Hz, CH_2CH_3), 86.2 (d, J = 157.0 Hz, C-1), 116.1 (d, J = 23.0 Hz, 2CHAr), 126.9 (d, J = 3.0 Hz, C-*ipso*), 127.9 (2CHAr), 128.0 (2CHAr), 128.4 (d, J = 6.0 Hz, 2CHAr), 128.6 (d, J = 2.0 Hz, CHAr), 133.4 (d, J = 4.0 Hz, C-*ipso*), 160.9 (d, J = 248.5 Hz, C-*ipso*), 162.2 (d, J = 12.0 Hz, C-3), 170.9 (d, J = 5.0 Hz, CO), 171.6 (d, J = 11.0 Hz, CO). HRMS $C_{22}H_{23}FN_2O_5P$ $[M + H]^+$445.1323; found, 445.1322. Anal. Calcd for $C_{22}H_{22}FN_2O_5P$: C, 59.46%; H, 4.99%; N, 6.30%. Found: C, 59.73%; H, 5.13%; N, 6.19%.

*Diethyl (1RS,3aSR,6aSR)-5-(4-Chlorophenyl)-4,6-dioxo-1-phenyl-1,3a,4,5,6,6a-hexahydropyrrolo[3,4-c]pyrrole-1-phosphonate (**9q**).* Following the general procedure, AgOAc (5 mg, 0.03 mmol), *N*-(4-chlorophenyl)maleimide (150 mg, 0.7 mmol), acetonitrile (4 mL), and diethyl α-phenylisocyanomethylphosphonate (118 mg, 0.5 mmol) gave **9q** (136 mg, 59%) as a white solid, after column chromatography (EtOAc). Mp 211−212 °C (EtOAc). IR (ATR) 3078, 2981, 2923, 2855, 1713, 1499, 1377, 1187, 1022, 773, 583 cm^{-1}. ^1H NMR (400 MHz, $CDCl_3$, HETCOR) δ 1.19 (t, J = 7.0 Hz, 3H, CH_2CH_3), 1.28 (t, J = 7.0 Hz, 3H, CH_2CH_3), 3.94 (m, 1H, CH_2CH_3), 4.11−4.19 (m, 3H, CH_2CH_3), 4.25 (dd, J = 18.0, 9.0 Hz, 1H, H-6a), 4.47 (ddd, J = 8.5, 3.0, 1.0 Hz, 1H, H-3a), 6.65−6.67 (m, 2H, ArH), 7.24−7.27 (m, 2H, ArH), 7.33−7.37 (m, 3H, ArH), 7.67 (br d, J = 7.5 Hz, 2H, ArH), 8.04 (dd, J = 5.5, 1.0 Hz, 1H, H-3). ^{13}C NMR (100.6 MHz) δ 16.4 (d, J = 3.0 Hz, CH_2CH_3), 16.4 (d, J = 4.0 Hz, CH_2CH_3), 48.4 (d, J = 2.0 Hz, C-6a), 60.2 (C-3a), 63.7 (d, J = 7.0 Hz, CH_2CH_3), 64.8 (d, J = 7.0 Hz, CH_2CH_3), 86.4 (d, J = 157.0 Hz, C-1), 127.4 (2CHAr), 128.1 (d, J = 1.0 Hz, 2CHAr), 128.5 (d, J = 6.0 Hz, 2CHAr), 128.7 (d, J = 2.0 Hz, CHAr), 129.4 (2CHAr), 129.6 (C-*ipso*), 133.6 (d, J = 4.0 Hz, C-*ipso*), 134.7 (C-*ipso*), 162.2 (d, J = 12.0 Hz, C-3), 170.8 (d, J = 5.0 Hz, CO), 171.5 (d, J = 12.0 Hz, CO). HRMS $C_{22}H_{23}ClN_2O_5P$ $[M + H]^+$ 461.1028; found, 461.1026. Anal. Calcd for $C_{22}H_{22}ClN_2O_5P$: C, 57.34%; H, 4.81%; N, 6.08%. Found: C, 57.71%; H, 4.92%; N, 5.96%.

*Diethyl (1RS,3aSR,6aSR)-5-(2-Chlorophenyl)-4,6-dioxo-1-phenyl-1,3a,4,5,6,6a-hexahydropyrrolo[3,4-c]pyrrole-1-phosphonate (**9r**).*

https://dx.doi.org/10.1021/acs.jmedchem.9b02080
J. Med. Chem. 2020, 63, 3610−3633

Following the general procedure, AgOAc (6 mg, 0.04 mmol), *N*-(2-chlorophenyl)maleimide (180 mg, 0.9 mmol), acetonitrile (5 mL), and diethyl α-phenylisocyanomethylphosphonate (152 mg, 0.6 mmol) gave **9r** (200 mg, 72%) as a white solid, after column chromatography (EtOAc/hexane 7:3). Mp 172−174 °C (EtOAc). IR (ATR) 3496, 2981, 2866, 1790, 1718, 1482, 1386, 1237, 1194, 1045, 1021, 973, 757, 579 cm^{-1}. ^1H NMR (400 MHz, $CDCl_3$, HETCOR) δ 1.14 (t, *J* = 7.0 Hz, 3H, CH_2CH_3-rotamer A), 1.19 (t, *J* = 7.0 Hz, 3H, CH_2CH_3-rotamer B), 1.29 (t, *J* = 7.0 Hz, 3H, CH_2CH_3-rotamer A), 1.30 (t, *J* = 7.0 Hz, 3H, CH_2CH_3-rotamer B), 3.82 (m, 1H, CH_2CH_3-rotamer A), 3.93 (m, 1H, CH_2CH_3-rotamer B), 4.05−4.20 (m, 6H, CH_2CH_3-rotamer A and B), 4.35 (dd, *J* = 18.0, 8.5 Hz, 1H, H-6a rotamer A), 4.36 (dd, *J* = 18.0, 8.5 Hz, 1H, H-6a rotamer B), 4.52 (ddd, *J* = 8.5, 4.5, 1.5 Hz, 1H, H-3a rotamer A), 4.56 (ddd, *J* = 8.5, 3.0, 1.5 Hz, 1H, H-3a rotamer B), 6.30 (dd, *J* = 8.0, 1.5 Hz, 1H, ArH rotamer B), 7.10 (m, 1H, ArH rotamer B), 7.13 (ddd, *J* = 16.0, 8.0, 2.0 Hz, 1H, ArH rotamer A), 7.25−7.43 (m, 10H, 6ArH rotamer A and 4ArH rotamer B), 7.42 (dd, *J* = 8.0, 1.5 Hz, 1H, ArH rotamer B), 7.71 (d, *J* = 8.0 Hz, 2H, ArH rotamer B), 7.78 (d, *J* = 8.0 Hz, 2H, ArH rotamer A), 8.03 (dd, *J* = 5.5 Hz, 1.5 Hz, 1H, H-3 rotamer A), 8.08 (dd, *J* = 5.0, 1.5 Hz, 1H, H-3 rotamer B). ^{13}C NMR (100.6 MHz) δ 16.2 (d, *J* = 6.0 Hz, CH_2CH_3 rotamer A or B), 16.2 (d, *J* = 6.0 Hz, CH_2CH_3 rotamer A or B), 16.3 (d, *J* = 6.0 Hz, CH_2CH_3 rotamer A or B), 16.3 (d, *J* = 5.5 Hz, CH_2CH_3 rotamer A or B), 48.0 (d, *J* = 2.5 Hz, C-6a rotamer A), 48.6 (d, *J* = 2.5 Hz, C-6a rotamer B), 60.3 (C-3a rotamer B), 60.1 (C-3a rotamer A), 63.5 (d, *J* = 7.5 Hz, CH_2CH_3 rotamer A), 63.6 (d, *J* = 7.5 Hz, CH_2CH_3 rotamer B), 64.7 (d, *J* = 7.5 Hz, CH_2CH_3 rotamer B), 64.8 (d, *J* = 7.5 Hz, CH_2CH_3 rotamer A), 86.0 (d, *J* = 157.5, C-1 rotamer A), 86.6 (d, *J* = 153.5, C-1 rotamer B), 127.6 (CHAr rotamer A or B), 127.7 (d, *J* = 2.0 Hz, CHAr rotamer A or B), 127.8 (CHAr rotamer A), 127.9 (CHAr rotamer A or B), 128.0 (CHAr rotamer A or B), 128.4 (d, *J* = 5.0 Hz, 2CHAr rotamer B), 128.5 (2CHAr rotamer A or B), 128.6 (d, *J* = 2.0 Hz, CHAr rotamer A or B), 128.9 (d, *J* = 6.0 Hz, CHAr rotamer A), 129.1 (C-*ipso* rotamer A), 129.2 (C-*ipso* rotamer B), 129.3 (CHAr rotamer B), 129.6 (CHAr rotamer A), 130.2 (CHAr rotamer B), 130.3 (CHAr rotamer A or B), 130.7 (CHAr rotamer A or B), 130.9 (CHAr rotamer A or B), 132.0 (C-*ipso* rotamer A), 132.2 (C-*ipso* rotamer B), 132.9 (d, *J* = 4.0 Hz, C-*ipso* rotamer A), 133.5 (d, *J* = 4.0 Hz, C-*ipso* rotamer B), 162.0 (d, *J* = 11.5 Hz, C-3 rotamer A), 162.2 (d, *J* = 12.5 Hz, C-3 rotamer B), 170.2 (d, *J* = 5.0 Hz, CO rotamer B), 170.3 (d, *J* = 5.5 Hz, CO rotamer A), 170.7 (d, *J* = 11.5 Hz, CO rotamer A or B), 170.8 (d, *J* = 15.0 Hz, CO rotamer B). HRMS $C_{22}H_{23}ClN_2O_5P$ $[M + H]^+$ 461.1028; found, 461.1025. Anal. Calcd for $C_{22}H_{22}ClN_2O_5P$: C, 57.34%; H, 4.81%; N, 6.08%. Found: C,57.18%; H,4.86%; N,5.88%.

*Diethyl (1RS,3aSR,6aSR)-5-(3-Chlorophenyl)-4,6-dioxo-1-phenyl-1,3a,4,5,6,6a-hexahydropyrrolo[3,4-c]pyrrole-1-phosphonate (**9s**).* Following the general procedure, AgOAc (8 mg, 0.05 mmol), *N*-(3-chlorophenyl)maleimide (250 mg, 1.2 mmol), acetonitrile (6 mL), and diethyl α-phenylisocyanomethylphosphonate (203 mg, 0.8 mmol) gave **9s** (167 mg, 45%) as a white solid, after column chromatography (EtOAc). Mp 186−187 °C (EtOAc). IR (ATR) 3488, 3084, 2962, 2928, 1709, 1587, 1475, 1382, 1241, 1183, 1051, 1022, 948, 705 cm^{-1}. ^1H NMR (400 MHz, $CDCl_3$, HETCOR) δ 1.19 (t, *J* = 7.0 Hz, 3H, CH_2CH_3), 1.28 (t, *J* = 7.0 Hz, 3H, CH_2CH_3), 3.94 (m, 1H, CH_2CH_3), 4.10−4.19 (m, 3H, CH_2CH_3), 4.26 (dd, *J* = 18.0, 9.0 Hz, 1H, H-6a), 4.48 (ddd, *J* = 8.5, 3.0, 1.5 Hz, 1H, H-3a), 6.63−6.68 (m, 2H, ArH), 7.22 (m, 1H, ArH), 7.26 (m, 1H, ArH), 7.35−7.39 (m, 3H, ArH), 7.68 (br d, *J* = 7.5 Hz, 2H, ArH), 8.05 (dd, *J* = 5.0, 1.5 Hz, 1H, H-3). ^{13}C NMR (100.6 MHz) δ 16.4 (d, *J* = 5.5 Hz, CH_2CH_3), 16.4 (d, *J* = 5.5 Hz, CH_2CH_3), 48.5 (d, *J* = 3.0 Hz, C-6a), 60.2 (C-3a), 63.7 (d, *J* = 7.0 Hz, CH_2CH_3), 64.8 (d, *J* = 7.0 Hz, CH_2CH_3), 86.4 (d, *J* = 157.0 Hz, C-1), 124.4 (CHAr), 126.5 (CHAr), 128.2 (d, *J* = 2.0 Hz, 2CHAr), 128.5 (d, *J* = 6.0 Hz, 2CHAr), 128.9 (d, *J* = 2.0 Hz, CHAr), 129.0 (CHAr), 130.1 (CHAr), 132.2 (C-*ipso*), 133.5 (d, *J* = 4.0 Hz, C-*ipso*), 134.7 (C-*ipso*), 162.3 (d, *J* = 12.0 Hz, C-3), 170.6 (d, *J* = 5.0 Hz, CO), 171.4 (d, *J* = 12.0 Hz, CO). HRMS $C_{22}H_{23}ClN_2O_5P$ $[M + H]^+$ 461.1028; found, 461.1029. Anal. Calcd for $C_{22}H_{22}ClN_2O_5P$: C, 57.34%; H, 4.81%; N, 6.08%. Found: C, 57.70%; H, 4.96%; N, 5.59%.

*Diethyl (1RS,3aSR,6aSR)-5-(4-Bromophenyl)-4,6-dioxo-1-phenyl-1,3a,4,5,6,6a-hexahydropyrrolo[3,4-c]pyrrole-1-phosphonate (**9t**).* Following the general procedure, AgOAc (7 mg, 0.04 mmol), *N*-(4-bromophenyl)maleimide (275 mg, 1.1 mmol), acetonitrile (5 mL), and diethyl α-phenylisocyanomethylphosphonate (177 mg, 0.7 mmol) gave **9t** (181 mg, 51%) as a white solid, after column chromatography (EtOAc/hexane 1:1). Mp 180−182 °C (EtOAc). IR (ATR) 3478, 2918, 2845, 1797, 1714, 1480, 1387, 1236, 1187, 1158, 1022, 973, 744, 578 cm^{-1}. ^1H NMR (400 MHz, $CDCl_3$, HETCOR) δ 1.19 (t, *J* = 7.0 Hz, 3H, CH_2CH_3), 1.28 (t, *J* = 7.0 Hz, 3H, CH_2CH_3), 3.93 (m, 1H, CH_2CH_3), 4.10−4.19 (m, 3H, CH_2CH_3), 4.25 (dd, *J* = 18.0, 9.0 Hz, 1H, H-6a), 4.47 (ddd, *J* = 9.0, 3.0, 1.5 Hz, 1H, H-3a), 6.59−6.61 (m, 2H, ArH), 7.34−7.36 (m, 3H, ArH), 7.40−7.42 (m, 2H, ArH), 7.67 (br s, *J* = 7.5 Hz, 2H, ArH), 8.04 (dd, *J* = 5.0, 1.5 Hz, 1H, H-3). ^{13}C NMR (100.6 MHz) δ 16.4 (d, *J* = 3.0 Hz, CH_2CH_3), 16.4 (d, *J* = 4.0 Hz, CH_2CH_3), 48.4 (d, *J* = 3.0 Hz, C-6a), 60.3 (C-3a), 63.7 (d, *J* = 8.0 Hz, CH_2CH_3), 64.8 (d, *J* = 7.0 Hz, CH_2CH_3), 86.4 (d, *J* = 157.0 Hz, C-1), 122.7 (C-*ipso*), 127.7 (2CHAr), 128.1 (d, *J* = 2.0 Hz, 2CHAr), 128.5 (d, *J* = 6.0 Hz, 2CHAr), 128.8 (d, *J* = 2.0 Hz, CHAr), 130.2 (C-*ipso*), 132.4 (2CHAr), 133.6 (d, *J* = 4.0 Hz, C-*ipso*), 162.2 (d, *J* = 12.0 Hz, C-3), 170.7 (d, *J* = 5.0 Hz, CO), 171.4 (d, *J* = 11.0 Hz, CO). HRMS $C_{22}H_{23}BrN_2O_5P$ $[M + H]^+$ 505.0522; found, 505.0522. Anal. Calcd for $C_{22}H_{22}BrN_2O_5P$: C, 52.99%; H, 4.90%; N, 5.24%. Found: C, 53.30%; H, 4.61%; N, 5.10%.

*Diethyl (1RS,3aSR,6aSR)-5-(3,5-Dichlorophenyl)-4,6-dioxo-1-phenyl-1,3a,4,5,6,6a-hexahydropyrrolo[3,4-c]pyrrole-1-phosphonate (**9u**).* Following the general procedure, AgOAc (12 mg, 0.07 mmol), *N*-(3,5-dichlorophenyl)maleimide (267 mg, 1.1 mmol), acetonitrile (5 mL), and diethyl α-phenylisocyanomethylphosphonate (177 mg, 0.7 mmol) gave **9u** (190 mg, 55%) as a white solid, after column chromatography (EtOAc/hexane 8:2). Mp 207−209 °C (EtOAc). IR (ATR) 3483, 3079, 2952, 2928, 1719, 1573, 1441, 1373, 1226, 1183, 1027, 973, 763, 734, 727, 588 cm^{-1}. ^1H NMR (400 MHz, $CDCl_3$, HETCOR) δ 1.20 (t, *J* = 7.0 Hz, 3H, CH_2CH_3), 1.28 (t, *J* = 7.0 Hz, 3H, CH_2CH_3), 3.94 (m, 1H, CH_2CH_3), 4.10−4.19 (m, 3H, CH_2CH_3), 4.25 (dd, *J* = 18.0, 8.5 Hz, 1H, H-6a), 4.47 (ddd, *J* = 9.0, 2.5, 1.5 Hz, 1H, H-3a), 6.60 (d, *J* = 2.0 Hz, 2H, ArH), 7.27 (m, 1H, ArH), 7.37−7.40 (m, 3H, ArH), 7.65 (br d, *J* = 5.0 Hz, 2H, ArH), 8.04 (dd, *J* = 5.0, 1.5 Hz, 1H, H-3). ^{13}C NMR (100.6 MHz) δ 16.3 (d, *J* = 5.5 Hz, CH_2CH_3), 16.4 (d, *J* = 5.5 Hz, CH_2CH_3), 48.6 (d, *J* = 3.0 Hz, C-6a), 60.9 (C-3a), 63.8 (d, *J* = 7.0 Hz, CH_2CH_3), 64.9 (d, *J* = 7.0 Hz, CH_2CH_3), 86.5 (d, *J* = 158.0 Hz, C-1), 124.8 (2CHAr), 128.3 (d, *J* = 2.0 Hz, 2CHAr), 128.5 (d, *J* = 5.0 Hz, 2CHAr), 129.0 (d, *J* = 2.0 Hz, CHAr), 129.1 (CHAr), 132.8 (C-*ipso*), 133.5 (d, *J* = 3.0 Hz, C-*ipso*), 135.3 (2C-*ipso*), 162.0 (d, *J* = 13.0 Hz, C-3), 170.2 (d, *J* = 5.0 Hz, CO), 171.1 (d, *J* = 11.0 Hz, CO). HRMS $C_{22}H_{22}Cl_2N_2O_5P$ $[M + H]^+$ 495.0638; found, 495.0638. Anal. Calcd for $C_{22}H_{21}Cl_2N_2O_5P$: C, 53.35%; H, 4.27%; N, 5.66%. Found: C, 53.69%; H, 4.35%; N, 5.42%.

*Diethyl (1RS,3aSR,6aSR)-5-(3,4-Dichlorophenyl)-4,6-dioxo-1-phenyl-1,3a,4,5,6,6a-hexahydropyrrolo[3,4-c]pyrrole-1-phosphonate (**9v**).* Following the general procedure, AgOAc (8 mg, 0.05 mmol), *N*-(3-chloro-4-chlorophenyl)maleimide (288 mg, 1.2 mmol), acetonitrile (6 mL), and diethyl α-phenylisocyanomethylphosphonate (202 mg, 0.8 mmol) gave **9v** (210 mg, 53%) as a white solid, after column chromatography (EtOAc/hexane 1:1). Mp 172−174 °C (EtOAc). IR (ATR) 3480, 3075, 2957, 1790, 1716, 1464, 1251, 1187, 1058, 1024, 737, 579 cm^{-1}. ^1H NMR (400 MHz, $CDCl_3$, HETCOR) δ 1.20 (t, *J* = 7.0 Hz, 3H, CH_2CH_3), 1.28 (t, *J* = 7.0 Hz, 3H, CH_2CH_3), 3.95 (m, 1H, CH_2CH_3), 4.10−4.20 (m, 3H, CH_2CH_3), 4.26 (dd, *J* = 18.0, 8.5 Hz, 1H, H-6a), 4.47 (ddd, *J* = 8.5, 3.0, 1.5 Hz, 1H, H-3a), 6.61 (dd, *J* = 9.0, 2.5 Hz, 1H, ArH), 6.78 (d, *J* = 2.5 Hz, 1H, ArH), 7.35−7.38 (m, 4H, ArH), 7.65−7.68 (m, 2H, ArH), 8.04 (dd, *J* = 4.5, 1.5 Hz, 1H, H-3). ^{13}C NMR (100.6 MHz) δ 16.2 (d, *J* = 6.0 Hz, CH_2CH_3), 16.3 (d, *J* = 6.0 Hz, CH_2CH_3), 48.4 (d, *J* = 3.0 Hz, C-6a), 60.0 (C-3a), 63.6 (d, *J* = 7.0 Hz, CH_2CH_3), 64.7 (d, *J* = 8.0 Hz, CH_2CH_3), 86.2 (d, *J* = 157.0 Hz, C-1), 125.2 (CHAr), 127.9 (CHAr), 128.0 (d, *J* = 2.0 Hz, 2CHAr), 128,3 (d, *J* = 6.0 Hz, 2CHAr), 128.7 (d, *J* = 2.0 Hz, CHAr), 130.2 (C-*ipso*), 130.6 (CHAr), 132.9 (C-*ipso*), 133.0 (C-*ipso*), 133.3 (d, *J* = 4.0 Hz, C-*ipso*), 161.9 (d, *J* = 13.0 Hz, C-3), 170.2 (d, *J* = 5.0 Hz, CO), 171.1 (d, *J* = 12.0 Hz, CO). HRMS

https://dx.doi.org/10.1021/acs.jmedchem.9b02080
J. Med. Chem. 2020, 63, 3610−3633

$C_{22}H_{22}Cl_2N_2O_5P$ $[M + H]^+$ 495.0638; found, 495.0637. Anal. Calcd for $C_{22}H_{21}Cl_2N_2O_5P$: C, 53.35%; H, 4.27%; N, 5.66%. Found: C, 53.42%; H, 4.30%; N, 5.48%.

*Diethyl (1RS,3aSR,6aSR)-4,6-Dioxo-1-phenyl-5-(2,4,6-trichlorophenyl)-1,3a,4,5,6,6a-hexahydropyrrolo[3,4-c]pyrrole-1-phosphonate (**9w**).* Following the general procedure, AgOAc (8.3 mg, 0.05 mmol), *N*-(2,4,6-trichlorophenyl)maleimide (194 mg, 0.7 mmol), acetonitrile (4 mL), and diethyl α-phenylisocyanomethylphosphonate (127 mg, 0.5 mmol) gave **9w** (215 mg, 81%) as a yellowish solid, after column chromatography (EtOAc). Mp 146−148 °C (EtOAc). IR (ATR) 3501, 2976, 2854, 1786, 1727, 1471, 1361, 1253, 1043, 1322, 961, 704 cm^{-1}. ^1H NMR (400 MHz, $CDCl_3$, HETCOR) δ 1.14 (t, *J* = 7.0 Hz, 3H, CH_2CH_3), 1.28 (t, *J* = 7.0 Hz, 3H, CH_2CH_3), 3.84 (m, 1H, CH_2CH_3), 4.03−4.17 (m, 3H, CH_2CH_3), 4.41 (dd, *J* = 18.0, 9.0 Hz, 1H, H-6a), 4.57 (ddd, *J* = 8.5, 4.0, 1.0 Hz, 1H, H-3a), 7.26 (d, *J* = 3.0 Hz, 1H, ArH), 7.28−7.34 (m, 3H, ArH), 7.36 (d, *J* = 2.0 Hz, 1H, ArH), 7.75 (br d, *J* = 8.0 Hz, 2H, ArH), 8.02 (dd, *J* = 5.0, 1.0 Hz, 1H, H-3). ^{13}C NMR (100.6 MHz) δ 16.3 (d, *J* = 6.0 Hz, CH_2CH_3), 16.4 (d, *J* = 6.0 Hz, CH_2CH_3), 48.3 (d, *J* = 3.0 Hz, C-6a), 61.0 (C-3a), 63.7 (d, *J* = 7.0 Hz, CH_2CH_3), 64.9 (d, *J* = 8.0 Hz, CH_2CH_3), 86.7 (d, *J* = 152.0 Hz, C-1), 126.6 (C-*ipso*), 127.8 (d, *J* = 2.0 Hz, 2CHAr), 128.6 (CHAr), 128.7 (CHAr), 128.8 (CHAr), 129.0 (d, *J* = 5.0 Hz, 2CHAr), 133.0 (d, *J* = 5.0 Hz, C-*ipso*), 135.1 (d, *J* = 10.0 Hz, C-*ipso*), 136.8 (2C-*ipso*), 161.8 (d, *J* = 11.0 Hz, C-3), 169.3 (d, *J* = 5.0 Hz, CO), 169.8 (d, *J* = 14.0 Hz, CO). HRMS $C_{22}H_{21}Cl_3N_2O_5P$ $[M + H]^+$ 529.0248; found, 529.0242. Purity 98% (t_R = 5.06 min).

*Diethyl (1RS,3aSR,6aSR)-5-(3-Nitrophenyl)-4,6-dioxo-1-phenyl-1,3a,4,5,6,6a-hexahydropyrrolo[3,4-c]pyrrole-1-phosphonate (**9x**).* Following the general procedure, AgOAc (4 mg, 0.02 mmol), *N*-(3-nitrophenyl)maleimide (131 mg, 0.6 mmol), acetonitrile (3 mL), and diethyl α-phenylisocyanomethylphosphonate (101 mg, 0.4 mmol) gave **9x** (101 mg, 54%) as a white solid, after column chromatography (EtOAc). Mp 192−195 °C (EtOAc). IR (NaCl) 2984, 1724, 1537, 1351, 1248, 1176, 1050, 971, 758, 674 cm^{-1}. ^1H NMR (400 MHz, $CDCl_3$, HETCOR) δ 1.21 (t, *J* = 7.0 Hz, 3H, CH_2CH_3), 1.29 (t, *J* = 7.0 Hz, 3H, CH_2CH_3), 3.98 (m, 1H, CH_2CH_3), 4.10−4.24 (m, 3H, CH_2CH_3), 4.30 (dd, *J* = 18.0, 9.0 Hz, 1H, H-6a), 4.53 (ddd, *J* = 9.0, 3.0, 1.0 Hz, H-3a), 7.11 (dq, *J* = 8.0, 1.0 Hz, 1H, ArH), 7.38−7.41 (m, 3H, ArH), 7.49 (t, *J* = 8.0 Hz, 1H, ArH), 7.58 (t, *J* = 2.0 Hz, 1H, ArH), 7.67−7.69 (m, 2H, ArH), 8.07 (dd, *J* = 5.0, 1.0 Hz, 1H, H-3), 8.14 (ddd, *J* = 8.5, 2.5, 1.0 Hz, 1H, ArH). ^{13}C NMR (100.6 MHz) δ 16.2 (d, *J* = 3.0 Hz, CH_2CH_3), 16.3 (d, *J* = 3.5 Hz, CH_2CH_3), 48.5 (d, *J* = 2.0 Hz, C-6a), 60.0 (C-3a), 63.6 (d, *J* = 7.5 Hz, CH_2CH_3), 64.7 (d, *J* = 7.5 Hz, CH_2CH_3), 86.2 (d, *J* = 158.0 Hz, C-1), 121.4 (CHAr), 123.3 (CHAr), 128.1 (2CHAr), 128.2 (CHAr), 128.3 (CHAr), 128.9 (d, *J* = 1.5 Hz, CHAr), 129.8 (CHAr), 131.9 (CHAr), 132.0 (C-*ipso*), 133.2 (d, *J* = 4.0 Hz, C-*ipso*), 148.3 (C-*ipso*), 161.7 (d, *J* = 12.0 Hz, C-3), 170.2 (d, *J* = 5.5 Hz, CO), 171.1 (d, *J* = 11.0 Hz, CO). HRMS $C_{22}H_{23}N_3O_7P$ $[M + H]^+$ 472.1268; found, 472.1276. Anal. Calcd for $C_{22}H_{22}N_3O_7P$: C, 56.05%; H, 4.70%; N, 8.91%. Found: C, 55.73%; H, 4.74%; N, 8.85%.

*Diethyl (1RS,3aSR,6aSR)-5-(2-Methyl-5-nitrophenyl)-4,6-dioxo-1-phenyl-1,3a,4,5,6,6a-hexahydropyrrolo[3,4-c]pyrrole-1-phosphonate (**9y**).* Following the general procedure, AgOAc (5 mg, 0.03 mmol), *N*-(2-methyl-5-nitrophenyl)maleimide (138 mg, 0.6 mmol), acetonitrile (3 mL), and diethyl α-phenylisocyanomethylphosphonate (101 mg, 0.4 mmol) gave **9y** (111 mg, 57%) as a white solid, after column chromatography (EtOAc). Mp 196−198 °C (EtOAc). IR (ATR) 3493, 3079, 2947, 2845, 1724, 1519, 1343, 1192, 1017, 739, 578 cm^{-1}. ^1H NMR (400 MHz, $CDCl_3$, HETCOR) δ 1.16 (td, *J* = 7.0, 0.5 Hz, 3H, CH_2CH_3 rotamer A), 1.22 (td, *J* = 7.0, 0.5 Hz, 3H, CH_2CH_3 rotamer B), 1.29 (td, *J* = 7.0, 0.5 Hz, 3H, CH_2CH_3 rotamer B), 1.30 (td, *J* = 7.0, 0.5 Hz, 3H, CH_2CH_3 rotamer A), 1.51 (s, 3H, CH_3 rotamer A), 2.15 (s, 3H, CH_3 rotamer B), 3.85 (m, 1H, CH_2CH_3 rotamer A), 3.99 (m, 1H, CH_2CH_3 rotamer B), 4.03−4.24 (m, 6H, CH_2CH_3 rotamer A and B), 4.35 (dd, *J* = 18.0, 9.0 Hz, 1H, H-6a rotamer B), 4.39 (dd, *J* = 18.5, 9.0 Hz, 1H, H-6a rotamer A), 4.55 (ddd, *J* = 10.0, 2.5, 1.5 Hz, 1H, H-3a rotamer B), 4.59 (ddd, *J* = 9.0, 3.5, 1.5 Hz, 1H, H-3a rotamer A), 6.88 (d, *J* = 2.5 Hz, 1H, ArH rotamer B), 7.47−7.19 (m, 8H, 4ArH rotamer A and 4ArH rotamer B), 7.69 (br s, 2H, ArH rotamer B), 7.77 (d, *J* = 7.5 Hz, 2H, ArH rotamer A), 7.91 (d, *J* = 2.5 Hz, 1H, ArH rotamer A), 8.05 (dd, *J* = 5.0, 1.5 Hz, 1H, C-3 rotamer A), 8.08 (dd, *J* = 5.5, 2.5 Hz, 1H, C-3 rotamer B), 8.08−8.11 (m, 2H, ArH rotamer A and rotamer B). ^{13}C NMR (100.6 MHz) δ 16.3 (d, *J* = 5.5 Hz, CH_2CH_3 rotamer A), 16.3 (d, *J* = 5.5 Hz, CH_2CH_3 rotamer B), 16.4 (d, *J* = 5.5 Hz, CH_2CH_3 rotamer A), 16.4 (d, *J* = 5.5 Hz, CH_2CH_3 rotamer B), 17.5 (CH_3 rotamer A), 18.2 (CH_3 rotamer B), 48.3 (d, *J* = 2.5 Hz, C-6a rotamer A), 49.2 (d, *J* = 2.5 Hz, C-6a rotamer B), 60.1 (C-3a rotamer B), 61.0 (C-3a rotamer A), 63.7 (d, *J* = 7.5 Hz, CH_2CH_3 rotamer A), 63.8 (d, *J* = 7.5 Hz, CH_2CH_3 rotamer B), 64.9 (d, *J* = 7.5 Hz, CH_2CH_3 rotamer B), 65.0((d, *J* = 7.5 Hz, CH_2CH_3 rotamer A), 86.3 (d, *J* = 159.0, C-1 rotamer B), 86.6 (d, *J* = 154.5, C-1 rotamer A), 123.5 (CHAr rotamer B), 123.7 (CHAr rotamer A), 124.3 (CHAr rotamer A), 124.5 (CHAr rotamer B), 127.9 (CHAr rotamer A), 128.0 (CHAr rotamer B), 128.3 (d, *J* = 5.5 Hz, 2CHAr rotamer B), 128.3 (CHAr rotamer A), 128.4 (CHAr rotamer B), 128.8 (d, *J* = 2.5 Hz, CHAr rotamer A), 128.9 (d, *J* = 6.5 Hz, 2CHAr rotamer A), 129.4 (d, *J* = 2.0 Hz, CHAr rotamer B), 131.1 (C-*ipso* rotamer A), 131.2 (C-*ipso* rotamer B), 131.8 (CHAr rotamer B), 131.9 (CHAr rotamer A), 133.3 (d, *J* = 4.5 Hz, C-*ipso* rotamer A), 133.4 (d, *J* = 4.0 Hz, C-*ipso* rotamer B), 143.8 (C-*ipso* rotamer A), 143.9 (C-*ipso* rotamer B), 146.6 (C-*ipso* rotamer A), 146.7 (C-*ipso* rotamer B), 161.8 (d, *J* = 12.5 Hz, C-3 rotamer B), 161.9 (d, *J* = 11.5 Hz, C-3 rotamer A), 170.4 (d, *J* = 5.0 Hz, CO rotamer B), 170.6 (d, *J* = 5.5 Hz, CO rotamer A), 171.0 (d, *J* = 13.5 Hz, CO rotamer A), 171.3 (d, *J* = 10.0 Hz, CO rotamer B). HRMS $C_{23}H_{25}N_3O_7P$ $[M + H]^+$ 486.1425; found, 486.1424. Anal. Calcd for $C_{23}H_{24}N_3O_7P$: C, 56.91%; H, 4.98%; N, 8.66%. Found: C, 57.33%; H, 5.11%; N, 8.59%.

*Diethyl (1RS,3aSR,6aSR)-5-(1,1′-Biphenyl)-4-yl-4,6-dioxo-1-phenyl-1,3a,4,5,6,6a-hexahydropyrrolo[3,4-c]pyrrole-1-phosphonate (**9z**).* Following the general procedure, AgOAc (5 mg, 0.03 mmol), *N*-(*p*-phenylphenyl)maleimide (200 mg, 0.8 mmol), acetonitrile (4 mL), and diethyl α-phenylisocyanomethylphosphonate (134 mg, 0.5 mmol) gave **9z** (129 mg, 49%) as a yellowish oil, after column chromatography (EtOAc). IR (NaCl) 3483, 2982, 2928, 1716, 1628, 1487, 1378, 1248, 1182, 1052, 1024, 969, 839, 792 cm^{-1}. ^1H NMR (400 MHz, $CDCl_3$, HETCOR) δ 1.20 (t, *J* = 7.0 Hz, 3H, CH_2CH_3), 1.29 (t, *J* = 7.0 Hz, 3H, CH_2CH_3), 3.97 (m, 1H, CH_2CH_3), 4.09−4.23 (m, 3H, CH_2CH_3), 4.30 (dd, *J* = 18.5, 9.0 Hz, 1H, H-6a), 4.51 (ddd, *J* = 9.0, 3.0, 1.5 Hz, 1H, H-3a), 6.80 (m, 2H, ArH), 7.31−7.42 (m, 6H, ArH), 7.47−7.51 (m, 4H, ArH), 7.71 (br d, *J* = 7.5 Hz, 2H, ArH), 8.08 (dd, *J* = 5.0, 1.5 Hz, 1H, H-3). ^{13}C NMR (100.6 MHz) δ 16.2 (d, *J* = 5.5 Hz, CH_2CH_3), 16.3 (d, *J* = 5.5 Hz, CH_2CH_3), 48.2 (d, *J* = 2.5 Hz, C-6a), 60.2 (C-3a), 63.5 (d, *J* = 7.0 Hz, CH_2CH_3), 64.6 (d, *J* = 7.5 Hz, CH_2CH_3), 86.5 (d, *J* = 157.0 Hz, C-1), 126.3 (2CHAr), 127.1 (2CHAr), 127.7 (CHAr), 127.8 (2CHAr), 127.9 (d, *J* = 1.5 Hz, 2CHAr), 128.4 (d, *J* = 6.0 Hz, 2CHAr), 128.6 (d, *J* = 2.0 Hz, CHAr), 128.8 (2CHAr), 130.0 (C-*ipso*), 133.4 (d, *J* = 4.0 Hz, C-*ipso*), 140.0 (C-*ipso*), 141.7 (C-*ipso*), 162.3 (d, *J* = 12.0 Hz, C-3), 170.9 (d, *J* = 5.5 Hz, CO), 171.7 (d, *J* = 11.5 Hz, CO). HRMS $C_{28}H_{28}N_2O_5P$ $[M + H]^+$503.1730; found, 503.1727. Purity 98.5% (t_R = 4.71 min).

*Diethyl (1RS,3aSR,6aSR)-4,6-Dioxo-1-phenyl-5-(p-tolyl)-1,3a,4,5,6,6a-hexahydropyrrolo[3,4-c]pyrrole-1-phosphonate (**9aa**).* Following the general procedure, AgOAc (6 mg, 0.04 mmol), *N*-(4-methylphenyl)maleimide (153 mg, 0.9 mmol), acetonitrile (4.5 mL), and diethyl α-phenylisocyanomethylphosphonate (168 mg, 0.6 mmol) gave **9aa** (199 mg, 75%) as a white solid, after column chromatography (EtOAc/hexane 3:2 to 9:1). Mp 156−158 °C (EtOAc). IR (ATR) 3476, 2936, 2863, 1711, 1632, 1520, 1368, 1240, 1181, 1025, 971, 740, 583 cm^{-1}. ^1H NMR (400 MHz, $CDCl_3$, HETCOR) δ 1.19 (t, *J* = 7.0 Hz, 3H, CH_2CH_3), 1.29 (t, *J* = 7.0 Hz, 3H, CH_2CH_3), 2.28 (s, 3H, CH_3−Ar), 3.93 (m, 1H, CH_2CH_3), 4.11−4.19 (m, 3H, CH_2CH_3), 4.24 (dd, *J* = 16.5, 9.0, 1H, H-6a), 4.46 (ddd, *J* = 8.5, 3.0, 1.5 Hz, 1H, H-3a), 6.60 (m, 2H, ArH), 7.09 (m, 2H, ArH), 7.31−7.38 (m, 3H, ArH), 7.68−7.70 (m, 2H, ArH), 8.05 (dd, *J* = 5.0, 1.5 Hz, 1H, H-3). ^{13}C NMR (100.6 MHz) δ 16.2 (d, *J* = 5.5 Hz, CH_2CH_3), 16.3 (d, *J* = 5.5 Hz, CH_2CH_3), 21.1 (CH_3−Ar), 48.1 (d, *J* = 3.0 Hz, C-6a), 60.2 (C-3a), 63.5 (d, *J* = 7.0 Hz, CH_2CH_3), 64.6 (d, *J* = 8.0 Hz, CH_2CH_3), 86.2 (d, *J* = 156.0 Hz, C-1), 125.8

https://dx.doi.org/10.1021/acs.jmedchem.9b02080
J. Med. Chem. 2020, 63, 3610−3633

(2CHAr), 127.9 (d, J = 2.0 Hz, 2CHAr), 128.3 (CHAr), 128.4 (CHAr), 128.5 (d, J = 2.0 Hz, CHAr), 128.5 (C-*ipso*), 129.6 (2CHAr), 133.5 (d, J = 4.0 Hz, C-*ipso*), 138.8 (C-*ipso*), 162.4 (d, J = 12.0 Hz, C-3), 171.1 (d, J = 5.0 Hz, CO), 171.7 (d, J = 11.0 Hz, CO). HRMS $C_{23}H_{26}N_2O_5P$ $[M + H]^+$ 441.1574; found, 441.1572. Anal. Calcd for $C_{23}H_{25}N_2O_5P$: C, 62.72%; H, 5.72%; N, 6.36%. Found: C, 62.87%; H, 5.82%; N, 6.18%.

*Diethyl (1RS,3aSR,6aSR)-4,6-Dioxo-5-(4-phenoxyphenyl)-1-phenyl-1,3a,4,5,6,6a-hexahydropyrrolo[3,4-c]pyrrole-1-phosphonate (**9ab**).* Following the general procedure, AgOAc (9 mg, 0.05 mmol), *N*-(4-phenoxyphenyl)maleimide (371 mg, 1.4 mmol), acetonitrile (7 mL), and diethyl α-phenylisocyanomethylphosphonate (228 mg, 0.9 mmol) gave **9ab** (302 mg, 65%) as a white solid, after column chromatography (EtOAc). Mp 165−167 °C (EtOAc). IR (NaCl) 3488, 3057, 2984, 1783, 1715, 1628, 1488, 1242, 1187, 1024, 700, 578 cm^{-1}. ^1H NMR (400 MHz, $CDCl_3$, HETCOR) δ 1.19 (t, J = 7.0 Hz, 3H, CH_2CH_3), 1.28 (t, J = 7.0 Hz, 3H, CH_2CH_3), 3.95 (m, 1H, CH_2CH_3), 4.10−4.19 (m, 3H, CH_2CH_3), 4.25 (dd, J = 18.0, 8.5 Hz, 1H, H-6a), 4.46−4,49 (ddd, J = 8.5, 3.0, 1.5 Hz, 1H, H-3a), 6.64−6.67 (m, 2H, ArH), 6.87−6.89 (m, 2H, ArH), 6.96−6.98 (m, 2H, ArH), 7.12 (m, 1H, ArH), 7.30−7.38 (m, 5H, ArH), 7.69 (d, J = 8.0 Hz, 2H, ArH), 8.01 (dd, J = 5.0, 1.5 Hz, 1H, H-3). ^{13}C NMR (100.6 MHz) δ 16.2 (d, J = 4.0 Hz, CH_2CH_3), 16.3 (d, J = 4.0 Hz, CH_2CH_3), 48.2 (d, J = 3.0 Hz, C-6a), 60.1 (C-3a), 63.5 (d, J = 7.0 Hz, CH_2CH_3), 64.6 (d, J = 7.0 Hz, CH_2CH_3), 86.2 (d, J = 157.0 Hz, C-1), 118.5 (2CHAr), 119.6 (2CHAr), 124.0 (2CHAr), 125.6 (C-*ipso*), 127.5 (2CHAr), 127.9 (d, J = 2.0 Hz, 2CHAr), 128.4 (d, J = 6.0 Hz, CHAr), 128.6 (d, J = 2.0. Hz, CHAr), 129.8 (2CHAr), 133.5 (d, J = 4.0 Hz, C-*ipso*), 156.2 (C-*ipso*), 157.6 (C-*ipso*), 162.2 (d, J = 12.0 Hz, C-3), 171.0 (d, J = 6.0 Hz, CO), 171.7 (d, J = 11.0 Hz, CO). HRMS $C_{28}H_{28}N_2O_6P$ $[M + H]^+$ 519.1679; found, 519.1675. Anal. Calcd for $C_{28}H_{27}N_2O_6P$: C, 64.86%; H, 5.25%; N, 5.40%. Found: C, 65.12%; H, 5.26%; N, 5.41%.

*Diethyl (1RS,3aSR,6aSR)-5-(Naphth-1-yl)-4,6-dioxo-1-phenyl-1,3a,4,5,6,6a-hexahydropyrrolo[3,4-c]pyrrole-1-phosphonate (**9ac**).* Following the general procedure, AgOAc (3 mg, 0.02 mmol), *N*-(naphth-1-yl)maleimide (100 mg, 0.5 mmol), acetonitrile (2 mL), and diethyl α-phenylisocyanomethylphosphonate (76 mg, 0.3 mmol) gave **9ac** (70 mg, 49%) as a white solid, after column chromatography (EtOAc/hexane 1:1 to 9:1). Mp 197−198 °C (EtOAc). IR (ATR) 3480, 2927, 2853, 1716, 1598, 1446, 1397, 1358, 1240, 1177, 1039, 1025, 961, 775, 706, 583 cm^{-1}. ^1H NMR (400 MHz, $CDCl_3$, HETCOR) δ 1.17 (td, J = 7.0, 0.5 Hz, 3H, CH_2CH_3 rotamer A), 1.20 (td, J = 7.0, 0.5 Hz, 3H, CH_2CH_3 rotamer B), 1.30 (t, J = 7.0 Hz, 3H, CH_2CH_3 rotamer A), 1.31 (t, J = 7.0 Hz, 3H, CH_2CH_3 rotamer B), 3.90 (m, 1H, CH_2CH_3 rotamer A), 3.98 (m, 1H, CH_2CH_3 rotamer B), 4.04−4.26 (m, 6H, CH_2CH_3 rotamer A and B), 4.43 (dd, J = 18.5, 9.0 Hz, 1H, H-6a rotamer A), 4.46 (dd, J = 18.0, 8.5 Hz, 1H, H-6a rotamer B), 4.63 (ddd, J = 9.0, 3.5, 1.5 Hz, 1H, H-3a rotamer A), 4.67 (ddd, J = 8.5, 3.0, 1.5 Hz, 1H, H-3a rotamer B), 6.33 (dd, J = 8.5, 1.0 Hz, 1H, ArH rotamer A), 6.39 (dd, J = 7.5, 1.0 Hz, 1H, ArH rotamer B), 7.12 (ddd, J = 8.5, 7.0, 1.5 Hz, 1H, ArH rotamer A), 7.21 (dd, J = 7.5, 1.0 Hz, 1H, ArH rotamer A), 7.28−7.49 (m, 12H, ArH rotamer A and B), 7.73−7.90 (m, 8H, ArH rotamer A and B), 8.12 (dd, J = 5.0 Hz, 1.5 Hz, 1H, H-3 rotamer B), 8.13 (dd, J = 5.0, 1.5 Hz, 1H, H-3 rotamer A). ^{13}C NMR (100.6 MHz) δ 16.2 (d, J = 5.0 Hz, CH_2CH_3 rotamer A or B), 16.3 (d, J = 5.0 Hz, CH_2CH_3 rotamer A or B), 16.3 (d, J = 6.0 Hz, $2CH_2CH_3$ rotamer A or B), 48.3 (d, J = 2.5 Hz, C-6a rotamer A), 48.6 (d, J = 2.5 Hz, C-6a rotamer B), 60.3 (C-3a rotamer B), 61.0 (C-3a rotamer A), 63.6 (d, J = 7.5 Hz, $2CH_2CH_3$ rotamer A and B), 64.7 (d, J = 7.0 Hz, CH_2CH_3 rotamer B), 64.7 (d, J = 7.5 Hz, CH_2CH_3 rotamer A), 86.2 (d, J = 157.5 Hz, C-1 rotamer B), 86.5 (d, J = 155.0 Hz, C-1 rotamer A), 121.2 (CHAr rotamer A), 121.6 (CHAr rotamer B), 125.0 (CHAr rotamer A), 125.1 (CHAr rotamer B), 125.7 (CHAr rotamer B), 126.0 (CHAr rotamer A), 126.3 (CHAr rotamer A), 126.5 (CHAr rotamer B), 127.0 (CHAr rotamer A), 127.2 (CHAr rotamer B), 127.6 (C-*ipso* rotamer A), 127.8 (C-*ipso* rotamer B), 127.9 (d, J = 2.0 Hz, 2CHAr rotamer A), 128.0 (d, J = 2.0 Hz, 2CHAr rotamer B), 128.3 (CHAr rotamer A), 128.4 (d, J = 6.0 Hz, CHAr rotamer B), 128.6 (d, J = 2.0 Hz, 2CHAr rotamer A), 128.7 (d, J = 2.5 Hz, 2CHAr rotamer B), 128.9 (CHAr rotamer B), 129.0 (CHAr rotamer A), 130.0 (CHAr rotamer A), 130.1 (CHAr rotamer B), 133.4 (d, J = 4.5 Hz, C-*ipso* rotamer A), 133.5 (d, J = 4.0 Hz, C-*ipso* rotamer B), 134.1 (C-*ipso* rotamer A), 134.2 (C-*ipso* rotamer B), 162.3 (d, J = 11.5 Hz, C-3 rotamer A), 162.4 (d, J = 12.0 Hz, C-3 rotamer B), 171.3 (d, J = 5.5 Hz, CO rotamer B), 171.4 (d, J = 5.5 Hz, CO rotamer A), 171.7 (d, J = 12.5 Hz, CO rotamer A), 171.9 (d, J = 11.5 Hz, CO rotamer B). HRMS $C_{26}H_{26}N_2O_5P$ $[M + H]^+$ 477.1574; found, 477.1571. Anal. Calcd For $C_{26}H_{25}N_2O_5P$: C, 65.54%; H, 5.29%; N, 5.88%. Found: C, 65.34%; H, 5.12%; N, 5.65%.

*Diethyl (1RS,3aSR,6aSR)-5-(2-Chloropyridin-3-yl)-4,6-dioxo-1-phenyl-1,3a,4,5,6,6a-hexahydropyrrolo[3,4-c]pyrrole-1-phosphonate (**9ad**).* Following the general procedure, AgOAc (12 mg, 0.07 mmol), *N*-(2-chloropyridin-3-yl)maleimide (250 mg, 1.2 mmol), acetonitrile (6 mL), and diethyl α-phenylisocyanomethylphosphonate (203 mg, 0.8 mmol) gave **9ad** (224 mg, 61%) as a white solid, after column chromatography (EtOAc). Mp 176−178 °C (EtOAc). IR (ATR) 3483, 2991, 2948, 1790, 1722, 1564, 1420, 1242, 1050, 752, 699, 574 cm^{-1}. ^1H NMR (400 MHz, $CDCl_3$, HETCOR) δ 1.14 (td, J = 7.0, 0.5 Hz, 3H, CH_2CH_3 rotamer A), 1.19 (td, J = 7.0, 0.5 Hz, 3H, CH_2CH_3 rotamer B), 1.28 (td, J = 7.0, 0.5 Hz, 3H, CH_2CH_3 rotamer A), 1.29 (td, J = 7.0, 0.5 Hz, 3H, CH_2CH_3 rotamer B), 3.82 (m, 1H, CH_2CH_3 rotamer A), 3.95 (m, 1H, CH_2CH_3 rotamer B), 4.05−4.20 (m, 6H, CH_2CH_3 rotamer A and B), 4.36 (dd, J = 18.0, 8.5 Hz, 1H, H-6a rotamer A), 4.38 (dd, J = 18.0, 8.5 Hz, 1H, H-6a rotamer B), 4.53 (ddd, J = 8.5, 4.0, 1.5 Hz, 1H, H-3a rotamer A), 4.58 (ddd, J = 8.5, 3.0, 1.5 Hz, 1H, H-3a rotamer B), 6.59 (dd, J = 8.0, 2.0 Hz, 1H, ArH rotamer B), 7.14 (dd, J = 8.0, 5.0 Hz, 1H, ArH rotamer B), 7.27 (dd, J = 8.0, 5.0 Hz, 1H, ArH rotamer A), 7.31−7.37 (m, 6H, 3ArH rotamer A and 3ArH rotamer B), 7.46 (dd, J = 8.0, 2.0 Hz, 1H, ArH rotamer A), 7.69 (m, 2H, ArH rotamer A), 7.76 (m, 2H, ArH rotamer B), 8.02 (dd, J = 5.5 Hz, 1.5 Hz, 1H, H-3 rotamer A), 8.07 (dd, J = 5.0, 1.5 Hz, 1H, H-3 rotamer B), 8.36 (dd, J = 5.0, 2.0 Hz, 2H, ArH rotamer A and rotamer B). ^{13}C NMR (100.6 MHz) δ 16.3 (d, J = 5.5 Hz, CH_2CH_3 rotamer A), 16.4 (d, J = 5.5 Hz, CH_2CH_3 rotamer B), 16.4 (d, J = 6.0 Hz, CH_2CH_3 rotamer A), 16.5 (d, J = 5.5 Hz, CH_2CH_3 rotamer B), 48.4 (d, J = 2.5 Hz, C-6a rotamer A), 49.0 (d, J = 2.5 Hz, C-6a rotamer B), 60.4 (C-3a rotamer A), 61.0 (C-3a rotamer B), 63.7 (d, J = 7.5 Hz, CH_2CH_3 rotamer A), 63.8 (d, J = 7.5 Hz, CH_2CH_3 rotamer B), 64.9 (d, J = 7.5 Hz, CH_2CH_3 rotamer B), 65.0 (d, J = 7.5 Hz, CH_2CH_3 rotamer A), 86.1 (d, J = 158.0 Hz, C-1 rotamer A or B), 86.9 (d, J = 153.0 Hz, C-1 rotamer A or B), 123.0 (CHAr rotamer A), 123.2 (CHAr rotamer B), 126.4 (C-*ipso* rotamer A), 126.5 (C-*ipso* rotamer B), 127.9 (d, J = 2.0 Hz, 2CHAr rotamer A), 128.1 (d, J = 1.5 Hz, 2CHAr rotamer B), 128.6 (d, J = 5.5 Hz, 2CHAr rotamer B), 128.8 (d, J = 4.5 Hz, CHAr rotamer A or B), 128.8 (CHAr rotamer A or B), 128.9 (d, J = 5.5 Hz, 2CHAr rotamer A), 132.9 (d, J = 4.5 Hz, C-*ipso* rotamer A), 133.6 (d, J = 4.0 Hz, C-*ipso* rotamer B), 138.4 (CHAr rotamer B), 138.6 (CHAr rotamer A), 149.2 (C-*ipso* rotamer A), 149.5 (C-*ipso* rotamer B), 150.3 (CHAr rotamer A), 150.5 (CHAr rotamer B), 161.6 (d, J = 11.5 Hz, C-3 rotamer A), 162.0 (d, J = 12.5 Hz, C-3 rotamer B), 169.7 (d, J = 5.0 Hz, CO rotamer A), 169.8 (d, J = 5.5 Hz, CO rotamer B), 170.5 (d, J = 11.5 Hz, CO rotamer A), 170.6 (d, J = 14.5 Hz, CO rotamer B). HRMS $C_{21}H_{22}ClN_3O_5P$ $[M + H]^+$ 462.0980; found, 462.0980. Anal. Calcd For $C_{21}H_{21}ClN_3O_5P$: C, 54.61%; H, 4.58%; N, 9.10%. Found: C, 55.01%; H, 4.67%; N, 8.86%.

Theoretical Calculations. The study of the [3 + 2] cycloaddition reaction (Scheme 1) was performed for model systems that include the reactants (dimethyl α-phenylisocyanomethylphosphonate and *N*-methylmaleimide) and a silver cation bound to acetonitrile as the catalytic moiety. Geometry optimizations were carried out using the B3LYP functional[63,64] and the 6-31+G(d) basis set[65] for all atoms but silver, which was treated with the LANL2DZ basis[66] in conjunction with the effective core potential for inner electrons. The nature of the stationary points (reactant, transition state, and products) was confirmed by inspection of the vibrational frequencies. Intrinsic reaction coordinate calculations[67] were carried out to check the connection between the transition states and the minimum energy structures. To further check the relative stabilities of transition states,

https://dx.doi.org/10.1021/acs.jmedchem.9b02080
J. Med. Chem. 2020, 63, 3610−3633

geometry optimizations were also performed using the MN15L functional.[68] Finally, solvation calculations were performed with the SMD version[69] of the IEFPCM model to take into account the contribution due to solvation in acetonitrile. All calculations were performed with Gaussian 16.[70]

Binding Studies. *Preparation of Cellular Membranes.* Male Swiss mice (final age 8−10 weeks) and Sprague−Dawley rats weighting 250−300 g (Harlan Interfauna Iberica, Spain) were killed, and the brain cortex was dissected and stored at −70 °C until assays were performed. Kidneys were also obtained from male Sprague−Dawley rats. All animal experimental protocols were performed in agreement with European Union regulations (O.J. of E.C. L 358/1 18/12/1986).

Human brain samples were obtained at autopsy in the Basque Institute of Legal Medicine, Bilbao, Spain. Samples from the prefrontal cortex (Brodmann's area 9) were dissected at the time of autopsy and immediately stored at −70 °C until assay. The study was developed in compliance with policies of research and ethical review boards for post-mortem brain studies.

To obtain cellular membranes (P2 fraction), the different samples were homogenized using an ultraturrax in 30 volumes of homogenization buffer (0.25 M sucrose, 1 mM $MgCl_2$, 5 mM Tris-HCl, pH 7.4). The crude homogenate was centrifuged for 5 min at 1000*g* (4 °C), and the supernatant was centrifuged again for 10 min at 40000*g* (4 °C). The resultant pellet was washed twice in 20 volumes of homogenization buffer and recentrifuged in similar conditions. Protein content was measured according to the method of Bradford using BSA as standard.

Competition Binding Assays. The pharmacological activity of the compounds was evaluated through competition binding studies against the I_2-IR selective radioligand [^{3}H]2-[(2-benzofuranyl)-2-imidazoline (2-BFI), the α_2-adrenergic receptor selective radioligand [^{3}H]RX821002 (2-methoxyidazoxan) or the I_1-IR selective radioligand [^{3}H]clonidine. Specific binding was measured in 0.25 mL aliquots (50 mM Tris-HCl, pH 7.5) containing 100 μg of membranes, which were incubated in 96-well plates either with [^{3}H]2-BFI (2 nM) for 45 min at 25 °C, [^{3}H]RX821002 (1 nM) for 30 min at 25 °C, or [^{3}H]clonidine (5 nM) for 45 min at 22 °C, in the absence or presence of the competing compounds (10^{-12} to 10^{-3} M, 10 concentrations). [^{3}H]Clonidine binding was performed in the presence of 10 μM adrenaline to preclude binding to α_2-AR.

Incubations were terminated by separating free ligand from bound ligand by rapid filtration under vacuum (1450 Filter Mate Harvester, PerkinElmer) through GF/C glass fiber filters. The filters were then rinsed three times with 300 μL of binding buffer, air-dried (120 min), and counted for radioactivity by liquid scintillation spectrometry using a MicroBeta TriLux counter (PerkinElmer). Specific binding was determined and plotted as a function of the compound concentration. Nonspecific binding was determined in the presence of idazoxan (10^{-5} M), a compound with well established affinity for I_2-IR and α_2-adrenergic receptors, in [^{3}H]2-BFI and [^{3}H]RX821002 assays or rilmenidine (10^{-5} M) in [^{3}H]clonidine experiments. Analyses of competition experiments to obtain the inhibition constant (K_i) were performed by nonlinear regression using the GraphPad Prism program. K_i values were normalized to pK_i values. I_2-IR/α_2 selectivity index was calculated as the antilogarithm of the difference between pK_i values for I_2-IR and pK_i values for α_2-AR. For [^{3}H]clonidine experiments, IC_{50} values were calculated (the concentration of tested ligand that displaces 50% of specifically bound [^{3}H]clonidine).

I_1-Binding Site Assay. Kidneys were obtained from male Sprague−Dawley rats (250−280 g) and cellular membranes (P2 fractions) prepared according to established methods. [^{3}H]RX821002 (2-methoxyidazoxan) binds to α_2-adrenoceptor subtypes and a nonadrenoceptor imidazoline binding site in rat kidney.[71]

Competition binding assays were performed as previously reported with minor modifications.[25] [^{3}H]Clonidine (5 nM, Perkin−Elmer) was bound in the presence of 10 μM adrenaline to preclude binding to α_2-adrenoceptors. The specific component was defined by 1 mM rilmenidine. Membrane aliquots (220 μL, 0.1−0.12 mg of protein) were incubated with 10 concentrations of the test compounds over the range 10^{-12} to 10^{-3} M.

Incubations were carried out in 96 well plates (final volume 250 μL/well) in 50 mM Tris−HCl buffer (pH 7.4) supplemented with 1 mM $MgCl_2$ at 22 °C for 45 min with agitation (400 rpm). Bound radioligand and free radioactivity were separated by rapid filtration through presoaked (0.5% polyethylenimine) glass-fiber filters (Whatman GFB). Trapped radioligand was determined by liquid scintillation counting, and the data were analyzed with GraphPad Prism version 5.0 for Windows (GraphPad Software, San Diego, CA, USA) to yield IC_{50} values (the concentration of tested ligand that displaces 50% of specifically bound [^{3}H]clonidine).

3D-QSAR Study. *Data Set Preparation.* The data set composed of previously synthesized and in vitro tested bicyclic α-iminophosphonates with different affinities on I_2-IR and α_2-AR receptors was used for the creation of the 3D-QSAR models (Table 1). Additionally, to compare and validate our results, we have added four standards in both data sets, tracizoline, idazoxan, BU99008, and LSL60101. Examined compounds cover wide range of experimental activity (pK_i I_2, 3.11−10.28; pK_i α_2, 3.59−10.27) and structural diversity, which ensure good quality and applicability of the created 3D-QSAR models. Selection of dominant forms of studied ligands at physiological pH 7.4 was obtained by the Marvin Sketch 5.5.1.0 program.[72] Subsequently, they were initially preoptimized with semiempirical/PM3 (Parameterized Model revision 3) method[73,74] and then by ab initio Hartree−Fock/3-21G method[75] using Gaussian 09 software[76] included in Chem3D Ultra program.[77] Obtained ligands' conformations were used for calculation of specific molecular descriptors (grid independent descriptors, GRIND)[78] and 3D-QSAR model building.

3D-QSAR Study. 3D-QSAR models were created using Pentacle program,[79] which calculates GRID independent descriptors (GRIND and GRIND2) from molecular interaction fields (MIFs). Four different probes were used to calculate MIFs: O probe (hydrogen bond acceptor groups), N1 probe (hydrogen bond donor groups), DRY probe (hydrophobic interactions), and TIP probe (the shape of molecule). The grid spacing was set to 0.5. ALMOND algorithm was used for the extraction of the most relevant regions, which represent favorable interaction positions between ligand and probe. Consistently Large Auto and Cross Correlation (CLACC) algorithm was used to calculate GRIND descriptors using the correlation between same and different nodes. The smoothing window was set to 0.8 Å. Partial Least Square (PLS) regression was applied for 3D-QSAR model building. Initial number of descriptors was reduced using Fractional Factorial Design (FFD) to obtain most significant GRIND variables. The results of node−node energies between the same or a different probe were then presented as correlograms.[79,80]

***In vivo* studies in mice.** Studies and procedures involving mouse brain dissection and extractions followed the ARRIVE[81] and standard ethical guidelines (European Communities Council Directive 2010/63/EU and Guidelines for the Care and Use of Mammals in Neuroscience and Behavioral Research, National Research Council 2003) and were approved by the respective Local Bioethical Committees (Universitat de les Illes Balears-CAIB and University of Barcelona-GenCat). All efforts were made to minimize the number of animals used and their suffering.

Hypothermia. For this study a total of 35 adult CD-1 mice and 9 adult Sprague−Dawley rats bred and housed in standard cages under defined environmental conditions (22 °C, 70% humidity, and 12 h light/dark cycle, lights on at 8:00 AM, with free access to a standard diet and tap water) in the animal facility at the University of the Balearic Islands were used. Animals were habituated to the experimenter by being handled and weighed for 2 days prior to any experimental procedures. For the acute treatment, mice or rats received a single dose of **9d** (20 mg/kg, ip, n = 12 for mice, and 20 or 35 mg/kg, ip, n = 3 per dose for rats) or vehicle (1 mL/kg of DMSO, ip, n = 13 for mice and n = 3 for rats), while for the repeated treatment, mice were daily treated with **9d** (20 mg/kg, ip, n = 5) or vehicle (ip, n = 5) for 5 consecutive days. The possible hypothermic effect exerted by **9d** was evaluated by measuring changes in rectal

https://dx.doi.org/10.1021/acs.jmedchem.9b02080
J. Med. Chem. 2020, 63, 3610−3633

temperature before any drug treatment (basal value) and 1 h (for mice) or 1, 2, and 3 h (for rats) after drug injection by a rectal probe connected to a digital thermometer (Compact LCD display thermometer, SA880-1M, RS, Corby, UK). Animals were sacrificed right after the last rectal temperature measurement, and the hippocampus was freshly dissected and kept at −80 °C for future biochemical analysis.

Western Blot Analysis for FADD Protein. Hippocampal sample proteins (40 μg) were separated by sodium dodecyl sulfate polyacrylamide electrophoresis (SDS-PAGE) on 10% polyacrylamide minigels (Bio-Rad) and transferred onto nitrocellulose membranes by standard Western blot procedures as described previously.[25] The membranes were incubated overnight with anti-FADD (H-181) Ab, no. sc-5559 (Santa Cruz Biotechnology, Santa Cruz, CA) and then stripped and reprobed for β-actin (clone AC-15) Ab, no. A1978 (Sigma). Following secondary antibody (anti-rabbit or anti-mouse) incubation and ECL detection system (Amersham, Buckinghamshire, UK), proteins were visualized on autoradiographic films (Amersham ECL Hyperfilm). Upon densitometric scanning (GS-800 Imaging Densitometer, Bio-Rad) of immunoreactive bands (integrated optical density, IOD) the amount of FADD protein in brain samples of mice from different treatment groups was compared with that of vehicle-treated controls (100%) in the same gel. Quantification of β-actin contents served as a loading control (no differences between treatment groups, data not shown). Each brain sample (and target protein) was quantified in 2−4 gels, and the mean value was used as a final estimate.

5xFAD *In Vivo* Experimental Design. Female 5xFAD and WT mice, 5-months-old (n = 51), were used to carry out cognitive and molecular analyses. The 5xFAD mouse is a double transgenic APP/PS1 that coexpresses five mutations associated with AD and that rapidly develops severe amyloid pathology with high levels of intraneuronal Aβ42 around 2 months of age. The model was generated by the introduction of human APP with the Swedish (K670N/M671L), Florida (I716V), and London (Val717Ile) mutations and the introduction of PS1 M146L and L286V. Moreover, 5xFAD mouse presents neuronal loss and cognitive deficits in spatial learning (at approximately four to five months).[82]

The animals were randomly allocated to three experimental groups: WT control (n = 12) and 5xFAD control (n = 14), animals administered vehicle (2-hydroxypropyl)-β-cyclodextrin 1.8%, and 5xFAD treated with **9d** 5 (mg/kg)/day (n = 25), diluted in 1.8% (2-hydroxypropyl)-β-cyclodextrin and administered through drinking water, up to euthanasia. Weight and water consumption were controlled each week, and the **9d** concentration was adjusted accordingly to reach the precise dose. Animals had free access to food and water and were kept under standard temperature conditions (22 ± 2 °C) and 12 h/12 h light−dark cycles (300 lx/0 lx).

After 4 weeks of treatment period, animals were subjected to cognitive tests to study the effect of treatment on learning and memory, including short- and long-term memory (NORT). Mice were euthanized 3 days after the behavioral test completion by cervical dislocation. Brains were immediately removed from the skull, and the hippocampus was then isolated and frozen on powdered dry ice. They were maintained at −80 °C for biochemical experiments.

Behavioral Testing: NORT. In brief, mice were placed in a black L-shape maze consisting of two arms at 90°, 25 cm long, 20 cm high, and 5 cm wide. The mice were habituated to the apparatus for 10 min on 3 consecutive days in the habituation phase. Afterward, on day 4, the training session took place, in which two identical objects (A) were placed in the maze and the mice were allowed to explore freely for 10 min. Two hours after training sessions, one of the objects was replaced with a novel object (B) to assess short-term-memory. Again, the amount of time spent exploring each object was scored. During this second trial, objects A and B were placed in the maze, and the times that the animal took to explore the new object (TN) and the old object (TO) were recorded. A discrimination index (DI) was calculated, defined as (TN − TO)/(TN + TO). Twenty-four hours after the acquisition trial, the mice were tested again to assess long-term memory, with a new object substituting object B and a new DI calculated. Exploration of an object by a mouse was defined as pointing the nose toward the object at a distance ≤2 cm or touching it with the nose. Turning or sitting around the object was not considered exploration. To avoid object preference biases, objects A and B were counterbalanced so that one-half of the animals in each experimental group were first exposed to object A and then to object B, whereas the other half first saw object B and then object A. All sessions were videotaped, and the time spent with each object was manually recorded. The maze, the surface, and the objects were cleaned with 70% ethanol between the animal trials to eliminate olfactory cues.

Determination of Oxidative Stress. Hydrogen peroxide from brain samples of 10 mice of each group was measured as an indicator of OS, and it was quantified using the Hydrogen Peroxide Assay Kit (Sigma-Aldrich, St. Louis, MI) according to the manufacturer's instructions.

RNA Extraction and Gene Expression Determination. Total RNA isolation was carried out using TRIzol reagent according to manufacturer's instructions. The yield, purity, and quality of RNA were determined spectrophotometrically with a NanoDrop ND-1000 (Thermo Scientific) apparatus and an Agilent 2100B Bioanalyzer (Agilent Technologies). RNAs with 260/280 ratios and RNA integrity number (RIN) higher than 1.9 and 7.5, respectively, were selected. Reverse transcription-polymerase chain reaction (RT-PCR) was performed as follows: 2 μg of mRNA (mRNA) was reverse-transcribed using the High Capacity cDNA Reverse Transcription Kit (Applied Biosystems). Real-time quantitative PCR (qPCR) from 48 mice of both strains (n = 4−6 per group) was used to quantify mRNA expression of OS and inflammatory genes.

SYBR Green real-time PCR was performed on a Step One Plus Detection System (Applied-Biosystems) employing SYBR Green PCR Master Mix (Applied-Biosystems). Each reaction mixture contained 6.75 μL (2 μg) of complementary DNA (cDNA), 0.75 μL of each primer (of which concentration was 100 nM), and 6.75 μL of SYBR Green PCR Master Mix (2×).

TaqMan-based real-time PCR (Applied Biosystems) was also performed in a Step One Plus Detection System (Applied-Biosystems). Each 20 μL of TaqMan reaction contained 9 μL (25 ng) of cDNA, 1 μL of 20× probe of TaqMan Gene Expression Assays, and 10 μL of 2× TaqMan Universal PCR Master Mix.

Data were analyzed utilizing the comparative cycle threshold (Ct) method (ΔΔCt), where the housekeeping gene level was used to normalize differences in sample loading and preparation.[49] Normalization of expression levels was performed with *β-actin* gene for SYBR Green-based real-time PCR and TATA-binding protein (*Tbp*) gene for TaqMan-based real-time PCR. Primers sequences and TaqMan probes used in this study are presented in Table S10. Each sample was analyzed in duplicate, and the results represent the n-fold difference of the transcript levels among different groups.

■ ASSOCIATED CONTENT

Supporting Information

The Supporting Information is available free of charge at https://pubs.acs.org/doi/10.1021/acs.jmedchem.9b02080.

Experimental procedures for synthesis of **10a−10c** and **11**, theoretical calculations, 3D-QSAR study, in vitro BBB assay, DMPK assays, receptor characterization panel, in vivo data, tables of ^{1}H and ^{13}C spectra, and X-ray crystallography data (PDF)

Molecular formula strings (CSV)

■ AUTHOR INFORMATION

Corresponding Author

Carmen Escolano − *Laboratory of Medicinal Chemistry (Associated Unit to CSIC), Department of Pharmacology, Toxicology and Medicinal Chemistry, Faculty of Pharmacy and Food Sciences, and Institute of Biomedicine (IBUB), University*

https://dx.doi.org/10.1021/acs.jmedchem.9b02080
J. Med. Chem. 2020, 63, 3610−3633

*of Barcelona, E-08028 Barcelona, Spain; orcid.org/0000-0002-9117-8239; Phone: +34 934024542; Email: cescolano@ub.edu

Authors

Sònia Abás – *Laboratory of Medicinal Chemistry (Associated Unit to CSIC), Department of Pharmacology, Toxicology and Medicinal Chemistry, Faculty of Pharmacy and Food Sciences, and Institute of Biomedicine (IBUB), University of Barcelona, E-08028 Barcelona, Spain*

Sergio Rodríguez-Arévalo – *Laboratory of Medicinal Chemistry (Associated Unit to CSIC), Department of Pharmacology, Toxicology and Medicinal Chemistry, Faculty of Pharmacy and Food Sciences, and Institute of Biomedicine (IBUB), University of Barcelona, E-08028 Barcelona, Spain*

Andrea Bagán – *Laboratory of Medicinal Chemistry (Associated Unit to CSIC), Department of Pharmacology, Toxicology and Medicinal Chemistry, Faculty of Pharmacy and Food Sciences, and Institute of Biomedicine (IBUB), University of Barcelona, E-08028 Barcelona, Spain*

Christian Griñán-Ferré – *Pharmacology Section, Toxicology and Medicinal Chemistry, Faculty of Pharmacy and Food Sciences, and Institut de Neurociències, University of Barcelona, E-08028 Barcelona, Spain*

Foteini Vasilopoulou – *Pharmacology Section, Toxicology and Medicinal Chemistry, Faculty of Pharmacy and Food Sciences, and Institut de Neurociències, University of Barcelona, E-08028 Barcelona, Spain*

Iria Brocos-Mosquera – *Department of Pharmacology, University of the Basque Country, UPV/EHU, E-48940 Leioa, Bizkaia, Spain*

Carolina Muguruza – *Department of Pharmacology, University of the Basque Country, UPV/EHU, E-48940 Leioa, Bizkaia, Spain; orcid.org/0000-0002-0477-5757*

Belén Pérez – *Department of Pharmacology, Therapeutic and Toxicology, Autonomous University of Barcelona, E-08193 Barcelona, Spain*

Elies Molins – *Institut de Ciència de Materials de Barcelona (CSIC), E-08193 Cerdanyola, Spain; orcid.org/0000-0003-1012-0551*

F. Javier Luque – *Department of Nutrition, Food Sciences and Gastronomy, School of Pharmacy and Food Sciences, Institute of Biomedicine (IBUB), and Institute of Theoretical and Computational Chemistry (IQTCUB), University of Barcelona, E-08921 Santa Coloma de Gramanet, Spain; orcid.org/0000-0002-8049-3567*

Pilar Pérez-Lozano – *Unit of Pharmaceutical Technology, Pharmacy and Pharmaceutical Technology, and Physical Chemistry Department, Faculty of Pharmacy and Food Sciences, University of Barcelona, E-08028 Barcelona, Spain; orcid.org/0000-0001-6899-066X*

Steven de Jonghe – *Rega Institute for Medical Research, Katholieke Universiteit Leuven, 3000 Leuven, Belgium; orcid.org/0000-0002-3872-6558*

Dirk Daelemans – *Rega Institute for Medical Research, Katholieke Universiteit Leuven, 3000 Leuven, Belgium*

Lieve Naesens – *Rega Institute for Medical Research, Katholieke Universiteit Leuven, 3000 Leuven, Belgium*

José Brea – *Innopharma screening platform, BioFarma research group, Centro de Investigación en Medicina Molecular y Enfermedades Crónicas (CIMUS), Universidad de Santiago de Compostela, 15782 Santiago de Compostela, Spain*

M. Isabel Loza – *Innopharma screening platform, BioFarma research group, Centro de Investigación en Medicina Molecular y Enfermedades Crónicas (CIMUS), Universidad de Santiago de Compostela, 15782 Santiago de Compostela, Spain*

Elena Hernández-Hernández – *IUNICS University of the Balearic Islands (UIB), and Health Research Institute of the Balearic Islands (IdISBa), E-07122 Palma de Mallorca, Spain*

Jesús A. García-Sevilla – *IUNICS University of the Balearic Islands (UIB), and Health Research Institute of the Balearic Islands (IdISBa), E-07122 Palma de Mallorca, Spain*

M. Julia García-Fuster – *IUNICS University of the Balearic Islands (UIB), and Health Research Institute of the Balearic Islands (IdISBa), E-07122 Palma de Mallorca, Spain*

Milica Radan – *Department of Pharmaceutical Chemistry, Faculty of Pharmacy, University of Belgrade, 11000 Belgrade, Serbia*

Teodora Djikic – *Department of Pharmaceutical Chemistry, Faculty of Pharmacy, University of Belgrade, 11000 Belgrade, Serbia*

Katarina Nikolic – *Department of Pharmaceutical Chemistry, Faculty of Pharmacy, University of Belgrade, 11000 Belgrade, Serbia*

Mercè Pallàs – *Pharmacology Section, Toxicology and Medicinal Chemistry, Faculty of Pharmacy and Food Sciences, and Institut de Neurociències, University of Barcelona, E-08028 Barcelona, Spain; orcid.org/0000-0003-3095-4254*

Luis F. Callado – *Department of Pharmacology, University of the Basque Country, UPV/EHU, E-48940 Leioa, Bizkaia, Spain*

Complete contact information is available at: https://pubs.acs.org/10.1021/acs.jmedchem.9b02080

Author Contributions

▲S.A. and S.R.-A. contributed equally to this work. C.G.-F., J.A.G.-S., M.J.G.-F., M.P., and C.E. designed the study. S.A., S.R.-A., and A.B. synthesized, purified, and characterized the I_2-IR ligands. C.G.-F., F.V., and M.P. carried out the behavior and cognition studies and cellular parameter determination. I.B.-M., C.M., and L.F.C. performed the binding experiments. B.P. performed the PAMPA–BBB permeation experiments. E.M. conducted the X-ray crystallographic analysis. F.J.L. was in charge of the theoretical studies. P.P.-L. performed the physicochemical studies. S.L., D.D., and L.N. carried out the cytotoxicity studies. J.B. and M.I.L. determined the ADMET parameters. E.H.-H., J.A.G.-S., and M.J.G.-S. performed the hypothermic studies and analysis of FADD protein content. M.R., T.D., and K.N. carried out the 3D-QSAR study. C.G.-F., F.J.L, P.P.-L., J.A.G.-S., M.J.G.-S., L.F.C., K.N., M.P., and C.E. contributed to writing the manuscript. All the authors have read and approved the final version of the manuscript.

Notes

The authors declare the following competing financial interest(s): C.E., M.P., C.G.-F., S.A., L.-F.C., and J.A.G.-S. are inventors of the patent application on I2 imidazoline receptor ligands, WO2019/121853 (reference 29).

■ ACKNOWLEDGMENTS

We strongly acknowledge the advice of Dr. Andrés G. Fernández (our mentor in the CaixaImpulse 2018 program) for invaluable advice. This study was supported by the Ministerio de Economía y Competitividad of Spain (SAF2016-77703) and the Basque Government (IT1211-19).

The project leading to these results has received funding from "la Caixa" Foundation (ID 100010434) under agreement CI18-00002. This activity has received funding from the European Institute of Innovation and Technology (EIT). This body of the European Union receives support from the European Union's Horizon 2020 research and innovation programme. C.G.-F, F.V., C.E., S.R.-A., A.B., and M.P. belong to 2017SGR106 (Generalitat de Catalunya). J.A.G.-S. is a member emeritus of the Institut d'Estudis Catalans. Financial support was provided for F.V. (University of Barcelona, APIF_2017), S.R.-A. (Generalitat de Catalunya, 2018FI_B_00227), A.B. (Institute of Biomedicine UB_2018), C.M. (Marie Sklodowska-Curie Actions Individual Fellowships H2020-MSCA-IF-2016, ID747487), and E.H.-H. (Consejería de Innovación, Investigación y Turismo del Gobierno de las Islas Baleares y del Fondo Social Europeo, FPI/2102/2018). F.J.L. acknowledges the financial support from the Spanish Ministerio de Economía, Industria y Competitividad (grant MDM-2017-0767; AEI/FEDER UE), and Generalitat de Catalunya (grant 2017SGR1746). M.R., T.D., and K.N. kindly acknowledge Ministry of Science and Technological Development of the Republic of Serbia, Project Contract No. 172033, and HORISON2020-COST-Action CA18133 ERNEST: European Research Network on Signal Transduction.

■ ABBREVIATIONS

α_2-AR, α_2 adrenergic receptor; 2-BFI, 2-[(2-benzofuranyl)-2-imidazoline]; B3LYP, 3-parameter hybrid Becke exchange/Lee−Yang−Parr correlation; BU224, 2-(4,5-dihydroimidazol-2-yl)quinoline; CCK_A, cholecystokinin type A receptor; CCK_B, cholecystokinin type B receptor; *Cxcl10*, C-X-C motif chemokine 10 gene; DI, discrimination index; 5xFAD, mouse model of amyloid deposition expressing five familial AD (FAD) mutations; FADD, Fas-associated protein with death domain; GRIND, Grid-independent descriptors; HeLa, human cervical carcinoma cell line; 4-HNE, 4-hydroxy-2-nonenal; Hmox1, heme oxygenase (decycling) 1; H_2O_2, hydrogen peroxide; IR, imidazoline receptors; I_1-IRs, imidazoline I_1 receptors; I_2-IRs, imidazoline I_2 receptors; I_3-IRs, imidazoline I_3 receptors; LANLD2DZ, Los Alamos National Laboratory 2-double-z (density functional theory); MDCK, Madin-Darby canine kidney; MT4, human T-lymphocyte; MRC-5, human embryonic lung fibroblast; NORT, novel object recognition test; iNOS, inducible nitric oxide synthase; OS, oxidative stress; PhosMic, diethyl isocyanomethylphosphonate; P_e, permeability; pK_I, antilog of K_i; pK_{iL}, low pK_i binding site; pK_{iH}, high pK_i binding site; 3D-QSAR, three-dimensional quantitative structure−activity relationship; QM, quantum mechanical; [^{3}H]-RX821002, ^{3}H-labeled 2-methoxyidazoxan; SAMP8, senescence accelerated mouse-prone 8; SEM, standard error of the mean; *Tnf-α*, tumor necrosis factor α gene; TPSA, topological polar surface area; Vero, African green monkey kidney cell line; WT, WT mice

■ REFERENCES

(1) Bousquet, P.; Feldman, J.; Schwartz, J. Central cardiovascular effects of alpha adrenergic drugs: differences between catecholamines and imidazolines. *J. Pharmacol. Exp. Ther.* **1984**, *230*, 232−236.
(2) Bousquet, P.; Hudson, A.; García-Sevilla, J. A.; Li, J.-X. Imidazoline receptor system: the past, the present, and the future. *Pharmacol. Rev.* **2020**, *72*, 50−79.
(3) Lowry, J. A.; Brown, J. T. Significance of the imidazoline receptors in toxicology. *Clin. Toxicol.* **2014**, *52*, 454−469.
(4) Regunathan, S.; Reis, D. J. Imidazoline receptors and their endogenous ligands. *Annu. Rev. Pharmacol. Toxicol.* **1996**, *36*, 511−544.
(5) Fenton, C.; Keating, G. M.; Lyseng-Williamson, K. A. Moxonidine: a review of its use in essential hypertension. *Drugs* **2006**, *66*, 477−496.
(6) Reid, J. L. Rilmenidine: a clinical overview. *Am. J. Hypertens.* **2000**, *13*, 106S−111S.
(7) Chan, S. L.; Brown, C. A.; Scarpello, K. E.; Morgan, N. G. The imidazoline site involved in control of insulin secretion: characteristics that distinguish it from I_1- and I_2-sites. *Br. J. Pharmacol.* **1994**, *112*, 1065−1070.
(8) Li, J. X. Imidazoline I_2 receptors: an update. *Pharmacol. Ther.* **2017**, *178*, 48−56.
(9) Li, J. X.; Zhang, Y. Imidazoline I_2 receptors: target for new analgesics? *Eur. J. Pharmacol.* **2011**, *658*, 49−56.
(10) Regunathan, S.; Feinstein, D. L.; Reis, D. J. Anti-proliferative and anti-inflammatory actions of imidazoline agents. Are imidazoline receptors involved? *Ann. N. Y. Acad. Sci.* **1999**, *881*, 410−419.
(11) Smith, K. L.; Jessop, D. S.; Finn, D. P. Modulation of stress by imidazoline binding sites: implications for psychiatric disorders. *Stress* **2009**, *12*, 97−114.
(12) Martín-Gómez, J. I.; Ruíz, J.; Callado, L. F.; Garibi, J. M.; Aguinaco, L.; Barturen, F.; Meana, J. J. Increased density of I_2-imidazoline receptors in human gliobastomas. *NeuroReport* **1996**, *7*, 1393−1396.
(13) Callado, L. F.; Martín-Gómez, J. I.; Ruiz, J.; Garibi, J. M.; Meana, J. J. Imidazoline I_2 receptors density increases with the malignancy of human gliomas. *J. Neurol., Neurosurg. Psychiatry* **2004**, *75*, 785−787.
(14) Reynolds, G. P.; Boulton, R. M.; Pearson, S. J.; Hudson, A. L.; Nutt, D. J. Imidazoline binding sites in Huntington's and Parkinson's disease putamen. *Eur. J. Pharmacol.* **1996**, *301*, R19−R21.
(15) Gargalidis-Moudanos, C.; Pizzinat, N.; Javoy-Agid, F.; Remaury, A.; Parini, A. I_2-imidazoline binding sites and monoamine oxidase activity in human postmortem brain from patients with Parkinson's disease. *Neurochem. Int.* **1997**, *30*, 31−36.
(16) Meana, J. J.; Barturen, F.; Martín, I.; García-Sevilla, J. A. Evidence of increased non-adrenoreceptor [^{3}H]idazoxan binding sites in the frontal cortex of depressed suicide victims. *Biol. Psychiatry* **1993**, *34*, 498−501.
(17) García- Sevilla, J.; Escribá, P. V.; Sastre, M.; Walzer, C.; Busquets, X.; Jaquet, G.; Reis, D. J.; Guimón, J. Immunodetection and quantitation of imidazoline receptor proteins in platelets of patients with major depression and in brains of suicide victims. *Arch. Gen. Psychiatry* **1996**, *53*, 803−810.
(18) Ruíz, J.; Martín, I.; Callado, L. F.; Meana, J. J.; Barturen, F.; García-Sevilla, J. A. Non-adrenoreceptor [^{3}H]idazoxan binding sites (I_2-imidazoline sites) are increased in postmortem brain from patients with Alzheimer's disease. *Neurosci. Lett.* **1993**, *160*, 109−112.
(19) García-Sevilla, J. A.; Escribá, P. V.; Walzer, C.; Bouras, C.; Guimón, J. Imidazoline receptor proteins in brains of patients with Alzheimer's disease. *Neurosci. Lett.* **1998**, *247*, 95−98.
(20) Comi, E.; Lanza, M.; Ferrari, F.; Mauri, V.; Caselli, G.; Rovati, L. C. Efficacy of CR4056, a first-in-class imidazoline-2 analgesic drug, in comparison with naproxen in two rat models of osteoarthritis. *J. Pain Res.* **2017**, *10*, 1033−1043.
(21) Rovati, L. C.; Brambilla, N.; Blicharski, T.; Connell, J.; Vitalini, C.; Bonazzi, A.; Giacovelli, G.; Girolami, F.; D'Amato, M. Efficacy and safety of the firts-in-classs imidazoline-2 receptor ligand CR4056 in pain from knee osteoarthritis and desease phenotypes: a randomized, double-blind, placebo-controlled phase 2 trial. *Osteoarthritis and Cartilage* **2020**, *28*, 22.
(22) Tyacke, R. J.; Myers, J. F. M.; Venkataraman, A. V.; Mick, I.; Turton, S.; Passchier, J.; Husbands, S. M.; Rabiner, E. A.; Gunn, R. N.; Murphy, P. S.; Parker, C. A.; Nutt, D. J. Evaluation of ^{11}C-

https://dx.doi.org/10.1021/acs.jmedchem.9b02080
J. Med. Chem. 2020, 63, 3610−3633

BU99008, a PET ligand for the imidazoline$_2$ binding site in human brain. *J. Nucl. Med.* **2018**, *59*, 1597−1602.
(23) Wilson, H.; Dervenoulas, G.; Pagano, G.; Tyacke, R. J.; Polychronis, S.; Myers, J.; Gunn, R. N.; Rabiner, E. A.; Nutt, D.; Politis, M. Imidazoline 2 binding sites reflecting astroglia pathology in Parkinson's disease: an *in vivo* ^{11}C-BU99008 PET study. *Brain* **2019**, *142*, 3116.
(24) Dardonville, C.; Rozas, I. Imidazoline binding sites and their ligands: an overview of the different chemical structures. *Med. Res. Rev.* **2004**, *24*, 639−661.
(25) Abás, S.; Erdozain, A. M.; Keller, B.; Rodríguez-Arévalo, S.; Callado, L. F.; García-Sevilla, J. A.; Escolano, C. Neuroprotective effects of a structurally new family of high affinity imidazoline I_2 receptors ligands. *ACS Chem. Neurosci.* **2017**, *8*, 737−742.
(26) Abás, S.; Estarellas, C.; Luque, F. J.; Escolano, C. Easy access to (2-imidazolin-4-yl)phosphonates by a microwave assisted multicomponent reaction. *Tetrahedron* **2015**, *71*, 2872−2881.
(27) Griñán-Ferré, C.; Vasilopoulou, F.; Abás, S.; Rodríguez-Arévalo, S.; Bagán, A.; Sureda, F. X.; Pérez, B.; Callado, L. F.; García-Sevilla, J. A.; García-Fuster, M. J.; Escolano, C.; Pallàs, M. Behavioral and cognitive improvement induced by novel imidazoline I_2 receptor ligands in female SAMP8 mice. *Neurotherapeutics* **2019**, *16*, 416−431.
(28) Arróniz, C.; Molina, J.; Abás, S.; Molins, E.; Campanera, J. M.; Luque, F. J.; Escolano, C. First diastereoselective [3 + 2] cycloaddition reaction of diethyl isocyanomethylphosphonate and maleimides. *Org. Biomol. Chem.* **2013**, *11*, 1640−1649.
(29) Escolano, C.; Pallás, M.; Griñán-Ferré, C.; Abás, S.; Callado, L.-F.; García-Sevilla, J. A. Synthetic I_2 Imidazoline Receptor Ligands for Prevention or Treatment of Human Brain Disorders. WO 2019/121853 A1, June 27, 2019.
(30) Grijalba, B.; Callado, L. F.; Meana, J. J.; García-Sevilla, J. A.; Pazos, A. α_2-Adrenoceptor subtypes in the human brain: a phamacological delineation of [^{3}H]RX-821002 binding to membranes and tissue sections. *Eur. J. Pharmacol.* **1996**, *310*, 83−93.
(31) Callado, L. F.; Maeztu, A. I.; Ballesteros, J.; Gutiérrez, M.; Meana, J. J. Differential [^{3}H]idazoxan and [^{3}H]2-(2-benzofuranyl)-2-imidazoline (2-BFI) binding to imidazoline I_2 receptors in human postmortem frontal cortex. *Eur. J. Pharmacol.* **2001**, *423*, 109−114.
(32) BU99008 was prepared according to the literature procedure: Tyacke, R. J.; Fisher, A.; Robinson, E. S. J.; Grundt, P.; Turner, E. M.; Husbands, S. M.; Hudson, A. L.; Parker, C. A.; Nutt, D. J. Evaluation and initial in vitro and in vivo characterization of the potential positron emission tomography ligand, BU99008 (2-(4,5-dihydro-1*H*-imidazol-2-yl)-1-methyl-1*H*-indole), for the imidazoline$_2$ binding site. *Synapse* **2012**, *66*, 542−551.
(33) CR4056 was prepared according to the literature procedure: Giordani, A.; Mandelli, S.; Verpilio, I.; Zanzola, S.; Tarchino, F.; Caselli, G.; Piepoli, T.; Mazzari, S.; Makovec, F.; Rovati, L. C. 6−1H-Imidazo-quinazoline and Quinolines Derivatives, New Potent Analgesics and Anti-inflammatory Agents. US 8,193,353 B2, June 5, 2012.
(34) Lione, L. A.; Nutt, D. J.; Hudson, A. L. [^{3}H]-2-(2-benzofuranyl)-2-imidazoline: a new selective high affinity radioligand for the study of rabbit brain imidazoline I_2 receptors. *Eur. J. Pharmacol.* **1996**, *304*, 221−229.
(35) Alemany, R.; Olmos, G.; García-Sevilla, J. A. Labelling I_{2B}-imidazoline receptors by [^{3}H]-2-(2-benzofuranyl)-2-imidazoline (2-BFI) in rat brain and liver: characterization, regulation and relation to monoamine oxidase enzymes. *Naunyn-Schmiedeberg's Arch. Pharmacol.* **1997**, *356*, 39−47.
(36) Lione, L. A.; Nutt, D. J.; Hudson, A. L. Characterisation and localisation of [^{3}H]-2-(2-benzofuranyl)-2-imidazoline binding in rat brain: a selective ligand for imidazoline I_2 receptors. *Eur. J. Pharmacol.* **1998**, *353*, 123−135.
(37) Quaglia, W.; Bousquet, P.; Pigini, M.; Carotti, A.; Carrieri, A.; Dontenwill, M.; Gentili, F.; Giannella, M.; Maranca, F.; Piergentili, A.; Brasili, L. 2-(2-Phenylcyclopropyl)imidazolines: reversed enantioselective interaction at I_1 and I_2 imidazoline receptors. *J. Med. Chem.* **1999**, *42*, 2737−2740.
(38) Alemany, R.; Olmos, G.; Escribá, P. V.; Menargues, A.; Obach, R.; García-Sevilla, J. A. LSL60101, a selective ligand for imidazoline I_2 receptors, on glial fibrillary acidic protein concentration. *Eur. J. Pharmacol.* **1995**, *280*, 205−210.
(39) Ferrari, F.; Fiorentino, S.; Mennuni, L.; Garofalo, P.; Letari, O.; Mandelli, S.; Giordani, A.; Lanza, M.; Caselli, G. Analgesic efficacy of CR4056, a novel imidazoline-2 receptor ligand, in rat models of inflammatory and neuropathic pain. *J. Pain Res.* **2011**, *4*, 111−115.
(40) *Pentacle*, version 1.0.6, Molecular Discovery Ltd., Perugia, Italy, 2009.
(41) Ghosh, J.; Lawless, M. S.; Waldman, M.; Gombar, V.; Fraczkiewicz, R. Modeling ADMET. *Methods Mol. Biol.* **2016**, *1425*, 63−83.
(42) ADMET Predictor, v. 9.5, Simulations Plus Inc., Lancaster, CA, USA, 2019, https://www.simulations-plus.com.
(43) Daina, A.; Michielin, O.; Zoete, V. Swiss ADME: a free web tool to evaluate pharmacokinetics, drug-likeness and medicinal chemistry friendliness of small mol. *Sci. Rep.* **2017**, *7*, 42717.
(44) Biopharmaceutics classification system-based biowaivers, International council for harmonisation of technical requirements for pharmaceutical for human use. https://www.ich.org/fileadmin/Public_Web_Site/ICH_Products/Guidelines/Multidisciplinary/M9/M9EWG_DraftGuideline_Step2_2018_0606.pdf.
(45) International council on harmonisation of technical requirements for registration of pharmaceuticals for human use. ICH harmonized tripartite guideline. "Stability testing of new drug substance and products". Q1A (R2), 2003.
(46) For information on the Eurofins Lead Profiling Screen, see http://www.eurofins.com.
(47) Cawston, E. E.; Miller, L. J. Therapeutic potential for novel drugs targeting the type 1 cholecystokinin receptor. *Br. J. Pharmacol.* **2010**, *159*, 1009−1021.
(48) Keller, B.; García-Sevilla, J. A. Inhibitory effects of imidazoline receptor ligands on basal and kainic acid-induced neurotoxic signalling in mice. *J. Psychopharmacol.* **2016**, *30*, 875−886.
(49) Thorn, D. A.; An, X. F.; Zhang, Y.; Pigini, M.; Li, J. X. Characterization of the hypothermic effects of imidazoline I_2 receptor agonists in rats. *Br. J. Pharmacol.* **2012**, *166*, 1936−1945.
(50) Craven, J. A.; Conway, E. L. Effects of alpha 2-adrenoceptor antagonists and imidazoline 2-receptor ligands on neuronal damage in global ischaemia in the rat. *Clin. Exp. Pharmacol. Physiol.* **1997**, *24*, 204−207.
(51) Marion, D. W.; Penrod, L. E.; Kelsey, S. F.; Obrist, W. D.; Kochanek, P. M.; Palmer, A. M.; Wisniewski, S. R.; DeKosky, S. T. Treatment of traumatic brain injury with moderate hypothermia. *N. Engl. J. Med.* **1997**, *336*, 540−546.
(52) Maier, C. M.; Ahern, K. V.; Cheng, M. L.; Lee, J. E.; Yenari, M. A.; Steinberg, G. K. Optimal depth and duration of mild hypothermia in focal model of transient cerebral ischemia: effects on neurologic outcome, infarct size, apopotosis, and inflammation. *Stroke* **1998**, *29*, 2171−2180.
(53) Hernández-Hernández, E.; Miralles, A.; Esteban, S.; García-Fuster, M. J. Improved age-related deficits in cognitive performance and affective-like behavior following acute, but not repeated , 8-OH-DPAT treatments in rats: regulation of hippocampal FADD. *Neurobiol. Aging* **2018**, *71*, 115−126.
(54) Hernández-Hernández, E.; Miralles, A.; Esteban, S.; Garcia-Fuster, M. J. Repeated treatment with the α2-adrenoceptor agonist UK-14304 improves cognitive performance in middle-age rats: role of hippocampal Fas-associated death domain. *J. Psychopharmacol.* **2018**, *32*, 248−255.
(55) Bilkei-Gorzo, A. Genetic mouse models of brain ageing and Alzheimer's disease. *Pharmacol. Ther.* **2014**, *142*, 244−257.
(56) Antunes, M.; Biala, G. The novel object recognition memory: neurobiology, test procedure, and its modifications. *Cogn. Process.* **2012**, *13*, 93−110.

https://dx.doi.org/10.1021/acs.jmedchem.9b02080
J. Med. Chem. 2020, 63, 3610−3633

(57) Heneka, M. T.; McManus, R. M.; Latz, E. Inflammasome signalling in brain function and neurodegenerative disease. *Nat. Rev. Neurosci.* **2018**, *19*, 610−621.
(58) Gao, H.-M.; Zhou, H.; Hong, J. S. Oxidative stress, neuroinflammation, and neurodegeneration. In *Neuroinflammation and neurodegeneration*; Peterson, P. K., Toborek, M., Eds.; Springer: New York, 2014; pp 81−104.
(59) Ekert, J. O.; Gould, R. L.; Reynolds, G.; Howard, R. J. TNF alpha inhibitors in Alzheimer's disease: a systematic review. *Int. J. Geriatr. Psychiatry* **2018**, *33*, 688−694.
(60) Iadecola, C.; Zhang, F.; Casey, R.; Nagayama, M.; Ross, M. E. Delayed reduction of ischemic brain injury and neurological deficits in mice lacking the inducible nitric oxide synthase gene. *J. Neurosci.* **1997**, *17*, 9157−9164.
(61) Schipper, H. M.; Song, W.; Tavitian, A.; Cressatti, M. The sinister face of heme oxygenase-1 in brain aging and disease. *Prog. Neurobiol.* **2019**, *172*, 40−70.
(62) Griñán-Ferré, C.; Sarroca, S.; Ivanova, A.; Puigoriol-Illamola, D.; Aguado, F.; Camins, A.; Sanfeliu, C.; Pallàs, M. Epigenetic mechanisms underlying cognitive impairment and Alzheimer disease hallmarks in 5xFAD mice. *Aging* **2016**, *8*, 664−684.
(63) Becke, A. D. Density-functional thermochemistry. III. The role of exact exchange. *J. Chem. Phys.* **1993**, *98*, 5648.
(64) Lee, C.; Yang, W.; Parr, R. G. Development of the Colle-Salvetti correlation-energy formula into a functional of the electron density. *Phys. Rev. B: Condens. Matter Mater. Phys.* **1988**, *37*, 785.
(65) Clark, T.; Chandrasekhar, J.; Spitznagel, G. W.; Schleyer, P. v. R. Efficient diffuse function-augmented basis sets for anion calculations. III. The 3-21+G basis set for first-row elements, Li−F. *J. Comput. Chem.* **1983**, *4*, 294−301.
(66) Wadt, W. R.; Hay, P. J. Ab initio effective core potentials for molecular calculations. Potentials for K to Au including the outermost core orbitals. *J. Chem. Phys.* **1985**, *82*, 284.
(67) Gonzalez, C.; Schlegel, H. B. An improved algorithm for reaction path following. *J. Chem. Phys.* **1989**, *90*, 2154.
(68) Yu, H. S.; He, X.; Truhlar, D. G. MN-15: A new local exchanged-correlation functional for Kohn-Sham density functional theory broad accuracy for atoms, molecules, and solids. *J. Chem. Theory Comput.* **2016**, *12*, 1280−1293.
(69) Marenich, A. V.; Cramer, C. J.; Truhlar, D. G. Universal solvation model based on solute electron density and on a continuum model of the solvent defined by the bulk dielectric constant and atomic surface tensions. *J. Phys. Chem. B* **2009**, *113*, 6378−6396.
(70) Frisch, M. J.; et al. *Gaussian 16*, revision B.01, Gaussian, Inc.: Wallingford, CT, 2016.
(71) Callado, L. F.; Gabilondo, A. M.; Meana, J. J. [^{3}H] RX821002 (2-methoxyidazoxan) binds to α_2-adrenoceptor subtypes and a non-adrenoceptor imidazoline binding site in rat kidney. *Eur. J. Pharmacol.* **1996**, *316*, 359−368.
(72) MarvinSketch 5.5.1.0. ChemAxon, Budapest, Hungary, 2011; software available at https://www.chemaxon.com.
(73) Stewart, J. J. P. Optimization of parameters for semiempirical methods I. Method. *J. Comput. Chem.* **1989**, *10*, 209−220.
(74) Stewart, J. J. P. Optimization of parameters for semiempirical methods II.Method. *J. Comput. Chem.* **1989**, *10*, 221−264.
(75) Hehre, W. J.; Radom, L.; Schleyer, PvR.; Pople, J. A. *Ab initio molecular orbital theory*; Wiley: New York, 1986; Vol *1*.
(76) Frisch, M. J.; Trucks, G. W.; Schlegel, H. B.; Scuseria, G. E.; Robb, M. A.; Cheeseman, J. R.; Scalmani, G.; Barone, V.; Mennucci, B.; Petersson, G. A.; Nakatsuji, H.; Caricato, M.; Li, X.; Hratchian, H. P.; Izmaylov, A. F.; Bloino, J.; Zheng, G.; Sonnenberg, J. L.; Hada, M.; Ehara, M.; Toyota, K.; Fukuda, R.; Hasegawa, J.; Ishida, M.; Nakajima, T.; Honda, Y.; Kitao, O.; Nakai, H.; Vreven, T.; Montgomery, J. A., Jr.; Peralta, J. E.; Ogliaro, F.; Bearpark, M.; Heyd, J. J.; Brothers, E.; Kudin, K. N.; Staroverov, V. N.; Kobayashi, R.; Normand, J.; Raghavachari, K.; Rendell, A.; Burant, J. C.; Iyengar, S. S.; Tomasi, J.; Cossi, M.; Rega, N.; Millam, J. M.; Klene, M.; Knox, J. E.; Cross, J. B.; Bakken, V.; Adamo, C.; Jaramillo, J.; Gomperts, R.; Stratmann, R. E.; Yazyev, O.; Austin, A. J.; Cammi, R.; Pomelli, C.; Ochterski, J. W.; Martin, R. L.; Morokuma, K.; Zakrzewski, V. G.; Voth, G. A.; Salvador, P.; Dannenberg, J. J.; Dapprich, S.; Daniels, A. D.; Farkas, O.; Foresman, J. B.; Ortiz, J. V.; Cioslowski, J.; Fox, D. J. *Gaussian 09*, revision D.01, Gaussian Inc.: Wallingford, CT, 2009.
(77) CambridgeSoft Corporation. *ChemBio3D Ultra*, version 13.0; CambridgeSoft, Cambridge, MA, USA, 2013.
(78) Durán, A.; Zamora, I.; Pastor, M. Suitability of GRIND-Based principal properties for the description of molecular similarity and ligand-based virtual screening. *J. Chem. Inf. Model.* **2009**, *49*, 2129−2138.
(79) Durán, Á.; Pastor, M. *Pentacle, An advanced tool for computing and handling grid-independent descriptors*. User Manual Version 1.06; 2011.
(80) Ojha, P. K.; Roy, K. Comparative QSARs for antimalarial endochins: Importance of descriptor-thinning and noise reduction prior to feature selection. *Chemom. Intell. Lab. Syst.* **2011**, *109*, 146−161.
(81) Kilkenny, C.; Browne, W. J.; Cuthill, I. C.; Emerson, M.; Altman, D. G. Improving biocesce research reporting: the ARRIVE guidelines for reporting animal research. *PLoS Biol.* **2010**, *8*, e1000412.
(82) Oakley, H.; Cole, S. L.; Logan, S.; Maus, E.; Shao, P.; Craft, J.; Guillozet-Bongaarts, A.; Ohno, M.; Disterhoft, J.; Van Eldik, L.; Berry, R.; Vassar, R. Intraneuronal beta-amyloid aggregates, neurodegeneration, and neuron loss in transgenic mice with five familial Alzheimer's desease mutations: potential factors in amyloid plaque formation. *J. Neurosci.* **2006**, *26*, 10129−10140.

https://dx.doi.org/10.1021/acs.jmedchem.9b02080
J. Med. Chem. 2020, 63, 3610−3633

Bicyclic α-iminophosphonates as highly affinity imidazoline I_2 receptor ligands for Alzheimer's Disease

*Sònia Abás,[†,▽] Sergio Rodríguez-Arévalo,[†,▽] Andrea Bagán,[†] Christian Griñán-Ferré,[‡] Foteini Vasilopoulou,[‡] Iria Brocos-Mosquera,[§] Carolina Muguruza,[§] Belén Pérez,[∥] Elies Molins,[⊥] F. Javier Luque,[#] Pilar Pérez-Lozano,[○] Steven de Jonghe,[△] Dirk Daelemans,[△] Lieve Naesens,[△] José Brea,[◆] M. Isabel Loza,[◆] Elena Hernández-Hernández,[ǂ] Jesús A. García-Sevilla,[ǂ] M. Julia García-Fuster,[ǂ] Milica Radan,[#] Teodora Djikic,[#] Katarina Nikolic,[#] Mercè Pallàs,[‡] Luis F. Callado,[§] Carmen Escolano[†,]**

[†] Laboratory of Medicinal Chemistry (Associated Unit to CSIC), Department of Pharmacology, Toxicology and Medicinal Chemistry, Faculty of Pharmacy and Food Sciences, and Institute of Biomedicine (IBUB), University of Barcelona, Av. Joan XXIII, 27-31, E-08028 Barcelona, Spain.

[‡] Pharmacology Section, Toxicology and Medicinal Chemistry, Faculty of Pharmacy and Food Sciences, and Institut de Neurociències, University of Barcelona, Av. Joan XXIII, 27-31, E-08028 Barcelona, Spain.

[§] Department of Pharmacology, University of the Basque Country, UPV/EHU, E-48940 Leioa, Bizkaia, and Centro de Investigación Biomédica en Red de Salud Mental, CIBERSAM, Spain.

‖ Department of Pharmacology, Therapeutic and Toxicology, Autonomous University of Barcelona, E-08193 Barcelona, Spain.

⊥ Institut de Ciència de Materials de Barcelona (CSIC), Campus UAB, E-08193 Cerdanyola, Spain.

Department of Nutrition, Food Sciences and Gastronomy, School of Pharmacy and Food Sciences, Institute of Biomedicine (IBUB), and Institute of Theoretical and Computational Chemistry (IQTCUB), University of Barcelona, E-08921, Santa Coloma de Gramanet, Spain.

○ Unit of Pharmaceutical Technology, Pharmacy and Pharmaceutical Technology, and Physical Chemistry Department, Faculty of Pharmacy and Food Sciences, University of Barcelona, Av. Joan XXIII, 27-31, E-08028 Barcelona, Spain.

Δ Rega Institute for Medical Research, Katholieke Universiteit Leuven, 3000 Leuven, Belgium.

♦ Innopharma screening platform. BioFarma research group. Centro de Investigación en Medicina Molecular y Enfermedades Crónicas (CIMUS). Universidad de Santiago de Compostela, Santiago de Compostela, Spain.

Department of Pharmaceutical Chemistry, Faculty of Pharmacy, University of Belgrade, Vojvode Stepe 450, 11000 Belgrade, Serbia.

ǂ IUNICS University of the Balearic Islands (UIB), and Health Research Institute of the Balearic Islands, IdISBa, Cra. Valldemossa km 7.5, E-07122 Palma de Mallorca, Spain.

CONTENTS:

Synthesis of α-substituted PhosMic derivatives 10a-10e and 11	**S4**
Theoretical calculations	**S8**
3D-QSAR study	**S25**
***In vitro* Blood-Brain Barrier Permeation Assay**	**S35**
Cytotoxicity assay	**S37**
Microsomal stability of human, rat and mice microsomes	**S38**
Solubility and chemical stability	**S40**
Cytochrome inhibition	**S41**
hERG ion channel inhibition	**S42**
Human and mouse plasma protein binding	**S43**
Receptor characterization panel	**S44**
***5xFAD In vivo* experimental design**	**S48**
NMR spectra data	**S49**
Table S12. Representative data of ^{1}H-NMR spectra of new compounds	**S50**
Table S13. Representative data of ^{13}C-NMR spectra of new compounds	**S53**
^{1}H-NMR and ^{13}C-NMR spectra of new compounds 9a – 15	**S56**
^{31}P-NMR of 9d	**S98**
X-ray crystallographic data for 9b, 9c, 9d, 9v and 9ab	**S99**
HPLC/MS analysis of 9a, 14c, 15c, 9f, 9g, 9h, 9i, 9j, 9k, 9w and 9z	**S125**
References	**S147**
Molecular Formula Strings (Smiles)	**S148**

Synthesis of α-substituted PhosMic derivatives

General conditions for the synthesis of compounds (10a-10e and 11). Reagents, solvents, dry solvents and starting products were acquired from commercial sources. The organic phases were dried with anhydrous Na_2SO_4. All the reactions were performed in dry conditions (inert atmosphere) and using dry solvents. The term "concentration" refers to the vacuum evaporation using a Büchi rotavapor. When indicated, the reaction products were purified by "flash" chromatography on silica gel (35-70 μm) with the indicated solvent system. The melting points were measured in a MFB 59510M Gallenkamp instruments. IR spectra were performed in a spectrophotometer Nicolet Avantar 320 FTR-IR or in a Spectrum Two FT-IR Spectrometer, and only noteworthy IR absorptions (cm^{-1}) are listed. NMR spectra were recorded in $CDCl_3$ at 400 MHz (^1H) and 100.6 MHz (^{13}C), and chemical shifts are reported in δ values downfield from TMS or relative to residual chloroform (7.26 ppm, 77.0 ppm) as an internal standard. Data are reported in the following manner: chemical shift, multiplicity, coupling constant (*J*) in hertz (Hz), integrated intensity and assignment (when possible). Multiplicities are reported using the following abbreviations: s, singlet; d, doublet; dd, doublet of doublets; t, triplet; m, multiplet; br s, broad signal. The accurate mass analyses were carried out using a LC/MSD-TOF spectrophotometer.

Diethyl α-phenylisocyanomethylphosphonate (10a). [1]

Diethyl [amino(4-fluorophenyl)methyl]phosphonate (step 1-10b).[2] A mixture of 4-fluorobenzaldehyde (3.32 mL, 31.0 mmol), HMDS (3.20 mL, 15.5 mmol), diethyl phosphite (2.0 mL, 15.5 mmol) and I_2 (393 mg, 1.55 mmol) was stirred at rt overnight. Then, the reaction mixture was evaporated and EtOAc was added to the resulting residue. The organic phase was washed with a 10% solution of $Na_2S_2O_4$, dried and evaporated. Then, the residue (imine intermediate), THF (7 mL) and HCl 2N (10 mL) was heated at 70˚C overnight. The THF was evaporated, water was added and the aqueous phase was washed with EtAOc. The aqueous phase was basified with NaOH 2N and the product was extracted with EtOAc. The organic phases were combined, dried and evaporated to give **step 1-10b** (1.17 g, 35%) as yellowish oil. IR (ATR) 3373, 3303, 2988, 1735, 1601, 1506, 1224, 1157, 1015, 961, 841, 790 cm^{-1}. representative peaks: ^1H NMR (400 MHz, $CDCl_3$) δ 1.20 (t, 3H, CH_2CH_3), 1.28 (t, 3H, CH_2CH_3), 3.59 (t, 1H, CH_2CH_3), 3.89-4.09 (m, 3H, CH_2CH_3), 4.25 (d, J = 16.0 Hz, 1H, C*H*), 7.02-7.13 (m, 2H, Ar*H*), 7.41-7.47 (m, 1H, Ar*H*), 7.62-7.70 (m, 1H, Ar*H*). HRMS $C_{11}H_{18}FNO_3P$ $[M+H]^+$ 262.1003; found, 262.0999.

Diethyl [amino(4-methoxyphenyl)methyl]phosphonate (step 1-10c).[2] A mixture of 4-methoxybenzaldehyde (4.22 mL, 31.0 mmol), HMDS (3.20 mL, 15.5 mmol), diethyl phosphite (2.0 mL, 15.5 mmol) and I_2 (393 mg, 1.55 mmol) was stirred at rt overnight. Then, the reaction mixture was evaporated and EtOAc was added to the resulting residue. The organic phase was washed with a 10% solution of $Na_2S_2O_4$, dried and evaporated. Then, the residue (imine intermediate), THF (7 mL) and HCl 2N (10 mL) was heated at 70˚C overnight. The THF was evaporated, water was added and the aqueous phase was washed with EtAOc. The aqueous phase was basified with NaOH 2N and the product was extracted with EtOAc. The organic phases were combined, dried and evaporated to give **step 1-10c** compound (1.78 mg, 42%) as yellowish oil. IR (ATR) 3382, 3296, 2902, 1610, 1509, 1243, 1179, 1023, 909, 833, 727 cm^{-1}. ^1H NMR (400 MHz, $CDCl_3$) δ 1.18 (t, 3H, CH_2CH_3), 1.27 (t, 3H, CH_2CH_3), 3.79 (s, 3H, OCH_3), 3.82-3.89 (m, 1H, CH_2CH_3), 3.95-4.04 (m, 3H, CH_2CH_3), 4.19 (d, J = 16.0 Hz, 1H, C*H*), 6.86-6.89 (m, 2H, Ar*H*), 7.35-7.38 (m, 2H, Ar*H*). HRMS $C_{12}H_{21}NO_4P$ $[M+H]^+$ 274.1203; found, 274.1206.

Diethyl [(4-fluorophenyl)(formamido)methyl]phosphonate (step 2-10b).[1] To a solution of **step 1-10b** (722 mg, 2.76 mmol) in formic acid (5.20 mL), acetic anhydride (1.84 mL, 19.31 mmol) was added dropwise. The reaction was stirred at rt for 1 h and the mixture was concentrated *in vacuo* to give **step 2-10b** compound (798 mg, 100%) as yellowish solid. IR (ATR) 3254, 3034, 2878, 1674, 1506, 1380, 1215, 1160, 1015, 960, 812 cm^{-1}. ^1H NMR (400 MHz, $CDCl_3$) δ 1.11 (t, 3H, CH_2CH_3), 1.33 (t, 3H, CH_2CH_3), 3.70-3.78 (m, 1H, CH_2CH_3), 3.90-3.96 (m, 1H, CH_2CH_3), 4.12-4.17 (m, 2H, CH_2CH_3), 5.55 (dd, J = 9.5, 21.0 Hz, 1H, C*H*), 7.01-7.06 (m, 2H, Ar*H*), 7.43-7.47 (m, 2H, Ar*H*), 7.71 (br s, 1H, N*H*), 8.23 (s, 1H, C*H*O). HRMS $C_{12}H_{18}FNO_4P$ $[M+H]^+$ 290.0952; found, 290.0953.

Diethyl [(4-methoxyphenyl)(formamido)methyl]phosphonate (step 2-10c).[1] To a solution of **step 1-10c** (1.36 g, 4.98 mmol) in formic acid (9.39 mL), acetic anhydride (3.30 mL, 34.87 mmol) was added dropwise. The reaction was stirred at rt for 1 h and the mixture was concentrated *in vacuo* to give **step 2-10c** compound (1.50 g, 100%) as a yellowish solid. IR (ATR) 3269, 3009, 2881, 1676, 1504, 1379, 1212, 1010, 964, 793, 727 cm^{-1}. ^1H NMR (400 MHz, $CDCl_3$) δ 1.10 (t, 3H, CH_2CH_3), 1.33 (t, 3H, CH_2CH_3), 3.66-3.72 (m, 1H, CH_2CH_3), 3.79 (s, 3H, OCH_3), 3.88-4.19 (m, 1H, CH_2CH_3), 4.09-4.19 (m, 2H, CH_2CH_3), 5.53 (dd, J = 9.5, 20.5 Hz, 1H, C*H*), 6.86-6.88 (m, 2H, Ar*H*), 7.38-7.40 (m, 2H, Ar*H*), 7.55 (br s, 1H, N*H*), 8.23 (s, 1H, C*H*O). HRMS $C_{13}H_{21}NO_5P$ $[M+H]^+$ 302.1152; found, 302.1157.

Diethyl [(4-fluorophenyl)isocyanomethyl]phosphonate (10b).[1] Et_3N (2.0 mL, 13.8 mmol) and $POCl_3$ (0.4 mL, 4.15 mmol) were added dropwise to a cooled solution (-78ºC) of **step 2-10b**

compound (800 mg, 2.77 mmol) in THF (7.5 mL). The reaction mixture was allowed to warm to rt. After 2 h, cold water (0 ºC) was added and the mixture was extracted with Et_2O. The combined organic layers were dried and concentrated *in vacuo* to give a residue which was purified by column chromatography (EtOAc-Hexane 4:1) to afford **10b** (616 mg, 82%) as yellowish oil. IR(ATR) 2975, 2911, 1679, 1510, 1247, 1177, 1016, 963, 836, 743 cm^{-1}. ^1H NMR (400 MHz, $CDCl_3$) δ 1.27 (t, 3H, CH_2CH_3), 1.31 (t, 3H, CH_2CH_3), 4.00-4.19 (m, 4H, CH_2CH_3), 5.00 (d, *J* = 21.0 Hz, 1H, C*H*), 7.09-7.13 (m, 2H, Ar*H*), 7.44-7.48 (m, 2H, Ar*H*). ^{13}C NMR (100.6 MHz) δ 16.4 (d, *J* = 5.5 Hz, CH_2CH_3), 16.5 (d, *J* = 5.5 Hz, CH_2CH_3), 55.0 (d, *J* = 152.0 Hz, *C*H), 64.6 (d, *J* = 7.0 Hz, CH_2CH_3), 65.1 (d, *J* = 7.5 Hz, CH_2CH_3), 116.0 (d, *J* = 2.5 Hz, *C*HAr), 116.2 (d, *J* = 2.5 Hz, *C*HAr), 125.8 (C-*ipso*), 129.3 (d, *J* = 5.0 Hz, *C*HAr), 129.4 (d, *J* = 5.0 Hz, *C*HAr), 161.6 (*C-ipso*), 162.0 (d, *J* = 3.0 Hz, NC). HRMS $C_{12}H_{16}FNO_3P$ $[M+H]^+$ 272.0846; found, 272.0854.

Diethyl [(4-methoxyphenyl)isocyanomethyl]phosphonate (10c).[1] Et_3N (3.5 mL, 24.9 mmol) and $POCl_3$ (0.7 mL, 7.47 mmol) were added dropwise to a cooled solution (-78ºC) of **step 2-10c** (1.50 g, 4.98 mmol) in THF (13.8 mL). The reaction mixture was allowed to warm to rt. After 2 h, cold water (0 ºC) was added and the mixture was extracted with Et_2O. The combined organic layers were dried and concentrated *in vacuo* to give a residue which was purified by column chromatography (EtOAc-Hexane 4:1) to afford **10c** (1.13g, 80%) as yellowish oil. IR(ATR): 2978, 2917, 1610, 1514, 1455, 1293, 1250, 1176, 1013, 963, 839, 763 cm^{-1}; ^1H NMR (400 MHz, $CDCl_3$) δ 1.28 (t, 3H, CH_2CH_3), 1.31 (t, 3H, CH_2CH_3), 3.82 (s, 3H, OCH_3), 4.03-4.16 (m, 4H, CH_2CH_3), 4.95 (d, *J* = 20.5 Hz, 1H, C*H*), 6.92-6.95 (m, 2H, Ar*H*), 7.38-7.41 (m, 2H, Ar*H*); ^{13}C NMR (100.6 MHz) δ 16.4 (d, *J* = 5.5 Hz, CH_2CH_3), 16.5 (d, *J* = 5.5 Hz, CH_2CH_3), 55.5 (OCH_3), 55.6 (d, *J* = 156.0 Hz, *C*H), 64.4 (d, *J* = 7.0 Hz, CH_2CH_3), 64.9 (d, *J* = 7.0 Hz, CH_2CH_3), 114.4 (d, *J* = 2.5 Hz, 2x*C*HAr), 121.8 (C-*ipso*), 128.8 (d, *J* = 5.0 Hz, 2x*C*HAr), 160.3 (*C-ipso*), 160.8 (d, *J* = 5.0 Hz, NC); HRMS $C_{13}H_{19}NO_4P$ $[M+H]^+$ 284.1046; found, 284.1052.

Diethyl (1-isocyano-2-phenylethyl)phosphonate (10d).[3] Potassium *tert*-butoxide (492 mg, 4.4 mmol) was added to a cooled solution (-78 ºC) of diethyl isocyanomethylphosphonate (672 mg, 4 mmol) in dichloromethane (DCM) (6.0 mL) and the mixture was stirred for 15 min at – 78 ˚C. Then, a solution of benzyl bromide (476 µL, 4 mmol) in DCM (2.0 mL) was added. The reaction mixture was stirred for additional 30 min at -78 ˚C and allowed to warm to rt. After 30 min stirring the mixture at rt, the organic phase was washed with water, dried and concentrated. The resulting residue was purified by column chromatography (AcOEt/Hexane 4:6 to 1:1) to furnish **10d** (516 mg, 45%) as yellowish oil. ^1H NMR (400 MHz, $CDCl_3$) δ 1.38 (t, *J* = 7.0 Hz, 6H, CH_2CH_3), 2.80-3.06 (m, 1H, CH_2), 3.23-3.29 (m, 1H, CH_2), 3.80-4.20 (m, 1H, C*H*), 4.10-

4.50 (m, 4H, CH_2CH$_3$), 7.27-7.38 (m, 5H, Ar*H*). ^{13}C NMR (100.6 MHz) δ 16.3 (CH$_2$*C*H$_3$), 16.4 (CH$_2$*C*H$_3$), 36.0 (*C*H$_2$Ar), 52.0 (d, *J* = 155.0 Hz, *C*H), 63.8 (d, *J* = 7.0 Hz, *C*H$_2$CH$_3$), 64.4 (d, *J* = 7.0 Hz, *C*H$_2$CH$_3$), 127.5 (*C*HAr), 129.0 (d, *J* = 38.0 Hz, 2x*C*HAr), 135.4 (d, *J* = 14.0 Hz, 2x*C*HAr), 160.8 (*C*N).

Diethyl [2-(4-fluorophenyl)-1-isocyanoethyl]phosphonate (10e).[3] Potassium *tert*-butoxide (711 mg, 5.8 mmol) was added to a cooled solution (-78 ˚C) of diethyl isocyanomethylphosphonate (937 mg, 5.3 mmol) in DCM (9.0 mL) and the mixture was stirred for 15 min at - 78˚C. Then, a solution of 4-fluorobenzyl bromide (660 µL, 5.3 mmol) in DCM (3.0 mL) was added. The reaction mixture was stirred for additional 30 min at -78 ˚C and allowed to warm to rt. After 30 min stirring the mixture at rt, the organic phase was washed with water, dried and concentrated. The resulting residue was purified by column chromatography (AcOEt/hexane 4:6 to 1:1) to furnish **10e** (662 mg, 44%) as yellowish oil. IR (ATR) 2984, 2914, 2140, 1735, 1510, 1264, 1224, 1106, 974, 801, 761 cm^{-1}. ^{1}H NMR (400 MHz, CDCl$_3$) δ 1.38-1.42 (m, 6H, CH$_2$CH_3), 2.96-3.04 (m, 1H, CH_2), 3.19 – 3.26 (m, 1H, CH_2), 3.75 – 3.79 (d, *J* = 16.0 Hz, 1H, C*H*), 4.22-4.31 (m, 4H, CH_2CH$_3$), 7.02-7.06 (m, 2H, Ar*H*), 7.24-7.27 (m, 2H, Ar*H*). HRMS $C_{13}H_{18}FNO_3P$ $[M+H]^+$ 286.1003; found, 286.1011.

Theoretical calculations

Table S1. Relative stabilities (kcal·mol^{-1}) between reactants, transition states and products for the *cis* and *trans* [3+2] cycloadditions between *N*-methyl maleimide and PhosMic in the gas phase and in solution. These latter values were obtained by combining the relative stabilities in the gas phase with the solvation free energies in acetonitrile. All values relative to the *trans* reactants.

Cycloaddition	Reactant	Transition State	Product
Gas phase			
cis	2.0	19.0	-13.7
trans	0.0	16.7	-15.5
Solvation free energy			
cis	-0.2	1.7	0.1
trans	0.0	1.7	0.9
Solution (acetonitrile)			
cis	1.8	20.7	-13.6
trans	0.0	18.4	-14.6

Optimized parameters of reactants, transition states and products derived for the cis [3+2] cicloaddition (geometry in Å; energy in atomic units) **from B3LYP calculations**

Reactant

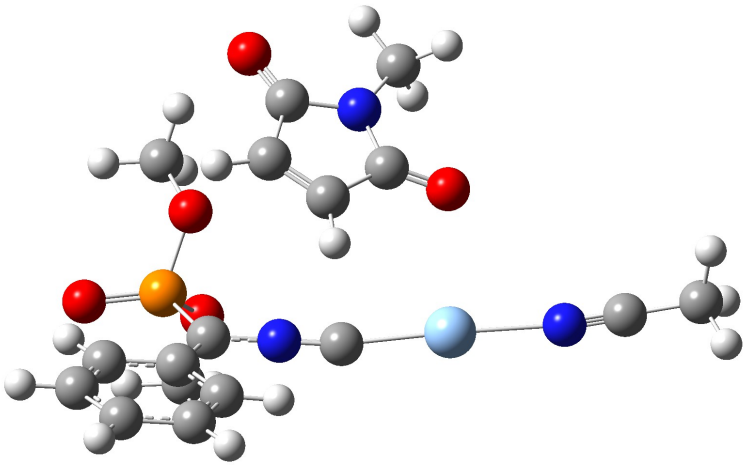

Geometry

1	7	0	1.268649	-2.808851	-1.346528
2	6	0	-0.076617	-3.023722	-1.700851
3	6	0	-0.579982	-1.717882	-2.238770
4	6	0	0.421592	-0.830149	-2.201931
5	6	0	1.627629	-1.494282	-1.610865
6	6	0	2.138597	-3.806413	-0.750263
7	8	0	2.729924	-1.007908	-1.382954
8	8	0	-0.664703	-4.081493	-1.592616
9	1	0	-1.602018	-1.587918	-2.569039
10	1	0	0.421207	0.209273	-2.501502
11	1	0	1.608165	-4.760406	-0.768818
12	1	0	3.067658	-3.887353	-1.322072
13	1	0	2.378814	-3.543071	0.285257
14	6	0	-2.032266	0.748012	0.431563
15	7	0	-0.704665	0.918878	0.589769
16	6	0	0.455087	1.084434	0.702369
17	47	0	2.515176	1.136068	0.600470

18	7	0	4.672354	1.271934	0.539087
19	6	0	5.820565	1.259409	0.405786
20	6	0	7.267567	1.239506	0.232561
21	1	0	7.751178	0.937920	1.167112
22	1	0	7.535258	0.528069	-0.555270
23	1	0	7.623177	2.235812	-0.048768
24	15	0	-2.725881	-0.574442	1.375203
25	8	0	-4.216108	-0.622123	1.466013
26	8	0	-2.037777	-1.928346	0.781170
27	6	0	-2.427462	-3.204148	1.329722
28	8	0	-1.977790	-0.550928	2.833494
29	6	0	-2.442209	0.386322	3.816607
30	1	0	-2.014034	-3.960659	0.660203
31	1	0	-2.015077	-3.322400	2.337729
32	1	0	-3.518111	-3.288996	1.360866
33	1	0	-3.504147	0.227092	4.028989
34	1	0	-2.287409	1.416638	3.473775
35	1	0	-1.848991	0.207145	4.716607
36	6	0	-2.719921	1.578414	-0.563379
37	6	0	-2.009322	2.557835	-1.298996
38	6	0	-4.104337	1.445711	-0.834071
39	6	0	-2.644834	3.355763	-2.252240
40	1	0	-0.949273	2.707038	-1.113348
41	6	0	-4.726184	2.245537	-1.790972
42	1	0	-4.685397	0.718087	-0.278518
43	6	0	-4.009519	3.207800	-2.513302
44	1	0	-2.063360	4.100802	-2.792199
45	1	0	-5.791449	2.115258	-1.970502
46	1	0	-4.504273	3.828855	-3.255613

Sum of electronic and zero-point Energies= -1686.455391 a.u.

Sum of electronic and thermal Free Energies= -1686.530633 a.u.

Transition state (C···C distances in Å; C-N-C angle in degrees)

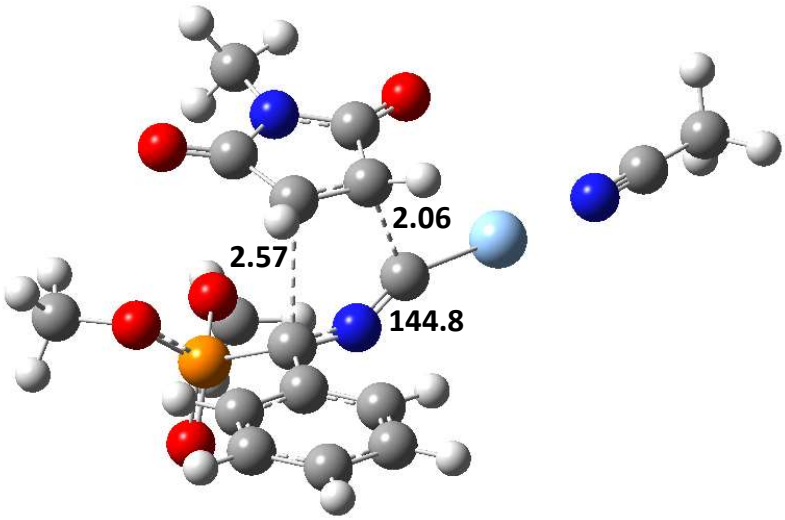

Geometry

1	7	0	0.237719	-2.379755	-1.613651
2	6	0	-1.102910	-1.932468	-1.794359
3	6	0	-1.044656	-0.465336	-1.914438
4	6	0	0.303233	-0.085596	-1.866392
5	6	0	1.124620	-1.324705	-1.708990
6	6	0	0.597613	-3.762417	-1.376312
7	8	0	2.352743	-1.409856	-1.623783
8	8	0	-2.045310	-2.705832	-1.878293
9	1	0	-1.869927	0.091598	-2.333640
10	1	0	0.727220	0.762734	-2.392668
11	1	0	0.169796	-4.401604	-2.154793
12	1	0	1.687281	-3.833788	-1.393795
13	1	0	0.219876	-4.098631	-0.404097
14	6	0	-1.677116	0.607524	0.336772
15	7	0	-0.356719	0.795744	0.511483
16	6	0	0.736991	0.690532	-0.003597
17	47	0	2.820033	0.768162	0.252874
18	7	0	4.990329	0.825244	0.459198
19	6	0	6.144135	0.772160	0.509296
20	6	0	7.599018	0.701562	0.568879

21	1	0	7.917118	0.404437	1.573246
22	1	0	7.963384	-0.034994	-0.154365
23	1	0	8.030008	1.679431	0.331810
24	15	0	-2.341260	-0.691538	1.429517
25	8	0	-2.812729	-0.267916	2.780686
26	8	0	-3.438170	-1.372129	0.474764
27	6	0	-4.138537	-2.563752	0.875974
28	8	0	-1.163007	-1.811992	1.491133
29	6	0	-0.360658	-1.972508	2.674538
30	1	0	-4.849631	-2.774343	0.076268
31	1	0	-3.435405	-3.396801	0.965366
32	1	0	-4.664491	-2.399542	1.822142
33	1	0	-0.937120	-1.728091	3.570438
34	1	0	0.520759	-1.325506	2.611597
35	1	0	-0.048285	-3.019524	2.698293
36	6	0	-2.494710	1.770874	-0.068406
37	6	0	-1.887214	3.014871	-0.339953
38	6	0	-3.891314	1.665633	-0.238337
39	6	0	-2.643535	4.105202	-0.768878
40	1	0	-0.817023	3.130356	-0.198824
41	6	0	-4.641193	2.759526	-0.668697
42	1	0	-4.386563	0.720099	-0.049187
43	6	0	-4.026477	3.986593	-0.937514
44	1	0	-2.149112	5.053845	-0.964773
45	1	0	-5.715699	2.649811	-0.793579
46	1	0	-4.616067	4.836964	-1.270056

Negative frequency: -353.8

Sum of electronic and zero-point Energies= -1686.432693

Sum of electronic and thermal Free Energies= -1686.503549

Product

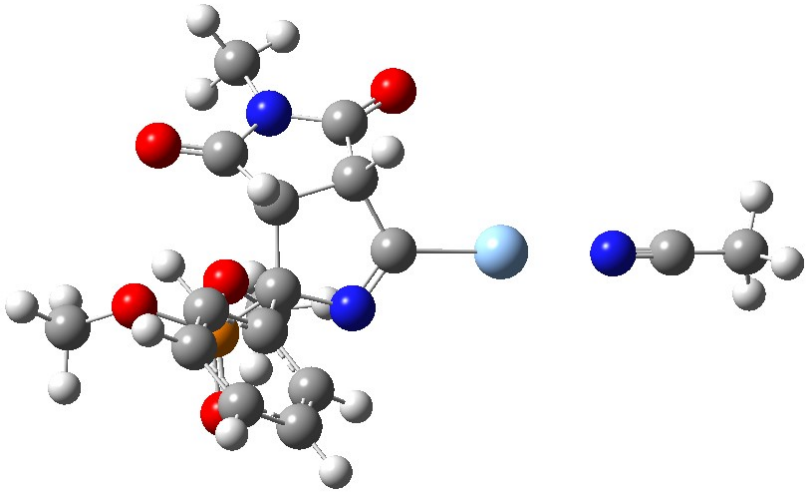

Geometry

1	7	0	-0.416099	-2.738848	-1.295412
2	6	0	-1.588707	-1.976860	-1.289394
3	6	0	-1.202721	-0.496463	-1.357802
4	6	0	0.325574	-0.519313	-1.553468
5	6	0	0.736169	-1.983693	-1.477967
6	6	0	-0.431865	-4.189861	-1.204277
7	8	0	1.864331	-2.440430	-1.562555
8	8	0	-2.700402	-2.466456	-1.316036
9	1	0	-1.738490	-0.071007	-2.208253
10	1	0	0.669896	-0.112939	-2.511829
11	1	0	-1.034332	-4.610071	-2.015166
12	1	0	0.598968	-4.539833	-1.279562
13	1	0	-0.867675	-4.497373	-0.248972
14	6	0	-1.395093	0.464913	-0.104699
15	7	0	-0.024059	0.829908	0.339732
16	6	0	0.891989	0.318479	-0.397144
17	47	0	2.951552	0.548001	-0.061391
18	7	0	5.106902	0.771428	0.299024
19	6	0	6.245056	0.857990	0.484448
20	6	0	7.680433	0.965852	0.718227
21	1	0	7.881276	1.000583	1.793721

22	1	0	8.193694	0.100588	0.286795
23	1	0	8.066535	1.878582	0.253406
24	15	0	-2.129531	-0.265289	1.454758
25	8	0	-2.154192	0.615577	2.654120
26	8	0	-3.554623	-0.789368	0.926361
27	6	0	-4.484281	-1.425344	1.818897
28	8	0	-1.305726	-1.656596	1.690224
29	6	0	-0.299660	-1.737583	2.720495
30	1	0	-5.392719	-1.593210	1.237852
31	1	0	-4.083822	-2.385856	2.160022
32	1	0	-4.697715	-0.777774	2.675008
33	1	0	-0.632079	-1.216648	3.621841
34	1	0	0.635567	-1.296159	2.363912
35	1	0	-0.159148	-2.801721	2.925283
36	6	0	-2.209580	1.714158	-0.462460
37	6	0	-1.773789	2.987026	-0.068278
38	6	0	-3.417174	1.601219	-1.170330
39	6	0	-2.518778	4.123587	-0.395555
40	1	0	-0.853940	3.075313	0.498640
41	6	0	-4.160478	2.737937	-1.495491
42	1	0	-3.790403	0.620009	-1.451540
43	6	0	-3.712100	4.005795	-1.112441
44	1	0	-2.164587	5.103331	-0.083769
45	1	0	-5.092813	2.630141	-2.044633
46	1	0	-4.290449	4.891050	-1.365641

Sum of electronic and zero-point Energies= -1686.486683

Sum of electronic and thermal Free Energies= -1686.555692

Optimized parameters of reactants, transition states and products derived for the trans [3+2] cicloaddition (geometry in Å; energy in atomic units) **from B3LYP calculations**

Reactant

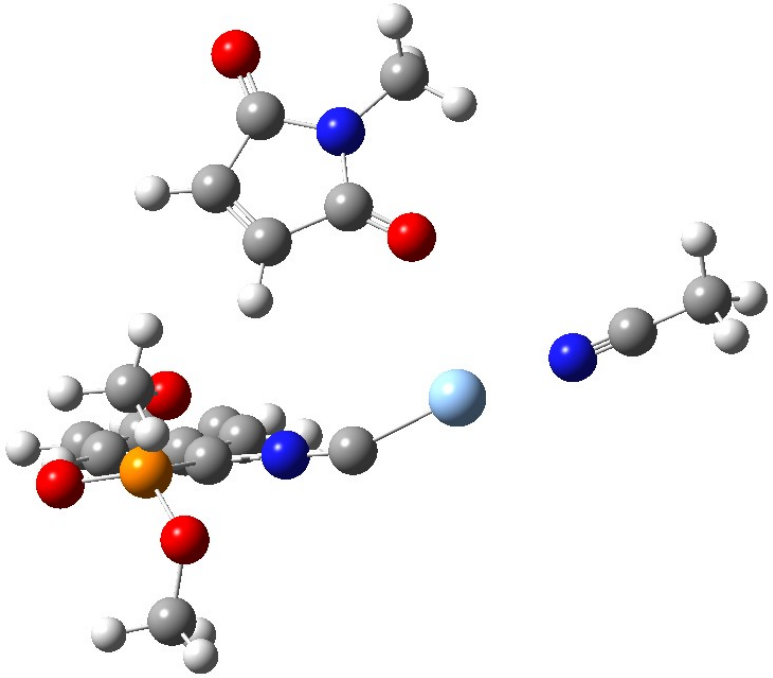

Geometry

1	7	0	2.186282	3.276484	0.716704
2	6	0	1.058999	4.027968	1.089597
3	6	0	-0.021349	3.034991	1.396232
4	6	0	0.463830	1.800216	1.213572
5	6	0	1.893743	1.917323	0.768711
6	6	0	3.459585	3.855061	0.325226
7	8	0	2.681910	1.019487	0.496387
8	8	0	1.021361	5.241470	1.141834
9	1	0	-1.014728	3.336501	1.703127
10	1	0	-0.043529	0.851771	1.344989
11	1	0	3.858259	4.477531	1.131927
12	1	0	4.147568	3.033733	0.116614
13	1	0	3.339818	4.473174	-0.569926
14	6	0	-2.244245	-0.637324	-0.343125
15	7	0	-0.990267	-1.088005	-0.557117
16	6	0	0.103601	-1.487679	-0.734587

17	47	0	2.171907	-1.517824	-0.644104
18	7	0	4.329549	-1.802504	-0.646964
19	6	0	5.481453	-1.889471	-0.600343
20	6	0	6.934070	-1.997202	-0.540485
21	1	0	7.219866	-2.986761	-0.169913
22	1	0	7.359672	-1.853213	-1.538682
23	1	0	7.335601	-1.233331	0.133013
24	15	0	-2.894123	-1.063274	1.238172
25	8	0	-4.312284	-0.687689	1.516774
26	8	0	-2.576744	-2.651031	1.499437
27	6	0	-3.443406	-3.621056	0.892045
28	8	0	-1.799765	-0.451398	2.292687
29	6	0	-1.972261	-0.700246	3.699498
30	1	0	-4.476299	-3.475923	1.224362
31	1	0	-3.395383	-3.551687	-0.201481
32	1	0	-3.080804	-4.600739	1.212180
33	1	0	-1.808413	-1.759762	3.921353
34	1	0	-1.223333	-0.093026	4.214040
35	1	0	-2.975219	-0.402065	4.021544
36	6	0	-2.872683	0.198820	-1.373316
37	6	0	-4.174458	0.735917	-1.225357
38	6	0	-2.181332	0.497061	-2.571588
39	6	0	-4.739819	1.525316	-2.225562
40	1	0	-4.736228	0.524225	-0.322463
41	6	0	-2.759865	1.285772	-3.567310
42	1	0	-1.182289	0.100677	-2.729453
43	6	0	-4.044717	1.811407	-3.406709
44	1	0	-5.742704	1.920667	-2.077219
45	1	0	-2.196501	1.489026	-4.476075
46	1	0	-4.494768	2.426262	-4.181955

Sum of electronic and zero-point Energies= -1686.456706

Sum of electronic and thermal Free Energies= -1686.533881

Transition state (C···C distances in Å; C-N-C angle in degrees)

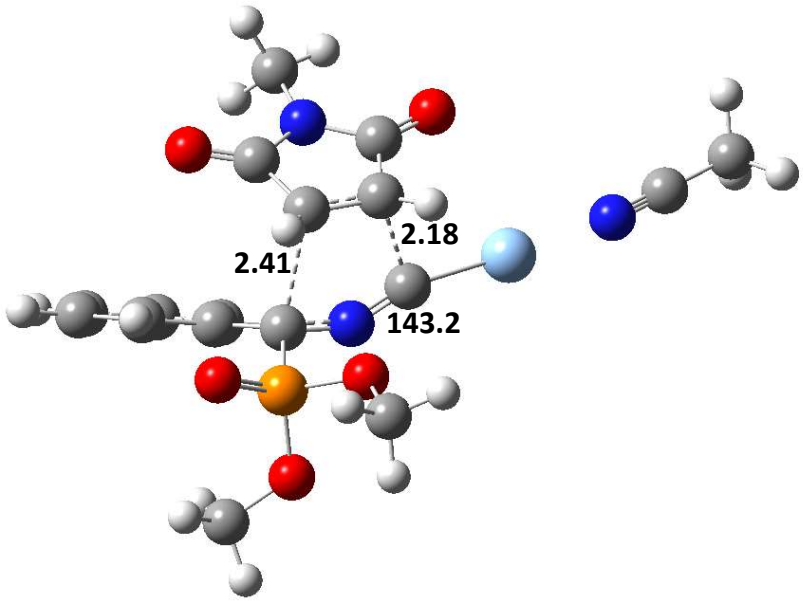

Geometry

1	7	0	-0.251238	-2.462516	1.474558
2	6	0	1.023941	-1.942589	1.792847
3	6	0	0.846622	-0.483582	1.992887
4	6	0	-0.519012	-0.208222	1.877917
5	6	0	-1.228008	-1.472602	1.584903
6	6	0	-0.499231	-3.855434	1.159300
7	8	0	-2.437184	-1.653248	1.412993
8	8	0	2.028204	-2.630849	1.883976
9	1	0	1.585380	0.082272	2.542700
10	1	0	-1.040037	0.627208	2.327784
11	1	0	-0.220098	-4.497206	2.001992
12	1	0	-1.565885	-3.965112	0.952097
13	1	0	0.084975	-4.158396	0.284357
14	6	0	1.611853	0.312917	-0.148526
15	7	0	0.333030	0.552905	-0.534866
16	6	0	-0.811761	0.528966	-0.153680
17	47	0	-2.877377	0.563043	-0.486971
18	7	0	-5.039034	0.538310	-0.746009
19	6	0	-6.186974	0.416364	-0.808240

20	6	0	-7.634141	0.257240	-0.881649
21	1	0	-8.127640	1.185820	-0.577740
22	1	0	-7.931265	0.012696	-1.906394
23	1	0	-7.950651	-0.551087	-0.214681
24	15	0	2.515700	1.798724	0.381145
25	8	0	3.754929	1.539554	1.168511
26	8	0	2.772102	2.746369	-0.923177
27	6	0	3.983400	2.608090	-1.690394
28	8	0	1.349804	2.638667	1.116482
29	6	0	1.664086	3.916358	1.700016
30	1	0	4.854460	2.573654	-1.029997
31	1	0	3.944357	1.701248	-2.302780
32	1	0	4.033801	3.486618	-2.337488
33	1	0	1.910909	4.639993	0.916656
34	1	0	0.764549	4.235407	2.229975
35	1	0	2.497960	3.823418	2.402870
36	6	0	2.357890	-0.743714	-0.876621
37	6	0	3.636508	-1.161787	-0.454067
38	6	0	1.781187	-1.381283	-1.994614
39	6	0	4.310823	-2.173575	-1.138169
40	1	0	4.089084	-0.703223	0.417692
41	6	0	2.460148	-2.396225	-2.668863
42	1	0	0.801903	-1.065062	-2.342072
43	6	0	3.732285	-2.796872	-2.247604
44	1	0	5.291616	-2.485499	-0.787981
45	1	0	1.996076	-2.868285	-3.531994
46	1	0	4.261886	-3.587480	-2.773233

Negative frequency: -349.4

Sum of electronic and zero-point Energies= -1686.437075

Sum of electronic and thermal Free Energies= -1686.507217

Product

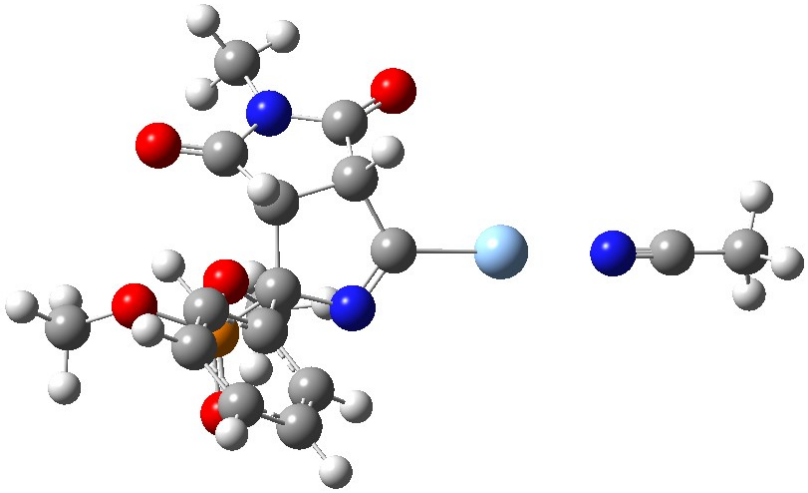

Geometry

1	7	0	0.101319	2.988086	-1.104607
2	6	0	1.337178	2.337019	-1.059663
3	6	0	1.103331	0.842178	-1.300501
4	6	0	-0.423816	0.723120	-1.454813
5	6	0	-0.960977	2.141590	-1.416876
6	6	0	-0.024760	4.429764	-0.955247
7	8	0	-2.112150	2.505783	-1.589044
8	8	0	2.392225	2.923906	-0.917226
9	1	0	1.667298	0.574205	-2.198475
10	1	0	-0.767619	0.217272	-2.362255
11	1	0	0.556835	4.941402	-1.728284
12	1	0	-1.081843	4.682619	-1.051374
13	1	0	0.351721	4.737227	0.024593
14	6	0	1.422284	-0.149827	-0.104177
15	7	0	0.114930	-0.496248	0.491317
16	6	0	-0.872978	-0.067557	-0.203951
17	47	0	-2.892798	-0.344373	0.294000
18	7	0	-5.013352	-0.603043	0.812613
19	6	0	-6.137895	-0.691438	1.067348
20	6	0	-7.556381	-0.800547	1.387921
21	1	0	-8.005637	-1.620471	0.818623

22	1	0	-7.683242	-0.996899	2.457289
23	1	0	-8.067945	0.133066	1.133060
24	15	0	2.136160	-1.718082	-0.842821
25	8	0	3.404477	-1.537357	-1.611508
26	8	0	2.226358	-2.822334	0.336995
27	6	0	3.458955	-3.062102	1.046505
28	8	0	0.883019	-2.260172	-1.710895
29	6	0	1.059950	-3.408770	-2.559859
30	1	0	4.312702	-3.000913	0.366224
31	1	0	3.568917	-2.333491	1.854501
32	1	0	3.377065	-4.069160	1.461774
33	1	0	1.212518	-4.306914	-1.952230
34	1	0	0.136810	-3.506292	-3.134616
35	1	0	1.909611	-3.262735	-3.234131
36	6	0	2.407150	0.339071	0.964232
37	6	0	3.724322	0.698672	0.632782
38	6	0	2.005222	0.411136	2.306730
39	6	0	4.612319	1.125632	1.621619
40	1	0	4.057117	0.645992	-0.397392
41	6	0	2.896038	0.842893	3.294519
42	1	0	0.994830	0.117426	2.568117
43	6	0	4.203608	1.200439	2.956771
44	1	0	5.625140	1.406155	1.343498
45	1	0	2.564737	0.894453	4.329213
46	1	0	4.897100	1.535965	3.724328

Sum of electronic and zero-point Energies= -1686.490065

Sum of electronic and thermal Free Energies= -1686.558641

Optimized parameters of transition states derived for the cis and trans [3+2] cicloaddition (geometry in Å; energy in atomic units) **from MN15L calculations**

Transition state for cis cicloaddition (C···C distances in Å; C-N-C angle in degrees)

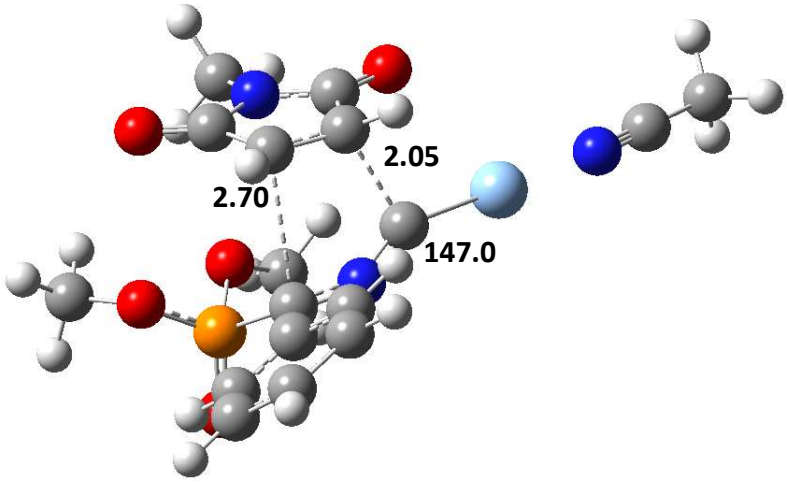

Geometry

1	7	0	0.206262	-2.308687	-1.545414
2	6	0	-1.146637	-1.885843	-1.752955
3	6	0	-1.100704	-0.436323	-1.967387
4	6	0	0.245668	-0.027813	-1.914749
5	6	0	1.083724	-1.252702	-1.657910
6	6	0	0.545034	-3.644103	-1.095077
7	8	0	2.310637	-1.314103	-1.494569
8	8	0	-2.074366	-2.688193	-1.758478
9	1	0	-1.962820	0.127320	-2.334358
10	1	0	0.679796	0.811388	-2.474744
11	1	0	0.466934	-4.375345	-1.922976
12	1	0	1.583144	-3.624560	-0.716368
13	1	0	-0.158450	-3.943119	-0.293016
14	6	0	-1.691941	0.637771	0.438896
15	7	0	-0.375337	0.890353	0.474759
16	6	0	0.703189	0.806324	-0.100243
17	47	0	2.771001	0.866242	0.170433

18	7	0	4.930341	0.922679	0.435952
19	6	0	6.086891	0.861518	0.556554
20	6	0	7.537170	0.783442	0.706152
21	1	0	7.793907	0.526072	1.749532
22	1	0	7.940905	0.006337	0.032419
23	1	0	7.994541	1.756308	0.451198
24	15	0	-2.148464	-0.811185	1.425741
25	8	0	-2.404350	-0.589624	2.873117
26	8	0	-3.340153	-1.401924	0.544597
27	6	0	-3.793129	-2.742625	0.815949
28	8	0	-0.962451	-1.867430	1.124878
29	6	0	0.223442	-1.901732	1.928249
30	1	0	-4.629199	-2.922584	0.121317
31	1	0	-2.977831	-3.459803	0.604731
32	1	0	-4.134754	-2.825892	1.867053
33	1	0	0.265765	-2.877432	2.448531
34	1	0	0.233732	-1.083788	2.675555
35	1	0	1.092773	-1.802880	1.243320
36	6	0	-2.624498	1.717456	0.070134
37	6	0	-2.191900	2.760291	-0.790145
38	6	0	-3.967998	1.720730	0.520340
39	6	0	-3.076777	3.768925	-1.188503
40	1	0	-1.152074	2.762072	-1.151920
41	6	0	-4.848683	2.733851	0.114547
42	1	0	-4.316752	0.935464	1.204762
43	6	0	-4.412097	3.760879	-0.740447
44	1	0	-2.726211	4.566509	-1.858967
45	1	0	-5.885815	2.724750	0.478024
46	1	0	-5.105570	4.553120	-1.054452

Negative frequency: -376.8

Sum of electronic and zero-point Energies= -1684.741793

Sum of electronic and thermal Free Energies= -1684.808303

Transition state for trans cicloaddition (C···C distances in Å; C-N-C angle in degrees)

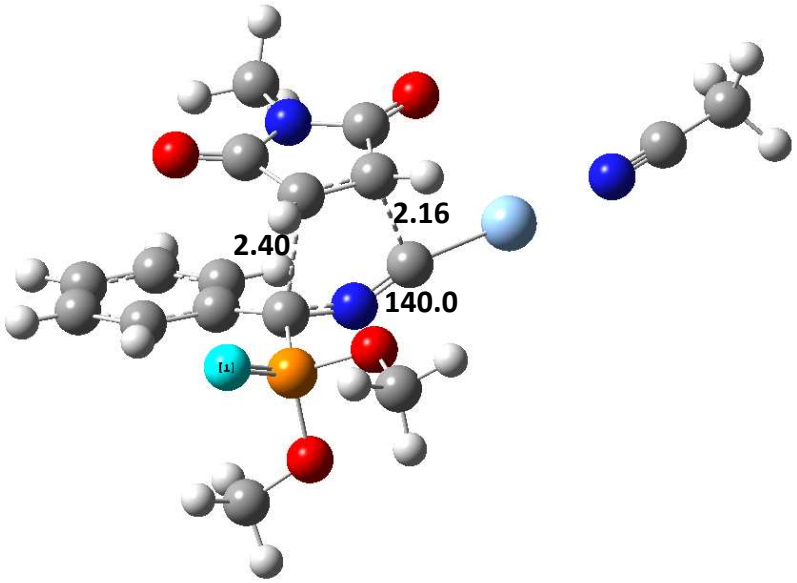

Geometry

1	7	0	-0.003238	-2.232897	1.360636
2	6	0	1.218572	-1.639438	1.767280
3	6	0	0.913623	-0.205053	1.990088
4	6	0	-0.475834	-0.029363	1.845418
5	6	0	-1.068672	-1.345744	1.506547
6	6	0	-0.137896	-3.606721	0.915552
7	8	0	-2.254417	-1.642851	1.300055
8	8	0	2.274069	-2.250726	1.865049
9	1	0	1.624844	0.447012	2.506861
10	1	0	-1.079146	0.780960	2.269048
11	1	0	-0.684339	-4.217143	1.661144
12	1	0	-0.693283	-3.634513	-0.042503
13	1	0	0.881405	-4.007914	0.773224
14	6	0	1.607298	0.362128	-0.235824
15	7	0	0.316441	0.525826	-0.657920
16	6	0	-0.818880	0.541715	-0.210582
17	47	0	-2.882922	0.460032	-0.452460
18	7	0	-5.044692	0.354406	-0.627083

19	6	0	-6.194745	0.174674	-0.656043
20	6	0	-7.636505	-0.052616	-0.689739
21	1	0	-8.041455	-0.036068	0.338131
22	1	0	-8.129750	0.735574	-1.286484
23	1	0	-7.848770	-1.037105	-1.144181
24	15	0	2.388240	1.923492	0.228603
25	8	0	3.625172	1.811149	1.044197
26	8	0	2.574725	2.813976	-1.116315
27	6	0	3.684406	2.461511	-1.961175
28	8	0	1.152190	2.702866	0.902153
29	6	0	1.433169	4.035594	1.368278
30	1	0	4.618917	2.404350	-1.369185
31	1	0	3.494288	1.487791	-2.456915
32	1	0	3.761876	3.257522	-2.721053
33	1	0	1.610644	4.709007	0.507538
34	1	0	0.538005	4.360662	1.924280
35	1	0	2.315927	4.033529	2.037035
36	6	0	2.369756	-0.777848	-0.794761
37	6	0	3.749248	-0.958617	-0.519568
38	6	0	1.687859	-1.787641	-1.522581
39	6	0	4.412997	-2.112856	-0.960957
40	1	0	4.287179	-0.216054	0.083400
41	6	0	2.360483	-2.937423	-1.954900
42	1	0	0.614702	-1.668590	-1.734511
43	6	0	3.729635	-3.108484	-1.678785
44	1	0	5.478404	-2.240459	-0.722974
45	1	0	1.808739	-3.708241	-2.513081
46	1	0	4.255007	-4.013785	-2.013214

Negative frequency: -380.8

Sum of electronic and zero-point Energies= -1684.743843

Sum of electronic and thermal Free Energies= -1684.810187

3D-QSAR study

Selection of training and test set compounds. Original data set, for both created 3D-QSAR models, was divided on training and test set according to the PCA (Principal Component Analysis) score plot. Approximately 70% of compounds were chosen for the training set, and 30% for test set considering that p*K*i values were homogeneously distributed in the whole range. Final data set for I_2-IR ligands contains 33 compounds, with 23 compounds in training set and 10 compounds in test set, while data set for α_2-receptor ligands contains 30 compounds, with 21 compounds in training set and 9 compounds in test set (Table S2 and S3). Training set compounds were used for model building, and test set compounds were used for model validation.

Validation of created 3D-QSAR models. Different internal and external validation methods were employed in order to ensure the reliability and predictive quality of created QSAR models. Internal predictivity was examined with parameters such as cross-validated squared correlation coefficient (Q^2), root mean square error of estimation (RMSEE) and predicted residual sum of squares (PRESS) (Eq. 1, 2 and 3). These parameters are calculated only for training set compounds. For a predictive QSAR model values of Q^2 should be higher than 0.5.[4,5]

$$PRESS = \sum_{i=1}^{n} e_{(i)}^2 \quad (1) \qquad RMSEE = \sqrt{\frac{PRESS}{n}} \quad (2) \qquad Q^2 = 1 - \frac{PRESS}{SSTo} \quad (3)$$

Very often high value of Q^2 does not present real predictive potential of created model.[6] For that reason, calculations of external validation parameters help us to truly clarify the predictive power of created models. Parameters of external validation are R^2_{pred}, RMSEP and r^2metrics parameters (r^2_m, $r^{2/}_m$, $\bar{r}^2_m$ and Δr^2_m) (Eq. 4, 5, 6 and 7). Value of R^2_{pred} should be higher than 0.5. Values of correlation coefficients $r^2_{m,}$ and $r^{/2}_m$ should be close and greater than 0.5, while their average value ($\bar{r}^2_m$) should be greater than 0.5 and the difference between r^2_m and $r^{/2}_m$ (Δr^2_m) should be lower than 0.2 for an acceptable model. Parameters of r^2metrics represent more stringent criterion of external validation and better reflect external predictive power of created models.[7]

$$R^2_{pred} = 1 - \frac{\Sigma(Y_{obs(test)} - \bar{Y}_{pred(test)})^2}{\Sigma(Y_{obs(test)} - \bar{Y}_{training})^2} \quad (4) \qquad r^2_{m=r^2\left(\sqrt{1-|r^2-r_0^2|}\right)} \quad (6)$$

$$RMSEP = \sqrt{\frac{PRESS}{n}} \quad (5) \qquad r^{/2}_{m=r^2\left(1-\sqrt{|r^2-r_0^{/2}|}\right)} \quad (7)$$

Obtained values of $R^2pred(I_2)$= 0.68, $R^2pred(\alpha_2)$= 0.87 and r^2 metrics parameters indicate that developed models have good predictive quality.

Table S2. Results of 3D-QSAR study for I_2-IR ligands

Training set			Test set		
	pKi(exp)	**pKi (pred)**		**pKi(exp)**	**pKi(pred)**
9c	10.28	9.39	**9d**	8.56	8.00
9b	9.74	9.09	**9a**	7.97	8.27
9f	8.37	7.78	**Idazoxan**	7.41	7.92
LSL60101	8.13	8.44	**BU99008**	7.05	7.84
9ad	7.96	7.52	**9i**	7.01	6.52
9z	7.90	7.37	**9x**	6.81	7.32
13d	7.87	8.00	**8a**	6.79	6.05
8c	7.73	7.76	**14c**	6.59	6.21
Tracizoline	7.58	7.36	**9u**	5.81	5.78
12d	7.55	8.55	**9r**	5.09	5.61
9h	7.35	7.94			
9ab	6.96	6.65	**R^2_{pred}=0.68 (>0.5)**		
9e	6.65	7.12	**RMSEP=0.53**		
9k	6.35	5.91	**r^2_m=0.59 (>0.5)**		
8b	5.74	6.87	**$r^{2/}_m$=0.64 (>0.5)**		
9aa	5.44	5.64	**Δr^2_m=0.05 (<0.2)**		
15c	5.35	4.44	**$\bar{r}^2_m$= 0.61 (>0.5)**		
9j	5.26	5.93	**$(r^2-r^{2/}_0)/r^2$=0.02 (<0.1)**		
8e	5.11	5.07	**k'= 1.00 (0.85≤k'≤1.15)**		
9g	4.02	4.98			
9m	3.84	3.30			
13c	3.39	3.16			
9ac	3.11	3.42			
R^2=0.90 (>0.7)					
Q^2=0.65 (>0.5)					
RMSEE=0.60					

Table S3. Results of 3D-QSAR study for α_2-AR ligands

Training set			Test set		
	pKi(exp)	**pKi (pred)**		**pKi(exp)**	**pKi(pred)**
8d	10.27	10.65	**8c**	8.49	8.47
8a	9.49	9.85	**12c**	6.77	6.15
9b	9.01	8.41	**9d**	6.27	6.15
Idazoxan	8.35	7.95	**9r**	6.15	5.36
9j	8.11	7.91	**9a**	5.93	5.63
15c	7.20	7.02	**9ab**	5.43	5.83
9h	6.77	6.88	**9w**	5.16	5.26
9u	6.22	6.18	**9n**	4.73	5.02
8e	6.14	6.13	**BU99008**	4.37	4.86
9f	5.85	5.53			
9l	5.65	5.77	**R^2_{pred}=0.87 (>0.5)**		
9p	5.34	5.33	**RMSEP=0.42**		
LSL60101	5.17	5.31	**r^2_m=0.83 (>0.5)**		
9z	5.12	5.13	**$r^{2/}_m$=0.71 (>0.5)**		
9e	4.59	4.64	**Δr^2_m=0.12 (<0.2)**		
Tracizoline	4.33	4.49	**$\bar{r}^2_m$= 0.77 (>0.5)**		
9i	4.31	4.48	**$(r^2-r^{2/}_0)/r^2$=0.04 (<0.1)**		
13c	3.85	4.31	**k'= 0.98 (0.85≤k'≤1.15)**		
9k	3.77	3.47			
14c	3.94	4.32			
12d	3.38	3.11			
R^2=0.98 (>0.7)					
Q^2=0.61 (>0.5)					
RMSEE=0.57					

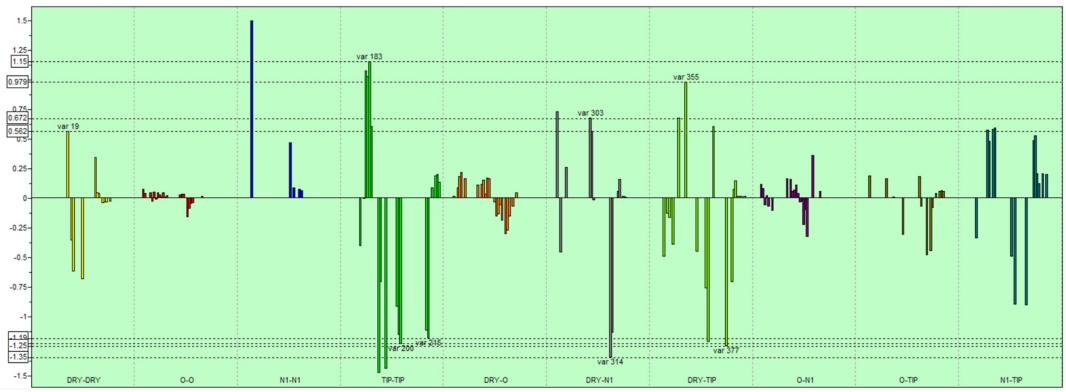

Figure S1. PLS coefficient plot for the I_2-IR 3D-QSAR model. The most significant variables are labelled.

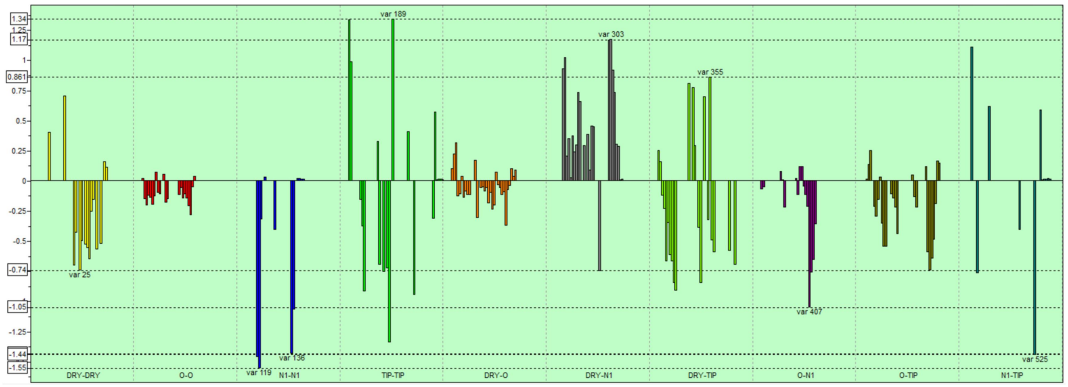

Figure S2. PLS coefficient plot for the α_2-AR 3D-QSAR model. The most significant variables are labelled.

Interpretation of created 3D-QSAR models. According to the correlogram shown in Figure S1, variables with most important positive influence on I_2-IR activity are: var19 (DRY-DRY: 7.60-8.00 Å), var183 (TIP-TIP: 6.00-6.40 Å), var303 (DRY-N1: 9.20-9.60 Å) and var355 (DRY-TIP: 7.60-8.00 Å). Positive variables are depicted in the Figure S3 for the most active compound, **9c** (pKi I_2 = 10.28), and for **13d** (pKi I_2 = 7.87) which possess the highest selectivity (I_2/ α_2=74131).

Created 3D-QSAR model for I_2-IR ligands shows that var183 possess strong positive influence on pKi values. It represents the distance of 6.00-6.40 Å between two steric hot spot regions located around electron withdrawing substituents of the *N*-phenyl. The

highest values are calculated for compounds **13d** and **12d** which possess high selectivity towards I_2-IR (Figure S3B). From created α_2-AR ligand model, it can be seen that this variable do not possess such significant impact on α_2-AR binding. Therefore, we hypothesize that presence of these substituents may be very importnat for enhancing I_2-IR binding activity and selectivity. GRIND variables DRY-N1 (var303) and DRY-TIP (var355) show positive impact on biological activity and signify the importance of hydrophobic interactions in the binding site of I_2-IR. Var303 define favourable distance (9.20-9.60 Å) between hydrophobic regions around bicyclic ring and nitrogen from imino group as hydrogen bond acceptor (Figure S3B). On the other hand, DRY-DRY variable from α_2-AR model, var25 (10.00-10.40 Å), describe unfavourable impact of hydrophobic regions around phenyl ring in α position, which could be related with higher affinity of *α*-unsubstituted ligands to α_2-AR (**8a**, **8c**, **8d** and **8e**). Var355 (DRY-TIP: 7.60-8.00 Å) delineate optimal distance between aforementioned hydrophobic regions around bicyclic ring and ethyl phosphonate group as steric hot spot (Figure S3A and S3B). Moreover, var19 (DRY-DRY: 7.60-8.00 Å), which is describing hydrophobic probes located around *N*-phenyl substituent, implies that presence of aromatic ring in that position establish favourable van der Waals interactions with amino acids of the active pocket (Figure S3A and S3B). Comparing to compounds which possess *N*-alkyl substituents instead of *N*-phenyl, such as **8a** or **9a**, we can conclude that introduction of this aromatic ring positively correlates with I_2-IR binding activity.

Variables with highest negative influence on I_2-IR binding activity are: var200 (TIP-TIP: 12.80-13.20 Å), var215 (TIP-TIP: 18.80-19.20 Å), var314 (DRY-N1: 13.60-14.00 Å) and var377 (DRY-TIP: 16.40-16.80 Å). Negative variables are depicted in Figure S4 on **9m** (pKi I_2=3.84) and **9ac** (pKi I_2=3.11), which possess low activity on I_2-IR.

From cross-correlogram TIP-TIP, it can be seen that var200 and var215 have strong negative influence on I_2-IR binding activity. Both variables are presented between two steric hot spots, substituents in the N-maleimide group and ethyl groups on phosphonate (Figure S4A and S4B). The highest values are calculated for compounds bearing longer distances (12.80-13.20 Å – var200 and 18.80-20.20 Å – var215) between these steric regions (**9e**, **8e**, **9m**, **9aa**, **9ab**, **9k**, **9ac** and **9z**). This molecular shape analysis implies that introduction of longer substituents in the *N*-maleimide group may not be the most complemented with the binding site of I_2-IR. Unfavourable impact of bulkier *N*-substituents is also defined with GRIND variable DRY-N1 (var314). It describes

unfavourable interaction between hydrophobic regions around aromatic ring separated from hydrogen bond acceptor group, nitrogen from imino group, at the longer distance (13.60-14.00 Å) (Figure S4A and S4B). This variable is pronounced in compounds **9z**, **9m**, **9j**, **9ab** and **9ac**. Furthermore, variable var377 (DRY-TIP) unfavourably impacts I_2-IR binding affinity describing hydrophobic and steric regions separated at the longer distance range (16.40-16.80 Å) than optimal (Figure S4A and S4B). The highest values are expressed in compounds **8e**, **9j**, **9k**, **9m**, **9z**, **9ab** and **9ac**, while the most potent compounds do not possess this negative variable. Overall, aforementioned negative variables confirm unfavourable fitting of longer molecules into I_2-IR binding pocket. Contrary, analysis of positive variables, var303 (DRY-N1: 13.20-13.60 Å) and var355 (DRY-TIP: 12.40-12.80 Å), from α_2-AR model show that introduction of steric regions at a longer distance from hydrogen bond acceptor or ethyl phosphonate group may lead to an increase in α_2-AR activity (**8e**, **9j**, **9l**).

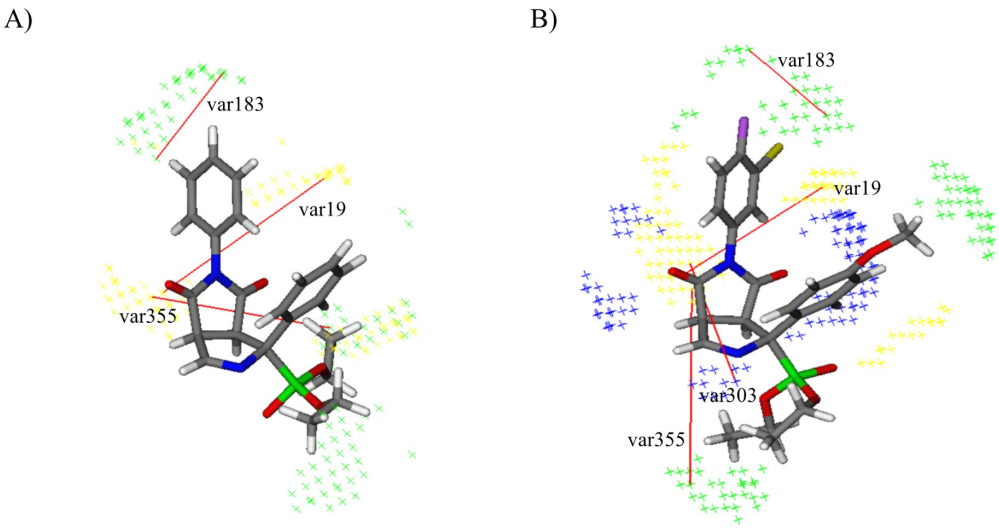

Figure S3. Representation of positive (in red) interactions of **9c** (A) and **13d** (B) in I_2-IR 3D-QSAR model. The steric hot spots (TIP) are presented in green, hydrophobic regions (DRY) in yellow and H-bond acceptor regions (N1) in blue.

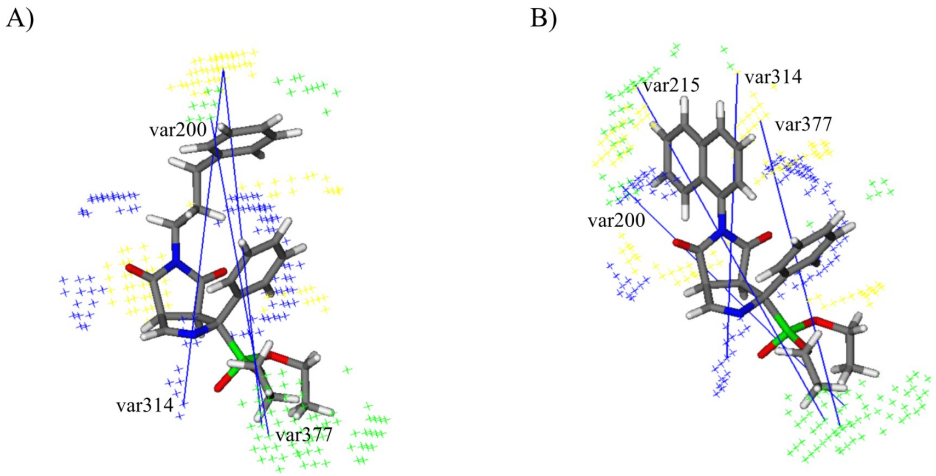

Figure S4. Representation of negative (in blue) interactions of **9m** (A) and **9ac** (B) in I_2-IR 3D-QSAR model. The steric hot spots (TIP) are presented in green, hydrophobic regions (DRY) in yellow and H-bond acceptor regions (N1) in blue.

The applicability domain (AD). In order to define AD of created I_2 and α_2 3D-QSAR models we have performed the leverage approach (Williams plot). SPSS v.18.0 software was used for this procedure.[8] The value of warning leverage h* was calculated according to relation $h^* = 3(p+1)/n$, where p presents the number of model variables (in this case we use five most significant variables according to PLS coefficient plot) and n is the number of compounds in training set. Figure S5 and S6 show that all compounds for both models are within of the defined AD.

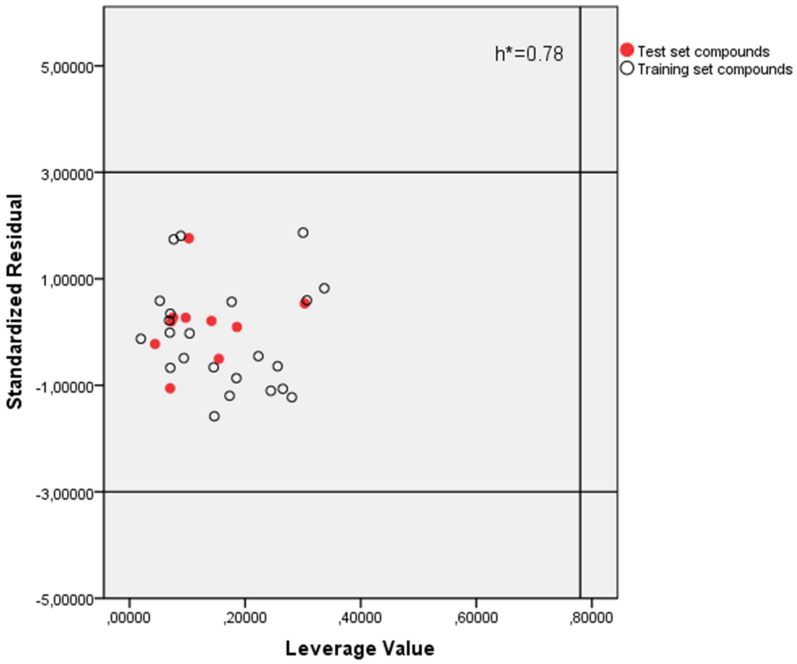

Figure S5. AD of developed I_2-IR 3D-QSAR model

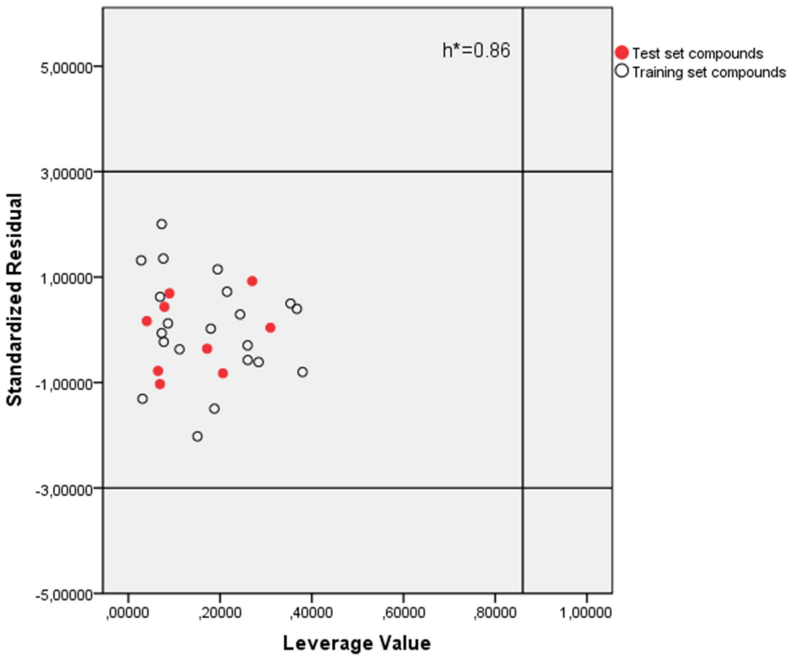

Figure S6. AD of developed α_2-AR 3D-QSAR model

Table S4. Results of physico-chemical parameters of I_2-IR ligands obtained from SwissADME web tool

Identifier	pKi(I_2)	MW <500 (g/mol)	Log S (ESOL) -10 to 0	Solubility class	Log $P_{o/w}$ (XLOGP3) < 5	Log $P_{o/w}$ (MLOGP) < 4.15	Log $P_{o/w}$ (WLOGP) < 5.6	Consensus Log $P_{o/w}$	RuleOf5	TPSA 20Å²<TPSA<130
Idazoxan, 4	7.41	204.23	-1.78	very soluble	0.70	0.99	0.07	1.23	Yes; 0 violation	42.85 Å²
Tracizoline, 5	7.58	173.23	-1.95	very soluble	1.31	2.10	-1.09	1.49	Yes; 0 violation	26.00 Å²
BU99008, 2	7.05	200.26	-2.27	soluble/ very soluble	1.29	1.95	-1.15	1.37	Yes; 0 violation	30.93 Å²
LSL60101, 3	8.13	214.22	-3.03	soluble	2.13	0.85	2.83	2.19	Yes; 0 violation	51.05 Å²
8c	7.73	350.31	-1.97	very soluble	0.27	0.98	1.71	1.34	Yes; 0 violation	95.08 Å²
9d	8.56	478.84	-4.19	moderately soluble	2.48	2.99	4.34	3.43	Yes; 0 violation	95.08 Å²
9b	9.74	432.45	-3.47	soluble	2.00	2.09	3.25	2.73	Yes; 0 violation	95.08 Å²
9c	10.28	426.40	-3.42	soluble	1.75	2.13	3.13	2.55	Yes; 0 violation	95.08 Å²
9a	7.97	364.33	-2.00	soluble/ very soluble	0.19	0.95	1.55	1.36	Yes; 0 violation	95.08 Å²
9z	7.90	502.50	-4.93	moderately soluble	3.38	3.16	4.79	3.89	Yes; 1 violation: MW>500	95.08 Å²
9f	8.37	378.36	-2.25	soluble	0.56	1.19	1.94	1.76	Yes; 0 violation	95.08 Å²
9h	7.35	406.41	-2.80	soluble	1.18	1.65	2.72	2.20	Yes; 0 violation	95.08 Å²
9i	7.01	498.55	-4.48	moderately soluble	3.10	3.13	4.14	3.63	Yes; 0 violation	95.08 Å²
12d	7.55	496.83	-4.35	moderately soluble	2.58	3.36	4.90	3.71	Yes; 0 violation	95.08 Å²
9ad	7.96	461.84	-3.56	soluble	1.64	1.61	3.17	2.44	Yes; 0 violation	107.97 Å²
13d	7.87	508.86	-4.27	moderately soluble	2.45	2.68	4.35	2.68	Yes; 1 violation: MW>500	104.31 Å²

Legend: MW – molecular weight; **Log S (ESOL)** – water solubility, topological method implemented from Delaney JS 2004 J. Chem. Inf. Model; **Solubility Class** - insoluble < -10 < poorly < -6 < moderately <-4 < soluble < -2 < very < 0 < highly; **XLOGP3 –** atomistic and knowledge-based method calculated by XLOGP program; **MLOGP** – topological method implemented from Moriguchi I. et al. 1992 Chem. Pharm. Bull.; **WLOGP** – atomistic method implemented from Wildman SA and Crippen GM. 1999 J. Chem. Inf. Model.; **Consensus Log Po/w –** average logP value of five predictions; **RuleOf5** - Lipinski's "Rule of Five"; **TPSA** – topological polar surface area.

Table S5. Selected pharmacokinetic properties of I_2-IR ligands obtained with ADMET Predictor program

Identifier	pKi(I_2)	S+Peff	BBB Filter	hum_ fup%	Pgp_ Substr	Pgp_Inh	CYP_ Risk	TOX_ Risk
Idazoxan, 4	7.41	3.854	High (98%)	60.075	No (93%)	No (96%)	2	1
Tracizoline, 5	7.58	3.042	High (98%)	57.803	No (93%)	No (96%)	1.451	3.365
BU99008, 2	7.05	3.145	High (98%)	57.69	No (93%)	No (96%)	1.215	2.927
LSL60101, 3	8.13	4.388	High (98%)	9.985	No (93%)	No (96%)	0.435	0
8c	7.73	2.273	High (77%)	23.11	No (93%)	No (96%)	0	1
9d	8.56	3.871	High (75%)	6.51	No (93%)	No (58%)	1.21	0.232
9b	9.74	2.707	High (74%)	10.274	No (93%)	No (63%)	1.541	0.386
9c	10.28	3.247	High (77%)	7.891	No (93%)	No (63%)	1.25	1
9a	7.97	3.01	High (76%)	27.813	No (93%)	No (96%)	0.772	0.677
9z	7.90	2.504	High (70%)	3.619	No (93%)	Yes (97%)	1.264	1.089
9f	8.37	2.972	High (76%)	22.087	No (93%)	No (96%)	0.996	0.66
9h	7.35	2.919	High (75%)	18.205	No (93%)	No (96%)	2.127	1.005
9i	7.01	2.391	High (74%)	6.64	No (93%)	No (46%)	2.198	1
12d	7.55	4.411	High (74%)	6.451	No (93%)	Yes (43%)	1.211	0.284
9ad	7.96	2.708	High (74%)	11.408	No (93%)	No (66%)	1.078	1
13d	7.87	3.248	High (74%)	6.596	No (93%)	Yes (43%)	1.191	0

Legend: S+Peff – estimated permeability, **BBB filter** - qualitative likelihood (High/Low) of crossing the blood-brain barrier; **hum_fup%** - percentage of unbound drug in plasma; **Pgp_Substr** - likelihood of P-glycoprotein efflux; **Pgp_Inh –** likelihood of a molecule being an inhibitor of P-glycoprotein; **CYP_Risk** – cytochrome P450 liability score; **Tox_Risk** – toxicity liability score.

***In vitro* Blood-Brain Barrier Permeation Assay**

To evaluate the brain penetration of the different compounds, a parallel artificial membrane permeation assay for blood-brain barrier was used, following the method described by Di et al (Table S6).[9] The *in vitro* permeability (P_e) of fourteen commercial drugs through lipid extract of porcine brain membrane together with the test compounds were determined. Commercial drugs and assayed compounds were tested using a mixture of PBS:ETOH (70:30). Assay validation was made by comparing the experimental permeability with the reported values of the commercial drugs by bibliography and lineal correlation between experimental and reported permeability of the fourteen commercial drugs using the parallel artificial membrane permeation assay was evaluated (y=1,572x-1,090; R^2=0,938). From this equation and taking into account the limits established by Di et al. for BBB permeation, we established the ranges of permeability as compounds of high BBB permeation (CNS+): *P*e (10^{-6} cms^{-1}) > 5,198; compounds of low BBB permeation(CNS-): *P*e (10^{-6} cm s^{-1}) < 2,054 and compounds of uncertain BBB permeation(CNS+/-): 5,198 > *P*e (10^{-6} cm s^{-1}) > 2,054.

Table S6. Permeability Results *P*e (10^{-6} cm s^{-1}) from the PAMPA-BBB Assay for new reported compounds and Their Prediction of BBB Penetration.

Compound	*P*e (10^{-6} cm s^{-1})[a]	Prediction
8a	1.2±0.04	CNS-
8b	7.5±0.6	CNS+
8c	4.3±0.3	CNS+/-
8d	9.4±1.2	CNS+
8e	5.13±0,95	CNS+/-
9a	0.75±0.13	CNS-
9b	25.9±0.6	CNS+
9c	7.8±0.6	CNS+
9d	9.7±0.7	CNS+
9e	3.9±0.15	CNS+/-
14c	6.9±0.3	CNS+
12c	3.2±0.16	CNS+/-
12d	4.4±0.09	CNS+/-
13c	1.8±0.06	CNS-
13d	1.9±0.06	CNS-
15c	9.5±0.5	CNS+
9f	3.7±0.5	CNS+/-
9g	6.2±0.3	CNS+
9h	6.3±0.3	CNS+
9i	6.7±0.3	CNS+
9j	>30	CNS+
9k	6.2±0.3	CNS+
9l	7.2±0.45	CNS+
9m	21.2±2.77	CNS+
9n	5.6±0,15	CNS+

9o	6.9±0.2	CNS+
9p	3.2±0.2	CNS+/-
9q	5.5±0.03	CNS+
9r	5.3±0.14	CNS+/-
9s	3.7±0.1	CNS+/-
9t	4.4±0.4	CNS+/-
9u	8.3±0.45	CNS+
9v	8.9±0.3	CNS+
9w	9.8±0.6	CNS+
9x	4.5±0.25	CNS+/-
9y	1.4±0.04	CNS-
9z	8.2±0.3	CNS+
9aa	8.75±0.5	CNS+
9ab	6.5±0.02	CNS+
9ac	1.4±0.06	CNS-
9ad	1.1±0.15	CNS-

a. PBS/EtOH (70:30) was used as solvent. Values are expressed as mean±SD of at least three independent experiments.

Cytotoxicity assays

All tumor cell lines were acquired from the American Type Culture Collection (ATCC, Manassas, VA, USA), except for the DND-41 cell line, which was purchased from the Deutsche Sammlung von Mikroorganismen und Zellkulturen (DSMZ Leibniz-Institut, Germany), and the Hap-1 cell line which was ordered from Horizon Discovery (Horizon Discovery Group, UK). All cell lines were cultured as recommended by the suppliers. Media were purchased from Gibco Life Technologies, USA, and supplemented with 10% fetal bovine serum (HyClone, GE Healthcare Life Sciences, USA). Adherent cell lines HCT-116, NCI-H460, LN-229, Hap-1 and Capan-1 cells were seeded at a density between 500 and 1500 cells per well, in 384-well, black walled, clear-bottomed tissue culture plates (Greiner). After overnight incubation, cells were treated with the test compounds at seven different concentrations ranging from 100 to 6.4 x 10^{-3} µM. Suspension cell lines HL-60, K-562, Z-138, and DND-41 were seeded at densities ranging from 2500 to 5500 cells per well in 384-well, black walled, clear-bottomed tissue culture plates containing the test compounds at the same seven concentration points. The plates were incubated and monitored at 37°C for 72 h in an IncuCyte® (Essen BioScience Inc., Ann Arbor, MI, USA) for real-time imaging. Images were taken every 3 h, with one field imaged per well under 10x magnification.

Microsomal stability of human, rat and mice microsomes

Human, rat and mice microsomes from Tebu-Xenotech were employed in the assay. They content 20 mg/mL of protein.

Brief protocol: The following quantities were added to each well of a 96-well microplate.

	Blank (µL)	Human (µL)	Mice (µL)	Rat (µL)
Phosphate buffer Na/K 50 mM pH 7.4	295	283.5	301.3	301.3
$MgCl_2$ 30 mM	50	50	50	50
NADP 10 mM	50	50	50	50
Glucose 6-P 100mM	50	50	50	50
Glucose 6-P DH 20 U/mL	25	25	25	25
Water	25			
Human microsomes		36.5		
Rat microsomes				18.7
Mice microsomes			18.7	
Test compound	5	5	5	5

Plates were incubated at 37°C and 75 µL samples were taken at 0, 10, 20, 40 and 60 min. Samples were transferred to a microplate and 75 µL Acetonitrile were added for inactivating the microsomes, and 30 µL of H_2O for improving the chromatographic conditions and kept at 4 °C. When all the samples were taken the plate was centrifuged at 46000 g for 30 min at 15 °C. Supernatant was taken and injected in the UPLC-MS/MS.

Stationary phase: Reverse phase Acquity UPLC® BEH C18 1,7 µm (2.1 mm x 50 mm) (Waters). Mobile phase: A: Water+0.1% formic; B: acetonitrile+0.1% formic acid.

Gradient:

Time (min)	A	B
0	95%	5%
0.1	95%	5%
1	0%	100%
2.5	0%	100%
2.6	95%	5%
3	95%	5%

Flow: 0.6 mL/min

The chromatographic equipment employed was an UPLC QSM Waters Acquity. Compound concentrations were calculated from the UV peak areas. The response was linear in the range between 10 ng/mL and 0.3125 ng/mL.

Metabolic stability was calculated from the logarithm of the remaining **9d** at each of the times evaluated.

Table S7. Microsomal stability of human, rat and mice microsomes

Rat			Mice			Human		
% remanent (sampling time 60 min)	*t1/2 (min)*	*Clint (µL/min* mg prot)*	*% remanent (sampling time 60 min)*	*t1/2 (min)*	*Clint (µL/min* mg prot)*	*% remanent (sampling time 60 min)*	*t1/2 (min)*	*Clint (µL/min *mg prot)*
44.79	52.81	13.1	65.08	91.72	7.55	50.87	64.16	10.8

Solubility

The stock solutions (10^{-2} M) of the assayed compound were diluted to decreased molarity, from 300 µM to 0.1µM, in 384 well transparent plate (*Greiner* 781801) with 1% DMSO: 99% PBS buffer. Incubated at 37ºC and read after 2 h in a *NEPHELOstar Plus* (*BMG LABTECH*). The results were adjusted to a segmented regression to obtain the maximum concentration in which compound is soluble. **9d**, solubility 92 µM.

The stock solutions (10^{-3} M) of **9d** were diluted to decreased molarity, from 50 µM to 4 µM, with MeOH, acetonitrile and water (with 17% added methanol). The different dilutions were filtrated thorough PVDF 0.45 µm filters and read in a spectrophotometer-DAD (Analytical Jena) at 215 and 220 nm in order to obtain a segmented regression. Additionally, a saturated solution was prepared, filtered, read and adjusted to calculate the maximum concentration in which compound is soluble. The solubility of **9d** in MeOH, acetonitrile and water and classification according to Ph. Eur. is 35.08 mg/mL (soluble), 102.7 mg/mL (freely soluble) and 0.17 mg/mL (very slightly soluble), respectively.

Chemical stability

In order to evaluate the stability, weekly HPLC were performed on the **9d** exposed sample to stress conditions (see manuscript). **9d** 0.2 mg/mL, phase mobil (A: H_20 + 0.05% formic acid and B: ACN + 0.05% formic acid) at 1:1 proportion. Stationary phase, Poroshell 120 EC-C15 (4.6x50 mm, 2.7-micro). Mobile phase (A: H_20 + 0.05% formic acid and B: ACN + 0.05% formic acid) using a gradient elution. Flow rate 0.6 mL/min. The DAD detector was set at 254 nm and the injection volume was 5 µL and oven temperature 40 ºC.

Cytochrome inhibition

The objective of this study was to screen the inhibition potential of the compounds using recombinant human cytochrome P450 enzymes (CYP1A2, CYP2C9, CYP2C19, CYP2D6 and CYP3A4) and probe substrates with fluorescent detection.

Incubations were conducted in a 200 µL volume in 96 well microtiter plates (COSTAR 3915). Addition of cofactor-buffer mixture (KH_2PO_4 buffer, 1.3mM $NADP^+$, 3.3mM $MgCl_2$, 3.3 mM Glucose-6-phosphate and 0.4U/mL Glucose-6-phosphate Dehydrogenase), supersomes control, standard inhibitors (Furafyline, Tranylzypromine, Ketoconazole, Sulfaphenazole and Quinidine; from Sigma Aldrich) and test compounds to plates were carried out by a liquid handling station (Zephyr Caliper). The plate was then pre-incubated at 37ºC for 5 min, and the reaction initiated by the addition of pre-warmed enzyme/substrate (E/S) mix. The E/S mix contained buffer (KH_2PO_4), c-DNA-expressed P450 in insect cell microsomes, substrate (3-cyano-7-ethoxycoumarin (CEC) for CYP1A2 and CYP2C19, 7-methoxy-4-(trifluoromethyl)coumarin (7-MFC) for CYP2C9, 3-[2-(*N*,*N*-diethyl-*N*-methylammonium)ethyl]-7-methoxy-4-methylcoumarin (AMMC) for CYP2D6, 7-benzyloxytrifluoromethyl coumarin (7-BFC) and Dibenzylfluorescein (DBF) for CYP3A4) to give the final assay concentrations in a reaction volume of 200 µL. Reactions were terminated after different incubation times depending on the each cytochrome by addition of STOP solution (ACN/TrisHCl 0.5M 80:20 and NaOH 2N for CYP3A4 (DBF) and ACN/TrisHCl 0.5M 80:20 for the other cytochromes).

Fluorescence per well was measured using a fluorescence plate reader (Tecan M1000 pro) and percentage of inhibition was calculated taking into account the compound-free wells and the wells with reference compounds.

Results for **9d**: CYP1A2 (%inhib 10 µM) 1 ± 1; CYP2C9 (%inhib 10 µM) 26 ± 6; CYP3A4 (BFC) (%inhib 10 µM) 53 ± 1; CYP3A4 (DBF) (%inhib 10 µM) 48 ± 1; CYP2D6 (%inhib 10 µM) 27 ± 4.

hERG ion channel inhibition

The assays were carried out at a CHO cell line transfected with the hERG potassium channel. Cells were grown in the presence of doxycycline for inducing the channel expression and kept at 30°C for 24 h before running the assay. Plate was primed with extracellular (2 mM $CaCl_2$; 1 mM $MgCl_2$; 10 mM Hepes; 4 mM KCl; 145 mM NaCl; 10 mM glucose; pH=7.4) and intracellular (5.374 mM $MgCl_2$; 1.75 mM $MgCl_2$; 10 mM EGTA; 10 mM Hepes; 120 mM KCl; 4 mM Na2-ATP; pH=7.2) solutions and the compounds dissolved in the extracellular solution. Cells were detached and suspended in the extracellular solution and dispensed in the assay plate at a density of 3*106 cells/well. Plate was introduced in the automated patch-clamp reader (Ionflux HT) and the hERG channel currents were evoked by a 5 sec depolarization step (from -80 mV to +20mV) which was followed by a 5 second tail step to -50mV.

Current was normalized to the maximum inhibition shown by controls and percentage of inhibition calculated. Inhibitory activity of **9d** at hERG channel, % inhibition (10 μM): 30.5 ± 7.7.

Human and mouse plasma protein binding

Human and mouse plasma from Seralab was employed in the assay.

Brief protocol: The assay was carried out by employing Rapid Equilibrium Dyalisis (RED) from Thermo Scientific. The compounds were dissolved at 5 µM in plasma and added to the corresponding insert of the RED device. Dialysis buffer was added to the corresponding insert of the RED device. Plate was incubated for 4h at 37°C. After the incubation period 50 µL aliquots of each chamber were transferred to empty vials. 50 µL of dialysis buffer were added to the plasma samples and 50 µL of plasma were added to the buffer samples. 300 µL of acetonitrile were added to all the samples and centrifuged at 4000 rpm 100 µL aliquots of the supernatants were transferred to a LC analysis plate and diluted with 100 µL of water. Samples were analyzed in a UPLC/MS/MS. Stationary phase: Reverse phase Acquity UPLC® BEH C18 1,7 µm (2.1 mm x 100 mm) (Waters). Mobile phase: 125 mM Ammonium hydroxide/acetonitrile

Gradient:

Time	Ammonium hydroxide	Acetonitrile
0	95%	5%
0.1	95%	5%
1	0%	100%
2	0%	100%
2.1	95%	5%
2.5	95%	5%

Flow: 0.6 mL/min

The chromatographic equipment employed was an UPLC QSM Waters Acquity. Compound concentrations were calculated from the MS peak areas.

Table S8. Human and mouse plasma protein binding

	Mouse		Human	
Compound	***Plasma protein binding***	***Unbound fraction***	***Plasma protein binding***	***Unbound fraction***
9d	96.29%	3.71%	91.97%	8.03%

Receptor characterization panel

Table S9. Eurofins radioligand displacement using 10 µM 9d. Displacement greater than 50% is considered significant.

Compound I.D.	Client Compound I.D.	Test Concentration	% Inhibition of Control Specific Binding 1st	2nd	Mean
A_{2A} *(h)* (agonist radioligand)					
100046828-1	B06	1.0E-05 M	1.4	-10.1	-4.4
α_{1A} *(h)* (antagonist radioligand)					
100046828-1	B06	1.0E-05 M	1.9	10.1	6.0
α_{2A} *(h)* (antagonist radioligand)					
100046828-1	B06	1.0E-05 M	14.2	2.2	8.2
β_1 *(h)* (agonist radioligand)					
100046828-1	B06	1.0E-05 M	-11.7	-10.3	-11.0
β_2 *(h)* (antagonist radioligand)					
100046828-1	B06	1.0E-05 M	1.1	-4.3	-1.6
BZD (central) (agonist radioligand)					
100046828-1	B06	1.0E-05 M	-5.7	7.7	1.0
CB_1 *(h)* (agonist radioligand)					
100046828-1	B06	1.0E-05 M	-10.5	2.3	-4.1
CB_2 *(h)* (agonist radioligand)					
100046828-1	B06	1.0E-05 M	2.7	6.1	4.4
CCK_1 (CCK_A) *(h)* (agonist radioligand)					
100046828-1	B06	1.0E-05 M	72.1	68.7	**70.4**
D_1 *(h)* (antagonist radioligand)					
100046828-1	B06	1.0E-05 M	10.4	29.8	20.1
D_{2S} *(h)* (agonist radioligand)					
100046828-1	B06	1.0E-05 M	14.6	-7.1	3.8
ET_A *(h)* (agonist radioligand)					
100046828-1	B06	1.0E-05 M	11.8	-2.4	4.7
NMDA (antagonist radioligand)					
100046828-1	B06	1.0E-05 M	9.1	3.4	6.3
H_1 *(h)* (antagonist radioligand)					
100046828-1	B06	1.0E-05 M	-3.7	-2.6	-3.2
H_2 *(h)* (antagonist radioligand)					
100046828-1	B06	1.0E-05 M	-16.7	-8.8	-12.7
MAO-A (antagonist radioligand)					
100046828-1	B06	1.0E-05 M	0.9	10.5	5.7

M_1 *(h)* (antagonist radioligand)					
100046828-1	B06	1.0E-05 M	-20.3	-9.3	-14.8
M_2 *(h)* (antagonist radioligand)					
100046828-1	B06	1.0E-05 M	0.1	-1.1	-0.5
M_3 *(h)* (antagonist radioligand)					
100046828-1	B06	1.0E-05 M	-8.9	-4.1	-6.5
N neuronal α4β2 *(h)* (agonist radioligand)					
100046828-1	B06	1.0E-05 M	-9.1	-5.3	-7.2
δ (DOP) *(h)* (agonist radioligand)					
100046828-1	B06	1.0E-05 M	-13.9	-7.4	-10.6
kappa (h) (KOP) (agonist radioligand)					
100046828-1	B06	1.0E-05 M	47.4	47.2	47.3
μ (MOP) *(h)* (agonist radioligand)					
100046828-1	B06	1.0E-05 M	1.9	11.2	6.6
5-HT_{1A} *(h)* (agonist radioligand)					
100046828-1	B06	1.0E-05 M	-1.1	1.6	0.2
5-HT1B(h) (antagonist radioligand)					
100046828-1	B06	1.0E-05 M	-14.8	1.2	-6.8
5-HT_{2A} *(h)* (agonist radioligand)					
100046828-1	B06	1.0E-05 M	-3.2	-11.6	-7.4
5-HT_{2B} *(h)* (agonist radioligand)					
100046828-1	B06	1.0E-05 M	13.4	-9.6	1.9
5-HT_3 *(h)* (antagonist radioligand)					
100046828-1	B06	1.0E-05 M	-15.2	-12.1	-13.7
GR *(h)* (agonist radioligand)					
100046828-1	B06	1.0E-05 M	-2.6	-6.0	-4.3
AR *(h)* (agonist radioligand)					
100046828-1	B06	1.0E-05 M	-12.6	-11.3	-12.0
$V_{1\,a}$ *(h)* (agonist radioligand)					
100046828-1	B06	1.0E-05 M	32.7	32.3	32.5
Ca^{2+} channel (L, dihydropyridine site) (antagonist radioligand)					
100046828-1	B06	1.0E-05 M	22.6	24.1	23.3
Potassium Channel hERG (human)- [3H] Dofetilide					
100046828-1	B06	1.0E-05 M	-10.1	-11.3	-10.7
K_V channel (antagonist radioligand)					
100046828-1	B06	1.0E-05 M	10.7	-4.8	2.9
Na^+ channel (site 2) (antagonist radioligand)					
100046828-1	B06	1.0E-05 M	13.0	10.8	11.9
norepinephrine transporter *(h)* (antagonist radioligand)					
100046828-1	B06	1.0E-05 M	-10.3	-5.1	-7.7
dopamine transporter *(h)* (antagonist radioligand)					
100046828-1	B06	1.0E-05 M	1.8	12.6	7.2
5-HT transporter *(h)* (antagonist radioligand)					
100046828-1	B06	1.0E-05 M	-9.2	0.7	-4.3

Reference compounds results:

Compound I.D.	IC_{50} (M)	K_i (M)	nH
A_{2A} *(h)* (agonist radioligand)			
NECA	8.1E-08 M	6.6E-08 M	0.8
α_{1A} *(h)* (antagonist radioligand)			
WB 4101	4.9E-10 M	2.5E-10 M	1.2
α_{2A} *(h)* (antagonist radioligand)			
yohimbine	1.2E-08 M	5.4E-09 M	1.0
β_1 *(h)* (agonist radioligand)			
atenolol	4.8E-07 M	2.7E-07 M	1.2
β_2 *(h)* (antagonist radioligand)			
ICI 118551	7.0E-10 M	2.3E-10 M	1.0
BZD (central) (agonist radioligand)			
diazepam	9.4E-09 M	7.9E-09 M	1.5
CB_1 *(h)* (agonist radioligand)			
CP 55940	1.8E-09 M	1.6E-09 M	1.0
CB_2 *(h)* (agonist radioligand)			
WIN 55212-2	3.1E-09 M	2.0E-09 M	1.0
CCK_1 (CCK_A) *(h)* (agonist radioligand)			
CCK-8s	4.5E-11 M	3.4E-11 M	0.6
D_1 *(h)* (antagonist radioligand)			
SCH 23390	3.1E-10 M	1.2E-10 M	1.4
D_{2S} *(h)* (agonist radioligand)			
7-OH-DPAT	1.5E-09 M	6.1E-10 M	1.2
ET_A *(h)* (agonist radioligand)			
endothelin-1	3.1E-11 M	1.5E-11 M	0.9
NMDA (antagonist radioligand)			
CGS 19755	3.5E-07 M	2.9E-07 M	1.0
H_1 *(h)* (antagonist radioligand)			
pyrilamine	3.0E-09 M	1.9E-09 M	1.1
H_2 *(h)* (antagonist radioligand)			
cimetidine	6.7E-07 M	6.6E-07 M	1.3
MAO-A (antagonist radioligand)			
clorgyline	1.5E-09 M	8.9E-10 M	2.5
M_1 *(h)* (antagonist radioligand)			
pirenzepine	2.2E-08 M	1.9E-08 M	1.3
M_2 *(h)* (antagonist radioligand)			
methoctramine	4.0E-08 M	2.8E-08 M	1.2
M_3 *(h)* (antagonist radioligand)			
4-DAMP	1.4E-09 M	9.8E-10 M	1.7
N neuronal α4β2 *(h)* (agonist radioligand)			
nicotine	3.1E-09 M	1.0E-09 M	0.9
δ (DOP) *(h)* (agonist radioligand)			
DPDPE	3.2E-09 M	1.7E-09 M	1.0
kappa (h) (KOP) (agonist radioligand)			
U50488	6.8E-10 M	3.7E-10 M	1.1
μ (MOP) *(h)* (agonist radioligand)			
DAMGO	8.1E-10 M	3.3E-10 M	1.1
5-HT_{1A} *(h)* (agonist radioligand)			
8-OH-DPAT	1.3E-09 M	6.4E-10 M	0.8

5-HT1B(h) (antagonist radioligand)			
Serotonine	1.9E-07 M	8.5E-08 M	0.7
5-HT_{2A} *(h)* (agonist radioligand)			
(±)DOI	3.8E-10 M	2.8E-10 M	1.0
5-HT_{2B} *(h)* (agonist radioligand)			
(±)DOI	2.6E-09 M	1.3E-09 M	1.3
5-HT_3 *(h)* (antagonist radioligand)			
MDL 72222	1.1E-08 M	7.6E-09 M	1.0
GR *(h)* (agonist radioligand)			
dexamethasone	3.7E-09 M	1.8E-09 M	0.9
AR *(h)* (agonist radioligand)			
testosterone	3.1E-09 M	1.4E-09 M	0.9
V_{1a} *(h)* (agonist radioligand)			
[d(CH_2)$_5$ ^{1},Tyr(Me)$_2$]-AVP	2.1E-09 M	1.3E-09 M	1.1
Ca^{2+} channel (L, dihydropyridine site) (antagonist radioligand)			
nitrendipine	1.8E-10 M	1.2E-10 M	1.2
Potassium Channel hERG (human)- [3H] Dofetilide			
Terfenadine	1.3E-07 M	9.2E-08 M	1.0
K_V channel (antagonist radioligand)			
α-dendrotoxin	1.1E-10 M	8.5E-11 M	0.9
Na^+ channel (site 2) (antagonist radioligand)			
veratridine	6.9E-06 M	6.2E-06 M	1.1
norepinephrine transporter *(h)* (antagonist radioligand)			
protriptyline	5.0E-09 M	3.7E-09 M	1.3
dopamine transporter *(h)* (antagonist radioligand)			
BTCP	1.5E-08 M	7.7E-09 M	1.1
5-HT transporter *(h)* (antagonist radioligand)			
imipramine	3.1E-09 M	1.4E-09 M	1.1

***5xFAD In vivo* experimental design**

Table S10. SYBR Green primers used in qPCR studies.

Target	Product size (bp)	Forward primer (5'-3')	Reverse primer (5'-3')
Cxcl10	72	GGCTAGTCCTAATTGCCCTTGG	TTGTCTCAGGACCATGGCTTG
Tnf-α	157	TCGGGGTGATCGGTCCCCAA	TGGTTTGCTACGACGTGGGCT
iNOS	125	GGCAGCCTGAGAGACCTTTG	GGAAGCGTTTCGGGATCTGAA
β-actin	190	CTGTCCCTGTATGCCTCTG	ATGTCACGCACGATTTCC

Table S11. TaqMan probes used in qPCR studies.

Target	Product size (bp)	Reference
Hmox1	69	Mm00516005_m1
Tbp	93	Mm00446971_m1

Statistical analysis

The statistical analysis was conducted using GraphPad Prism ver.7 statistical software. Data were expressed as the mean ± Standard Error of the Mean (SEM) from at least 10 samples per group. Means were compared to One-Way ANOVA analysis of variance, followed by Tukey-Kramer multiple comparison post-hoc analysis. Comparisons between groups were also performed by two-tail Student's *t*-test for independent samples. Statistical significance was considered when p-values were <0.05. The statistical outliers were carried out with Grubss' test and subsequently removed from the analysis.

NMR spectra data

The ^{1}H and ^{13}C spectra of the 37 new synthetized compounds **9-15** showed coupling constants (*J*) between ^{1}H-P and ^{13}C-P. Significant coupling constants ^{1}H-P (in green) and ^{1}H-^{1}H (in blue) for representative compound **9c** are depicted (Figure). In particular, the imine proton H-3 exhibits a ^{1}H-P *J* of ~ 5 Hz, and the bridged protons H-3a and H-6a have ^{1}H-P *J* of ~ 3 Hz and ~ 18 Hz (in green), respectively. Additionally, ^{1}H-^{1}H *J* of 1.5 Hz between H-3 and H-3a, and 9 Hz of the geminal H-3a and H-6a are observed (in blue). In the ^{13}C spectra a *J* of ~ 160 Hz was observed between C1 and the P. In a similar fashion the peaks corresponding to C3a appears as doblets due to the *J* of ~ 12 Hz with the P atom (in red). Noteworthy, spectra of compounds **9r**, **9y**, **9ac** and **9ad** with an *ortho* substituted *N*-phenyl showed the presence of rotamers, same multiplicity (^{1}H-NMR) different shift (^{1}H-NMR and ^{13}C-NMR), due to the restricted rotation of the *N*-C*ipso* phenyl bond. For a complete table on the representative peaks in the ^{1}H-NMR and ^{13}C-NMR spectra of all the new compunds see Tables S12 and S13.

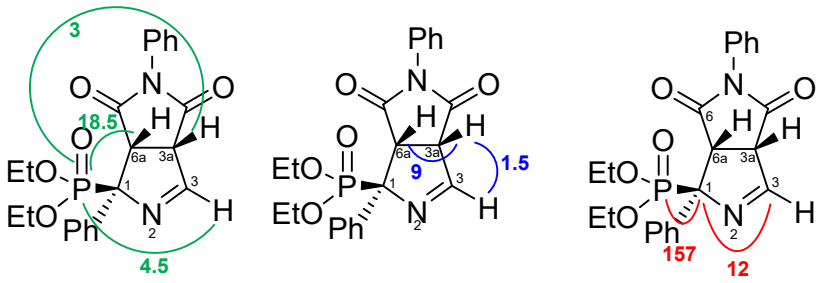

Figure. Coupling constants for **9c**, ^{1}H-P (in green), ^{1}H-H (in blue), ^{13}C-P (in red).

Table S12. ^{1}H chemical shifts (ppm) for new compounds including both the multiplicity and the coupling constants (*J* Hz).

Compound	**H3**	**H3a**	**H6a**
9a	7.95, dd 5.5, 1.0	4.34, ddd 8.5, 4.0, 1.0	4.01, m
9b	8.00, dd 5.0, 1.5	4.25, ddd 8.5, 3.0, 1.5	4.03, dd 18.5, 8.5
9c	7.97, dd 4.5, 1.6	4.40, ddd 8.5, 3.0, 1.5	4.17, dd 18.5, 9.0
9d	8.05, d 4.5	4.47, m	4.25, dd 18.0, 8.0
9e	8.04, dd 5.0, 1.5	4.45, ddd 8.5, 3.0, 1.5	4.25, dd 18.0, 8.5
14c	7.82, dd 5.0, 1.5	4.39, dq 9.0, 1.5	3.97, dd 19.0, 9.0
15c	7.82, dd 5.0, 1.5	4.39, ddd 9.5, 3.5, 1.5	3.96, dd 19.0, 9.5
12c	8.04, dd 5.0, 1.5	4.49, dq 8.5, 1.5	4.25, dd 18.0, 8.5
13c	8.02, dd 5.5, 1.5	4.46, ddd 8.5, 3.0, 1.5	4.23, dd 18.0, 8.5
12d	8.02, dd 5.0, 1.5	4.49, ddd 8.5, 3.0, 1.5	4.25, dd 18.0, 8.5
13d	8.02, dd 5.0, 1.5	4.46, ddd 8.5, 3.0, 1.5	4.22, dd 18.0, 8.5
9f	7.96, dd 5.0, 1.5	4.29, ddd 8.5, 3.5, 1.5	4.10, m
9g	7.95, dd 5.0, 1.5	4.30, ddd 8.5, 3.5, 1.5	4.06, m
9h	7.93, dd 5.0, 1.5	4.08, m	3.91, m
9i	7.95, dd 5.0, 1.0	4.29, ddd 8.5, 3.0, 1.0	4.11, dd 19.0, 8.5
9j	7.92, dd 5.0, 1.5	4.33, ddd 8.5, 3.5, 1.5	4.18, m
9k	7.85, dd 5.0, 1.0	4.24, ddd 8.5, 4.0, 1.0	4.16, m

9l	7.83, dd 5.5, 1.5	4.24, ddd 8.0, 4.0, 1.5	4.15, m
9m	8.00, dd 5.0, 1.5	4.31, ddd 9.0, 3.0, 1.5	4.17, m
9n	8.05, dd 5.0, 1.5	4.51, ddd 8.5, 3.0, 1.5	4.28, dd 18.0, 9.0
9o	8.06, dd 5.0, 1.5	4.50, ddd 9.0, 2.5, 1.5	4.27, dd 18.0, 9.0
9p	8.05, dd 5.0, 1.5	4.48, ddd 8.5, 3.0, 1.5	4.26, dd 18.0, 9.0
9q	8.04, dd 5.5, 1.0	4.47, ddd 8.5, 3.0, 1.0	4.25, dd 18.0, 9.0
9r **(rotamer A)**	8.03, dd 5.5, 1.5	4.52, ddd 8.5, 4.5, 1.5	4.35, dd 18.0, 8.5
9r **(rotamer B)**	8.08, dd 5.0, 1.5	4.56, ddd 8.5, 3.0, 1.5	4.36, dd 18.0, 8.5
9s	8.05, dd 5.0, 1.5	4.48, ddd 8.5, 3.0, 1.5	4.26, dd 18.0, 9.0
9t	8.04, dd 5.0, 1.5	4.47, ddd 9.0, 3.0, 1.5	4.25, dd 18.0, 9.0
9u	8.04, dd 5.0, 1.5	4.47, ddd 9.0, 2.5, 1.5	4.25, dd 18.0, 8.5
9v	8.04, dd 4.5, 1.5	4.47, ddd 8.5, 3.0, 1.5	4.26, dd 18.0, 8.5
9w	8.02, dd 5.0, 1.0	4.57, ddd 8.5, 4.0, 1.0	4.41, dd 18.0, 9.0
9x	8.07, dd 5.0, 1.0	4.53, ddd 9.0, 3.0, 1.0	4.30, dd 18.0, 9.0
9y **(rotamer A)**	8.05, dd 5.0, 1.5	4.59, ddd 9.0, 3.5, 1.5	4.39, dd 18.5, 9.0
9y **(rotamer B)**	8.08, dd 5.5, 2.5	4.55, ddd 10.0, 2.5, 1.5	4.35, dd 18.0, 9.0
9z	8.08, dd 5.0, 1.5	4.51, ddd 9.0, 3.0, 1.5	4.30, dd 18.5, 9.0
9aa	8.05, dd 5.0, 1.5	4.46, ddd 8.5, 3.0, 1.5	4.24, dd 16.5, 9.0
9aa	8.01, dd 5.0, 1.5	4.48, ddd 8.5, 3.0, 1.5	4.25, dd 18.0, 8.5
9ac **(rotamer A)**	8.13, dd 5.0, 1.5	4.63, ddd 9.0, 3.5, 1.5	4.43, dd 18.5, 9.0

9ac (rotamer B)	8.12, dd 5.0, 1.5	4.67, ddd 8.5, 3.0, 1.5	4.46, dd 18.0, 8.5
9ad (rotamer A)	8.02, dd 5.5, 1.5	4.53, ddd 8.5, 4.0, 1.5	4.36, dd 18.0, 8.5
9ad (rotamer B)	8.07, dd 5.0, 1.5	4.58, ddd 8.5, 3.0, 1.5	4.36, dd 18.0, 8.5

Table S13. ^{13}C chemical shifts for new compounds (ppm) including both the multiplicity and the coupling constants (*J* Hz).

Compound	**C1**	**C3**	**C3a**	**C6a**
9a	85.6, d 154.0	162.5, d 11.5	60.5	47.7, d 2.0
9b	85.7, d 156.0	162.8, d 12.0	59.9	47.5, d 2.5
9c	86.2, d 157.0	162.5, d 12.0	60.2	48.2, d 2.0
9d	86.2, d 156.0	162.0, d 12.5	60.1	48.5
9e	86.2, d 157.5	162, d 12.0	60.1	48.1, d 2.0
14c	83.7, d 158.0	161.3,d 13.0	59.9	45.9, d 3.0
15c	87.3, d 159.5	161.5, d 12.5	59,9	45.9, d 2.5
12c	85.9, d 156.0	162.8,d 12.0	60.5	48.1, d 3.0
13c	86.0, d 157.0	162.3, d 12.0	60.3	48.3, d 3.0
12d	86.0, d 156.0	162.4, d 12.0	60.3	48.2, d 3.0
13d	86.0, d 158.0	161.8, d 13.0	60.1	48.6, d 3.0
9f	85.8, d 155.0	162.7, d 12.0	60.5	47.9, d 2.0
9g	85.9, d 154.0	162.8, d 12.0	60.5	47.8, d 3.0
9h	86.6, d 158.0	163.3, d 12.0	60.2	48.1 ,d 2.0
9i	86.0, d 155.0	162.6, d 12.0	60.6	47.7, d 2.0
9j	85.7, d 155.0	162.3, d 11.5	60.4	47.8, d 2.0

9k	---	162.6, d 11.5	60.2	47.5, d 2.5
9l	85.7, d 153.0	162.5, d 12.0	60.3	47.5, d 2.0
9m	86.1, d 157.0	162.7, d 12.0	60.2	48.0, d 2.0
9n	86.3, d 157.0	162.0, d 13.0	60.1	48.3, d 3.0
9o	86.4, d 158.0	162.1, d 12.0	60.2	48.6, d 2.0
9p	86.2, d 157.0	162.2, d 12.0	60.1	48.2, d 3.0
9q	86.4, d 157.0	162.2, d 12.0	60.2	48.4, d 2.0
9r (rotamer A)	86.0, d 157.5	162.0, d 11.5	60.1	48.0, d 2.5
9r (rotamer B)	86.6, d 153.5	162.2, d 12.5	60.3	48.6, d 2.5
9s	86.4, d 157.0	162.3, d 12.0	60.2	48.5, d 3.0
9t	86.4, d 157.0	162.2, d 12.0	60.3	48.4, d 3.0
9u	86.5, d 158.0	162.0, d 13.0	60.9	48.6, d 3.0
9v	86.2, d 157.0	161.9, d 13.0	60.0	48.4, d 3.0
9w	86.7, d 152.0	161.8, d 11.0	61.0	48.3, d 3.0
9x	86.2, d 158.0	161.7, d 12.0	60.0	48.5, d 2.0
9y (rotamer A)	86.6, d 154.5	161.9, d 11.5	61.0	48.3, d 2.5
9y (rotamer B)	86.3, d 159.0	161.8, d 12.5	60.1	49.2, d 2.5
9z	86.5, d 157.0	162.3, d 12.0	60.2	48.2, d 2.5

9aa	86.2, d 156.0	162.4, d 12.0	60.2	48.1, d 3.0
9aa	86.2, d 157.0	162.2, d 12.0	60.1	48.2, d 3.0
9ac **(rotamer A)**	86.5, d 155.0	162.3, d 11.5	61.0	48.3, d 2.5
9ac **(rotamer B)**	86.2, d 157.5	162.4, d 12.0	60.3	48.6, d 2.5
9ad **(rotamer A)**	86.1, d 158.0	161.6, d 11.5	60.4	48.4, d 2.5
9ad **(rotamer B)**	86.9, d 153.0	162.0, d 12.5	61.0	49.0, d 2.5

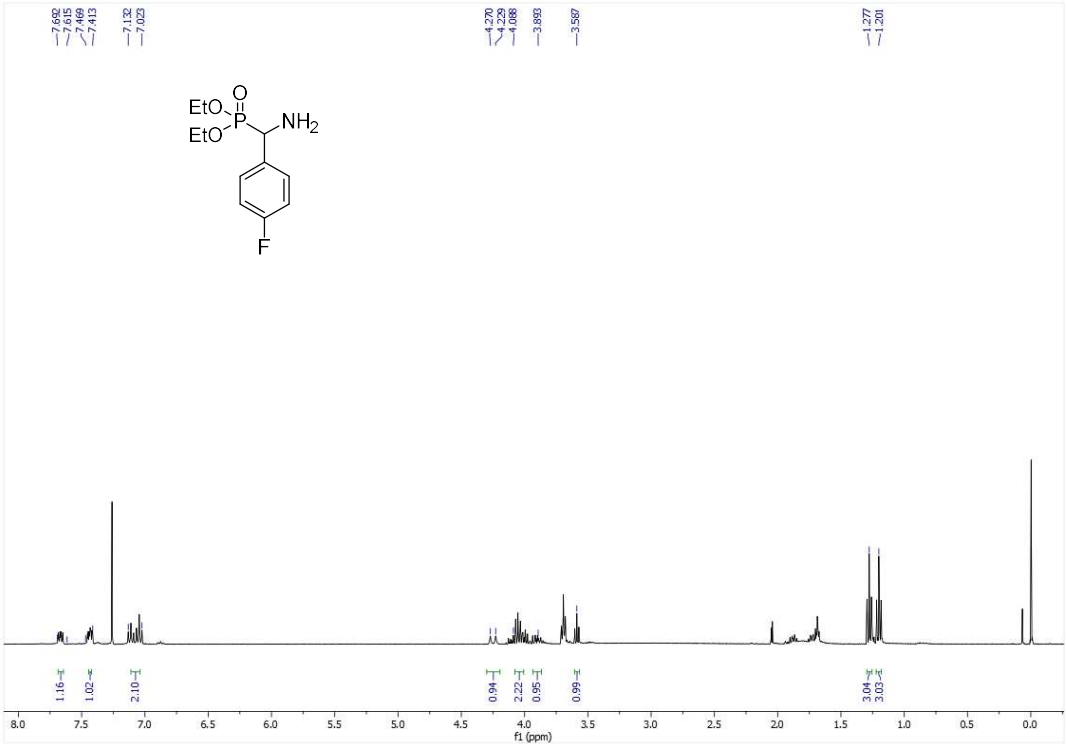

Diethyl [amino(4-fluorophenyl)methyl]phosphonate (step 1-10b)

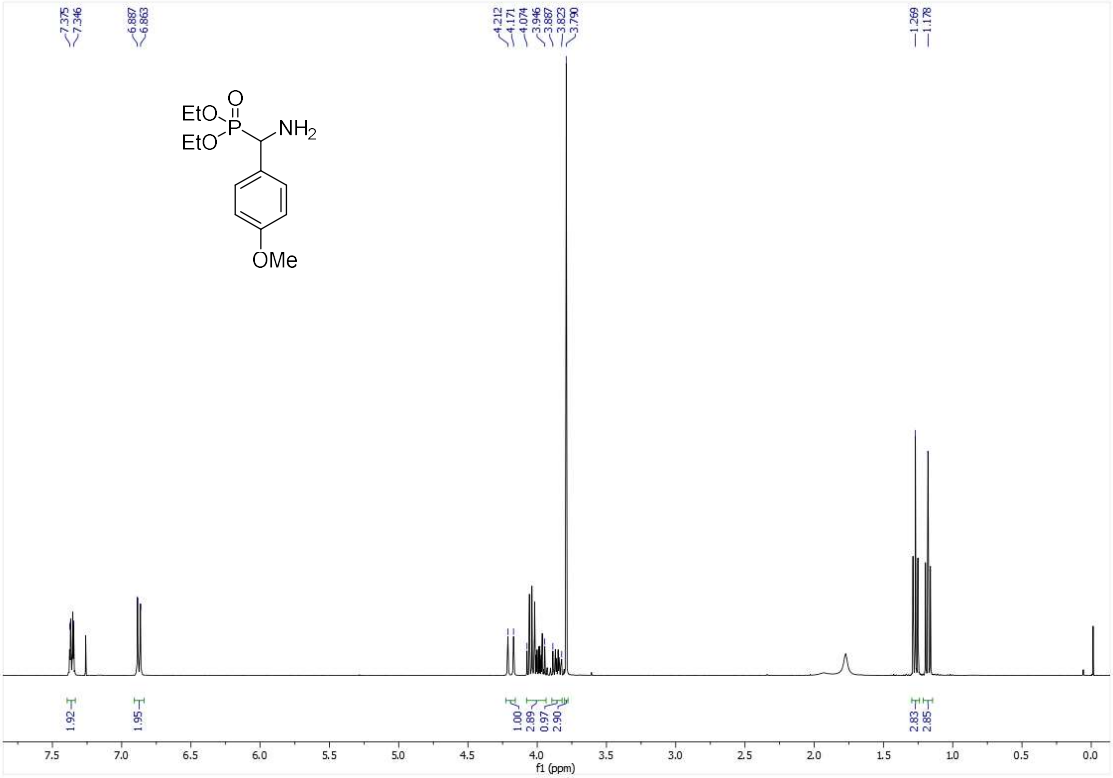

Diethyl [amino(4-methoxyphenyl)methyl]phosphonate (step 1-10c)

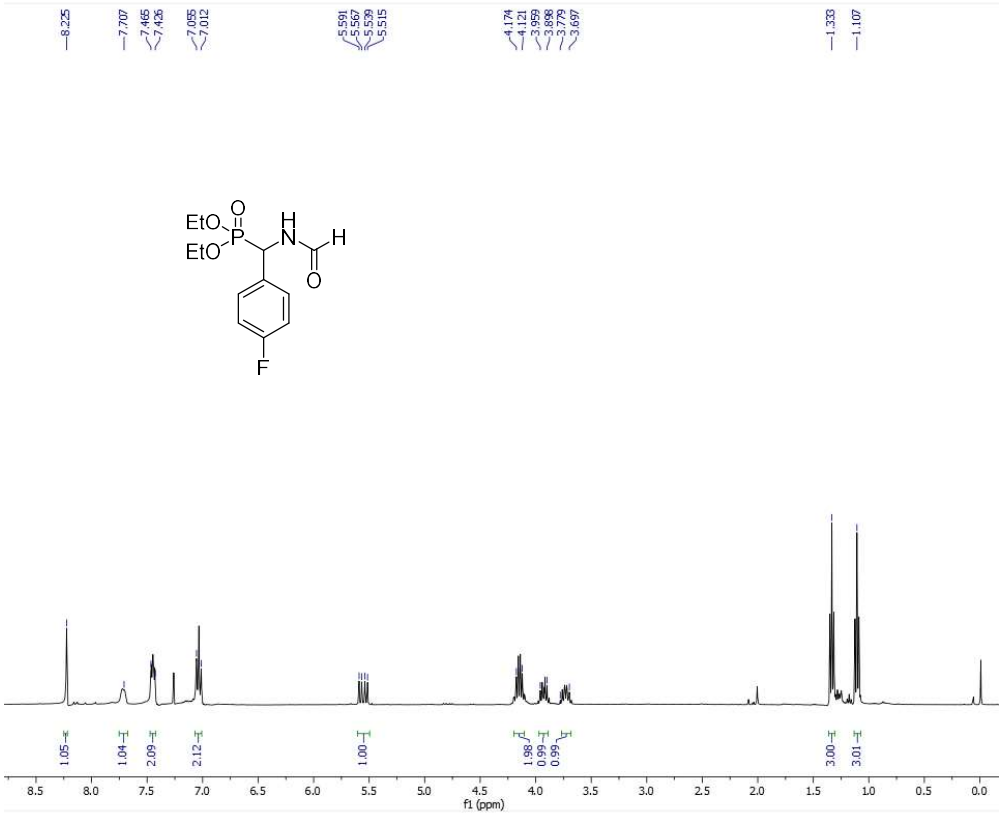

Diethyl [(4-fluorophenyl)(formamido)methyl]phosphonate (step 2-10b)

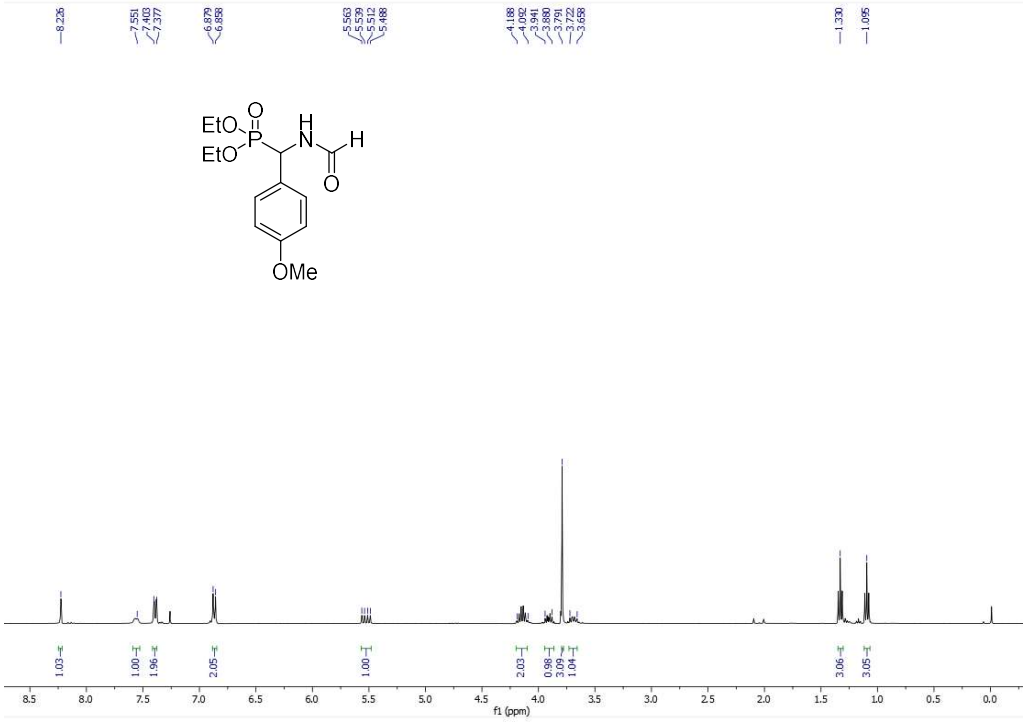

Diethyl [(4-methoxyphenyl)(formamido)methyl]phosphonate (step 2-10c)

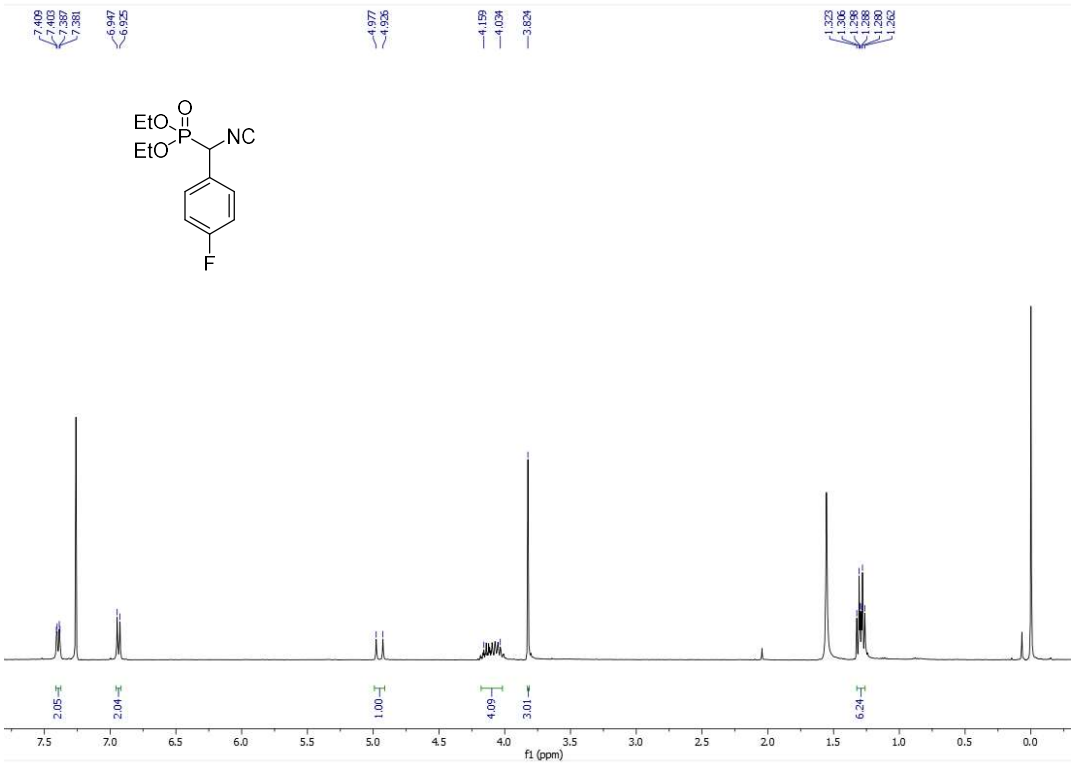

Diethyl [(4-methoxyphenyl)isocyanomethyl]phosphonate (10b)

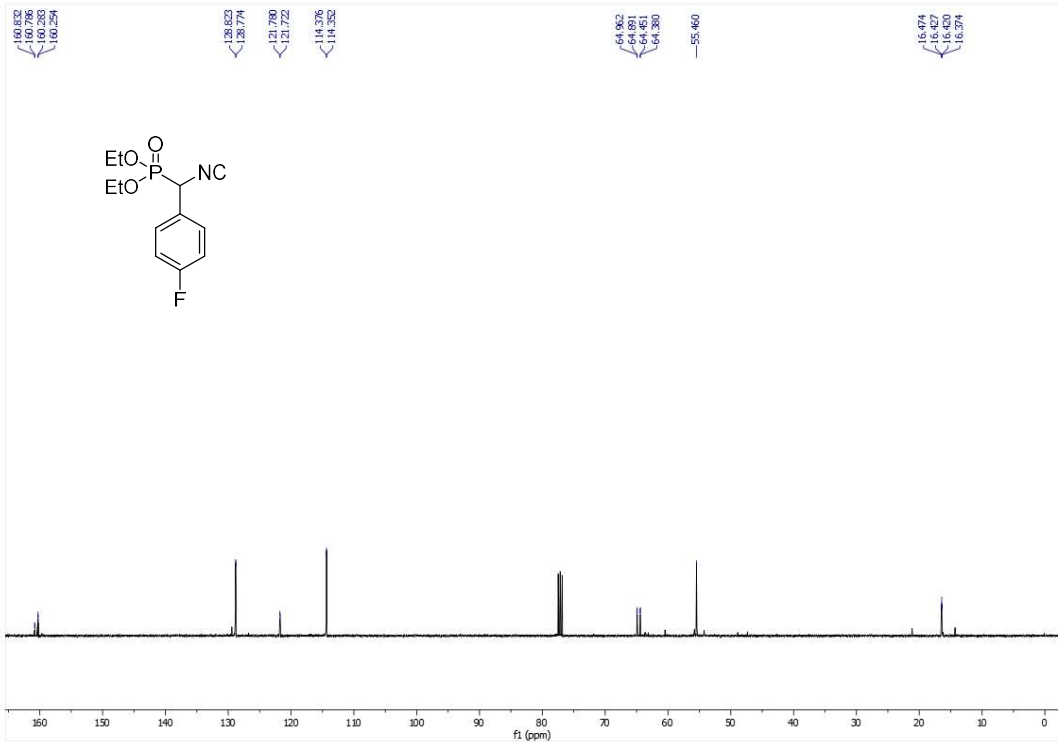

Diethyl [(4-methoxyphenyl)isocyanomethyl]phosphonate (10b)

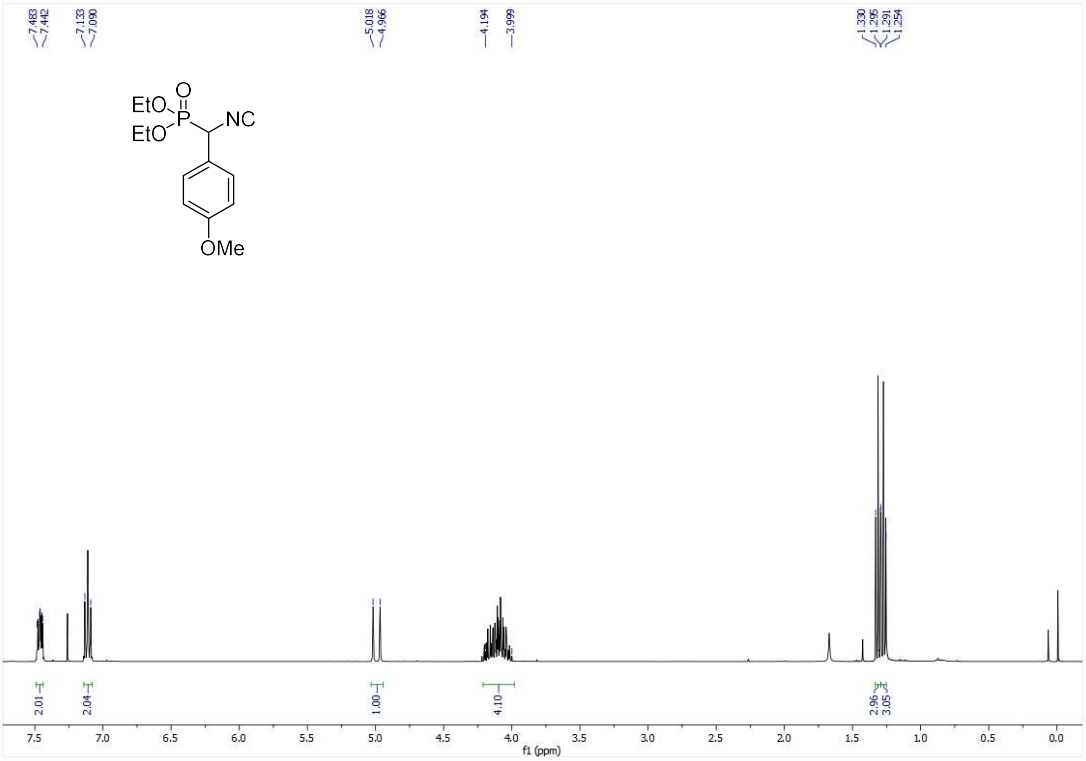

Diethyl [(4-fluorophenyl)isocyanomethyl]phosphonate (10c)

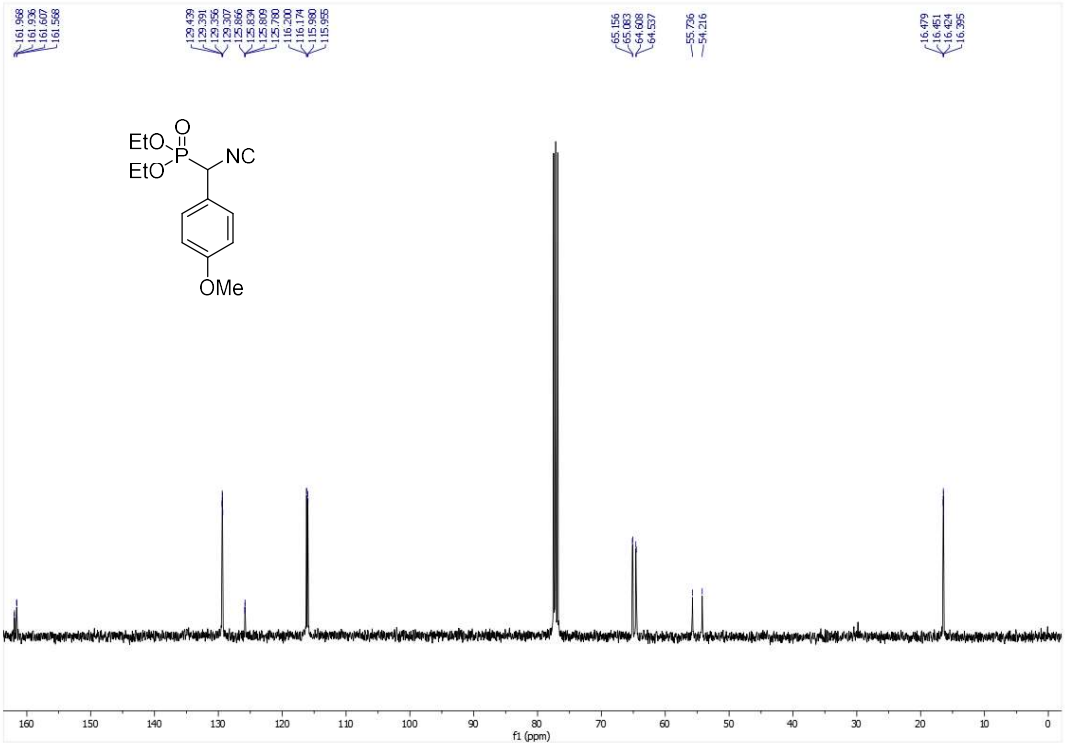

Diethyl [(4-fluorophenyl)isocyanomethyl]phosphonate (10c)

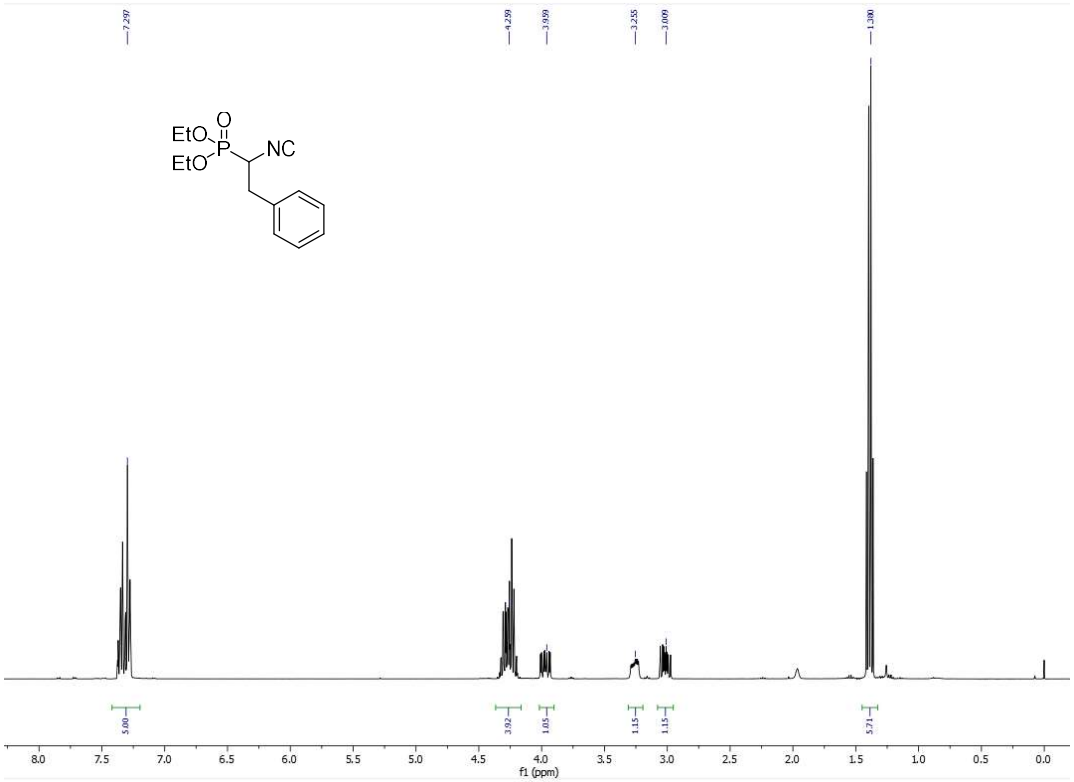

Diethyl (1-isocyano-2-phenylethyl)phosphonate (10d)

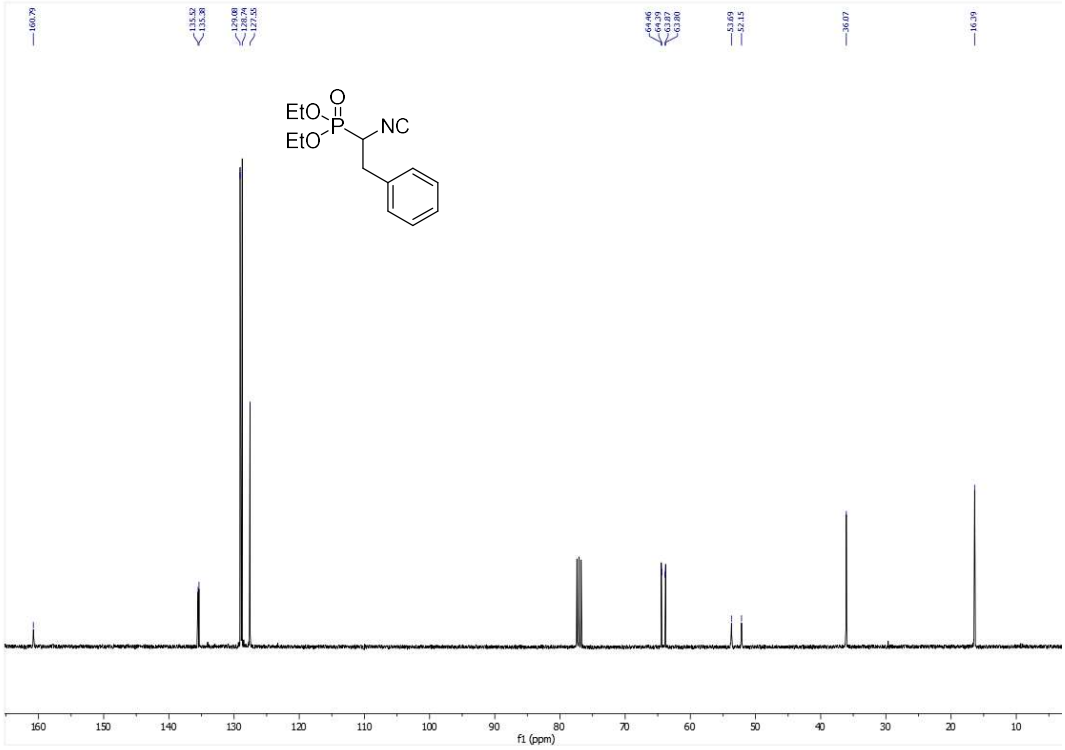

Diethyl (1-isocyano-2-phenylethyl)phosphonate (10d)

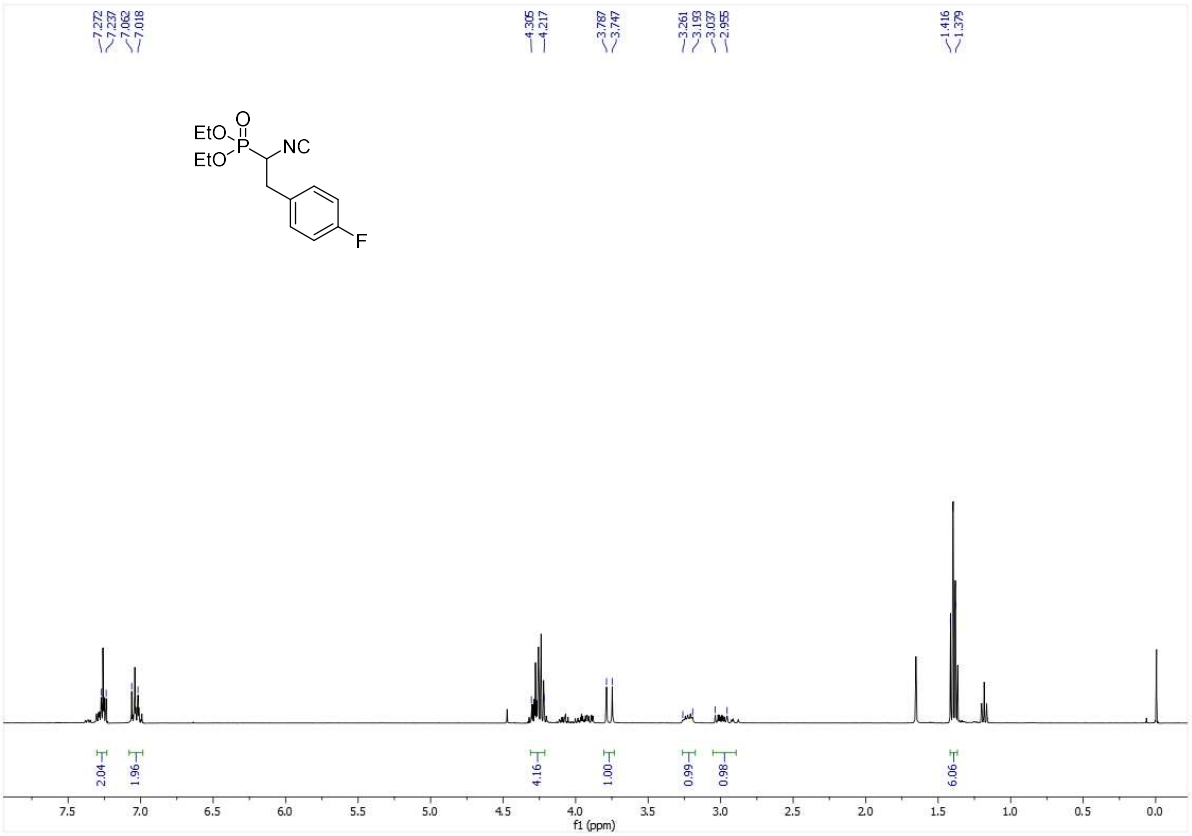

Diethyl [2-(4-fluorophenyl)-1-isocyanoethyl]phosphonate (10e)

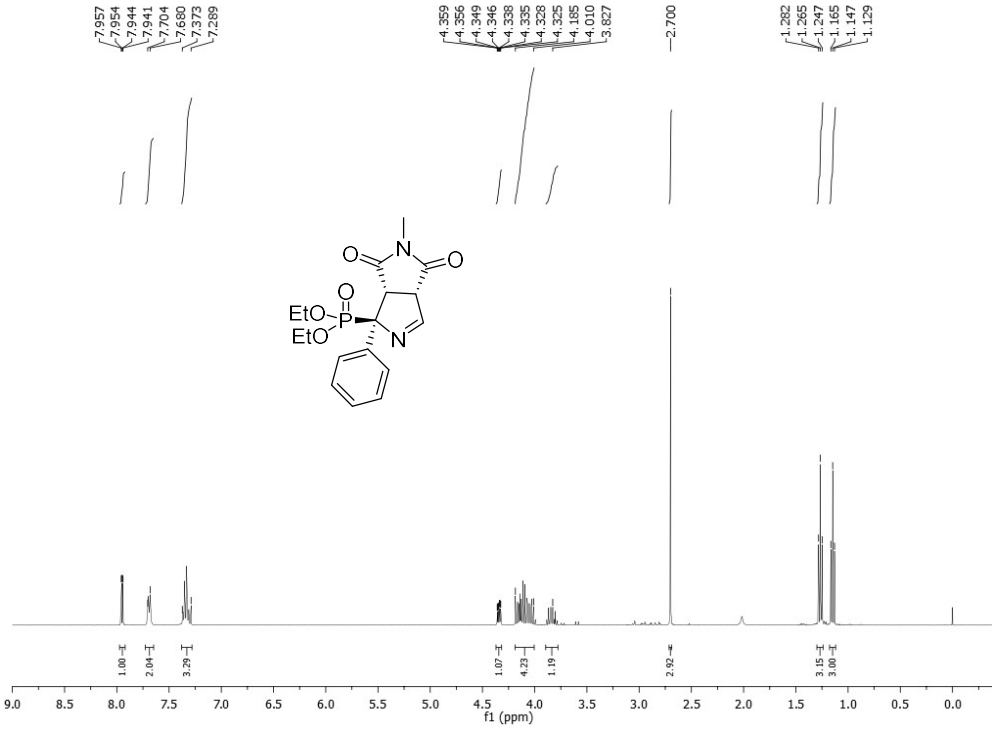

Diethyl (1*RS*,3a*SR*,6a*SR*)-5-methyl-4,6-dioxo-1-phenyl-1,3a,4,5,6,6a-hexahydropyrrolo[3,4-*c*]pyrrole-1-phosphonate (9a)

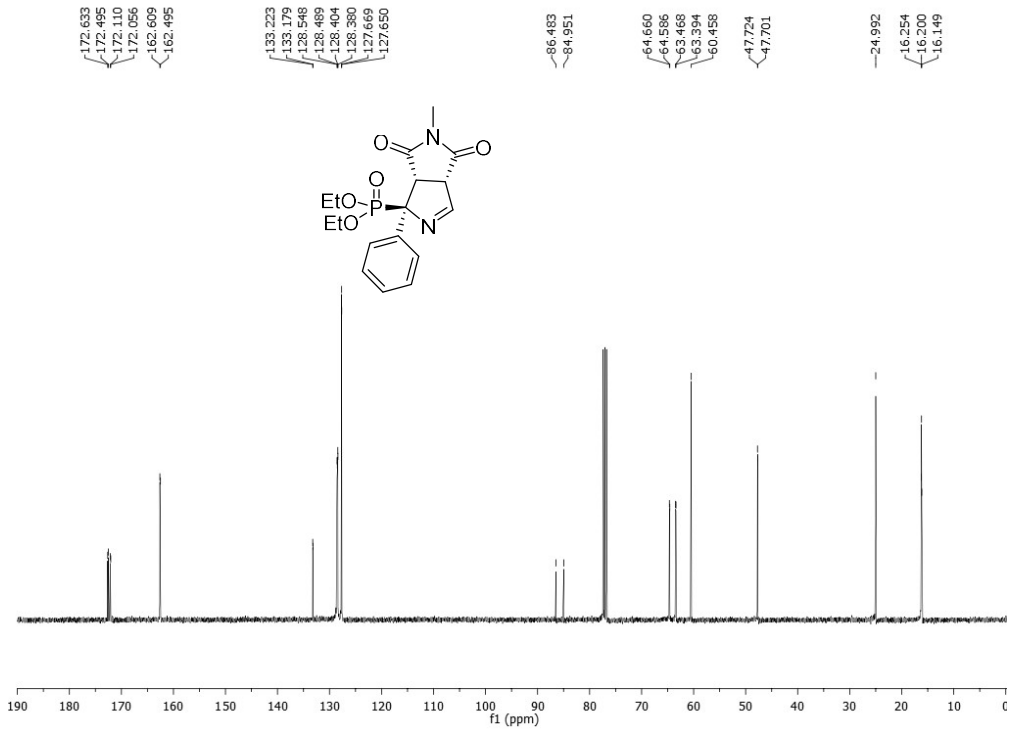

Diethyl (1*RS*,3a*SR*,6a*SR*)-5-methyl-4,6-dioxo-1-phenyl-1,3a,4,5,6,6a-hexahydropyrrolo[3,4-*c*]pyrrole-1-phosphonate (9a)

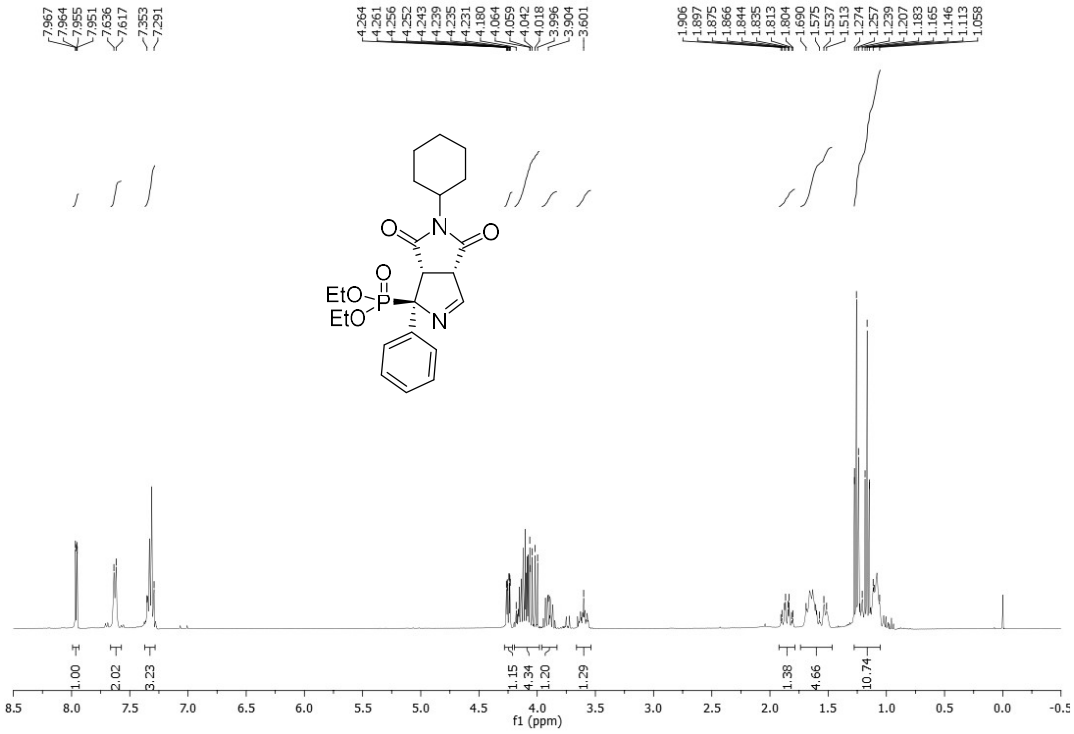

Diethyl (1*RS*,3a*SR*,6a*SR*)-5-cyclohexyl-4,6-dioxo-1-phenyl-1,3a,4,5,6,6a-hexahydropyrrolo[3,4-*c*]pyrrole-1-phosphonate (9b)

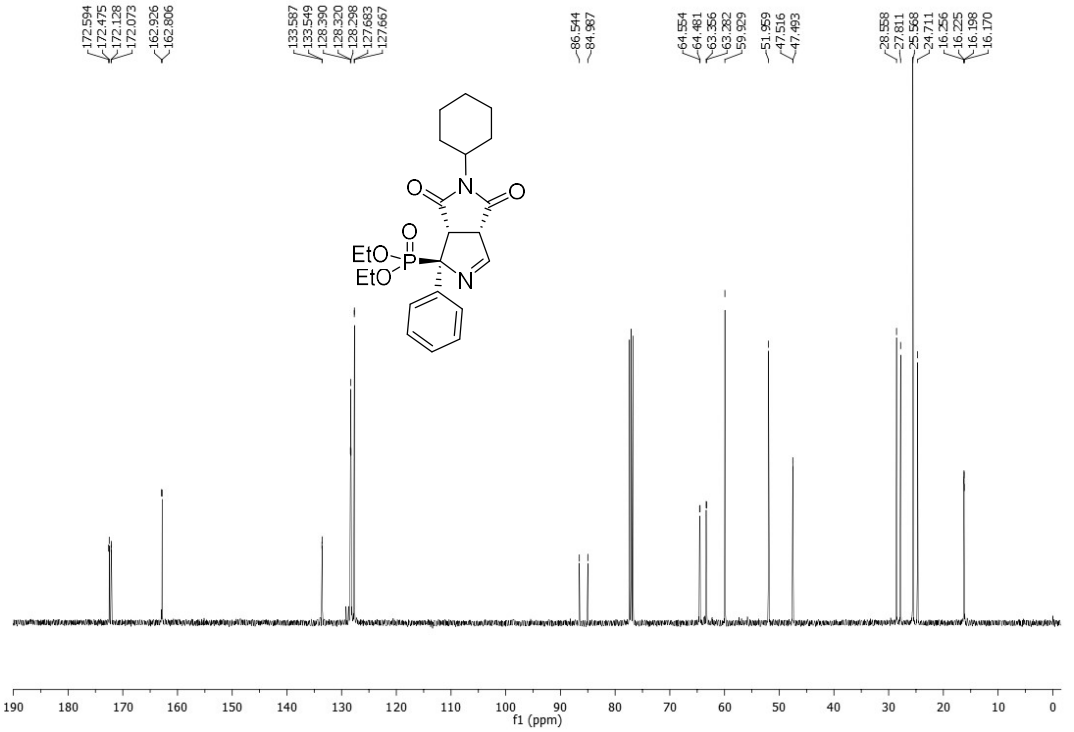

Diethyl (1*RS*,3a*SR*,6a*SR*)-5-cyclohexyl-4,6-dioxo-1-phenyl-1,3a,4,5,6,6a-hexahydropyrrolo[3,4-*c*]pyrrole-1-phosphonate (9b)

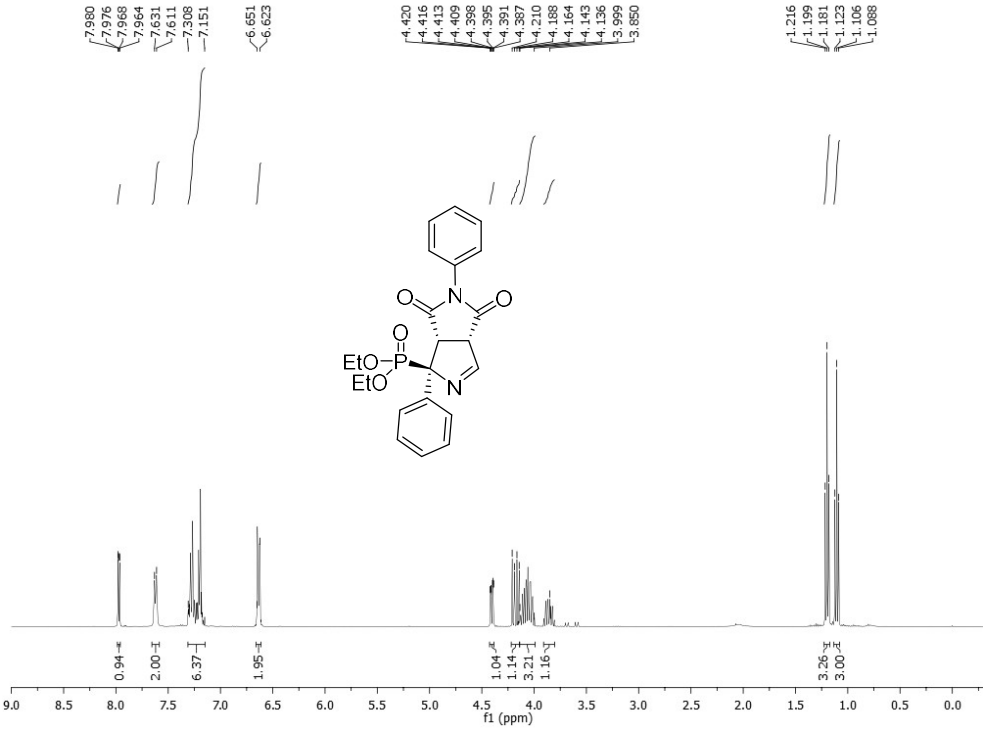

Diethyl (1*RS*,3a*SR*,6a*SR*)-4,6-dioxo-1,5-diphenyl-1,3a,4,5,6,6a-hexahydropyrrolo[3,4-*c*]pyrrole-1-phosphonate (9c)

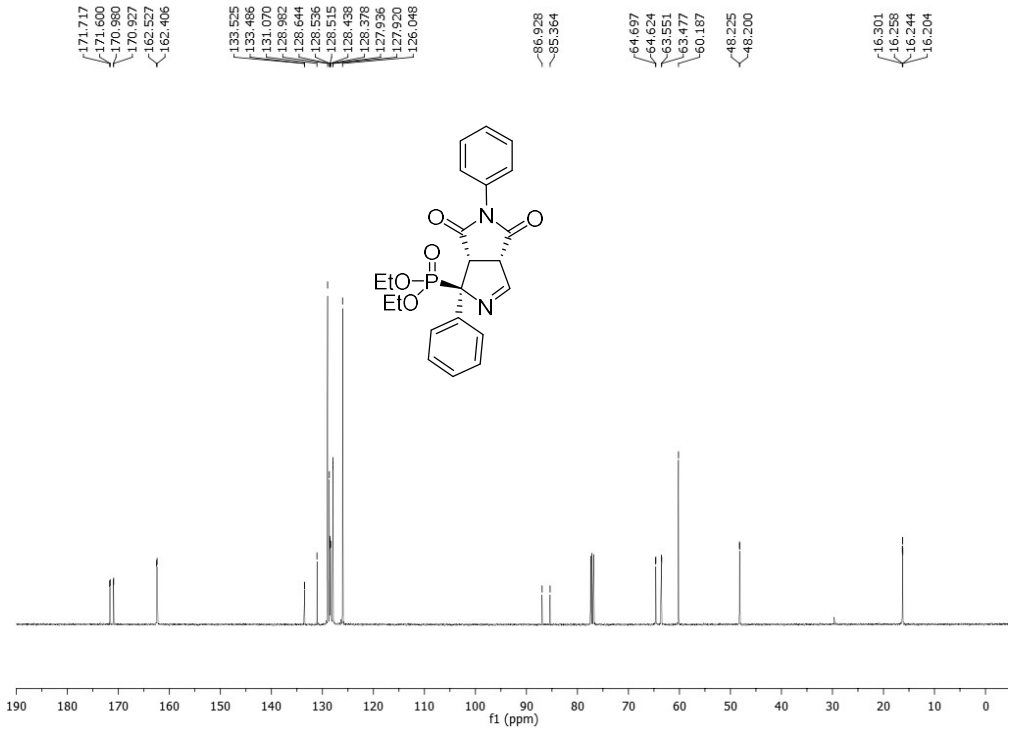

Diethyl (1*RS*,3a*SR*,6a*SR*)-4,6-dioxo-1,5-diphenyl-1,3a,4,5,6,6a-hexahydropyrrolo[3,4-*c*]pyrrole-1-phosphonate (9c)

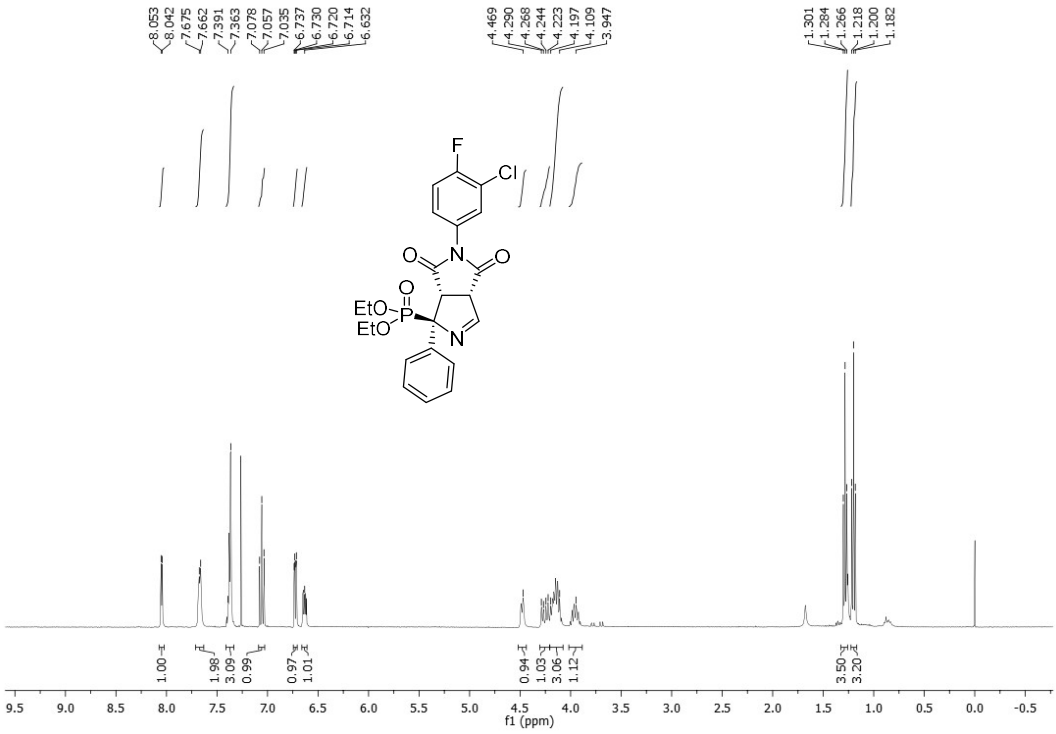

Diethyl (1*RS*,3a*SR*,6a*SR*)-5-(3-chloro-4-fluorophenyl)-4,6-dioxo-1-phenyl-1,3a,4,5,6,6a-hexahydropyrrolo[3,4-*c*]pyrrole-1-phosphonate (9d)

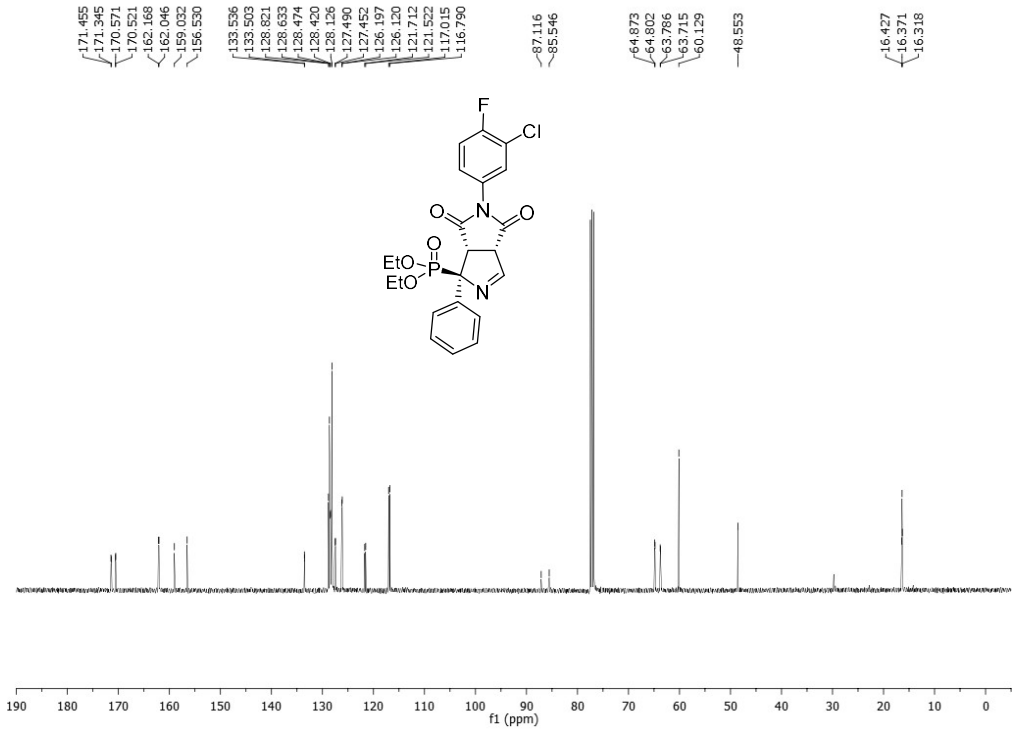

Diethyl (1*RS*,3a*SR*,6a*SR*)-5-(3-chloro-4-fluorophenyl)-4,6-dioxo-1-phenyl-1,3a,4,5,6,6a-hexahydropyrrolo[3,4-*c*]pyrrole-1-phosphonate (9d)

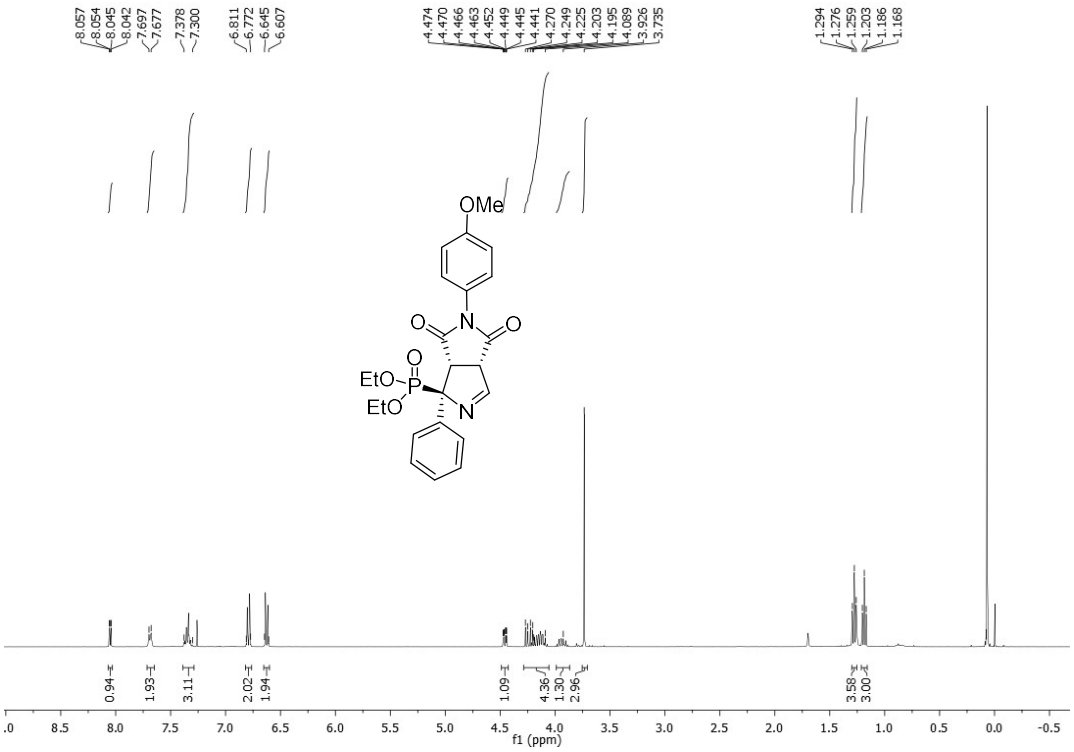

Diethyl (1*RS*,3a*SR*,6a*SR*)-5-(4-methoxyphenyl)-4,6-dioxo-1-phenyl-1,3a,4,5,6,6a-hexahydropyrrolo[3,4-*c*]pyrrole-1-phosphonate (9e)

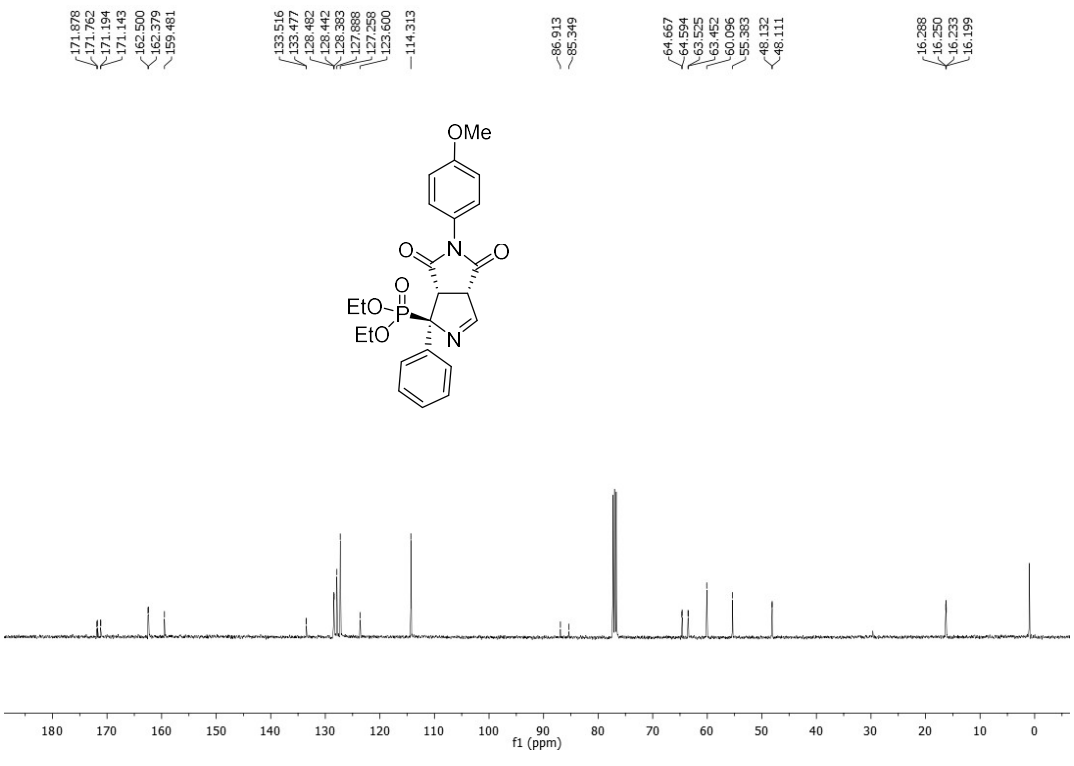

Diethyl (1*RS*,3a*SR*,6a*SR*)-5-(4-methoxyphenyl)-4,6-dioxo-1-phenyl-1,3a,4,5,6,6a-hexahydropyrrolo[3,4-*c*]pyrrole-1-phosphonate (9e)

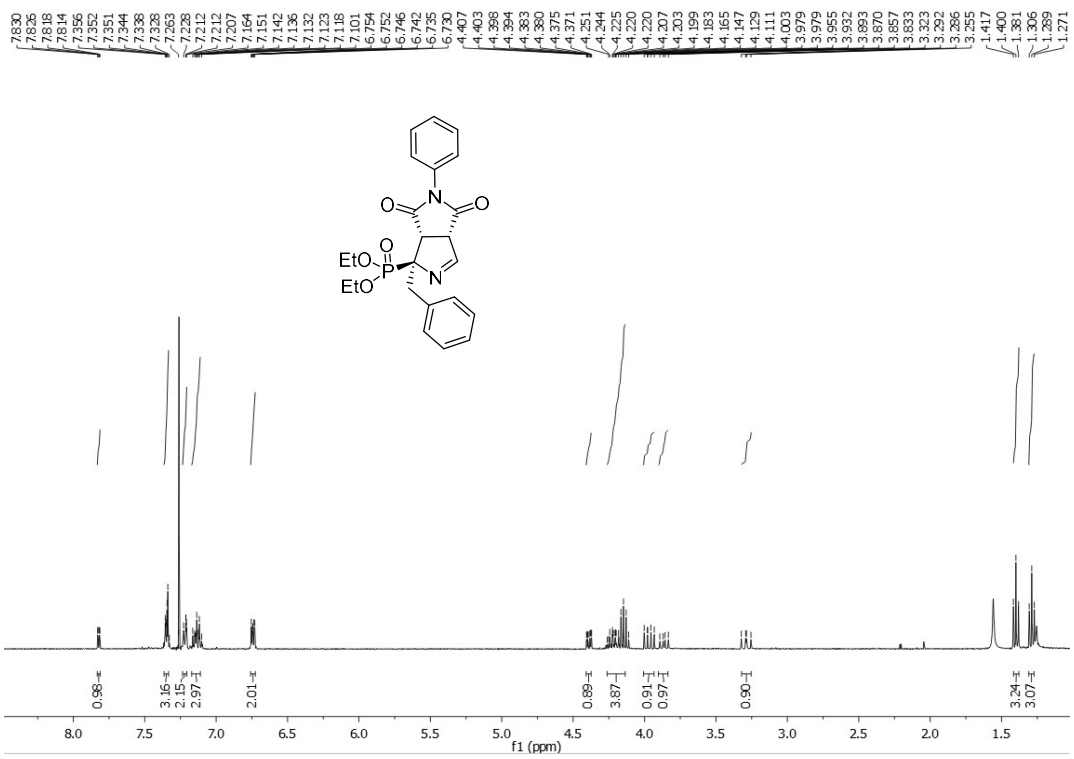

Diethyl (1*RS*,3a*SR*,6a*SR*)-1-benzyl-4,6-dioxo-5-phenyl-1,3a,4,5,6,6a-hexahydropyrrolo[3,4-*c*]pyrrole-1-phosphonate (14c)

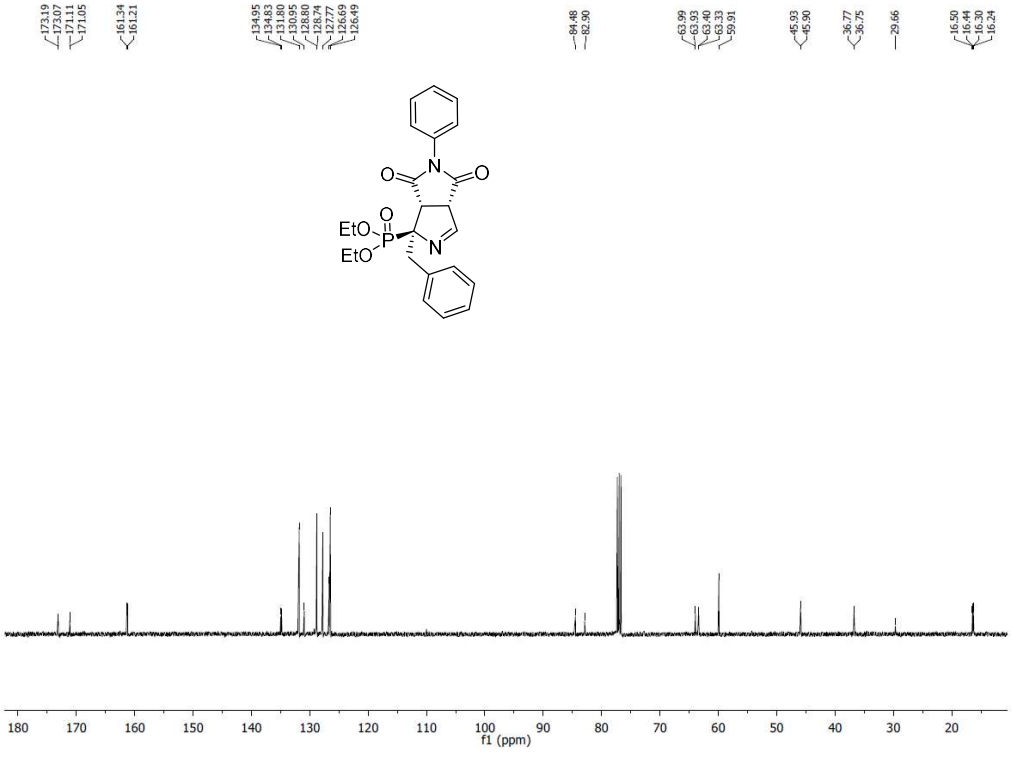

Diethyl (1*RS*,3a*SR*,6a*SR*)-1-benzyl-4,6-dioxo-5-phenyl-1,3a,4,5,6,6a-hexahydropyrrolo[3,4-*c*]pyrrole-1-phosphonate (14c)

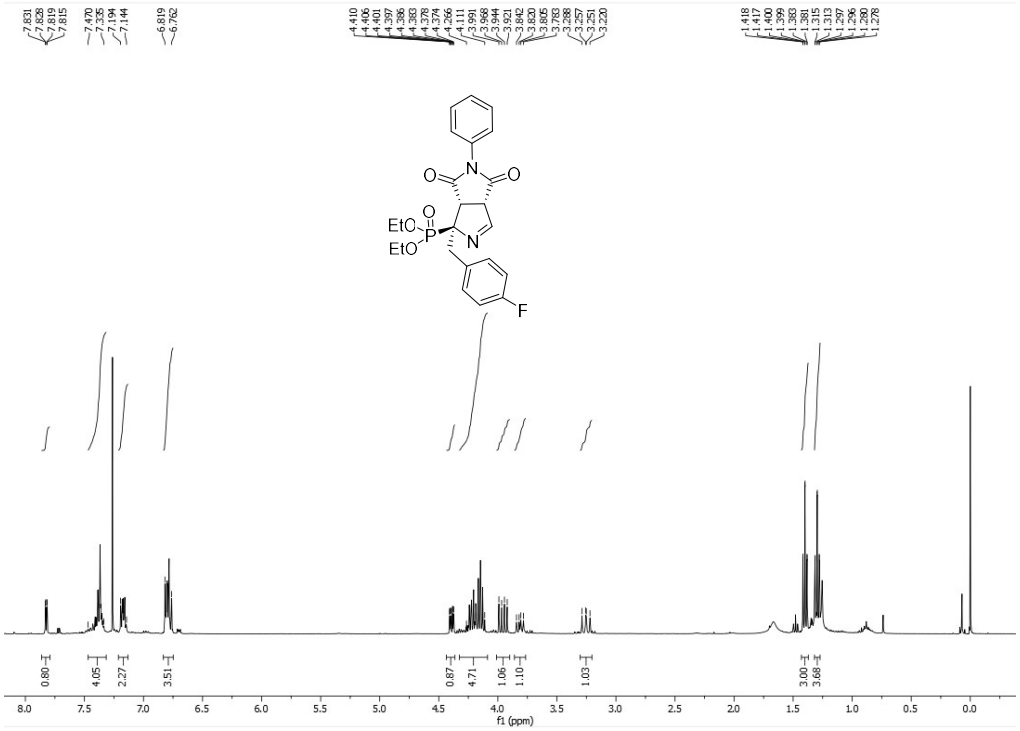

Diethyl (1*RS*,3a*SR*,6a*SR*)-1-(4-fluorobenzyl)-4,6-dioxo-5-phenyl-1,3a,4,5,6,6a-hexahydropyrrolo[3,4-*c*]pyrrole-1-phosphonate (15c)

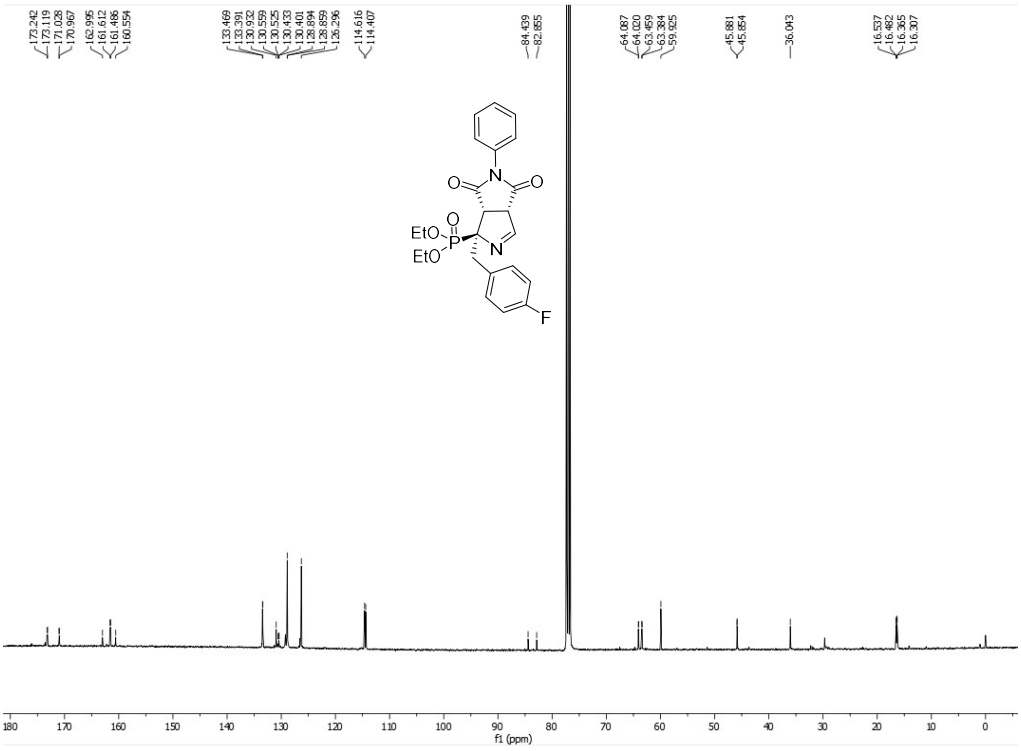

Diethyl (1*RS*,3a*SR*,6a*SR*)-1-(4-fluorobenzyl)-4,6-dioxo-5-phenyl-1,3a,4,5,6,6a-hexahydropyrrolo[3,4-*c*]pyrrole-1-phosphonate (15c)

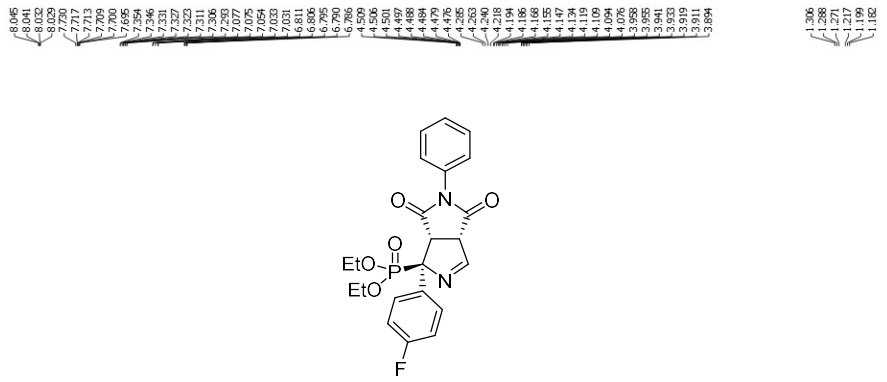

Diethyl (1*RS*,3a*SR*,6a*SR*)-1-(4-fluorophenyl)-4,6-dioxo-5-phenyl-1,3a,4,5,6,6a-hexahydropyrrolo[3,4-*c*]pyrrole-1-phosphonate (12c)

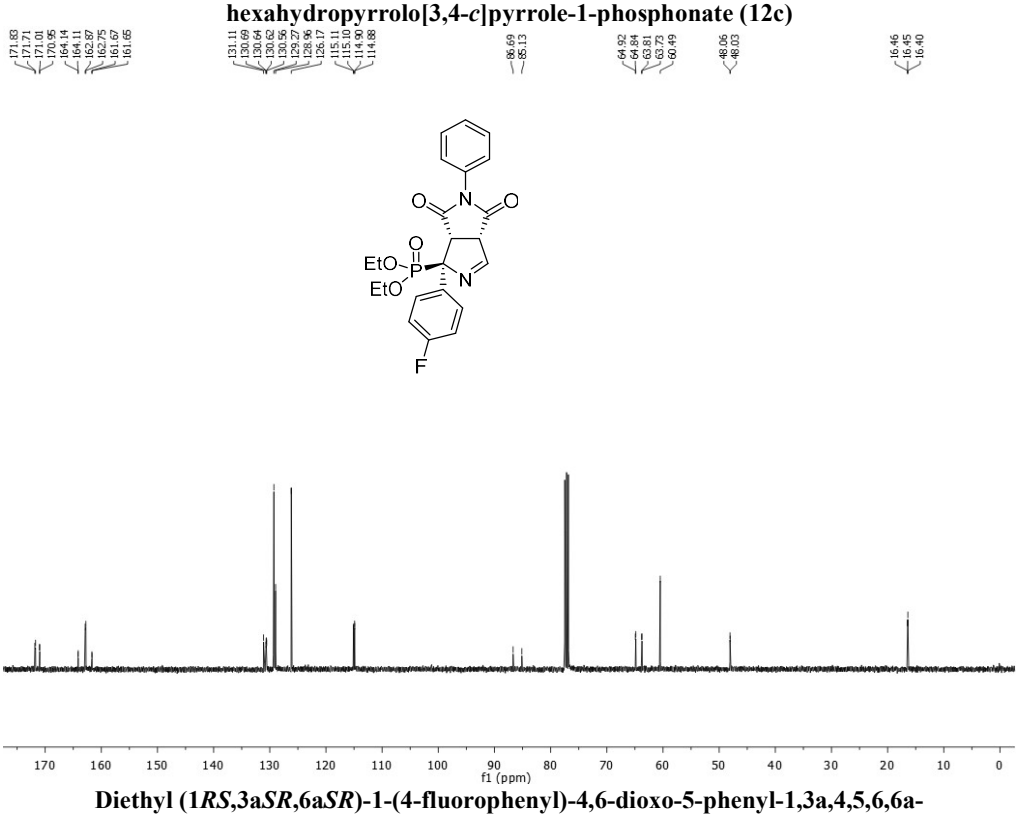

Diethyl (1*RS*,3a*SR*,6a*SR*)-1-(4-fluorophenyl)-4,6-dioxo-5-phenyl-1,3a,4,5,6,6a-hexahydropyrrolo[3,4-*c*]pyrrole-1-phosphonate (12c)

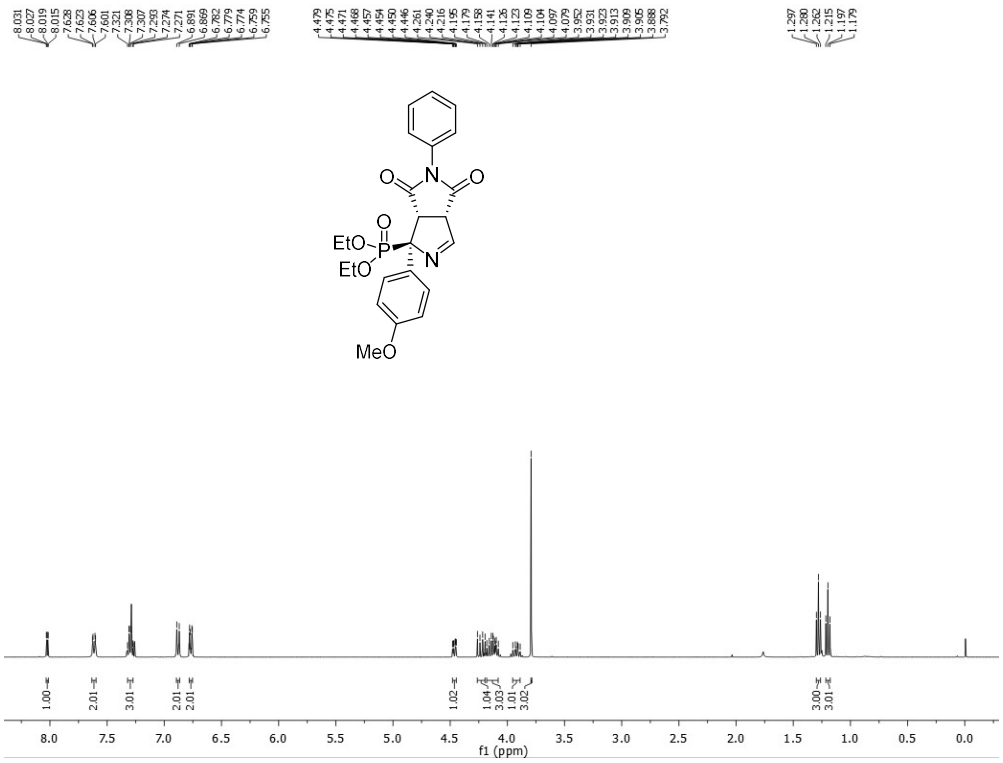

Diethyl (1*RS*,3a*SR*,6a*SR*)-1-(4-methoxyphenyl)-4,6-dioxo-5-phenyl-1,3a,4,5,6,6a-hexahydropyrrolo[3,4-*c*]pyrrole-1-phosphonate (13c)

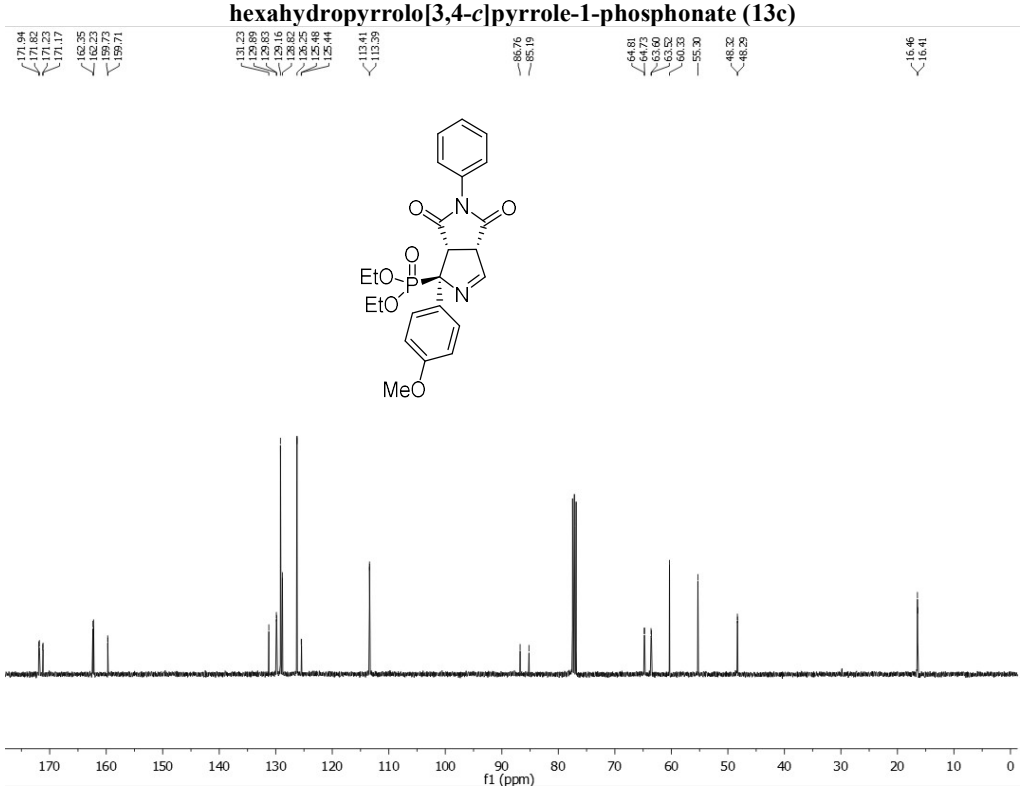

Diethyl (1*RS*,3a*SR*,6a*SR*)-1-(4-methoxyphenyl)-4,6-dioxo-5-phenyl-1,3a,4,5,6,6a-hexahydropyrrolo[3,4-*c*]pyrrole-1-phosphonate (13c)

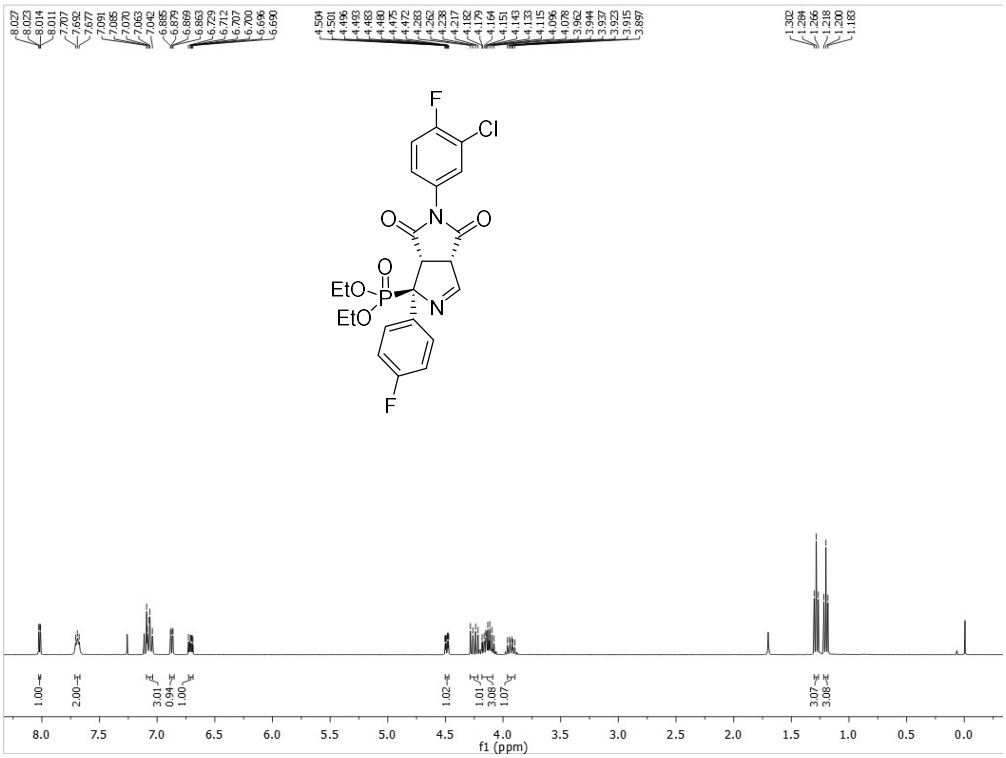

Diethyl (1*RS*,3a*SR*,6a*SR*)-5-(3-chloro-4-fluorophenyl)-1-(4-fluorophenyl)-4,6-dioxo-1,3a,4,5,6,6a-hexahydropyrrolo[3,4-*c*]pyrrole-1-phosphonate (12d)

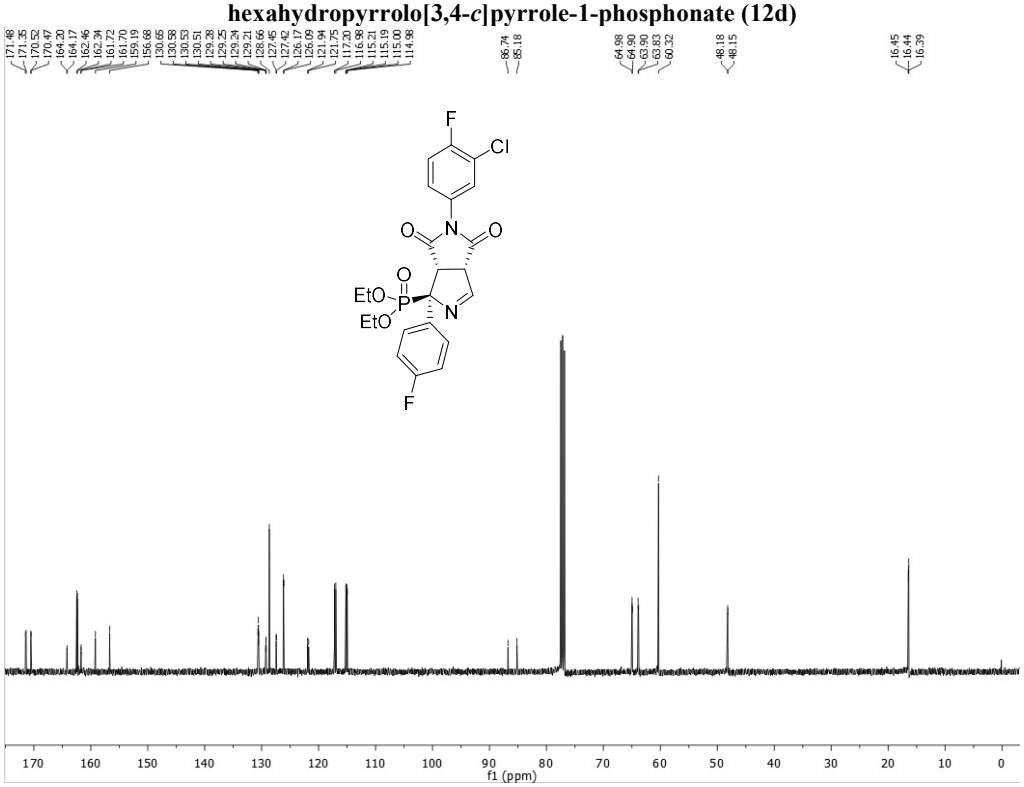

Diethyl (1*RS*,3a*SR*,6a*SR*)-5-(3-chloro-4-fluorophenyl)-1-(4-fluorophenyl)-4,6-dioxo-1,3a,4,5,6,6a-hexahydropyrrolo[3,4-*c*]pyrrole-1-phosphonate (12d)

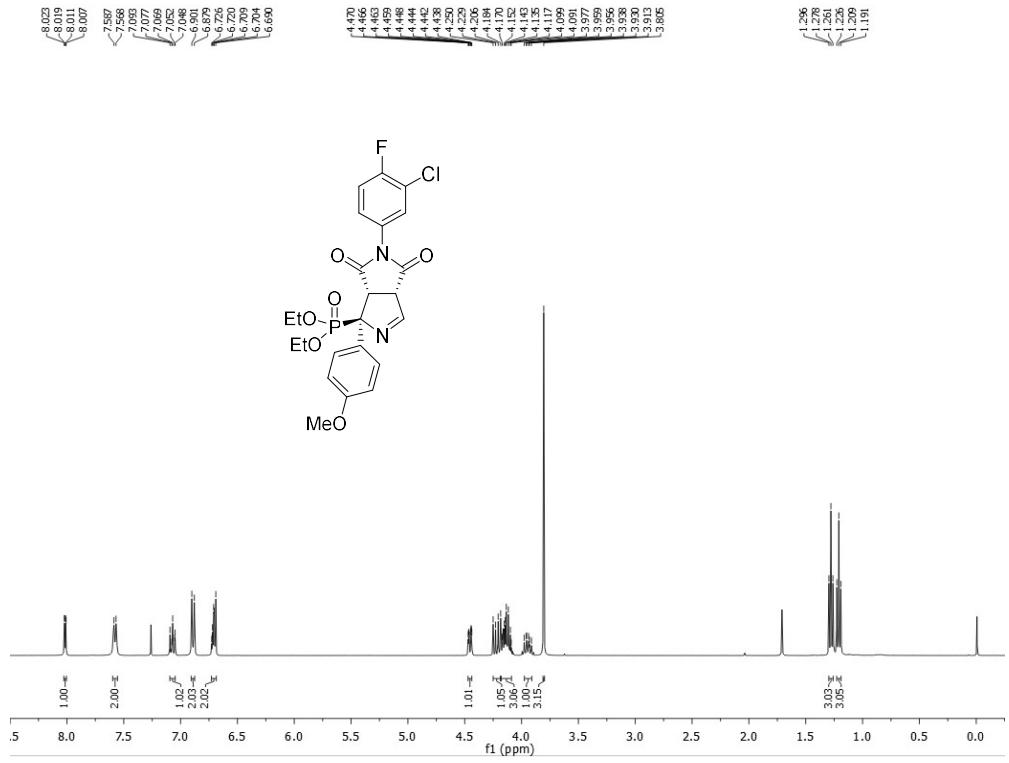

Diethyl (1*RS*,3a*SR*,6a*SR*)-5-(3-chloro-4-fluorophenyl)-1-(4-methoxyphenyl)-4,6-dioxo-1,3a,4,5,6,6a-hexahydropyrrolo[3,4-*c*]pyrrole-1-phosphonate (13d)

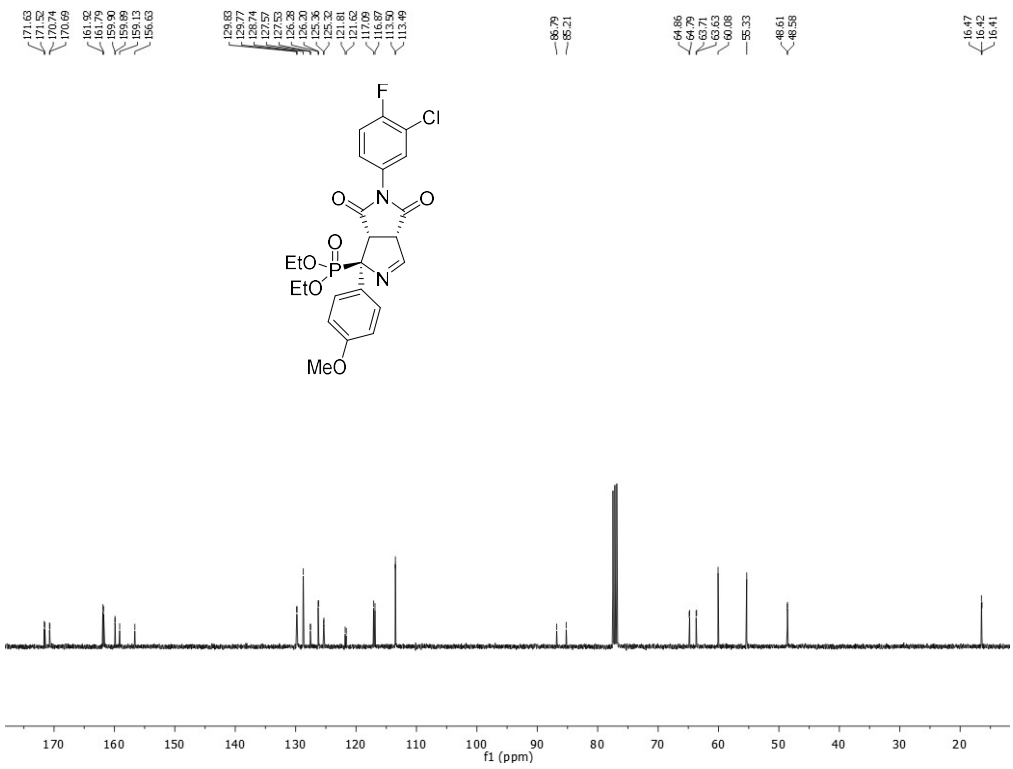

Diethyl (1*RS*,3a*SR*,6a*SR*)-5-(3-chloro-4-fluorophenyl)-1-(4-methoxyphenyl)-4,6-dioxo-1,3a,4,5,6,6a-hexahydropyrrolo[3,4-*c*]pyrrole-1-phosphonate (13d)

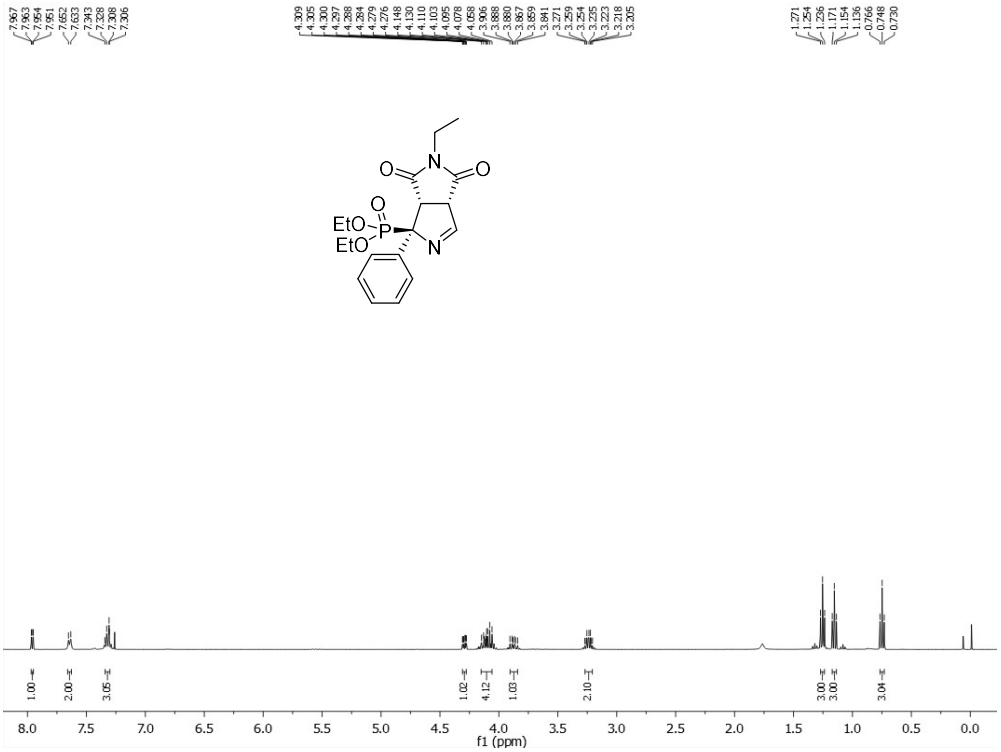

Diethyl (1*RS*,3a*SR*,6a*SR*)-5-ethyl-4,6-dioxo-1-phenyl-1,3a,4,5,6,6a-hexahydropyrrolo[3,4-*c*]pyrrole-1-phosphonate (9f)

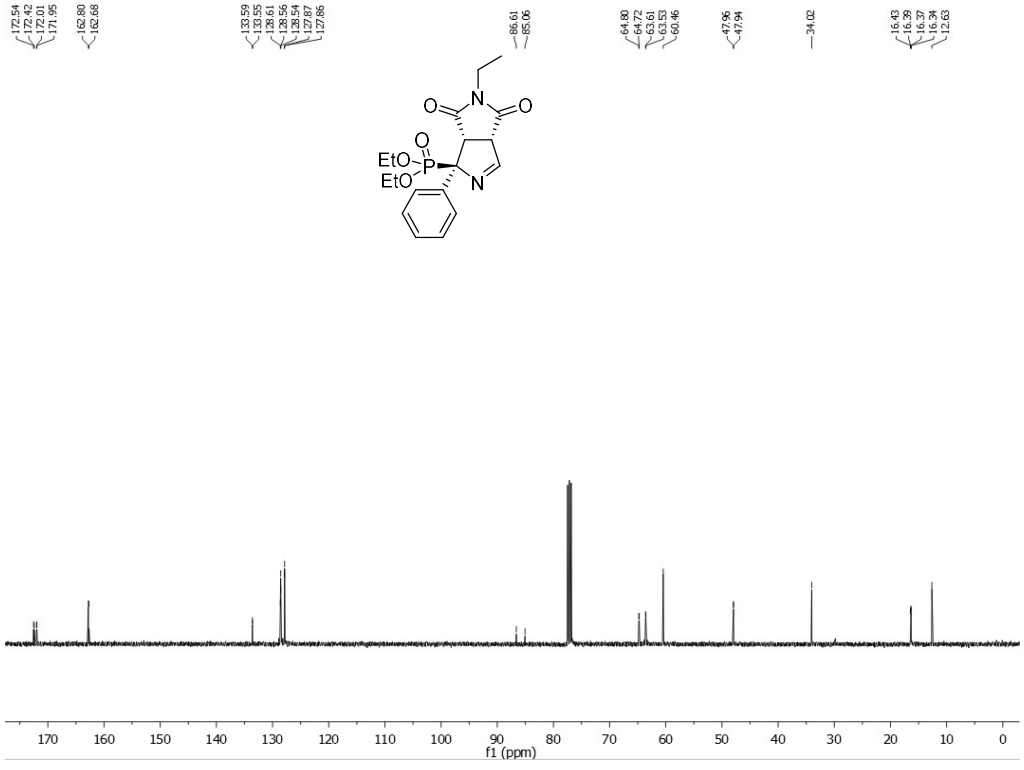

Diethyl (1*RS*,3a*SR*,6a*SR*)-5-ethyl-4,6-dioxo-1-phenyl-1,3a,4,5,6,6a-hexahydropyrrolo[3,4-*c*]pyrrole-1-phosphonate (9f)

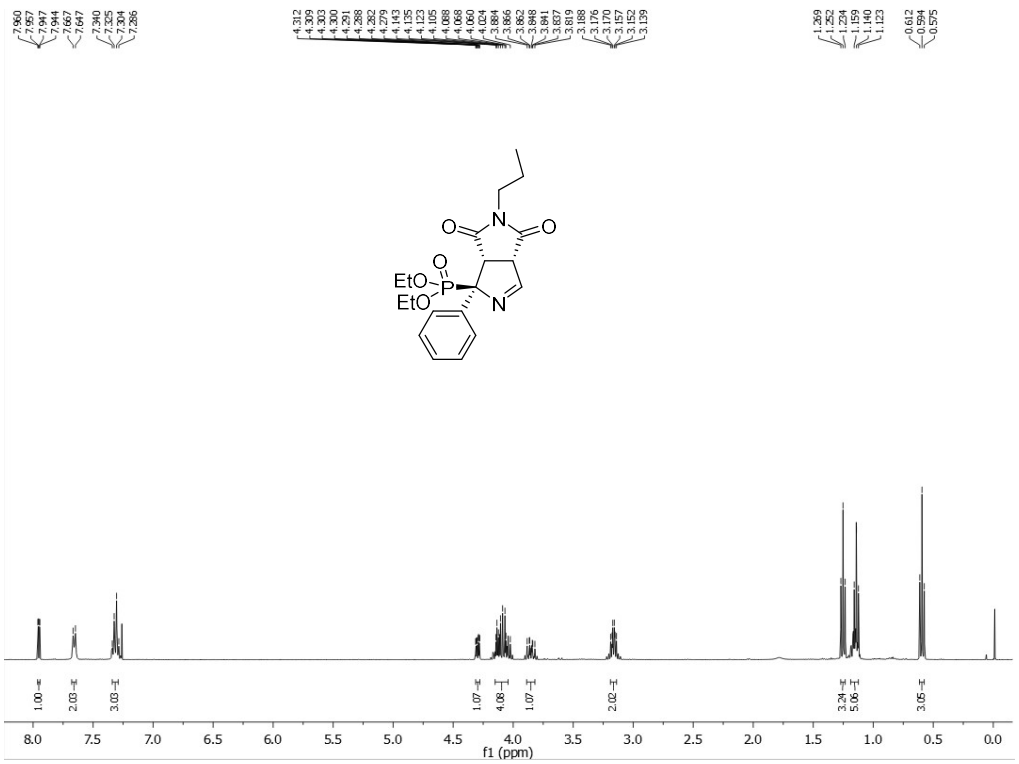

Diethyl (1*RS*,3a*SR*,6a*SR*)-4,6-dioxo-1-phenyl-5-propyl-1,3a,4,5,6,6a-hexahydropyrrolo[3,4-*c*]pyrrole-1-phosphonate (9g)

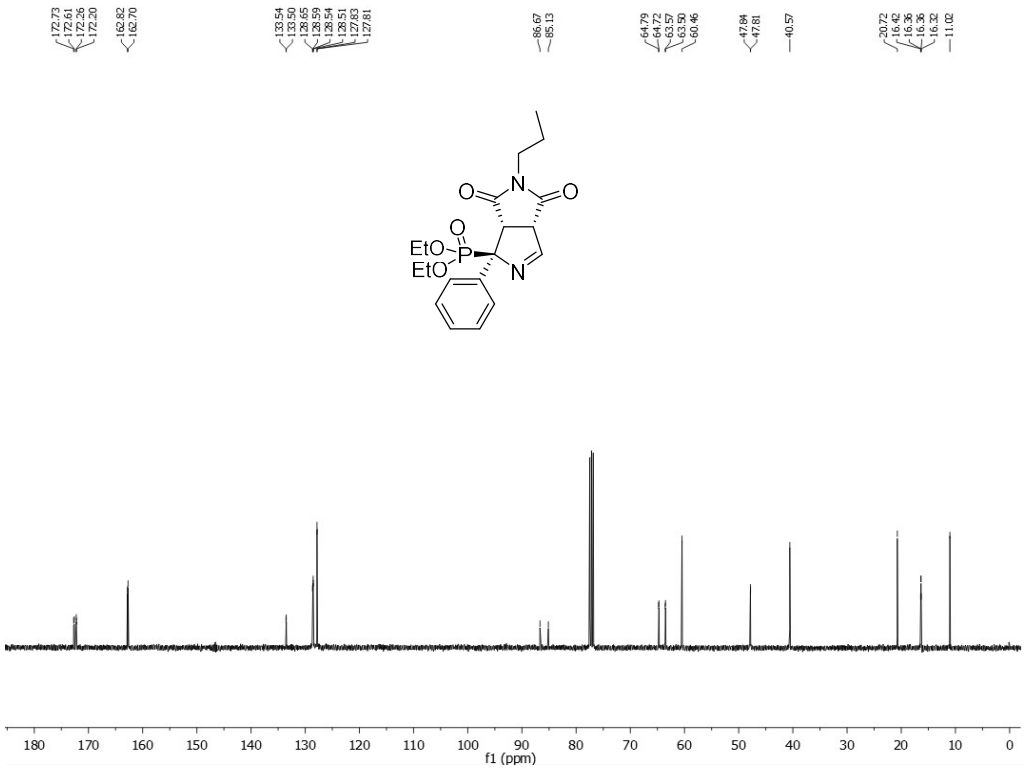

Diethyl (1*RS*,3a*SR*,6a*SR*)-4,6-dioxo-1-phenyl-5-propyl-1,3a,4,5,6,6a-hexahydropyrrolo[3,4-*c*]pyrrole-1-phosphonate (9g)

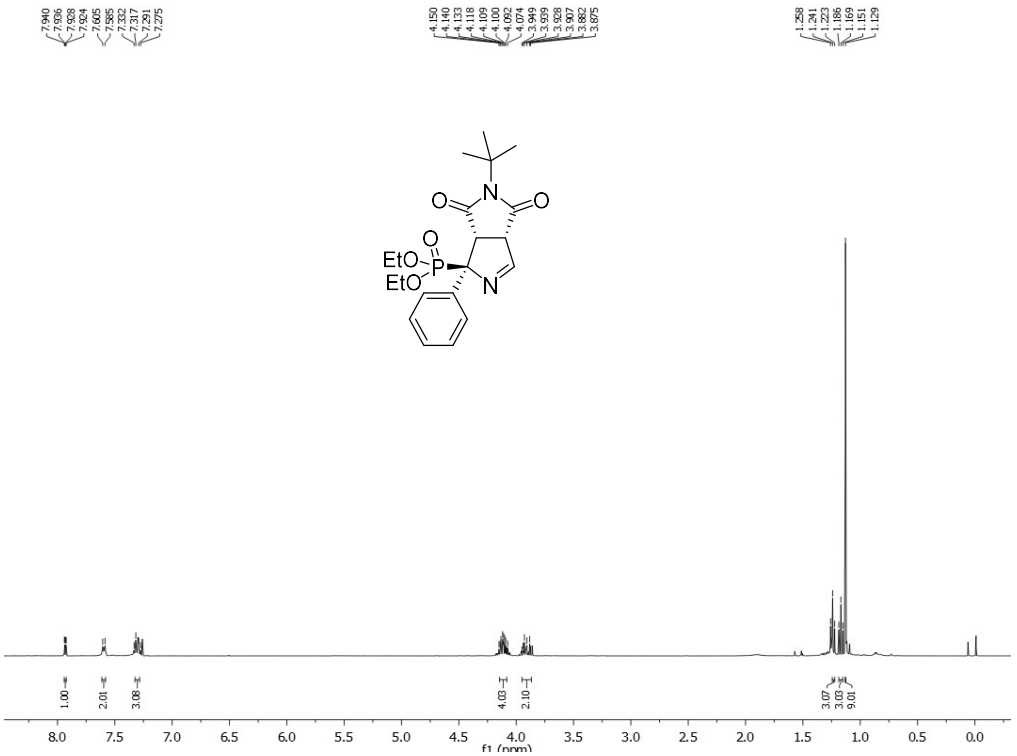

Diethyl (1*RS*,3a*SR*,6a*SR*)-5-(tert-butyl)-4,6-dioxo-1-phenyl-1,3a,4,5,6,6a-hexahydropyrrolo[3,4-*c*]pyrrole-1-phosphonate (9h)

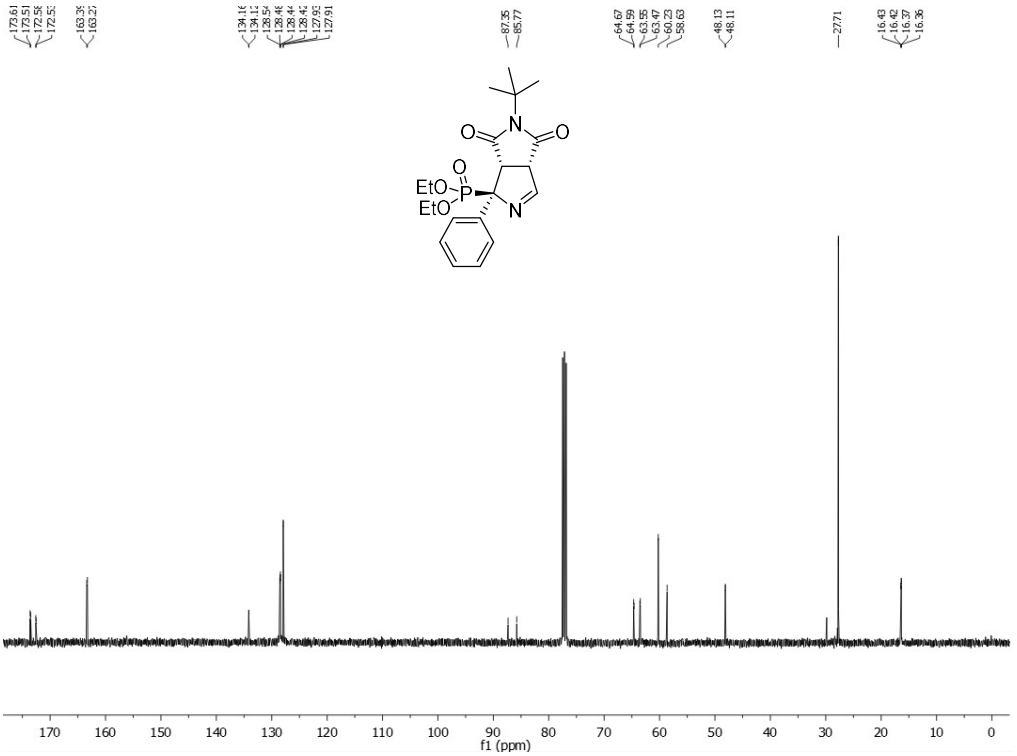

Diethyl (1*RS*,3a*SR*,6a*SR*)-5-(tert-butyl)-4,6-dioxo-1-phenyl-1,3a,4,5,6,6a-hexahydropyrrolo[3,4-*c*]pyrrole-1-phosphonate (9h)

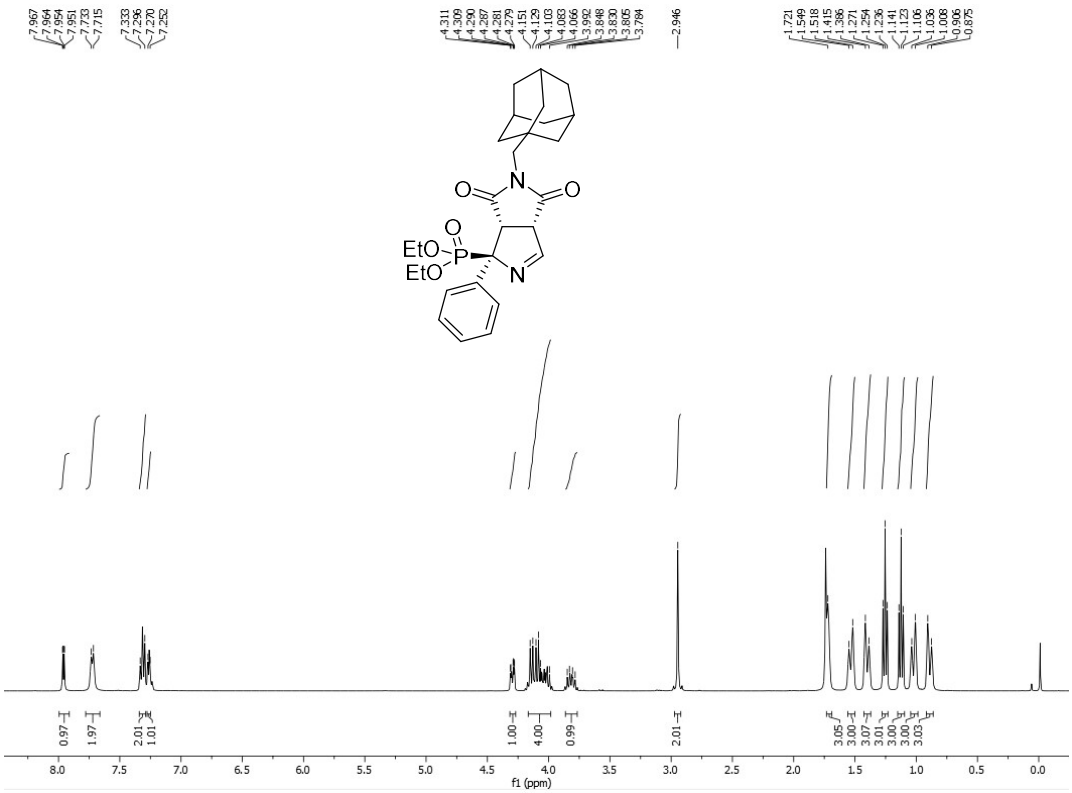

Diethyl (1*RS*,3a*SR*,6a*SR*)-5-(adamantan-1-yl)methyl)-4,6-dioxo-1-phenyl-1,3a,4,5,6,6a-hexahydropyrrolo[3,4-*c*]pyrrole-1-phosphonate (9i)

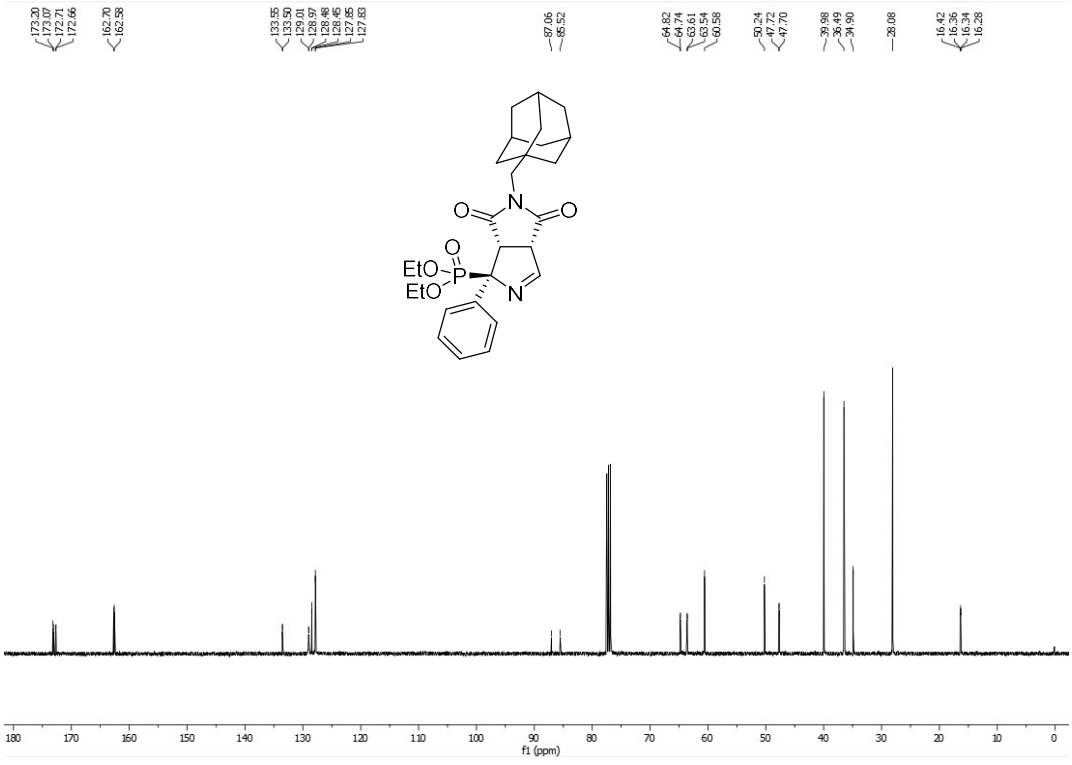

Diethyl (1*RS*,3a*SR*,6a*SR*)-5-(adamantan-1-yl)methyl)-4,6-dioxo-1-phenyl-1,3a,4,5,6,6a-hexahydropyrrolo[3,4-*c*]pyrrole-1-phosphonate (9i)

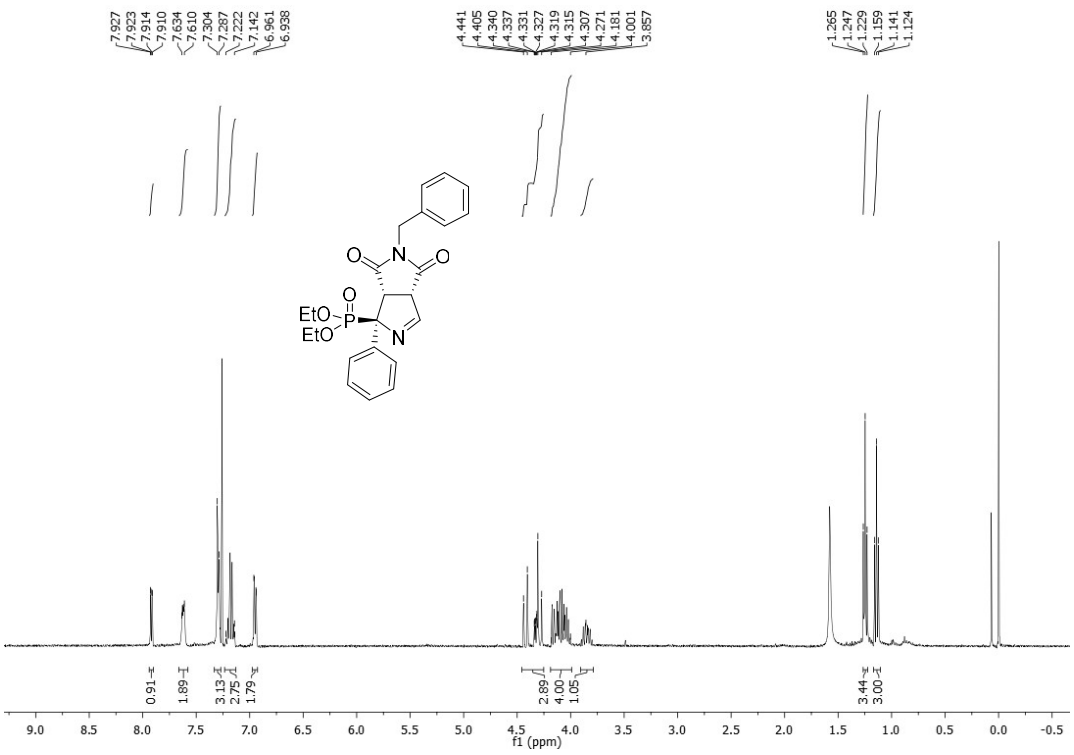

Diethyl (1*RS*,3a*SR*,6a*SR*)-5-benzyl-4,6-dioxo-1-phenyl-1,3a,4,5,6,6a-hexahydropyrrolo[3,4-*c*]pyrrole-1-phosphonate (9j)

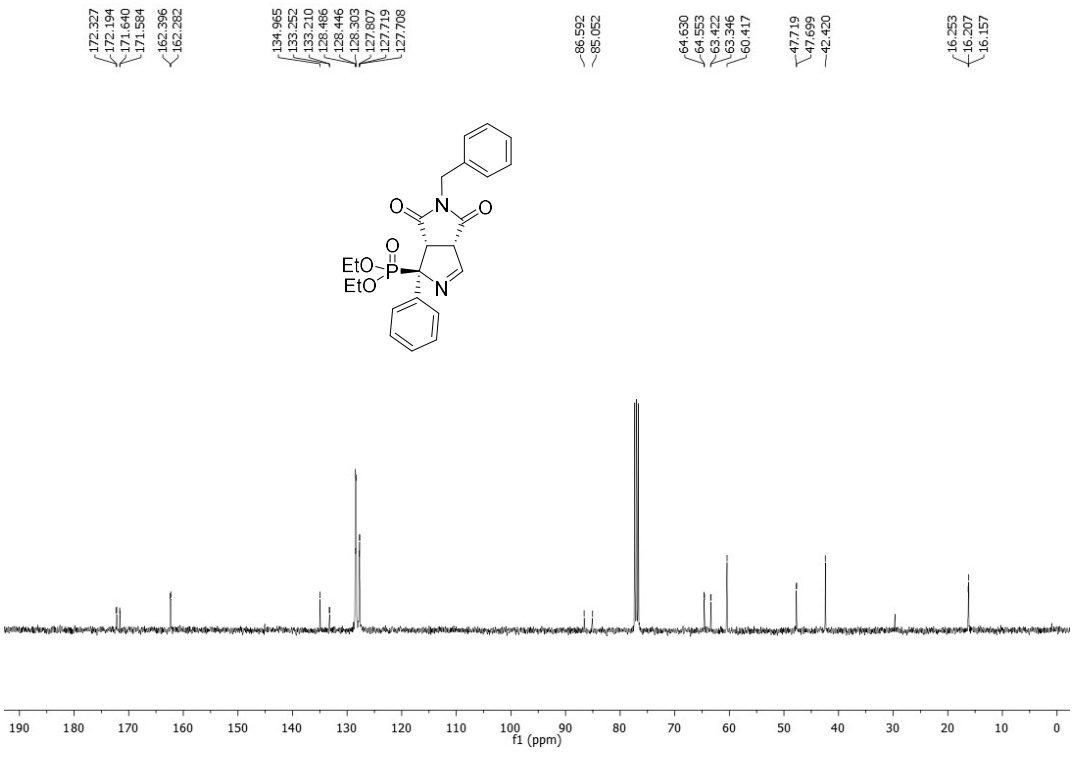

Diethyl (1*RS*,3a*SR*,6a*SR*)-5-benzyl-4,6-dioxo-1-phenyl-1,3a,4,5,6,6a-hexahydropyrrolo[3,4-*c*]pyrrole-1-phosphonate (9j)

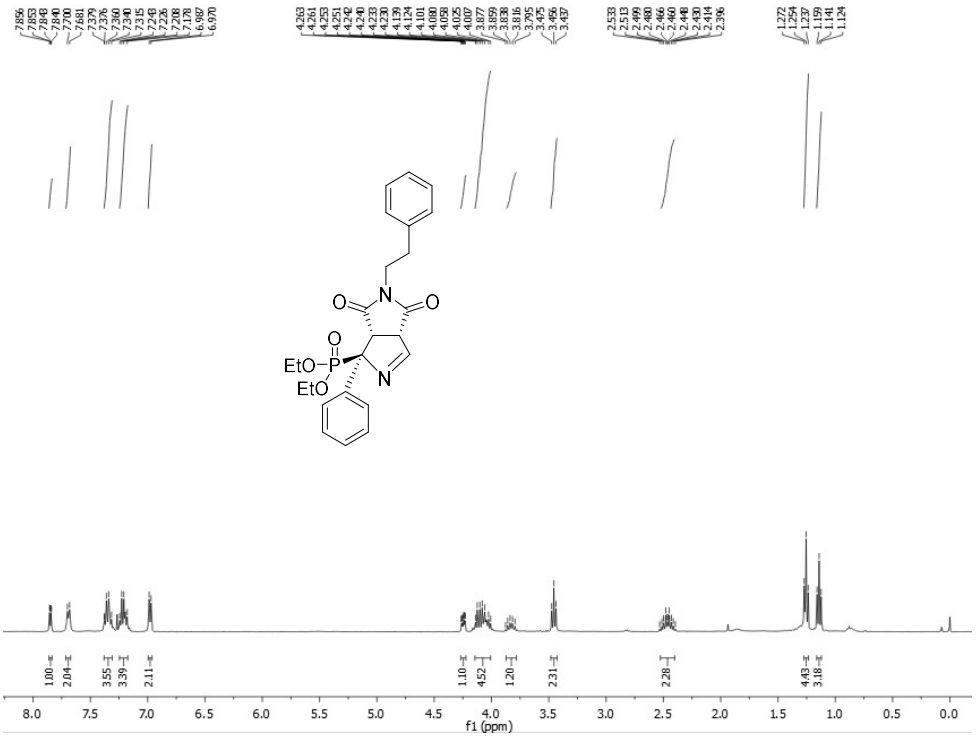

Diethyl (1*RS*,3a*SR*,6a*SR*)-4,6-dioxo-5-phenethyl-1-phenyl-1,3a,4,5,6,6a-hexahydropyrrolo[3,4-*c*]pyrrole-1-phosphonate (9k)

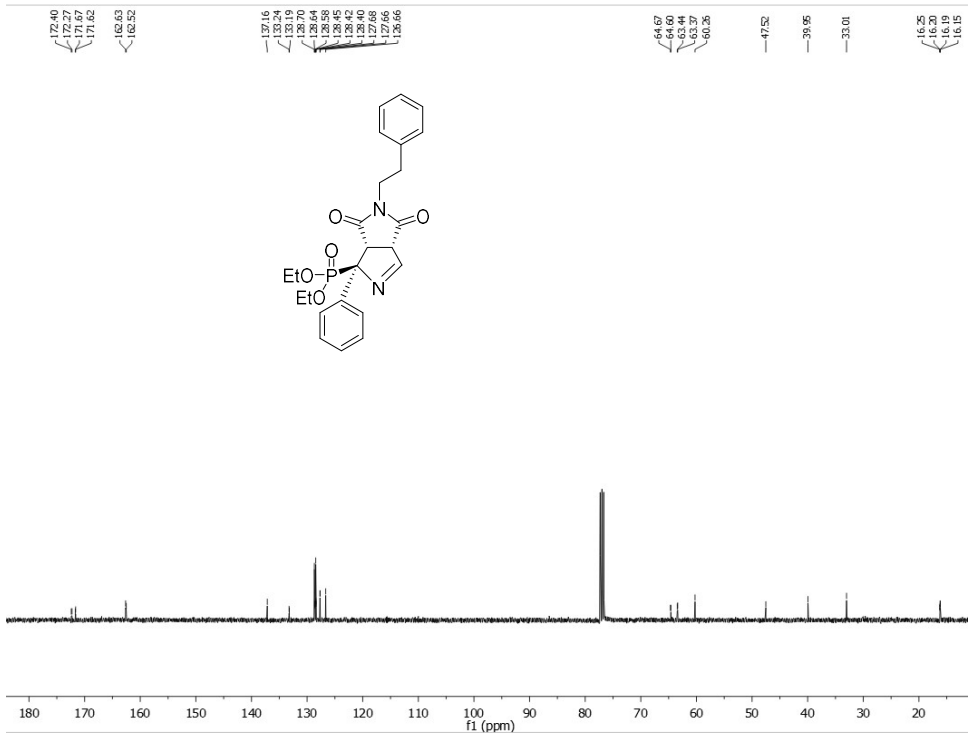

Diethyl (1*RS*,3a*SR*,6a*SR*)-4,6-dioxo-5-phenethyl-1-phenyl-1,3a,4,5,6,6a-hexahydropyrrolo[3,4-*c*]pyrrole-1-phosphonate (9k)

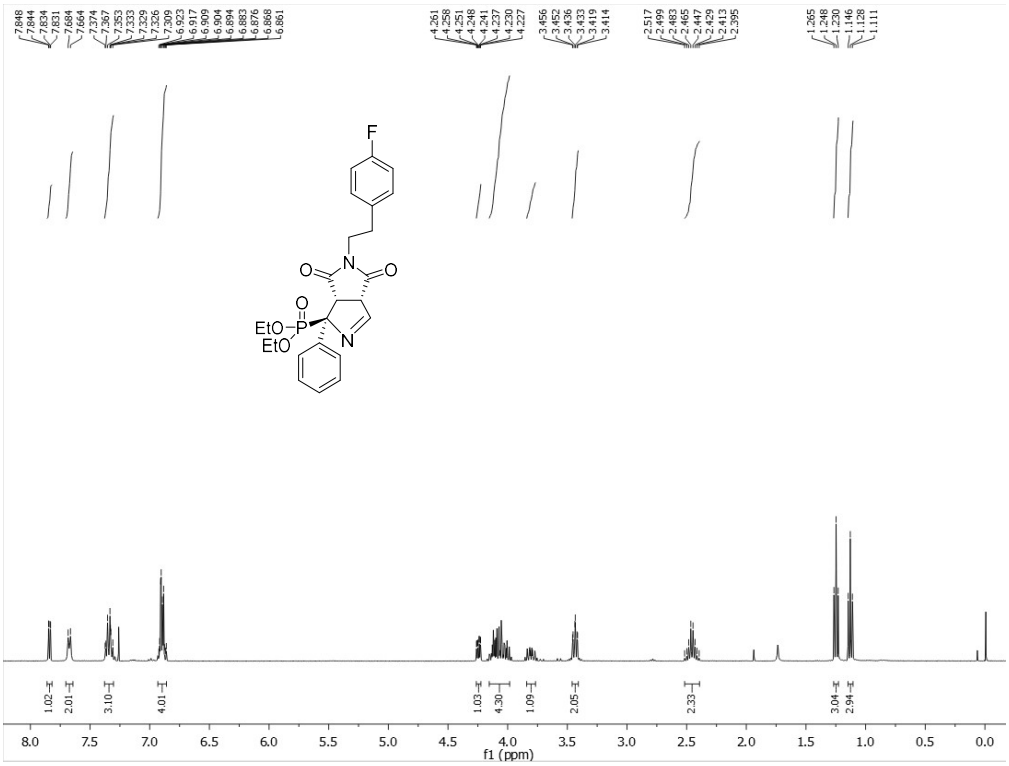

Diethyl (1*RS*,3a*SR*,6a*SR*)-5-(4-fluorophenethyl)-4,6-dioxo-1-phenyl-1,3a,4,5,6,6a-hexahydropyrrolo[3,4-*c*]pyrrole-1-phosphonate (9l)

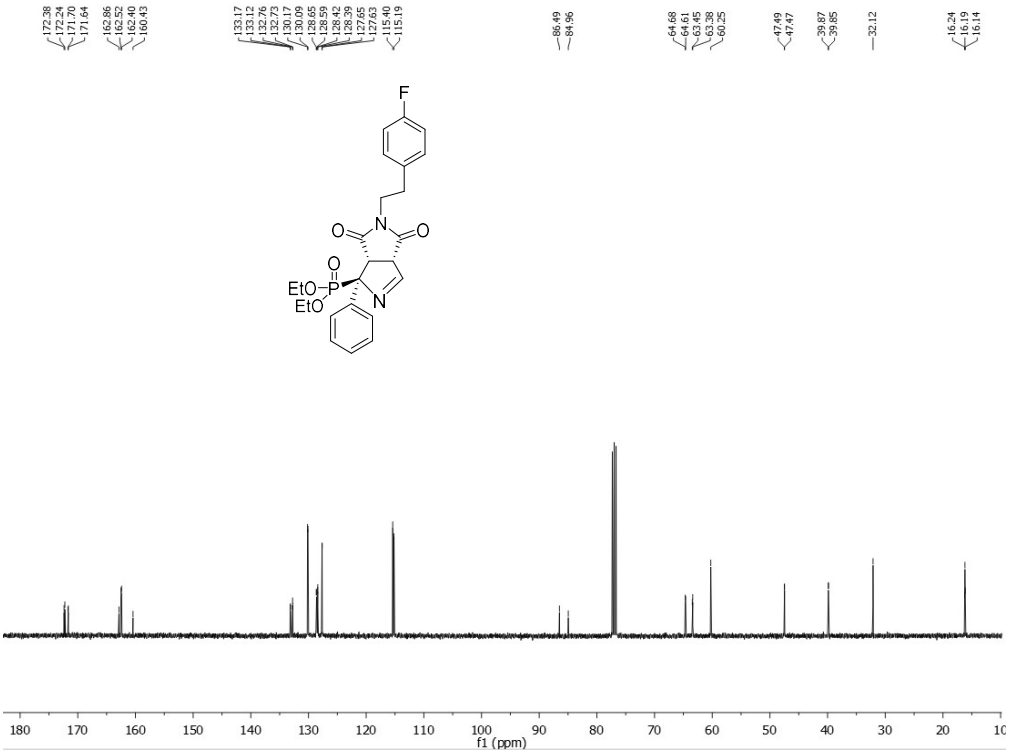

Diethyl (1*RS*,3a*SR*,6a*SR*)-5-(4-fluorophenethyl)-4,6-dioxo-1-phenyl-1,3a,4,5,6,6a-hexahydropyrrolo[3,4-*c*]pyrrole-1-phosphonate (9l)

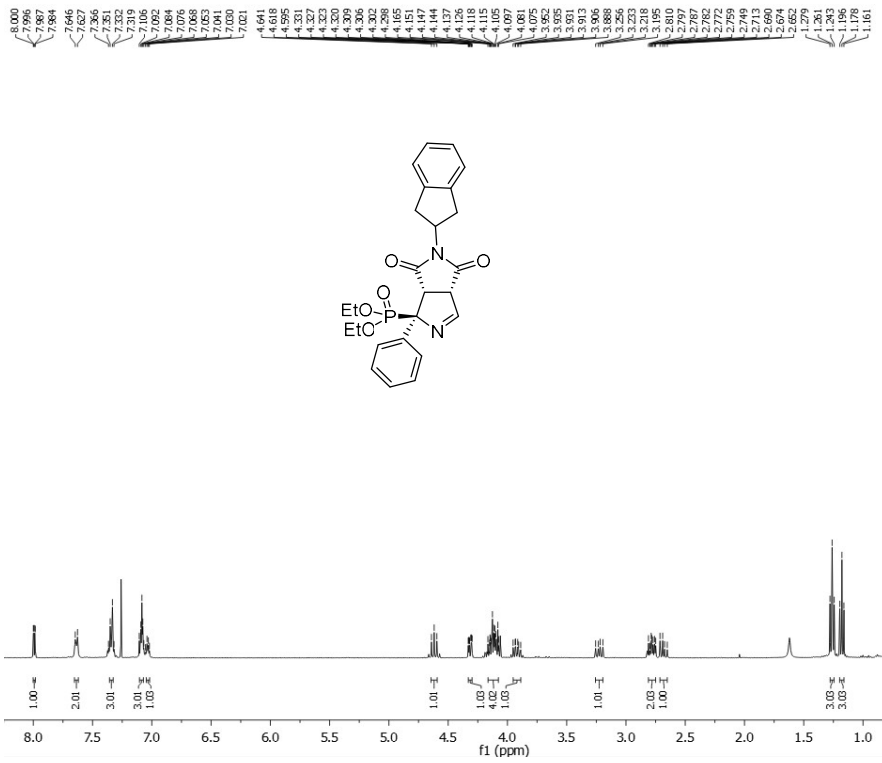

Diethyl (1*RS*,3a*SR*,6a*SR*)-5-(2,3-dihydro-1H-inden-2-yl)-4,6-dioxo-1-phenyl-1,3a,4,5,6,6a-hexahydropyrrolo[3,4-*c*]pyrrole-1-phosphonate (9m)

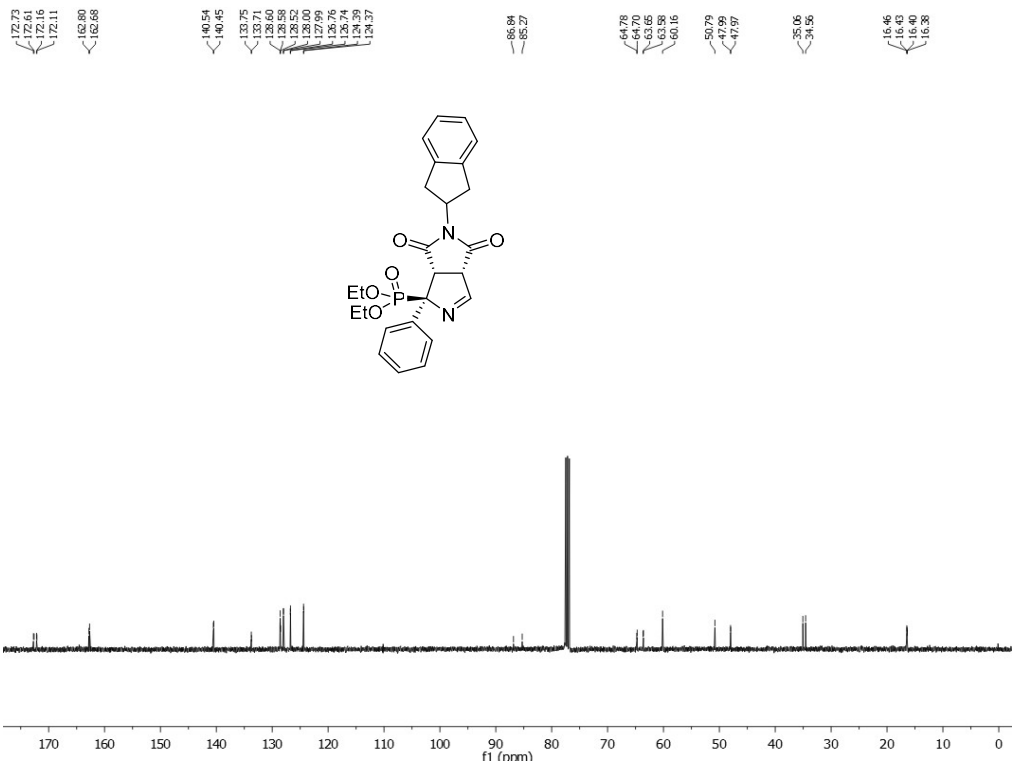

Diethyl (1*RS*,3a*SR*,6a*SR*)-5-(2,3-dihydro-1H-inden-2-yl)-4,6-dioxo-1-phenyl-1,3a,4,5,6,6a-hexahydropyrrolo[3,4-*c*]pyrrole-1-phosphonate (9m)

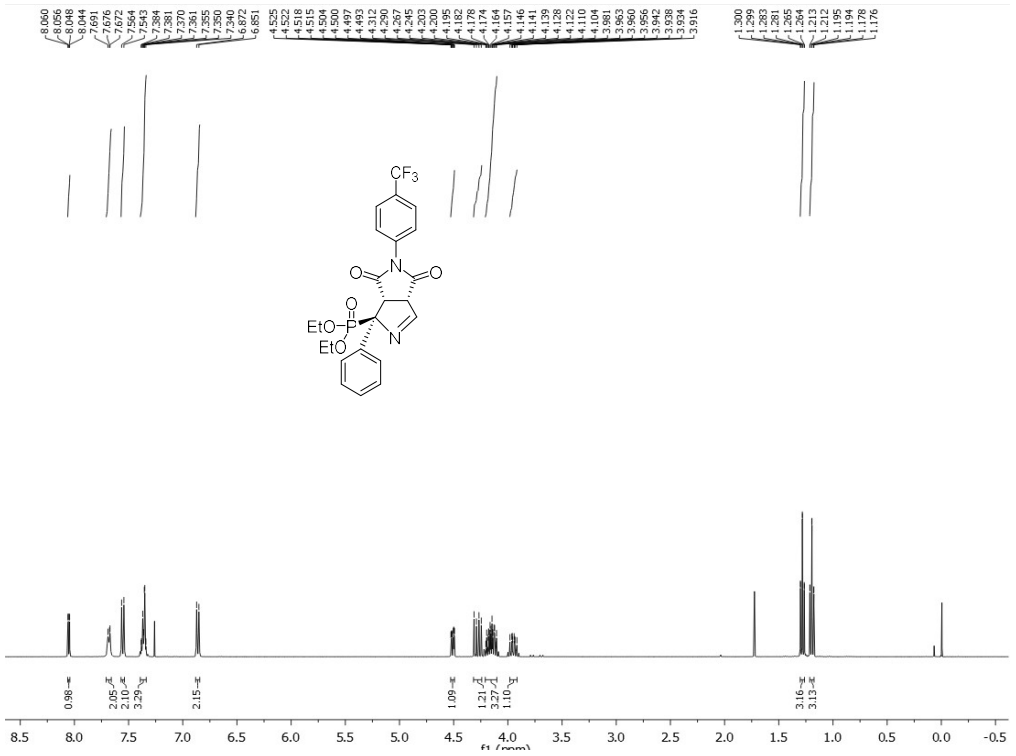

Diethyl (1*RS*,3a*SR*,6a*SR*)-4,6-dioxo-1-phenyl-5-[4-(trifluoromethyl)phenyl]-1,3a,4,5,6,6a-hexahydropyrrolo[3,4-*c*]pyrrole-1-phosphonate (9n)

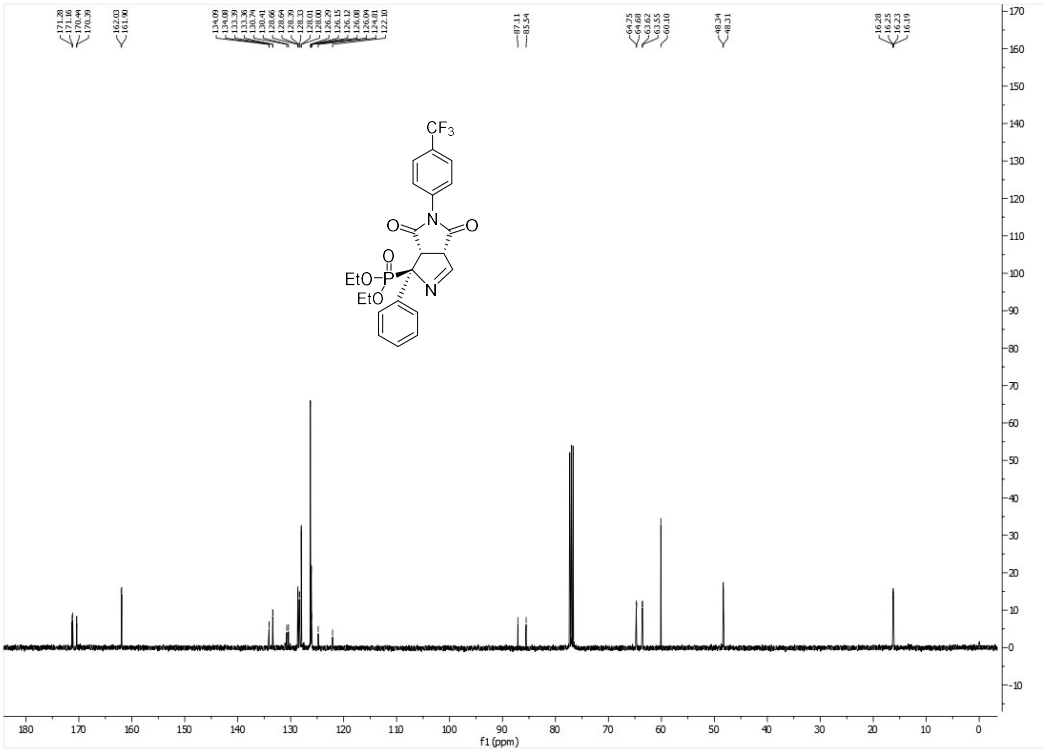

Diethyl (1*RS*,3a*SR*,6a*SR*)-4,6-dioxo-1-phenyl-5-[4-(trifluoromethyl)phenyl]-1,3a,4,5,6,6a-hexahydropyrrolo[3,4-*c*]pyrrole-1-phosphonate (9n)

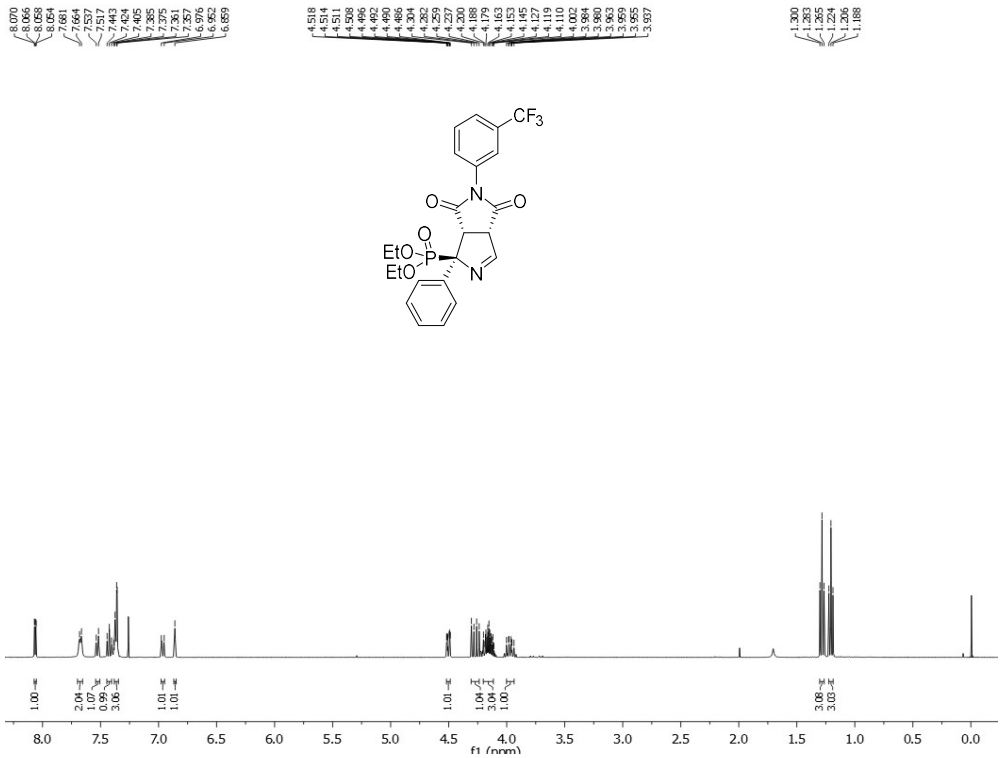

Diethyl (1*RS*,3a*SR*,6a*SR*)-4,6-dioxo-1-phenyl-5-[3-(trifluoromethyl)phenyl]-1,3a,4,5,6,6a-hexahydropyrrolo[3,4-*c*]pyrrole-1-phosphonate (9o)

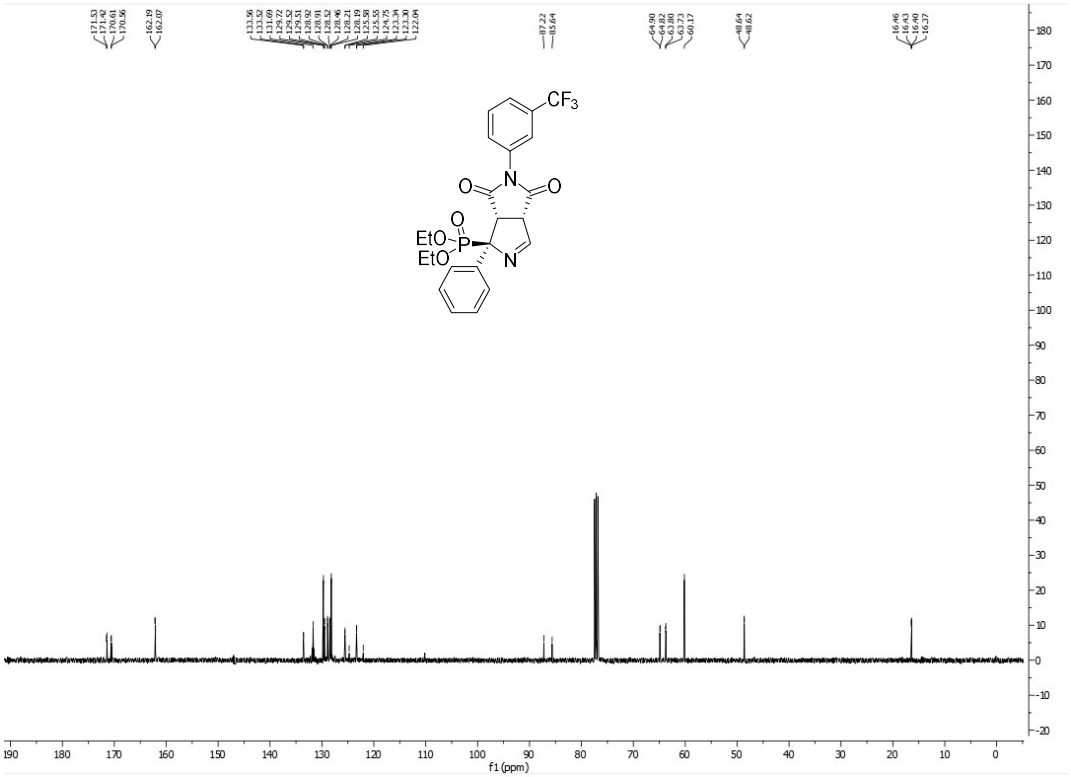

Diethyl (1*RS*,3a*SR*,6a*SR*)-4,6-dioxo-1-phenyl-5-[3-(trifluoromethyl)phenyl]-1,3a,4,5,6,6a-hexahydropyrrolo[3,4-*c*]pyrrole-1-phosphonate (9o)

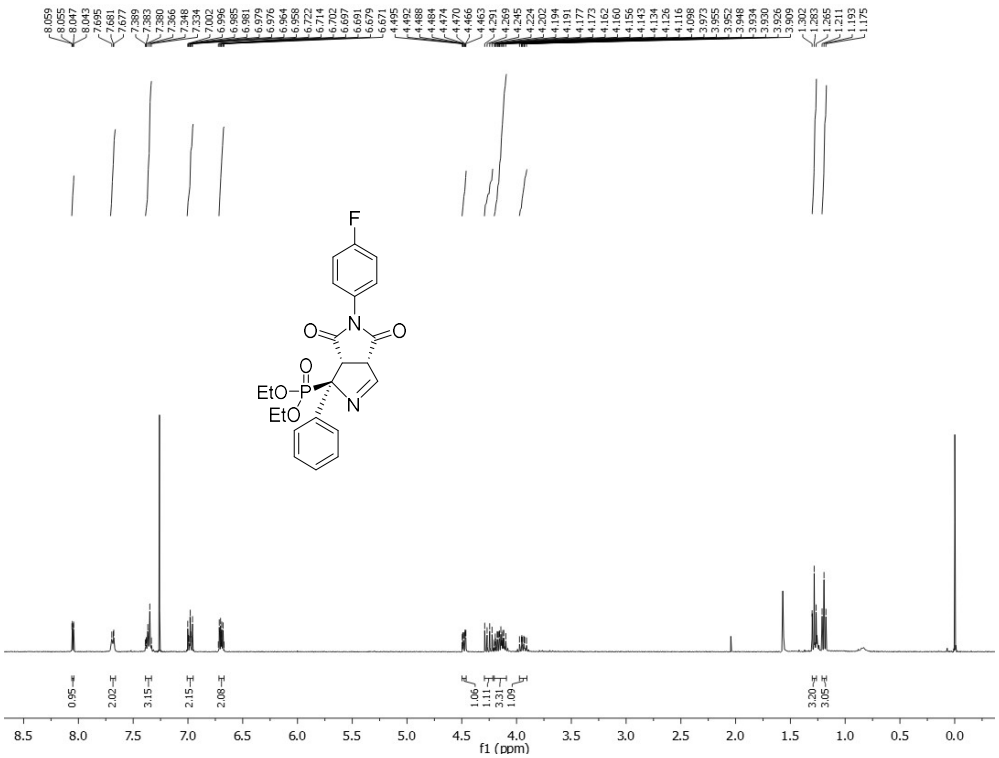

Diethyl (1*RS*,3a*SR*,6a*SR*)-5-(4-fluorophenyl)-4,6-dioxo-1-phenyl-1,3a,4,5,6,6a-hexahydropyrrolo[3,4-*c*]pyrrole-1-phosphonate (9p)

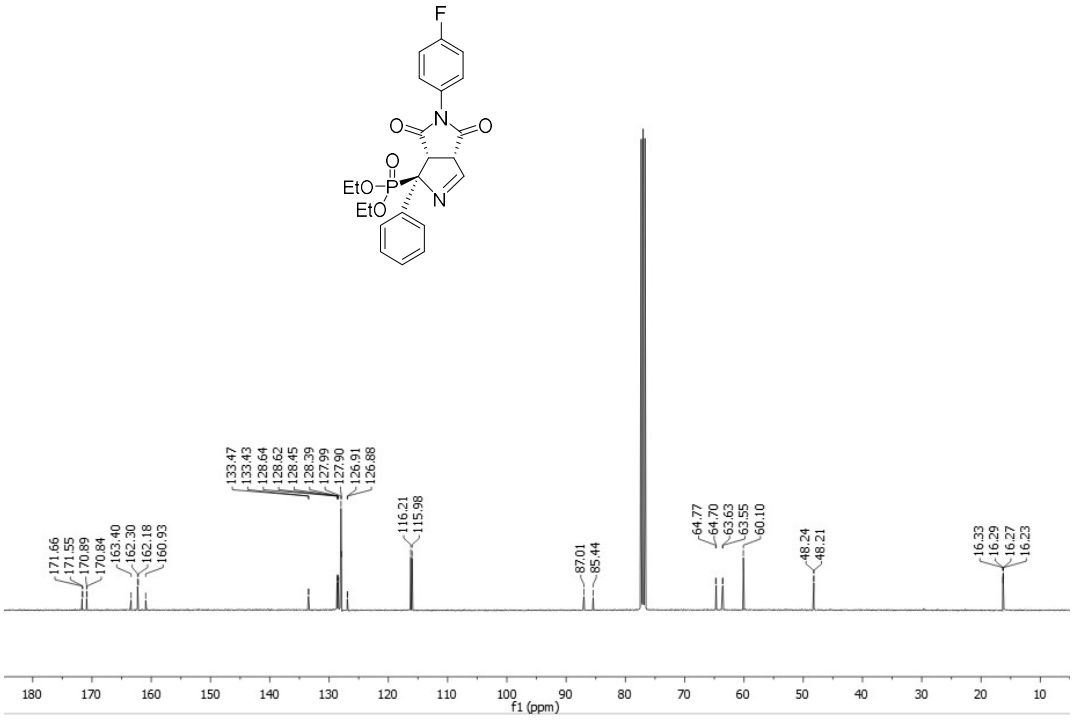

Diethyl (1*RS*,3a*SR*,6a*SR*)-5-(4-fluorophenyl)-4,6-dioxo-1-phenyl-1,3a,4,5,6,6a-hexahydropyrrolo[3,4-*c*]pyrrole-1-phosphonate (9p)

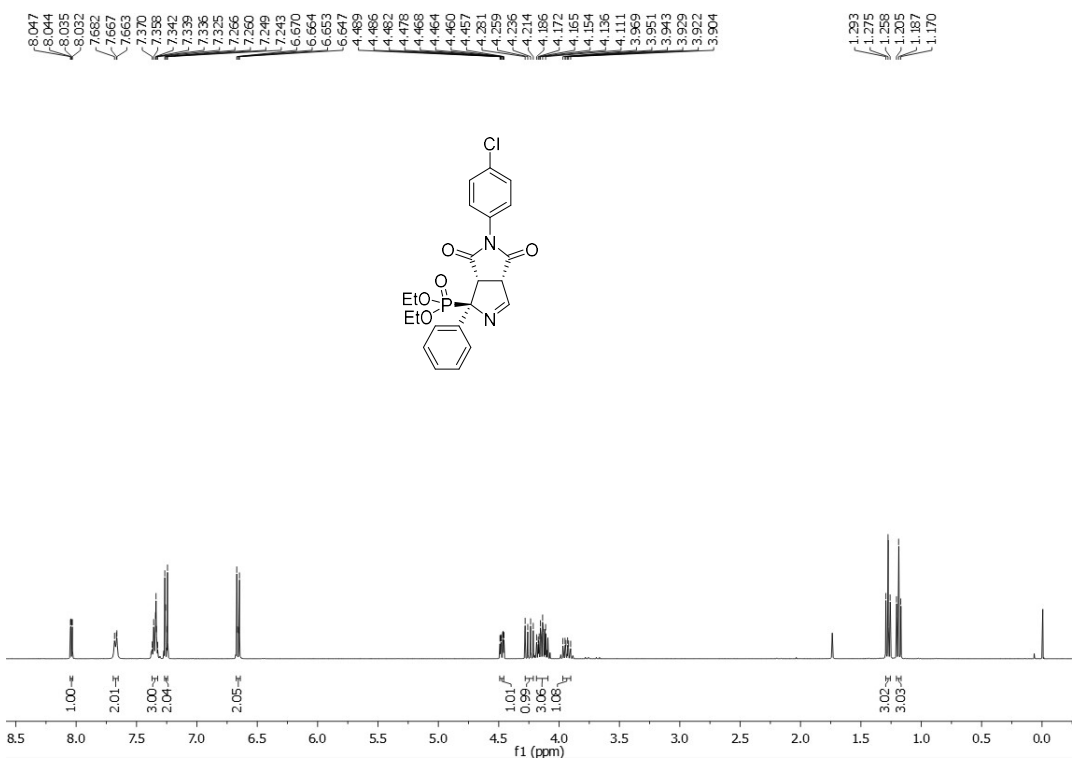

Diethyl (1*RS*,3a*SR*,6a*SR*)-5-(4-chlorophenyl)-4,6-dioxo-1-phenyl-1,3a,4,5,6,6a-hexahydropyrrolo[3,4-*c*]pyrrole-1-phosphonate (9q)

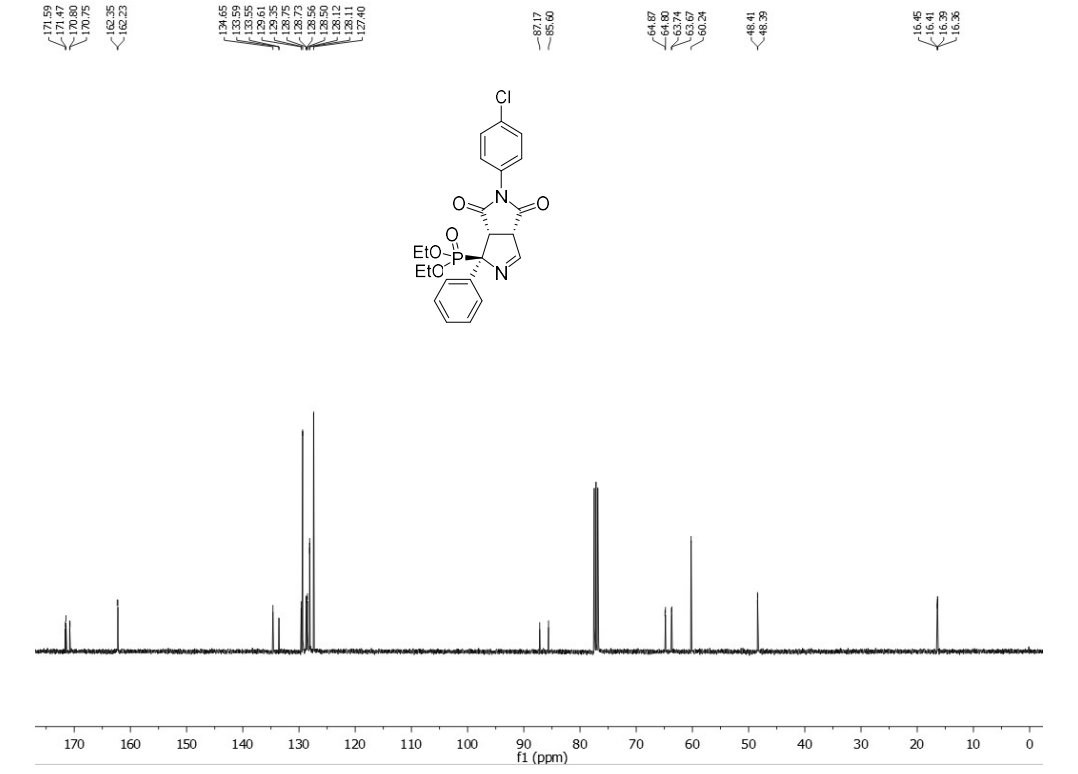

Diethyl (1*RS*,3a*SR*,6a*SR*)-5-(4-chlorophenyl)-4,6-dioxo-1-phenyl-1,3a,4,5,6,6a-hexahydropyrrolo[3,4-*c*]pyrrole-1-phosphonate (9q)

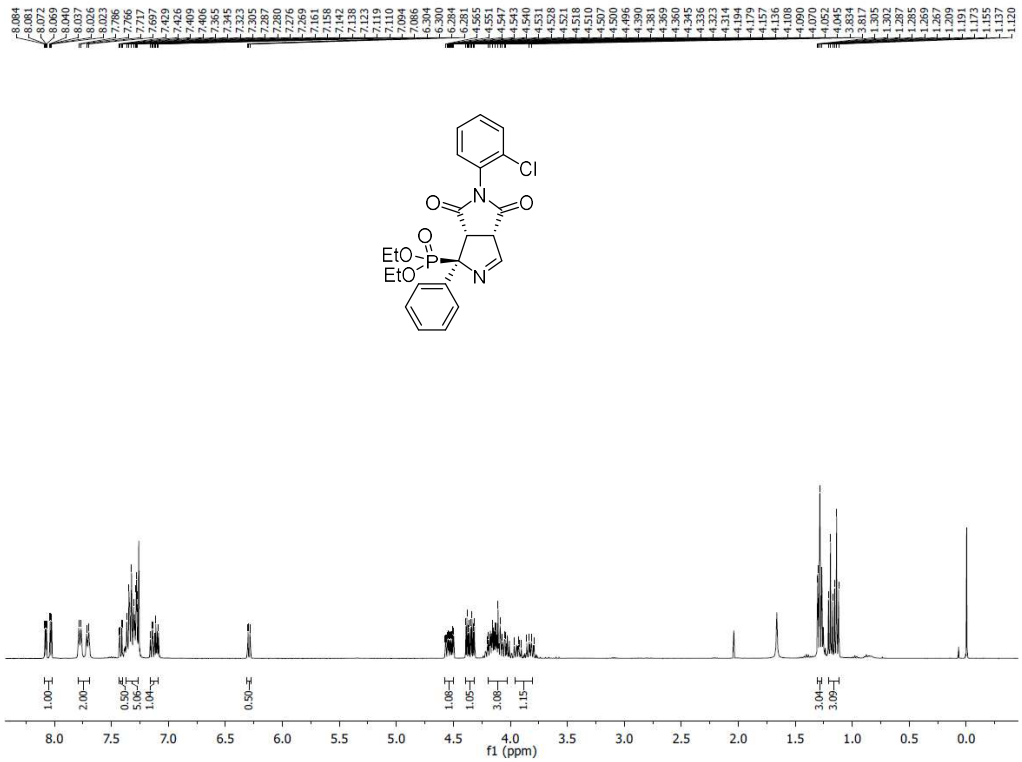

Diethyl (1*RS*,3a*SR*,6a*SR*)-5-(2-chlorophenyl)-4,6-dioxo-1-phenyl-1,3a,4,5,6,6a-hexahydropyrrolo[3,4-*c*]pyrrole-1-phosphonate (9r)

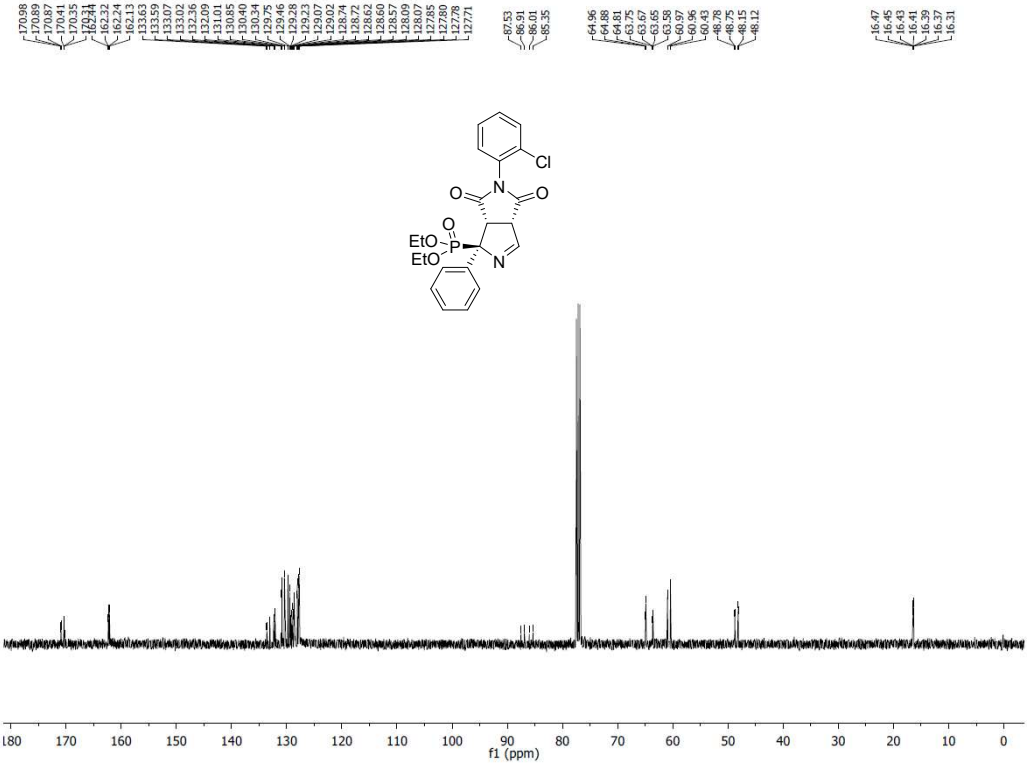

Diethyl (1*RS*,3a*SR*,6a*SR*)-5-(2-chlorophenyl)-4,6-dioxo-1-phenyl-1,3a,4,5,6,6a-hexahydropyrrolo[3,4-*c*]pyrrole-1-phosphonate (9r)

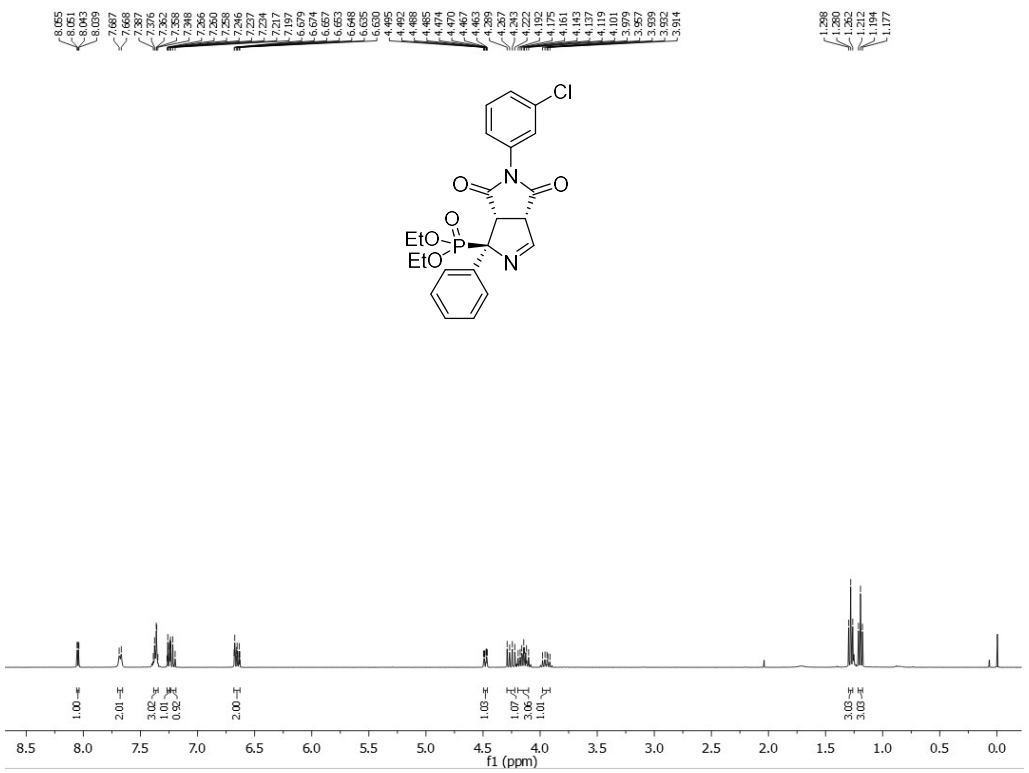

Diethyl (1*RS*,3a*SR*,6a*SR*)-5-(3-chlorophenyl)-4,6-dioxo-1-phenyl-1,3a,4,5,6,6a-hexahydropyrrolo[3,4-*c*]pyrrole-1-phosphonate (9s)

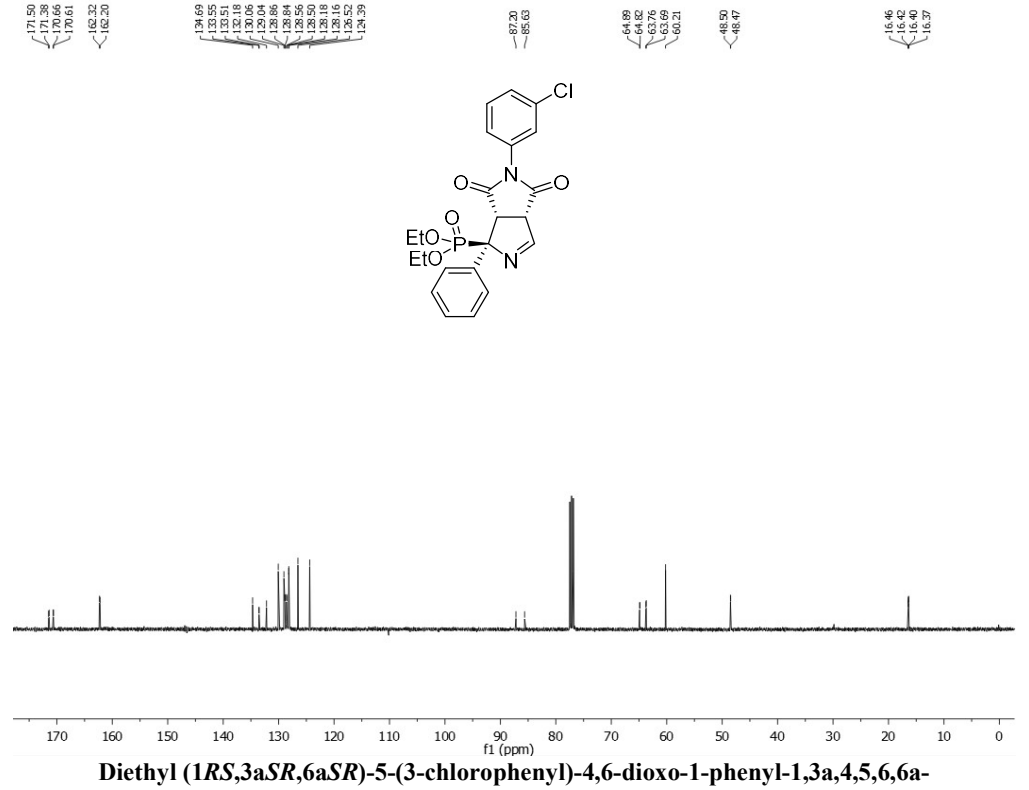

Diethyl (1*RS*,3a*SR*,6a*SR*)-5-(3-chlorophenyl)-4,6-dioxo-1-phenyl-1,3a,4,5,6,6a-hexahydropyrrolo[3,4-*c*]pyrrole-1-phosphonate (9s)

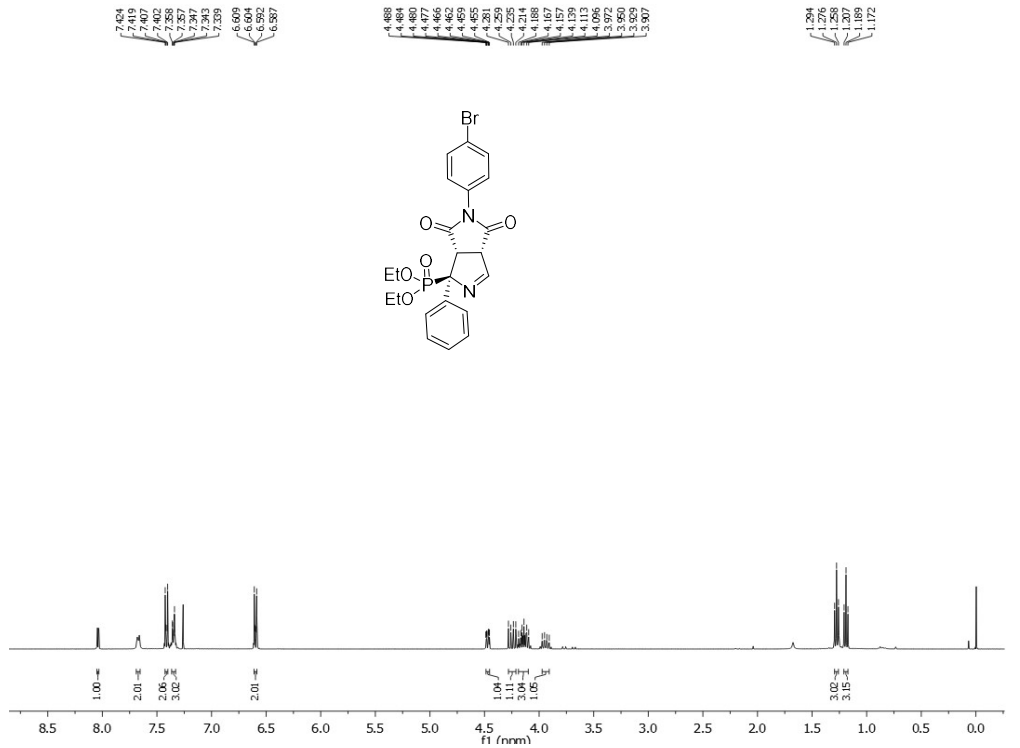

Diethyl (1*RS*,3a*SR*,6a*SR*)-5-(4-bromophenyl)-4,6-dioxo-1-phenyl-1,3a,4,5,6,6a-hexahydropyrrolo[3,4-*c*]pyrrole-1-phosphonate (9t)

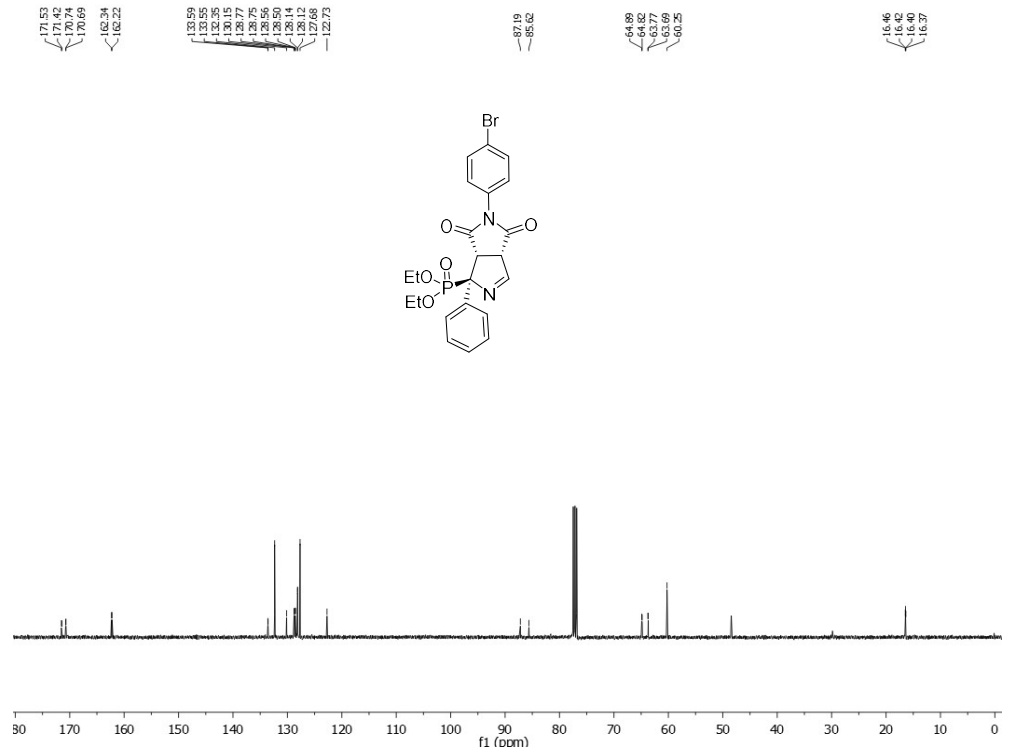

Diethyl (1*RS*,3a*SR*,6a*SR*)-5-(4-bromophenyl)-4,6-dioxo-1-phenyl-1,3a,4,5,6,6a-hexahydropyrrolo[3,4-*c*]pyrrole-1-phosphonate (9t)

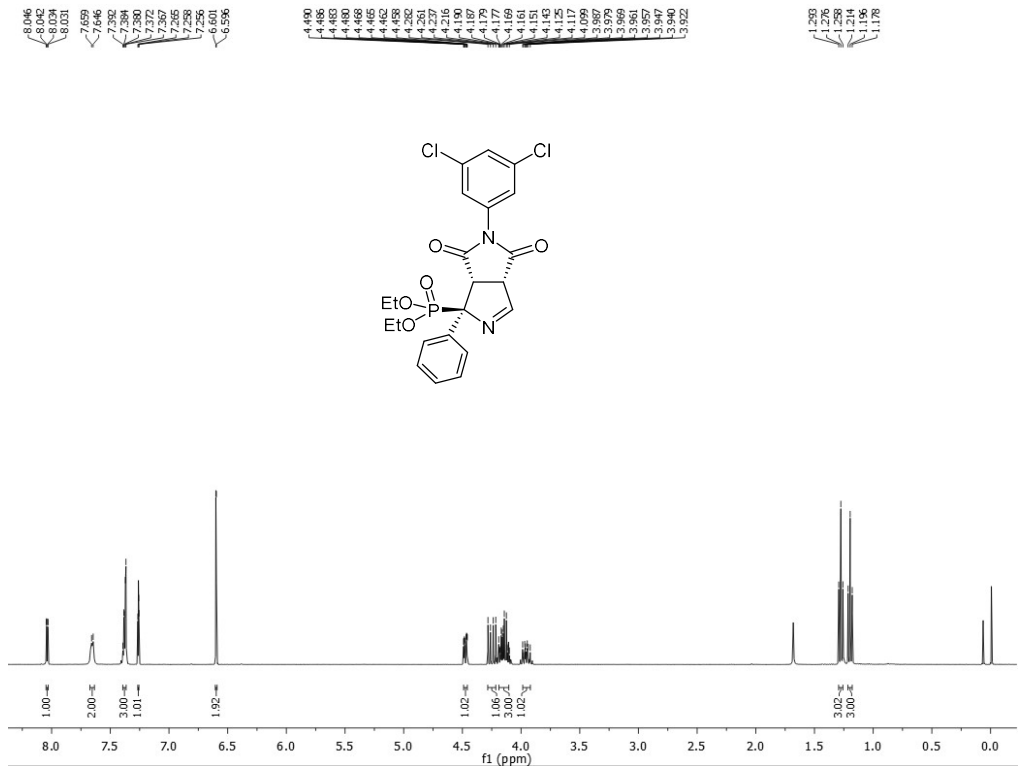

Diethyl (1*RS*,3a*SR*,6a*SR*)-5-(3,5-dichlorophenyl)-4,6-dioxo-1-phenyl-1,3a,4,5,6,6a-hexahydropyrrolo[3,4-*c*]pyrrole-1-phosphonate (9u)

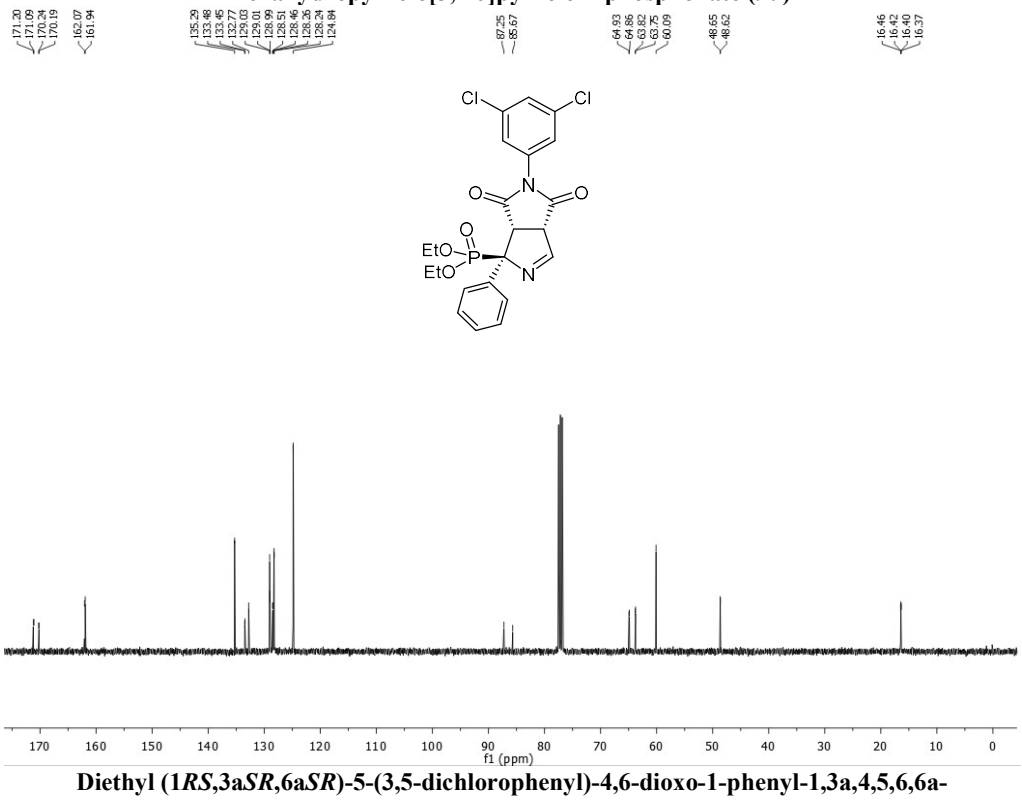

Diethyl (1*RS*,3a*SR*,6a*SR*)-5-(3,5-dichlorophenyl)-4,6-dioxo-1-phenyl-1,3a,4,5,6,6a-hexahydropyrrolo[3,4-*c*]pyrrole-1-phosphonate (9u)

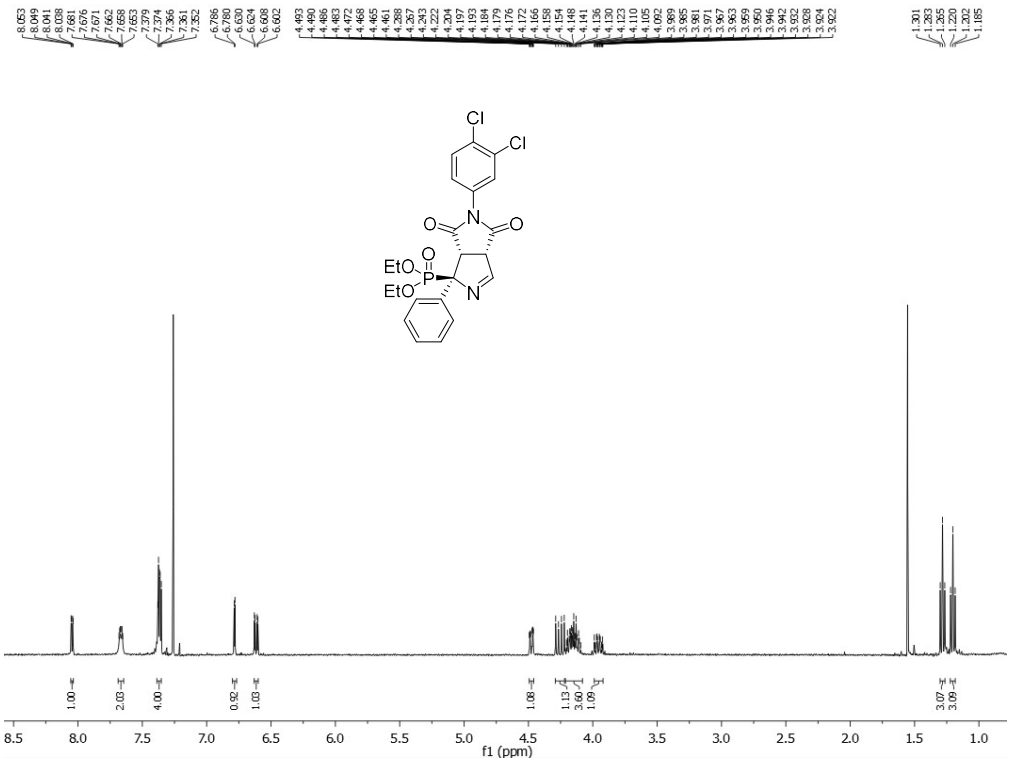

Diethyl (1*RS*,3a*SR*,6a*SR*)-5-(3,4-dichlorophenyl)-4,6-dioxo-1-phenyl-1,3a,4,5,6,6a-hexahydropyrrolo[3,4-*c*]pyrrole-1-phosphonate (9v)

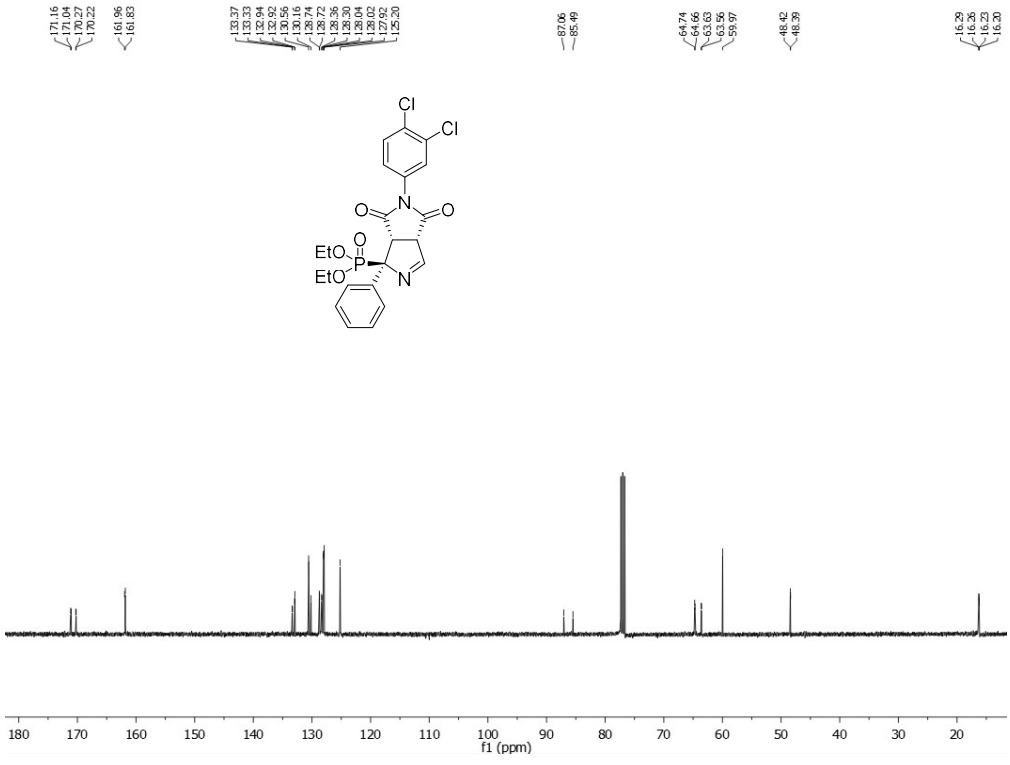

Diethyl (1*RS*,3a*SR*,6a*SR*)-5-(3,4-dichlorophenyl)-4,6-dioxo-1-phenyl-1,3a,4,5,6,6a-hexahydropyrrolo[3,4-*c*]pyrrole-1-phosphonate (9v)

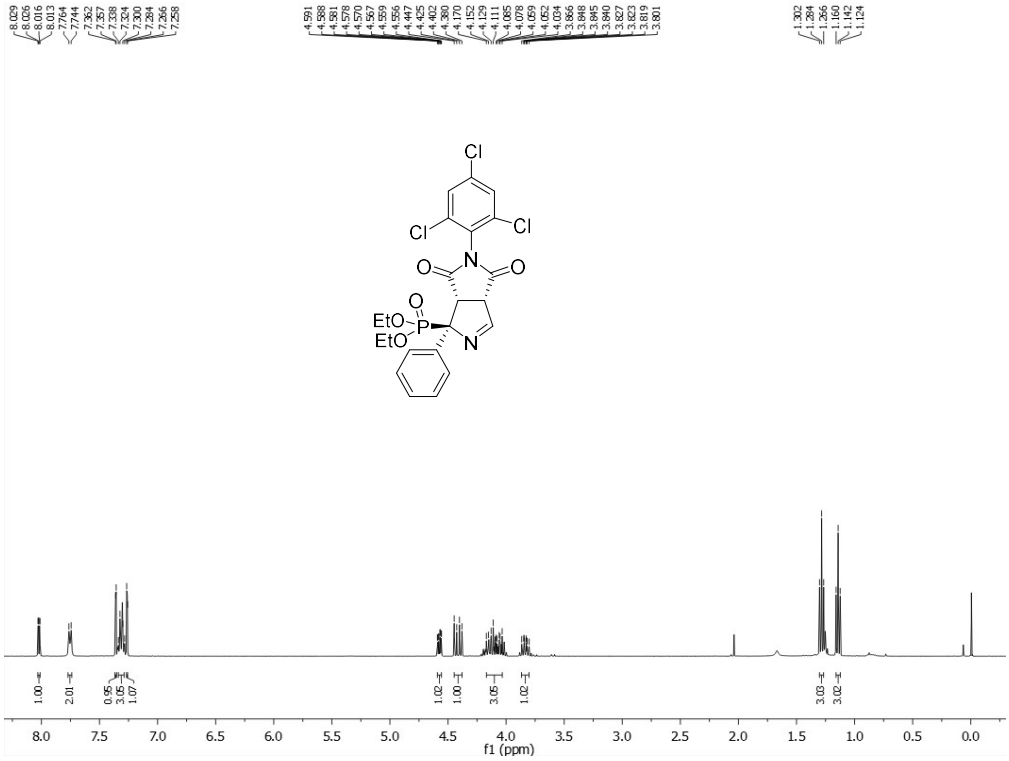

Diethyl (1*RS*,3a*SR*,6a*SR*)-4,6-dioxo-1-phenyl-5-(2,4,6-trichlorophenyl)-1,3a,4,5,6,6a-hexahydropyrrolo[3,4-*c*]pyrrole-1-phosphonate (9w)

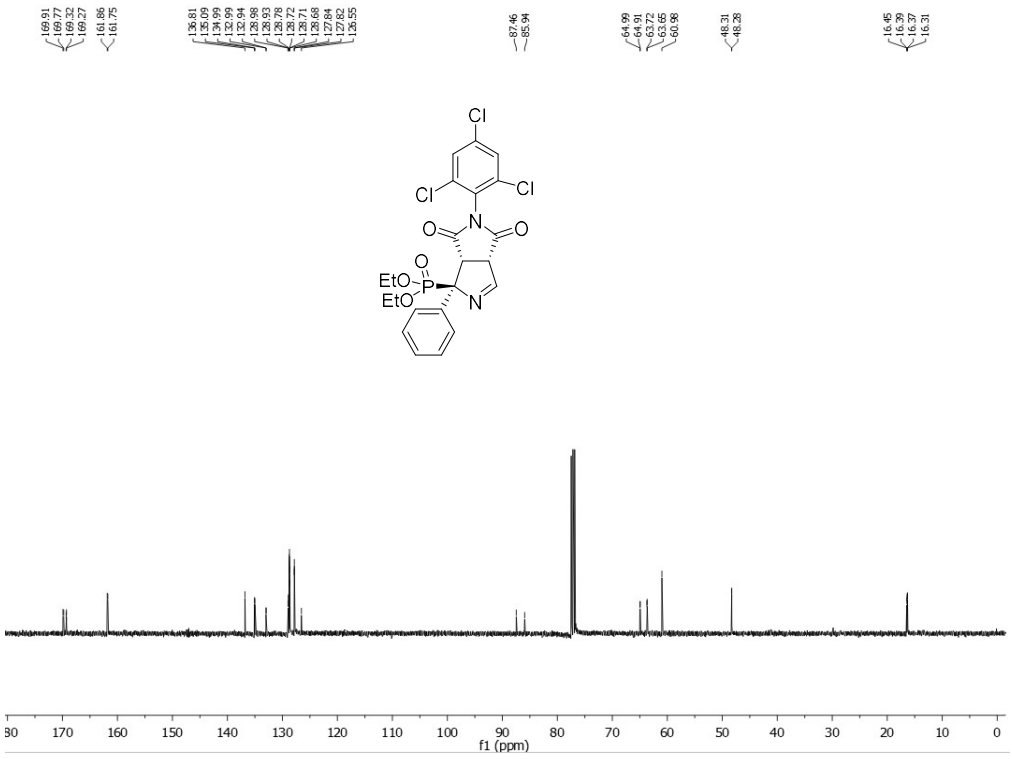

Diethyl (1*RS*,3a*SR*,6a*SR*)-4,6-dioxo-1-phenyl-5-(2,4,6-trichlorophenyl)-1,3a,4,5,6,6a-hexahydropyrrolo[3,4-*c*]pyrrole-1-phosphonate (9w)

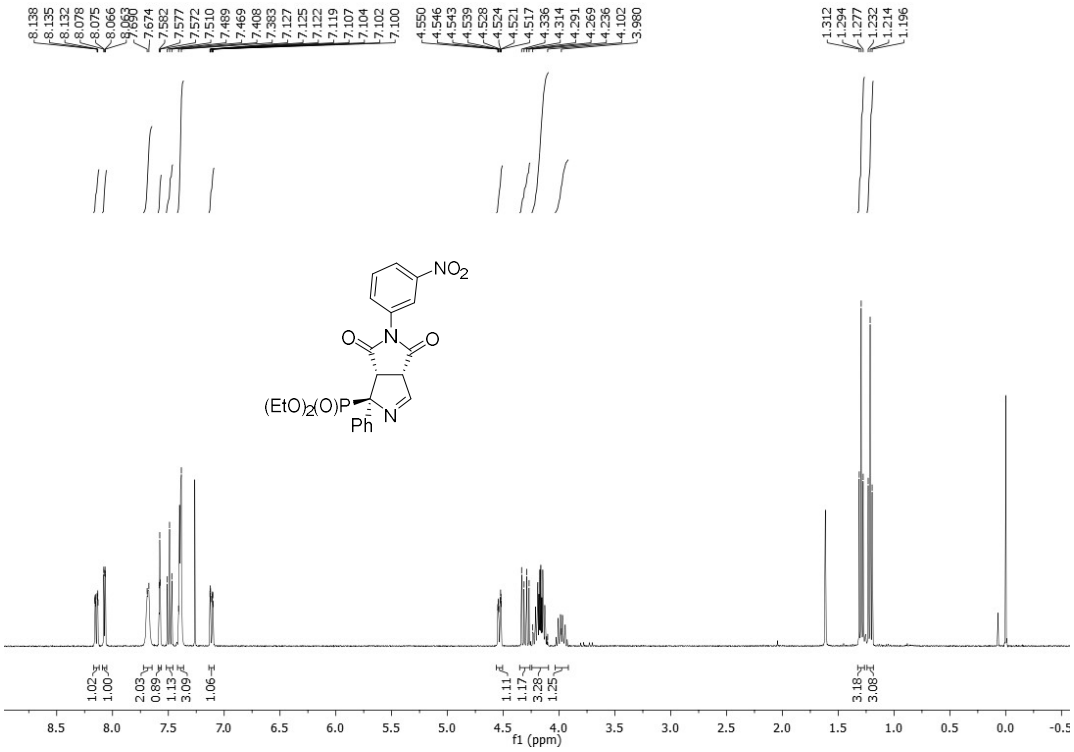

Diethyl (1*RS*,3a*SR*,6a*SR*)-5-(3-nitrophenyl)-4,6-dioxo-1-phenyl-1,3a,4,5,6,6a-hexahydropyrrolo[3,4-*c*]pyrrole-1-phosphonate (9x)

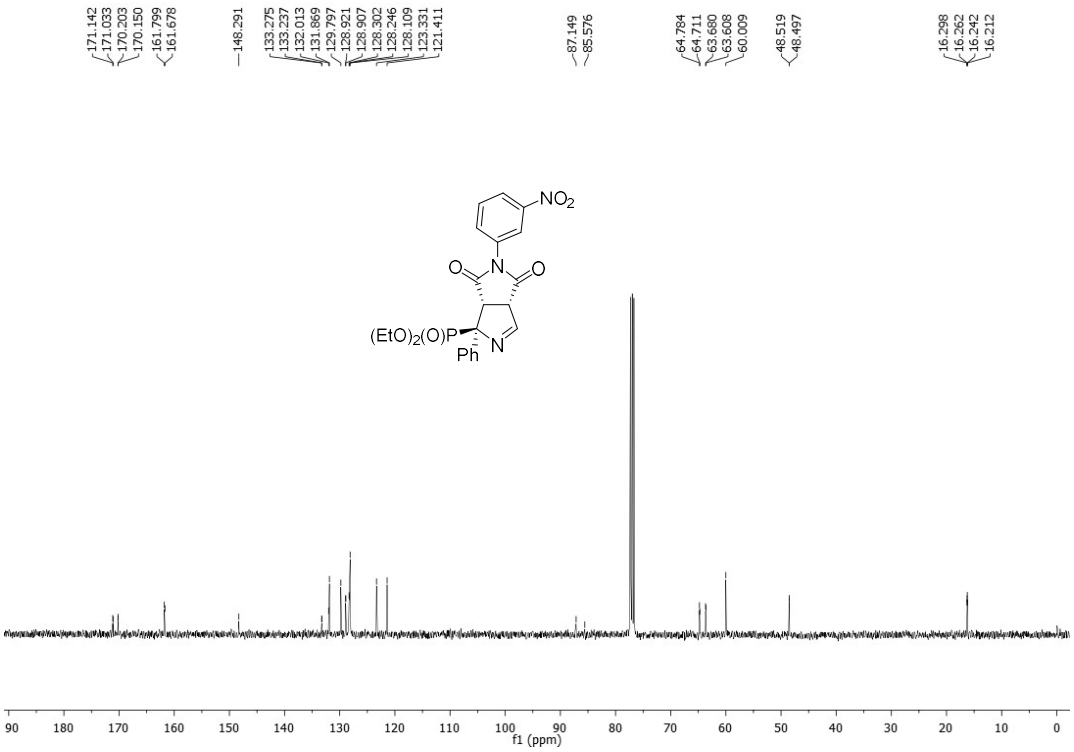

Diethyl (1*RS*,3a*SR*,6a*SR*)-5-(3-nitrophenyl)-4,6-dioxo-1-phenyl-1,3a,4,5,6,6a-hexahydropyrrolo[3,4-*c*]pyrrole-1-phosphonate (9x)

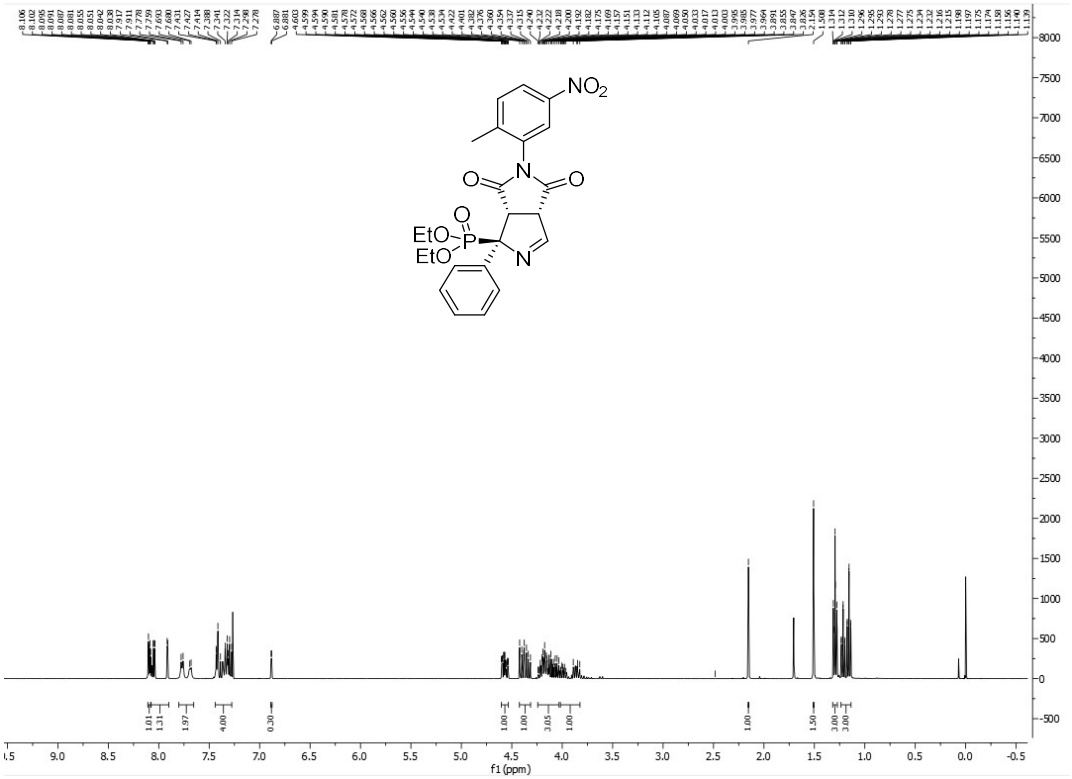

Diethyl (1*RS*,3a*SR*,6a*SR*)-5-(2-methyl-5-nitrophenyl)-4,6-dioxo-1-phenyl-1,3a,4,5,6,6a-hexahydropyrrolo[3,4-*c*]pyrrole-1-phosphonate(9y)

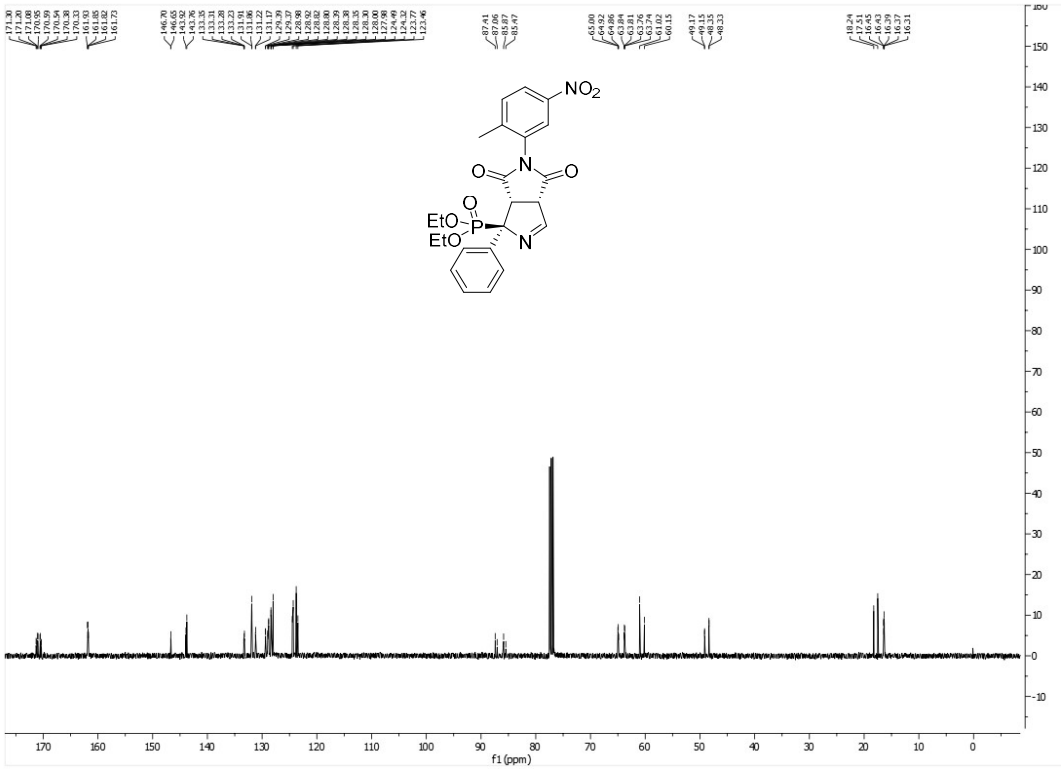

Diethyl (1*RS*,3a*SR*,6a*SR*)-5-(2-methyl-5-nitrophenyl)-4,6-dioxo-1-phenyl-1,3a,4,5,6,6a-hexahydropyrrolo[3,4-*c*]pyrrole-1-phosphonate(9y)

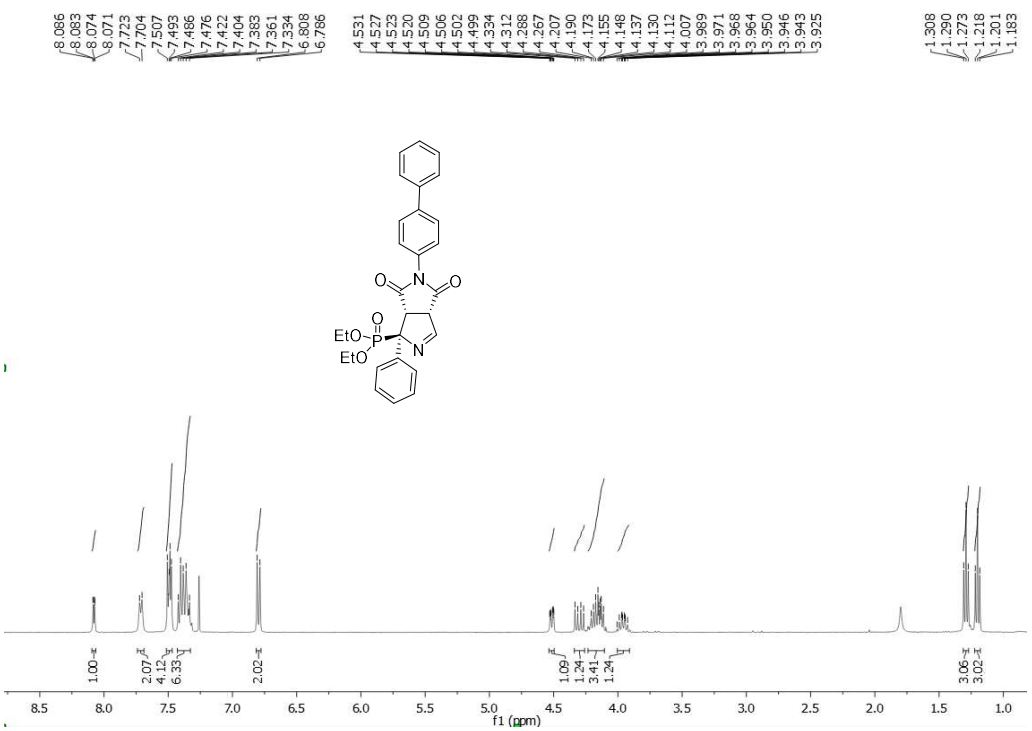

Diethyl (1*RS*,3*aSR*,6*aSR*)-5-(1,1'-biphenyl)-4-yl-4,6-dioxo-1-phenyl-1,3a,4,5,6,6a-hexahydropyrrolo[3,4-c]pyrrole-1-phosphonate (9z)

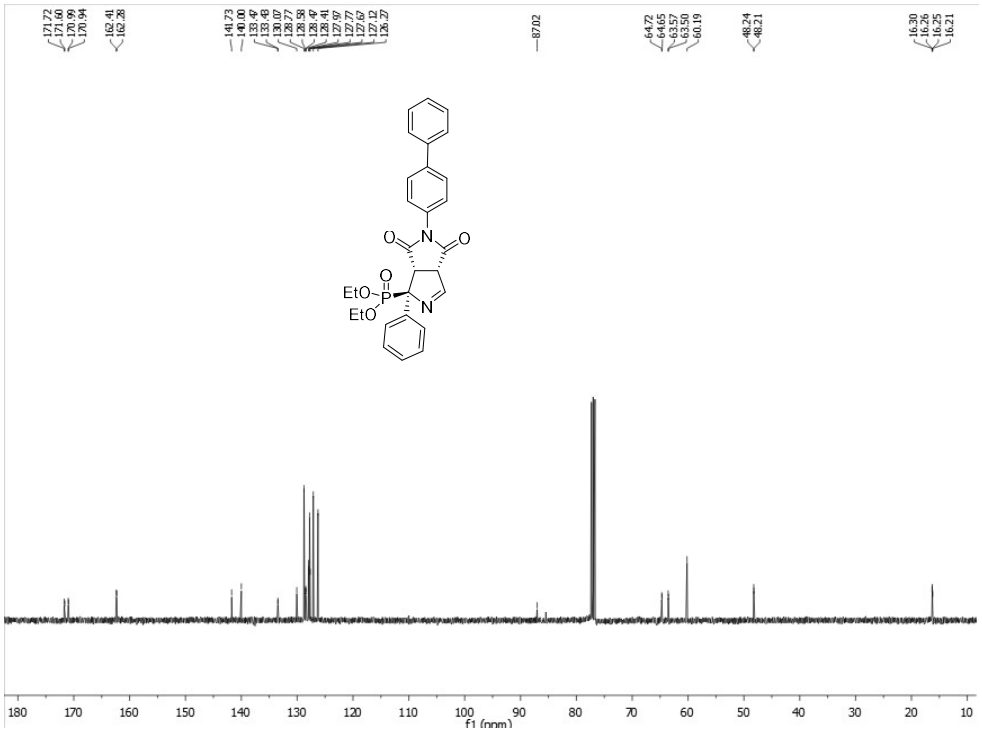

Diethyl (1*RS*,3*aSR*,6*aSR*)-5-(1,1'-biphenyl)-4-yl-4,6-dioxo-1-phenyl-1,3a,4,5,6,6a-hexahydropyrrolo[3,4-c]pyrrole-1-phosphonate (9z)

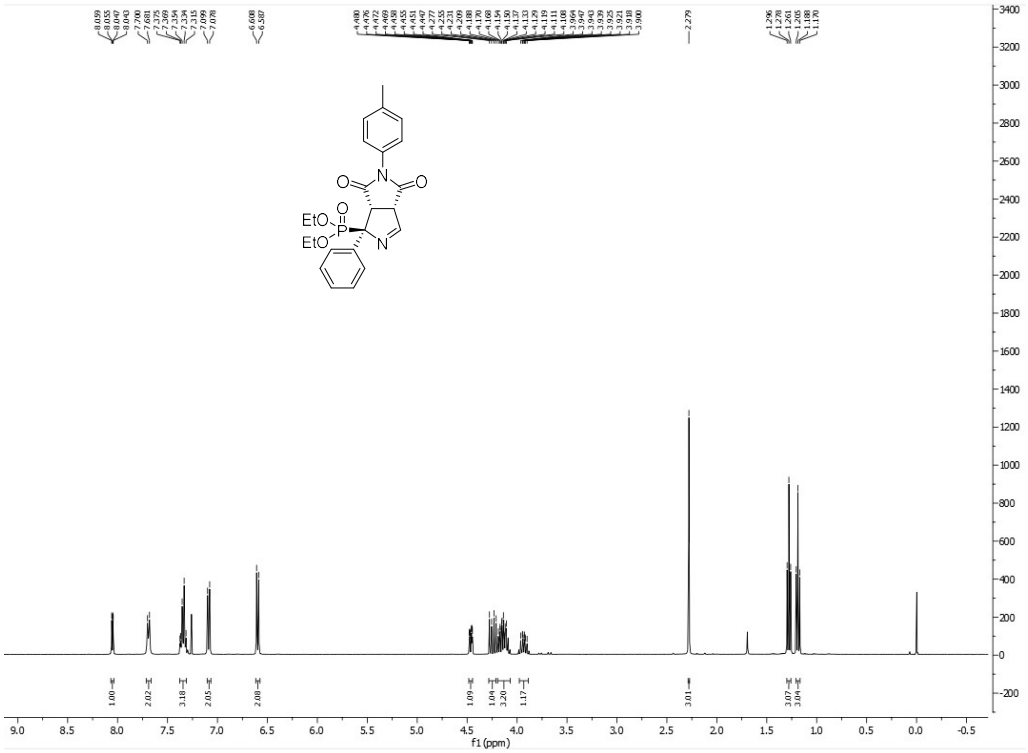

Diethyl (1*RS*,3a*SR*,6a*SR*)-4,6-dioxo-1-phenyl-5-(p-tolyl)-1,3a,4,5,6,6a-hexahydropyrrolo[3,4-*c*]pyrrole-1-phosphonate (9aa)

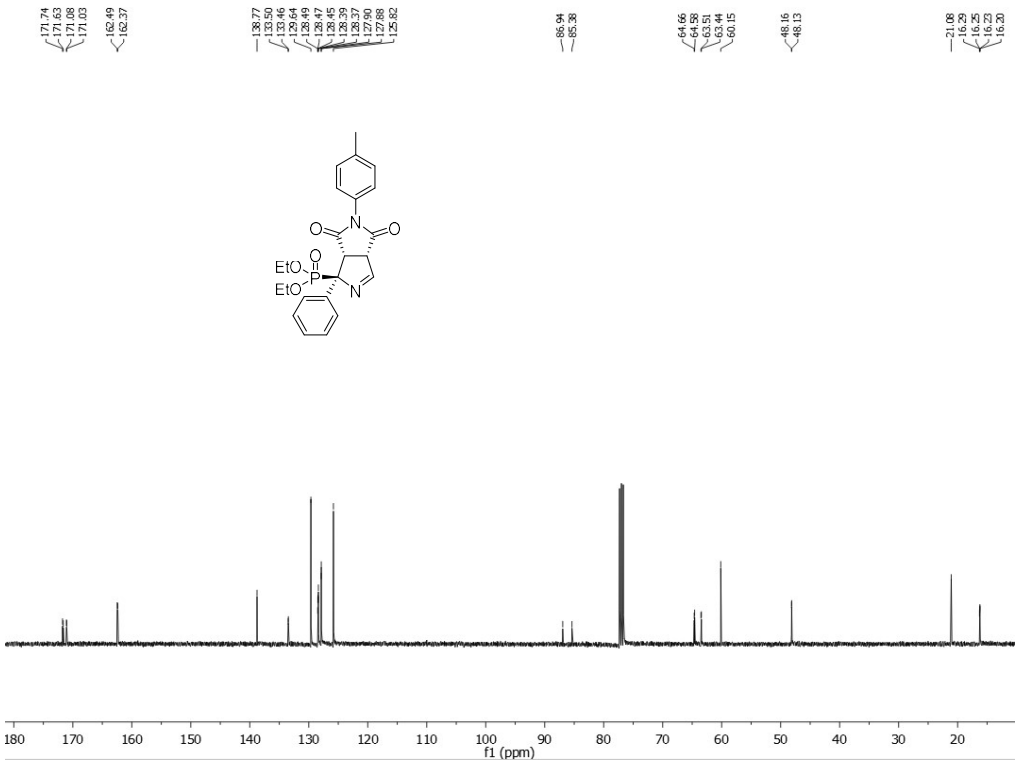

Diethyl (1*RS*,3a*SR*,6a*SR*)-4,6-dioxo-1-phenyl-5-(p-tolyl)-1,3a,4,5,6,6a-hexahydropyrrolo[3,4-*c*]pyrrole-1-phosphonate (9aa)

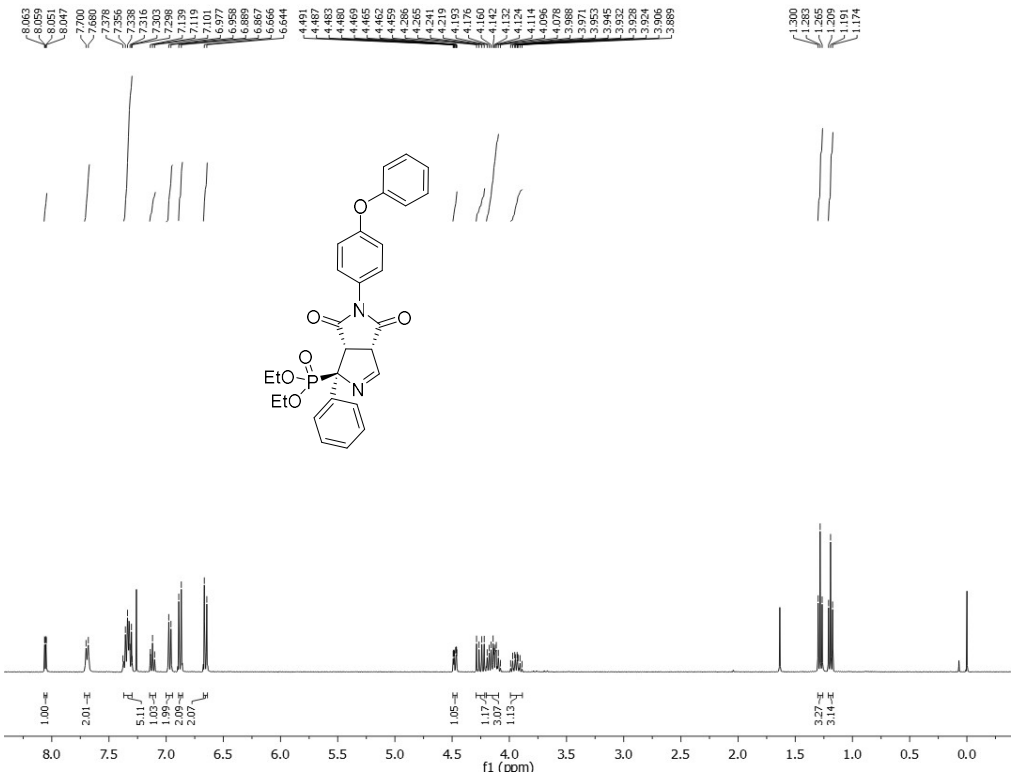

Diethyl (1*RS*,3a*SR*,6a*SR*)-4,6-dioxo-5-(4-phenoxyphenyl)-1-phenyl-1,3a,4,5,6,6a-hexahydropyrrolo[3,4-*c*]pyrrole-1-phosphonate (9ab)

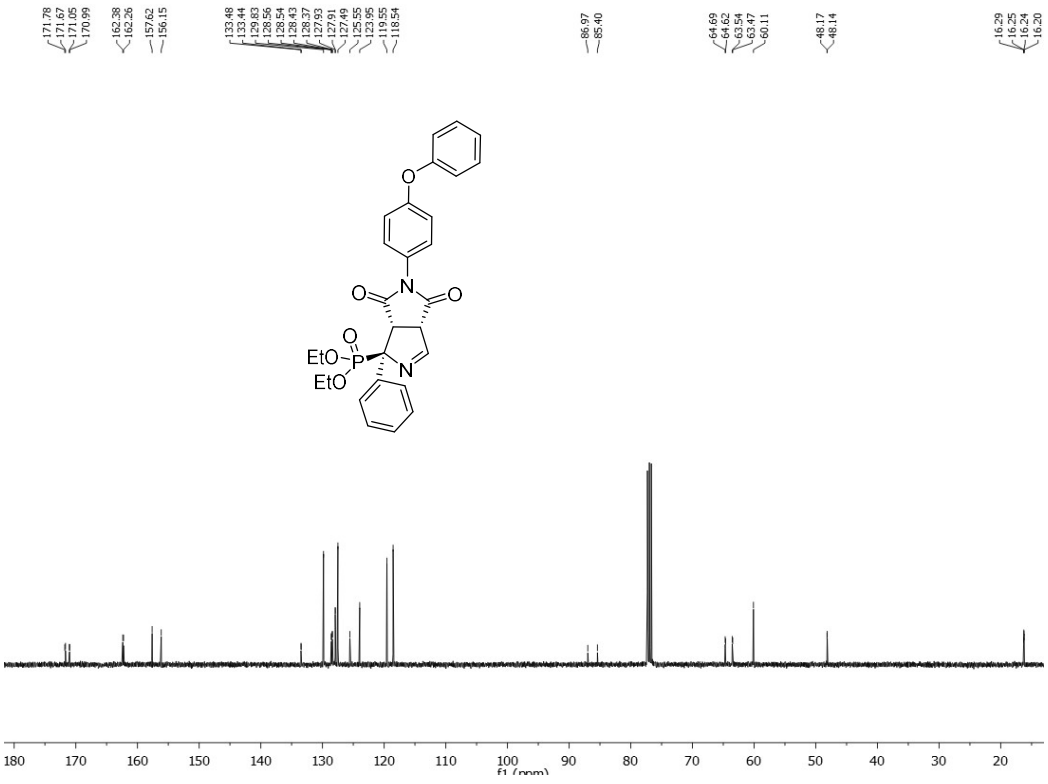

Diethyl (1*RS*,3a*SR*,6a*SR*)-4,6-dioxo-5-(4-phenoxyphenyl)-1-phenyl-1,3a,4,5,6,6a-hexahydropyrrolo[3,4-*c*]pyrrole-1-phosphonate (9ab)

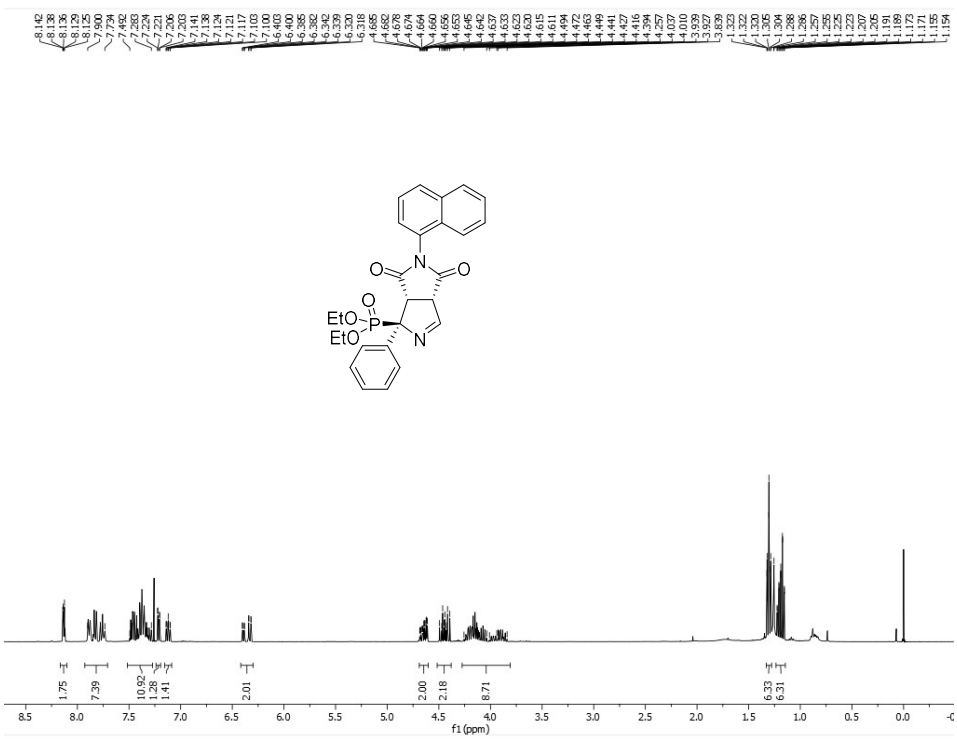

Diethyl (1*RS*,3a*SR*,6a*SR*)-5-(naphth-1-yl)-4,6-dioxo-1-phenyl-1,3a,4,5,6,6a-hexahydropyrrolo[3,4-*c*]pyrrole-1-phosphonate (9ac)

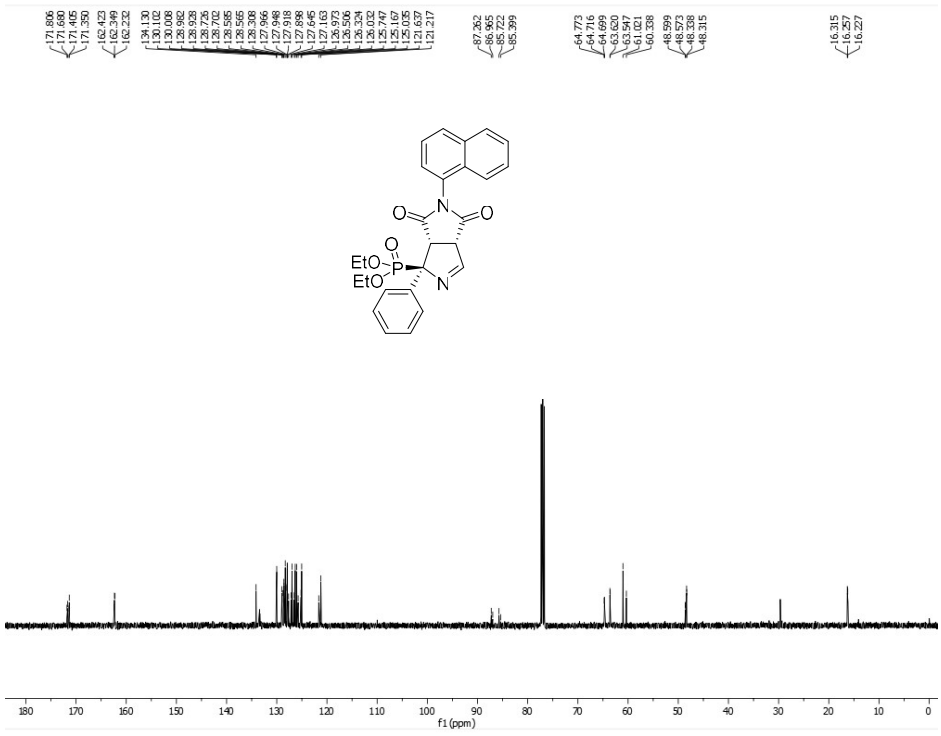

Diethyl (1*RS*,3a*SR*,6a*SR*)-5-(naphth-1-yl)-4,6-dioxo-1-phenyl-1,3a,4,5,6,6a-hexahydropyrrolo[3,4-*c*]pyrrole-1-phosphonate (9ac)

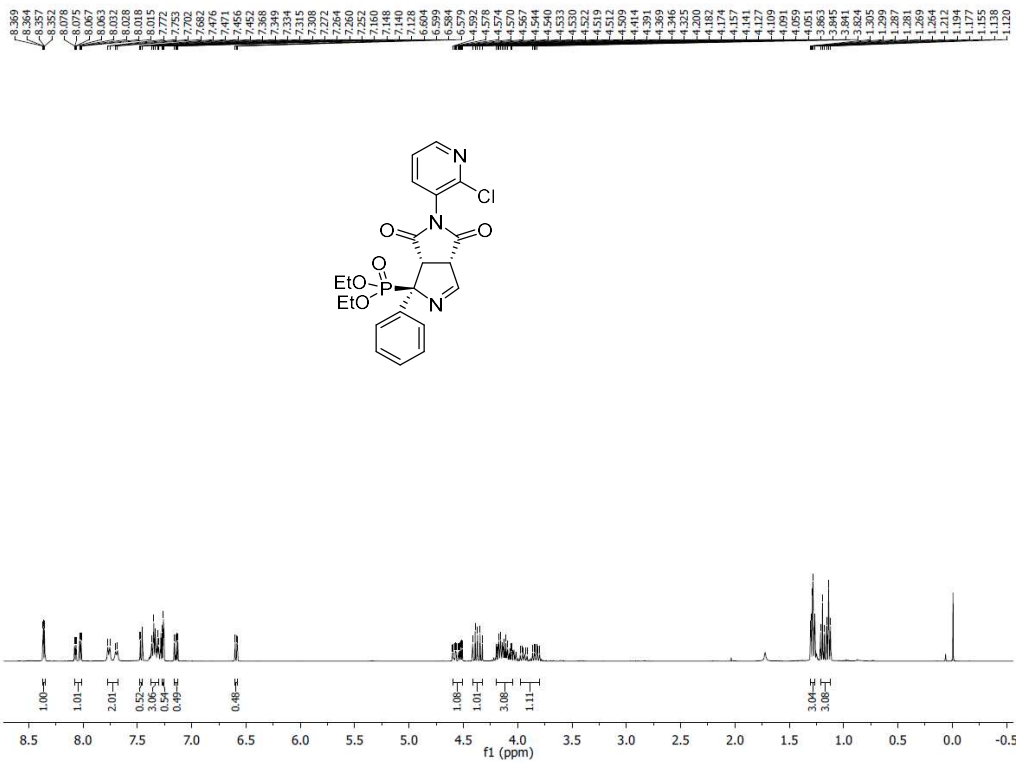

Diethyl (1*RS*,3a*SR*,6a*SR*)-5-(2-chloropyridin-3-yl)-4,6-dioxo-1-phenyl-1,3a,4,5,6,6a-hexahydropyrrolo[3,4-*c*]pyrrole-1-phosphonate (9ad)

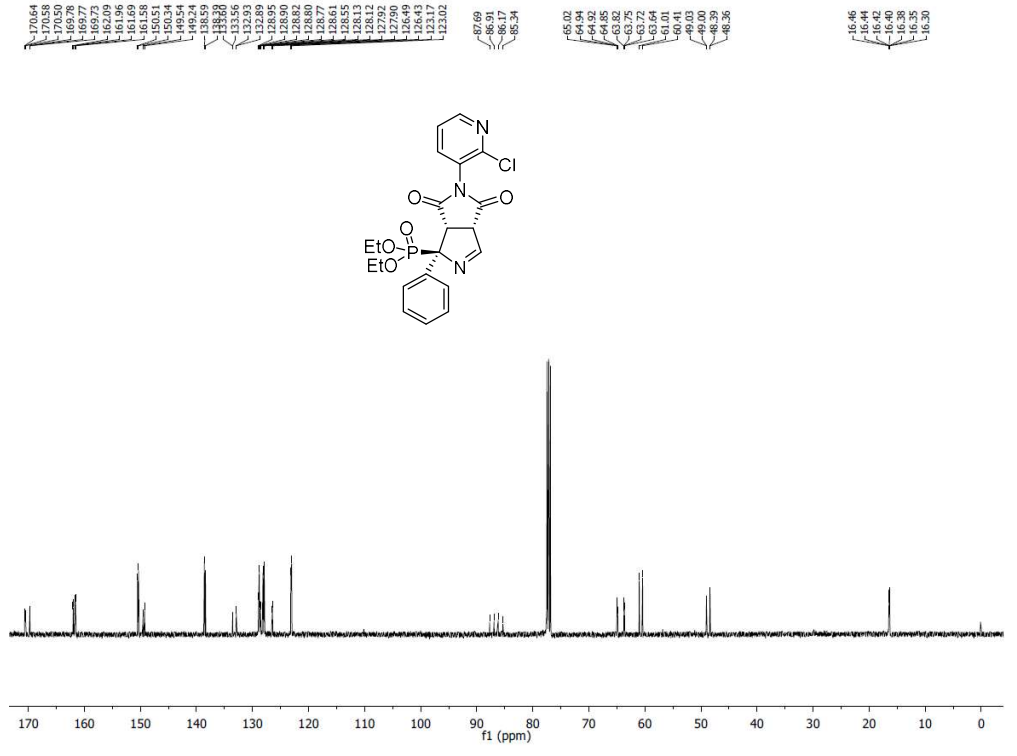

Diethyl (1*RS*,3a*SR*,6a*SR*)-5-(2-chloropyridin-3-yl)-4,6-dioxo-1-phenyl-1,3a,4,5,6,6a-hexahydropyrrolo[3,4-*c*]pyrrole-1-phosphonate (B9ad)

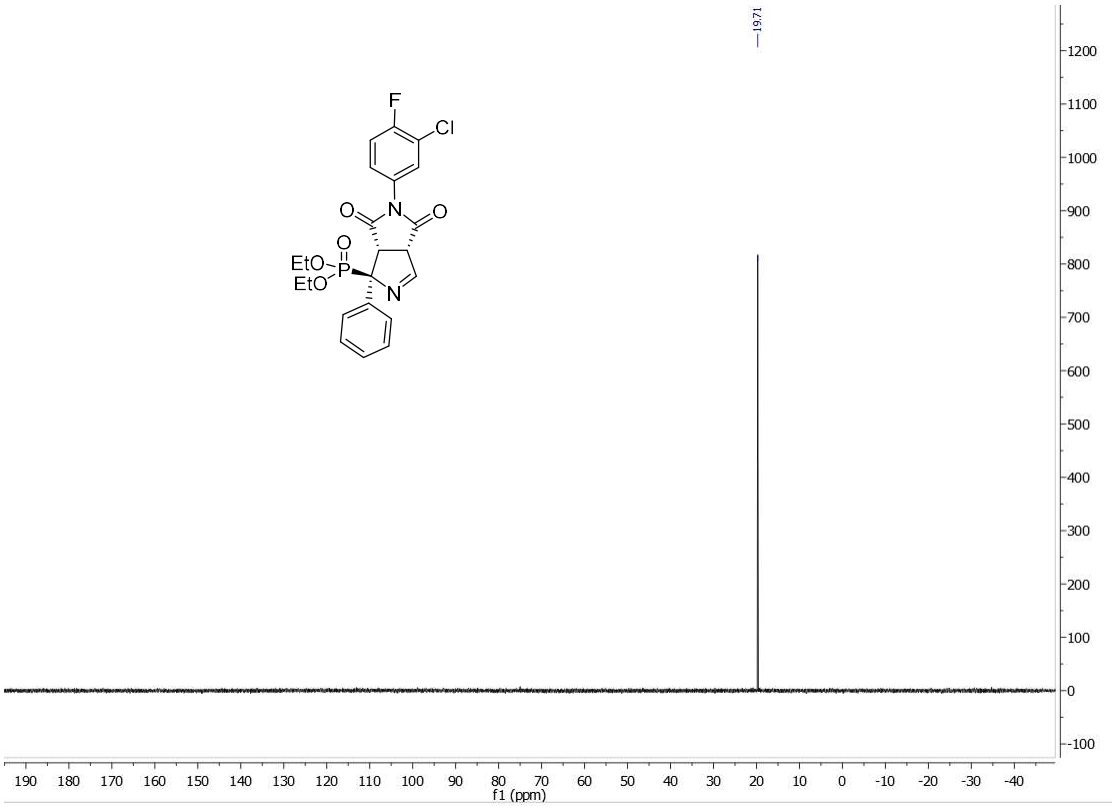

Diethyl (1*RS*,3a*SR*,6a*SR*)-5-(3-chloro-4-fluorophenyl)-4,6-dioxo-1-phenyl-1,3a,4,5,6,6a-hexahydropyrrolo[3, 4-*c*]pyrrole-1-phosphonate (9d)

Diethyl (1*RS*,3a*SR*,6a*SR*)-5-cyclohexyl-4,6-dioxo-1-phenyl-1,3a,4,5,6,6a-hexahydropyrrolo[3,4-*c*]pyrrole-1-phosphonate (9b): Deposition number: 1960886

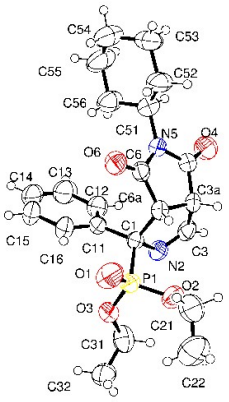

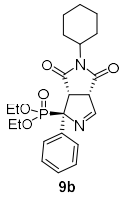

9b

Table 1. Crystal data and structure refinement for **9b**.

Identification code	Jb135	
Empirical formula	C22 H29 N2 O5 P	
Formula weight	432.44	
Temperature	294(2) K	
Wavelength	0.71073 Å	
Crystal system	Monoclinic	
Space group	P 21/n	
Unit cell dimensions	a = 15.0774(9) Å	α= 90°.
	b = 9.6740(6) Å	β= 97.8160(10)°.
	c = 15.2961(9) Å	γ = 90°.
Volume	2210.3(2) Å^3	
Z	4	
Density (calculated)	1.299 Mg/m^3	
Absorption coefficient	0.160 mm^{-1}	
F(000)	920	
Crystal size	0.27 x 0.24 x 0.29 mm^3	
Theta range for data collection	2.040 to 30.486°.	
Index ranges	-21<=h<=16, -13<=k<=13, -14<=l<=21	
Reflections collected	12714	
Independent reflections	5178 [R(int) = 0.0311]	
Completeness to theta = 25.242°	72.9 %	
Refinement method	Full-matrix least-squares on F^2	
Data / restraints / parameters	5178 / 0 / 273	
Goodness-of-fit on F^2	0.864	
Final R indices [I>2sigma(I)]	R1 = 0.0620, wR2 = 0.1659	
R indices (all data)	R1 = 0.1119, wR2 = 0.1874	
Largest diff. peak and hole	0.364 and -0.217 e.Å^{-3}	

Table 2. Atomic coordinates (x 10^4) and equivalent isotropic displacement parameters ($Å^2$x 10^3) for **9b** U(eq) is defined as one third of the trace of the orthogonalized U^{ij} tensor.

	x	y	z	U(eq)
P(1)	8854(1)	2180(1)	8747(1)	60(1)
O(1)	8706(2)	3060(2)	7961(2)	91(1)
O(2)	9345(1)	776(2)	8634(1)	67(1)
O(3)	9400(2)	2944(2)	9518(2)	92(1)
O(4)	5763(2)	-1688(2)	9103(2)	82(1)
O(6)	6140(2)	2228(2)	7554(1)	71(1)
N(2)	8040(1)	601(2)	9850(1)	52(1)
N(5)	5737(1)	360(2)	8336(1)	53(1)
C(1)	7811(1)	1600(2)	9111(1)	43(1)
C(3)	7673(2)	-548(2)	9639(2)	54(1)
C(3A)	7142(2)	-665(2)	8745(2)	50(1)
C(4)	6137(2)	-773(2)	8767(2)	54(1)
C(6)	6338(2)	1240(2)	8013(2)	51(1)
C(6A)	7277(2)	736(2)	8330(1)	45(1)
C(11)	7266(2)	2790(2)	9440(2)	50(1)
C(12)	6718(2)	2520(3)	10082(2)	67(1)
C(13)	6179(2)	3564(4)	10356(3)	90(1)
C(14)	6213(2)	4877(4)	10024(3)	94(1)
C(15)	6753(3)	5144(3)	9403(3)	92(1)
C(16)	7284(2)	4107(3)	9102(2)	73(1)
C(21)	9736(3)	442(4)	7836(2)	88(1)
C(22)	10698(3)	611(5)	8001(4)	113(1)
C(31)	10035(3)	2401(3)	10224(2)	78(1)
C(32)	10800(2)	3319(4)	10362(3)	83(1)
C(51)	4736(2)	464(3)	8177(2)	67(1)
C(52)	4392(2)	203(4)	7231(2)	82(1)
C(53)	3383(2)	364(4)	7032(3)	92(1)
C(54)	3061(2)	1683(5)	7397(3)	98(1)
C(55)	3392(2)	1845(5)	8338(3)	98(1)
C(56)	4403(2)	1737(4)	8551(2)	81(1)

Table 3. Bond lengths [Å] and angles [°] for **9b.**

P(1)-O(1)	1.466(2)
P(1)-O(3)	1.532(2)
P(1)-O(2)	1.5674(19)
P(1)-C(1)	1.827(2)
O(2)-C(21)	1.462(4)
O(3)-C(31)	1.441(4)
O(4)-C(4)	1.202(3)
O(6)-C(6)	1.199(3)
N(2)-C(3)	1.264(3)
N(2)-C(1)	1.491(3)
N(5)-C(4)	1.376(3)
N(5)-C(6)	1.381(3)
N(5)-C(51)	1.500(3)
C(1)-C(11)	1.538(3)
C(1)-C(6A)	1.586(3)
C(3)-C(3A)	1.493(4)
C(3)-H(3)	0.9300
C(3A)-C(6A)	1.522(3)
C(3A)-C(4)	1.524(3)
C(3A)-H(3A)	0.9800
C(6)-C(6A)	1.514(3)
C(6A)-H(6A)	0.9800
C(11)-C(16)	1.377(4)
C(11)-C(12)	1.391(4)
C(12)-C(13)	1.396(4)
C(12)-H(12)	0.9300
C(13)-C(14)	1.371(6)
C(13)-H(13)	0.9300
C(14)-C(15)	1.358(6)
C(14)-H(14)	0.9300
C(15)-C(16)	1.399(5)
C(15)-H(15)	0.9300
C(16)-H(16)	0.9300
C(21)-C(22)	1.448(6)
C(21)-H(21A)	0.9700
C(21)-H(21B)	0.9700
C(22)-H(22A)	0.9600
C(22)-H(22B)	0.9600
C(22)-H(22C)	0.9600
C(31)-C(32)	1.448(5)
C(31)-H(31A)	0.9700
C(31)-H(31B)	0.9700
C(32)-H(32A)	0.9600
C(32)-H(32B)	0.9600
C(32)-H(32C)	0.9600
C(51)-C(56)	1.474(4)
C(51)-C(52)	1.490(4)
C(51)-H(51)	0.9800
C(52)-C(53)	1.518(5)
C(52)-H(52A)	0.9700
C(52)-H(52B)	0.9700
C(53)-C(54)	1.500(6)
C(53)-H(53A)	0.9700
C(53)-H(53B)	0.9700
C(54)-C(55)	1.467(6)
C(54)-H(54A)	0.9700
C(54)-H(54B)	0.9700

C(55)-C(56)	1.518(5)
C(55)-H(55A)	0.9700
C(55)-H(55B)	0.9700
C(56)-H(56A)	0.9700
C(56)-H(56B)	0.9700
O(1)-P(1)-O(3)	110.92(15)
O(1)-P(1)-O(2)	115.77(14)
O(3)-P(1)-O(2)	106.87(12)
O(1)-P(1)-C(1)	112.74(12)
O(3)-P(1)-C(1)	107.95(14)
O(2)-P(1)-C(1)	101.94(10)
C(21)-O(2)-P(1)	122.2(2)
C(31)-O(3)-P(1)	129.27(18)
C(3)-N(2)-C(1)	109.18(19)
C(4)-N(5)-C(6)	113.4(2)
C(4)-N(5)-C(51)	119.8(2)
C(6)-N(5)-C(51)	126.5(2)
N(2)-C(1)-C(11)	108.47(19)
N(2)-C(1)-C(6A)	105.74(16)
C(11)-C(1)-C(6A)	113.72(17)
N(2)-C(1)-P(1)	107.99(15)
C(11)-C(1)-P(1)	112.98(15)
C(6A)-C(1)-P(1)	107.56(15)
N(2)-C(3)-C(3A)	117.53(19)
N(2)-C(3)-H(3)	121.2
C(3A)-C(3)-H(3)	121.2
C(3)-C(3A)-C(6A)	103.25(18)
C(3)-C(3A)-C(4)	113.3(2)
C(6A)-C(3A)-C(4)	105.05(18)
C(3)-C(3A)-H(3A)	111.6
C(6A)-C(3A)-H(3A)	111.6
C(4)-C(3A)-H(3A)	111.6
O(4)-C(4)-N(5)	126.2(2)
O(4)-C(4)-C(3A)	125.9(2)
N(5)-C(4)-C(3A)	107.9(2)
O(6)-C(6)-N(5)	125.3(2)
O(6)-C(6)-C(6A)	126.2(2)
N(5)-C(6)-C(6A)	108.49(18)
C(6)-C(6A)-C(3A)	104.38(18)
C(6)-C(6A)-C(1)	115.40(17)
C(3A)-C(6A)-C(1)	103.76(17)
C(6)-C(6A)-H(6A)	110.9
C(3A)-C(6A)-H(6A)	110.9
C(1)-C(6A)-H(6A)	110.9
C(16)-C(11)-C(12)	118.9(2)
C(16)-C(11)-C(1)	122.1(3)
C(12)-C(11)-C(1)	119.0(2)
C(11)-C(12)-C(13)	120.1(3)
C(11)-C(12)-H(12)	119.9
C(13)-C(12)-H(12)	119.9
C(14)-C(13)-C(12)	120.4(4)
C(14)-C(13)-H(13)	119.8
C(12)-C(13)-H(13)	119.8
C(15)-C(14)-C(13)	119.4(3)
C(15)-C(14)-H(14)	120.3
C(13)-C(14)-H(14)	120.3
C(14)-C(15)-C(16)	121.2(3)
C(14)-C(15)-H(15)	119.4

C(16)-C(15)-H(15)	119.4
C(11)-C(16)-C(15)	119.9(4)
C(11)-C(16)-H(16)	120.1
C(15)-C(16)-H(16)	120.1
C(22)-C(21)-O(2)	109.8(3)
C(22)-C(21)-H(21A)	109.7
O(2)-C(21)-H(21A)	109.7
C(22)-C(21)-H(21B)	109.7
O(2)-C(21)-H(21B)	109.7
H(21A)-C(21)-H(21B)	108.2
C(21)-C(22)-H(22A)	109.5
C(21)-C(22)-H(22B)	109.5
H(22A)-C(22)-H(22B)	109.5
C(21)-C(22)-H(22C)	109.5
H(22A)-C(22)-H(22C)	109.5
H(22B)-C(22)-H(22C)	109.5
O(3)-C(31)-C(32)	108.7(3)
O(3)-C(31)-H(31A)	109.9
C(32)-C(31)-H(31A)	109.9
O(3)-C(31)-H(31B)	109.9
C(32)-C(31)-H(31B)	109.9
H(31A)-C(31)-H(31B)	108.3
C(31)-C(32)-H(32A)	109.5
C(31)-C(32)-H(32B)	109.5
H(32A)-C(32)-H(32B)	109.5
C(31)-C(32)-H(32C)	109.5
H(32A)-C(32)-H(32C)	109.5
H(32B)-C(32)-H(32C)	109.5
C(56)-C(51)-C(52)	115.2(3)
C(56)-C(51)-N(5)	112.4(2)
C(52)-C(51)-N(5)	110.8(3)
C(56)-C(51)-H(51)	105.9
C(52)-C(51)-H(51)	105.9
N(5)-C(51)-H(51)	105.9
C(51)-C(52)-C(53)	112.6(3)
C(51)-C(52)-H(52A)	109.1
C(53)-C(52)-H(52A)	109.1
C(51)-C(52)-H(52B)	109.1
C(53)-C(52)-H(52B)	109.1
H(52A)-C(52)-H(52B)	107.8
C(54)-C(53)-C(52)	112.2(3)
C(54)-C(53)-H(53A)	109.2
C(52)-C(53)-H(53A)	109.2
C(54)-C(53)-H(53B)	109.2
C(52)-C(53)-H(53B)	109.2
H(53A)-C(53)-H(53B)	107.9
C(55)-C(54)-C(53)	111.9(4)
C(55)-C(54)-H(54A)	109.2
C(53)-C(54)-H(54A)	109.2
C(55)-C(54)-H(54B)	109.2
C(53)-C(54)-H(54B)	109.2
H(54A)-C(54)-H(54B)	107.9
C(54)-C(55)-C(56)	113.6(3)
C(54)-C(55)-H(55A)	108.8
C(56)-C(55)-H(55A)	108.8
C(54)-C(55)-H(55B)	108.8
C(56)-C(55)-H(55B)	108.8
H(55A)-C(55)-H(55B)	107.7

C(51)-C(56)-C(55)	111.1(3)
C(51)-C(56)-H(56A)	109.4
C(55)-C(56)-H(56A)	109.4
C(51)-C(56)-H(56B)	109.4
C(55)-C(56)-H(56B)	109.4
H(56A)-C(56)-H(56B)	108.0

Table 4. Anisotropic displacement parameters ($Å^2 x\ 10^3$) for **9b**.The anisotropic displacement factor exponent takes the form: $-2\pi^2[\ h^2 a^{*2} U^{11} + ... + 2\ h\ k\ a^*\ b^*\ U^{12}\ ]$

	U^{11}	U^{22}	U^{33}	U^{23}	U^{13}	U^{12}
P(1)	46(1)	46(1)	87(1)	13(1)	8(1)	-1(1)
O(1)	73(1)	81(1)	123(2)	50(1)	30(1)	4(1)
O(2)	58(1)	60(1)	86(1)	6(1)	24(1)	9(1)
O(3)	60(1)	54(1)	151(2)	-18(1)	-21(1)	0(1)
O(4)	72(1)	64(1)	112(2)	17(1)	19(1)	-10(1)
O(6)	80(1)	55(1)	70(1)	13(1)	-19(1)	3(1)
N(2)	55(1)	47(1)	51(1)	10(1)	1(1)	6(1)
N(5)	46(1)	45(1)	65(1)	-8(1)	0(1)	4(1)
C(1)	42(1)	36(1)	51(1)	5(1)	0(1)	1(1)
C(3)	56(1)	44(1)	62(1)	17(1)	9(1)	10(1)
C(3A)	49(1)	32(1)	67(1)	-2(1)	10(1)	3(1)
C(4)	52(1)	42(1)	67(1)	-2(1)	5(1)	-1(1)
C(6)	57(1)	41(1)	51(1)	-4(1)	-7(1)	4(1)
C(6A)	49(1)	39(1)	47(1)	1(1)	7(1)	2(1)
C(11)	47(1)	43(1)	56(1)	-9(1)	-5(1)	2(1)
C(12)	68(2)	64(1)	70(2)	-12(1)	14(1)	5(1)
C(13)	75(2)	98(3)	98(2)	-36(2)	16(2)	9(2)
C(14)	69(2)	80(2)	128(3)	-52(2)	-11(2)	19(2)
C(15)	82(2)	49(1)	136(3)	-18(2)	-17(2)	19(2)
C(16)	73(2)	45(1)	97(2)	2(1)	-2(2)	12(1)
C(21)	98(3)	84(2)	80(2)	-14(2)	10(2)	-4(2)
C(22)	100(3)	130(3)	119(3)	11(3)	49(3)	15(3)
C(31)	105(3)	58(1)	70(2)	4(1)	11(2)	1(2)
C(32)	67(2)	86(2)	90(2)	-16(2)	-16(2)	10(2)
C(51)	50(1)	68(2)	83(2)	-2(1)	4(1)	5(1)
C(52)	57(2)	104(2)	82(2)	-36(2)	-7(2)	5(2)
C(53)	56(2)	107(3)	108(3)	-19(2)	-10(2)	-9(2)
C(54)	56(2)	121(3)	113(3)	2(2)	0(2)	15(2)
C(55)	62(2)	130(3)	104(3)	-16(2)	14(2)	31(2)
C(56)	60(2)	102(2)	78(2)	-27(2)	6(2)	15(2)

Diethyl (1*RS*,3a*SR*,6a*SR*)-4,6-dioxo-1,5-diphenyl-1,3a,4,5,6,6a-hexahydropyrrolo[3,4-*c*]pyrrole-1-phosphonate (9c): Deposition number: 1960883

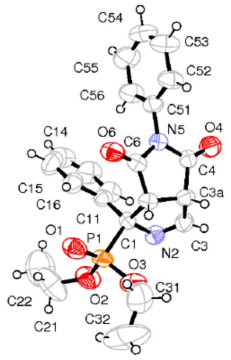

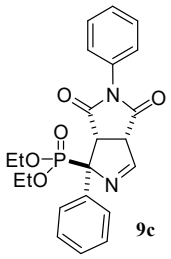

9c

Table 1. Crystal data and structure refinement for **9c.**

Identification code	Jb104	
Empirical formula	C22 H23 N2 O5 P	
Formula weight	426.39	
Temperature	293(2) K	
Wavelength	0.71073 Å	
Crystal system	Orthorhombic	
Space group	P 21 c n	
Unit cell dimensions	a = 9.151(3) Å	α= 90°.
	b = 13.035(8) Å	β= 90°.
	c = 18.159(2) Å	γ = 90°.
Volume	2166.1(15) $Å^3$	
Z	4	
Density (calculated)	1.308 Mg/m^3	
Absorption coefficient	0.162 mm^{-1}	
F(000)	896	
Crystal size	0.42 x 0.33 x 0.30 mm^3	
Theta range for data collection	1.923 to 24.975°.	
Index ranges	-10<=h<=10, -15<=k<=15, 0<=l<=21	
Reflections collected	6335	
Independent reflections	3805 [R(int) = 0.0490]	
Completeness to theta = 25.242°	97.6 %	
Refinement method	Full-matrix least-squares on F^2	
Data / restraints / parameters	3805 / 4 / 294	
Goodness-of-fit on F^2	1.030	
Final R indices [I>2sigma(I)]	R1 = 0.0579, wR2 = 0.1457	
R indices (all data)	R1 = 0.0786, wR2 = 0.1605	
Absolute structure parameter	0.1(2)	
Extinction coefficient	0.036(5)	
Largest diff. peak and hole	0.235 and -0.284 $e.Å^{-3}$	

Table 2. Atomic coordinates (x 10^4) and equivalent isotropic displacement parameters ($Å^2$x 10^3)
For **9c.** U(eq) is defined as one third of the trace of the orthogonalized U^{ij} tensor._

	x	y	z	U(eq)
P(1)	6646(2)	917(1)	3588(1)	55(1)
O(1)	7754(6)	1101(3)	4147(2)	74(1)
O(2)	7204(6)	1011(4)	2770(3)	83(2)
O(3)	5271(6)	1623(3)	3625(3)	76(1)
O(4)	2761(5)	-2695(3)	4262(3)	79(1)
O(6)	6669(5)	-1196(3)	5357(2)	64(1)
N(2)	4635(5)	-416(4)	3094(2)	53(1)
N(5)	4910(5)	-2196(3)	4797(2)	45(1)
C(1)	5821(5)	-364(4)	3642(3)	43(1)
C(3)	3475(6)	-710(4)	3398(3)	55(1)
C(3A)	3558(6)	-906(4)	4213(3)	49(1)
C(4)	3638(6)	-2046(4)	4410(3)	52(1)
C(6)	5680(6)	-1291(4)	4922(3)	46(1)
C(6A)	5040(6)	-489(4)	4419(3)	45(1)
C(11)	6973(6)	-1178(4)	3465(3)	50(1)
C(12)	6759(8)	-1874(5)	2898(3)	66(2)
C(13)	7797(10)	-2613(6)	2740(5)	87(2)
C(14)	9041(11)	-2692(7)	3134(5)	99(3)
C(15)	9286(8)	-1997(8)	3698(5)	89(3)
C(16)	8265(7)	-1248(6)	3858(4)	69(2)
C(21)	8665(13)	1236(10)	2580(7)	135(4)
C(22)	9330(16)	483(12)	2182(8)	169(6)
C(31)	4930(30)	2395(17)	4118(14)	108(8)
C(32)	5240(50)	3413(18)	3790(20)	190(20)
C(31A)	5540(20)	2708(13)	3811(13)	86(6)
C(32A)	4260(30)	3070(20)	4199(14)	116(9)
C(51)	5310(6)	-3155(4)	5132(3)	50(1)
C(52)	4704(9)	-3443(5)	5793(4)	68(2)
C(53)	5104(10)	-4364(6)	6106(4)	82(2)
C(54)	6052(9)	-4995(5)	5762(4)	82(2)
C(55)	6644(11)	-4711(5)	5106(5)	91(2)
C(56)	6279(8)	-3786(5)	4782(4)	75(2)

Table 3. Bond lengths [Å] and angles [°] for **9c**

P(1)-O(1)	1.454(5)
P(1)-O(3)	1.561(5)
P(1)-O(2)	1.576(5)
P(1)-C(1)	1.835(5)
O(2)-C(21)	1.411(11)
O(3)-C(31)	1.38(2)
O(3)-C(31A)	1.473(16)
O(4)-C(4)	1.197(7)
O(6)-C(6)	1.208(7)
N(2)-C(3)	1.256(8)
N(2)-C(1)	1.474(7)
N(5)-C(4)	1.374(7)
N(5)-C(6)	1.392(7)
N(5)-C(51)	1.438(7)
C(1)-C(11)	1.530(8)
C(1)-C(6A)	1.590(7)
C(3)-C(3A)	1.503(8)
C(3A)-C(6A)	1.509(8)
C(3A)-C(4)	1.530(7)
C(6)-C(6A)	1.506(7)
C(11)-C(16)	1.384(9)
C(11)-C(12)	1.385(8)
C(12)-C(13)	1.383(10)
C(13)-C(14)	1.349(14)
C(14)-C(15)	1.386(13)
C(15)-C(16)	1.382(11)
C(21)-C(22)	1.362(16)
C(31)-C(32)	1.48(3)
C(31A)-C(32A)	1.44(2)
C(51)-C(56)	1.366(8)
C(51)-C(52)	1.374(9)
C(52)-C(53)	1.378(10)
C(53)-C(54)	1.349(11)
C(54)-C(55)	1.360(11)
C(55)-C(56)	1.383(10)
O(1)-P(1)-O(3)	115.8(3)
O(1)-P(1)-O(2)	114.8(3)
O(3)-P(1)-O(2)	104.8(3)
O(1)-P(1)-C(1)	113.5(2)
O(3)-P(1)-C(1)	101.7(3)
O(2)-P(1)-C(1)	104.8(3)
C(21)-O(2)-P(1)	123.6(6)
C(31)-O(3)-P(1)	129.7(12)
C(31A)-O(3)-P(1)	116.3(8)
C(3)-N(2)-C(1)	109.8(4)
C(4)-N(5)-C(6)	113.0(4)
C(4)-N(5)-C(51)	123.8(4)
C(6)-N(5)-C(51)	122.7(4)
N(2)-C(1)-C(11)	109.5(4)
N(2)-C(1)-C(6A)	105.3(4)
C(11)-C(1)-C(6A)	115.2(4)
N(2)-C(1)-P(1)	108.0(3)
C(11)-C(1)-P(1)	109.7(4)
C(6A)-C(1)-P(1)	109.0(3)
N(2)-C(3)-C(3A)	116.2(5)
C(3)-C(3A)-C(6A)	103.2(4)

C(3)-C(3A)-C(4)	113.4(4)
C(6A)-C(3A)-C(4)	104.4(4)
O(4)-C(4)-N(5)	125.6(5)
O(4)-C(4)-C(3A)	127.0(5)
N(5)-C(4)-C(3A)	107.4(5)
O(6)-C(6)-N(5)	124.9(5)
O(6)-C(6)-C(6A)	128.0(5)
N(5)-C(6)-C(6A)	107.1(4)
C(6)-C(6A)-C(3A)	104.5(4)
C(6)-C(6A)-C(1)	115.7(4)
C(3A)-C(6A)-C(1)	102.7(4)
C(16)-C(11)-C(12)	117.4(6)
C(16)-C(11)-C(1)	121.7(5)
C(12)-C(11)-C(1)	120.8(5)
C(13)-C(12)-C(11)	120.9(7)
C(14)-C(13)-C(12)	121.5(8)
C(13)-C(14)-C(15)	118.6(7)
C(16)-C(15)-C(14)	120.5(8)
C(15)-C(16)-C(11)	121.0(7)
C(22)-C(21)-O(2)	113.8(10)
O(3)-C(31)-C(32)	111(2)
C(32A)-C(31A)-O(3)	107.1(19)
C(56)-C(51)-C(52)	120.2(6)
C(56)-C(51)-N(5)	119.5(5)
C(52)-C(51)-N(5)	120.3(5)
C(51)-C(52)-C(53)	119.5(6)
C(54)-C(53)-C(52)	120.7(7)
C(53)-C(54)-C(55)	119.7(6)
C(54)-C(55)-C(56)	120.9(7)
C(51)-C(56)-C(55)	119.0(7)

Table 4. Anisotropic displacement parameters ($Å^2 x\ 10^3$) for **9c.** The anisotropic displacement factor exponent takes the form: $-2\pi^2[\ h^2 a^{*2} U^{11} + ... + 2\ h\ k\ a^*\ b^*\ U^{12}\ ]$

	U^{11}	U^{22}	U^{33}	U^{23}	U^{13}	U^{12}
P(1)	71(1)	47(1)	46(1)	10(1)	-5(1)	-9(1)
O(1)	90(3)	66(3)	66(3)	10(2)	-19(2)	-25(2)
O(2)	95(3)	100(4)	53(3)	23(2)	7(2)	-20(3)
O(3)	99(3)	49(2)	79(3)	6(2)	-9(3)	6(2)
O(4)	68(3)	62(3)	107(4)	10(2)	-23(3)	-13(2)
O(6)	82(3)	58(2)	53(2)	9(2)	-22(2)	-15(2)
N(2)	57(3)	56(3)	44(3)	-3(2)	-8(2)	1(2)
N(5)	50(2)	40(2)	44(2)	1(2)	1(2)	0(2)
C(1)	45(3)	44(3)	39(3)	-1(2)	-1(2)	-5(2)
C(3)	51(3)	59(3)	54(3)	2(3)	-8(3)	6(3)
C(3A)	55(3)	43(3)	49(3)	3(2)	6(2)	9(2)
C(4)	49(3)	46(3)	60(3)	3(3)	0(3)	-3(2)
C(6)	59(3)	40(3)	39(3)	-2(2)	7(3)	-3(2)
C(6A)	60(3)	36(2)	38(3)	-1(2)	3(2)	0(2)
C(11)	58(3)	50(3)	42(3)	7(2)	5(2)	2(2)
C(12)	79(4)	61(3)	60(3)	-7(3)	7(3)	1(3)
C(13)	106(6)	71(5)	84(5)	-12(4)	26(5)	17(4)
C(14)	118(7)	82(6)	96(6)	21(5)	53(6)	38(5)
C(15)	66(4)	117(7)	85(6)	26(5)	12(4)	27(5)
C(16)	62(4)	84(5)	61(4)	12(3)	1(3)	6(3)
C(21)	153(10)	142(10)	110(8)	-14(7)	53(7)	-60(8)
C(22)	146(11)	191(15)	169(13)	-20(11)	41(10)	-7(10)
C(31)	111(16)	84(16)	128(18)	-28(14)	21(14)	20(14)
C(32)	280(50)	55(15)	240(40)	-24(17)	-140(40)	15(19)
C(31A)	88(13)	51(12)	119(16)	5(9)	14(11)	-8(8)
C(32A)	132(18)	85(18)	130(18)	-19(13)	38(14)	-18(14)
C(51)	60(3)	36(3)	53(3)	-3(2)	-5(3)	0(2)
C(52)	95(5)	56(4)	55(4)	7(3)	15(3)	10(3)
C(53)	127(6)	63(4)	56(4)	12(3)	7(4)	7(4)
C(54)	117(6)	45(3)	83(5)	11(3)	-19(4)	9(4)
C(55)	103(5)	55(4)	117(6)	-2(4)	13(5)	28(4)
C(56)	89(5)	58(4)	77(4)	4(3)	27(4)	20(3)

Table 5. Hydrogen bonds for **9c** [Å and °].

D-H...A	d(D-H)	d(H...A)	d(D...A)	<(DHA)
C(3A)-H(3A)...O(1)#1	0.98	2.59	3.079(7)	110.6
C(3A)-H(3A)...O(6)#1	0.98	2.51	3.332(7)	140.8
C(21)-H(21B)...O(1)	0.97	2.46	2.970(12)	112.8

Symmetry transformations used to generate equivalent atoms:
#1 x-1/2,-y,-z+1

Diethyl (1*RS*,3a*SR*,6a*SR*)-5-(3-chloro-4-fluorophenyl)-4,6-dioxo-1-phenyl-1,3a,4,5,6,6a-hexahydropyrrolo[3,4-*c*]pyrrole-1-phosphonate (9d)*:* Deposition number: 1960884

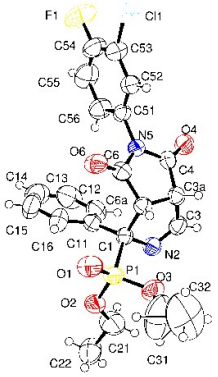

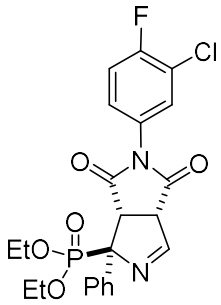

B06, **9d**

Table 1. Crystal data and structure refinement for **9d.**

Identification code	Jb128	
Empirical formula	C22 H21 Cl F N2 O5 P	
Formula weight	478.83	
Temperature	294(2) K	
Wavelength	0.71073 Å	
Crystal system	Monoclinic	
Space group	P 21/n	
Unit cell dimensions	a = 15.288(3) Å	α= 90°.
	b = 9.269(3) Å	β= 92.653(17)°.
	c = 15.874(3) Å	γ = 90°.
Volume	2247.0(10) $Å^3$	
Z	4	
Density (calculated)	1.415 Mg/m^3	
Absorption coefficient	0.286 mm^{-1}	
F(000)	992	
Crystal size	0.390 x 0.240 x 0.240 mm^3	
Theta range for data collection	1.808 to 24.977°.	
Index ranges	-18<=h<=0, 0<=k<=11, -18<=l<=18	
Reflections collected	4436	
Independent reflections	3935 [R(int) = 0.0541]	
Completeness to theta = 24.977°	99.9 %	
Refinement method	Full-matrix least-squares on F^2	
Data / restraints / parameters	3935 / 0 / 291	
Goodness-of-fit on F^2	1.029	
Final R indices [I>2sigma(I)]	R1 = 0.0572, wR2 = 0.1443	
R indices (all data)	R1 = 0.1212, wR2 = 0.1627	
Largest diff. peak and hole	0.427 and -0.328 $e.Å^{-3}$	

Table 2. Atomic coordinates (x 10^4) and equivalent isotropic displacement parameters ($Å^2$x 10^3) for **9d.** U(eq) is defined as one third of the trace of the orthogonalized U^{ij} tensor.

	x	y	z	U(eq)
Cl(1)	-1852(1)	-86(2)	6496(1)	130(1)
P(1)	3957(1)	1969(1)	8665(1)	53(1)
F(1)	-2539(2)	1507(4)	7907(2)	136(1)
O(1)	3806(2)	2876(3)	7927(2)	73(1)
O(2)	4426(2)	2844(3)	9389(2)	67(1)
O(3)	4499(2)	568(3)	8526(2)	68(1)
O(4)	832(2)	-1912(3)	9149(2)	63(1)
O(6)	1443(2)	1974(3)	7530(2)	67(1)
C(1)	2945(2)	1219(4)	9048(2)	44(1)
N(2)	3166(2)	108(3)	9693(2)	51(1)
C(3)	2789(2)	-1062(4)	9491(2)	53(1)
C(3A)	2246(2)	-1090(4)	8681(2)	48(1)
C(4)	1269(2)	-1053(4)	8786(2)	46(1)
N(5)	946(2)	180(3)	8388(2)	44(1)
C(6)	1594(2)	978(4)	8000(2)	50(1)
C(6A)	2457(2)	368(3)	8291(2)	45(1)
C(11)	2375(2)	2376(4)	9437(2)	50(1)
C(12)	1905(3)	2078(5)	10135(3)	69(1)
C(13)	1340(3)	3067(7)	10453(4)	98(2)
C(14)	1229(3)	4384(7)	10094(4)	101(2)
C(15)	1698(4)	4708(5)	9405(4)	97(2)
C(16)	2268(3)	3725(4)	9079(3)	73(1)
C(21)	4831(3)	2232(6)	10143(3)	101(2)
C(22)	5361(3)	3293(5)	10590(3)	100(2)
C(31)	5264(6)	600(8)	8010(6)	184(4)
C(32)	5431(7)	-321(10)	7528(6)	218(5)
C(51)	32(2)	504(4)	8271(2)	48(1)
C(52)	-410(2)	59(4)	7551(2)	59(1)
C(53)	-1279(3)	394(5)	7417(3)	75(1)
C(54)	-1687(3)	1155(5)	8022(3)	82(1)
C(55)	-1254(3)	1602(5)	8744(3)	89(1)
C(56)	-372(3)	1274(5)	8872(3)	69(1)

Table 3. Bond lengths [Å] and angles [°] for **9d.**

Cl(1)-C(53)	1.728(4)
P(1)-O(1)	1.452(2)
P(1)-O(2)	1.553(3)
P(1)-O(3)	1.562(3)
P(1)-C(1)	1.826(3)
F(1)-C(54)	1.346(5)
O(2)-C(21)	1.439(5)
O(3)-C(31)	1.459(7)
O(4)-C(4)	1.203(4)
O(6)-C(6)	1.202(4)
C(1)-N(2)	1.481(4)
C(1)-C(11)	1.529(5)
C(1)-C(6A)	1.593(4)
N(2)-C(3)	1.262(4)
C(3)-C(3A)	1.499(5)
C(3A)-C(4)	1.511(5)
C(3A)-C(6A)	1.527(4)
C(4)-N(5)	1.386(4)
N(5)-C(6)	1.402(4)
N(5)-C(51)	1.433(4)
C(6)-C(6A)	1.489(5)
C(11)-C(12)	1.377(5)
C(11)-C(16)	1.380(5)
C(12)-C(13)	1.371(6)
C(13)-C(14)	1.355(7)
C(14)-C(15)	1.368(7)
C(15)-C(16)	1.379(6)
C(21)-C(22)	1.440(6)
C(31)-C(32)	1.182(8)
C(51)-C(52)	1.364(5)
C(51)-C(56)	1.362(5)
C(52)-C(53)	1.372(5)
C(53)-C(54)	1.366(6)
C(54)-C(55)	1.362(6)
C(55)-C(56)	1.389(6)
O(1)-P(1)-O(2)	110.21(16)
O(1)-P(1)-O(3)	115.64(16)
O(2)-P(1)-O(3)	108.04(14)
O(1)-P(1)-C(1)	112.48(15)
O(2)-P(1)-C(1)	108.79(15)
O(3)-P(1)-C(1)	101.17(15)
C(21)-O(2)-P(1)	125.1(3)
C(31)-O(3)-P(1)	120.4(3)
N(2)-C(1)-C(11)	108.9(3)
N(2)-C(1)-C(6A)	105.1(3)
C(11)-C(1)-C(6A)	113.4(3)
N(2)-C(1)-P(1)	109.0(2)
C(11)-C(1)-P(1)	112.0(2)
C(6A)-C(1)-P(1)	108.2(2)
C(3)-N(2)-C(1)	109.6(3)
N(2)-C(3)-C(3A)	117.4(3)
C(3)-C(3A)-C(4)	114.5(3)
C(3)-C(3A)-C(6A)	102.3(3)
C(4)-C(3A)-C(6A)	104.7(3)
O(4)-C(4)-N(5)	124.8(3)
O(4)-C(4)-C(3A)	127.7(3)

N(5)-C(4)-C(3A)	107.5(3)
C(4)-N(5)-C(6)	113.1(3)
C(4)-N(5)-C(51)	123.8(3)
C(6)-N(5)-C(51)	122.5(3)
O(6)-C(6)-N(5)	124.0(3)
O(6)-C(6)-C(6A)	128.8(3)
N(5)-C(6)-C(6A)	107.3(3)
C(6)-C(6A)-C(3A)	105.1(3)
C(6)-C(6A)-C(1)	115.0(3)
C(3A)-C(6A)-C(1)	103.5(2)
C(12)-C(11)-C(16)	117.2(4)
C(12)-C(11)-C(1)	120.9(3)
C(16)-C(11)-C(1)	121.8(3)
C(13)-C(12)-C(11)	121.6(5)
C(14)-C(13)-C(12)	121.1(5)
C(13)-C(14)-C(15)	118.3(5)
C(14)-C(15)-C(16)	121.3(5)
C(15)-C(16)-C(11)	120.6(4)
C(22)-C(21)-O(2)	110.6(4)
C(32)-C(31)-O(3)	123.4(9)
C(52)-C(51)-C(56)	121.5(3)
C(52)-C(51)-N(5)	119.2(3)
C(56)-C(51)-N(5)	119.4(3)
C(51)-C(52)-C(53)	120.0(4)
C(54)-C(53)-C(52)	118.6(4)
C(54)-C(53)-Cl(1)	119.8(3)
C(52)-C(53)-Cl(1)	121.5(4)
F(1)-C(54)-C(55)	118.1(5)
F(1)-C(54)-C(53)	120.0(5)
C(55)-C(54)-C(53)	121.9(4)
C(54)-C(55)-C(56)	119.2(4)
C(51)-C(56)-C(55)	118.7(4)

Table 4. Anisotropic displacement parameters ($Å^2 x\ 10^3$) for **9d**.The anisotropic displacement factor exponent takes the form: $-2\pi^2[\ h^2 a^{*2} U^{11} + ... + 2\ h\ k\ a^*\ b^*\ U^{12}\ ]$

	U^{11}	U^{22}	U^{33}	U^{23}	U^{13}	U^{12}
Cl(1)	83(1)	160(2)	143(1)	-24(1)	-53(1)	7(1)
P(1)	44(1)	58(1)	57(1)	11(1)	-2(1)	-4(1)
F(1)	51(2)	165(3)	193(3)	0(3)	5(2)	29(2)
O(1)	63(2)	88(2)	66(2)	36(2)	-2(1)	-9(2)
O(2)	60(2)	63(2)	78(2)	7(1)	-22(1)	-6(1)
O(3)	49(1)	73(2)	83(2)	2(2)	18(1)	8(1)
O(4)	57(2)	54(2)	80(2)	16(1)	10(1)	-4(1)
O(6)	58(2)	77(2)	66(2)	28(2)	-12(1)	-9(1)
C(1)	44(2)	42(2)	45(2)	5(2)	0(2)	0(2)
N(2)	53(2)	51(2)	49(2)	7(2)	-3(1)	0(2)
C(3)	50(2)	49(2)	60(2)	11(2)	4(2)	5(2)
C(3A)	49(2)	44(2)	50(2)	-5(2)	6(2)	2(2)
C(4)	53(2)	40(2)	46(2)	-3(2)	2(2)	-1(2)
N(5)	42(2)	43(2)	47(2)	2(1)	-1(1)	-1(1)
C(6)	54(2)	54(2)	40(2)	2(2)	-1(2)	-6(2)
C(6A)	41(2)	49(2)	45(2)	-2(2)	6(2)	-1(2)
C(11)	51(2)	49(2)	50(2)	-7(2)	-6(2)	-2(2)
C(12)	72(3)	62(2)	75(3)	-13(2)	20(2)	-6(2)
C(13)	79(3)	104(4)	113(4)	-52(4)	28(3)	-7(3)
C(14)	67(3)	101(4)	134(5)	-59(4)	0(3)	16(3)
C(15)	106(4)	61(3)	122(4)	-13(3)	-24(3)	31(3)
C(16)	84(3)	58(3)	77(3)	3(2)	1(2)	17(2)
C(21)	105(4)	96(4)	96(3)	24(3)	-50(3)	-14(3)
C(22)	120(4)	81(3)	94(3)	-11(3)	-44(3)	18(3)
C(31)	205(8)	129(6)	228(9)	22(6)	130(7)	48(6)
C(32)	267(11)	201(9)	198(9)	-75(7)	140(8)	-11(8)
C(51)	40(2)	48(2)	57(2)	6(2)	5(2)	1(2)
C(52)	53(2)	58(2)	66(2)	-8(2)	-5(2)	4(2)
C(53)	58(3)	75(3)	90(3)	7(3)	-15(2)	3(2)
C(54)	45(2)	88(3)	113(4)	15(3)	1(3)	9(2)
C(55)	70(3)	99(4)	101(4)	-1(3)	32(3)	17(3)
C(56)	58(2)	83(3)	67(3)	-3(2)	8(2)	8(2)

Table 5. Hydrogen bonds for **9d** [Å and °].

D-H...A	d(D-H)	d(H...A)	d(D...A)	<(DHA)
C(3A)-H(3A)...O(6)#1	0.98	2.49	3.359(4)	147.7
C(22)-H(22B)...O(6)#2	0.96	2.56	3.436(5)	151.8
C(31)-H(31A)...O(1)	0.97	2.57	3.067(8)	112.2
C(52)-H(52)...O(1)#1	0.93	2.54	3.295(5)	139.0

Symmetry transformations used to generate equivalent atoms:
#1 -x+1/2,y-1/2,-z+3/2 #2 x+1/2,-y+1/2,z+1/2

Diethyl (1*RS*,3a*SR*,6a*SR*)-5-(3,4-dichlorophenyl)-4,6-dioxo-1-phenyl-1,3a,4,5,6,6a-hexahydropyrrolo[3,4-*c*]pyrrole-1-phosphonate (9v): Deposition number: 1960887

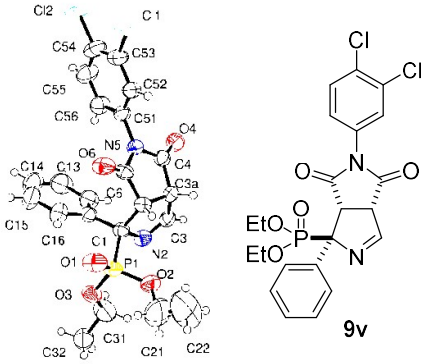

Table 1. Crystal data and structure refinement for **9v.**

Identification code	Jb137	
Empirical formula	C22 H21 Cl2 N2 O5 P	
Formula weight	495.28	
Temperature	294(2) K	
Wavelength	0.71073 Å	
Crystal system	Monoclinic	
Space group	P 21/n	
Unit cell dimensions	a = 15.769(3) Å	α= 90°.
	b = 9.234(2) Å	β= 93.672(5)°.
	c = 15.789(3) Å	γ = 90°.
Volume	2294.3(9) Å^3	
Z	4	
Density (calculated)	1.434 Mg/m^3	
Absorption coefficient	0.389 mm^{-1}	
F(000)	1024	
Crystal size	0.33 x 0.12 x 0.11 mm^3	
Theta range for data collection	1.769 to 28.326°.	
Index ranges	-21<=h<=21, -12<=k<=12, -21<=l<=21	
Reflections collected	49110	
Independent reflections	5704 [R(int) = 0.0892]	
Completeness to theta = 25.242°	100.0 %	
Refinement method	Full-matrix least-squares on F^2	
Data / restraints / parameters	5704 / 0 / 291	
Goodness-of-fit on F^2	1.012	
Final R indices [I>2sigma(I)]	R1 = 0.0598, wR2 = 0.1362	
R indices (all data)	R1 = 0.1155, wR2 = 0.1653	
Largest diff. peak and hole	0.533 and -0.336 e.Å^{-3}	

Table 2. Atomic coordinates (x 10^4) and equivalent isotropic displacement parameters ($Å^2$x 10^3) for **9v**. U(eq) is defined as one third of the trace of the orthogonalized U^{ij} tensor.

	x	y	z	U(eq)
Cl(1)	3639(1)	9847(2)	6664(1)	98(1)
Cl(2)	2190(1)	8305(2)	7622(1)	129(1)
P(1)	1326(1)	8053(1)	1087(1)	48(1)
O(1)	2074(1)	7137(3)	1246(1)	68(1)
O(2)	1474(1)	9464(2)	565(1)	61(1)
O(3)	602(1)	7175(2)	608(1)	63(1)
O(4)	817(1)	11917(2)	4120(1)	58(1)
O(6)	2493(1)	8094(2)	3515(1)	61(1)
N(2)	269(1)	9893(3)	1838(2)	46(1)
N(5)	1618(1)	9857(2)	4004(1)	41(1)
C(1)	932(2)	8810(3)	2062(2)	39(1)
C(3)	454(2)	11070(3)	2217(2)	47(1)
C(3A)	1279(2)	11121(3)	2740(2)	43(1)
C(4)	1190(2)	11077(3)	3696(2)	42(1)
C(6)	2005(2)	9077(3)	3377(2)	43(1)
C(6A)	1689(2)	9691(3)	2534(2)	40(1)
C(11)	557(2)	7643(3)	2618(2)	45(1)
C(12)	-133(2)	7961(4)	3085(2)	63(1)
C(13)	-439(3)	6967(5)	3647(3)	87(1)
C(14)	-77(3)	5635(6)	3736(3)	94(2)
C(15)	592(3)	5292(4)	3267(3)	92(1)
C(16)	914(2)	6284(4)	2714(2)	69(1)
C(21)	1969(5)	9381(7)	-188(4)	142(2)
C(22)	2528(5)	10365(8)	-264(5)	184(4)
C(31)	-151(3)	7780(4)	185(3)	86(1)
C(32)	-531(2)	6744(4)	-422(2)	76(1)
C(51)	1746(2)	9521(3)	4891(2)	43(1)
C(52)	2513(2)	9859(3)	5309(2)	50(1)
C(53)	2658(2)	9483(4)	6153(2)	60(1)
C(54)	2026(2)	8794(4)	6571(2)	68(1)
C(55)	1263(2)	8484(4)	6146(2)	72(1)
C(56)	1118(2)	8843(4)	5303(2)	59(1)

Table 3. Bond lengths [Å] and angles [°] for **9v.**

Cl(1)-C(53)	1.731(3)
Cl(2)-C(54)	1.723(3)
P(1)-O(1)	1.460(2)
P(1)-O(3)	1.556(2)
P(1)-O(2)	1.567(2)
P(1)-C(1)	1.835(3)
O(2)-C(21)	1.466(5)
O(3)-C(31)	1.438(4)
O(4)-C(4)	1.203(3)
O(6)-C(6)	1.200(3)
N(2)-C(3)	1.267(4)
N(2)-C(1)	1.474(3)
N(5)-C(4)	1.386(3)
N(5)-C(6)	1.396(3)
N(5)-C(51)	1.435(3)
C(1)-C(11)	1.532(4)
C(1)-C(6A)	1.589(4)
C(3)-C(3A)	1.496(4)
C(3A)-C(6A)	1.515(4)
C(3A)-C(4)	1.524(4)
C(6)-C(6A)	1.503(4)
C(11)-C(16)	1.380(4)
C(11)-C(12)	1.385(4)
C(12)-C(13)	1.385(5)
C(13)-C(14)	1.359(6)
C(14)-C(15)	1.363(7)
C(15)-C(16)	1.384(5)
C(21)-C(22)	1.277(7)
C(31)-C(32)	1.455(5)
C(51)-C(56)	1.371(4)
C(51)-C(52)	1.377(4)
C(52)-C(53)	1.382(4)
C(53)-C(54)	1.385(5)
C(54)-C(55)	1.371(5)
C(55)-C(56)	1.377(5)
O(1)-P(1)-O(3)	109.94(13)
O(1)-P(1)-O(2)	115.26(14)
O(3)-P(1)-O(2)	107.91(12)
O(1)-P(1)-C(1)	112.89(12)
O(3)-P(1)-C(1)	109.18(13)
O(2)-P(1)-C(1)	101.20(12)
C(21)-O(2)-P(1)	119.2(3)
C(31)-O(3)-P(1)	125.6(2)
C(3)-N(2)-C(1)	109.3(2)
C(4)-N(5)-C(6)	113.3(2)
C(4)-N(5)-C(51)	123.6(2)
C(6)-N(5)-C(51)	122.7(2)
N(2)-C(1)-C(11)	108.7(2)
N(2)-C(1)-C(6A)	105.3(2)
C(11)-C(1)-C(6A)	113.4(2)
N(2)-C(1)-P(1)	109.28(17)
C(11)-C(1)-P(1)	112.15(19)
C(6A)-C(1)-P(1)	107.70(17)
N(2)-C(3)-C(3A)	117.0(3)
C(3)-C(3A)-C(6A)	102.8(2)
C(3)-C(3A)-C(4)	114.5(2)

C(6A)-C(3A)-C(4)	104.9(2)
O(4)-C(4)-N(5)	124.9(3)
O(4)-C(4)-C(3A)	127.8(3)
N(5)-C(4)-C(3A)	107.2(2)
O(6)-C(6)-N(5)	124.4(3)
O(6)-C(6)-C(6A)	128.3(3)
N(5)-C(6)-C(6A)	107.3(2)
C(6)-C(6A)-C(3A)	105.1(2)
C(6)-C(6A)-C(1)	114.8(2)
C(3A)-C(6A)-C(1)	103.3(2)
C(16)-C(11)-C(12)	117.6(3)
C(16)-C(11)-C(1)	122.2(3)
C(12)-C(11)-C(1)	120.1(3)
C(13)-C(12)-C(11)	121.2(4)
C(14)-C(13)-C(12)	120.3(4)
C(13)-C(14)-C(15)	119.2(4)
C(14)-C(15)-C(16)	121.1(4)
C(11)-C(16)-C(15)	120.5(4)
C(22)-C(21)-O(2)	116.5(6)
O(3)-C(31)-C(32)	110.1(3)
C(56)-C(51)-C(52)	121.0(3)
C(56)-C(51)-N(5)	120.1(3)
C(52)-C(51)-N(5)	118.9(3)
C(51)-C(52)-C(53)	119.5(3)
C(52)-C(53)-C(54)	119.7(3)
C(52)-C(53)-Cl(1)	119.2(3)
C(54)-C(53)-Cl(1)	121.1(3)
C(55)-C(54)-C(53)	119.9(3)
C(55)-C(54)-Cl(2)	119.3(3)
C(53)-C(54)-Cl(2)	120.7(3)
C(54)-C(55)-C(56)	120.6(3)
C(51)-C(56)-C(55)	119.3(3)

Table 4. Anisotropic displacement parameters ($Å^2 x\ 10^3$) for **9v.** The anisotropic displacement factor exponent takes the form: $-2\pi^2[\ h^2 a^{*2} U^{11} + ... + 2\ h\ k\ a^*\ b^*\ U^{12}\ ]$

	U^{11}	U^{22}	U^{33}	U^{23}	U^{13}	U^{12}
Cl(1)	84(1)	143(1)	62(1)	4(1)	-26(1)	-7(1)
Cl(2)	145(1)	195(2)	45(1)	35(1)	7(1)	-3(1)
P(1)	50(1)	57(1)	37(1)	-5(1)	-3(1)	10(1)
O(1)	62(1)	85(2)	56(1)	-11(1)	-2(1)	34(1)
O(2)	75(2)	66(1)	43(1)	2(1)	12(1)	1(1)
O(3)	71(1)	59(1)	54(1)	-7(1)	-23(1)	5(1)
O(4)	72(1)	50(1)	52(1)	-4(1)	13(1)	11(1)
O(6)	57(1)	74(2)	51(1)	-8(1)	-10(1)	27(1)
N(2)	41(1)	51(2)	45(1)	3(1)	-2(1)	9(1)
N(5)	40(1)	45(1)	37(1)	1(1)	1(1)	1(1)
C(1)	36(1)	44(2)	37(1)	-2(1)	-2(1)	5(1)
C(3)	51(2)	46(2)	44(2)	8(1)	1(1)	9(1)
C(3A)	48(2)	42(2)	40(1)	4(1)	6(1)	-4(1)
C(4)	42(2)	42(2)	43(2)	0(1)	4(1)	-2(1)
C(6)	36(1)	49(2)	43(2)	-7(1)	-3(1)	3(1)
C(6A)	33(1)	50(2)	38(1)	-3(1)	4(1)	-3(1)
C(11)	46(2)	48(2)	40(2)	-1(1)	-3(1)	-8(1)
C(12)	63(2)	68(2)	60(2)	-2(2)	12(2)	-14(2)
C(13)	93(3)	100(3)	69(3)	-5(2)	22(2)	-40(3)
C(14)	121(4)	93(3)	66(3)	20(2)	-5(3)	-53(3)
C(15)	118(4)	61(2)	94(3)	26(2)	-11(3)	-11(3)
C(16)	75(2)	56(2)	75(2)	14(2)	2(2)	6(2)
C(21)	207(7)	120(4)	110(4)	8(4)	86(5)	-6(5)
C(22)	170(6)	172(7)	222(8)	-49(6)	114(6)	-88(5)
C(31)	79(3)	75(3)	99(3)	-11(2)	-35(2)	19(2)
C(32)	75(2)	71(2)	78(3)	9(2)	-29(2)	-7(2)
C(51)	48(2)	46(2)	37(1)	1(1)	5(1)	4(1)
C(52)	51(2)	56(2)	42(2)	0(1)	1(1)	-2(2)
C(53)	65(2)	71(2)	41(2)	-2(2)	-7(2)	5(2)
C(54)	82(3)	86(3)	37(2)	8(2)	10(2)	9(2)
C(55)	74(2)	89(3)	54(2)	12(2)	20(2)	-6(2)
C(56)	52(2)	73(2)	52(2)	3(2)	11(1)	-5(2)

Table 5. Hydrogen bonds for **9v** [Å and °].

D-H...A	d(D-H)	d(H...A)	d(D...A)	<(DHA)
C(3A)-H(3A)...O(6)#1	0.98	2.52	3.391(3)	147.8
C(32)-H(32C)...O(6)#2	0.96	2.57	3.448(4)	152.8
C(52)-H(52)...O(1)#1	0.93	2.61	3.329(4)	134.9

Symmetry transformations used to generate equivalent atoms:
#1 -x+1/2,y+1/2,-z+1/2 #2 x-1/2,-y+3/2,z-1/2

Diethyl (1*RS*,3a*SR*,6a*SR*)-4,6-dioxo-5-(4-phenoxyphenyl)-1-phenyl-1,3a,4,5,6,6a-hexahydropyrrolo[3,4-*c*]pyrrole-1-phosphonate (9ab): Deposition number: 1960885

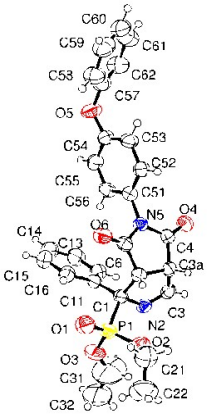

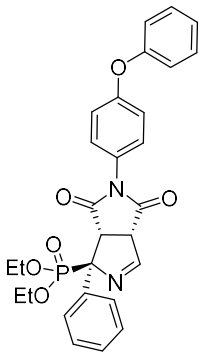

9ab

Table 1. Crystal data and structure refinement for **9ab.**

Identification code	Jb131	
Empirical formula	C28 H27 N2 O6 P	
Formula weight	518.48	
Temperature	294(2) K	
Wavelength	0.71073 Å	
Crystal system	Monoclinic	
Space group	I 2/a	
Unit cell dimensions	a = 22.065(4) Å	α= 90°.
	b = 9.314(2) Å	β= 112.776(16)°.
	c = 27.263(4) Å	γ = 90°.
Volume	5166.0(17) Å^3	
Z	8	
Density (calculated)	1.333 Mg/m^3	
Absorption coefficient	0.152 mm^{-1}	
F(000)	2176	
Crystal size	0.39 x 0.33 x 0.15 mm^3	
Theta range for data collection	1.620 to 25.124°.	
Index ranges	-16<=h<=26, -11<=k<=10, -32<=l<=17	
Reflections collected	9131	
Independent reflections	4559 [R(int) = 0.0846]	
Completeness to theta = 25.124°	98.7 %	
Refinement method	Full-matrix least-squares on F^2	
Data / restraints / parameters	4559 / 0 / 337	
Goodness-of-fit on F^2	0.997	
Final R indices [I>2sigma(I)]	R1 = 0.0526, wR2 = 0.1177	
R indices (all data)	R1 = 0.1383, wR2 = 0.1478	
Extinction coefficient	0.00136(18)	
Largest diff. peak and hole	0.512 and -0.393 e.Å^{-3}	

Table 2. Atomic coordinates (x 10^4) and equivalent isotropic displacement parameters ($Å^2$x 10^3) for **9ab.** U(eq) is defined as one third of the trace of the orthogonalized U^{ij} tensor.

	x	y	z	U(eq)
P(1)	5656(1)	-1033(1)	3648(1)	53(1)
O(1)	5820(1)	39(3)	3328(1)	70(1)
O(2)	6057(1)	-2460(3)	3741(1)	66(1)
O(3)	5743(1)	-450(3)	4204(1)	79(1)
O(4)	3308(1)	-4767(3)	2426(1)	56(1)
O(5)	1346(1)	-394(3)	690(1)	71(1)
O(6)	4267(1)	-800(3)	2068(1)	58(1)
N(2)	4720(1)	-2802(3)	3694(1)	45(1)
N(5)	3636(1)	-2605(3)	2202(1)	40(1)
C(1)	4809(2)	-1672(3)	3346(1)	41(1)
C(3)	4519(2)	-3942(4)	3435(1)	48(1)
C(3A)	4438(2)	-3931(4)	2864(1)	43(1)
C(4)	3725(2)	-3886(4)	2481(1)	41(1)
C(6)	4213(2)	-1819(4)	2322(1)	44(1)
C(6A)	4718(2)	-2471(4)	2805(1)	42(1)
C(11)	4314(2)	-465(4)	3288(1)	43(1)
C(12)	3784(2)	-683(4)	3436(1)	56(1)
C(13)	3308(2)	358(5)	3347(2)	69(1)
C(14)	3354(2)	1629(5)	3107(2)	77(1)
C(15)	3885(2)	1876(4)	2972(2)	72(1)
C(16)	4356(2)	836(4)	3056(1)	56(1)
C(21)	6617(2)	-2671(6)	3588(2)	88(1)
C(22)	7230(2)	-2531(7)	4045(2)	125(2)
C(31)	5866(4)	-1140(9)	4658(2)	196(4)
C(32)	6183(3)	-583(8)	5132(2)	178(3)
C(51)	3027(2)	-2137(4)	1804(1)	43(1)
C(52)	2824(2)	-2641(4)	1294(1)	54(1)
C(53)	2256(2)	-2100(4)	909(1)	58(1)
C(54)	1909(2)	-1040(4)	1041(1)	49(1)
C(55)	2108(2)	-562(4)	1550(1)	53(1)
C(56)	2667(2)	-1106(4)	1933(1)	52(1)
C(57)	1083(2)	-882(4)	163(1)	58(1)
C(58)	1360(2)	-480(5)	-186(2)	78(1)
C(59)	1072(3)	-919(6)	-704(2)	86(1)
C(60)	519(3)	-1714(5)	-870(2)	85(2)
C(61)	245(2)	-2075(6)	-521(2)	99(2)
C(62)	520(2)	-1651(5)	9(2)	80(1)

Table 3. Bond lengths [Å] and angles [°] for **9ab.**

P(1)-O(1)	1.461(3)
P(1)-O(3)	1.549(3)
P(1)-O(2)	1.562(3)
P(1)-C(1)	1.826(3)
O(2)-C(21)	1.463(4)
O(3)-C(31)	1.328(6)
O(4)-C(4)	1.197(4)
O(5)-C(54)	1.378(4)
O(5)-C(57)	1.400(4)
O(6)-C(6)	1.208(4)
N(2)-C(3)	1.258(4)
N(2)-C(1)	1.480(4)
N(5)-C(4)	1.387(4)
N(5)-C(6)	1.393(4)
N(5)-C(51)	1.431(4)
C(1)-C(11)	1.532(5)
C(1)-C(6A)	1.595(4)
C(3)-C(3A)	1.497(4)
C(3A)-C(4)	1.514(4)
C(3A)-C(6A)	1.528(4)
C(6)-C(6A)	1.487(4)
C(11)-C(16)	1.387(5)
C(11)-C(12)	1.391(4)
C(12)-C(13)	1.380(5)
C(13)-C(14)	1.376(6)
C(14)-C(15)	1.376(6)
C(15)-C(16)	1.373(5)
C(21)-C(22)	1.447(6)
C(31)-C(32)	1.313(7)
C(51)-C(52)	1.368(4)
C(51)-C(56)	1.376(4)
C(52)-C(53)	1.381(5)
C(53)-C(54)	1.380(5)
C(54)-C(55)	1.359(4)
C(55)-C(56)	1.367(4)
C(57)-C(62)	1.351(5)
C(57)-C(58)	1.366(5)
C(58)-C(59)	1.369(6)
C(59)-C(60)	1.346(6)
C(60)-C(61)	1.352(6)
C(61)-C(62)	1.390(6)
O(1)-P(1)-O(3)	112.26(17)
O(1)-P(1)-O(2)	115.03(15)
O(3)-P(1)-O(2)	106.99(16)
O(1)-P(1)-C(1)	113.62(15)
O(3)-P(1)-C(1)	105.79(15)
O(2)-P(1)-C(1)	102.23(14)
C(21)-O(2)-P(1)	123.7(3)
C(31)-O(3)-P(1)	130.2(4)
C(54)-O(5)-C(57)	118.4(3)
C(3)-N(2)-C(1)	110.2(3)
C(4)-N(5)-C(6)	113.7(3)
C(4)-N(5)-C(51)	124.8(3)
C(6)-N(5)-C(51)	121.5(3)
N(2)-C(1)-C(11)	108.7(2)
N(2)-C(1)-C(6A)	105.1(3)

C(11)-C(1)-C(6A)	114.6(2)
N(2)-C(1)-P(1)	108.1(2)
C(11)-C(1)-P(1)	111.8(2)
C(6A)-C(1)-P(1)	108.0(2)
N(2)-C(3)-C(3A)	116.9(3)
C(3)-C(3A)-C(4)	113.1(3)
C(3)-C(3A)-C(6A)	103.1(3)
C(4)-C(3A)-C(6A)	105.0(3)
O(4)-C(4)-N(5)	125.5(3)
O(4)-C(4)-C(3A)	127.6(3)
N(5)-C(4)-C(3A)	106.9(3)
O(6)-C(6)-N(5)	124.3(3)
O(6)-C(6)-C(6A)	128.4(3)
N(5)-C(6)-C(6A)	107.3(3)
C(6)-C(6A)-C(3A)	105.1(3)
C(6)-C(6A)-C(1)	114.3(3)
C(3A)-C(6A)-C(1)	103.2(2)
C(16)-C(11)-C(12)	118.1(3)
C(16)-C(11)-C(1)	121.2(3)
C(12)-C(11)-C(1)	120.6(3)
C(13)-C(12)-C(11)	121.0(4)
C(14)-C(13)-C(12)	119.8(4)
C(13)-C(14)-C(15)	119.8(4)
C(16)-C(15)-C(14)	120.4(4)
C(15)-C(16)-C(11)	120.9(4)
C(22)-C(21)-O(2)	110.7(4)
C(32)-C(31)-O(3)	124.4(8)
C(52)-C(51)-C(56)	120.4(3)
C(52)-C(51)-N(5)	120.6(3)
C(56)-C(51)-N(5)	118.9(3)
C(51)-C(52)-C(53)	119.3(3)
C(54)-C(53)-C(52)	119.8(3)
C(55)-C(54)-O(5)	114.6(3)
C(55)-C(54)-C(53)	120.5(3)
O(5)-C(54)-C(53)	125.0(3)
C(54)-C(55)-C(56)	119.9(3)
C(55)-C(56)-C(51)	120.1(3)
C(62)-C(57)-C(58)	122.2(4)
C(62)-C(57)-O(5)	117.2(4)
C(58)-C(57)-O(5)	120.3(4)
C(57)-C(58)-C(59)	118.8(4)
C(60)-C(59)-C(58)	120.6(4)
C(59)-C(60)-C(61)	119.7(5)
C(60)-C(61)-C(62)	121.7(5)
C(57)-C(62)-C(61)	116.9(4)

Table 4. Anisotropic displacement parameters ($Å^2 x\ 10^3$) for **9ab**. The anisotropic displacement factor exponent takes the form: $-2\pi^2[\ h^2 a^{*2} U^{11} + ... + 2\ h\ k\ a^*\ b^*\ U^{12}\ ]$

	U^{11}	U^{22}	U^{33}	U^{23}	U^{13}	U^{12}
P(1)	42(1)	59(1)	50(1)	3(1)	10(1)	-9(1)
O(1)	56(2)	74(2)	76(2)	16(2)	22(1)	-16(1)
O(2)	40(1)	76(2)	80(2)	13(2)	20(1)	7(1)
O(3)	81(2)	90(2)	49(2)	-16(2)	5(1)	-7(2)
O(4)	51(1)	50(2)	64(2)	2(1)	18(1)	-10(1)
O(5)	63(2)	89(2)	51(2)	-2(2)	9(1)	29(2)
O(6)	58(2)	69(2)	45(1)	9(1)	16(1)	-16(1)
N(2)	44(2)	45(2)	46(2)	8(2)	14(1)	0(1)
N(5)	34(2)	43(2)	42(2)	-2(1)	13(1)	-2(1)
C(1)	42(2)	41(2)	38(2)	4(2)	14(2)	-6(2)
C(3)	39(2)	47(2)	56(2)	10(2)	15(2)	2(2)
C(3A)	37(2)	41(2)	51(2)	-2(2)	17(2)	4(2)
C(4)	43(2)	38(2)	45(2)	-6(2)	19(2)	-3(2)
C(6)	44(2)	51(2)	39(2)	-4(2)	17(2)	-6(2)
C(6A)	34(2)	50(2)	43(2)	-3(2)	16(2)	0(2)
C(11)	44(2)	45(2)	39(2)	-3(2)	13(2)	-4(2)
C(12)	58(2)	54(2)	59(2)	-2(2)	26(2)	0(2)
C(13)	58(3)	72(3)	78(3)	-17(3)	28(2)	7(2)
C(14)	75(3)	66(3)	77(3)	-17(3)	15(3)	23(3)
C(15)	84(3)	48(3)	74(3)	1(2)	20(3)	7(2)
C(16)	60(2)	50(2)	57(2)	5(2)	22(2)	3(2)
C(21)	75(3)	101(4)	92(3)	-4(3)	38(3)	10(3)
C(22)	52(3)	161(6)	148(5)	-9(4)	23(3)	4(3)
C(31)	265(10)	244(10)	63(4)	-9(5)	44(5)	50(8)
C(32)	215(8)	180(7)	73(4)	-20(5)	-17(4)	19(6)
C(51)	41(2)	47(2)	40(2)	-3(2)	16(2)	-4(2)
C(52)	54(2)	54(2)	49(2)	-9(2)	16(2)	11(2)
C(53)	56(2)	69(3)	40(2)	-11(2)	10(2)	9(2)
C(54)	44(2)	54(2)	45(2)	3(2)	14(2)	6(2)
C(55)	46(2)	56(2)	58(2)	-3(2)	20(2)	13(2)
C(56)	49(2)	62(2)	44(2)	-11(2)	19(2)	0(2)
C(57)	54(2)	65(3)	46(2)	4(2)	9(2)	12(2)
C(58)	77(3)	92(4)	60(3)	4(3)	22(2)	-6(3)
C(59)	105(4)	97(4)	60(3)	15(3)	36(3)	11(3)
C(60)	105(4)	79(4)	53(3)	0(3)	10(3)	23(3)
C(61)	86(4)	103(4)	86(4)	-9(3)	10(3)	-22(3)
C(62)	68(3)	100(4)	67(3)	6(3)	22(2)	-8(3)

Table 5. Hydrogen bonds for **9ab** [Å and °].

D-H...A	d(D-H)	d(H...A)	d(D...A)	<(DHA)
C(3A)-H(3A)...O(6)#1	0.98	2.42	3.290(4)	147.1
C(31)-H(31B)...O(2)	0.97	2.46	2.959(7)	111.9

Symmetry transformations used to generate equivalent atoms:
#1 -x+1,y-1/2,-z+1/2

Diethyl (1*RS*,3a*SR*,6a*SR*)-5-methyl-4,6-dioxo-1-phenyl-1,3a,4,5,6,6a-hexahydropyrrolo[3,4-*c*]pyrrole-1-phosphonate (9a)

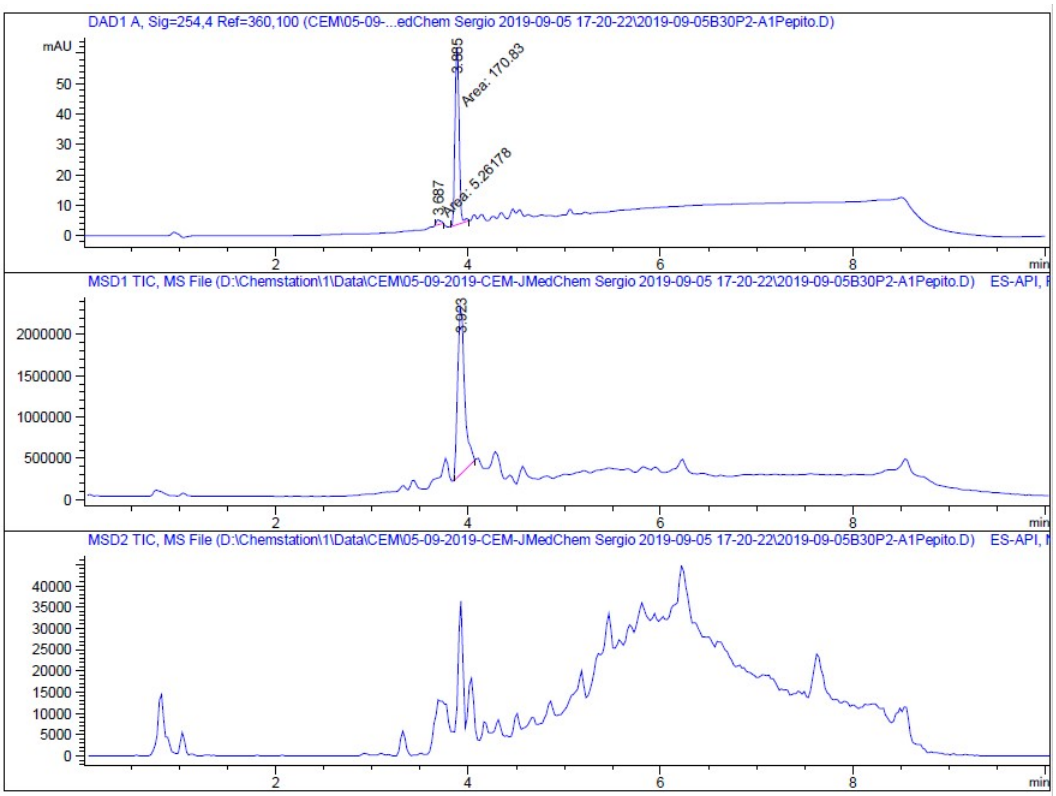


```
=====================================================================
                    Area Percent Report
=====================================================================

Sorted By             :      Signal
Multiplier            :      1.0000
Dilution              :      1.0000
Do not use Multiplier & Dilution Factor with ISTDs


Signal 1: DAD1 A, Sig=254,4 Ref=360,100

Peak RetTime Type  Width     Area      Height     Area
  #   [min]       [min]   [mAU*s]     [mAU]       %
----|-------|----|-------|----------|----------|--------|
   1   3.687 MM    0.0518    5.26178    1.69342   2.9881
   2   3.885 MM    0.0486  170.82957   58.59513  97.0119

Totals :                  176.09135   60.28854
```

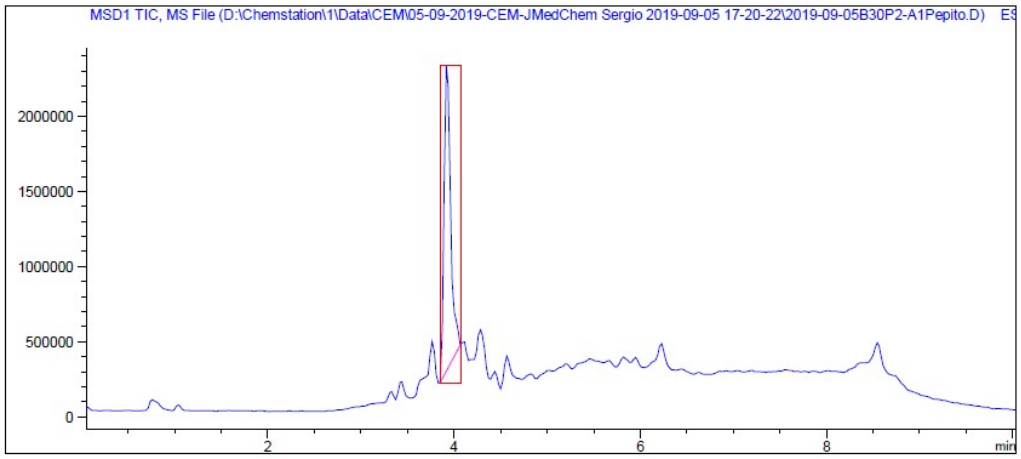
MSD1 TIC, MS File (D:\Chemstation\1\Data\CEM\05-09-2019-CEM-JMedChem Sergio 2019-09-05 17-20-22\2019-09-05B30P2-A1Pepito.D)
2000000
1500000
1000000
500000
0
2
4
6
8
min

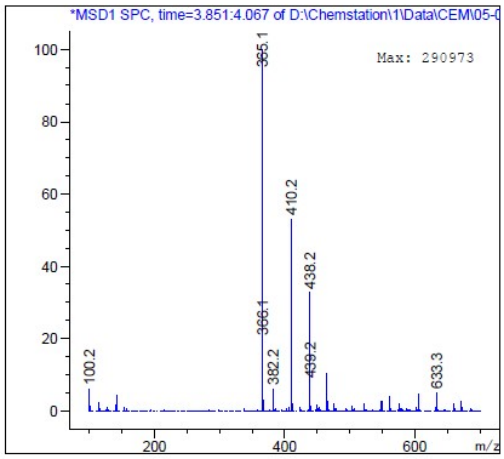
*MSD1 SPC, time=3.851:4.067 of D:\Chemstation\1\Data\CEM\05-0
Max: 290973
365.1
410.2
438.2
366.1
382.2
439.2
633.3
100.2
100
80
60
40
20
0
200
400
600
m/z

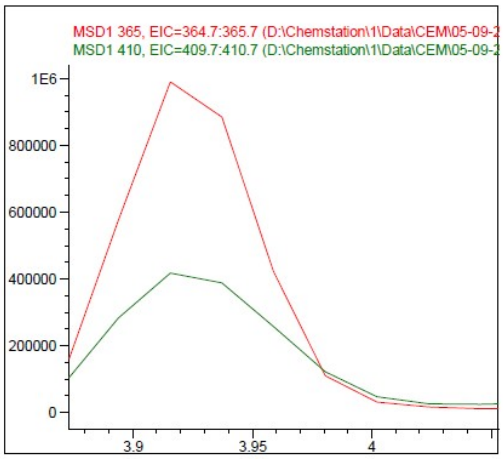
MSD1 365, EIC=364.7:365.7 (D:\Chemstation\1\Data\CEM\05-09-2
MSD1 410, EIC=409.7:410.7 (D:\Chemstation\1\Data\CEM\05-09-2
1E6
800000
600000
400000
200000
0
3.9
3.95
4

Diethyl (1*RS*,3a*SR*,6a*SR*)-1-benzyl-4,6-dioxo-5-phenyl-1,3a,4,5,6,6a-hexahydropyrrolo[3,4-*c*]pyrrole-1-phosphonate (14c)

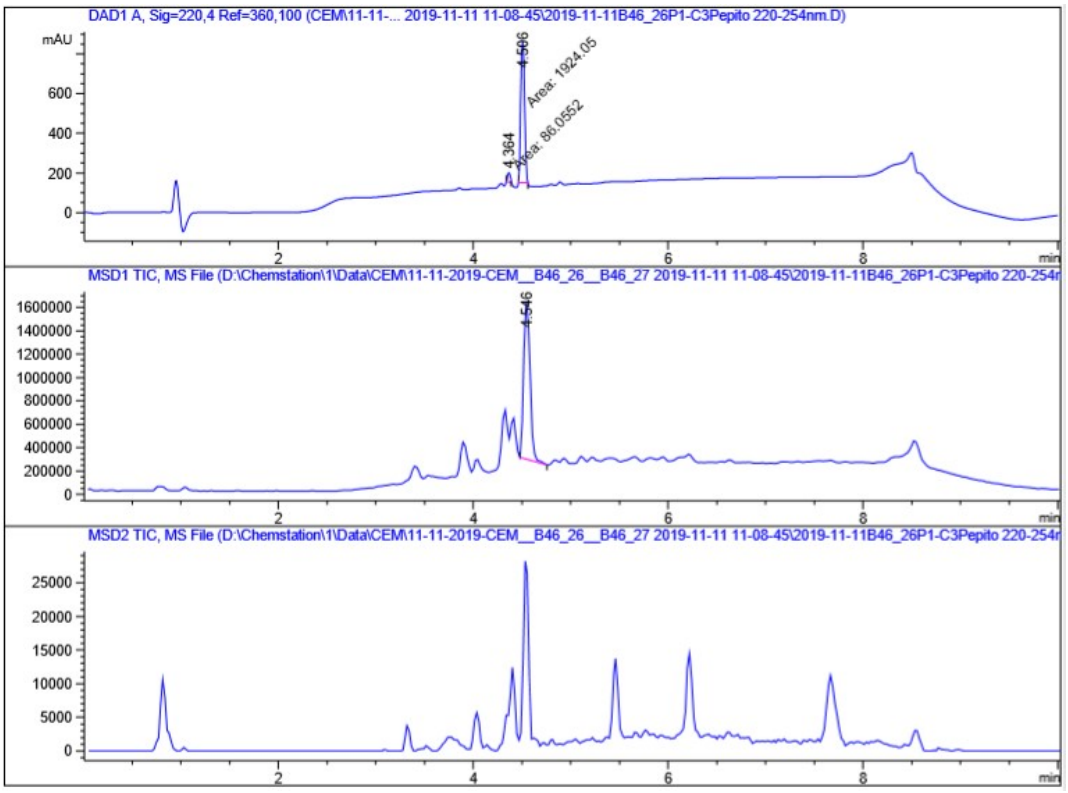


```
=====================================================================
                      Area Percent Report
=====================================================================

Sorted By             :      Signal
Multiplier            :      1.0000
Dilution              :      1.0000
Use Multiplier & Dilution Factor with ISTDs


Signal 1: DAD1 A, Sig=220,4 Ref=360,100

Peak RetTime Type  Width     Area      Height     Area
  #   [min]        [min]   [mAU*s]     [mAU]       %
----|-------|----|-------|----------|----------|--------|
   1   4.364 MM    0.0311   86.05524   46.19073   4.2811
   2   4.506 MM    0.0448 1924.05261  716.32135  95.7189

Totals :                  2010.10786  762.51208
```

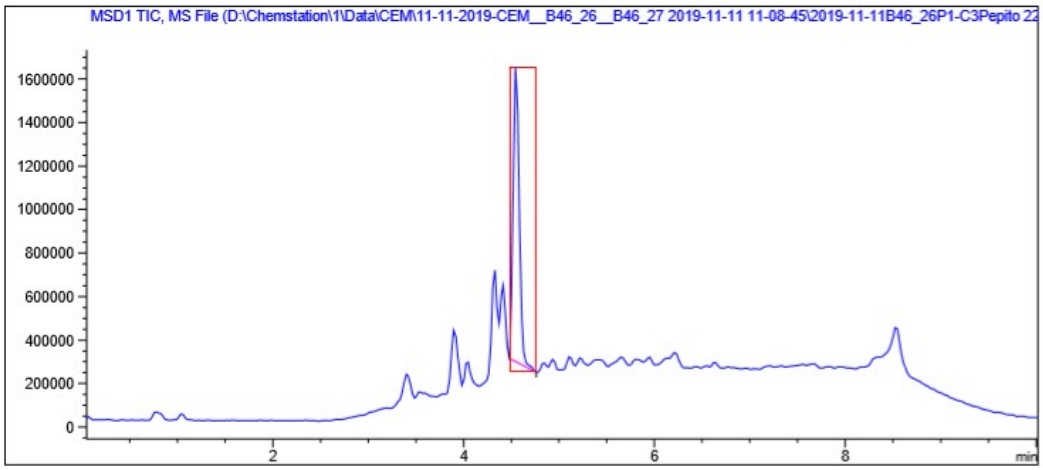
MSD1 TIC, MS File (D:\Chemstation\1\Data\CEM\11-11-2019-CEM__B46_26__B46_27 2019-11-11 11-08-45\2019-11-11B46_26P1-C3Pepito 22
1600000
1400000
1200000
1000000
800000
600000
400000
200000
0
2
4
6
8
min

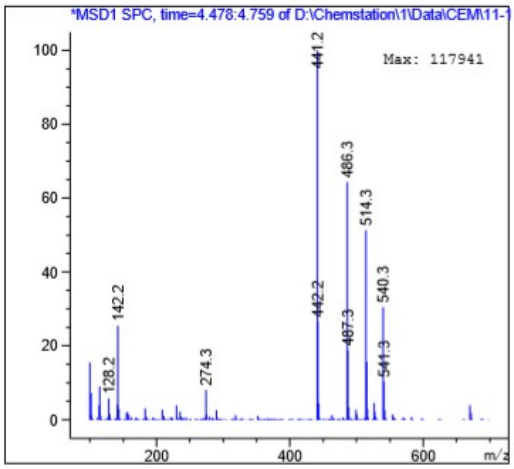
*MSD1 SPC, time=4.478:4.759 of D:\Chemstation\1\Data\CEM\11-1
Max: 117941
100
80
60
40
20
0
441.2
486.3
514.3
540.3
142.2
442.2
487.3
541.3
128.2
274.3
200
400
600
m/z

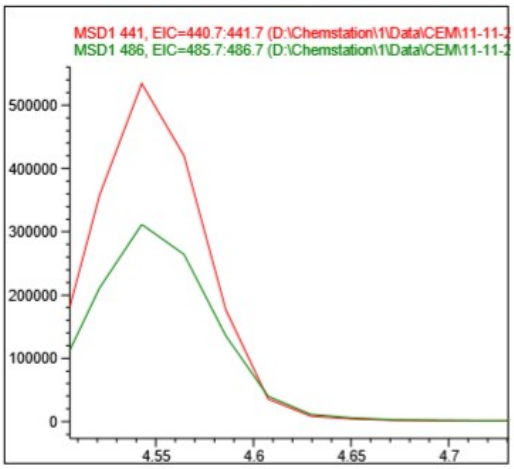
MSD1 441, EIC=440.7:441.7 (D:\Chemstation\1\Data\CEM\11-11-2
MSD1 486, EIC=485.7:486.7 (D:\Chemstation\1\Data\CEM\11-11-2
500000
400000
300000
200000
100000
0
4.55
4.6
4.65
4.7

Diethyl (1*RS*,3a*SR*,6a*SR*)-1-(4-fluorobenzyl)-4,6-dioxo-5-phenyl-1,3a,4,5,6,6a-hexahydropyrrolo[3,4-*c*]pyrrole-1-phosphonate (15c)

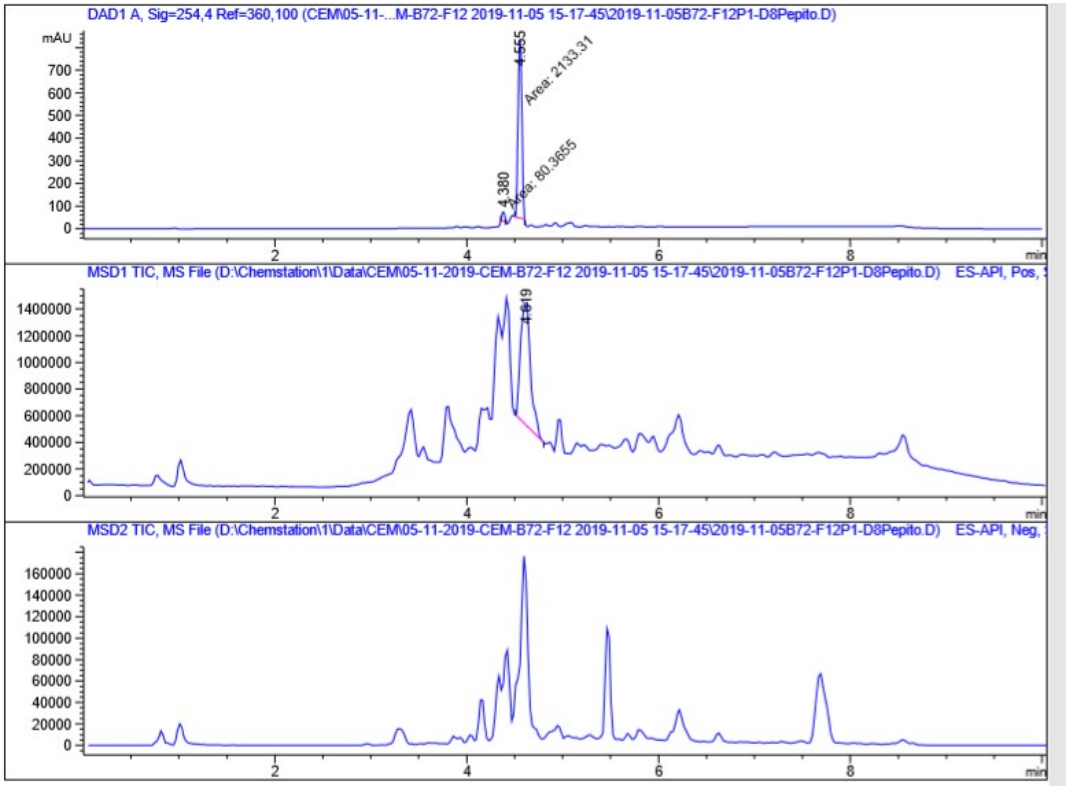


```
=====================================================================
                        Area Percent Report
=====================================================================

Sorted By             :      Signal
Multiplier            :      1.0000
Dilution              :      1.0000
Do not use Multiplier & Dilution Factor with ISTDs

 Signal 1: DAD1 A, Sig=254,4 Ref=360,100

 Peak RetTime Type  Width     Area      Height     Area
   #   [min]        [min]   [mAU*s]     [mAU]       %
----|-------|----|-------|----------|----------|--------|
   1   4.380 MM    0.0321   80.36546   41.77053   3.6304
   2   4.555 MM    0.0450 2133.30615  790.23047  96.3696

 Totals :                  2213.67161  832.00100
```

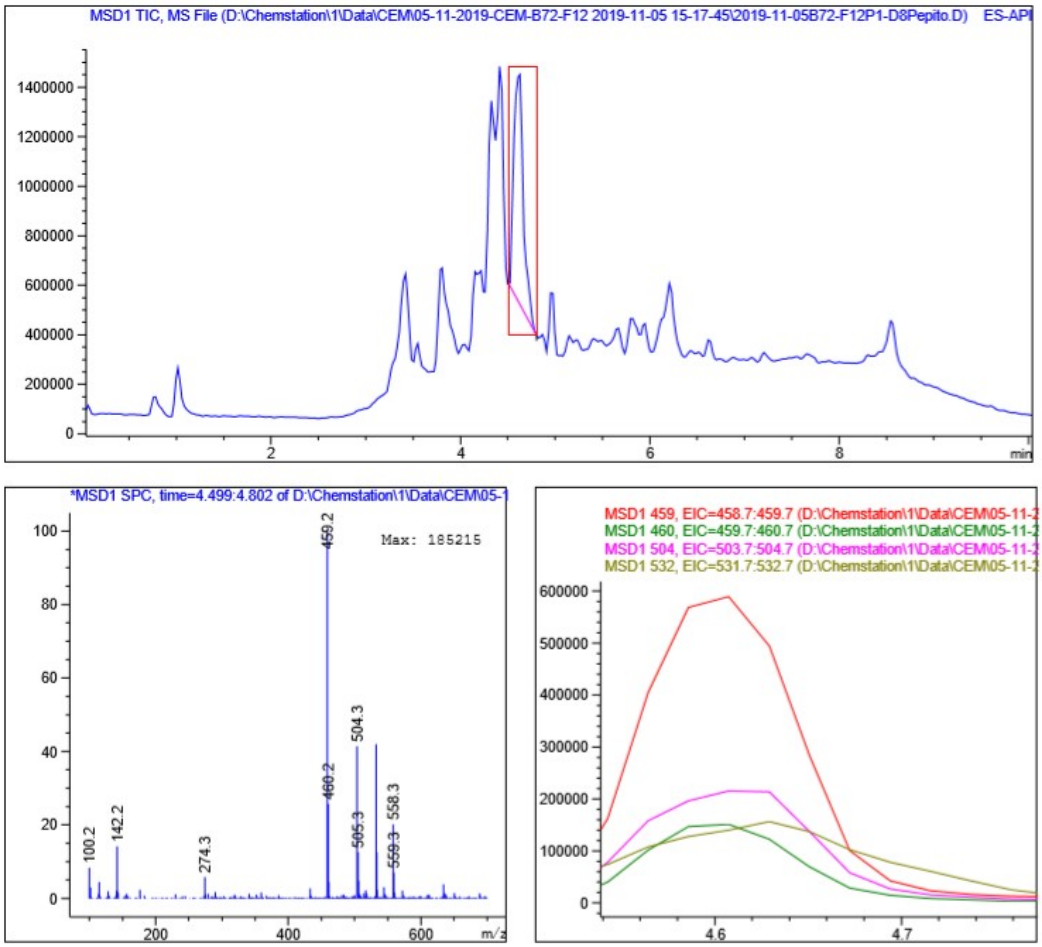
MSD1 TIC, MS File (D:\Chemstation\1\Data\CEM\05-11-2019-CEM-B72-F12 2019-11-05 15-17-45\2019-11-05B72-F12P1-D8Pepito.D) ES-API
1400000
1200000
1000000
800000
600000
400000
200000
0
2
4
6
8
min
*MSD1 SPC, time=4.499:4.802 of D:\Chemstation\1\Data\CEM\05-1
Max: 185215
459.2
504.3
460.2
505.3
559.3
558.3
142.2
100.2
274.3
100
80
60
40
20
0
200
400
600
m/z
MSD1 459, EIC=458.7:459.7 (D:\Chemstation\1\Data\CEM\05-11-2
MSD1 460, EIC=459.7:460.7 (D:\Chemstation\1\Data\CEM\05-11-2
MSD1 504, EIC=503.7:504.7 (D:\Chemstation\1\Data\CEM\05-11-2
MSD1 532, EIC=531.7:532.7 (D:\Chemstation\1\Data\CEM\05-11-2
600000
500000
400000
300000
200000
100000
0
4.6
4.7

Diethyl (1*RS*,3a*SR*,6a*SR*)-5-ethyl-4,6-dioxo-1-phenyl-1,3a,4,5,6,6a-hexahydropyrrolo[3,4-*c*]pyrrole-1-phosphonate (9f)

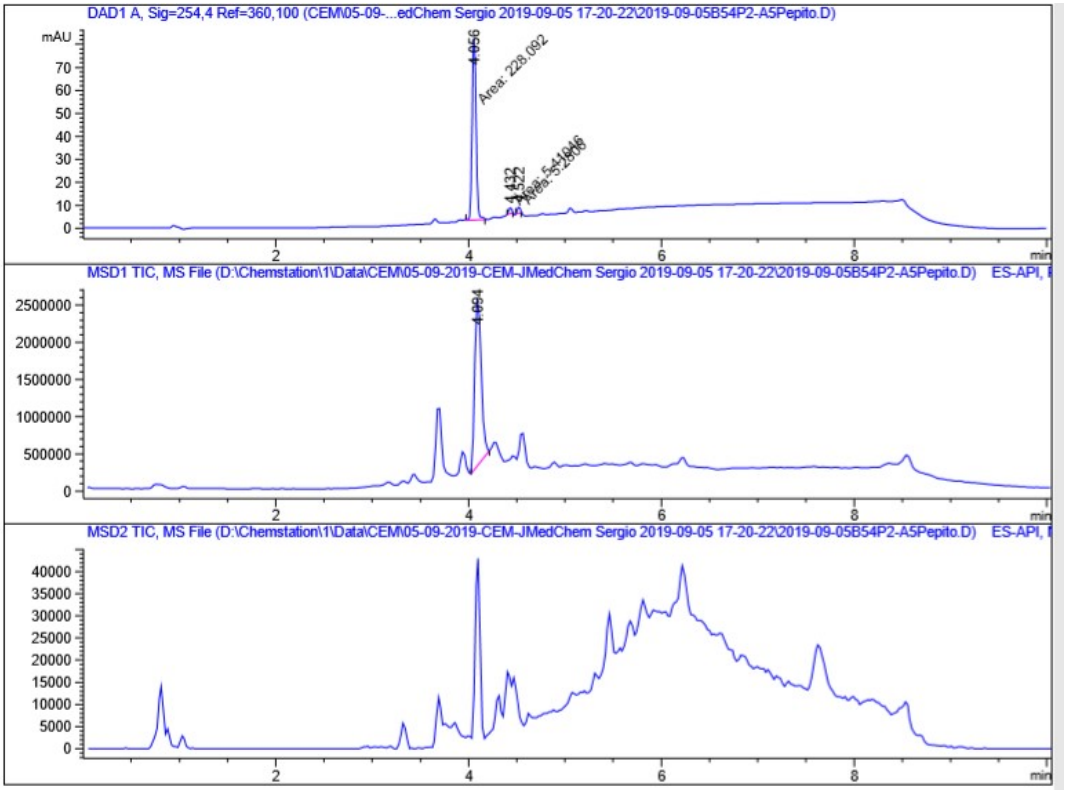


```
=====================================================================
                        Area Percent Report
=====================================================================

Sorted By             :      Signal
Multiplier            :      1.0000
Dilution              :      1.0000
Do not use Multiplier & Dilution Factor with ISTDs


 Signal 1: DAD1 A, Sig=254,4 Ref=360,100

 Peak RetTime Type  Width     Area      Height     Area
   #   [min]        [min]   [mAU*s]     [mAU]       %
 ----|-------|----|-------|----------|----------|--------|
    1   4.056 MM    0.0480  228.09171   79.25881  95.5227
    2   4.432 MM    0.0360    5.41046    2.50647   2.2659
    3   4.522 MM    0.0328    5.28060    2.68492   2.2115

 Totals :                    238.78277   84.45021
```

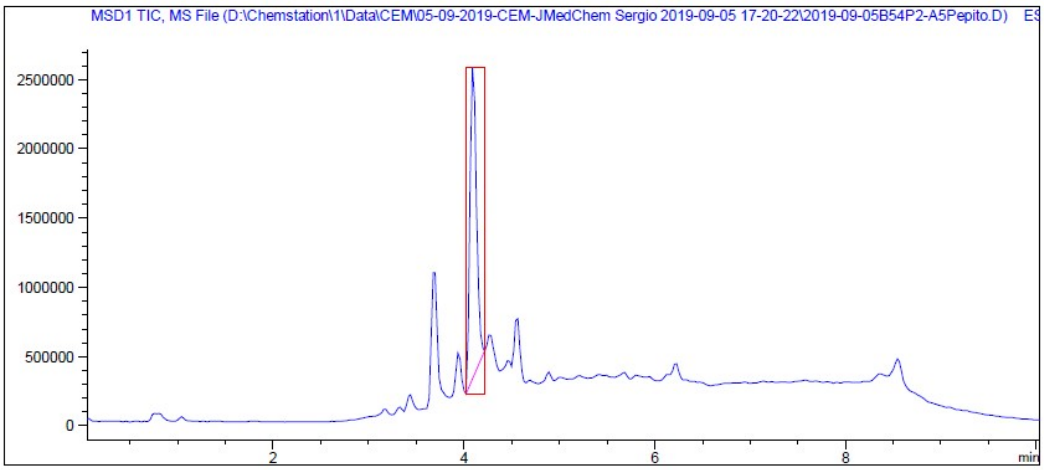
MSD1 TIC, MS File (D:\Chemstation\1\Data\CEM\05-09-2019-CEM-JMedChem Sergio 2019-09-05 17-20-22\2019-09-05B54P2-A5Pepito.D)
2500000
2000000
1500000
1000000
500000
0
2
4
6
8
min

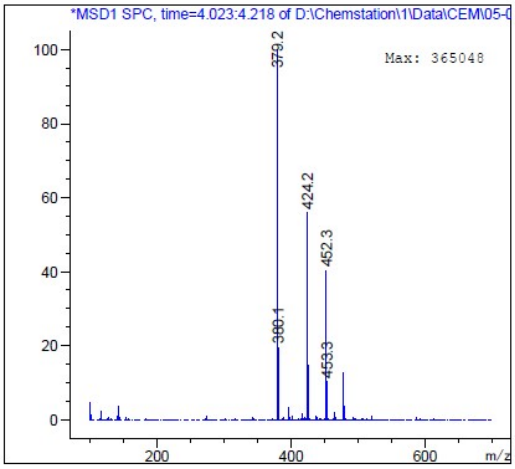
*MSD1 SPC, time=4.023:4.218 of D:\Chemstation\1\Data\CEM\05-0
Max: 365048
379.2
424.2
452.3
380.1
453.3
100
80
60
40
20
0
200
400
600
m/z

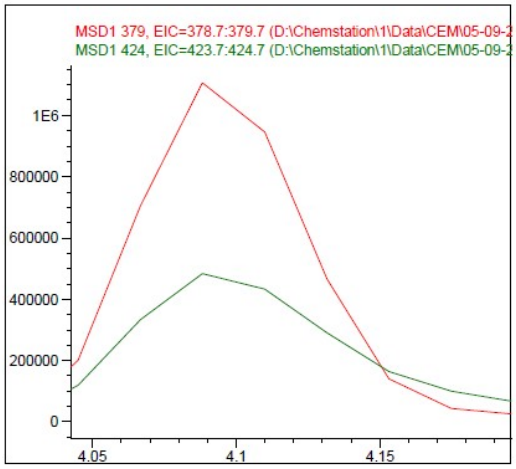
MSD1 379, EIC=378.7:379.7 (D:\Chemstation\1\Data\CEM\05-09-2
MSD1 424, EIC=423.7:424.7 (D:\Chemstation\1\Data\CEM\05-09-2
1E6
800000
600000
400000
200000
0
4.05
4.1
4.15

Diethyl (1*RS*,3a*SR*,6a*SR*)-4,6-dioxo-1-phenyl-5-propyl-1,3a,4,5,6,6a-hexahydropyrrolo[3,4-*c*]pyrrole-1-phosphonate (9g)

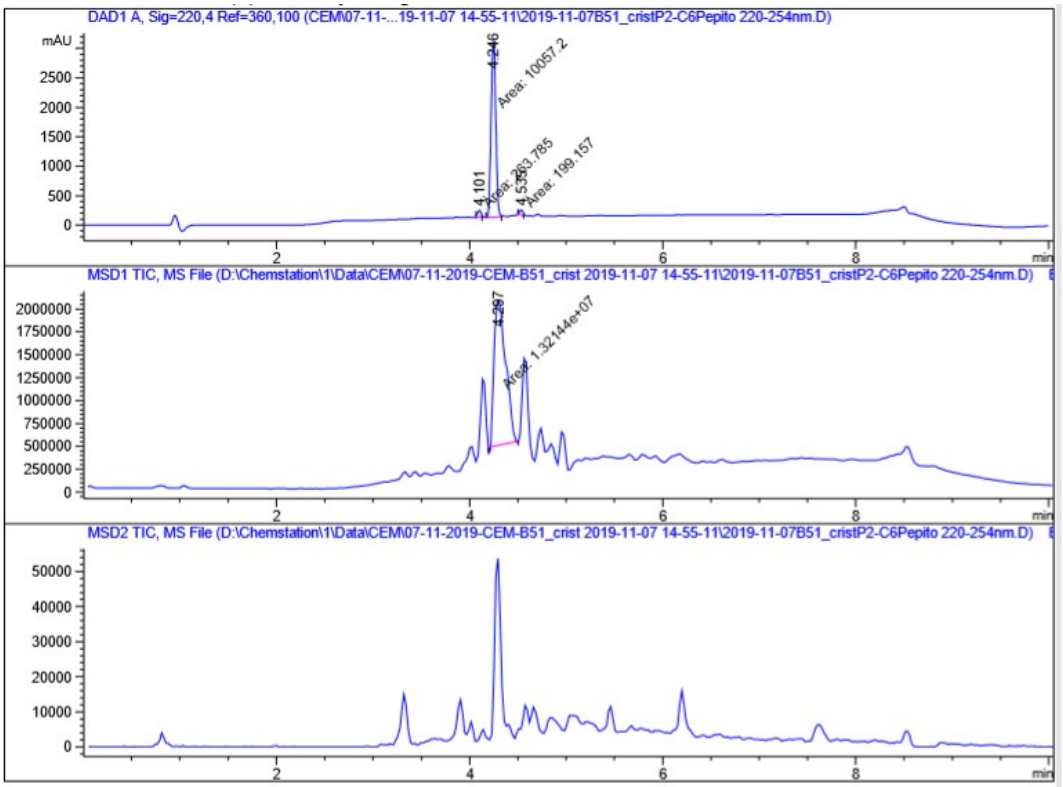


```
=====================================================================
                      Area Percent Report
=====================================================================

Sorted By             :      Signal
Multiplier            :      1.0000
Dilution              :      1.0000
Do not use Multiplier & Dilution Factor with ISTDs


Signal 1: DAD1 A, Sig=220,4 Ref=360,100

Peak RetTime Type  Width     Area      Height     Area
  #   [min]        [min]   [mAU*s]     [mAU]       %
----|-------|----|-------|----------|----------|--------|
   1   4.101 MM    0.0399  263.78546  110.05743   2.5074
   2   4.246 MM    0.0558 1.00572e4  3001.36499  95.5995
   3   4.535 MM    0.0399  199.15672   83.17267   1.8931

Totals :                  1.05202e4  3194.59509
```

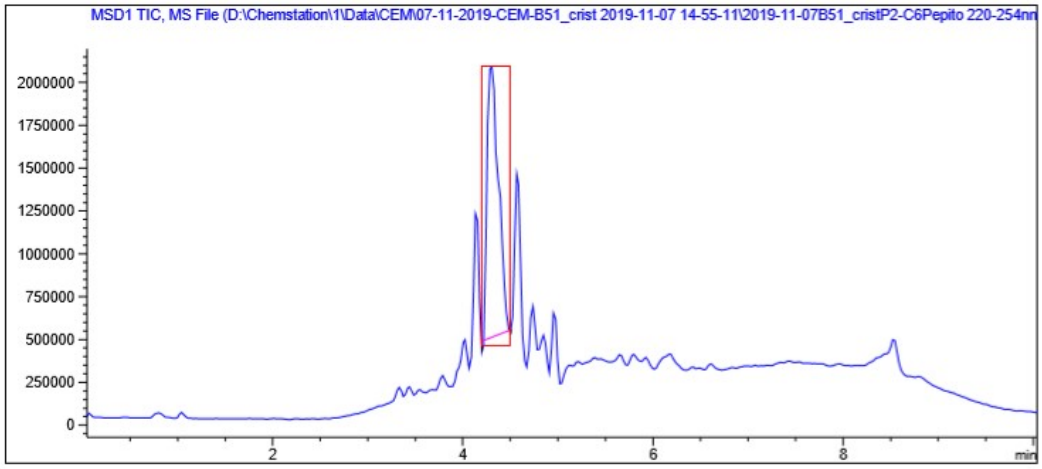
MSD1 TIC, MS File (D:\Chemstation\1\Data\CEM\07-11-2019-CEM-B51_crist 2019-11-07 14-55-11\2019-11-07B51_cristP2-C6Pepito 220-254nm
2000000
1750000
1500000
1250000
1000000
750000
500000
250000
0
2
4
6
8
min

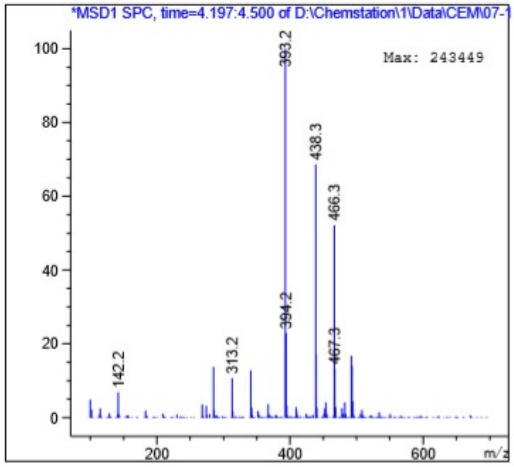
*MSD1 SPC, time=4.197:4.500 of D:\Chemstation\1\Data\CEM\07-1
Max: 243449
393.2
438.3
466.3
394.2
467.3
142.2
313.2
100
80
60
40
20
0
200
400
600
m/z

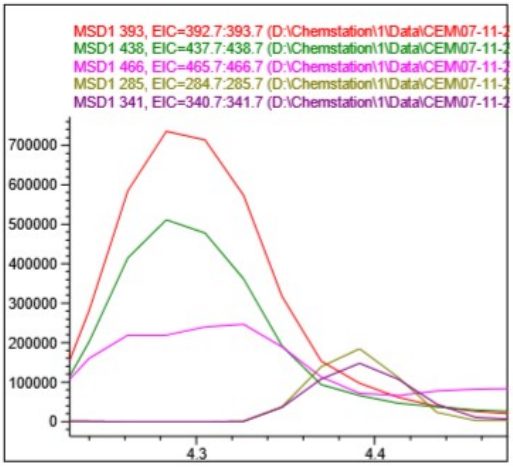
MSD1 393, EIC=392.7:393.7 (D:\Chemstation\1\Data\CEM\07-11-2
MSD1 438, EIC=437.7:438.7 (D:\Chemstation\1\Data\CEM\07-11-2
MSD1 466, EIC=465.7:466.7 (D:\Chemstation\1\Data\CEM\07-11-2
MSD1 285, EIC=284.7:285.7 (D:\Chemstation\1\Data\CEM\07-11-2
MSD1 341, EIC=340.7:341.7 (D:\Chemstation\1\Data\CEM\07-11-2
700000
600000
500000
400000
300000
200000
100000
0
4.3
4.4

Diethyl (1*RS*,3a*SR*,6a*SR*)-5-(tert-butyl)-4,6-dioxo-1-phenyl-1,3a,4,5,6,6a-hexahydropyrrolo[3,4-*c*]pyrrole-1-phosphonate (9h)

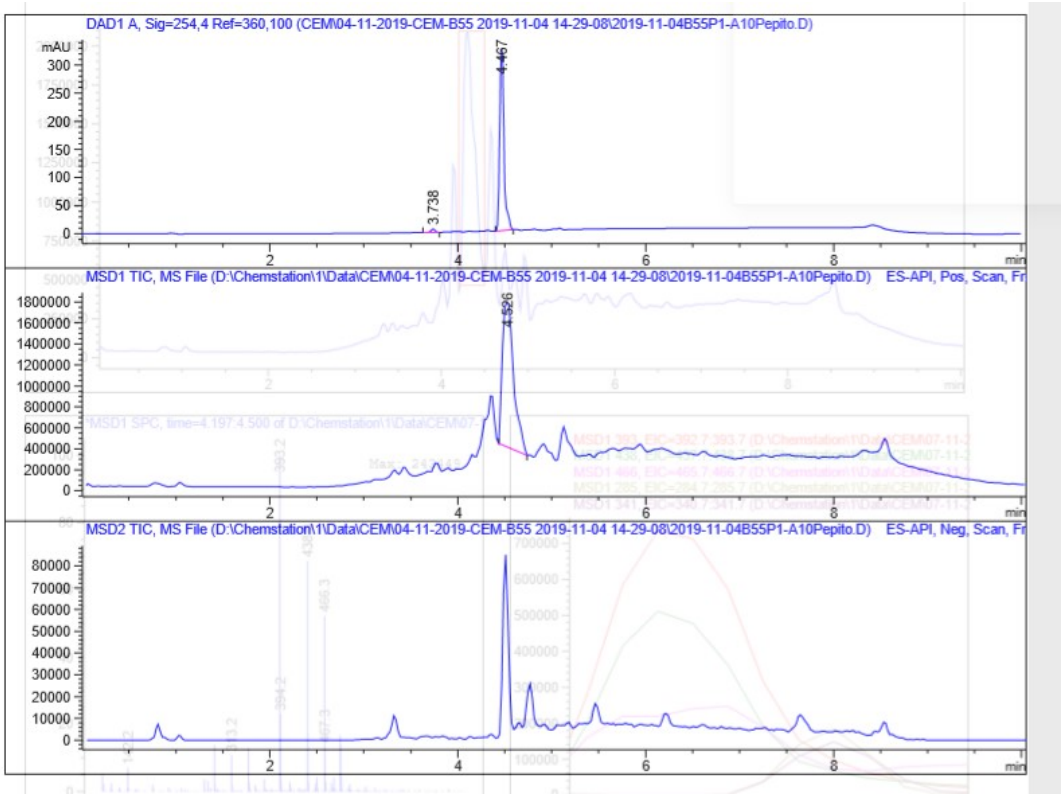


```
=====================================================================
                        Area Percent Report
=====================================================================

Sorted By             :      Signal
Multiplier            :      1.0000
Dilution              :      1.0000
Do not use Multiplier & Dilution Factor with ISTDs


Signal 1: DAD1 A, Sig=254,4 Ref=360,100

Peak RetTime Type  Width     Area      Height     Area
  #   [min]        [min]   [mAU*s]     [mAU]       %
----|-------|----|-------|----------|----------|--------|
   1   3.738 BB    0.0468   17.44491    5.85403   1.6787
   2   4.467 BB    0.0487 1021.77124  324.38782  98.3213

Totals :                  1039.21615  330.24185
```

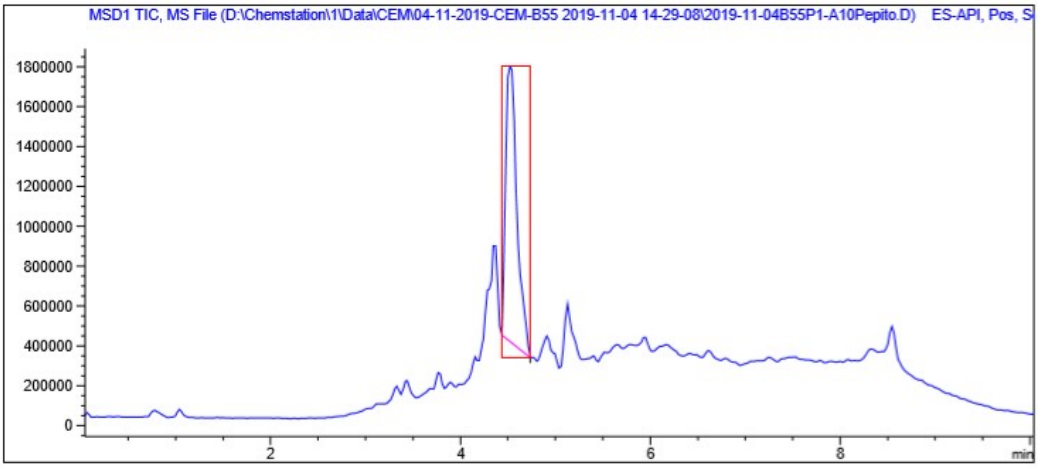
MSD1 TIC, MS File (D:\Chemstation\1\Data\CEM\04-11-2019-CEM-B55 2019-11-04 14-29-08\2019-11-04B55P1-A10Pepito.D) ES-API, Pos, S
1800000
1600000
1400000
1200000
1000000
800000
600000
400000
200000
0
2
4
6
8
min

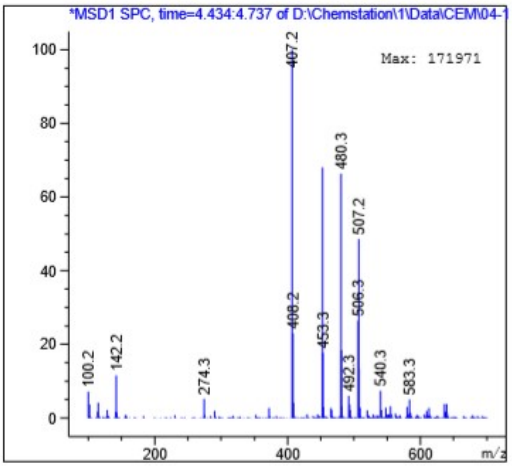
*MSD1 SPC, time=4.434:4.737 of D:\Chemstation\1\Data\CEM\04-1
Max: 171971
100
80
60
40
20
0
100.2
142.2
274.3
406.2
407.2
453.3
480.3
492.3
506.3
507.2
540.3
583.3
200
400
600
m/z

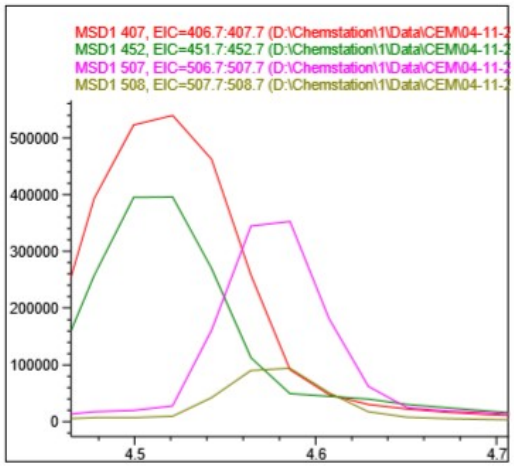
MSD1 407, EIC=406.7:407.7 (D:\Chemstation\1\Data\CEM\04-11-2
MSD1 452, EIC=451.7:452.7 (D:\Chemstation\1\Data\CEM\04-11-2
MSD1 507, EIC=506.7:507.7 (D:\Chemstation\1\Data\CEM\04-11-2
MSD1 508, EIC=507.7:508.7 (D:\Chemstation\1\Data\CEM\04-11-2
500000
400000
300000
200000
100000
0
4.5
4.6
4.7

Diethyl (1*RS*,3a*SR*,6a*SR*)-5-(adamantan-1-yl)methyl)-4,6-dioxo-1-phenyl-1,3a,4,5,6,6a-hexahydropyrrolo[3,4-*c*]pyrrole-1-phosphonate (9i)

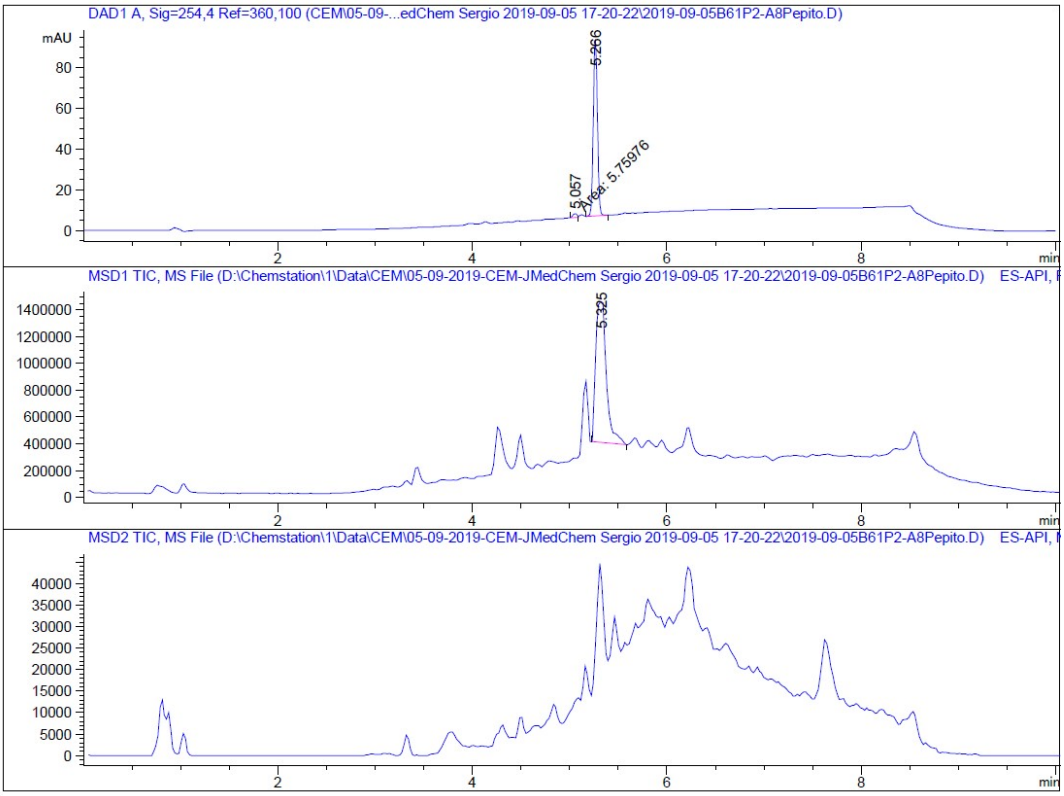


```
=====================================================================
                        Area Percent Report
=====================================================================

Sorted By             :      Signal
Multiplier            :      1.0000
Dilution              :      1.0000
Do not use Multiplier & Dilution Factor with ISTDs


Signal 1: DAD1 A, Sig=254,4 Ref=360,100

Peak RetTime Type  Width     Area      Height     Area
  #   [min]        [min]   [mAU*s]     [mAU]       %
----|-------|----|-------|----------|----------|--------|
   1   5.057 MF    0.0487    5.75976    1.97158   2.1773
   2   5.266 BB    0.0489  258.77179   86.45103  97.8227

Totals :                    264.53155   88.42261
```

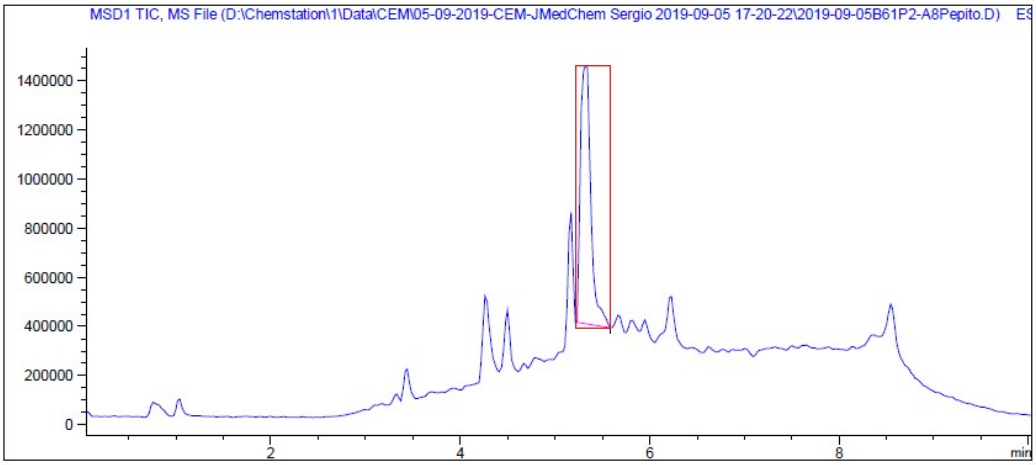
MSD1 TIC, MS File (D:\Chemstation\1\Data\CEM\05-09-2019-CEM-JMedChem Sergio 2019-09-05 17-20-22\2019-09-05B61P2-A8Pepito.D)
1400000
1200000
1000000
800000
600000
400000
200000
0
2
4
6
8

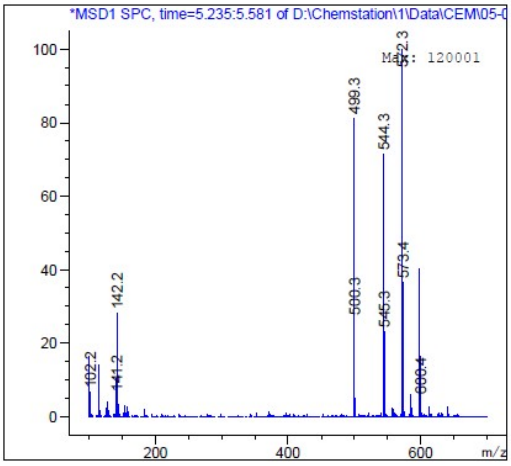
*MSD1 SPC, time=5.235:5.581 of D:\Chemstation\1\Data\CEM\05-0
Max: 120001
499.3
544.3
572.3
573.4
500.3
545.3
142.2
102.2
141.2
100
80
60
40
20
0
200
400
600
m/z

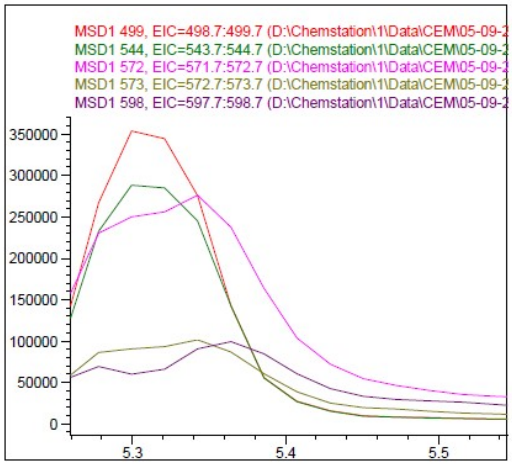
MSD1 499, EIC=498.7:499.7 (D:\Chemstation\1\Data\CEM\05-09-2
MSD1 544, EIC=543.7:544.7 (D:\Chemstation\1\Data\CEM\05-09-2
MSD1 572, EIC=571.7:572.7 (D:\Chemstation\1\Data\CEM\05-09-2
MSD1 573, EIC=572.7:573.7 (D:\Chemstation\1\Data\CEM\05-09-2
MSD1 598, EIC=597.7:598.7 (D:\Chemstation\1\Data\CEM\05-09-2
350000
300000
250000
200000
150000
100000
50000
0
5.3
5.4
5.5

Diethyl (1*RS*,3a*SR*,6a*SR*)-5-benzyl-4,6-dioxo-1-phenyl-1,3a,4,5,6,6a-hexahydropyrrolo[3,4-*c*]pyrrole-1-phosphonate (9j)

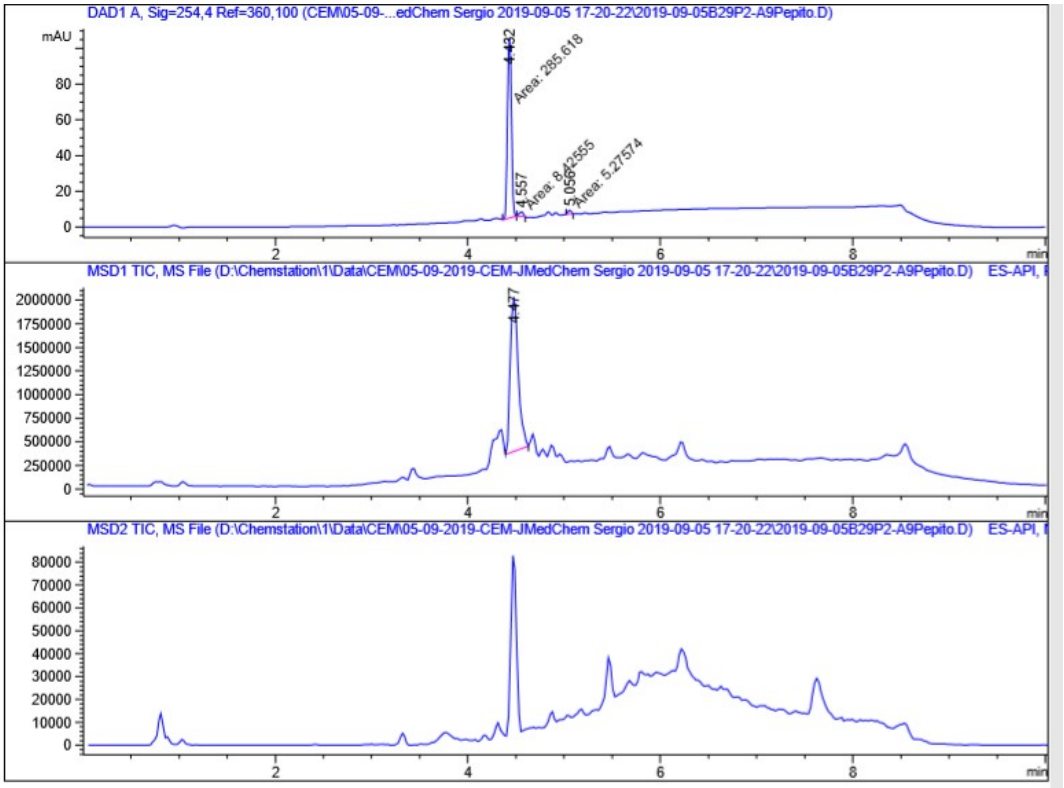


```
================================================================================
                            Area Percent Report
================================================================================

Sorted By             :      Signal
Multiplier            :      1.0000
Dilution              :      1.0000
Do not use Multiplier & Dilution Factor with ISTDs


 Signal 1: DAD1 A, Sig=254,4 Ref=360,100

 Peak RetTime Type  Width     Area      Height     Area
   #   [min]        [min]   [mAU*s]     [mAU]       %
----|-------|----|-------|----------|----------|--------|
   1   4.432 MM    0.0470  285.61795  101.35640  95.4225
   2   4.557 MM    0.0523    8.42555    2.68248   2.8149
   3   5.056 MM    0.0398    5.27574    2.21116   1.7626

 Totals :                  299.31924  106.25004
```

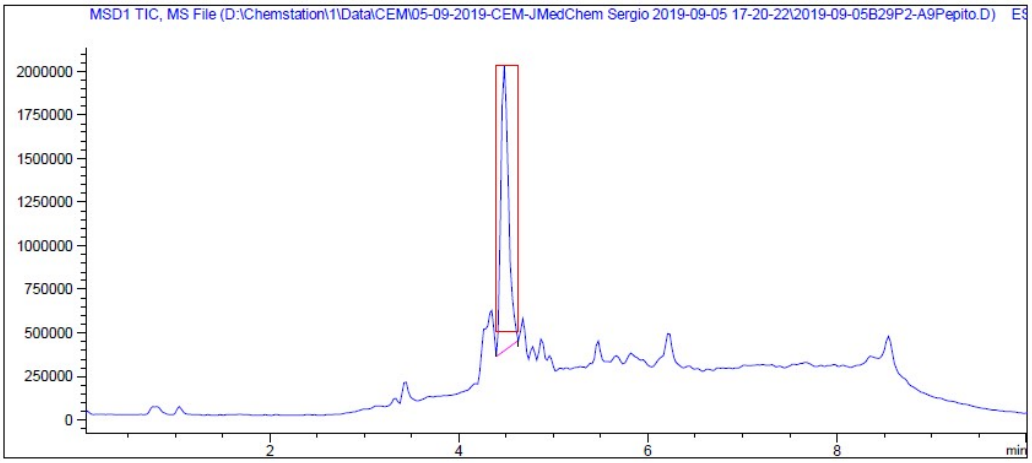
MSD1 TIC, MS File (D:\Chemstation\1\Data\CEM\05-09-2019-CEM-JMedChem Sergio 2019-09-05 17-20-22\2019-09-05B29P2-A9Pepito.D)
2000000
1750000
1500000
1250000
1000000
750000
500000
250000
0
2
4
6
8

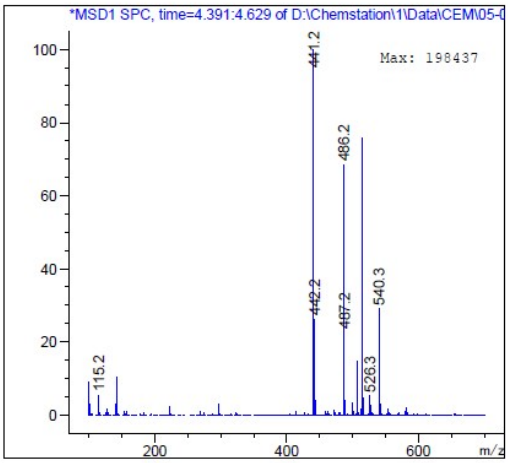
*MSD1 SPC, time=4.391:4.629 of D:\Chemstation\1\Data\CEM\05-0
Max: 198437
441.2
486.2
442.2
487.2
540.3
526.3
115.2
100
80
60
40
20
0
200
400
600
m/z

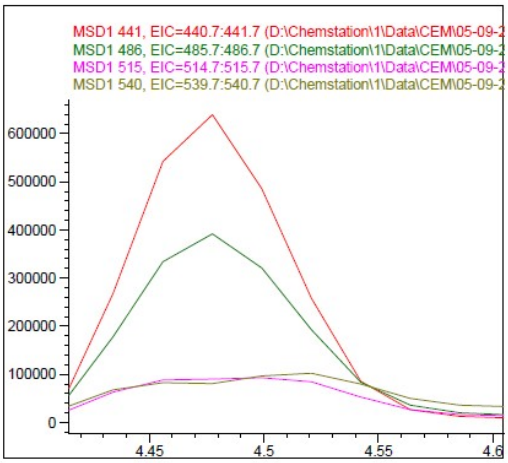
MSD1 441, EIC=440.7:441.7 (D:\Chemstation\1\Data\CEM\05-09-2
MSD1 486, EIC=485.7:486.7 (D:\Chemstation\1\Data\CEM\05-09-2
MSD1 515, EIC=514.7:515.7 (D:\Chemstation\1\Data\CEM\05-09-2
MSD1 540, EIC=539.7:540.7 (D:\Chemstation\1\Data\CEM\05-09-2
600000
500000
400000
300000
200000
100000
0
4.45
4.5
4.55
4.6

Diethyl (1*RS*,3a*SR*,6a*SR*)-4,6-dioxo-5-phenethyl-1-phenyl-1,3a,4,5,6,6a-hexahydropyrrolo[3,4-*c*]pyrrole-1-phosphonate (9k)

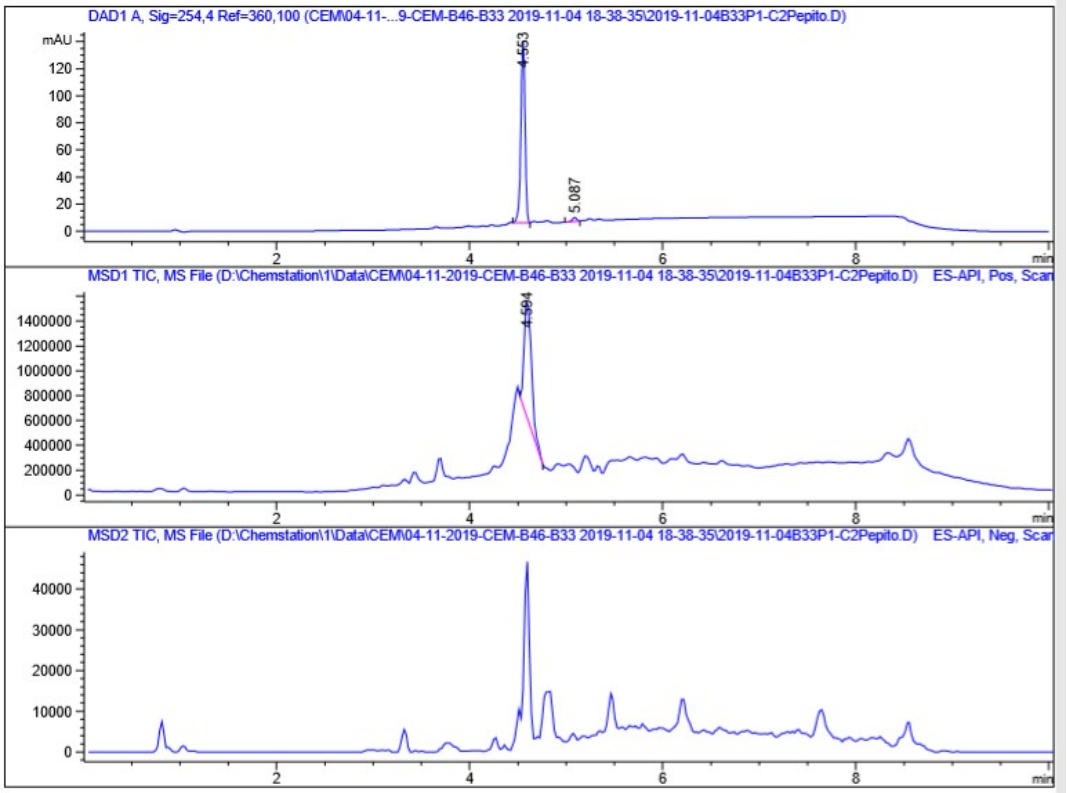


```
=====================================================================

                        Area Percent Report

=====================================================================

Sorted By             :      Signal
Multiplier            :      1.0000
Dilution              :      1.0000
Do not use Multiplier & Dilution Factor with ISTDs


Signal 1: DAD1 A, Sig=254,4 Ref=360,100

Peak RetTime Type  Width     Area      Height     Area
  #   [min]        [min]   [mAU*s]     [mAU]       %
----|-------|----|-------|----------|----------|--------|
   1   4.553 BB    0.0497  410.48108  133.97070  98.0419
   2   5.087 BB    0.0482    8.19819    2.79994   1.9581

Totals :                   418.67927  136.77065
```

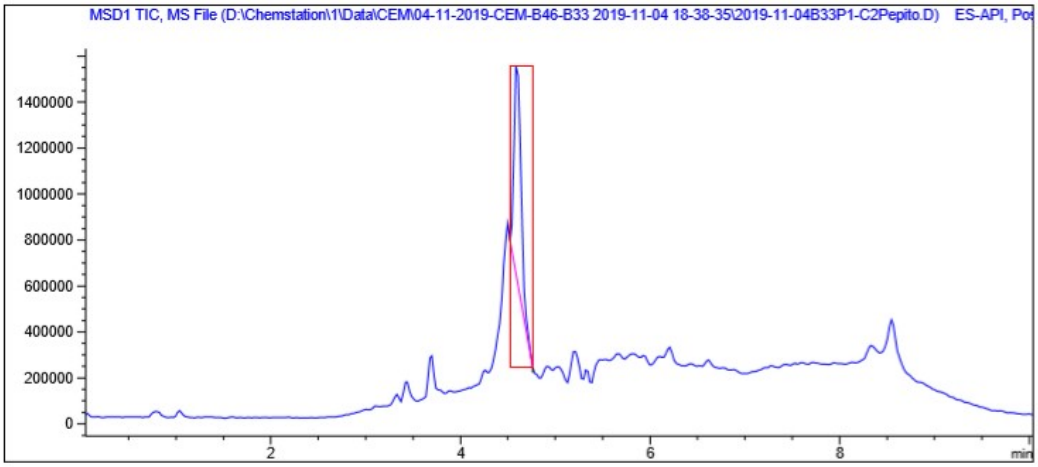
MSD1 TIC, MS File (D:\Chemstation\1\Data\CEM\04-11-2019-CEM-B46-B33 2019-11-04 18-38-35\2019-11-04B33P1-C2Pepito.D) ES-API, Pos
1400000
1200000
1000000
800000
600000
400000
200000
0
2
4
6
8
min

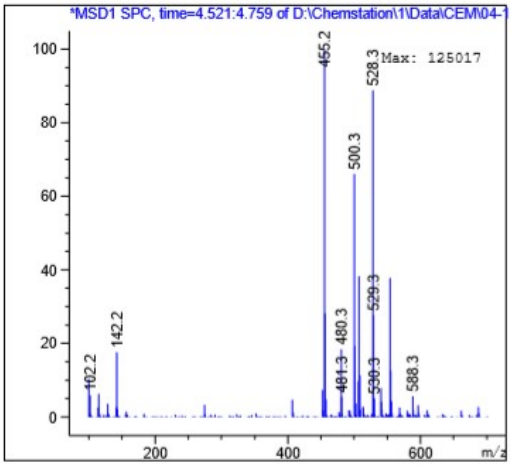
*MSD1 SPC, time=4.521:4.759 of D:\Chemstation\1\Data\CEM\04-1
Max: 125017
455.2
528.3
500.3
529.3
480.3
142.2
102.2
481.3
530.3
588.3
100
80
60
40
20
0
200
400
600
m/z

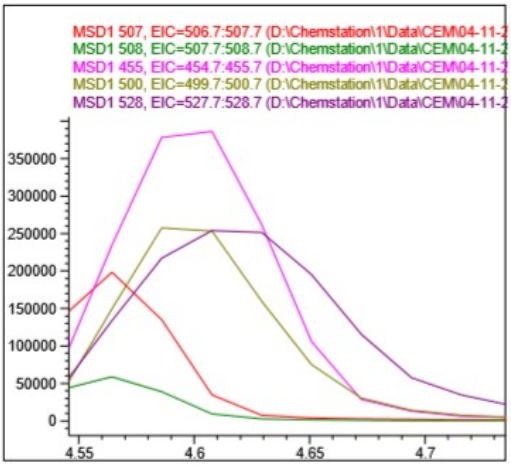
MSD1 507, EIC=506.7:507.7 (D:\Chemstation\1\Data\CEM\04-11-2
MSD1 508, EIC=507.7:508.7 (D:\Chemstation\1\Data\CEM\04-11-2
MSD1 455, EIC=454.7:455.7 (D:\Chemstation\1\Data\CEM\04-11-2
MSD1 500, EIC=499.7:500.7 (D:\Chemstation\1\Data\CEM\04-11-2
MSD1 528, EIC=527.7:528.7 (D:\Chemstation\1\Data\CEM\04-11-2
350000
300000
250000
200000
150000
100000
50000
0
4.55
4.6
4.65
4.7

Diethyl (1*RS*,3a*SR*,6a*SR*)-4,6-dioxo-1-phenyl-5-(2,4,6-trichlorophenyl)-1,3a,4,5,6,6a-hexahydropyrrolo[3,4-*c*]pyrrole-1-phosphonate (9w)

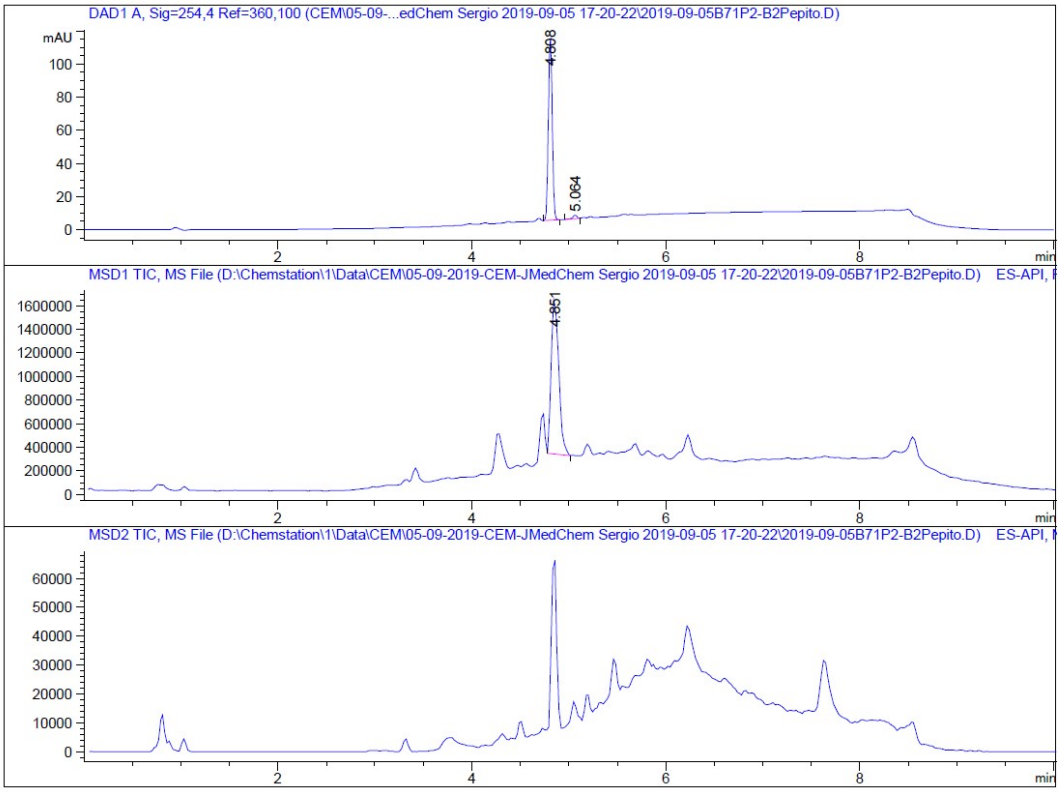


```
=====================================================================
                        Area Percent Report
=====================================================================

Sorted By             :      Signal
Multiplier            :      1.0000
Dilution              :      1.0000
Do not use Multiplier & Dilution Factor with ISTDs


Signal 1: DAD1 A, Sig=254,4 Ref=360,100

Peak RetTime Type  Width     Area      Height     Area
  #   [min]        [min]   [mAU*s]     [mAU]       %
----|-------|----|-------|----------|----------|--------|
   1   4.808 BB    0.0453  314.69922  110.17357  97.9988
   2   5.064 BB    0.0477    6.42630    2.10232   2.0012

Totals :                   321.12552  112.27588
```

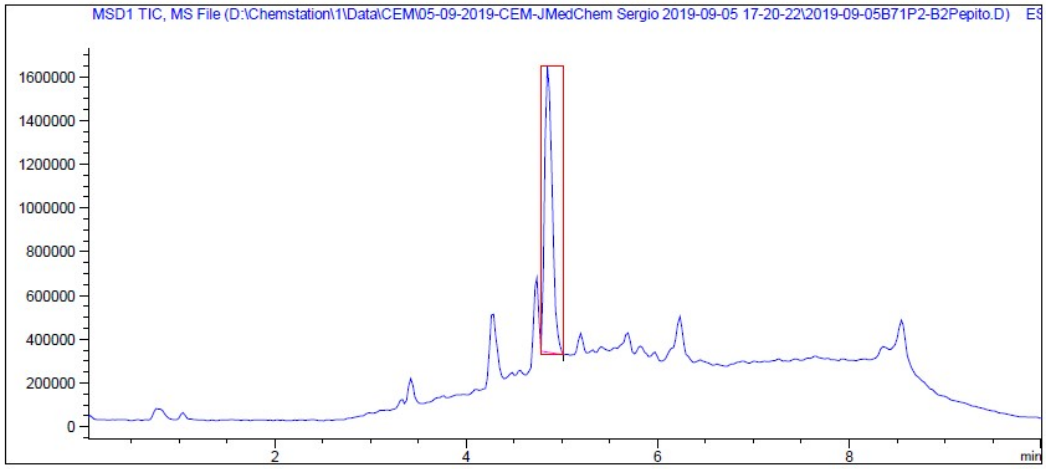
MSD1 TIC, MS File (D:\Chemstation\1\Data\CEM\05-09-2019-CEM-JMedChem Sergio 2019-09-05 17-20-22\2019-09-05B71P2-B2Pepito.D)
1600000
1400000
1200000
1000000
800000
600000
400000
200000
0
2
4
6
8
min

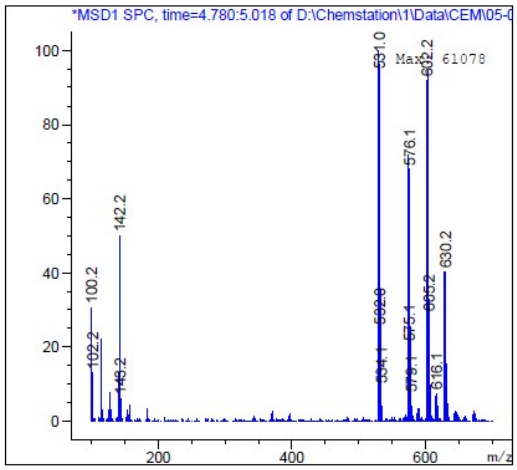
*MSD1 SPC, time=4.780:5.018 of D:\Chemstation\1\Data\CEM\05-0
Max. 61078
531.0
602.2
576.1
142.2
100.2
630.2
592.8
605.2
575.1
554.1
579.1
616.1
102.2
148.2
100
80
60
40
20
0
200
400
600
m/z

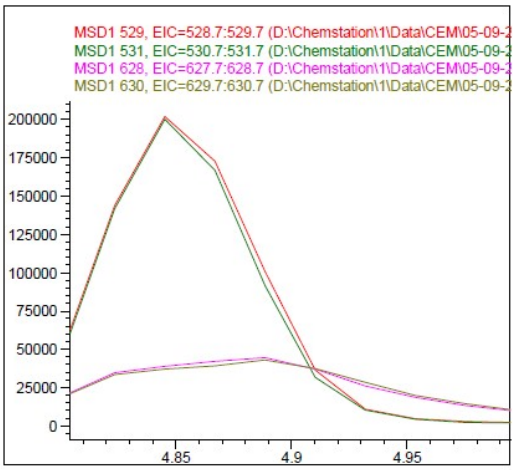
MSD1 529, EIC=528.7:529.7 (D:\Chemstation\1\Data\CEM\05-09-2
MSD1 531, EIC=530.7:531.7 (D:\Chemstation\1\Data\CEM\05-09-2
MSD1 628, EIC=627.7:628.7 (D:\Chemstation\1\Data\CEM\05-09-2
MSD1 630, EIC=629.7:630.7 (D:\Chemstation\1\Data\CEM\05-09-2
200000
175000
150000
125000
100000
75000
50000
25000
0
4.85
4.9
4.95

Diethyl (1*RS*,3a*SR*,6a*SR*)-5-(1,1'-biphenyl)-4-yl-4,6-dioxo-1-phenyl-1,3a,4,5,6,6a-hexahydropyrrolo[3,4-c]pyrrole-1-phosphonate (9z)

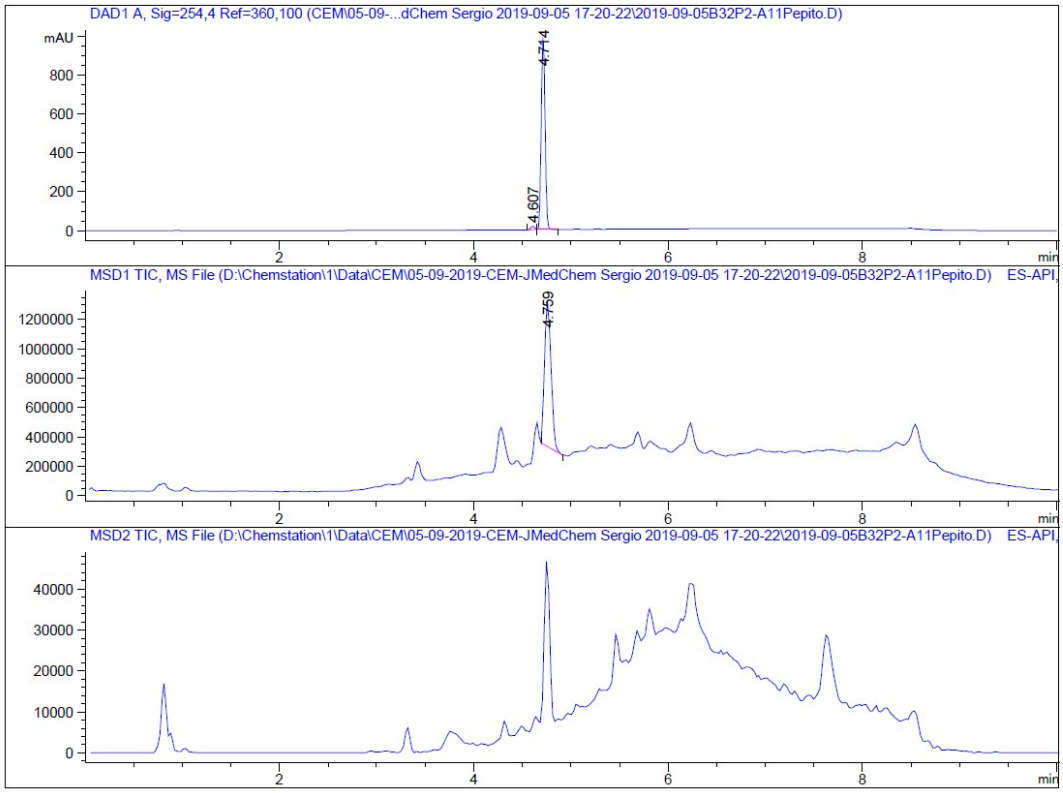


```
=====================================================================
                      Area Percent Report
=====================================================================

Sorted By             :      Signal
Multiplier            :      1.0000
Dilution              :      1.0000
Do not use Multiplier & Dilution Factor with ISTDs


Signal 1: DAD1 A, Sig=254,4 Ref=360,100

Peak RetTime Type  Width     Area      Height     Area
  #   [min]        [min]   [mAU*s]     [mAU]       %
----|-------|----|-------|----------|----------|--------|
   1   4.607 BB    0.0432   43.25058   16.18649   1.5320
   2   4.714 BB    0.0449 2779.87134  985.41620  98.4680

Totals :                  2823.12191 1001.60269
```

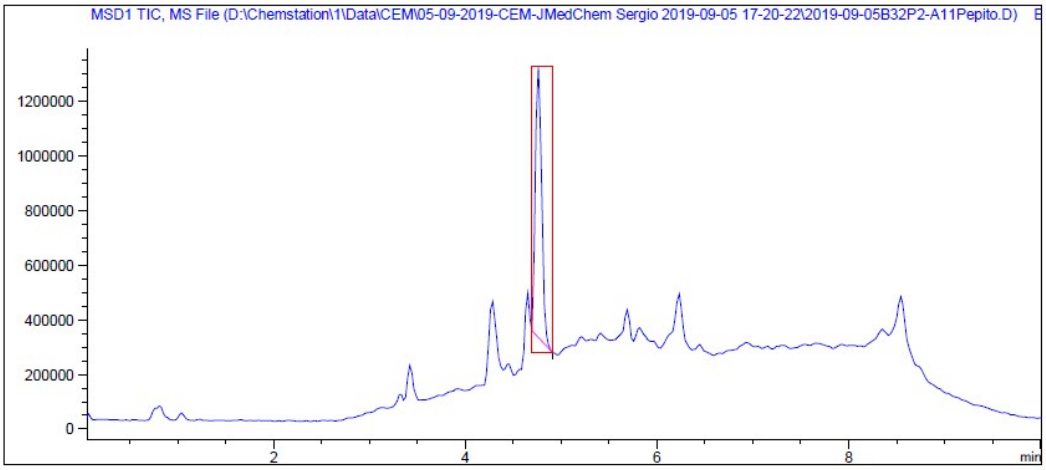
MSD1 TIC, MS File (D:\Chemstation\1\Data\CEM\05-09-2019-CEM-JMedChem Sergio 2019-09-05 17-20-22\2019-09-05B32P2-A11Pepito.D)
1200000
1000000
800000
600000
400000
200000
0
2
4
6
8
min

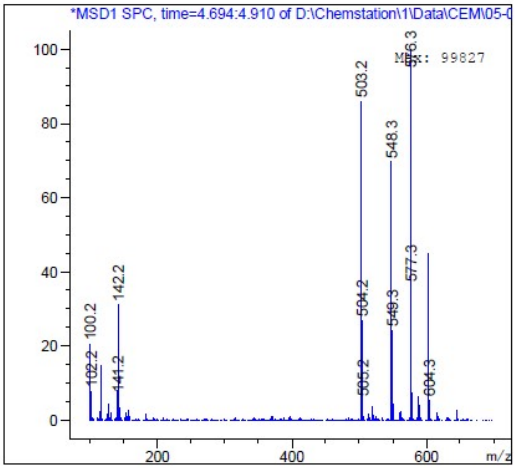
*MSD1 SPC, time=4.694:4.910 of D:\Chemstation\1\Data\CEM\05-0
Max: 99827
503.2
548.3
576.3
142.2
100.2
504.2
549.3
577.3
102.2
141.2
505.2
604.3
100
80
60
40
20
0
200
400
600
m/z

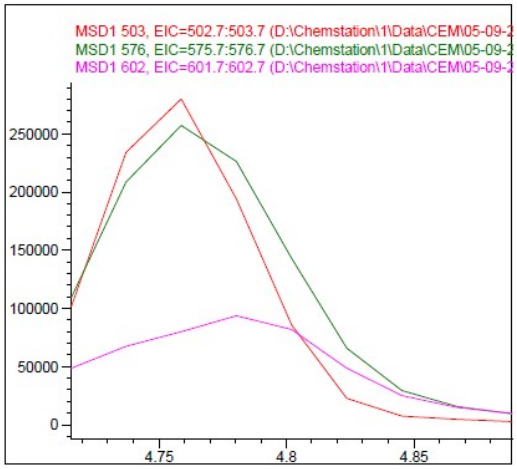
MSD1 503, EIC=502.7:503.7 (D:\Chemstation\1\Data\CEM\05-09-2
MSD1 576, EIC=575.7:576.7 (D:\Chemstation\1\Data\CEM\05-09-2
MSD1 602, EIC=601.7:602.7 (D:\Chemstation\1\Data\CEM\05-09-2
250000
200000
150000
100000
50000
0
4.75
4.8
4.85

References

(1) Abás, S.; Estarellas, C.; Luque, F.J.; Escolano, C. Easy access to (2-imidazolin-4-yl)phosphonates by a microwave assisted multicomponent reaction. *Tetrahedron*, **2015**, *7*, 2872-2881.

(2) Sobhani, S.; Vafaee, A. Molecular Iodine: An Efficient Catalyst for the One-Pot Synthesis of Primary 1-Aminophosphonates. *J. Iran. Chem. Soc.* **2010**, *7*, 227-236.

(3) Rachon, J.; Schöllkopf, U.; Wintel, T. 1-Aminoalkylphosphonsäuren durch Alkylieren von α-metalliertem isocyanmethylphosphonsäuren-diethylester. *Liebigs Ann Chem.* **1981**, 709-718.

(4) Tropsha, A.; Best Practices for QSAR Model Development, Validation, and Exploitation. *Mol. Inform*. **2010**, *29*, 476–488.

(5) Golbraikh, A.; Tropsha, A. Beware of q2. *J. Mol. Graph. Model*. **2002**, *20*, 269–276.

(6) Roy, K.; Mitra, I.; Kar, S.; Ojha, P. K.; Das, R. N.; Kabir, H. Comparative studies on some metrics for external validation of QSPR models. *J. Chem. Inf. Model.* **2012**, *52*, 396–408.

(7) Gramatica, P. (2007). Principles of QSAR models validation: internal and external. *QSAR & Comb. Sci.* **2007**, *26*, 694–701.

(8) SPSS Inc. Released 2009. PASW Statistics for Windows, Version 18.0. Chicago: SPSS Inc.

(9) Di, L.; Kerns, E. H.; Fan, K.; McConnell, O. J.; and Carter, G. T. High throughput artificial membrane permeability assay for blood-brain barrier. *Eur. J. Med. Chem*. **2003**, *38*, 223-232.

Compound	SMILE	I_2-IR Binding Affinities (pKi)	α_2-AR Binding Affinities (pKi)	Selectivity (I_2/α_2)
9a	O=C(N1C)[C@@H]2C=N[C@](P(OCC)(OCC)=O)(C3=CC=CC=C3)[C@@H]2C1=O	7.97	5.93	110
9b	O=C1N(C2CCCCC2)C(C3C(P(OCC)(OCC)=O)(C4=CC=CC=C4)N=CC31)=O	9.74	9.01	5
9c	O=C(C1C(P(OCC)(OCC)=O)(C2=CC=CC=C2)N=CC13)N(C4=CC=CC=C4)C3=O	10.28	10.38	1
9d	O=C(C1C(P(OCC)(OCC)=O)(C2=CC=CC=C2)N=CC13)N(C4=CC=C(F)C(Cl)=C4)C3=O	8,56	6,27	195
9e	O=C(N1C2=CC=C(OC)C=C2)[C@@H]3C=N[C@](P(OCC)(OCC)=O)(C4=CC=CC=C4)[C@@H]3C1=O	6,65	4,59	115
14c	O=C1N(C2=CC=CC=C2)C([C@@H]3[C@H]1C=N[C@@]3(CC4=CC=CC=C4)P(OCC)(OCC)=O)=O	5,51	---	---
15c	O=C(N1C2=CC=CC=C2)[C@H]3[C@H]([C@@](P(OCC)(OCC)=O)(CC4=CC=C(F)C=C4)N=C3)C1=O	<3	7,69	---
12c	O=C([C@H]1[C@@](P(OCC)(OCC)=O)(C2=CC=C(F)C=C2)N=C[C@H]13)N(C4=CC=CC=C4)C3=O	<3	6,77	---
13c	O=C([C@H]1[C@@](P(OCC)(OCC)=O)(C2=CC=C(OC)C=C2)N=C[C@H]13)N(C4=CC=CC=C4)C3=O	3,39	3,85	---
12d	O=C([C@H]1[C@@](P(OCC)(OCC)=O)(C2=CC=C(F)C=C2)N=C[C@H]13)N(C4=CC(Cl)=C(F)C=C4)C3=O	7,55	3,38	14791
13d	O=C([C@H]1[C@@](P(OCC)(OCC)=O)(C2=CC=C(OC)C=C2)N=C[C@H]13)N(C4=CC(Cl)=C(F)C=C4)C3=O	7.87	<3	74131
9f	O=C([C@@H]1[C@H]2C=N[C@]1(P(OCC)(OCC)=O)C3=CC=CC=C3)N(C2=O)CC	8.37	5.85	331
9g	O=C([C@@H]1[C@H]2C=N[C@@]1(C3=CC=CC=C3)P(OCC)(OCC)=O)N(C2=O)CCC	4,02	---	---
9h	O=C([C@@H]1[C@H]2C=N[C@]1(P(OCC)(OCC)=O)C3=CC=CC=C3)N(C2=O)C(C)(C)C	7.25	6.77	3
9i	O=C([C@@H]([C@](C1=CC=CC=C1)(P(OCC)(OCC)=O)N=C2)[C@@H]2C3=O)N3CC4(C5)C[C@@H](CC5C6)C[C@@H]6C4	7.01	4,31	401
9i	O=C([C@@H]([C@](C1=CC=CC=C1)(P(OCC)(OCC)=O)N=C2)[C@@H]2C3=O)N3CC4(C5)C[C@@H](CC5C6)C[C@@H]6C4	7.01	4,31	401
9j	O=C(N1CC2=CC=CC=C2)[C@@H]3C=N[C@@](C4=CC=CC=C4)(P(OCC)(OCC)=O)[C@@H]3C1=O	5.26	8.11	---
9k	O=C1N(C([C@@H]2[C@H]1C=N[C@]2(P(OCC)(OCC)=O)C3=CC=CC=C3)=O)CCC4=CC=CC=C4	5.85	3.59	182

9l	O=C1N(C([C@@H]2[C@H]1C=N[C@]2(P(OCC)(OCC)=O)C3=CC=CC=C3)=O)CCC4=CC=C(F)C=C4	<3	5,65	---
9m	O=C([C@@H]1[C@H]2C=N[C@]1(P(OCC)(OCC)=O)C3=CC=CC=C3)N(C4CC5=CC=CC=C5C4)C2=O	3.84	3.442	2
9n	O=C1N(C([C@@H]2[C@H]1C=N[C@]2(P(OCC)(OCC)=O)C3=CC=CC=C3)=O)C4=CC=C(C(F)(F)F)C=C4	<3	4.73	---
9o	O=C([C@@H]1[C@H]2C=N[C@]1(P(OCC)(OCC)=O)C3=CC=CC=C3)N(C2=O)C4=CC(C(F)(F)F)=CC=C4	<3	---	---
9p	O=C1N(C([C@@H]2[C@H]1C=N[C@]2(P(OCC)(OCC)=O)C3=CC=CC=C3)=O)C4=CC=C(F)C=C4	<3	5.34	---
9q	O=C([C@@H]1[C@H]2C=N[C@@]1(C3=CC=CC=C3)P(OCC)(OCC)=O)N(C2=O)C4=CC=C(Cl)C=C4	<3	---	---
9r	O=C([C@@H]([C@](C1=CC=CC=C1)(P(OCC)(OCC)=O)N=C2)[C@@H]2C3=O)N3C4=C(Cl)C=CC=C4	5.09	6.15	---
9s	O=C([C@@H]1[C@H]2C=N[C@]1(P(OCC)(OCC)=O)C3=CC=CC=C3)N(C2=O)C4=CC(Cl)=CC=C4	<3	---	---
9t	O=C1N(C2=CC=C(Br)C=C2)C([C@@H]3[C@H]1C=N[C@@]3(C4=CC=CC=C4)P(OCC)(OCC)=O)=O	<3	---	---
9u	O=C([C@@H]([C@](C1=CC=CC=C1)(P(OCC)(OCC)=O)N=C2)[C@@H]2C3=O)N3C4=CC(Cl)=CC(Cl)=C4	5,81	6,22	---
9b	O=C1N(C([C@@H]2[C@H]1C=N[C@]2(P(OCC)(OCC)=O)C3=CC=CC=C3)=O)C4=CC(Cl)=C(Cl)C=C4	<3	---	---
9w	O=C([C@@H]([C@](C1=CC=CC=C1)(P(OCC)(OCC)=O)N=C2)[C@@H]2C3=O)N3C4=C(Cl)C=C(Cl)C=C4Cl	<3	5,16	---
9x	O=C(N1C2=CC([N+]([O-])=O)=CC=C2)[C@@H]3C=N[C@](P(OCC)(OCC)=O)(C4=CC=CC=C4)[C@@H]3C1=O	6,81	10,18	---
9y	O=C([C@@H]1[C@H]2C=N[C@@]1(C3=CC=CC=C3)P(OCC)(OCC)=O)N(C2=O)C4=CC([N+]([O-])=O)=CC=C4C	<3	---	---
9z	O=C(N1C2=CC=C(C3=CC=CC=C3)C=C2)[C@@H]4C=N[C@](P(OCC)(OCC)=O)(C5=CC=CC=C5)[C@@H]4C1=O	7,90	5,12	602
9aa	O=C1N(C([C@@H]2[C@H]1C=N[C@]2(P(OCC)(OCC)=O)C3=CC=CC=C3)=O)C4=CC=C(C)C=C4	5,44	---	---
9ab	O=C1N(C2=CC=C(OC3=CC=CC=C3)C=C2)C([C@@H]4[C@H]1C=N[C@]4(P(OCC)(OCC)=O)C5=CC=CC=C5)=O	6,96	5,34	34
9ac	O=C([C@@H]1[C@H]2C=N[C@]1(P(OCC)(OCC)=O)C3=CC=CC=C3)N(C2=O)C4=C(C=CC=C5)C5=CC=C4	3,11	<3	---
9ad	O=C([C@@H]([C@](C1=CC=CC=C1)(P(OCC)(OCC)=O)N=C2)[C@@H]2C3=O)N3C4=C(Cl)N=CC=C4	7,96	<3	91201
16	O=C(N1C2=CC=CC=C2)[C@@H]3C=N[C@](P(OC4=CC=CC=C4)(OC5=CC=CC=C5)=O)(C6=CC=CC=C6)[C@@H]3C1=O	5,86	11,64	---

2.2. Resultados no publicados

En este apartado se muestran resultados continuación al trabajo descrito en la publicación en la revista *Journal of Medicinal Chemistry* que aún no han sido publicados. Para hacer más fácil la exposición de los resultados, se ha utilizado la numeración que aparece en el artículo cuando se hace referencia a alguno de los compuestos ya descritos (apartado 2.1).[42] Como ya se ha comentado, en este artículo se describe la síntesis y perfil farmacológico de compuestos con núcleo de α-iminofosfonato bicíclico que actúan como ligandos altamente selectivos de I_2-IR, siendo la primera familia de ligandos de estos receptores que no tienen estructura de imidazolina o imidazol.

Es importante destacar la presencia en la bibliografía de estudios donde la afinidad por los I_2-IR varía dependiendo del enantiómero del ligando evaluado. Estos resultados destacan la existencia de requisitos estereoespecíficos de estos receptores, junto a sus homólogos I_1-R, presentando mejores afinidades por uno de los enantiómeros puros en comparación con el racémico.[34b,64] Por tanto, podríamos contemplar una mejora en la actividad de los productos preparados si se considera la existencia de un posible eutómero y un distómero en la familia de α-iminofosfonatos bicíclicos.

La síntesis de α-iminofosfonatos bicíclicos implica una reacción de cicloadición [3+2] diastereoselectiva y los productos obtenidos corresponden a la mezcla racémica de los dos posibles enantiómeros. Debido al interés por encontrar ligandos mejorados de I_2-IR, nos propusimos separar la mezcla racémica en los dos enantiómeros de los tres α-iminofosfonatos bicíclicos que presentaban mayor afinidad por I_2-IR como son **B06 (9d)** (Figura 2.1), **9b** y **9c**, con valores de unión expresados en pK_i de 8.56, 9.74 y 10.28, respectivamente y, posteriormente, determinar la afinidad de cada enantiómero por los I_2-IR para poder compararlos con la mezcla racémica.

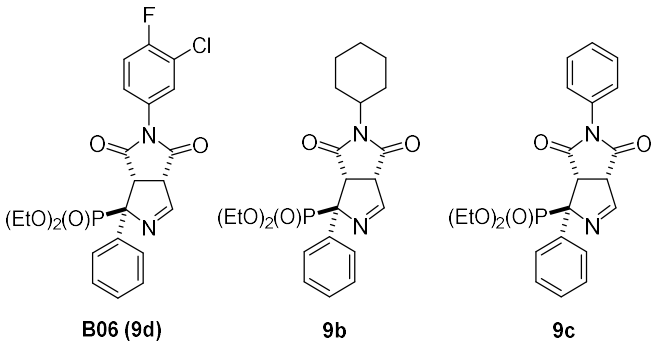

[64] (a) Quaglia, W.; Bousquet, P.; Pigini, M.; Carotti, A.; Carrieri, A.; Dontenwill, M.; Gentili, F.; Giannella, M.; Maranca, F.; Piergentili, A.; Brasili, L. *J. Med. Chem.* **1999,** *42,* 2737-2740; (b) Glennon, R.A.; Grella, B.; Tyacke, R.J.; Lau, A.; Westaway, J.; Hudson, A. L. *Bioorg. Med. Chem*. **2004**, *14*, 527-529.

Figura 2.1. Estructura de **B06 (9d)**, **9b** y **9c**.

El compuesto **B06** se envió a la Dra. Pilar Franco de la empresa Chiral Technologies, Inc. para la búsqueda de las condiciones necesarias para separar ambos enantiómeros por HPLC preparativo. Se seleccionó la columna Chiralpack IC y una mezcla isocrática de heptano y diclorometano (+2% EtOH + 0.2% DEA) como fase móvil para la separación enantiomérica del compuesto. En nuestro laboratorio, al no disponer de HPLC preparativo, los enantiómeros se separaron siguiendo las condiciones establecidas en un HPLC analítico. Dado el éxito con este método para separar los enantiómeros de la mezcla racémica, los otros miembros seleccionados de esta familia de compuestos, **9b** y **9c**, se separaron en las mismas condiciones.

Una vez separados los enantiómeros de **B06**, **9b** y **9c** se enviaron para su evaluación farmacológica al grupo del Prof. L. F. Callado (UPV), que procedió como en casos anteriores, a determinar la afinidad y selectividad por I_2-IR, mediante estudios de unión competitiva frente a radioligandos selectivos de I_2-IR ([^{3}H]-2-BFI) y de α_2-AR ([^{3}H]-RX821002) en membranas del córtex frontal humano *post-mortem* En la Tabla 2.1 se presentan las pK_i de cada enantiómero, así como los valores de las muestras racémicas y de estándares (**idazoxan**, **2-BFI**, **CR4056**,**BU99008**, **LSL60101**). Se denominan a los dos posibles enantiómeros de **B06**, **9b** y **9c**, como **Enant 1** o **Enant 2** según el tiempo de retención de cada uno de ellos en el HPLC analítico, siendo **Enant 1** el que tiene un tiempo de retención menor y **Enant 2** el que tiene un tiempo de retención mayor.

Tabla 2.1. Afinidades por I_2-IR y α_2-AR de ligandos conocidos (**idazoxan**, **2-BFI**, **CR4056**, **BU99008**, **LSL60101**) y de racémico y enantiómeros de **B06**, **9b** y **9c**.

Compuesto	[^{3}H]-2-BFI I_2 pK_i (un lugar)	[^{3}H]-2-BFI I_2 pK_i (dos lugares)		Lugar de alta afinidad (% ocupación)	[^{3}H]-RX821002 α_2 pK_i	Selectividad I_2/α_2
Idazoxan	7.41±0.63	7.87±0.74	5.76±0.57	40±7	7.92±0.07	-
2-BFI	8.31±0.13	9.08±0.22	7.15±0.31	58±9	4.58±0.22	5370
CR4056	5.95±0.11	-	-	-	2.65±1.24	1995
BU99008	7.05±0.17	-	-	-	4.37±0.17	479
LSL60101	6.67±0.09	8.17±0.19	6.02±0.10	34±4	3.18±0.17	3090
B06 (9d)	8.56±0.32	-	-	-	6.27±0.56	195
B06-Enant 1	5.68±0.12	-	-	-	5.38±0.19	2
B06-Enant 2	8.19±0.20	-	-	-	3.11±0.64	120226
9b	9.74±0.29	-	-	-	9.01±0.51	5
9b-Enant 1	<3	-	-	-	-	-
9b-Enant 2	3.99±0.18	10.41±0.57	3.81±0.23	25±5	-	-
9c	10.28±0.37	-	-	-	10.38±0.22	1
9c-Enant 1	8.74±0.24	9.17±0.18	3.79±0.43	53±6	-	-
9c-Enant 2	7.84±0.26	8.63±0.19	3.06±0.89	35±3	-	-

Los datos indicados en la Tabla 2.1 determinan un comportamiento diferente de los racémicos frente a los enantiómeros de **B06**, **9b** y **9c**. En el caso de **B06** el enantiómero que denominamos **B06-Enant 2** (tiempo de retención mayor en la columna de HPLC quiral) tiene un valor de pK_i de 8.19 (similar a la muestra racémica, 8.56) respecto a su pareja que lo tiene de 5.68, además de una excelente selectividad I_2/α_2 (120226). Por tanto, en este caso sí que podríamos hablar de un posible eutómero, presentando unos valores de afinidad y, sobretodo, selectividad I_2/α_2 superiores al de los ligandos I_2-IR conocidos. En el caso de **9b**, el enantiómero más afín, como sucede con el compuesto anterior, es el que se retiene más en la columna, **9b-Enant 2**, presentando, a diferencia del racémico, una curva bifásica con dos lugares de unión, uno de alta afinidad y otro de baja afinidad, pK_i de 10.41 y 3.81, respectivamente, con un porcentaje de ocupación del 25% para el de alta afinidad. Los enantiómeros de **9c** disponían de actividades similares, demostrando tener curvas bifásicas con porcentajes de ocupación del lugar de alta afinidad, 53% para **9c-Enant 1** y 35% para **9c-Enant 2**. Finalmente, cabe destacar que al igual de la muestra racémica de la que proceden, los enantiómeros de **9b** y **9c** no presentan selectividad I_2/α_2.

Seguidamente, teniendo en cuenta la localización de estos receptores en el SNC, la Dra. Belén Pérez de la UAB llevó a cabo el ensayo de permeabilidad *in vitro* PAMPA-BBB. Todos los enantiómeros, a excepción de los **9c** que no presentan una permeabilidad óptima (SNC +/-: 5.198 > P_e (10^{-6} cm·s^{-1}) > 2.054), al igual que sus homólogos racémicos, resultaron situarse por encima del umbral establecido para una alta permeabilidad de la BHE (SNC +: P_e (10^{-6} cm·s^{-1}) > 5.198), considerándose adecuados para contemplar más estudios (Tabla 2.2).

Tabla 2.2. Resultado de permeabilidad (PAMPA-BBB) y predicción de penetración en BHE de los compuestos racémico y enantiómeros de **B06**, **9b** y **9c**.

	Permeabilidad P_e (10^{-6} cm·s^{-1})	**Predicción**
B06 (9d)	9.7 ± 0.7	SNC +
B06-Enant 1	8.3 ± 1.0	SNC +
B06-Enant 2	8.4 ± 0.6	SNC +
9b	25.9 ± 0.6	SNC +
9b-Enant 1	13.3 ± 0.8	SNC +
9b-Enant 2	17.6 ± 1.3	SNC +
9c	7.8 ± 0.6	SNC +
9c-Enant 1	2.9 ± 0.1	SNC +/-
9c-Enant 2	2.8 ± 0.1	SNC +/-

Adicionalmente, en la USC se realizó un estudio preliminar *in vitro* de ADME de los enantiómeros de **B06** considerando la solubilidad, la estabilidad microsomal, la inhibición de citocromos y del canal hERG y, finalmente, la unión a proteínas plasmáticas. La solubilidad de ambos enantiómeros en 1% DMSO + 99% tampón de PBS fue excelente (>90 μM). Seguidamente, los datos mostrados en la Tabla 2.3 revelan que el eutómero (**B06-Enant 2**) presenta similitud en los resultados entre las diferentes especies, a diferencia del distómero y el racémico. Esto indica poca diferencia en el metabolismo dependiendo de la especie, factor favorable para poder trasladar los estudios en rata/ratón a humano si fuera necesario en posteriores estudios.

Tabla 2.3. Estabilidad microsomal de los compuestos en diferentes especies.

	Ratón			**Humano**			**Rata**		
	% remanente (tiempo muestreo 60 min)	$t_{1/2}$ (min)	**Clint** (μL/min* mg prot)	**% remanente** (tiempo muestreo 60 min)	$t_{1/2}$ (min)	**Clint** (μL/min* mg prot)	**% remanente** (tiempo muestreo 60 min)	$t_{1/2}$ (min)	**Clint** (μL/min* mg prot)
B06	65.08	91.72	7.55	50.87	64.16	10.8	44.79	52.81	13.1
B06-Enant 1	55.43	77.82	8.91	62.58	89.21	7.77	67.88	124.74	5.56
B06-Enant 2	47.81	56.88	12.18	53.91	61.71	11.23	43.44	47.07	14.72

El potencial de inhibición de **B06** y sus enantiómeros se evaluó utilizando enzimas recombinantes del citocromo P450 humano [CYP1A2, CYP2C9, CYP2C19, CYP2D6, CYP3A4 (BFC y DBF)]. Los resultados representados en la Tabla 2.4 mostraron que la inhibición de los citocromos no era relevante, teniendo en cuenta el rango de afinidad del orden nM y considerando la concentración de 10 μM del ensayo. Por lo tanto, no se espera que a dosis terapéuticas el compuesto pueda interferir con el metabolismo de otros fármacos mediados por el citocromo P450.

Tabla 2.4. Inhibición citocrómica de los compuestos.

	CYP1A2	**CYP2D6**	**CYP3A4 (BFC)**	**CYP3A4 (DBF)**
B06	1 ± 1	27 ± 4	53 ± 1	48 ± 1
B06-Enant 1	22 ± 1	1 ± 1	16 ± 1	20 ± 3
B06-Enant 2	26 ± 3	7 ± 3	18 ± 1	30 ± 1

Asimismo, se evaluó la posible inhibición de los canales hERG del racémico y los enantiómeros de **B06**, mostrando inhibiciones inferiores al 30% a una concentración de 10 μM, descantando así el riesgo de este posible *off-target*.

Finalmente, el grado de unión a proteínas plasmáticas fue ligeramente superior en ratones que, en humanos en todos los compuestos, presentando aproximadamente un

8% de producto libre en humanos (Tabla 2.5). Este dato hay que tenerlo presente en el caso de que el producto progresara en fases clínicas y se plantearan ensayos en humanos.

Tabla 2.5. Unión a proteínas plasmáticas de los compuestos en diferentes especies.

	Ratón		Humano	
	Unión proteína plasmática (%)	**Fracción no unida**	**Unión proteína plasmática (%)**	**Fracción no unida**
B06	96.29	3.71	91.97	8.03
B06-Enant 1	99.99	0.01	91.88	8.12
B06-Enant 2	97.73	2.26	91.97	8.03

Dado el interés generado por los resultados obtenidos, en un futuro el grupo se plantea la posibilidad de llegar a sintetizar los enantiómeros de **B06** de manera enantioselectiva o bien realizar la separación de un racemato con un HPLC semipreparativo. De esta manera se podrían obtener cantidades suficientes para plantear un estudio preliminar *in vivo* en el modelo murino predeterminado y comparar los resultados farmacológicos con los obtenidos para **B06**. La introducción de un átomo pesado en uno de los enantiómeros y la obtención de un monocristal para análisis de cristalografía de rayos X permitirá determinar la estereoquímica absoluta del eutómero/distómero. A continuación, se incluyen las condiciones experimentales de separación de los enantiómeros y los cromatogramas de HPLC.

PARTE EXPERIMENTAL

Cromatograma/condiciones utilizadas por Chiral Technologies, Inc. parala separación de los enantiómeros de una mezcla racémica de **B06**.

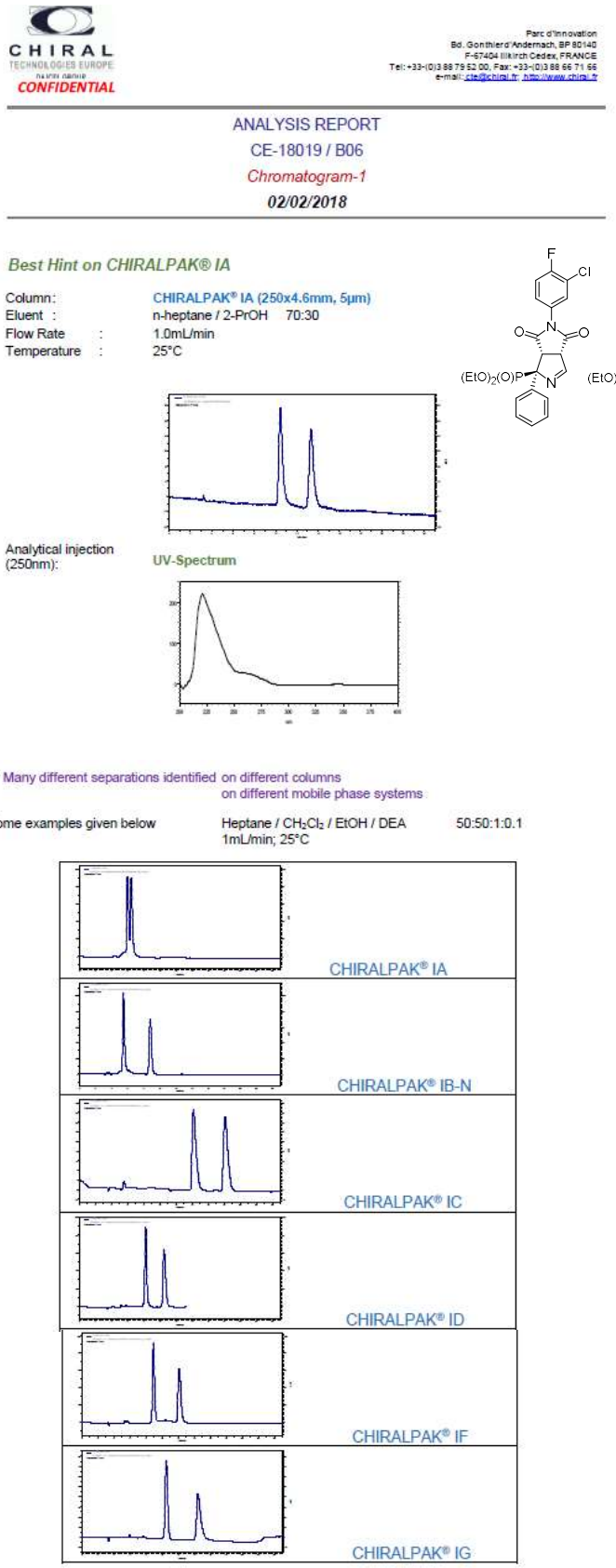

Chiral HPLC Method for Identification and enantiomeric separation of racemic samples of **B06**, **9b** and **9c**.

HPLC Equipment: All analyses and separations were carried out with an Agilent 1100 series HPLC system with a quaternary pump coupled to a UV detector set at 254 nm.

Sample concentration: Solid sample 3 mg **B06** in 1 mL of a mixture 50:50 Heptane-DCM; solid sample 3 mg **9b** in 1 mL of a mixture 50:50 Heptane-DCM; and solid sample 3 mg **9c** in 1 mL of a mixture 50:50 Heptane-DCM.

Chromatographic conditions: The column was a Chiralpack IC (Daicel Chemical Ind., Ltd., Tokyo, Japan) 5 ODS 4.6 mm x 250 mm (5 μm), with a constant flow of 1.0 mL min^{-1} and a controlled temperature of 25 ºC. The injection volume was 100 μL, and the detection wavelength was λ = 254 nm. The mobile phase consisted of heptane and a mixture of DCM + 2% EtOH + 0,2% DEA. Isocratic methods were developed and are detailed in Tables S1-3.

Table S1. Detailed gradient for the developed method for **B06**.

Time (min)	Heptane	DCM + 2% EtOH + 0,2% DEA
0	40	60
15	40	60

Table S2. Detailed gradient for the developed method for **9b**.

Time (min)	Heptane	DCM + 2% EtOH + 0,2% DEA
0	50	50
10	50	50

Table S3. Detailed gradient for the developed method for **9c**.

Time (min)	Heptane	DCM + 2% EtOH + 0,2% DEA
0	50	50
30	50	50

Enantiomeric separation: A racemic sample of **B06**, **9b** and **9c** was injected in the HPLC with the appropriate method. Each enantiomer was collected in two different round-bottom flasks. The procedure was repeated several times until to obtain 10 mg of each enantiomer. Finally, the different solutions containing the enantiomers were concentrated *in vacuo*.

MATERIAL SUPLEMENTARIO

HPLC/MS analysis of **B06, 9b and 9c.**

Diethyl (1RS,3aSR,6aSR)-5-(3-chloro-4-fluorophenyl)-4,6-dioxo-1-phenyl-1,3a,4,5,6,6a-hexahydropyrrolo[3,4-c]pyrrole-1-phosphonate (B06).

```
Sample Info     : 3mg/ml 50:50 Heptane-DCM_mixture.

Additional Info : Peak(s) manually integrated
```

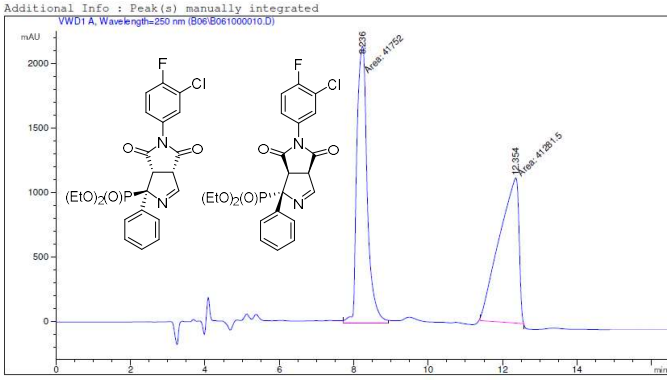


```
================================================================
                      Area Percent Report
================================================================

Sorted By             :      Signal
Multiplier:                   :      1.0000
Dilution:                     :      1.0000
Use Multiplier & Dilution Factor with ISTDs


Signal 1: VWD1 A, Wavelength=250 nm

Peak RetTime Type  Width     Area      Height     Area
  #   [min]        [min]  mAU   *s   [mAU   ]      %
----|-------|----|-------|----------|----------|--------|
   1   8.236 MM    0.3244 4.17520e4  2145.11987  50.2834
   2  12.354 MM    0.6112 4.12815e4  1125.60815  49.7166

Totals :                  8.30335e4  3270.72803
```

Diethyl (1RS,3aSR,6aSR)-5-cyclohexyl-4,6-dioxo-1-phenyl-1,3a,4,5,6,6a-hexahydropyrrolo[3,4-c]pyrrole-1-phosphonate (9b)

```
Sample Info     : Blank, 50:50 Heptane:DCM/EtOH/TEA

Additional Info : Peak(s) manually integrated
```

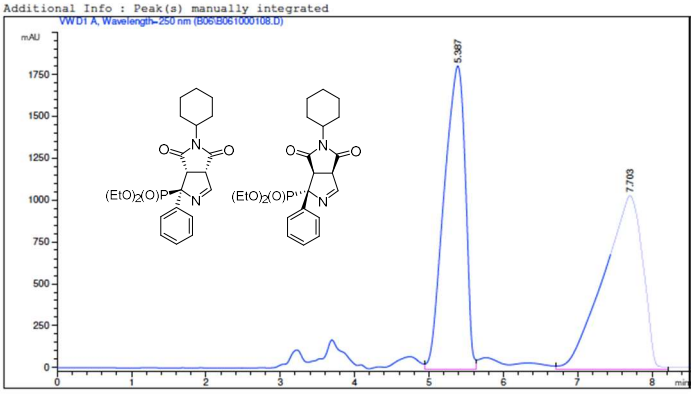


```
================================================================
                      Area Percent Report
================================================================

Sorted By             :      Signal
Multiplier:                   :      1.0000
Dilution:                     :      1.0000
Use Multiplier & Dilution Factor with ISTDs


Signal 1: VWD1 A, Wavelength=250 nm

Peak RetTime Type  Width     Area      Height     Area
  #   [min]        [min]  mAU   *s   [mAU   ]      %
----|-------|----|-------|----------|----------|--------|
   1   5.387 VV    0.3445 3.57616e4  1806.61951  48.6436
   2   7.703 VV    0.5034 3.77559e4  1033.37463  51.3564

Totals :                  7.35174e4  2839.99414
```

Diethyl (1RS,3aSR,6aSR)-4,6-dioxo-1,5-diphenyl-1,3a,4,5,6,6a-hexahydropyrrolo [3,4-c]pyrrole-1-phosphonate (9c)

```
Sample Info     : Blank, 50:50 Heptane:DCM/EtOH/TEA

Additional Info : Peak(s) manually integrated
```

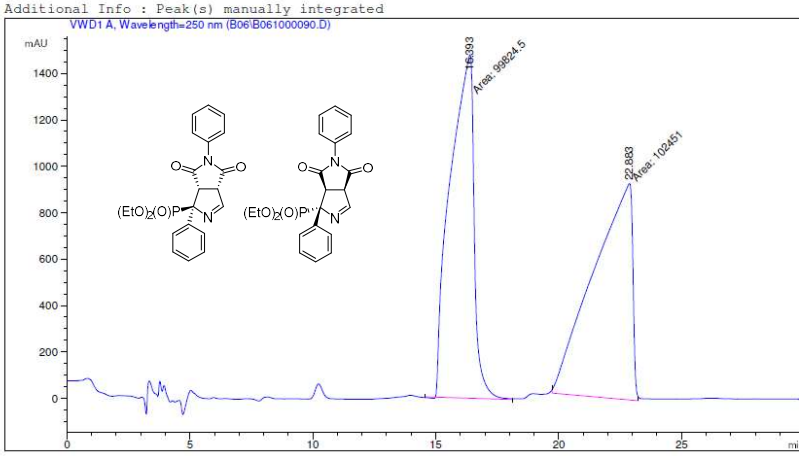


```
=====================================================================
                        Area Percent Report
=====================================================================

Sorted By             :      Signal
Multiplier:                   :      1.0000
Dilution:                     :      1.0000
Use Multiplier & Dilution Factor with ISTDs


Signal 1: VWD1 A, Wavelength=250 nm

Peak RetTime Type  Width     Area      Height     Area
  #   [min]        [min]  mAU   *s    [mAU   ]      %
----|-------|----|-------|----------|----------|--------|
   1  16.393 MM    1.1249 9.98245e4  1479.01001  49.3507
   2  22.883 MM    1.8323 1.02451e5   931.91986  50.6493

Totals :                  2.02276e5  2410.92987
```

Capítulo 3. *Benzofuranyl-2-imidazoles as Imidazoline I_2 Receptor Ligands for Alzheimer's Disease*

3.1. *European Journal Medicinal Chemistry* 2021, *222*, 113540

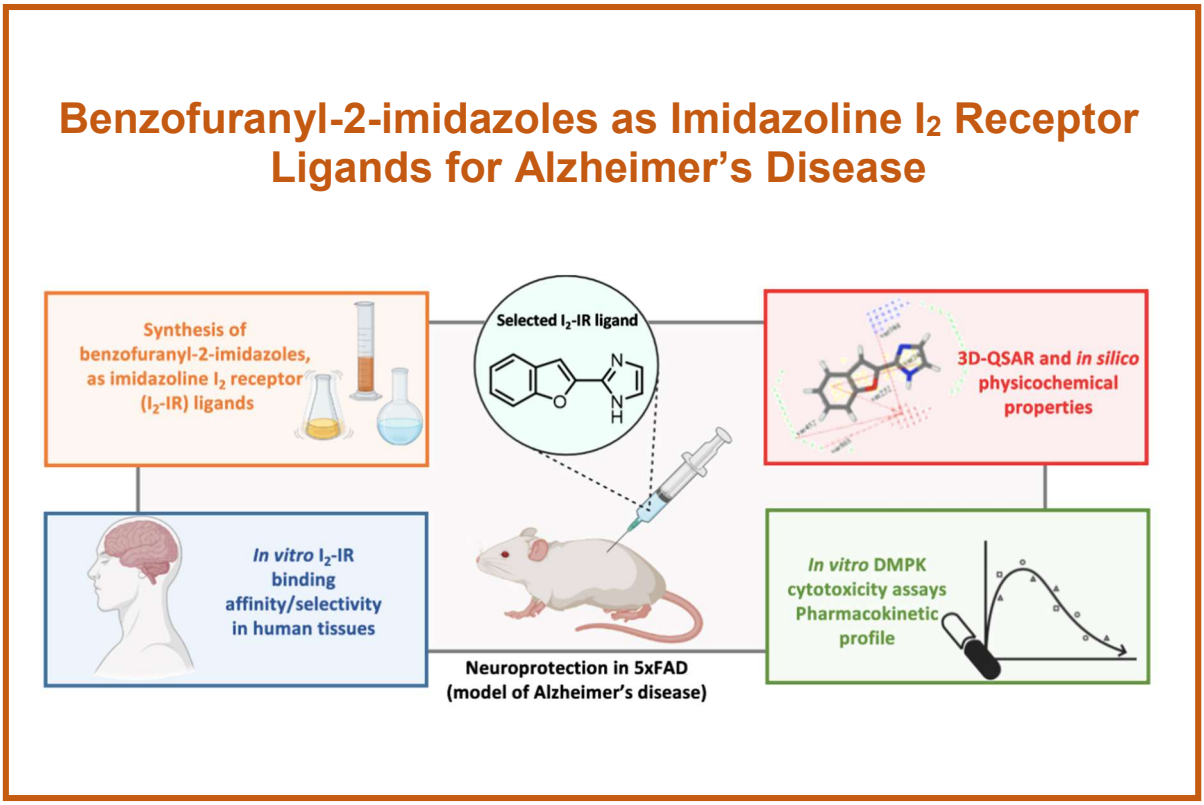

European Journal of Medicinal Chemistry 222 (2021) 113540

Contents lists available at ScienceDirect

European Journal of Medicinal Chemistry

journal homepage: http://www.elsevier.com/locate/ejmech

Benzofuranyl-2-imidazoles as imidazoline I_2 receptor ligands for Alzheimer's disease

Sergio Rodriguez-Arévalo [a, 1], Andrea Bagán [a], Christian Griñán-Ferré [b, 1], Foteini Vasilopoulou [b], Mercè Pallàs [b], Iria Brocos-Mosquera [c, d], Luis F. Callado [c, d], M. Isabel Loza [e], Antón L. Martínez [e], José Brea [e], Belén Pérez [f], Elies Molins [g], Steven De Jonghe [h], Dirk Daelemans [h], Milica Radan [i], Teodora Djikic [i], Katarina Nikolic [i], Elena Hernández-Hernández [j], M. Julia García-Fuster [j], Jesús A. García-Sevilla [j], Carmen Escolano [a, *]

[a] Laboratory of Medicinal Chemistry (Associated Unit to CSIC), Department of Pharmacology, Toxicology and Medicinal Chemistry, Faculty of Pharmacy and Food Sciences, Institute of Biomedicine (IBUB), University of Barcelona, Av. Joan XXIII, 27-31, E-08028, Barcelona, Spain
[b] Pharmacology Section, Toxicology and Medicinal Chemistry, Faculty of Pharmacy and Food Sciences, Institut de Neurociències, University of Barcelona, Av. Joan XXIII, 27-31, E-08028, Barcelona, Spain
[c] Department of Pharmacology, University of the Basque Country, UPV/EHU, E-48940, Leioa, Bizkaia, Spain
[d] Centro de Investigación Biomédica en Red de Salud Mental, CIBERSAM, Spain
[e] Innopharma Screening Platform, BioFarma Research Group, Centro de Investigación en Medicina Molecular y Enfermedades Crónica (CIMUS), Universidad de Santiago de Compostela, E-15782, Santiago de Compostela, Spain
[f] Department of Pharmacology, Therapeutic and Toxicology, Autonomous University of Barcelona, E-08193, Cerdanyola, Spain
[g] Institut de Ciència de Materials de Barcelona (CSIC), Campus UAB, E-08193, Cerdanyola, Spain
[h] KU Leuven, Department of Microbiology, Immunology and Transplantation, Rega Institute, Laboratory of Virology and Chemotherapy, Herestraat 49, 3000, Leuven, Belgium
[i] Department of Pharmaceutical Chemistry, Faculty of Pharmacy, University of Belgrade, 11000, Belgrade, Serbia
[j] IUNICS University of the Balearic Islands (UIB), Health Research Institute of the Balearic Islands (IdISBa), E-07122, Palma de Mallorca, Spain

ARTICLE INFO

Article history:
Received 23 February 2021
Received in revised form
26 April 2021
Accepted 10 May 2021
Available online 20 May 2021

Keywords:
Imidazoline I_2 receptors
Imidazoline I_2 receptor ligands
Neuroprotection
5xFAD
Benzofuranyl-2-imidazoles
Oxidative stress

ABSTRACT

Recent findings unveil the pharmacological modulation of imidazoline I_2 receptors (I_2-IR) as a novel strategy to face unmet medical neurodegenerative diseases. In this work, we report the chemical characterization, three-dimensional quantitative structure-activity relationship (3D-QSAR) and ADMET *in silico* of a family of benzofuranyl-2-imidazoles that exhibit affinity against human brain I_2-IR and most of them have been predicted to be brain permeable. Acute treatment in mice with 2-(2-benzofuranyl)-2-imidazole, known as **LSL60101** (garsevil), showed non-warning properties in the ADMET studies and an optimal pharmacokinetic profile. Moreover, LSL60101 induced hypothermia in mice while decreased pro-apoptotic FADD protein in the hippocampus. *In vivo* studies in the familial Alzheimer's disease 5xFAD murine model with the representative compound, revealed significant decreases in the protein expression levels of antioxidant enzymes superoxide dismutase and glutathione peroxidase in hippocampus. Overall, **LSL60101** plays a neuroprotective role by reducing apoptosis and modulating oxidative stress.

1. Introduction

Imidazoline I_2 receptors (I_2-IR) are heterogeneous entities, often described as nonadrenergic binding sites for imidazolines [1], that bind with high affinity to [^{3}H]idazoxan and with lower affinity to [^{3}H]*p*-aminoclonidine and [^{3}H]clonidine [2,3]. I_2-IR are present in many organs, tissues and cell types, including brain, kidney, liver, astrocytes, platelets [4], pancreatic cells and, vascular smooth muscle cells [5]. Modifications in the levels of I_2-IR have been associated with analgesia [6], inflammation [7] and with human brain disorders [8] such as depression [9], Alzheimer's type

* Corresponding author.
E-mail address: cescolano@ub.edu (C. Escolano).
[1] Both authors contribute equally to this work.

https://doi.org/10.1016/j.ejmech.2021.113540
0223-5234/

dementia [10], Parkinson's disease [11], and glial tumors [12]. The fact that I_2-IR are altered in many pathophysiological processes and the availability of known I_2-IR ligands have permitted to place I_2-IR in a privileged position as new promising therapeutic targets. Representative I_2-IR ligands [13] emerged from the literature as useful tools to reveal the biological implications of these non-structurally described receptors (Fig. 1). The compelling evidence has demonstrated the neuroprotective role of I_2-IR through the pharmacological activities observed for their ligands. Agmatine, identified as the endogenous I_2-IR ligand, has modulated actions in several neurotransmitters leading to neuroprotection in both *in vitro* and in rodent models [14]. Idazoxan reduced neuron damage in the rat brain hippocampus after global ischemia [15]. 2-(2-Benzofuranyl)-2-imidazoline (2-BFI), a selective I_2-IR ligand, provided neuroprotective benefits against cerebral ischemia in models of chronic opioid therapy [16]. Idazoxan and 2-BFI have been proposed to exert neuroprotection by direct blocking of *N*-methyl-D-aspartate receptor (NMDA) mediated intracellular [Ca^{2+}] influx [17].

Two out of these seven ligands depicted in Fig. 1, CR4056 and [^{11}C]BU99008, are in the process of validating their therapeutic potential by progressing in clinical trials for osteoarthritis [18], and for PET diagnosis for patients that suffer from Alzheimer's disease (AD) [19,20], respectively. Due to the clinical implications of I_2-IR, the discovery of new I_2-IR ligands that could modulate the pharmacology involved is a challenging goal for a medicinal chemistry program. In this framework, we recently provided two structurally new families of I_2-IR ligands and validated their properties ameliorating the devastating cognitive decline in two murine models of neurodegeneration [21–23].

At the subcellular level in the central nervous system (CNS), I_2-IR are mainly located on the outer membrane of mitochondria in astrocytes [24,25]. Mitochondria are one of the main sources of reactive oxygen species (ROS) and reactive nitrogen species (RNS). The amyloid cascade hypothesis, that dominates the field of AD, has been replaced by alternative explanations arising from the connection of mitochondrial dysfunction and increased ROS. There is evidence that indicates a pro-oxidant ability of Aβ, mediating an accelerated production of ROS by directly binding to the mitochondrial membranes. Consequently, mitochondrial dynamics and function are altered, disrupting the energy metabolism, and leading to the loss of synaptic function. An excess in ROS/RNS production and a mitochondrial dysfunction could lead to oxidative stress (OS), which is implicated in several neurodegenerative diseases, such as AD [26–28]. In fact, there is growing evidence for the contribution of OS and neuroinflammation to the pathogenesis of AD [29,30]. Recent studies have investigated the role of I_2-IR in OS processes. Selective 2-BFI [31] decreased OS and altered the levels of antioxidant enzymes in an AD rat model and protected against OS-induced astrocytic cell death. Moreover, our group reported decreased levels of hydrogen peroxide levels and OS markers induced by two new I_2-IR ligands in aged SAMP8 mice [32].

In this manuscript, we focused our attention on 2-(2-benzofuranyl)-2-imidazole, named as **LSL60101** (garsevil), first described in 1995 by García-Sevilla's group as a I_2-IR selective ligand involved in astrocyte activation and neuronal regeneration [33,34]. In the following years, some outstanding papers described the biological relevance of **LSL60101** in the attenuation of morphine tolerance and hence proposing a neuroprotective role [35], such as provoking morphological/biochemical changes in astroglia that were neuroprotective after neonatal axotomy [36], and producing discriminable stimulus [37], amongst others. Of note, astrocytes as the main supportive cells in the CNS are significantly involved in the redox homeostasis, and consequently, this could be an indicative of a possible effect of **LSL60101** on OS balance.

From the structural chemical point of view, the nature of known I_2-IR ligands (Fig. 1) is relatively restricted and the pharmacophore moiety is generally related to 2-imidazoline-like structures.

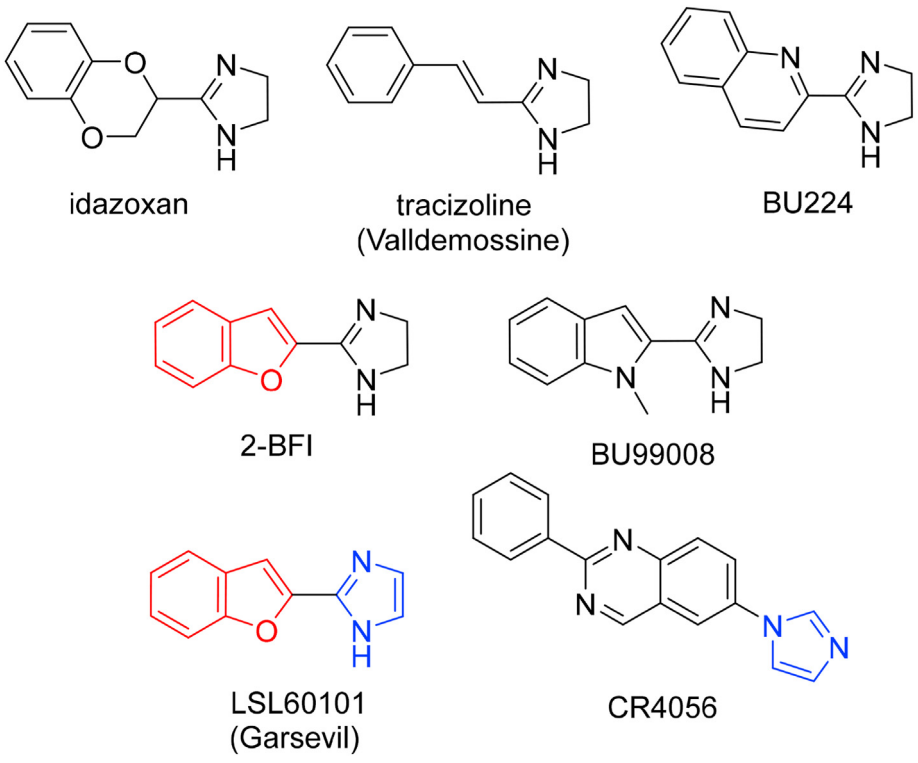

Fig. 1. Representative I_2-IR ligands.

Structural comparison of **LSL60101** with other known I_2-IR ligands, and in particular with 2-BFI that shares a benzofuran moiety, suggest a pharmacomodulation involving an unsaturation of the imidazoline ring, a drug optimization strategy appealed in the design of new drugs. The presence of an imidazole ring in the successful CR4056 ligand encourages the proposal.

Herein we describe the synthesis and full characterization of ten benzofuranyl-2-imidazole derivatives to shed light on the structural-activity relationship of this family. Note, that the structural exploration involves substituents, either eletron donating (methoxy) or electron attractor by inductive effect (bromide), located in different positions of the phenyl ring, and alkylation of the imidazole ring of the benzofuranyl-2-imidazole scaffold. We assessed the pharmacological profile of the ten analogues and selectivity through competition binding studies against the selective I_2-IR radioligand [^{3}H]2-BFI. Selectivity *versus* two related targets, the imidoline I_1 receptor (I_1-IR) and the α_2-adrenergic receptor (α_2-AR) was evaluated through competition studies using the selective radioligands [^{3}H]clonidine and [^{3}H]RX821002 (2-methoxyidazoxan), respectively. Complementarily, we performed three-dimensional quantitative structure−activity relationship (3D-QSAR) studies of this compound family and predicted *in silico* the ADMET properties. **LSL60101** endowed with the best I_2-IR affinity and an excellent selectivity index regarding I_1-IR and α_2-AR was selected for further studies. We carried out preliminary drug metabolism and pharmacokinetics (DMPK) studies for **LSL60101**, including chemical stability, PAMPA-BBB permeability assay, solubility, cytotoxicity, microsomal stability, cytochromes inhibition, and safety. The hypothermic properties and FADD multifunctional protein (as a marker of neuroplasticity) regulation were also studied following several **LSL60101** treatments in mice. Pharmacokinetics was carried out prior to an *in vivo* treatment in a proper murine model of AD. Thus, we further assessed the neuroprotective effects of **LSL60101** by evaluating specific OS markers under oxidative damage and several transcription factors related to OS machinery in 5xFAD mice (an early-onset mouse transgenic model of AD).

2. Results and discussion

2.1. Chemistry

The preparation of the required final benzofuranyl-2-imidazoles was accomplished, based on previous described procedure [33], starting from the corresponding commercially available benzofuran-2-carboxylic acid derivatives (Scheme 1). Except for the commercially available benzofuran-2-carbonitrile, **2a**, the other derivatives **2b**, **2c**, and **2d**, were prepared in two steps. Treatment of the corresponding benzofuran-2-carboxylic acid derivatives with thionyl chloride and ammonium hydroxide furnished the carboxamides **1b**, **1c**, and **1d** in excellent yields. Dehydration reaction with phosphorus oxychloride gave benzofuran-2-carbonitriles, **2b**, **2c**, and **2d**, that were efficiently transformed in the corresponding benzofuran-2-carbimididates hydrochlorides **3a**, **3b**, **3c** and **3d** after treatment with ethereal HCl 2 M. To construct the imidazole moiety, the reaction with 2,2-dimethoxyethylamine was undertaken to give **4a**, **4b**, **4c** and **4d** in quantitative yields, that were treated with aqueous hydrochloric acid accomplish the attack of the nitrogen atom to the ketal electrophilic carbon, affording benzofuranyl-2-imidazoles **5a** (named **LSL60101**), **5b**, **5c** and **5d**. Recrystallization of **5a** as monocrystal confirmed its structure by X-ray crystallographic analysis (see supporting information S51).

To access hydroxybenzofuran-2-imidazole derivatives **6b** and **6c**, hydrolysis of the methylether group of **5b** and **5c** was achieved by treatment with hydrobromic acid. The alkylation of the *N*-imidazole of compound **5a** with methyl iodide gave compound **7a** and with ethyl iodide yielded **7aa**. Analogously, the reaction of **5b** and **5c** with ethyl bromide furnished the expected products **7b** and **7c** in excellent yields.

All final products **5a-5d**, **6b-6c** and **7a**, **7aa**, **7b** and **7c**, were completely characterized (see experimental section and supporting information S19−S29) and all the tested compounds possess a purity of at least 95% (see supporting information S30−S49).

2.2. Pharmacological evaluation

2.2.1. Radioligand I_2-IR binding assays

The pharmacological profile of the ten compounds with the structures **5**, **6** and **7** (Scheme 1) was evaluated through competition binding studies against the selective I_2-IR radioligand [^{3}H]2-BFI and the selective α_2-AR radioligand [^{3}H]RX821002. The studies were performed in membranes from post-mortem human frontal cortex, a brain area that shows an important density of I_2-IR and α_2-AR. Idazoxan, a compound with well-established affinity for I_2-IR ($pK_i = 7.41 \pm 0.63$) and α_2-AR ($pK_i = 8.35 \pm 0.16$) was used as reference. The inhibition constant (K_i) for each compound was obtained and is expressed as the corresponding pK_i. The selectivity for these two receptors was expressed by the I_2/α_2 index, calculated as the antilogarithm of the ratio between pK_i values for I_2-IR and pK_i values for α_2-AR. Competition experiments against [^{3}H]2-BFI were biphasic for most of the compounds (Table 1).

We have previously reported the affinity of 2-BFI in I_2-IR human brain ($pK_{iH} = 9.08$ and $pK_{iL} = 7.15$). The structural differences between 2-BFI and **LSL60101** rely on the presence of an additional double bond in the five membered ring, from a 2-imidazoline to an imidazole conferring a planar structure to **LSL60101** (see X-ray crystallography discussion in the experimental section). The mentioned structural difference rendered a decrease in the affinity to $pK_{iH} = 8.17 \pm 0.19$ and $pK_{iL} = 6.02 \pm 0.10$, with 34% occupancy of the high affinity site. The decreased affinity upon α_2-AR plays in our favor and selectivity had an excellent ratio of 3090.

Next, electron-donating groups in the phenyl ring, such as a methoxy group was considered. Thus, compounds **5b** and **5c** bearing a methoxy group in the position −5 and −6, gave affinity values of $pK_i = 6.41 \pm 0.16$ and $pK_{iH} = 6.77 \pm 0.29$ and $pK_{iL} = 4.58 \pm 0.39$, respectively. The introduction of a 5-bromine furnished compound **5d** with similar affinity values as **LSL60101** ($pK_{iH} = 8.63 \pm 0.51$ and $pK_{iL} = 5.85 \pm 0.18$) but showing less selectivity against α_2-AR. The hydroxybenzofuran-2-imidazole derivatives **6b** and **6c** showed affinities of $pK_{iH} = 9.57 \pm 0.63$ and $pK_{iL} = 4.6 \pm 0.26$ and $pK_i = 5.48 \pm 0.11$, respectively, with a drop in the I_2/α_2 selectivity in relation to their methoxy derivative partners **5b** and **5c**. Compounds **7a**, **7aa** and **7b** bearing a *N*-alkylated imidazole nucleus showed affinity that better fit to a two-site binding model with $pK_{iH} = 6.99 \pm 0.28$ and $pK_{iL} = 5.35 \pm 0.21$, $pK_{iH} = 7.09 \pm 0.42$ and $pK_{iL} = 4.72 \pm 0.15$, and $pK_{iH} = 6.95 \pm 0.16$ and $pK_{iL} = 4.16 \pm 0.12$, with high affinity site occupancy of 38, 22 and 35%, respectively. Compared to the non-alkylated partners **LSL60101** and **5b**, the additional *N*-alkyl group did not result in a significant increase in the pK_i value but in a drop in the I_2/α_2 selectivity. *N*-Ethyl substituted **7c** gave an outstanding $pK_{iH} = 9.13 \pm 0.47$ value of I_2 affinity with a 12% high occupancy affinity site, whereas the non-alkylated homologous **5c** displayed a and $pK_{iL} = 5.11 \pm 0.06$.

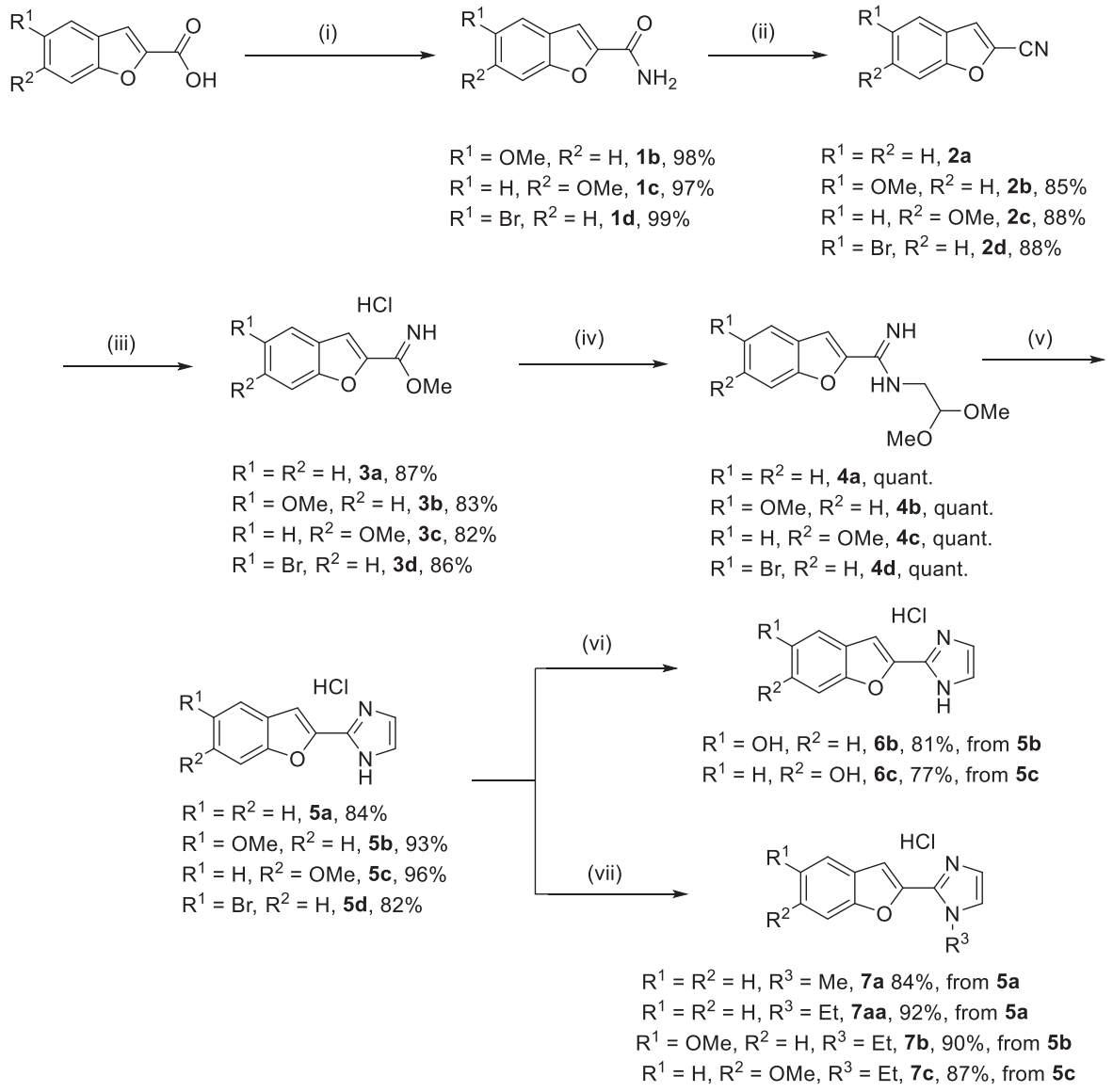

Scheme. 1. *Reagents and conditions*: (i) $SOCl_2$, toluene, 3 h, reflux; 25% aq. NH_4OH, rt; (ii) $POCl_3$, dichloroethane, 75 °C, 2 h; (iii) Et_2O·HCl 2 M, 4 °C, 48 h; (iv) 2,2-dimethoxyethylamine, methanol, 60 °C, 16 h; (v) HCl 2 M, 60 °C, 16 h; (vi) HBr 47%, 100 °C, 7 h; (vii) NaH, methyl iodide or ethyl bromide, DMF, 0 °C to rt, 75 min.

The study highlighted **LSL60101** as the most promising candidate of the benzofuran-2-imidazole family to tackle further *in vitro* and *in vivo* studies.

2.2.2. Comparison of I_2-IR binding affinities of ***LSL60101*** across species

The literature is non-uniform in the I_2-IR affinity values across species (human, rat, rabbit, mouse, and monkey), given the radioligand considered as a reference (idazoxan, 2-BFI) and the tissues used for analysis (from different anatomical parts: kidney, whole brain, cortex, etc). Thus, we made an effort in the comparison of affinities of standard I_2-IR ligands, 2-BFI, tracizoline, and clinically prominent [^{11}C]BU99008 and CR4056 [23]. When evaluating **LSL60101** a two-site model of binding was observed in human post-mortem brain cortical membranes with a pK_{iH} 8.17 ± 0.19 and pK_{iL} = 6.02 ± 0.10, and an occupancy of the high site of 34%. In rat cerebral cortex using idazoxan as radioligand, **LSL60101** was reported a lower affinity than in human tissues, with a pK_{iH} = 6.45 and pK_{iL} = 1.16, but a higher percentage fraction of occupancy (79%) [34]. In mice brain cortical membranes, the competition curve against [^{3}H]2-BFI binding was significantly better with a two-site fit than a one-site binding model, providing a pK_{iH} 9.92 ± 0.17 and pK_{iL} = 6.00 ± 0.14. These values were close to those found in human tissues including a similar occupancy of the high site (41%) supporting the *in vivo* experiments in mice.

2.3. 3D-QSAR study

The 3D-QSAR method was used to analyse the most significant descriptors that were interpreted in terms of identifying and quantifying structural elements important for I_2-IR and α_2-AR activity. The study was conducted on structurally diverse I_2-IR ligands that were divided into two clusters, based on their chemical structures. Cluster 1 represents compounds synthesized in this manuscript, while cluster 2 contains bicyclic α-iminophosphonate I_2-IR ligands previously described by our group (Fig. S1) [23]. To

Table 1
I_2-IR and α_2-AR Binding Affinities (pK_i) of compound idazoxan and 2-BFI and new compounds **5a-5d**, **6b, 6c**, **7a**, **7aa**, **7b** and **7c**.

Compound $R^1/R^2/R^3$ **General structure** 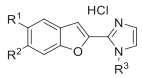	[a][^{3}H]2-BFI **I_2** pK_i one site	[b][^{3}H]-2-BFI **I_2** pK_i two sites		**High-affinity site %**	[^{3}H]-RX821002 **α_2** pK_i	**Selectivity I_2/α_2**
Idazoxan	7.41 ± 0.63	7.87 ± 0.74	5.76 ± 0.57	40 ± 7	8.35 ± 0.16	_
2-BFI	8.31 ± 0.13	9.08 ± 0.22	7.15 ± 0.31	58 ± 9	4.58 ± 0.22	5370
5a, LSL60101 $R^1 = R^2 = R^3 = H$	6.67 ± 0.09	8.17 ± 0.19	6.02 ± 0.10	34 ± 4	3.18 ± 0.17	3090
5b $R^1 = OMe$, $R^2 = R^3 = H$	6.41 ± 0.16	_	_	_	3.94 ± 0.07	295
5c $R^1 = H$, $R^2 = OMe$, $R^3 = H$	5.88 ± 0.16	6.77 ± 0.29	4.58 ± 0.39	46 ± 9	3.01 ± 0.45	741
5d $R^1 = Br$, $R^2 = H$, $R^3 = H$	6.28 ± 0.18	8.63 ± 0.51	5.85 ± 0.18	20 ± 5	4.92 ± 0.25	23
6b $R^1 = OH$, $R^2 = H$, $R^3 = H$	4.87 ± 0.23	9.57 ± 0.63	4.6 ± 0.25	29 ± 5	3.84 ± 0.16	11
6c $R^1 = H$, $R^2 = OH$, $R^3 = H$	5.48 ± 0.11	_	_	_	3.76 ± 0.12	52
7a $R^1 = R^2 = H$, $R^3 = Me$	5.98 ± 0.08	6.99 ± 0.28	5.35 ± 0.21	38 ± 10	3.75 ± 0.12	170
7aa $R^1 = R^2 = H$, $R^3 = Et$	5.05 ± 0.10	7.09 ± 0.42	4.72 ± 0.15	22 ± 6	3.77 ± 0.08	19
7b $R^1 = OMe$, $R^2 = H$, $R^3 = Et$	4.96 ± 0.15	6.95 ± 0.16	4.16 ± 0.12	35 ± 3	4.21 ± 0.19	6
7c $R^1 = H$, $R^2 = OMe$, $R^3 = Et$	5.26 ± 0.08	9.13 ± 0.47	5.11 ± 0.06	12 ± 2	3.17 ± 0.25	123

[a] Selectivity I_2-IR/α_2-AR expressed as the antilog (pK_i I_2-IR − pK_i α_2-AR).
[b] The best fit of the data for most of the compounds was to a two-site binding model with high pK_i (pK_{iH}) and low pK_i (pK_{iL}) affinities for both binding sites, respectively.

compare and validate our results, we have added three I_2-IR standard ligands (tracizoline, idazoxan, and BU99008, Fig. 1), in both data sets. Structural diversity of prepared data set enabled us not only to deeper analyse the most important structural characteristics, but also to suggest modifications to come up with novel compounds with improved I_2-IR activity and selectivity.

The Pentacle program [38] was used for calculation of GRID independent descriptors (GRIND and GRIND2) and 3D-QSAR model building. The reliability and predictive power of the created 3D-QSAR models were assessed using different internal and external validation parameters (Tables S1 and S2). Obtained results indicated that both models possessed good predictive capability and could be used for activity prediction of newly designed compounds. PLS coefficient plots presented the most important variables with positive and negative influence on I_2-IR and α_2-AR activity (Figs. S2 and S3).

Compounds from cluster 1 are compounds reported here (Scheme 1) with pK_i ranges between 4.87 and 6.67 for I_2-IR, and 3.01–4.92 for α_2-AR, while cluster 2 compounds present our bicyclic α-iminophosphonate derivatives (Fig. S1) with pK_i ranging from 4.02 to 8.56 for I_2-IR, and 3.38–6.77 for α_2-AR. Comparing to molecules from cluster 2, cluster 1 compounds possess lower pK_i values for I_2-IR as well as α_2-AR.

The most potent compound from cluster 1, **LSL60101** (pK_i = 6.67), displayed all significant variables with the most positive impact on the activity. Positive influence on both I_2-IR and α_2-AR activity showed variables var24 (DRY-DRY: 9.60–10.00 Å) and var25 (DRY-DRY: 10.00–10.40 Å), respectively. They described the optimal distance range between two hydrophobic regions, around benzofuranyl and imidazole rings, which may be crucial for establishing favourable van der Waals interactions with amino acids in the active pocket of both receptors (Fig. 2a). Moreover, I_2-IR 3D-QSAR model pointed out var232 (DRY-O: 6.40–6.80 Å) as the variable with the strongest positive influence on I_2-IR binding activity. This variable implies the importance of hydrogen bond donor group, −NH from imidazoline ring, located at a certain distance from hydrophobic region, benzofuranyl ring (Fig. 2a). Contrary, it did not possess such a significant influence in the compounds from cluster 2, since they lack hydrogen bond donor groups (Fig. S4). GRIND variable O–N1 (var394: 6.40–6.80 Å) signified a positive influence of the imidazole ring on I_2-IR activity, describing the distance between hydrogen bond acceptor and donor probes located around nitrogen atoms (Fig. 2a). On the other hand, it did not show a significant effect on α_2-AR activity. Furthermore, the importance of hydrogen bonding interactions in the binding site of I_2 receptor was confirmed with variables var452 (O-TIP: 8.00–8.40 Å) and var503 (N1-TIP: 6.80–7.20 Å), which underlined optimal distances between the steric region around the benzofuranyl ring and −NH from the imidazoline ring as a hydrogen bond donor or acceptor (Fig. 2a). Therefore, we can conclude that the substitution of the −NH imidazole group (R3) and losing of the hydrogen bond donating characteristics negatively correlated with I_2-IR binding activity and selectivity (**7a**, **7aa**, **7c**, **7b**). Analysis of α_2-AR 3D-QSAR model showed that the sole introduction of a hydrogen bond acceptor-group, at a certain distance from hydrophobic or steric region around heterocyclic ring, induced a positive impact on α_2-AR activity.

The compound with the lowest activity within the cluster 1 is **6b** (pK_i = 4.87). The introduction of a hydroxy or methoxy group on the carbon atom of the benzofuranyl nucleus resulted in reduced affinity, which could be described with var197 (TIP-TIP: 14.00–14.40 Å) and var350 (DRY-TIP: 10.40–10.80 Å) (Fig. 2b). Additionally, the unfavourable impact of these groups is also defined with the negative variable var408 (O–N1), which explains the distance of 12.00–12.40 Å between −NH of imidazoline, as a hydrogen bond donor and the oxygen atom in hydroxy or methoxy substituent as a hydrogen bond acceptor (Fig. 2b). Based on these findings we can conclude that the introduction of a hydrogen bond

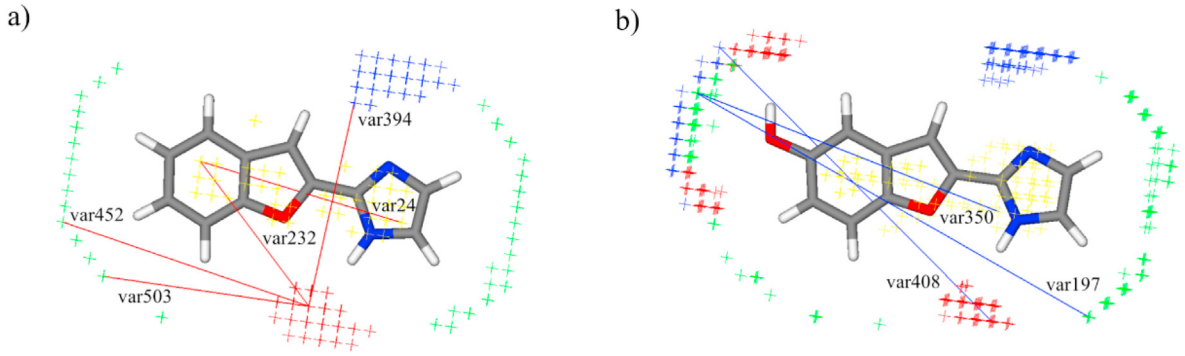

Fig. 2. Representation of positive interactions (in red) of **LSL60101** (a) and negative interactions (in blue) of **6b**; (b) in I_2-IR 3D-QSAR model. The steric hot spots (TIP) are presented in green, hydrophobic regions (DRY) in yellow, H-bond acceptor regions (N1) in blue, and H-bond donor regions (N1) in red.

acceptor substituent on the benzofuranyl ring may not be considered as the most complemental with the binding site of I_2-IR.

2.4. *In silico ADMET analysis of physicochemical and pharmacokinetic parameters*

The drug discovery pipeline has more and more relied on *in silico* predictions to optimize lead compounds and reduce investments [39]. *In silico* ADMET prediction aims to evaluate individual ADMET behaviours of examined compounds. Pharmacokinetic properties such as absorption, distribution, metabolism, excretion, and toxicity (ADMET) profiling of compounds were determined using ADMET Predictor software [40], while physico-chemical parameters were assessed with SwissADME online programme [41]. The obtained results are presented in Tables S3 and S4. Based on the results obtained from the performed calculations, we can conclude that all studied compounds present good water solubility and lipophilicity. Compounds reported here satisfy the Lipinski's Rule of 5, which supports their drug-likeness properties and potential chance to be orally bioavailable. Moreover, the polarity of compounds was evaluated by the TPSA (topological polar surface area) descriptor and results revealed that benzofuranyl-2-imidazoles possessed lower polarity, similar to idazoxan, when compared to previously described bicyclic α-iminophosphonate derivatives (see supporting information, Fig. S1) [23]. Regarding pharmacokinetic properties, we noted that all molecules possessed high BBB permeation. Compared to standard molecules, such as idazoxan, all examined compounds possessed lower percentage of unbound drug in plasma. Furthermore, this family showed lower metabolic CYP risk and TOX risk comparing to idazoxan and bicyclic α-iminophosphonate derivatives. P-gp is believed to play an important role in drug distribution and resistance to CNS drug treatment. The examined compounds were not identified as potential substrates for P-gp transporters. Since blocking hERG channels represents a major therapeutic challenge in drug discovery, we note that the compounds synthesized in this manuscript did not show affinity to inhibit hERG channels.

The absence of warnings of this theoretical study gave us confidence for undertaking further *in vitro* and eventually, *in vivo* experiments to assess the benzofuranyl-2-imidazole family and **LSL60101** as a neuroprotective agent.

2.5. *Blood brain barrier permeation assay*

Considering the localization of I_2-IR in the CNS, a good ability to cross the BBB is an essential requirement for developing effective I_2-IR ligands with potential therapeutic applications in the neuroprotective field. Guaranteed by the *in silico* parameters the *in vitro* permeability (P_e) of all the novel compounds was determined by using the PAMPA-BBB permeability assay (Table 2). The new compounds prepared were well above the threshold established for high BBB permeation ($P_e > 5.198 \times 10^{-6}$ cm s^{-1}), except for compound**s 6b** and **6c**. The aforementioned two compounds bear a hydroxyl group increasing their polarity and decreasing their capability to permeate the artificial PAMPA-BBB membrane with P_e values of $0.1 \pm 0.03 \times 10^{-6}$ cm s^{-1} and $0.32 \pm 0.1 \times 10^{-6}$ cm s^{-1}, respectively. In particular, the most I_2-IR affine compound **LSL60101** had a P_e value of $13.6 \pm 0.4 \times 10^{-6}$ cm s^{-1} and was considered suitable to envisage further *in vitro* and *in vivo* studies oriented to in-depth the pharmacological profile of the new family of I_2-IR ligands.

According to these data, compounds including a hydroxyl group in its structure, such as **6b** and **6c**, were not suitable for considering their potential in neurodegenerative diseases. In particular, **LSL60101** showed the best affinity and selectivity values and since it had a good ability to cross the BBB it will be used to undertake further studies.

2.6. *Selectivity I_2-IR versus I_1-IR in **LSL60101***

LSL60101 showed a remarkable affinity for I_2-IR and selectivity I_2/α_2-AR with a ratio 3090. Then, we assessed the affinity/selectivity

Table 2
Permeability results (Pe 10^{-6} cm s^{-1}) from the PAMPA-BBB assay for new report compounds and their prediction of BBB permeation.

Compound	[a]P_e 10^{-6} cm s^{-1}	[b]Prediction
Idazoxan	3.3 ± 0.1	CNS ±
2-BFI	6.1 ± 0.2	CNS+
5a, LSL60101	13.6 ± 0.4	CNS+
5b	8.3 ± 1.2	CNS+
5c	7.6 ± 0.1	CNS+
5d	20.3 ± 0.2	CNS+
6b	0.32 ± 0.1	CNS-
6c	0.1 ± 0.03	CNS-
7a	17.4 ± 0.85	CNS+
7aa	19.2 ± 1.1	CNS+
7b	12.4 ± 0.8	CNS+
7c	14.85 ± 0.1	CNS+

[a] PBS/EtOH (70:30) was used as solvent. Values are expressed as mean ± SD of at least three independent experiments.
[b] The *in vitro* permeability (P_e) of fourteen commercial drugs through lipid extract of porcine brain membrane together with the test compounds were determined (for the commercial drug values see Table S5).

for the very close receptors I_1-IR. Specific binding of [^{3}H]clonidine (20 nM) to I_1-IR of rat or human hypothalamic membranes was accomplished after pre-incubation with benextramine (10 μM) to alkylate population of α_2-AR. Under these experimental conditions [^{3}H]clonidine only labelled I_1-IR and in drug competition experiments moxonidine, a known I_1-IR selective compound, showed subnanomolar affinity for these I_1-sites; $K_{iH} = 0.2$ nM; $K_{iL} = 12$ μM. **LSL60101** displayed a very low affinity for I_1-IR, in rat samples $K_i = 115$ μM and in human samples $K_i = 250$ μM.

2.7. Acute toxicity

Based on the excellent affinity/selectivity upon I_2-IR of **LSL60101**, the safety evaluation was undertaken to determine the acute toxicity of the compound. **LSL60101** was safe up to a dose level of 100 mg/kg body weight after an intraperitoneal administration, since the LD_{50} was considered to be greater than 100 mg/kg (Probit analysis) in male albino mice (lack of toxicity in the range of doses tested: 10−100 mg/kg; n = 10 mice per dose tested).

2.8. ADME-DMPK profiling of *LSL60101*

With a compound showing promising binding properties/selectivity, devoid to α_2-AR and I_1-IR, and optimal safety, we undertook *in vitro* assays to define its physicochemical properties and chemical stability.

The solubility of **LSL60101** in 1% DMSO and 99% PBS buffer was excellent (52.5 μM). For a better definition, the solubility of **LSL60101** at different pH 1.13, 4.61 and 6.97, simulating the pH range of the gastric and intestinal fluids, was studied (see supporting information S10). Following the solubility terms stablished in *European Pharmacopoeia* vs.10.0, **LSL60101** is a soluble substance at pH 1.13 and 4.61 and a very slightly soluble substance at pH 6.97 (Table S6).

The chemical evaluation of **LSL60101** implied forced degradation studies under different stress conditions for a period of nine weeks, monitoring weekly the assays by HPLC and ^{1}H NMR. In particular, **LSL60101** was subjected to the effect of daylight with temperatures between 0 and 23 °C and a relative humidity of 25−85%, to the effect of high temperature (thermal stability at 75 °C), and to the continuous light of a 100W (230V) bulb. Analysis by HPLC showed that the compound was completely stable under all the aforementioned conditions. Calculated lipophilicity of **LSL60101** referring to the consensus log $P_{o/w}$ value calculated using the SwissADME program for five predictive log $P_{o/w}$ models, iLOGP, XLOGP3, WLOGP, MLOGP and SILICOS-IT, which gave values of 1.51, 2.16, 2.82, 1.15 and 3.02, respectively. Therefore, the calculated log $P_{o/w}$ and the other parameters of Lipinski were within the limits and the compounds are suitable for undertaking the characterization of *in vitro* ADME properties.

Microsomal stability, which is widely used to determine the likely degree of primary metabolic clearance in the liver, was assessed in human and mouse recombinant microsomes. The data shown in Table S7 reveals a 36% percentage of remaining compound, after 60 min of incubation in mouse microsomes, and 58% in human, indicating moderate differences in the metabolism depending on the species. The $t_{1/2}$ is 1.4-fold bigger in human than in mice, therefore the difference should be taken into consideration through additional preclinical studies.

The inhibition potential of **LSL60101** was evaluated using recombinant human cytochrome P450 enzymes [CYP1A2, CYP2C9, CYP2C19, CYP2D6, CYP3A4 (7-BFC) and CYP3A4 (DBF)] and probe substances with fluorescent detection. The results depicted in Table S8 showed no inhibition of the cytochromes considered at 10 μM concentration. Taking into account the range of nM in the affinity values of **LSL60101** it is not expected that at therapeutic doses the compound may interfere with the cytochrome P450-mediated metabolism of other drugs.

The plasma stability of **LSL60101** assessed in humans pooled from healthy donors was measured up to 6 h (0 h, 1 h, 2 h and 6 h) revealing 100, 83, 77 and 57% of the remaining percentage (Table S9). In mouse plasma **LSL60101** was inert under the conditions studied, remaining as 100% of the initial compound after 6 h (Table S10).

The extent of plasma protein binding was slightly superior in human that in mouse plasma. The fraction unbound value is also reported in Table S11. Whereas a 7.1% of **LSL60101** can be found in humans as free drug, a 16.0% was observed in mouse.

The effect of **LSL60101** over the activity of hERG, an important safety issue in drug discovery, was assessed and showed an inhibitory activity (%) of 4 ± 1 at 10 μM concentration, discarding any worries on this issue.

2.9. Cytotoxicity

In order to exclude compounds with adverse cellular effects, the newly synthesized compounds were evaluated for cytotoxicity. Human primary cells are physiologically more relevant. However, because of the difficulties of working with primary cultures, immortalized cell lines were used as an *in vitro* screening tool for cytotoxicity. In a panel of cancer cell lines, including LN-229 (glioblastoma), Capan-1 (pancreatic adenocarcinoma), HCT-116 (colorectal carcinoma), NCI−H460 (lung carcinoma), DND-41 (acute lymphoblastic leukemia), HL-60 (acute myeloid leukemia), K-562 (chronic myeloid leukemia) and Z-138 (non-Hodgkin lymphoma) cell lines, none of the compounds displayed any cytotoxicity at 100 μM (the highest concentration tested), as determined by a real-time IncuCyte proliferation assay.

2.10. Pharmacokinetics

The pharmacokinetic profile of **LSL60101** was investigated prior to the treatment of a murine model of AD (5xFAD). Following a single oral administration of 10 mg/kg of **LSL60101** in CD1 mice, plasma concentrations of drug were found after 15 min of treatment and were detected for 24 h. Absorption of drug from the gastrointestinal tract was slowly reaching C_{max} (3.24 μM) at 2 h after dosing and $t_{1/2\beta}$ was around 7 h. The narrow differences in AUC_0^t and AUC_0^∞ showed complete exposure, good bioavailability and appropriate elimination of **LSL60101** to reach the therapeutic potential of I_2-IR ligands in the experimental conditions described (Fig. 3).

Furthermore, the remarkable affinity of **LSL60101** for I_2-IR (pK_i in mouse brain cortical membranes ranged from 9.92 to 6) and the excellent selectivity ratio I_2/α_2-AR (3090) could guarantee, from the kinetic profile observed in plasma, that the concentrations reached at the site of action are enough to demonstrate the efficacy of this drug.

Overall, these studies confirmed that **LSL60101** is orally bioavailable and metabolically stable and can be used for further *in vivo* experiments.

2.11. Hypothermic effects of *LSL60101* in naïve mice

Several previous studies have proven the induction of acute hypothermia by I_2-IR ligands in rats [42,43] and mice [21−23]. In this regard, the present study evaluated the hypothermic effects of **LSL60101** in a wide range of doses (1, 5, 10, 20, 30, 50 mg/kg i.p.) in adult male and female CD1 mice at different times post-injection. The results showed a sharp drop in core body temperature

Pharmacokinetic parameters	
AUC_0^{∞}(ug*h/ml)	2.6
AUC_0^{t}(ug*h/ml)	2.7
T_{max}	2 h
C_{max}	0.6 μg/ml
$t_{1/2\,\beta}$	6.7 h

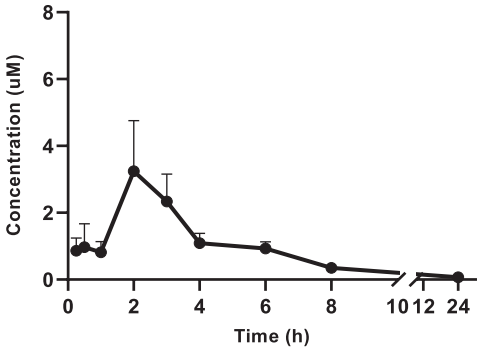

Fig. 3. Plasma concentration of **LSL60101** at different times (15 min–24 h) after an oral administration of 10 mg/kg, determined by HPLC/UV-VS at 290 nm. Basic pharmacokinetic parameters were calculated.

(ranging from −1.1 to −3.9 °C) for the larger dose tested (50 mg/kg) and observed 1 and up to 2 h post-injection (Fig. 4). Core body temperature returned to basal levels 3 h after drug administration.

The present results, in line with prior data [42], suggest the need for high doses of **LSL60101** to induce the expected hypothermia characteristic of I_2-IR ligands [21–23,43]. As for the role of this acute pharmacological effect, hypothermia is known to provide neuroprotection in models of cerebral ischemia; even mild temperature drops can cause significant neuroprotection [44]. In fact, hypothermia has been used to improve the neurological outcome under various pathological conditions, including stroke and traumatic brain injury [45,46]. In this line of thought, **LSL60101** has proven to partially prevent neuronal death in rats following neonatal axotomy [36], and thus, its hypothermic effects might be a relevant feature that could be mediating certain degree of neuroprotection.

Although the agonist or antagonist nature of I_2-IR ligands has been a topic of debate [2], it has been suggested that I_2-IR agonists reliably decrease body temperature in a highly quantitative manner in rodents [42], suggesting this assay could be used as a sensitive *in vivo* assay for studying I_2 receptor ligands, and in line with the hypothermic effects observed in the present study in mice treated with **LSL60101**.

2.12. Effects of acute *LSL60101* on hippocampal FADD protein content in naïve mice

In the context of neuroprotection, FADD adaptor emerges as a key multifunctional protein involved in the mechanisms

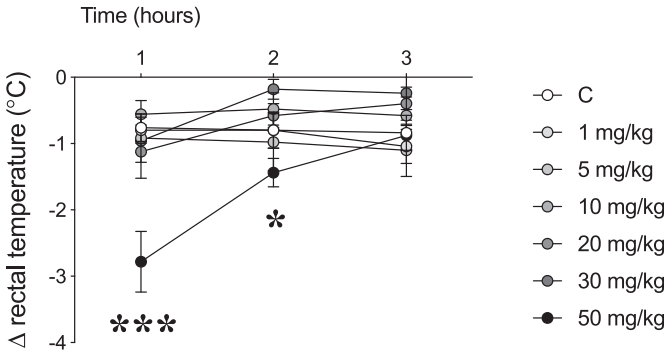

Fig. 4. Acute effects of **LSL60101** treatment on core body temperature in mice. Symbols represent means ± SEM of the difference (Δ, 1, 2 or 3 h minus basal value) in body temperature (°C) for each treatment group. ***$p < 0.001$ and *$p < 0.05$ when comparing the dose of 50 mg/kg with the control group (repeated measures ANOVA followed by Sidak's comparison test).

controlling cell fate regulation, balancing pro-apoptotic and/or neuroprotective actions in rodents [21,47,48]. The acute treatment with a high dose of **LSL60101** (50 mg/kg, i.p.) significantly decreased (by ~34%) hippocampal FADD protein content as compared to vehicle-treated mice (Fig. 5). The present results replicated earlier studies in which other I_2-IR ligands decreased FADD hippocampal content [21,23], and suggested the induction of non-apoptotic (e.g., neuroplastic and or neuroprotective) actions initiated by acute **LSL60101** treatment in mice brain and in parallel to the hypothermic effects.

2.13. Effects of chronic *LSL60101* at a low dose in a mice model of Alzheimer's disease

Accumulating evidence support that I_2-IR exert neuroprotective roles in a plethora of neurodegenerative disorders, such as AD [8,9,11,49,50]. Previous studies suggested that I_2-IR in the CNS are mainly located on the outer membrane of mitochondria in astrocytes [51]. Given that alterations in mitochondrial function promote an increased ROS production, which combined with an altered antioxidant defence contribute to the early stages of AD before the development of Aβ pathology and cognitive dysfunction [29,30,52], here we tested the effects of a low dose of **LSL60101** administered following a chronic paradigm (1 mg/kg/day, for 4 weeks) on specific OS markers under oxidative damage in 5XFAD mice, an early-onset mouse transgenic model of AD, and as compared to a wild type strain. The results showed increased gene expression of the so-called antioxidant response element (AREs), such as heme oxygenase 1 (Hmox1), aldehyde dehydrogenase 2 (Aldh2) and iNOS [53] in 5xFAD vs. wild type mice (Fig. 6). By contrast, in 5xFAD mice treated with **LSL60101**, the expression of those decreased in a significant way.

On the other hand, an excess in ROS is removed by antioxidant enzymes (e.g., superoxide dismutase, SOD1, and glutathione peroxidase, GPX-1). 5XFAD mice showed a significant decrease in both proteins levels in reference to wild type mice. Interestingly, **LSL60101** was able to significantly increase the levels of these key protein, indicating that **LSL60101** induced the activation of a cellular signalling cascade that led to a reduced OS, and that in turn could have a neuroprotective role in an oxidative environment related with neurodegenerative processes such as AD (Fig. 7).

These results are in agreement with recent studies that demonstrated a key role for I_2-IR ligands in the OS process. In particular, 2-BFI (a selective ligand to I_2-IR), decreased OS and altered the level of anti-oxidant enzymes in an AD rat model [54], protecting against OS-induced astrocytic cell death [55]. Ultimately, previous work from our group reported a decrease in hydrogen peroxide levels and OS markers induced by the I_2-IR ligands **MCR5**

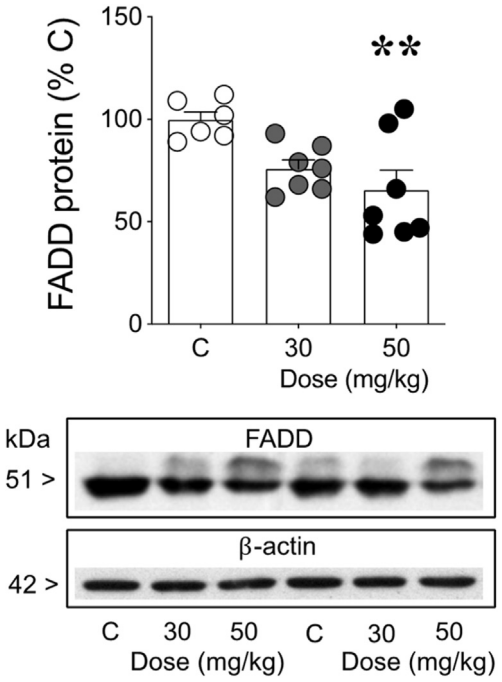

Fig. 5. Acute effects of **LSL60101** (30 or 50 mg/kg, i.p.) on hippocampal FADD protein. Columns are means ± SEM of FADD content (% C) for each treatment group. Individual symbols are shown for each animal. One-way ANOVA followed by Sidak's multiple comparisons tests: $^{**}p < 0.01$ vs. C (control-treated mice). Representative immunoblots depicting the labelling of FADD and β-actin (as a loading control) for each treatment group are shown below.

and **MCR9** in aged SAMP8 mice [22]. Recently, we demonstrated that **LSL60101** can ameliorate the AD hallmarks and neuroinflammation [56]. Moreover, the chronic treatment with **LSL60101** led to the induction of reactive astrocytes and the up-regulation of the expression of the astrocyte marker glial fibrillary acidic protein (GFAP) [34]. As mentioned, astrocytes are the main supportive cells in the CNS and are significantly involved in the redox homeostasis [57], and thus, and as a consequence, this could be proposed as a possible effect of **LSL60101** on OS balance.

3. Conclusions

We have evaluated the binding and selective properties upon I_2-IR in human brain tissues of a series of benzofuranyl-2-imidazoles diversely substituted in both benzofuranyl and imidazole rings. Due to the lack of structural description of these receptors, 3D-QSAR and *in silico* physicochemical properties were performed in order to determine the relevant elements that may allow the further structural optimization of new molecules. The secure theoretical DMPK of the family led us to undertake *in vitro* studies including PAMPA to confirm their penetration into the CNS to address neurodegenerative issues. The safe *in vitro* DMPK and cytotoxicity assays of the selected **LSL60101** opened the door to *in vivo* studies. After the determination of its pharmacokinetic profile, the treatment of animals with **LSL60101** confirmed a decrease in the content of hippocampal FADD protein, a key signalling mediator of neuroprotective actions. The I_2-IR ligand **LSL60101** also fostered a diminution in oxidative stress biomarkers in an AD murine model (5xFAD). Thus, the modulation of I_2-IR by **LSL60101** is proposed as a promising opportunity for addressing AD therapeutics and invites for the further design of new promising benzofuranyl-2-imidazole-base structures to be added to the scarce arsenal of I_2-IR ligands.

4. Experimental section

4.1. Chemistry

Reagents, solvents and starting products were acquired from commercial sources. The term "concentration" refers to the vacuum evaporation using a Büchi rotavapor. When indicated, the reaction products were purified by "flash" chromatography on silica gel (35–70 μm) with the indicated solvent system. IR spectra were performed in a Spectrum Two FT-IR Spectrometer, and only noteworthy IR absorptions (cm^{-1}) are listed. NMR spectra were recorded in DMSO-d_6 at 400 MHz (^{1}H) and 100.6 MHz (^{13}C), and chemical shifts are reported in δ values downfield from TMS or relative to residual DMSO-d_6 (2.50 ppm, 39.5 ppm) as an internal standard. Data are reported in the following manner: chemical shift, multiplicity, coupling constant (J) in hertz (Hz) and integrated intensity. Multiplicities are reported using the following abbreviations: s, singlet; d, doublet; dd, double doublet; q, quadrupet; t, triplet; m, multiplet; br s, broad signal. The accurate mass analyses were carried out using a LC/MSD-TOF spectrophotometer. HPLC-MS (Agilent 1260 Infinity II) analysis was conducted on a Poroshell 120 EC-C15 (4.6 mm × 50 mm, 2.7 μm) at 40 °C with mobile phase A (H_2O + 0.05% formic acid) and B (ACN + 0.05% formic acid) using a gradient elution and flow rate 0.6 mL/min. The DAD detector was set at 254 nm, the injection volume was 5 μL, and oven temperature was 40 °C. All tested compounds possess a purity of at least 95%.

4.1.1. General procedures for the synthesis of benzofuran-2-carboxamides ***1b***, ***1c*** and ***1d***

Thionyl chloride (1.65 equiv) was added to a suspension of benzofuran-2-carboxylic acid derivatives (1 equiv) in anhydrous toluene (0.4 mmol/mL). After stirring the mixture for 3 h, at reflux, the reaction was cooled and concentrated. Then, the resulting benzofuran-2-carbonyl chloride derivative (1 equiv) was added in small portions to an ice-cold solution of 25% aq. NH_4OH (0.5 mmol/mL). Upon completion of the addition the reaction mixture was allowed to reach rt and a precipitate was formed. The solid was collected by filtration, washed with cold water and dried under vacuum.

*4.1.1.1. 5-Methoxybenzofuran-2-carboxamide (**1b**).* Following the general procedure, thionyl chloride (17.2 mmol, 1.25 mL), 5-bromobenzofuran-2-carboxylic acid (10.4 mmol, 2.0 g), anhydrous toluene (25 mL) and 25% aq. NH_4OH (20 mL) gave **1b** (1.87 g, 98%) as a beige solid.

*4.1.1.2. 6-Methoxybenzofuran-2-carboxamide (**1c**).* Following the general procedure, thionyl chloride (8.60 mmol, 0.63 mL), 6-methoxybenzofuran-2-carboxylic acid (5.20 mmol, 1.0 g), anhydrous toluene (13 mL) and 25% aq. NH_4OH (10 mL) gave **1c** (930 mg, 97%) as a beige solid.

*4.1.1.3. 5-Bromobenzofuran-2-carboxamide (**1d**).* Following the general procedure, thionyl chloride (13.7 mmol, 1.0 mL), 5-bromobenzofuran-2-carboxylic acid (8.30 mmol, 2.0 g), anhydrous toluene (21 mL) and 25% aq. NH_4OH (17 mL) gave **1d** (1.98 g, 99%) as a white solid.

4.1.2. General procedure for the synthesis of benzofuran-2-carbonitrile ***2b***, ***2c*** and ***2d***

Phosphoryl chloride (3 equiv) was added to a solution of benzofuran-2-carboxamide derivative (1 equiv) in dichloroethane (0.48 mmol/mL). The reaction was stirred at 75 °C for 2 h. Then, the reaction mixture was evaporated and neutralized with saturated $NaHCO_3$ solution. The aqueous phase was extracted with AcOEt, the

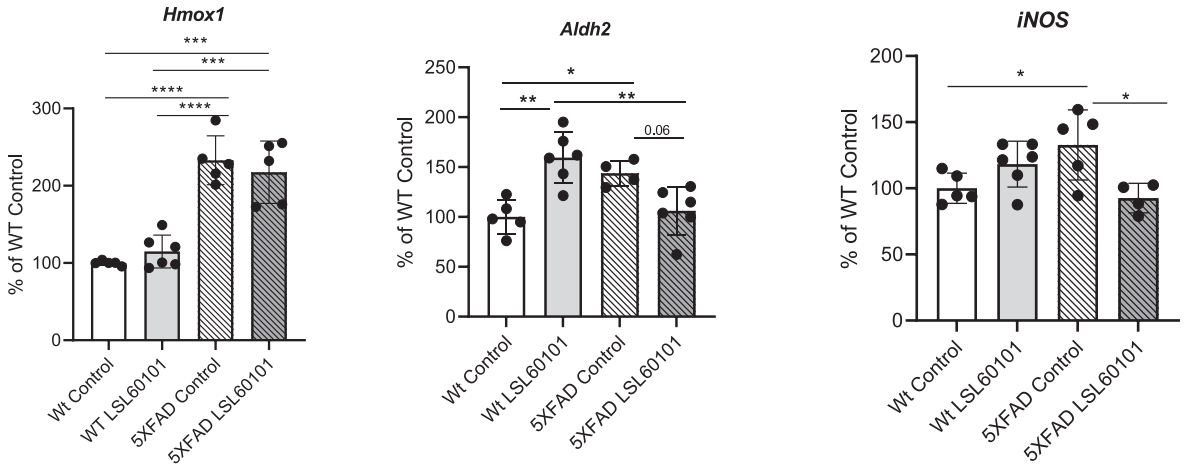

Fig. 6. Chronic effects of **LSL60101** (1 mg/kg/day, per os.) on *Hmox1, Aldh2* and *iNOS* gene expression in hippocampus. Columns are the mean ± SEM for each treatment group. Individual symbols are shown for each animal. Means were compared with two-way ANOVAs, followed by Tukey-Kramer multiple comparison post-hoc analysis: ****$p < 0.0001$; ***$p < 0.001$; **$p < 0.01$; *$p < 0.05$ vs. Wt Controls.

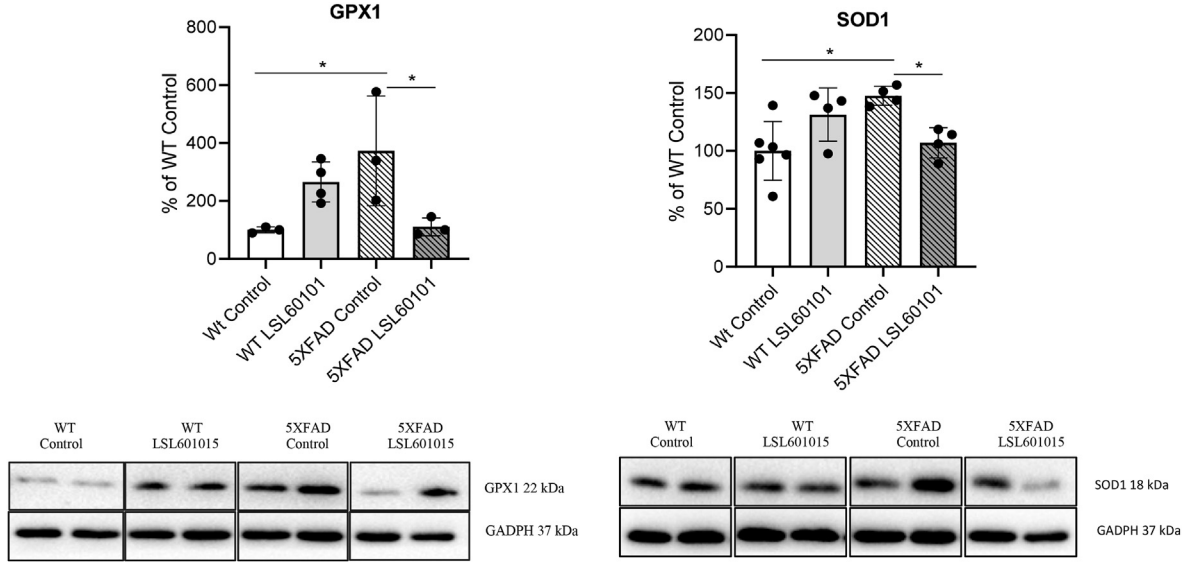

Fig. 7. Chronic effects of **LSL60101** (1 mg/kg/day, per os.) on the expression of SOD1 and GPX-1 protein levels in hippocampus. Columns are the mean ± SEM for each treatment group. Individual symbols are shown for each animal. Means were compared with two-way ANOVAs, followed by Tukey-Kramer multiple comparisons post-hoc analysis. *$p < 0.01$ vs. Wt control mice).

combined organic phases were washed with brine, dried over Na_2SO_4, and evaporated to give a residue, which was purified by flash column chromatography.

*4.1.2.1. 5-Methoxybenzofuran-2-carbonitrile (**2b**).* Following the general procedure, **1b** (9.62 mmol, 1.84 g), dichloroethane (20 mL) and phosphoryl chloride (28.9 mmol, 2.70 mL) gave **2b** (1.42 g, 85%) as a beige solid, after column chromatography (dichloromethane 100%).

*4.1.2.2. 6-Methoxybenzofuran-2-carbonitrile (**2c**).* Following the general procedure, **1c** (4.87 mmol, 930 mg), dichloroethane (10 mL) and phosphoryl chloride (14.6 mmol, 1.36 mL) gave **2c** (740 mg, 88%) as a beige solid, after column chromatography (dichloromethane 100%).

*4.1.2.3. 5-Bromobenzofuran-2-carbonitrile (**2d**).* Following the general procedure, **1d** (7.92 mmol, 1.90 g), dichloroethane (17 mL) and phosphoryl chloride (23.8 mmol, 2.21 mL) gave **2d** (1.55 g, 88%) as a white solid, after column chromatography (dichloromethane 100%).

*4.1.3. General procedure for the synthesis of methyl benzofuran-2-carbimididate hydrochlorides **3a**, **3b**, **3c** and **3d***

The 2-cyanobenzofuran derivative (1 equiv) was dissolved in ethereal HCl 2 M (0.25 mmol/mL) and methanol (5 mmol/mL). The resulting mixture was kept at 4 °C for 48 h. The resulting solid was filtered, washed with cold ether and dried in order to obtain the desired carbimidate hydrochloride.

*4.1.3.1. Methyl benzofuran-2-carbimididate hydrochloride (**3a**).* Following the general procedure, benzofuran-2-carbonitrile (6.99 mmol, 1.0 g), ethereal HCl 2 M (28 mL) and methanol (1.4 mL) gave **3a** (1.29 g, 87%) as a white solid.

*4.1.3.2. Methyl 5-methoxybenzofuran-2-carbimididate hydrochloride (**3b**).* Following the general procedure, **2b** (8.08 mmol, 1.40 g), ethereal HCl 2 M (32 mL), methanol (2 mL) gave **3b** (1.62 g, 83%) as a white solid.

*4.1.3.3. Methyl 6-methoxybenzofuran-2-carbimididate hydrochloride (**3c**).* Following the general procedure, **2c** (4.04 mmol, 700 mg), ethereal HCl 2 M (16 mL) and methanol (1 mL) gave **3c** (797 mg, 82%) as a white solid.

*4.1.3.4. Methyl 5-bromobenzofuran-2-carbimididate hydrochloride (**3d**).* Following the general procedure, **2d** (4.82 mmol, 1.10 g), ethereal HCl 2 M (19 mL) and methanol (1 mL) gave **3d** (1.20 g, 86%) as a white solid.

*4.1.4. General procedure for the synthesis of N-(2,2-dimethoxyethyl)benzofuran-2-carboximidamide **4a**, **4b**, **4c** and **4d***

A solution of 2,2-dimethoxyehtylamine (1.1 equiv) and methyl benzofuran-2-carbimidate hydrochloride derivative (1 equiv) in methanol (0.47 mmol/mL) was stirred at 60 °C for 16 h. The mixture was evaporated to dryness, which was used directly in the next step without further purification.

*4.1.4.1. N-(2,2-dimethoxyethyl)benzofuran-2-carboximidamide (**4a**).* Following the general procedure, **3a** (5.20 mmol, 1.10 g), 2,2-dimethoxyethylamine (5.72 mmol, 0.62 ml) and methanol (11 mL) gave **4a** (1.29 g, quantitative) as a beige solid.

*4.1.4.2. N-(2,2-Dimethoxyethyl)-5-methoxybenzofuran-2-carboximidamide (**4b**).* Following the general procedure, **3b** (4.34 mmol, 1.05 g), 2,2-dimethoxyethylamine (4.78 mmol, 0.52 mL) and methanol (9 mL) gave **4b** (1.29 g, quantitative) as a beige solid.

*4.1.4.3. N-(2,2-Dimethoxyethyl)-6-methoxybenzofuran-2-carboximidamide (**4c**).* Following the general procedure, **3c** (2.93 mmol, 708 mg), 2,2-dimethoxyethylamine (3.22 mmol, 0.35 mL) and methanol (6 mL) gave **4c** (815 mg, quantitative) as a beige solid.

*4.1.4.4. N-(2,2-Dimethoxyethyl)-5-bromobenzofuran-2-carboximidamide (**4d**).* Following the general procedure, **3d** (2.01 mmol, 584 mg), 2,2-dimethoxyethylamine (2.21 mmol, 0.24 mL) and methanol (4 mL) gave **4d** (657 mg, quantitative) as a beige solid.

*4.1.5. General procedure for the synthesis of 2-(benzofuran-2-yl)-1H-imidazole hydrochlorides **LSL60101**, **5b**, **5c** and **5d***

The corresponding *N*-(2,2-dimethoxyethyl)benzofuran-2-carboximidamide was treated with HCl 2 M (0.1 mmol/mL) and the resulting mixture was stirred at 60 °C for 16 h. After cooling, the solution was washed with dichloromethane. The aqueous layer was basified with NaOH 5 M and the free base extracted with AcOEt. The combined organic phases were washed with brine, dried over Na_2SO_4, and evaporated to give a residue which was dissolved in diethyl ether/ethanol (5:1). Ethereal HCl 2 M (1.5 mmmol/mL) was added and the precipitated salt was collected by filtration and was crystallized with acetonitrile.

*4.1.5.1. 2-(Benzofuran-2-yl)-1H-imidazole hydrochloride (**5a**).* Following the general procedure, **4a** (5.20 mmol, 1.29 g), HCl 2 M (52 mL) and ethereal HCl 2 M (3.5 mL) gave **LSL60101** (960 mg, 84%) as a white solid. IR (ATR) 3477, 3168, 2535, 1651, 1457, 1310, 1140, 1009, 879, 737, 706 cm^{-1}. ^1H NMR (400 MHz, DMSO-d_6) δ 7.40 (t, $J = 7.5$ Hz, 1H), 7.52 (t, $J = 8.5$ Hz, 1H), 7.74 (d, $J = 8.5$ Hz, 1H), 7.83 (s, 2H), 7.88 (d, $J = 7.5$ Hz, 1H), 8.12 (s, 1H). ^{13}C NMR (100.6 MHz) δ 109.8, 111.6, 120.8 (2C), 122.9, 124.4, 127.1, 127.3, 135.1, 140.6, 154.6. HRMS $C_{11}H_9N_2O$ $[M+H]^+$ 185.0709; found, 185.0706. Purity 99.6% ($t_R = 3.08$ min).

*4.1.5.2. 2-(5-Methoxybenzofuran-2-yl)-1H-imidazole hydrochloride (**5b**).* Following the general procedure, **4b** (4.10 mmol, 1.14 g), HCl 2 M (41 mL) and ethereal HCl 2 M (2.7 mL) gave **5b** (950 mg, 93%) as a white solid. IR (ATR) 3449, 3076, 2587, 1647, 1457, 1434, 1206, 1157, 1018, 812, 776, 712 cm^{-1}. ^1H NMR (400 MHz, DMSO-d_6) δ 3.81 (s, 3H), 7.08 (dd, $J = 9.0$, 2.5 Hz, 1H), 7.38 (d, $J = 2.5$ Hz, 1H), 7.61 (d, $J = 9.0$ Hz, 1H), 7.82 (s, 2H), 8.10 (s, 1H). ^{13}C NMR (100.6 MHz) δ 55.7, 104.4, 110.2, 112.2, 116.5, 120.7 (2C), 127.8, 135.0, 141.1, 149.5, 156.5. HRMS $C_{12}H_{11}N_2O_2$ $[M+H]^+$ 215.0815; found, 215.0816. Purity 98.5% ($t_R = 3.19$ min).

*4.1.5.3. 2-(6-Methoxybenzofuran-2-yl)-1H-imidazole hydrochloride (**5c**).* Following the general procedure, **4c** (2.93 mmol, 815 mg), HCl 2 M (29 mL) and ethereal HCl 2 M (2.0 mL) gave **5c** (702 mg, 96%) as a white solid. IR (ATR) 3349, 3089, 2731, 1614, 1492, 1269, 1151, 1110, 1023, 842, 773, 709 cm^{-1}. ^1H NMR (400 MHz, DMSO-d_6) δ 3.86 (s, 3H), 7.02 (dd, $J = 8.5$, 2.0 Hz, 1H), 7.23 (s, 1H), 7.74 (d, $J = 8.5$ Hz, 1H), 7.77 (s, 2H), 8.06 (s, 1H). ^{13}C NMR (100.6 MHz) δ 55.9, 95.8, 110.2, 113.8, 120.2, 120.4 (2C), 123.2, 135.2, 139.6, 156.0, 159.8. HRMS $C_{12}H_{11}N_2O_2$ $[M+H]^+$ 215.0815; found, 215.0814. Purity 99.6% ($t_R = 3.20$ min).

*4.1.5.4. 2-(5-Bromobenzofuran-2-yl)-1H-imidazole hydrochloride (**5d**).* Following the general procedure, **4d** (1.99 mmol, 650 mg), HCl 2 M (20 mL) and ethereal HCl 2 M (1.3 mL) gave **5d** (536 mg, 82%) as a white solid. IR (ATR) 3379, 3171, 2703, 1650, 1566, 1447, 1143, 1047, 879, 749, 718 cm^{-1}. ^1H NMR (400 MHz, DMSO-d_6) δ 7.62 (dd, $J = 9.0$, 2.0 Hz, 1H), 7.70 (d, $J = 9.0$ Hz, 1H), 7.83 (s, 2H), 8.07 (s, 1H), 8.12 (d, $J = 2.0$ Hz, 1H). ^{13}C NMR (100.6 MHz) δ 108.9, 113.7, 116.6, 121.1 (2C), 125.3, 129.4, 129.8, 134.6, 142.0, 153.3. HRMS $C_{11}H_8BrN_2O$ $[M+H]^+$ 262.9815; found, 262.9813. Purity 98.6% ($t_R = 3.47$ min).

*4.1.6. General procedure for the synthesis of 1-alkyl-2-(benzofuran-2-yl)-1H-imidazole hydrochlorides **6b** and **6c***

2-(Benzofuran-2-yl)-1*H*-imidazole hydrochlorides derivatives were neutralized with NaOH 2 N and the free base was extracted with AcOEt. The combined organic phases were washed with brine, dried over Na_2SO_4, and evaporated to give the desired amine. To a solution of the free base (1 equiv) generated from the corresponding 2-(benzofuran-2-yl)-1*H*-imidazole hydrochloride was treated with HBr 47% acid solution (0.5 mL) and the mixture was stirred at 100 °C for 7 h. After cooling the resulting solid was filtered, dissolved in water and basified with saturated $NaHCO_3$ solution. The free base was extracted with AcOEt. The combined organic phases were washed with brine, dried over Na_2SO_4, and evaporated to give a residue which was dissolved in diethyl ether/ethanol. Ethereal HCl 2 M (1.5 mmol/mL) was added and the precipitated salt was collected by filtration and was crystallized with acetonitrile.

*4.1.6.1. 2-(5-Hydroxybenzofuran-2-yl)-1H-imidazole hydrochloride (**6b**).* Following the general procedure, **5b** (0.93 mmol, 200 mg), HBr 47% acid solution (2 mL) and ethereal HCl 2 M (0.6 mL) gave **6b** (191 mg, 81%) as a yellowish solid. IR (ATR) 3266, 3009, 2819, 2731, 1593, 1443, 1370, 1246, 1195, 1157, 1090, 850, 802, 700 cm^{-1}. ^1H NMR (400 MHz, DMSO-d_6) δ 6.99 (dd, $J = 9.0$, 2.0 Hz, 1H), 7.14 (d, $J = 2.0$ Hz, 1H), 7.51 (d, $J = 9.0$ Hz, 1H), 7.80 (s, 2H), 7.97 (d, $J = 1.0$ Hz, 1H). ^{13}C NMR (100.6 MHz) δ 106.4, 109.9, 111.9, 116.7, 120.6 (2C), 127.9, 135.2, 140.7, 148.9, 154.5. HRMS $C_{11}H_9N_2O_2$ $[M+H]^+$

201.0659; found, 201.0656. Purity 98.1% ($t_R = 2.92$ min).

*4.1.6.2. 2-(6-Hydroxybenzofuran-2-yl)-1H-imidazole hydrochloride (**6c**).* Following the general procedure, **5c** (0.93 mmol, 200 mg), HBr 47% acid solution (1.9 mL) and ethereal HCl 2 M (0.6 mL) gave **6c** (183 mg, 77%) as a yellowish solid. IR (ATR) 3388, 3092, 2813, 2755, 1624, 1430, 1377, 1283, 1150, 1122, 1096, 839, 766, 708 cm^{-1}. ^1H NMR (400 MHz, DMSO-d_6) δ 6.92 (dd, $J = 8.5$, 2.0 Hz, 1H), 7.10 (s, 1H), 7.63 (d, $J = 8.5$ Hz, 1H), 7.77 (s, 2H), 8.01 (s, 1H), 10.30 (br s, 1H). ^{13}C NMR (100.6 MHz) δ 97.5, 110.6, 114.4, 118.9, 120.2 (2C), 123.2, 135.4, 138.7, 156.2, 158.4. HRMS $C_{11}H_9N_2O_2$ [M+H]+ 201.0659; found, 201.0657. Purity 97.6% ($t_R = 2.91$ min).

*4.1.7. General procedure for the synthesis of 1-alkyl-2-(benzofuran-2-yl)-1H-imidazole hydrochlorides **7a**, **7aa**, **7b** and **7c***

2-(Benzofuran-2-yl)-1*H*-imidazole hydrochlorides derivatives were neutralized with NaOH 2 N and the free base was extracted with AcOEt. The combined organic phases were washed with brine, dried over Na_2SO_4, and evaporated to give the desired amine. To a solution of the free base (1 equiv) generated from the corresponding 2-(benzofuran-2-yl)-1*H*-imidazole hydrochloride in DMF (0.34 mmol/mL) at 0 °C was added sodium hydride (1.5 equiv, 60% in mineral oil). After 30 min at rt, methyl iodide/ethyl bromide (1.1 equiv) was added dropwise over 15 min at 0 °C. Then, the mixture was stirred for 30 min at rt, poured into water and extracted with AcOEt. The organic layer was washed with and the product was extracted with HCl 1 M. The aqueous layer was basified with NaOH 2 M and the free base was extracted with AcOEt. The combined organic phases were washed with brine, dried over Na_2SO_4, and evaporated to give a residue which was dissolved in diethyl ether/ethanol. Ethereal HCl 2 M (1.5 mmol/mL) was added and the precipitated salt was collected by filtration and was crystallized with acetonitrile.

*4.1.7.1. 1-Methyl-2-(benzofuran-2-yl)-1H-imidazole hydrochloride (**7a**).* Following the general procedure, **LSL60101** (0.76 mmol, 140 mg), methyl iodide (0.84 mmol, 0.05 mL), sodium hydride 60% in mineral oil (1.14 mmol, 45.8 mg), DMF (2.3 mL) and ethereal HCl 2 M (0.5 mL) gave **7a** (150 mg, 84%) as a white solid. IR (ATR) 3306, 3095, 2569, 1634, 1445, 1270, 1188, 1131, 1033, 883, 756, 708 cm^{-1}. ^1H NMR (400 MHz, DMSO-d_6) δ 4.13 (s, 3H), 7.43 (t, $J = 7.5$ Hz, 1H), 7.55 (t, $J = 8.5$ Hz, 1H), 7.77 (d, $J = 8.5$ Hz, 1H), 7.80 (d, $J = 2.0$ Hz, 1H), 7.86–7.91 (m, 2H), 8.01 (s, 1H). ^{13}C NMR (100.6 MHz) δ 36.8, 111.5, 112.2, 121.0, 123.2, 124.9, 126.0, 127.4, 127.9, 135.6, 140.5, 154.9. HRMS $C_{12}H_{11}N_2O$ $[M+H]^+$ 199.0866; found, 199.0866. Purity 99.7% ($t_R = 3.15$ min).

*4.1.7.2. 1-Ethyl-2-(benzofuran-2-yl)-1H-imidazole hydrochloride (**7aa**).* Following the general procedure**, LSL60101** (1.36 mmol, 250 mg), ethyl bromide (1.42 mmol, 0.10 mL), sodium hydride 60% in mineral oil (2.04 mmol, 82 mg), DMF (4.0 mL) and ethereal HCl 2 M (0.9 mL) gave **7aa** (310 mg, 92%) as a white solid. IR (ATR) 3394, 3104, 2618, 1628, 1428, 1266, 1177, 1111, 929, 836, 761, 708 cm^{-1}. ^1H NMR (400 MHz, DMSO-d_6) δ 1.50 (t, $J = 7.0$ Hz, 3H), 4.55 (q, $J = 7.0$ Hz, 2H), 7.41 (d, $J = 7.5$ Hz, 1H), 7.53 (t, $J = 8.0$ Hz, 1H), 7.76 (d, $J = 8.5$ Hz, 1H), 7.86–7.88 (m, 2H), 8.00 (d, $J = 1.5$ Hz, 1H), 8.12 (s, 1H). ^{13}C NMR (100.6 MHz) δ 15.2, 44.3, 111.6, 111.8, 120.8, 122.8, 123.9, 124.5, 126.8, 127.5, 134.1, 139.7, 154.6. HRMS $C_{13}H_{13}N_2O$ $[M+H]^+$ 213.1022; found, 213.1021. Purity 100% ($t_R = 3.35$ min).

*4.1.7.3. 1-Ethyl-2-(5-methoxybenzofuran-2-yl)-1H-imidazole hydrochloride (**7b**).* Following the general procedure, **5b** (0.93 mmol, 200 mg), ethyl bromide (0.98 mmol, 0.07 mL), sodium hydride 60% in mineral oil (1.40 mmol, 56 mg), DMF (3 mL) and ethereal HCl 2 M (0.6 mL) gave **7b** (220 mg, 90%) as a white solid. IR (ATR) 3410, 3143, 2532, 1610, 1490, 1420, 1255, 1209, 1021, 928, 810, 758, 709 cm^{-1}. ^1H NMR (400 MHz, DMSO-d_6) δ 1.49 (t, $J = 7.0$ Hz, 3H), 3.82 (s, 3H), 4.54 (q, $J = 7.0$ Hz, 2H), 7.10 (dd, $J = 9.0$, 2.5 Hz, 1H), 7.35 (d, $J = 2.5$ Hz, 1H), 7.66 (d, $J = 9.0$ Hz, 1H), 7.85 (d, $J = 2.0$ Hz, 1H), 7.98 (d, $J = 2.0$ Hz, 1H), 8.06 (s, 1H). ^{13}C NMR (100.6 MHz) δ 15.2, 44.3, 55.7, 104.1, 111.7, 112.5, 116.8, 120.7, 123.8, 127.5, 134.1, 140.3, 149.6, 156.5. HRMS $C_{14}H_{15}N_2O_2$ $[M+H]^+$ 243.1128; found, 243.1128. Purity 98.4% ($t_R = 3.44$ min).

*4.1.7.4. 1-Ethyl-2-(6-methoxybenzofuran-2-yl)-1H-imidazole hydrochloride (**7c**).* Following the general procedure, **5c** (0.93 mmol, 200 mg), ethyl bromide (0.98 mmol, 0.07 mL), sodium hydride 60% in mineral oil (1.40 mmol, 56 mg), DMF (2.7 mL) and ethereal HCl 2 M (0.6 mL) gave **7c** (212 mg, 87%) as a white solid. IR (ATR) 3474, 3151, 2728, 1614, 1495, 1417, 1276, 1150, 1108, 1021, 928, 853, 813, 778, 701 cm^{-1}. ^1H NMR (400 MHz, DMSO-d_6) δ 1.49 (t, $J = 7.0$ Hz, 3H), 3.86 (s, 3H), 4.52 (q, $J = 7.0$ Hz, 2H), 7.03 (dd, $J = 8.5$, 2.0 Hz, 1H), 7.33 (s, 1H), 7.73 (d, $J = 8.5$ Hz, 1H), 7.82 (d, $J = 2.0$ Hz, 1H), 7.95 (d, $J = 2.0$ Hz, 1H), 8.05 (s, 1H). ^{13}C NMR (100.6 MHz) δ 15.2, 44.2, 55.9, 95.8, 112.0, 114.2, 119.9, 120.3, 123.1, 123.6, 134.3, 138.6, 156.1, 159.9. HRMS $C_{14}H_{15}N_2O_2$ $[M+H]^+$ 243.1128; found, 243.1128. Purity 99.2% ($t_R = 3.37$ min).

4.2. X-ray crystallographic analysis

Crystals of **LSL60101** were obtained from slow evaporation of methanol solutions. The single crystal X-Ray diffraction data set was collected at 294 K up to a max 2θ of ca. 57° on a Bruker Smart APEX II diffractometer, using monochromatic MoKα radiation λ = 0.71073 Å and 0.3° separation between frames. Data integration was performed using SAINT V6.45A and SORTAV (Blessing, 1995) in the diffractometer package. The crystal and collection data and structural refinement parameters are given in Table S14. The structure was solved by direct methods using SHELXT-2014 (Sheldrick, 2014) and Fourier's difference methods, and refined by least squares on F^2 using SHELXL-2014/7 (Sheldrick, 2014) inside the WinGX program environment (Farrugia, 2012). Atom coordinates are given in Table S15 and bond distances and angles in Table S16. The crystal structure shows the chlorohydrate form of **LSL60101**, which is as almost planar, as well as a methanol solvent molecule. Anisotropic displacement parameters were used for non-H atoms (Table S17) and the H-atoms were positioned in calculated positions (except H2) and refined riding on their parent atoms. Fig. 8 exhibits an ORTEP view of the molecule with the atom labelling, as well as its closest intermolecular bonds (Table S18) with the chloride anion (N12—H12···Cl1) and the methanol molecule (N9—H9···O2). These two intermolecular bonds are slightly out of the plane of the **LSL60101** molecule, producing a small torsion of the imidazolium group respect to the molecular mean plane (τ(O1—C2—C8—N9) = −4.3(11), τ(C3—C2—C8—N12) = −1.8(14)°). Methanol is also bonded to the chloride anion through the contact O2—H2···Cl1^i (i = x-1,y,z), giving rise to corrugated chains along **a,** assembled by parallel stacking along **c**. Crystallographic data (excluding structure factors) for the reported structure has been deposited in the Cambridge Crystallographic Data Centre as supplementary publication, CCDC No. 2063533. Copies of this information may be obtained free of charge from The Director, CCDC, 12 Union Road, Cambridge CB2 1EZ, UK. Fax: +44 1223 336 033. E-mail: data_request@ccdc.cam.ac.uk. Web page: http://www.ccdc.cam.ac.uk.

4.3. Binding studies

4.3.1. Preparation of cellular membranes

Male Swiss mice (final age 8–10 weeks) were killed, and the

brain cortex dissected and stored at −70 °C until assays were performed. All animal experimental protocols were performed in agreement with European Union regulations (O.J. of E.C. L 358/1 18/12/1986).

Human brain samples were obtained at autopsy in the Basque Institute of Legal Medicine, Bilbao, Spain. Samples from the prefrontal cortex (Brodmann's area 9) were dissected at the time of autopsy and immediately stored at −70 °C until assay. The study was developed in compliance with policies of research and ethical review boards for postmortem brain studies.

To obtain cellular membranes (P2 fraction) the different samples were homogenized using an ultraturrax in 10 vol of homogenization buffer (0.25 M sucrose, 5 mM Tris−HCl, pH 7.4). The crude homogenate was centrifuged for 5 min at 1000 g (4 °C) and the supernatant was centrifuged again for 10 min at 40,000 g (4 °C). The resultant pellet was washed twice in 5 vol of homogenization buffer and recentrifuged in similar conditions. Protein content was measured according to the method of Bradford using BSA as standard.

4.3.2. Competition binding assays

The pharmacological activity of the compounds was evaluated through competition binding studies against the I_2-IR selective radioligand [^{3}H]2-BFI or the α_2-adrenergic receptor selective radioligand [^{3}H]RX821002. Specific binding was measured in 0.25 mL aliquots (50 mM Tris-HCl, pH 7.5) containing 100 μg of membranes, which were incubated in 96-well plates either with [^{3}H]2-BFI (2 nM) for 45 min at 25 °C or [^{3}H]RX821002 (1 nM) for 30 min at 25 °C, in the absence or presence of the competing compounds (10^{-12} to 10^{-3} M, 10 concentrations).

Specific binding of [^{3}H]clonidine (20 nM) to rat or human hypothalamic membranes pre-incubated with benextramine (100 μM) to alkylate the population of α_2-adrenoceptors. Under these experimental conditions [^{3}H]clonidine only labelled I_1-sites. In drug competition experiments, moxonidine (the reference compound for I_1-IR) showed sub-nanomolar affinity for these I_1-sites ($K_{iH} = 0.2$ nM; $K_{iL} = 32$ mM).

Incubations were terminated by separating free ligand from bound ligand by rapid filtration under vacuum (1450 Filter Mate Harvester, PerkinElmer) through GF/C glass fiber filters. The filters were then rinsed three times with 300 μL of binding buffer, air-dried (120 min), and counted for radioactivity by liquid scintillation spectrometry using a MicroBeta TriLux counter (PerkinElmer). Specific binding was determined and plotted as a function of the compound concentration. Nonspecific binding was determined in the presence of idazoxan (10^{-5} M), a compound with well stablished affinity for I_2-IR and α_2-adrenergic receptors, in [^{3}H]2-BFI and [^{3}H]RX821002 assays. To obtain the inhibition constant (K_i) analyses of competition experiments were performed by nonlinear regression using the GraphPad Prism program. K_i values were normalized to pK_i values. I_2-IR/α_2 selectivity index was calculated as the antilogarithm of the difference between pK_i values for I_2-IR and pK_i values for α_2-AR.

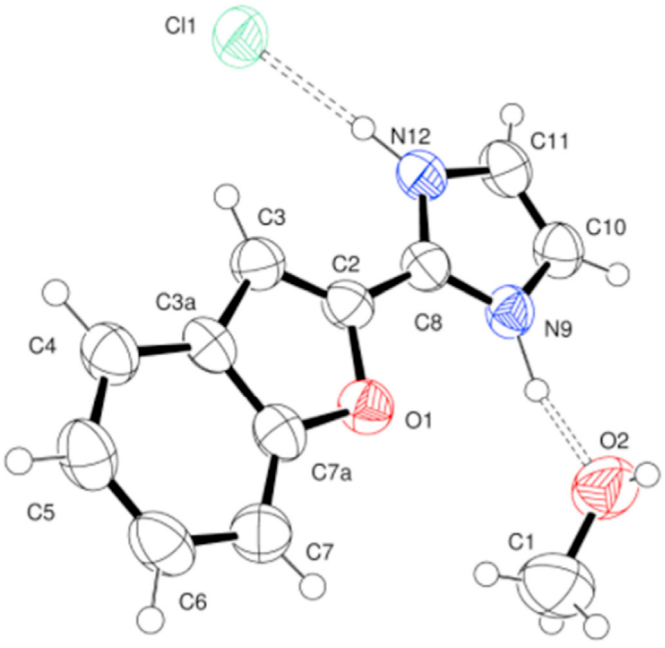

Fig. 8. X-ray crystal structure of **LSL60101**.

4.4. Acute toxicity

Lethal dose (LD_{50}) is a statistical derived amount of a compound that can be expected to cause death in 50% of the animals, rodents in general and is used as a measure of its acute toxicity. In this particular study, LD_{50} was calculated using the Logarithmic-Probit method, as initially described in Miller and Tainter (1944) [58], and the calculations further elaborated by Randhawa (2009) [59]. Male albino mice were administered i.p. with LSL60101 at a range of doses (10−100 mg/kg; n = 10 mice per dose tested), percentage mortalities were transformed to probits for each dose, and log-doses vs. probits were plotted to calculate LD_{50} (see further details in Ref. [59]).

4.5. 3D-QSAR study. Data set preparation

The original data set was divided on training set, that was used for model building and test set, used for model evaluation. The I_2-IR 3D-QSAR model contains 24 compounds (Fig. S1), with 16 compounds in the training set and 8 compounds in the test set, while data set for the α_2-AR 3D-QSAR model contains 22 compounds, with 14 compounds in the training set and 8 compounds in the test set (Tables S1 and S2). In order to compare and validate our results, we added three I_2-IR standard ligands (tracizoline, idazoxan, and BU99008, Fig. 1), in both data sets. Test set compounds were chosen based on PCA (Principal Component Analysis) plot, considering that pK_i values were homogeneously distributed in the whole range.

After dividing all data sets into training and test sets, variable selection was performed using fractional factorial design (FFD), and Partial Least Square (PLS) regression was applied for building 3D-QSAR models (Figs. S2 and S3).

Dominant forms of ligands at physiological pH 7.4 were obtained with the Marvin Sketch 5.5.1.0 program [60], while geometry was optimized with semiempirical/PM3 (Parameterized Model revision 3) method [61,62] followed by ab initio Hartree-Fock/3-21G method [63] using Gaussian 09 software [64] included in ChemBio3D Ultra 13 program [65].

The Pentacle program [38] was used for calculation of GRID independent descriptors (GRIND and GRIND2) and 3D-QSAR model building. Computation of descriptors is based on Molecular Interaction Fields (MIF), by using four different probes: O probe (hydrogen bond acceptor groups), N1 probe (hydrogen bond donor groups), TIP probe (the shape of molecule), and DRY probe (hydrophobic interactions). After MIFs calculation, ALMOND algorithm was used for the extraction of the most relevant regions, which represented the positions of favourable interactions between the ligand and probe. In the final step, Consistently Large Auto and Cross Correlation (CLACC) algorithm was used to plot node-node energies, between the same or a different probe, into auto- and

cross-correlograms, with the smoothing window set to 0.8 Å [66].

4.6. Cytotoxicity assays

Cancer cell lines LN-229, Capan-1, HCT-116, NCI–H460, HL-60, K-562 and Z-138 were acquired from the American Type Culture Collection (ATCC, Manassas, VA, USA) and the DND-41 cell line was purchased from the Deutsche Sammlung von Mikroorganismen und Zellkulturen (DSMZ Leibniz-Institut, Germany). All cell lines were cultured as recommended by the suppliers. Adherent cell lines LN-229, Capan-1, HCT-116 and NCI–H460 were seeded at a density between 500 and 1500 cells per well, in 384-well tissue culture plates (Greiner). After overnight incubation, cells were treated with different concentrations of the test compounds. Suspension cell lines HL-60, K-562, Z-138 and DND-41 were seeded at densities ranging from 2500 to 5500 cells per well in 384-well culture plates containing the test compounds at the same concentration points. The plates were incubated and monitored at 37 °C for 72 h in an IncuCyte® (Essen BioScience Inc., Sartorius) for real-time imaging of cell proliferation. Brightfield images were taken every 3 h, with one field imaged per well under 10x magnification. Cell growth was then quantified based on the percent cellular confluence as analysed by the IncuCyte® image analysis software, and used to calculate CC_{50} values by linear interpolation.

4.7. Pharmacokinetic analysis and analysis conditions

The pharmacokinetic study was carried on in male CD1 mice (Envigo Laboratories) with a body weight between 40 and 50 g (n = 3–4 per group). Animals were randomized to be included in the treated or control groups. A single intraperitoneal dose of **LSL60101** (10 mg/kg, 10 ml/kg) was administered early in the morning (between 8 and 11 a.m.) without anaesthesia. Compound was dissolved in 10% of 2-hydroxypropyl)-β-cyclodextrin in physiological saline). Mice were monitored for signs of pain or distress during the time between injection and euthanasia. Mice were sacrificed by cervical dislocation and blood (0.6 mL) was collected at different time points (15 min, 30 min, 45 min, 60 min, 2 h, 3 h, 4 h, 5 h, 8 h and 24 h after injection) in tubes with serum gel and clotting activator (Sarstedt Micro tube 1.1 mL Z-Gel). Samples were centrifugated at 10.000 rpm for 10 min to obtain plasma and stored at −80 °C up to analysis of compound concentration by HPLC-UV. Experimental procedures were in line with the Directive 2010/63/EU and approved by the Institutional Animal Care and Generalitat de Catalunya (#10291, 1/28/2018).

LSL60101 plasma concentrations versus time curves for the mean of animals were analysed by a non-compartmental model based on statistical moment theory using the "PK Solutions" computer program. The pharmacokinetic parameters calculated were the area under the concentration vs time curve (AUC), calculated using the trapezoidal rule in the interval 0–24 h; the half-life ($t_{1/2\beta}$), determined as $ln_{2/\beta}$, being β, calculated from the slope of the linear, least-squares regression line; the C_{max} and T_{max} were read directly from the mean concentration curves.

The HPLC system was a PerkinElmer LC (Perkin Elmer INC, Massachussets, U.S.) consisting of a Flexar LC pump, a chromatography interface (NCI 900 network), a Flexar LC autosampler PE, and a Waters 2487 dual λ absorbance detector. The chromatographic column was a kromasil 100-5-C18 (4.0 × 200 mm-Teknokroma Analítica S.A. Sant Cugat, Spain). Flux was 0.8 ml/mn and the mobile phase consisted in 0.05 M KH_2PO_4 (30%):acetonitrile (70%) in isocratic conditions. The elution time of **LSL60101** was 4.4 min, and it was detected at 290 nm. The assay had a range of 0,025-5 μg/mL. The calibration curves were constructed by plotting the peak area ratio of the analysed peak against the known concentrations.

4.8. In vivo studies in mice

Studies and procedures involving mouse brain dissection and extractions were approved by the respective Local Bioethical Committees (Universitat de les Illes Balears-CAIB and University of Barcelona-GenCat) and followed the ARRIVE [67] and standard ethical guidelines (European Communities Council Directive 2010/63/EU and Guidelines for the Care and Use of Mammals in Neuroscience and Behavioural Research, National Research Council 2003). All efforts were made to minimize the number of animals used and their suffering.

4.9. Hypothermia in naïve mice

This study was performed in male and female adult CD-1 mice bred and housed in the animal facility at the University of the Balearic Islands in standard cages in set environmental conditions (22 °C, 70% humidity, and 12 h light/dark cycle, lights on at 8:00 a.m.) with free access to a standard diet and tap water. Prior to any experimental procedures, mice were habituated to the experimenter by being handled and weighed for 2 days. Mice were treated with a single dose of **LSL60101** (1, 5, 10, 20, 30 or 50 mg/kg, i.p., n = 5 for treatment group) or vehicle (2 ml/kg of saline, i.p., n = 5), and changes in rectal temperature were measured by comparing basal values (before drug treatment) with that obtained 1, 2 and 3 h post-treatment by a rectal probe connected to a digital thermometer (Compact LCD display thermometer, SA880-1 M, RS, Corby, UK).

4.10. Western blot analysis for FADD protein in naïve mice

For evaluating FADD protein regulation, a subgroup of mice received a single dose of **LSL60101** (30 or 50 mg/kg, i.p., n = 7 for treatment group) or vehicle (2 ml/kg of saline, i.p., n = 6) and were sacrificed 1 h after treatment. The hippocampus was freshly dissected and kept at −80 °C until hippocampal sample proteins (40 μg) were separated by SDS-PAGE on 10% polyacrylamide minigels (Bio-Rad) and transferred onto nitrocellulose membranes by standard Western blot (Wb) procedures as described previously [21]. Membranes were incubated overnight with anti-FADD (H-181; sc-5559; Santa Cruz Biotechnology, Santa Cruz, CA), and following secondary antibody (anti-rabbit) incubation and ECL detection system (Amersham, Buckinghamshire, UK), proteins were visualized on autoradiographic films (Amersham ECL Hyperfilm). The amount of FADD protein in mice brain samples from different treatment groups was compared with that of vehicle-treated controls (100%) in the same gel by densitometric scanning (GS-800 Imaging Densitometer, Bio-Rad) of immunoreactive bands (integrated optical density, IOD). Each brain sample was quantified in 2–4 gels, and the mean value was used as a final estimate. Quantification of β-actin contents (clone AC-15; Ab, no. A1978; Sigma) was used as a house-keeping control (no differences between treatment groups, 15 μg per sample).

4.11. 5XFAD as an animal model of AD: pharmacological treatments

The 5XFAD is a double transgenic APP/PS1 that co-expresses five mutations of AD and presents robust oxidative levels [68]. 6-month-old female 5XFAD mice (n = 20) and wild type (Wt) mice (n = 20) were used to carry out the molecular analyses. The animals were randomly allocated into four experimental groups: Control 5XFAD and Wt, administered with vehicle (2-hydroxypropyl)-β-cyclodextrin 1.8%), and treated 5XFAD and Wt administered with **LSL60101** diluted in vehicle (1 mg/kg/day). Treatment length was 4 weeks. Water consumption was controlled each week and the I_2-IR

ligand concentration was adjusted accordingly to reach the precise dose. Animals had free access to food and water, and were kept under standard temperature conditions (22 ± 2 °C) and 12 h: 12 h light-dark cycles (300 lux/0 lux).

4.12. Western blot analysis in 5xFAD and Wt mice

For subcellular fractionation, 150 μL of buffer A (10 mM HEPES pH 7.9, 10 mM KCl, 0.1 mM EDTA pH 8, 0.1 mM EGTA pH 8, 1 mM DTT, 1 mM PMSF, protease inhibitors) were added to each sample and incubated on ice for 15 min. After this time, the samples were homogenized with a tissue homogenizer, 12.5 μL Igepal 1% were added, and the each eppendorf was vortexed for 15 s. Following 30 s of full-speed centrifugation at 4 °C, supernatants were collected (cytoplasmic fraction); 80 μL of buffer C (20 mM HEPES pH 7.9, 0,4 M NaCl, 1 mM EDTA pH 8, 0.1 mM EGTA pH 8, 20% Glycerol 1 mM DTT, 1 mM PMSF, protease inhibitors) was added to each pellet and incubated under agitation at 4 °C for 15 min. Subsequently, samples were centrifuged for 10 min at full speed at 4 °C. Supernatants were collected (nuclear fraction).

For Western blot analysis, aliquots of 20 μg of total hippocampal protein were used. Protein samples from mice (n = 3–5 per group) were separated by Sodium dodecyl sulphate-polyacrylamide gel electrophoresis (SDS-PAGE) (8–12%) and transferred onto (Polyvinylidene difluoride) PVDF membranes (Millipore). Afterward, membranes were blocked in 5% non-fat milk in 0.1% Tris-buffered saline - Tween20 (TBS-T) for 1 h at room temperature, followed by overnight incubation at 4 °C with the primary antibodies listed in Table S12.

Membranes were washed and incubated with the corresponding secondary antibodies for 1 h at room temperature. Immunoreactive proteins were viewed with a chemiluminescence-based detection kit, following the manufacturer's protocol (ECL Kit; Millipore) and digital images were acquired using a ChemiDoc XRS + System (Bio-Rad). Semi-quantitative analyses were carried out using ImageLab software (Bio-Rad), and results were expressed in Arbitrary Units (AU), considering control protein levels as 100%. Protein loading was routinely monitored by immunodetection of Glyceraldehyde-3-phosphate dehydrogenase (GADPH) (Table S12).

4.13. RNA extraction and gene expression determination in 5xFAD and Wt mice

Total RNA isolation was carried out using TRIzol® reagent according to manufacturer's instructions. The yield, purity, and quality of RNA were determined spectrophotometrically with a NanoDrop™ ND-1000 (Thermo Scientific) apparatus and an Agilent 2100B Bioanalyzer (Agilent Technologies). RNAs with 260/280 ratios and RIN higher than 1.9 and 7.5, respectively, were selected. Reverse Transcription-Polymerase Chain Reaction (RT-PCR) was performed as follows: 2 μg of messenger RNA (mRNA) was reverse-transcribed using the High Capacity cDNA Reverse Transcription Kit (Applied Biosystems). Real-time quantitative PCR (qPCR) from 24 mice of both strains (n = 4–6 per group) was used to quantify mRNA expression of OS and inflammatory genes.

SYBR® Green real-time PCR was performed on a Step One Plus Detection System (Applied-Biosystems) employing SYBR® Green PCR Master Mix (Applied-Biosystems). Each reaction mixture contained 6.75 μL of complementary DNA (cDNA) (which concentration was 2 μg), 0.75 μL of each primer (which concentration was 100 nM), and 6.75 μL of SYBR® Green PCR Master Mix (2X). Data were analysed utilizing the comparative Cycle threshold (Ct) method (ΔΔCt), where the housekeeping gene level was used to normalize differences in sample loading and preparation. The primers sequences used in this study are presented in Supplementary Table S10b. Normalization of expression levels was performed with β-actin for SYBR® Green-based real-time PCR. Each sample was analysed in duplicate, and the results represent the n-fold difference of the transcript levels among different groups.

4.14. Statistical analysis for 5xFAD and Wt mice comparisons

The statistical analysis was conducted using the statistical software GraphPad Prism version 8. Data were expressed as the mean ± Standard Error of the Mean (SEM). Means were compared with two-way ANOVAs, followed by Tukey-Kramer multiple comparisons post-hoc analysis. Statistical significance was considered when p-values were <0.05. The statistical outliers were carried out with Grubss' test and subsequently removed from the analysis.

Declaration of competing interest

The authors declare that they have no known competing financial interests or personal relationships that could have appeared to influence the work reported in this paper.

Acknowledgment

This work was supported by Ministerio de Ciencia, Innovación y Universidades, Agencia Estatal de Investigación (Spain, PID2019-107991RB-I00, PID2019-106285RB), the Basque Government (IT1211/19) and Generalitat de Catalunya (GC) (2017SGR106). The project leading to these results has received funding from "la Caixa" Foundation (ID 100010434) under agreement CI18-00002. This activity has received funding from the European Institute of Innovation and Technology (EIT). This body of the European Union receives support from the European Union's Horizon 2020 research and innovation programme. C.G.-F, F.V., C.E., S.R.-A., A.B., and M.P. Financial support was provided for F.V. (University of Barcelona, APIF_2017), S.R.-A. (Generalitat de Catalunya, 2018FI_B_00227), A.B. (Institute of Biomedicine UB_2018), J.A.G.-S. is a member emeritus of the Institut d'Estudis Catalans (Barcelona, Catalonia). E.H.-H. is supported by a predoctoral scholarship (FPI/2102/2018; Consejería de Innovación, Investigación y Turismo del Gobierno de las Islas Baleares y del Fondo Social Europeo). M.R., T.D., and K.N. kindly acknowledge the project funded by the Ministry of Science and Technological Development of the Republic of Serbia, Contract No. 451-03-68/2020-14/200161, and HORISON 2020-COST-Action CA18133 ERNEST: European Research Network on Signal Transduction. E. M. acknowledges funding to Severo Ochoa: CEX2019-917S. M.I.L, A.L.M. and J.B. gratefully acknowledge support from Xunta de Galicia (ED431C 2018/21 and ED431G 2019/02) and European Regional Development Fund (ERDF).

The authors thanks Dr. Rossend Obach and Dr. Ángel Menargues (LASA Laboratorios and later Ipsen Pharma SA, Barcelona, Spain) for initially providing the compound **LSL60101**.

Appendix A. Supplementary data

Supplementary data to this article can be found online at https://doi.org/10.1016/j.ejmech.2021.113540.

References

[1] P. Bousquet, J. Feldman, J. Schwartz, Central cardiovascular effects of alpha adrenergic drugs: differences between catecholamines and imidazolines,

J. Pharmacol. Exp. Therapeut. 230 (1984) 232–236.
[2] P. Bousquet, A. Hudson, J.A. García-Sevilla, J.X. Li, Imidazoline receptor system: the past, the present, and the future, Pharmacol. Rev. 72 (2020) 50–79.
[3] J.X. Li, Imidazoline I_2 receptors: an update, Pharmacol. Ther. 178 (2017) 48–56.
[4] J. García-Sevilla, P.V. Escribá, M. Sastre, C. Walzer, X. Busquets, G. Jaquet, D.J. Reis, J. Guimón, Immunodetection and quantitation of imidazoline receptor proteins in platelets of patients with major depression and in brains of suicide victims, Arch. Gen. Psychiatr. 53 (1996) 803–810.
[5] J.A. Lowry, J.T. Brown, Significance of the imidazoline receptors in toxicology, Clin. Toxicol. 52 (2014) 454–469.
[6] J.X. Li, Y. Zhang, Imidazoline I_2 receptors: target for new analgesics? Eur. J. Pharmacol. 658 (2011) 49–56.
[7] S. Regunathan, D.L. Feinstein, D.J. Reis, Anti-proliferative and anti-inflammatory actions of imidazoline agents. Are imidazoline receptors involved? Ann. N. Y. Acad. Sci. 881 (1999) 410–419.
[8] K.L. Smith, D.S. Jessop, D.P. Finn, Modulation of stress by imidazoline binding sites: implications for psychiatric disorders, Stress 12 (2009) 97–114.
[9] J.J. Meana, F. Barturen, I. Martín, J.A. García-Sevilla, Evidence of increased non-adrenoreceptor [^{3}H]idazoxan binding sites in the frontal cortex of depressed suicide victims, Biol. Psychiatr. 34 (1993) 498–501.
[10] J. Ruíz, I. Martín, L.F. Callado, J.J. Meana, F. Barturen, J.A. García-Sevilla, Non-adrenoreceptor [^{3}H]idazoxan binding sites (I_2-imidazoline sites) are increased in postmortem brain from patients with Alzheimer's disease, Neurosci. Lett. 160 (1993) 109–112.
[11] C. Gargalidis-Moudanos, N. Pizzinat, F. Javoy-Agid, A. Remaury, A. Parini, I_2-imidazoline binding sites and monoamine oxidase activity in human post-mortem brain from patients with Parkinson's disease, Neurochem. Int. 30 (1997) 31–36.
[12] L.F. Callado, J.I. Martín-Gómez, J. Ruiz, J.M. Garibi, J.J. Meana, Imidazoline I_2 receptors density increases with the malignancy of human gliomas, J. Neurol. Neurosurg. Psychiatry 75 (2004) 785–787.
[13] C. Dardonville, I. Rozas, Imidazoline binding sites and their ligands: an overview of the different chemical structures, Med. Res. Rev. 24 (2004) 639–661.
[14] G.M. Gilad, V.H. Gilad, Accelerated functional recovery and neuroprotection by agmatine after spinal cord ischemia in rats, Neurosci. Lett. 296 (2000) 97–100.
[15] K. Maiese, L. Pek, S.B. Berger, D.J. Reis, Reduction in focal cerebral ischemia by agents acting at imidazole receptors, J. Cerebr. Blood Flow Metabol. 12 (1992) 53–63.
[16] Z. Han, M.J. Xiao, B. Shao, R.Y. Zheng, G.Y. Yang, K. Jin, Attenuation of ischemia induced rat brain injury by 2-(2-benzofuranyl)-2-imidazoline, a high selectivity ligand for imidazoline I(2)receptors, Neurol. Res. 31 (2009) 390–395.
[17] S.X. Jiang, R.Y. Zheng, J.Q. Zheng, X.L. Li, Z. Han, S.T. Hou, Reversible inhibition of intracellular calcium influx through NMDA receptors by imidazoline (I)2 receptor antagonists, Eur. J. Pharmacol. 629 (2010) 12–19.
[18] L.C. Rovati, N. Brambilla, T. Blicharski, J. Connell, C. Vitalini, A. Bonazzi, G. Giacovelli, F. Girolami, M. D'Amato, Efficacy and safety of the firts-in-classs imidazoline-2 receptor ligand CR4056 in pain from knee osteoarthritis and disease phenotypes: a randomized, double-blind, placebo-controlled phase 2 trial, Osteoarthritis Cartilage 28 (2020) 22–30.
[19] R.J. Tyacke, J.F.M. Myers, A.V. Venkataraman, I. Mick, S. Turton, J. Passchier, S.M. Husband, E.A. Rabiner, R.N. Gunn, P.S. Murphy, C.A. Parker, D.J. Nutt, Evaluation of ^{11}C-BU99008, a PET ligand for the imidazoline2 binding site in human brain, J. Nucl. Med. 59 (2018) 1597–1602.
[20] H. Wilson, G. Dervenoulas, G. Pagano, R.J. Tyacke, S. Polychronis, J. Myers, R.N. Gunn, E.A. Rabiner, D. Nutt, M. Politis, Imidazoline 2 binding sites reflecting astroglia pathology in Parkinson's disease: an in vivo ^{11}C-BU99008 PET study, Brain 10 (2019) 3116–3128.
[21] S. Abás, A.M. Erdozain, B. Keller, S. Rodríguez-Arévalo, L.F. Callado, J.A. García-Sevilla, C. Escolano, Neuroprotective effects of a structurally new family of high affinity imidazoline I_2 receptors ligands, ACS Chem. Neurosci. 8 (2017) 737–742.
[22] C. Griñán-Ferré, F. Vasilopoulou, S. Abás, S. Rodríguez-Arévalo, A. Bagán, F.X. Sureda, B. Pérez, L.F. Callado, J.A. García-Sevilla, M.J. García-Fuster, C. Escolano, M. Pallàs, Behavioral and cognitive improvement induced by novel imidazoline I_2 receptor ligands in female SAMP8 mice, Neurotherapeutics 16 (2019) 416–431.
[23] S. Abás, S. Rodríguez-Arévalo, A. Bagán, C. Griñán-Ferré, F. Vasilopoulou, I. Brocos-Mosquera, C. Muguruza, B. Pérez, E. Molins, F.J. Luque, P. Pérez-Lozano, S. de Jonghe, D. Daelemans, L. Naesens, J. Brea, M.I. Loza, E. Hernández-Hernández, J.A. García-Sevilla, M.J. García-Fuster, M. Radan, T. Djikic, K. Nikolic, M. Pallàs, L.F. Callado, C. Escolano, Bicyclic α-iminophosphonates as high affinity imidazoline I_2 receptor ligands for alzheimer's disease, J. Med. Chem. 7 (2020) 3610–3633.
[24] D.A. Ruggiero, S. Regunathan, H. Wang, T.A. Milner, D.J. Reis, Immunocytochemical localization of an imidazoline receptor protein in the central nervous system, Brain Res. 780 (1998) 270–293.
[25] J.A. García-Sevilla, P.V. Escribá, C. Walzer, C. Bouras, J. Guimón, Imidazoline receptor proteins in brains of patients with Alzheimer's disease, Neurosci. Lett. 247 (1998) 95–98.
[26] D.S. Albers, M.F. Beal, Mitochondrial dysfunction and oxidative stress in aging and neurodegenerative diseases, J. Neural. Transm. Suppl. 5 (2000) 133–154.
[27] J.P. Bolaños, M.A. Moro, I. Lizasoain, A. Almeida, Mitochondrial and reactive oxygen and nitrogen species in neurological disorders and stroke: therapeutic implications, Adv. Drug Deliv. Rev. 61 (2009) 1299–1315.
[28] Z. Liu, T. Zhou, A.C. Ziegler, P. Dimitrion, L. Zuo, Oxidative stress in neurodegenerative diseases: from molecular mechanisms to clinical applications, Oxid. Med. Cell Longev. 2017 (2017) 1–11.
[29] M. Johnstone, A.J. Geraing, K.M. Miller, A central role for astrocytes in the inflammatory response to beta-amyloid: chemokines, cytokines and reactive oxygen species are produced, J. Neuroinmunol. 93 (1999) 182–193.
[30] D.J. Bonda, X. Wang, G. Perry, A. Nunomura, M. Tabaton, X. Zhu, M.A. Smith, Oxidative stress in Alzheimer disease: a possibility for prevention, Neuropharmacology 59 (2010) 290–294.
[31] L.A. Lione, D.J. Nutt, A.L. Hudson, Characterisation and localisation of [^{3}H]-2-(2-benzofuranyl)-2-imidazoline binding in rat brain: a selective ligand for imidazoline I_2 receptors, Eur. J. Pharmacol. 353 (1998) 123–135.
[32] F. Vasilopoulou, C. Griñán-Ferré, S. Rodríguez-Arévalo, A. Bagán, S. Abás, C. Escolano, M. Pallàs, I_2 imidazoline receptor modulation protects aged SAMP8 mice against cognitive decline by suppressing the calcineurin pathway, GeroScience 43 (2021) 965–983.
[33] J.A. García-Sevilla, J.J. Meana, F. Barturen, F.A. Geijo, A. Menargues, R. Obach, F. Pla, Benzofuranylimidazole Derivatives and Therapeutical Compositions Containing the Same, 1994. US5354769(A), October 11.
[34] R. Alemany, G. Olmos, P.V. Escribá, A. Menargues, R. Obach, J.A. García-Sevilla, LSL60101, a selective ligand for imidazoline I_2 receptors, on glial fibrillary acidic protein concentration, Eur. J. Pharmacol. 280 (1995) 205–210.
[35] M.A. Boronat, G. Olmos, J.A. García-Sevilla, Attenuation of tolerance to opioid-induced antinociception and protection against morphine-induced decrease of neurofilament proteins by idazoxan and other I_2-imidazoline ligands, Br. J. Pharmacol. 125 (1998) 175–185.
[36] A. Casanova, G. Olmos, J. Ribera, M.A. Boronat, J.E. Esquerda, J.A. García-Sevilla, Induction of reactive astrocytosis and prevention of motoneuron cell death by the I_2-imidazoline receptor ligand LSL60101, Br. J. Pharmacol. 130 (2000) 1767–1776.
[37] N. MacInnes, S.L. Handley, Characterization of the discriminable stimulus produced by 2-BFI: effects of imidazoline I_2-site ligands, MAOIs, β-carbolines, agmatine and ibogaine, Br. J. Pharmacol. 135 (2002) 1227–1234.
[38] Pentacle, Version1.0.6, MolecularDiscoveryLtd., Perugia, Italy, 2009.
[39] A. Krüger, V. Gonçalves, C. Wrenger, T. Kronenberger, ADME Profiling in Drug Discovery and a New Path Paved on Silica, Drug Discovery and Development - New Advances, 2019.
[40] ADMET Predictor, V. 9.5, Simulations Plus Inc., Lancaster, CA, USA. https://www.simulations-plus.com.
[41] A. Daina, O. Michielin, V. Zoete, SwissADME: a free web tool to evaluate pharmacokinetics, drug-likeness and medicinal chemistry friendliness of small mol, Sci. Rep. 7 (2017) 1–13.
[42] D.A. Thorn, X. An, Y. Zhang, M. Pigini, J. Li, Characterization of the hypothermic effects of imidazoline I_2 receptor agonists in rats, Br. J. Pharmacol. 166 (2012) 1936–1945.
[43] E. Hernández-Hernández, M.J. García-Fuster, Evaluating the effects of 2-BFI and tracizoline, two potent I_2-imidazoline receptor agonists, on cognitive performance and affect in middle-aged rats, Naunyn-Schmiedeberg's Arch. Pharmacol. Pharmacology 394 (2021) 989–996.
[44] J.A. Craven, E.L. Conway, Effects of alpha 2-adrenoceptor antagonists and imidazoline 2-receptor ligands on neuronal damage in global ischemia in the rat, Clin. Exp. Pharmacol. Physiol. 24 (1997) 204–207.
[45] D.W. Marion, L.E. Penrod, S.F. Kelsey, W.D. Obrist, P.M. Kochanek, A.M. Palmer, S.R. Wisniewski, S.T. DeKosky, Treatment of traumatic brain injury with moderate hypothermia, N. Engl. J. Med. 336 (1997) 540–546.
[46] C.M. Maier, K.V. Ahern, M.L. Cheng, J.E. Lee, M.A. Yenari, G.K. Steinberg, J.R. Kirsch, Optimal depth and duration of mild hypothermia in a focal model of transient cerebral ischemia: effects on neurologic outcome, infarct size, apoptosis, and inflammation, Stroke 29 (10) (1998) 2171–2180.
[47] E. Hernández-Hernández, A. Miralles, S. Esteban, M.J. García-Fuster, Improved age-related deficits in cognitive performance and affective-like behavior following acute, but not repeated, 8-OH-DPAT treatments in rats: regulation of hippocampal FADD, Neurobiol. Aging 71 (2018) 115–126.
[48] E. Hernández-Hernández, A. Miralles, S. Esteban, M.J. García-Fuster, Repeated treatment with the α2-adrenoceptor agonist UK-14304 improves cognitive performance in middle-age rats: role of hippocampal Fas-associated death domain, J. Psychopharmacol. 32 (2) (2018) 248–255.
[49] E. Comi, M. Lanza, F. Ferrari, V. Mauri, G. Caselli, L.C. Rovati, Efficacy of CR4056, a first-in-class imidazoline-2 analgesic drug, in comparison with naproxen in two rat models of osteoarthritis, J. Pain Res. 10 (2017) 1033–1043.
[50] N. Mirzaei, B.C. Mota, A.M. Birch, N. Davis, C. Romero-Molina, L. Katsouri, E.O.C. Palmer, A. Golbano, L.J. Riggall, I. Nagy, R. Tyacke, D.J. Nutt, M. Sastre, Imidazoline ligand BU224 reverses cognitive deficits, reduces microgliosis and enhances synaptic connectivity in a mouse model of Alzheimer's disease, Br. J. Pharmacol. 178 (3) (2021) 654–671.
[51] J.A. Garcia-Sevilla, P.V. Escriba, C. Walzer, C. Bouras, J. Guimon, Imidazoline receptor proteins in brains of patients with Alzheimer's disease, Neurosci. Lett. 247 (1998) 95–98.
[52] B. Uttara, A.V. Singh, P. Zamboni, R.T. Mahajan, Oxidative stress and neurodegenerative diseases: a review of upstream and downstream antioxidant therapeutic options, Curr. Neuropharmacol. 7 (1) (2009) 65–74.
[53] E. Birben, U.M. Sahiner, C. Sackesen, S. Erzurum, O. Kalayci, Oxidative stress and antioxidant defense, World Allergy Organ. J. 5 (1) (2012) 9–19.
[54] J.S. Tian, Q.J. Zhai, Y. Zhao, R. Chen, L.D. Zhao, 2-(2-benzofuranyl)-2-imidazoline (2-BFI) improved the impairments in AD rat models by

inhibiting oxidative stress, inflammation and apoptosis, J. Integr. Neurosci. 16 (4) (2017) 385–400.
[55] D.H. Choi, J.H. Yun, J. Lee, Protective effect of the imidazoline I_2 receptor agonist 2-BFI on oxidative cytotoxicity in astrocytes, Biochem. Biophys. Res. Commun. 503 (4) (2018) 3011–3016.
[56] F. Vasilopoulou, S. Rodríguez-Arévalo, A. Bagán, C. Escolano, C. Griñán-Ferré, M. Pallàs, Disease-modifying treatment with I2 imidazoline receptor ligand LSL60101 in an Alzheimer's disease mouse model: a Comparative study with donepezil, Br. J. Pharmacol. (2021) 1–17.
[57] Y. Chen, C. Qin, J. Huang, X. Tang, C. Liu, K. Huang, J. Xu, G. Guo, A. Tong, L. Zhou, The role of astrocytes in oxidative stress of central nervous system: a mixed blessing, Cell Prolif 53 (3) (2020) e12781.
[58] L.C. Miller, M.L. Tainter, Estimation of the ED_{50} and its error by means of logarithmic-probit graph paper, Proc. Soc. Exp. Bio. Med. 57 (1944) 261–264.
[59] M.A. Randhawa, Calculation of LD_{50} values from the method of miller and tainter, 1944, J. Ayub Med. Coll. Abbottabad 21 (3) (2009) 184–185.
[60] MarvinSketch 5.5.1.0, ChemAxon, Budapest, Hungary, 2011 software available at, https://www.chemaxon.com.
[61] J.J.P. Stewart, Optimization of parameters for semiempirical methods I. Method, J. Comput. Chem. 10 (1989) 209–220.
[62] J.J.P. Stewart, Optimization of parameters for semiempirical methods II. Applications, J. Comput. Chem. 10 (1989) 221–264.
[63] W.J. Hehre, L. Radom, PvR. Schleyer, J. Pople, AB Initio Molecular Orbital Theory, Wiley, 1986.
[64] M.J. Frisch, Gaussian 98 (RevisionA.7), 1998.
[65] CambridgeSoft Corporation, ChemBio3D Ultra, Version 13.0, 2013. Cambridge, MA, USA.
[66] A. Duran, M. Pastor, An advanced tool for computing and handling grid-independent descriptors, User Manual (2011). Version 1.06.
[67] N. Percie du Sert, A. Ahluwalia, S. Alam, M.T. Avey, M. Baker, W.J. Browne, A. Clark, I.C. Cuthill, U. Dirnagl, M. Emerson, P. Garner, S.T. Holgate, D.W. Howells, V. Hurst, N.A. Karp, S.E. Lazic, K. Lidster, C.J. MacCallum, M. Macleod, E.J. Pearl, O.H. Petersen, F. Rawle, P. Reynolds, K. Rooney, E.S. Sena, S.D. Silberberg, T. Steckler, H. Würbel, Reporting animal research: explanation and elaboration for the ARRIVE guidelines 2.0, PLoS Biol. 18 (7) (2020), https://doi.org/10.1371/journal.pbio.3000411.
[68] H. Oakley, S.L. Cole, S. Logan, E. Maus, P. Shao, J. Craft, A. Guillozet-Bongaarts, M. Ohno, J. Disterhoft, L. Van Eldik, R. Berry, R. Vassar, Intraneuronal β-amyloid aggregates, neurodegeneration, and neuron loss in transgenic mice with five familial Alzheimer's disease mutations: potential factors in amyloid plaque formation, J. Neurosci. 26 (2006) 10129–10140.

Benzofuranyl-2-imidazoles as Imidazoline I_2 Receptor Ligands for Alzheimer's Disease

*Sergio Rodriguez-Arévalo[a,#] Andrea Bagán[a], Christian Griñán-Ferré[b,#] Foteini Vasilopoulou[b], Mercè Pallàs[b], Iria Brocos-Mosquera[c], Luis F. Callado[c], M. Isabel Loza[d], Antón L. Martínez[d], José Brea[d], Belén Pérez[e], Elies Molins[f], Steven De Jonghe[g], Dirk Daelemans[g], Milica Radan[h], Teodora Djikic[h], Katarina Nikolic[h], Elena Hernández-Hernández[i], M. Julia García-Fuster[i], Jesús A. García-Sevilla[i] and Carmen Escolano[a],**

CONTENTS:

3D-QSAR study and physicochemical parameters **S1**

***In vitro* Blood-Brain Barrier Permeation Assay** **S9**

Solubility of LSL60101 under various pH environments **S10**

Chemical stability of LSL60101 **S12**

Microsomal stability of LSL60101 of human and mice microsomes **S13**

Cytochrome inhibition of LSL60101 **S14**

Plasma stability of LSL60101 **S15**

Human and mouse plasma protein binding of LSL60101 **S16**

hERG ion channel inhibition of LSL60101 **S16**

Cytotoxicity assays **S17**

Antibodies and primers used **S18**

Table of representative data of ^{1}H-NMR spectra of new compounds 5a – 7c **S19**

^{1}H-NMR and ^{13}C-NMR spectra of new compounds 5a – 7c **S20**

HPLC/MS analysis of 5a-7c **S30**

Molecular Formula Strings (Smiles) **S50**

X-ray crystallographic data for LSL60101 **S51**

References **S56**

3D-QSAR study and physico-chemical parameters

The study was conducted on structurally diverse I_2-IR ligands that were divided into two clusters, based on their chemical structures. Cluster 1 represents compounds prepared in this work (Scheme 1 in the manuscript), while cluster 2 contains bicyclic α-iminophosphonate I_2-IR ligands previously described by our group (Figure S1) [1].

The original data set was divided on training set, that was used for model building and test set, used for model evaluation. I_2-IR 3D-QSAR model contains 24 compounds, with 16 compounds in training set and 8 compounds in test set, while data set for α_2-AR 3D-QSAR model contains 22 compounds, with 14 compounds in training set and 8 compounds in test set (Table S1 and S2). Test set compounds were chosen based on PCA (Principal Component Analysis) plot, considering that pK_i values were homogeneously distributed in the whole range.

After dividing data set into training and test set, variable selection was performed using fractional factorial design (FFD), while Partial Least Square (PLS) regression was applied for building 3D-QSAR models.

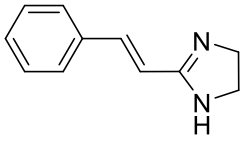

tracizoline

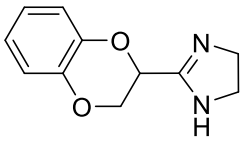

idazoxan

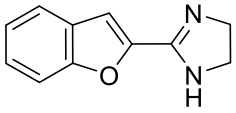

2-BFI

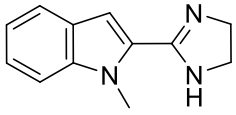

BU99008

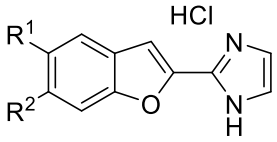

R^1 = R^2 = H, **5a, LSL60101**
R^1 = OMe, R^2 = H, **5b**
R^1 = H, R^2 = OMe, **5c**
R^1 = Br, R^2 = H, **5d**

R^1 = OH, R^2 = H, **6b**
R^1 = H, R^2 = OH, **6c**

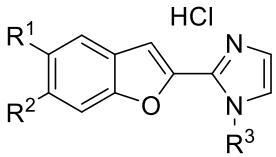

R^1 = R^2 = H, R^3 = Me, **7a**
R^1 = R^2 = H, R^3 = Et, **7aa**
R^1 = OMe, R^2 = H, R^3 = Et, **7b**
R^1 = H, R^2 = OMe, R^3 = Et, **7c**

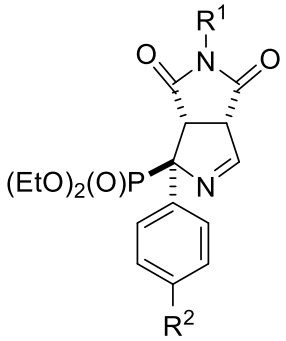

R^1 = 3Cl, 4FPh, R^2= H, **9d**
R^1 = Et, R^2 = H, **9f**
R^1 = 4-PhPh, R^2 = H, **9z**
R^1 = tBu, R^2 = H, **9h**
R^1 = propyl, R^2 = H, **9g**
R^1 = 4PhOPh, R^2 = H, **9ab**
R^1 = 4-OMePh, R^2 = H, **9e**
R^1 = $Ph(CH_2)_2CH_2$, R^2 = H, **9k**
R^1 = 3Cl, 4FPh, R^2 = OMe, **13d**
R^1 = 3Cl, 4FPh, R^2 = F, **12d**

Figure S1. Structures of compounds for I_2-IR and α_2-AR 3D-QSAR models.

Validation of created 3D-QSAR models. In order to ensure the reliability and good predicted power of the created 3D-QSAR models, we have utilized different internal and external validation methods. Training set compounds were used for the internal validation of model, calculating parameters such as Q^2 (Cross-validated Squared Correlation Coefficient), RMSEE (Root Mean Square Error of Estimation) and PRESS (Predicted Residual Sum of Squares) (Eq. 1, 2 and 3). For a predictive QSAR models, values of Q^2 should be higher than 0.5 [2,3].

$$PRESS = \sum_{i=1}^{n} e_{(i)}^2 \quad (1) \qquad RMSEE = \sqrt{\frac{PRESS}{n}} \quad (2) \qquad Q^2 = 1 - \frac{PRESS}{SSTo} \quad (3)$$

Even though, high value of Q^2 is important for good model quality, it does not present sufficient condition for a high predictive ability of a 3D-QSAR model [4]. For that reason, we have employed test set compounds for external validation, to truly clarify the predictive power of the created models. Parameters of external validation are correlation coefficient for the test set - R^2_{pred}, RMSEP (Root Mean Square Error of Prediction) and r^2metrics parameters (r^2_m, $r^{2/}_m$, $\overline{r}^2_m$ and Δr^2_m) (Eq. 4, 5, 6 and 7). For an acceptable model, value of R^2_{pred} should be higher than 0.5, while values of correlation coefficients r^2_m, and $r^{/2}_m$ should be close and greater than 0.5, their average value ($\overline{r}^2_m$) should be greater than 0.5, and the difference between r^2_m and $r^{/2}_m$ (Δr^2_m) should be lower than 0.2. Parameters of r^2metrics represent more rigorous criterion of external validation and better reflect external predictive quality of the created 3D-QSAR models [4].

$$R^2_{pred} = 1 - \frac{\Sigma(Y_{obs(test)} - \bar{Y}_{pred(test)})^2}{\Sigma(Y_{obs(test)} - \bar{Y}_{training})^2} \quad (4) \qquad r^2_{m=r^2\left(\sqrt{1-|r^2-r_0^2|}\right)} \quad (6)$$

$$RMSEP = \sqrt{\frac{PRESS}{n}} \quad (5) \qquad r^{/2}_{m=r^2\left(1-\sqrt{|r^2-r_0^{/2}|}\right)} \quad (7)$$

Table S1. Results of 3D-QSAR study for I_2-IR ligands.

Training set			Test set		
	pKi(exp)	pKi(pred)		pKi(exp)	pKi(pred)
9d	8.56	8.40	**2-BFI**	8.31	7.20
9f	8.37	7.74	**Tracizoline**	7.58	6.96
9z	7.90	8.11	**12d**	7.55	7.37
13d	7.87	7.73	**9h**	7.35	7.55
Idazoxan	7.41	7.44	**9ab**	6.96	7.25
BU99008	7.05	7.73	**7a**	5.98	5.56
LSL60101	6.67	6.40	**6c**	5.48	6.34
9e	6.65	7.17	**7b**	4.96	4.64
5b	6.41	5.34			
9k	6.35	5.89	**R^2_{pred}=0.71 (>0.5)**		
5d	6.28	6.39	**RMSEP=0.59**		
5c	5.88	5.87	**r^2_m=0.70 (>0.5)**		
7c	5.26	5.40	**$r^{2\prime}_m$=0.55 (>0.5)**		
7aa	5.05	5.26	**Δr^2_m=0.15 (<0.2)**		
6b	4.87	5.24	**$\overline{r}^2_m$= 0.62 (>0.5)**		
9g	4.02	4.50	**$(r^2-r^{\prime 2}_0)/r^2$=0.09 (<0.1)**		
			k'= 0.97 (0.85≤k'≤1.16)		
R^2=0.88 (>0.7)					
Q^2=0.60 (>0.5)					
RMSEE=0.62					

Table S2. Results of 3D-QSAR study for α_2-AR ligands.

Training set			Test set		
	pKi(exp)	pKi(pred)		pKi(exp)	pKi(pred)
Idazoxan	7.92	7.35	**9h**	6.77	6.50
9d	6.27	6.51	**9z**	5.12	4.90
9f	5.85	5.96	**5d**	4.92	4.07
9ab	5.43	5.62	**Tracizoline**	4.33	3.95
9e	4.59	4.53	**7b**	4.21	4.23
2-BFI	4.58	4.86	**6b**	3.84	4.18
BU99008	4.37	4.35	**6c**	3.76	3.11
5b	3.94	4.26	**7a**	3.75	3.21
7aa	3.77	3.31			
9k	3.77	3.53	**R^2_{pred}=0.75 (>0.5)**		
12d	3.38	3.08	**RMSEP=0.48**		
LSL60101	3.18	3.35	**r^2_m=0.71 (>0.5)**		
7c	3.17	3.59	**$r^{2\prime}_m$=0.84 (>0.5)**		
5c	3.01	2.92	**Δr^2_m=0.12 (<0.2)**		
			$\overline{r}^2_m$= 0.78 (>0.5)		
R^2=0.95 (>0.7)			**$(r^2-r^{\prime 2}_0)/r^2$=0.00 (<0.1)**		
Q^2=0.53 (>0.5)			**k'= 0.93 (0.85≤k'≤1.16)**		
RMSEE=0.34					

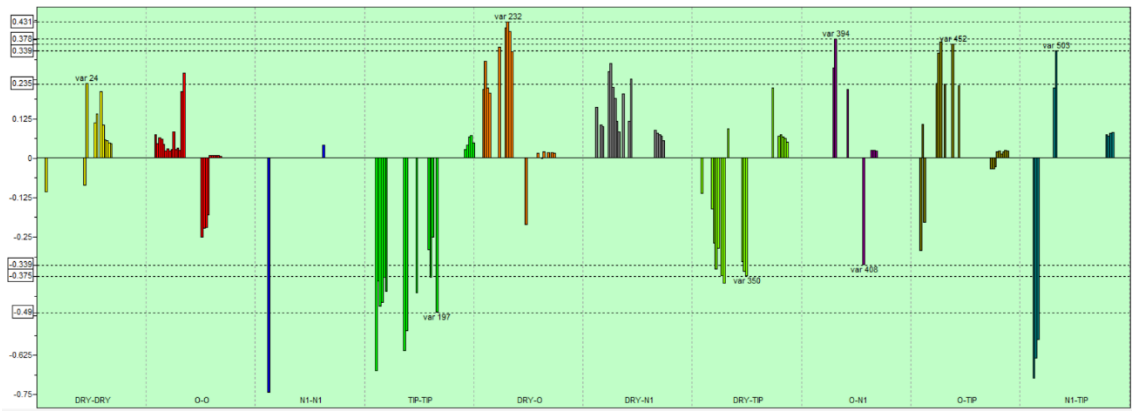

Figure S2. PLS coefficient plot for the I_2-IR 3D-QSAR model. The most significant variables are labelled.

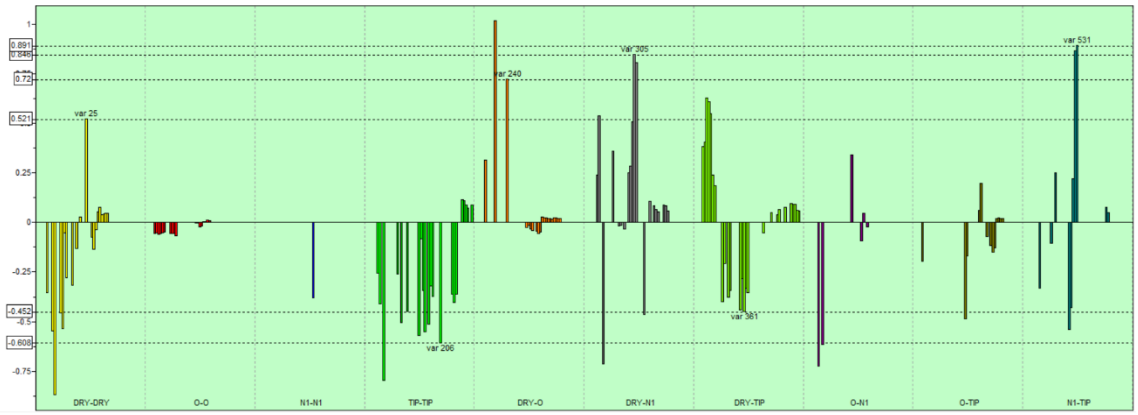

Figure S3. PLS coefficient plot for the α_2-AR 3D-QSAR model. The most significant variables are labelled.

Interpretation of created 3D-QSAR models. According to the correlogram shown in Figure S2, the most significant positive variables within cluster 2 are var24 (DRY-DRY: 9.60-10.00 Å) and var503 (N1-TIP: 6.80-7.20 Å). Var24 explain favourable impact of hydrophobic regions around phenyl ring in α position, while var503 delineate optimal distance between oxygen atom of the carbonyl of the maleimide, acting as a hydrogen bond acceptor group, and ethyl groups on phosphonate as steric regions (Figure S4a). The most influential negative variables for I_2-IR 3D-QSAR model within cluster 2 are var197 (TIP-TIP: 14.00-14.40 Å) and var350 (DRY-TIP: 10.40-10.80 Å). Both variables emphasize that introduction of bulkier substituent in the *N*-maleimide group leads to a decrease in activity (**9k**, **9ab**) (Figure S4b).

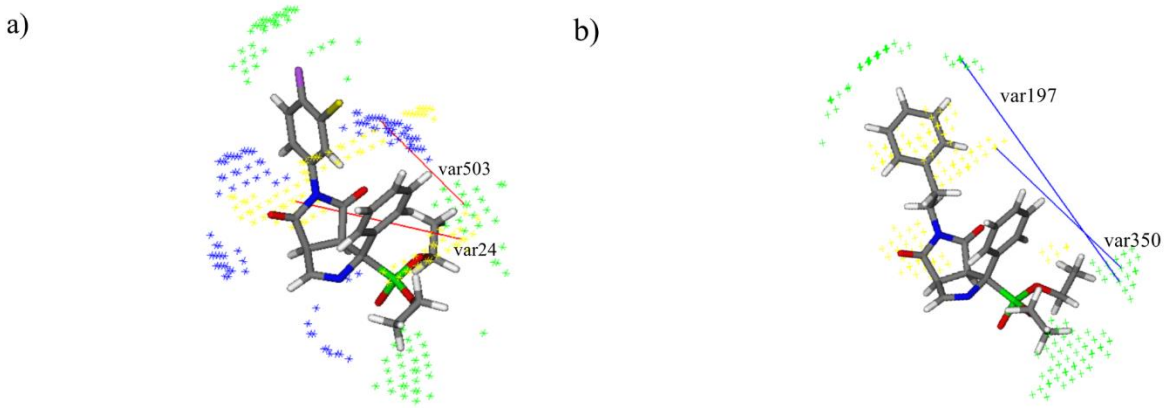

Figure S4. Representation of positive interactions (in red) of 9d (a) and negative interactions (in blue) of 9k (b) in I_2-IR 3D-QSAR model. The steric hot spots (TIP) are presented in green, hydrophobic regions (DRY) in yellow, and H-bond acceptor regions (N1) in blue.

The applicability domain (AD). Even though performed internal and external validations suggest that the created 3D-QSAR models are stable and reliable, and exhibits good predictive ability, in fact, each model has its own applicability domain. The leverage approach, presented using the Williams plot, is commonly used to define applicability domain of a model. In this study, we have used SPSS v.18.0 software for this procedure [4]. The critical leverage h* (the vertical line) is generally calculated according to relation h* = 3(p+1)/n, where p presents the number of model variables (in this case we used most significant variables according to PLS coefficient plot) and n is the number of compounds in training set. When the absolute standardized residual for a molecule exceed three standard deviation units, and/or the leverage value of a compound is greater than the critical value (h*), the compound is outside the AD of the model and the created models are not reliable. Figure S5 and S6 show that all compounds for both models are within of the defined AD.

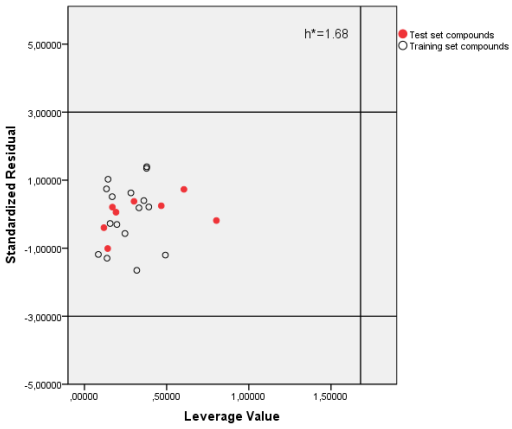

Figure S5. AD of developed I_2-IR 3D-QSAR model.

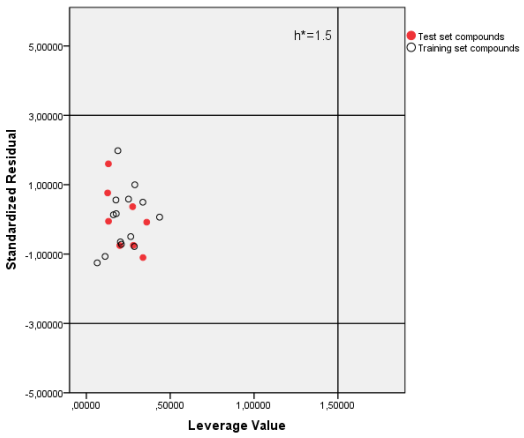

Figure S6. AD of developed α_2-AR 3D-QSAR model

Table S3. Results of physicochemical parameters of I_2-IR ligands obtained with SwissADME web tool.

Identifier	pKi(I_2)	Log S (ESOL) -10 to 0	Solubility class	Log $P_{o/w}$ (XLOGP3 < 5)	Log $P_{o/w}$ (MLOGP < 4.15)	Log $P_{o/w}$ (WLOGP < 5.6)	RuleOf 5	TPSA 20Å²<TPSA< 130
9d	8.56	-4.24	Moderately soluble	2.56	2.66	3.90	0	102.02
9f	8.37	-2.30	Soluble	0.64	0.86	1.50	0	102.02
2-BFI	8.31	-2.42	Soluble	1.62	1.67	1.02	0	37.53
9z	7.90	-4.98	Moderately soluble	3.46	2.82	4.35	1; Mw	102.02
13d	7.87	-4.33	Moderately soluble	2.53	2.35	3.91	1; Mw	111.25
Tracizoline	7.58	-1.95	very soluble	1.31	2.10	-1.09	0	26.00
12d	7.55	-4.41	Moderately soluble	2.66	3.03	4.46	0	102.02
Idazoxan	7.41	-1.78	Very soluble	0.70	0.99	0.07	0	42.85
9h	7.35	-2.86	Soluble	1.26	1.32	2.28	0	102.02
BU99008	7.05	-2.27	soluble	1.29	1.95	-1.15	0	30.93
9ab	6.96	-4.94	Moderately soluble	3.36	2.57	4.48	1; Mw	111.25
LSL60101	6.67	-3.02	Soluble	2.16	1.15	2.82	0	41.82
9e	6.65	-3.56	Soluble	1.80	1.50	2.70	0	111.25
5b	6.41	-3.03	Soluble	2.13	0.85	2.83	0	51.05
9k	6.35	-3.75	Soluble	2.23	1.96	2.73	0	102.02
5d	6.28	-3.89	Soluble	2.85	1.83	3.59	0	41.82
7a	5.98	-3.02	Soluble	2.11	1.43	2.83	0	30.96
5c	5.88	-3.03	Soluble	2.13	0.85	2.83	0	51.05
6c	5.48	-2.85	Soluble	1.81	0.56	2.53	0	62.05
7c	5.26	-3.23	Soluble	2.39	1.38	3.32	0	40.19
7aa	5.05	-3.19	Soluble	2.41	1.70	3.32	0	30.96
7b	4.96	-3.23	Soluble	2.39	1.38	3.32	0	40.19
6b	4.87	-2.85	Soluble	1.81	0.56	2.53	0	62.05
9g	4.02	-2.65	Soluble	1.17	1.10	1.89	0	102.02

Legend: Log S (ESOL) – water solubility, topological method implemented from Delaney JS 2004 J. Chem. Inf. Model; Solubility Class - insoluble < -10 < poorly < -6 < moderately < -4 < soluble < -2 < very < 0 < highly; XLOGP3 – atomistic and knowledge-based method calculated by XLOGP program; MLOGP – topological method implemented from Moriguchi I. et al. 1992 Chem. Pharm. Bull.; WLOGP – atomistic method implemented from Wildman SA and Crippen GM. 1999 J. Chem. Inf. Model.; RuleOf5 - Lipinski's "Rule of Five"; TPSA – topological polar surface area.

Table S4. Results of pharmacokinetic parameters of I_2-IR ligands obtained with ADMET Predictor software.

Identifier	pKi(I_2)	BBB Filter	hum_fup%	Pgp_Substr	Pgp_Inh	CYP_Risk	TOX_Risk	hERG_Filter
9d	8.56	High (75%)	6.51	No (93%)	No (58%)	1.21	1.23	Yes (98%)
9f	8.37	High (76%)	22.09	No (93%)	No (96%)	1.00	2.00	No (96%)
2-BFI	8.31	High (98%)	33.04	No (93%)	No (96%)	0.40	4.29	No (87%)
9z	7.90	High (70%)	3.62	No (93%)	Yes (97%)	1.26	1.09	Yes (91%)
13d	7.87	High (74%)	6.60	No (93%)	Yes (43%)	1.19	0.85	Yes (78%)
Tracizoline	7.58	High (98%)	57.80	No (93%)	No (96%)	1.45	2.00	No (96%)
12d	7.55	High (74%)	6.45	No (93%)	Yes (43%)	1.21	0.72	Yes (87%)
Idazoxan	7.41	High (98%)	60.08	No (93%)	No (96%)	2.00	1.00	No (96%)
9h	7.35	High (75%)	18.21	No (93%)	No (96%)	2.13	2.00	No (81%)
BU99008	7.05	High (98%)	57.69	No (93%)	No (96%)	1.22	1.91	No (81%)
9ab	6.96	High (76%)	3.79	No (93%)	Yes (97%)	1.23	1.99	Yes (81%)
LSL60101	6.67	High (98%)	9.90	No (93%)	No (96%)	0.44	1.99	No (81%)
9e	6.65	High (77%)	7.43	No (93%)	No (57%)	1.22	1.92	Yes (63%)
5b	6.41	High (98%)	9.41	No (93%)	No (96%)	0.54	0.73	No (81%)
9k	6.35	High (73%)	7.39	No (93%)	Yes (59%)	2.00	1.00	No (49%)
5d	6.28	High (98%)	6.04	No (93%)	No (81%)	0.62	1.16	No (61%)
7a	5.98	High (98%)	10.91	No (93%)	No (96%)	1.25	1.00	No (96%)
5c	5.88	High (98%)	9.99	No (93%)	No (96%)	0.44	0.60	No (81%)
6c	5.48	High (98%)	13.30	No (93%)	No (96%)	0.10	1.00	No (96%)
7c	5.26	High (98%)	9.01	No (93%)	No (96%)	1.58	0.00	No (96%)
7aa	5.05	High (98%)	9.00	No (93%)	No (96%)	0.92	0.00	No (96%)
7b	4.96	High (98%)	8.79	No (93%)	No (96%)	1.41	0.00	No (96%)
6b	4.87	High (98%)	12.95	No (93%)	No (96%)	0.10	1.00	No (96%)
9g	4.02	High (76%)	17.78	No (93%)	No (96%)	1.27	1.82	No (96%)

Legend: S+Peff – estimated permeability, BBB filter - qualitative likelihood (High/Low) of crossing the blood-brain barrier; hum_fup% - percentage of unbound drug in plasma; Pgp_Substr - likelihood of P-glycoprotein efflux; Pgp_Inh – likelihood of a molecule being an inhibitor of P-glycoprotein; CYP_Risk – cytochrome P450 liability score; Tox_Risk – toxicity liability score; hERG_Filter - qualitative estimation of the likelihood of the hERG potassium channel inhibition in human.

In vitro Blood-Brain Barrier Permeation Assay

To evaluate the brain penetration of the different compounds, a parallel artificial membrane permeation assay for blood-brain barrier was used, following the method described by Di et al [5]. The *in vitro* permeability (P_e) of fourteen commercial drugs (see table) through lipid extract of porcine brain membrane together with the test compounds were determined. Commercial drugs and assayed compounds were tested using a mixture of PBS:ETOH (70:30). Assay validation was made by comparing the experimental permeability with the reported values of the commercial drugs by bibliography and lineal correlation between experimental and reported permeability of the fourteen commercial drugs using the parallel artificial membrane permeation assay was evaluated ($y = 1.572x-1.090$; $R^2=0.938$). From this equation and taking into account the limits established by Di et al. for BBB permeation, we established the ranges of permeability as compounds of high BBB permeation (CNS+): *P*e (10^{-6} cms^{-1}) > 5.198; compounds of low BBB permeation(CNS-): *P*e (10^{-6} cm s^{-1}) < 2.054 and compounds of uncertain BBB permeation (CNS+/-): 5.198 > *P*e (10^{-6} cm s^{-1}) > 2.054.

Table S5. Permeability (*Pe* 10^{-6} cm s^{-1}) in the PAMPA-BBB assay of the 14 commercial drugs predictive penetration in the CNS used as references.

Compound	**Bibliography value[(a)]**	**Experimental value (n=3) ± S.D.**	***CNS Prediction***
Verapamil	16,0	25,4±0,6	*CNS*+
Testosterone	17,0	27,1±0,5	CNS+
Costicosterone	5,1	6,7±0,1	CNS+
Clonidine	5,3	6,5±0,05	CNS+
Ofloxacin	0,8	0,1±0,08	CNS-
Lomefloxacin	0,0	0,85±0,03	CNS-
Progesterone	9,3	16,8±0,3	CNS+
Promazine	8,8	13,8±0,3	CNS+
Imipramine	13,0	12,5±0,2	CNS+
Hidrocortisone	1,9	1,4±0,05	CNS-
Piroxicam	2,5	1,9±0,07	CNS-
Desipramine	12,0	17,8±0,1	CNS+
Cimetidine	0,0	0,7±0,03	CNS-
Norfloxacine	0,1	8,8±0,5	CNS+

Solubility of LSL60101

The stock solutions (10^{-2} M) of the assayed compound were diluted to decreased molarity, from 300 µM to 0.1µM, in 384 well transparent plate (Greiner 781801) with 1 % DMSO: 99 % PBS buffer. Incubated at 37 ºC and read after 2 h in a NEPHELOstar Plus (BMG LABTECH). The results were adjusted to a segmented regression to obtain the maximum concentration in which compound is soluble. **LSL60101**, solubility 52.5 µM.

Solubility of LSL60101 under various pH environments

The objective of this study is to establish the solubility of **LSL60101** at pH 1.13, 4.61 and 6.97 at 30 °C through the saturation method. This pH range simulates the gastric and intestinal fluids and cover the physiological pH range of the gastrointestinal tract.

Methods: The absorbance was measured by using the Agilent 708-DS Spectrophotometer and the pHmeter used to determinate the pH was MicropH 2001 Crison. The pH 1.13 buffer solution was prepared dissolving 20 mL of hydrochloric acid 5 M in 1 litre of deionised water. The pH 4.61 buffer solution was prepared dissolving 6.81 g of potassium dihydrogen phosphate in 1 litre of deionised water. The pH 6.97 buffer solution was prepared dissolving 1.03 g of potassium dihydrogen phosphate, 2.01 g of dipotassium hydrogen phosphate and 8.52 g of sodium chloride in 1 litre of deionised water.

Assay: In order to carry out the study, a seven-point calibration curves were prepared (2 µg/mL to 40 µg/mL) for each pH value considering the absorbances obtained at different pH and in compliance with the Lambert-Beer Law. The linear equation and the R^2 determination coefficient obtained for pH 1.13, 4.61 and 6.97 are shown in figure S5, respectively.

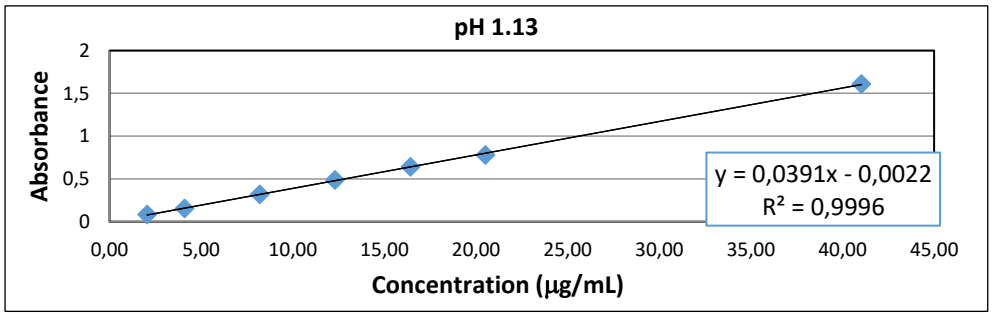

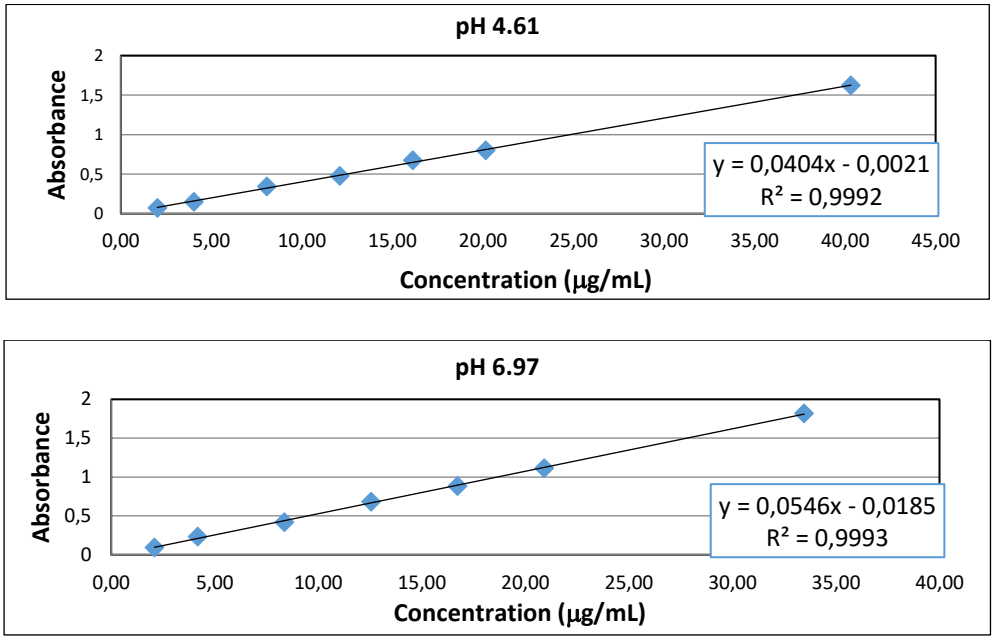

Figure S7.

In order to establish the solubility of **LSL60101**, the necessary amount of the sample was weighed to get a saturated solution in 2 mL of each buffer solution. Then, the samples were filtered through 0,45 µm PVDF filters and the corresponding dilutions were prepared in order to obtain a specific concentration which are within the established concentrations of the calibration curves. The absorbance of the samples was measured with the spectrophotometer at 275 nm wavelength, and calculations were done with the results in order to obtain the solubility of the compound at the different pH. Table S6 shows the results depending on the pH.

Table S6. Classification based on Eur. Ph. 10 th depending on the pH 1.13, 4.61 and 6.97.

pH	Concentration (mg/mL)	Classification Eur. Ph.
1.13	58.78 mg/mL	Soluble
4.61	43.86 mg/mL	Soluble
6.97	0.129 mg/mL	very slightly soluble

For **LSL60101**, a solubility of 58.78 mg/mL was obtained at pH 1.13, 43.86 mg/mL at pH 4.61 and 0.129 mg/mL at pH 6.97. Following the solubility terms stablished in European Pharmacopoeia (Ph. Eur.) 10th, it corresponds to a soluble substance at pH 1.13 (1 g in 17.01

mL of buffer solution) and at pH 4.61 (1 g in 22.80 mL of buffer solution) and a very slightly soluble substance at pH 6.97 (1 g in 7769.48 mL of buffer solution). Therefore, it is concluded from the results obtained in the study performed that the sample subject of study is soluble at pH 1.13 and pH 4.61 and very slightly soluble at pH 6.97.

Chemical stability of LSL60101

In order to evaluate the stability, weekly HPLC were performed on the **LSL60101** exposed sample to stress conditions (see results and discussion). **LSL60101** 0.2 mg/mL, phase mobil (A: H_20 + 0.05 % formic acid and B: ACN + 0.05 % formic acid) at 1:1 proportion. Stationary phase, Poroshell 120 EC-C15 (4.6x50 mm, 2.7-micro). Mobile phase (A: H_20 + 0.05 % formic acid and B: ACN + 0.05 % formic acid) using a gradient elution. Flow rate 0.6 mL/min. The DAD detector was set at 254 nm and the injection volume was 5 µL and oven temperature 40 °C. NMR spectra were recorded in $CDCl_3$ at 400 MHz (^1H) and 100.6 MHz (^{13}C), and chemical shifts are reported in δ values downfield from TMS or relative to residual chloroform (7.26 ppm, 77.0 ppm) as an internal standard. Data are compared taking into consideration: chemical shift, multiplicity, coupling constant (*J*) in hertz (Hz), integrated intensity and assignment.

Microsomal stability of LSL60101 at human and mice microsomes

Human and mice microsomes from Tebu-Xenotech were employed in the assay. They content 20 mg/mL of protein.

The following quantities were added to each well of a 96-well microplate.

	Blank (µL)	Human (µL)	Mice (µL)
Phosphate buffer Na/K 50 mM pH 7.4	295	283.5	301.3
$MgCl_2$ 30 mM	50	50	50
NADP 10 mM	50	50	50
Glucose 6-P 100mM	50	50	50
Glucose 6-P DH 20 U/mL	25	25	25
Water	25		
Human microsomes		36.5	
Mice microsomes			18.7
Test compound	5	5	5

Plates were incubated at 37 °C and 75 µL samples were taken at 0, 10, 20, 40 and 60 min. Samples were transferred to a microplate and 75 µL Acetonitrile were added for inactivating the microsomes, and 30 µL of H_2O for improving the chromatographic conditions and kept at 4 °C. When all the samples were taken the plate was centrifuged at 46000 g for 30 min at 15 °C. Supernatant was taken and injected in the UPLC-MS/MS. Stationary phase: Reverse phase Acquity UPLC® BEH C18 1.7 µm (2.1 mm x 50 mm) (Waters). Mobile phase: A: H_20 + 0.1 % formic; B: acetonitrile + 0.1 % formic acid.

Gradient:

Time	Water	Acetonitrile
0	95%	5%
0.1	95%	5%
1	0%	100%
2	0%	100%
2.1	95%	5%
2.5	95%	5%

Flow: 0.6 mL/min. The chromatographic equipment employed was an UPLC QSM Waters Acquity. Compound concentrations were calculated from the UV peak areas. The response was linear in the range between 10 ng/mL and 0.3125 ng/mL. Metabolic stability was calculated from the logarithm of the remaining **LSL60101** at each of the times evaluated.

Table S7. Microsomal stability of LSL60101 at human and mice microsomes.

Mice			Human		
% remanent (sampling time 60 min)	**$t_{1/2}$** (min)	**Clint** (µL/min*mg prot)	**% remanent** (sampling time 60 min)	**$t_{1/2}$** (min)	**Clint** (µL/min*mg prot)
35.58	68.99	10.04	57.76	97.9	7.07

Cytochrome inhibition of LSL60101

The objective of this study was to screen the inhibition potential of the compound using recombinant human cytochrome P450 enzymes (CYP1A2, CYP2C9, CYP2C19, CYP2D6, CYP3A4 (BFC) and CYP3A4 (DBF)) and probe substrates with fluorescent detection.

Assays were conducted in a 200 µl volume in 96 well microtiter plates (COSTAR 3915). Addition of cofactor-buffer mixture (KH_2PO_4 buffer, 1.3mM NADP, 3.3mM $MgCl_2$, 3.3 mM Glucose-6-phosphate and 0.4U/mL Glucose-6phosphate Dehydrogenase), supersomes control, standard inhibitors (Furafyline, Tranylzypromine, Ketoconazole, Sulfaphenazole and Quinidine; from Sigma Aldrich) previously diluted and compound to plates were carried out by a liquid handling station (Zephyr Caliper). The plate was then pre-incubated at 37 ºC for 5 min, and the reaction initiated by the addition of pre-warmed enzyme/substrate (E/S) mix. The E/S mix contained buffer (KH2PO4), c-DNA- pre-warmed enzyme/substrate (E/S) mix. The E/S mix contained buffer (KH_2PO_4), c-DNA-expressing P450 in insect cell microsomes, substrate (3-cyano-7-ethoxycoumarin (CEC) for CYP1A2 and CYP2C19, 7-Methoxy-4(trifluoromethyl)coumarin (7-MFC) for CYP2C9, 3-[2-(N,N-Diethyl-N-methylammonium)ethyl]-7-Methoxy-4-Methylcoumarin (AMMC) for CYP2D6 and 7-benzyloxytrifluoromethyl coumarin (7-BFC) and Dibenzylfluorescein (DBF) for CYP3A4) and other components to give the final assay concentrations in a reaction volume of 200 µl. Reactions were terminated after various times (a specific time for each cytochrome) by addition of STOP (0.5 M ACN/TrisHCl 80:20, and 2 N NaOH for CYP3A4 (DBF).

Fluorescence per well was measured using a fluorescence plate reader (Tecan Infinite M1000 pro) and percentage of inhibition was calculated.

Table S8. Results of inhibition of LSL60101.

	CYP1A2 (%inhib 10 µM)	**CYP2C9 (%inhib 10 µM)**	**CYP2C19 (%inhib 10 µM)**	**CYP2D6 (%inhib 10 µM)**	**CYP3A4 (7-BFC) (%inhib 10 µM)**	**CYP3A4 (DBF) (%inhib 10 µM)**
LSL60101	62 ± 2	1 ± 1	8 ± 3	19 ± 5	18 ± 1	10 ± 2

Plasma stability of LSL60101

Human and mouse plasma pooled from healthy donors extracted in citrate tubes was employed in the assay. Plates containing 10 µM compounds in plasma (total volume: 50 µL) were incubated at 37 ºC at the different times (0, 60, 180 and 360 min). Then 100 µl Acetonitrile were added for precipitating plasma protein, and the plate was centrifuged at 46000 g for 60 min at 5 ºC. Supernatant was taken and analyzed by UPLC/MS/MS for sample quantification. Stationary phase: Reverse phase Acquity UPLC® BEH C18 1.7 µm (2.1 mm x 50 mm) (Waters). Mobile phase: 0.1 % formic acid in H_20/0.1 % formic acid in acetonitrile.

Gradient:

Time	Water	Acetonitrile
0	95%	5%
0.1	95%	5%
1	0%	100%
2	0%	100%
2.1	95%	5%
2.5	95%	5%

Flow: 0.6 mL/min. The chromatographic equipment employed was an UPCL QSM Waters Acquity. Compound concentrations were calculated from the MS peak areas.

Table S9. Remaining percentage for LSL60101 at human plasma at the different times.

	0 h	**1 h**	**2 h**	**6 h**
LSL60101	100	83	77	57

Table S10. Remaining percentage for 5a at mouse plasma at the different times.

	0 h	**1 h**	**2 h**	**6 h**
LSL60101	100	100	100	100

Human and mouse plasma protein binding of LSL60101

Human and mouse plasma from Seralab was employed in the assay which was carried out by employing Rapid Equilibrium Dyalisis (RED) from Thermo Scientific. The compounds were dissolved at 5 µM in plasma and added to the corresponding insert of the RED device. Dialysis buffer was added to the corresponding insert of the RED device. Plate was incubated for 4 h at 37 ºC. After the incubation period 50 µL aliquots of each chamber were transferred to empty vials. 50 µL of dialysis buffer were added to the plasma samples and 50 µL of plasma were added to the buffer samples. 300 µL of acetonitrile were added to all the samples and centrifuged at 4000 rpm. 100 µL aliquots of the supernatants were transferred to a LC analysis plate and diluted with 100 µL of water. Samples were analyzed in a UPLC/MS/MS. Stationary phase: Reverse phase Acquity UPLC® BEH C18 1.7 µm (2.1 mm x 100 mm) (Waters). Mobile phase: 125 mM Ammonium hydroxide/acetonitrile. Gradient:

Time	Ammonium hydroxide	Acetonitrile
0	95%	5%
0.1	95%	5%
1	0%	100%
2	0%	100%
2.1	95%	5%
2.5	95%	5%

Flow: 0.6 mL/min. The chromatographic equipment employed was an UPLC QSM Waters Acquity. Compound concentrations were calculated from the MS peak areas.

Table S11. Human and mouse plasma protein binding.

	Mouse		Human	
Compound	**Plasma protein binding** (%)	**Unbound fraction** (%)	**Plasma protein binding** (%)	**Unbound fraction** (%)
LSL60101	84.0	16.0	92.9	7.1

hERG ion channel inhibition of LSL60101

The assay was carried out at a CHO cell line transfected with the hERG potassium channel. 72 h before the assay, 2500 cells were seeded on a 384 well black plate (Greiner 781091). Cell line were maintained at 37 ºC in a 5 % CO_2 atmosphere for 24 h and at 30 ºC in a 5 % CO_2 atmosphere for 48 h plus. hERG activity was measured by using the FluxorTM Potassium Ion Chanel Assay Kit (Thermo Fisher F10016). Medium was replaced for 20 µl Loading Buffer and the cells were incubated for 60 min at 25 ºC, protected from direct light. After incubation, Loading Buffer was replaced for Assay buffer and the compounds were incubated for 30 min at 25 ºC. 5µl of Stimulus Buffer was added to each well and the fluorescence was read (λex = 490 nm, λem = 525nm) using imaging plate reader system (FDSS7000EX, Hamamatsu®) every second after the establishment of a baseline line. The fluorescent signal was normalized to the maximum inhibition shown by controls and percentage of inhibition calculated. Inhibitory activity of **LSL60101** at hERG channel, % inhibition (10 µM): 4 ± 1.

Cytotoxicity assays

All tumor cell lines were acquired from the American Type Culture Collection (ATCC, Manassas, VA, USA), except for the DND-41 cell line, which was purchased from the Deutsche Sammlung von Mikroorganismen und Zellkulturen (DSMZ Leibniz-Institut, Germany), and the Hap-1 cell line which was ordered from Horizon Discovery (Horizon Discovery Group, UK). All cell lines were cultured as recommended by the suppliers. Media were purchased from Gibco Life Technologies, USA, and supplemented with 10 % fetal bovine serum (HyClone, GE Healthcare Life Sciences, USA). Adherent cell lines HCT-116, NCI-H460, LN-229, Hap-1 and Capan-1 cells were seeded at a density between 500 and 1500 cells per well, in 384-well, black walled, clear-bottomed tissue culture plates (Greiner). After overnight incubation, cells were treated with the test compounds at seven different concentrations ranging from 100 to 6.4 x 10^{-3} μM. Suspension cell lines HL-60, K-562, Z-138, and DND-41 were seeded at densities ranging from 2500 to 5500 cells per well in 384-well, black walled, clear-bottomed tissue culture plates containing the test compounds at the same seven concentration points. The plates were incubated and monitored at 37 °C for 72 h in an IncuCyte® (Essen BioScience Inc., Ann Arbor, MI, USA) for real-time imaging. Images were taken every 3 h, with one field imaged per well under 10x magnification.

Antibodies and primers used

Table S12. Reagents used for WB and qPCR experiments.

a) Antibodies used in WB studies.

Antibody	Host	Source/Catalog	WB dilution
SOD1	Rabbit	*Novus Biologicals/NBP2-24915*	1:1000
GPX1/Glutathion Peroxidase 1	Rabbit	*Novus Biologicals.NBP1 33620*	1:1000
GAPDH	Mouse	Millipore/MAB374	1:2500

b) SYBR Green primers used in qPCR studies.

Target	Product size (bp)	Forward primer (5'-3')	Reverse primer (5'-3')
Aldh2	***136***	***GCAGGCGTACACAGAAGTGA***	***TGAGCTTCATCCCCTACCCA***
iNOS	**125**	***GGCAGCCTGAGAGACCTTTG***	***GGAAGCGTTTCGGGATCTGAA***
Hmox1	***69***	***TGACACCTGAGGTCAAGCAC***	***GTCTCTGCAGGGGCAGTATC***
β-actin	***190***	***CTGTCCCTGTATGCCTCTG***	***ATGTCACGCACGATTTCC***

Table of representative data of ^{1}H-NMR spectra of new compounds

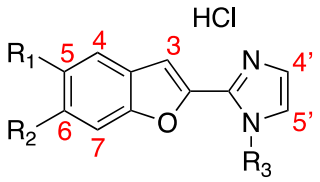

Table S13. ^{1}H chemical shifts for new compounds including both the multiplicity and the coupling constants.

Compound	**H3**	**H4**	**H5**	**H6**	**H7**	**H4' / H5' imidazole**
LSL60101	8.12, s	7.88, d 7.5	7.52, t 8.5	7.40, t 7.5	7.74, d 8.5	7.83, s
5b	8.10, s	7.61, d 9.0	---	7.08, dd 9.0, 2.5	7.38, d 2.5	7.82, s
5c	8.06, s	7.74, d 8.5	7.02, dd 8.5, 2.0	---	7.23, s	7.77, s
5d	8.07, s	8.12, d 2.0	---	7.62, dd 9.0, 2.0	7.70, d 9.0	7.83, s
6b	7.97, s	7.51, d 9.0	---	6.99, dd 9.0, 2.0	7.14, d 2.0	7.80, s
6c	8.01, s	7.63, d 8.5	6.92, dd 8.5, 2.0	---	7.10, s	7.77, s
7a	8.01, s	7.88, d 7.5	7.55, t 8.5	7.43, t 7.5	7.77, d 8.5	7.80, d, 2.0 7.88, d, 1.5
7aa	8.12, s	7.87, d 7.5	7.53, t 8.0	7.41, t 7.5	7.76, d 8.5	7.86, d, 20 8.00, d, 1.5
7b	8.06 s	7.66, d 9.0	---	7.10, dd 9.0, 2.5	7.35, d 2.5	7.98, d, 2.0 7.85, d, 2.0
7c	8.05, s	7.73, d 8.5	7.03, dd 8.5, 2.0	---	7.33, s	7.95, d, 2.0 7.82, d, 2.0

^{1}H-NMR and ^{13}C-NMR spectra of new compounds 5a – 7c

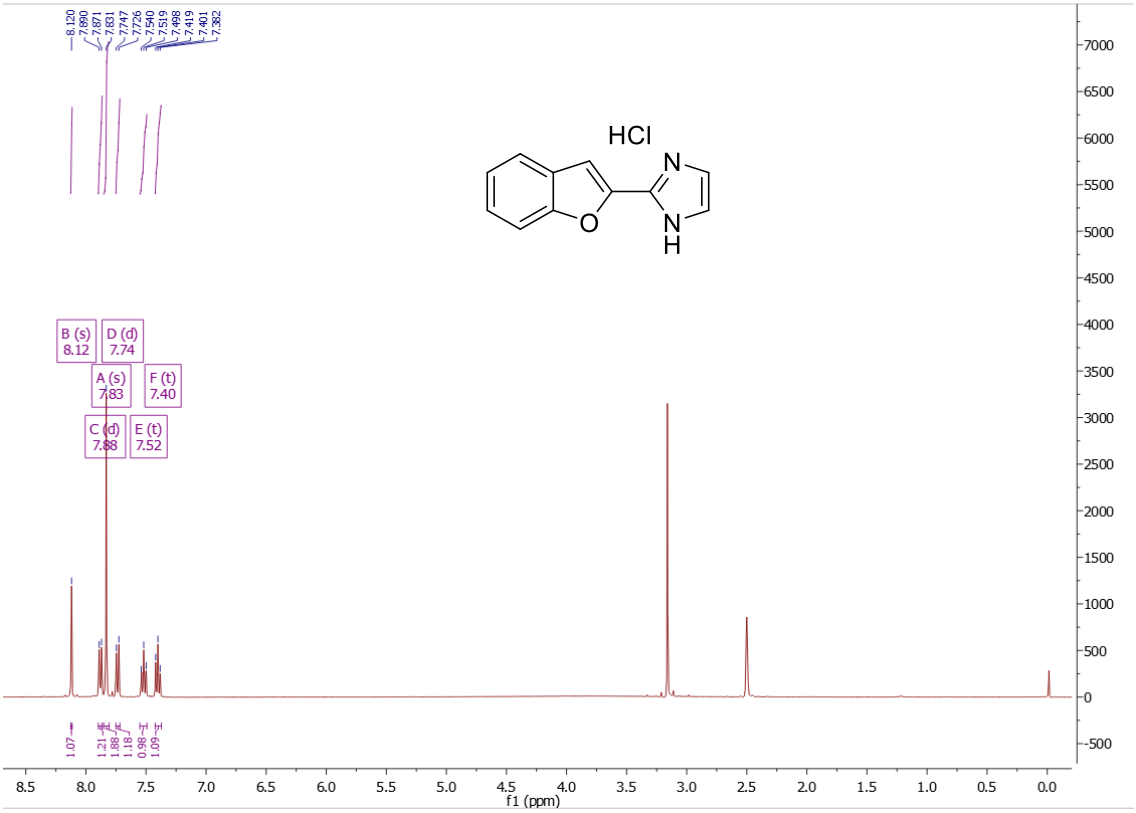

2-(Benzofuran-2-yl)-1*H*-imidazole hydrochloride (LSL60101)

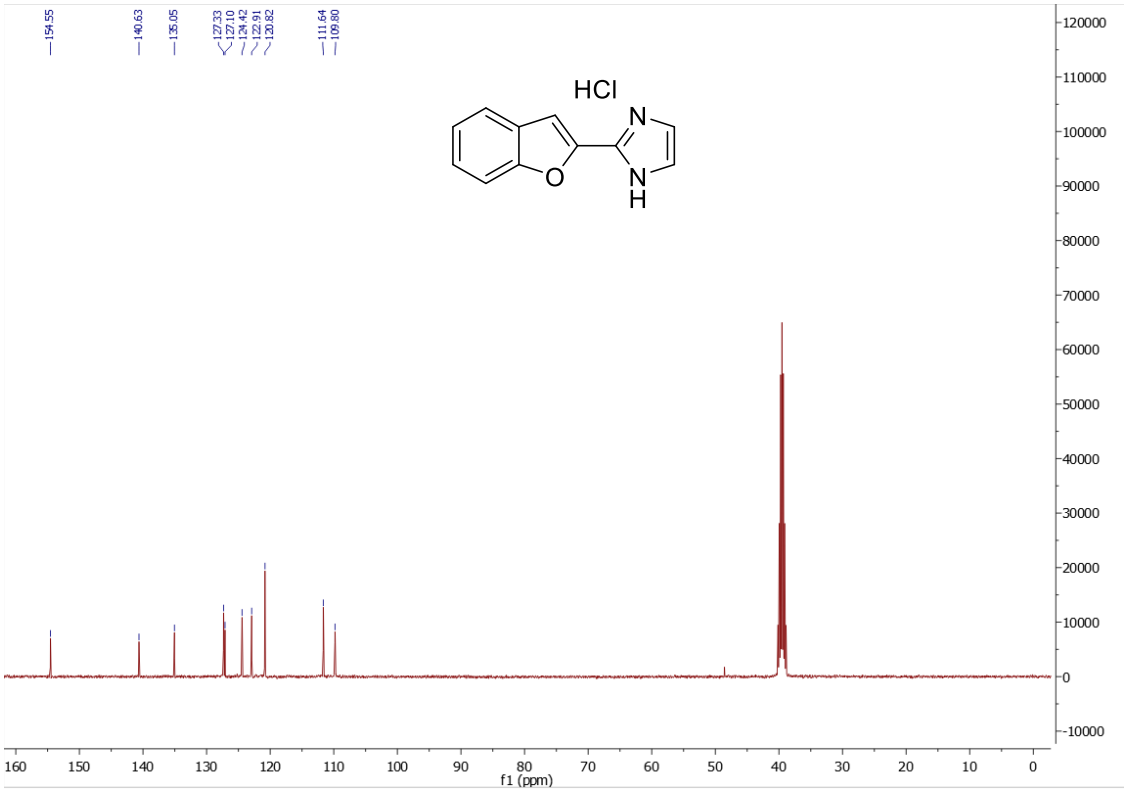

2-(Benzofuran-2-yl)-1*H*-imidazole hydrochloride (LSL60101)

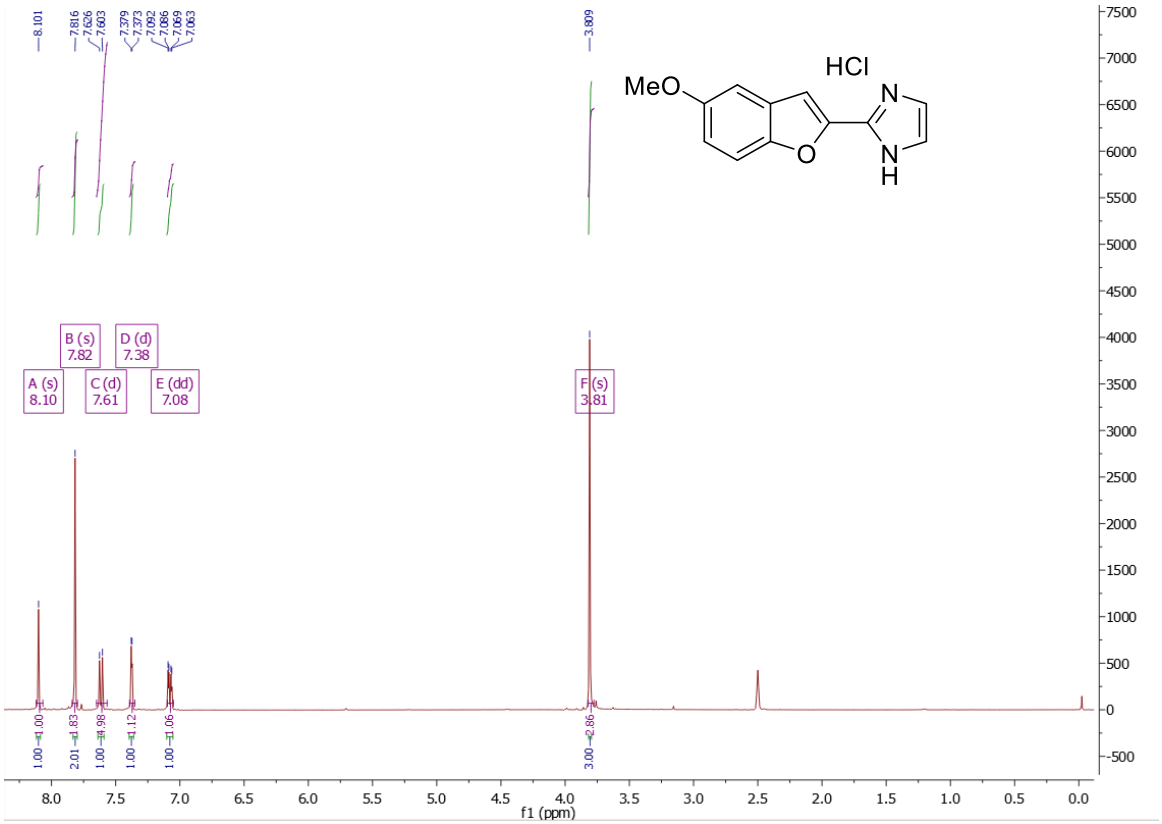

2-(5-Methoxybenzofuran-2-yl)-1*H*-imidazole hydrochloride (5b)

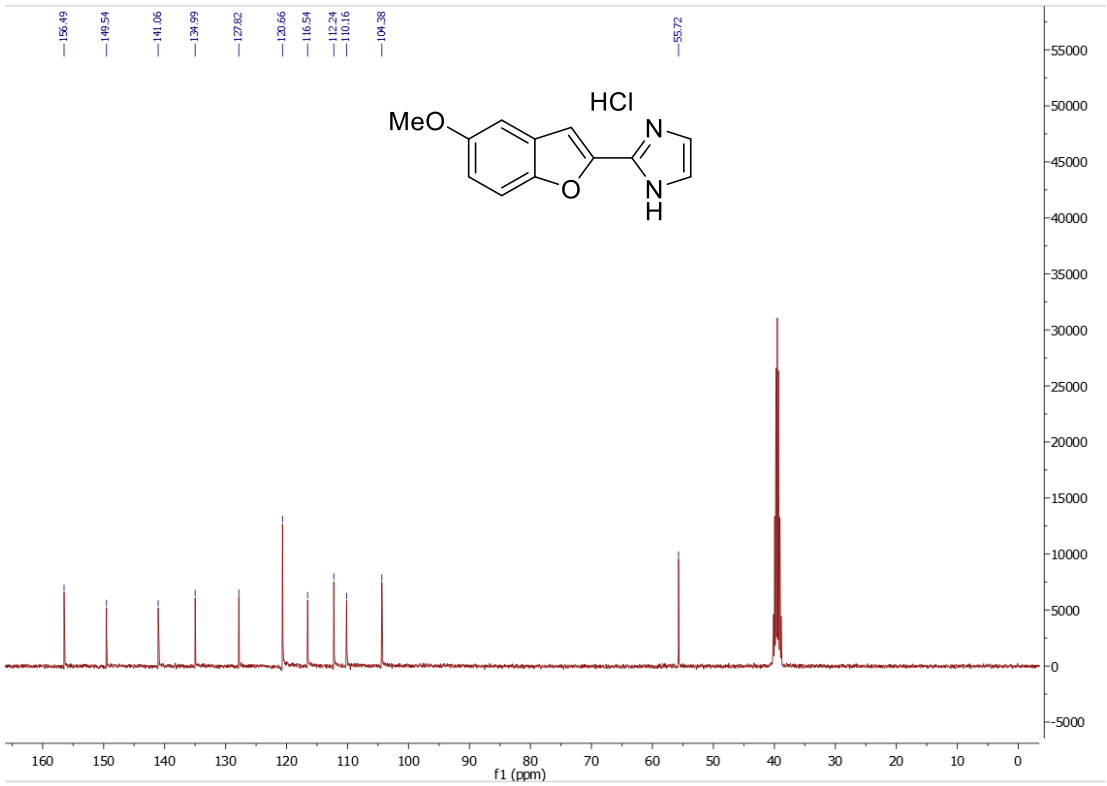

2-(5-Methoxybenzofuran-2-yl)-1*H*-imidazole hydrochloride (5b)

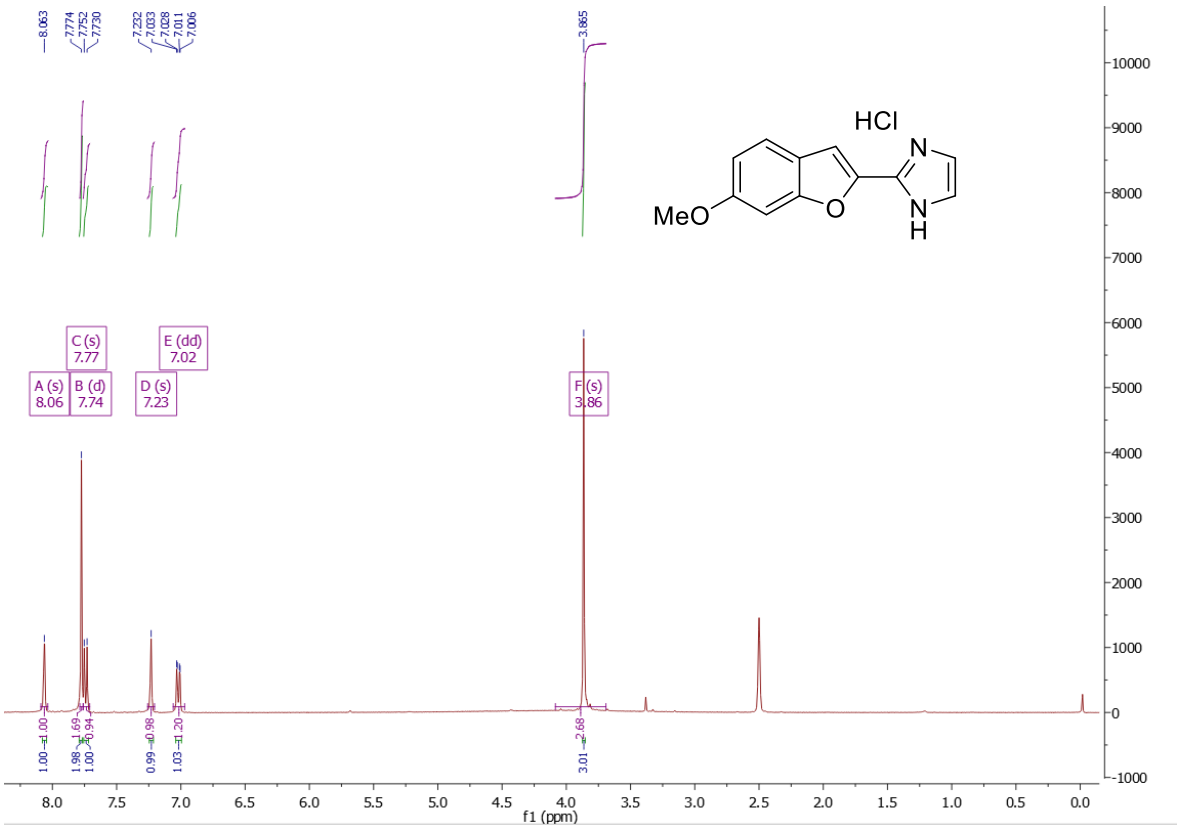

2-(6-Methoxybenzofuran-2-yl)-1*H*-imidazole hydrochloride (5c)

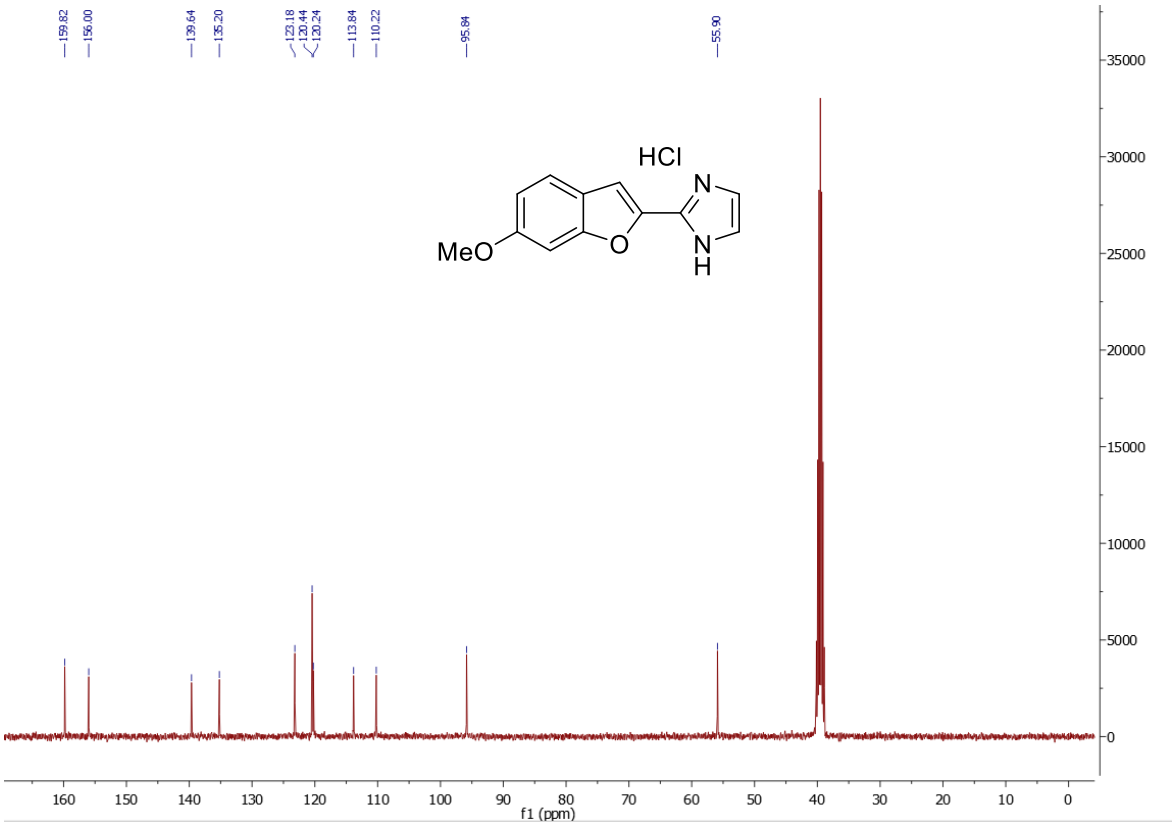

2-(6-Methoxybenzofuran-2-yl)-1*H*-imidazole hydrochloride (5c)

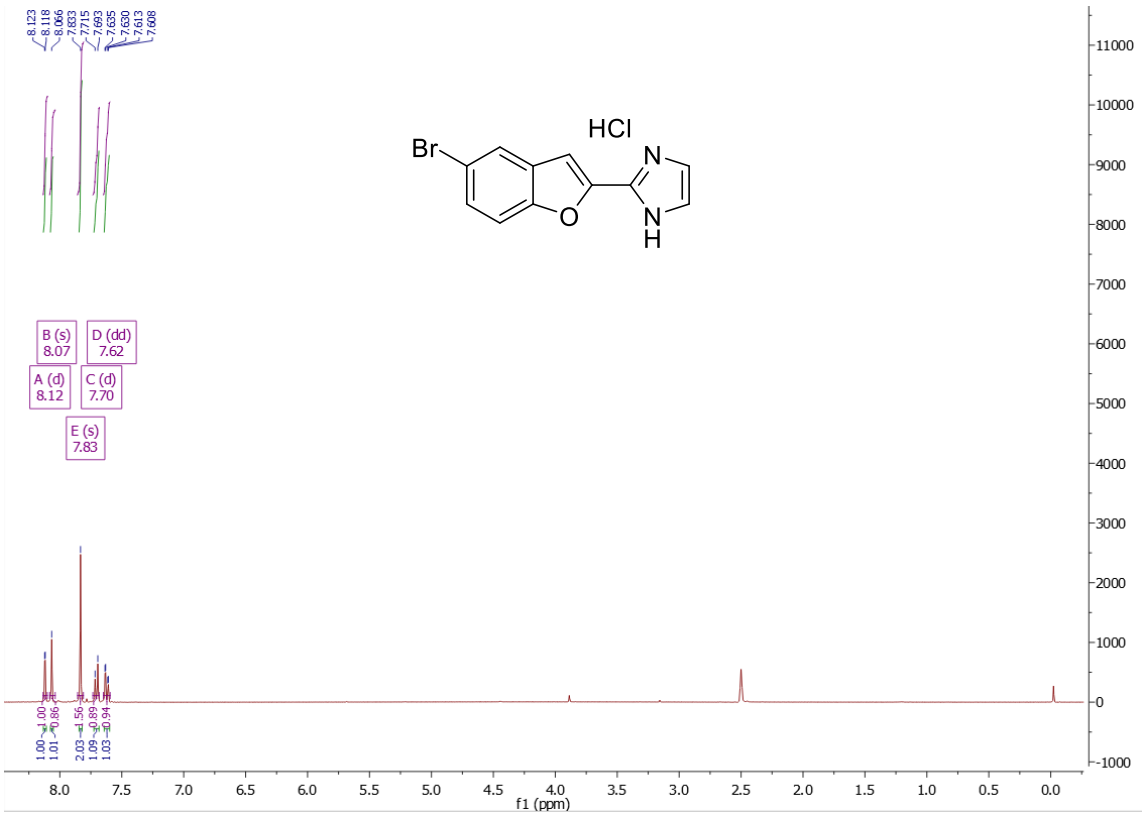

2-(5-Bromobenzofuran-2-yl)-1*H*-imidazole hydrochloride (5d)

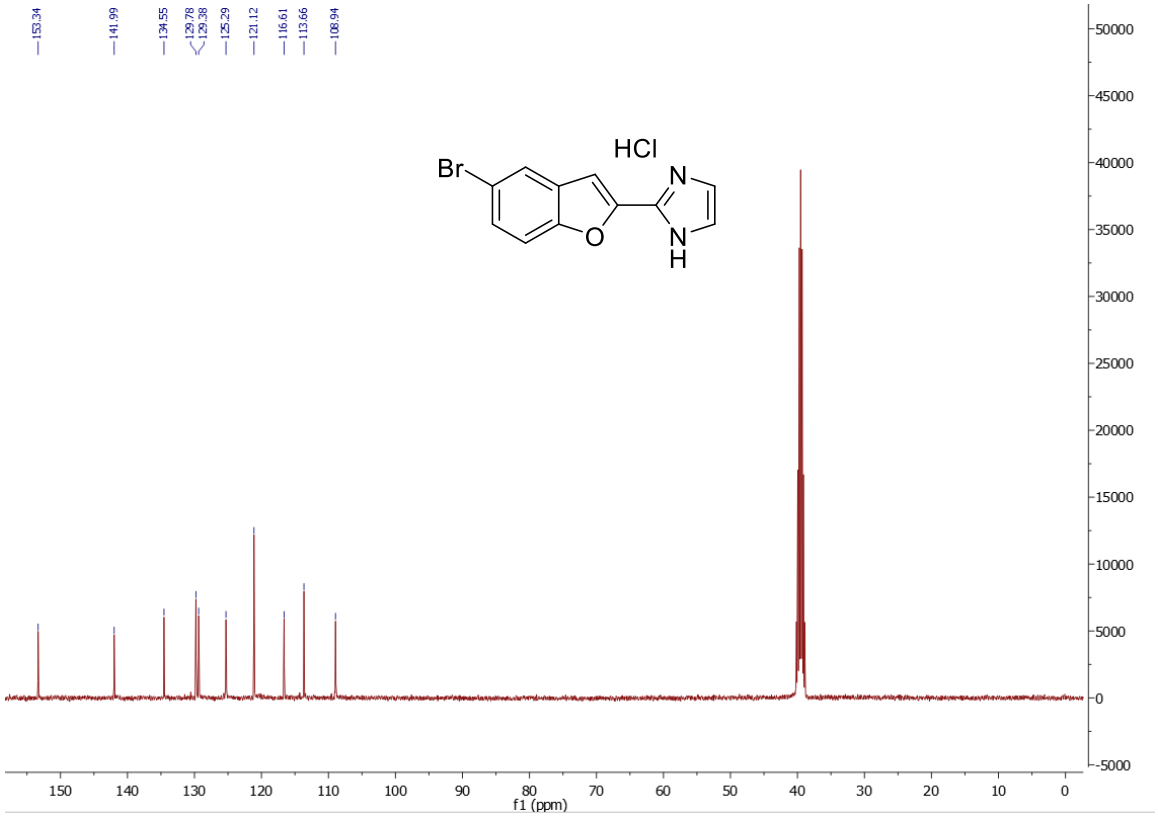

2-(5-Bromobenzofuran-2-yl)-1*H*-imidazole hydrochloride (5d)

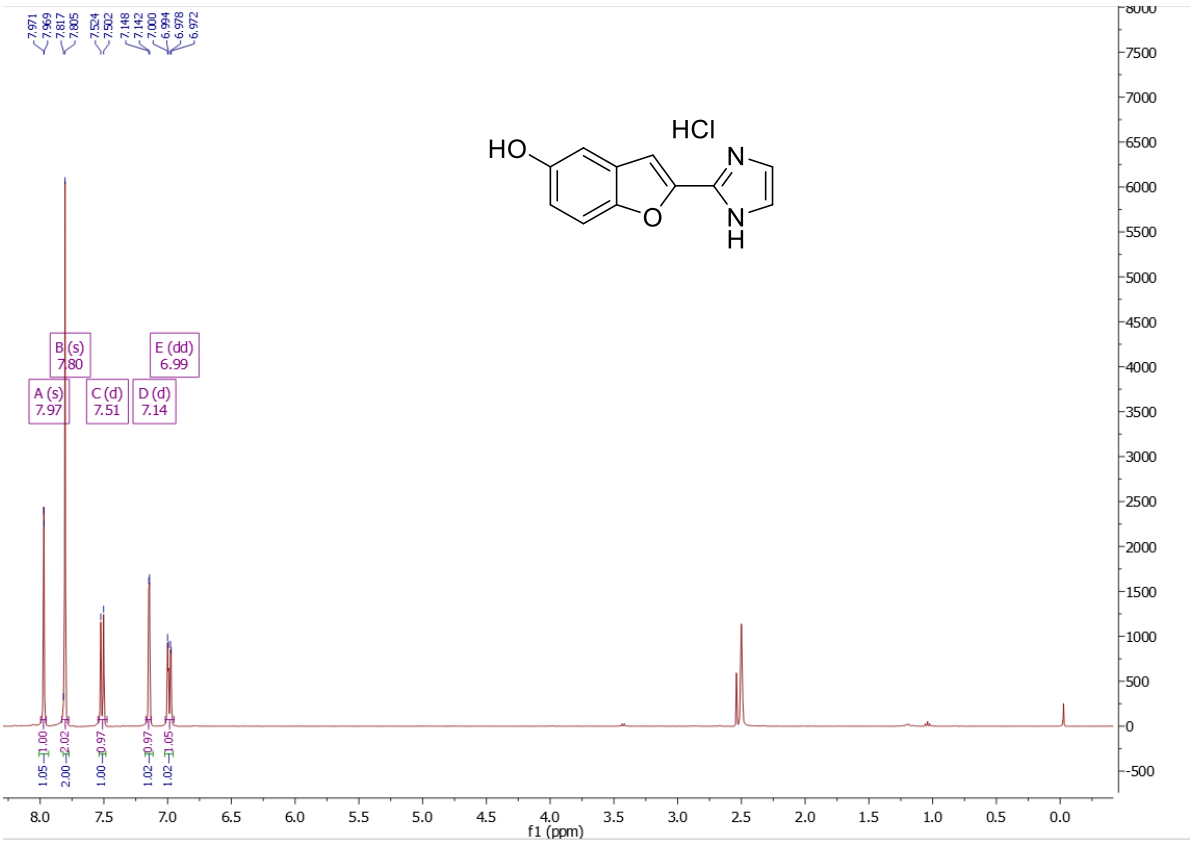

2-(5-Hydroxybenzofuran-2-yl)-1*H*-imidazole hydrochloride (6b)

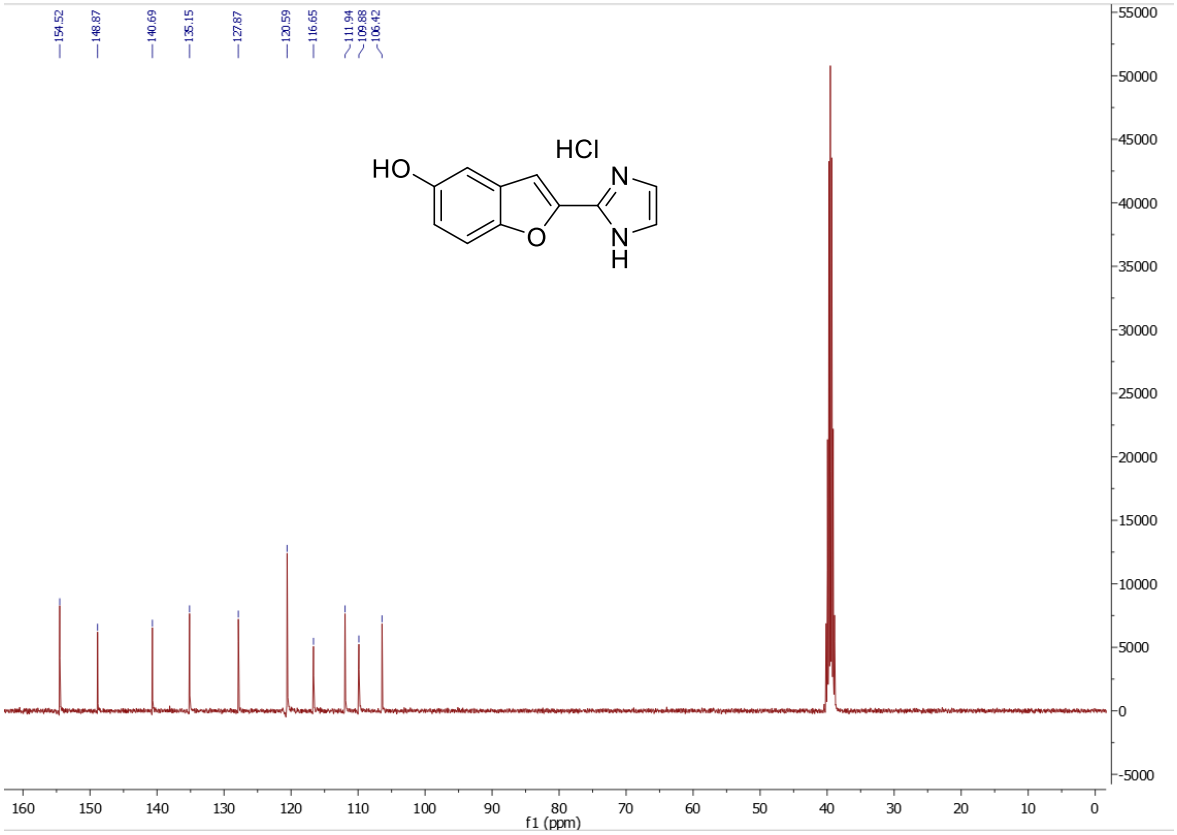

2-(5-Hydroxybenzofuran-2-yl)-1*H*-imidazole hydrochloride (6b)

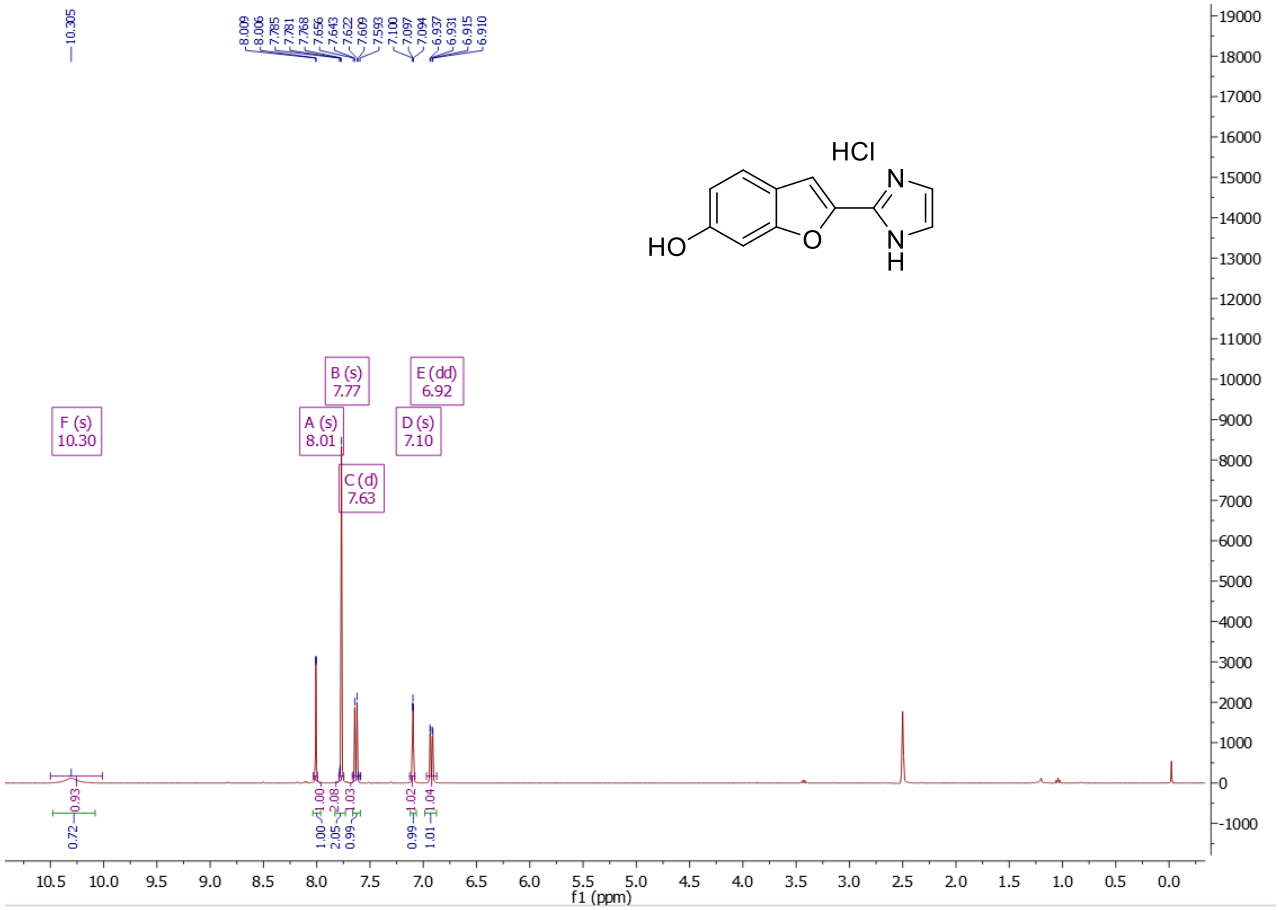

2-(6-Hydroxybenzofuran-2-yl)-1*H*-imidazole hydrochloride (6c)

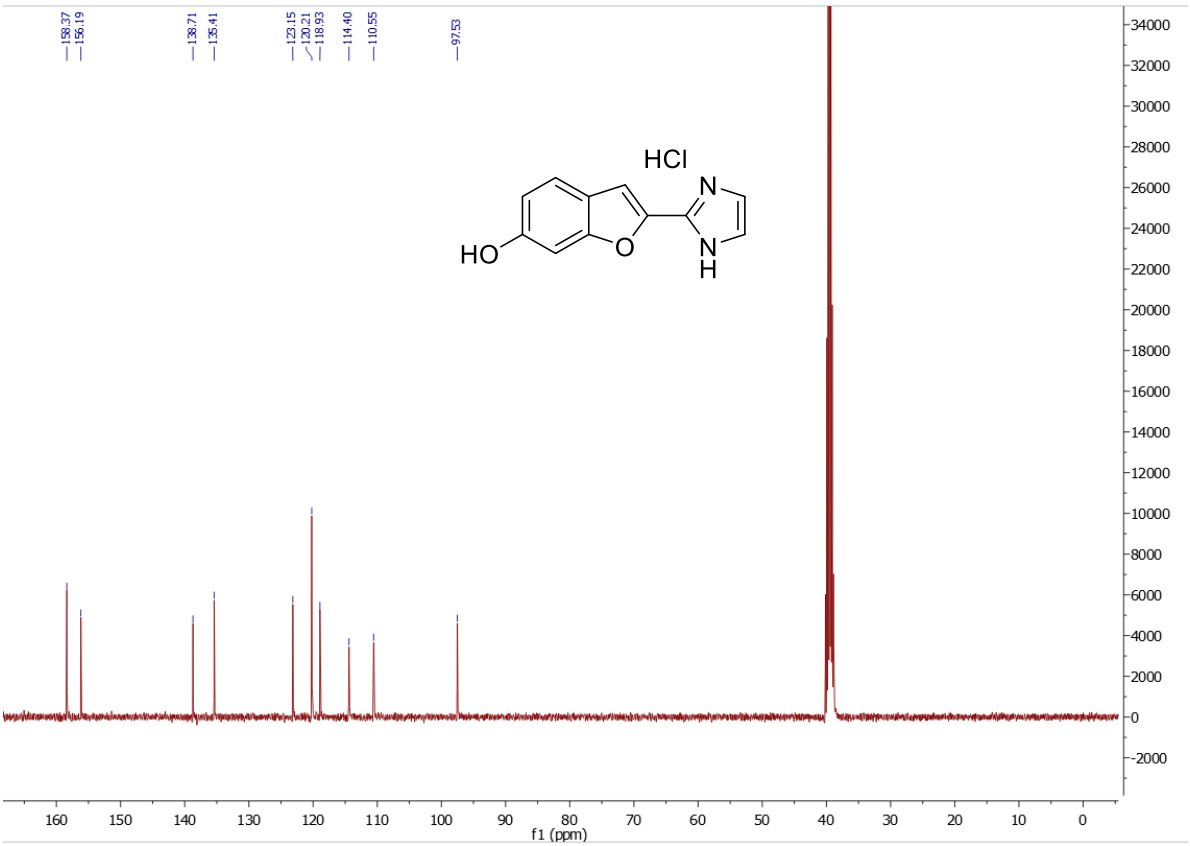

2-(6-Hydroxybenzofuran-2-yl)-1*H*-imidazole hydrochloride (6c)

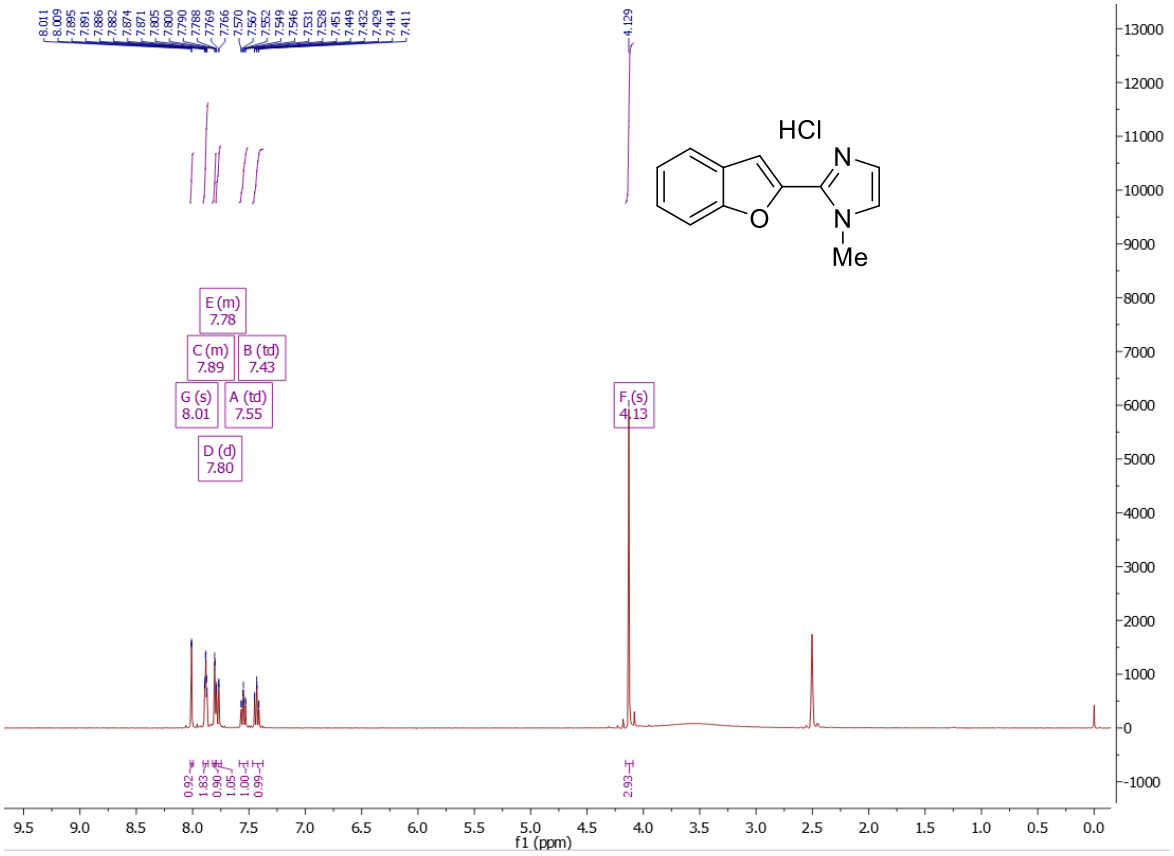

1-Methyl-2-(benzofuran-2-yl)-1*H*-imidazole hydrochloride (7a)

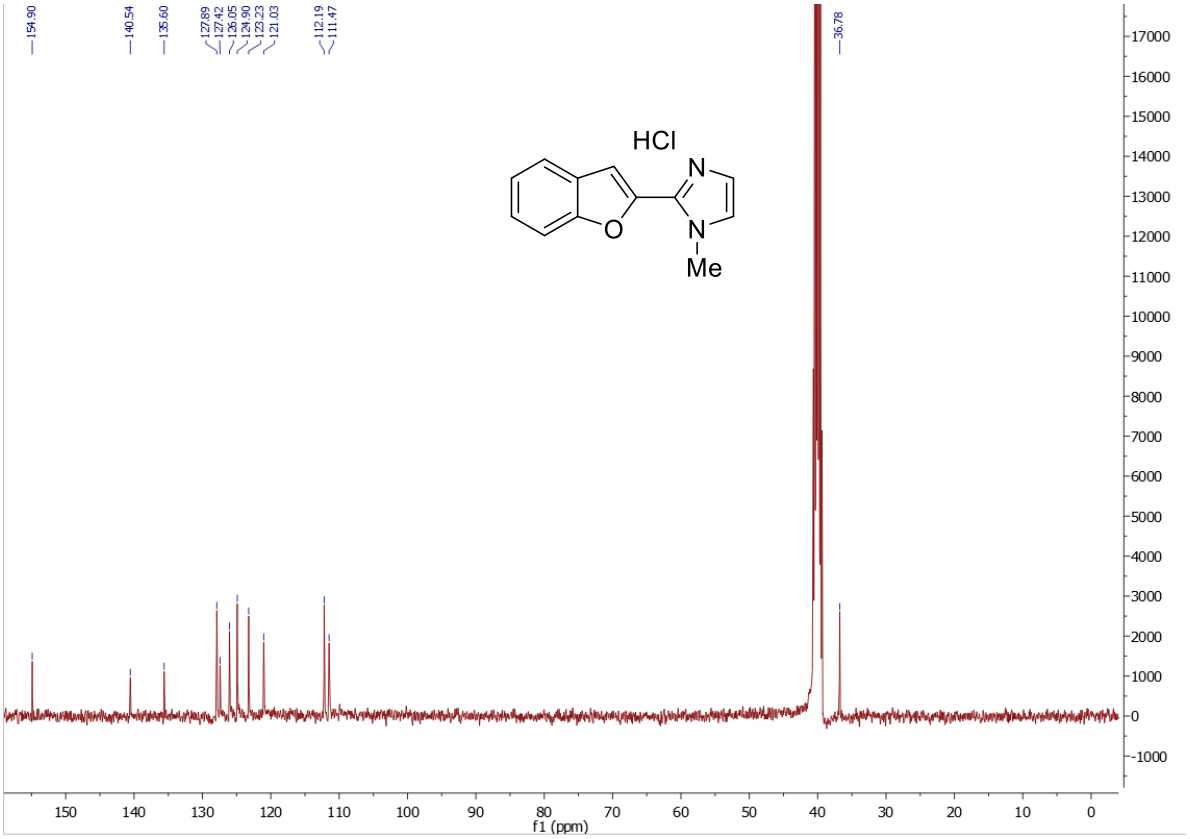

1-Methyl-2-(benzofuran-2-yl)-1*H*-imidazole hydrochloride (7a)

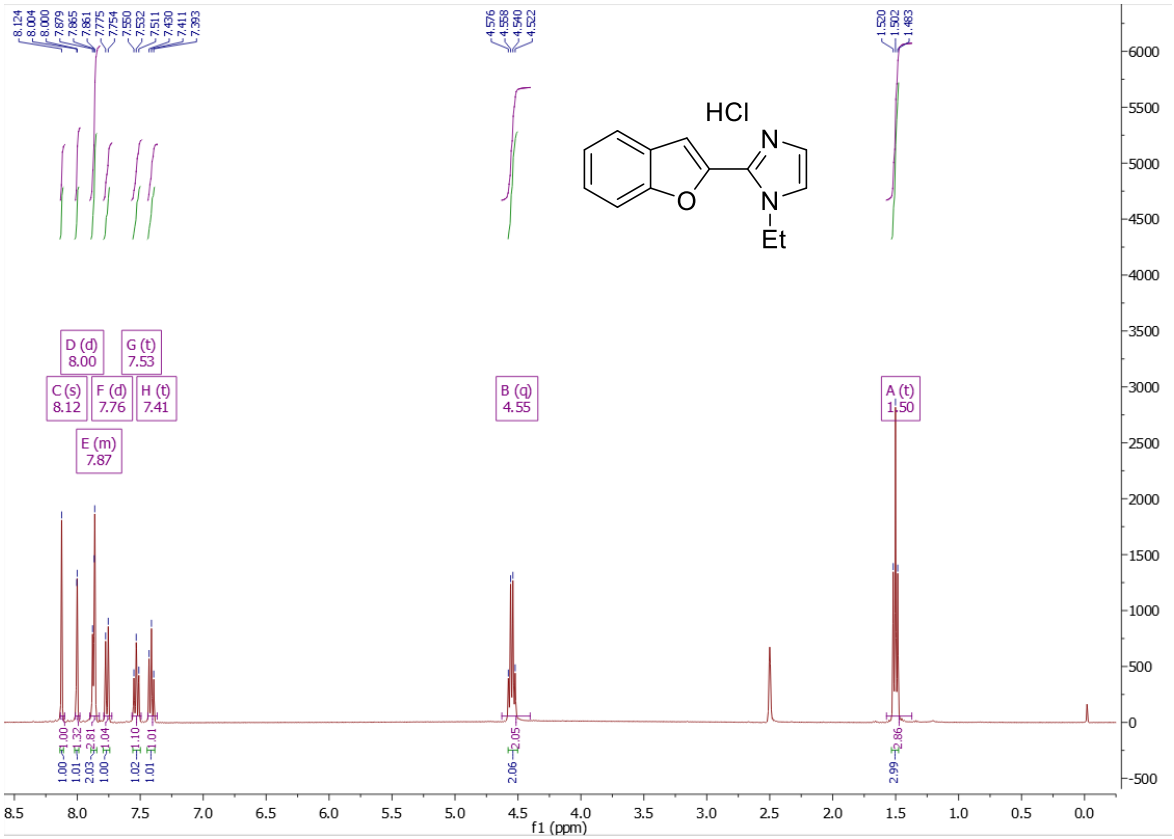

1-Ethyl-2-(benzofuran-2-yl)-1*H*-imidazole hydrochloride (7aa)

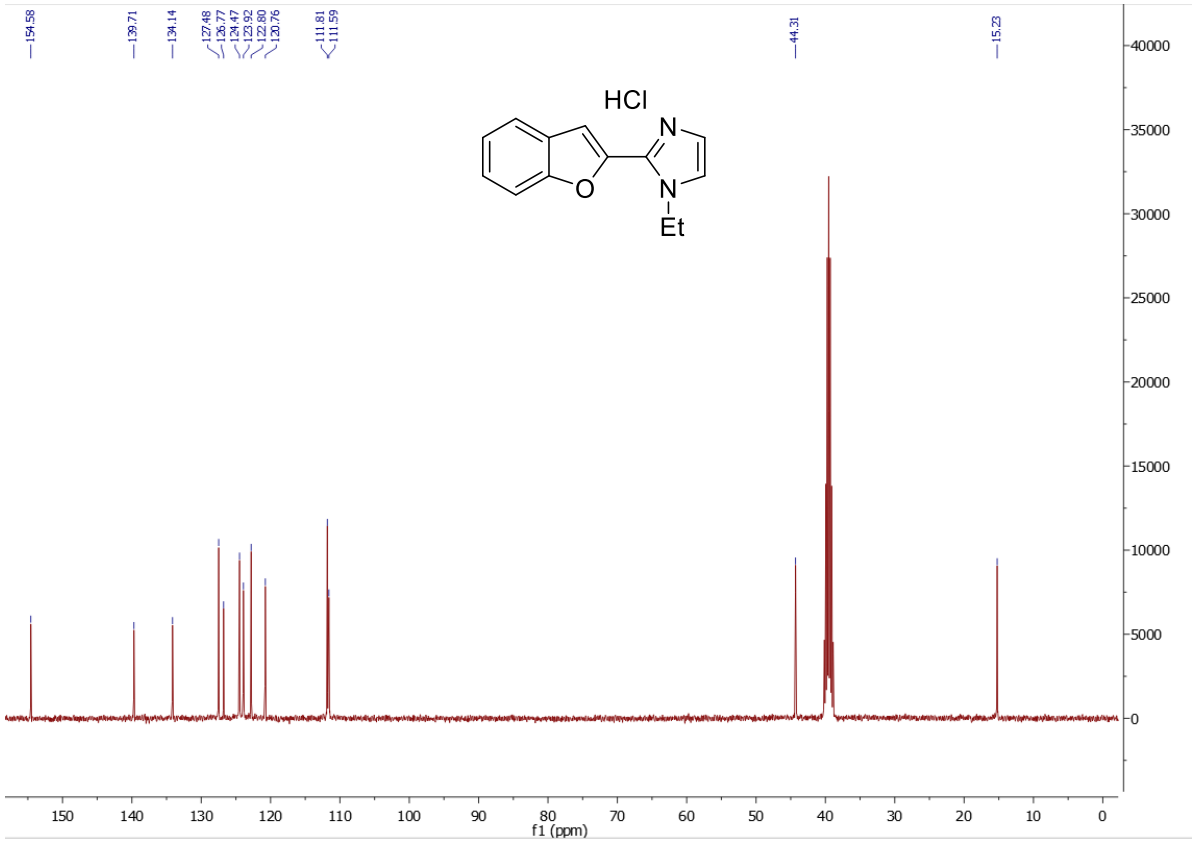

1-Ethyl-2-(benzofuran-2-yl)-1*H*-imidazole hydrochloride (7aa)

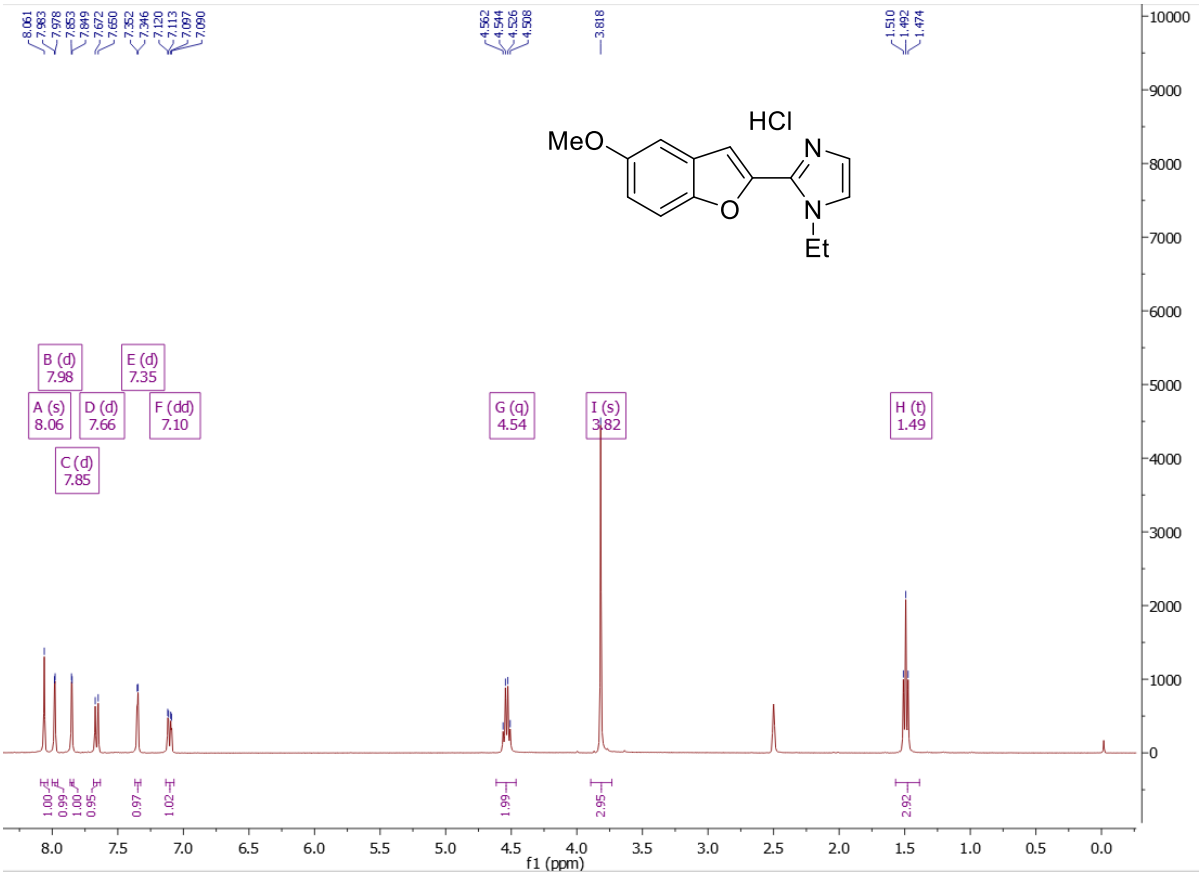

1-Ethyl-2-(5-methoxybenzofuran-2-yl)-1*H*-imidazole hydrochloride (7b)

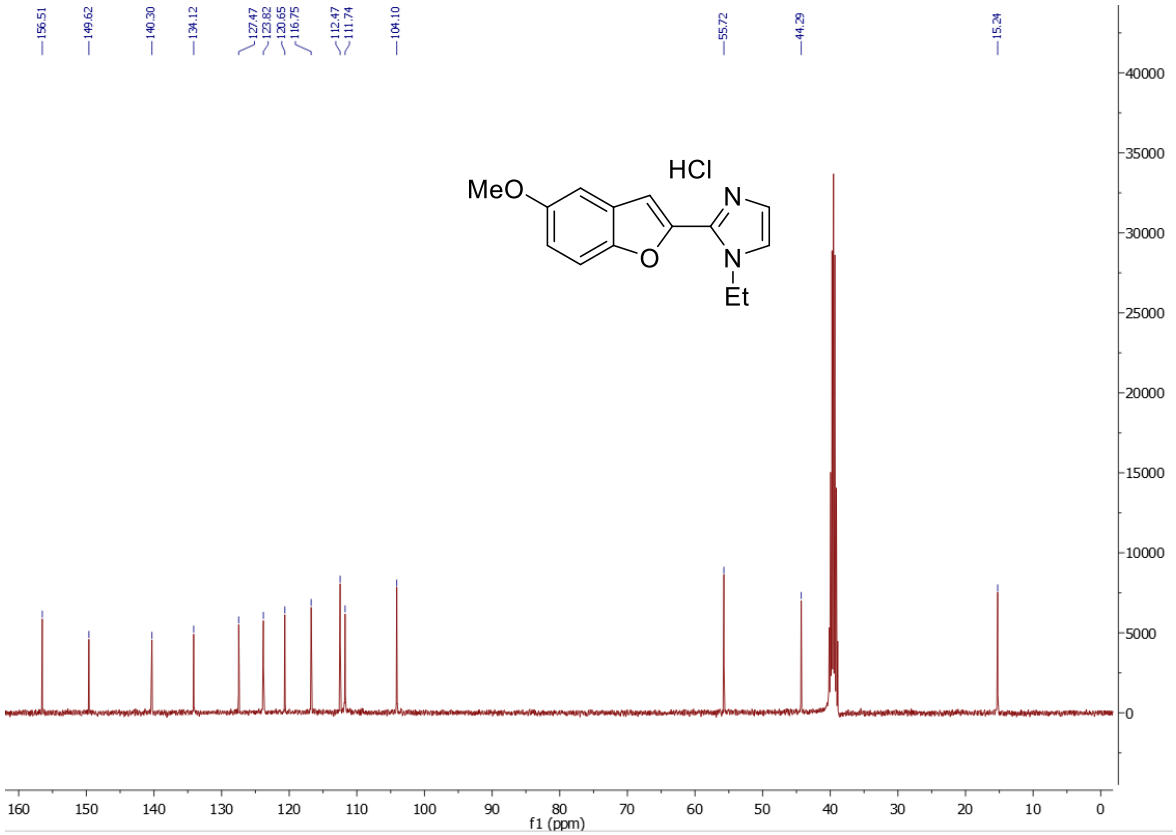

1-Ethyl-2-(5-methoxybenzofuran-2-yl)-1*H*-imidazole hydrochloride (7b)

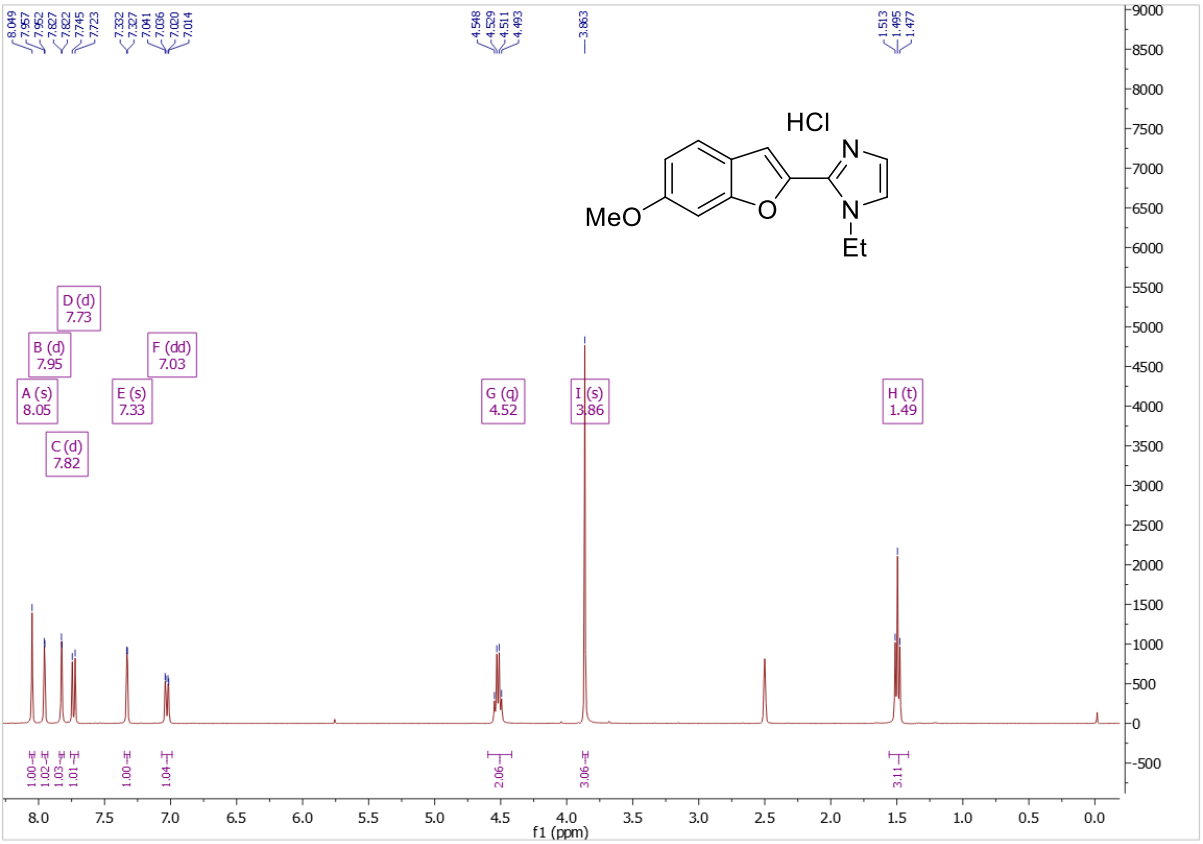

1-Ethyl-2-(6-methoxybenzofuran-2-yl)-1*H*-imidazole hydrochloride (7c)

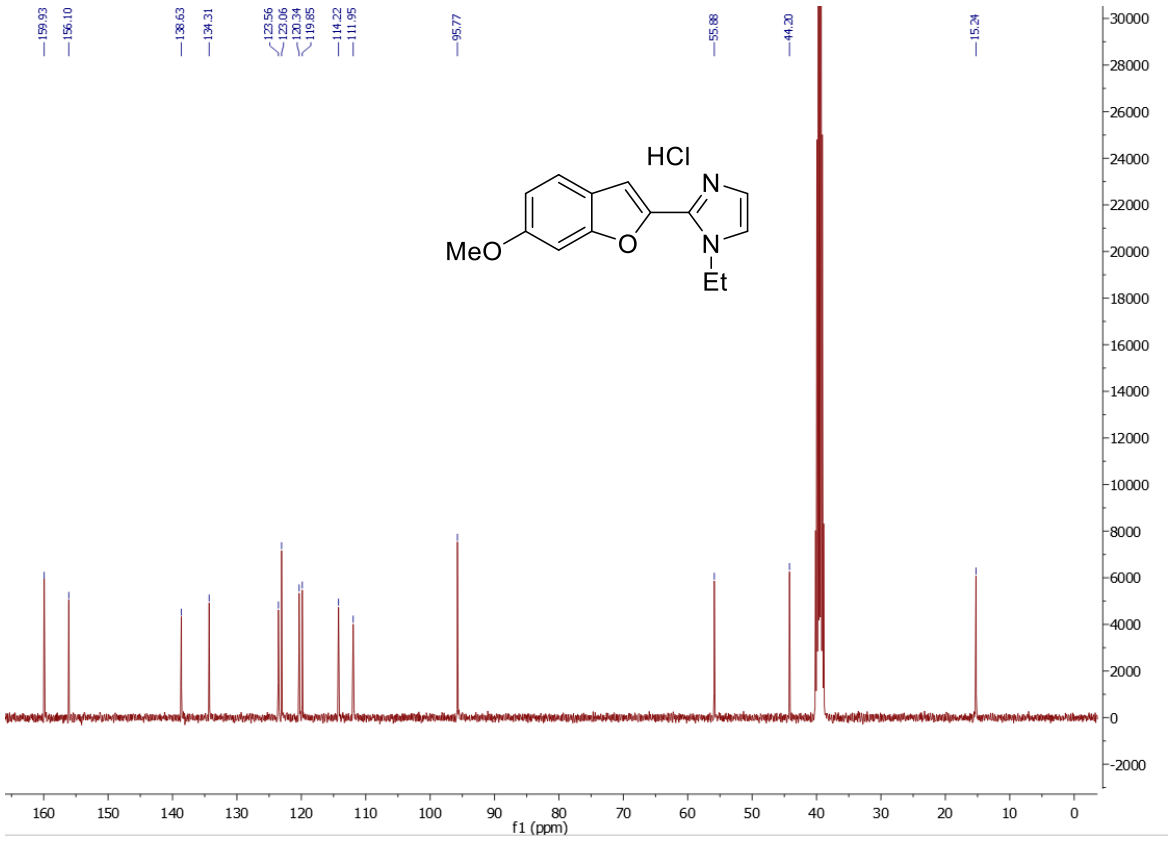

1-Ethyl-2-(6-methoxybenzofuran-2-yl)-1*H*-imidazole hydrochloride (7c)

HPLC/MS analysis of 5a-7c

2-(Benzofuran-2-yl)-1*H*-imidazole hydrochloride (LSL60101)

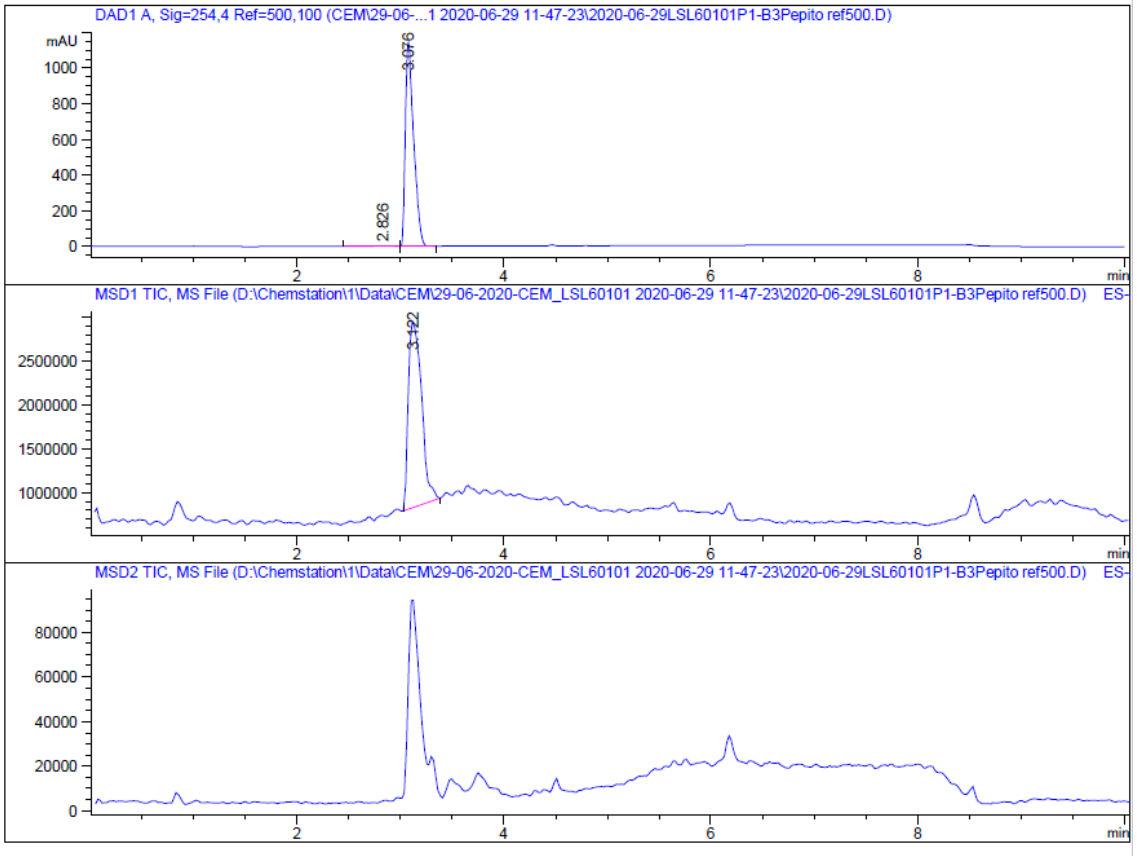


```
=====================================================================
                        Area Percent Report
=====================================================================

Sorted By             :      Signal
Multiplier            :      1.0000
Dilution              :      1.0000
Do not use Multiplier & Dilution Factor with ISTDs


Signal 1: DAD1 A, Sig=254,4 Ref=500,100

Peak RetTime Type  Width     Area      Height     Area
  #   [min]        [min]   [mAU*s]     [mAU]       %
----|-------|----|-------|----------|----------|--------|
   1   2.826 BB    0.2216   23.13766    1.57324   0.3621
   2   3.076 BB    0.0809 6367.33203 1144.69751  99.6379

Totals :                  6390.46970 1146.27075
```

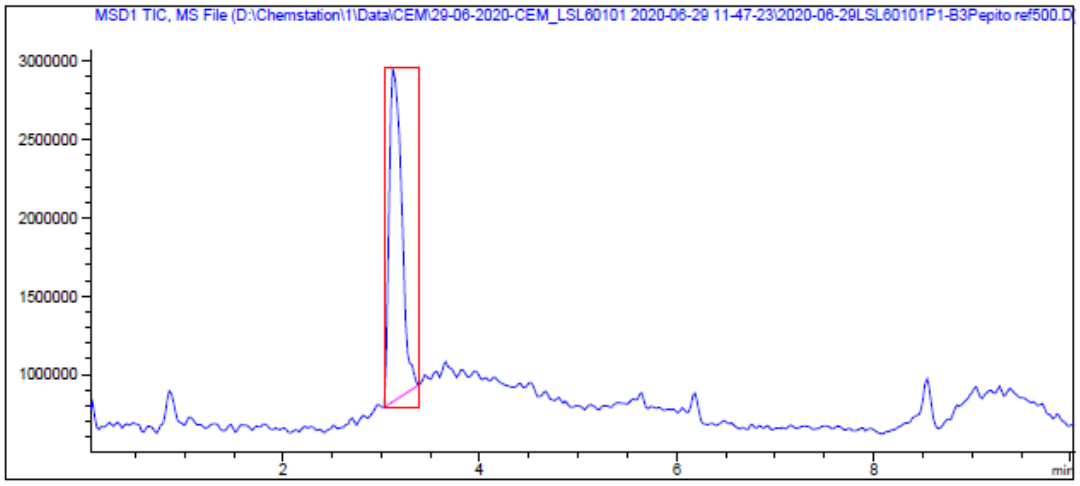
MSD1 TIC, MS File (D:\Chemstation\1\Data\CEM\29-06-2020-CEM_LSL60101 2020-06-29 11-47-23\2020-06-29LSL60101P1-B3Pepito ref500.D
3000000
2500000
2000000
1500000
1000000
2
4
6
8
min

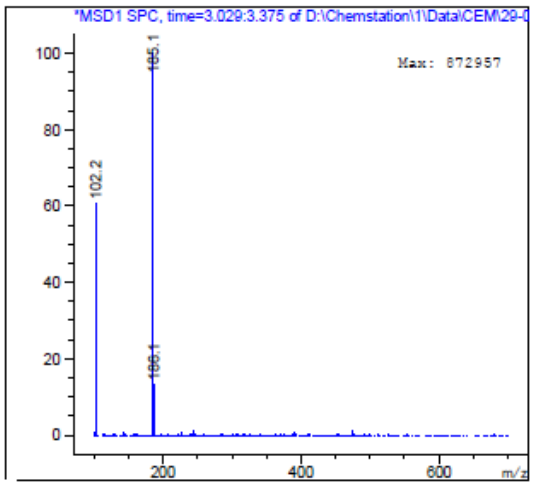
*MSD1 SPC, time=3.029:3.375 of D:\Chemstation\1\Data\CEM\29-0
Max: 872957
185.1
102.2
186.1
100
80
60
40
20
0
200
400
600
m/z

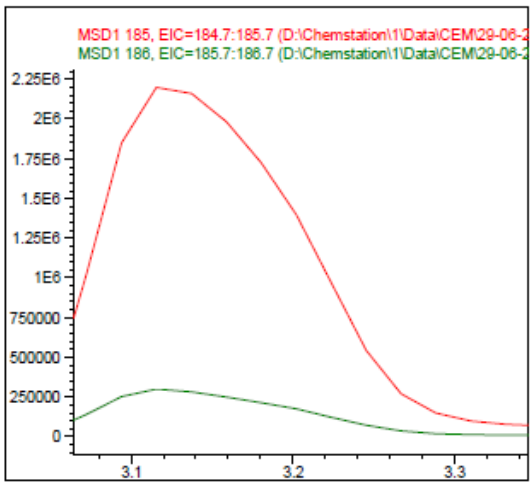
MSD1 185, EIC=184.7:185.7 (D:\Chemstation\1\Data\CEM\29-06-2
MSD1 186, EIC=185.7:186.7 (D:\Chemstation\1\Data\CEM\29-06-2
2.25E6
2E6
1.75E6
1.5E6
1.25E6
1E6
750000
500000
250000
0
3.1
3.2
3.3

2-(5-Methoxybenzofuran-2-yl)-1*H*-imidazole hydrochloride (5b)

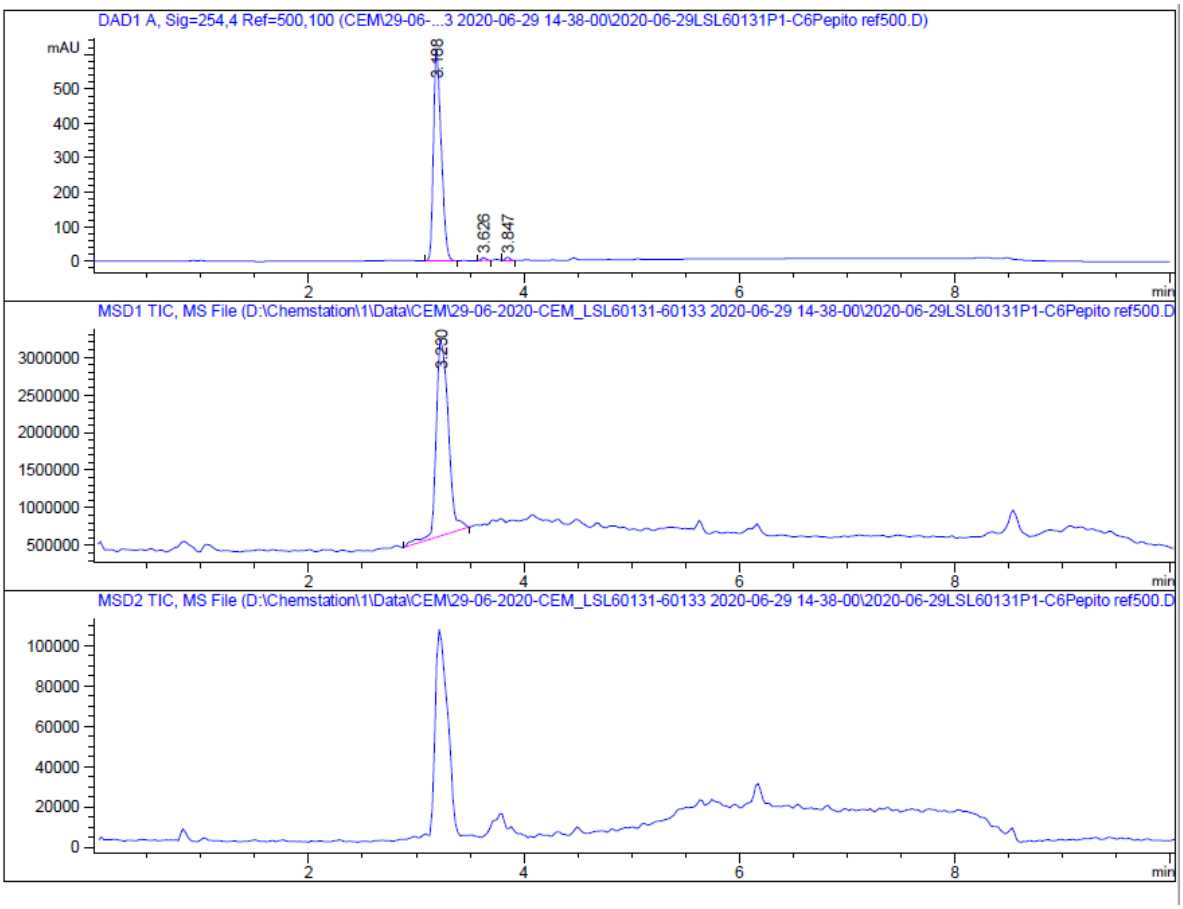


```
=====================================================================
                        Area Percent Report
=====================================================================

Sorted By             :      Signal
Multiplier            :      1.0000
Dilution              :      1.0000
Do not use Multiplier & Dilution Factor with ISTDs


Signal 1: DAD1 A, Sig=254,4 Ref=500,100

Peak RetTime Type  Width     Area      Height     Area
  #   [min]        [min]   [mAU*s]     [mAU]       %
----|-------|----|-------|----------|----------|--------|
   1   3.188 BB    0.0765 3075.78931  613.73615  98.4553
   2   3.626 BB    0.0463   24.02009    8.17429   0.7689
   3   3.847 BB    0.0476   24.23633    8.41937   0.7758

Totals :                  3124.04572  630.32981
```

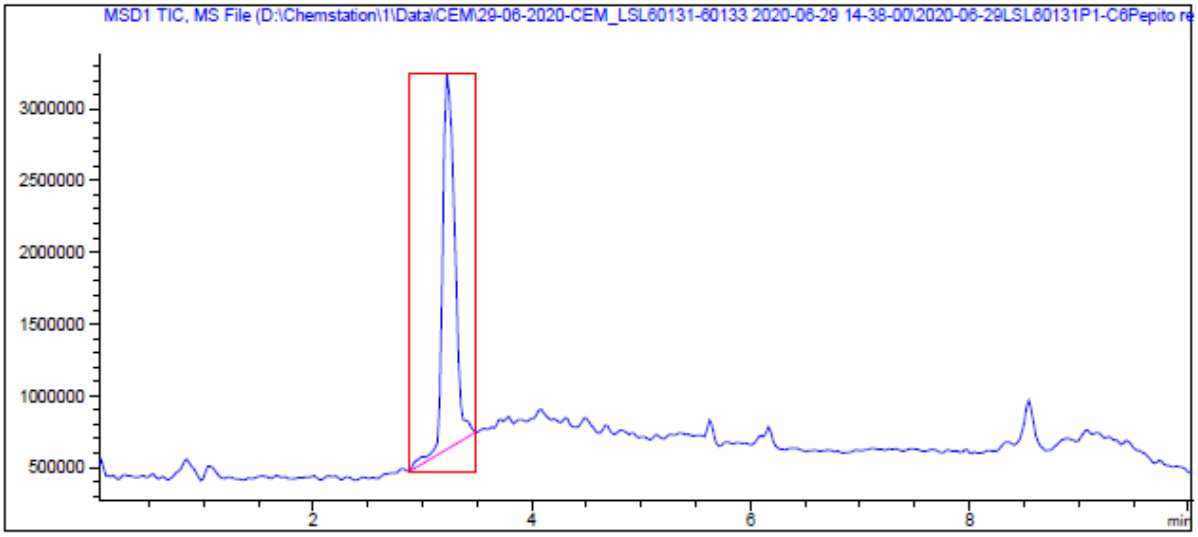
MSD1 TIC, MS File (D:\Chemstation\1\Data\CEM\29-06-2020-CEM_LSL60131-60133 2020-06-29 14-38-00\2020-06-29LSL60131P1-C6Pepito re
3000000
2500000
2000000
1500000
1000000
500000
2
4
6
8
min

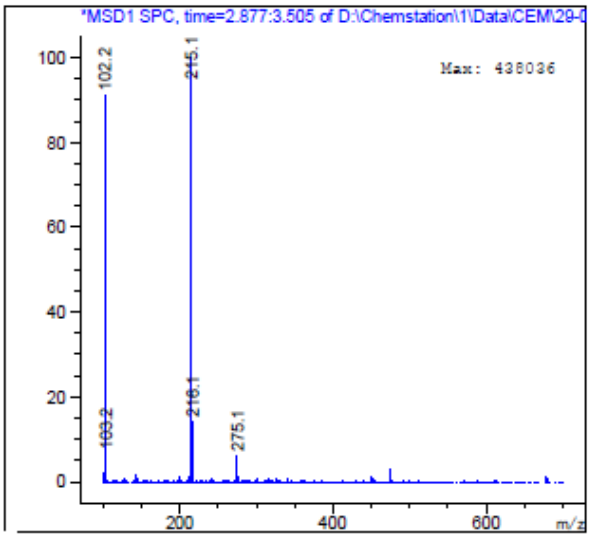
*MSD1 SPC, time=2.877:3.505 of D:\Chemstation\1\Data\CEM\29-0
Max: 436036
102.2
215.1
216.1
275.1
100
80
60
40
20
0
200
400
600
m/z

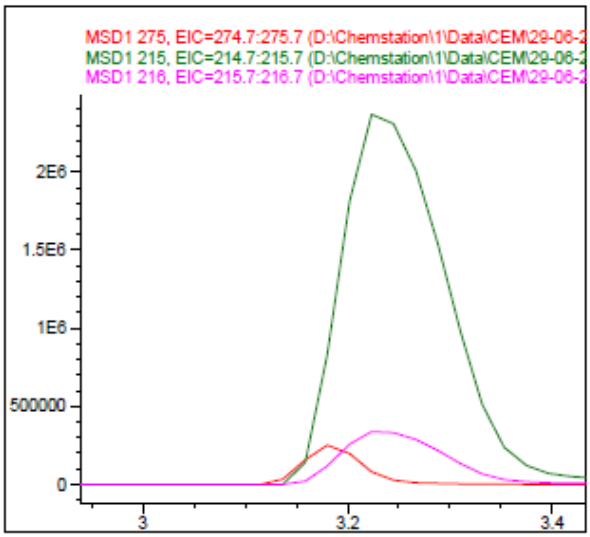
MSD1 275, EIC=274.7:275.7 (D:\Chemstation\1\Data\CEM\29-06-2
MSD1 215, EIC=214.7:215.7 (D:\Chemstation\1\Data\CEM\29-06-2
MSD1 216, EIC=215.7:216.7 (D:\Chemstation\1\Data\CEM\29-06-2
2E6
1.5E6
1E6
500000
0
3
3.2
3.4

2-(6-Methoxybenzofuran-2-yl)-1*H*-imidazole hydrochloride (5c)

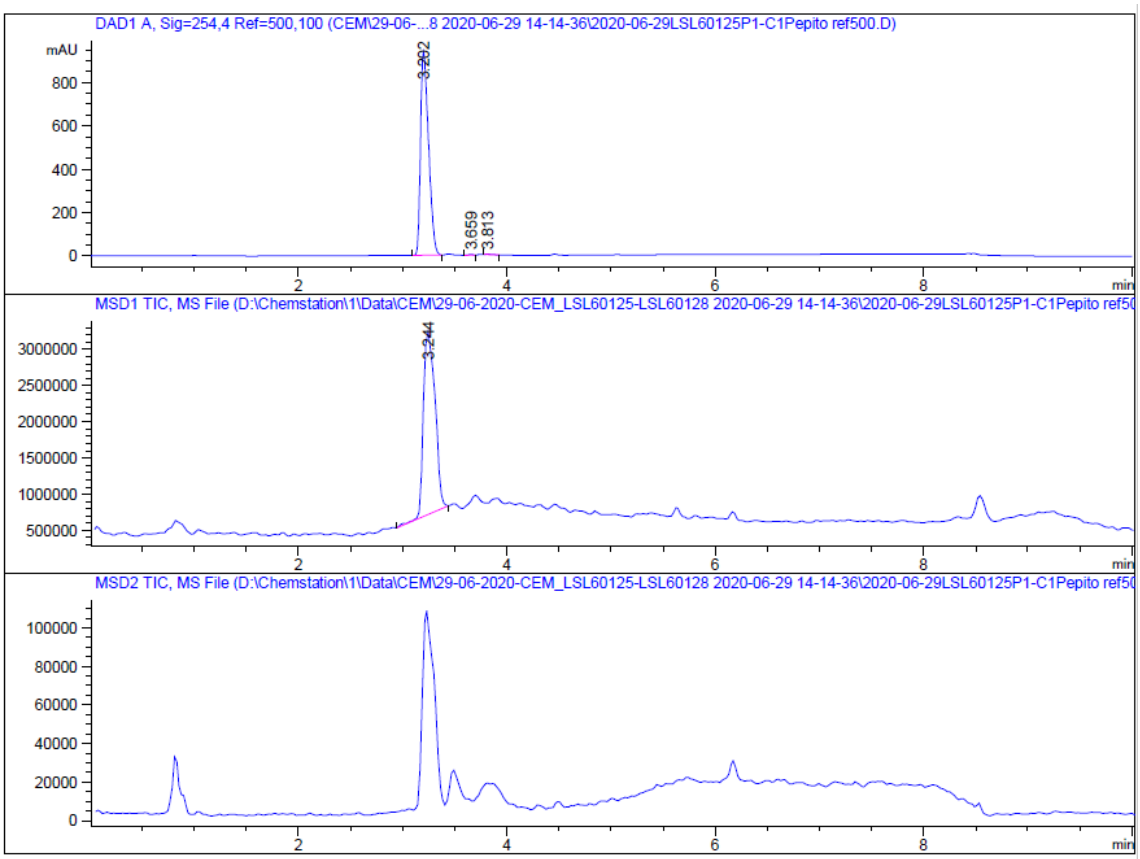


```
=====================================================================
                        Area Percent Report
=====================================================================

Sorted By             :      Signal
Multiplier            :      1.0000
Dilution              :      1.0000
Do not use Multiplier & Dilution Factor with ISTDs


Signal 1: DAD1 A, Sig=254,4 Ref=500,100

Peak RetTime Type  Width     Area      Height     Area
  #   [min]        [min]   [mAU*s]     [mAU]       %
----|-------|----|-------|----------|----------|--------|
   1   3.202 BB    0.0802 5028.13477  943.71252  99.6391
   2   3.659 BB    0.0461    8.19546    2.80256   0.1624
   3   3.813 BB    0.0733   10.01648    1.90532   0.1985

Totals :                  5046.34671  948.42041
```

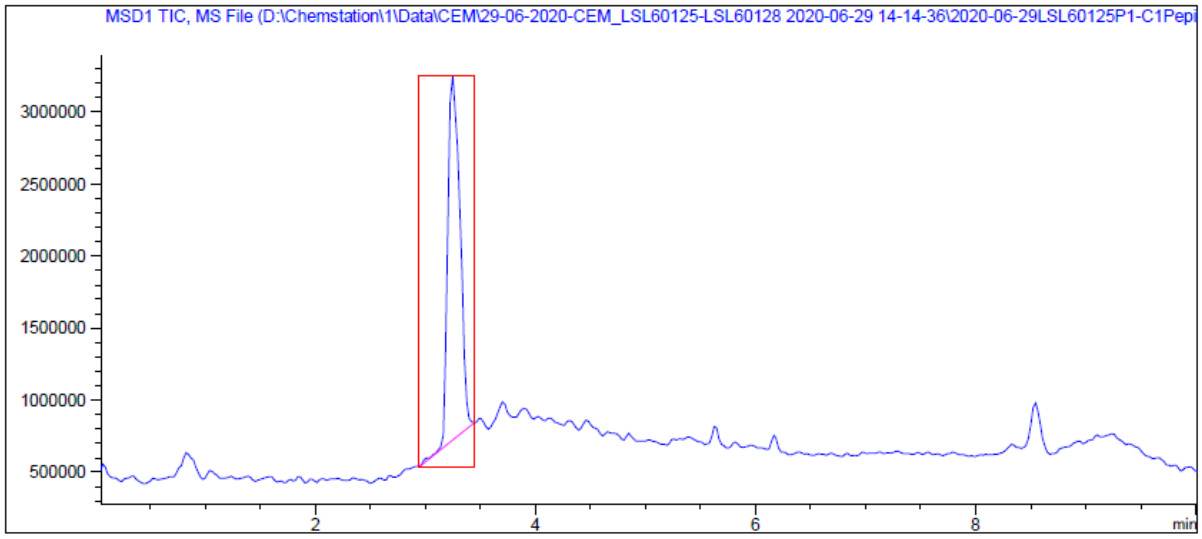
MSD1 TIC, MS File (D:\Chemstation\1\Data\CEM\29-06-2020-CEM_LSL60125-LSL60128 2020-06-29 14-14-36\2020-06-29LSL60125P1-C1Pep
3000000
2500000
2000000
1500000
1000000
500000
2
4
6
8
min

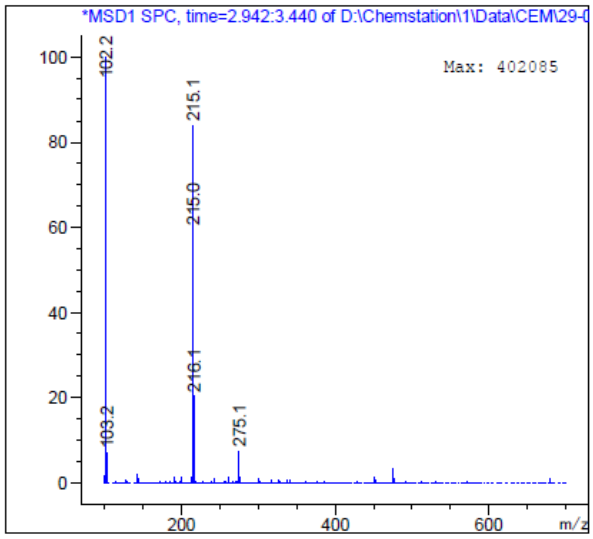
*MSD1 SPC, time=2.942:3.440 of D:\Chemstation\1\Data\CEM\29-0
Max: 402085
100
80
60
40
20
0
402.2
215.1
215.0
216.1
103.2
275.1
200
400
600
m/z

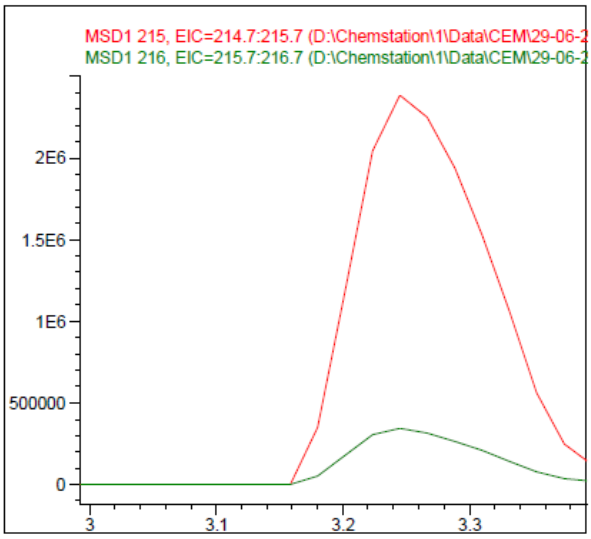
MSD1 215, EIC=214.7:215.7 (D:\Chemstation\1\Data\CEM\29-06-2
MSD1 216, EIC=215.7:216.7 (D:\Chemstation\1\Data\CEM\29-06-2
2E6
1.5E6
1E6
500000
0
3
3.1
3.2
3.3

2-(5-Bromobenzofuran-2-yl)-1*H*-imidazole hydrochloride (5d)

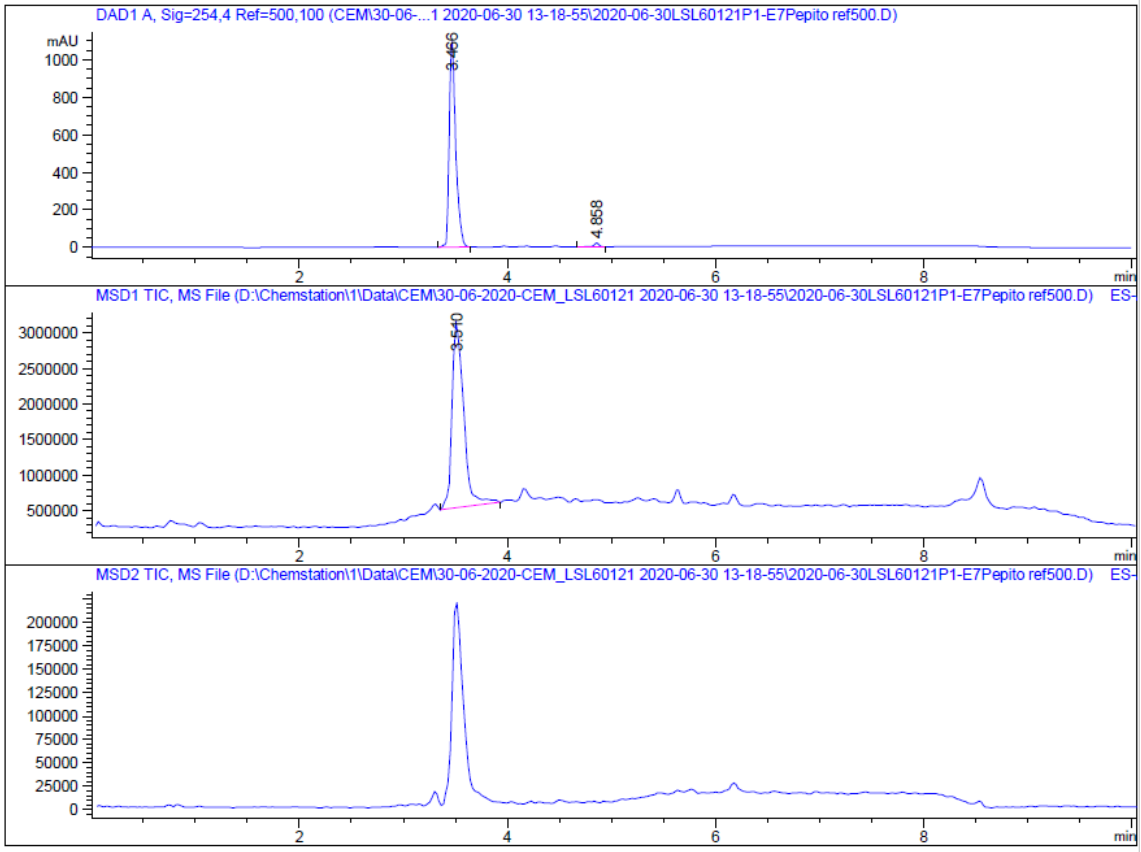

==========

Area Percent Report

==========

Sorted By : Signal
Multiplier : 1.0000
Dilution : 1.0000
Do not use Multiplier & Dilution Factor with ISTDs

Signal 1: DAD1 A, Sig=254,4 Ref=500,100

Peak #	RetTime [min]	Type	Width [min]	Area [mAU*s]	Height [mAU]	Area %
1	3.466	BB	0.0623	4700.52295	1089.63074	98.6140
2	4.858	BB	0.0519	66.06541	19.32478	1.3860
Totals :				4766.58836	1108.95552	

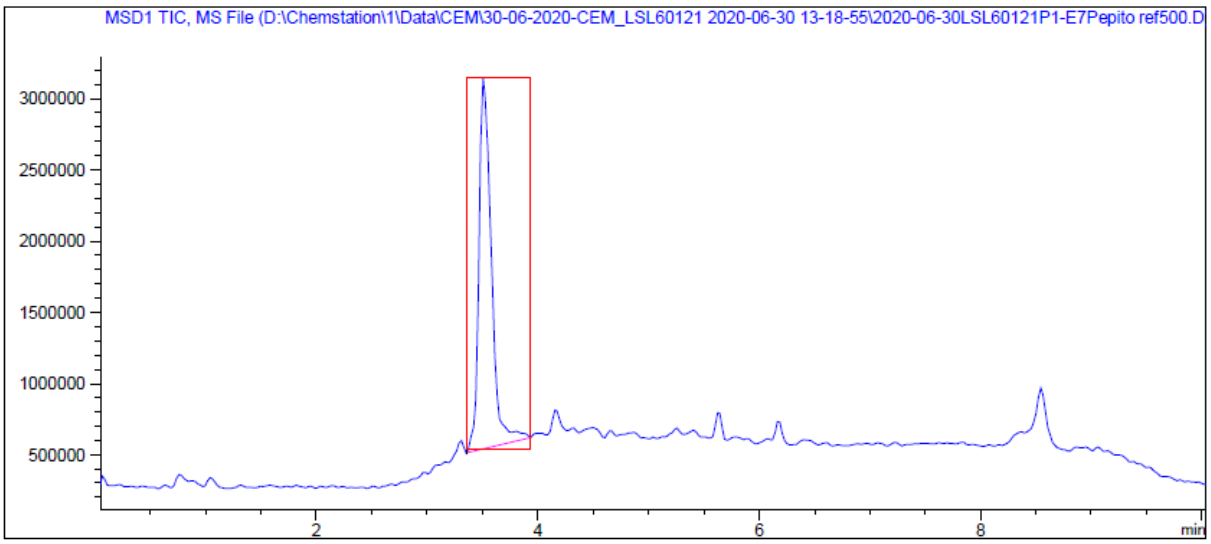
MSD1 TIC, MS File (D:\Chemstation\1\Data\CEM\30-06-2020-CEM_LSL60121 2020-06-30 13-18-55\2020-06-30LSL60121P1-E7Pepito ref500.D
3000000
2500000
2000000
1500000
1000000
500000
2
4
6
8
min

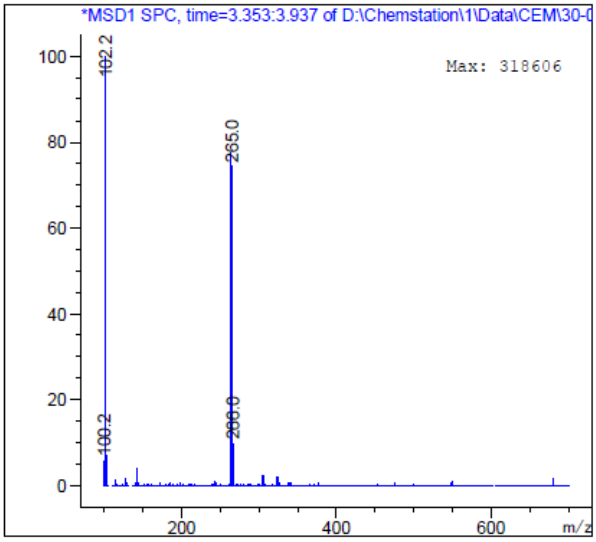
*MSD1 SPC, time=3.353:3.937 of D:\Chemstation\1\Data\CEM\30-0
Max: 318606
102.2
265.0
100.2
280.0
100
80
60
40
20
0
200
400
600
m/z

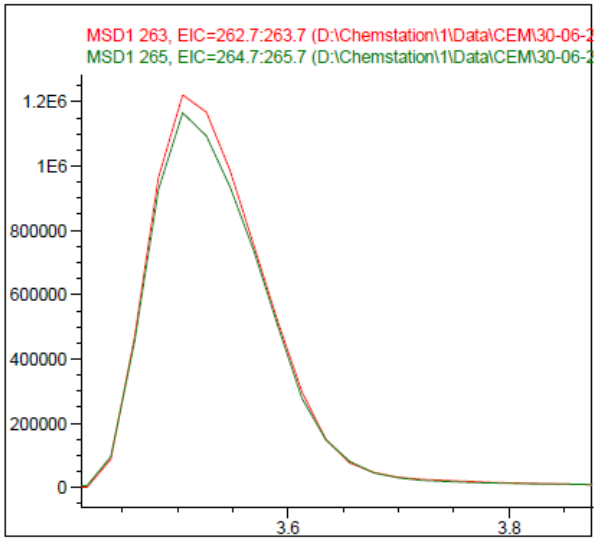
MSD1 263, EIC=262.7:263.7 (D:\Chemstation\1\Data\CEM\30-06-2
MSD1 265, EIC=264.7:265.7 (D:\Chemstation\1\Data\CEM\30-06-2
1.2E6
1E6
800000
600000
400000
200000
0
3.6
3.8

2-(5-Hydroxybenzofuran-2-yl)-1*H*-imidazole hydrochloride (6b)

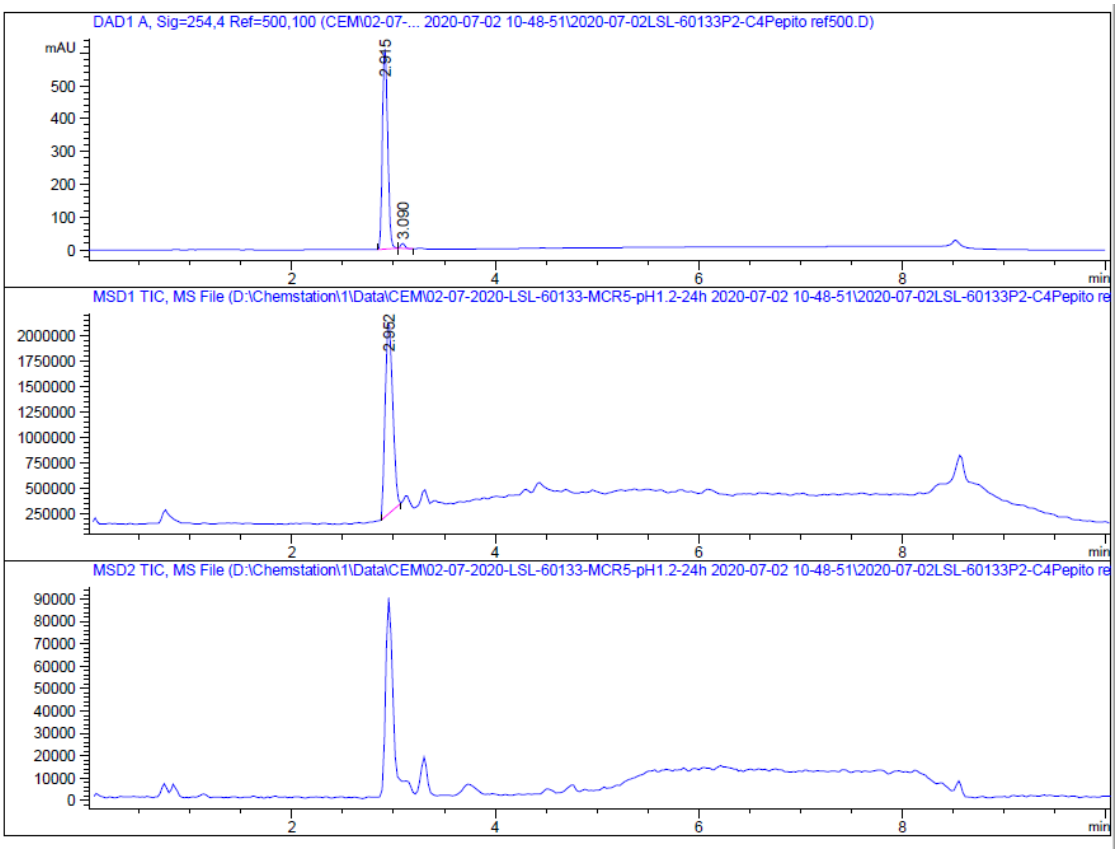


```
=====================================================================
                        Area Percent Report
=====================================================================

Sorted By             :      Signal
Multiplier            :      1.0000
Dilution              :      1.0000
Do not use Multiplier & Dilution Factor with ISTDs


Signal 1: DAD1 A, Sig=254,4 Ref=500,100

Peak RetTime Type  Width     Area      Height     Area
  #   [min]        [min]   [mAU*s]     [mAU]       %
----|-------|----|-------|----------|----------|--------|
   1   2.915 BB    0.0559 2186.83765  609.37555  98.0891
   2   3.090 BB    0.0452   42.60264   14.98559   1.9109

Totals :                  2229.44029  624.36114
```

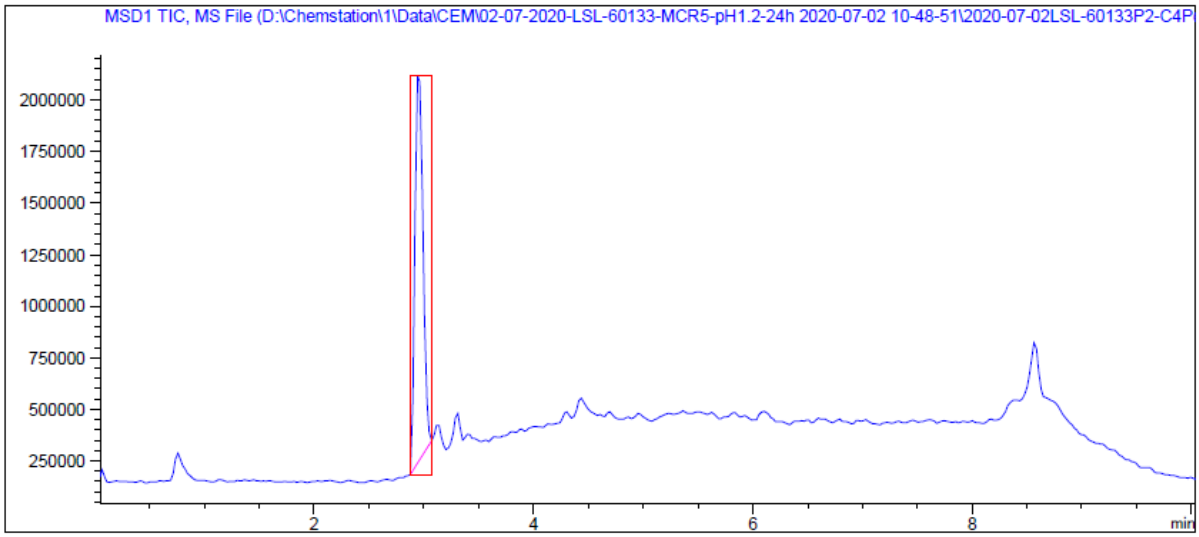
MSD1 TIC, MS File (D:\Chemstation\1\Data\CEM\02-07-2020-LSL-60133-MCR5-pH1.2-24h 2020-07-02 10-48-51\2020-07-02LSL-60133P2-C4P
2000000
1750000
1500000
1250000
1000000
750000
500000
250000
2
4
6
8
min

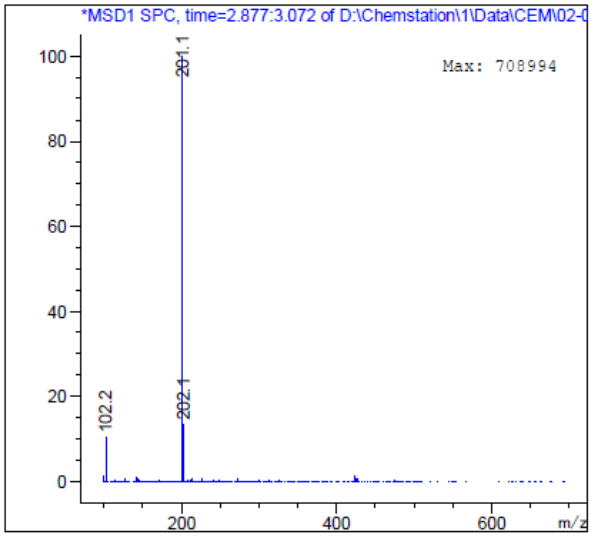
*MSD1 SPC, time=2.877:3.072 of D:\Chemstation\1\Data\CEM\02-0
Max: 708994
201.1
102.2
202.1
100
80
60
40
20
0
200
400
600
m/z

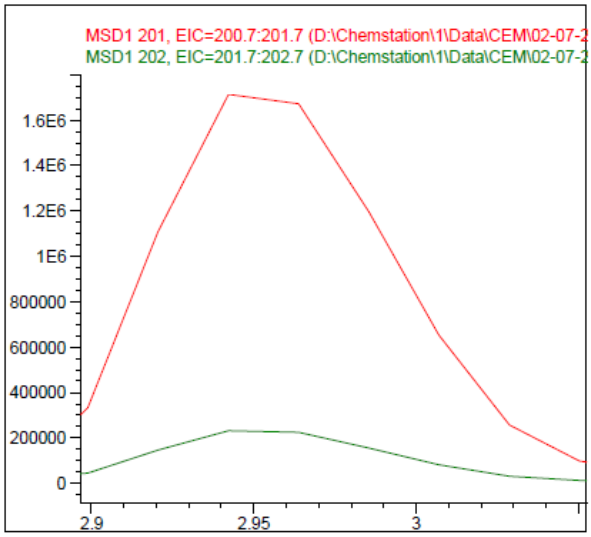
MSD1 201, EIC=200.7:201.7 (D:\Chemstation\1\Data\CEM\02-07-2
MSD1 202, EIC=201.7:202.7 (D:\Chemstation\1\Data\CEM\02-07-2
1.6E6
1.4E6
1.2E6
1E6
800000
600000
400000
200000
0
2.9
2.95
3

2-(6-Hydroxybenzofuran-2-yl)-1*H*-imidazole hydrochloride (6c)

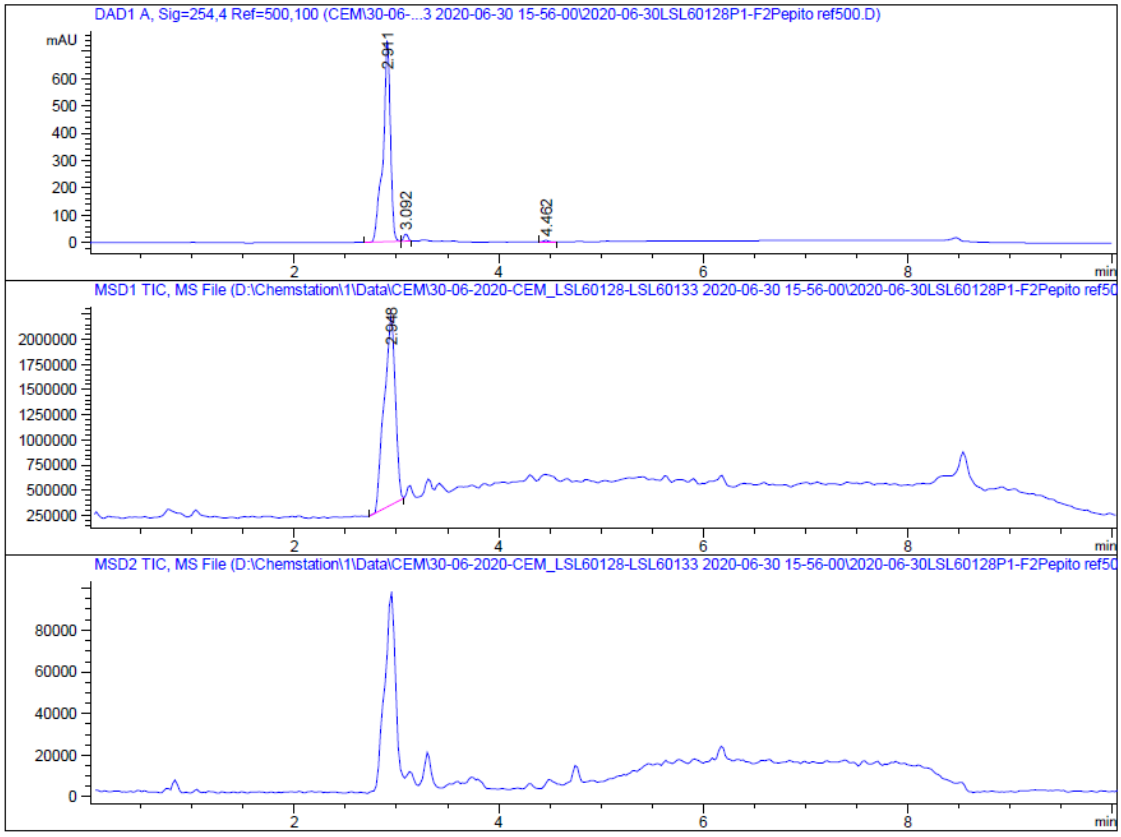

==========

Area Percent Report

==========

Sorted By : Signal
Multiplier : 1.0000
Dilution : 1.0000
Do not use Multiplier & Dilution Factor with ISTDs

Signal 1: DAD1 A, Sig=254,4 Ref=500,100

Peak #	RetTime [min]	Type	Width [min]	Area [mAU*s]	Height [mAU]	Area %
1	2.911	BB	0.0751	3718.08862	734.25549	97.6147
2	3.092	BB	0.0446	72.39094	25.91696	1.9006
3	4.462	BB	0.0528	18.46445	5.55345	0.4848
Totals :				3808.94401	765.72590	

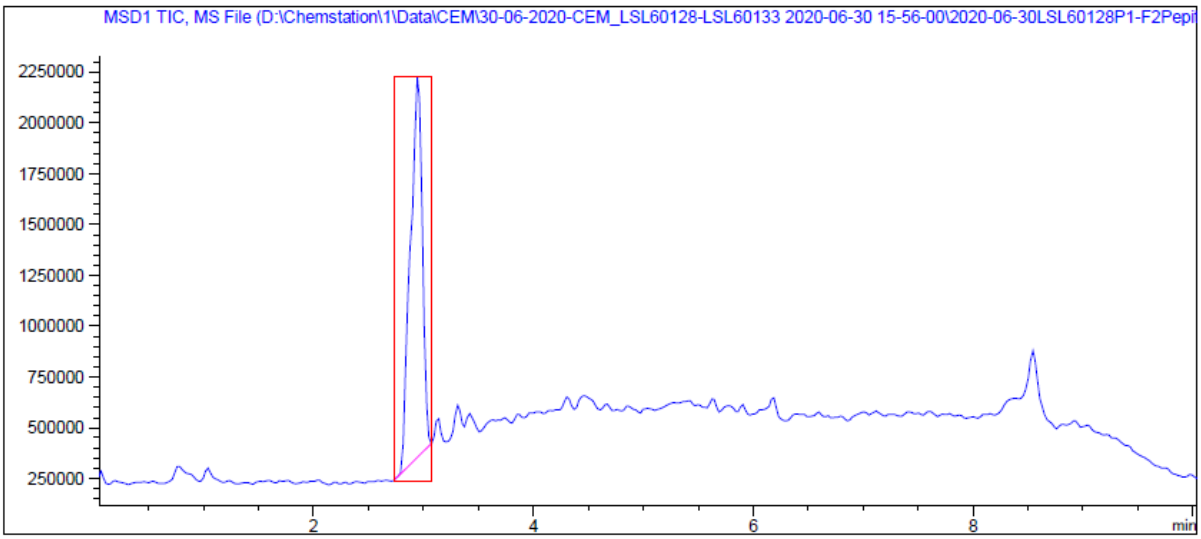
MSD1 TIC, MS File (D:\Chemstation\1\Data\CEM\30-06-2020-CEM_LSL60128-LSL60133 2020-06-30 15-56-00\2020-06-30LSL60128P1-F2Pepi
2250000
2000000
1750000
1500000
1250000
1000000
750000
500000
250000
2
4
6
8
min

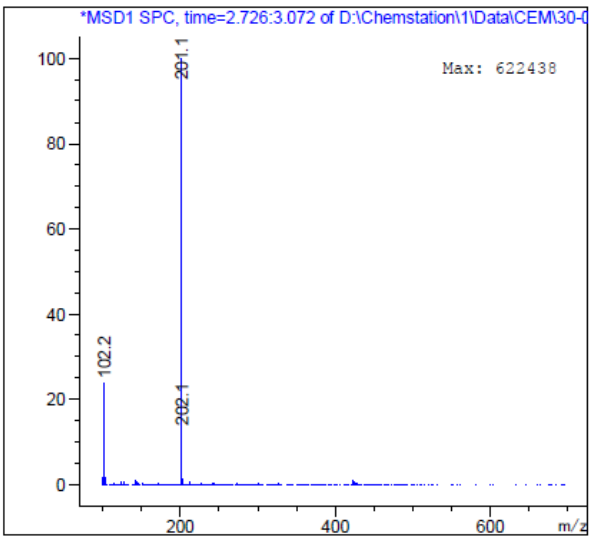
*MSD1 SPC, time=2.726:3.072 of D:\Chemstation\1\Data\CEM\30-0
Max: 622438
201.1
202.1
102.2
100
80
60
40
20
0
200
400
600
m/z

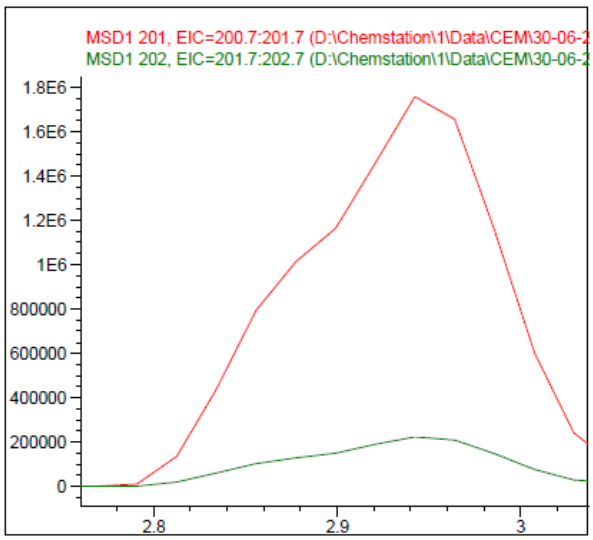
MSD1 201, EIC=200.7:201.7 (D:\Chemstation\1\Data\CEM\30-06-2
MSD1 202, EIC=201.7:202.7 (D:\Chemstation\1\Data\CEM\30-06-2
1.8E6
1.6E6
1.4E6
1.2E6
1E6
800000
600000
400000
200000
0
2.8
2.9
3

1-Methyl-2-(benzofuran-2-yl)-1*H*-imidazole hydrochloride (7a)

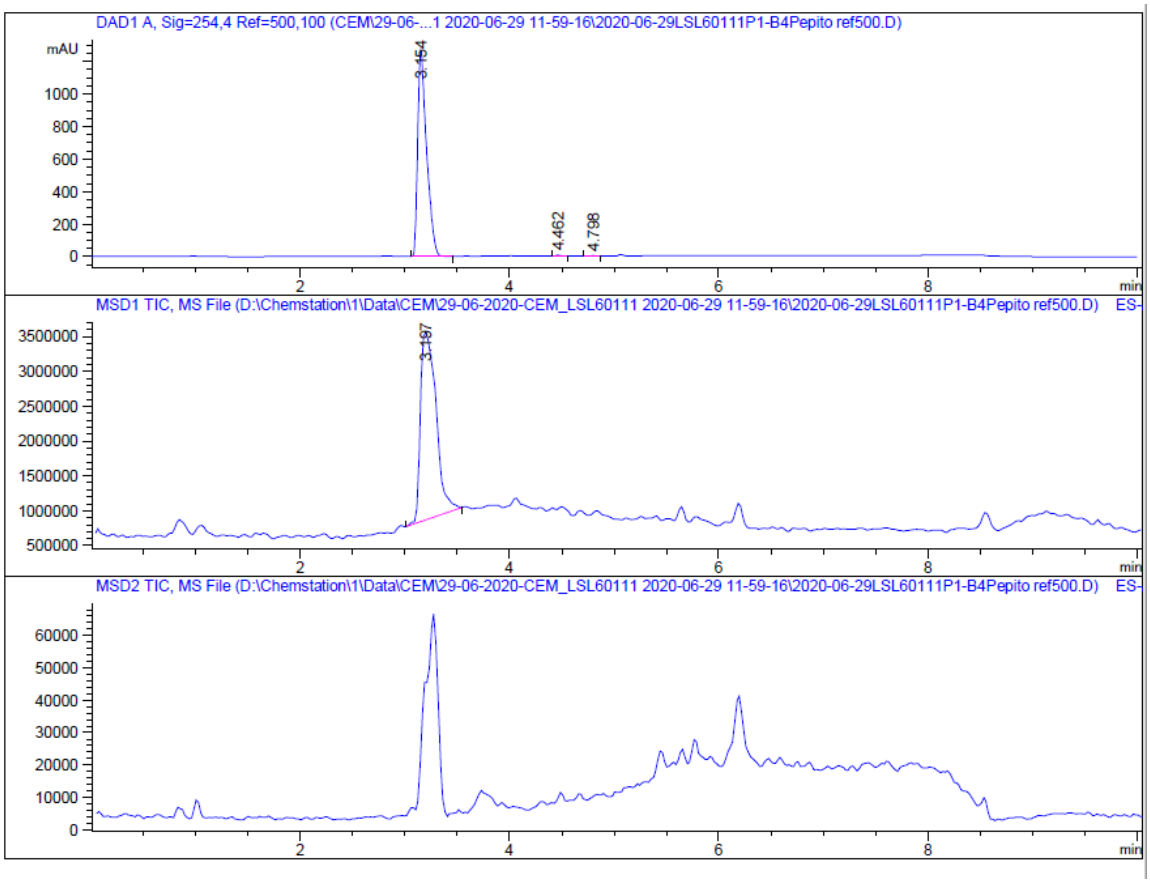


```
=====================================================================
                        Area Percent Report
=====================================================================

Sorted By             :      Signal
Multiplier            :      1.0000
Dilution              :      1.0000
Do not use Multiplier & Dilution Factor with ISTDs


Signal 1: DAD1 A, Sig=254,4 Ref=500,100

Peak RetTime Type  Width     Area      Height     Area
  #   [min]        [min]   [mAU*s]     [mAU]       %
----|-------|----|-------|----------|----------|--------|
   1   3.154 BB    0.0866 7458.54102 1268.48767  99.6504
   2   4.462 BB    0.0540   18.69691    5.45366   0.2498
   3   4.798 BB    0.0611    7.47288    1.85068   0.0998

Totals :                  7484.71080 1275.79201
```

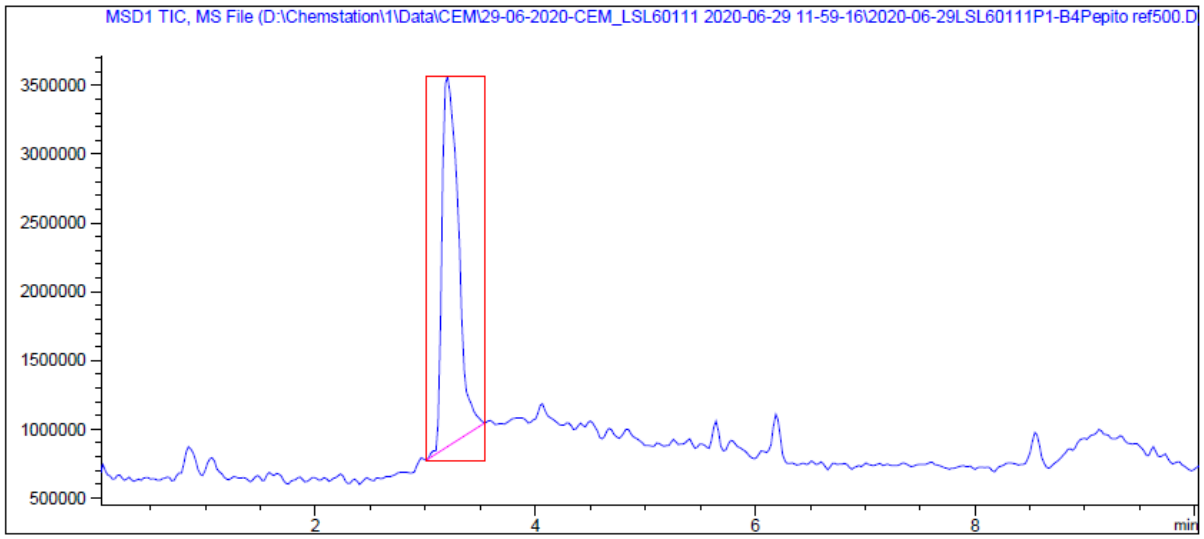
MSD1 TIC, MS File (D:\Chemstation\1\Data\CEM\29-06-2020-CEM_LSL60111 2020-06-29 11-59-16\2020-06-29LSL60111P1-B4Pepito ref500.D
3500000
3000000
2500000
2000000
1500000
1000000
500000
2
4
6
8
min

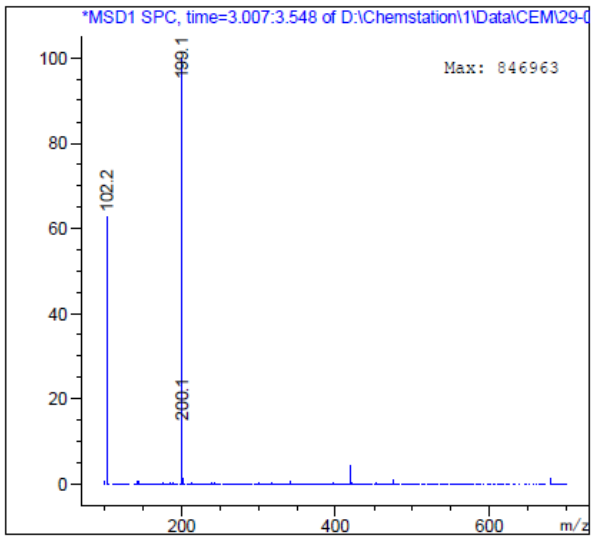
*MSD1 SPC, time=3.007:3.548 of D:\Chemstation\1\Data\CEM\29-0
Max: 846963
199.1
102.2
200.1
100
80
60
40
20
0
200
400
600
m/z

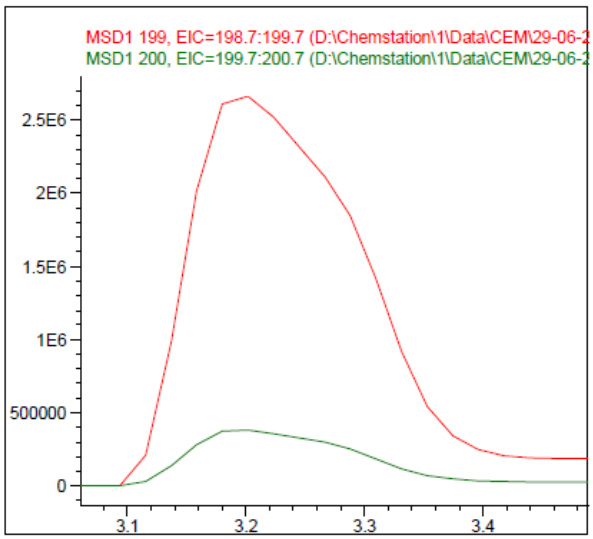
MSD1 199, EIC=198.7:199.7 (D:\Chemstation\1\Data\CEM\29-06-2
MSD1 200, EIC=199.7:200.7 (D:\Chemstation\1\Data\CEM\29-06-2
2.5E6
2E6
1.5E6
1E6
500000
0
3.1
3.2
3.3
3.4

1-Ethyl-2-(benzofuran-2-yl)-1*H*-imidazole hydrochloride (7aa)

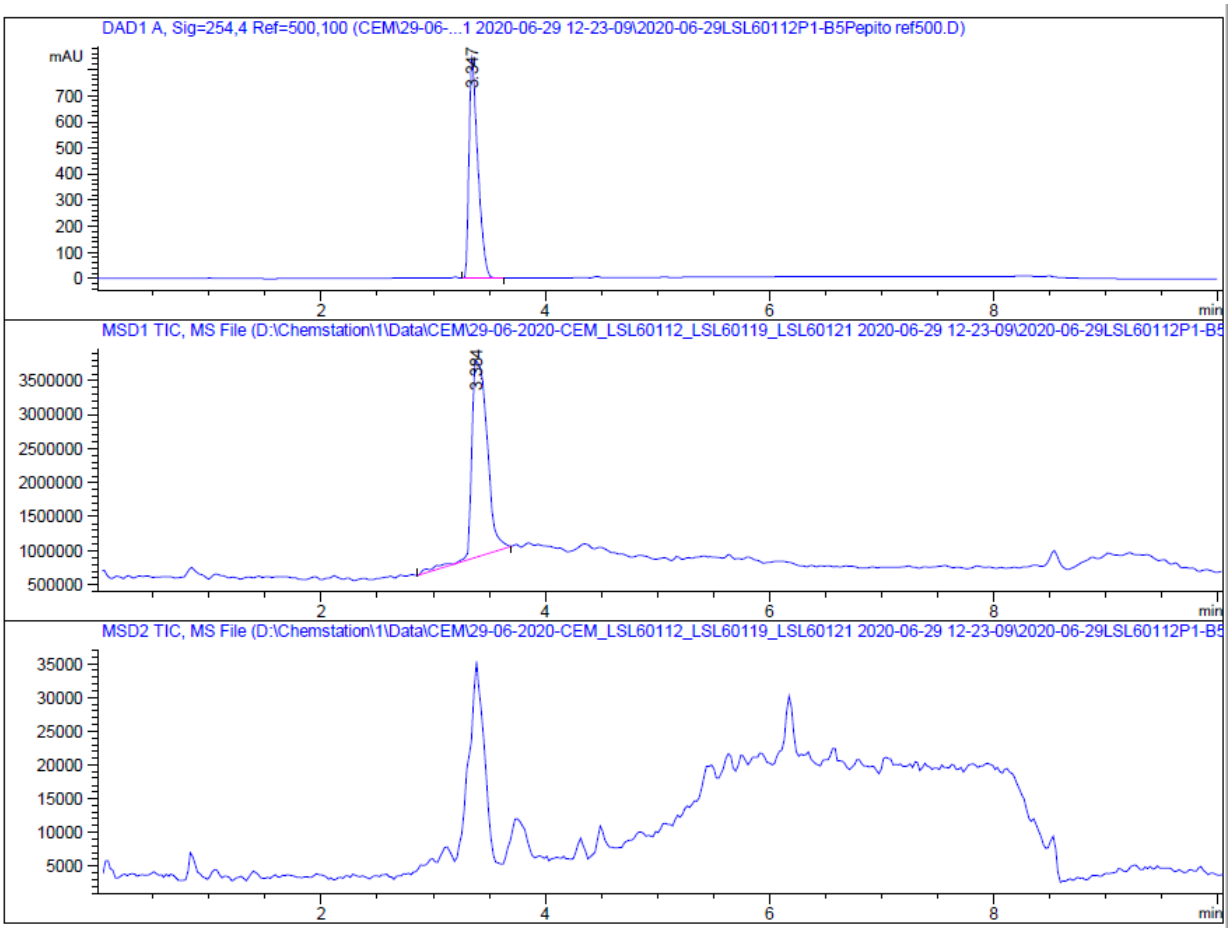


```
=====================================================================
                        Area Percent Report
=====================================================================

Sorted By             :      Signal
Multiplier            :      1.0000
Dilution              :      1.0000
Do not use Multiplier & Dilution Factor with ISTDs


Signal 1: DAD1 A, Sig=254,4 Ref=500,100

Peak RetTime Type  Width     Area      Height     Area
  #   [min]        [min]   [mAU*s]     [mAU]       %
----|-------|----|-------|----------|----------|--------|
   1   3.347 BB    0.0802 4639.06592  842.49225 100.0000

Totals :                  4639.06592  842.49225
```

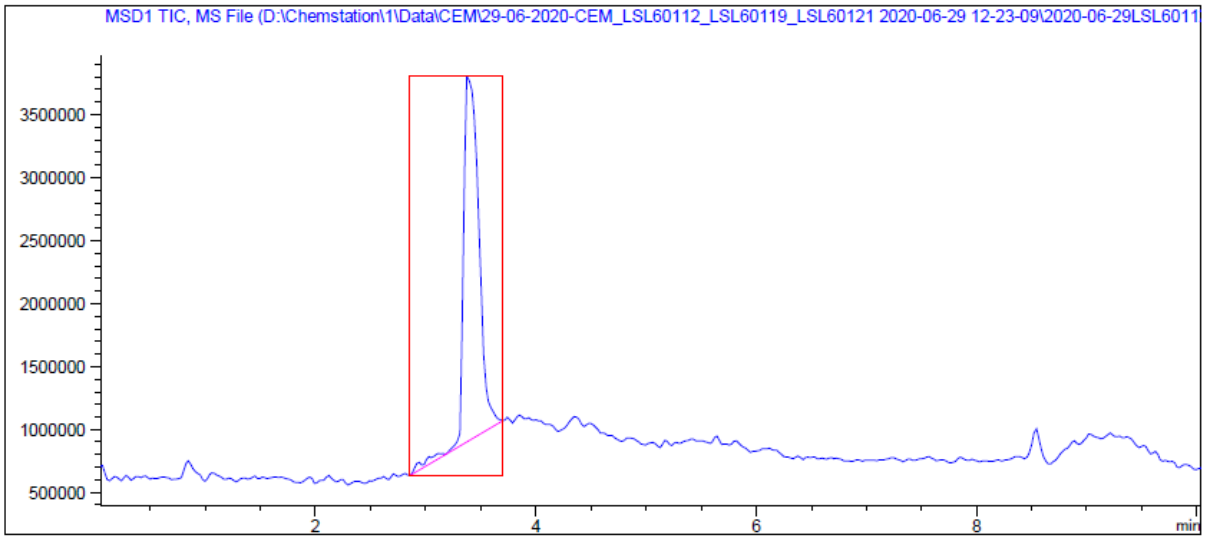
MSD1 TIC, MS File (D:\Chemstation\1\Data\CEM\29-06-2020-CEM_LSL60112_LSL60119_LSL60121 2020-06-29 12-23-09\2020-06-29LSL6011
3500000
3000000
2500000
2000000
1500000
1000000
500000
2
4
6
8
min

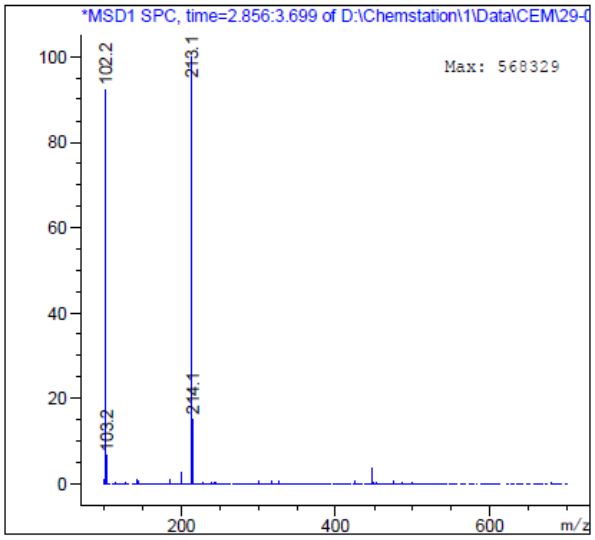
*MSD1 SPC, time=2.856:3.699 of D:\Chemstation\1\Data\CEM\29-0
Max: 568329
102.2
213.1
103.2
214.1
100
80
60
40
20
0
200
400
600
m/z

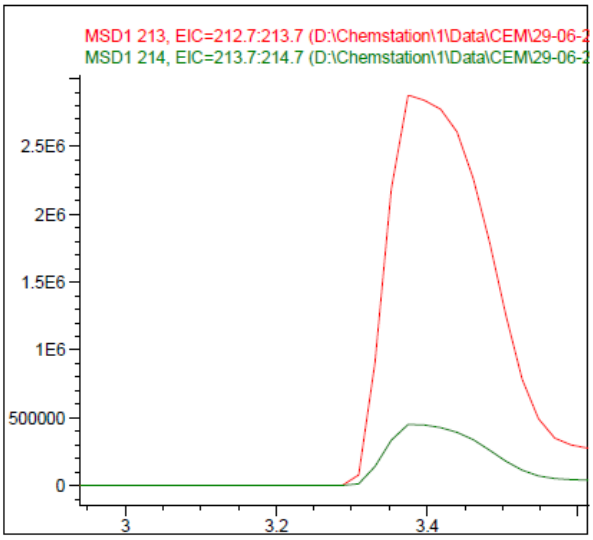
MSD1 213, EIC=212.7:213.7 (D:\Chemstation\1\Data\CEM\29-06-2
MSD1 214, EIC=213.7:214.7 (D:\Chemstation\1\Data\CEM\29-06-2
2.5E6
2E6
1.5E6
1E6
500000
0
3
3.2
3.4

1-Ethyl-2-(5-methoxybenzofuran-2-yl)-1*H*-imidazole hydrochloride (7b)

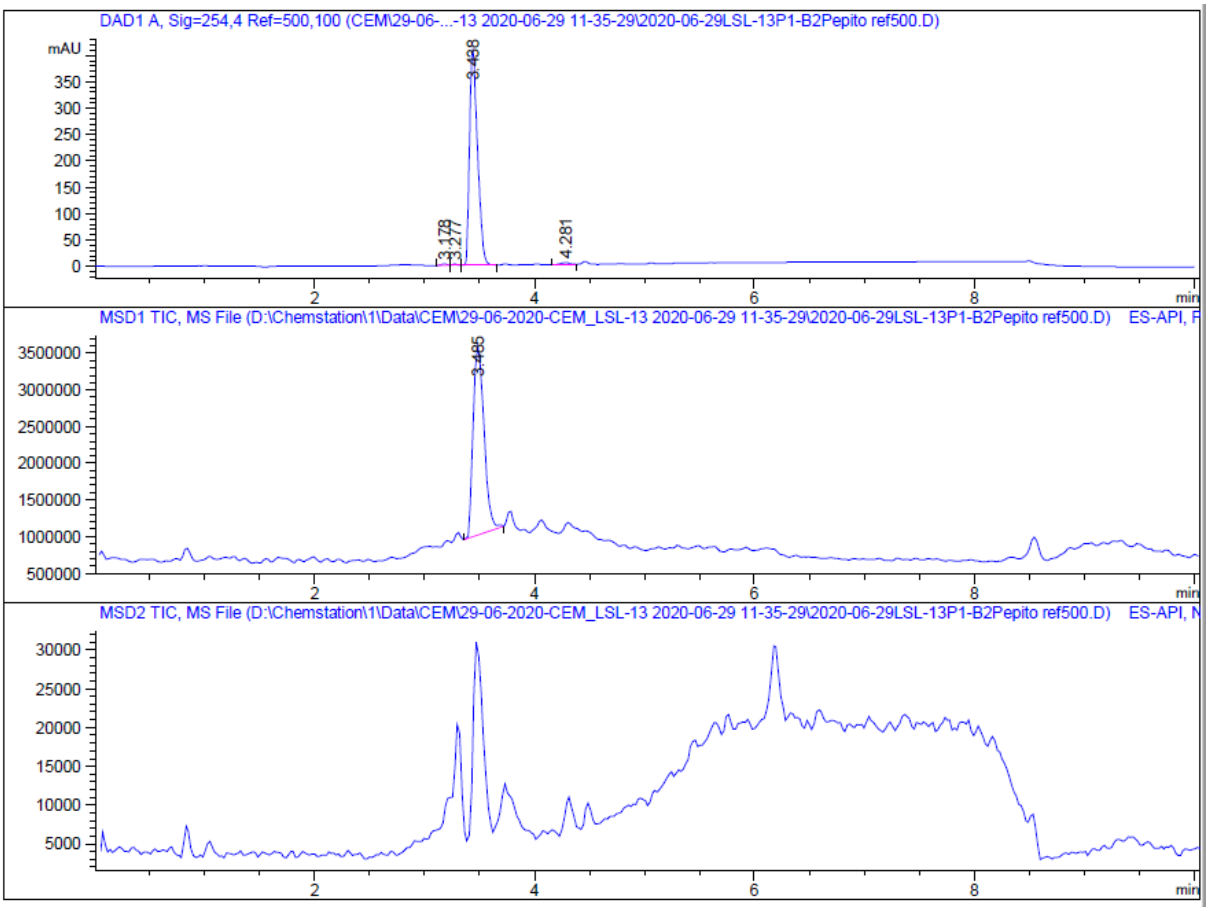


```
============================================================
                      Area Percent Report
============================================================

Sorted By             :      Signal
Multiplier            :      1.0000
Dilution              :      1.0000
Do not use Multiplier & Dilution Factor with ISTDs


Signal 1: DAD1 A, Sig=254,4 Ref=500,100

Peak RetTime Type  Width     Area      Height     Area
  #   [min]        [min]   [mAU*s]     [mAU]       %
----|-------|----|-------|----------|----------|--------|
   1   3.178 BB    0.0592    9.26722    2.62444   0.4410
   2   3.277 BB    0.0423    5.66840    2.18320   0.2697
   3   3.438 BB    0.0770 2067.37280  408.49457  98.3747
   4   4.281 BB    0.0769   19.22038    3.68104   0.9146

Totals :                  2101.52879  416.98325
```

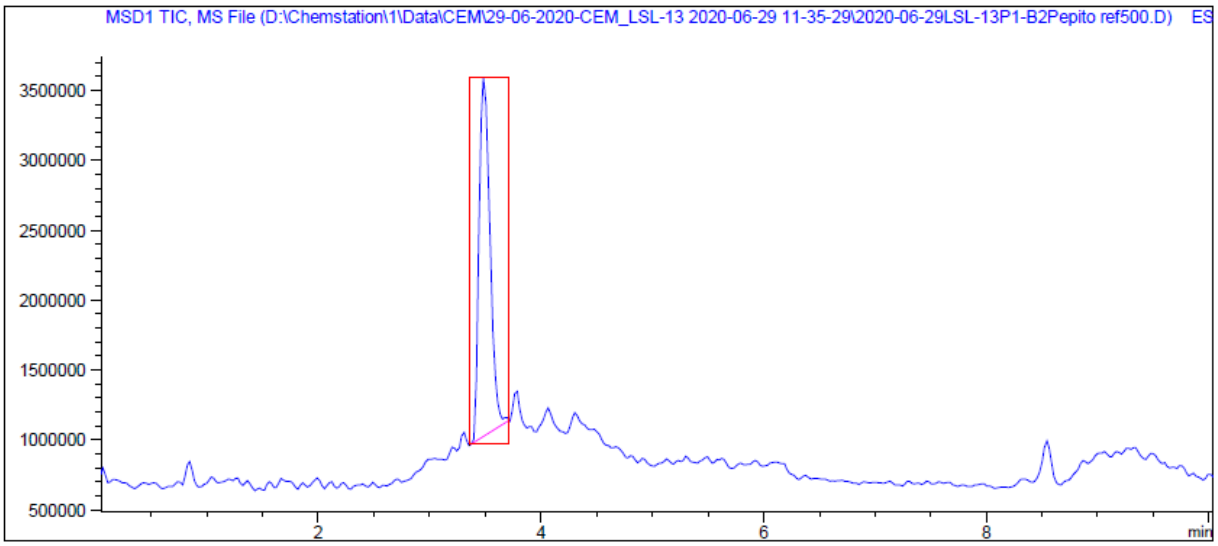
MSD1 TIC, MS File (D:\Chemstation\1\Data\CEM\29-06-2020-CEM_LSL-13 2020-06-29 11-35-29\2020-06-29LSL-13P1-B2Pepito ref500.D) ES
3500000
3000000
2500000
2000000
1500000
1000000
500000
2
4
6
8
min

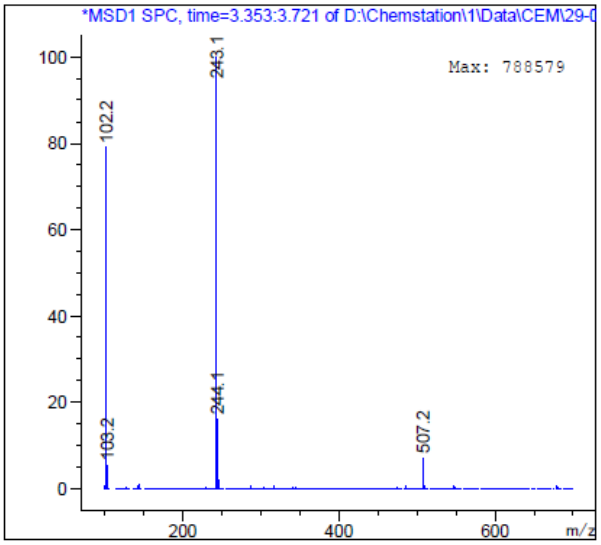
*MSD1 SPC, time=3.353:3.721 of D:\Chemstation\1\Data\CEM\29-0
Max: 788579
100
80
60
40
20
0
102.2
243.1
244.1
103.2
507.2
200
400
600
m/z

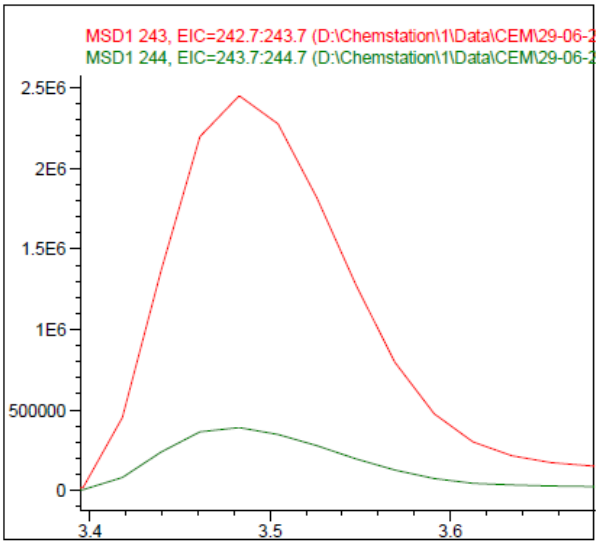
MSD1 243, EIC=242.7:243.7 (D:\Chemstation\1\Data\CEM\29-06-2
MSD1 244, EIC=243.7:244.7 (D:\Chemstation\1\Data\CEM\29-06-2
2.5E6
2E6
1.5E6
1E6
500000
0
3.4
3.5
3.6

1-Ethyl-2-(6-methoxybenzofuran-2-yl)-1*H*-imidazole hydrochloride (7c)

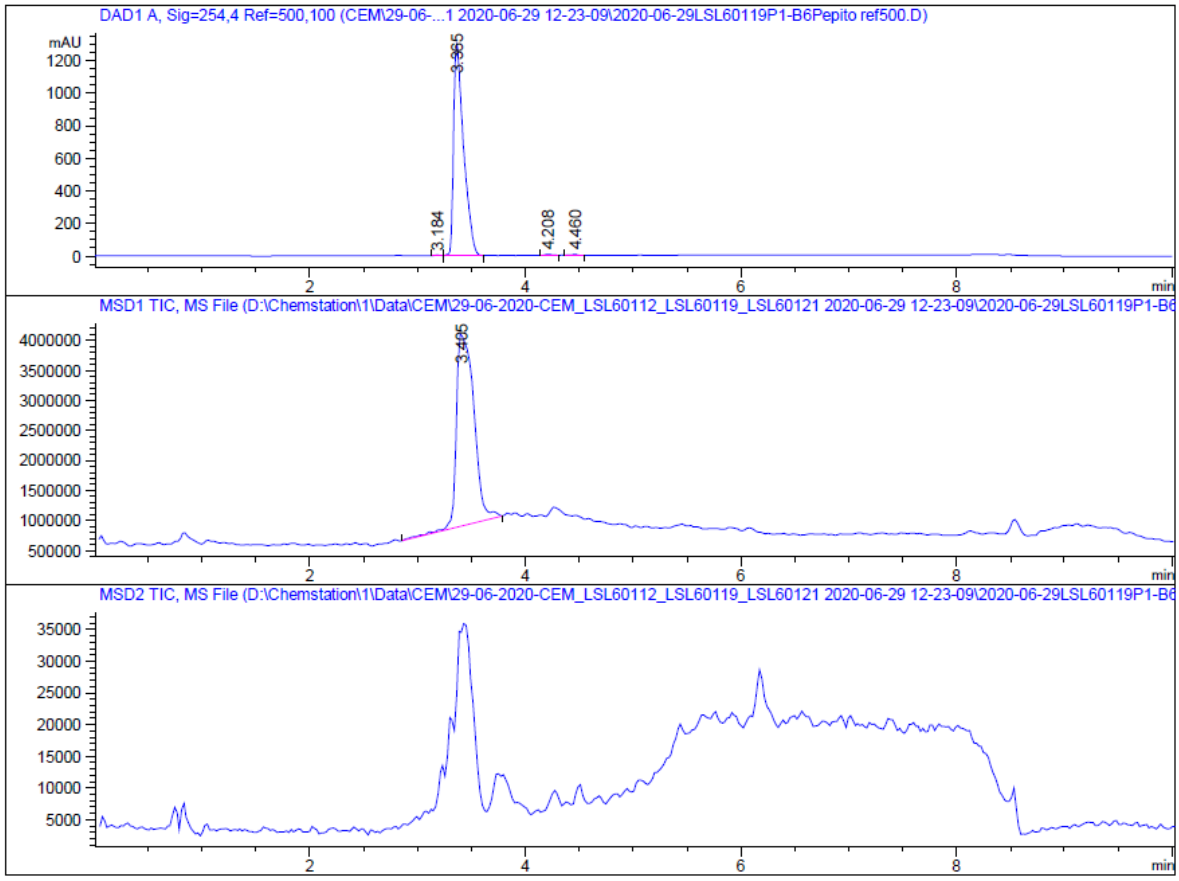


```
============================================================
                      Area Percent Report
============================================================

Sorted By             :      Signal
Multiplier            :      1.0000
Dilution              :      1.0000
Do not use Multiplier & Dilution Factor with ISTDs


Signal 1: DAD1 A, Sig=254,4 Ref=500,100

Peak RetTime Type  Width     Area      Height     Area
  #   [min]        [min]   [mAU*s]     [mAU]       %
----|-------|----|-------|----------|----------|--------|
   1   3.184 BB    0.0484   15.03643    4.82012   0.1780
   2   3.365 BB    0.0911 8379.78711 1301.08167  99.2089
   3   4.208 BB    0.0748   28.80082    5.91957   0.3410
   4   4.460 BB    0.0593   22.98279    5.67076   0.2721

Totals :                  8446.60715 1317.49211
```

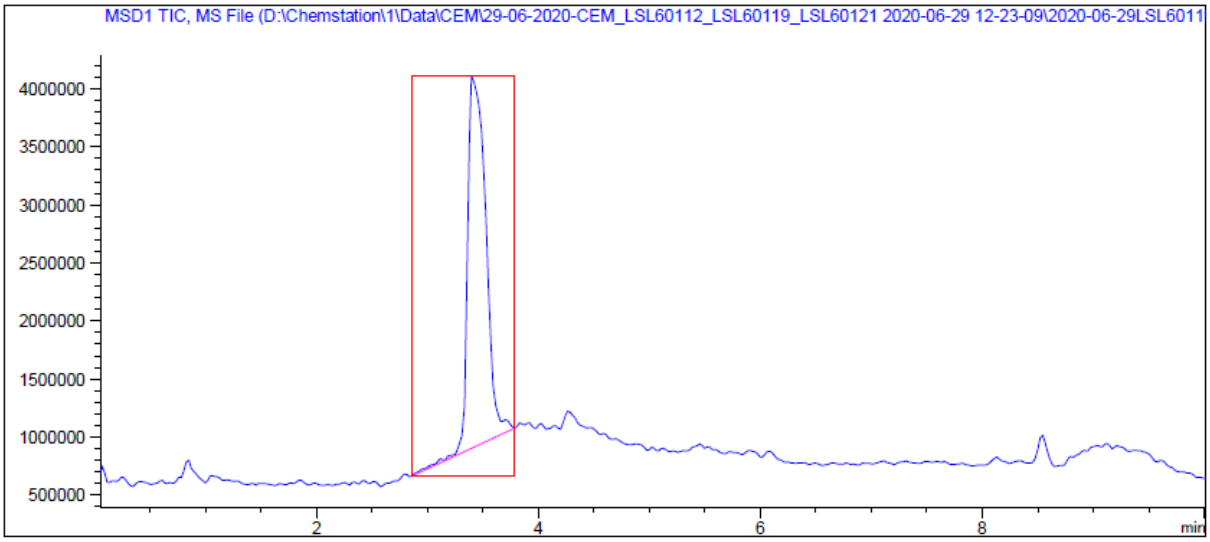
MSD1 TIC, MS File (D:\Chemstation\1\Data\CEM\29-06-2020-CEM_LSL60112_LSL60119_LSL60121 2020-06-29 12-23-09\2020-06-29LSL6011
4000000
3500000
3000000
2500000
2000000
1500000
1000000
500000
2
4
6
8
min

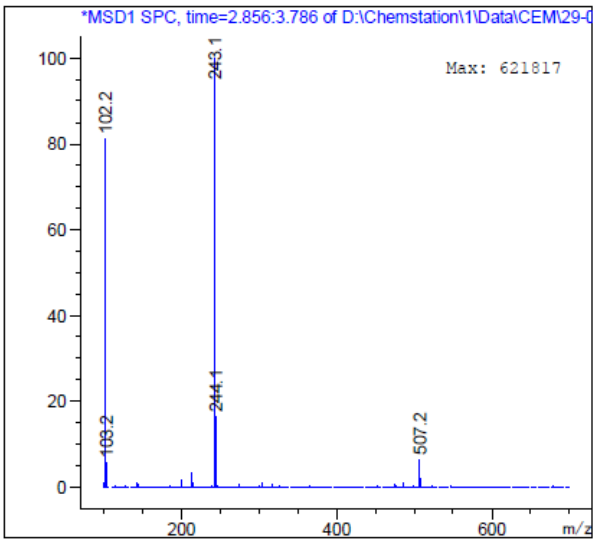
*MSD1 SPC, time=2.856:3.786 of D:\Chemstation\1\Data\CEM\29-0
Max: 621817
243.1
102.2
244.1
103.2
507.2
100
80
60
40
20
0
200
400
600
m/z

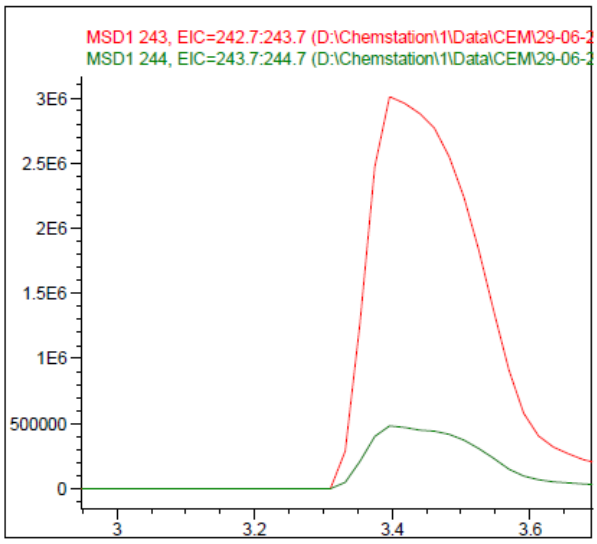
MSD1 243, EIC=242.7:243.7 (D:\Chemstation\1\Data\CEM\29-06-2
MSD1 244, EIC=243.7:244.7 (D:\Chemstation\1\Data\CEM\29-06-2
3E6
2.5E6
2E6
1.5E6
1E6
500000
0
3
3.2
3.4
3.6

Molecular Formula Strings (Smiles)

Compound	SMILE	I_2-IR Binding Affinities (pKi)	α_2-AR Binding Affinities (pKi)	Selectivity (I_2/α_2)
LSL60101	C12=CC=CC=C1C=C(C3=NC=CN3)O2.Cl	6.67±0.09	3.18±0.17	3090
5b	COC1=CC=C(OC(C2=NC=CN2)=C3)C3=C1.Cl	6.41±0.16	3.94±0.07	295
5c	COC1=CC=C2C(OC(C3=NC=CN3)=C2)=C1.Cl	5.88±0.16	3.01±0.45	741
5d	BrC1=CC=C(OC(C2=NC=CN2)=C3)C3=C1.Cl	6.28±0.18	4.92±0.25	23
6b	OC1=CC=C(OC(C2=NC=CN2)=C3)C3=C1.Cl	4.87±0.23	3.84±0.16	11
6c	OC1=CC=C2C(OC(C3=NC=CN3)=C2)=C1.Cl	5.48±0.11	3.76±0.12	52
7a	CN1C(C2=CC3=CC=CC=C3O2)=NC=C1.Cl	5.98±0.08	3.75±0.12	170
7aa	CCN1C(C2=CC3=CC=CC=C3O2)=NC=C1.Cl	5.05±0.10	3.77±0.08	19
7b	CCN1C(C2=CC3=CC(OC)=CC=C3O2)=NC=C1.Cl	4.96±0.15	4.21±0.19	6
7c	CCN1C(C2=CC3=CC=C(OC)C=C3O2)=NC=C1.Cl	5.26±0.08	3.17±0.25	123

X-ray crystallographic data for LSL60101

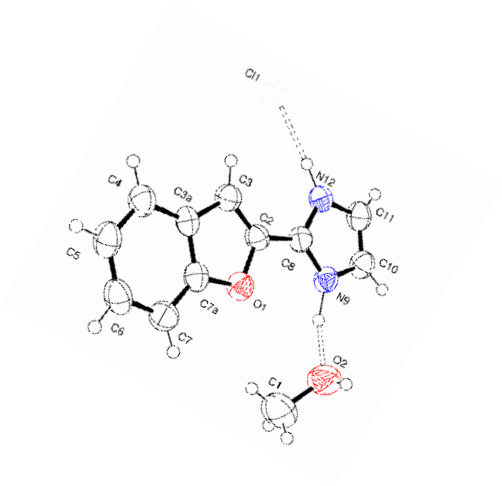

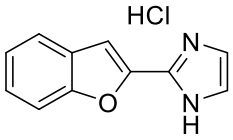

Table S14. Crystal data and structure refinement for **LSL60101**.

Identification code	Jb151	
Empirical formula	C12 H13 Cl N2 O2	
Formula weight	252.69	
Temperature	294(2) K	
Wavelength	0.71073 Å	
Crystal system	Monoclinic	
Space group	C c	
Unit cell dimensions	a = 9.1405(18) Å	α= 90°.
	b = 19.166(4) Å	β= 98.090(5)°.
	c = 7.1170(15) Å	γ = 90°.
Volume	1234.4(4) $Å^3$	
Z	4	
Density (calculated)	1.360 Mg/m^3	
Absorption coefficient	0.301 mm^{-1}	
F(000)	528	
Crystal size	0.22 x 0.14 x 0.07 mm^3	
Theta range for data collection	2.125 to 28.319°.	
Index ranges	-12<=h<=12, -25<=k<=25, -9<=l<=9	
Reflections collected	12563	
Independent reflections	3077 [R(int) = 0.0895]	
Completeness to theta = 25.242°	100.0 %	
Refinement method	Full-matrix least-squares on F^2	
Data / restraints / parameters	3077 / 2 / 192	
Goodness-of-fit on F^2	0.962	

Final R indices [I>2sigma(I)]	R1 = 0.0592, wR2 = 0.1181
R indices (all data)	R1 = 0.1340, wR2 = 0.1492
Absolute structure parameter	0.5
Largest diff. peak and hole	0.261 and -0.229 e.Å^{-3}

Table S15. Atomic coordinates (x 10^4) and equivalent isotropic displacement parameters (Å^{2}x 10^3) for **LSL60101**. U(eq) is defined as one third of the trace of the orthogonalized U^{ij} tensor.

	x	y	z	U(eq)
Cl(1)	9423(2)	3730(1)	7317(3)	70(1)
O(1)	4031(4)	4937(2)	5034(6)	50(1)
N(9)	3885(6)	3474(2)	5060(8)	46(1)
N(12)	6180(6)	3365(2)	6258(8)	49(1)
C(2)	5276(7)	4569(3)	5778(10)	44(1)
C(3)	6402(8)	4985(3)	6445(10)	50(2)
C(3A)	5871(7)	5683(3)	6149(9)	44(2)
C(4)	6480(9)	6352(3)	6536(11)	55(2)
C(5)	5578(8)	6922(4)	6014(11)	60(2)
C(6)	4156(9)	6842(4)	5123(11)	61(2)
C(7)	3526(9)	6193(3)	4730(11)	57(2)
C(7A)	4415(7)	5630(3)	5268(9)	48(2)
C(8)	5100(8)	3823(3)	5672(11)	45(1)
C(10)	4181(7)	2770(3)	5217(10)	53(2)
C(11)	5588(8)	2703(3)	5948(10)	55(2)
O(2)	1078(5)	3819(3)	3826(9)	80(2)
C(1)	597(11)	4428(4)	2738(14)	95(3)

Table S16. Bond lengths [Å] and angles [°] for **LSL60101**.

O(1)-C(7A)	1.379(7)
O(1)-C(2)	1.380(7)
N(9)-C(8)	1.317(8)
N(9)-C(10)	1.377(7)
N(12)-C(8)	1.343(8)
N(12)-C(11)	1.385(8)
C(2)-C(3)	1.335(8)
C(2)-C(8)	1.439(7)
C(3)-C(3A)	1.429(8)
C(3A)-C(7A)	1.393(8)
C(3A)-C(4)	1.410(9)
C(4)-C(5)	1.386(9)
C(5)-C(6)	1.372(10)
C(6)-C(7)	1.383(10)
C(7)-C(7A)	1.372(9)
C(10)-C(11)	1.324(10)
O(2)-C(1)	1.436(9)
C(7A)-O(1)-C(2)	105.3(5)
C(8)-N(9)-C(10)	108.9(5)
C(8)-N(12)-C(11)	107.2(6)
C(3)-C(2)-O(1)	112.6(5)
C(3)-C(2)-C(8)	133.4(6)
O(1)-C(2)-C(8)	114.0(6)
C(2)-C(3)-C(3A)	106.2(6)
C(7A)-C(3A)-C(4)	118.7(6)
C(7A)-C(3A)-C(3)	106.3(6)
C(4)-C(3A)-C(3)	135.0(7)
C(5)-C(4)-C(3A)	117.4(7)
C(6)-C(5)-C(4)	121.7(7)
C(5)-C(6)-C(7)	122.3(7)
C(7A)-C(7)-C(6)	115.9(7)
C(7)-C(7A)-O(1)	126.4(6)
C(7)-C(7A)-C(3A)	124.0(7)
O(1)-C(7A)-C(3A)	109.6(6)

N(9)-C(8)-N(12)	108.6(5)
N(9)-C(8)-C(2)	127.2(6)
N(12)-C(8)-C(2)	124.1(6)
C(11)-C(10)-N(9)	107.2(6)
C(10)-C(11)-N(12)	108.1(6)

Table S17. Anisotropic displacement parameters ($Å^2 x\ 10^3$) for **LSL60101**. The anisotropic displacement factor exponent takes the form: $-2\pi^2[\ h^2 a^{*2} U^{11} + ... + 2\ h\ k\ a^*\ b^*\ U^{12}\ ]$

	U^{11}	U^{22}	U^{33}	U^{23}	U^{13}	U^{12}
Cl(1)	59(1)	46(1)	103(1)	6(1)	2(1)	0(1)
O(1)	54(3)	40(2)	55(3)	-3(2)	9(2)	1(2)
N(9)	48(3)	37(3)	54(3)	-3(2)	7(3)	-4(2)
N(12)	52(3)	37(3)	59(3)	6(2)	6(3)	2(2)
C(2)	47(3)	38(3)	47(3)	2(3)	7(3)	5(3)
C(3)	53(4)	42(4)	53(4)	0(3)	2(3)	-1(3)
C(3A)	58(4)	34(3)	42(4)	2(3)	12(3)	1(3)
C(4)	65(5)	41(4)	58(5)	-1(3)	7(4)	-3(3)
C(5)	71(5)	39(4)	75(5)	-3(4)	22(4)	0(3)
C(6)	72(5)	44(4)	71(5)	9(4)	25(4)	14(4)
C(7)	53(4)	48(4)	70(5)	2(4)	12(4)	8(3)
C(7A)	58(4)	39(3)	46(4)	0(3)	10(3)	-3(3)
C(8)	50(3)	43(3)	42(3)	1(3)	7(3)	-2(3)
C(10)	58(4)	40(3)	62(4)	-3(3)	10(4)	-4(3)
C(11)	66(5)	35(3)	64(5)	-1(3)	12(4)	-1(3)
O(2)	63(4)	64(3)	112(5)	3(3)	5(3)	8(3)
C(1)	95(6)	69(5)	118(7)	10(5)	3(6)	16(5)

Table S18. Hydrogen bonds for **LSL60101** [Å and °].

D-H...A	d(D-H)	d(H...A)	d(D...A)	<(DHA)
O(2)-H(2)...Cl(1)#1	0.82	2.27	3.091(6)	173.9
C(3)-H(3)...Cl(1)	0.96(6)	2.86(6)	3.649(7)	140(4)
N(9)-H(9)...O(2)	1.11(6)	1.59(7)	2.675(7)	164(5)
N(12)-H(12)...Cl(1)	1.01(6)	2.03(6)	3.036(6)	174(5)

Symmetry transformations used to generate equivalent atoms:

#1 x-1,y,z

References

[1] Abás S.; Rodríguez-Arévalo S.; Bagán A.; Griñán-Ferré C.; Vasilopoulou F.; Brocos-Mosquera I.; Muguruza C.; Pérez B.; Molins E.; Luque F. J.; Pérez-Lozano P.; de Jonghe S.; Daelemans D.; Naesens L.; Brea J.; Loza M. I.; Hernández-Hernández E.; García-Sevilla J. A.; García-Fuster M. J.; Radan M.; Djikic T.; Nikolic K.; Pallàs M.; Callado L. F.; Escolano C. Bicyclic α-Iminophosphonates as High Affinity Imidazoline I2 Receptor Ligands for Alzheimer's Disease. J. Med. Chem. 7 (2020) 3610-3633.
[2] Tropsha, A.; Best Practices for QSAR Model Development, Validation, and Exploitation. Mol. Inform. 29 (2010) 476-488.
[3] Golbraikh, A.; Tropsha, A. Beware of q2. J. Mol. Graph. Model. 20 (2002) 269-276.
[4] SPSS Inc. Released 2009. PASW Statistics for Windows, Version 18.0. Chicago: SPSS Inc.
[5] Di, L.; Kerns, E. H.; Fan, K.; McConnell, O. J.; and Carter, G. T. High throughput artificial membrane permeability assay for blood-brain barrier. Eur. J. Med. Chem. 38 (2003) 223-232.

3.2. Resultados no publicados

En este apartado se recoge el trabajo que se ha generado a partir de los resultados publicados en el artículo *European Journal of Medicinal Chemistry*.[43] Este estudio, llevado a cabo durante el periodo final de mi Tesis Doctoral, ha dado lugar a resultados prometedores siendo uno de los objetivos de trabajo actuales del grupo.

En el artículo mostrado anteriormente (apartado 3.1) se ha reportado la síntesis y perfil farmacológico de una familia de compuestos con núcleo de benzofuranil-2-imidazol, derivados de **LSL60101**, un ligando de I_2-IR.

Desde el punto de vista de la estructura química, como ya se ha comentado anteriormente, la naturaleza de los ligandos I_2-IR conocidos está relativamente restringida (Figura 3.1A). El farmacóforo generalmente se relaciona con estructuras que presentan un núcleo de 2-imidazolina sustituida en la posición 2 (**idazoxan**, **2-BFI** y **BU224**). La comparación estructural de **LSL60101** con otros ligandos I_2-IR conocidos, y en particular **2-BFI** con el que comparte un heterociclo de benzofurano, sugiere la farmacomodulación por insaturación del anillo imidazolínico como una estrategia de optimización de fármacos con estructura alternativa a las imidazolinas. La presencia de un anillo de imidazol en el ligando I_2-IR en fase clínica, **CR4056** respalda la propuesta.

Con el objetivo de ampliar el arsenal sintético de ligandos I_2-IR, y conocer mejor la relación estructura-actividad, se propuso sintetizar una serie de productos estructuralmente homólogos a ligandos I_2-IR conocidos incluyendo modificaciones sobre sus anillos aromáticos. Posteriormente, se propone la evaluación del perfil farmacológico de los compuestos sintetizados.

Las farmacomodulaciones realizadas durante mi Tesis Doctoral fueron, como sucede con la relación de **LSL60101** y **2-BFI**, la insaturación del anillo imidazolínico de **BU224** e **idazoxan** para obtener las estructuras **LSL42** y **LSL39**, respectivamente. Además, se realizó la sustitución del átomo de oxígeno del anillo de benzofurano de **LSL60101** por -NH-, -S-, dando lugar a los bioisósteros **LSL33** y **LSL29**. Algunas de las propuestas, **LSL34** y **LSL35,** presentan la unión al heterociclo por el nitrogeno del imidazol como en el caso de **CR4056** (Figura 3.1B).

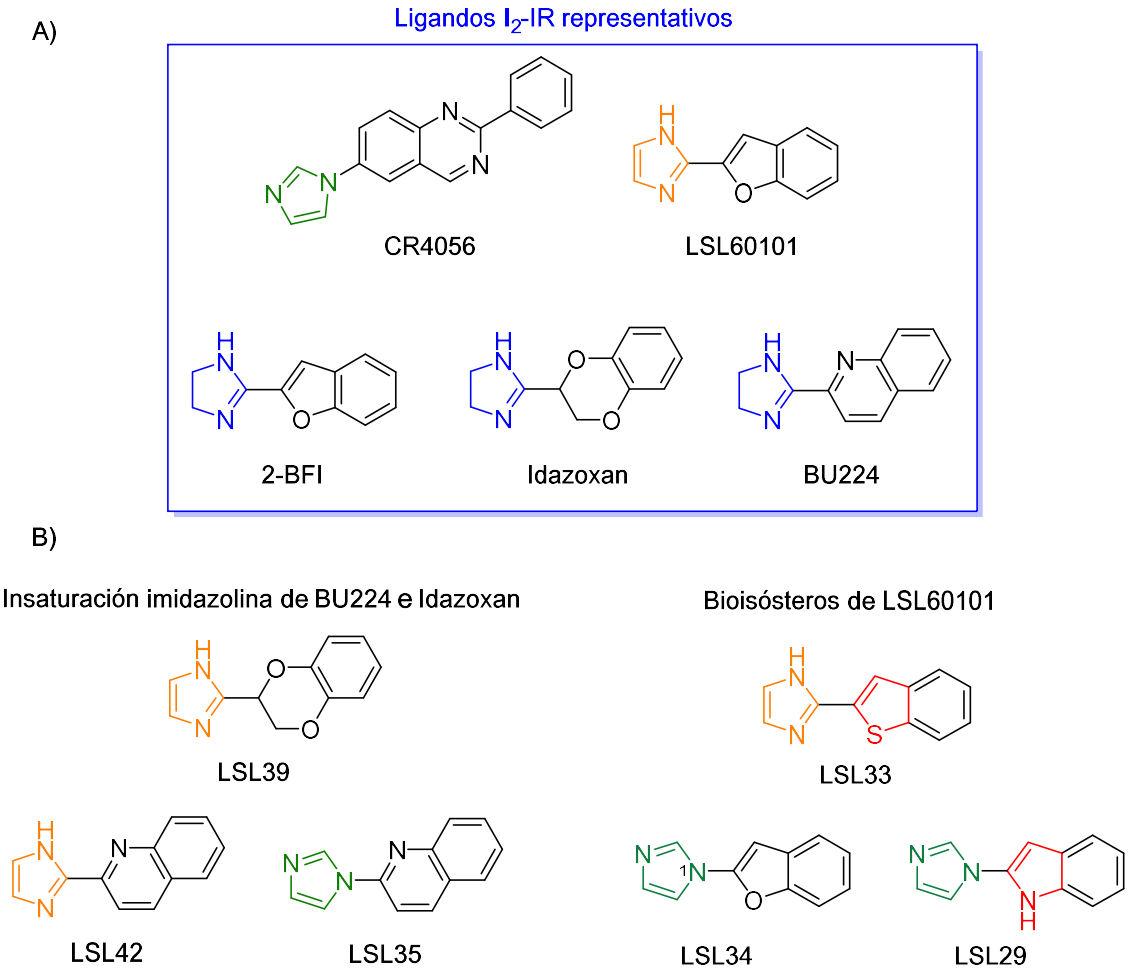

Figura 3.1. **A)** Estructura ligandos I_2-IR representativos. **B)** Modificaciones estructurales realizadas inspiradas en ligandos I_2-IR representativos.

Preparación de LSL42 y de LSL 39.

La preparación de los análogos de **BU224** e **idazoxan** en los que el núcleo de imidazolina se sustituye por el núcleo de 2-imidazol (**LSL42** y **LSL39**) se llevó a cabo siguiendo la ruta sintética descrita en el artículo *European Journal of Medicinal Chemistry*.[48] Partiendo de los derivados quinolina-2-carbonitrilo (**1a**) y 2,3-dihidro-1,4-benzodioxina-2-carbonitrilo (**1b**), en presencia de éter clorhídrico y metanol se obtuvieron los correspondientes carbimidatos **2a** y **2b**. Seguidamente, se hicieron reaccionar con 2,2-dimetoxietilamina para dar **3a** y **3b** que, tras tratamiento con HCl 2N condujeron a **LSL42** y **LSL39** con rendimientos adecuados (Esquema 3.1A).

Además, se propuso un ejemplo donde el anillo de imidazol estuviese enlazado a la estructura por el átomo de nitrógeno y no por el carbono de la posición 2, como sucede en el caso de **CR4056**. La síntesis del compuesto deseado, **LSL35,** fue descrita por el

Prof. Choudhury en el 2016, por medio de un acoplamiento de Ullmann catalizado por cobre entre 2-bromoquinolina e imidazol (Esquema 3.1B).[65]

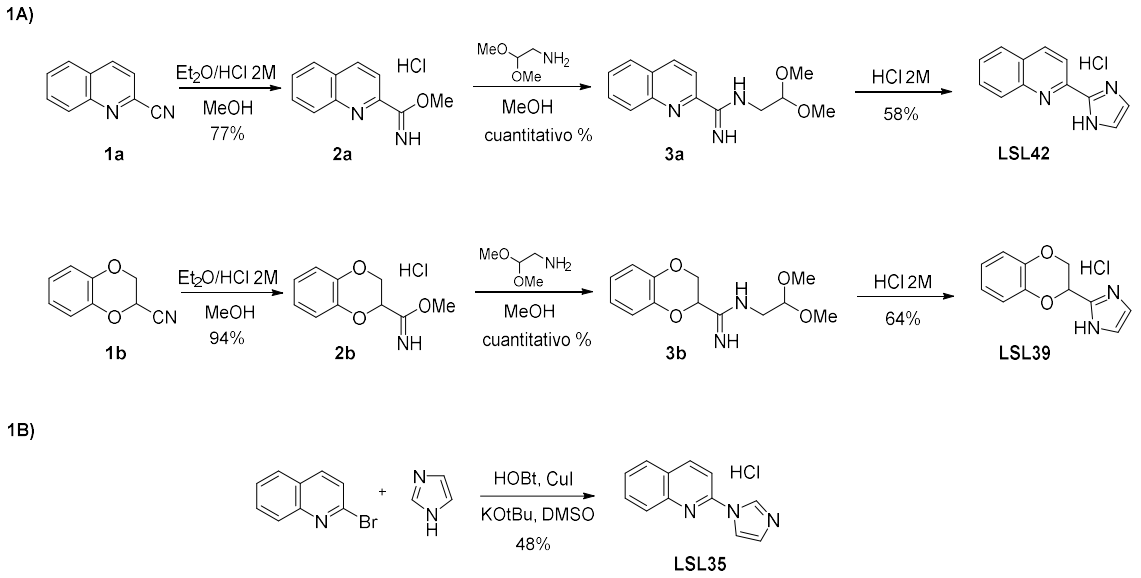

Esquema 3.1. **A)** Ruta sintética para **LSL42** y **LSL39**. **B)** Ruta sintética para **LSL35**.

Sustitución del anillo heterocíclico de benzofurano por un sistema heterocíclico bioisóstero en ***LSL60101***

En este caso, a diferencia del artículo mencionado anteriormente donde las modificaciones mantenían siempre el núcleo de benzofuranil-2-imidazol, se propuso sintetizar derivados del ligando I_2-IR **LSL60101** en los que se sustituye el anillo de benzofurano por un sistema heterocíclico biosóstero con estructura de benzotiofeno. Además, como sucede con **LSL35**, se pretende generar el derivado con el anillo imidazólico unido al benzofurano directamente por el átomo de nitrógeno (*N*1), de manera análoga a como ocurre en **CR4056**.

Para sintetizar el derivado de **LSL60101** que contiene anillo de benzotiofeno, **LSL33**, se siguió la ruta sintética descrita previamente en el *European Journal of Medicinal Chemistry*.[43] Partiendo del benzotiofeno-2-carbonitrilo (**1c**) y con las transformaciones pertinentes para la formación del anillo de imidazol (Esquema 3.2A). Seguidamente, mediante los acoplamientos adecuados descritos en la literatura (Esquema 3.2B), se obtuvieron los derivados en que el imidazol está unido al núcleo de benzofurano (**LSL34**) o indol (**LSL29**) por el átomo nitrógeno y no por el carbono de la posición 2. El compuesto **LSL34** se relaciona con **LSL60101** y, en el caso de **LSL29**, se llevan a cabo dos modificaciones el punto de unión del anillo imidazólico y la sustitución del sistema

[65] Ghorai, D.; Dutta, C.; Choudhury, J. *ACS Catal*. **2016**, *6*, 709-713.

de benzofurano por un indol. Las síntesis de estos dos últimos compuestos fueron publicadas en los años 2014 y 2012, respectivamente.[66]

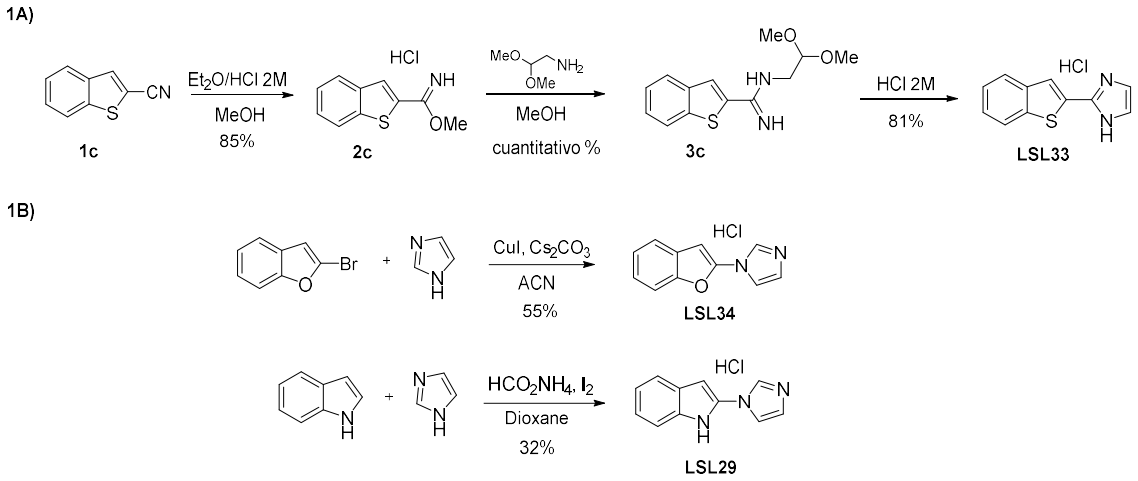

Esquema 3.2. **A)** Ruta sintética para **LSL33**. **B)** Ruta sintética para **LSL34** y **LSL29**.

Posteriormente, se procedió a evaluar la actividad farmacológica de la nueva familia de compuestos (**LSL29**, **LSL33**, **LSL34**, **LSL35**, **LSL39** y **LSL42**) mediante estudios competitivos frente a radioligandos selectivos de I_2-IR ([^{3}H]-2-BFI) y de α_2-AR ([^{3}H]-RX821002) en el grupo del Prof. L. F. Callado (UPV).

En la Tabla 3.1 se representan las constantes de inhibición obtenidas para cada compuesto expresadas como pK_i, así como los valores de los ligandos I_2-IR conocidos. Como se puede observar, todos los compuestos sintetizados tienen buenos valores de afinidad por I_2-IR, pero a su vez también son afines por los α_2-AR y, por lo tanto, han perdido la selectividad I_2-IR respecto a **LSL60101** (selectividad I_2/α_2 de 3090). Los productos derivados de **BU224** e **idazoxan** obtenidos mediante la de insaturación del anillo imidazolínico (**LSL35**, **LSL39** y **LSL42**), presentaron valor de afinidad inferiores a **idazoxan** y, al igual que este, fueron no selectivos por I_2-IR. Por otro lado, los compuestos bioisósteros de **LSL60101** (**LSL29**, **LSL33** y **LSL34**), cabe destacar **LSL33** y **LSL34** los cuales presentan curvas bifásicas con dos lugares de unión, uno de alta afinidad y otro de baja afinidad, con buenos porcentajes de ocupación del lugar de alta afinidad, 27 y 37% respectivamente, siendo los valores de **LSL34** superiores a **LSL60101**. El compuestos **LSL29**, bioisóstero de **LSL34** que contiene un indol, resultó no presentar una afinidad destacable. Los nuevos compuestos sintetizados carecen de selectividad I_2-IR frente a α_2-AR.

[66] (a) Wu, W-B.; Huang, J-M. *Org. Lett*. **2012**, *14*, 5832-5835; (b) Hededi, M.; Bentabed-Ababsa, G.; Derdour, A.; Roisnel, T.; Dorcet, V.; Chavallier, F.; Picot, L.; Thiery, V.; Mongin, F. *Bioorg. Med. Chem*. **2014**, *22*, 3498-3507.

Tabla 3.1. Valores de la afinidad de unión para I_2-IR y α_2-AR de los nuevos compuestos.

Compuesto	[^{3}H]-2-BFI I_2 p*K*i (un lugar)	[^{3}H]-2-BFI I_2 p*K*i (dos lugares)		Lugar de alta afinidad (% ocupación)	[^{3}H]-RX821002 α_2 p*K*i	Selectividad I_2/α_2
Idazoxan	7.41±0.63	7.87±0.74	5.76±0.57	40±7	7.92±0.07	-
2-BFI	8.31±0.13	9.08±0.22	7.15±0.31	58±9	4.58±0.22	5370
CR4056	5.95±0.11				2.65±1.24	1995
BU99008	7.05±0.17				4.37±0.17	479
LSL60101	6.67±0.09	8.17±0.19	6.02±0.10	34±4	3.18±0.17	3090
LSL29	4.57±0.23	8.54±0.71	4.09±0.22	22±5	4.99±0.18	
LSL33	5.95±0.24	10.1±0.57	5.68±0.25	27±6	4.70±0.12	
LSL34	5.58±0.31	9.23±0.36	4.64±0.32	37±6	5.40±0.21	
LSL35	5.49±0.14	-	-	-	5.24±0.26	
LSL39	6.10±0.25	-	-	-	3.97±0.25	
LSL42	5.24±0.12	-	-	-	5.32±0.24	

Todos los compuestos, a excepción de **LSL39**, se sometieron a estudios de PAMPA-BBB por la Dra. B. Pérez (UAB) y resultaron situarse por encima del umbral establecido para una alta permeabilidad de la BHE (SNC +: P_e (10^{-6} cm·s^{-1}) > 5.198) (Tabla 3.2).

Tabla 3.2. Resultado de permeabilidad por ensayo PAMPA-BBB y predicción de penetración en BHE de los compuestos **LSL29**-**LSL42**.

	Permeabilidad P_e (10^{-6} cm·s^{-1})	**Predicción**
LSL60101	13.6 ± 0.4	SNC +
LSL29	10.8 ± 0.4	SNC +
LSL33	8.1 ± 0.4	SNC +
LSL34	14.1 ± 0.5	SNC +
LSL35	16.2 ± 0.9	SNC +
LSL42	5.8 ± 0.2	SNC +

Finalmente, viendo los resultados alentadores de esta nueva familia de compuestos derivados de ligandos I_2-IR conocidos, se ha planteado en un futuro realizar modificaciones estructurales basadas en los compuestos con el perfil farmacológico más atractivo, **LSL33** y **LSL34**. Dichas modificaciones están por concretar, pero podrían contemplar la introducción de sustituyentes en el anillo bencénico o bien en uno de los nitrógenos del anillo de cinco miembros, entre otras, con el objetivo establecer relaciones estructura-actividad que permitan acceder a moléculas con un mejor perfil farmacológico.

PARTE EXPERIMENTAL

Reagents, solvents and starting products were acquired from commercial sources. The term "concentration" refers to the vacuum evaporation using a Büchi rotavapor. When indicated, the reaction products were purified by "flash" chromatography on silica gel (35-70 μm) with the indicated solvent system. IR spectra were performed in a Spectrum Two FT-IR Spectrometer, and only noteworthy IR absorptions (cm^{-1}) are listed. NMR spectra were recorded in DMSO-d_6 or CD_3OD at 400 MHz (^1H) and 100.6 MHz (^{13}C), and chemical shifts are reported in δ values downfield from TMS or relative to residual DMSO-d_6 (2.50 ppm, 39.5 ppm) or CD_3OD (3.31 ppm) as an internal standard. Data are reported in the following manner: chemical shift, multiplicity, coupling constant (*J*) in hertz (Hz) and integrated intensity. Multiplicities are reported using the following abbreviations: s, singlet; d, doublet; dd, doublet of doublets; t, triplet; m, multiplet; br s, broad signal. The accurate mass analyses were carried out using a LC/MSD-TOF spectrophotometer.

2-Imidazol-1-yl-1H-indole hydrochloride (LSL29).[66a]

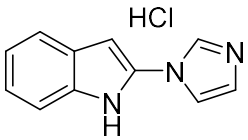

I_2 (317 mg, 1.25 mmol) was added to a mixture of indole (59 mg, 0.5 mmol), imidazole (272 mg, 4 mmol) and a saturated aqueous ammonium formate solution (0.3 mL) in 1,4-dioxane (0.3 mL). The reaction mixture was stirred at room temperature for 24 h. Then, a saturated aqueous $Na_2S_2O_3$ solution (1 mL) was added. The reaction mixture was extracted with EtOAc. The combined organic layer was washed with brine and dried over anhydrous Na_2SO_4, filtered, and concentrated *in vacuo*. The crude product was purified by flash chromatography on silica gel (DCM 100%). The product was dissolved in DCM and ethereal HCl 2M (0.4 mL) was added and the precipitated salt was collected by filtration to give **LSL29** (35 mg, 32%). The characterization is coincident with the previously reported.[66a] IR (ATR) 3105, 2688, 2617, 1579, 1564, 1391, 1328, 1236, 1068, 898, 824, 779 cm^{-1}. ^1H-NMR (400 MHz, DMSO-d_6): *δ* 6.89 (d, *J* = 5.0 Hz, 1H), 7.12 (t, *J* = 7.0 Hz, 1H), 7.23 (t, *J* = 7.0 Hz, 1H), 7.47 (d, *J* = 8.5 Hz, 1H), 7.62 (d, *J* = 7.5 Hz, 1H), 7.84 (s, 1H), 8.26 (s, 1H), 9.59 (s, 1H), 12.52 (br s, 1H). HRMS $C_{11}H_{10}N_3$ $[M+H]^+$ 184.0869; found, 184.0870.

1-(Benzofuran-2-yl)-1H-imidazole hydrochloride (LSL34).[66b]

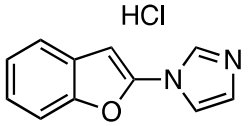

To a solution of 2-bromobenzofurane (197 mg, 1 mmol) in ACN (5 mL) was added imidazole (102 mg, 1.5 mmol), Cs_2CO_3 (651 mg, 2.0 mmol) and CuI (38 mg, 0.2 mmol). The reaction mixture was stirred under reflux for 24 h. After completion of the reaction, the resulting residue was

filtered over Celite®, washed with EtOAc and concentrated *in vacuo*. Then, the crude product was purified by flash chromatography (DCM 100%). The product was dissolved in DCM and ethereal HCl 2M (0.7 mL) was added and the precipitated salt was collected by filtration to give **LSL34** (121 mg, 55%). The characterization is coincident with the previously reported.[66b] IR (ATR) 3385, 3075, 2883, 1905, 1628, 1579, 1536, 1455, 1389, 1198, 1056, 990, 801 cm^{-1}. ^{1}H-NMR (400 MHz, DMSO-d_6): *δ* 7.04 (s, 1H), 7.19 (s, 1H), 7.29-7.37 (m, 2H), 7.62-7.65 (m, 1H), 7.68 (dd, *J* = 7.5, 1.5 Hz, 1H), 7.83 (s, 1H), 8.35 (s, 1H). HRMS $C_{11}H_9N_2O$ $[M+H]^+$ 185.0711; found, 185.0711.

1-(Quinoline-2-yl)-1H-imidazole hydrochloride (LSL35).[65]

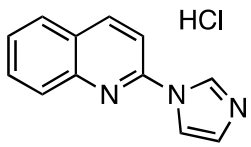

To a solution of 2-bromoquinoline (104 mg, 0.5 mmol) in DMSO (2 mL) was added imidazole (17 mg, 0.25 mmol), HOBt (3.4 mg, 0.025 mmol), KOtBu (42.1 mg, 0.375 mmol) and CuI (2.5 mg, 0.013 mmol). The reaction mixture was stirred under reflux for 24 h. After completion of the reaction, the resulting residue was filtered over Celite® and washed with EtOAc. The resulting solution was washed with brine, dried over Na_2SO_4, and concentrated *in vacuo*. Then, the crude product was purified by flash chromatography (DCM 100%). The product was dissolved in DCM and ethereal HCl 2M (0.2 mL) was added and the precipitated salt was collected by filtration to give **LSL35** (55 mg, 48%). The characterization is coincident with the previously reported.[65] IR (ATR) 3426, 3096, 3010, 2638, 1588, 1541, 1507, 1434, 1355, 1328, 1225, 989, 903, 821 cm^{-1}. ^{1}H-NMR (400 MHz, DMSO-d_6): *δ* 7.74 (t, *J* = 8.0 Hz, 1H), 7.88 (s, 1H), 7.92 (t, *J* = 7.0 Hz, 1H), 8.07 (d, *J* = 8.5 Hz, 1H), 8.14 (d, *J* = 7.5 Hz, 1H), 8.21 (d, *J* = 9.0 Hz, 1H), 8.58 (s, 1H), 8.79 (d, *J* = 9.0 Hz, 1H), 9.98 (s, 1H). HRMS $C_{12}H_{10}N_3$ [M+H]+ 196.0869; found, 196.0871.

1. General procedure for the synthesis of 2-carbimididate hydrochlorides derivatives ***2a, 2b*** *and* ***2c***.[43]

The 2-cyanobenzofuran derivative 1a, 1b or 1c (1 equiv) was dissolved in ethereal HCl 2M (0.25 mmol/mL) and methanol (5 mmol/mL). The resulting mixture was kept at 4 ºC for 48 h. The resulting solid was filtered, washed with cold diethyl ether, and dried to obtain the desired carbimidate hydrochloride.

1.1. ***Methyl quinoline-2-carbimidate hydrochloride (2a)***. Following the general procedure, quinoline-2-carbonitrile **1a** (500 mg, 3.25 mmol), ethereal HCl 2M (13 mL) and methanol (0.65 mL) gave **2a** (555 mg, 77%) as a white solid.

1.2. ***Methyl 2,3-dihydrobenzo[1,4]dioxine-2-carbimidate hydrochloride*** *(**2b**).* Following the general procedure, 2,3-dihydro-1,4-benzodioxine-2-carbonitrile **1b** (500 mg, 3.10 mmol), ethereal HCl 2M (12.5 mL) and methanol (0.62 mL) gave **2b** (668 mg, 94%) as a white solid.

1.3. ***Methyl benzothiophene-2-carbimidate hydrochloride*** *(**2c**).* Following the general procedure, benzothiophene-2-carbonitrile **1c** (500 mg, 3.14 mmol), ethereal HCl 2M (12.6 mL) and methanol (0.63 mL) gave **2c** (608 mg, 85%) as a white solid.

*2. General procedure for the synthesis of N-(2,2-dimethoxyethyl)-2-carboximidamide derivatives **3a**, **3b** and **3c**.*

A solution of 2,2-dimethoxyehtylamine (1.1 equiv) and 2-carbimidate hydrochloride derivative, 2a, 2b or 2c, (1 equiv) in methanol (0.47 mmol/mL) was stirred at 60 ºC for 16 h. The mixture was evaporated to dryness and was used directly in the next step without further purification.

2.1. ***N-(2,2-Dimethoxyethyl)quinoline-2-carboximidamide (3a)***. Following the general procedure, **2a** (500 mg, 2.25 mmol), 2,2-dimethoxyethylamine (0.27 mL, 2.48 mmol) and methanol (5.4 mL) gave **3a** (583 mg, quantitative yield) as a beige solid.

2.2. ***N-(2,2-Dimethoxyethyl)-2,3-dihydrobenzo[1,4]dioxine-2-carboximidamide*** *(**3b**).* Following the general procedure, **2b** (650 mg, 2.84 mmol), 2,2-dimethoxyethylamine (0.34 mL, 3.12 mmol) and methanol (6.0 mL) gave **3b** (755 mg, quantitative yield) as a beige solid.

2.3. ***N-(2,2-Dimethoxyethyl)benzothiophene-2-carboximidamide*** *(**3c**).* Following the general procedure, **2c** (590 mg, 2.60 mmol), 2,2-dimethoxyethylamine (0.31 mL, 2.86 mmol) and methanol (5.5 mL) gave **3c** (687 mg, quantitative yield) as a beige solid.

*3. General procedure for the synthesis of 1H-imidazole hydrochlorides derivatives **LSL33**, **LSL39** and **LSL42**.*

The corresponding *N*-(2,2-dimethoxyethyl)-2-carboximidamide 3a, 3b, 3c (1 equiv) was treated with HCl 2M (0.1 mmol/mL) and the resulting mixture was stirred at 60 ºC for 16 h. After cooling, the solution was washed with DCM. The aqueous layer was basified with NaOH 5M and the free base extracted with EtOAc. The combined organic phases were washed with brine, dried over Na_2SO_4, and evaporated to give a residue which was

dissolved in diethyl ether/ethanol (5:1). Ethereal HCl 2M (1.5 mmmol/mL) was added and the precipitated salt was collected by filtration and was crystallized with ACN.

3.1. ***2-(Benzothiophene-2-yl)-1H-imidazole hydrochloride (LSL33).***

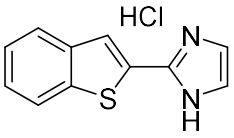

Following the general procedure, **3c** (680 mg, 2.57 mmol), HCl 2M (25.7 mL) and ethereal HCl 2M (1.7 mL) gave **LSL33** (492 mg, 81%) as a white solid. IR (ATR) 3395, 3172, 3146, 2562, 1623, 1455, 1445, 1140, 1094, 860, 842, 736 cm^{-1}. ^{1}H-NMR (400 MHz, DMSO-d_6) *δ* 7.49-7.55 (m, 2H), 7.77 (s, 2H), 8.02 (d, *J* = 8.5 Hz, 1H), 8.15 (d, *J* = 8.5 Hz, 1H), 8.38 (s, 1H). ^{13}C NMR (100.6 MHz, DMSO-d_6) *δ* 120.8 (2C), 123.0, 124.9, 125.1, 125.7, 126.9, 127.3, 138.5, 138.6, 139.9. HRMS $C_{11}H_9N_2O$ $[M+H]^+$ 201.0481; found, 201.0482.

3.2. ***2-(2,3-Dihydrobenzo[1,4]dioxin-2-yl)-1H-imidazole hydrochloride (LSL39)***.

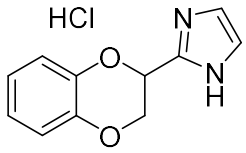

Following the general procedure, **3b** (700 mg, 2.63 mmol), HCl 2M (26.3 mL) and ethereal HCl 2M (1.8 mL) gave **LSL39** (401 mg, 64%) as a white solid. IR (ATR) 3365, 2877, 2673, 1595, 1490, 1262, 1074, 1041, 875, 751 cm^{-1}. ^{1}H-NMR (400 MHz, DMSO-d_6) *δ* 4.64 (d, *J* = 5.0 Hz, 2H), 5.85 (t, *J* = 4.0 Hz, 1H), 6.92-7.04 (m, 4H), 7.74 (s, 2H). ^{13}C-NMR (100.6 MHz, DMSO-d_6) *δ* 64.4, 67.0, 117.4, 117.6, 120.2 (2C), 122.1, 122.4, 141.4, 141.6, 142.5. HRMS $C_{11}H_{11}N_2O_2$ $[M+H]^+$ 203.0815; found, 203.0816.

3.3. ***2-(Quinoline-2-yl)-1H-imidazole hydrochloride (LSL42).***

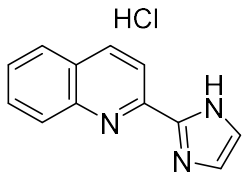

Following the general procedure, **3a** (550 mg, 2.12 mmol), HCl 2M (21.2 mL) and ethereal HCl 2M (1.4 mL) gave **LSL42** (284 mg, 58%) as a white solid. IR (ATR) 3398, 2996, 2608, 1618, 1557, 1404, 1351, 1289, 1205, 1019, 803, 798, 721 cm^{-1}. ^{1}H-NMR (400 MHz, CD_3OD) *δ* 7.75 (t, *J* = 8.0 Hz, 1H), 7.78 (s, 2H), 7.91 (t, *J* = 8.5 Hz, 1H), 8.06 (d, *J* = 8.0 Hz, 1H), 8.17 (d, *J* = 8.5 Hz, 1H), 8.23 (d, *J* = 9.0 Hz, 1H), 8.63 (d, *J* = 8.5 Hz, 1H). HRMS $C_{12}H_{10}N_3$ $[M+H]^+$ 196.0869; found, 196.0873.

MATERIAL SUPLEMENTARIO

^{1}H-NMR and ^{13}C-NMR spectra of compounds **LSL29**, **LSL33**, **LSL34**, **LSL35**, **LSL39** and **LSL42**

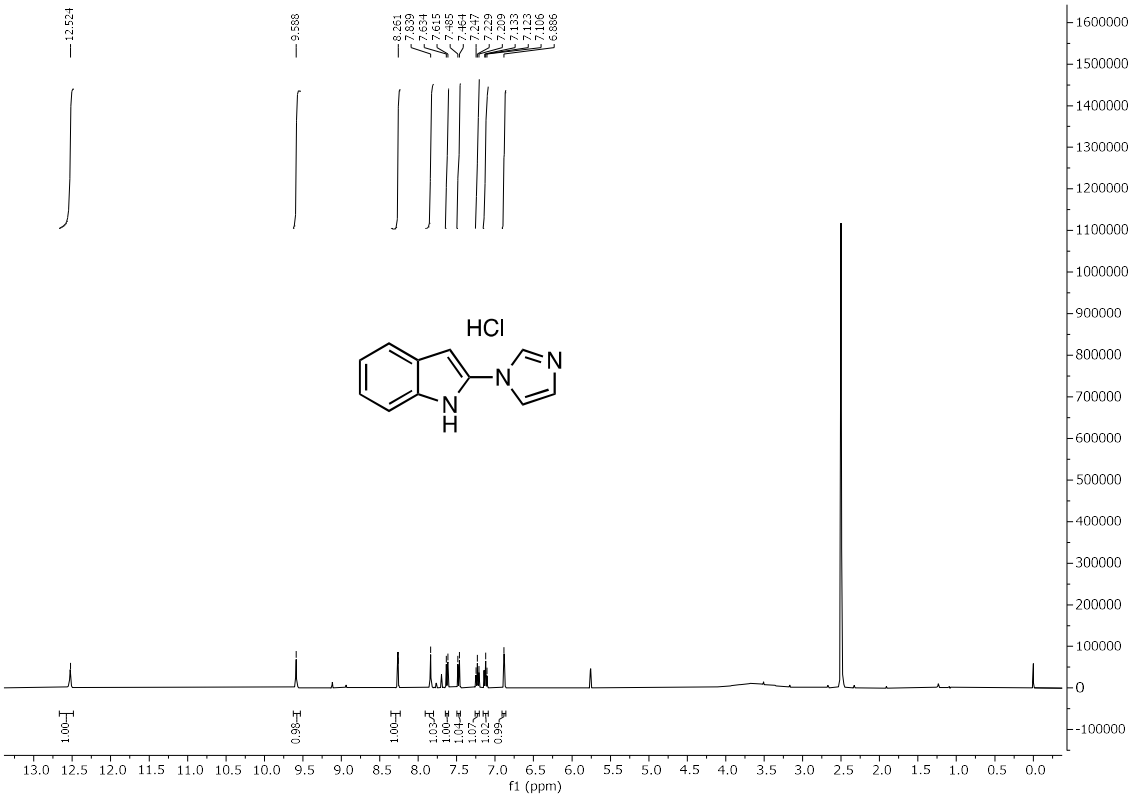

2-Imidazol-1-yl-1H-indole hydrochloride (LSL29)

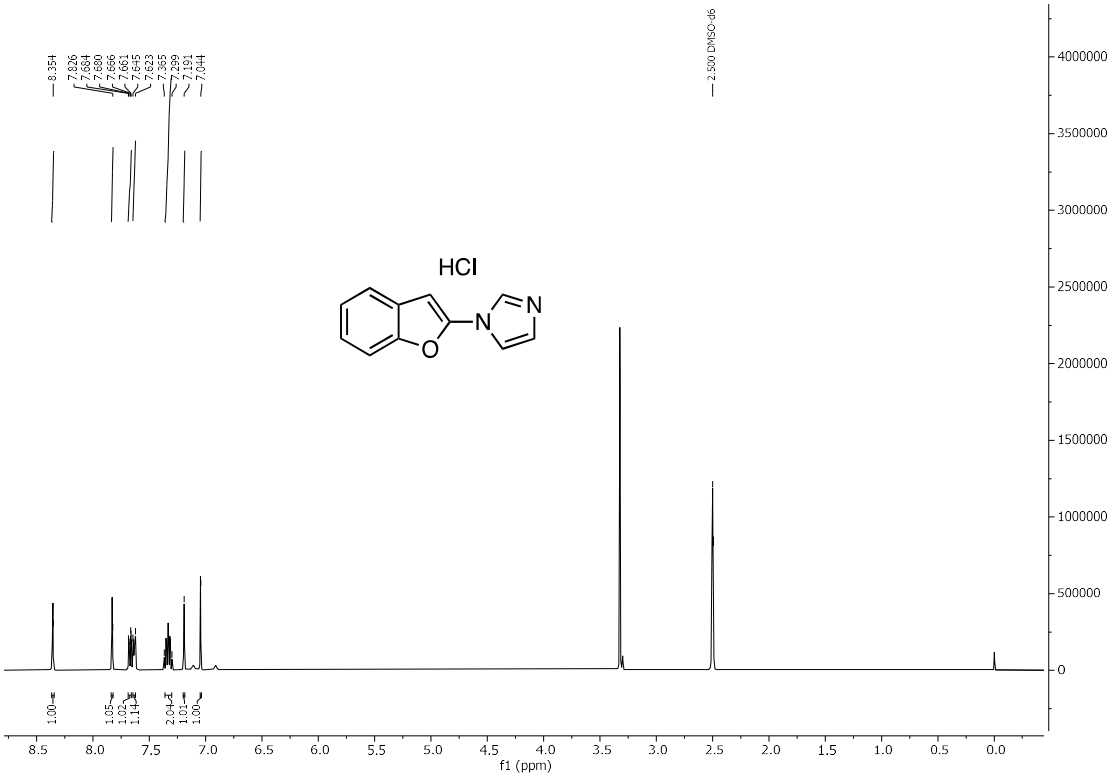

1-(Benzofuran-2-yl)-1H-imidazole hydrochloride (LSL34)

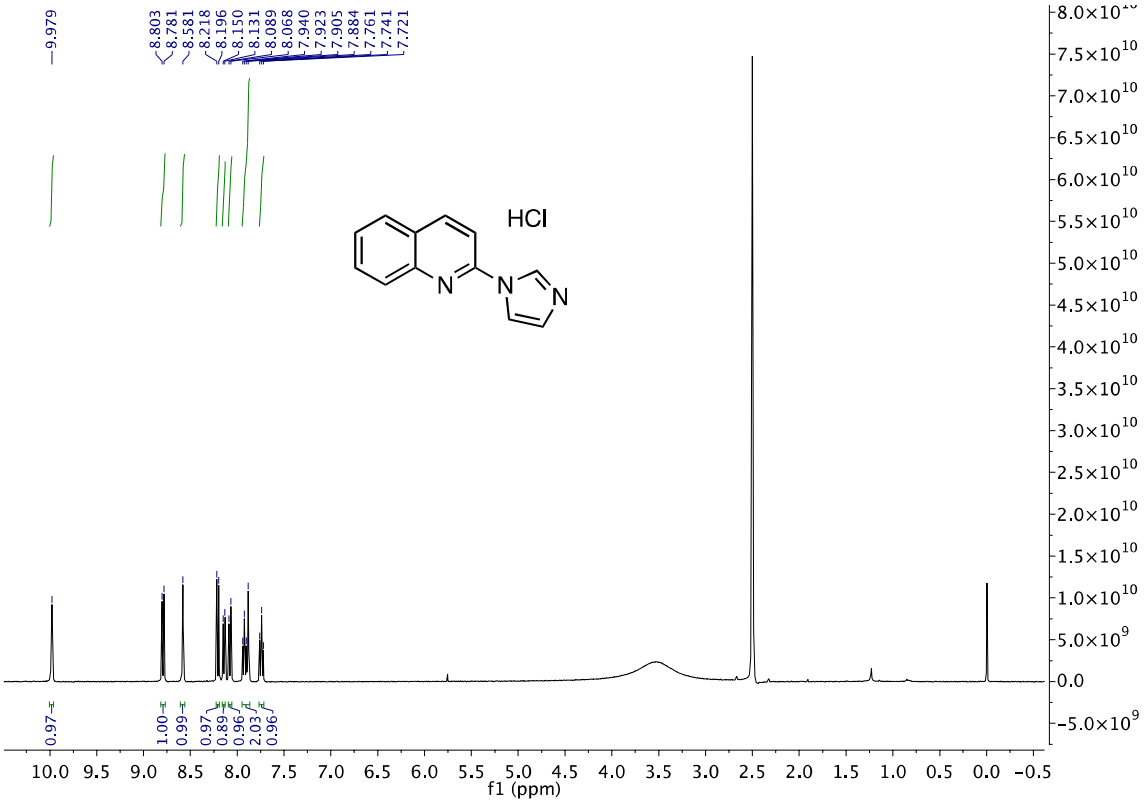

1-(Quinoline-2-yl)-1H-imidazole hydrochloride (LSL35)

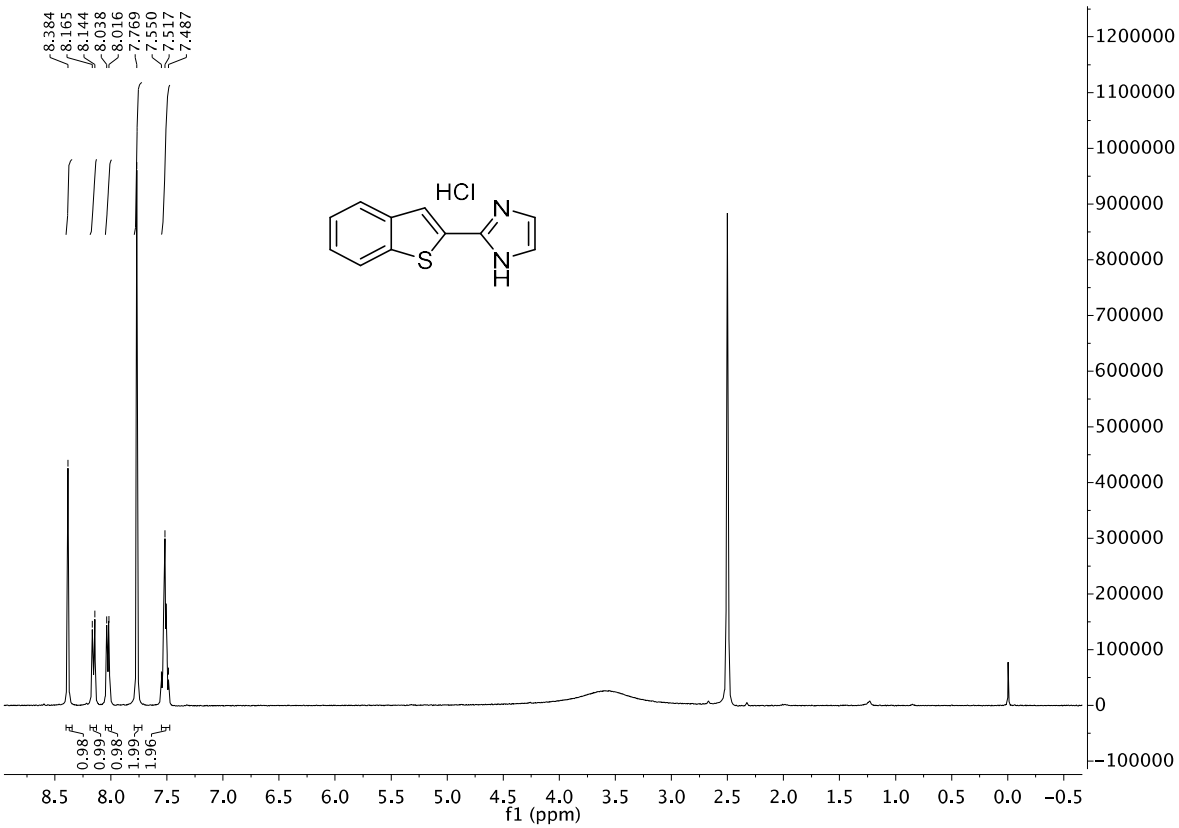

2-(Benzothiophene-2-yl)-1H-imidazole hydrochloride (LSL33)

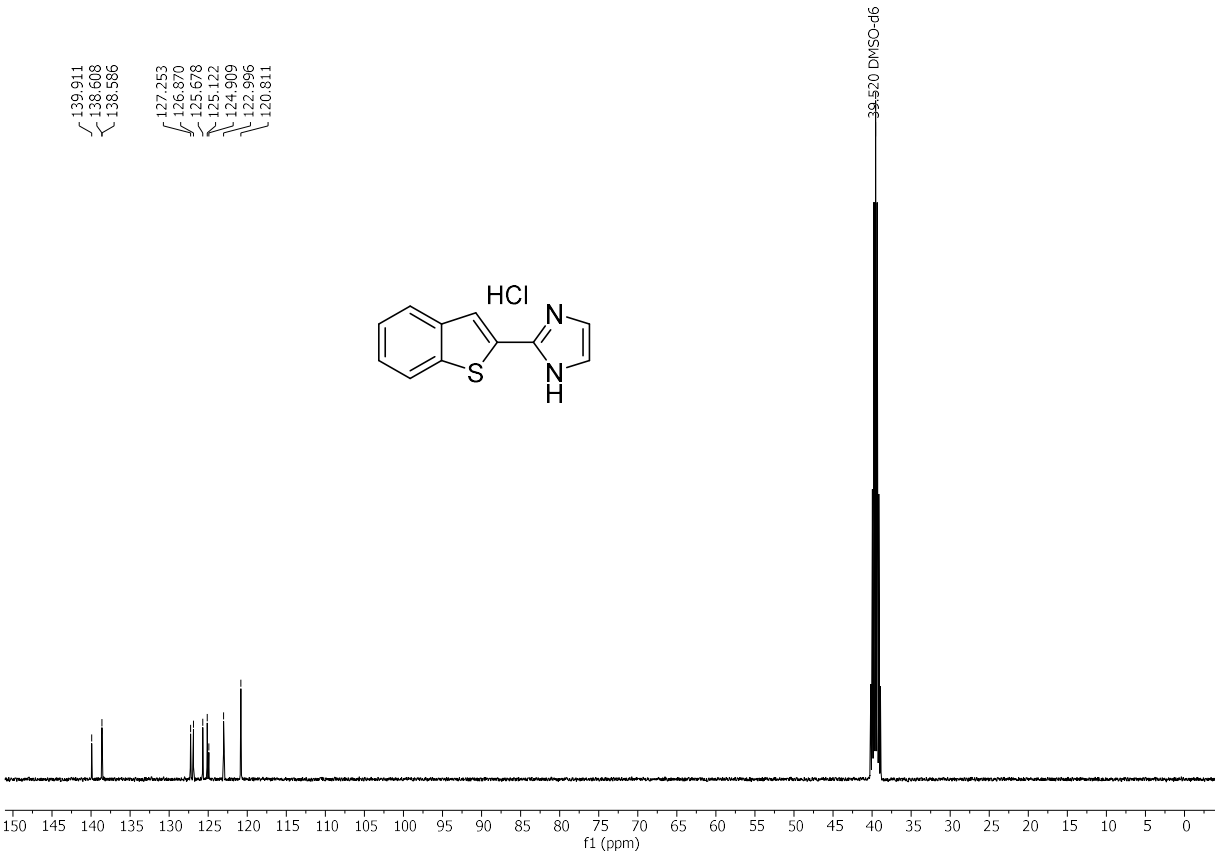

2-(Benzothiophene-2-yl)-1H-imidazole hydrochloride (LSL33)

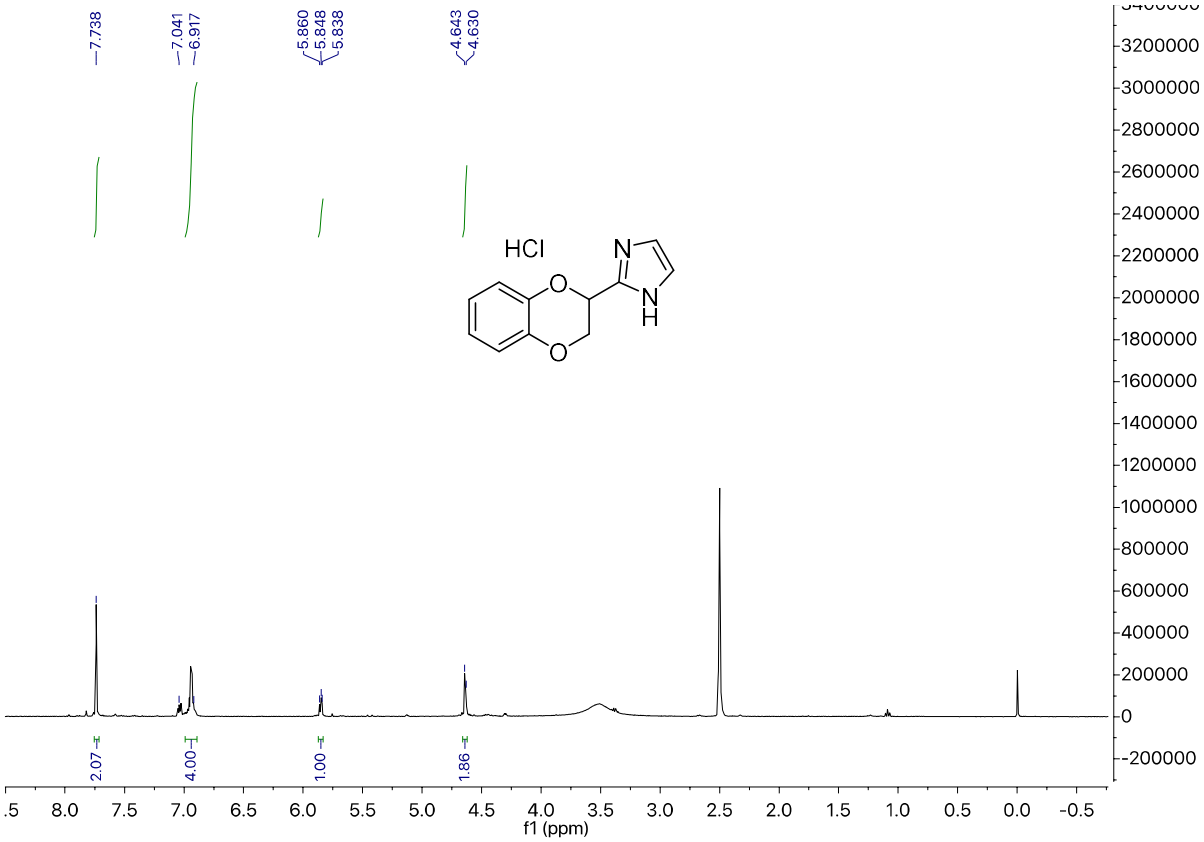

2-(2,3-Dihydrobenzo[1,4]dioxin-2-yl)-1H-imidazole hydrochloride (LSL39)

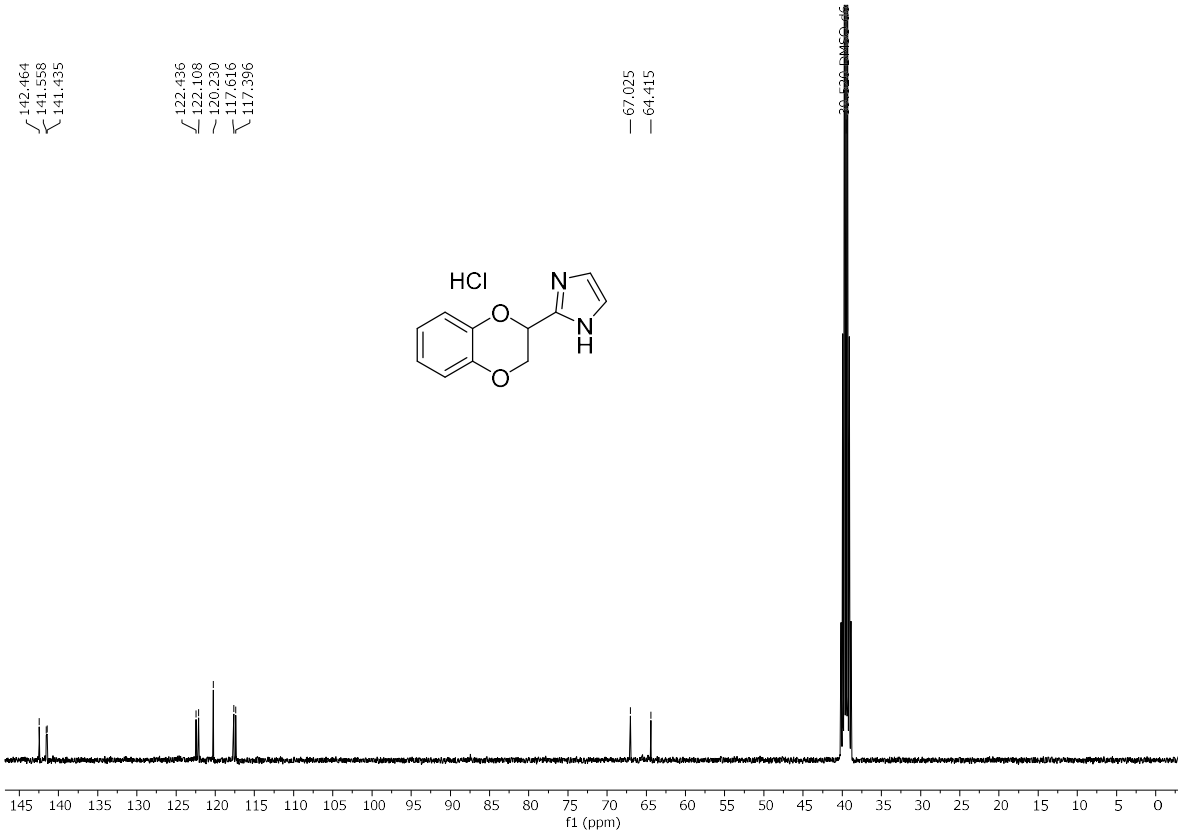

2-(2,3-Dihydrobenzo[1,4]dioxin-2-yl)-1H-imidazole hydrochloride (LSL39)

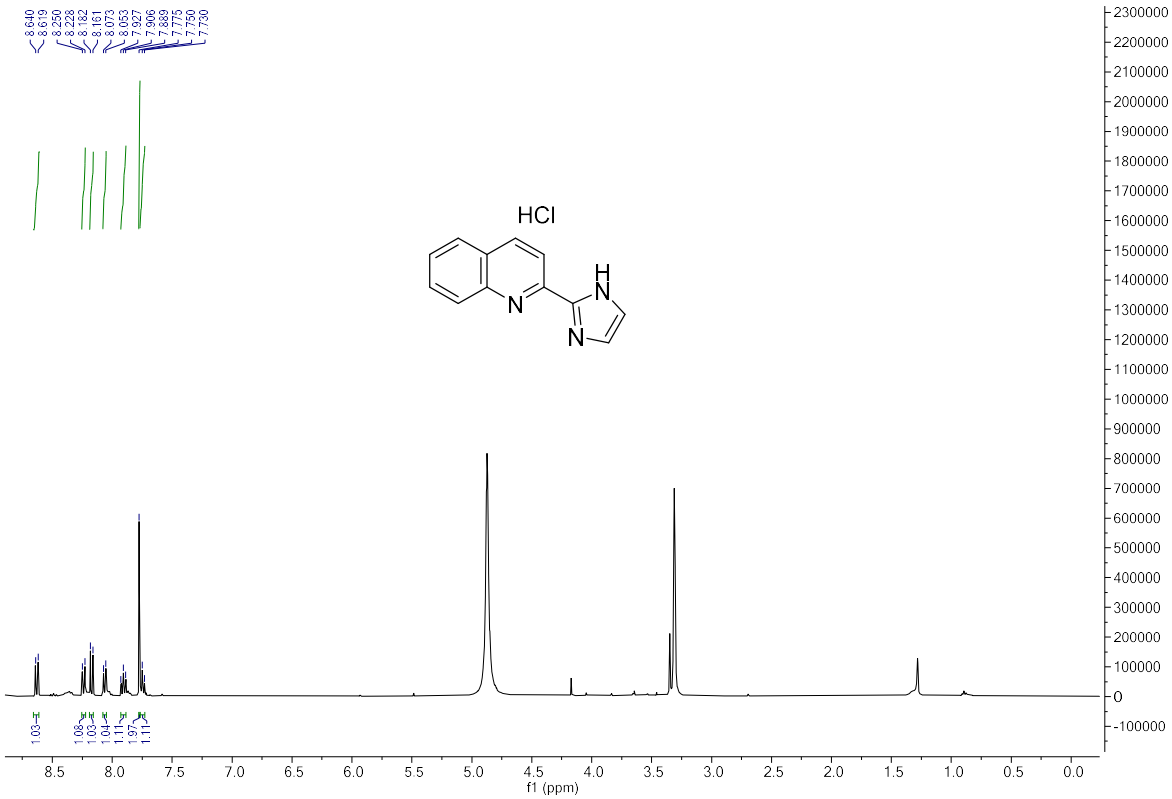

2-(Quinoline-2-yl)-1H-imidazole hydrochloride (LSL42)

Capítulo 4. ***The first consecutive multicomponent reaction leading diastereoselectively to bis(2-imidazolin-4-yl)phosphonates***

The first consecutive multicomponent reaction leading diastereoselectively to bis(2-imidazolin-4-yl)phosphonates

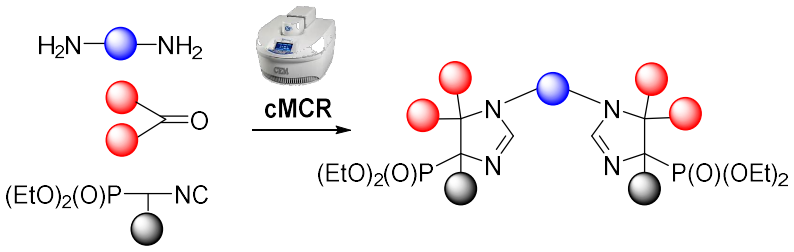

Capítulo 4. *The first consecutive multicomponent reaction leading diastereoselectively to bis(2-imidazolin-4-yl)phosphonates*

En este capítulo se recogen los estudios encaminados a la exploración de nuevas reacciones multicomponente complejas que implican isocianofosfonatos. El trabajo se encuentra avanzado y actualmente estamos a la espera de finalizar la parte experimental y preparar un manuscrito para enviar a una revista especializada en síntesis orgánica para su evaluación.

4.1. Introducción

Las reacciones multicomponente (MCR), tal y como se detalla en la introducción de la presente Tesis Doctoral (apartado 1.1), son reacciones que implican tres o más reactivos de partida que interaccionan en una única etapa sintética y recipiente (*one-pot*), dando lugar a productos finales con una elevada economía de átomo y eficiencia en la formación de enlaces.[67]

Recientemente, las MCR consecutivas (cMCR, también conocidas como MCR secuenciales o múltiples) han surgido como una herramienta sintética interesante para la obtención de moléculas complejas de gran diversidad siguiendo los principios de la química sostenible. Las cMCR son reacciones privilegiadas que emplean de manera consecutiva la combinación de dos o más MCR generando, como mínimo, seis enlaces covalentes mediante la presencia de reactivos de partida bifuncionales o multifuncionales (Esquema 4.1).[68]

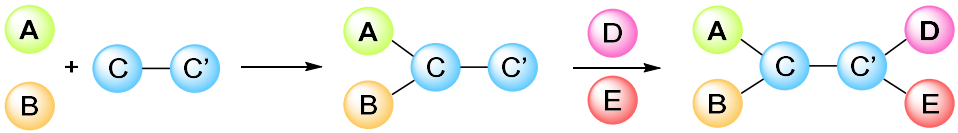

Esquema 4.1. Esquema conceptual de las cMCR.[69]

Por lo tanto, las cMCR emergen como un proceso sintético de utilidad para la obtención de productos simétricos o asimétricos altamente funcionalizados, a partir de sustratos simples y accesibles. El principal desafío en el desarrollo de cMCR es la compatibilidad

[67] (a) Zhu, J.; Wang Q.; Wang, M.-X. *Multicomponent Reactions in Organic Synthesis*, Wiley-VCH, Weinheim, **2015**; (b) Wender, P. A. *Tetrahedron* **2013**, *69*, 7529-7550.
[68] (a) Wessjohann, L.A.; Neves-Filh, R.A.W.; Rivera, D. G. *in Isocyanide Chemistry, Applications in Synthesis and Material Science*, ed. V.G. Nenajdenko, Wiley-VCH, **2014**, pp. 33–262; (b) Barreto, A.F.S.; Vercillo, O.E.; Wessjohann, L.A.; Andrade, C.K.Z. *Beilstein J. Org. Chem*. **2014**, *10*, 1017–1022; (c) Zhang, Z.; You, Y.-Z.; Wu, D.C.; Hong, C.-Y. *Macromolecules* **2015**, *48*, 3414−3421.
[69] Zhi, S.; Ma, Z.; Zhang, W. *Org. Biomol. Chem*. **2019**, *17*,7632-7650.

y selectividad de los grupos funcionales. De hecho, en muchas ocasiones en que los grupos funcionales se ven comprometidos, es necesario recurrir agrupos protectores.[70]

A lo largo de los años, el grupo de investigación dirigido por la Prof. Carmen Escolano ha desarrollado varias estrategias para la construcción de heterociclos mediante el uso de derivados que contienen grupos isocianuro y ésteres fosfónicos en su estructura (*Capítulo 1*). Dado el interés en satisfacer la demanda de compuestos que contienen un núcleo de 2-imidazolina, heterociclo localizado productos naturales y compuestos orgánicos de interés biológico, en el contexto de la Tesis Doctoral de la Dra. Sònia Abás se describió la síntesis mediante MCR de (2-imidazolin-4-il)fosfonatos sustituidos (Esquema 4.2).[18] Además, estos compuestos fueron evaluados como ligandos I_2-IR y presentaron una elevada afinidad y selectividad por estos receptores.[30]

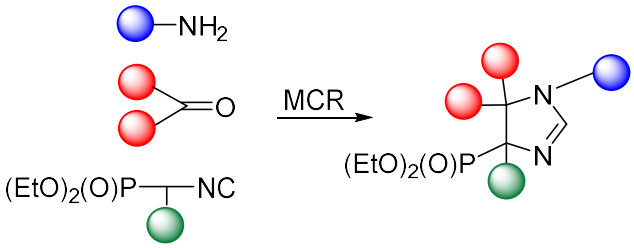

Esquema 4.2. Esquema de la síntesis de (2-imidazolin-4- il)fosfonatos por MCR.

Cabe destacar que, si bien los derivados de isocianuros se encuentran ampliamente descritos en la literatura como reactivos privilegiados en MCR (del inglés, *isocyanide-based multicomponent reactions* IMCRs), el uso de estos en cMCRs se encuentra prácticamente restringido a reacciones tipo Ugi (Esquema 4.3A)[71] o Groebke-Blackburn-Bienaymé (Esquema 4.3B)[72] y por combinación de ellas u otras, tipo Biginelli, Passerini o Huisgen, proporcionando (macro)heterociclos (Esquema 4.3C).[69]

El grupo de investigación del Prof. Orru describió la primera cMCR que incluye un grupo 2-imidazolina en su estructura final mediante dos IMCR consecutivas (Esquema 4.3D).[73]

[70] Ghashghaei, O.; Seghetti, F.; Lavilla, R. *Beilstein J. Org. Chem*. **2019**, *15*, 521–534.
[71] Barreto, A.F.S.; Andrade, C.K.Z. *Beilstein J. Org. Chem*. **2019**, *15*, 906-930.
[72] Ghashghaei, O.; Caputo, S.; Sintes, M.; Revés, M.; Kielland, N.; Estarellas, C.; Luque, F.J.; Avino, A.; Eritja, R.; Serna-Gallego, A.; Marrugal-Lorenzo, J.A.; Pachon, J.; Sanchez-Céspedes, J.; Treadwell, R.; de Moliner, F.; Vendrell, M.; Lavilla, R. *Chem.- Eur. J.* **2018**, *24*, 14513–14521.
[73] Elders, N.; Born, D.; Hendrickx, L.J.D.; Timmer, B.J.J.; Krause, A.; Janssen, E.; Kanter, F.J.J.; Ruijter, E.; Orru, R.V.A. *Angew. Chem. Int. Ed*. **2009**, *48*, 5856– 5859.

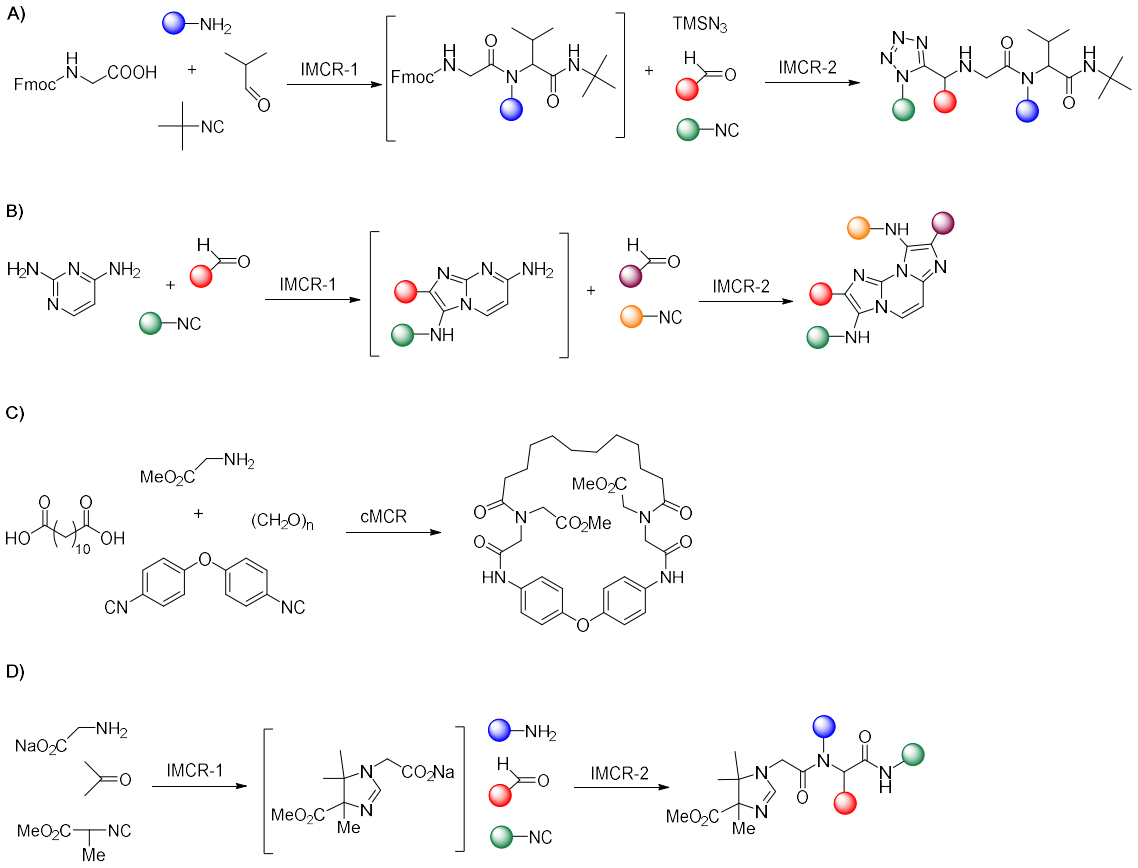

Esquema 4.3. Ejemplos de cMCRs que incluyen isocianuros.

Con la atención puesta en la complejidad de los compuestos obtenidos mediante estas reacciones de fácil experimental y aprovechando nuestra experiencia previa en reacciones de tipo ICMR,[22] nos propusimos explorar el potencial de algunos de los productos de partida empleados anteriormente para generar nuevas cMCR (Esquema 4.2).[74]

4.2. Objetivo

Considerando el interés del grupo en el desarrollo de reacciones que involucran isocianometilfosfonatos respectando las recomendaciones de la química sostenible, se propuso una cMCR entre isocianuros α-sustituidos, en especial isocianometilfosfonatos, cetonas y diaminas diversamente sustituidas para la formación de compuestos complejos que contengan en su estructura bis(2-imidazolin-4-il)fosfonatos (Esquema 4.4). Este proyecto de metodología sintética daría lugar al primer estudio de obtención de bisimidazolinas por cMCR y al primer trabajo sintético de cMCR que emplea isocianuros que contienen ésteres fosfónicos.[75]

[74] Sinha, M.K.; Khoury, K.; Herdtweck, E.; Dömling, A. *Chem.-Eur. J.* **2013**, *19*, 8048-8052.
[75] Bhat, S.I. *ChemistrySelect* **2020**, *5*, 8040-8061.

Además, estos compuestos podrían ser potenciales ligandos I_2-IR ya que se podrían considerar estructuras resultantes de la duplicación molecular de los (2-imidazolin-4-il)fosfonato descritos anteriormente.[35] Por lo tanto, la evaluación farmacológica de los productos resultantes es una de las tareas que se consideraron.

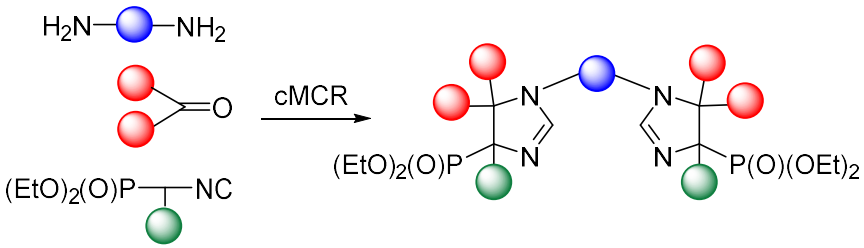

Esquema 4.4. cMCR propuesta para la obtención de bis(2-imidazolin-4-il)fosfonatos.

4.3. Discusión de los resultados

En primer lugar, se propuso explorar una reacción de tres componentes (diaminas, isocianometilfosfonatos y acetona) a través de dos cMCR, generando los bis(2-imidazolin-4-il)fosfonatos propuestos siguiendo las condiciones de reacción descritas para sus análogos (2-imidazolin-4-il)fosfonato.[22] La síntesis se llevó a cabo en un horno microondas (10 min a 40 ºC), instrumento excepcional para la química orgánica sostenible, permitiendo reducir tiempo y energía requerida para la reacción.[76] Los componentes implicados en la reacción inicial fueron α-fenilisocianometilfosfonato de dietilo (α-Ph-PhosMic), 1,4-diaminobutano, acetona (que desempeña la función dual de reactivo y disolvente) y $AgNO_3$ como catalizador.[18]

Siguiendo las condiciones comentadas, se accedió al producto deseado **1a** con una conversión de un 61 % y un 45% de rendimiento e, inesperadamente, de forma diastereoselectiva, aislándose únicamente uno de los dos posibles diastereómeros, teniendo en cuenta la generación de dos centros cuaternarios.

Con estos buenos resultados iniciales nos propusimos optimizar la reacción anterior realizando distintas modificaciones en las condiciones experimentales, las cuales aparecen recogidas en la Tabla 4.1.

4.3.1. Búsqueda de las condiciones de reacción óptimas

Tal y como se puede observar en la Tabla 4.1 (y en la Tabla S2 de la información complementaria), variando las condiciones de reacción empleando: horno microondas (entradas 1 y 2), temperatura ambiente durante 16 h (entrada 3) o ultrasonidos, otra

[76] Majumder, A.; Gupta, R.; Jain, A. *Green Chem. Lett. Rev.* **2013**, *6*, 151-182.

herramienta que sigue los fundamentos de la química sostenible ampliamente utilizada en las MCR (entrada 4), se aumenta la formación de **1a**, pasando a ser el porcentaje de conversión de un 61% a un 82, 75 y 80 %, respectivamente.[77]

Tabla 4.1. Optimización de las condiciones de reacción para la obtención de **1a**.[a]

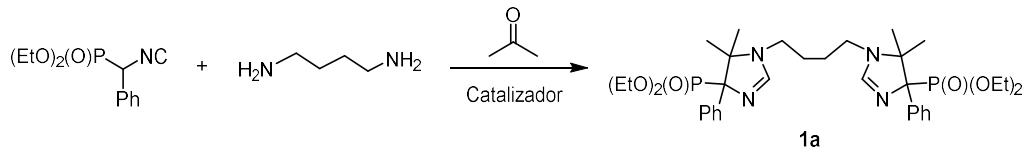

1a

Entrada	Condiciones	Catalizador	Conversión a 1a[b]
1	MW, 40ºC, 10 min	$AgNO_3$	61
2	**MW, 40ºC, 20 min**	**$AgNO_3$**	**82**
3	t.a., 16 h	$AgNO_3$	75
4	US, 40ºC, 1 h	$AgNO_3$	80
5	MW, 40ºC, 20 min	---	0
6	MW, 40ºC, 20 min	$AgNO_3$[c]	52
7	MW, 40ºC, 20 min	CF_3COOH	8
8	MW, 40ºC, 20 min	$AgBF_4$	70[d]
9	MW, 40ºC, 20 min	AgF	67[d]
10	MW, 40ºC, 20 min	AgOAc	58[d]

[a] Porcentajes de los reactivos:α-Ph-PhosMic (2.2 equiv), 1,4-diaminobutano (1 equiv), acetona (0.13 mmol/ml) y catalizador (10%-mmol). **[b]** Conversión (%) a **1a** determinada por HPLC-MS**. [c]** $AgNO_3$ 6%-mmol. **[d]** El producto de ciclodimerización **A** fue detectado por HPLC-MS en el crudo de reacción (entrada 8, 4%; entrada 9, 7%; entrada 10, 10%).

Asimismo, la ausencia de catalizador (entrada 5) impide la obtención del compuesto **1a**. Al disminuir la cantidad de $AgNO_3$ del 10% al 6% se reduce la conversión en el producto final (entrada 6). Por tanto, la nueva cMCR requiere el 10% de catalizador para que transcurra de manera óptima.

Finalmente, la reacción tiene lugar de igual modo cuando se utilizan otras sales de plata, $AgBF_4$, AgF o AgOAc, con acidez superior a $AgNO_3$ como catalizador, observándose la formación **A** (Figura 4.1) (entradas 8-10). Para poder afirmar que el compuesto que se obtenía como secundario en las reacciones llevadas a cabo en las condiciones de las entradas 8, 9 y 10 era el de reacción del isocianuro consigo mismo, se decidió proceder a su síntesis. Para ello, se sometió el α-Ph-PhosMic a las condiciones de la entrada 2 en ausencia de la diamina, conduciendo al producto **A** con un rendimiento del 78%. En trabajos anteriores del grupo ya se había observado la formación del producto resultante

[77] Banerjee, B. *Ultrasonics Sonochemistry* **2017**, *35*, 15-35.

de la reacción de PhosMic consigo mismo (**B**) de manera muy considerable cuando se utilizaba AgOAc como catalizador y era inapreciable con el uso de $AgNO_3$.[22]

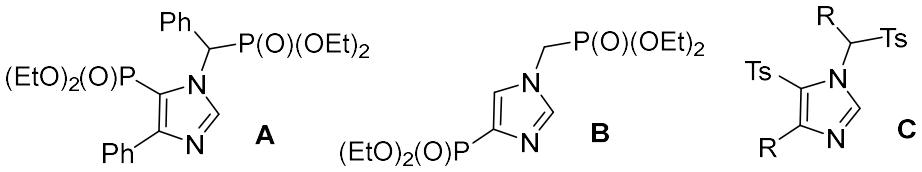

Figura 4.1. Producto de ciclodimerización **A**.

Posteriormente, en base a estudios del Prof. Bi, donde se describe el producto resultante de la reacción de ciclodimerización de tosilmetilisocianuros (TosMIC) α-sustituidos (**C**),[78] se propuso un posible mecanismo para la formación de **A** (Esquema 4.5). El mecanismo propuesto implica, en primer lugar, la formación de un complejo del α-Ph-PhosMic con la plata. En segundo lugar, se da una reacción de cicloadición [3+2] entre los isocianofosfonatos. Seguidamente, en el intermedio que presenta un ion nitrilo se produce la transposición 1,2 del fosfonato formándose un carbocation que, finalmente, mediante la protonación y desmetalación, se obtiene como resultado el producto **A**. La reacción de migración 1,2 de fosfonatos en imidazolinas no está descrita como tal, pero si hay algunas referencias en para otros heterociclos en medios básicos.[79]

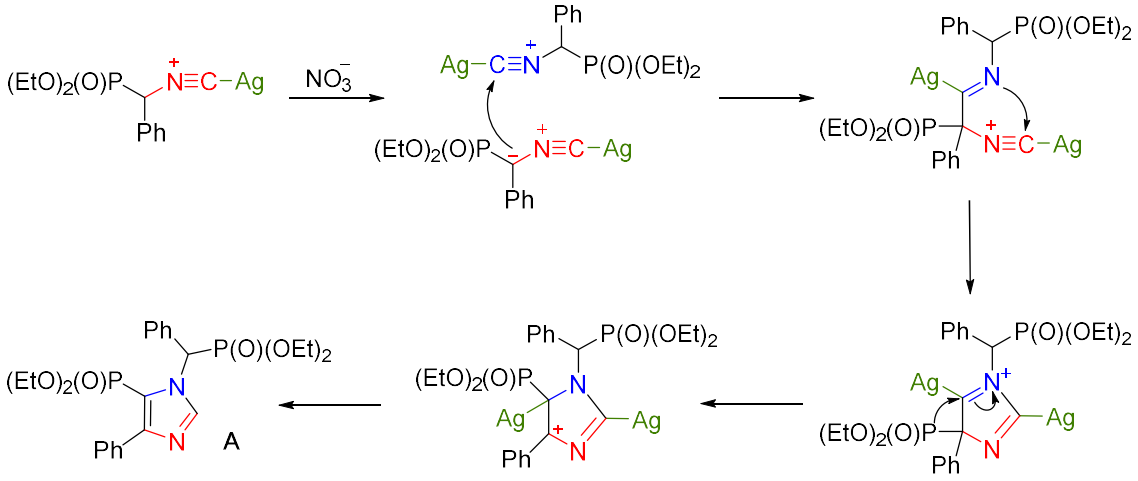

Esquema 4.5. Propuesta del mecanismo de reacción para la formación de **A**.

Una vez encontradas unas condiciones de reacción adecuadas, horno microondas durante 20 minutos a 40 ºC en presencia de $AgNO_3$ al 10% (Tabla 4.1, entrada 2),

[78] Wang, H.; Kumar, R.K.; Yu, Y.; Zhang, L.; Liu, Z.; Liao, P.; Bi, X. *Chem. Asian J.* **2016**, *11*, 2841-2845.
[79] (a) Anderson, D.K.; Sikorski, J.A. *J. Heterocycl. Chem.* **1992**, *29*, 177-180; (b) Sudau, A.; Münch, W.; Bats, J.-W.; Nubbemeyer, U. *Eur. J. Org. Chem*. **2002**, 3315-3325; (c) Khan, S.; Battula, S.; Ahmed, Q.N. *Tetrahedron* **2016**, *72*, 4273-4279.

decidimos aplicarlas a una variedad de reactivos de partida para acceder a una familia de bis(2-imidazolinas) diversamente sustituidas.

En esta Tesis, se exploró el alcance de la reacción utilizando otras diaminas primarias simétricas y asimétricas de diferente naturaleza y patrón de sustitución como son aminas alifáticas, bencílicas o arílicas (Tabla 4.2). También, se exploró la reacción utilizando diferentes compuestos carbonílicos.

4.3.2. Estudio de la reacción con diferentes diaminas alifáticas

Los resultados obtenidos al utilizar diferentes diaminas se exponen en la Tabla 4.2, donde se muestran los rendimientos de los bis(2-imidazolin-4-il)fosfonatos **1a-9b** que van de moderados a buenos (41-82%), considerando que se generan varios enlaces covalentes, incluidos dos centros esterogénicos.

Tabla 4.2. Rendimiento (%) de los bis(2-imidazolin-4-il)fosfonatos **1a-9b**.[a]

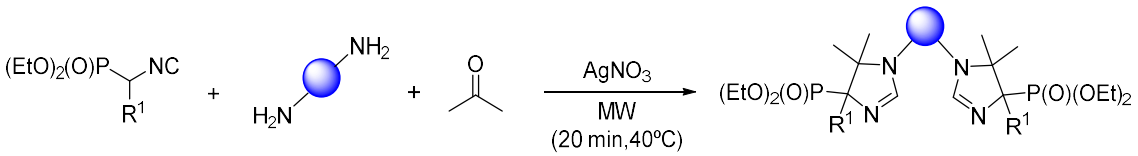

Entrada	R^1	Diamina	Producto	Rendimiento
1	Ph	1,4-Diaminobutano	**1a**	82
2	H	1,4-Diaminobutano	**1b**	54
3	Bn	1,4-Diaminobutano	**nd**	-
4	Ph	1,6-Diaminohexano	**2**	67
5	H	1,10-Diaminodecano	**3**	41
6	H	1,8-Diamino-3,6-dioxaoctano	**4**	66
7	Ph	biciclo(2.2.1)heptametanodiamina	**5**	65
8	Ph	*p*-Xilenodiamina	**6a**	67
9	H	*p*-Xilenodiamina	**6b**	62
10	Ph	*m*-Xilenodiamina	**7**	72
11	Bn	*p*-Xilenodiamina	**nd**	-
12	Ph	*p*-Ciclohexanodiamina	**nd**	33[b][c]
13	H	*p*-Ciclohexanodiamina	**8a**	30
14	Ph	*p*-Fenilenodiamina	**nd**	51[b][c]
15	H	*p*-Fenilenodiamina	**nd**	-
16	Ph	4-Aminobencilamina	**nd**	56[b][c]
17	Ph	2-Metilpentano-1,5-diamina	**9a**	57
18	H	2-Metilpentano-1,5-diamina	**9b**	53

[a] Condiciones de reacción: isocianometilfosfonato (2.2 equiv), diamina (1 equiv), acetona (0.13 mmol/ml) y $AgNO_3$ (10%-mmol) en horno microondas (20 min/40ºC); **1a-9b** rendimiento del producto aislado (%), nd = no detectado. **[b]** Rendimiento (%) de los correspondientes (2-imidazolin-4-il)fosfonatos **Ia, II y III**. **[c]** El producto **A** detectado por HPLC-MS en el crudo de reacción (entrada 12, 40%; entrada 14, 39%, entrada 18, 17%).

El estudio se inició sintetizando los bis(2-imidazolin-4-il)fosfonatos **1a-3** con rendimientos de 82, 54, 67 y 41%, respectivamente (entradas 1-5). Estos compuestos se caracterizan por tener una cadena carbonada que une los dos sistemas imidazolínicos de diferente longitud, 4, 6 y 10 carbonos, así como la presencia (**1a**, **2**, **4** y **5**), o no (**1b** y **3**), de sustituyentes en el carbono alfa del grupo isocianuro.

El compuesto **1a**, que incorporado un fenilo en el carbono alfa del grupo isocianuro (entrada 1) y una cadena carbonada de 4 carbonos, presentó mayor rendimiento (82%) que su homólogo sin sustituyente en esta posición **1b** (54%) (entrada 2). A su vez, los compuestos **2** (entrada 4) y **3** (entrada 5), que presentan cadenas carbonadas de mayor longitud que sus homólogos **1a** y **1b**, se aislaron con rendimientos del 67 y 41%, respectivamente. Por eso, se puede deducir que la incorporación de un fenilo en el carbono alfa del grupo isocianuro y el uso de diaminas de cadenas carbonadas de longitud corta-media son condiciones estructurales favorables para la formación de los compuestos, presentando rendimientos más elevados. Como se observa en la entrada 3, al añadir α-bencilisocianometilfosfonato de dietilo (α-Bn-PhosMic) la reacción no tuvo lugar, aislándose los reactivos de partida, probablemente debido a la menor acidez del protón en α del isocianuro respecto a los derivados anteriores. Al hacer reaccionar α-Bn-PhosMic con catalizadores de una acidez superior al $AgNO_3$, como el AgOAc, tampoco se obtiene el producto deseado y, además, se observa la formación del subproducto **A**.

Al compuesto **4**, el cual contiene una cadena carbonada que incorpora átomos de oxígeno, se accedió con un rendimiento del 66% (entrada 6). El objetivo con la preparación de **4** consistía en incrementar solubilidad, ya que los compuestos descritos anteriormente (**1a-3**) eran pocos solubles en los disolventes orgánicos comunes del laboratorio y generaban problemas para ser purificados.

Asimismo, también se describe el producto resultante de la reacción con una diamina policíclica (biciclo(2.2.1)heptametanodiamina), obteniendo el compuesto **5** con un rendimiento del 65% (entrada 7) (Figura 4.2).

Hasta el momento habíamos conseguido preparar seis compuestos mediante el uso de diaminas alifáticas, que repiten el sistema heterocíclico de (2-imidazol-4-il)fosfonato unido por una cadena carbonada.

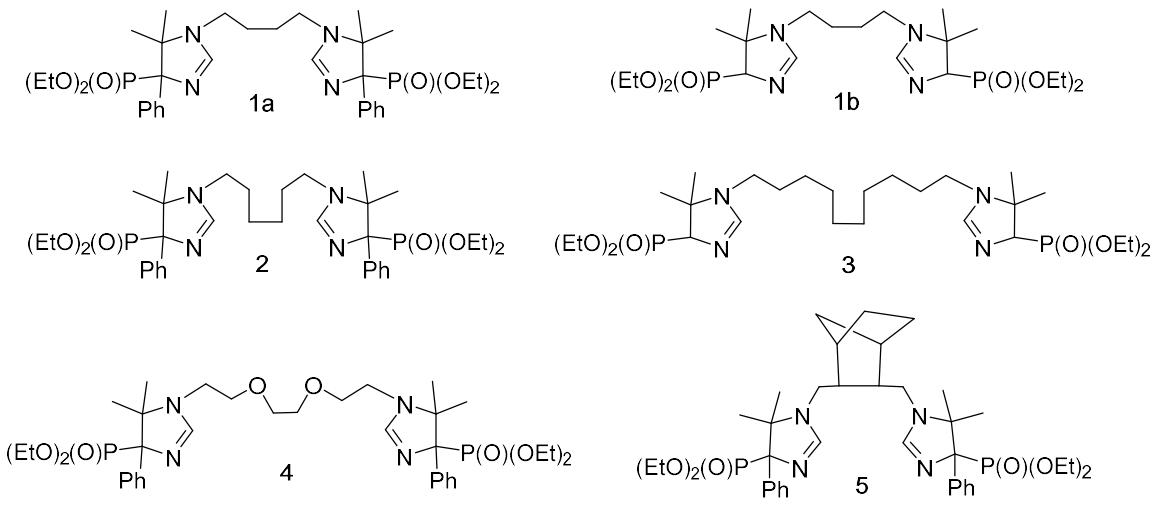

Figura 4.2. Bis(2-imidazolin-4-il)fosfonatos **1a-5**.

4.3.3. Estudio de la reacción con diferentes diaminas bencílicas

Seguidamente, se continuó el cribado empleando diaminas bencílicas. La reacción con *p*-xilenodiamina en presencia de α-Ph-PhosMic condujo al compuesto **6a** con un 67% de rendimiento (Tabla 4.2, entrada 8). De manera análoga a como se procedió anteriormente para la preparación de **1a** y **1b**, se llevó a cabo la reacción con PhosMic y se accedió a **6b** con un 62% de rendimiento (Tabla 4.2, entrada 9). En este caso la presencia o no de un fenilo en la posición alfa del grupo isocianuro no representó una variación en rendimiento en el producto final. Considerando otra diamina aromática como la *m*-xilenodiamina se obtuvieron resultados satisfactorios de un 72% en la obtención de **7** (Tabla 4.2, entrada 10). Sin embargo, al considerar α-Bn-PhosMic y aminas *p*-xilenodiamna la reacción, tal y como había ocurrido anteriormente con las aminas aromáticas, no dió el resultado deseado (Tabla 4.2, entrada 11), aislando únicamente los reactivos de partida (Figura 4.3). Así, habíamos accedido a tres compuestos que contenían en su estructura 2-imidazolinas con el patrón particular de sustitución unidas por una cadena que contenía un benceno (**6a**, **6b**, **7**).

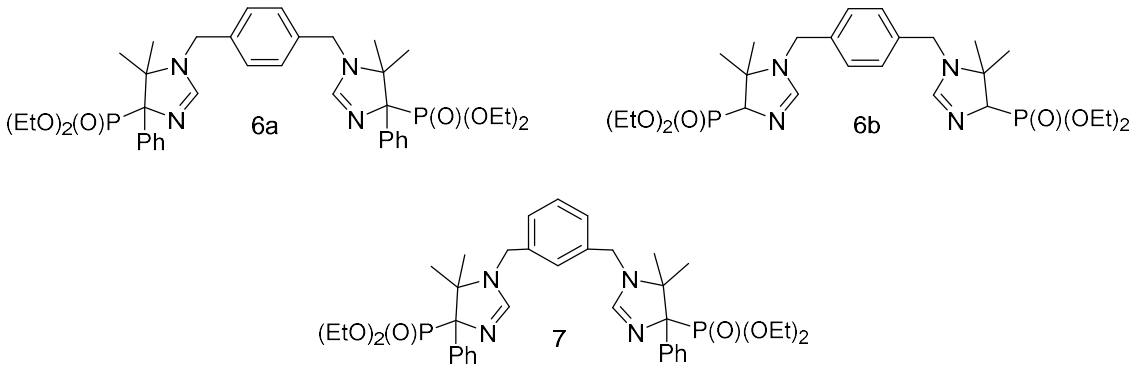

Figura 4.3. Bis(2-imidazolin-4-il)fosfonatos **6a**, **6b** y **7**.

4.3.4. Estudio de la reacción con diferentes diaminas impedidas estéricamente o dianilina

A continuación, se propuso estudiar como transcurría la reacción al emplear diaminas con mayor impedimento estérico o dianilina, tales como *p*-ciclohexanodiamina (Tabla 4.2, entradas 12 y 13) o *p*-fenilendiamina (Tabla 4.2, entradas 14 y 15). En este caso, la cMCR para la formación de bis(2-imidazolin-4-il)fosfonatos no tuvo lugar en las condiciones estándares de microondas a 40 ºC durante 20 min.

Es importante destacar que al usar α-Ph-PhosMic da como resultado el producto **A**, así como la IMCR en una de las dos aminas, aislando así los correspondientes (2-imidazolin-4-il)fosfonatos **Ia-III** (Esquema 4.6).

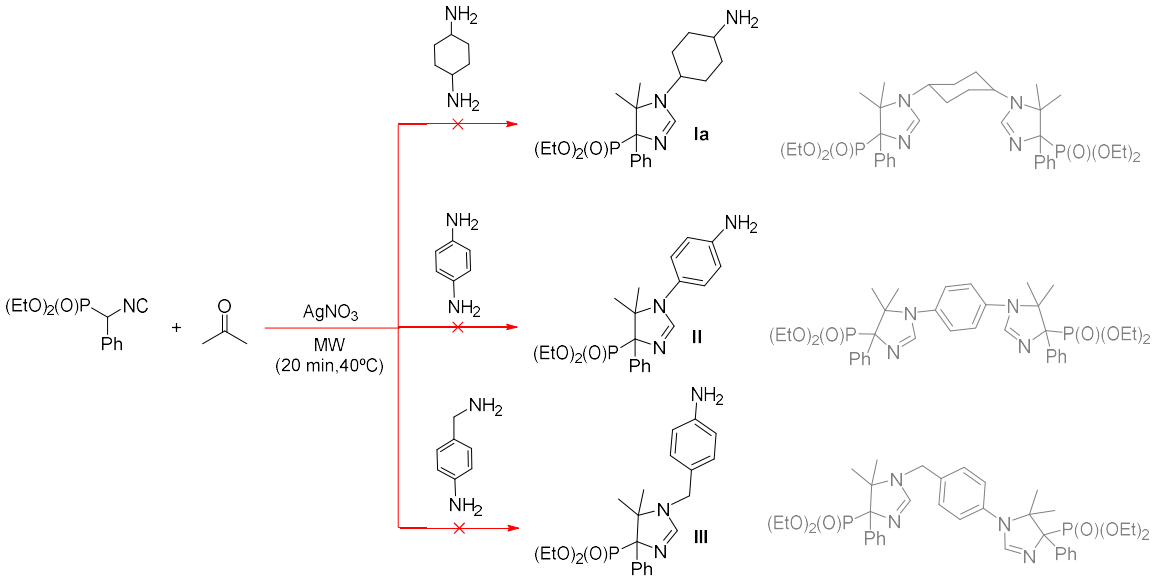

Esquema 4.6. (2-imidazolin-4-il)fosfonatos **Ia-III**.

Con la intención de sintetizar algún ejemplo de bis(2-imidazolin-4-il)fosfonato con *p*-ciclohexanodiamina y α-Ph-PhosMic se realizaron múltiples modificaciones en las condiciones de reacción en microondas (Tabla 4.3), tales como el aumento del tiempo de reacción de 20 a 60 min (entrada 2), cambiar el catalizador por AgOAc (entrada 3) o incorporar un disolvente a la reacción como es el metanol (entrada 4).

Ninguna de estas modificaciones resultó dar el producto deseado, por ello se realizó la reacción en ultrasonidos durante 2 h a 40 ºC (entrada 5) o bajo agitación constante a temperatura ambiente durante 48 h (entrada 6). En este último caso, aunque el producto deseado no pudo ser aislado, fue detectada por HPLC-MS la presencia en baja proporción de este.

Tabla 4.3. Optimización de las condiciones de reacción para la obtención del bis(2-imidazolin-4-il)fosfonato **8a**-**8b**.[a, b]

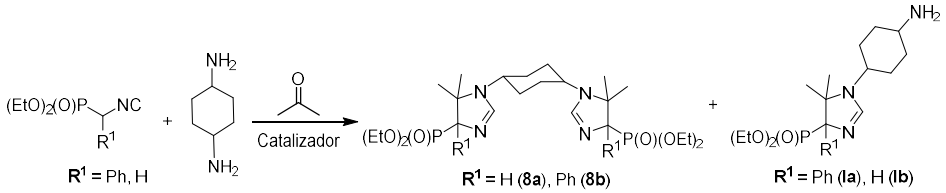

Entrada	R^1	Condiciones	Conversión a 8a-8b	Conversión a Ia-Ib	Conversión a A o B
1	Ph	MW, 40 ºC, 20 min	5	45	40
2	Ph	MW, 40 ºC, 60 min	8	40	45
3	Ph	MW, 40 ºC, 60 min [c]	0	32	55
4	Ph	MW, 40 ºC, 60 min [d]	0	24	37
5	Ph	US, 40 ºC, 2 h	0	34	59
6	Ph	r.t., 48 h	16	32	47
7	H	MW, 40 ºC, 20 min	45	44	0
8	H	r.t., 48 h	75	18	0
9	H	US, 40 ºC, 2 h	84	0	0

[a]Cantidades de reactivos: isocianometilfosfonato (2.2 equiv), *p*-ciclohexanodiamina (1 equiv), acetona (0.13 mmol/ml) y $AgNO_3$ (10%-mmol). **[b]** Conversión (%) determinada por HPLC-MS. **[c]** AgOAc (10%-mmol). **[d]** Acetona (4 equiv) en metanol (0.13 mmol/ml).

Se realizaron estudios considerando el uso de PhosMic para comparar su comportamiento respecto a su homólogo α-Ph-PhosMic. Por ello, se repitieron las condiciones comentadas anteriormente: microondas a 40 ºC durante 20 min (entrada 7), agitación a temperatura ambiente durante 48h (entrada 8) y ultrosonidos a 40 ºC durante 2 h (entrada 9), en presencia de PhosMic y la diamina monocíclica, observando en todos los casos la formación del producto final deseado, resultando ser la reacción en ultrasonidos la que mayor conversión generaba para obtener el compuesto **8a**. En un futuro próximo se seguirán realizando ensayos encaminados a la obtención de **8b**.

4.3.5. Estudio de la reacción con diamina asimétrica

Finalmente, se seleccionó una diamina alifática asimétrica (2-metilpentano-1,5-diamina) para la síntesis de los (2-imidazolin-4-il)fosfonatos asimétricos **9a** y **9b** que difieren en la presencia o no de un fenilo en la posición alfa del grupo isocianuro, con rendimientos del 57 y 53%, respectivamente (Tabla 4.2, entrada 17 y 18). En ambos casos, aunque se genera un nuevo centro cuaternario, solo se observó y aisló un diastereómero (HPLC-MS del crudo de **9b**, Apartado 3 información complementaria).

Este acontecimiento inesperado, la obtención de un único diastereómero en presencia de una diamina asimétrica, ya se había observado en trabajos previos del grupo al

sintetizar (2-imidazolin-4-il)fosfonatos empleando una amina alifática asimétrica (Figura 4.4).[22]

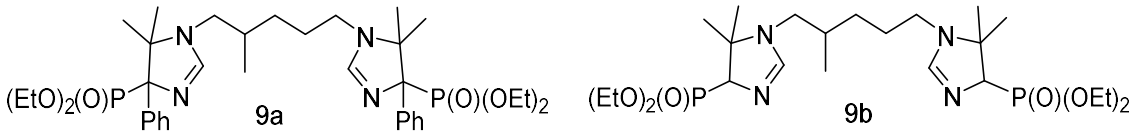

Figura 4.4. Bis(2-imidazolin-4-il)fosfonatos **9a** y **9b**.

Con el objetivo de sintetizar bis(2-imidazolin-4-il)fosfonatos asimétricos, se propuso obtener el producto resultante **6c** por medio de la reacción *one-pot* de *p*-xilenodiamina, PhosMic, α-Ph-PhosMic y acetona, simultáneamente (Esquema 4.7).

Desafortunadamente, no se accedió al compuesto final esperado con diferentes sustituyentes en el carbono en alfa del fosfonato de cada anillo, sino que únicamente se observó la formación de (**A**) (30%) y el bis(2-imidazolin-4-il)fosfonato simétrico **6a** (20%), así como un exceso de PhosMic sin reaccionar. Se plantea como hipótesis de que esto sucede debido a la menor reactividad del PhosMic a su derivado α-sustituido.

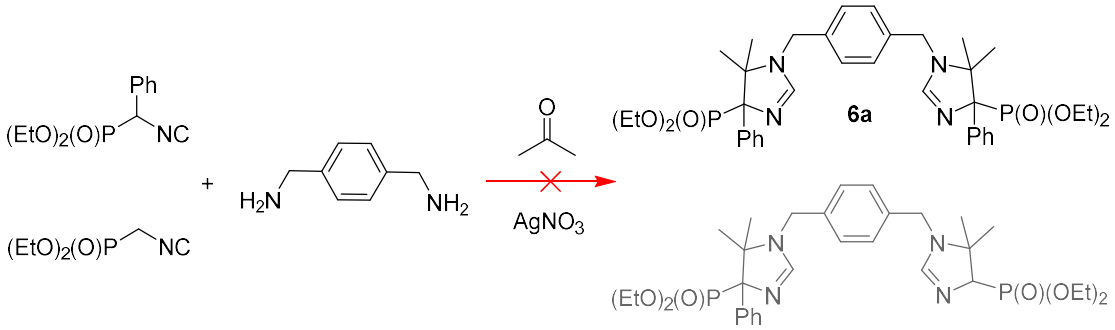

Esquema 4.7. cMCR para obtención del bis(2-imidazolin-4-il)fosfonato asimétrico **6c**.

4.3.6. Estudio de la reacción con triamina alifática

Además, se propuso una reacción cMCR triple que, bajo las condiciones estándares de reacción, condujese a una estructura de tris(2-imidazolin-4-il)fosfonatos. Así **10** se sintetizó por reacción de α-Ph-PhosMic en presencia de tris(2-aminoetil)amina (Figura 4.5), con un buen rendimiento (52%) teniendo en cuenta que para formarse tiene lugar tres IMCRs y se generan nueve enlaces (Tabla 4.2, entrada 17).

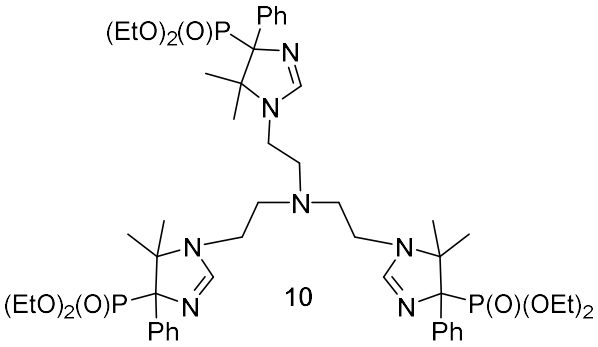

Figura 4.5. Tris(2-imidazolin-4-il)fosfonatos **10**.

A continuación, los esfuerzos se dirigieron a explorar la cMCR resultante de emplear un compuesto carbonilo diferente a la acetona.

4.3.7. Estudio de la reacción con diferentes carbonilos

Con la intención de sustituir la acetona, se llevó a cabo la reacción utilizando ciclohexanona, como uno de los componentes de la cMCR, *p*-xilenodiamina y PhosMic o α-Ph-PhosMic, dando como resultado los derivados bisespiránicos de los bis(2-imidazolin-4-il)fosfonatos **11a** y **11b** de manera diastereoselectiva con rendimientos de 45 y 49%, respectivamente (Figura 4.6).

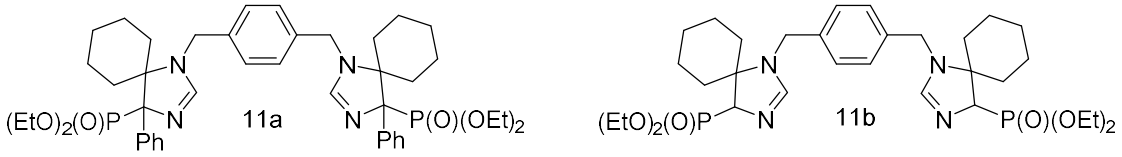

Figura 4.6. Bis(2-imidazolin-4-il)fosfonatos **11a** y **11b**.

Además, se propuso utilizar una cetona asimétrica, la 3,3-dimetilbutan-2-ona en presencia de α-Ph-PhosMic y *p*-xilenodiamina. En este caso, la reacción no funcionó, aislándose únicamente el producto (**A**), probablemente debido al impedimento estérico que presenta esta cetona (Esquema 4.8).

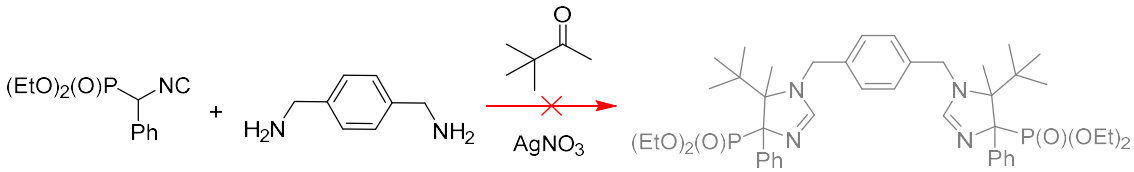

Esquema 4.8. cMCR empleando una cetona asimétrica.

4.3.8. Determinación de la diastereoselectividad de la reacción para la formación de 1a.

Es importante destacar que para todos los (2-imidazolin-4-il)fosfonatos obtenidos por cMCR únicamente se observa la formación de uno de los posibles diastereómeros, confirmando que se trata de una reacción diastereoselectiva. Este hecho se corroboró mediante el análisis de los crudos de reacción de los compuestos por ^{1}H-RMN, indicando la presencia de un grupo señales correspondientes a uno de los posibles diastereómero, en lugar de dos. Asimismo, **1a** fue cristalizado en una mezcla de disolventes (IPA-hexano) obteniendo un monocristal. La estructura del producto ha sido confirmada inequívocamente por los estudios cristalográficos de rayos X (Figura 4.7) realizados por el Prof. Molins del Institut de Ciència de Materials de Barcelona (CSIC).

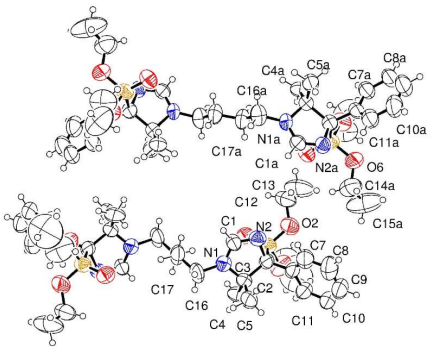

Figura 4.7. Estructura de rayos X de **1a**.

Los resultados indican quelos ésteres fosfónicos presentes en los centros estereogénicos de cada sistema imidazolínico presentan una relación *trans* entre ellos, obteniendo de los dos posibles diastereómeros la pareja de enantiómeros *SR* y *RS* (Figura 4.8).

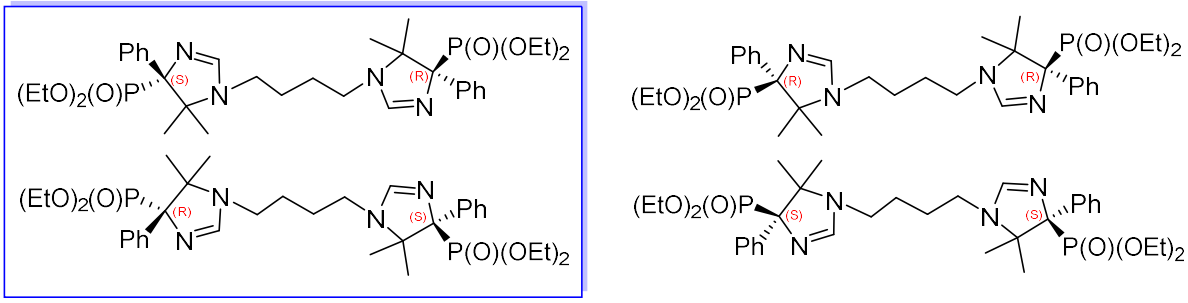

Figura 4.8. Estructura del par de enantiómeros de **1a**.

Actualmente, el Prof. F. Javier Luque está realizando estudios teóricos para justificar la estereoquímica observada en la reacción, aunque aún no hay resultados concluyentes.

Como era de esperar, los espectros de RMN de ^{1}H y ^{13}C de los derivados **1a-11b** que contienen en su estructura ésteres fosfónicos resultaron ser complejos debido a las constantes de acoplamiento adicionales entre ^{1}H-P y ^{13}C-P (Tabla 4.4).

Tabla 4.4. Desplazamientos químicos (ppm), multiplicidad y constantes de acoplamiento (*J* Hz, verde (^{1}H-P) y azul (^{13}C-P)) de ^{1}H y ^{13}C para los nuevos compuestos **1a-11b**.

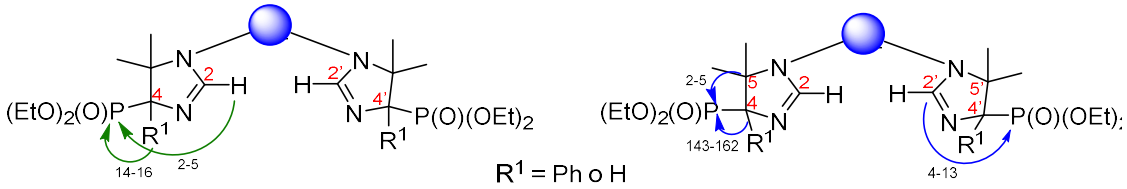

R^1 = Ph o H

Compuesto	H2/H2'	H4/H4'	C2/C2'	C4/C4'	C5/C5'
1a	7.11, d 3.0	---	155.9, d 6.0	81.8, d 146.0	67.7, d 4.0
1b	7.11, br s	3.96, dd 14.0, 2.0	156.8, d 12.0	70.5, d 162.0	65.3, d 3.0
2	7.10, d 3.5	---	155.9, d 6.0	81.6, d 147.0	68.6, d 4.0
3	7.12, br s	3.94, dd 16.0, 1.5	156.5, d 13.0	72.0, d 162.0	64.9, d 2.0
4	7.29, d 4.0	---	156.5, dd 7.0, 3.0	81.4, dd 145.0, 3.0	68,3, d 4.0
5	7.34, s	---	155.9, d 5.0	81.3, d 145.0	68.8, d 3.0
6a	7.03, d 4.5	---	156.5, d 5.0	82.1, d 146.5	68.9, d 4.5
6b	6.94, br s	3.99, dd 16.0, 1.5	156.9, d 12.0	73.1, d 162.0	66.8, d 3.0
7	7.06, t 3.0	---	156.6, d 6.0	82.0, dd 146.5, 3.0	68.9, d 4.5
8a	7.36, br s	3.93, dd 15.0, 2.0	154.2, d 9.0	72.4, d 161.0	65.3, d 4.0
9a	7.08, d 3.5 7.15, dd 19.0, 3.5	---	157.1, d 5.0 157.3, d 5.0	81.4, d 145.0 81.5, d 143.0	69.3, d 3.0 69.4, d 3.0
9b	6.82, d 2.5 6.87, d 2.0	3.89, d 2.0 3.93, d 2.0	156.2, d 4.0 157.0, d 4.0	73.6, d 163 73.7, d 164	64.4, d 3.0 64.5, d 3.0
10	7.39, s	---	156.3, d 5.0	80.9, d 153.0	69.0, d 4.0
11a	7.01, t 4.0	---	157.1, d 6.0	83.5, d 145.0	70.8, d 4.0
11b	7.14, br d 3.0	4.37, d 16.0	157.9, dd 7.0, 1.0	68.6, d 151.0	63.1, d 4.0

Con el propósito de explorar el potencial de la reacción, se propuso sustituir los isocianofosfonatos por sus ésteres alquílicos homólogos y, mediante cMCR, sintetizar

las bis(2-imidazolinas) derivadas de la reacción de la diamina (aromática o alifática, *p*-xilenodiamina y 1,4-diaminobutano, respectivamente), acetona y isocianoacetato de metilo. Asimismo, el grupo de investigación donde se enmarca esta Tesis Doctoral tiene años de experiencia en el uso de isocianoacetatos como reactivos de partida, permitiendo acceder a núcleos de 2-pirrolinas,[11] (2-imidazolin-4-il)carboxilatos[22] y 1-pirrolinas bicíclicas.[13]

El interés en preparar estos compuestos bis(2-imidazolin-4-il)carboxilatos radica en la observación realizada por el grupo de investigación de la Prof. Carmen Escolano al sintetizar y 1-pirrolinas bicíclicas por medio de una reacción de cicloadición [3+2] entre isocianuros y maleimidas.[13] Este estudio demostró que al utilizar PhosMic como isocianuro la reacción era diastereoselectiva, a diferencia de estudios publicados por el Prof. Grigg empleando su homólogo isocianoacetato, que resultaba dar una mezcla diastereomérica.[9] Por ello, se consideró que al emplear un isocianuro no fosforado, la cMCR no cursaría con diastereoselectividad.

4.3.9. cMCR utilizando isocianoacetato de metilo

En primer lugar, se sugirió obtener los bis(2-imidazolin-4-il)carboxilatos de metilo por cMCR siguiendo el método para sintetizar (2-imidazolin-4-il)carboxilatos de metilo descrito por el grupo del profesor Orru (Esquema 4.9, condiciones A)[19c] y, posteriormente, por nuestro grupo de investigación (Esquema 4.9, condiciones B), empleando metanol o acetona como disolvente y la presencia (o no) de catalizador, ya que los protones en α de los isocianoacetatos son más ácidos que sus análogos de ésteres fosfónicos.[22]

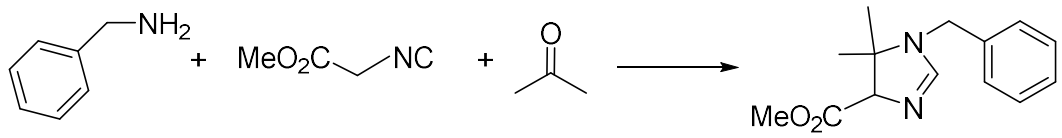

Esquema 4.9. Síntesis de (2-imidazolin-4-il)carboxilatos de metilo por MCR. **A)** Na_2SO_4, MeOH, 5 h a t.a. 89%. **B)** $AgNO_3$, MW, 10 min a 40 ºC. 94%.

En nuestro caso, la formación de los productos deseados no tuvo lugar en ausencia de catalizador. Por esa razón, se planteó la opción de sintetizarlos bajo las condiciones generales óptimas para los ésteres fosfónicos, es decir, utilizando catalizador ($AgNO_3$), en ausencia de disolvente y en horno microondas (20 min a 40 ºC). Con estas condiciones se accedió a los compuestos **12** y **13** con rendimientos de 72 y 75%, respetivamente (Figura 4.9).

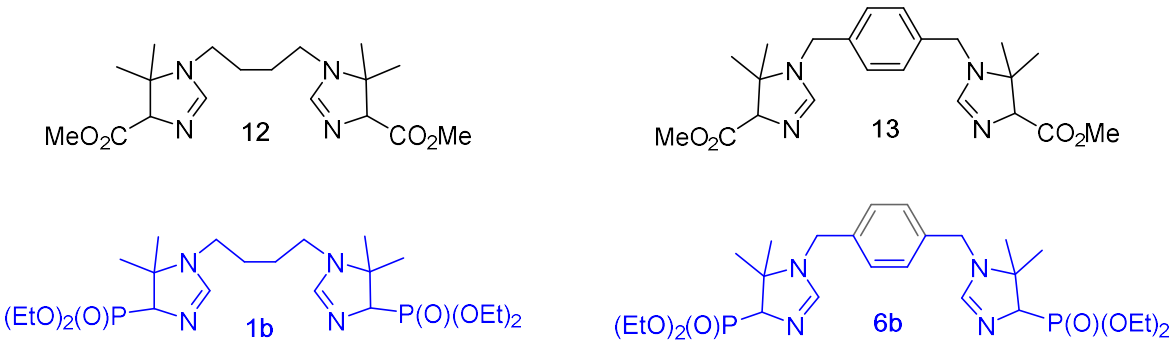

Figura 4.9. Bis(2-imidazolin-4-il)carboxilatos **12** y **13** y bis(2-imidazolin-4-il)fosfonatos **1b** y **6b**.

En estos ejemplos, a diferencia de sus análogos fosforados (**1b** y **6b**), la reacción no cursó de manera diastereoselectiva, sino que dió lugar a una mezcla de diastereómeros. La relación diastereoisomérica obtenida es variable en función de las condiciones en las que se lleva a cabo la reacción. En la reacción en horno microondas (20 min a 40 ºC), los productos **12** y **13** se aíslan en una relación diastereomérica de 8:1 (A:B) (Figura 4.10A). En cambio, si el compuesto **12** se sintetiza por condiciones convencionales de agitación durante 16 h a temperatura ambiente en matraz, se forma una mezcla de diastereómeros en una proporción 1:1 (A:B) (Figura 4.10B). Por último, al llevar a cabo la reacción en ultrasonidos durante 1 h a 40ºC, se observa como la relación diastereomérica se invierte a 1:2 (A:B) (Figura 4.10C). Las proporciones de ambos diastereómeros en las diferentes condiciones de reacción se determinaron mediante el análisis por ^{1}H-RMN de los crudos de reacción del compuesto **12** sintetizado en las diferentes condiciones. En los espectros de la Figura 4.10 se observa la presencia de dos grupos de señales en los protones de diagnóstico encuadrados con diferentes colores [posición: *H*2 (azul), *H*4 (naranja), C*H*$_3$O (verde) y C*H*$_3$x2 (lila)] en distinta proporción correspondientes a cada diastereómero (Tabla 4.5).

Tabla 4.5. Comparación de formación de diastereómeros para el compuesto **12**.

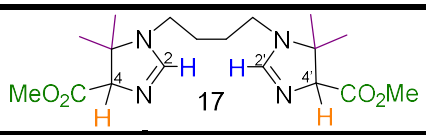

Posición	Desplazamiento químico (ppm)	Relación diastereomérica (A:B) en diferentes condiciones		
		MW, 40 ºC, 20 min	r.t., 16 h	US, 40 ºC, 1 h
*H*2	≈ 7.0	8:1	1:1	1:2
*H*4	≈ 4.5	8:1	1:1	1:2
C*H*$_3$O	≈ 3.7	8:1	1:1	1:2
C*H*$_3$x2	≈ 1.2	8:1	1:1	1:2

Actualmente, los esfuerzos se focalizan en la cristalización de los diastereómeros mayoritarios de los bis(2-imidazolin-4-il)carboxilatos **12** y **13**, con el objetivo de determinar, de manera inequívoca, la configuración relativa de estos compuestos por estudios cristalográficos de rayos X.

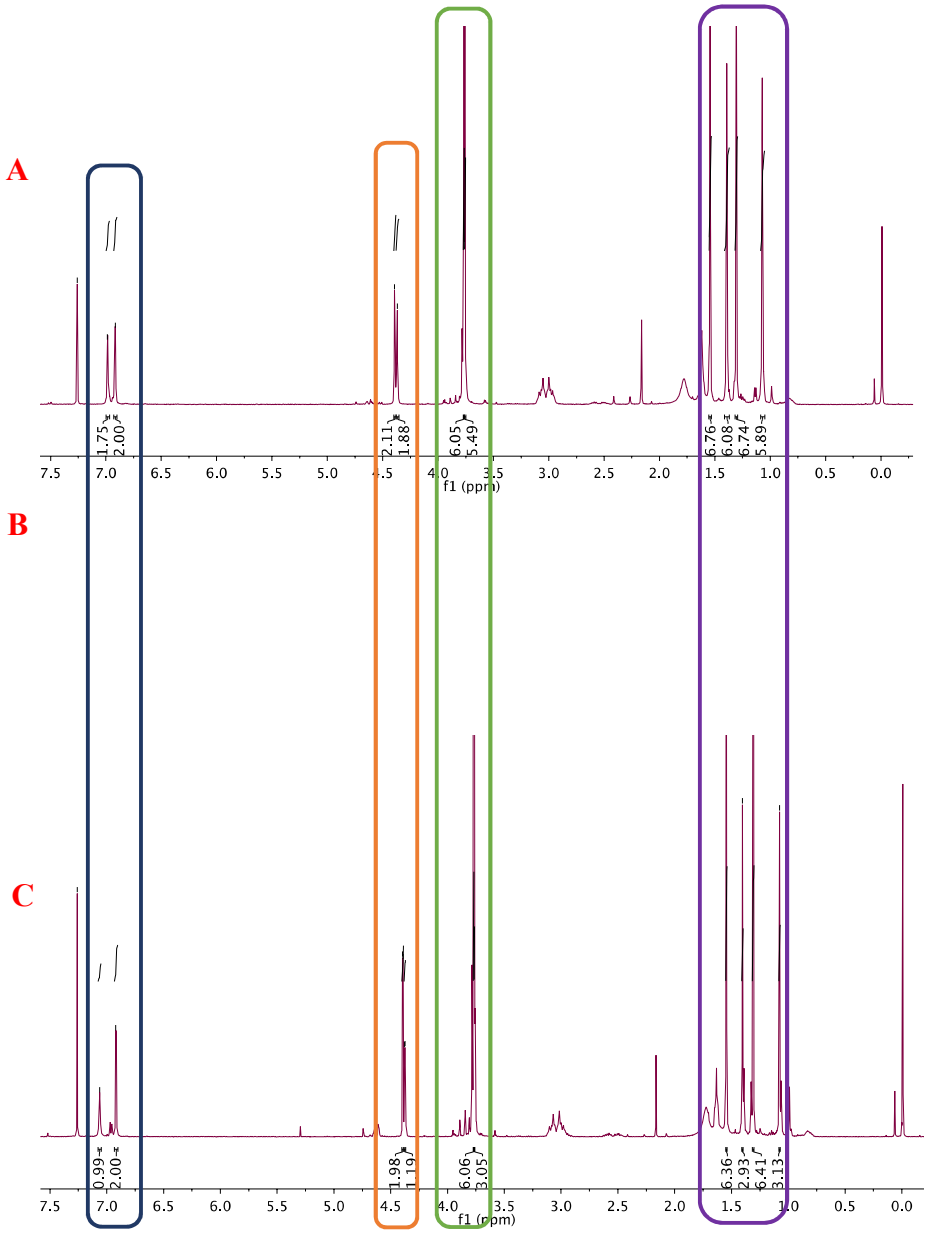

Figura 4.10. ^{1}H-RMN de **12** en diferentes condiciones de reacción.

4.3.10. Propuesta del mecanismo de reacción

A continuación, conociendo la estructura rayos X del compuesto **1a** se ha planteado la posibilidad, aunque no hay descrito ningún trabajo de cMCR que refuerce esta hipótesis,

de que el mecanismo de reacción para la cMCR descrita tenga lugar por etapas, formándose primero una MCR y seguidamente otra, y no de manera simultánea. Esta conclusión deriva de la obtención de productos con un sistema imidazolínico procedentes de la reacción por únicamente una de las dos aminas por falta de reactividad para dar la segunda MCR (**Ia**-**III**). Esto puede ser debido a que el grupo fosfonato tiene una geometría molecular tetraédrica, a diferencia de los ésteres, cuya geometría es trigonal plana, lo que podría suponer que están favorecidos para que la reacción se dé indistintamente por cualquiera de los dos planos.

4.3.11. Estudio farmacológico

Finalmente, como se comenta en el apartado de objetivos, este proyecto no se basa únicamente en un estudio de metodología química de las cMCR y isocianometilfosfonatos, sino también, en el descubrimiento de ligandos para los I_2-IR por duplicación molecular de los (2-imidazolin-4-il)fosfonato descritos previamente por el grupo de investigación.

Por ello, los compuestos sintetizados han sido enviados al Prof. Callado de la UPV para la evaluación de su afinidad y selectividad por I_2-IR, ello mediante estudios competitivos frente a radioligandos selectivos de I_2-IR ([^{3}H]-2-BFI) y de α_2-AR ([^{3}H]-RX821002).

La afinidad (expresadas como pK_i) y la selectividad I_2-IR/ α_2-AR obtenida para el compuesto **1a** resultó ser inferior a la familia de compuestos homólogos sin duplicar, como por ejemplo los compuesto **MCR2**, **MCR4**, **MCR5** y **MCR8** (Figura 4.11), los cuales presentan una afinidad y selectividad frente a α_2-AR media de entre 7 a 10 y de 300 a 1000, respectivamente. El bis(2-imidazolin-4-il)fosfonato **1a** presenta una curva bifásica con dos lugares de unión, uno de alta afinidad (6.39) y otro de baja afinidad (3.47), con bajos porcentajes de ocupación del lugar de alta afinidad (19%). Además, cabe resaltar que presenta un buen valor de selectividad frente a α_2-AR en el lugar de unión de alta afinidad (575).

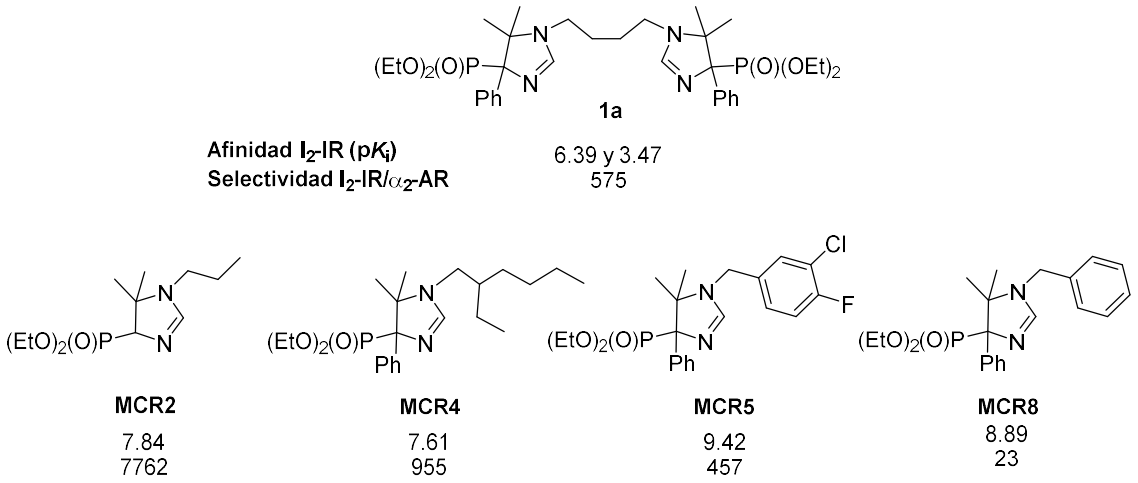

Figura 4.11. Afinidad por los I_2-IR para **1a** y los (2-imidazolin-4-il)fosfonatos **MCR2**, **MCR4**, **MCR5** y **MCR8.**

4.4. Conclusiones

En resumen, en el presente capítulo se ha puesto en manifiesto la primera cMCR que emplea isocianuros fosforados como componentes de la reacción. Además, estos isocianometilfosfonatos (PhosMic y derivados) en combinación con una diamina y una cetona ha permitido obtener una colección variada de bis(2-imidazolin-4-il)fosfonatos de manera diastereoselectiva, siendo la primera vez que describe la obtención de bisimidazolinas por cMCR y el primer trabajo sintético de cMCR que emplea isocianofosforados. La reacción desarrollada para la síntesis de estos heterociclos complejos transcurre con buenos rendimientos y economía de átomo, ausencia de disolvente y mediante unas condiciones suaves de reacción en microondas.

Asimismo, desde el punto de vista estereoquímico, la estructura del producto final **1a** ha podido ser determinada de manera inequívoca mediante análisis cristalográfico de rayos X. Además, es importante resaltar el contraste de estereoselectivadad obtenida en los productos finales dependiendo de la naturaleza del isocianuro.

Por lo tanto, la combinación de cMCR e isocianofosforados hace a este trabajo de metodología atractivo y útil, lo que nos da libertad para concluir que la química de cMCR puede ser una gran fuente para la formación de nuevos compuestos en beneficio de diferentes campos de investigación.

PARTE EXPERIMENTAL

Reagents, solvents and starting products were acquired from commercial sources. Evaporation of solvents was accomplished with a rotary evaporator. Chromatography refers to flash column chromatography and was carried out on silica gel (35-70 μm) with the indicated solvent system. IR spectra were performed in a Spectrum Two FT-IR Spectrometer, and only noteworthy IR absorptions (cm^{-1}) are listed. NMR spectra were recorded in $CDCl_3$ at 400 MHz (^1H) and 100.6 MHz (^{13}C), and chemical shifts are reported in *δ* values downfield from TMS or relative to residual chloroform (7.26 ppm, 77.0 ppm) as an internal standard. Data are reported in the following manner: chemical shift, multiplicity, coupling constant (*J*) in hertz (Hz), integrated intensity and assignment (when possible). Multiplicities are reported using the following abbreviations: s, singlet; d, doublet; dd, doublet of doublets; t, triplet; q, quadruplet; m, multiplet; br s, broad singlet; br d, broad doublet. Assignments and stereochemical determinations are given only when they are derived from definitive two-dimensional NMR experiments (g-HSQC). The accurate mass analyses were carried out using a LC/MSD-TOF spectrophotometer. Optical rotation was measured on a PerkinElmer 341 polarimeter. HPLC-MS (Agilent 1260 Infinity II) analysis was conducted on a Poroshell 120 EC-C15 (4.6 mm × 50 mm, 2.7 μm) at 40°C with mobile phase A (H_2O + 0.05% formic acid) and B (ACN + 0.05% formic acid) using a gradient elution and flow rate 0.6 mL/min. The DAD detector was set at 254 nm, the injection volume was 5 μL, and oven temperature was 40°C. Microwave reactions were performed on a Biotage Initiator Classic.

General procedure. A mixture of $AgNO_3$ (10%-mmol), ketone, amine (1.0 equiv.) and PhosMic or α-Ph-PhosMic (2.2 equiv.) was stirred under microwave irradiation at 40ºC for 20 min. The mixture was filtered and evaporated and the resulting residue was purified by flash column chromatography.

Tetraethyl [butane-1,4-diylbis(5,5-dimethyl-4-phenyl-4,5-dihydro-1H-imidazole-1,4-diyl)]bis(phosphonate) (1a).

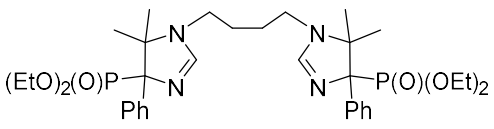

Following the general procedure, $AgNO_3$ (8.5 mg, 0.05 mmol), acetone (3.8 mL), 1,4-diaminobutane (44 m g, 0.5 mmol) and α-PhPhosMic (278 mg, 1.10 mmol) afforded **1a** (275 mg, 82%) as a yellowish solid, after column chromatography (DCM/5%MeOH). The product was crystallized from a mixture between IPA and hexane (1:9) to afford **1a** as a white crystal. IR (ATR) 3203, 2954, 2922, 1629, 1554, 1401, 1309, 1286, 1098, 912, 823, 782, 702 cm^{-1}. ^1H NMR (400 MHz,

$CDCl_3$) δ 0.59 (s, 6H, 2xC*H*$_3$), 0.98 (t, *J* = 7.0 Hz, 6H, 2xOCH$_2$C*H*$_3$), 1.25 (t, *J* = 7.0 Hz, 6H, 2xOCH$_2$C*H*$_3$), 1.68-1.72 (m, 4H, 2xC*H*$_2$), 1.78 (s, 6H, 2xC*H*$_3$), 2.96-2.99 (m, 2H, NC*H*$_2$), 3.10-3.14 (m, 2H, NC*H*$_2$), 3.44-3.54 (m, 2H, OC*H*$_2$CH$_3$), 3.72-3.78 (m, 2H, OC*H*$_2$CH$_3$), 4.01-4.15 (m, 4H, 2xOC*H*$_2$CH$_3$), 7.11 (t, *J* = 3.0 Hz, 2H, 2x*H*-2), 7.28-7.32 (m, 6H, ArH), 7.81 (br d, *J* = 22.5 Hz, 4H, Ar*H*). ^{13}C NMR (100.6 MHz) δ 16.3 (d, *J* = 5.0 Hz, 2xOCH$_2$*C*H$_3$), 16.7 (d, *J* = 6.0 Hz, 2xOCH$_2$*C*H$_3$), 23.2 (d, *J* = 15.0 Hz, 2x*C*H$_3$), 24.2 (d, *J* = 8.0 Hz, 2x*C*H$_3$), 28.3 [CH$_2$(*C*H$_2$)$_2$CH$_2$], 28.4 (CH$_2$(*C*H$_2$)$_2$CH$_2$), 41.8 (NCH$_2$), 41.9 (N*C*H$_2$), 63.0 (d, *J* = 4.0 Hz, O*C*H$_2$CH$_3$), 63.1 (d, *J* = 4.0 Hz, O*C*H$_2$CH$_3$), 63.3 (d, *J* = 7.0 Hz, 2xO*C*H$_2$CH$_3$), 68.7 (d, *J* = 4.0 Hz, 2x*C*-5), 81.8 (d, *J* = 146.0, Hz, 2x*C*-4), 127.3 (2x*C*HAr), 127.5 (4x*C*HAr), 128.3 (2x*C*HAr), 128.8 (2x*C*HAr), 137.3 (2x*C*-*ipso*), 155.9 (d, *J* = 6.0 Hz, 2x*C*-2). HRMS $C_{34}H_{54}N_4O_6P_2$ $[M+2H]^{2+}$ 338.1754; found, 338.1746. $[\alpha]^{22}_D$ = ± 0.00 (c 0.15, EtOH).

Tetraethyl [butane-1,4-diylbis(5,5-dimethyl-4,5-dihydro-1H-imidazole-1,4-diyl)]bis(phosphonate) (1b).

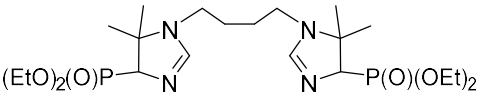

Following the general procedure, $AgNO_3$ (8.5 mg, 0.05 mmol), acetone (3.8 mL), 1,4-diaminobutane (44 mg, 0.5 mmol) and PhosMic (177 μL, 1.10 mmol) afforded **1b** (140 mg, 54%) as a yellowish oil, after column chromatography (EtOAc/5%MeOH). IR (ATR) 3103, 2941, 1620, 1366, 1312, 1245, 1166, 966, 833, 791, 714 cm^{-1}. ^{1}H NMR (400 MHz, $CDCl_3$) δ 1.28-1.33 (m, 12H, 2xOCH$_2$C*H*$_3$), 1.25 (t, *J* = 7.0 Hz, 6H, 2xOCH$_2$C*H*$_3$), 1.35 (s, 6H, 2xC*H*$_3$), 1.41 (s, 6H, 2xC*H*$_3$), 1.63-1.68 (m, 4H, 2xC*H*$_2$), 3.11-3.16 (m, 2H, NC*H*$_2$), 3.66-3.70 (m, 2H, NC*H*$_2$), 3.96 (dd, *J* = 14.0, 2.0 Hz, 2H, 2x*H*-4), 4.09-4.24 (m, 8H, 4xOC*H*$_2$CH$_3$), 7.11 (br s, 2H, 2x*H*-2). ^{13}C NMR (100.6 MHz) δ 16.5 (d, *J* = 6.0 Hz, 2xOCH$_2$*C*H$_3$), 16.6 (d, *J* = 6.0 Hz, 2xOCH$_2$*C*H$_3$), 21.2 (d, *J* = 6.0 Hz, 2x*C*H$_3$), 27.6 (d, *J* = 11.0 Hz, 2x*C*H$_3$), 27.8 (2x*C*H$_2$), 41.5 (2xNCH$_2$), 62.3 (d, *J* = 7.0 Hz, 2xO*C*H$_2$CH$_3$), 63.3 (d, *J* = 8.0 Hz, 2xO*C*H$_2$CH$_3$), 65.3 (d, *J* = 3.0 Hz, 2x*C*-5), 70.5 (d, *J* = 162.0 Hz, 2x*C*-4), 156.8 (d, *J* = 12.0 Hz, 2x*C*-2). HRMS $C_{22}H_{46}N_4O_6P_2$ $[M+2H]^{2+}$ 262.1446; found, 262.1449.

Tetraethyl [hexane-1,6-diylbis(5,5-dimethyl-4-phenyl-4,5-dihydro-1H-imidazole-1,4-diyl)]bis(phosphonate) (2).

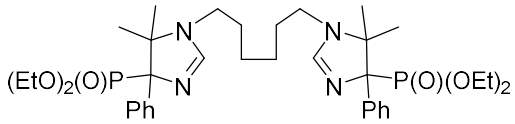

Following the general procedure, $AgNO_3$ (4.4 mg, 0.026 mmol), acetone (2.0 mL), 1,6-diaminohexane (30.2 mg, 0.26 mmol) and α-Ph-PhosMic (145 mg, 0.57 mmol) afforded **2** (122 mg, 67%) as a yellowish oil, after

column chromatography (DCM/5%MeOH). IR (ATR) 2982, 2941, 1529, 1425, 1323, 1211, 1118, 922, 881, 821, 797, 765, 699 cm^{-1}. ^1H NMR (400 MHz, $CDCl_3$) δ 0.59 (s, 6H, 2xC*H*$_3$), 0.96 (t, *J* = 7.0 Hz, 6H, 2xOCH$_2$C*H*$_3$), 1.26 (t, *J* = 7.0 Hz, 6H, 2xOCH$_2$C*H*$_3$), 1.39-1.42 (m, 4H, 2xC*H*$_2$), 1.60-1.63 (m, 4H, 2xC*H*$_2$), 1.78 (s, 6H, 2xC*H*$_3$), 2.91-2.98 (m, 2H, NC*H*$_2$), 3.05-3.12 (m, 2H, NC*H*$_2$), 3.41-3.50 (m, 2H, OC*H*$_2$CH$_3$), 3.70-3.76 (m, 2H, OC*H*$_2$CH$_3$), 4.03-4.16 (m, 4H, 2xOC*H*$_2$CH$_3$), 7.10 (d, *J* = 3.5 Hz, 2H, *H*-2), 7.28-7.33 (m, 6H, Ar*H*), 7.82 (br d, *J* = 21.0 Hz, 4H, Ar*H*). ^{13}C NMR (100.6 MHz) δ 16.3 (d, *J* = 6.0 Hz, 2xOCH$_2$*C*H$_3$), 16.6 (d, *J* = 6.0 Hz, 2xOCH$_2$*C*H$_3$), 23.2 (d, *J* = 14.0 Hz, 2x*C*H$_3$), 24.2 (d, *J* = 8.0 Hz, 2x*C*H$_3$), 26.7 [2xCH$_2$(*C*H$_2$)$_4$CH$_2$], 31.0 (2xCH$_2$(*C*H$_2$)$_4$CH$_2$), 41.8 (2xN*C*H$_2$), 62.9 (d, *J* = 9.0 Hz, 2xO*C*H$_2$CH$_3$), 63.4 (d, *J* = 7.0 Hz, 2xO*C*H$_2$CH$_3$), 68.6 (d, *J* = 4.0 Hz, 2x*C*-5), 81.6 (d, *J* = 147.0, Hz, 2x*C*-4), 127.3 (2x*C*HAr), 127.5 (4x*C*HAr), 128.4 (2x*C*HAr), 128.8 (2x*C*HAr), 137.2 (2x*C*-*ipso*), 155.9 (d, *J* = 6.0 Hz, 2x*C*-2). HRMS $C_{36}H_{58}N_4O_6P_2$ $[M+2H]^{2+}$ 352.1915; found, 352.1917.

Tetraethyl [decane-1,10-diylbis(5,5-dimethyl-4,5-dihydro-1H-imidazole-1,4-diyl)]bis(phosphonate) (3).

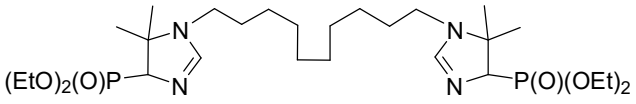

Following the general procedure, $AgNO_3$ (4.9 mg, 0.029 mmol), acetone (4.5 mL), 1,10-diaminodecane (50 mg, 0.29 mmol) and PhosMic (103 μL, 0.64 mmol) afforded **3** (72 mg, 41%) as a yellowish oil, after column chromatography (EtOAc/5%MeOH). IR (ATR) IR (ATR) 2945, 1619, 1355, 1221, 1123, 1006, 932, 888, 837, 787, 754, 712, 688 cm^{-1}. ^1H NMR (400 MHz, $CDCl_3$) δ 1.24-1.29 (m, 12H, 6xC*H*$_2$), 1.31-1.36 (m, 18H, 4xOCH$_2$C*H*$_3$ + 2xC*H*$_3$), 1.41 (s, 6H, 2xC*H*$_3$), 1.55-1.58 (m, 4H, 2xC*H*$_2$), 2.99-3.05 (m, 4H, 2xNC*H*$_2$), 3.94 (dd, *J* = 16.0, 1.5 Hz, 2H, 2x*H*-4), 4.13-4.24 (m, 8H, 4xOC*H*$_2$CH$_3$), 7.12 (br s, 2H, *H*-2). ^{13}C NMR (100.6 MHz) δ 16.5 (d, *J* = 6.0 Hz, 2xOCH$_2$*C*H$_3$), 16.6 (d, *J* = 5.0 Hz, 2xOCH$_2$*C*H$_3$), 21.3 (d, *J* = 7.0 Hz, 2x*C*H$_3$), 27.9 (d, *J* = 11.0 Hz, 2x*C*H$_3$), 26.9 (2xCH$_2$), 29.3 (2xCH$_2$), 29.5 (2xCH$_2$), 30.8 (2xCH$_2$), 41.8 (2xN*C*H$_2$), 62.2 (d, *J* = 7.0 Hz, 2xO*C*H$_2$CH$_3$), 63.1 (d, *J* = 7.0 Hz, 2xO*C*H$_2$CH$_3$), 64.9 (d, *J* = 2.0 Hz, 2x*C*-5), 72.0 (d, *J* = 162.0 Hz, 2x*C*-4), 156.5 (d, *J* = 13.0 Hz, 2x*C*-2). HRMS $C_{28}H_{58}N_4O_6P_2$ $[M+2H]^{2+}$ 304.1910; found, 304.1913.

Tetraethyl {[(ethane-1,2-diylbis(oxy))bis(ethane-2,1-diyl)]bis(5,5-dimethyl-4-phenyl-4,5-dihydro-1H-imidazole-1,4-diyl)}bis(phosphonate) (4).

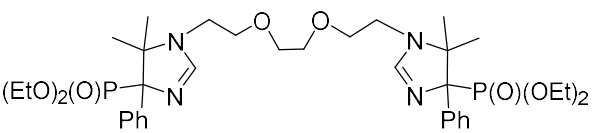

Following the general procedure, $AgNO_3$ (8.5 mg, 0.05 mmol), acetone (3.8 mL), 1,8-diamino-3,6-dioxaoctane

(74 μL, 0.5 mmol) and α-PhPhosMic (278 mg, 1.10 mmol) afforded **4** (241 mg, 66%) as a yellowish oil, after column chromatography (DCM/5%MeOH). IR (ATR) 3117, 2972, 2902, 1721, 1568, 1371, 1279, 1176, 992, 878,732 cm^{-1}. ^{1}H NMR (400 MHz, $CDCl_3$) δ 0.60 (s, 6H, 2xC*H*$_3$), 0.98 (t, *J* = 7.0 Hz, 6H, 2xOCH$_2$C*H*$_3$), 1.27 (t, *J* = 7.0 Hz, 6H, 2xOCH$_2$C*H*$_3$), 1.79 (s, 6H, 2xC*H*$_3$), 3.11-3.18 (m, 2H, NC*H*$_2$), 3.27-3.35 (m, 2H, OC*H*$_2$), 3.46-3.52 (m, 2H, OC*H*$_2$), 3.56-3.62 (m, 4H, NC*H*$_2$ + OC*H*$_2$CH$_3$), 3,64 (s, 4H, O(C*H*$_2$)$_2$O), 3.73-3.79 (m, 2H, OC*H*$_2$CH$_3$), 4.02-4.20 (m, 4H, 2xOC*H*$_2$CH$_3$), 7.24 (t, *J* = 4.0 Hz, 2H, Ar*H*), 7.29 (d, *J* = 4.0 Hz, 2H, 2x*H*-2),7.31-7.33 (m, 4H, ArH), 7.85 (br d, *J* = 26.5 Hz, 4H, Ar*H*). ^{13}C NMR (100.6 MHz) δ 16.2 (d, *J* = 6.0 Hz, 2xOCH$_2$*C*H$_3$), 16.5 (d, *J* = 5.0 Hz, 2xOCH$_2$*C*H$_3$), 23.2 (d, *J* = 14.5 Hz, 2x*C*H$_3$), 24.1 (d, *J* = 9.0 Hz, 2x*C*H$_3$), 46.1 (2xN*C*H$_2$), 63.0 (d, *J* = 8.0 Hz, 2xO*C*H$_2$CH$_3$), 63.2 (d, *J* = 7.0 Hz, 2xO*C*H$_2$CH$_3$), 68.3 (t, *J* = 4.0 Hz, 2x*C*-5), 70.6 (2xO*C*H$_2$), 71.4 (2xO(*C*H$_2$)$_2$O), 81.4 (dd, *J* = 145.0, 3.0 Hz, 2x*C*-4), 127.2 (2x*C*HAr), 127.3 (4x*C*HAr), 128.2 (2x*C*HAr), 128.7 (2x*C*HAr), 137.2 (2x*C-ipso*), 156.5 (dd, *J* = 7.0, 3.0 Hz, 2x*C*-2). HRMS $C_{36}H_{57}N_4O_8P_2$ $[M+H]^+$ 735.3646; found, 735.3662.

***Tetraethyl [(bicyclo[2.2.1]heptane-2,3-diyl)bis(methylene))bis(5,5-dimethyl-4-phenyl-4,5-dihydro-1H-imidazole-1,4-diyl)]bis(phosphonate) (5)*.**

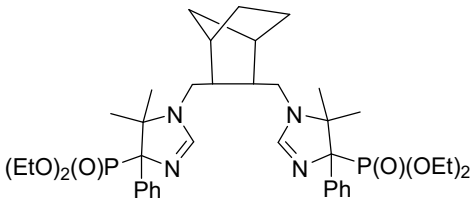

Following the general procedure, $AgNO_3$ (5.4 mg, 0.03 mmol), acetone (2.5 mL), Bicyclo(2.2.1)heptanedimethanamine (50 mg, 0.32 mmol) and α-Ph-PhosMic (178 mg, 0.70 mmol) afforded **5** (153 mg, 65%) as a yellowish oil, after column chromatography (DCM/5%MeOH). IR (ATR) 3002, 2912, 1701, 1577, 1377,1234, 1109, 1077, 954, 932, 883, 755, 712 cm^{-1}.^{1}H NMR (400 MHz, $CDCl_3$) δ ^{1}H NMR (400 MHz, $CDCl_3$) δ 0.60 (s, 6H, 2xC*H*$_3$), 0.96 (dt, *J* = 7.0, 5.0 Hz, 6H, 2xOCH$_2$C*H*$_3$), 1.27-1.29 (m, 14H, 2xOCH$_2$C*H*$_3$ + 3xC*H*$_2$ + 2xC*H*), 1.80 (s, 6H, 2xC*H*$_3$), 2.18-2.20 (m, 1H, C*H*), 2.32-2.37 (m, 1H, C*H*), 2.70-3.06 (m, 4H, 2xNC*H*$_2$), 3.38-3.47 (m, 2H, OC*H*$_2$CH$_3$), 3.70-3.75 (m, 2H, OC*H*$_2$CH$_3$), 4.06-4.15 (m, 4H, 2xOC*H*$_2$CH$_3$), 7.13-7.23 (m, 2H, Ar*H*), 7.29-7.30 (m, 4H, ArH), 7.34 (s, 2H, 2x*H*-2),7.84 (br s, 4H, Ar*H*). ^{13}C NMR (100.6 MHz) δ 16.3 (d, *J* = 5.0 Hz, 2xOCH$_2$*C*H$_3$), 16.6 (d, *J* = 6.0 Hz, 2xOCH$_2$*C*H$_3$), 22.9 (d, *J* = 18.0 Hz, 2x*C*H$_3$), 23.3 (d, *J* = 11.0 Hz, 2x*C*H$_3$), 29.8 (2xC*H*), 35.1 (C*H*$_2$), 38.9 (2xC*H*), 39.2 (2xC*H*$_2$),47.4 (N*C*H$_2$), 41.9 (N*C*H$_2$), 62.8 (d, *J* = 4.0 Hz, O*C*H$_2$CH$_3$), 62.9 (d, *J* = 9.0 Hz, O*C*H$_2$CH$_3$), 63.6 (d, *J* = 6.0 Hz, 2xO*C*H$_2$CH$_3$), 68.8 (d, *J* = 3.0 Hz, 2x*C*-5), 81.3 (d, *J* = 145.0, Hz, 2x*C*-4), 127.4 (2x*C*HAr), 127.6 (4x*C*HAr), 128.3 (2x*C*HAr), 128.8 (2x*C*HAr), 137.0 (2x*C-ipso*), 155.9 (d, *J* = 5.0 Hz, 2x*C*-2). HRMS $C_{39}H_{60}N_4O_6P_2$ $[M+2H]^{2+}$ 371.1989; found, 371.1989.

Tetraethyl {[1,4-phenylenebis(methylene)]bis(5,5-dimethyl-4-phenyl-4,5-dihydro-1H-imidazole-1,4-diyl)}bis(phosphonate) (6a).

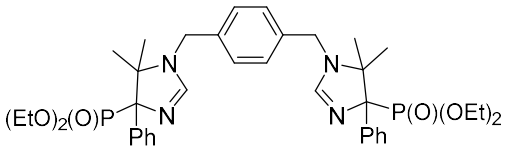

Following the general procedure, $AgNO_3$ (12.4 mg, 0.07 mmol), acetone (5.6 mL), *p*-xylylenediamine (100 mg, 0.73 mmol) and α-PhPhosMic (407 mg, 1.61 mmol) afforded **6a** (351 mg, 67%) as a yellowish oil, after column chromatography (DCM/5%MeOH). IR (ATR) 2987, 2941, 1821, 1587, 1449, 1341, 1182, 1061, 922, 712 cm^{-1}. ^1H NMR (400 MHz, $CDCl_3$) δ 0.66 (s, 6H, 2xC*H*$_3$), 0.97 (t, *J* = 7.0 Hz, 6H, 2xOCH$_2$C*H*$_3$), 1.29 (t, *J* = 7.0 Hz, 6H, 2xOCH$_2$C*H*$_3$), 1.76 (s, 6H, 2xC*H*$_3$), 3.42-3.50 (m, 2H, OC*H*$_2$CH$_3$), 3.72-3.78 (m, 2H, OC*H*$_2$CH$_3$), 4.05-4.30 (m, 8H, 2xOC*H*$_2$CH$_3$ + 2xC*H*$_2$Ar), 7.03 (d, *J* = 4.5 Hz, 2H, *H*-2), 7.27-7.38 (m, 10H, Ar*H*), 7.85 (br d, *J* = 29.5 Hz, 4H, Ar*H*). ^{13}C NMR (100.6 MHz) δ 16.3 (d, *J* = 5.0 Hz, 2xOCH$_2$*C*H$_3$), 16.7 (d, *J* = 6.0 Hz, 2xOCH$_2$*C*H$_3$), 23.2 (d, *J* = 14.5 Hz, 2x*C*H$_3$), 24.4 (d, *J* = 8.5 Hz, 2x*C*H$_3$), 46.1 (2x*C*H$_2$Ar), 63.0 (d, *J* = 8.5 Hz, 2xO*C*H$_2$CH$_3$), 63.5 (d, *J* = 7.0 Hz, 2xO*C*H$_2$CH$_3$), 68.9 (d, *J* = 4.5 Hz, 2x*C*-5), 82.1 (d, *J* = 146.5 Hz, 2x*C*-4), 127.3 (2x*C*HAr), 127.6 (d, *J* = 3.0 Hz, 2x*C*HAr), 128.1 (4x*C*HAr), 128.3 (2x*C*HAr), 128.9 (4x*C*HAr), 137.3 (2x*C-ipso*), 137.8 (2x*C-ipso*), 156.5 (d, *J* = 6.0 Hz, 2x*C*-2). HRMS $C_{38}H_{54}N_4O_6P_2$ $[M+2H]^{2+}$ 362.1754; found, 362.1762.

Tetraethyl {[1,4-phenylenebis(methylene)]bis(5,5-dimethyl-4,5-dihydro-1H-imidazole-1,4-diyl)}bis(phosphonate) (6b).

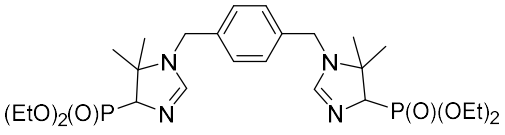

Following the general procedure, $AgNO_3$ (12.4 mg, 0.07 mmol), acetone (5.6 mL), *p*-xylylenediamine (100 mg, 0.73 mmol) and PhosMic (259 μL, 1.61 mmol) afforded **6b** (274 mg, 62%) as a yellowish oil, after column chromatography (EtOAc/5%MeOH). IR (ATR) 2952, 2911, 1819, 1607, 1587, 1409, 1371, 1212, 1082, 1001, 812, 699 cm^{-1}. ^1H NMR (400 MHz, $CDCl_3$) δ 1.29 (s, 6H, 2xC*H*$_3$), 1.32 (t, *J* = 7.0 Hz, 6H, 2xOCH$_2$C*H*$_3$), 1.36 (t, *J* = 7.0 Hz, 6H, 2xOCH$_2$C*H*$_3$), 1.42 (s, 6H, 2xC*H*$_3$), 3.99 (dd, *J* = 16.0, 1.5 Hz, 2H, 2x*H*-4), 4.15-4.28 (m, 12H, 4xOC*H*$_2$CH$_3$, 2xC*H*$_2$Ar), 6.94 (br s, 2H, *H*-2), 7.27, (s, 4H, Ar*H*). ^{13}C NMR (100.6 MHz) δ 16.6 (d, *J* = 5.0 Hz, 2xOCH$_2$*C*H$_3$), 16.7 (d, *J* = 5.0 Hz, 2xOCH$_2$*C*H$_3$), 21.4 (d, *J* = 7.0 Hz, 2x*C*H$_3$), 27.9 (d, *J* = 11.0 Hz, 2x*C*H$_3$), 45.5 (2x*C*H$_2$Ar), 62.1 (d, *J* = 7.0 Hz, 2xO*C*H$_2$CH$_3$), 63.1 (d, *J* = 7.0 Hz, 2xO*C*H$_2$CH$_3$), 64.8 (d, *J* = 3.0 Hz, 2x*C*-5), 73.1 (d, *J* = 162.0 Hz, 2x*C*-4), 128.1 (4x*C*HAr), 137.6 (2x*C-ipso*), 156.9 (d, *J* = 12.0 Hz, 2x*C*-2). HRMS $C_{26}H_{46}N_4O_6P_2$ $[M+2H]^{2+}$ 286.1441; found, 286.1448.

Tetraethyl {[1,3-phenylenebis(methylene)]bis(5,5-dimethyl-4-phenyl-4,5-dihydro-1H-imidazole-1,4-diyl)}bis(phosphonate) (7).

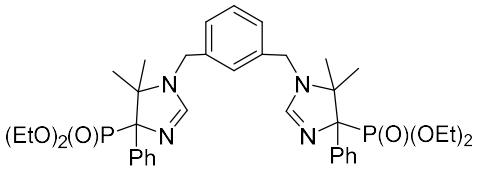

Following the general procedure, $AgNO_3$ (3.1 mg, 0.017 mmol), acetone (1.4 mL), *m*-xylylenediamine (24 μL, 0.18 mmol) and α-PhPhosMic (102 mg, 0.40 mmol) afforded **7** (95 mg, 72%) as a yellowish oil, after column chromatography (DCM/5%MeOH). IR (ATR) 3001, 2950, 1792, 1577, 1473, 1333, 1201, 1071, 892, 723 cm^{-1}. ^1H NMR (400 MHz, $CDCl_3$) δ 0.66 (s, 6H, 2xC*H*$_3$), 0.97 (t, *J* = 7.0 Hz, 6H, 2xOCH$_2$C*H*$_3$), 1.26 (t, *J* = 7.0 Hz, 6H, 2xOCH$_2$C*H*$_3$), 1.75 (s, 6H, 2xC*H*$_3$), 3.44-3.51 (m, 2H, OC*H*$_2$CH$_3$), 3.72-3.79 (m, 2H, OC*H*$_2$CH$_3$), 4.04-4.16 (m, 4H, 2xOC*H*$_2$CH$_3$), 4.18-4.32 (m, 4H, 2xC*H*$_2$Ar), 7.06 (t, *J* = 3.0 Hz, 2H, *H*-2), 7.27-7.37 (m, 10H, Ar*H*), 7.83 (br d, *J* = 30.0 Hz, 4H, Ar*H*). ^{13}C NMR (100.6 MHz) δ 16.3 (d, *J* = 6.0 Hz, 2xOCH$_2$*C*H$_3$), 16.7 (d, *J* = 6.0 Hz, 2xOCH$_2$*C*H$_3$), 23.2 (d, *J* = 13.0 Hz, 2x*C*H$_3$), 24.3 (dd, *J* = 8.0, 4.0 Hz, 2x*C*H$_3$), 46.3 (2x*C*H$_2$Ar), 63.2 (d, *J* = 9.0 Hz, 2xO*C*H$_2$CH$_3$), 63.4 (d, *J* = 7.0 Hz, 2xO*C*H$_2$CH$_3$), 68.9 (d, *J* = 4.5 Hz, 2x*C*-5), 82.0 (dd, *J* = 146.5, 3.0 Hz, 2x*C*-4), 127.0 (*C*HAr), 127.2 (4x*C*HAr), 127.6 (4x*C*HAr), 128.3 (2x*C*HAr), 128.8 (*C*HAr), 129.2 (2x*C*HAr), 137.2 (2x*C-ipso*), 137.8 (2x*C-ipso*), 156.6 (d, *J* = 6.0 Hz, 2x*C*-2). HRMS $C_{38}H_{54}N_4O_6P_2$ $[M+2H]^{2+}$ 362.1754; found, 362.1751.

Tetraethyl [cyclohexane-1,4-diylbis(5,5-dimethyl-4,5-dihydro-1H-imidazole-1,4-diyl)]bis(phosphonate) (8a).

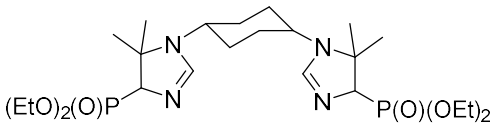

A mixture of $AgNO_3$ (4.3 mg, 0.025 mmol), acetone (1.9 mL), *p*-cyclohexanediamine (29 mg, 0.25 mmol) and PhosMic (89 μL, 0.55 mmol) was stirred at room temperature for 16 h to afford **8a** (40 mg, 30%) as a yellowish oil, after column chromatography (EtOAc/5% MeOH). IR (ATR) 2998, 2911, 1522, 1333, 1291, 1232, 1172, 1098, 977, 912, 843, 767, 732 cm^{-1}. ^1H NMR (400 MHz, $CDCl_3$) δ 1.25 (s, 6H, 2xC*H*$_3$), 1.31-1.37 (m, 16H, 4xOCH$_2$C*H*$_3$ + 4xC*H*), 1.43 (s, 6H, 2xC*H*$_3$), 1.77-1.90 (m, 4H, 4xC*H*), 3.15-3.16 (m, 2H, 2xNC*H*), 3.93 (dd, *J* = 15.0, 2.0 Hz, 2H, 2x*H*-4), 4.17-4.26 (m, 8H, 4xOC*H*$_2$CH$_3$), 7.36 (br s, 2H, 2x*H*-2). ^{13}C NMR (100.6 MHz) δ 16.6 (d, *J* = 5.0 Hz, 2xOCH$_2$*C*H$_3$), 16.7 (d, *J* = 8.0 Hz, 2xOCH$_2$*C*H$_3$), 21.8 (d, *J* = 7.0 Hz, 2x*C*H$_3$), 21.9 (d, *J* = 6.0 Hz, 2x*C*H$_3$), 28.5 (2x*C*H$_2$), 29.8 (2x*C*H$_2$), 48.0 (2xN*C*H), 62.1 (d, *J* = 7.0 Hz, 2xO*C*H$_2$CH$_3$), 63.1 (d, *J* = 6.0 Hz, 2xO*C*H$_2$CH$_3$), 65.3 (d, *J* = 4.0 Hz, 2x*C*-5), 72.4 (d, *J* = 161.0 Hz, 2x*C*-4), 154.2 (d, *J* = 9.0 Hz, 2x*C*-2). HRMS $C_{24}H_{48}N_4O_6P_2$ $[M+2H]^{2+}$ 275.1524; found, 275.1528.

Tetraethyl [4-methylpentane-1,5-diylbis(5,5-dimethyl-4-phenyl-4,5-dihydro-1H-imidazole-1,4-diyl)]bis(phosphonate)(9a).

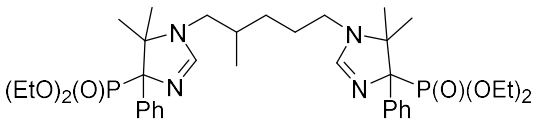

Following the general procedure, $AgNO_3$ (8.5 mg, 0.05 mmol), acetone (3.8 mL), 2-methylpentane-1,5-diamine (67 μL, 0.5 mmol) and α-PhPhosMic (278 mg, 1.10 mmol) afforded **9a** (220 mg, 57%) as a yellowish oil, after column chromatography (DCM/5%MeOH). IR (ATR) 2977, 2922, 1600, 1475, 1223, 1189, 1003, 966, 878, 826, 794, 756, 702, 688 cm^{-1}. ^1H NMR (400 MHz, $CDCl_3$) δ 0.58 (d *J* = 2.5 Hz, 3H, CHC*H*$_3$), 0.59 (s, 3H, C*H*$_3$), 0.94-1.00 (m, 9H, CH_3 + 2xOCH$_2$C*H*$_3$), 1.10-1.19 (m, 2H, C*H*$_2$), 1.26 (t, *J* = 16.0 Hz, 6H, 2xOCH$_2$C*H*$_3$), 1.43-1.57 (m, 2H, C*H*$_2$), 1.68-1.72 (m, 1H, C*H*CH$_3$), 1.76 (s, 3H, C*H*$_3$), 1.78 (s, 3H, C*H*$_3$), 2.78-3.15 (m, 4H, 2xNC*H*$_2$), 3.39-3.49 (m, 2H, OC*H*$_2$CH$_3$), 3.68-3.78 (m, 2H, OC*H*$_2$CH$_3$), 4.03-4.16 (m, 4H, 2xOC*H*$_2$CH$_3$), 7.08 (d, *J* = 3.5 Hz, *H*-2), 7.15 (dd, *J* = 19.0, 3.5 Hz, *H*-2), 7.27-7.33 (m, 6H, Ar*H*), 7.82 (br s, 4H, Ar*H*). ^{13}C NMR (100.6 MHz) δ 16.3 (d, *J* = 6.0 Hz, 2xOCH$_2$*C*H$_3$), 16.6 (d, *J* = 6.0 Hz, 2xOCH$_2$*C*H$_3$), 17.4 (CH*C*H$_3$), 23.0 (d, *J* = 15.0 Hz, 2x*C*H$_3$), 23.9 (d, *J* = 8.0 Hz, *C*H$_3$), 23.9 (d, *J* = 8.0 Hz, *C*H$_3$), *2*6.8 (d, *J* = 8.0 Hz, *C*HCH$_3$), 26.8 (*C*H$_2$), 27.7 (*C*H$_2$), 30.0 (*C*H$_2$), 42.0 (d, *J* = 8.0 Hz, N*C*H$_2$), 45.0 (N*C*H$_2$), 63.1 (d, *J* = 6.0 Hz, 2xO*C*H$_2$CH$_3$), 64.3 (d, *J* = 8.0 Hz, 2xO*C*H$_2$CH$_3$), 69.3 (d, *J* = 3.0 Hz, *C*-5), 69.4 (d, *J* = 3.0 Hz, 2x*C*-5), 81.4 (d, *J* = 145.0, Hz, *C*-4), 81.5 (d, *J* = 143.0, Hz, *C*-4), 127.0 (2x*C*HAr), 127.8 (4x*C*HAr), 128.5 (2x*C*HAr), 128.8 (2x*C*HAr), 136.7 (2x*C*-*ipso*), 157.1 (d, *J* = 5.0 Hz, *C*-2), 157.3 (d, *J* = 5.0 Hz, *C*-2). HRMS $C_{36}H_{58}N_4O_6P_2$ $[M+2H]^{2+}$ 352.1910; found, 352.1913.

Tetraethyl [4-methylpentane-1,5-diylbis(5,5-dimethyl-4,5-dihydro-1H-imidazole-1,4-diyl)]bis(phosphonate) (9b).

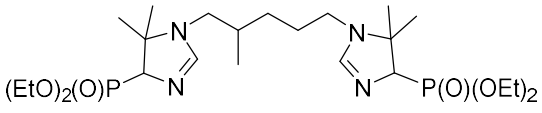

Following the general procedure, $AgNO_3$ (8.5 mg, 0.05 mmol), acetone (3.8 mL), 2-methylpentane-1,5-diamine (67 μL, 0.5 mmol) and PhosMic (177 μL, 1.10 mmol) afforded **9b** (145 mg, 53%) as a yellowish oil, after column chromatography (EtOAc/5%MeOH). IR (ATR) 2947, 1515, 1333, 1222, 1123, 1006, 977, 877, 811, 791, 722, 701, 676 cm^{-1}. ^1H NMR (400 MHz, $CDCl_3$) δ 0.89 (d *J* = 3.0 Hz, 3H, CHC*H*$_3$), 1.04-1.11 (m, 2H, C*H*$_2$), 1.29-1.36 (m, 24H, 4xCH_3 + 4xOCH$_2$C*H*$_3$), 1.45-1.55 (m, 2H, C*H*$_2$), 1.59-1.65 (m, 1H, C*H*CH$_3$), 2.80-3.01 (m, 4H, 2xNC*H*$_2$), 3.89 (d *J* = 2.0 Hz, 1H, *H*-4), 3.93 (d *J* = 2.0 Hz, 1H, *H*-4), 4.13-4.23 (m, 8H, 4xOC*H*$_2$CH$_3$), 6.82 (d, *J* = 2.5 Hz, *H*-2), 6.87 (d, *J* = 2.0 Hz, *H*-2). ^{13}C NMR (100.6 MHz) δ 16.5 (d, *J* = 6.0 Hz, 2xOCH$_2$*C*H$_3$), 16.6 (CH*C*H$_3$), 16.7 (d, *J* = 3.0 Hz, OCH$_2$*C*H$_3$), 17.5

(d, *J* = 6.0 Hz, OCH_2CH_3), 21.0 ($CHCH_3$), 23.0 (d, *J* = 6.0 Hz, CH_3), 23.3 (d, *J* = 12.0 Hz, CH_3), 28.8 (d, *J* = 8.0 Hz, CH_3), 28.5 (d, *J* = 4.0 Hz, CH_3), 31.7 (CH_2), 34.0 (CH_2), 41.7 (NCH_2), 48.2 (NCH_2), 61.8 (d, *J* = 5.0 Hz, OCH_2CH_3), 61.9 (d, *J* = 5.0 Hz, OCH_2CH_3), 63.0 (d, *J* = 7.0 Hz, 2xOCH_2CH_3), 64.4 (d, *J* = 3.0 Hz, *C*-5), 64.5 (d, *J* = 3.0 Hz, *C*-5), 73.6 (d, *J* = 163.0 Hz, *C*-4), 73.7 (d, *J* = 164.0 Hz, *C*-4), 156.2 (d, *J* = 4.0 Hz, *C*-2), 157.0 (d, *J* = 4.0 Hz, *C*-2). HRMS $C_{24}H_{50}N_4O_6P_2$ $[M+2H]^{2+}$ 276.1597; found, 257.1600.

Hexaethyl [nitrilotris(ethane-2,1-diyl)]tris(5,5-dimethyl-4-phenyl-4,5-dihydro-1H-imidazole-1,4-diyl)tris(phosphonate) (10).

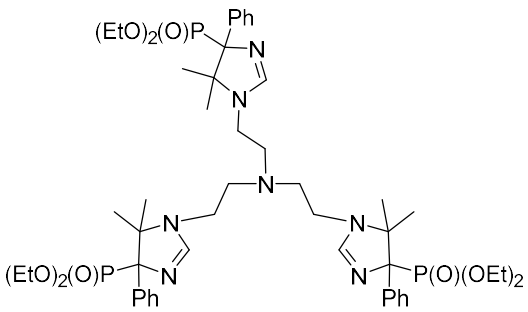

A mixture of $AgNO_3$ (5.8 mg, 0.034 mmol), acetone (2.6 mL), tris(2-aminoethyl)amine (51 μL, 0.34 mmol) and α-PhPhosMic (284 mg, 1.12 mmol) was stirred under microwave irradiation at 40 ºC for 20 min. The mixture was filtered and evaporated to yield a residue, which was purified by flash column chromatography (DCM/5%MeOH) to afford **10** (181 mg, 52%) as a yellowish oil. IR (ATR) 3311, 3112, 2974, 2909, 1701, 1656, 1461, 1275, 1182, 1007, 924, 818, 712 cm^{-1}. ^1H NMR (400 MHz, $CDCl_3$) δ 0.62 (s, 9H, 3xCH_3), 1.02 (t, *J* = 7.0 Hz, 9H, 3xOCH_2CH_3), 1.23 (t, *J* = 7.0 Hz, 9H, 3xOCH_2CH_3), 1.79 (s, 9H, 3xCH_3), 2.73-2.77 (m, 6H, CH_2N), 3.03-3.12 (m, 3H, NCH_2), 3.24-3.32 (m, 3H, NCH_2), 3.55-3.63 (m, 3H, OCH_2CH_3), 3.75-3.81 (m, 3H, OCH_2CH_3), 4.03-4.13 (m, 6H, 6xOCH_2CH_3), 7.27-7.31 (m, 9H, ArH), 7.39 (s, 3H, 3x*H*-2), 7.73-7.81 (br d, *J* = 33.5 Hz, 6H, Ar*H*). ^{13}C NMR (100.6 MHz) δ 16.3 (d, *J* = 5.0 Hz, 3xOCH_2CH_3), 16.7 (d, *J* = 5.0 Hz, 3xOCH_2CH_3), 23.5 (d, *J* = 14.0 Hz, 3xCH_3), 24.1 (d, *J* = 8.0 Hz, 3xCH_3), 40.5 (CH_2N), 40.6 (CH_2N), 40.7 (CH_2N), 45.8 (3xNCH_2), 63.2 (d, *J* = 8.0 Hz, 2xOCH_2CH_3), 63.3 (d, *J* = 8.0 Hz, OCH_2CH_3), 63.4 (d, *J* = 8.0 Hz, 2xOCH_2CH_3), 63.5 (d, *J* = 8.0 Hz, OCH_2CH_3), 69.0 (d, *J* = 4.0 Hz, 3x*C*-5), 80.9 (d, *J* = 153.0, Hz, 3x*C*-4), 127.3 (3x*C*HAr), 127.7 (6x*C*HAr), 128.1 (3x*C*HAr), 128.4 (3x*C*HAr), 136.7 (3x*C-ipso*), 156.3 (d, *J* = 5.0 Hz, 3x*C*-2). HRMS $C_{51}H_{79}N_7O_9P_3$ $[M+H]^+$ 1026.5147; found, 1026.5149.

Tetraethyl [(1,4-phenylenebis(methylene))bis(4-phenyl-1,3-diazaspiro[4.5]dec-2-ene-1,4-diyl)]bis(phosphonate) (11a).

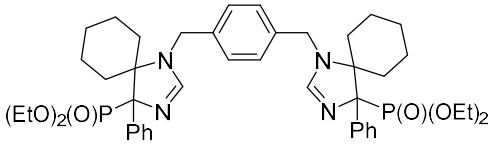

Following the general procedure, $AgNO_3$ (4.3 mg, 0.025 mmol), cyclohexanone (206 μL, 2.0 mmol), *p*-xylylenediamine (34 mg, 0.25 mmol) and α-PhPhosMic (139 mg, 0.55 mmol) in methanol (1.3 mL) afforded **11a** (118 mg,

59%) as a yellowish oil, after column chromatography (DCM/5%MeOH). IR (ATR) 2931, 1721, 1657, 1321, 1261, 1083, 1023, 991, 854, 741, 688 cm^{-1}. ^1H NMR (400 MHz, $CDCl_3$) δ 0.66-0.74 (m, 2H, *H*-cycloh), 0.99 (t, *J* = 7.0 Hz, 6H, 2xOCH_2CH_3), 1.11-1.17 (m, 2H, *H*-cycloh), 1.25-1.29 (m, 14H, 12x*H*-cycloh + 2xOCH_2CH_3), 1.63-1.70 (m, 2H, *H*-cycloh), 1.91-2.00 (m, 2H, *H*-cycloh), 2.01-2.09 (m, 2H, *H*-cycloh), 2.62-2.68 (m, 2H, *H*-cycloh), 3.54-3.64 (m, 2H, OCH_2CH_3), 3.86-3.94 (m, 2H, OCH_2CH_3), 4.04-4.18 (m, 4H, 2xOCH_2CH_3), 4.46 (s, 4H, CH_2Ar), 7.01 (t, *J* = 4.0 Hz, 2H, *H*-2), 7.29-7.37 (m, 6H, Ar*H*), 7.41 (d, *J* = 1.0 Hz, 4H, Ar*H*), 7.82 (d, *J* = 1.0 Hz, 2H, Ar*H*), 8.20 (d, *J* = 1.0 Hz, 2H, Ar*H*). ^{13}C NMR (100.6 MHz) δ 16.3 (d, *J* = 5.0 Hz, 2xOCH_2CH_3), 16.7 (d, *J* = 6.0 Hz, 2xOCH_2CH_3), 21.9 (2xCH_2cycloh), 22.7 (2xCH_2cycloh), 24.8 (2xCH_2cycloh), 32.4 (d, *J* = 8.0 Hz, 2xCH_2cycloh), 32.7 (d, *J* = 15.0 Hz, 2xCH_2cycloh), 46.7 (2xCH_2Ar), 63.2 (d, *J* = 4.5 Hz, OCH_2CH_3), 63.3 (d, *J* = 4.0 Hz, OCH_2CH_3), 63.5 (d, *J* = 7.0 Hz, 2xOCH_2CH_3), 70.8 (d, *J* = 4.0 Hz, 2x*C-5*), 83.5 (d, *J* = 145.0 Hz, 2x*C*-4), 127.0 (2xCHAr), 127.7 (2xCHAr), 128.1 (4xCHAr), 128.4 (2xCHAr), 129.7 (2xCHAr), 129.8 (2xCHAr), 137.2 (2x*C-ipso*), 138.0 (2x*C-ipso*), 157.1 (d, *J* = 6.0 Hz, 2x*C*-2). HRMS $C_{44}H_{61}N_4O_6P_2$ $[M+H]^+$ 803.4070; found, 803.4066.

Tetraethyl [(1,4-phenylenebis(methylene))bis(1,3-diazaspiro[4.5]dec-2-ene-1,4-diyl)]bis(phosphonate) (11b).

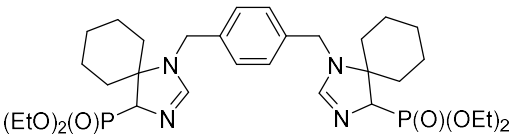

Following the general procedure, $AgNO_3$ (4.3 mg, 0.025 mmol), cyclohexanone (206 μL, 2.0 mmol), *p*-xylylenediamine (34 mg, 0.25 mmol) and PhosMic (89 μL, 0.55 mmol) in methanol (1.3 mL) afforded **11b** (88 mg, 54%) as a yellowish oil, after column chromatography (EtOAc/5%MeOH). IR (ATR) 2971, 2926, 1911, 1599, 1341, 1302, 1093, 1032, 969, 814, 747, 691 cm^{-1}. ^1H NMR (400 MHz, $CDCl_3$) δ 1.06-1.12 (m, 2H, *H*-cycloh), 1.30-1.37 (m, 20H, 8x*H*-cycloh + 4xOCH_2CH_3), 1.48-1.55 (m, 2H, *H*-cycloh), 1.66-1.68 (m, 2H, *H*-cycloh), 1.74-1.87 (m, 4H, *H*-cycloh), 2.23-2.26 (m, 2H, *H*-cycloh), 4.14-4.26 (m, 12H, 4xOCH_2CH_3, 2xCH_2Ar), 4.37 (d, *J* = 16.0, 2H, 2x*H*-4), 7.14 (br d, *J* = 3.0 Hz, 2H, *H*-2), 7.34, (s, 4H, Ar*H*). ^{13}C NMR (100.6 MHz) δ 16.6 (d, *J* = 5.0 Hz, 2xOCH_2CH_3), 16.7 (d, *J* = 6.0 Hz, 2xOCH_2CH_3), 22.2 (2xCH_2cycloh), 23.8 (2xCH_2cycloh), 25.3 (2xCH_2cycloh), 30.7 (d, *J* = 9.0 Hz, 2xCH_2cycloh), 32.8 (d, *J* = 12.0 Hz, 2xCH_2cycloh), 45.5 (2xCH_2Ar), 62.2 (d, *J* = 7.0 Hz, 2xOCH_2CH_3), 63.1 (d, *J* = 4.0 Hz, 2x*C*-5), 63.2 (d, *J* = 7.0 Hz, 2xOCH_2CH_3), 68.6 (d, *J* = 151.0 Hz, 2x*C*-4), 127.9 (4xCHAr), 137.5 (2x*C-ipso*), 157.9 (dd, *J* = 7.0, 1.0 Hz, 2x*C*-2). HRMS $C_{32}H_{54}N_4O_6P_2$ $[M+2H]^{2+}$ 326.1754; found, 326.1754.

Dimethyl (butane-1,4-diyl)bis(5,5-dimethyl-4,5-dihydro-1H-imidazole-4-carboxylate) (12).

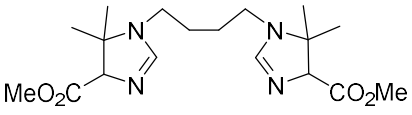

A mixture of $AgNO_3$ (8.5 mg, 0.05 mmol), acetone (3.8 mL), 1,4-diaminobutane (44 mg, 0.5 mmol) and methyl isocyanoacetate (100 μL, 1.10 mmol) was stirred under microwave irradiation at 40ºC for 20 min. The mixture was filtered and evaporated to yield a residue, which was purified by flash column chromatography (EtOAc/5%MeOH/0.33%TEA) to afford **12** (137 mg, 75%) as an 8:1 mixture of diastereomers A (122 mg, 67%) and B (15 mg, 8%) (confirmed by ^{1}H-RMN). **Diastereomer A:** IR (ATR) 2972, 1788, 1583, 1353, 1243, 1120, 941, 882, 743, 692 cm^{-1}. ^{1}H NMR (400 MHz, $CDCl_3$) δ 1.08 (s, 6H, 2xC*H*$_3$), 1.40 (s, 6H, 2xC*H*$_3$), 1.62-1.65 (m, 4H, 2xCH_2), 2.98-3.02 (m, 2H, NCH_2), 3.06-3.11 (m, 2H, NCH_2), 3.75 (s, 6H, 2xOC*H*$_3$), 4.38 (d, *J* = 1.5 Hz, 2H, 2x*H*-4), 7.12 (s, 2H, 2x*H*-2). ^{13}C NMR (100.6 MHz) δ 20.2 (2xCH_3), 27.1 (2xCH_2), 28.2 (2xCH_3), 41.6 (2xNCH_2), 52.1 (2xOCH_3), 65.2 (2x*C*-5), 77.9 (2x*C*-4), 156.4 (2x*C*-2), 171.3 (2xCO). HRMS $C_{18}H_{32}N_4O_4$ $[M+2H]^{2+}$ 184.107; found, 184.1210. **Diastereomer B:** IR (ATR) 2981, 1779, 1572, 1380, 1254, 1152, 963, 866, 732, 694 cm^{-1}. ^{1}H NMR (400 MHz, $CDCl_3$) δ 1.07 (s, 6H, 2xC*H*$_3$), 1.39 (s, 6H, 2xC*H*$_3$), 1.62-1.64 (m, 4H, 2xCH_2), 2.98-3.01 (m, 2H, NCH_2), 3.06-3.10 (m, 2H, NCH_2), 3.75 (s, 6H, 2xOC*H*$_3$), 4.37 (d, *J* = 1.5 Hz, 2H, 2x*H*-4), 7.06 (s, 2H, 2x*H*-2). ^{13}C NMR (100.6 MHz) δ 20.2 (2xCH_3), 27.1 (2xCH_2), 28.3 (2xCH_3), 41.6 (2xNCH_2), 52.1 (2xOCH_3), 65.1 (2x*C*-5), 78.2 (d, *J* = 1.5 Hz, 2x*C*-4), 156.5 (2x*C*-2), 171.3 (2xCO). HRMS $C_{18}H_{32}N_4O_4$ $[M+2H]^{2+}$ 184.106; found, 184.1210.

Dimethyl [1,4-phenylenebis(methylene)]bis(5,5-dimethyl-4,5-dihydro-1H-imidazole-4-carboxylate) (13).

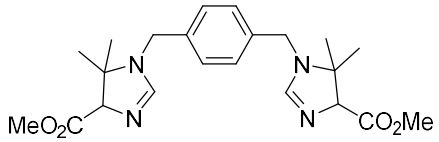

A mixture of $AgNO_3$ (8.5 mg, 0.05 mmol), acetone (3.8 mL), *p*-xylylenediamine (68 mg, 0.5 mmol) and methyl isocyanoacetate (100 μL, 1.10 mmol) was stirred under microwave irradiation at 40ºC for 20 min. The mixture was filtered and evaporated to yield a residue, which was purified by flash column chromatography (EtOAc/5%MeOH/0.33%TEA) to afford **13** (160 mg, 72%) as an 8:1 mixture of diastereomers A (142 mg, 64%) and B (18 mg, 8%) (confirmed by HPLC-MS). **Diastereomer A:** IR (ATR) 2982, 1802, 1617, 1583, 1321, 1237, 1032, 931, 765 cm^{-1}. ^{1}H NMR (400 MHz, $CDCl_3$) δ 1.00 (s, 6H, 2xC*H*$_3$), 1.35 (s, 6H, 2xC*H*$_3$), 3.76 (s, 6H, 2xOC*H*$_3$), 4.21 (q, *J* = 22.0, 10.0 Hz, 4H, 2xC*H*$_2$Ar), 4.44 (d, *J* = 1.5 Hz, 2H, 2x*H*-4), 6.94 (s, 2H, 2x*H*-2), 7.27 (s, 4H, Ar*H*). ^{13}C NMR (100.6 MHz) δ 20.3 (2xCH_3), 27.3 (2xCH_3), 45.9 (2xCH_2Ar), 52.1 (2xOCH_3), 65.0 (2x*C*-5), 78.7 (2x*C*-4), 128.3 (4x*C*HAr), 137.6 (2x*C*-

ipso), 156.8 (2x*C*-2), 171.4 (2xCO). HRMS $C_{22}H_{32}N_4O_4$ $[M+2H]^{2+}$ 208.1206; found, 208.1201. **Diastereomer B:** IR (ATR) 2971, 1819, 1622, 1596, 1317, 1241, 1021, 901, 791 cm^{-1}. ^1H NMR (400 MHz, $CDCl_3$) δ 1.12 (s, 6H, 2xCH_3), 1.37 (s, 6H, 2xCH_3), 3.78 (s, 6H, 2xOCH_3), 4.24 (q, *J* = 20.0, 9.0 Hz, 4H, 2xCH_2Ar), 4.46 (d, *J* = 1.5 Hz, 2H, 2x*H*-4), 7.04 (s, 2H, 2x*H*-2), 7.29 (s, 4H, Ar*H*). ^{13}C NMR (100.6 MHz) δ 20.4 (2xCH_3), 27.3 (2xCH_3), 46.0 (2xCH_2Ar), 52.2 (2xOCH_3), 65.3 (2x*C*-5), 78.1 (2x*C*-4), 128.5 (4x*C*HAr), 137.4 (2x*C*-*ipso*), 156.9 (2x*C*-2), 171.1 (2xCO). HRMS $C_{22}H_{32}N_4O_4$ $[M+2H]^{2+}$ 208.1206; found, 208.1208.

Diethyl {[5-(diethoxyphosphoryl)-4-phenyl-1H-imidazol-1-yl)](phenyl)methyl} phosphonate (A).

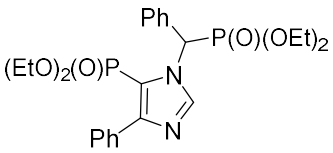

A mixture of $AgNO_3$ (8.5 mg, 0.05 mmol), acetone (3.8 mL) and α-Ph-PhosMic (126.5 mg, 0.5 mmol) was stirred under microwave irradiation at 40 ºC for 20 min. The mixture was filtered and evaporated to yield a residue which was purified by flash column chromatography (DCM/5% MeOH) to obtain **A** (197 mg, 78%) as a yellowish oil. IR (ATR) 3022, 2944, 1771, 1615, 1485, 1331, 1121, 1012, 961, 823, 785 cm^{-1}. ^1H NMR (400 MHz, $CDCl_3$) δ 0.95 (t, *J* = 7.0 Hz, 3H, OCH_2CH_3), 0.99 (t, *J* = 7.0 Hz, 3H, OCH_2CH_3), 1.14 (t, *J* = 7.0 Hz, 3H, OCH_2CH_3), 1.22 (t, *J* = 7.0 Hz, 3H, OCH_2CH_3), 3.52-3.58 (m, 1H, OCH_2CH_3), 3.71-3.77 (m, 2H, OCH_2CH_3), 3.81-3.88 (m, 1H, OCH_2CH_3), 3.95-4.06 (m, 3H, OCH_2CH_3), 4.08-4.15 (m, 1H, OCH_2CH_3), 7.02 (d, *J* = 23.5 Hz, 1H, C*H*Ph), 7.34-7.38 (m, 6H, Ar*H*), 7.55 (d, *J* = 7.5 Hz, 2H, Ar*H*), 7.68 (d, *J* = 8.0 Hz, 2H, Ar*H*), 8.62 (d, *J* = 3.0 Hz, 1H, C*H*N). ^{13}C NMR (100.6 MHz) δ 15.8 (d, *J* = 7.5, OCH_2CH_3), 15.9 (d, *J* = 7.5, OCH_2CH_3), 16.3 (d, *J* = 6.0, OCH_2CH_3), 16.4 (d, *J* = 5.5, OCH_2CH_3), 56.8 (d, *J* = 152.5, *C*HPh), 62.4 (d, *J* = 5.0, O*C*H$_2$CH$_3$), 62.5 (d, *J* = 5.0, O*C*H$_2$CH$_3$), 63.7 (d, *J* = 7.5, O*C*H$_2$CH$_3$), 64.0 (d, *J* = 7.0, O*C*H$_2$CH$_3$), 127.8 (3x*C*HAr), 128.3 (N*C*P), 128.9 (*C*HAr), 128.9 (*C*HAr), 128.9 (*C*HAr), 129.0 (*C*HAr), 129.4 (2x*C*HAr), 133.9 (*C*-ipso), 134.1 (*C*-ipso), 141.8 (d, *J* = 2.5), 141.9 (d, *J* = 2.5, *C*HN), 151.8 (d, *J* = 17.5, N*C*N). HRMS $C_{24}H_{33}N_2O_6P_2$ $[M+H]^+$ 507.1814; found, 507.1817.

Diethyl [1-(4-aminocyclohexyl)-5,5-dimethyl-4-phenyl-4,5-dihydro-1H-imidazol-4-yl]phosphonate (Ia)

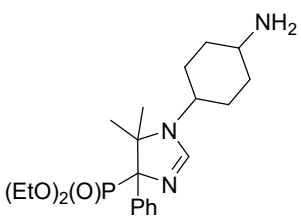

Following the general procedure, $AgNO_3$ (4.4 mg, 0.026 mmol), acetone (1.9 mL), *p*-cyclohexanediamine (30 mg, 0.26 mmol) and α-PhPhosMic (141.5 mg, 0.56 mmol) afforded **Ia** (35 mg, 33%) as a yellowish oil, after column chromatography (DCM/5%MeOH). IR (ATR) 3228, 2975, 2912, 1630, 1402,

1255, 1173, 1054, 975, 854 801, 792, 727 cm^{-1}. ^{1}H NMR (400 MHz, $CDCl_3$) δ 0.57 (s, 3H, C*H*$_3$), 0.96 (t, *J* = 7.0 Hz, 3H, OCH$_2$C*H*$_3$), 1. (t, *J* = 7.0 Hz, 3H, OCH$_2$C*H*$_3$), 1.50-1.52 (m, 1H, *H*-cycloh), 1.58-1.67 (m, 2H, *H*-cycloh), 1-73-1.78 (m, 4H, *H*-cycloh + C*H*$_3$), 1.80-1.90 (m, 2H, *H*-cycloh), 1.95-2.07 (m, 2H, *H*-cycloh), 2.73-2.89 (m, 1H, C*H*N), 3.29-3.30 (m, 1H, C*H*NH$_2$), 3.43-3.48 (m, 1H, OC*H*$_2$CH$_3$), 3.72-3.78 (m, 1H, OC*H*$_2$CH$_3$), 4.01-4.06 (m, 1H, OC*H*$_2$CH$_3$), 4.09-4.14 (m, 1H, OC*H*$_2$CH$_3$), 7.27-7.35 (m, 4H, *H*-2 + Ar*H*), 7.81 (br d, *J* = 21.0 Hz, 2H, Ar*H*). ^{13}C NMR (100.6 MHz) δ 16.4 (d, *J* = 4.0 Hz, OCH$_2$*C*H$_3$), 16.7 (d, *J* = 5.0 Hz, OCH$_2$*C*H$_3$), 24.3 (d, *J* = 8.0 Hz, *C*H$_3$), 24.7 (d, *J* = 12.0 Hz, *C*H$_3$), 28.5 (*C*H$_2$cycloh), 29.5 (*C*H$_2$cycloh), 29.8 (*C*H$_2$cycloh), 31.6 (*C*H$_2$cycloh), 44.6 (N*C*Hcycloh), 51.3 (NH$_2$*C*Hcycloh), 62.9 (O*C*H$_2$CH$_3$), 63.5 (O*C*H$_2$CH$_3$), 68.7 (*C*-5), 81.5 (d, *J* = 116.0, Hz, *C*-4), 127.2 (*C*HAr), 127.5 (2x*C*HAr), 128.3 (*C*HAr), 128.9 (*C*HAr), 137.3 (*C-ipso*), 153.9 (*C*-2). HRMS $C_{21}H_{35}N_3O_3P$ $[M+H]^+$ 408.2420; found, 408.2422.

Diethyl [1-(4-aminophenyl)-5,5-dimethyl-4-phenyl-4,5-dihydro-1H-imidazol-4-yl] phosphonate (II).

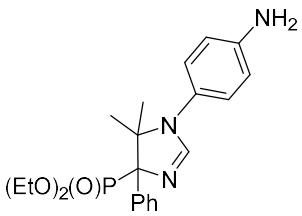

Following the general procedure, $AgNO_3$ (4.4 mg, 0.026 mmol), acetone (1.9 mL), *p*-phenylenediamine (28 mg, 0.26 mmol) and α-PhPhosMic (141.5 mg, 0.56 mmol) afforded **II** (53 mg, 51%) as a yellowish oil, after column chromatography (DCM/5%MeOH). IR (ATR) 3222, 2966, 2932, 1666, 1511, 1442, 1261, 1132, 1032, 944, 812, 765 cm^{-1}. ^{1}H NMR (400 MHz, $CDCl_3$) δ 0.60 (s, 3H, C*H*$_3$), 0.99 (t, *J* = 7.0 Hz, 3H, OCH$_2$C*H*$_3$), 1.30 (t, *J* = 7.0 Hz, 3H, OCH$_2$C*H*$_3$), 1.81 (s, 3H, C*H*$_3$), 3.48-3.54 (m, 1H, OC*H*$_2$CH$_3$), 3.74-3.81 (m, 1H, OC*H*$_2$CH$_3$), 4.10-4.24 (m, 2H, OC*H*$_2$CH$_3$), 6.64 (d, *J* = 8.5 Hz, 2H, Ar*H*), 6.93 (d, *J* = 8.5 Hz, 2H, Ar*H*), 7.22 (d, *J* = 4.0 Hz, 1H, *H*-2), 7.29-7.35 (m, 3H, Ar*H*), 7.89 (br d, *J* = 41.5 Hz, 2H, Ar*H*). ^{13}C NMR (100.6 MHz) δ 16.3 (d, *J* = 5.0 Hz, OCH$_2$*C*H$_3$), 16.7 (d, *J* = 6.0 Hz, OCH$_2$*C*H$_3$), 24.3 (d, *J* = 14.5 Hz, *C*H$_3$), 25.1 (d, *J* = 8.0 Hz, *C*H$_3$), 63.1 (d, *J* = 9.0 Hz, O*C*H$_2$CH$_3$), 63.5 (d, *J* = 7.0 Hz, O*C*H$_2$CH$_3$), 68.9 (d, *J* = 4.5 Hz, *C*-5), 81.7 (d, *J* = 146.0 Hz, *C*-4), 115.4 (4x*C*HAr), 127.6 (d, *J* = 3.0 Hz, *C*HAr), 128.3 (*C-ipso*), 129.0 (4x*C*HAr), 137.1 (*C-ipso*), 146.0 (*C-ipso*), 156.0 (d, *J* = 6.0 Hz, *C*-2). HRMS $C_{21}H_{29}N_3O_3P$ $[M+H]^+$ 402.1947; found, 402.1951.

Diethyl [1-(4-aminobenzyl)-5,5-dimethyl-4-phenyl-4,5-dihydro-1H-imidazol-4-yl] phosphonate (III).

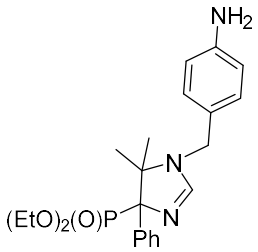

Following the general procedure, $AgNO_3$ (5.3 mg, 0.031 mmol), acetone (2.4 mL), 4-aminobenzylamine (35 μL, 0.31 mmol) and α-PhPhosMic (172.2 mg, 0.68 mmol) afforded **III** (72 mg, 56%) as a yellowish oil, after column chromatography (DCM/5%MeOH). IR (ATR) 3198, 2956, 2924, 1789, 1530, 1422, 1255, 1161, 1034, 955, 835, 799 cm^{-1}. ^1H NMR (400 MHz, $CDCl_3$) δ 0.66 (s, 3H, C*H*$_3$), 0.95 (t, *J* = 7.0 Hz, 3H, OCH_2CH_3), 1.28 (t, *J* = 7.0 Hz, 3H, OCH_2CH_3), 1.79 (s, 3H, C*H*$_3$), 3.39-3.46 (m, 1H, OCH_2CH_3), 3.70-3.76 (m, 1H, OCH_2CH_3), 4.02-4.18 (m, 4H, OCH_2CH_3 + CH_2Ar), 6.66 (d, *J* = 8.5 Hz, 2H, Ar*H*), 7.05 (d, *J* = 4.0 Hz, 1H, *H*-2), 7.12 (d, *J* = 8.5 Hz, 2H, Ar*H*), 7.27-7.33 (m, 3H, Ar*H*), 7.85 (br d, *J* = 20.0 Hz, 2H, Ar*H*). ^{13}C NMR (100.6 MHz) δ 16.3 (d, *J* = 5.0 Hz, OCH_2CH_3), 16.6 (d, *J* = 6.0 Hz, OCH_2CH_3), 23.2 (d, *J* = 14.0 Hz, CH_3), 24.2 (d, *J* = 8.0 Hz, CH_3), 46.0 (CH_2Ar), 63.1 (d, *J* = 9.0 Hz, OCH_2CH_3), 63.6 (d, *J* = 8.0 Hz, OCH_2CH_3), 68.9 (d, *J* = 4.0 Hz, *C*-5), 81.7 (d, *J* = 146.0 Hz, *C*-4), 115.3 (4x*C*HAr), 127.6 (d, *J* = 3.0 Hz, *C*HAr), 128.3 (*C-ipso*), 129.2 (4x*C*HAr), 137.0 (*C-ipso*), 146.2 (*C-ipso*), 156.4 (d, *J* = 6.0 Hz, *C*-2). HRMS $C_{22}H_{31}N_3O_3P$ $[M+H]^+$ 416.2103; found, 416.2101.

MATERIAL SUPLEMENTARIO

TABLE OF CONTENTS:

1. **Representative data of ^{1}H and ^{13}C-NMR spectra of new compounds** 364
2. **^{1}H-NMR and ^{13}C-NMR spectra of new compounds 1a – III** 365
3. **^{1}H-NMR and HPLC-MS spectra of new some reaction crudes** 388
4. **Comparative ^{1}H-NMR spectra of 12 at different reaction conditions** 390
5. **X-ray crystallographic data for 1a** 392
6. **Optimization synthesis of 1a** 408
7. **Optimization synthesis of 8a** 410
8. **Optimization synthesis of II** 412

1. Representative data of ^{1}H and ^{13}C-NMR spectra of new compounds

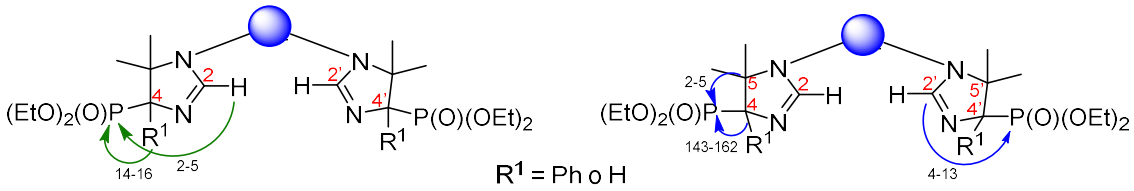

Tabla S1. ^{1}H and ^{13}C chemical shifts (ppm) for new compounds **1a-11b** including both the multiplicity and the coupling constants (J Hz). Coupling constants for ^{1}H-P (in green), ^{13}C-P (in blue).

Compuesto	H2/H2'	H4/H4'	C2/C2'	C4/C4'	C5/C5'
1a	7.11, d 3.0	---	155.9, d 6.0	81.8, d 146.0	67.7, d 4.0
1b	7.11, br s	3.96, dd 14.0, 2.0	156.8, d 12.0	70.5, d 162.0	65.3, d 3.0
2	7.10, d 3.5	---	155.9, d 6.0	81.6, d 147.0	68.6, d 4.0
3	7.12, br s	3.94, dd 16.0, 1.5	156.5, d 13.0	72.0, d 162.0	64.9, d 2.0
4	7.29, d 4.0	---	156.5, dd 7.0, 3.0	81.4, dd 145.0, 3.0	68,3, d 4.0
5	7.34, s	---	155.9, d 5.0	81.3, d 145.0	68.8, d 3.0
6a	7.03, d 4.5	---	156.5, d 5.0	82.1, d 146.5	68.9, d 4.5
6b	6.94, br s	3.99, dd 16.0, 1.5	156.9, d 12.0	73.1, d 162.0	66.8, d 3.0
7	7.06, t 3.0	---	156.6, d 6.0	82.0, dd 146.5, 3.0	68.9, d 4.5
8a	7.36, br s	3.93, dd 15.0, 2.0	154.2, d 9.0	72.4, d 161.0	65.3, d 4.0
9a	7.08, d 3.5 7.15, dd 19.0, 3.5	---	157.1, d 5.0 157.3, d 5.0	81.4, d 145.0 81.5, d 143.0	69.3, d 3.0 69.4, d 3.0
9b	6.82, d 2.5 6.87, d 2.0	3.89, d 2.0 3.93, d 2.0	156.2, d 4.0 157.0, d 4.0	73.6, d 163 73.7, d 164	64.4, d 3.0 64.5, d 3.0
10	7.39, s	---	156.3, d 5.0	80.9, d 153.0	69.0, d 4.0
11a	7.01, t 4.0	---	157.1, d 6.0	83.5, d 145.0	70.8, d 4.0
11b	7.14, br d 3.0	4.37, d 16.0	157.9, dd 7.0, 1.0	68.6, d 151.0	63.1, d 4.0

2. ^{1}H-NMR and ^{13}C-NMR spectra of new compounds 1a – III

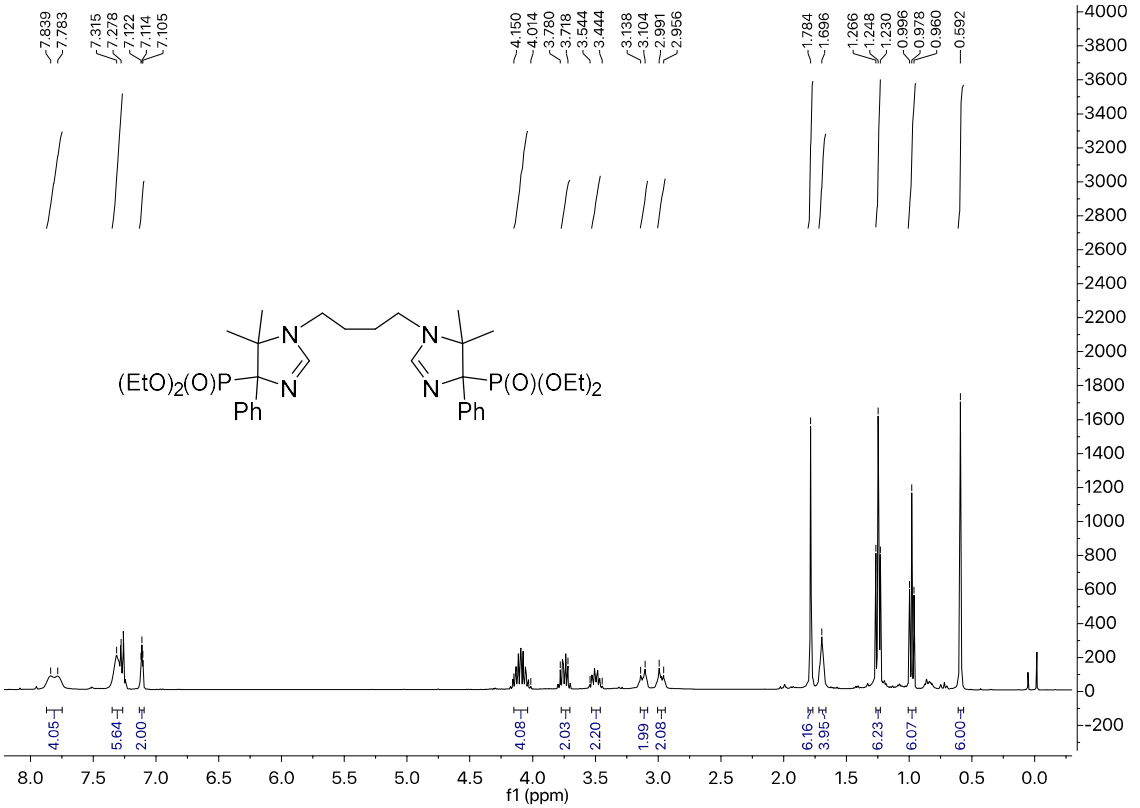

Tetraethyl [butane-1,4-diylbis(5,5-dimethyl-4-phenyl-4,5-dihydro-1H-imidazole-1,4-diyl)]bis(phosphonate) (1a)

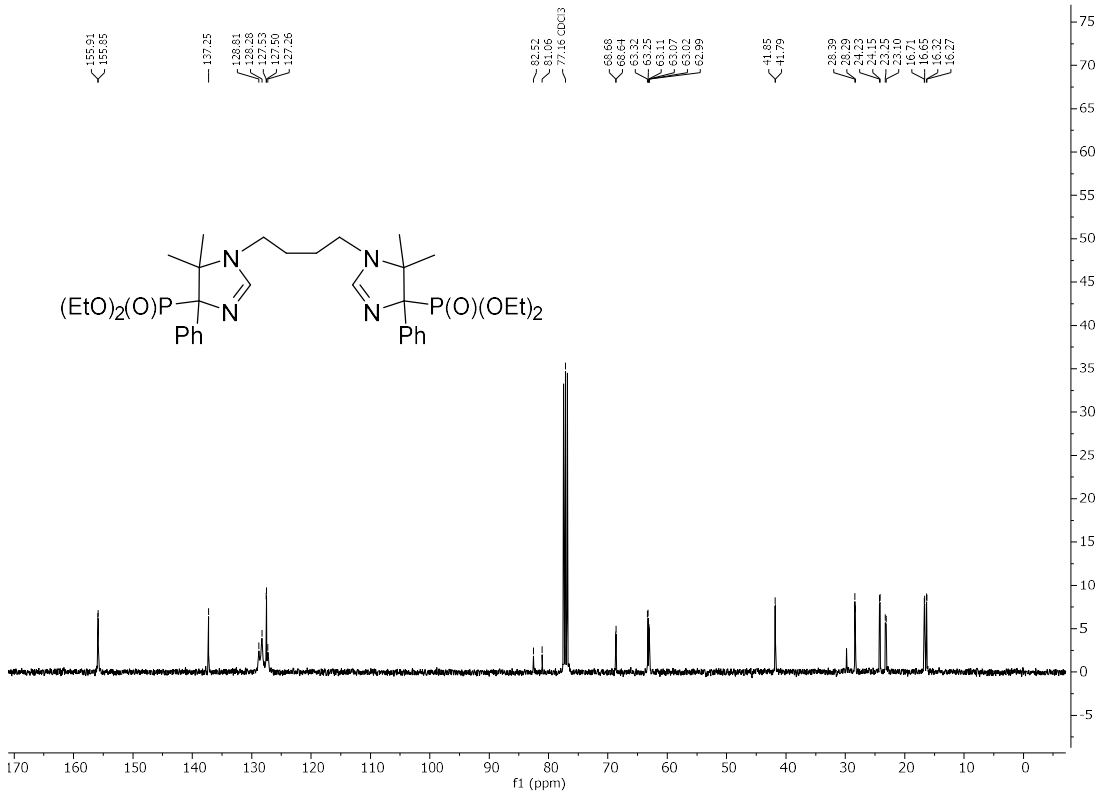

Tetraethyl [butane-1,4-diylbis(5,5-dimethyl-4-phenyl-4,5-dihydro-1H-imidazole-1,4-diyl)]bis(phosphonate) (1a)

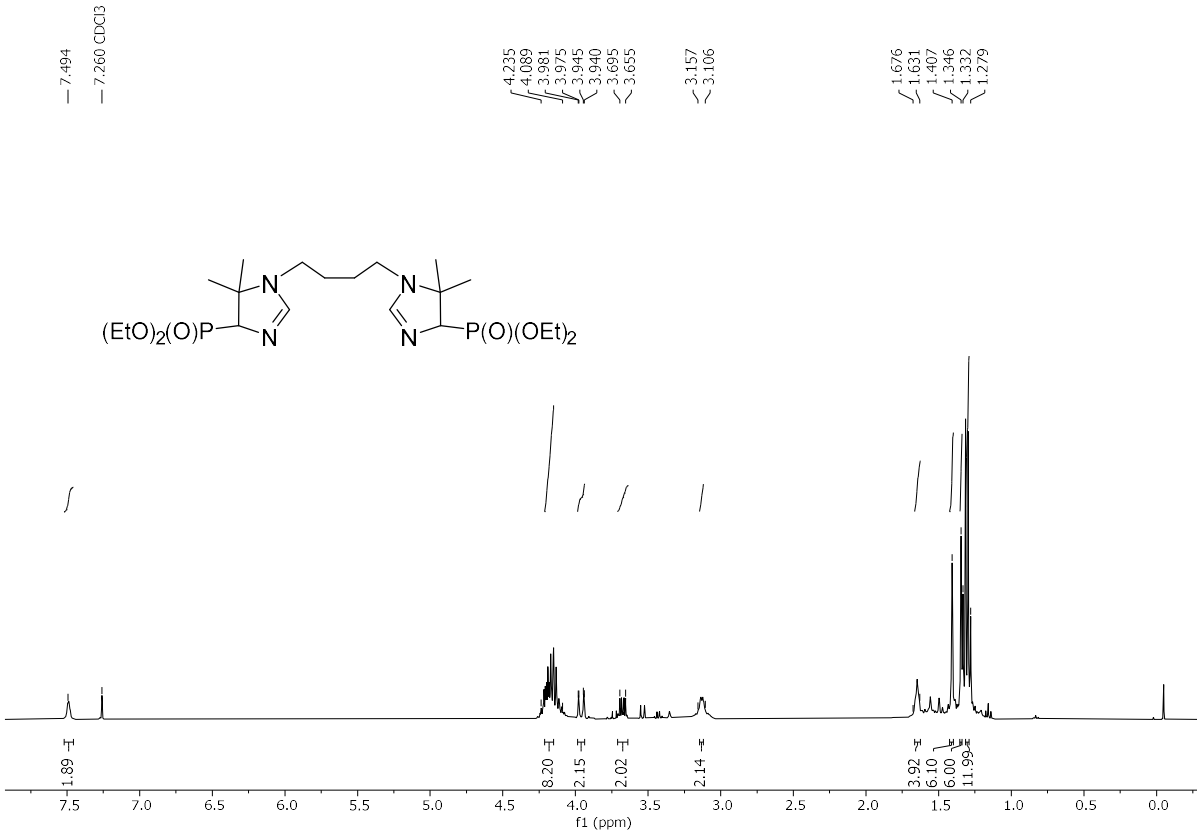

Tetraethyl [butane-1,4-diylbis(5,5-dimethyl-4,5-dihydro-1H-imidazole-1,4-diyl)]bis(phosphonate) (1b)

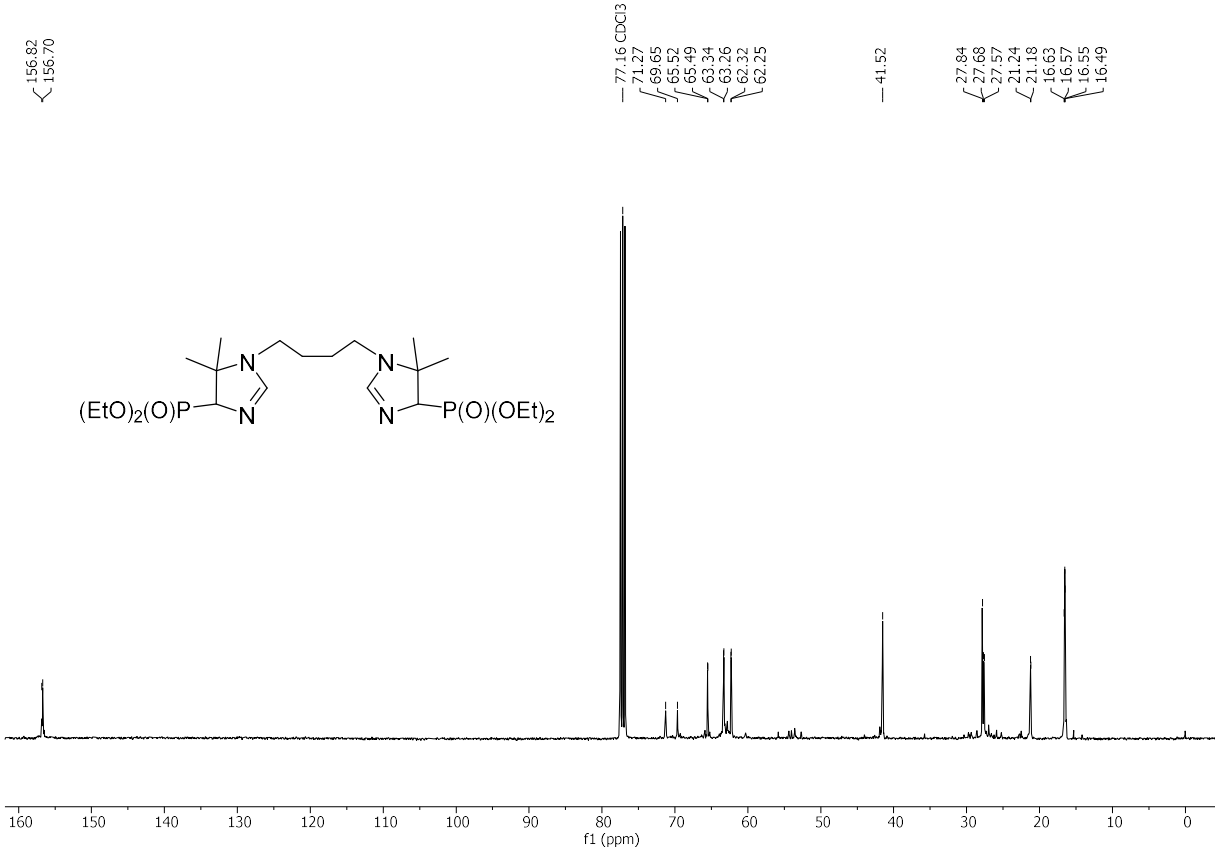

Tetraethyl [butane-1,4-diylbis(5,5-dimethyl-4,5-dihydro-1H-imidazole-1,4-diyl)]bis(phosphonate) (1b)

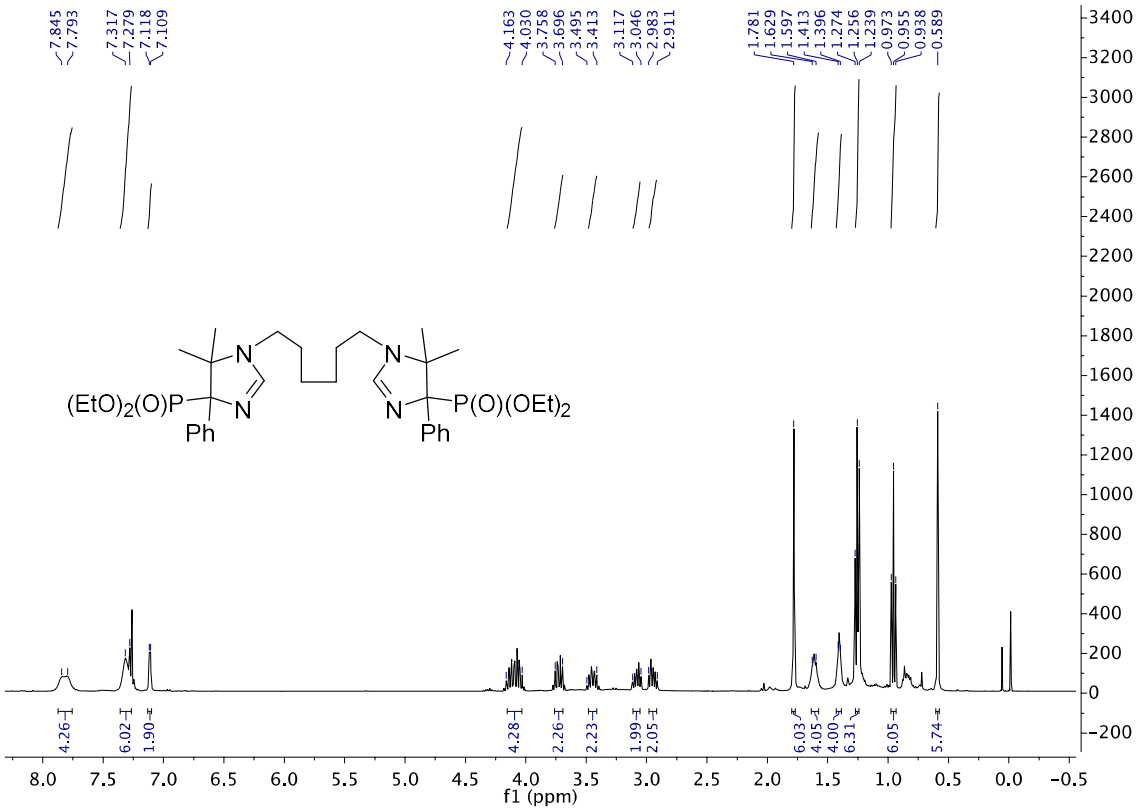

Tetraethyl [hexane-1,6-diylbis(5,5-dimethyl-4-phenyl-4,5-dihydro-1H-imidazole-1,4-diyl)]bis(phosphonate) (2)

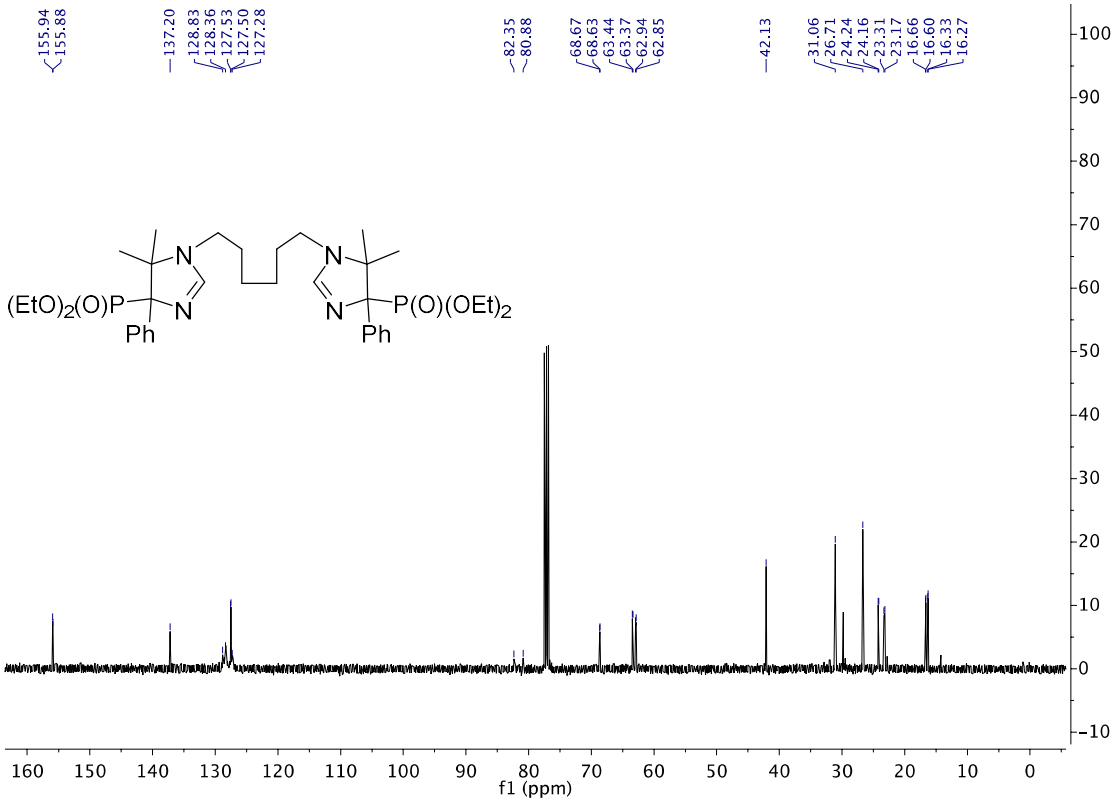

Tetraethyl [hexane-1,6-diylbis(5,5-dimethyl-4-phenyl-4,5-dihydro-1H-imidazole-1,4-diyl)]bis(phosphonate) (2)

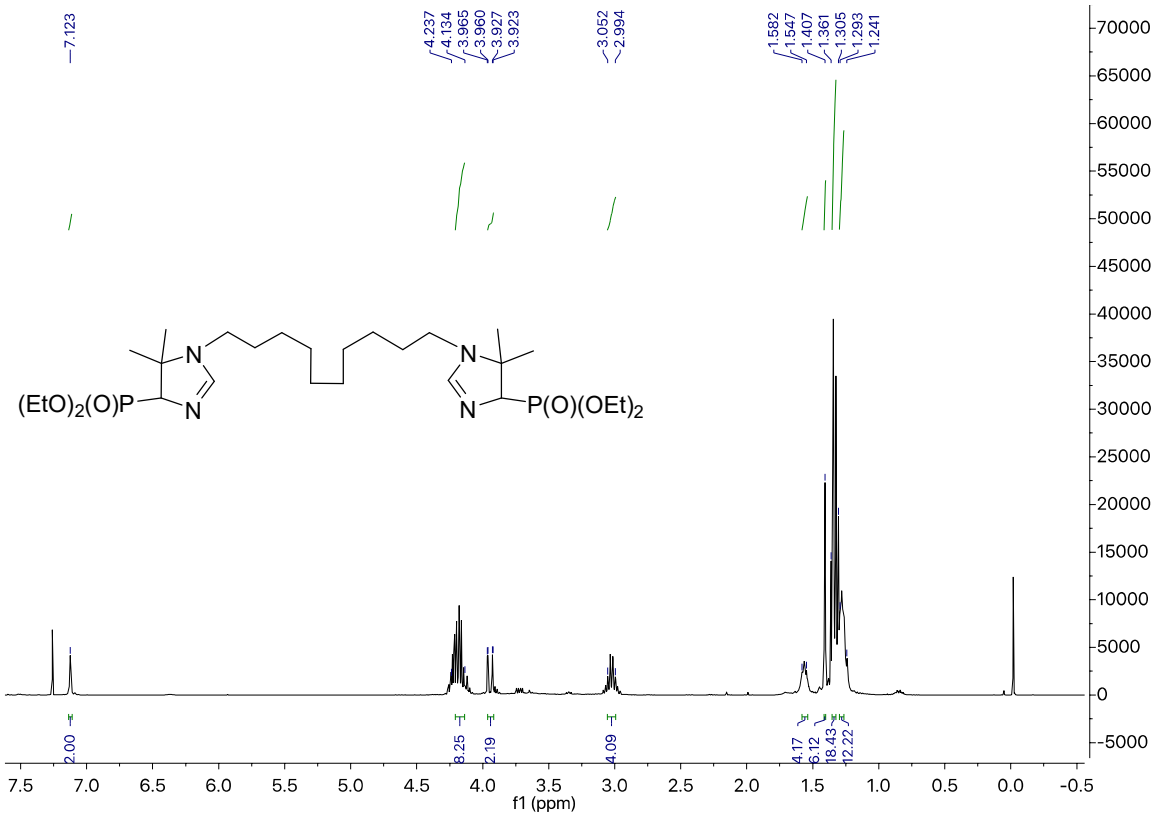

Tetraethyl [decane-1,10-diylbis(5,5-dimethyl-4,5-dihydro-1H-imidazole-1,4-diyl)]bis(phosphonate) (3)

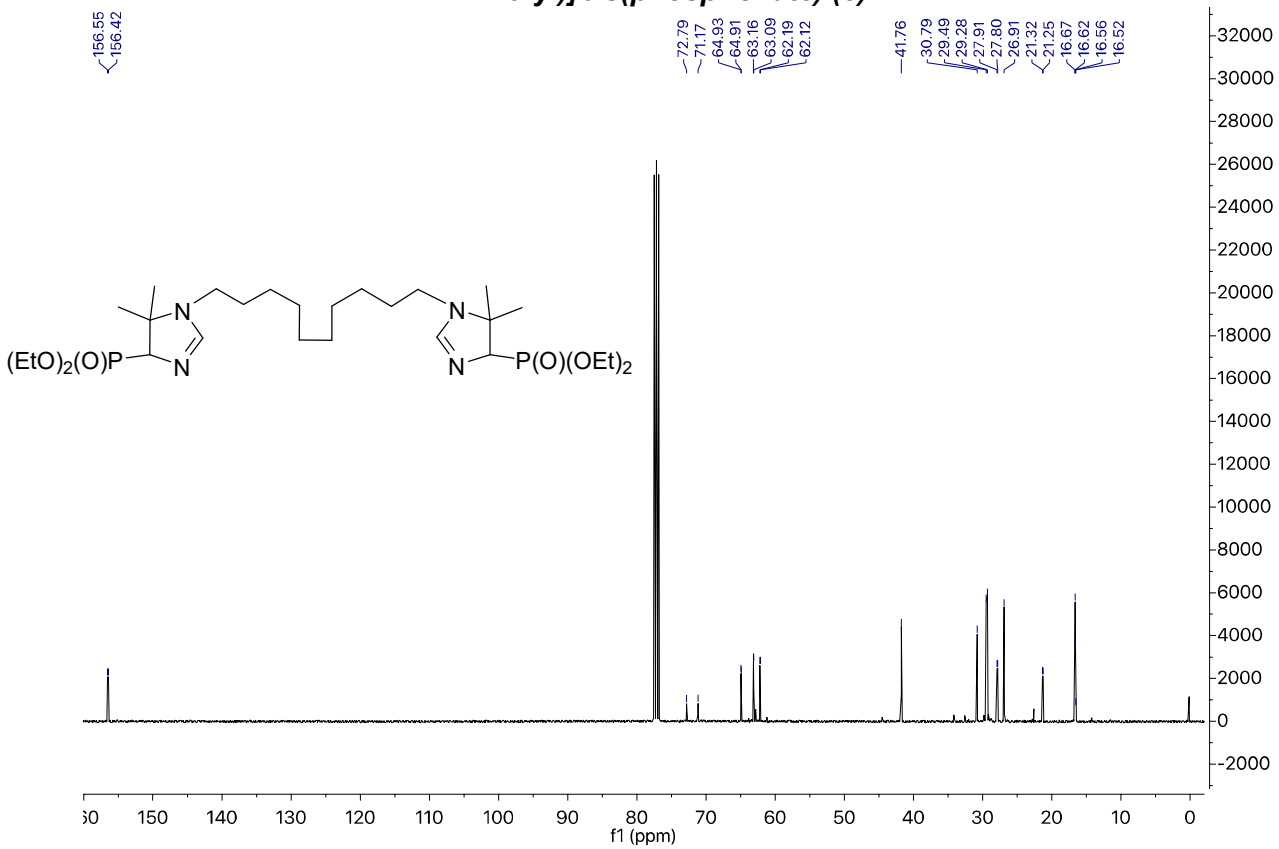

Tetraethyl [decane-1,10-diylbis(5,5-dimethyl-4,5-dihydro-1H-imidazole-1,4-diyl)]bis(phosphonate) (3)

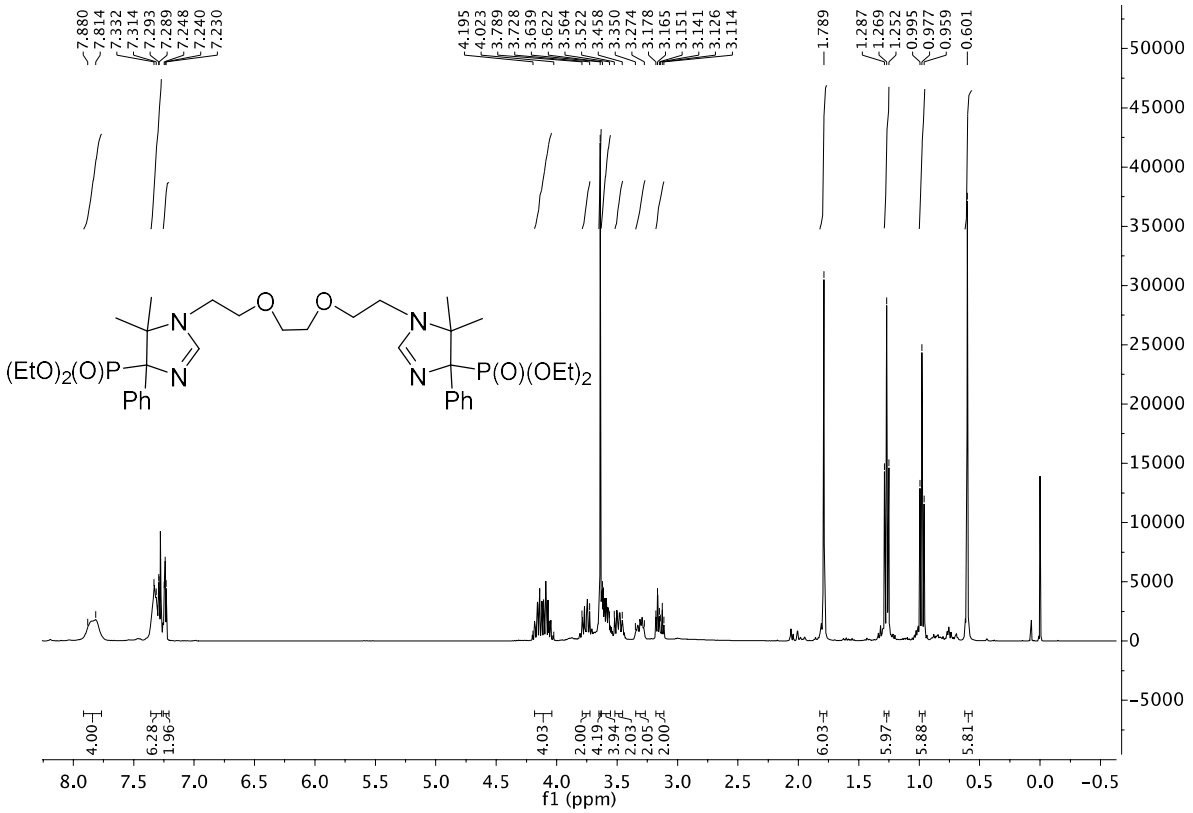

Tetraethyl {[(ethane-1,2-diylbis(oxy))bis(ethane-2,1-diyl)]bis(5,5-dimethyl-4-phenyl-4,5-dihydro-1H-imidazole-1,4-diyl)}bis(phosphonate) (4)

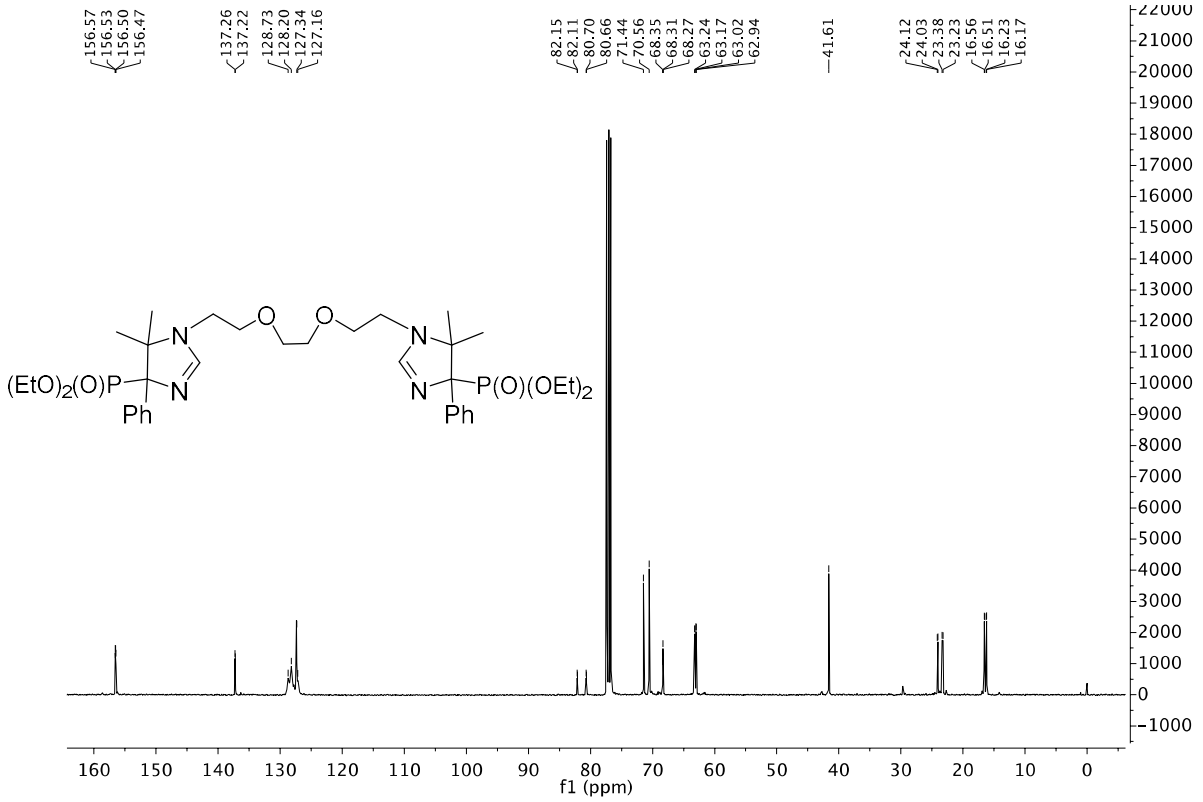

Tetraethyl {[(ethane-1,2-diylbis(oxy))bis(ethane-2,1-diyl)]bis(5,5-dimethyl-4-phenyl-4,5-dihydro-1H-imidazole-1,4-diyl)}bis(phosphonate) (4)

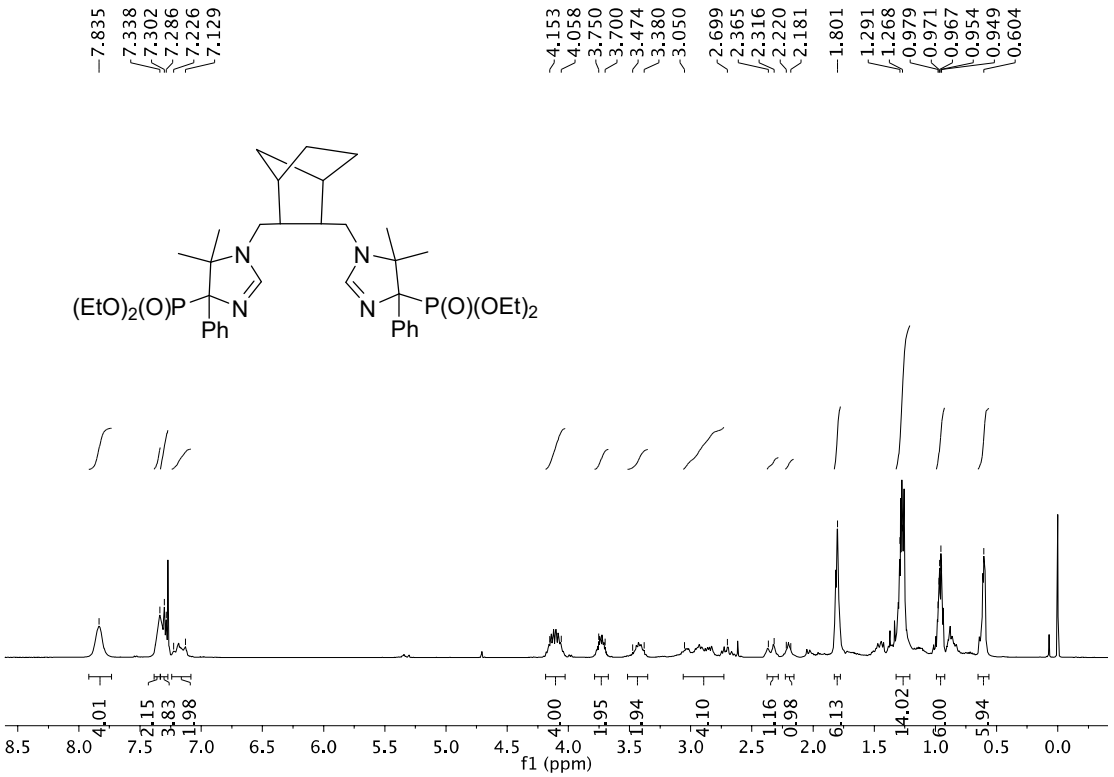

Tetraethyl [(bicyclo[2.2.1]heptane-2,3-diyl)bis(methylene))bis(5,5-dimethyl-4-phenyl-4,5-dihydro-1H-imidazole-1,4-diyl)]bis(phosphonate) (5)

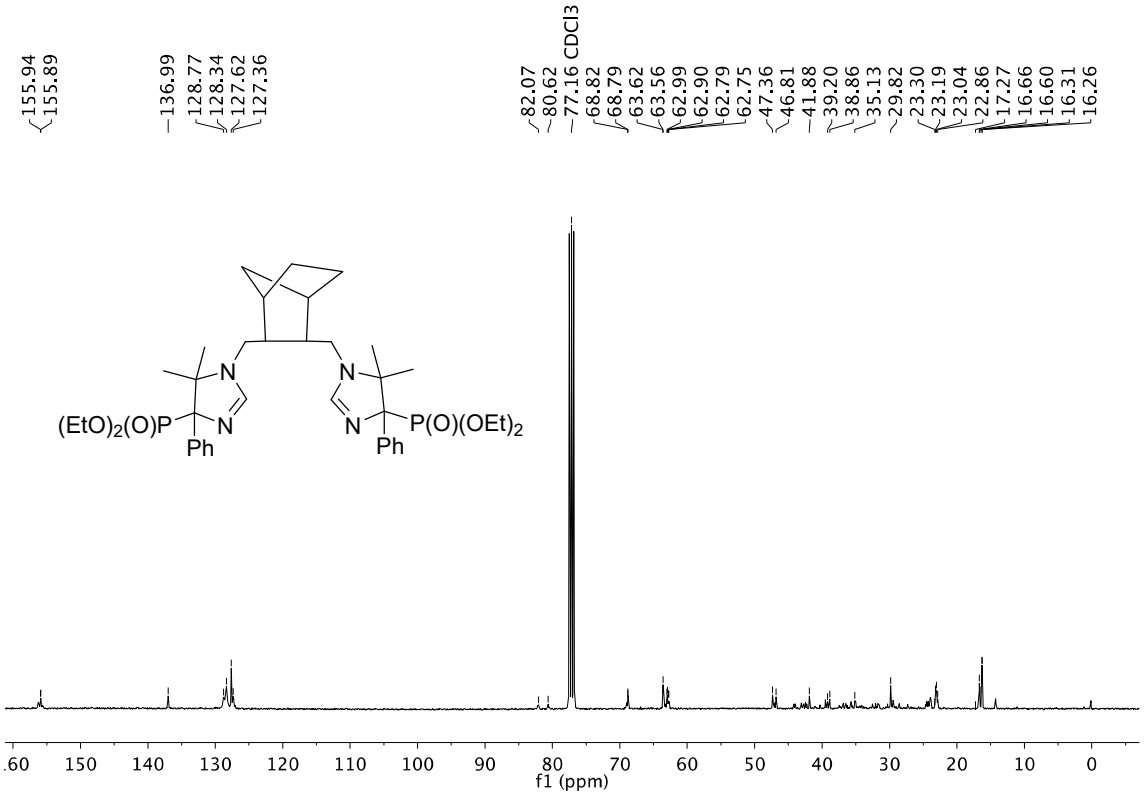

Tetraethyl [(bicyclo[2.2.1]heptane-2,3-diyl)bis(methylene))bis(5,5-dimethyl-4-phenyl-4,5-dihydro-1H-imidazole-1,4-diyl)]bis(phosphonate) (5)

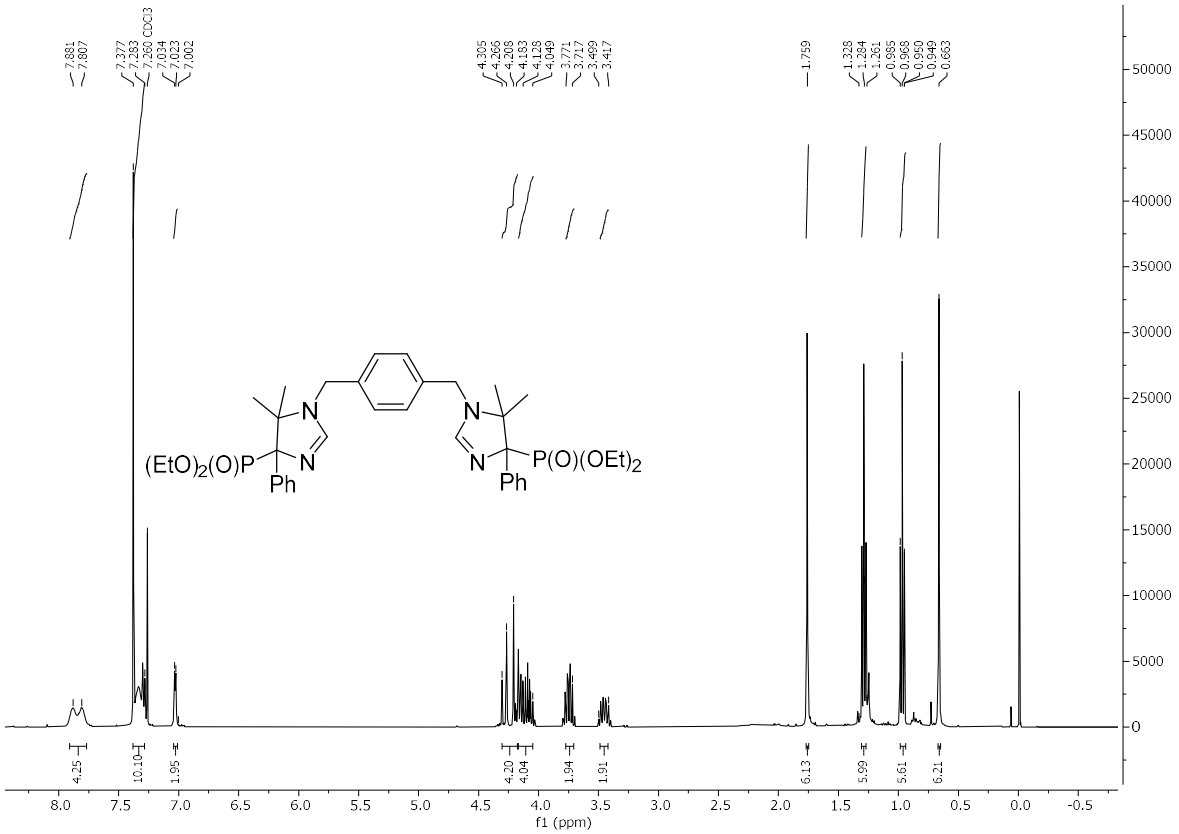

Tetraethyl {[1,4-phenylenebis(methylene)]bis(5,5-dimethyl-4-phenyl-4,5-dihydro-1H-imidazole-1,4-diyl)}bis(phosphonate) (6a)

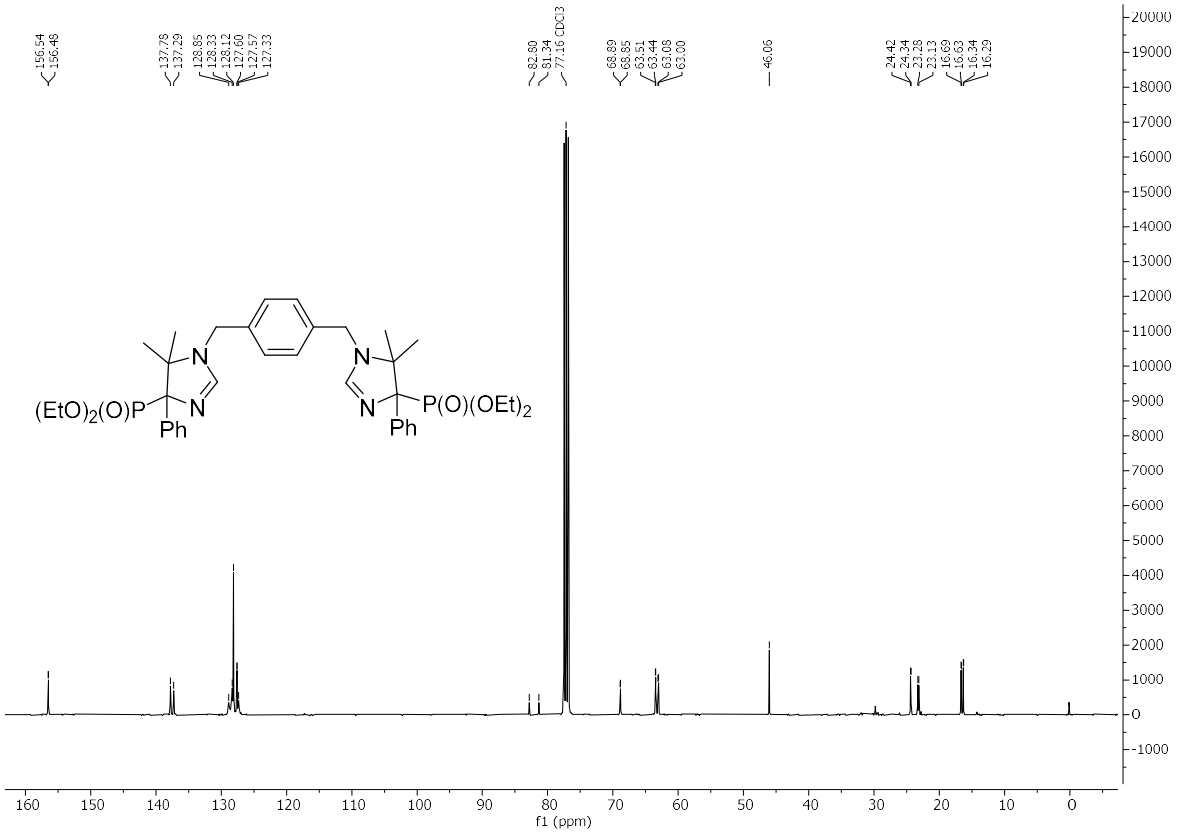

Tetraethyl {[1,4-phenylenebis(methylene)]bis(5,5-dimethyl-4-phenyl-4,5-dihydro-1H-imidazole-1,4-diyl)}bis(phosphonate) (6a)

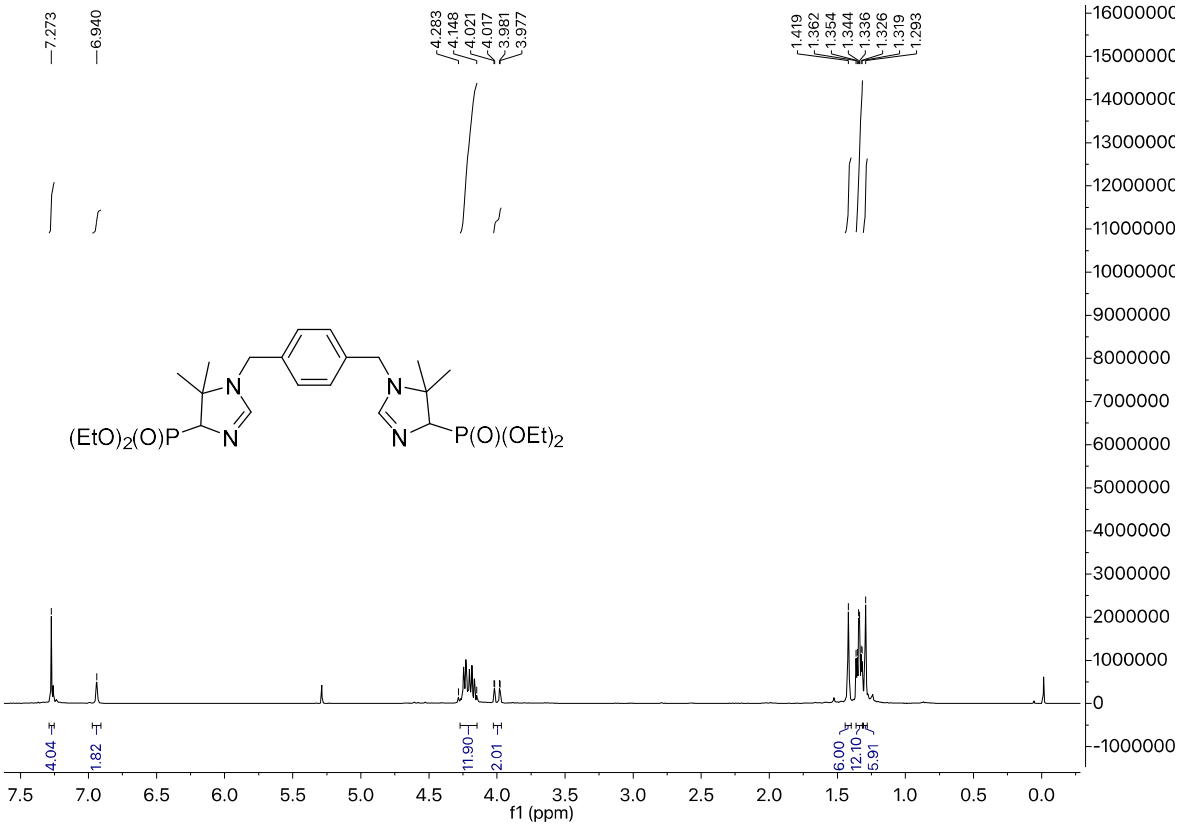

Tetraethyl {[1,4-phenylenebis(methylene)]bis(5,5-dimethyl-4,5-dihydro-1H-imidazole-1,4-diyl)}bis(phosphonate) (6b)

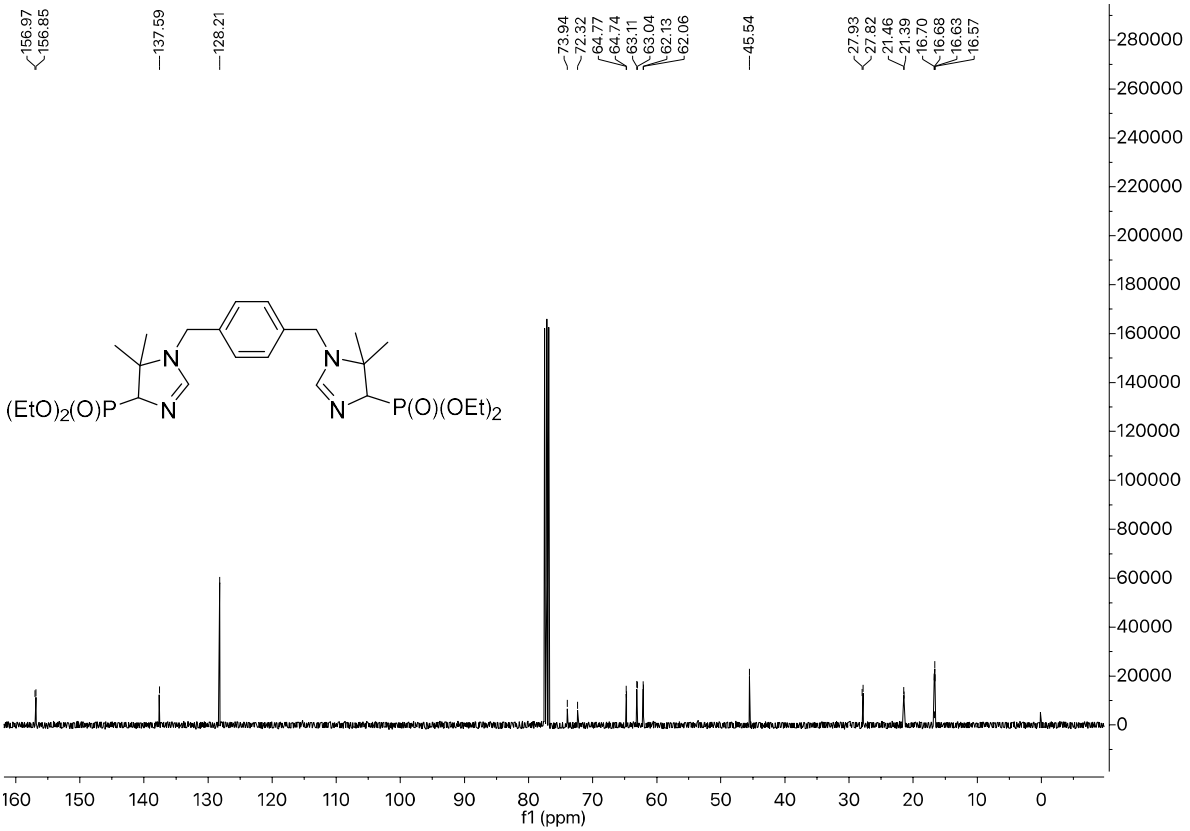

Tetraethyl {[1,4-phenylenebis(methylene)]bis(5,5-dimethyl-4,5-dihydro-1H-imidazole-1,4-diyl)}bis(phosphonate) (6b)

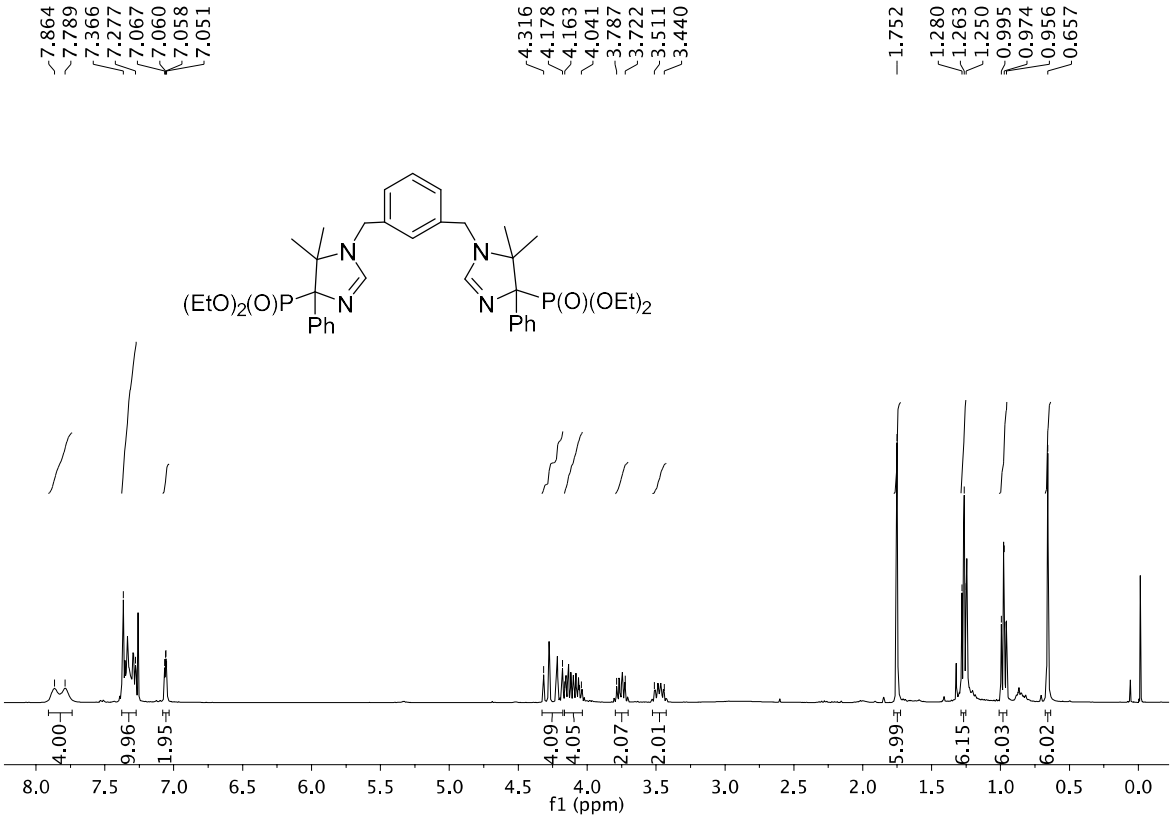

Tetraethyl {[1,3-phenylenebis(methylene)]bis(5,5-dimethyl-4-phenyl-4,5-dihydro-1H-imidazole-1,4-diyl)}bis(phosphonate) (7)

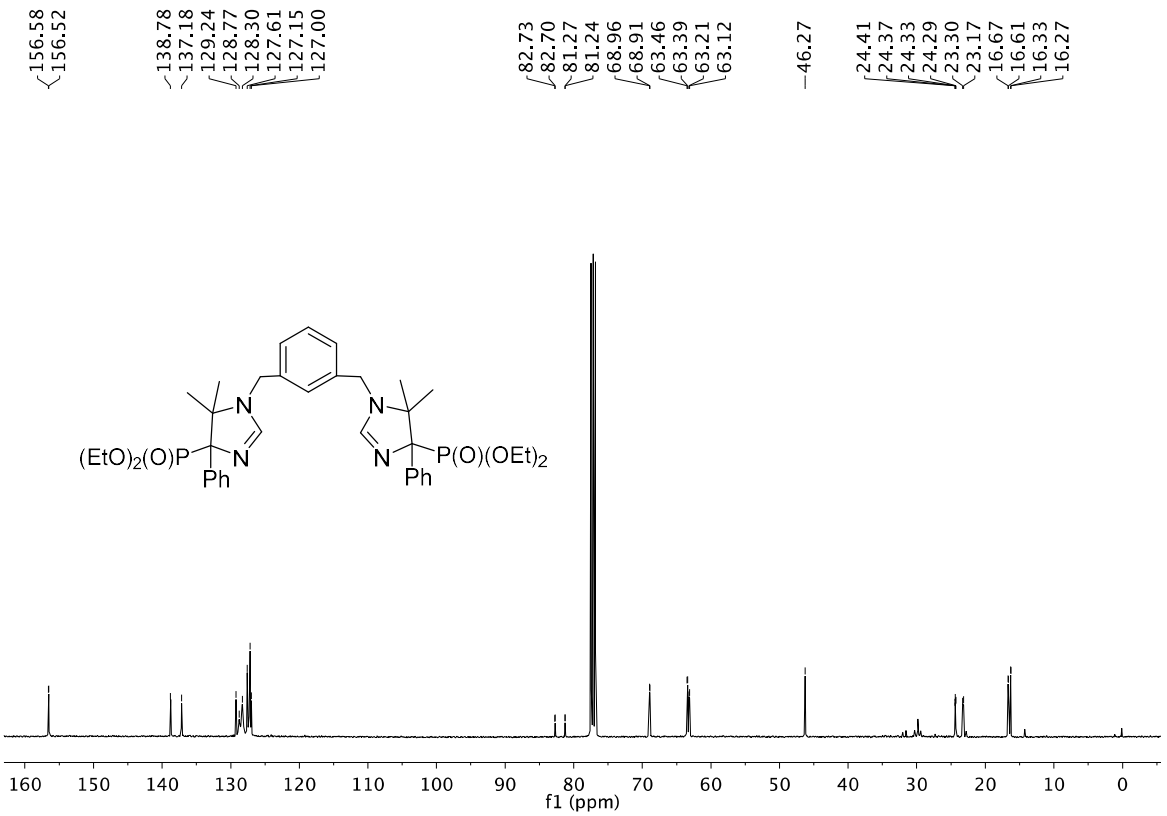

Tetraethyl {[1,3-phenylenebis(methylene)]bis(5,5-dimethyl-4-phenyl-4,5-dihydro-1H-imidazole-1,4-diyl)}bis(phosphonate) (7)

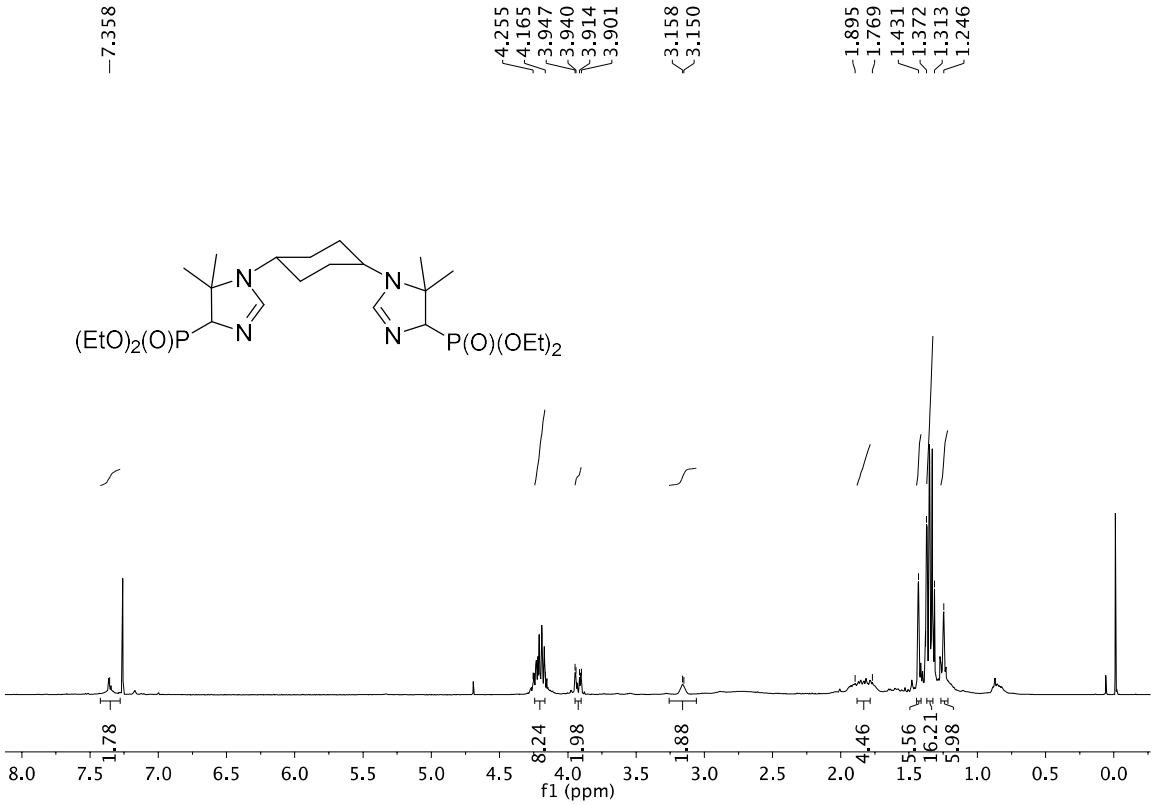

Tetraethyl [cyclohexane-1,4-diylbis(5,5-dimethyl-4,5-dihydro-1H-imidazole-1,4-diyl)]bis(phosphonate)(8a)

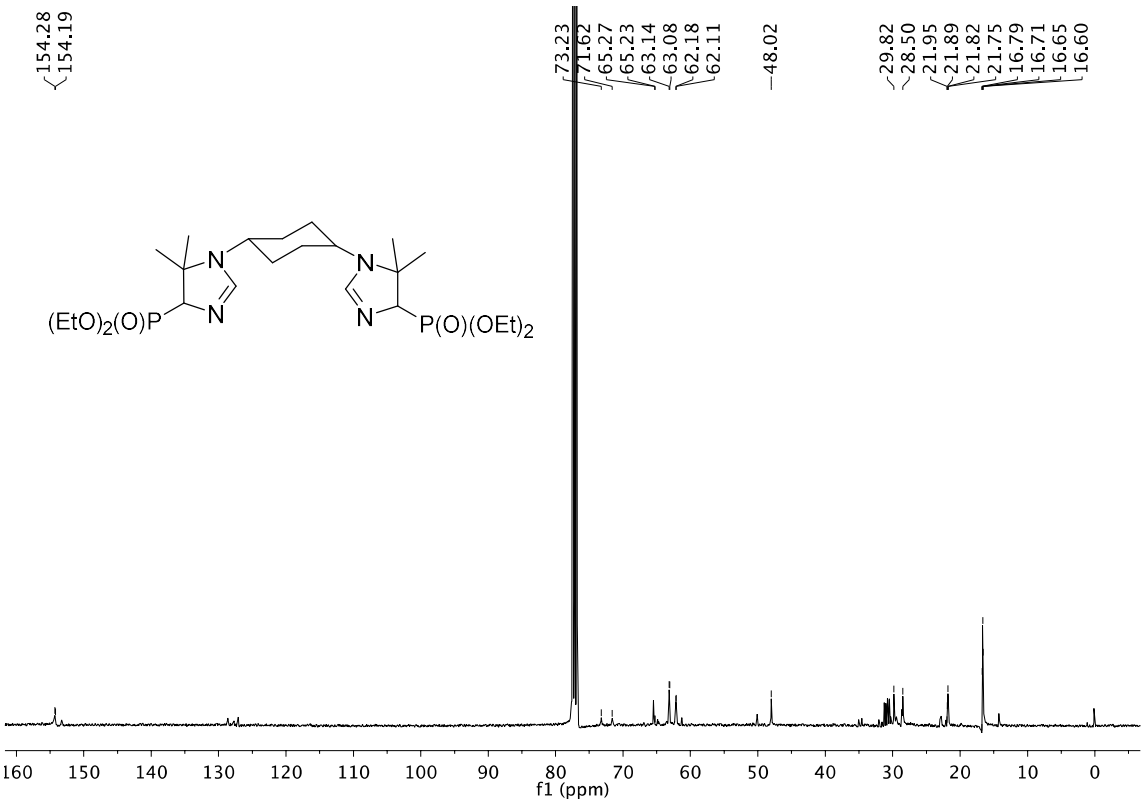

Tetraethyl [cyclohexane-1,4-diylbis(5,5-dimethyl-4,5-dihydro-1H-imidazole-1,4-diyl)]bis(phosphonate) (8a)

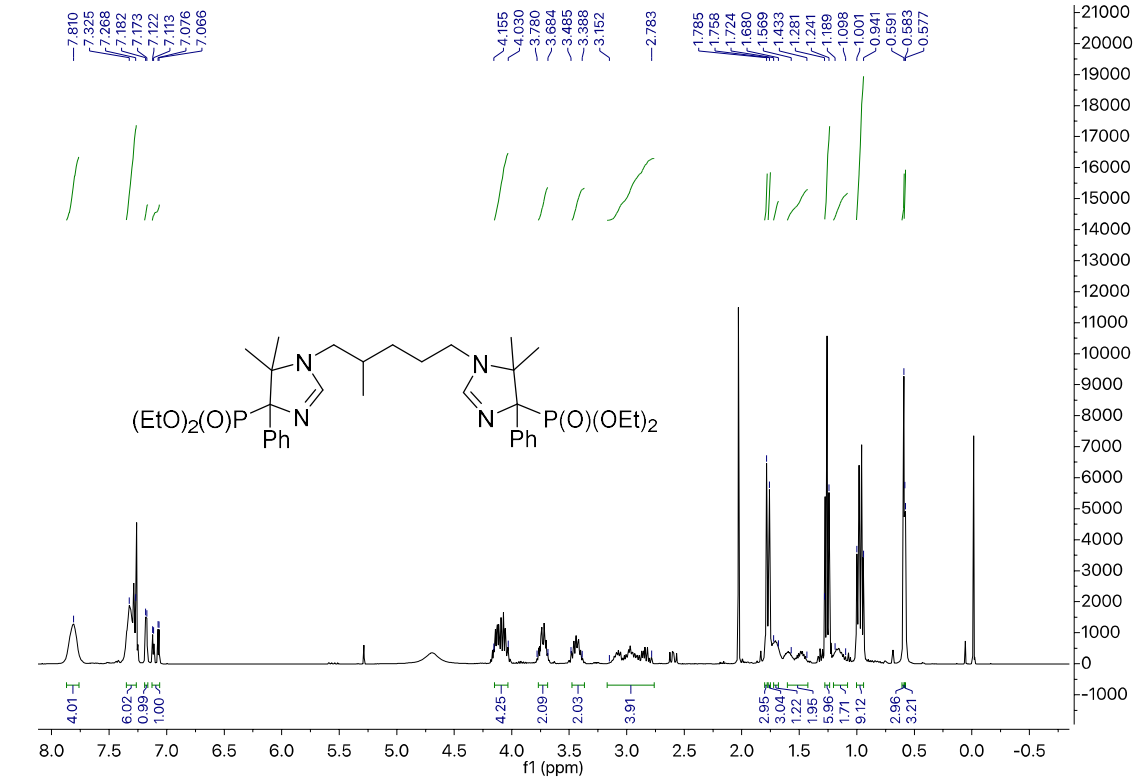

Tetraethyl [4-methylpentane-1,5-diylbis(5,5-dimethyl-4-phenyl-4,5-dihydro-1H-imidazole-1,4-diyl)]bis(phosphonate)(9a)

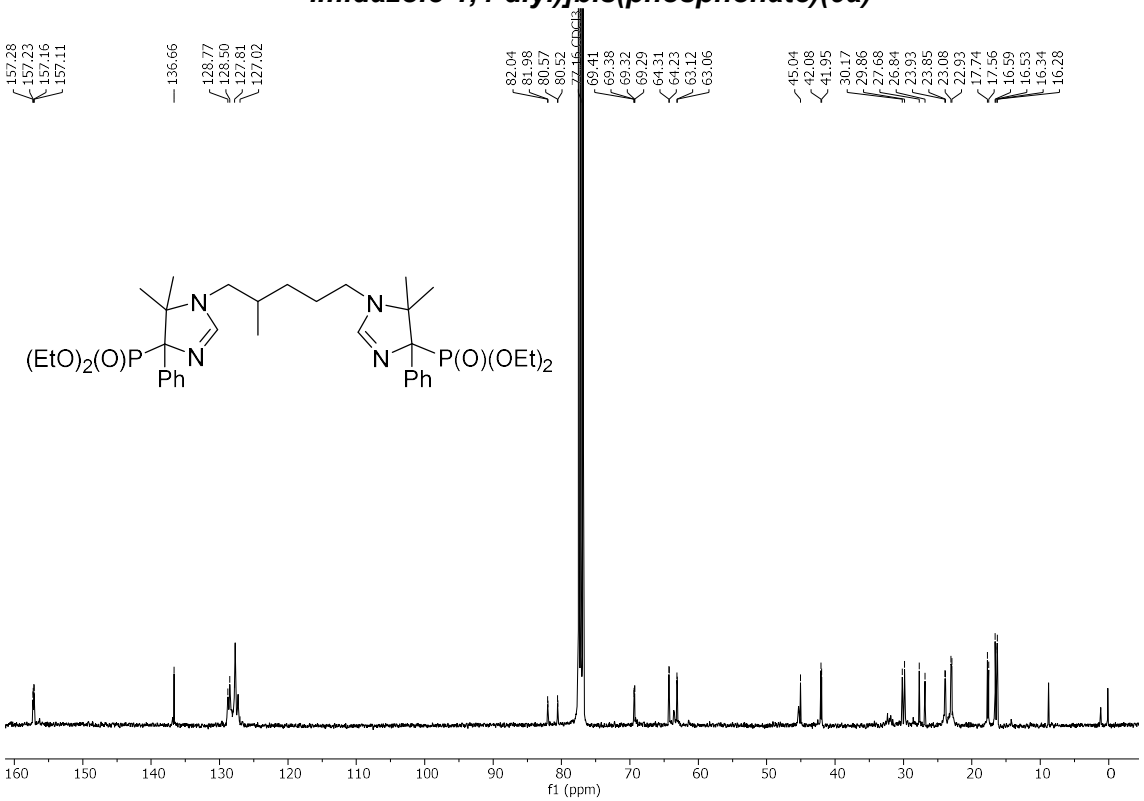

Tetraethyl [4-methylpentane-1,5-diylbis(5,5-dimethyl-4-phenyl-4,5-dihydro-1H-imidazole-1,4-diyl)]bis(phosphonate)(9a)

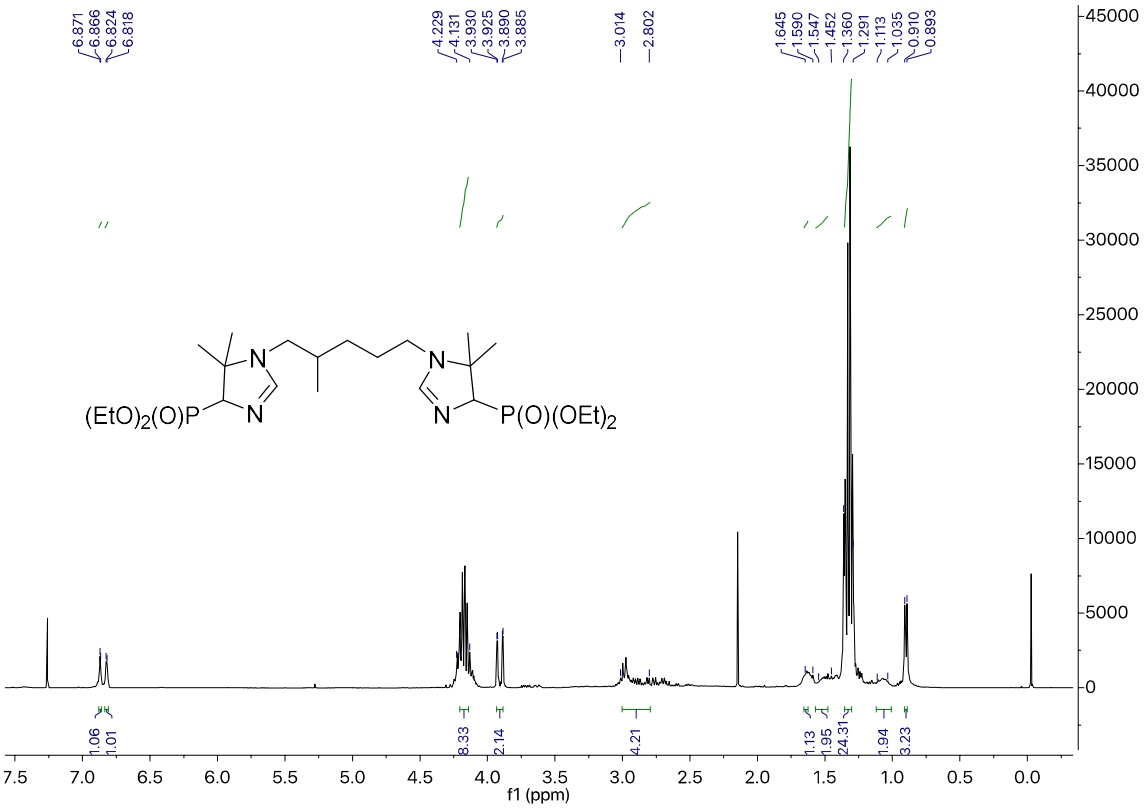

tetraethyl [4-methylpentane-1,5-diylbis(5,5-dimethyl-4,5-dihydro-1H-imidazole-1,4-diyl)]bis(phosphonate) (9b)

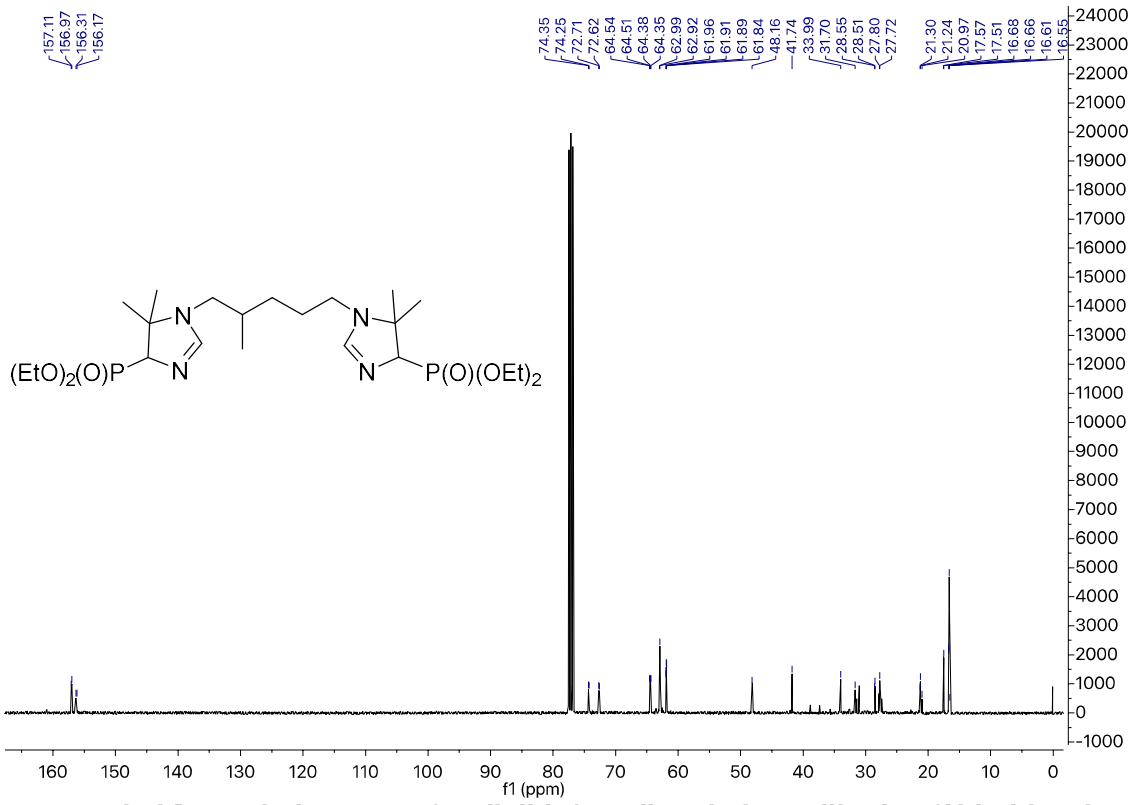

tetraethyl [4-methylpentane-1,5-diylbis(5,5-dimethyl-4,5-dihydro-1H-imidazole-1,4-diyl)]bis(phosphonate) (9b)

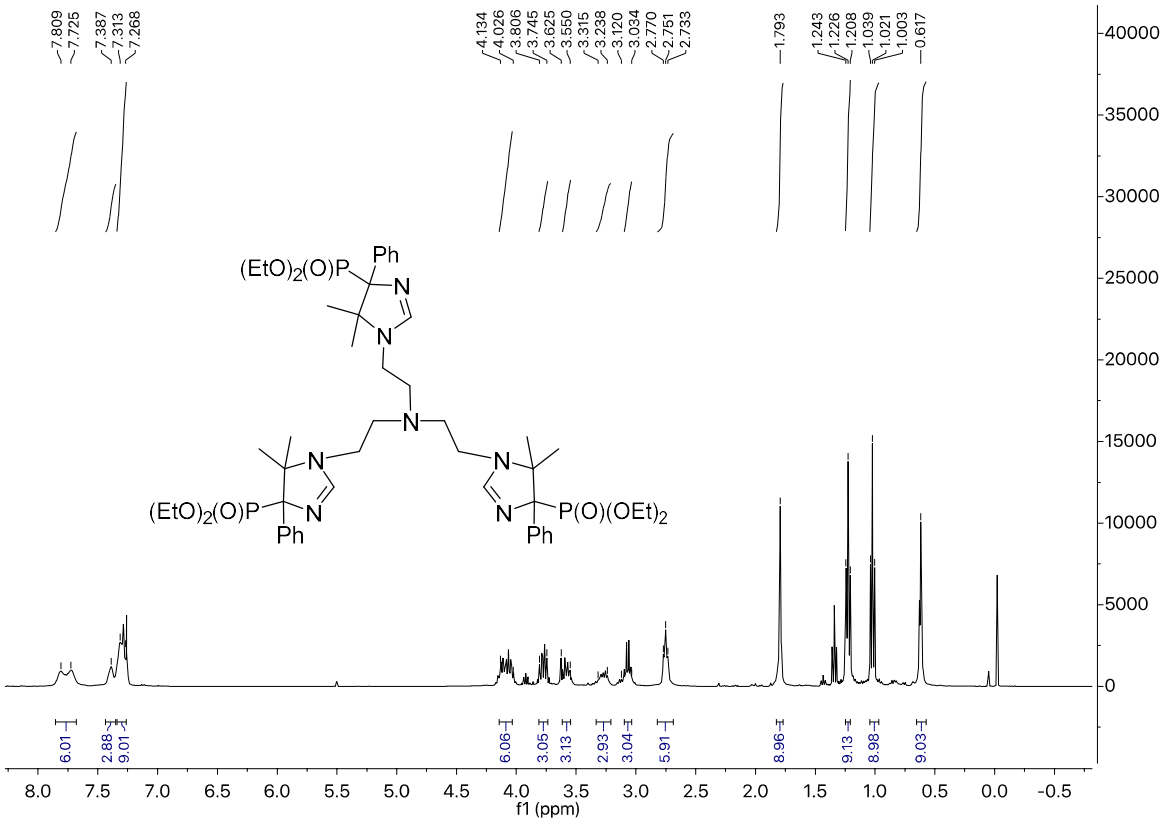

Hexaethyl [(nitrilotris(ethane-2,1-diyl))tris(5,5-dimethyl-4-phenyl-4,5-dihydro-1H-imidazole-1,4-diyl)]tris(phosphonate) (10)

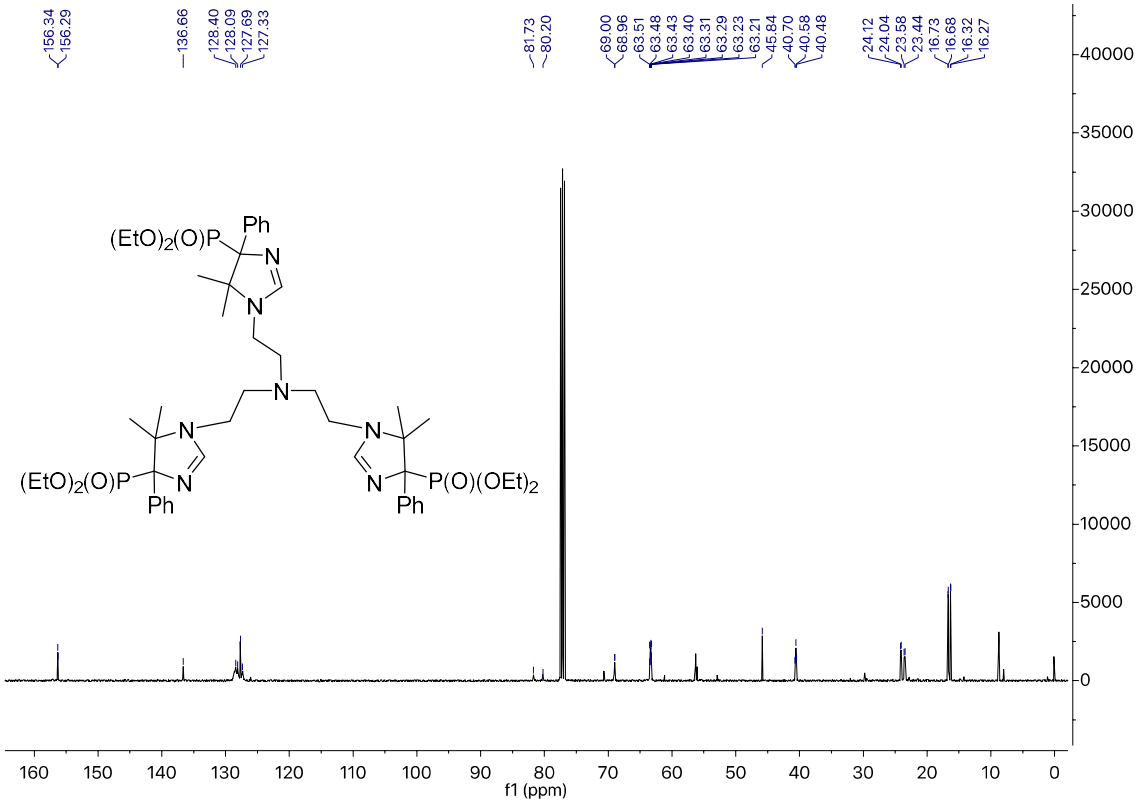

Hexaethyl [(nitrilotris(ethane-2,1-diyl))tris(5,5-dimethyl-4-phenyl-4,5-dihydro-1H-imidazole-1,4-diyl)]tris(phosphonate) (10)

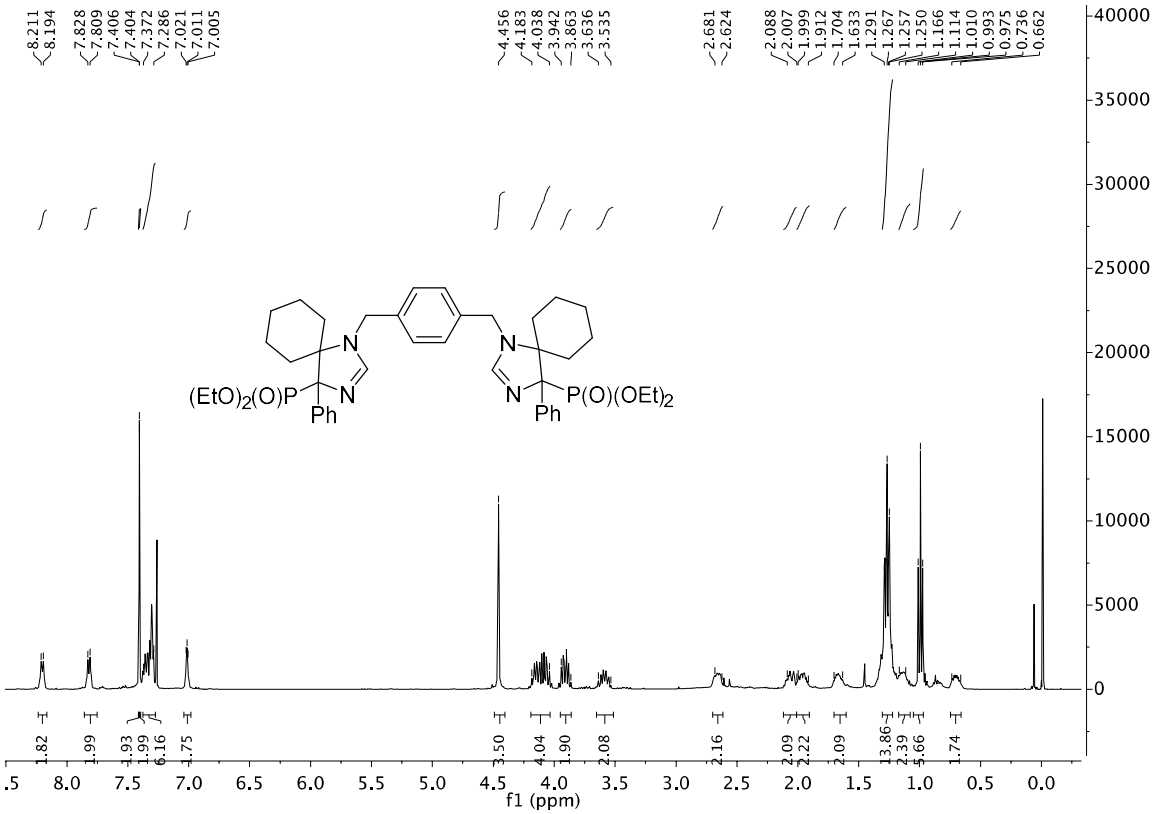

Tetraethyl [(1,4-phenylenebis(methylene))bis(4-phenyl-1,3-diazaspiro[4.5]dec-2-ene-1,4-diyl)]bis(phosphonate) (11a)

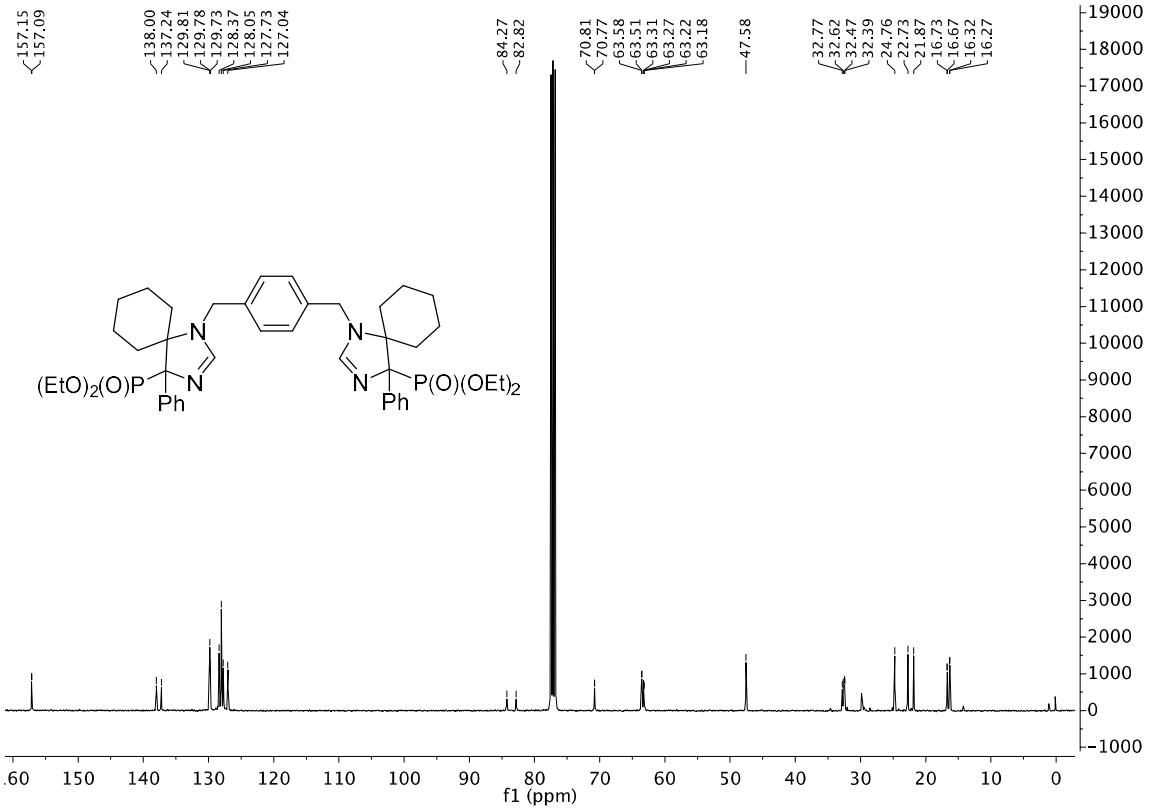

Tetraethyl [(1,4-phenylenebis(methylene))bis(4-phenyl-1,3-diazaspiro[4.5]dec-2-ene-1,4-diyl)]bis(phosphonate) (11a)

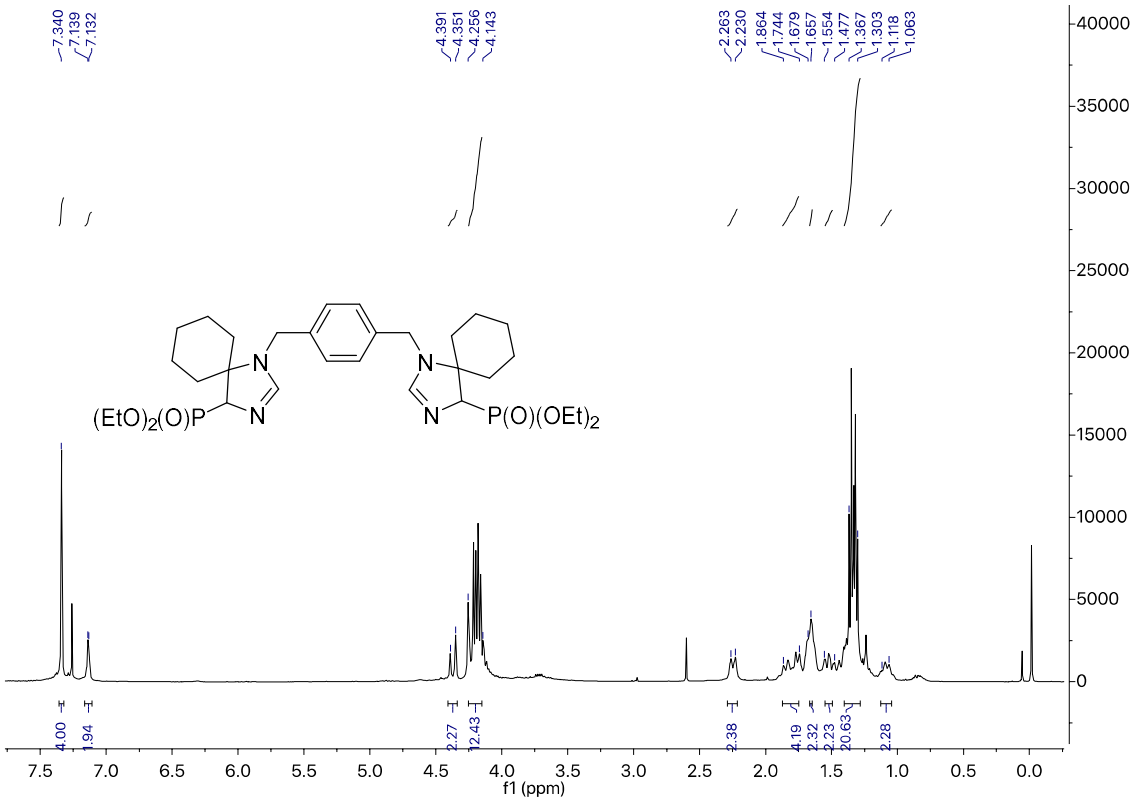

Tetraethyl [(1,4-phenylenebis(methylene))bis(1,3-diazaspiro[4.5]dec-2-ene-1,4-diyl)]bis(phosphonate) (11b)

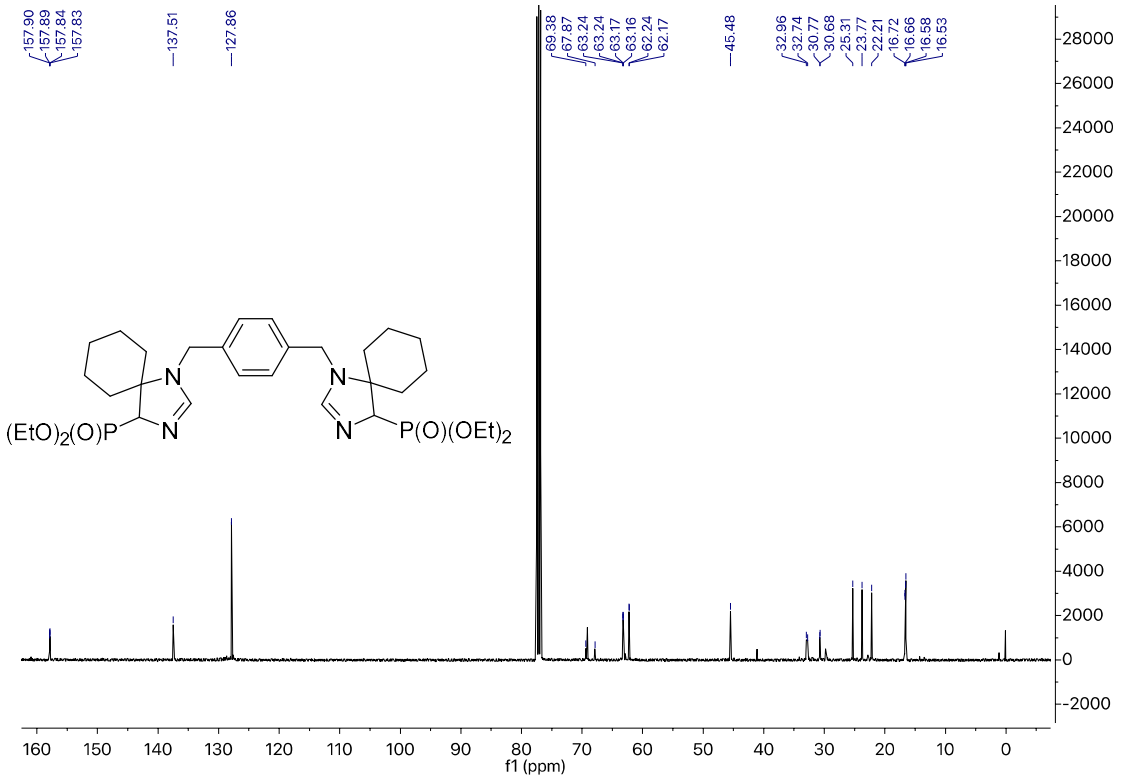

Tetraethyl [(1,4-phenylenebis(methylene))bis(1,3-diazaspiro[4.5]dec-2-ene-1,4-diyl)]bis(phosphonate) (11b)

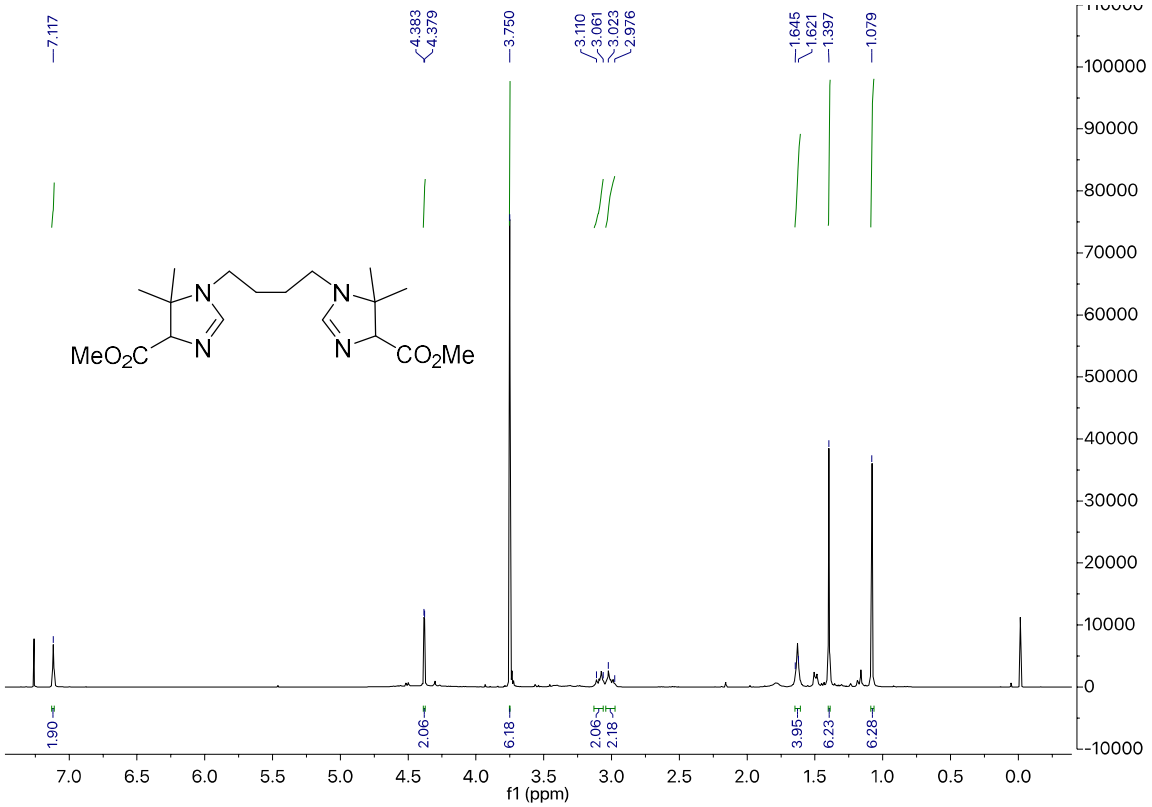

Dimethyl (butane-1,4-diyl)bis(5,5-dimethyl-4,5-dihydro-1H-imidazole-4-carboxylate) (12-Diast A)

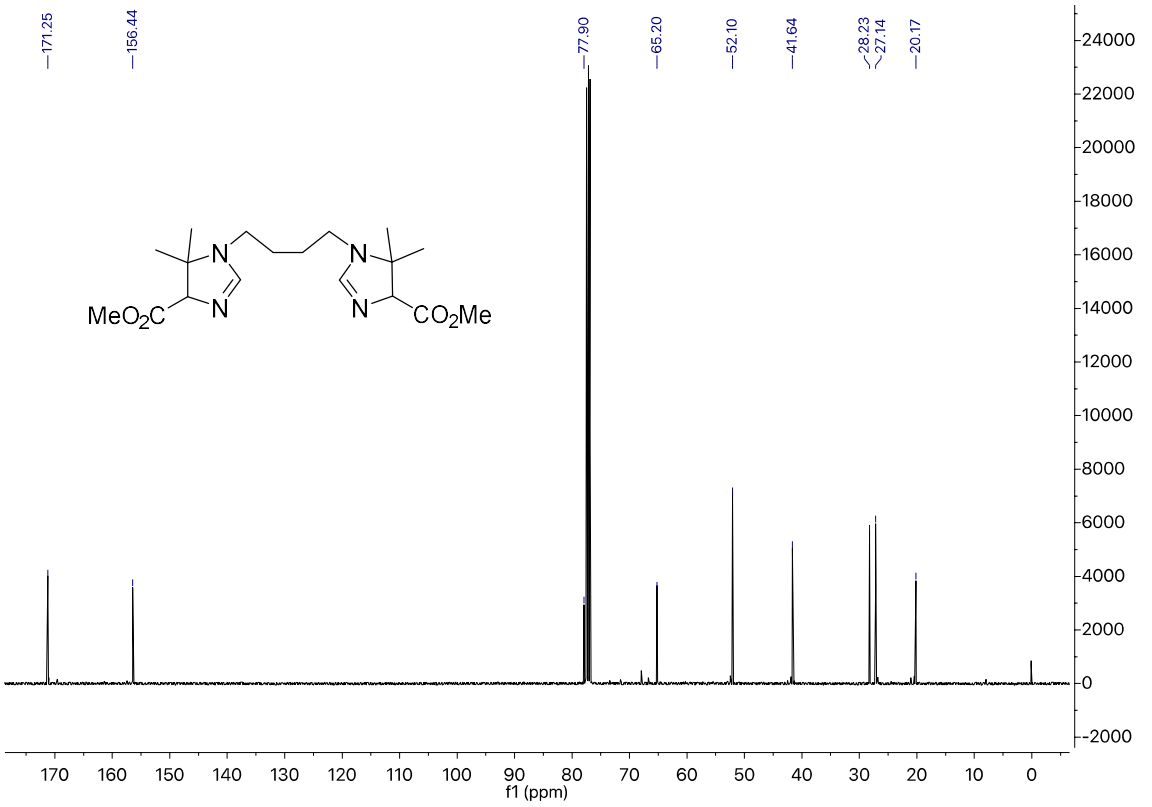

Dimethyl (butane-1,4-diyl)bis(5,5-dimethyl-4,5-dihydro-1H-imidazole-4-carboxylate) (12-Diast A)

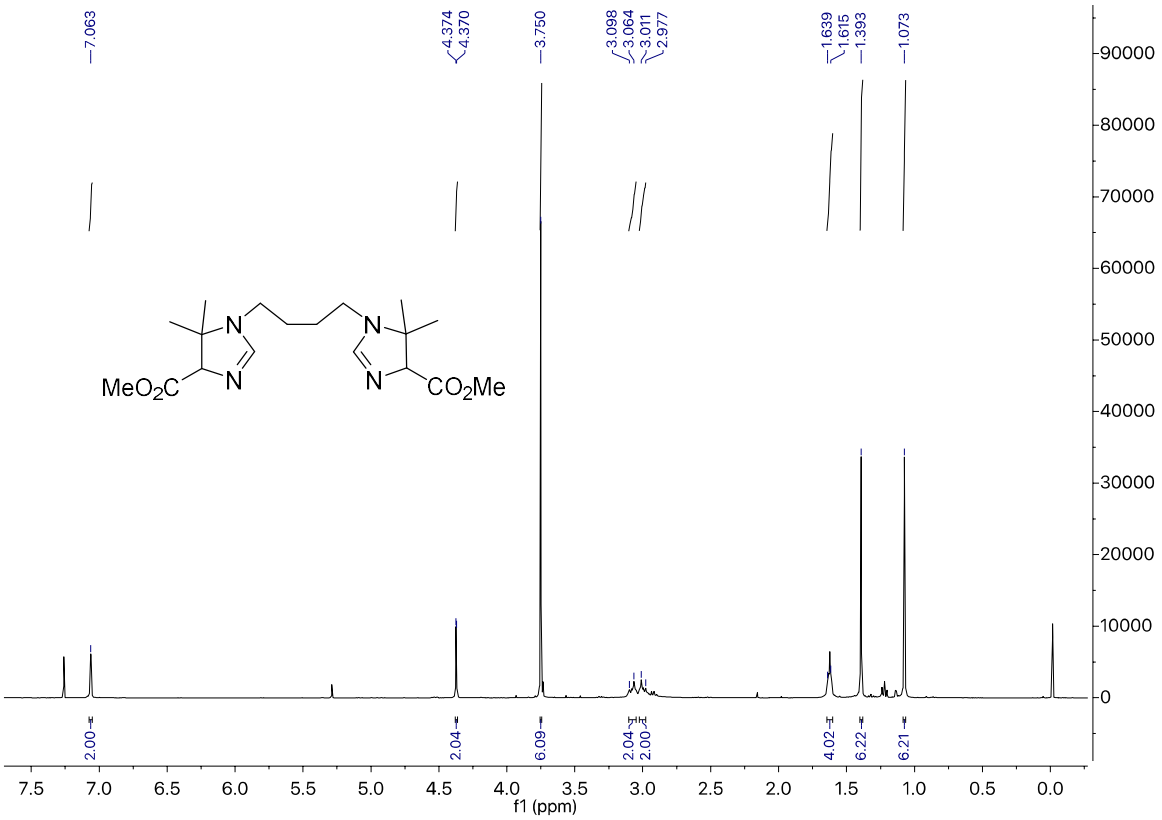

Dimethyl (butane-1,4-diyl)bis(5,5-dimethyl-4,5-dihydro-1H-imidazole-4-carboxylate) (12-Diast B)

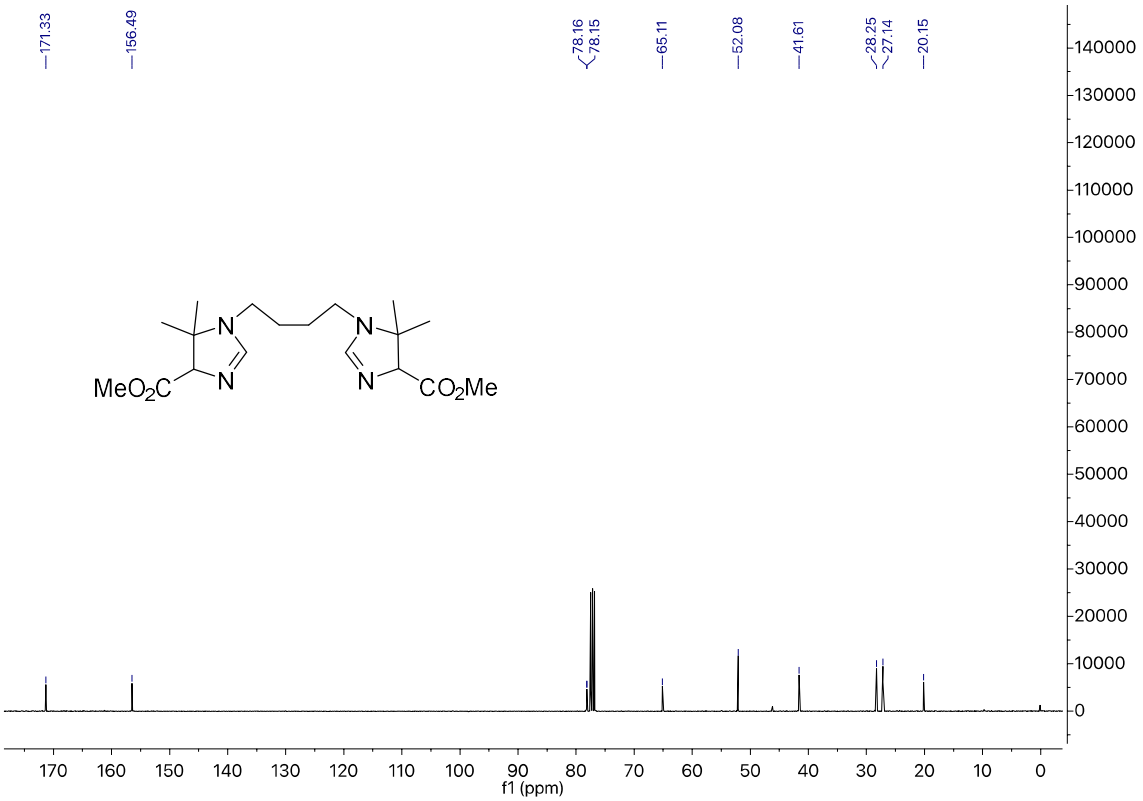

Dimethyl (butane-1,4-diyl)bis(5,5-dimethyl-4,5-dihydro-1H-imidazole-4-carboxylate) (12-Diast B)

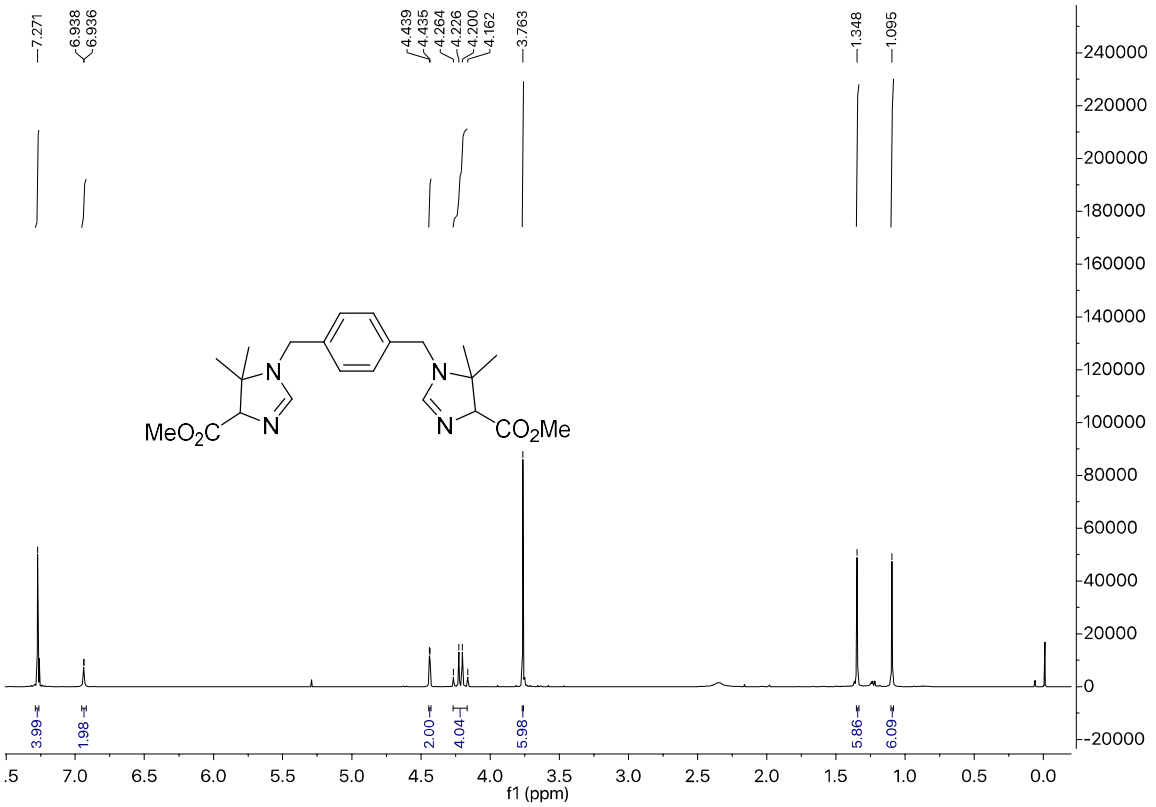

Dimethyl [1,4-phenylenebis(methylene)]bis(5,5-dimethyl-4,5-dihydro-1H-imidazole-4-carboxylate) (13-Diast A)

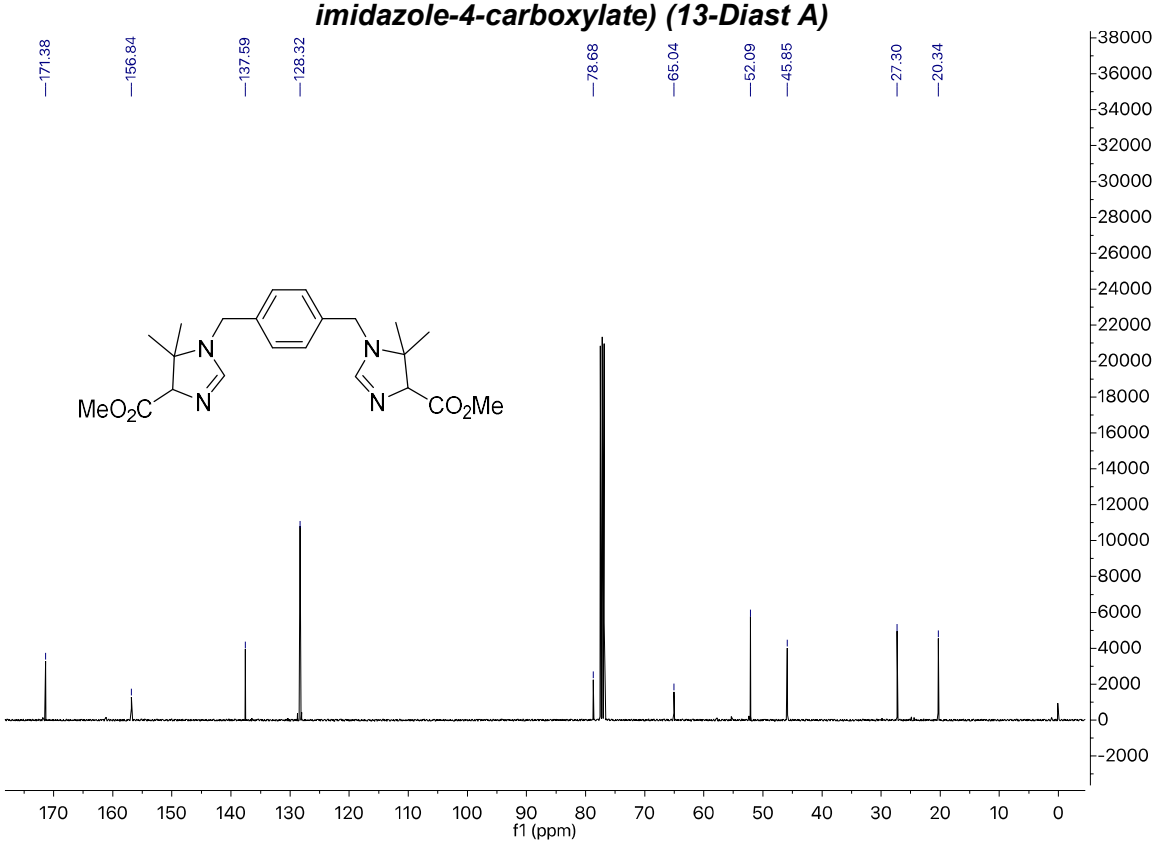

Dimethyl [1,4-phenylenebis(methylene)]bis(5,5-dimethyl-4,5-dihydro-1H-imidazole-4-carboxylate) (13-Diast A)

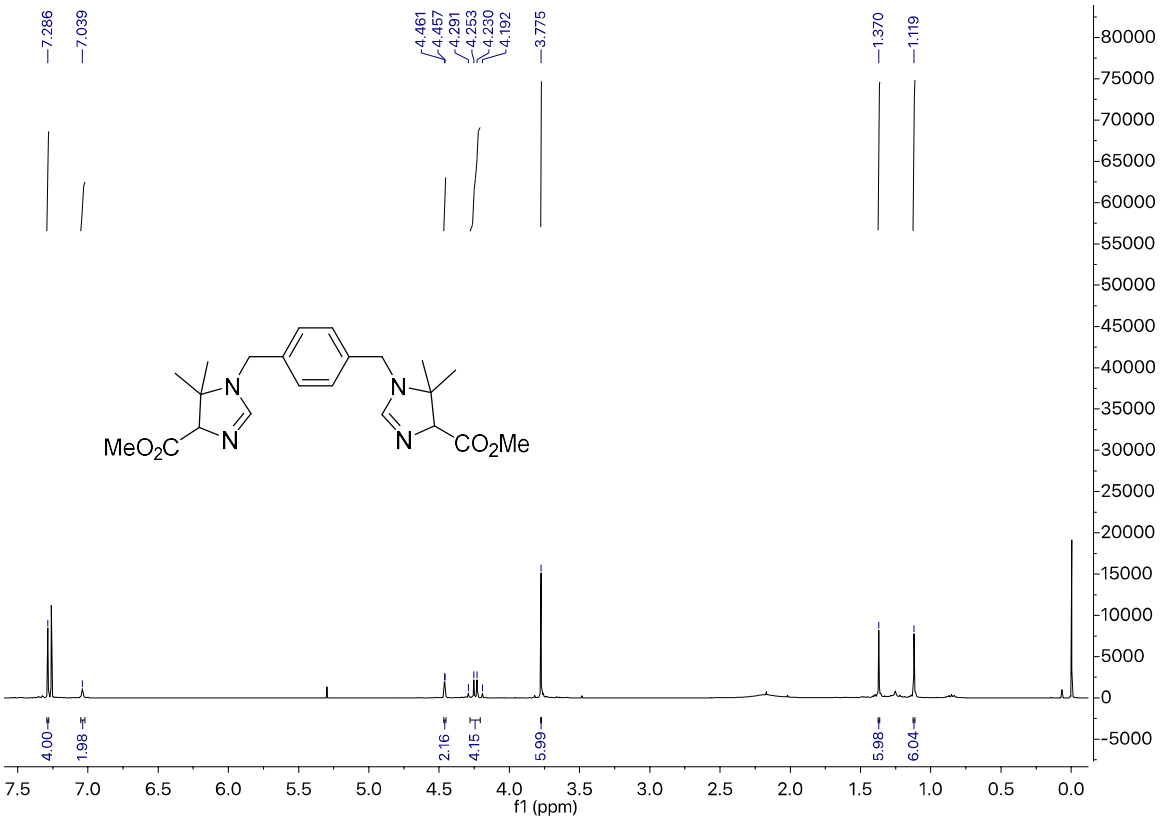

Dimethyl [1,4-phenylenebis(methylene)]bis(5,5-dimethyl-4,5-dihydro-1H-imidazole-4-carboxylate) (13-Diast B)

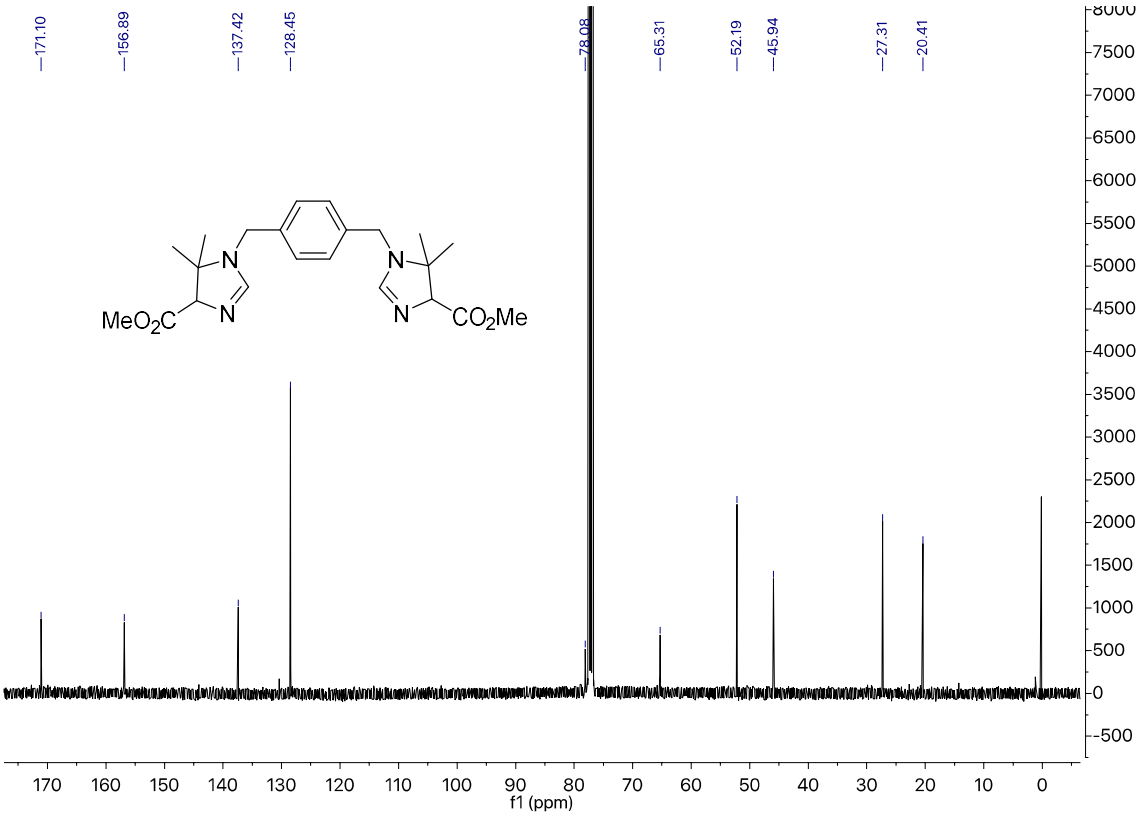

Dimethyl [1,4-phenylenebis(methylene)]bis(5,5-dimethyl-4,5-dihydro-1H-imidazole-4-carboxylate) (13-Diast B)

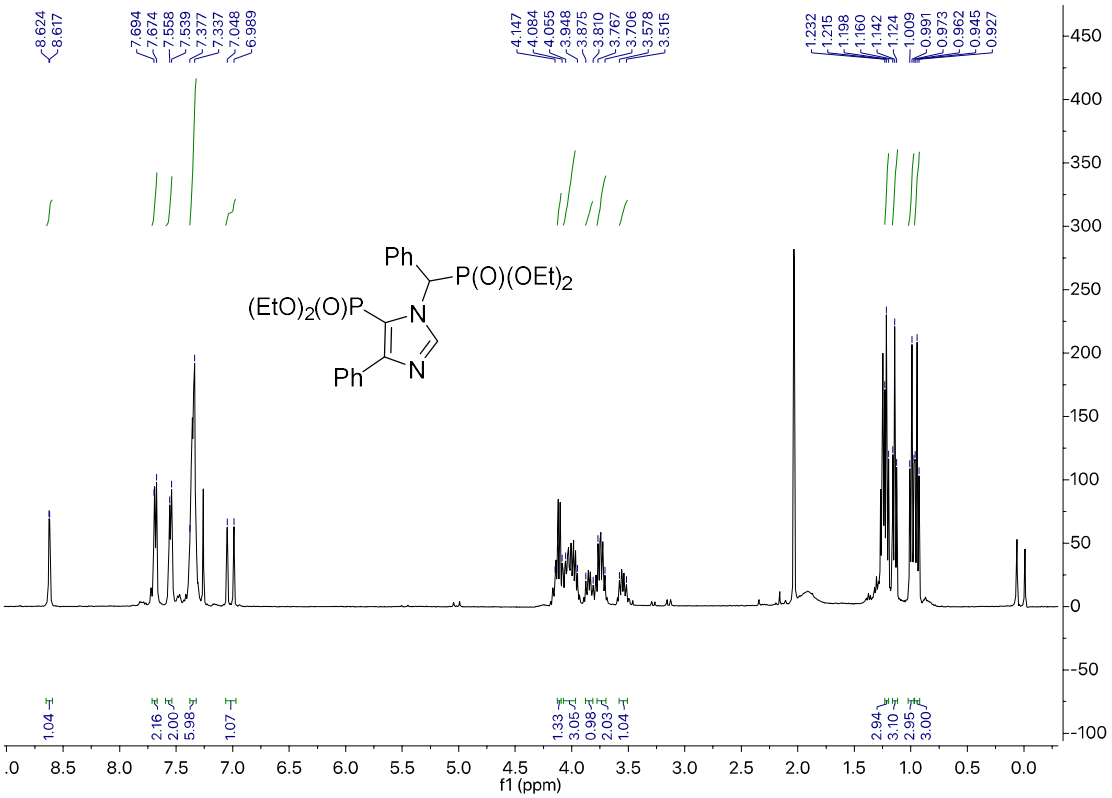

Diethyl {[5-(diethoxyphosphoryl)-4-phenyl-1H-imidazol-1-yl)](phenyl)methyl}phosphonate (A)

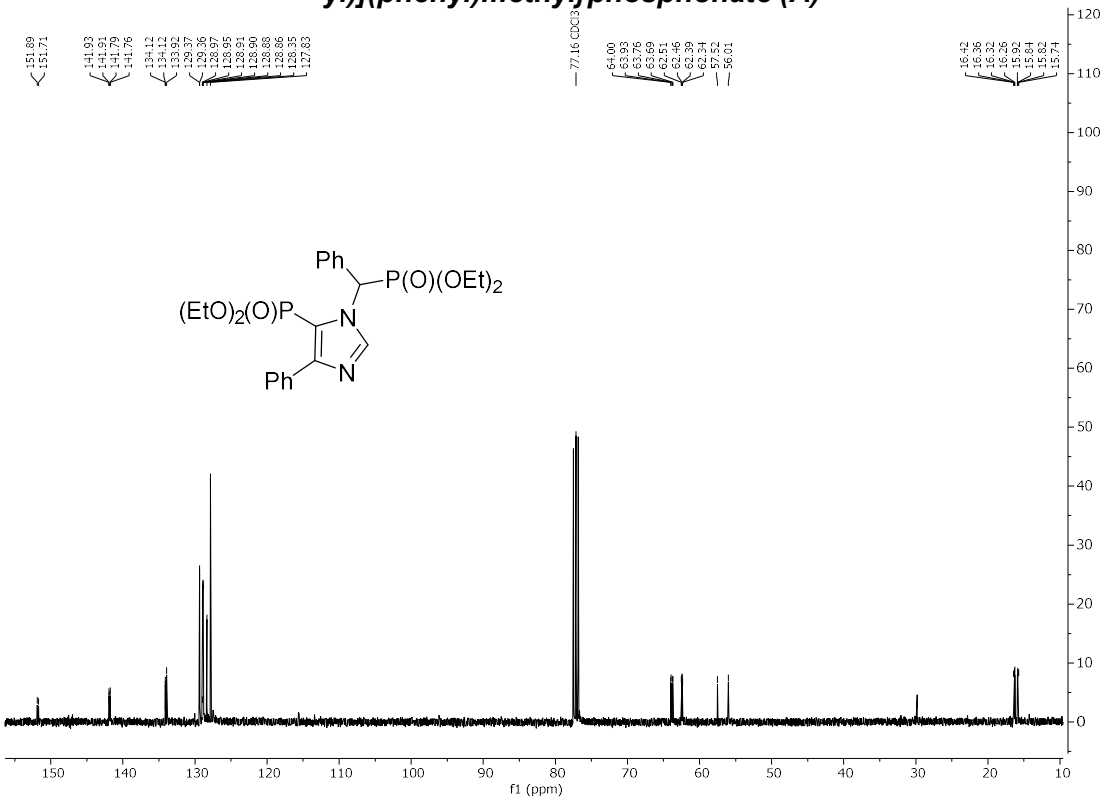

Diethyl {[5-(diethoxyphosphoryl)-4-phenyl-1H-imidazol-1-yl)](phenyl)methyl}phosphonate (A)

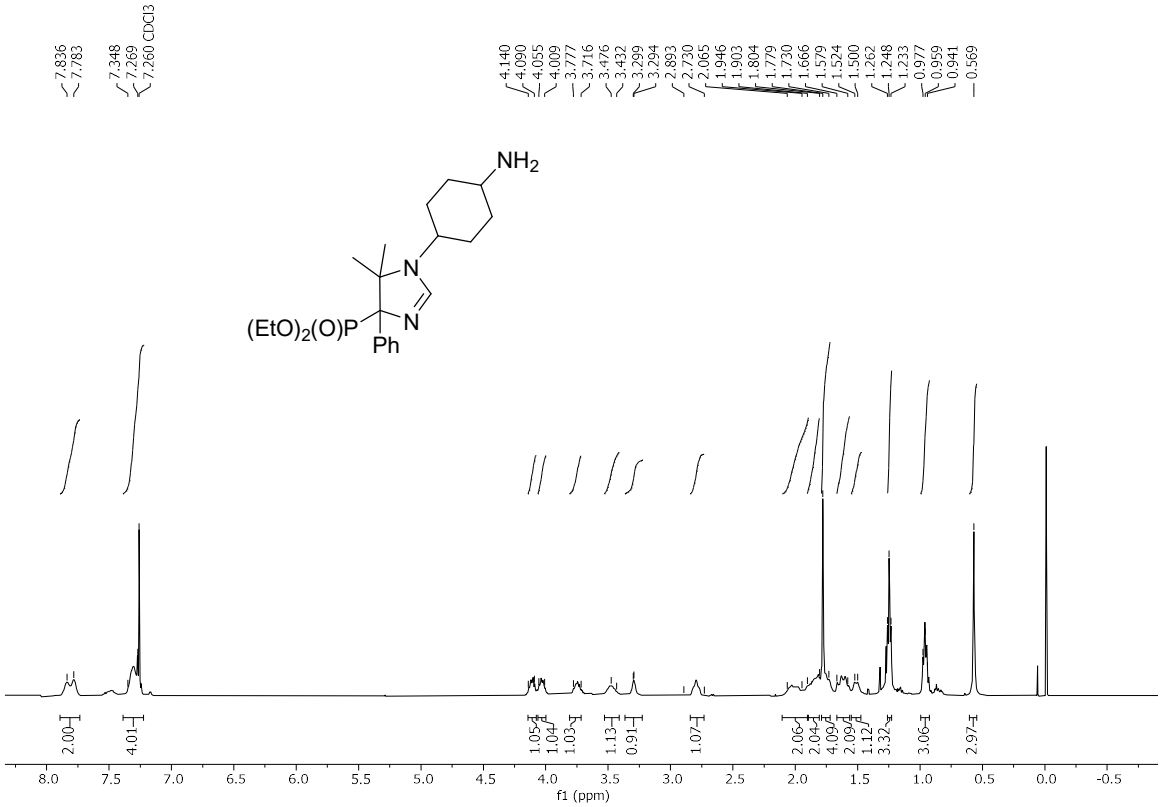

Diethyl [1-(4-aminocyclohexyl)-5,5-dimethyl-4-phenyl-4,5-dihydro-1H-imidazol-4-yl]phosphonate (Ia)

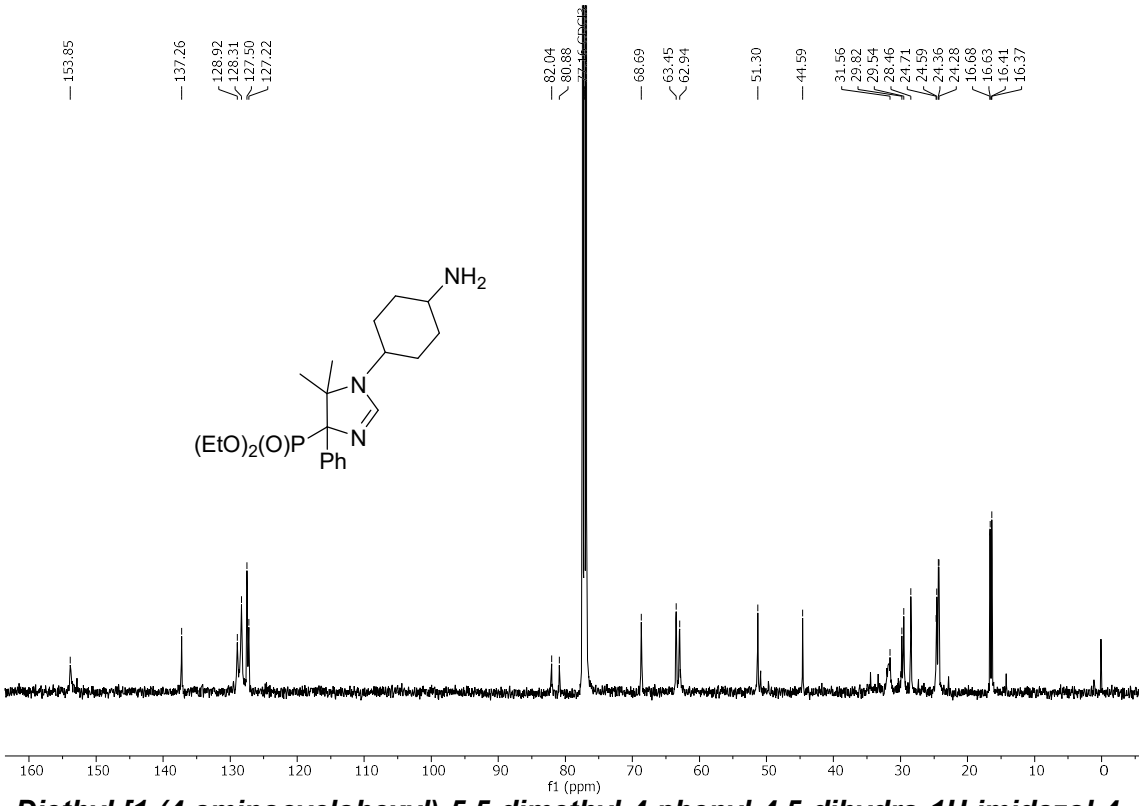

Diethyl [1-(4-aminocyclohexyl)-5,5-dimethyl-4-phenyl-4,5-dihydro-1H-imidazol-4-yl]phosphonate (Ia)

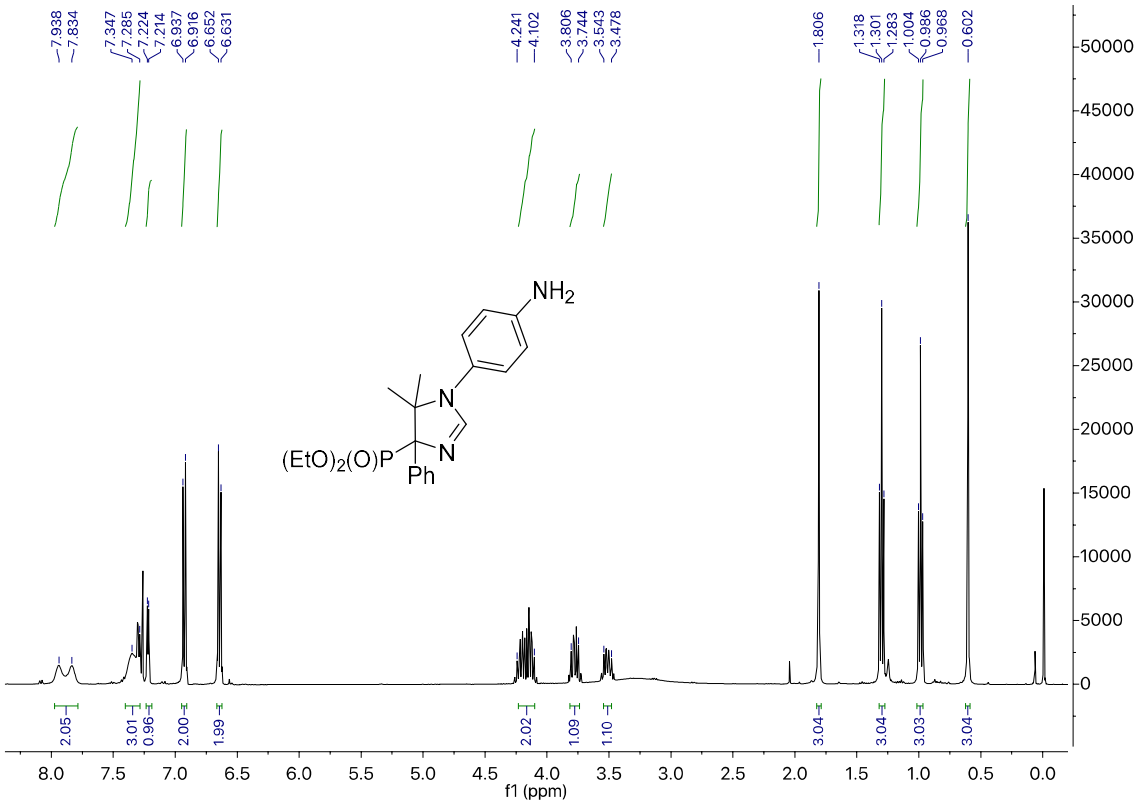

Diethyl [1-(4-aminophenyl)-5,5-dimethyl-4-phenyl-4,5-dihydro-1H-imidazol-4-yl]phosphonate (II)

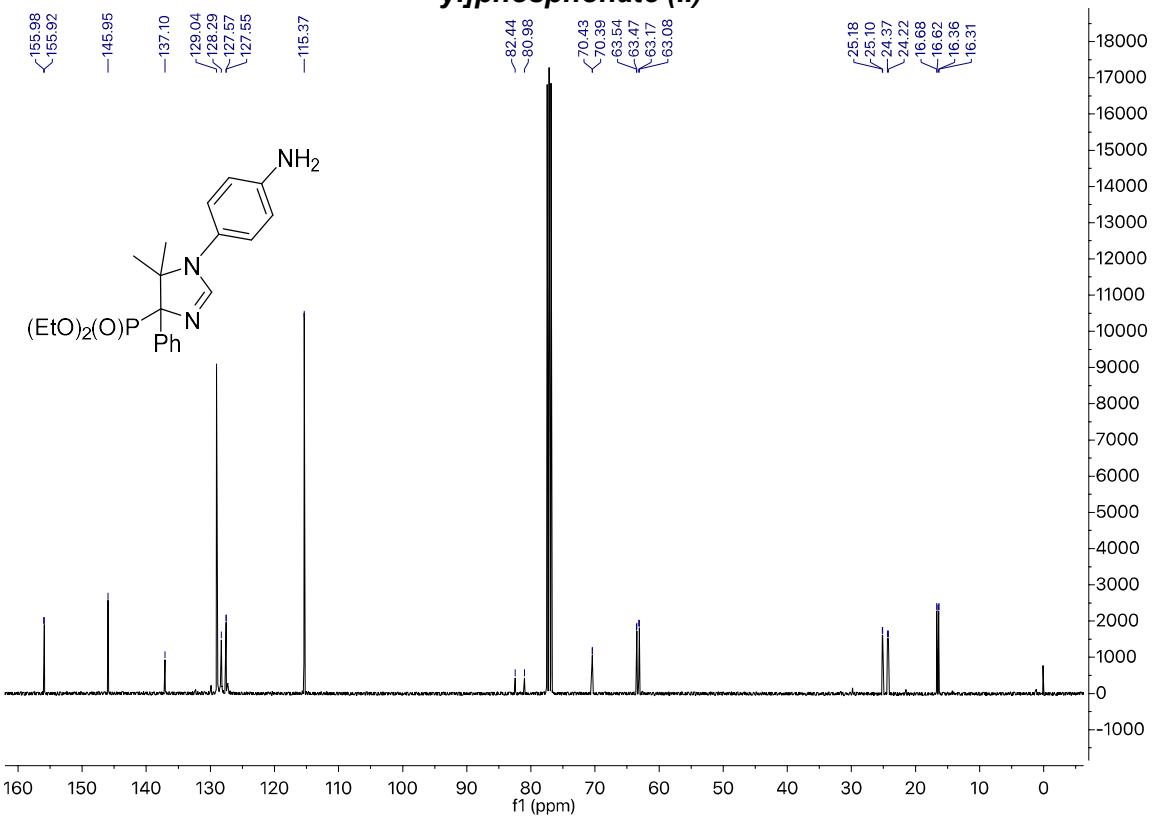

Diethyl [1-(4-aminophenyl)-5,5-dimethyl-4-phenyl-4,5-dihydro-1H-imidazol-4-yl]phosphonate (II)

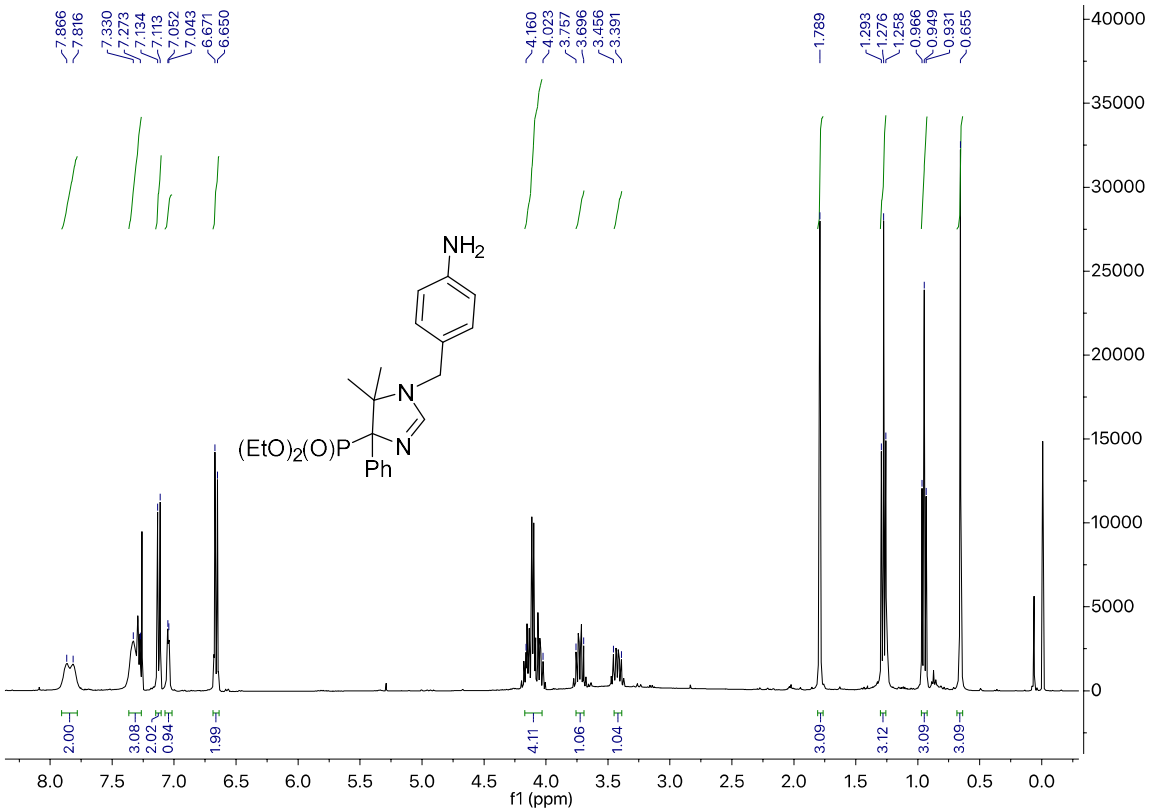

Diethyl [1-(4-aminobenzyl)-5,5-dimethyl-4-phenyl-4,5-dihydro-1H-imidazol-4-yl]phosphonate (III)

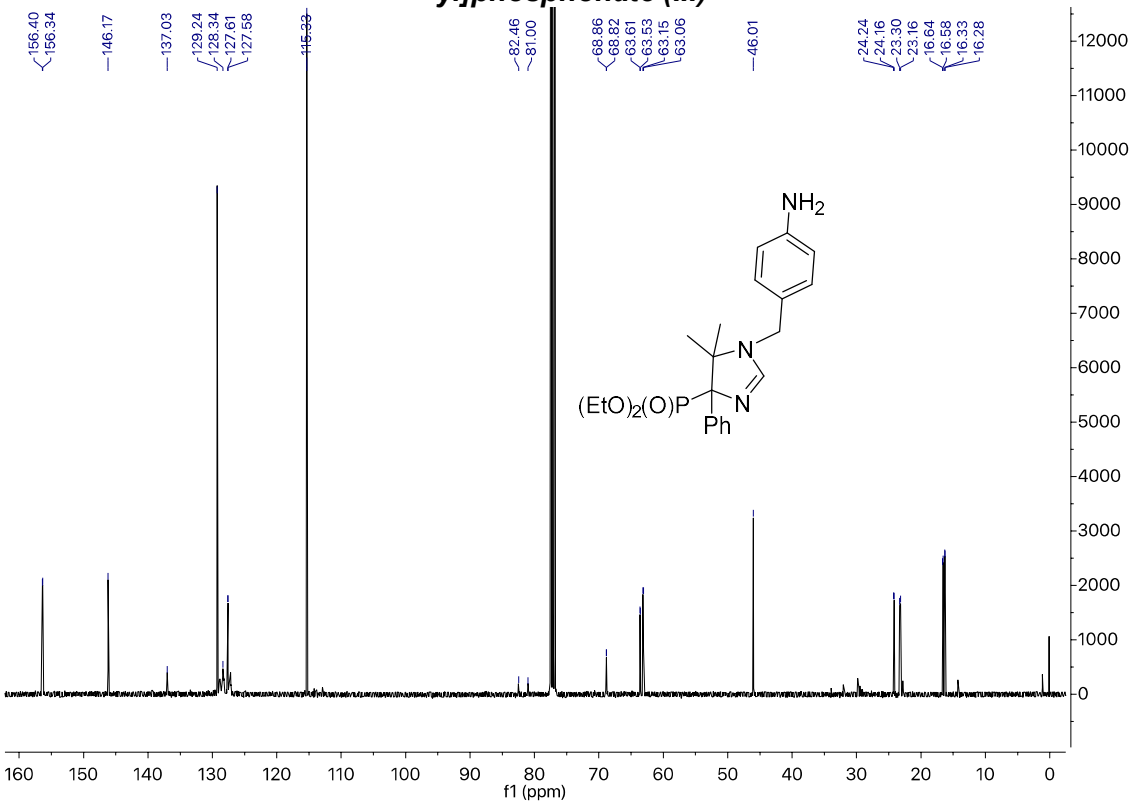

Diethyl [1-(4-aminobenzyl)-5,5-dimethyl-4-phenyl-4,5-dihydro-1H-imidazol-4-yl]phosphonate (III)

3. ^{1}H-NMR and HPLC-MS spectra of some reaction crudes

Tetraethyl [butane-1,4-diylbis(5,5-dimethyl-4-phenyl-4,5-dihydro-1H-imidazole-1,4-diyl)]bis(phosphonate) (1a)

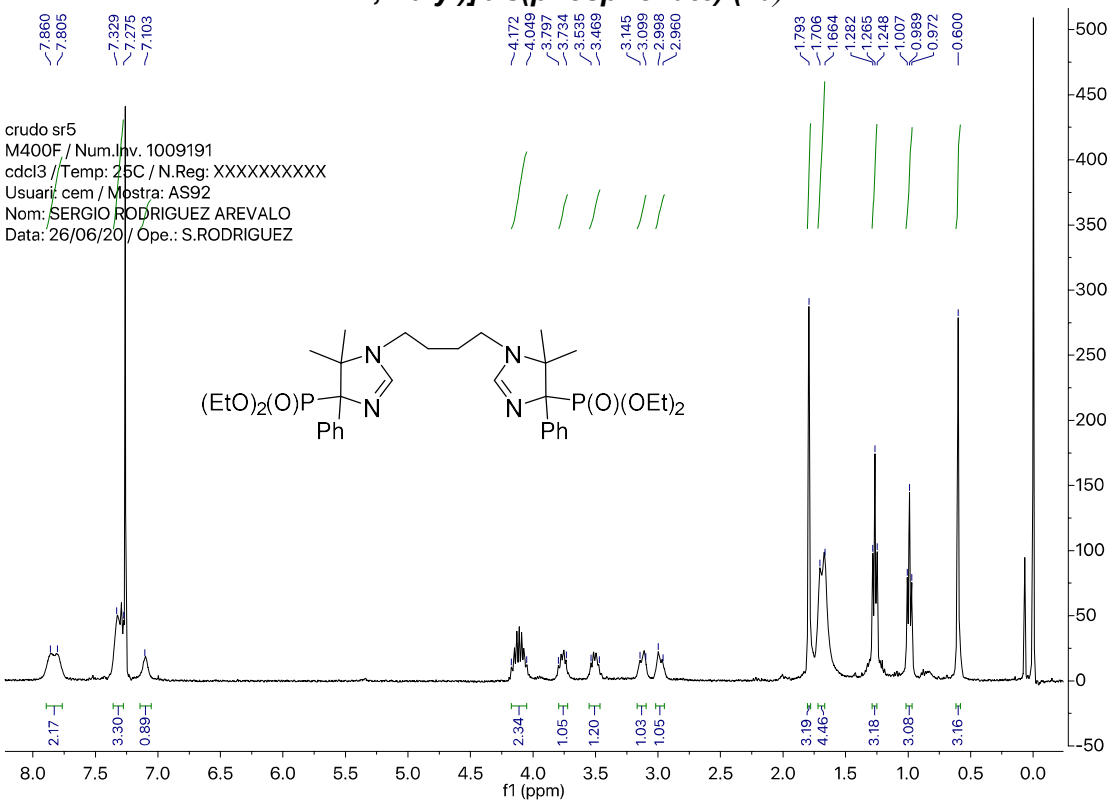

Diethyl (1-(5-(4-(diethoxyphosphoryl)-5,5-dimethyl-4,5-dihydro-1H-imidazol-1-yl)-2-methylpentyl)-5,5-dimethyl-4,5-dihydro-1H-imidazol-4-yl)phosphonate (9b)

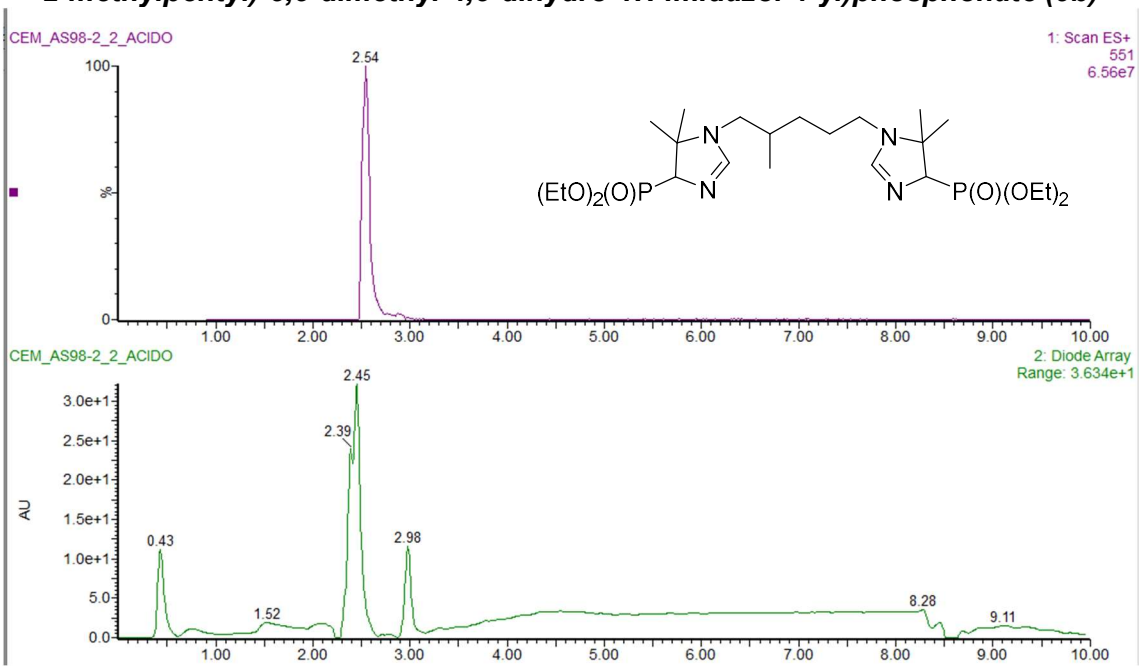

Dimethyl 1,1'-(1,4-phenylenebis(methylene))bis(5,5-dimethyl-4,5-dihydro-1H-imidazole-4-carboxylate) (13)

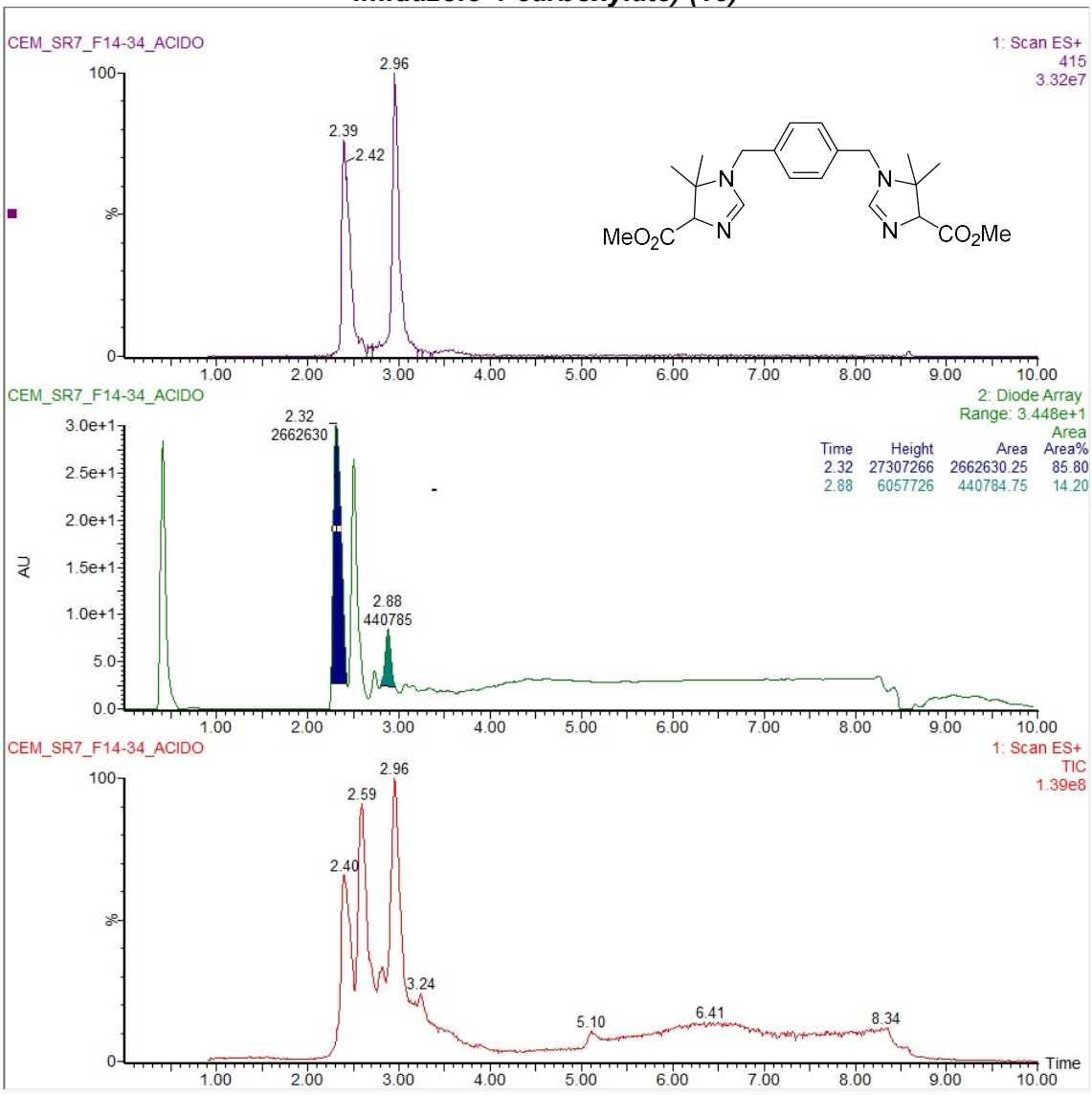

Comparative ^{1}H-NMR spectra of 12 at different reaction conditions

1) Optimized microwave irradiation conditions (20 min at 40 ºC), product **12** was isolated in a diastereomeric ratio of 8:1 (Diast A:Diast B).

2) Overnight at room temperature condition product **12** was isolated in a diastereomeric ratio of 1:1 (Diast A:Diast B).

3) Ultrasound irradiation conditions (10 min at 40 ºC) product **12** was isolated in a diastereomeric ratio of 1:2 (Diast A:Diast B).

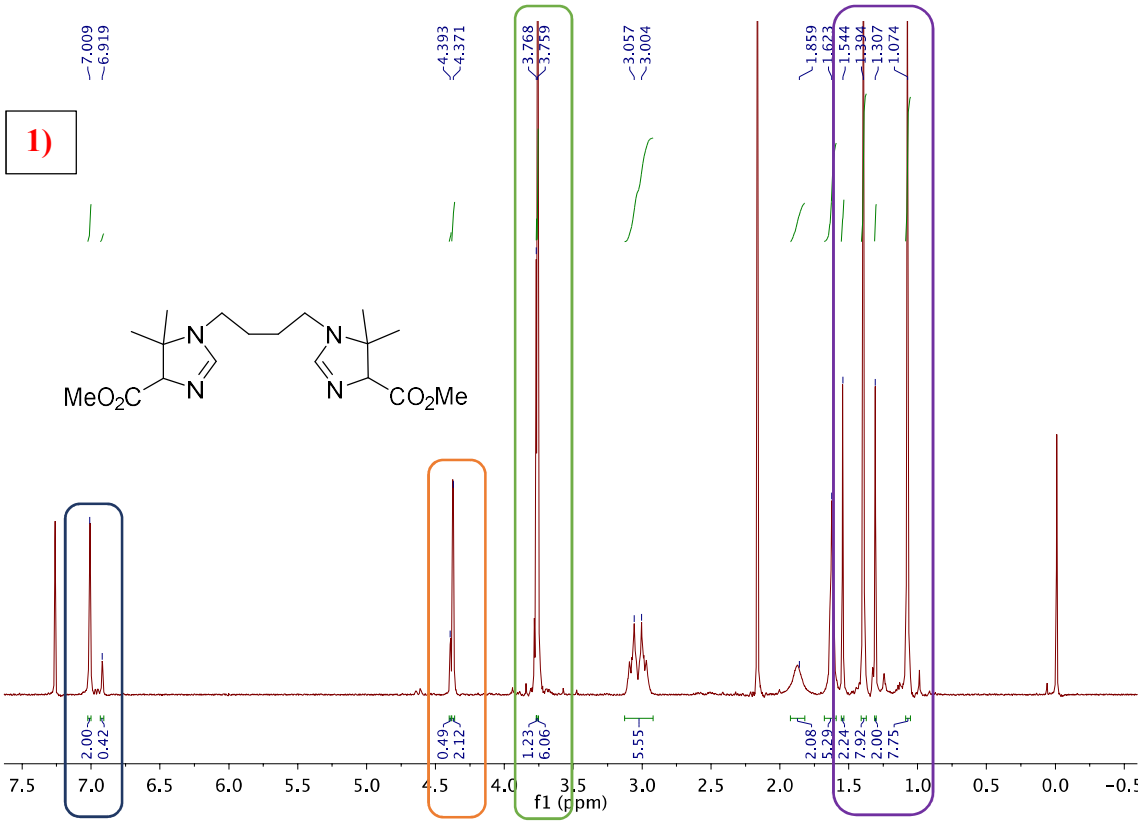

Dimethyl 1,1'-(butane-1,4-diyl)bis(5,5-dimethyl-4,5-dihydro-1H-imidazole-4-carboxylate) (12)

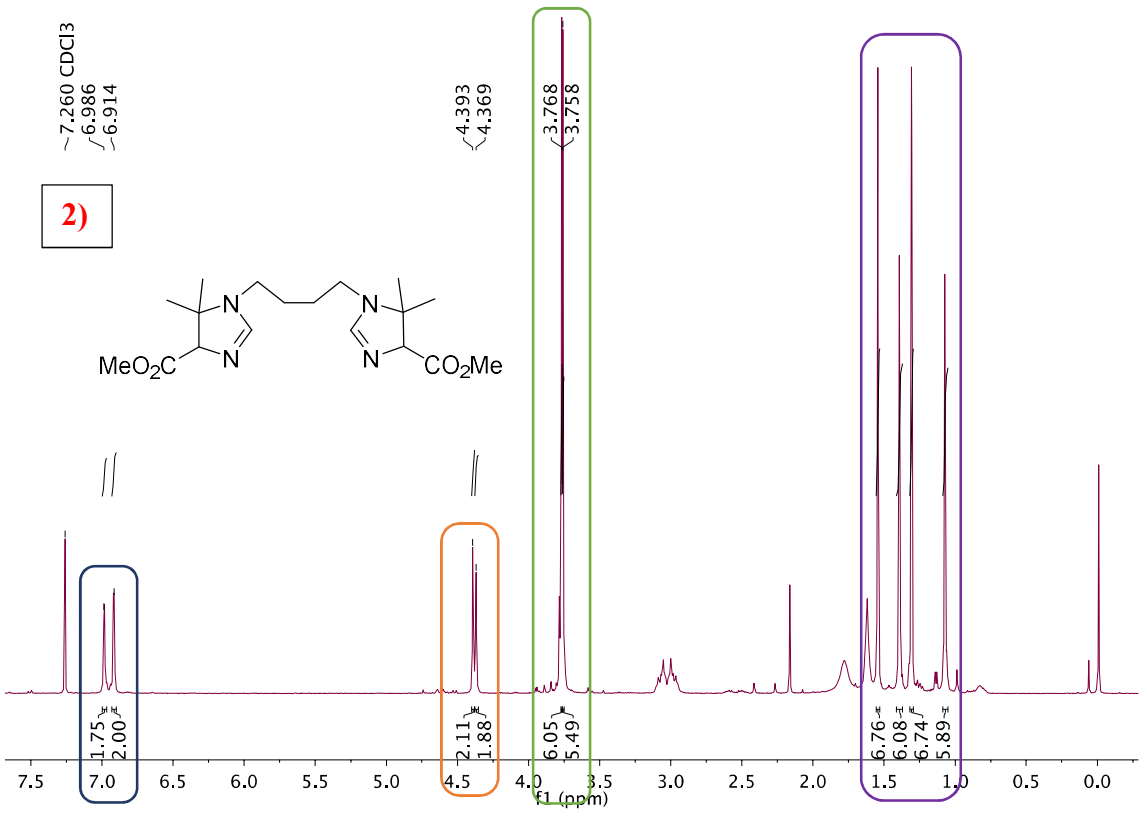

Dimethyl 1,1'-(butane-1,4-diyl)bis(5,5-dimethyl-4,5-dihydro-1H-imidazole-4-carboxylate) (12)

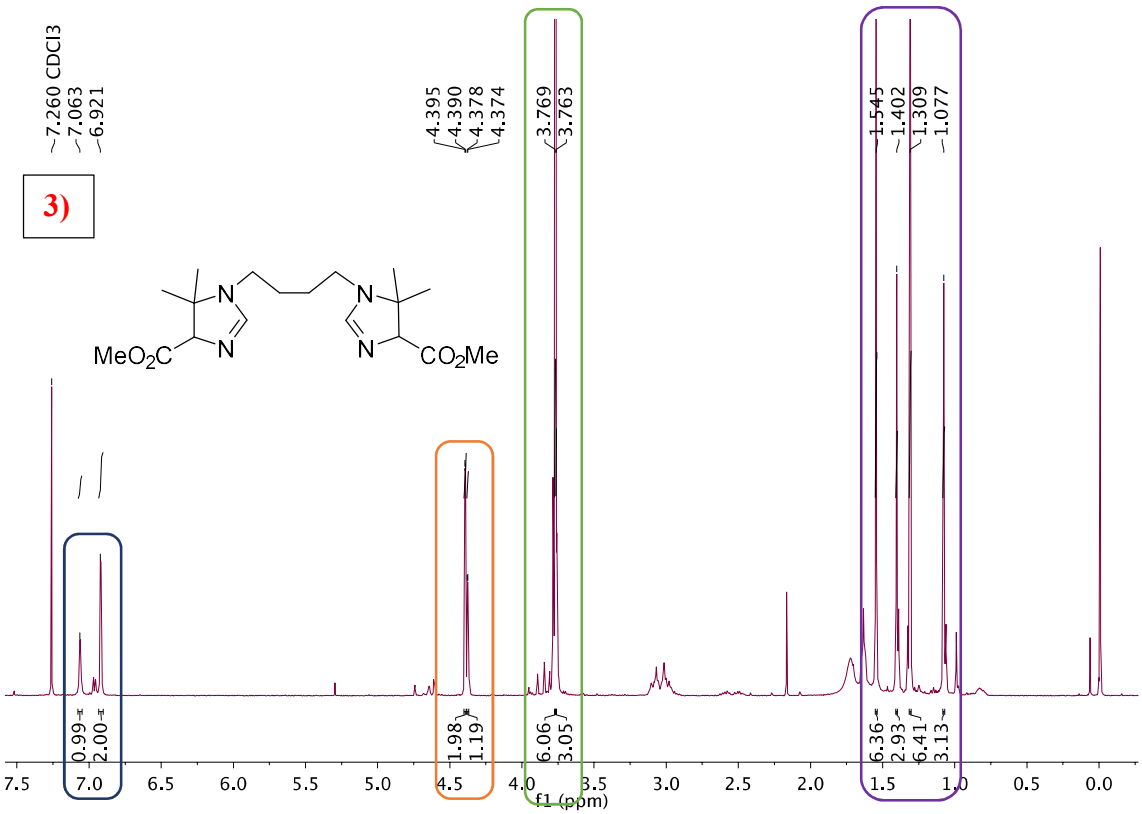

Dimethyl 1,1'-(butane-1,4-diyl)bis(5,5-dimethyl-4,5-dihydro-1H-imidazole-4-carboxylate) (12)

5. X-ray crystallographic data for 1a

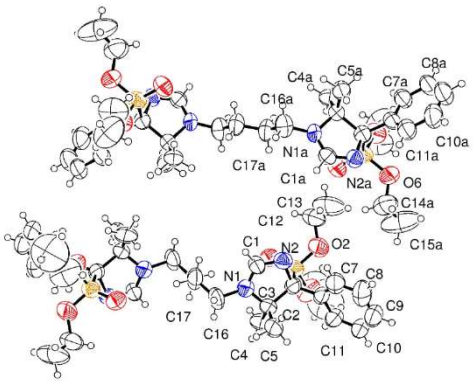

Table 1. Crystal data and structure refinement for **1a**.

Identification code	Jb142h	
Empirical formula	$C_{34}H_{58}N_4O_9P_2$	
Formula weight	728.78	
Temperature	294(2) K	
Wavelength	0.71073 Å	
Crystal system	Triclinic	
Space group	P -1	
Unit cell dimensions	a = 9.433(7) Å	α= 93.566(5)°
	b = 13.827(9) Å	β= 98.615(6)°
	c = 15.541(11) Å	γ = 92.072(6)°
Volume	1998(2) $Å^3$	
Z	2	
Density (calculated)	1.211 Mg/m^3	
Absorption coefficient	0.162 mm^{-1}	
F(000)	784	
Crystal size	0.280 x 0.140 x 0.110 mm^3	
Theta range for data collection	1.328 to 28.681°	
Index ranges	-8<=h<=12, -18<=k<=18, -20<=l<=17	
Reflections collected	16438	
Independent reflections	9949 [R(int) = 0.0866]	
Completeness to theta = 25.242°	100.0 %	
Refinement method	Full-matrix least-squares on F^2	
Data / restraints / parameters	9949 / 11 / 468	
Goodness-of-fit on F^2	0.744	
Final R indices [I>2sigma(I)]	R1 = 0.0739, wR2 = 0.1715	
R indices (all data)	R1 = 0.3308, wR2 = 0.2580	
Largest diff. peak and hole	0.340 and -0.237 $e.Å^{-3}$	

Table 2. Atomic coordinates (x 10^4) and equivalent isotropic displacement parameters ($Å^2$x 10^3)for **1a**. U(eq) is defined as one third of the trace of the orthogonalized U^{ij} tensor.

	x	y	z	U(eq)
P(1)	6606(2)	9536(1)	7148(1)	75(1)
P(2)	1335(2)	5761(1)	7021(1)	73(1)
O(1)	7961(5)	9127(3)	7494(3)	84(1)
O(2)	5424(6)	8780(4)	6660(3)	109(2)
O(3)	6700(6)	10262(4)	6408(3)	115(2)
O(4)	2768(5)	6167(3)	7383(3)	83(1)
O(5)	1338(5)	4926(3)	6295(3)	92(2)
O(6)	307(5)	6496(4)	6527(3)	90(2)
O(7)	3978(7)	7574(4)	8791(3)	111(2)
O(8)	1273(7)	2185(4)	1202(3)	110(2)
O(9)	3188(9)	2671(5)	111(4)	157(3)
N(1)	7305(6)	10370(4)	9236(3)	79(2)
N(1A)	1899(6)	5286(4)	9088(3)	67(2)
N(2)	5460(6)	9410(4)	8525(4)	81(2)
N(2A)	218(6)	6166(4)	8375(3)	69(2)
C(1)	6423(8)	9576(5)	9197(4)	73(2)
C(1A)	1196(8)	6098(5)	9026(4)	67(2)
C(2)	5711(8)	10231(5)	7928(4)	73(2)
C(2A)	296(7)	5253(5)	7813(4)	64(2)
C(3)	6704(8)	10979(5)	8578(4)	72(2)
C(3A)	1156(7)	4550(4)	8438(4)	62(2)
C(4)	7908(8)	11455(5)	8144(5)	97(3)
C(4A)	2158(7)	3878(4)	8036(4)	82(2)
C(5)	5806(8)	11742(5)	8970(4)	97(3)
C(5A)	140(7)	3942(5)	8900(4)	90(2)
C(6)	4298(9)	10585(5)	7506(4)	73(2)
C(6A)	-1205(9)	4854(5)	7403(4)	71(2)
C(7)	3012(11)	10203(6)	7665(5)	99(3)
C(7A)	-1341(9)	4021(5)	6825(4)	87(2)
C(8)	1737(10)	10564(9)	7284(6)	124(3)
C(8A)	-2681(12)	3617(7)	6505(6)	119(3)
C(9)	1735(14)	11300(8)	6750(7)	129(4)

C(9A)	-3863(13)	4028(8)	6739(7)	132(4)
C(10)	2985(13)	11701(7)	6576(6)	113(3)
C(10A)	-3761(10)	4856(8)	7280(6)	122(3)
C(11)	4256(9)	11326(5)	6950(5)	89(2)
C(11A)	-2419(10)	5270(6)	7632(5)	93(2)
C(12)	5434(10)	7738(6)	6780(5)	118(3)
C(12A)	2063(11)	5109(7)	5558(6)	142(4)
C(13)	5344(13)	7232(6)	5979(6)	177(5)
C(13A)	2402(12)	4322(8)	5126(6)	182(5)
C(14)	7367(15)	9980(9)	5644(7)	176(5)
C(14A)	446(10)	7533(6)	6719(6)	125(3)
C(15)	7327(18)	10599(11)	5106(9)	267(9)
C(15A)	404(14)	8038(7)	5967(7)	212(6)
C(16)	8303(9)	10741(5)	10052(4)	99(3)
C(16A)	2944(7)	5060(5)	9821(5)	88(2)
C(17)	9447(8)	10033(6)	10313(4)	97(3)
C(17A)	4496(8)	5079(6)	9627(4)	96(2)

Table 3. Bond lengths [Å] and angles [°] for **1a**.

P(1)-O(1)	1.459(5)
P(1)-O(2)	1.573(5)
P(1)-O(3)	1.582(5)
P(1)-C(2)	1.824(7)
P(2)-O(4)	1.461(4)
P(2)-O(5)	1.564(4)
P(2)-O(6)	1.584(5)
P(2)-C(2A)	1.841(6)
O(2)-C(12)	1.465(8)
O(3)-C(14)	1.463(11)
O(5)-C(12A)	1.450(9)
O(6)-C(14A)	1.443(8)
O(7)-H(71)	0.93(2)
O(7)-H(72)	0.93(2)
O(8)-H(81)	0.92(2)
O(8)-H(82)	0.90(2)
O(9)-H(91)	1.04(3)
O(9)-H(92)	0.94(3)
N(1)-C(1)	1.346(7)
N(1)-C(3)	1.430(7)
N(1)-C(16)	1.510(7)
N(1A)-C(1A)	1.325(7)
N(1A)-C(16A)	1.449(8)
N(1A)-C(3A)	1.468(7)
N(2)-C(1)	1.280(7)
N(2)-C(2)	1.545(8)
N(2A)-C(1A)	1.273(7)
N(2A)-C(2A)	1.500(7)
C(1)-H(1)	0.9300
C(1A)-H(1A)	0.9300
C(2)-C(6)	1.506(9)
C(2)-C(3)	1.577(8)
C(2A)-C(6A)	1.531(9)
C(2A)-C(3A)	1.576(8)
C(3)-C(5)	1.529(8)
C(3)-C(4)	1.552(9)

C(3A)-C(4A)	1.522(8)
C(3A)-C(5A)	1.538(8)
C(4)-H(4A)	0.9600
C(4)-H(4B)	0.9600
C(4)-H(4C)	0.9600
C(4A)-H(4A1)	0.9600
C(4A)-H(4A2)	0.9600
C(4A)-H(4A3)	0.9600
C(5)-H(5A)	0.9600
C(5)-H(5B)	0.9600
C(5)-H(5C)	0.9600
C(5A)-H(5A1)	0.9600
C(5A)-H(5A2)	0.9600
C(5A)-H(5A3)	0.9600
C(6)-C(7)	1.367(10)
C(6)-C(11)	1.379(9)
C(6A)-C(11A)	1.383(9)
C(6A)-C(7A)	1.405(9)
C(7)-C(8)	1.383(10)
C(7)-H(7)	0.9300
C(7A)-C(8A)	1.372(10)
C(7A)-H(7A)	0.9300
C(8)-C(9)	1.352(12)
C(8)-H(8)	0.9300
C(8A)-C(9A)	1.357(12)
C(8A)-H(8A)	0.9300
C(9)-C(10)	1.356(12)
C(9)-H(9)	0.9300
C(9A)-C(10A)	1.369(12)
C(9A)-H(9A)	0.9300
C(10)-C(11)	1.386(10)
C(10)-H(10)	0.9300
C(10A)-C(11A)	1.390(10)
C(10A)-H(10A)	0.9300
C(11)-H(11)	0.9300
C(11A)-H(11A)	0.9300
C(12)-C(13)	1.380(9)
C(12)-H(12A)	0.9700

C(12)-H(12B)	0.9700
C(12A)-C(13A)	1.318(10)
C(12A)-H(12C)	0.9700
C(12A)-H(12D)	0.9700
C(13)-H(13A)	0.9600
C(13)-H(13B)	0.9600
C(13)-H(13C)	0.9600
C(13A)-H(13D)	0.9600
C(13A)-H(13E)	0.9600
C(13A)-H(13F)	0.9600
C(14)-C(15)	1.232(13)
C(14)-H(14A)	0.9700
C(14)-H(14B)	0.9700
C(14A)-C(15A)	1.396(10)
C(14A)-H(14C)	0.9700
C(14A)-H(14D)	0.9700
C(15)-H(15A)	0.9600
C(15)-H(15B)	0.9600
C(15)-H(15C)	0.9600
C(15A)-H(15D)	0.9600
C(15A)-H(15E)	0.9600
C(15A)-H(15F)	0.9600
C(16)-C(17)	1.511(9)
C(16)-H(16A)	0.9700
C(16)-H(16B)	0.9700
C(16A)-C(17A)	1.538(9)
C(16A)-H(16C)	0.9700
C(16A)-H(16D)	0.9700
C(17)-C(17)#1	1.531(13)
C(17)-H(17A)	0.9700
C(17)-H(17B)	0.9700
C(17A)-C(17A)#2	1.420(12)
C(17A)-H(17C)	0.9700
C(17A)-H(17D)	0.9700
O(1)-P(1)-O(2)	115.1(3)
O(1)-P(1)-O(3)	115.1(3)
O(2)-P(1)-O(3)	100.2(3)
O(1)-P(1)-C(2)	116.5(3)

O(2)-P(1)-C(2)	105.0(3)
O(3)-P(1)-C(2)	102.9(3)
O(4)-P(2)-O(5)	113.6(3)
O(4)-P(2)-O(6)	114.9(3)
O(5)-P(2)-O(6)	101.6(3)
O(4)-P(2)-C(2A)	115.5(3)
O(5)-P(2)-C(2A)	105.0(3)
O(6)-P(2)-C(2A)	104.7(3)
C(12)-O(2)-P(1)	123.5(5)
C(14)-O(3)-P(1)	120.6(6)
C(12A)-O(5)-P(2)	118.5(5)
C(14A)-O(6)-P(2)	123.2(5)
H(71)-O(7)-H(72)	81(5)
H(81)-O(8)-H(82)	82(5)
H(91)-O(9)-H(92)	82(5)
C(1)-N(1)-C(3)	107.8(6)
C(1)-N(1)-C(16)	123.3(6)
C(3)-N(1)-C(16)	123.7(6)
C(1A)-N(1A)-C(16A)	125.5(6)
C(1A)-N(1A)-C(3A)	108.7(5)
C(16A)-N(1A)-C(3A)	123.5(6)
C(1)-N(2)-C(2)	104.8(5)
C(1A)-N(2A)-C(2A)	104.3(5)
N(2)-C(1)-N(1)	118.4(6)
N(2)-C(1)-H(1)	120.8
N(1)-C(1)-H(1)	120.8
N(2A)-C(1A)-N(1A)	118.7(6)
N(2A)-C(1A)-H(1A)	120.6
N(1A)-C(1A)-H(1A)	120.6
C(6)-C(2)-N(2)	110.4(6)
C(6)-C(2)-C(3)	116.7(5)
N(2)-C(2)-C(3)	101.7(5)
C(6)-C(2)-P(1)	111.9(4)
N(2)-C(2)-P(1)	98.1(4)
C(3)-C(2)-P(1)	115.7(5)
N(2A)-C(2A)-C(6A)	111.1(6)
N(2A)-C(2A)-C(3A)	104.6(5)
C(6A)-C(2A)-C(3A)	114.1(5)

N(2A)-C(2A)-P(2)	98.0(4)
C(6A)-C(2A)-P(2)	113.4(4)
C(3A)-C(2A)-P(2)	114.0(5)
N(1)-C(3)-C(5)	110.0(6)
N(1)-C(3)-C(4)	110.4(6)
C(5)-C(3)-C(4)	111.6(6)
N(1)-C(3)-C(2)	101.8(5)
C(5)-C(3)-C(2)	110.5(6)
C(4)-C(3)-C(2)	112.1(6)
N(1A)-C(3A)-C(4A)	113.9(5)
N(1A)-C(3A)-C(5A)	107.2(5)
C(4A)-C(3A)-C(5A)	108.9(6)
N(1A)-C(3A)-C(2A)	98.2(5)
C(4A)-C(3A)-C(2A)	116.7(5)
C(5A)-C(3A)-C(2A)	111.2(5)
C(3)-C(4)-H(4A)	109.5
C(3)-C(4)-H(4B)	109.5
H(4A)-C(4)-H(4B)	109.5
C(3)-C(4)-H(4C)	109.4
H(4A)-C(4)-H(4C)	109.5
H(4B)-C(4)-H(4C)	109.5
C(3A)-C(4A)-H(4A1)	109.5
C(3A)-C(4A)-H(4A2)	109.5
H(4A1)-C(4A)-H(4A2)	109.5
C(3A)-C(4A)-H(4A3)	109.5
H(4A1)-C(4A)-H(4A3)	109.5
H(4A2)-C(4A)-H(4A3)	109.5
C(3)-C(5)-H(5A)	109.5
C(3)-C(5)-H(5B)	109.5
H(5A)-C(5)-H(5B)	109.5
C(3)-C(5)-H(5C)	109.5
H(5A)-C(5)-H(5C)	109.5
H(5B)-C(5)-H(5C)	109.5
C(3A)-C(5A)-H(5A1)	109.4
C(3A)-C(5A)-H(5A2)	109.5
H(5A1)-C(5A)-H(5A2)	109.5
C(3A)-C(5A)-H(5A3)	109.5
H(5A1)-C(5A)-H(5A3)	109.5

H(5A2)-C(5A)-H(5A3)	109.5
C(7)-C(6)-C(11)	117.2(7)
C(7)-C(6)-C(2)	122.1(8)
C(11)-C(6)-C(2)	120.7(8)
C(11A)-C(6A)-C(7A)	119.9(7)
C(11A)-C(6A)-C(2A)	120.8(7)
C(7A)-C(6A)-C(2A)	119.1(8)
C(6)-C(7)-C(8)	120.5(9)
C(6)-C(7)-H(7)	119.8
C(8)-C(7)-H(7)	119.8
C(8A)-C(7A)-C(6A)	119.5(9)
C(8A)-C(7A)-H(7A)	120.2
C(6A)-C(7A)-H(7A)	120.2
C(9)-C(8)-C(7)	120.8(10)
C(9)-C(8)-H(8)	119.6
C(7)-C(8)-H(8)	119.6
C(9A)-C(8A)-C(7A)	120.0(11)
C(9A)-C(8A)-H(8A)	120.0
C(7A)-C(8A)-H(8A)	120.0
C(8)-C(9)-C(10)	120.7(12)
C(8)-C(9)-H(9)	119.7
C(10)-C(9)-H(9)	119.6
C(8A)-C(9A)-C(10A)	121.6(11)
C(8A)-C(9A)-H(9A)	119.2
C(10A)-C(9A)-H(9A)	119.2
C(9)-C(10)-C(11)	118.1(10)
C(9)-C(10)-H(10)	121.0
C(11)-C(10)-H(10)	120.9
C(9A)-C(10A)-C(11A)	119.8(10)
C(9A)-C(10A)-H(10A)	120.1
C(11A)-C(10A)-H(10A)	120.1
C(6)-C(11)-C(10)	122.7(9)
C(6)-C(11)-H(11)	118.6
C(10)-C(11)-H(11)	118.7
C(6A)-C(11A)-C(10A)	119.1(8)
C(6A)-C(11A)-H(11A)	120.4
C(10A)-C(11A)-H(11A)	120.5
C(13)-C(12)-O(2)	109.4(7)

C(13)-C(12)-H(12A)	109.8
O(2)-C(12)-H(12A)	109.8
C(13)-C(12)-H(12B)	109.8
O(2)-C(12)-H(12B)	109.8
H(12A)-C(12)-H(12B)	108.2
C(13A)-C(12A)-O(5)	114.5(9)
C(13A)-C(12A)-H(12C)	108.6
O(5)-C(12A)-H(12C)	108.7
C(13A)-C(12A)-H(12D)	108.6
O(5)-C(12A)-H(12D)	108.6
H(12C)-C(12A)-H(12D)	107.6
C(12)-C(13)-H(13A)	109.5
C(12)-C(13)-H(13B)	109.4
H(13A)-C(13)-H(13B)	109.5
C(12)-C(13)-H(13C)	109.5
H(13A)-C(13)-H(13C)	109.5
H(13B)-C(13)-H(13C)	109.5
C(12A)-C(13A)-H(13D)	109.4
C(12A)-C(13A)-H(13E)	109.5
H(13D)-C(13A)-H(13E)	109.5
C(12A)-C(13A)-H(13F)	109.5
H(13D)-C(13A)-H(13F)	109.5
H(13E)-C(13A)-H(13F)	109.5
C(15)-C(14)-O(3)	113.9(13)
C(15)-C(14)-H(14A)	108.8
O(3)-C(14)-H(14A)	108.8
C(15)-C(14)-H(14B)	108.8
O(3)-C(14)-H(14B)	108.7
H(14A)-C(14)-H(14B)	107.7
C(15A)-C(14A)-O(6)	112.2(8)
C(15A)-C(14A)-H(14C)	109.2
O(6)-C(14A)-H(14C)	109.2
C(15A)-C(14A)-H(14D)	109.1
O(6)-C(14A)-H(14D)	109.2
H(14C)-C(14A)-H(14D)	107.9
C(14)-C(15)-H(15A)	109.5
C(14)-C(15)-H(15B)	109.5
H(15A)-C(15)-H(15B)	109.5

C(14)-C(15)-H(15C) 109.5
H(15A)-C(15)-H(15C) 109.5
H(15B)-C(15)-H(15C) 109.5
C(14A)-C(15A)-H(15D) 109.5
C(14A)-C(15A)-H(15E) 109.5
H(15D)-C(15A)-H(15E) 109.5
C(14A)-C(15A)-H(15F) 109.4
H(15D)-C(15A)-H(15F) 109.5
H(15E)-C(15A)-H(15F) 109.5
N(1)-C(16)-C(17) 111.7(5)
N(1)-C(16)-H(16A) 109.3
C(17)-C(16)-H(16A) 109.3
N(1)-C(16)-H(16B) 109.3
C(17)-C(16)-H(16B) 109.3
H(16A)-C(16)-H(16B) 107.9
N(1A)-C(16A)-C(17A) 113.6(6)
N(1A)-C(16A)-H(16C) 108.8
C(17A)-C(16A)-H(16C) 108.9
N(1A)-C(16A)-H(16D) 108.8
C(17A)-C(16A)-H(16D) 108.8
H(16C)-C(16A)-H(16D) 107.7
C(16)-C(17)-C(17)#1 112.8(8)
C(16)-C(17)-H(17A) 109.1
C(17)#1-C(17)-H(17A) 109.0
C(16)-C(17)-H(17B) 109.0
C(17)#1-C(17)-H(17B) 109.0
H(17A)-C(17)-H(17B) 107.8
C(17A)#2-C(17A)-C(16A)112.3(9)
C(17A)#2-C(17A)-H(17C)109.1
C(16A)-C(17A)-H(17C) 109.1
C(17A)#2-C(17A)-H(17D)109.2
C(16A)-C(17A)-H(17D) 109.1
H(17C)-C(17A)-H(17D) 107.9

Symmetry transformations used to generate equivalent atoms:
#1 -x+2,-y+2,-z+2 #2 -x+1,-y+1,-z+2

Table 4. Anisotropic displacement parameters ($Å^2 x\ 10^3$) for **1a**. The anisotropic displacement factor exponent takes the form: $-2\pi^2[\ h^2 a^{*2} U^{11} + ... + 2\ h\ k\ a^*\ b^*\ U^{12}\ ]$

	U^{11}	U^{22}	U^{33}	U^{23}	U^{13}	U^{12}
P(1)	87(2)	69(1)	69(1)	-6(1)	16(1)	6(1)
P(2)	82(2)	69(1)	68(1)	2(1)	20(1)	-12(1)
O(1)	85(4)	82(3)	89(3)	4(3)	23(3)	18(3)
O(2)	124(5)	82(4)	111(4)	-31(3)	-4(3)	17(3)
O(3)	136(5)	147(5)	77(4)	35(3)	46(4)	38(4)
O(4)	74(4)	91(3)	81(3)	-9(2)	20(3)	-17(3)
O(5)	123(5)	97(4)	57(3)	-7(3)	30(3)	-8(3)
O(6)	103(4)	78(4)	90(3)	25(3)	10(3)	-3(3)
O(7)	139(6)	111(5)	82(4)	2(3)	21(4)	-32(4)
O(8)	128(5)	109(4)	98(4)	-1(3)	25(4)	37(4)
O(9)	159(7)	167(6)	153(6)	68(5)	21(5)	46(5)
N(1)	82(5)	75(4)	77(4)	0(3)	3(4)	2(4)
N(1A)	63(4)	77(4)	56(3)	3(3)	-7(3)	2(3)
N(2)	82(5)	74(4)	84(4)	9(3)	7(4)	-5(3)
N(2A)	67(4)	72(4)	65(4)	-5(3)	2(3)	6(3)
C(1)	77(6)	84(6)	55(4)	9(4)	9(4)	-17(4)
C(1A)	69(5)	64(5)	68(5)	-8(4)	18(4)	-4(4)
C(2)	95(6)	64(5)	56(4)	-1(3)	1(4)	11(4)
C(2A)	66(5)	70(5)	57(4)	6(3)	15(4)	-5(4)
C(3)	91(6)	54(4)	67(4)	-2(4)	-2(4)	10(4)
C(3A)	57(5)	59(4)	68(4)	-2(4)	5(4)	-4(4)
C(4)	98(6)	70(5)	129(7)	25(4)	37(5)	-27(4)
C(4A)	93(6)	50(4)	98(5)	-8(4)	1(5)	5(4)
C(5)	112(7)	85(5)	86(5)	-25(4)	-7(5)	17(5)
C(5A)	91(6)	93(6)	82(5)	33(4)	-6(4)	-27(5)
C(6)	81(6)	68(5)	64(5)	-3(4)	-8(5)	18(5)
C(6A)	76(6)	77(5)	57(4)	17(4)	-1(4)	-22(4)
C(7)	98(8)	97(6)	98(6)	2(5)	9(6)	4(6)
C(7A)	86(7)	88(6)	82(5)	9(4)	-4(5)	-21(5)
C(8)	66(7)	166(11)	133(9)	-6(7)	-6(6)	19(7)
C(8A)	102(8)	122(8)	116(8)	29(6)	-33(7)	-37(7)
C(9)	140(12)	102(9)	132(9)	-4(7)	-27(9)	40(8)
C(9A)	114(10)	132(10)	133(9)	34(7)	-34(8)	-54(8)

C(10)	120(9)	88(7)	116(7)	3(5)	-31(7)	15(7)
C(10A)	64(7)	159(10)	136(9)	54(7)	-12(6)	-25(7)
C(11)	92(7)	80(6)	92(6)	13(4)	-6(5)	21(5)
C(11A)	94(7)	100(6)	82(6)	19(4)	7(6)	-15(6)
C(12)	146(9)	77(6)	129(8)	-3(6)	27(6)	-21(6)
C(12A)	195(11)	133(9)	110(8)	-24(6)	76(8)	8(7)
C(13)	286(15)	91(7)	157(9)	-51(7)	75(9)	-10(8)
C(13A)	244(15)	206(12)	112(8)	21(8)	55(8)	85(10)
C(14)	238(14)	192(13)	120(10)	25(8)	88(10)	38(10)
C(14A)	140(9)	86(7)	154(9)	5(6)	31(7)	22(6)
C(15)	370(20)	300(20)	158(13)	36(12)	130(15)	-41(17)
C(15A)	356(19)	122(9)	197(12)	72(8)	144(12)	30(10)
C(16)	102(7)	110(6)	72(5)	-31(4)	-20(5)	10(5)
C(16A)	64(6)	116(6)	86(5)	-5(4)	18(5)	5(4)
C(17)	90(7)	112(6)	77(6)	-15(5)	-19(4)	24(5)
C(17A)	74(7)	112(6)	95(6)	16(5)	-17(5)	8(5)

Table 5. Hydrogen coordinates (x 10^4) and isotropic displacement parameters ($Å^2$x 10^3) for **1a**.

	x	y	z	U(eq)
H(71)	3540(110)	7200(60)	8300(40)	235
H(72)	4390(110)	7880(70)	8370(50)	235
H(81)	1470(120)	1900(70)	1720(40)	235
H(82)	1040(120)	2680(50)	1550(60)	235
H(91)	4000(50)	2470(70)	590(50)	235
H(92)	2690(70)	2730(80)	590(30)	235
H(1)	6512	9158	9646	87
H(1A)	1413	6609	9449	80
H(4A)	8208	12074	8443	145
H(4B)	7550	11542	7544	145
H(4C)	8709	11044	8177	145
H(4A1)	2796	4252	7745	124
H(4A2)	1604	3414	7622	124
H(4A3)	2708	3544	8486	124
H(5A)	4975	11429	9139	146
H(5B)	5509	12197	8545	146
H(5C)	6371	12077	9473	146
H(5A1)	694	3589	9335	136
H(5A2)	-435	3495	8481	136
H(5A3)	-473	4363	9174	136
H(7)	2995	9697	8031	119
H(7A)	-529	3745	6662	105
H(8)	870	10298	7397	149
H(8A)	-2778	3062	6127	143
H(9)	867	11533	6499	155
H(9A)	-4765	3741	6527	159
H(10)	2988	12213	6215	136
H(10A)	-4588	5141	7411	146
H(11)	5118	11584	6820	107
H(11A)	-2338	5820	8016	111
H(12A)	6312	7591	7150	142
H(12B)	4628	7545	7062	142

H(12C)	1450	5483	5159	170
H(12D)	2934	5502	5766	170
H(13A)	4436	7335	5634	265
H(13B)	5427	6553	6060	265
H(13C)	6106	7457	5685	265
H(13D)	3129	3999	5487	273
H(13E)	2759	4498	4608	273
H(13F)	1566	3895	4968	273
H(14A)	8361	9843	5838	211
H(14B)	6885	9386	5362	211
H(14C)	-325	7735	7028	150
H(14D)	1348	7696	7099	150
H(15A)	6357	10791	4957	401
H(15B)	7662	10335	4591	401
H(15C)	7929	11153	5349	401
H(15D)	1147	7826	5649	317
H(15E)	550	8720	6125	317
H(15F)	-514	7915	5608	317
H(16A)	7751	10851	10525	119
H(16B)	8757	11356	9952	119
H(16C)	2700	4421	9995	106
H(16D)	2888	5524	10309	106
H(17A)	8993	9395	10332	116
H(17B)	9937	10231	10895	116
H(17C)	4574	4582	9169	115
H(17D)	4723	5702	9415	115

Table 6. Hydrogen bonds for **1a** [Å and °].

D-H...A	d(D-H)	d(H...A)	d(D...A)	<(DHA)
O(7)-H(71)...O(4)	0.93(2)	1.98(3)	2.905(7)	168(10)
O(7)-H(72)...N(2)	0.93(2)	2.30(8)	2.935(8)	126(8)
O(8)-H(81)...O(1)#3	0.92(2)	1.97(4)	2.835(8)	157(10)
O(8)-H(82)...N(2A)#4	0.90(2)	2.03(6)	2.816(8)	145(9)
O(9)-H(91)...O(7)#3	1.04(3)	2.01(2)	2.991(9)	156(9)
O(9)-H(92)...O(8)	0.94(3)	1.91(2)	2.750(10)	147(7)
C(1)-H(1)...O(9)#3	0.93	2.60	3.366(10)	140.0
C(4)-H(4B)...O(3)	0.96	2.44	3.113(9)	126.5
C(4A)-H(4A1)...O(5)	0.96	2.70	3.156(8)	110.1
C(12)-H(12B)...O(4)	0.97	2.66	3.533(10)	149.3
C(14A)-H(14D)...O(4)	0.97	2.57	3.048(10)	110.5
C(16A)-H(16C)...O(9)#5	0.97	2.49	3.373(11)	150.9

Symmetry transformations used to generate equivalent atoms:

#1 -x+2,-y+2,-z+2 #2 -x+1,-y+1,-z+2 #3 -x+1,-y+1,-z+1

#4 -x,-y+1,-z+1 #5 x,y,z+1

6. Optimization of the synthesis of 1a

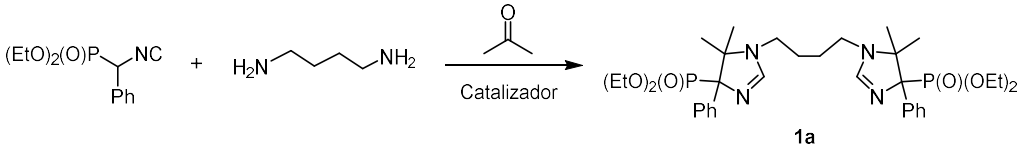

Table S2. Optimization of reaction conditions to obtain **1a**. [a, b]

Entry	Conditions	Catalyst	Conversion to 1a
1	MW, 40ºC, 10 min	$AgNO_3$	61
2	MW, 40ºC, 20 min	$AgNO_3$	82
3	r.t., 16 h	$AgNO_3$	75
4	US, 40ºC, 1 h	$AgNO_3$	80
5	MW, 40ºC, 20 min	---	0
6	MW, 40ºC, 20 min	$AgNO_3$[c]	52
7	MW, 40ºC, 20 min	CF_3COOH	8
8	MW, 40ºC, 20 min	$AgBF_4$	70[d]
9	MW, 40ºC, 20 min	AgF	67[d]
10	MW, 40ºC, 20 min	AgOAc	58[d]

[a] Reaction conditions: Ph-Phosmic (2.2 equiv), 1,4-diaminobutane (1 equiv), acetone (0.13 mmol/ml) and catalyst (10%-mmol). **[b]** The conversion (%) to **1a** was determined by HPLC-MS. **[c]** $AgNO_3$ (6%-mmol). **[d]** The cyclodimerization product **A** was detected in the mixture crude by HPLC-MS (entry 8, 4%; entry 9, 7%; entry 10, 10%)

Entry 1:
A mixture of $AgNO_3$ (2.2 mg, 0.013 mmol), acetone (1.0 mL), 1,4-diaminobutane (12 mg, 0.13 mmol) and α-Ph-PhosMic (71 mg, 0.28 mmol) was stirred under microwave irradiation at 40ºC for 10 min. The mixture was filtered and evaporated to yield a residue which was injected to HPLC-MS in order to determined the conversion to **1a** (61%).

Entry 2:
A mixture of $AgNO_3$ (2.2 mg, 0.013 mmol), acetone (1.0 mL), 1,4-diaminobutane (12 mg, 0.13 mmol) and α-Ph-PhosMic (71 mg, 0.28 mmol) was stirred under microwave irradiation at 40ºC for 20 min. The mixture was filtered and evaporated to yield a residue which was injected to HPLC-MS in order to determined the conversion to **1a** (82%).

Entry 3:
A mixture of $AgNO_3$ (2.2 mg, 0.013 mmol), acetone (1.0 mL), 1,4-diaminobutane (12 mg, 0.13 mmol) and α-Ph-PhosMic (71 mg, 0.28 mmol) was stirred at room temperture overnight. The mixture was filtered and evaporated to yield a residue which was injected to HPLC-MS in order to determined the conversion to **1a** (75%).

Entry 4:
A mixture of $AgNO_3$ (2.2 mg, 0.013 mmol), acetone (1.0 mL), 1,4-diaminobutane (12 mg, 0.13 mmol) and α-Ph-PhosMic (71 mg, 0.28 mmol) was stirred under ultrasound

irradiation at 40ºC for 1 h. The mixture was filtered and evaporated to yield a residue which was injected to HPLC-MS in order to determined the conversion to **1a** (80%).

Entry 5:
A mixture of acetone (1.0 mL), 1,4-diaminobutane (12 mg, 0.13 mmol) and α-Ph-PhosMic (71 mg, 0.28 mmol) was stirred under microwave irradiation at 40ºC for 20 min. The mixture was filtered and evaporated to yield a residue which was injected to HPLC-MS in order to determined the conversion to **1a** (0%).

Entry 6:
A mixture of $AgNO_3$ (1.4 mg, 0.008 mmol), acetone (1.0 mL), 1,4-diaminobutane (12 mg, 0.13 mmol) and α-Ph-PhosMic (71 mg, 0.28 mmol) was stirred under microwave irradiation at 40ºC for 20 min. The mixture was filtered and evaporated to yield a residue which was injected to HPLC-MS in order to determined the conversion to **1a** (52%).

Entry 7:
A mixture of trifluoroacetic acid (1.2 μL, 0.013 mmol), acetone (1.0 mL), 1,4-diaminobutane (12 mg, 0.13 mmol) and α-Ph-PhosMic (71 mg, 0.28 mmol) was stirred under microwave irradiation at 40ºC for 20 min. The mixture was filtered and evaporated to yield a residue which was injected to HPLC-MS in order to determined the conversion to **1a** (8%).

Entry 8:
A mixture of $AgBF_4$ (2.4 mg, 0.013 mmol), acetone (1.0 mL), 1,4-diaminobutane (12 mg, 0.13 mmol) and α-Ph-PhosMic (71 mg, 0.28 mmol) was stirred under microwave irradiation at 40ºC for 20 min. The mixture was filtered and evaporated to yield a residue which was injected to HPLC-MS in order to determined the conversion to **1a** (70%).

Entry 9:
A mixture of AgF (1.6 mg, 0.013 mmol), acetone (1.0 mL), 1,4-diaminobutane (12 mg, 0.13 mmol) and α-Ph-PhosMic (71 mg, 0.28 mmol) was stirred under microwave irradiation at 40ºC for 20 min. The mixture was filtered and evaporated to yield a residue which was injected to HPLC-MS in order to determined the conversion to **1a** (67%).

Entry 10:
A mixture of AgOAc (2.1 mg, 0.013 mmol), acetone (1.0 mL), 1,4-diaminobutane (12 mg, 0.13 mmol) and α-Ph-PhosMic (71 mg, 0.28 mmol) was stirred under microwave irradiation at 40ºC for 20 min. The mixture was filtered and evaporated to yield a residue which was injected to HPLC-MS in order to determined the conversion to **1a** (58%).

7. Optimization synthesis of 8a

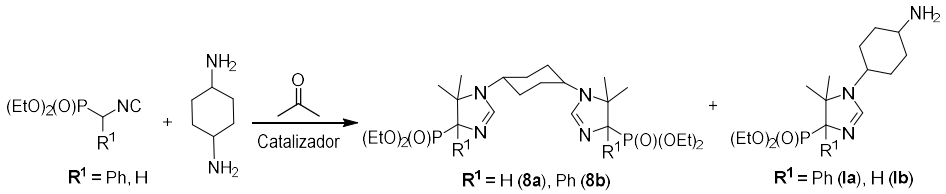

Table S3. Optimization of reaction conditions to obtain bis(2-imidazolin-4-yl)phosphonates **8a**. [a, b]

Entry	R^1	Conditions	Conversion to 8a-8b	Conversion to Ia-Ib	Conversion to A
1	Ph	MW, 40ºC, 20 min	5	45	40
2	Ph	MW, 40ºC, 60 min	8	40	45
3	Ph	MW, 40ºC, 60 min [c]	0	32	55
4	Ph	MW, 40ºC, 60 min [d]	0	24	37
5	Ph	r.t., 48 h	16	32	47
6	Ph	US, 40ºC, 2 h	0	34	59
7	H	MW, 40ºC, 20 min	45	44	0
8	H	r.t., 48 h	75	18	0
9	H	US, 40ºC, 2 h	84	0	0

[a] Reaction conditions: PhosMic or α-Ph-PhosMic (2.2 equiv), *p*-cyclohexanediamine (1 equiv), acetone (0.13 mmol/ml) and $AgNO_3$ (10%-mmol). **[b]** The conversion (%) was determined by HPLC-MS. **[c]** AgOAc (10%-mmol). **[d]** Acetone (4 equiv) and methanol (0.13 mmol/ml).

Entry 1:
A mixture of $AgNO_3$ (2.2 mg, 0.013 mmol), acetone (1.0 mL), *p*-cyclohexanediamine (15 mg, 0.13 mmol) and α-Ph-PhosMic (71 mg, 0.28 mmol) was stirred under microwave irradiation at 40ºC for 20 min. The mixture was filtered and evaporated to yield a residue which was injected to HPLC-MS in order to determined the conversion to **8b** (5%).

Entry 2:
A mixture of $AgNO_3$ (2.2 mg, 0.013 mmol), acetone (1.0 mL), *p*-cyclohexanediamine (15 mg, 0.13 mmol) and α-Ph-PhosMic (71 mg, 0.28 mmol) was stirred under microwave irradiation at 40ºC for 60 min. The mixture was filtered and evaporated to yield a residue which was injected to HPLC-MS in order to determined the conversion to **8b** (8%).

Entry 3:
A mixture of AgOAc (2.1 mg, 0.013 mmol), acetone (1.0 mL), *p*-cyclohexanediamine (15 mg, 0.13 mmol) and α-Ph-PhosMic (71 mg, 0.28 mmol) was stirred under microwave irradiation at 40ºC for 60 min. The mixture was filtered and evaporated to yield a residue which was injected to HPLC-MS in order to determined the conversion to **8b** (0%).

Entry 4:
A mixture of AgOAc (2.2 mg, 0.013 mmol), acetone (39 μL, 0.52 mmol), *p*-cyclohexanediamine (15 mg, 0.13 mmol) and α-Ph-PhosMic (71 mg, 0.28 mmol) in methanol (0.95 mL) was stirred under microwave irradiation at 40ºC for 60 min. The

mixture was filtered and evaporated to yield a residue which was injected to HPLC-MS in order to determined the conversion to **8b** (0%).

Entry 5:
A mixture of $AgNO_3$ (2.2 mg, 0.013 mmol), acetone (1.0 mL), *p*-cyclohexanediamine (15 mg, 0.13 mmol) and α-Ph-PhosMic (71 mg, 0.28 mmol) was stirred at room temperature for 48 h. The mixture was filtered and evaporated to yield a residue which was injected to HPLC-MS in order to determined the conversion to **8b** (16%).

Entry 6:
A mixture of $AgNO_3$ (2.2 mg, 0.013 mmol), acetone (1.0 mL), *p*-cyclohexanediamine (15 mg, 0.13 mmol) and α-Ph-PhosMic (71 mg, 0.28 mmol) was stirred under ultrasound irradiation at 40ºC for 2 h. The mixture was filtered and evaporated to yield a residue which was injected to HPLC-MS in order to determined the conversion to **8b** (0%).

Entry 7:
A mixture of $AgNO_3$ (2.2 mg, 0.013 mmol), acetone (1.0 mL), *p*-cyclohexanediamine (15 mg, 0.13 mmol) and PhosMic (45 μL, 0.28 mmol) was stirred under microwave irradiation at 40ºC for 20 min. The mixture was filtered and evaporated to yield a residue which was injected to HPLC-MS in order to determined the conversion to **8a** (45%).

Entry 8:
A mixture of $AgNO_3$ (2.2 mg, 0.013 mmol), acetone (1.0 mL), *p*-cyclohexanediamine (15 mg, 0.13 mmol) and PhosMic (45 μL, 0.28 mmol) was stirred at room temperature for 48 h. The mixture was filtered and evaporated to yield a residue which was injected to HPLC-MS in order to determined the conversion to **8a** (75%).

Entry 9:
A mixture of $AgNO_3$ (2.2 mg, 0.013 mmol), acetone (1.0 mL), *p*-cyclohexanediamine (15 mg, 0.13 mmol) and PhosMic (45 μL, 0.28 mmol) was stirred under ultrasound irradiation at 40ºC for 2 h. The mixture was filtered and evaporated to yield a residue which was injected to HPLC-MS in order to determined the conversion to **8a** (84%).

8. Optimization synthesis of II

Table S4. Optimization of reaction conditions to obtain (2-imidazolin-4-yl)phosphonate **II**. [a, b]

Entry	Isocyanide	Conditions	Catalyst	Conversion to II	Conversion to A or B
1	α–Ph-PhosMic	MW, 40ºC, 20 min	$AgNO_3$	58	39
2	α–Ph-PhosMic	MW, 40ºC, 60 min	$AgNO_3$	55	40
3	α–Ph-PhosMic	r.t., 48 h	$AgNO_3$	60	33
4	α–Ph-PhosMic	MW, 40ºC, 20 min	AgOAc	30	65
5	α–Ph-PhosMic	US, 40ºC, 3 h	$AgNO_3$	62	22
6	α–Ph-PhosMic	MW, 40ºC, 20 min	$AgBF_4$	55	41
7	α–Ph-PhosMic	MW, 40ºC, 20 min	AgF	40	54
8	PhosMic	MW, 40ºC, 20 min	$AgNO_3$	0	0
9	PhosMic	MW, 40ºC, 20 min	AgOAc	0	56
10	PhosMic	r.t., 48 h	$AgNO_3$	8	0
11	PhosMic	US, 40ºC, 3 h	$AgNO_3$	12	0

[a] Reaction conditions: Phosmic derivative (2.2 equiv), *p*-phenylenediamine (1 equiv), acetone (0.13 mmol/ml) and $AgNO_3$ (10%-mmol). **[b]** The conversion (%) was determined by HPLC-MS.

Entry 1:
A mixture of $AgNO_3$ (2.2 mg, 0.013 mmol), acetone (1.0 mL), *p*-phenylenediamine (14 mg, 0.13 mmol) and α-Ph-PhosMic (71 mg, 0.28 mmol) was stirred under microwave irradiation at 40ºC for 20 min. The mixture was filtered and evaporated to yield a residue which was injected to HPLC-MS in order to determined the conversion to **II** (58%).

Entry 2:
A mixture of $AgNO_3$ (2.2 mg, 0.013 mmol), acetone (1.0 mL), *p*-phenylenediamine (14 mg, 0.13 mmol) and α-Ph-PhosMic (71 mg, 0.28 mmol) was stirred under microwave irradiation at 40ºC for 60 min. The mixture was filtered and evaporated to yield a residue which was injected to HPLC-MS in order to determined the conversion to **II** (55%).

Entry 3:
A mixture of $AgNO_3$ (2.2 mg, 0.013 mmol), acetone (1.0 mL), *p*-phenylenediamine (14 mg, 0.13 mmol) and α-Ph-PhosMic (71 mg, 0.28 mmol) was stirred at room temperature for 48 h. The mixture was filtered and evaporated to yield a residue which was injected to HPLC-MS in order to determined the conversion to **II** (60%).

Entry 4:
A mixture of AgOAc (2.1 mg, 0.013 mmol), acetone (1.0 mL), *p*-phenylenediamine (14 mg, 0.13 mmol) and α-Ph-PhosMic (71 mg, 0.28 mmol) was stirred under microwave irradiation at 40ºC for 20 min. The mixture was filtered and evaporated to yield a residue which was injected to HPLC-MS in order to determined the conversion to **II** (30%).

Entry 5:
A mixture of $AgBF_4$ (2.4 mg, 0.013 mmol), acetone (1.0 mL), *p*-phenylenediamine (14 mg, 0.13 mmol) and α-Ph-PhosMic (71 mg, 0.28 mmol) was stirred under ultrasound irradiation at 40ºC for 3 h. The mixture was filtered and evaporated to yield a residue which was injected to HPLC-MS in order to determined the conversion to **II** (62%).

Entry 6:
A mixture of $AgBF_4$ (2.4 mg, 0.013 mmol), acetone (1.0 mL), *p*-phenylenediamine (14 mg, 0.13 mmol) and α-Ph-PhosMic (71 mg, 0.28 mmol) was stirred under microwave irradiation at 40ºC for 20 min. The mixture was filtered and evaporated to yield a residue which was injected to HPLC-MS in order to determined the conversion to **II** (55%).

Entry 7:
A mixture of AgF (1.6 mg, 0.013 mmol), acetone (01.0 mL), *p*-phenylenediamine (14 mg, 0.13 mmol) and α-Ph-PhosMic (71 mg, 0.28 mmol) was stirred under microwave irradiation at 40ºC for 20 min. The mixture was filtered and evaporated to yield a residue which was injected to HPLC-MS in order to determined the conversion to **II** (40%).

Entry 8:
A mixture of $AgNO_3$ (2.2 mg, 0.013 mmol), acetone (1.0 mL), *p*-phenylenediamine (14 mg, 0.13 mmol) and PhosMic (45 μL, 0.28 mmol) was stirred under microwave irradiation at 40ºC for 20 min. The mixture was filtered and evaporated to yield a residue which was injected to HPLC-MS in order to determined the conversion to **II** derivative (0%).

Entry 9:
A mixture of AgOAc (2.1 mg, 0.013 mmol), acetone (1.0 mL), *p*-phenylenediamine (14 mg, 0.13 mmol) and PhosMic (45 μL, 0.28 mmol) was stirred under microwave irradiation at 40ºC for 20 min. The mixture was filtered and evaporated to yield a residue which was injected to HPLC-MS in order to determined the conversion to **II** derivative (0%).

Entry 10:
A mixture of $AgNO_3$ (2.2 mg, 0.013 mmol), acetone (1.0 mL), *p*-phenylenediamine (14 mg, 0.13 mmol) and PhosMic (45 μL, 0.28 mmol) was stirred at room temperature for 48

h. The mixture was filtered and evaporated to yield a residue which was injected to HPLC-MS in order to determined the conversion to **II** derivative (8%).

Entry 11:

A mixture of $AgNO_3$ (2.2 mg, 0.013 mmol), acetone (1.0 mL), *p*-phenylenediamine (14 mg, 0.13 mmol) and PhosMic (45 μL, 0.28 mmol) was stirred under ultrasound irradiation at 40ºC for 3 h. The mixture was filtered and evaporated to yield a residue which was injected to HPLC-MS in order to determined the conversion to **II** derivative (12%).

Capítulo 5. ***Pharmacology and preclinical validation of a novel anticancer compound targeting PEPCK-M***

5.1. *Biomedicine & Pharmacotherapy* 2020, *121*, 109601

Pharmacology and preclinical validation of a novel anticancer compound targeting PEPCK-M

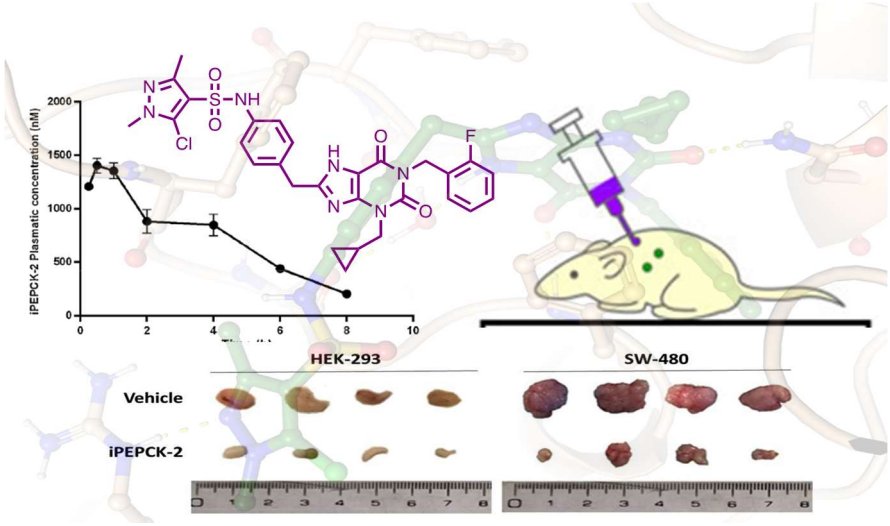

Biomedicine & Pharmacotherapy 121 (2020) 109601

Contents lists available at ScienceDirect

Biomedicine & Pharmacotherapy

journal homepage: www.elsevier.com/locate/biopha

Pharmacology and preclinical validation of a novel anticancer compound targeting PEPCK-M

Marc Aragó[a], Juan Moreno-Felici[a], Sonia Abás[b], Sergio Rodríguez-Arévalo[b], Petra Hyroššová[a], Agnes Figueras[c], Francesc Viñals[a,c], Belén Pérez[d], Maria I. Loza[e], Jose Brea[e], Pedro Latorre[f], Jose A. Carrodeguas[f], Pablo M. García-Rovés[a], Carlos Galdeano[g], Tiziana Ginex[h], Francisco J. Luque[h], Carmen Escolano[b], Jose C. Perales[a,*]

[a] Department of Physiological Sciences, School of Medicine, University of Barcelona, L'Hospitalet del Llobregat, Spain
[b] Laboratory of Medicinal Chemistry (Associated Unit to CSIC), Faculty of Pharmacy and Food Sciences, and Institute of Biomedicine (IBUB), University of Barcelona, Barcelona, Spain
[c] Programs of Molecular Mechanisms and Experimental Therapeutics in Oncology (ONCOBell), and Cancer Therapeutics Resistance (ProCURE), Catalan Institute of Oncology, Bellvitge Institute for Biomedical Research (IDIBELL), L'Hospitalet del Llobregat, Spain
[d] Department of Pharmacology, Therapeutic and Toxicology, Autonomous University of Barcelona, Bellaterra, Spain
[e] Innopharma Screening Platform, BioFarma Research Group, Centro de Investigación en Medicina Molecular y Enfermedades Crónicas (CIMUS), Universidad de Santiago de Compostela, Santiago de Compostela, Spain
[f] Instituto de Biocomputación y Física de Sistemas Complejos (BIFI), BIFI-IQFR (CSIC), Departamento de Bioquímica y Biología Molecular y Celular, Facultad de Ciencias, Universidad de Zaragoza, Zaragoza, Spain
[g] Department of Pharmacy, Pharmaceutical Technology and Physical Chemistry, School of Pharmacy, and Institute of Biomedicine (IBUB), University of Barcelona, Barcelona, Spain
[h] Department of Nutrition, Food Sciences and Gastronomy, School of Pharmacy and Food Sciences, Institute of Biomedicine (IBUB), and Institute of Theoretical and Computational Chemistry (IQTCUB), University of Barcelona, Santa Coloma de Gramanet, Spain

ARTICLE INFO

Keywords:
PEPCK-M
Xanthine derivatives
PEPCK inhibitors
Cancer metabolism
Xenograft
Gluconeogenesis
Breast carcinoma
Colon carcinoma
Preclinical
Mitochondrial physiology
CETSA
Insulin secretion

ABSTRACT

Background: Phosphoenolpyruvate carboxykinase (PEPCK) catalyzes the decarboxylation of oxaloacetate to phosphoenolpyruvate. The mitochondrial isozyme, PEPCK-M is highly expressed in cancer cells, where it plays a role in nutrient stress response. To date, pharmacological strategies to target this pathway have not been pursued.

Methods: A compound embodying a 3-alkyl-1,8-dibenzylxanthine nucleus (iPEPCK-2), was synthesized and successfully probed *in silico* on a PEPCK-M structural model. Potency and target engagement *in vitro* and *in vivo* were evaluated by kinetic and cellular thermal shift assays (CETSA). The compound and its target were validated in tumor growth models *in vitro* and in murine xenografts.

Results: Cross-inhibitory capacity and increased potency as compared to 3-MPA were confirmed *in vitro* and *in vivo*. Treatment with iPEPCK-2 inhibited cell growth and survival, especially in poor-nutrient environment, consistent with an impact on colony formation in soft agar. Finally, daily administration of the PEPCK-M inhibitor successfully inhibited tumor growth in two murine xenograft models as compared to vehicle, without weight loss, or any sign of apparent toxicity.

Conclusion: We conclude that iPEPCK-2 is a compelling anticancer drug targeting PEPCK-M, a hallmark gene product involved in metabolic adaptations of the tumor.

1. Background

Phosphoenolpyruvate carboxykinase (PEPCK) (GTP; EC 4.1.1.32) catalyzes the GTP-dependent conversion of oxaloacetate (OAA) to phosphoenolpyruvate (PEP) from two very similar isozymes localized to the cytosol (PEPCK-C) or the mitochondria (PEPCK-M) [1,2], and

Abbreviations: PEPCK, phosphoenolpyruvate carboxykinase; 3-MPA, 3-mercaptopicolinic acid; PEP, phosphoenolpyruvate; OAA, oxaloacetate; MA, malic acid; GSIS, glucose stimulated insulin secretion; AARE, amino acid response element; ER, endoplasmic reticulum; CETSA, cellular thermal shift assay; ITDRF, isothermal dose-response fingerprint; ADMET, absorption, distribution, metabolism, excretion, and toxicity; BBB, blood brain barrier

* Corresponding author at: Professor "Serra Hunter", School of Medicine, University of Barcelona, 08907, Barcelona, Spain.
E-mail address: jperales@ub.edu (J.C. Perales).

https://doi.org/10.1016/j.biopha.2019.109601
Received 22 July 2019; Received in revised form 24 October 2019; Accepted 25 October 2019

encoded by different nuclear genes (PCK1 and PCK2, respectively). Interestingly, both isozymes are differentially expressed and regulated. Whereas PEPCK-C is restricted to gluconeogenic and glyceroneogenic tissues (liver, small intestine, kidney cortex, and adipose tissue), and responds to insulin, glucagon and dexamethasone, PEPCK-M mRNA content is not regulated by hormonal cues, but it is more widely expressed (*i.e.*, T- and B-cells, pancreatic β-cells, liver, neurons, and undifferentiated tissues such as embryonal stem cells and tumors) [3–8]. In differentiated tissues PEPCK-M role is not completely understood, although it clearly impinges on cataplerosis and TCA cycle flux in the liver [6], and pancreatic β-cells [5].

In tumor cells, on the other hand, this enzyme promotes amino-acid homeostasis, 1-carbon metabolism and several biosynthetic processes crucial to sustain cancer cell and neuroprogenitor metabolism [8–10]. Indeed, the gene encoding for PEPCK-M, PCK2, is a target for ATF4, the master regulator of ER- and amino-acid stress responses [7]. PEPCK-M protein and mRNA was upregulated by effectors of this pathway by recruiting ATF4 to a consensus AARE site located at the PCK2 proximal promoter. Consistently, knocking-down PEPCK-M under stress tipped the balance of the cell towards apoptosis, whereas overexpressing PEPCK-M enhanced cell survival [7]. The importance of chronic ER-stress to induce adaptive responses in cancer cells *in vivo* suggested that the pathway is crucial to cancer cell metabolism and progression. In agreement with this view, loss-of-function genetic models have shown the relevance of PEPCK-M in cell growth and chemoresistance in lung and colon cancer, respectively [10–12].

Thus, we have aimed to identify the potential for this pathway in cancer therapeutic intervention by evaluating a small molecule targeting this enzyme, and its pharmacological validation in a murine preclinical cancer indication. A compound embodying a 3-alkyl-1,8-dibenzylxanthine skeleton previously described as GTP competitive inhibitor for PEPCK-C [13] in an *in vitro* assay, was retargeted against PEPCK-M and systematically assessed for target engagement, efficacy *in vitro*, and pharmacokinetics and activity *in vivo*. PEPCK-M inhibition leads to metabolic imbalances comparable to down-regulation of the enzyme using genetic models (*i.e.*, CRISPR/*cas*9), hindering cell viability *in vitro* and in xenograft models of transformed embryonal kidney (HEK-293) and colon carcinoma (SW-480) tumor growth. Therefore, we conclude that the PEPCK-M inhibitor described here have potent anticancer activities, underscoring the potential of this pathway as a novel therapeutic target.

2. Methods

2.1. Synthesis

The details of the synthesis and characterization of iPEPCK-2 are given in Methods S1 in Supporting Information.

2.2. Computational protocol

Pairwise sequence alignment for PEPCK-C and PEPCK-M isoforms was performed using stretcher (https://www.ebi.ac.uk/Tools/psa/; see Fig. S2 in Supporting Information). The PDB structure of human PEPCK-C co-crystallized with the GDP-competitive inhibitor, *N*-(4-{[3-butyl-1-(2-fluorobenzyl)-2,6-dioxo-2,3,6,7-tetrahydro-1*H*-purin-8-yl] methyl}phenyl)-1-methyl-1*H*-imidazole-4-sulfonamide (PDB ID: 2GMV) [13] was used as a template to generate the protein model for PEPCK-M with Swissmodel [14]. Choice of this X-ray structure was motivated by the high resemblance between the crystallographic ligand and iPEPCK-2.

AutoDock4 [15] was used to dock iPEPCK-2 in PEPCK-M generated by homology modeling from the cytosolic isoform. A structural water molecule (wat740 in 2GMV), mediating ligand interactions with protein residues W527 and W516, was included in the PEPCK-M structure, and its position was determined upon alignment of the 3D structures of the homology model built for PEPCK-M and the reference PDB (2GMV) structure. A grid spacing of 0.375 Å was used in conjunction with 62 × 62 × 62 grid points to define the box considered to explore the arrangement of the ligand in the binding pocket. A genetic algorithm was used to guide the docking search during pose generation. A total of 30 docking conformations were finally generated and analyzed.

2.3. Recombinant human PEPCK-C and PEPCK-M

Open reading frames from human PCK1 coding for PEPCK-C and PCK2 coding for PEPCK-M were cloned and transferred to the pET15b vector, and competent BL21 *E. coli* cells were transformed with the expression construct. Cells were precultured in 10 mL of 2xYT overnight, and the next day were grown at 37 °C in 200 mL of 2xYT medium until they grew to an optical density of 0.5-0.6 at λ_{600}. Then, IPTG was added to a final concentration of 1 mM to induce protein expression. The cells were incubated at room temperature for 5 h under moderate shaking (110 rpm). PEPCK-M was produced and isolated from Arctic express *E. coli* cells as described [16].

Cells were harvested by centrifugation and resuspended in lysis buffer, then lysozyme was added, and the mix was incubated 30 min in ice. The suspension was sonicated on ice for six cycles of 10 s ON and 30 s OFF. Then, DNAse was added, and after 15 min incubation, the cell debris was removed by centrifugation and the supernatants were purified using Qiagen Ni-NTA Agarose following the manufacturer protocol. The purified enzymes were used immediately or stored at −80 °C until needed.

2.4. PEPCK activity assays

Kinetic assays were performed analyzing NADH consumption by spectrophotometry. Absorbance was measured at 340 nm during 6 min at 37 °C in a total volume of 1 mL. The following reaction was studied in the presence of different concentrations of PEPCK inhibitors:

$$PEP + CO_2 + GTP \ (PEPCK) \rightarrow GDP + OAA + NADH \ (MDH) \rightarrow MA + NAD^+$$

The reaction was performed in 50 mM Tris-HCl (pH 7.4), 20 mM $NaHCO_3$, 1 mM $MnCl_2$, in the presence of CO_2 (carbogen infusion for 10 min). Then the following components were added: 0.5 mM PEP, 0.1 mM NADH, 2 UI/mL Malate dehydrogenase (MDH), 5 μM rotenone, 25 mM DTT. Recombinant PEPCK-C or PEPCK-M and the inhibitors were then added, and the reaction started by the addition of 0.2 mM of GDP.

2.5. Cell culture

All cell lines, except otherwise indicated, were grown in DMEM medium supplemented with 10% of fetal bovine/calf serum, 100 IU/mL penicillin + 100 μg/mL streptomycin, and 2 mM glutamine. INS-1 rat insulinoma cells were grown in complete RPMI-1640 supplemented with 71 μM of β-mercaptoethanol. For glucose deprivation experiments cells were seeded with glucose-free DMEM, and it was supplemented with 10% of dialyzed FBS, 100 IU/mL penicillin + 100 μg/mL streptomycin, and 2 mM glutamine.

2.6. Cellular thermal shift assay (CETSA)

Intact and viable mouse embryonal fibroblast (MEF) cells were harvested and resuspended to a final concentration of 2×10^6 cells/mL. Different PEPCK-M inhibitors were added to this suspension, to a final concentration of 5 μM, and incubated for 30 min at 37 °C. Cells were washed and resuspended with PBS to a final concentration of 3×10^7 cells/mL. They were split in different tubes and treated with a gradient of temperatures between 40 and 60 °C for 3 min, cells were incubated

3 min at room temperature and snap frozen with liquid nitrogen. Cells were lysed using a freeze/thaw cycle with liquid nitrogen and centrifuged at 20000 *g* 20 min at 4 °C. Finally, stable PEPCK-M present in the supernatant was quantified by western blot.

The analysis was also performed treating the cells with a gradient of PEPCK-M inhibitor concentrations and a thermal treatment at a single temperature (60 °C). IsoThermal Dose-Response Fingerprint ($ITDRF_{CE-TSA}$) concentrations were calculated as described [17].

2.7. Cell viability and anchorage-independent growth

Proliferation assays were performed on MCF7, HEK-293, HCT-116 and SW-480 cells seeded at 5×10^3 cells/well in 96-well plates. After overnight incubation cells were treated with the different PEPCK inhibitors between 24 and 72 h. Then viability was measured by MTT.

Anchorage-independent growth capacity was tested counting the colonies formed when cells have been seeded in soft agar. Firstly, the wells of 6-well plates were filled with 2 mL of complete medium with 0.6% melted agar. When agar solidified, 10^5 cells were seeded in 1 mL of complete medium (DMEM) with 0.3% agar with or without PEPCK-M inhibitors. Once the superior layer solidified, 500 μL of treatment medium was renewed, and changed twice a week. The plate was incubated for two weeks, and the colonies were stained with MTT and counted.

2.8. Glucose-stimulated insulin secretion (GSIS)

Insulin secretion experiments were performed in INS-1 rat insulinoma cells and fasted ICR mice. GSIS in INS1 cells; four hundred thousand cells/well were seeded in a 24 well and incubated with 2.8 mM of glucose KRBH medium in the presence or absence of iPEPCK-2 for 2 h. Then, the medium was discarded and 500 μL of KRBH medium with 2.8 mM of glucose were added for 1 h. Next, supernatants were collected and incubated in 500 μL of KRBH medium with 16.7 mM of glucose for 1 h. Finally, cells were lysed with RIPA and total protein was quantified for normalization. GSIS in fasted ICR mice; a GSIS assay was performed in male ICR white mice between 30 and 40 g (at least n = 4 per group given that insulin concentrations are quite dispersed in the population at baseline) and all animals were randomized to either the experimental and control groups. A single intraperitoneal dose of iPEPCK-2 (dissolved in 40 % PEG 400 in physiological saline), was administered at the described doses in the morning (between 8 and 10 a.m.) without anesthesia. Later (2 h or 5 h), a bolus of glucose (2 g/kg) was administered *via* IP to induce insulin secretion. Mice were monitored for signs of pain or distress during the time between either injection and euthanasia (at the earliest time of 15 min and the latest at 1 h after glucose bolus injection). Blood (50 μL) was collected from the tail vein after incision at the stated time points, and animals were subsequently sacrificed by cervical dislocation. The content of insulin of the different supernatants (*basal* in 2.8 mM glucose, or *GSIS* in 16.7 mM glucose) was measured by ELISA using the *Mercodia Mouse Insulin ELISA* kit.

2.9. Pharmacokinetics

The pharmacokinetic study was carried on in male ICR white mice between 30 and 40 g (n = 4 per group, which is a small cohort based on the potency of the analytical and quantification techniques utilized) and all animals were randomized to either the experimental and control groups. A single intraperitoneal dose of iPEPCK-2 (dissolved in 40 % PEG 400 in physiological saline), was administered at 8 mg/kg early in the morning (between 8 and 10 a.m.) without anesthesia. Mice were monitored for signs of pain or distress during the time between injection and euthanasia (at the earliest time of 15 min and the latest at 8 h after injection) and sacrificed by cervical dislocation for blood and brain collection. Brain and plasma were immediately frozen at -80 °C for pK analysis. iPEPCK-2 was extracted from plasma and homogenate brain in PBS with acetonitrile, in the presence of 1 M DTT and quantified by HPLC/UV. The solid phase was C18 RP column (5 m, 20 × 0.4 cm; Kromasil 100; Teknokroma) and the mobile phase consisting in a 0.05 M KH_2PO_4 (45%): acetonitrile (55%). The elution time of iPEPCK-2 was 3.7 min, and it was detected at 290 nm. The assay had a range of 0.125–5 μg/mL. Calibration curves were constructed by plotting the peak area ratio of analyzed peak against known concentrations.

iPEPCK-2 plasma concentrations *versus* time curves for the mean of animals were analyzed by a non-compartmental model based on statistical moment theory using the "PK Solutions" computer program. The pharmacokinetic parameters calculated were the area under the concentration *vs* time curve (AUC), which was calculated using the trapezoidal rule in the interval 0–8 h, and the half-life ($t_{1/2\beta}$), which was determined as ln2/β (β was calculated from the slope of the linear, least-squares regression line). The C_{max} and T_{max} were read directly from the mean concentration curves.

2.10. Xenograft subcutaneous models

Two subcutaneous tumor xenograft models were generated by injecting transformed cells in both flanks of female 5–6-week-old BALB/c nude mice (at least n = 5 per group, given the large dispersion on the size of the tumors grown in flanks of immunocompromised mice). In the first model, 1×10^6 HEK-293 cells were injected per flank; whereas on the colon carcinoma model, 5×10^6 SW-480 cells were utilized. Handling for the injections was in the absence of anesthesia or analgesia, and no signs of distress or pain were evident afterwards. Mice were monitored for signs of cancer disease, pain or distress during the time of the experiment and sacrificed by cervical dislocation and removed from the experiment if so advised by the Veterinarian in charge of the animal facility. When the tumors grew enough to be measured, mice were randomly split in two groups, and kept in grouped cages of at least 4 animals per cage. One group received a daily (between 8 and 10 a.m.) IP injection with 8 mg/kg of iPEPCK-2 without analgesia. No signs of distress or pain resulted from the injection. The other group was treated with vehicle (20% PEG400. 5% DMSO, H_2O) instead, following the same therapeutic regimen. The tumors were measured, and mice weighted twice a week. After 15 days (SW-480) or 24 days (HEK-293), mice were euthanized by cervical dislocation, and the tumors and organs processed for further analysis.

2.11. Histopathology

Tissues were fixed twelve hours in 4% Paraformaldehyde Buffer after trimming them into appropriate size and shape and placing them in histology cassettes. They were then dehydrated following an ethanol gradient process and embedded in paraffin. Tissue sections (3–4 μM) were stained with Harris hematoxylin & eosin stain for morphological analysis.

2.12. Statistics and data analysis

Cohort size (greater than 5 per group) for all experiments were based on statistical power calculations using GraphPad Prizm. Animals studies were not replicated to avoid utilization of additional animals and given that a sufficient number of animals in each group was utilized to provide good statistical power. All data was analyzed for variance and represented as means ± standard error of the mean (SEM) for at least 3 independent experiments with 3–8 replicates per group. One-way analysis of the variance (ANOVA) was utilized to unmask significant differences, and a Sidak multiple comparison test was used when indicated in assays containing more than two group comparisons. Minimum statistical significance was set at $*p < 0.05$.

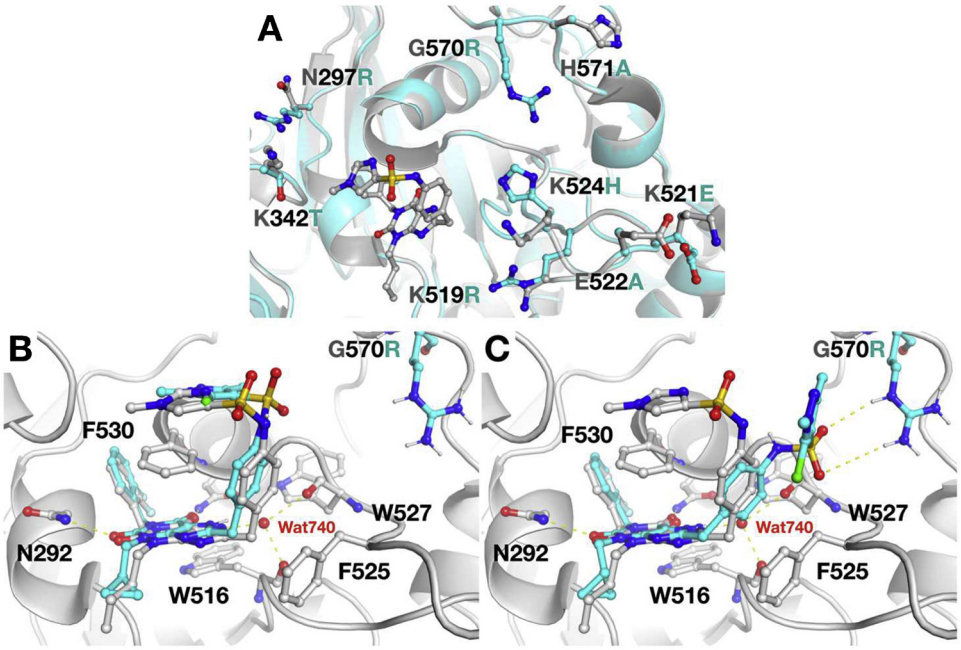

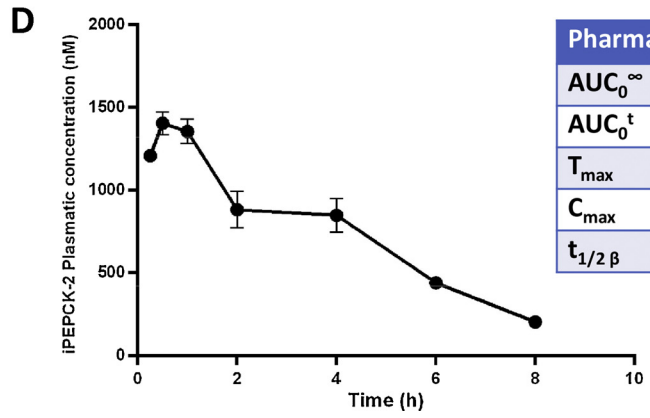

Pharmacokinetic parameters	
AUC_0^{∞}	238.2 µg*min/ml
AUC_0^{t}	218.7 µg*min/ml
T_{max}	0.5 h
C_{max}	0.86 µg/ml
$t_{1/2\,\beta}$	1.8 h

Fig. 1. Docking and pharmacokinetics (A) Superposition of human PEPCK-C (PDB ID: 2GMV; grey) and human PEPCK-M (in cyan). Changes in residue content at/around the binding pocket are highlighted, and the crystallographic pose of the inhibitor (N-(4-{[3-butyl-1-(2-fluorobenzyl)-2,6-dioxo-2,3,6,7-tetrahydro-1H-purin-8-yl]methyl}phenyl)-1-methyl-1H-imidazole-4-sulfonamide) is shown as sticks. (B, C) Representative docking poses for iPEPCK-2 (in cyan) in the GDP-binding site. The reference crystallographic protein-ligand complex (PDB ID: 2GMV) is shown in grey. The G570R mutation is highlighted in cyan/blue. Numbering of residues based on the sequence of PEPCK-C. (D) Plasma concentration of iPEPCK-2 at various times (15 min to 8 h) after an intraperitoneal administration of 8 mg/kg, as determined by HPLC/UV-VIS at 290 nm. Basic pharmacokinetic parameters are shown (in-chart panel). Data are means ± SEM (n = 4 in each time point for panel D).

3. Results

3.1. iPECK-2 is a potent on-target inhibitor of PEPCK-M with drug-like characteristics

We prepared and fully characterized (see Methods S1) 5-chloro-*N*-{4-[(3-(cyclopropylmethyl)-1-(2-fluorobenzyl)-2,6-dioxo-2,3,6,9-tetrahydro-1*H*-purin-8-yl)methyl]phenyl}-1,3-dimethyl-1*H*-pyrazole-4-sulfonamide (iPEPCK-2; chemical structure in Fig. S1 in Supporting Information) previously described by Pietranico et al. as a potent inhibitor of PEPCK-C [13].

The PDB structure of human PEPCK-C co-crystallized with a GTP-competitive inhibitor (PDB ID: 2GMV), was used as template to generate the structural model of PEPCK-M, taking advantage of the high sequence identity (69 %) and similarity (82 %) between the two isoforms (see Fig. S2 in Supporting Information). Superposition of the reference PDB structure for PEPCK-C, and the homology model built for PEPCK-M is shown in Fig. 1A. This comparison highlighted the preservation of residues in the binding pocket, and a few differences in residues around the edges of the pocket filled by the crystallographic ligand. Among them, K342T, K524H, K529R, and G570R are located at less than 8 Å from the ligand in the GDP-binding site. Autodock4 was used to dock iPEPCK-2 in the GDP-binding site of PEPCK-M. The two most interesting docking poses found for iPEPCK-2 are reported in Fig. 1B and C. The xanthine moiety is stably placed in a sub-cavity surrounded by N292, W516, F525, W527, and F530. The two oxygen atoms participate in hydrogen-bonding interactions with N292 and N533. Water-mediated polar interactions are also observed between the protonated nitrogen of the xanthine scaffold and the backbone oxygens of W527 and W516. The 2 F-benzene is inserted in a subpocket and stabilized by hydrophobic interactions with L293 and M296 (not shown). Two different orientations were, however, found for the pyrazole-4-sulfonamide moiety. In one case (Fig. 1B), this fragment matches the arrangement found in the crystallographic ligand in 2GMV, which involves the stacking of the pyrazole ring with F530. In the second case (Fig. 1C), a key difference in the vicinity of the binding pocket is the sulfonamide group interaction exclusive for the guanidine moiety of R570 in PEPCK-M (G570 in PEPCK-C).

Before evaluating iPEPCK-2 as an on-target inhibitor of PEPCK-M *in vitro* and *in vivo*, we performed basic ADMET and pharmacokinetic studies. *In vitro* ADMET assays showed good human and murine microsomal stability with a half-life of 119 min and a 75% of compound

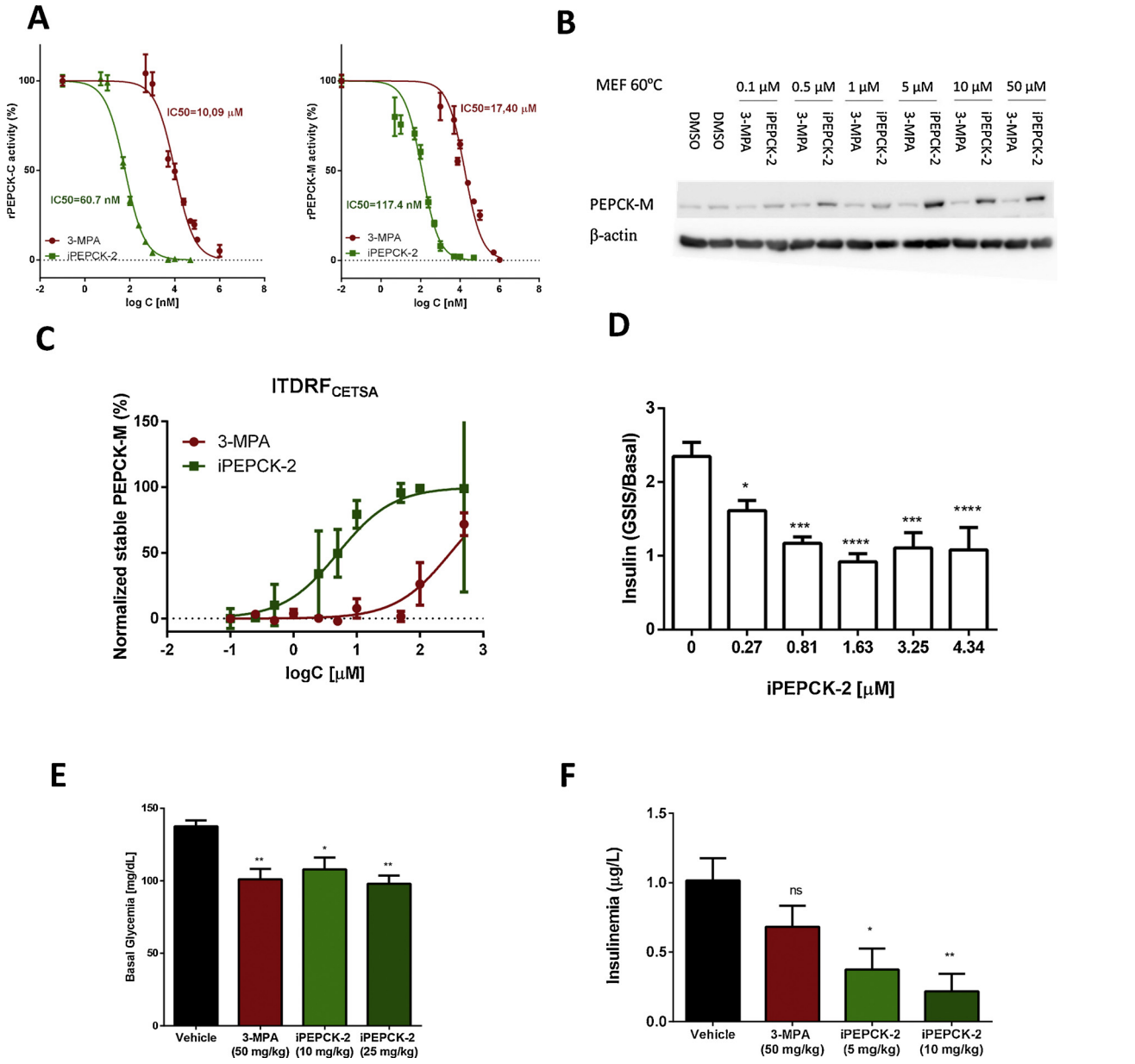

Fig. 2. iPEPCK-2 activity and target engagement. (A) Inhibition of purified human recombinant PEPCK-C and PEPCK-M by iPEPCK-2 and 3-MPA. IC_{50} for both isoforms are noted for every plot. (B) Representative Cellular Thermal Shift Assay (CETSA) at varying concentrations of inhibitors. PEPCK-M specific signal is detected by western blot in MEF cell extracts after 30 min incubation with different concentrations of 3-MPA and iPEPCK-2, prior to thermal treatment at 60 °C. (C) Calculated isothermal dose response fingerprint ($ITDRF_{CETSA}$) for both inhibitors. (D) Effects of iPEPCK-2 and 3-MPA on INS1 glucose-stimulated insulin production shown as a ratio of insulin concentration measured in the presence of 20 mM over 3 mM glucose. (E) Basal glycemia 5 h after an intraperitoneal administration of 3-MPA (50 mg/kg), iPEPCK-2 (10 or 25 mg/kg) or vehicle under fasting conditions. (F) Plasma Insulin at 15 min after an administration of a glucose bolus (2 g/kg) in the presence of inhibitors and vehicle. Data are means ± SEM (3 independent experiments were performed with n ≥ 3 in experiments shown in panels A and D; n ≥ 2 in experiments shown in panels B and C; n = 6 in experiments shown in panels E and F). A one-way Anova and a Sidak multiple comparison test was used. Statistical significance at *p < 0.05, **p < 0.01, ***p < 0.001 *vs* vehicle control.

remaining after 60 min in mice microsomes, predicting good *in vivo* pharmacokinetics (see Table S1 in Supporting Information). This was confirmed in murine *in vivo* pharmacokinetics studies with plasma concentrations of iPEPCK-2 measurable after 15 min of administration and maintained for 8 h, with a C_{max} (0.86 µg/mL or 1405 nM) at 30 min and $t_{1/2\beta}$ at around 2 h (Fig. 1D). The narrow differences in AUC_0^t and AUC_0^∞ showed complete exposure and good bioavailability of iPEPCK-2 after intraperitoneal administration in the described conditions. iPEPCK-2 was not found in the brain at the working concentrations, suggesting that the compound did not cross the blood brain barrier. We classified iPEPCK-2 as to have uncertain BBB permeation based on data from *in vitro* PAMPA assays (Pe value of 2.6 ± 0.2; see Table S2 in Supporting Information). No additional warning on toxicity were measured on cell viability assays in human MRC-5 fibroblast at 100 µM or on hERG inhibition (see Table S3 in Supporting Information). Finally, we found that iPEPCK-2 has acceptable solubility (61 µM at 37 °C in 1% DMSO, 99% PBS).

The inhibitory capacity of iPEPCK-2 and 3-MPA, was assayed on human recombinant PEPCK-C and PEPCK-M produced in our laboratory (Fig. 2A). iPEPCK-2 was the most potent inhibitor for both isoforms with an IC_{50} of 117.4 nM for PEPCK-M and 60.7 nM for the cytosolic isoform. The capacity to reach the mitochondria and inhibit PEPCK-M was confirmed using a cellular thermal shift assay (CETSA) (Fig. 2B). All inhibitors tested thermally stabilized PEPCK-M in live MEF cells,

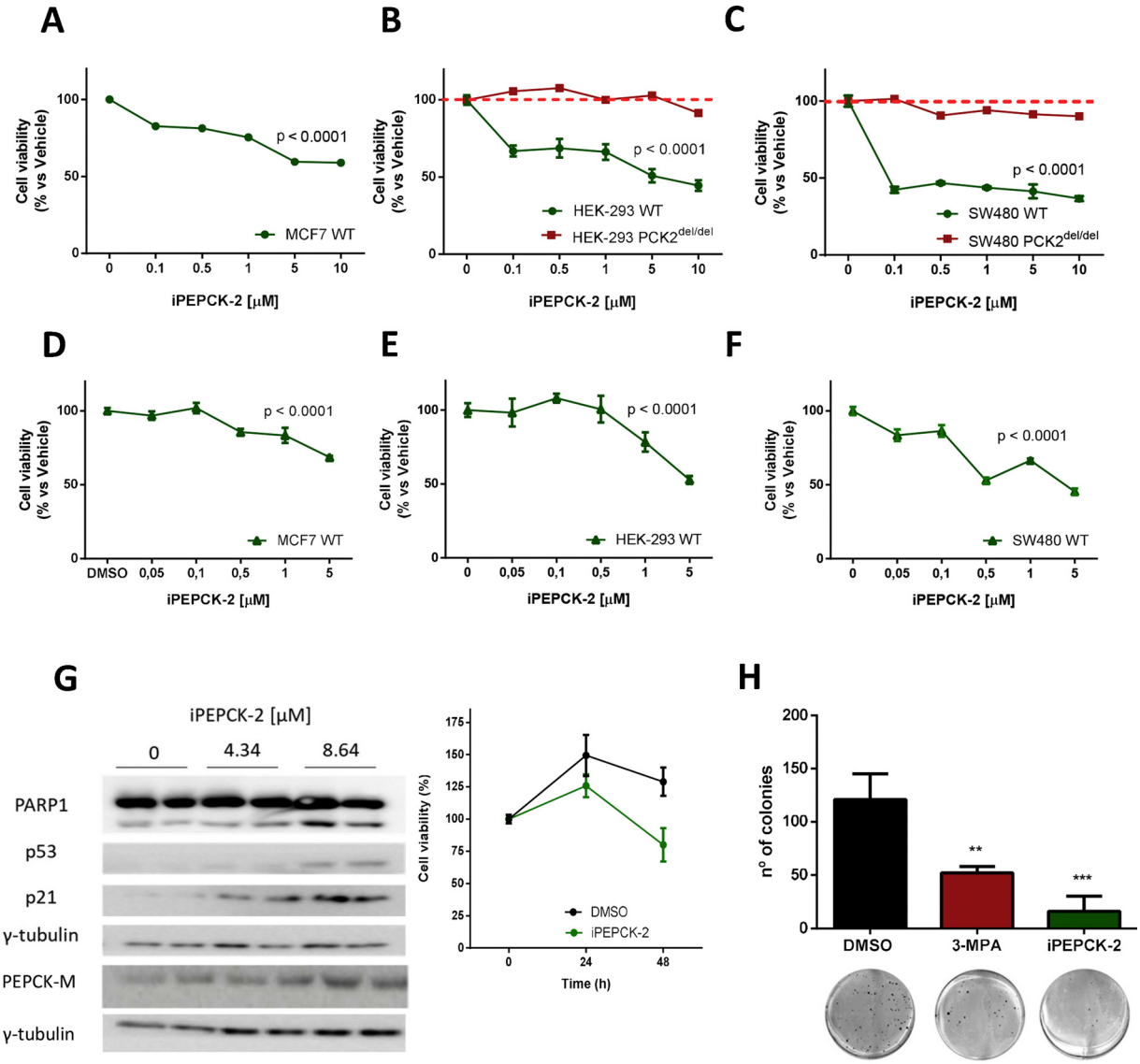

Fig. 3. Target selectivity and validation in cultured cancer cells. (A–C) Proliferation of MCF7 (A), HEK-293 wild-type and PCK2$^{del/del}$ (B) and SW-480 wild-type and PCK2$^{del/del}$ (C) after a 72-h treatment with iPEPCK-2. (D-F) Cell survival of wild-type MCF7 (D), HEK-293 (E) and SW-480 (F) in glucose-free media after 48 -hs of treatment with iPEPCK-2. (G) Survival (right panel) and mechanism of apoptotic cell-death (left panel) because of iPEPCK-2 treatment in limiting glucose conditions in HCT-116 wild-type cells. (H) Colonies formed when MCF7 cells were seeded in soft agar and treated with PEPCK-M inhibitors (5 μM) for 2 weeks. Representative photographs of 2-week colonies formed in each treatment group are noted. Data are means ± SEM (3 independent experiments were performed with n = 5 in each experiment shown in panels A thorough F, and plot shown in panel G; 2 independent experiments were performed with n ≥ 2 to produce the representative western blot shown in panel G; 3 independent experiments were performed with n ≥ 3 to produce panel H plot and representative photographs). A one-way Anova and a Sidak multiple comparison test was used. Statistical significance at *p < 0.05, **p < 0.01, ***p < 0.001 *vs* vehicle control.

which express exclusively the PEPCK-M isoform [7], confirming the accessibility to, and the binding and interaction with PEPCK-M in the mitochondrial matrix by both inhibitors. The capacity of the inhibitors to stabilize PEPCK-M against thermal denaturation was dose-dependent. A quantitative evaluation of target engagement at various doses of inhibitor demonstrated that iPEPCK-2 had the highest affinity for PEPCK-M, as compared to 3-MPA ($ITDRF_{cetsa}$, dose of inhibitor achieving a 50% stabilization at 60°C, was 5.08 *vs* 303.9 μM for iPEPCK-2 and 3-MPA, respectively) (Fig. 2C).

To evaluate the capacity of iPEPCK-2 to inhibit PEPCK-M driven pathways in an *in-cell* assay where PEPCK-C is not present, we took advantage of the role of this isoenzyme relaying glucose metabolism and insulin secretion (GSIS) in pancreatic β-cells or rat insulinoma INS-1, demonstrated using genetic models and oligonucleotides [5]. We therefore characterized iPEPCK-2 inhibition efficiency (EC_{50}) in INS-1 cells by quantifying glucose-stimulated insulin production (GSIS) in the presence of various concentrations of inhibitor. These studies confirmed that iPEPCK-2 treatment inhibited GSIS in a dose-dependent manner with an approximate EC_{50} of 250 nM (Fig. 2D).

To further evaluate the capacity of iPEPCK-2 to antagonize PEPCK driven pathways, we assayed hepatic gluconeogenesis and insulin secretion *in vivo*. Hepatic gluconeogenesis in rodents is mainly driven by PEPCK-C [4,6]. In fasted mice, systemic *in vivo* glucose production is assayed in response to a bolus administration of pyruvate. In this setting, glycemia reflects the net contribution of glucose synthesis to glucose homeostasis. iPEPCK-2 (10 and 25 mg/kg) and 3-MPA (50 mg/kg) had a significant negative impact on basal glycemia 5 -hs after administration (Fig. 2E), and over the glycemia excursion observed after the pyruvate bolus (see Fig. S3A–B in Supporting Information), as compared to DMSO treated mice. These data suggest that 3-MPA and iPEPCK-2 inhibit hepatic gluconeogenesis *in vivo*.

Finally, to assess PEPCK-M specific inhibition *in vivo*, we evaluated

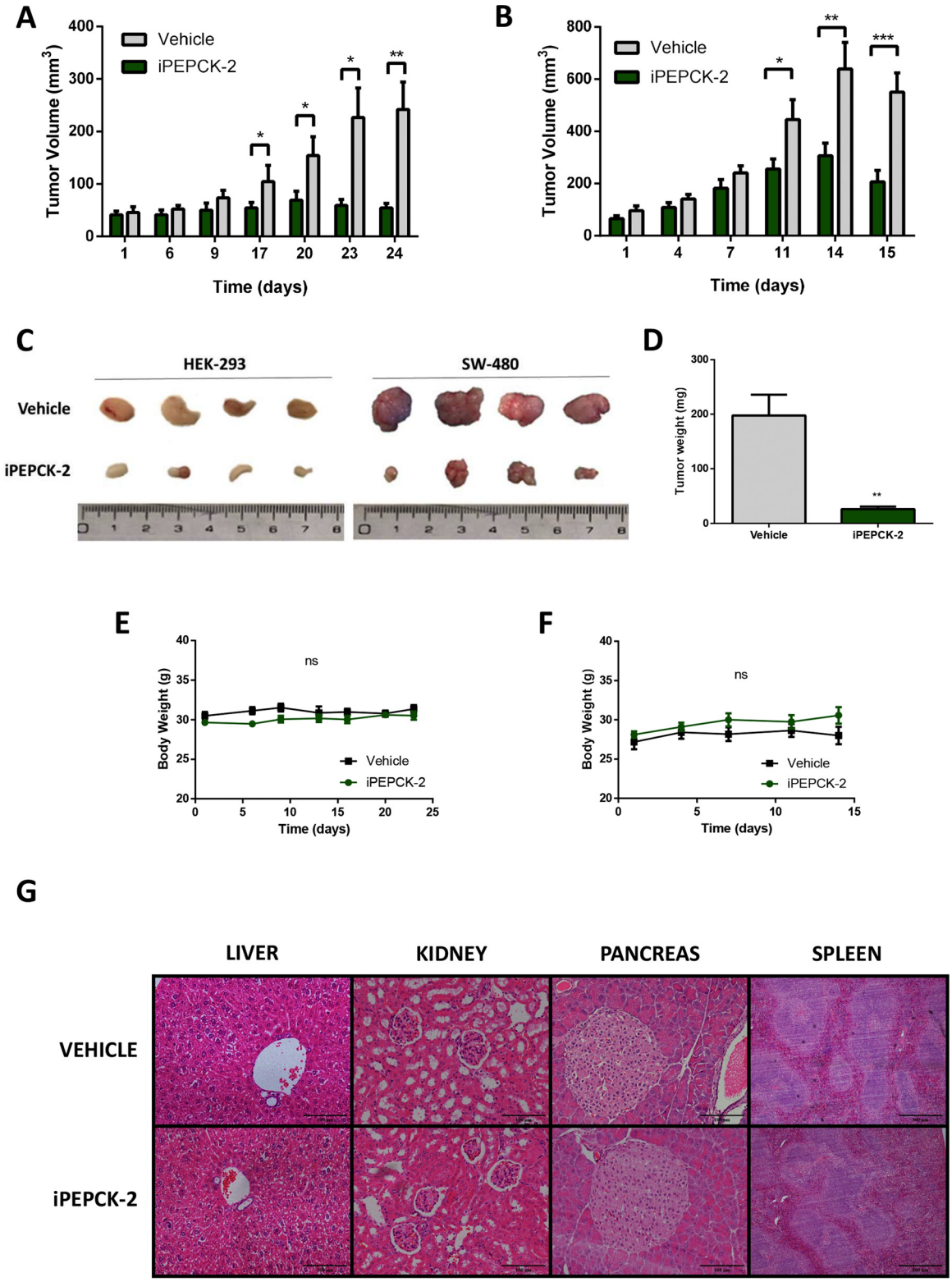

Fig. 4. ***In vivo*** **evaluation of iPEPCK-2 antitumoral activity in two murine subcutaneous xenograft models.** (A–B) Over-the-skin tumor volume ([short length^2 x long length]/2) from HEK-293 (A) and SW-480 (B) cells implanted into the flanks of BALB/C nude mice. Once the tumors grew sufficiently large to be measurable, animals were randomly grouped and daily treated with 8 mg/kg of iPEPCK-2 or vehicle intraperitoneally. (C) Representative tumor explants are shown. (D) HEK-293 tumors were weighted at the time of sacrifice. (E–F) Animals growing HEK-293 (E) and SW-480 (F) tumors were weighted periodically over the course of the experiment to detect health-related issues. (G) Representative H&E stained sections from various organs (liver, kidney, pancreas and spleen) to show no sign of apparent toxicity. Data are means ± SEM (n = 5 in each experiment shown in panels A thorough F, except for HEK-293 control group containing n = 3 due to animal issues upon tumor over growth; at least n = 3 sections per tumor were produced and examined to produced panel G and representative photographs).

pancreatic β-cell secretion of insulin in response to an intraperitoneal glucose bolus (IGTT). In this assay, glucose-stimulated insulin secretion generates a peak of plasma insulin concentration after a 2 g/kg glucose bolus is administered intraperitoneally in fasted mice. The animals for this test were submitted to inhibitor treatment just 2 -hs before the glucose bolus to avoid significant effects on basal glycemia (Fig. S3C). Treatment with iPEPCK-2 (10 mg/kg) showed a blunted insulin secretion response to glucose as compared to vehicle and 3-MPA (50 mg/kg) treated mice (Fig. 2F). The dose of iPEPCK-2 utilized confirmed that a single intraperitoneal administration of 8–10 mg/kg was enough to achieve efficacy, as supported by pharmacokinetic data (Fig. 1D) showing plasma concentrations of the drug 8 h post-administration always above the approximate EC_{50} calculated for insulinoma cells. 3-MPA reduction of insulin secretion was not statistically significant, suggesting inefficient target engagement as compared to the successful targeting of liver PEPCK-C demonstrated in the previous experiment (Figs. 2E and S3A-B; gluconeogenesis), or a problem to successfully reach pancreatic β-cells. Therefore, iPEPCK-2 targets PEPCK-M *in vivo* in pancreas β-cells, but it is non-selective for the mitochondrial isoform (Fig. 2D–F).

3.2. Preclinical validation of iPEPCK-2 and its target in cancer indications

PEPCK-M is present in pancreatic β-cells, tumor cells [5,7] and progenitors (neuroprogenitor cells [8];), hinting at a possible role for the enzyme in cancer cell metabolic adaptations. Indeed, we and others have validated this enzyme as a cancer target in several genetic models, both *in vitro* and *in vivo* [7,10–12]. Therefore, we aimed to validate iPEPCK-2 in a preclinical cancer indication by assaying viability, invasion, and *in vivo* tumor growth using epithelial MCF7 and HEK-293, and human colon carcinoma cells from epithelial HCT-116 and mesenchymal SW-480 origins. These cell lines express high levels of PEPCK-M and the cytosolic isoform is undetectable (Expression Atlas RNAseq geneset E-MTAB-2770). To evaluate target selectivity and test for off-target events, the impact of iPEPCK-2 in tumor cell viability was also assessed in cells lacking PEPCK-M using knock-out clones of HEK-293 (HEK-293-PCK2$^{del/del}$) and SW-480 (SW-480-PCK2$^{del/del}$) previously generated in our laboratory using CRISPR*Cas9* (Fig. S4, and Hyrossova et al, publication pending).

Treatment with iPEPCK-2 significantly reduced DMSO-normalized viability in wild type MCF7, HEK-293, and SW-480 cells grown in optimal culture conditions (Fig. 3A–C). Changes in viability with iPEPCK-2 were dependent on the presence of PEPCK-M, since when tested in HEK-293-PCK2$^{del/del}$ and SW-480-PCK2$^{del/del}$ cells the compound did not show additional effects beyond those consequence of knocking-out the gene, at least within the range of iPEPCK-2 (0.1–10 μM) utilized in the validation assays. All in all, these data suggest target selectivity and a no significant off-target effects (Fig. 3A–C).

PEPCK-M participates in pro-survival mechanisms engaged by nutrient limitation through the ER-stress pathway, and silencing the gene exacerbates ER-stress-mediated apoptosis [7]. Consistently, PEPCK-M inhibitors decreased the DMSO-normalized viability of cancer cells coping with nutrient stress after 48 h of glucose deprivation (Fig. 3D–F). These effects mimicked the consequences of PEPCK-M loss in HEK-293-PCK2$^{del/del}$ and SW-480-PCK2$^{del/del}$ when compared to their wild-type counterparts (Hyrossova et al, publication pending). The inhibition of PEPCK-M with iPEPCK-2 also copied the response observed in genetic models by Mendez-Lucas et al, as iPEPCK-2 compromised growth and enhanced PARP cleavage and apoptosis upon activation of p53 and p21 in HCT-116 cells in limiting glucose conditions (Fig. 3G). A physiologically relevant model to evaluate the response of cancer cells to diffusion constraints in nutrient supply is colony formation and growth in an anchorage-independent manner. Anchorage-independent growth during invasion and metastatic processes is also an important hallmark in cancer progression. iPEPCK-2 and 3-MPA treatment significantly reduced MCF7 colony formation when seeded in soft agar (Fig. 3H), although 3-MPA was less effective. Similar results were obtained in HCT-116 (data not shown).

We next examined the capacity of inhibitor iPEPCK-2 to blunt tumor growth in two xenograft murine models. Colon carcinoma (SW-480) or transformed kidney embryonal cells (HEK-293) cells were subcutaneously injected in both flanks of athymic mice and allowed to grow until measurable at the surface of the skin. Mice were randomly split into two different groups treated with a daily intraperitoneal injection of 8 mg/kg of iPEPCK-2 or vehicle for a variable period depending on the biological features of each model. Whereas vehicle treatment did not impede tumor growth, iPEPCK-2 treatment halted tumor growth in either xenograft mode, as measured both by continuous evaluation of volume under-the-skin and final weight (Fig. 4A–D). Histopathology of tumor samples from treated or untreated breast carcinoma or colon carcinoma tumors showed marked differences in both groups, with prominent necrosis observed in iPEPCK-2 treated tumors and reduced tumor cell burden overall (quantified in Fig. S5A–E in Supporting Information). Furthermore, no signs of apparent toxicity were observed upon close inspection; specifically, there was no macroscopic affectation of the liver or the spleen, weight loss (Fig. 4E and F), lethargy or major health-related disturbance apparent on mucosae or skin quality. The histopathological analysis of eosin and hematoxylin stained tissue sections from different organs did not show any sign of toxicity (Fig. 4G).

4. Discussion

The dominant role of hepatic PEPCK-C in the imbalance of glucose homeostasis in obese and diabetic patients [3] has justified the development of several low-potency compounds targeting this enzyme in the past 30–40 years (Jomain Baum et al., 1976), including compounds that mimic OAA [20], or analogs of 3-MPA [21]. In 2007, Pietranico et al. [13] described a series of C-8 modifications of xanthine derivatives with increased potency against PEPCK-C in the context of diabetes indications, although, it is unclear whether these compounds are being further pursued.

Because of recent findings on the mitochondrial isoform, PEPCK-M, and its impact in cancer biology [22], development of compounds targeting this pathway for cancer indications has gained new interest. Based on the sequence identity (69%) and similarity (82%), we hypothesized that PEPCK-C inhibitory compounds described by Pietranico et al. (synthesized here as iPEPCK-2) would properly dock onto PEPCK-M, especially since the binding pocket is mostly preserved. Consistently, the two orientations predicted from docking calculations for the benzyl-4-sulfonamide-5-chloro-1,3-dimethyl-1*H*-pyrazole moiety matched the arrangement found in the crystallographic ligand in 2GMV (on PEPCK-C), which is characterized by the stacking of the pyrazole ring with the benzene moiety of F530, with a minor deviation on the second case due to the interaction of the sulfonamide group with the guanidine moiety of R570. Notably, this interaction is enabled by the replacement of G570 in PEPCK-C by R in PEPCK-M, it being one of the few differences found close to the binding pocket. These data unveil the possibility to explore selectivity toward PEPCK-M in the future by exploiting the differences in residues located at the edge of the binding site in the two isoforms.

Activity assays on recombinant PEPCK-M and PEPCK-C from human confirmed cross-inhibition by inhibitor iPEPCK-2. IC_{50} values obtained in PEPCK-C activity assays were in the expected range [13], and 2-orders of magnitude lower than 3-MPA [19,23]. Similar potencies were found for PEPCK-C and PEPCK-M, as can be realized from the resemblance of the binding pockets in the two isoforms and the results from docking calculations. Furthermore, thermal stabilization of PEPCK-M by iPEPCK-2 presented similar kinetics to PEPCK-C in *in-cell* conditions, ruling out that compartmentalization of the mitochondrial isoform presents a relevant hinder to target engagement. Mitochondrial targeting was functionally demonstrated in rat insulinoma cells (INS-1) by

asserting the capacity of inhibitor iPEPCK-2 to interfere with glucose-stimulated insulin secretion in a dose-dependent manner. In the same model, Stark et al. [5] had shown an identical response using siRNA-driven down-regulation of PCK2 mRNA, identifying a role for this protein in the coupling mechanism responsible for insulin secretion secondary to the metabolism of glucose. Similarly, effective targeting of PEPCK-M *in vivo* by iPEPCK-2 was corroborated by a higher than 50% impact on short-term insulin secretion in fasted mice after an intraperitoneal administration of glucose, demonstrating the bioavailability of iPEPCK-2. These data provided the first evidence of PEPCK-M druggability in this physiological context, and an initial assessment of iPEPCK-2 usefulness in a pre-clinical setting, as prior data using oligonucleotide silencing of PEPCK-M in rats had not provided evidence for direct action on the healthy pancreas [24]. Overall, PEPCK-M molecular and functional target engagement was appropriately demonstrated both *in vitro*, *in-cell and in vivo*.

Once druggability was confirmed, iPEPCK-2 was further validated as an anticancer strategy starting off by contrasting the consequences of pharmacological inhibition and genetic ablation using PCK2-KO models produced using CRISPR/*Cas9*. Importantly, PCK2-KO cells also allowed us to demonstrate that the effects on tumor cell growth are PEPCK-M dependent, since iPEPCK-2 was ineffective at altering growth rates at concentrations utilized throughout the study in the absence of PEPCK-M, discarding off-target effects with consequences on tumor biology. In HEK-293 and SW-480 PEPCK-M inhibition by iPEPCK-2 mimicked genetic down-regulation of PEPCK-M by reducing cell proliferation and increasing cell death (not shown; Méndez-Lucas et al., 2014). Finally, even though PEPCK-C has been also implicated in metabolic adaptations specifically in melanoma [25], the participation of this isozyme in some of the effects observed here can be ruled-out as all cancer cell lines utilized in the present study have null expression of this isoform (Expression Atlas RNAseq geneset E-MTAB-2770). All-in-all, these data suggest that PEPCK-M is the plausible target for iPEPCK-2 in tumor cells at the concentrations tested.

Its potential as anticancer target resides in the capacity of PEPCK-M to flux glutamine carbons entering the TCA towards the glycolytic pool for the synthesis or serine/glycine, especially under nutrient deprivation, balancing ER stress and increasing cell survival [6,7,10]. This is exemplified in the marked effects observed after PEPCK-M inhibition in anchorage-independent growth in soft-agar, further validating PEPCK-M role in tumor cell metabolism, but also in invasiveness and metastasis. This idea was reinforced *in vivo* where both xenografted tumors stalled by daily administration of iPEPCK-2 as compared with vehicle. Reduced tumor growth confirmed that PEPCK-M expression offers a growth advantage to cancer cells and its inhibition could be a useful anticancer strategy. Pharmacokinetics profile and good bioavailability, with no crossing of the BBB, are good starting grounds for the prospective use of this compound in further clinical testing. Importantly, possible toxicity issues secondary to the inhibition of liver PEPCK-C or pancreatic PEPCK-M were not substantiated in xenografted mice by our limited evaluation of liver histology, weight gain or other health related signs, or changes in plasma insulin or glucose (Fig. S5F–G). Besides, insulin being a well-known growth factor, reduced insulinemia could work in synergy with PEPCK-M inhibition in the tumor. However, a full-blown toxicity assessment will be required to confirm these claims in the future.

In summary, we report here the first validation of a compound that target PEPCK-M as cancer therapeutics. PEPCK-M's crucial role in conditions of glucose limitation are accompanied by the capacity of the pathway to balance ER-stress and amino acid availability to warrant the anticancer effectiveness of iPEPCK-2 in our xenografted models. Hence, PEPCK-M is an exceptional element of the tumor metabolic toolbox to cope with huge variations in nutrient and metabolite availability in the heterogenous tumor. As clinical evidence mounts on the relevance of targeting metabolic enzymes for cancer therapy, it is indeed becoming clearer that pursuing key tumor metabolic hallmarks such as glycolysis or glutamine addiction might not be enough in the long run [26]. Therefore, a double-sword strategy, where PEPCK-M is one of the hits, might be ideal to deal with the demonstrated metabolic flexibility of tumors cells.

Ethics statement for research with animals

All animals were treated according to protocols approved by the Department of the Environment and Housing (DMAH, Generalitat de Catalunya, Spain) in an SPF housing facility located at the IDIBELL/Bellvitge Campus of the University of Barcelona with free access to food and water under a physiological light/dark cycle. No breeding was necessary for the experimental procedures described and all animals were provided by commercial vendors prior to utilization. A one-week adaptation period was allowed before handling for experimental procedures. The research was conducted in compliance with the Spanish legislation on "Protection of Animals Used for Experimental and Other Scientific Purposes" and in accordance with the EU Directive 2010/63/EU on this subject. Besides, the study complies with the ARRIVE guidelines developed by the NC 3Rs and the efforts to reduce the number of subjects used.

Consent for publication

N/A.

Data availability

No datasets were generated in the course of the work presented here, therefore data archival does not apply for this study. All data is available from the authors, and will be archived for a certain amount of time subject to regulations by the Institution (University of Barcelona).

Funding

This work was supported by grants from the Spanish "Ministerio de Economia y Competitividad" (MINECO; BFU2015-66030-R and SAF2017-85869-R) to JCP and FV, respectively (co-funded by the European Regional Development Fund, ERDF, A Way to Build Europe), and with support by Secretariat for Universities and Research of the Department of Business and Knowledge of the Government of Catalonia (2017SGR106, 2017SGR204, 2017SGR449 and 2017SGR1746). We are indebted to the "Ministerio de Educación" FPU and the "Ministerio de Economia y Competitividad" (MINECO) FPI for financial support for PH and JMF, respectively, and to the Generalitat de Catalunya FI program for partial financial support for MA and SRA, and the CERCA Program/Generalitat de Catalunya for their institutional support to IDIBELL.

Author contributions

MA: performed experiments, collected and analyze data. Wrote the manuscript.

JMF: performed experiments, collected and analyze data, and discussed the preliminary draft and provided feedback on general and specific details of the manuscript.

SA: performed experiments, collected and analyze data.

SRA: performed experiments, collected and analyze data.

PH: performed experiments, collected and analyze data, and discussed the preliminary draft and provided feedback on general and specific details of the manuscript.

AF: performed experiments, collected and analyze data, and discussed the preliminary draft and provided feedback on general and specific details of the manuscript.

FV: analyzed data, discussed the preliminary draft and provided feedback on general and specific details of the manuscript.

BP. performed experiments, collected and analyze data, and

discussed the preliminary draft and provided feedback on general and specific details of the manuscript.

MIL: analyzed data, discussed the preliminary draft and provided feedback on general and specific details of the manuscript.

JB: analyzed data, discussed the preliminary draft and provided feedback on general and specific details of the manuscript.

PL: contributed original materials, discussed the preliminary draft and provided feedback on general and specific details of the manuscript

JAC: contributed original materials, discussed the preliminary draft and provided feedback on general and specific details of the manuscript

PMGR: discussed the preliminary draft and provided feedback on general and specific details of the manuscript

CG: discussed the preliminary draft and provided feedback on general and specific details of the manuscript

TG: performed experiments, collected and analyze data.

FJL: analyzed data, discussed the preliminary draft and provided feedback on general and specific details of the manuscript. Conceived of the work.

CE: analyzed data, discussed the preliminary draft and provided feedback on general and specific details of the manuscript. Conceived of the work.

JCP: analyzed data, discussed the preliminary draft and provided feedback on general and specific details of the manuscript. Conceived of the work. Wrote the manuscript.

Declaration of Competing Interest

We declare no conflict of interest, financial or otherwise, in relation to the work described here.

Acknowledgements

We acknowledge the skillful technical support by the Scientific and Technical Services at the University of Barcelona, Bellvitge Campus, and to the “Consorci de Serveis Universitaris de Catalunya” (CSUC) for computational facilities.

Appendix A. Supplementary data

Supplementary material related to this article can be found, in the online version, at doi:https://doi.org/10.1016/j.biopha.2019.109601.

References

[1] H.C. Chang, M.D. Lane, The enzymatic carboxylation of phosphoenolpyruvate. II. Purification and properties of liver mitochondrial phosphoenolpyruvate carboxykinase, J. Biol. Chem. 241 (1966) 2413–2420.

[2] R.C. Nordlie, H.A. Lardy, Mammalian liver phosphoneolpyruvate carboxykinase activities, J. Biol. Chem. 238 (1963) 2259–2263.

[3] R.W. Hanson, A.J. Garber, Phosphoenolpyruvate carboxykinase. I. Its role in gluconeogenesis, Am. J. Clin. Nutr. 25 (1972) 1010–1021.

[4] J. Semakova, P. Hyroššová, A. Méndez-Lucas, E. Cutz, J. Bermudez, S. Burgess, S. Alcántara, J.C. Perales, PEPCK-C reexpression in the liver counters neonatal hypoglycemia in Pck1 $^{del/del}$ mice, unmasking role in non-gluconeogenic tissues, J. Physiol. Biochem. 73 (2017), https://doi.org/10.1007/s13105-016-0528-y.

[5] R. Stark, F. Pasquel, A. Turcu, R.L. Pongratz, M. Roden, G.W. Cline, G.I. Shulman, R.G. Kibbey, Phosphoenolpyruvate cycling via mitochondrial phosphoenolpyruvate carboxykinase links anaplerosis and mitochondrial GTP with insulin secretion, J. Biol. Chem. 284 (2009) 26578–26590, https://doi.org/10.1074/jbc.M109.011775.

[6] A. Méndez-Lucas, J.A.G. Duarte, N.E. Sunny, S. Satapati, T. He, X. Fu, J. Bermúdez, S.C. Burgess, J.C. Perales, PEPCK-M expression in mouse liver potentiates, not replaces, PEPCK-C mediated gluconeogenesis, J. Hepatol. 59 (2013) 105–113, https://doi.org/10.1016/j.jhep.2013.02.020.

[7] A. Méndez-Lucas, P. Hyroššová, L. Novellasdemunt, F. Viñals, J.C. Perales, Mitochondrial phosphoenolpyruvate carboxykinase (PEPCK-M) is a pro-survival, endoplasmic reticulum (ER) stress response gene involved in tumor cell adaptation to nutrient availability, J. Biol. Chem. 289 (2014) 22090–22102, https://doi.org/10.1074/jbc.M114.566927.

[8] Z. Alvarez, P. Hyrossova, J.C. Perales, S. Alcantara, Neuronal progenitor maintenance requires lactate metabolism and PEPCK-M-directed cataplerosis, Cereb. Cortex. 26 (2016), https://doi.org/10.1093/cercor/bhu281.

[9] K. Leithner, A. Triebl, M. Trötzmüller, B. Hinteregger, P. Leko, B.I. Wieser, G. Grasmann, A.L. Bertsch, T. Züllig, E. Stacher, A. Valli, R. Prassl, A. Olschewski, A.L. Harris, H.C. Köfeler, H. Olschewski, A. Hrzenjak, The glycerol backbone of phospholipids derives from noncarbohydrate precursors in starved lung cancer cells, Proc. Natl. Acad. Sci. 115 (2018) 6225–6230, https://doi.org/10.1073/pnas.1719871115.

[10] E.E. Vincent, A. Sergushichev, T. Griss, M.-C. Gingras, B. Samborska, T. Ntimbane, P.P. Coelho, J. Blagih, T.C. Raissi, L. Choinière, G. Bridon, E. Loginicheva, B.R. Flynn, E.C. Thomas, J.M. Tavaré, D. Avizonis, A. Pause, D.J.E. Elder, M.N. Artyomov, R.G. Jones, Mitochondrial phosphoenolpyruvate carboxykinase regulates metabolic adaptation and enables glucose-independent tumor growth, Mol. Cell 60 (2015) 195–207, https://doi.org/10.1016/j.molcel.2015.08.013.

[11] J.-W. Park, S.C. Kim, W.K. Kim, J.P. Hong, K.-H. Kim, H.Y. Yeo, J.Y. Lee, M.S. Kim, J.H. Kim, S.Y. Yang, D.Y. Kim, J.H. Oh, J.Y. Cho, B.C. Yoo, Expression of phosphoenolpyruvate carboxykinase linked to chemoradiation susceptibility of human colon cancer cells, BMC Cancer 14 (2014) 1–24, https://doi.org/10.1186/1471-2407-14-160.

[12] K. Leithner, A. Hrzenjak, M. Trötzmüller, T. Moustafa, H.C. Köfeler, C. Wohlkoenig, E. Stacher, J. Lindenmann, L. Harris, A. Olschewski, H. Olschewski, PCK2 activation mediates an adaptive response to glucose depletion in lung cancer, Oncogene 34 (2015) 1044–1050, https://doi.org/10.1038/onc.2014.47.

[13] S.L. Pietranico, L.H. Foley, N. Huby, W. Yun, P. Dunten, J. Vermeulen, P. Wang, K. Toth, G. Ramsey, M.-L. Gubler, S.J. Wertheimer, C-8 modifications of 3-alkyl-1,8-dibenzylxanthines as inhibitors of human cytosolic phosphoenolpyruvate carboxykinase, Bioorg. Med. Chem. Lett. 17 (2007) 3835–3839, https://doi.org/10.1016/j.bmcl.2007.05.013.

[14] A. Waterhouse, M. Bertoni, S. Bienert, G. Studer, G. Tauriello, R. Gumienny, F.T. Heer, T.A.P. de Beer, C. Rempfer, L. Bordoli, R. Lepore, T. Schwede, SWISS-MODEL: homology modelling of protein structures and complexes, Nucleic Acids Res. 46 (2018) W296–W303, https://doi.org/10.1093/nar/gky427.

[15] G.M. Morris, R. Huey, W. Lindstrom, M.F. Sanner, R.K. Belew, D.S. Goodsell, A.J. Olson, AutoDock4 and AutoDockTools4: automated docking with selective receptor flexibility, J. Comput. Chem. 30 (2009) 2785–2791, https://doi.org/10.1002/jcc.21256.

[16] M. Escós, P. Latorre, J. Hidalgo, R. Hurtado-Guerrero, J.A. Carrodeguas, P. López-Buesa, Kinetic and functional properties of human mitochondrial phosphoenolpyruvate carboxykinase, Biochem. Biophys. Rep. 7 (2016) 124–129, https://doi.org/10.1016/j.bbrep.2016.06.007.

[17] R. Jafari, H. Almqvist, H. Axelsson, M. Ignatushchenko, T. Lundbäck, P. Nordlund, D.M. Molina, The cellular thermal shift assay for evaluating drug target interactions in cells, Nat. Protoc. 9 (2014) 2100–2122, https://doi.org/10.1038/nprot.2014.138.

[19] M. Jomain Baum, V.L. Schramm, R.W. Hanson, Mechanism of 3 mercaptopicolinic acid inhibition of hepatic phosphoenolpyruvate carboxykinase (GTP), J. Biol. Chem. 251 (1976) 37–44.

[20] R.M. Stiffin, S.M. Sullivan, G.M. Carlson, T. Holyoak, Differential inhibition of cytosolic PEPCK by substrate analogues. Kinetic and structural characterization of inhibitor recognition, Biochemistry 47 (2008) 2099–2109, https://doi.org/10.1021/bi7020662.

[21] M.D. Balan, M.J. Mcleod, W.R. Lotosky, M. Ghaly, T. Holyoak, Inhibition and allosteric regulation of monomeric phosphoenolpyruvate carboxykinase by 3-mercaptopicolinic acid, Biochemistry 54 (2015) 5878–5887, https://doi.org/10.1021/acs.biochem.5b00822.

[22] G. Grasmann, E. Smolle, H. Olschewski, K. Leithner, Gluconeogenesis in cancer cells – repurposing of a starvation-induced metabolic pathway? Biochim. Biophys. Acta – Rev. Cancer 1872 (2019) 24–36, https://doi.org/10.1016/j.bbcan.2019.05.006.

[23] J.A. Urbina, C.E. Osorno, A. Rojas, Inhibition of phosphoenolpyruvate carboxykinase from Trypanosoma (Schizotrypanum) cruzi epimastigotes by 3-mercaptopicolinic acid: in vitro and in vivo studies, Arch. Biochem. Biophys. 282 (1990) 91–99.

[24] R. Stark, F. Guebre-Egziabher, X. Zhao, C. Feriod, J. Dong, T.C. Alves, S. Ioja, R.L. Pongratz, S. Bhanot, M. Roden, G.W. Cline, G.I. Shulman, R.G. Kibbey, A role for mitochondrial phosphoenolpyruvate carboxykinase (PEPCK-M) in the regulation of hepatic gluconeogenesis, J. Biol. Chem. 289 (2014) 7257–7263, https://doi.org/10.1074/jbc.C113.544759.

[25] Y. Li, S. Luo, R. Ma, J. Liu, P. Xu, H. Zhang, K. Tang, J. Ma, Y. Zhang, X. Liang, Y. Sun, T. Ji, N. Wang, B. Huang, Upregulation of cytosolic phosphoenolpyruvate carboxykinase is a critical metabolic event in melanoma cells that repopulate tumors, Cancer Res. 75 (2015) 1191–1196, https://doi.org/10.1158/0008-5472.CAN-14-2615.

[26] C. Vernieri, S. Casola, M. Foiani, F. Pietrantonio, F. de Braud, V. Longo, Targeting cancer metabolism: dietary and pharmacologic interventions, Cancer Discov. 6 (2016) 1315–1333, https://doi.org/10.1158/2159-8290.CD-16-0615.

Methods S1

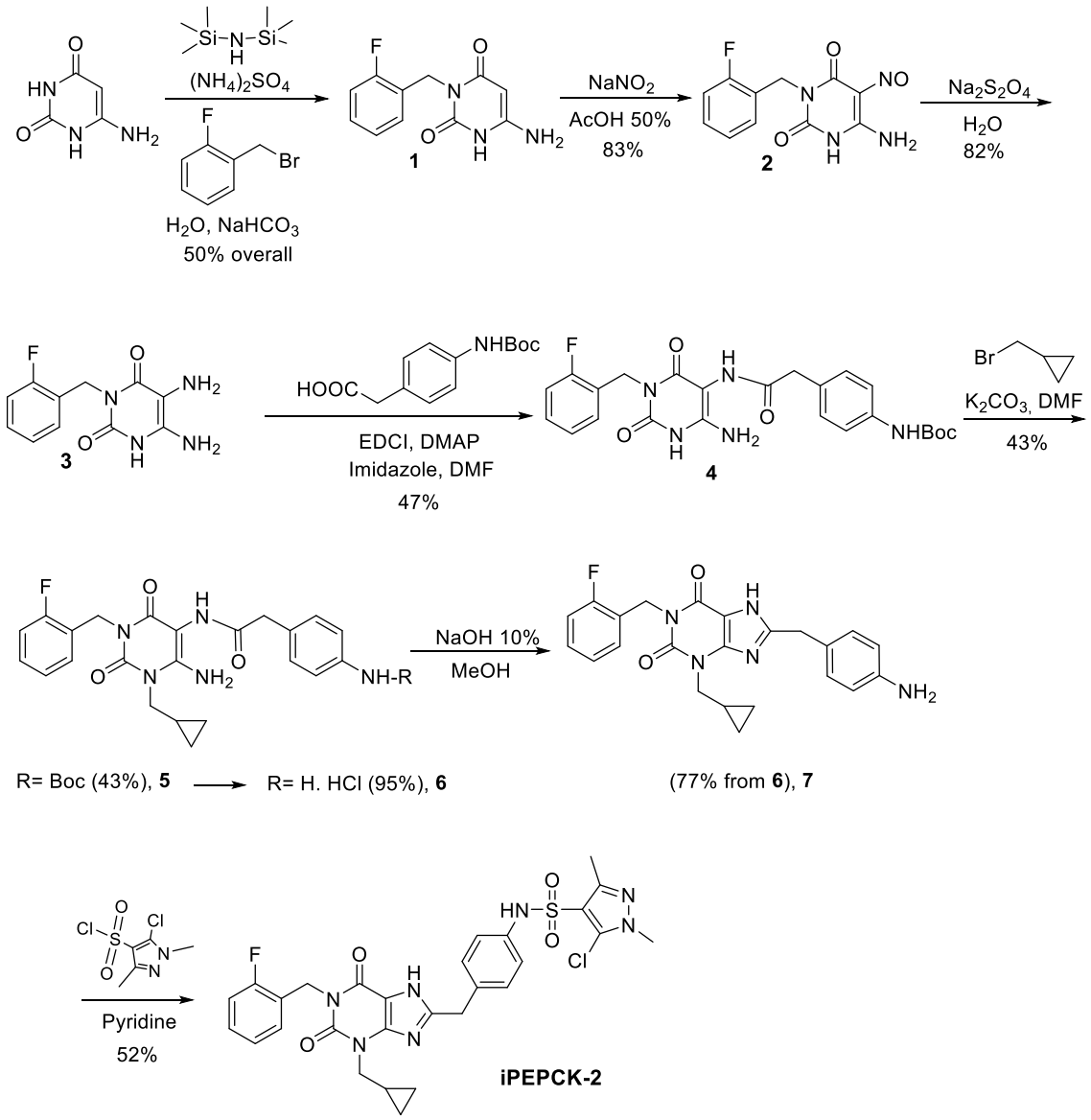

General scheme for the synthesis of iPEPCK-2

General experimental procedure:

NMR spectra were recorded in d_6-DMSO at 400 MHz (^{1}H) and chemical shifts are reported in δ values downfield from TMS or relative to residual d_6-DMSO (2.50 ppm, 77.0 ppm) as an internal standard. Data are reported in the following manner: chemical shift, multiplicity, coupling constant (J) in hertz (Hz), integrated intensity. Multiplicities are reported using the following abbreviations: s, singlet; d, doublet; m, multiplet; and br s, broad signal. Evaporation of solvents was accomplished with a rotary evaporator. Thin layer chromatography was done on SiO_2 (silica gel 60 F254). Chromatography refers to flash column chromatography was carried out on SiO_2 (silica gel 60, SDS, 230–400 mesh). Automatized chromatography was carried out with a Biotage Isolera System Single Channel, standard arm, variable detector (ISO-1SV) using Biotage® SNAP Cartridge, 10 g. Mass spectra were recorded on an LTQ spectrometer using electrospray (ES^+) ionization techniques. Elemental analyses were obtained with a Microanalyzez (EA 1108 CHNSO-O Carlo Erba Instruments) from the service of microanalysis located in Centre d'Investigació i Desenvolupament (CID), Barcelona.

6-Amino-3-(2-fluorobenzyl)pyrimidine-2,4-(1*H*,3*H*)-dione (1)

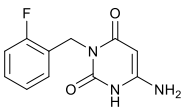

A mixture of 6-aminouracil (2 g, 15.7 mmol), $(NH_4)_2SO_4$ (114 mg, 0.86 mmol) and HMDS (12 mL, 59.5 mmol) under argon atmosphere was heated at reflux for 5 h. Then, the reaction mixture was concentrated *in vacuo* to afford *N*-(trimethylsilyl)-2,6-bis[(trimethylsilyl)oxy]pyrimidin-4-amine as a white solid (4.28 g), which was used directly in the next step without purification. The solid and 2-fluorobenzylbromide (1.7 mL, 13.6 mmol) was heated at 80°C for 2 h. The reaction mixture was cooled to 50°C and then treated with a solution of $Na_2S_2O_3$ (474 mg, 3 mmol) in water (8 mL). The mixture was cooled in an ice bath, and a saturated solution of $NaHCO_3$ was added in small portions until effervescence ceased. The mixture was stirred at 0°C for 30 min and a solid was formed. The solid was collected by filtration and washed with cold water and Et_2O to give **1** (1.85 g, 50% overall yield). Analytical samples were obtained by crystallization from methanol.

^{1}H-NMR (400 MHz, d_6-DMSO) *δ*: 4.62 (s, 1H, CH), 4.91 (s, 2H, CH_2), 6.31 (s, 2H, NH_2), 7.11 (m, 4H, ArH), 10.54 (bs, 1H, NH). The ^{1}H-NMR values are coincident with the described in the literature (ref. 1).

6-Amino-3-(2-fluorobenzyl)-5-nitrosopyrimidine-2,4-(1*H*,3*H*)dione (2)

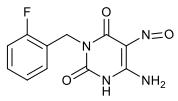

To a solution of compound **1** (2.17 g, 9.2 mmol) in 50% aqueous AcOH (46 mL) heated at 70°C, $NaNO_2$ (1.27 g, 18.4 mmol) was added in small portions over a period of 15 min. The mixture was further stirred for 30 min and then allowed to cool. An orange solid precipitated and was collected by filtration, washed with water, and dried *in vacuo* to give compound **2** (2.03 g, 83%) as an orange solid.

^{1}H-NMR (400 MHz, d_6-DMSO) *δ*: 5.08 (s, 2H, CH_2), 7.31 (m, 4H, ArH), 8.06 (s, 2H, NH_2), 11.49 (bs, 1H, NH). The ^{1}H-NMR values are coincident with the described in the literature (ref. 1).

5,6-Diamino-3-(2-fluorobenzyl)pyrimidine-2,4-(1*H*,3*H*)dione (3)

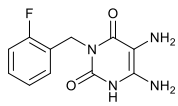

To a solution of **2** (1.39 g, 5.15 mmol) in water (25 mL), $Na_2S_2O_4$ (2.86 g, 16.5 mmol) was added and the mixture was stirred at 80°C for 30 min. Then, the reaction mixture was cooled to 0°C for 10 min and a precipitate appears. The precipitate was collected by filtration, rinsed with cold water and cold Et_2O, and dried *in vacuo* to afford compound **3** (1.07 g, 82%) as a white solid.

^{1}H-NMR (400 MHz, d_6-DMSO) *δ*: 4.96 (s, 2H, NH_2), 5.08 (s, 2H, CH_2), 5.93 (s, 2H, NH_2), 7.11 (m, 4H, ArH), 11.26 (bs, 1H, NH).

4-[*N*-(*tert*-Butyloxycarbonyl)amino]phenylacetic acid

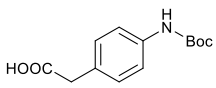

A solution of *p*-aminophenylacetic acid (2 g, 13.2 mmol) in a mixture of dioxane (26 mL) and water (13 mL), and Na_2CO_3 (1.4 g in 13 mL of water) was stirred and cooled in an ice bath. Di-*tert*-butyldicarbonate (3.1 g, 14.6 mmol) was added in one portion, and stirring was continued at room temperature for 4 h. The dioxane was removed *in vacuo* and saturated solution of $NaHSO_4$ was added to the reaction mixture until pH 4. The product was extracted with EtOAc. The organic layers were combined, dried over anhydrous Na_2SO_4, filtered and concentrated *in*

vacuo to give a brown solid which was purified by flash column chromatography (1:1:0.1 EtOAc/hexane/AcOH) to yield 4-[*N*-(*tert*-butyloxycarbonyl)amino]phenylacetic acid as a white solid (3.01 g, 90%).

^{1}H-NMR (400 MHz, d_6-DMSO) *δ*: 1.47 [s, 9H, $(CH_3)_3$], 3.46 (s, 2H, CH_2Ar), 7.11 (d, 2H, ArH), 7.38 (d, 2H, ArH), 9.27 (s, 1H, NHCOO), 12.23 (bs, 1H, COOH). The ^{1}H-NMR values are coincident with the described in the literature (ref. 2).

The synthesis of compounds **4**, **5**, **6**, **7** and **iPEPCK-2** was accomplished following the sequence reported in ref. 3. Spectral data for compounds **4**, **5**, **6**, **7**, and **iPEPCK-2** are reported in this supplementary material.

tert-Butyl {4-[2-((6-amino-3-(2-fluorobenzyl)-2,4-dioxo-1,2,3,4-tetrahydropyrimidin-5-yl) amino)-2-oxoethyl]phenyl}carbamate (4)

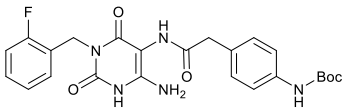

To a solution of compound 4-[*N*-(*tert*-Butyloxycarbonyl)amino]phenylacetic acid (1.36 g, 5.41 mmol) in dry DMF (14 mL) under argon at 25°C, EDCI (980 mg, 5.11 mmol), DMAP (27.5 mg, 0.22 mmol) and imidazole (15.3 mg, 0.22 mmol) were added. The reaction was stirred for 5 min and **3** (1.24 g, 4.95 mmol) was added. The resulting solution was stirred at room temperature overnight. The crude reaction was diluted with water (30 mL) and then acidified to pH 5 with 1 N HCl. The precipitated was collected by filtration, rinsed with water and Et_2O. The solid was crystallised from methanol to furnish **4** (1.12 g, 47%).

^{1}H-NMR (400 MHz, d_6-DMSO) *δ*: 1.47 [s, 9H, $(CH_3)_3$], 3.48 (s, 2H, C*H*$_2$CONH-), 4.94 (s, 2H, CH_2Ar), 6.07 (s, 2H, NH_2), 7.21 (m, 8H, ArH), 8.60 (s, 1H, N*H*COCH$_2$), 9.24 (s, 1H, NHCOO), 10.64 (s, 1H, NH).

tert-Butyl {4-[2-((6-amino-1-(cyclopropylmethyl)-3-(2-fluorobenzyl)-2,4-dioxo-1,2,3,4-tetrahydropyrimidin-5-yl)amino)-2-oxoethyl]phenyl}carbamate (5)

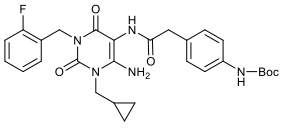

To a solution of **4** (964 mg, 2 mmol) in dry DMF (5 mL) at 25°C under argon, K_2CO_3 (276 mg, 2 mmol) and (bromomethyl)cyclopropane (194 µL, 2 mmol) were added. The

suspension was stirred at 50°C for 48 h and concentrated *in vacuo*. The resulting residue was treated with a 1N HCl (2 mL) and $CHCl_3$ (2 mL) and the phases were separated. The aqueous layer was neutralized and extracted with $CHCl_3$. The organic layers were combined, dried over anhydrous Na_2SO_4, filtered and concentrated *in vacuo* to give an orange oil that was purified by flash column chromatography (100% EtOAc) to yield **5** (460 mg, 43%) as an orange foam.

^{1}H-NMR (400 MHz, d_6-DMSO) δ: 0.11 [m, 4H, CH(C*H*$_2$)$_2$], 0.88 [m, 1H, C*H*(CH$_2$)$_2$], 1.12 [s, 9H, (CH$_3$)$_3$], 3.15 (s, 2H, C*H*$_2$CONH-), 3.50 [m, 2H, C*H*$_2$CH(CH$_2$)$_2$], 4.65 (s, 2H, CH$_2$Ar), 6.37 (s, 2H, NH$_2$), 6.87 (m, 8H, ArH), 8.23 (s, 1H, N*H*COCH$_2$), 8.89 (s, 1H, NHCOO).

N-[6-Amino-1-(cyclopropylmethyl)-3-(2-fluorobenzyl)-2,4-dioxo-1,2,3,4-tetrahydropyrimidin-5-yl]-2-(4-aminophenyl)acetamide, hydrochloride salt (6)

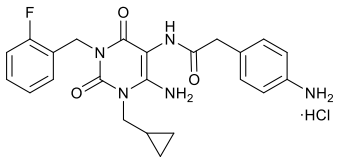

A solution of compound **5** (110 mg, 0.21 mmol) in 4N HCl in dioxane (2.1 mL, 0.02 mmol) was stirred at 25°C for 1 h. The reaction mixture was cooled to 0°C. The resulting solid was collected by filtration, washed with dioxane and Et_2O, and dried *in vacuo* to afford **6** (92 mg, 95%) as a yellow solid, which was used directly in the next step.

8-(4-Aminobenzyl)-3-(cyclopropylmethyl)-1-(2-fluorobenzyl)-3,7-dihydro-1*H*-purine-2,6-dione (7)

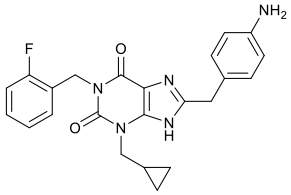

To a solution of **6** (195 mg, 0.41 mmol) in methanol (5 mL) at 25°C a 10% aqueous NaOH (3 mL) was added. The reaction mixture was stirred at 55°C for 4.5 h. The methanol was removed *in vacuo*. Then, the reaction mixture was diluted with CH_2Cl_2 (3 mL) and neutralized with a 1N HCl (pH 6). The layers were separated and the aqueous phase extracted with CH_2Cl_2. The organic layers were combined, dried over anhydrous Na_2SO_4, filtered and concentrated *in vacuo* to give a yellow oil which was purified by flash column chromatography (1:0.05 of CH_2Cl_2/methanol) to yield **7** (133 mg, 77 %) as a pale yellow solid.

^{1}H-NMR (400 MHz, d_6-DMSO) *δ*: 0.38 [m, 4H, CH(C*H*$_2$)$_2$], 1.23 [m, 1H, C*H*(CH$_2$)$_2$], 3.84 [m, 2H, C*H*$_2$CH(CH$_2$)$_2$], 3.86 (s, 2H, C*H*$_2$CNNH), 4.95 (s, 2H, NH$_2$), 5.12 (s, 2H, CH$_2$Ar), 6.49 (d, 2H, *J*= 8.4 Hz, Ar*H*-CHCNH$_2$,), 6.95 (d, 2H, *J* = 8.4 Hz, Ar*H*-CNH$_2$), 7.17 (m, 4H, ArH-F), 13.37 (s, 1H, NH). HRMS calculated for $C_{23}H_{23}ClFN_5O_2$ $[M+H]^+$ 420.1830, found 420.1821.

5-Chloro-*N*-{4-[(3-(cyclopropylmethyl)-1-(2-fluorobenzyl)-2,6-dioxo-2,3,6,9-tetrahydro-1*H*-purin-8-yl)methyl]phenyl}-1,3-dimethyl-4,5-dihydro-1*H*-pyrazole-4-sulfonamide iPEPCK-2.

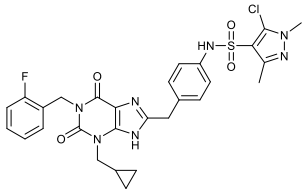

To a solution of **7** (93 mg, 0.22 mmol) in pyridine (1.4 mL) at 25°C, 5-chloro-1,3-dimethyl-1*H*-pyrazole-4-sulfonylchloride (63 mg, 0.28 mmol) was added. The reaction was stirred at room temperature for 24 h. The mixture was concentrated *in vacuo*. The reaction mixture was resuspended in CH_2Cl_2 (2 mL) and washed with 1N HCl. The organic layers were dried over anhydrous Na_2SO_4, filtered and concentrated *in vacuo* to give a yellow oil. Analytical samples were obtained by crystallization from methanol to afford **iPEPCK-2** (71 mg, 52%) as a solid.

^{1}H-NMR (400 MHz, d_6-DMSO) *δ*: 035 [m, 4H, CH(C*H*$_2$)$_2$], 1.23 [m, 1H, C*H*(CH$_2$)$_2$], 2.20 (s, 3H, CH$_3$CNN), 3.69 (s, 3H, C*H*$_3$NN), 3.85 [d, 2H, *J* = 6.8 Hz, C*H*$_2$CH(CH$_2$)$_2$], 3.98 (s, 2H, CH$_2$CNNH), 5.10 (s, 2H, C*H*$_2$Ar), 7.02-7.20 (m, 4H, ArH-F + m, 2H, Ar*H*CHCNH$_2$), 7.30 (m, 2H, Ar*H*-CNH$_2$), 10.38 (s, 1H, NHSO$_2$), 13.46 (s, 1H, NH). HRMS calculated for $C_{28}H_{29}ClFN_7O_4S$ $[M+H]^+$ 612.1598, found 612.1598. Analysis elemental calculated for $C_{28}H_{27}ClFN_7O_2S.2/3CH_3OH$: C, 54.41; H, 4.69; N 15.53; S, 5.08. Found C, 54.72; H, 4.47; N 15.23; S, 4.77 (%).

References:

1.- Hayallah AM, Famulok M (2007). Synthesis of new 1,3,8-trisubstituted purine-2,6-diones and 1,3,6-trisubstituted thiazolo[2,3-*f*]purine-2,4-diones. Heterocycles 74: 369-382. Müller CE, Sandoval-Ramírez J (1995). A new versatile synthesis of xanthines with variable substituents in the 1-, 3-, 7- and 8-positions. Synthesis, 1295-1299.

2.- Rai R, Katzenellenbogen JA. (1992). Guanidinophenyl-substituted enol lactones as selective, mechanism-based inhibitors of trypsin-like serine proteases. J. Med. Chem. 35: 4150-4159.

3.- Foley LH, Huby NJS, Pietranico-Cole SL, Yun W, Dunten PW. (2004). Sulfonamide substituted xanthine derivatives for use as PEPCK inhibitors. WO 2004/074288 A1.

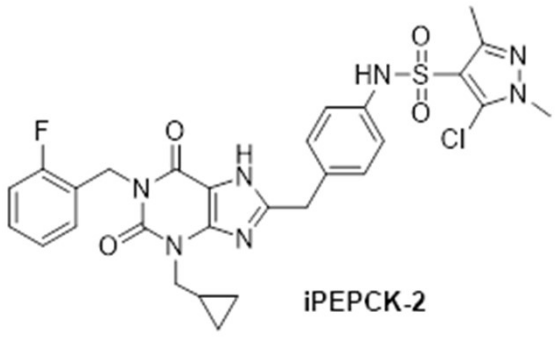

Figure S1. Chemical structure of iPEPCK-2

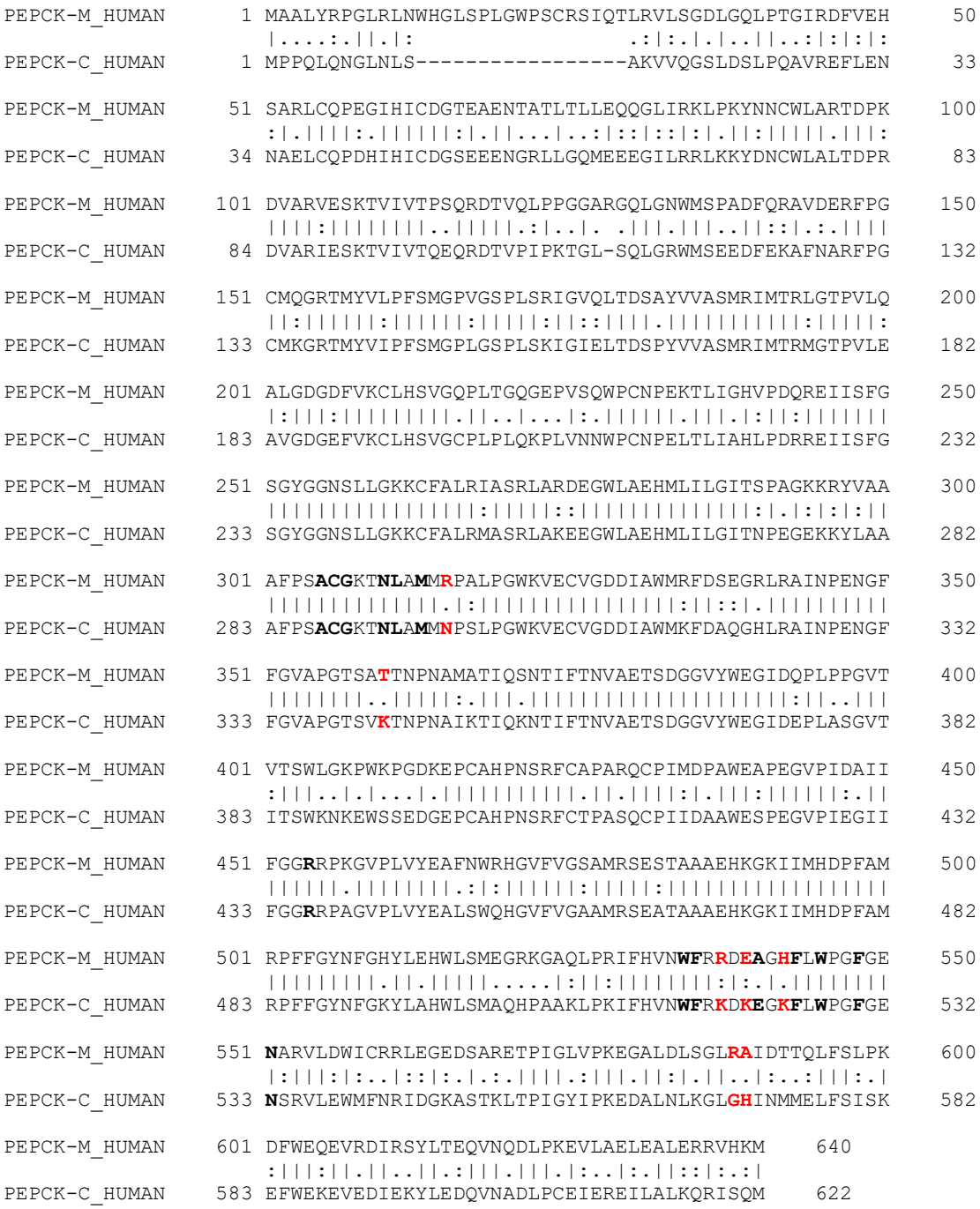

Figure S2. Pairwise sequence alignment for human PEPCK-C (PCK1; UniProtKB: P35558) and PEPCK-M (PCK2; UniProtKB: Q16822). Aminoacidic changes located at / near the inhibitor binding site are highlighted in red.

A

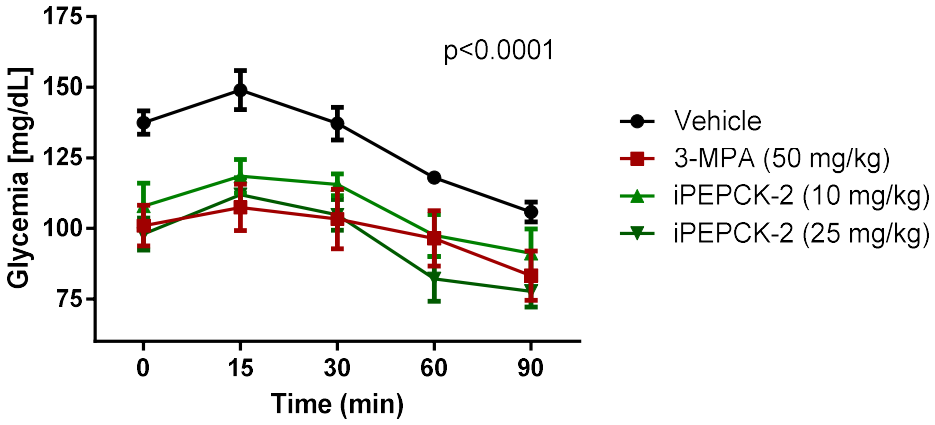

B

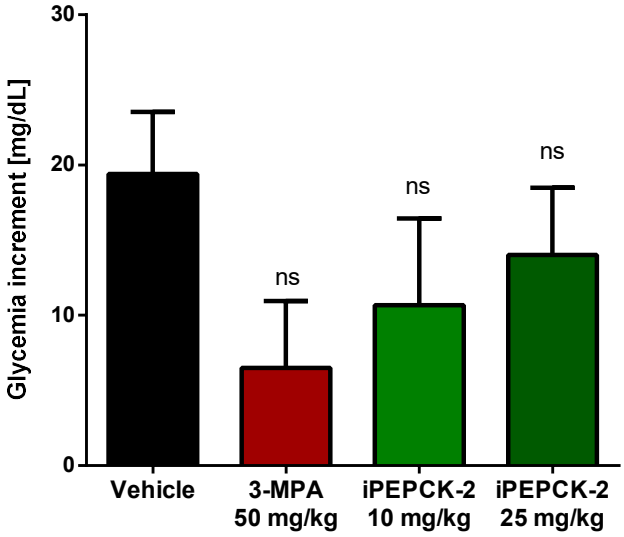

C

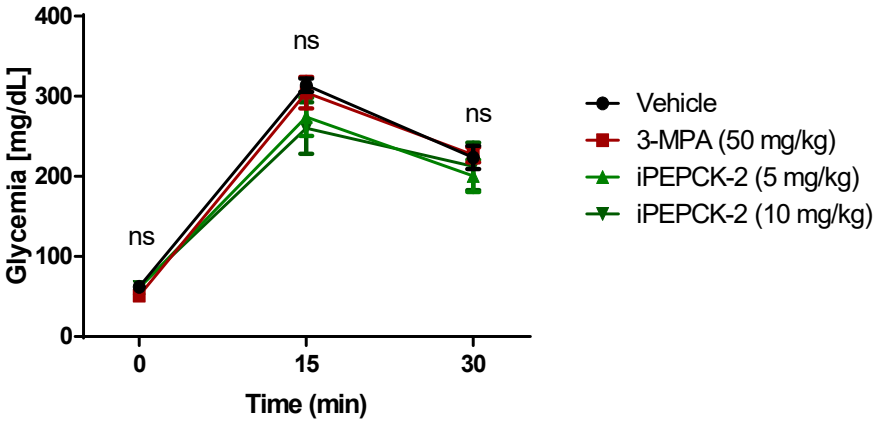

Figure S3. Glycemia excursion after the pyruvate tolerance test and the intraperitoneal glucose tolerance test. Animals were fasted overnight prior to inhibitors administration. The pyruvate bolus was administrated five hours after inhibitors treatment. Glycemia excursion **(A)** and glycemia increment **(B)** 15 min after the pyruvate bolus is shown. **(C)** The glucose bolus was administrated two hours after inhibitors treatment. Data are means ± SEM; n = 6. Statistical analysis was performed by one-way ANOVA with a Sidak multiple comparation test.

A

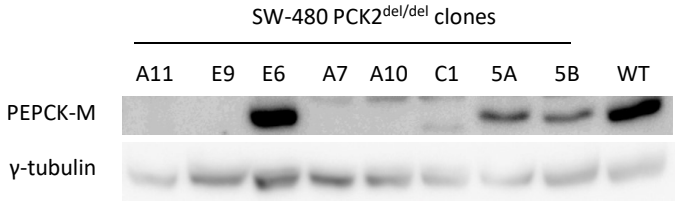

B

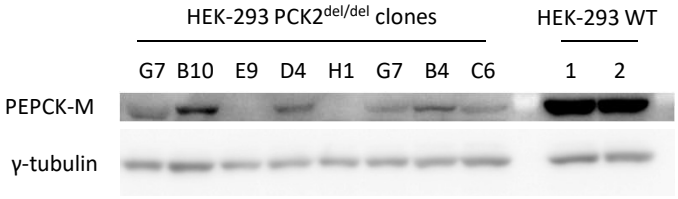

C

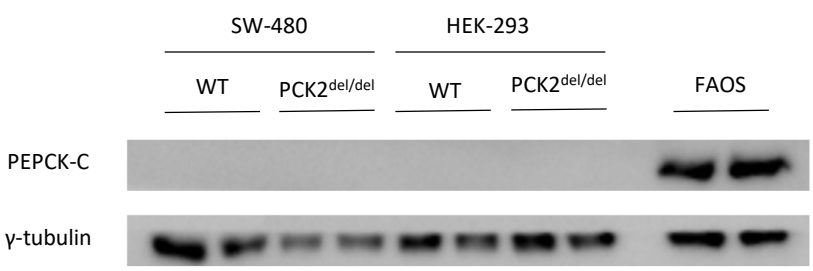

Figure S4. Western blot analysis of PEPCK-M and PEPCK-C levels in HEK-293 and SW-480 wild type and PCK2$^{del/del}$ clones. PEPCK-M levels of different SW-480 **(A)** and HEK-293 **(B)** PCK2$^{del/del}$ CRISPRCas9 clones. SW-480 A7 and HEK-203 H1 clones were the clones used in further experiments. PEPCK-C levels of WT and PCK2$^{del/del}$ clones **(C)**. FAO cell line lysate, which express high levels of PCK1 and PCK2, was added as a positive control.

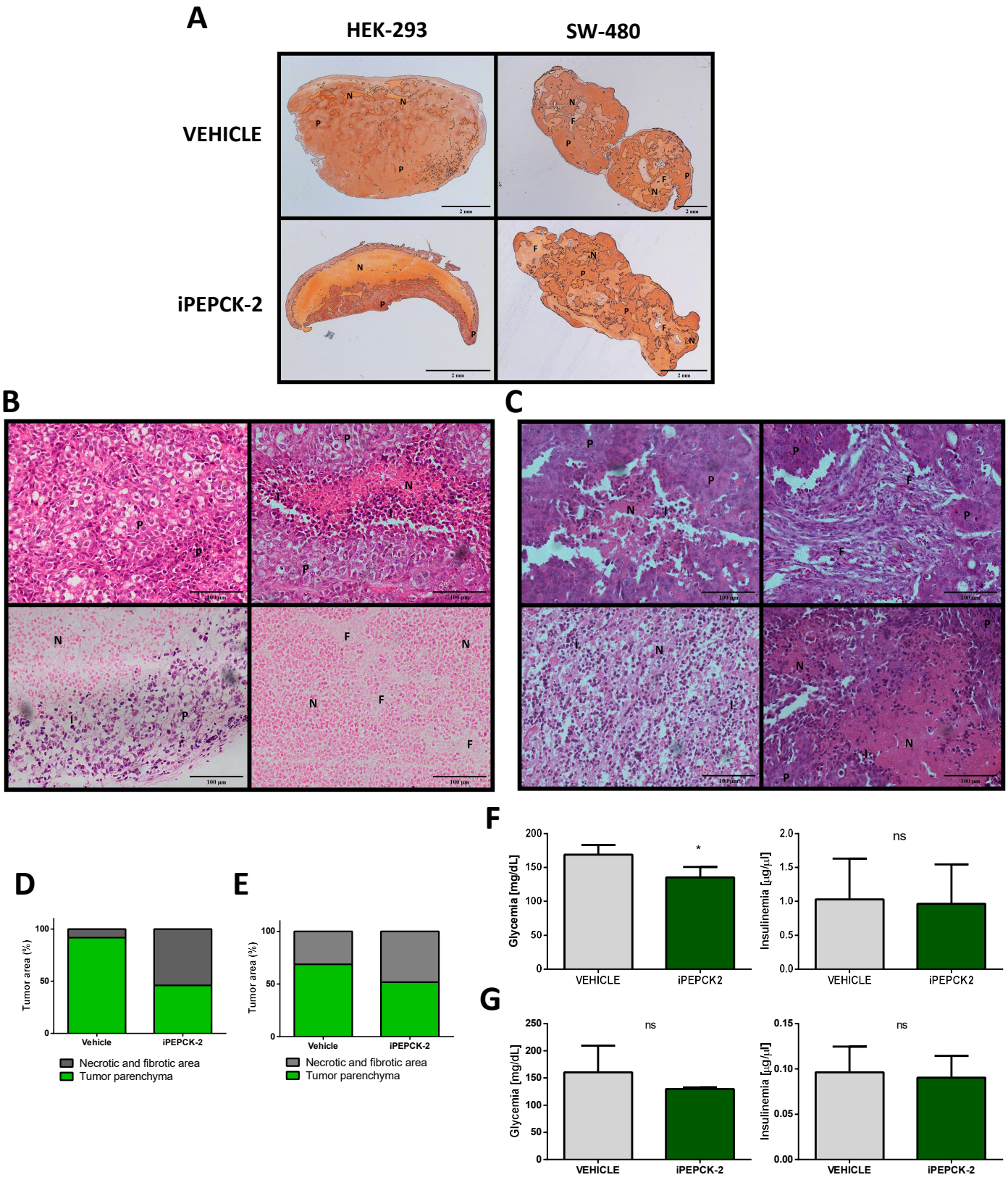

Figure S5. Analysis of tumor histopathology from HEK-293 and SW-480 explants. Full size H&E stained tumor sections (**A**). Reference H&E stained tumor sections (200x) from HEK-293 (**B**) and SW480 (**C**) explants indicating various histology features: P: tumor parenchyma; F: fibroblasts; N: necrotic areas; I: immune system infiltration. (**D-E**) Quantification of tumor parenchyma versus necrotic plus fibrotic areas of HEK-293 (**D**) and SW480 (**E**) tumors. The area means were quantified using Image J "Trainable Weka segmentation" Plug-in in full size tumor sections. 100x and 200x sections were used as a template to detect the different areas and the results were confirmed by microscopy. (**F-G**) Glycemia and insulinemia at the final point for HEK-293 (**F**) and SW-480 (**G**) models. Data are means ± SEM (n = 3 sections per tumor were produced at a minimum, and quantified).

	Human			Mice		
Compound	% remanent (sampling time 60 min)	t ½ (min)	Clint (µL/min*mg prot)	% remanent (sampling time 60 min)	t ½ (min)	Clint (µL/min* mg prot)
iPEPCK-2	68.71%	123.36	5.62	74.95%	119.66	5.79

Table S1. Microsomal stability of iPEPCK-2 in human and mice microsomes. Human and mice microsomes were purchased from Tebu-Xenotech. The compounds were incubated at 37ºC with the microsomes in a 50 mM phosphate buffer (pH=7.4) containing 3 mM $MgCl_2$, 1 mM NADP, 10 mM glucose-6-phosphate and 1 U/mL glucose-6-phosphate-dehydrogenase. Samples (75 µL) were taken from each well at 0, 10, 20, 40 and 60 min and transferred to a plate at 4ºC containing 75 µL acetonitrile and 30 µL of 0.5% formic acid in water were added for improving the chromatographic conditions. The plate was centrifuged (46000 g, 30 min) and supernatants were taken and analyzed in a UPLC-MS/MS (Xevo-TQD, Waters) by employing a BEH C18 column and a gradient of 0.1% formic acid in water: 0.1% formic acid acetonitrile (95%/5% for 60 s, 0%/100% for 90 s and 95%/5% for 30 s). The metabolic stability of the compounds was calculated from the logarithm of the remaining compounds at each of the time points studied.

Compound	Bibliography value	Experimental value (n=3) ± S.D.	CNS Prediction
Verapamil	16.0	28.5±0.9	CNS +
Testosterone	17.0	27.2±0.8	CNS +
Corticosterone	5.1	6.7±0.1	CNS +
Clonidine	5.3	6.5±0.05	CNS +
Ofloxacin	0.8	1.1±0.09	CNS -
Lomefloxacin	0.0	0.8±0.07	CNS -
Progesterone	9.3	16.8±0.03	CNS +
Promazine	8.8	13.8±0.3	CNS +
Imipramine	13.0	12.3±0.1	CNS +
Hydrocortisone	1.9	1.4±0.05	CNS -
Piroxicam	2.5	1.9±0.06	CNS +/-
Desipramine	12.0	17.8±0.1	CNS +
Cimetidine	0.0	0.7±0.03	CNS -
Norfloxacin	0.1	0.9±0.02	CNS -
iPEPCK-2		2.6±0.2	CNS +/-

Table S2. Permeability (*Pe* 10^{-6} cm s^{-1}) in the PAMPA-BBB assay of 14 commercial drugs and tested compounds and predictive penetration in the CNS (taken *from Di, L.; Kerns, E. H.; Fan, K.; McConnell, O. J.; CarTer, G. T. High throughput artificial membrane permeability assay for blood-brain barrier. Eur. J. Med.Chem.* ***2003****, 38, 223-232.*). The *in vitro* permeability (Pe) of iPEPCK-2 through a lipid extract of the porcine brain was determined using a mixture of phosphate-buffered saline (PBS)/EtOH 70:30. The concentration of drugs was determined using a UV/VIS (250-500 nm) plate reader. Assay validation was carried out by comparison of the experimental and reported permeability values of 14 commercial drugs, which provided a good linear correlation: Pe (exp) = 1.647 Pe (lit) – 1.416 (R^2 = 0.94). Using this equation, the following ranges of permeability were established: Pe (10^{-6} cm/s) > 5.17 for compounds with high BBB permeation (CNS+); Pe (10^{-6} cm/s) < 1.88 for compounds with low BBB permeation (CNS–); and 5.17 > Pe (10^{-6} cm/s) > 1.88 for compounds with uncertain BBB permeation (CNS±).

A

	hERG Channel inhibition (%)
iPEPCK-2	5±1

B

	Growth inhibition (%)
iPEPCK-2	39±3

Table S3. Toxicity. **(A)** Functional value over the activity of hERG channels at 10µM. CHO-hERG cell line was purchased from B'Sys. Cells and grown in F-12 Ham's supplemented with Glutamax, 10% FBS, 100 IU/mL penicillin + 100 mg/mL streptomycin, 100 µg/mL hygromycin and 100 µg/mL neomycin at 37°C in an atmosphere of 5% CO_2. 2500 cells were seeded on a 384 well black plate (Greiner 781091) and incubated at 37ºC in a 5% CO_2 atmosphere for 24 h and at 30ºC in a 5% CO_2 atmosphere for 48 min plus. hERG activity was measured by using the FluxorTM Potassium Ion Chanel Assay Kit (Thermo Fisher). Culture medium was replaced by 20 µL of loading buffer provided in the kit and the cells were incubated for 60 min at RT, protected from direct light. After incubation, loading buffer was replaced for assay buffer provided in the kit and the compounds were incubated for 30 min at RT. 5 µL of stimulus buffer provided in the kit was added to each well and the fluorescence (λex=490 nm, λem=525 nm) was measured using a fluorescence imaging plate reader system (FDSS7000EX, Hamamatsu®) every second after the establishment of a baseline**. (B)** Inhibition of cellular growth at 100 µM. The cytotoxicity of the compounds was measured by employing the non-tumoral lung fibroblast cell line MRC5 (ATCC). Cells were grown in Eagle's Minimum Essential Medium supplemented with 10% FBS at 37°C in an atmosphere of 5% CO_2. Cells (10000 /well) were seeded in a 96-well microplate and maintained for 24 min at 37°C in an atmosphere of 5% CO_2. Then compounds were added and incubated for 7 days under culture conditions. After the incubation time 10 µL of a 5 mg/mL MTT solution in PBS was added to each well and incubated for 4 h. After this incubation 100 µL of 10% sodium dodecyl sulphate in 0.01M HCl was added to each well and incubated for 12 min under the same experimental conditions. Absorbance at 595 nm was obtained in a multilabel reader (Tecan M1000 Pro). The percentage of inhibition of cell viability was calculated from the formula: % inhibition = 100-((AO*100)/AV); where AO is the observed absorbance in the compounds-treated wells and AV is the observed absorbance in the vehicle-treated wells.

5.2. Resultados no publicados

En este apartado, se presentan resultados complementarios que no se han recogido en la publicación y los métodos experimentales para preparar los productos propuestos. Los resultados que se recogen están estrechamente relacionados con los artículos, de los cuáles soy coautor, publicados en las revistas *Biomedicine & Pharmacotherapy*[53] (apartado 4.1) y *Cells* (anexo).[56] En estos trabajos se describe y valida la relevancia de la enzima fosfoenolpiruvato carboxiquinasa mitocondrial (PEPCK-M) como posible diana terapéutica para procesos cancerosos. Se determina su interés mediante su inhibición por **iPEPCK-2** un compuesto con núcleo de 3-alquil-1,8-dibencilxantina descrito por el Prof. Foley,[51] con propiedades antitumorales que podría ser un punto de partida como aproximación terapéutica novedosa para el tratamiento del cáncer (Figura 5.1).

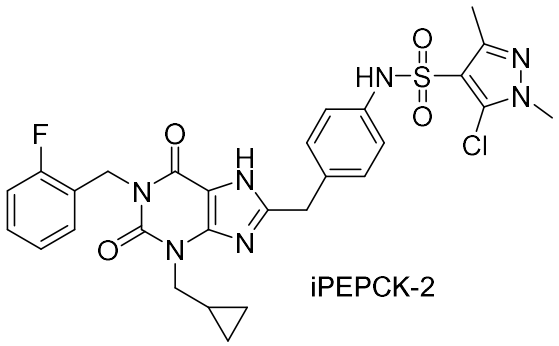

Figura 5.1. Estructura de **iPEPCK-2**.

La PEPCK, tal y como se ha explicado anteriormente, es la enzima que cataliza, empleando un nucleósido trifosfato (GTP) como donador del grupo fosforilo, la conversión del oxalacetato a fosfonoenolpiruvato en la gluconeogénesis. La PEPCK está formada por dos isoenzimas localizadas en el citosol, PEPCK-C, o en la mitocondria, PEPCK-M, codificadas por distintos genes nucleares, PCK1 y la PCK2, y presentes en tejido gluconeogénico y no gluconeogénicos, respectivamente. Además, está reportado la sobreexpresión del gen PCK2 en tumores, teniendo la PEPCK-M posiblemente un papel relevante para terapias anticancerosas.[49] Por ello, en un proyecto conjunto con el Prof. José Carlos Perales de la UB, con amplia experiencia en el estudio de la PEPCK-M y su implicación en cáncer, nos propusimos diseñar inhibidores enzimáticos de la isoforma mitocondrial como agentes antitumorales.

El compuesto **iPEPCK-2** inhibe la PEPCK-M pero no de manera selectiva, ya que es activo con el mismo rango de potencia frente a la isoenzima citosólica y, dado que no existe descrito ningún compuesto que disminuya forma selectiva la isoforma

mitocondrial de la PEPCK, el objetivo de este apartado era el diseño de un potente inhibidor selectivo para dicha isoforma.

El descubrimiento de compuestos que se dirigen de manera selectiva a mitocondria ha generado interés debido a los múltiples procesos fisiológicos que tienen lugar en ellas, como: ciclo de Krebs, oxidación de ácidos grasos, fosforilación oxidativa, entre otros. En la actualidad, existen diferentes métodos descritos de focalización mitocondrial: péptidos señal dirigidos a mitocondria, péptidos de penetración celular y cationes lipófilos.[80] Estas herramientas aprovechan la maquinaria de importación de mitocondrias o el alto potencial de membrana a través de la membrana mitocondrial interna. Los cationes lipófilos, como el trifenilfosfonio (TPP), pueden ser atraídos por las mitocondrias a través de interacciones electrostáticas y acumularse en su matriz debido al potencial de membrana negativo, llegando a concentrarse hasta 100 veces más que en citosol (Figura 5.2). En la bibliografía se describen varios ejemplos de compuestos que su estructura tiene unido un grupo de TPP, permitiéndoles acceder a mitocondria y detener ciclos celulares e inducir a la muerte celular de células cancerosa.[81]

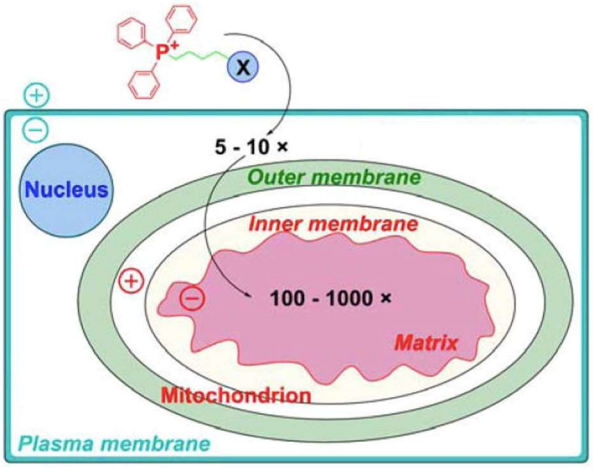

Figura 5.2. Mecanismo de internalización de compuestos con TPP.

Mediante un diseño racional, el Prof. F. Javier Luque de la UB propuso una serie de estructuras derivadas de **iPEPCK-2** que incluían el fragmento TPP. La adición del grupo TPP debería dirigir la molécula selectivamente a las mitocondrias, disminuyendo potencialmente posibles efectos adversos por inhibición de PEPCK-C, describiendo, la primera familia de inhibidores enzimáticos selectivos de PEPCK-M con un grupo TPP.

[80] Chen, Z-P.; Li, M; Zhang, L-J. J. *Drug Target*. **2016**, *24*, 492-502.
[81] (a) Millard, M.; Gallagher, J.D.; Olenyuk, B.Z. *J. Med. Chem.* **2013**, *56*, 9170-9179; (b) Pathak, R.K.; Marrache, S.; Harn, D.A.; Dhar, S. *ACS Chem Biol.* **2014**, *9*, 1178-1187.

Considerando el inhibidor enzimático **iPEPCK-2** descrito anteriormente como punto de partida, se sintetizaron y evaluaron una serie de productos con estructura de 3-alquil-1,8-dibencilxantina unidos a un grupo TPP mediante una cadena alquílica. Los inhibidores resultantes llamados **iPEPO-1**, **iPEPO-2** e **iPEPO-3** difieren en el número de carbonos 2, 3 o 4, respectivamente, de la cadena lineal que une el núcleo policíclico al fragmento de TPP.

Se propuso obtener los compuestos deseados a través de la reacción de acoplamiento entre la amina libre del intermedio de xantina 1,3,8-trisustituida **I**, previamente descrita por nuestro grupo,[53] con el grupo acido carboxílico de los bromuros de 2-(carboxietil) (**II**), 3-(carboxipropil) (**III**), 4-(carboxibutil) (**IV**) fenilfosfonio, en presencia de una base orgánica (trietilamina, TEA), los agentes acoplantes hidroxibenzotriazol (HOBt) y etil-3-(3-dimetilaminopropil)carbodiimida (EDCI) en dimetilformamida durante 16h a temperatura ambiente. Los compuestos resultantes **iPEPO-1**, **iPEPO-2** e **iPEPO-3** se purificaron por cromatografía en columna presentando rendimientos moderados de 42, 30 y 26%, respectivamente (Esquema 5.1).[41, 82]

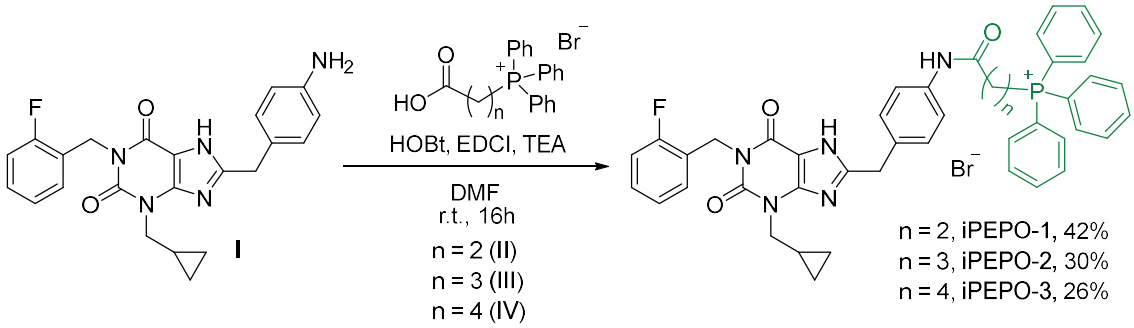

Esquema 5.1. Reacción para la obtención de **iPEPO-1**, **iPEPO-2** e **iPEPO-3**.

Seguidamente, se evaluó la actividad inhibitoria de los compuestos sintetizados frente a los enzimas PEPCK-M y PEPCK-C recombinante humana por parte del grupo del Prof. Perales en el contexto de la Tesis Doctoral del Sr. Marc Aragó.

Los resultados se compararon con dos compuestos de referencia, un inhibidor no competitivo alostérico de la PEPCK, el ácido 3-mercaptopicolínico (**3-MPA**)[51] y, otro más potente descrito por el prof. Foley y preparado posteriormente en nuestro grupo que actúa como GTP competitivo, **iPEPCK-2**.

Los nuevos productos descritos inhiben ambas isoformas de manera similar sin ser selectivos por la isoenzima mitocondrial como se puede observar en la Tabla 5.1. El compuesto **iPEPO-2** presenta una mayor inhibición (IC_{50} = 0.558 μM para la PEPCK-M

[82] Faucher, N.E.; Martres, P. Meunier, S. Indole derivatives useful as PPAR activators. WO2008/063371 A1, October 9, **2008**

y IC_{50} = 0.157 μM para la PEPCK-C) que sus análogos **iPEPO-1** (IC_{50} = 4.742 μM para la PEPCK-M y IC_{50} = 1.179 μM para la PEPCK-C) e **iPEPO-3** (IC_{50} = 3.090 μM para la PEPCK-M y IC_{50} = 0.771 μM para la PEPCK-C). Se puede deducir que **iPEPO-2** dispone la longitud óptima del *linker* carbonado unido el TPP, comparado con los compuestos unidos al TPP con *linkers* de menor (**iPEPO-1**) o mayor (**iPEPO-3**) distanciamiento de carbonos, 2 y 4 respectivamente, los cuales presentan actividades inferiores. Los tres derivados de TPP ofrecen una potencia global más baja que **iPEPCK-2** (IC_{50} = 0.117 μM para la PEPCK-M y IC_{50} = 0.061 μM para la PEPCK-C), producto del que provienen descrito anteriormente, aunque en el mismo orden de magnitud para **iPEPO-2**.

Tabla 5.1. Valores de IC_{50} (μM) de los compuestos sintetizados y de referencia frente a PEPCK-M y PEPCK-C recombinante humana.

Compuesto	PEPCK-C	PEPCK-M
3-MPA	10.097	17.402
iPEPCK-2	0.061	0.117
iPEPO-1	1.179	4.752
iPEPO-2	0.157	0.558
iPEPO-3	0.771	3.090

En un contexto celular, se realizó un ensayo de desplazamiento térmico celular (CETSA) utilizando la línea de células de hepatoma de rata (FAO). Las células de la FAO expresan ambas isoformas de PEPCK, tanto la mitocondrial como citosólica. En este ensayo, el compuesto más potente de la familia (**iPEPO-2**) se comparó con los inhibidores de PEPCK descritos anteriormente, **iPEPCK-2** y **3-MPA** (Figura 5.3).

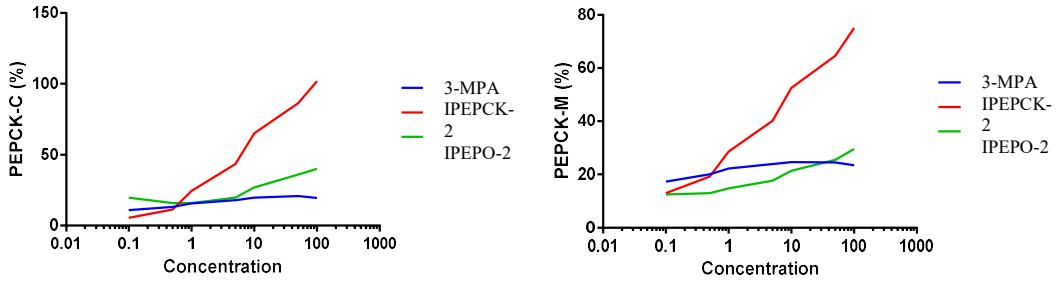

Figura 5.3. Ensayo cinético frente a la PEPCK-M y PEPCK-C de **iPEPO-2, iPEPCK-2** y **3-MPA**.

Dado que **iPEPO-2** mostró una potencia ligeramente más baja pero similar que **iPEPCK-2** en el ensayo cinético, se esperaba que **iPEPO-2** hubiera mostrado una estabilización térmica mejorada por la PEPCK-M (o, al menos, la misma que **iPEPCK-2**) debido a la focalización mitocondrial. Sin embargo, **iPEPCK-2** fue el mejor compuesto para estabilizar térmicamente ambas isoformas de PEPCK. Además, **iPEPO-2** no

resultó ser selectivo de PEPCK-M, ya que estabiliza la isoforma citosólica con la misma potencia que la mitocondrial (Figura 5.4).

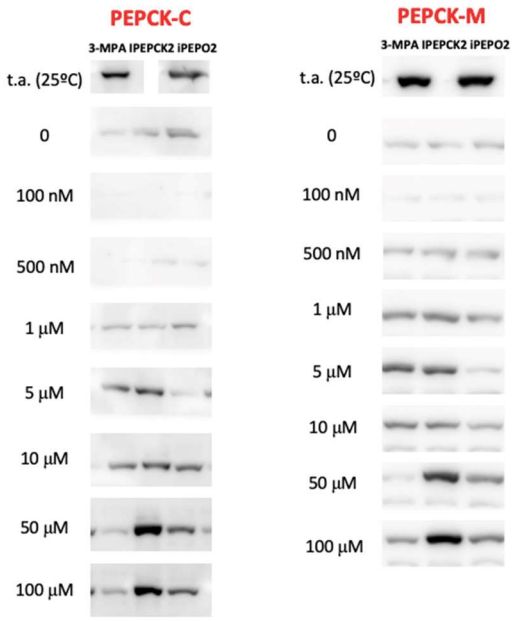

Figura 5.4. Estabilización de la PEPCK-M y PEPCK-C en células FAO tras el ensayo CETSA a 60 ºC durante 3 min en concentraciones crecientes de **iPEPO-2, iPEPCK-2** y **3-MPA**.

En conclusión, se han diseñado y sintetizado una serie de compuestos inhibidores de la PEPCK que incorporan un grupo de TPP con la intención de que inhiban selectivamente la isoenzima mitocondrial. Se describe como la primera familia de inhibidores de la PEPCK con valores submicromolar que contienen un grupo TPP en su estructura. Aunque los valores de inhibición de los compuestos diseñados y sintetizados son relevantes, no son tan potentes como **iPEPCK-2** ni degradan selectivamente la PEPCK-M.

PARTE EXPERIMENTAL

Reagents, solvents and starting products were acquired from commercial sources. Evaporation of solvents was accomplished with a rotary evaporator. Thin layer chromatography was done on SiO_2 (silica gel 60 F254). Chromatography refers to flash column chromatography was carried out on SiO_2 (silica gel 60, SDS, 230-400 mesh). NMR spectra were recorded in $CDCl_3$ at 400 MHz (^1H) and chemical shifts are reported in δ values downfield from TMS or relative to residual $CDCl_3$ (7.26 ppm) or CD_3OD (3.31 ppm) as an internal standard. Data are reported in the following manner: chemical shift, multiplicity, coupling constant (*J*) in hertz (Hz), integrated intensity. Multiplicities are reported using the following abbreviations: s, singlet; d, doublet m, multiplet; and br s, broad signal. The accurate mass analyses were carried out using a LC/MSD-TOF spectrophotometer.

***(3-[(4-((3-(Cyclopropylmethyl)-1-(2-fluorobenzyl)-2,6-dioxo-2,3,6,7-tetrahydro-1H-purin-8-yl)methyl)phenyl)amino]-3-oxopropyl)triphenylphosphonium bromide (iPEPO-1)*.**

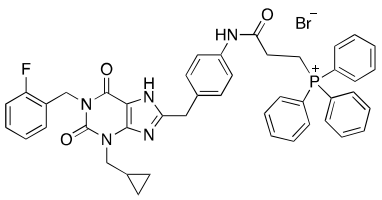

To a solution of hydroxybenzotriazole (HOBt) (19.3 mg, 0.143 mmol), 1-ethyl-3-(3-dimethylaminopropyl)carbodiimide (EDCI) (22.2 mg, 0.143 mmol) and triethylamine (TEA) (52 µL, 0.357 mmol) in 5 mL of dry DMF under argon at room temperature, (2-carboxyethyl)triphenylphosphonium bromide was added (54.4 mg, 0.131 mmol). The reaction was stirred for 15 min and 8-(4-aminobenzyl)-3-(cyclopropylmethyl)-1-(2-fluorobenzyl)-3,7-dihydro-1*H*-purine-2,6-dione (50.0 mg, 0.119 mmol) was added. The resulting solution was stirred at room temperature overnight. Then, the reaction mixture was evaporated and neutralized with saturated $NaHCO_3$ solution. The aqueous phase was extracted with EtOAc, the combined organic phases were washed with brine, dried over Na_2SO_4, and evaporated to give a residue, which was purified by flash column chromatography (EtOAc/MeOH 95:5) to afford **iPEPO-1** (41 mg, 22%) as a solid. ^1H-RMN (400 MHz, CD_3OD) *δ*: 0.46-0.50 [m, 4H, $CH(CH_2)_2$], 1.36-1.43 [m, 1H, $CH(CH_2)_2$], 2.81-2.91 [m, 2H, $CH_2CH(CH_2)_2$], 3.76-3.83 (m, 2H, CH_2CH_2), 3.98-3.99 (s, 2H, CH_2CNNH), 4.09-4.13 (m, 2H, CH_2CH_2), 5.26 (s, 2H, CH_2Ar), 7.06-7.10 (m, 2H, Ar*H*), 7.25 (d, *J* = 8.5 Hz, 2H, Ar*H*), 7.42 (d, *J* = 8.0 Hz, 2H, Ar*H*), 7.75-7.80 (m, 7H, Ar*H*), 7.84-7.90 (m, 10H, Ar*H*). HRMS $C_{44}H_{40}FN_5O_3P$ $[M+H]^+$ 736.2847, found 736.2841.

(4-[(4-((3-(Cyclopropylmethyl)-1-(2-fluorobenzyl)-2,6-dioxo-2,3,6,7-tetrahydro-1H-purin-8-yl)methyl)phenyl)amino]-4-oxobutyl)triphenylphosphonium bromide (iPEPO-2).

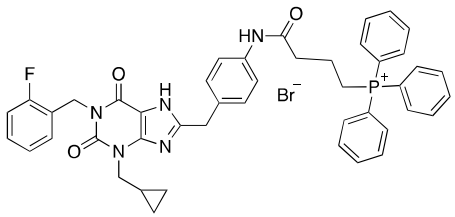

To a solution of HOBt (11.6 mg, 0.086 mmol), EDCI (13.4 mg, 0.086 mmol) and TEA (30 µL, 0.216 mmol) in 3 mL of dry DMF under argon at room temperature, (3-carboxypropyl)triphenylphosphonium bromide was added (33.8 mg, 0.079 mmol). The reaction was stirred for 15 min and 8-(4-aminobenzyl)-3-(cyclopropylmethyl)-1-(2-fluorobenzyl)-3,7-dihydro-1H-purine-2,6-dione (30.0 mg, 0.072 mmol) was added. The resulting solution was stirred at room temperature overnight. Then, the reaction mixture was evaporated and neutralized with saturated $NaHCO_3$ solution. The aqueous phase was extracted with EtOAc, the combined organic phases were washed with brine, dried over Na_2SO_4, and evaporated to give a residue, which was purified by flash column chromatography (EtOAc/MeOH 95:5) to afford **iPEPO-2** (18 mg, 26%) as a solid. ^{1}H-RMN (400 MHz, $CDCl_3$) *δ*: 0.43-0.47 [m, 4H, CH(C*H*$_2$)$_2$], 1.32–1.36 (m, 1H, $CH_2CH_2CH_2$), 1.39–1.42 [m, 2H, C*H*$(CH_2)_2$ + $CH_2CH_2CH_2$], 1.81-1.92 (m, 2H, $CH_2CH_2CH_2$), 2.95-3.5 [m, 1H, C*H*$_2$CH$(CH_2)_2$], 3.44-3.49 (m, 2H, $CH_2CH_2CH_2$), 3.87-3.97 [m, 1H, C*H*$_2$CH$(CH_2)_2$], 4.13 (s, 2H, C*H*$_2$CNNH), 5.10 (s, 2H, C*H*$_2$Ar), 6.92–6.95 (m, 1H, Ar*H*), 6.99 –7.01 (m, 1H, Ar*H*), 7.10–7.15 (m, 1H, Ar*H*), 7.21–7.23 (m, 1H, Ar*H*), 7.63–7.78 (m, 17H, Ar*H*), 7.82–7.87 (m, 2H, Ar*H*), 11.12 (bs, 1H, N*H*), 12.45 (bs, 1H, NH). HRMS $C_{46}H_{44}FN_5O_3P$ $[M+H]^+$ 764.3160, found 764.3150.

(5-[(4-((3-(Cyclopropylmethyl)-1-(2-fluorobenzyl)-2,6-dioxo-2,3,6,7-tetrahydro-1H-purin-8-yl)methyl)phenyl)amino]-5-oxopentyl)triphenylphosphonium bromide (iPEPO-3).

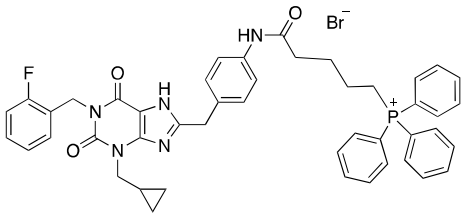

To a solution of HOBt (19.3 mg, 0.143 mmol), EDCI (22.2 mg, 0.143 mmol) and TEA (52 µL, 0.357 mmol) in 5 mL of dry DMF under argon at room temperature, (4-carboxybutyl)triphenylphosphonium bromide was added (58.1 mg, 0.131 mmol). The reaction was stirred for 15 min and 8-(4-aminobenzyl)-3-(cyclopropylmethyl)-1-(2-fluorobenzyl)-3,7-dihydro-1H-purine-2,6-dione (50.0 mg, 0.119 mmol) was added. The resulting solution was stirred at room temperature overnight. Then, the reaction mixture was evaporated and neutralized with saturated $NaHCO_3$ solution. The aqueous phase was extracted with EtOAc, the combined organic phases were washed with brine, dried over Na_2SO_4, and evaporated to give a residue, which was purified by flash column

chromatography (EtOAc/MeOH 95:5) to afford **iPEPO-3** (26 mg, 26%) as a solid. ^{1}H-RMN (400 MHz, $CDCl_3$) *δ*: 0.45-0.47 [m, 4H, CH(C*H*$_2$)$_2$], 0.82-0.85 [m, 2H, CH$_2$(C*H*$_2$)$_2$CH$_2$], 1.07–1.27 [m, 2H, CH$_2$(C*H*$_2$)$_2$CH$_2$], 1.29–1.37 (m, 1H, C*H*(CH$_2$)$_2$), 2.03-2.06 [m, 2H, C*H*$_2$(CH$_2$)$_2$CH$_2$], 2.94-2.97 [m, 1H, C*H*$_2$CH(CH$_2$)$_2$], 3.62-3.65 [m, 2H, CH$_2$(CH$_2$)$_2$C*H*$_2$], 3.96-3.98 [m, 1H, C*H*$_2$CH(CH$_2$)$_2$], 4.07 (s, 2H, C*H*$_2$CNNH), 5.13 (s, 2H, C*H*$_2$Ar), 6.90–6.97 (m, 2H, Ar*H*), 7.01 –7.04 (m, 1H, Ar*H*), 7.11 –7.14 (m, 1H, Ar*H*), 7.17–7.19 (m, 2H, Ar*H*), 7.58–7.61 (m, 3H, Ar*H*), 7.55–7.72 (m, 12H, Ar*H*), 7.79–7.84 (m, 2H, Ar*H*), 10.45 (bs, 1H, N*H*), 12.52 (bs, 1H, N*H*). HRMS $C_{45}H_{42}FN_5O_3P$ $[M+H]^+$ 750.3004, found 750.2997.

MATERIAL SUPLEMENTARIO

^{1}H-NMR and ^{13}C-NMR spectra of compounds **iPEPO-1**, **iPEPO-2** and **iPEPO-3**.

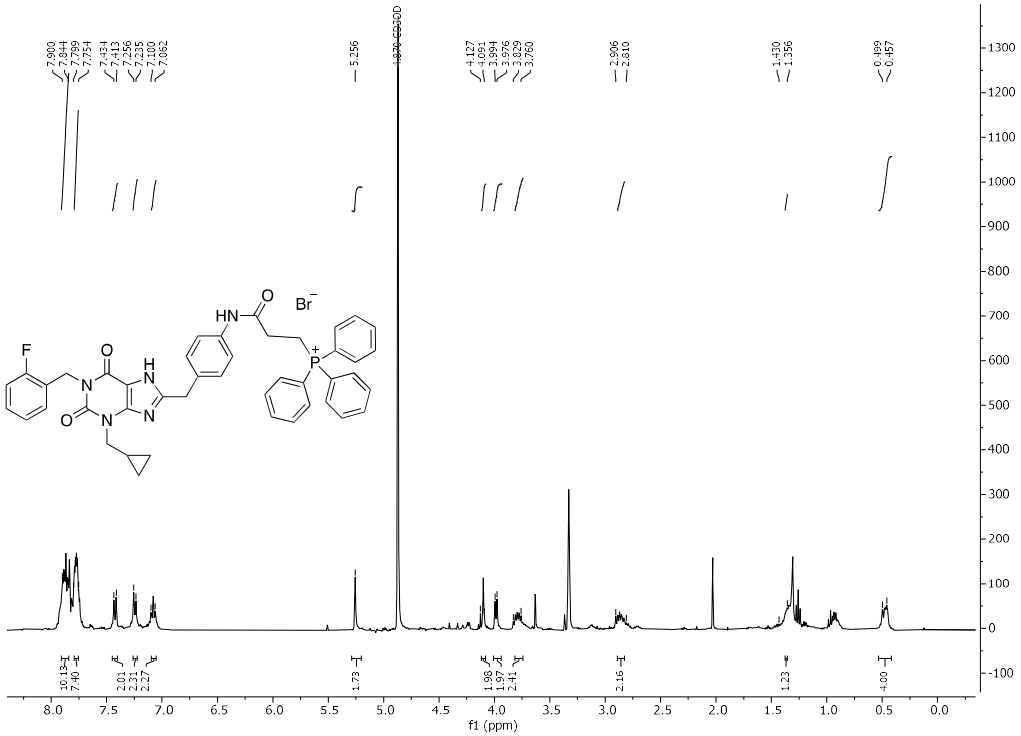

(3-[(4-((3-(Cyclopropylmethyl)-1-(2-fluorobenzyl)-2,6-dioxo-2,3,6,7-tetrahydro-1H-purin-8-yl)methyl)phenyl)amino]-3-oxopropyl)triphenylphosphonium bromide (iPEPO-1)

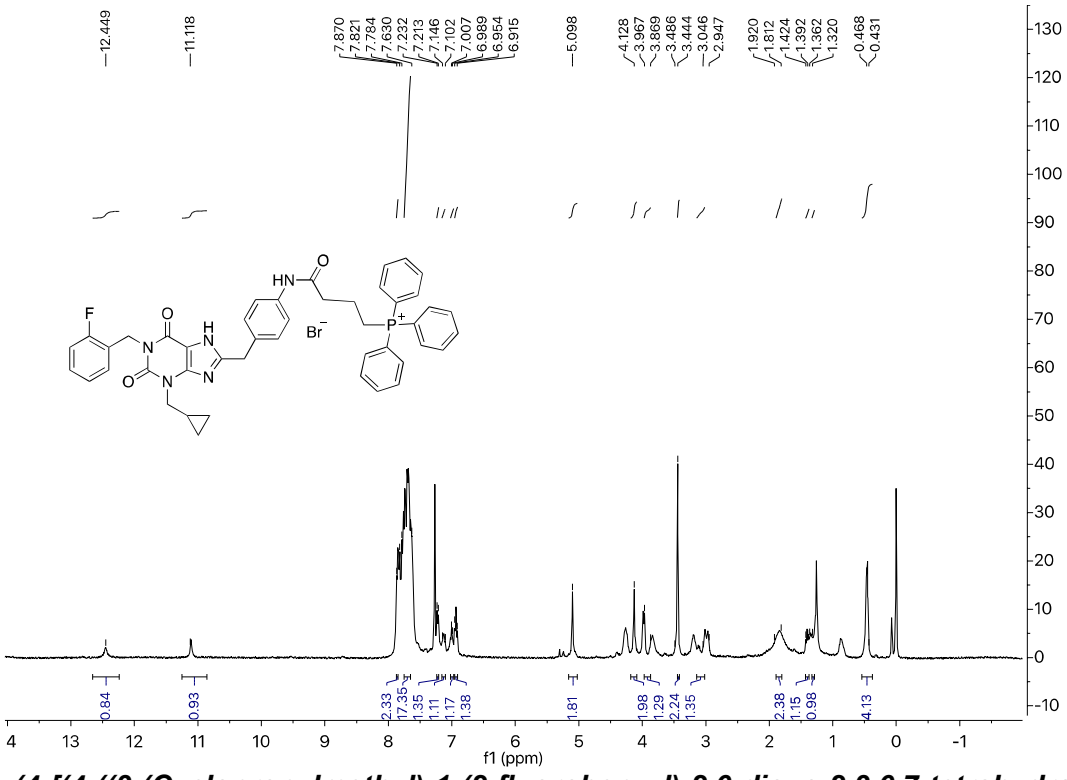

(4-[(4-((3-(Cyclopropylmethyl)-1-(2-fluorobenzyl)-2,6-dioxo-2,3,6,7-tetrahydro-1H-purin-8-yl)methyl)phenyl)amino]-4-oxobutyl)triphenylphosphonium bromide (iPEPO-2)

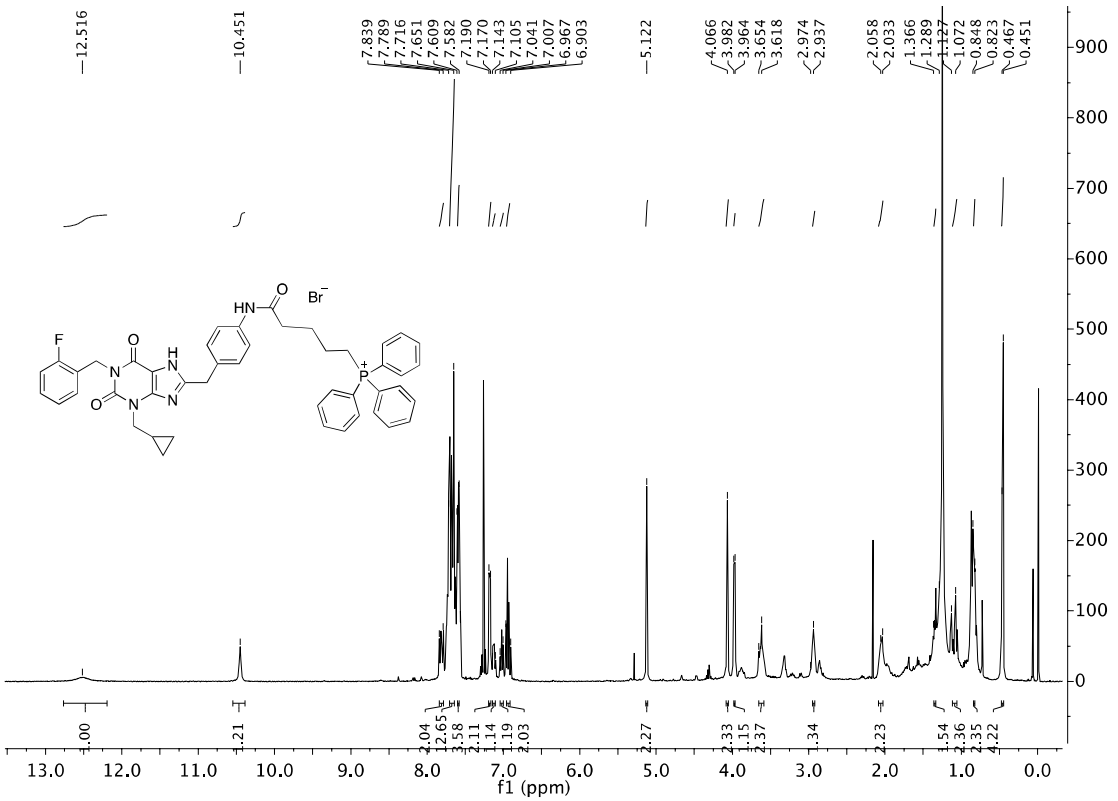

(5-[(4-((3-(Cyclopropylmethyl)-1-(2-fluorobenzyl)-2,6-dioxo-2,3,6,7-tetrahydro-1H-purin-8-yl)methyl)phenyl)amino]-5-oxopentyl)triphenylphosphonium bromide (iPEPO-3)

Capítulo 6. *Synthesis, Characterization and HPLC Analysis of the (1S,2S,5R)-Diastereomer and the Enantiomer of the Clinical Candidate AR-15512*

6.1. *Molecules* 2021, *26*, 906

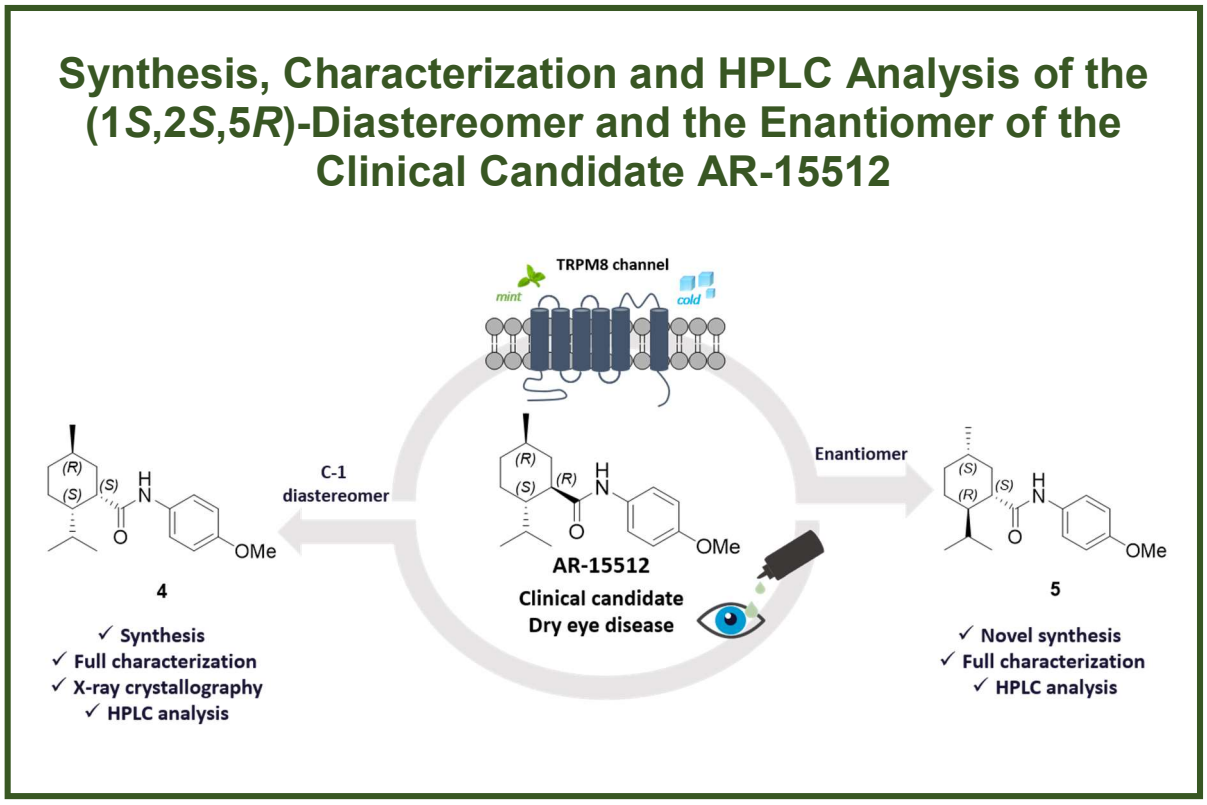

molecules

MDPI

Article

Synthesis, Characterization and HPLC Analysis of the (1*S*,2*S*,5*R*)-Diastereomer and the Enantiomer of the Clinical Candidate AR-15512

Sergio Rodríguez-Arévalo [1], Eugènia Pujol [1], Sònia Abás [1], Carles Galdeano [2], Carmen Escolano [1,*] and Santiago Vázquez [1,*]

[1] Laboratori de Química Farmacèutica (Unitat Associada al CSIC), Facultat de Farmàcia i Ciències de l'Alimentació, Institute of Biomedicine (IBUB), Universitat de Barcelona, Av. Joan XXIII, 27-31, 08028 Barcelona, Spain; rodriguez.arevalo@ub.edu (S.R.-A.); epujol@ub.edu (E.P.); soniaabas88@gmail.com (S.A.)

[2] Department of Pharmacy and Pharmaceutical Technology and Physical Chemistry, Faculty of Pharmacy and Food Sciences, Institute of Biomedicine (IBUB), University of Barcelona, Av. Joan XXIII, 27-31, 08028 Barcelona, Spain; cgaldeano@ub.edu

* Correspondence: cescolano@ub.edu (C.E.); svazquez@ub.edu (S.V.); Tel.: +34-934-024-542 (C.E.); +34-934-024-533 (S.V.)

Abstract: AR-15512 (formerly known as AVX-012 and WS-12) is a TRPM8 receptor agonist currently in phase 2b clinical trials for the treatment of dry eye. This bioactive compound with menthol-like cooling activity has three stereogenic centers, and its final structure and absolute configuration, (1*R*,2*S*,5*R*), have been previously solved by cryo-electron microscopy. The route of synthesis of AR-15512 has also been reported, revealing that epimerization processes at the C-1 can occur at specific stages of the synthesis. In order to confirm that the desired configuration of AR-15512 does not change throughout the process and to discard the presence of the enantiomer in the final product due to possible contamination of the initial starting material, both the enantiomer of AR-15512 and the diastereomer at the C-1 were synthesized and fully characterized. In addition, the absolute configuration of the (1*S*,2*S*,5*R*)-diastereomer was determined by X-ray crystallographic analysis, and new HPLC methods were designed and developed for the identification of the two stereoisomers and their comparison with the clinical candidate AR-15512.

Keywords: absolute configuration; AR-15512; diastereomer; enantiomer; HPLC analytical method

Citation: Rodríguez-Arévalo, S.; Pujol, E.; Abás, S.; Galdeano, C.; Escolano, C.; Vázquez, S. Synthesis, Characterization and HPLC Analysis of the (1*S*,2*S*,5*R*)-Diastereomer and the Enantiomer of the Clinical Candidate AR-15512. *Molecules* **2021**, *26*, 906. https://doi.org/10.3390/molecules26040906

Academic Editors: Patrizia Ferraboschi and Silvia Schenone

Received: 30 December 2020
Accepted: 5 February 2021
Published: 9 February 2021

1. Introduction

AR-15512 ((1*R*,2*S*,5*R*)-*N*-(4-methoxyphenyl)-5-methyl-2-(1-methylethyl) cyclohexan ecarboxamide) is a bioactive compound with menthol-like cooling effects that is currently being evaluated in phase 2b clinical trials as an ophthalmic solution for the treatment of dry eye, a chronic, highly prevalent, and age-related condition associated with pain and limitations in performing daily activities [1–4]. Indeed, dry eye disease is nowadays considered an unmet medical need, causing a significant socioeconomic burden in the general population [5,6]. AR-15512 acts as a potent and selective agonist of the TRPM8 (transient receptor potential melastatin member 8) cold thermoreceptor. TRPM8 is a calcium-permeable ion channel that serves as the principal detector of cold in humans and is involved in the regulation of tear production and blink rate [7,8]. Importantly, this stimulation can ultimately lead to a restoration of tear film volume and a reduction of ocular discomfort in patients suffering from dry eye syndrome [4]. AR-15512, formerly known as AVX-012, was developed by Avizorex Pharma, S. L. (Barcelona, Spain), a Spanish ophthalmic pharmaceutical company working on new therapeutics for tackling dry eye syndrome [9]. In November 2019, Avizorex and AR-15512 were acquired by Aerie Pharmaceuticals (Durham, NC, USA), a company that has further progressed this clinical candidate from successful

phase 2a studies performed by Avizorex to the aforementioned phase 2b, with a topline readout expected in the third quarter of 2021 [10,11]. Curiously, this molecule was first described in the literature in 1971, when it was patented as a menthol-derived cooling agent under the name of WS-12 [12]. Since then, other patents and several published works have followed, including studies confirming its exact stereochemistry and its binding to the TRPM8 receptor [13].

AR-15512 is easily synthesized starting from (1*R*,2*S*,5*R*)-(−)-menthol (**1**), a small molecule terpenoid from peppermint oil, as previously reported (Scheme 1) [12,14,15]. Hence, the first step is the reaction of the commercially available **1** with zinc chloride in the presence of hydrochloric acid to give (1*S*,2*R*,4*R*)-2-chloro-1-isopropyl-4-methylcyclohexane (**2**). Then, treatment of this intermediate with magnesium in diethyl ether to prepare the Grignard reagent followed by in situ reaction with CO_2 provides the corresponding carboxylic acid (**3**). Finally, a reaction between **3** and *p*-anisidine in the presence of the coupling reagent benzotriazol-1-yl-oxytripyrrolidinophosphonium hexafluorophosphate (PyBOP), *N*,*N*-diisopropylethylamine (DIPEA) as a base and dimethylacetamide (DMA) as a solvent furnishes AR-15512. Alternatively, amide formation can also be achieved via the corresponding acid chloride of **3**, readily prepared by reaction with $SOCl_2$ and like reagents, which reacts with the same *p*-anisidine in appropriate base and solvent.

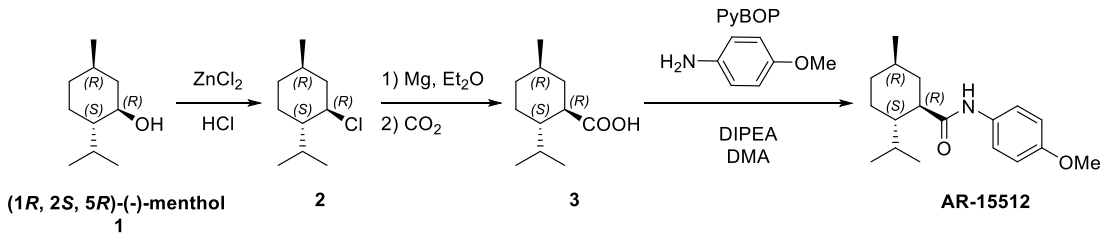

Scheme 1. Structure of the product AR-15512 and its reported synthetic procedure.

Bearing in mind both the chemical structure of AR-15512 and its synthesis, it has not been fully discarded whether epimerization processes at the C-1 can take place during its obtention [16]. Therefore, in order to rule this out and to confirm that the synthetic sequence indicated in Scheme 1 is stereochemically robust, the synthesis of the (1*S*,2*S*,5*R*)-diastereoisomer of AR-15512 (*neo*-AR-15512, **4**) was envisaged. Furthermore, in order to discard the presence of the enantiomer of AR-15512 (*ent*-AR-15512, **5**) in the final product coming from possible contamination of the initial (1*R*,2*S*,5*R*)-(−)menthol with its enantiomer (1*S*,2*R*,5*S*)-(+)menthol, a synthetic sequence was developed to access to the enantiomer of AR-15512 (Figure 1).

***neo*-AR-15512** ***ent*-AR-15512**

4 **5**

Figure 1. Structure and configuration of the target compounds in this work.

Here, we report for the first time the synthesis and full characterization of both the (1*S*,2*S*,5*R*)-diastereoisomer, **4**, and the enantiomer of AR-15512, **5**. In addition, we provide detailed information on the high-performance liquid chromatography (HPLC) analytical methods that have been developed for the identification of both compounds and comparison with the clinical candidate. Finally, X-ray crystallographic analysis has been performed to confirm the absolute configuration of the (1*S*,2*S*,5*R*)-diastereoisomer **4**.

2. Results and Discussion

2.1. Synthesis of (1S,2S,5R)-diastereomer of AR-15512, neo-AR-15512, **4**

As previously mentioned, the synthetic sequence depicted in Scheme 1 to approach AR-15512 starts from the commercially available (1*R*,2*S*,5*R*)-(−)-menthol (**1**). In order to access to (1*S*,2*S*,5*R*)-*N*-(4-methoxyphenyl)-5-methyl-2-(1-methylethyl)cyclohexanecarboxamide (*neo*-AR-15512) **4**, the diastereoisomer of AR-15512 at the C-1, an inversion in the configuration of the stereocenter C-1 is required from the same starting material. For its obtention, we took advantage of the fact that the synthesis of the carboxylic acid derivative (**9**) had already been published (Scheme 2) [17]. Worth to highlight, in this reference, the author reported that the aldehyde (**8**) was prone to epimerization.

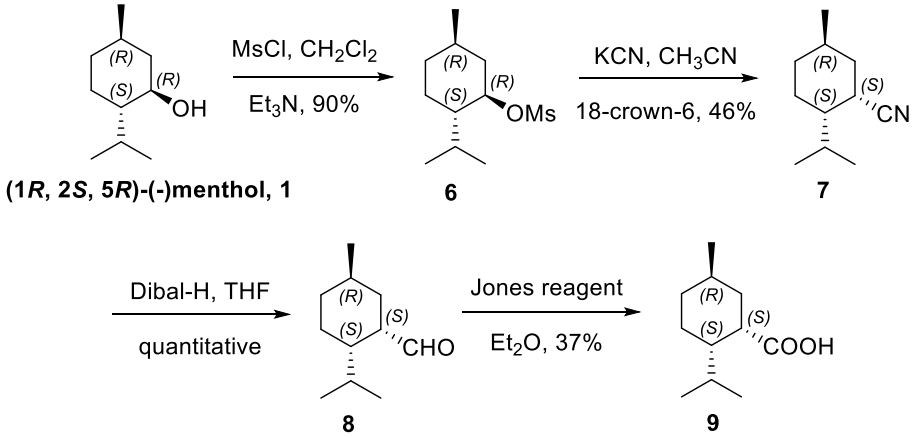

Scheme 2. Synthetic procedure reported for the carboxylic acid **9** [17].

Hence, starting from the known compound **9,** the corresponding acid chloride (**10**) was prepared by treatment with oxalyl chloride in dry dichloromethane (DCM) and in the presence of a catalytic amount of dimethylformamide (DMF) under argon. Intermediate **10** was used without further purification into the next synthetic step. Finally, the formation of compound **4** was achieved in 80% overall yield by reaction of **10** with *p*-anisidine in dry DCM as a solvent and in the presence of pyridine as a base (Scheme 3).

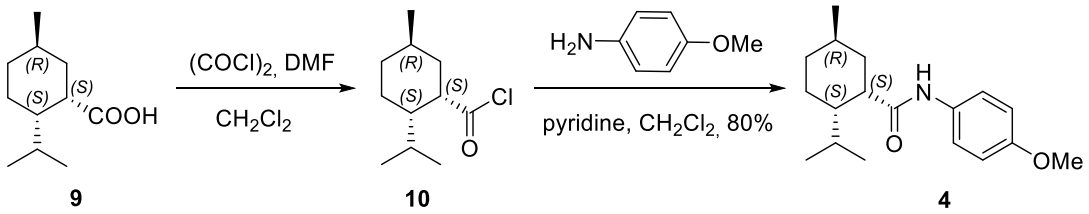

Scheme 3. Synthesis of *neo*-AR-15512, **4**, from the known carboxylic acid **9**.

2.1.1. Characterization and X-ray Structure Analysis of **4**

The diastereoisomer of AR-15512 at the C-1, compound **4**, was completely characterized by means of ^{1}H, ^{13}C, COSY and HSQC NMR experiments, infrared, elemental analysis, specific optical rotation, and melting point (see Material and Methods section and Supplementary Materials for further details). Moreover, the chiral identity of its three stereogenic centers was unambiguously confirmed by X-ray crystallography of a monocrystal obtained by recrystallization from ethyl acetate (Figure 2). Compound **4** was found to crystallize in the orthorhombic system, space group P 21 21 21, with the following cell parameters: *a* = 9.1371(2) Å, *b* = 10.3821(3) Å, *c* = 17.4893(7) Å, V = 1659.98(7) Å^3 and Z = 4 (further crystal data can be found in Supplementary Materials) [18].

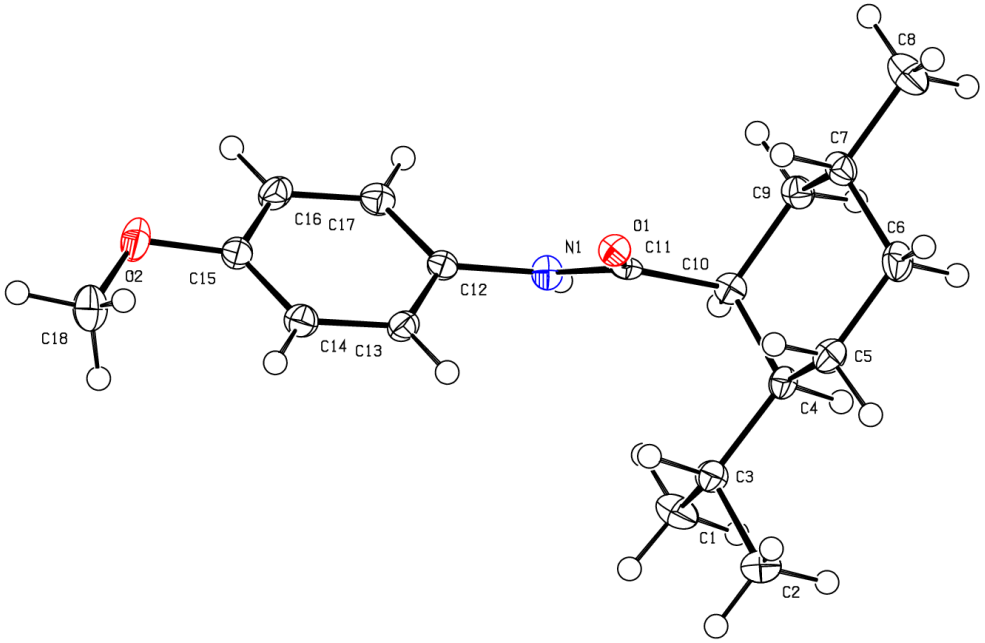

Figure 2. Crystal structure for (1*S*,2*S*,5*R*)-diastereomer of AR-15512, **4**.

2.1.2. HPLC Method for the Analysis of AR-15512 and Its Diastereoisomer **4** (*neo*-AR-15512)

Importantly, once the diastereoisomer of AR-15512 at the C-1 was synthesized, an HPLC method for its identification and differentiation from AR-15512 was designed and developed. Thus, AR-15512 and **4** were distinguished by comparison of the retention times of both compounds separately and in a mixture by using an Ultrabase C-18 (Akady) 5 ODS column 250 mm × 4.6 mm (particle size 5 μM) as stationary phase and an acetonitrile, water and trifluoroacetic acid (TFA) (0.1%) as a mobile phase, with a UV detector set at 254 nm (Table 1) (see Materials and Methods and Supplementary Materials for further details).

Table 1. Retention times of AR-15512 and its diastereomer **4**.

Compound	Retention Time (min)
AR-15512	11.8
neo-AR-15512, **4**	15.6

*2.2. Synthesis of the Enantiomer of AR-15512, **5** (ent-AR-15512)*

In pursuance of the enantiomer of AR-15512, (1*S*,2*R*,5*S*)-*N*-(4-methoxyphenyl)-5-methyl-2-(1-methylethyl)cyclohexanecarboxamide **5**, we first considered following the synthetic route previously shown in Scheme 1, but starting from the corresponding enantiomer, i.e., (1*S*,2*R*,5*S*)-(+)-menthol. However, an interesting alternative was found based on the synthetic accessibility of the epimerization-prone aldehyde **8**, which had indeed been used for obtaining diastereomer **4**, according to the bibliographic reference (see Scheme 2) [17].

Therefore, considering the known lability of the hydrogen in the α-position of the aldehyde derivative **8**, we reasoned that following the same sequence depicted in Scheme 2, but starting from the enantiomer of **1**, (1*S*,2*R*,5*S*)-(+)-menthol (**11**), we may gain access to the enantiomer of **8**, the aldehyde (**14**). We hypothesized that epimerization at C-1 of the intermediate aldehyde **14** should take place under acidic conditions as it would produce the thermodynamically more stable diastereoisomer **15**, in which all three substituents (aldehyde, isopropyl and methyl) are in equatorial (Scheme 4). The latter would then serve as an intermediate for the synthesis of the final compound **5**.

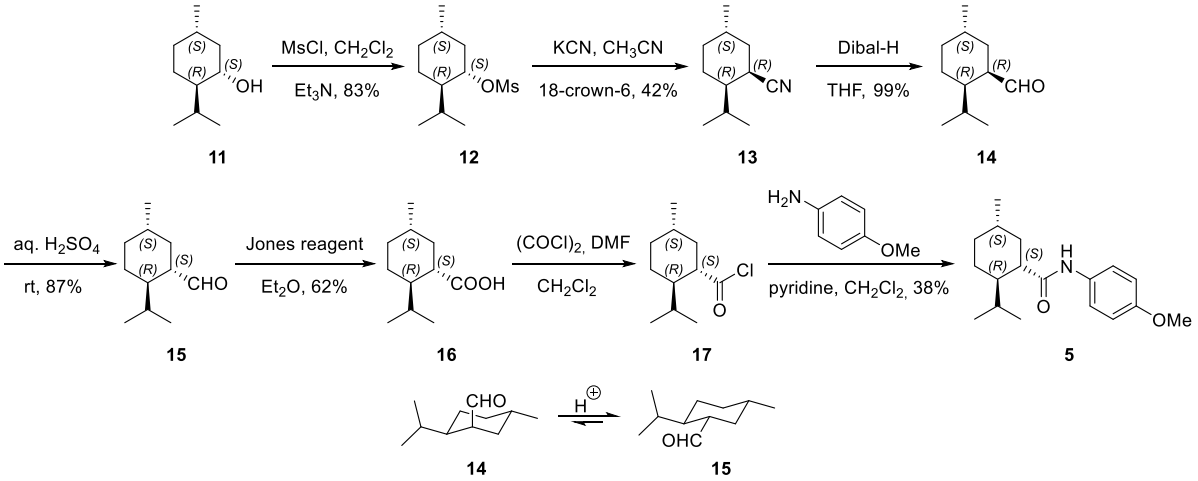

Scheme 4. Route of synthesis for **5**, *ent*-AR-15512, and key epimerization of **14** to **15**.

To our delight, the envisaged synthetic strategy turned out to be successful and allowed us to synthesize **5**. In this manner, the first synthetic step involved the treatment of **11** with mesyl chloride in dry DCM and in the presence of triethylamine as a base to yield the mesylate derivative (**12**) in 83% yield. In the next step, the inversion of the configuration in the C-1 occurred by means of an S_N2 reaction of the mesylate group by cyanide. The reaction of mesylate **12** with potassium cyanide in dry acetonitrile and in the presence of equimolecular quantities of 18-crown-6 furnished the nitrile derivative (**13**) as a unique product with an *R* configuration in the C-1 and in 42% yield. The following step involved the reduction of the nitrile to the aldehyde **14** in nearly quantitative yield with DIBAL-H in dry THF. As expected, the aldehyde **14** is susceptible to epimerization by treatment with aqueous sulfuric acid furnishing in 87% yield its epimer **15** that has the required stereochemistry in the three stereogenic centers to access the enantiomer of AR-15512. Oxidation of **15** using the Jones reagent yielded carboxylic acid **16** in 62% yield. Subsequently, treatment of **16** with oxalyl chloride in dry DCM and in the presence of a catalytic amount of DMF provided acid chloride (**17**), which was then reacted with *p*-anisidine in DCM under basic conditions to give the final compound, enantiomer **5**, with 38% yield (Scheme 4).

2.2.1. Characterization of **5**

The final compound **5** was fully characterized by ^{1}H, ^{13}C, COSY and HSQC NMR experiments, infrared, elemental analysis, specific optical rotation, and melting point (see Material and Methods section and Supplementary Materials for further details).

2.2.2. Chiral HPLC Method for the Analysis of AR-15512 and Its Enantiomer 5 (*ent*-AR-15512)

Just as we proceeded with the diastereomer **4**, a specific HPLC method was designed and developed to demonstrate that compound **5** was indeed the enantiomer of the clinical candidate AR-15512 and to discern between them. In particular, the chiral HPLC method was set up using a chiral column (Chiralpack IC 250 mm × 4.6 mm (particle size 5 μM)) as stationary phase and a mixture of hexane and 2-propanol as mobile phase, with a UV detector set at 254 nm (for detailed information, see Materials and Methods and Supplementary Materials). The retention times of the two compounds are shown below (Table 2).

Table 2. Retention times of AR-15512 and its enantiomer **5**.

Compound	Retention Time (min)
AR-15512	12.0
ent-AR-15512, **5**	10.0

3. Materials and Methods

3.1. Chemical Synthesis

3.1.1. General Methods

Commercially available reagents and solvents were used without further purification unless stated otherwise. Column chromatography was performed on silica gel 60 (35–70 μm) with the indicated solvent system. Thin-layer chromatography was performed with aluminum-backed sheets with silica gel 60 F_{254} (Merck, ref 1.05554), and spots were visualized with UV light and 1% aqueous solution of $KMnO_4$. Melting points were determined in open capillary tubes with an MFB 595010M Gallenkamp instrument. IR spectra were performed in a Shimadzu IRAffinity-1S spectrophotometer, and only noteworthy IR absorptions (cm^{-1}) are listed. Optical rotations were measured on a PerkinElmer 341 polarimeter. NMR spectra were recorded in $CDCl_3$ at 400 MHz (^1H) and 100.6 MHz (^{13}C). Chemical shifts are reported in δ values downfield from TMS or relative to residual chloroform (7.26 ppm, 77.0 ppm) as an internal standard. Data are reported in the following manner: chemical shift, multiplicity, coupling constants (*J*) in hertz (Hz), integrated intensity, and assignment. Multiplicities are reported using the following abbreviations: s, singlet; dd, doublet of doublets; ddd, doublet of a doublet of doublets; dddd, doublet of a doublet of a doublet of doublets; m, multiplet; dm, double multiplet; br s, broad signal. Assignments given for the NMR spectra of the compounds were carried out on the basis of COSY $^1H/^1H$ (standard procedures) and COSY $^1H/^{13}C$ (gHSQC) experiments. The elemental analyses were carried out in a Flash 1112 series ThermoFinnigan elemental microanalyzer (A5) to determine C, H, and N. The two final compounds possessed purity ≥95%, as evidenced by their elemental analyses.

3.1.2. Synthesis of Intermediates **6**–**9**

Compounds **6**, **7**, **8** and **9** were synthesized according to previously published procedures [17].

3.1.3. Synthesis of (1*S*,2*S*,5*R*)-5-methyl-2-(1-methylethyl)cyclohexanecarbonyl Chloride, **10**

The carboxylic acid **9** (293 mg, 1.6 mmol) and a catalytic amount of dry DMF (6 μL, 0.08 mmol) were put in dry DCM (10 mL) under argon and cooled to 0 °C, followed by the slow addition of oxalyl chloride (0.17 mL, 1.9 mmol) over a 10 min period. When the reaction was completed (monitored by NMR), the solvent was removed in vacuo. A yellow oil was obtained (323 mg, 100%) and was used in the next step without further purification. Its ^1H NMR spectrum was in agreement with the reported data [19].

3.1.4. Synthesis of neo-AR-15512, (1*S*,2*S*,5*R*)-*N*-(4-methoxyphenyl)-5-methyl-2-(1-methylethyl)cyclohexanecarboxamide, **4**

To a solution of *p*-anisidine (296 mg, 2.4 mmol) in dry DCM (8 mL) under argon, pyridine (0.2 mL, 2.4 mmol) was added. The solution was cooled to 0 °C and treated with the previously obtained compound **10** (323 mg, 1 mmol) dissolved in DCM (2 mL). The reaction mixture was stirred at room temperature overnight. The mixture was filtered, and the resulting filtrate was treated with 5 N aqueous NaOH until pH = 14 and subsequently extracted with DCM (3 × 50 mL). The combined organic extracts were dried over anhydrous Na_2SO_4, filtered and concentrated under reduced pressure to provide a yellow solid. Purification by column chromatography on silica with 100% DCM as eluent gave pure compound **4** as white crystals (360 mg, 78%), mp (ethyl acetate) 152 °C (151 °C [19]). $[\alpha]^{22}_D$ = +17.6 (*c* 0.23, EtOH) ($[\alpha]^{22}_D$ = +16.4 (*c* 1.0, EtOH) [19]). IR (KBr) ν: 527, 679, 822, 826,

1036, 1165, 1246, 1510, 1520, 1643, 1651, 2920, 2938, 2949, 3289, 3412, 3480 cm^{-1}. ^1H NMR (400 MHz, COSY, HETCOR, $CDCl_3$), δ: 0.84 (d, *J* = 6.4 Hz, 3 H, 5C-CH_3), 0.90 (m, 1 H, 4-H_{ax}), 0.91 [d, *J* = 6.4 Hz, 3 H, CH(C$\underline{H}_3$)$_2$], 0.94 [d, *J* = 6.8 Hz, 3 H, CH(C$\underline{H}_3$)$_2$], 1.08 (ddd, *J* = 16.8 Hz, *J′* = 8.0 Hz, *J″* = 4.0 Hz, 1 H, 2-H), 1.25 (m, 1 H, 6-H_{ax}), 1.67–1.73 (m, 2 H, 3-H_a, 5-H), 1.81 (dm, *J* = 12.8 Hz, 1 H, 4-H_{eq}), 1.89–1.99 [m, 3 H, 3-H_b, 6-H_{eq}, C$\underline{H}$(CH$_3$)$_2$], 2.67 (br s, 1 H, 1-H), 3.78 (s, 3 H, OCH_3), 6.84 [m, 2 H, 3(5)-ArH], 7.04 (br s, 1 H, NH), 7.39 [m, 2 H, 2(6)-ArH]. ^{13}C NMR (100.6 MHz, $CDCl_3$), δ: 21.3 [CH_3, CH(C$\underline{H}_3$)$_2$], 21.7 [CH_3, CH(C$\underline{H}_3$)$_2$], 22.5 (CH_3, 5C-CH_3), 25.5 (CH_2, 3-C), 27.1 [CH, C$\underline{H}$(CH$_3$)$_2$], 30.5 (CH, 5-C), 35.3 (CH_2, 4-C), 39.3 (CH_2, 6-C), 44.3 (CH, 1-C), 46.8 (CH, 2-C), 55.3 (CH_3, OCH_3), 114.1 [CH, 3(5)-ArC], 121.7 [CH, 2(6)-ArC], 131.3 (C, 1-ArC), 156.2 (C, 4-ArC), 173.4 (C, CON). Anal. calcd for $C_{18}H_{27}NO_2$: C 74.70, H 9.40, N 4.84. Found: C 74.90, H 9.34, N 4.69.

3.1.5. Synthesis of (1*S*,2*R*,5*S*)-(+)-menthol Mesylate, **12**

A solution of (1*S*,2*R*,5*S*)-(+)-menthol (**11**) (15 g, 96 mmol) in dry DCM (188 mL) under argon was cooled to 0 °C, and to that methane sulfonyl chloride (9.3 mL, 120 mmol) was added in one portion. The mixture was stirred for 20 min, followed by a dropwise addition of triethylamine (17.5 mL, 124.8 mmol) to the cold solution. The mixture was stirred for 24 h at 20 °C, whereupon complete consumption of starting material was shown by TLC analysis on SiO_2 using 15% ethyl acetate in hexane as eluent. The mixture was diluted with DCM (200 mL) and washed with water (2 × 100 mL), saturated aqueous $NaHCO_3$ (100 mL) and saturated aqueous NaCl (50 mL). The organic solution was dried over anhydrous Na_2SO_4, filtered, and the solvent removed in vacuo. The pale yellow oil was chromatographed on silica using 10% ethyl acetate in hexane as eluent to give **12** as a colorless oil (18.6 g, 83%). Its ^1H NMR spectrum was in agreement with the reported data for ent-**12** [17]. ^1H (400 MHz, $CDCl_3$), δ: 0.83 (d, *J* = 6.8 Hz, 3 H, 5C-C$\underline{H}_3$), 0.87 (m, 1 H, 4-H_{ax}), 0.92 [d, *J* = 6.8 Hz, 3 H, CH(C$\underline{H}_3$)$_2$], 0.93 [d, *J* = 6.8 Hz, 3 H, CH(C$\underline{H}_3$)$_2$], 1.04 (m, 1 H), 1.20 (m, 1 H), 1.30–1.49 (complex signal, 2 H), 1.57–1.69 (complex signal, 2 H), 2.00 (m, 1 H), 2.19 (dm, *J* = 12.0 Hz, 1 H), 3.00 (s, 3 H, $SO_2C\underline{H}_3$), 4.54 (ddd, *J* = 10.8 Hz, *J′* = 10.8 Hz, *J″* = 4.4 Hz, 1 H, 1-H).

3.1.6. Synthesis of (1*R*,2*R*,5*S*)-2-isopropyl-5-methylcyclohexane-1-carbonitrile, **13**

To a solution of the mesylate **12** (5.76 g, 24.6 mmol) in dry acetonitrile (70 mL) under argon was added potassium cyanide (8 g, 123 mmol) and 18-crown-6 (6.5 g, 24.6 mmol) and the resulting mixture was heated to reflux for 48 h. The mixture was poured into DCM (100 mL). The yellow solution was washed with water (5 × 30 mL) to remove excess cyanide and 18-crown-6. The organic phase was washed with saturated aqueous NaCl (50 mL) and dried over anhydrous Na_2SO_4. The solution was filtered, and the solvents were removed in vacuo. The resulting orange oil was chromatographed on silica with 5% ethyl acetate in hexane as eluent, affording compound **13** as a pale yellow oil (1.68 g, 42%). Its ^1H NMR spectrum was in agreement with the reported data for ent-**13** [20]. ^1H (400 MHz, $CDCl_3$), δ: 0.85 (m, 1 H), 0.92 (d, *J* = 6.8 Hz, 3 H, 5C-C$\underline{H}_3$), 0.96 [d, *J* = 6.4 Hz, 6 H, CH(C$\underline{H}_3$)$_2$], 1.00 (m, 1 H), 1.15 (ddd, *J* = 13.2 Hz, *J′* = 12.0 Hz, *J″* = 4.0 Hz, 1 H), 1.28 (m, 1 H), 1.59 (m, 1 H), 1.68–1.82 (complex signal, 2 H), 1.89 (m, 1 H), 1.99 (dq, *J* = 13.2 Hz, *J′* = 2.8 Hz, 1 H), 3.06 (m, 1 H, 1-H).

3.1.7. Synthesis of (1*R*,2*R*,5*S*)-2-isopropyl-5-methylcyclohexane-1-carboxaldehyde, **14**

A solution of nitrile **13** (1.41 g, 8.5 mmol) in dry THF (10 mL) under argon was cooled to 0 °C. Diisobutylaluminum hydride (17.5 mL, 1.2 M in toluene, 21.3 mmol) was added dropwise. The resulting solution was stirred at 0 °C for 4 h, then allowed to warm to 25 °C, and stirred for 18 additional hours. To quench, 200 mL of diethyl ether and 100 mL of 2% aqueous H_2SO_4 were cooled to 0 °C. The reaction mixture was added in 5 mL aliquots to the two-phase mixture with stirring between additions. After complete addition, the two-phase mixture was further acidified with 4 mL of 2% aqueous H_2SO_4. The organic phase was separated, and the aqueous phase was extracted with diethyl ether (3 × 150 mL).

The organic phases were combined and washed with saturated aqueous NaCl (100 mL), then dried over anhydrous Na_2SO_4, filtered, and the solvents removed in vacuo. **14** was isolated as a pale yellow oil (1.41 g, 99%). Due to its instability upon chromatography, this compound was used without further purification. Its ^{1}H NMR was in agreement with the reported data for *ent*-**14** [17].

3.1.8. Synthesis of (1*S*,2*R*,5*S*)-2-isopropyl-5-methylcyclohexane-1-carboxaldehyde, **15**

A solution of aldehyde **14** (0.84 g, 5 mmol) in diethyl ether (50 mL) was cooled to 0 °C, followed by a dropwise addition of 25% aqueous H_2SO_4 (18 mL) to the cold solution. The resulting solution was stirred at 0 °C for 4 h and at room temperature overnight. The organic phase was separated, and the aqueous phase was extracted with diethyl ether (3 × 100 mL). The organic phases were combined and washed with saturated aqueous NaCl (100 mL), then dried over anhydrous Na_2SO_4, filtered, and the solvents removed in vacuo. Aldehyde **15** was isolated as a pale orange oil (732 mg, 87%). Due to its instability upon chromatography, **15** was used in the next step without further purification. Its ^{1}H NMR was in agreement with previously reported data [21].

3.1.9. Synthesis of (1*S*,2*R*,5*S*)-2-isopropyl-5-methylcyclohexane-1-carboxylic Acid, **16**

To a solution of the aldehyde **15** (732 mg, 4.35 mmol) in 30 mL of diethyl ether and cooled to 0 °C, whereupon an excess of Jones reagent (8 mL) was transferred dropwise via pipet until the reaction solution remained orange colored. This mixture was vigorously stirred at room temperature for 60 min. A few drops of 2-propanol were then added until the mixture remained dark green colored and the solvents were removed under reduced pressure. The green solid residue was dissolved in water (50 mL), and this mixture was extracted with diethyl ether (4 × 50 mL). The combined organic layers were concentrated under reduced pressure until about 50 mL of the solvent remained. Then, it was washed with 2 N aqueous NaOH (3 × 50 mL), the combined basic layers acidified at 0 °C with conc. HCl until the pH was adjusted to about 2. The white precipitate thus formed was extracted with diethyl ether (3 × 40 mL); the combined ethereal layers were successively washed with one portion of water and saturated aqueous NaCl and dried over anhydrous Na_2SO_4. The dried ethereal solution was filtered through Celite® to remove any remaining chromium impurities, and the solvent was then removed in vacuo to give yellow crystals of acid **16** (500 mg, 62%). Its ^{1}H NMR was in agreement with previously reported data [22].

3.1.10. Synthesis of (1*S*,2*R*,5*S*)-2-isopropyl-5-methylcyclohexane-1-carbonyl Chloride, **17**

The carboxylic acid **16** (0.45 g, 2.44 mmol) and a catalytic amount of dry DMF (9 µL, 0.12 mmol) were put in dry DCM (15 mL) under argon and cooled to 0 °C, followed by the slow addition of oxalyl chloride (0.25 mL, 2.93 mmol) over a 10 min period. When the reaction was completed (monitored by NMR), the solvent was removed in vacuo. Compound **17** was obtained as a yellow oil (493 mg, 100%). Its ^{1}H NMR was in agreement with the reported data for ent-**17** [19].

3.1.11. Synthesis of ent-AR-15512, (1*S*,2*R*,5*S*)-*N*-(4-methoxyphenyl)-5-methyl-2-(1-methylethyl)cyclohexanecarboxamide, **5**

To a solution of the *p*-anisidine (451 mg, 3.66 mmol) in dry DCM (16 mL) under argon, pyridine (0.3 mL, 3.66 mmol) was added. The solution was then cooled to 0 °C and treated with the corresponding acid chloride **17** (493 mg, 2.44 mmol) dissolved in DCM (4 mL). The reaction mixture was stirred at room temperature overnight. The mixture was filtered, and the resulting filtrate treated with 5 N aqueous NaOH until pH = 14 and subsequently extracted with DCM (3 × 50 mL). The combined organic extracts were dried over anhydrous Na_2SO_4, filtered and concentrated under reduced pressure to provide a yellow solid. The resulting solid was chromatographed on silica with 100% DCM as eluent. The final compound **5** was obtained as white crystals (245 mg, 38%), mp (ethyl acetate) 178.6 °C. $[\alpha]^{22}_D$ = +56.0 (*c* 0.25, EtOH).

The specific optical rotation of AR-15512 was also measured $[\alpha]^{22}_{D} = -57.6$ (*c* 0.25, EtOH) ($[\alpha]^{22}_{D} = -58.6$ (*c* 1.0, EtOH) [19]). IR (KBr) ν: 725, 833, 1032, 1165, 1236, 1302, 1510, 1539, 1645, 1651, 2909, 2967, 3044, 3231 cm^{-1}. ^{1}H (400 MHz, COSY, HETCOR, $CDCl_3$), δ: 0.83 (d, *J* = 6.8 Hz, 3 H, 5C-C$\underline{H}_3$), 0.91 [d, *J* = 6.0 Hz, 3 H, CH(C$\underline{H}_3$)$_2$], 0.92 [d, *J* = 6.8 Hz, 3 H, CH(C$\underline{H}_3$)$_2$], 0.99 (m, 1 H, 4-H_{ax}), 1.07 (m, 1 H, 3-H_b), 1.29 (m, 1 H, 6-H_{ax}), 1.30 (m, 1 H, 5-H), 1.61 (dddd, *J* = 11.2 Hz, *J′* = 11.2 Hz, *J″*= 2.8 Hz, *J‴* = 2.8 Hz, 1 H, 2-H), 1.70 (m, 1 H, 3-H), 1.75 (m, 1 H, 4-H_{eq}), 1.82 [m, 1 H, C$\underline{H}$(CH$_3$)$_2$], 1.87 (dm, *J* = 11.6 Hz, 1 H, 6-H_{eq}), 2.12 (ddd, *J* = 11.2 Hz, *J′* = 11.2 Hz, *J″* = 3.2 Hz, 1 H, 1-H), 3.78 (s, 3 H, OCH_3), 6.84 [m, 2 H, 3(5)-ArH], 7.12 (br s, 1 H, NH), 7.42 [m, 2 H, 2(6)-ArH]. ^{13}C NMR (100.6 MHz, $CDCl_3$), δ: 16.3 (CH_3, 5C-CH_3), 21.4 [CH_3, CH(C$\underline{H}_3$)$_2$], 22.3 [CH_3, CH(C$\underline{H}_3$)$_2$], 24.0 (CH_2, 3-C), 28.8 [CH, C$\underline{H}$(CH$_3$)$_2$], 32.3 (CH, 5-C), 34.5 (CH_2, 4-C), 39.4 (CH_2, 6-C), 44.6 (CH, 2-C), 50.6 (CH, 1-C), 55.5 (CH_3, OCH_3), 114.1 [CH, 3(5)-ArC], 121.7 [CH, 2(6)-ArC], 131.1 (C, 1-ArC), 156.3 (C, 4-ArC), 174.0 (C, CON). Anal. calcd for $C_{18}H_{27}NO_2$: C 74.70, H 9.40, N 4.84. Found: C 74.62, H 9.26, N 4.64.

3.2. X-ray Crystallographic Analysis of neo-AR-15512, **4**

A colorless needle-like specimen of $C_{18}H_{27}NO_2$ (M = 289.42 g/mol), compound **4**, approximate dimensions 0.046 mm × 0.101 mm × 0.576 mm, was used for the X-ray crystallographic analysis. The X-ray intensity data were measured with a D8 Venture system equipped with a multilayer monochromator and a Cu microfocus (λ = 1.54178 Å) at 100.2 K. The frames were integrated with the Bruker SAINT software package using a narrow-frame algorithm. The structure was solved and refined using the Bruker SHELXTL Software Package, using the space group P 21 21 21, with Z = 4 for the formula unit $C_{18}H_{27}NO_2$ (orthorhombic system). The final cell constants of *a* = 9.1371(2) Å, *b* = 10.3821(3) Å, *c* = 17.4893(7) Å, V = 1659.98(7) $Å^3$, are based upon the refinement of the XYZ-centroids of reflections above 20 σ(I). Data were corrected for absorption effects using the multiscan method (SADABS). For further information, refer to Supplementary Materials [18].

3.3. HPLC Equipment and Methods

3.3.1. HPLC Equipment

All analyses were carried out with a Waters HPLC system with a 1525 binary pump coupled to a UV detector Waters 2489 set at 254 nm and using Waters Breeze software.

3.3.2. HPLC Method for Identification of AR-15512 and *neo*-AR-15512, **4**

Sample concentration. Solid sample 1 mg AR-15512 in 1 mL acetonitrile; solid sample 1 mg compound **4** in 1 mL acetonitrile; and solid sample mixture 1 mg AR-15512/1 mg compound **4** in 2 mL acetonitrile.

Chromatographic conditions. The employed column was a Ultrabase C-18 (Akady) 5 ODS 4.6 mm × 250 mm (5 µm), with a constant flow of 1.0 mL min^{-1} and a controlled temperature of 25 °C. The injection volume was 10 µL, and the detection wavelength was set at λ = 254 nm. The mobile phase consisted of acetonitrile + 0.1% TFA and water + 0.1% TFA. A gradient method was developed and is detailed in Table 3.

Table 3. Detailed gradient for the developed method.

Time (min)	% Acetonitrile + 0.1% TFA	% Water + 0.1% TFA
0	5	95
0.5	5	95
3	65	35
15	65	35
20	95	5
22	95	5
25	5	95

3.3.3. Chiral HPLC Method for Identification of AR-15512 and ent-AR15512, **5**

Sample concentration. Solid sample 1 mg AR-15512 in 1 mL 2-propanol; solid sample 1 mg compound **5** in 1 mL 2-propanol; and solid sample mixture 1 mg AR-15512/1 mg compound **5** in 2 mL 2-propanol; then, from the first two solutions, a new solution was prepared with 0.75 mL of AR-15512 solution and 0.25 mL of compound **5** solution.

Chromatographic conditions. The employed column was a Chiralpack IC (Daicel Chemical Ind., Ltd., Tokyo, Japan) 5 ODS 4.6 mm × 250 mm (5 µm), with a constant flow of 1.0 mL min^{-1} and a controlled temperature of 25 °C. The injection volume was 10 µL, and the detection wavelength was λ = 254 nm. The mobile phase consisted of isocratic 90% hexane and 10% 2-propanol.

4. Conclusions

In this work, two stereoisomers of AR-15512, a TRPM8 agonist currently in clinical trials for the treatment of the very common ophthalmological disorder dry eye, were synthesized and fully characterized. On one hand, its diastereomer at the C-1 was obtained, and its absolute configuration was confirmed by X-ray crystallographic analysis. On the other hand, and to our knowledge, we report for the first time a synthetic sequence to access the enantiomer of AR-15512. In addition, we provide two different HPLC methods designed and developed to identify both stereoisomers and to differentiate them from the clinical candidate AR-15512.

Supplementary Materials: The following are available online, Figure S1. ^{1}H, ^{13}C, HSQC and COSY NMR and IR spectra of compound **4**, Figure S2. ^{1}H, ^{13}C, HSQC and COSY NMR and IR spectra of compound **5**, Tables S1–S5. X-ray crystallographic data for compound **4**, Figure S3. HPLC chromatograms of compounds AR-15512 and **4**, Figure S4. HPLC chromatograms of compounds AR-15512 and **5**.

Author Contributions: C.E. and S.V. designed and supervised the work; S.R.-A. performed the chemical synthesis and full characterization; S.A. and C.G. performed HPLC chromatography and analyzed the analytical data; E.P. wrote and edited the manuscript. All authors have read and agreed to the published version of the manuscript.

Funding: This research was funded by AVIZOREX PHARMA, S. L.

Institutional Review Board Statement: Not applicable.

Informed Consent Statement: Not applicable.

Data Availability Statement: Not applicable.

Conflicts of Interest: The authors declare no conflict of interest. The funder had no role in the design of the study; in the collection, analyses, or interpretation of data; in the writing of the manuscript, or in the decision to publish the results.

Sample Availability: Samples of the compounds are available from the authors.

References

1. Belmonte, C.; Gallar, J.; Ferrer, A.; Fernandez, A.; Viana, F. Pharmaceutical Composition for the Treatment of Dry Eye. WO2012/032209A2, 15 March 2012.
2. Aerie Pharmaceuticals Initiates Phase 2b Clinical Trial of AR-15512 (TRPM8 Agonist) Ophthalmic Solution for the Treatment of Patients with Dry Eye Disease. Available online: https://investors.aeriepharma.com/news-releases/news-release-details/aerie-pharmaceuticals-initiates-phase-2b-clinical-trial-ar-15512 (accessed on 13 December 2020).
3. A Phase 2b Study Evaluating the Safety and Efficacy of AR-15512 Ophthalmic Solution for the Treatment of Dry Eye Disease (COMET-1). Available online: https://clinicaltrials.gov/ct2/show/NCT04498182 (accessed on 15 December 2020).
4. Craig, P.; Nelson, J.D.; Azar, D.T.; Belmonte, C.; Bron, A.J.; Chauhan, S.K.; de Paiva, C.S.; Gomez, J.A.P.; Hammitt, K.M.; Jones, L.; et al. TFOS DEWS II report executive summary. *Ocul. Surf.* **2017**, *15*, 802–812. [CrossRef] [PubMed]
5. O'Neil, E.C.; Henderson, M.; Massaro-Giordano, M.; Bunya, V.Y. Advances in dry eye disease treatment. *Curr. Opin. Ophthalmol.* **2019**, *30*, 166–178. [CrossRef] [PubMed]
6. Clayton, J.A. Dry Eye. *N. Engl. J. Med.* **2018**, *378*, 2212–2223. [CrossRef] [PubMed]

7. Watson, H.R.; Hems, R.; Rowsell, D.G.; Spring, D.J. New compounds with the menthol cooling effect. *J. Soc. Cosmet. Chem.* **1978**, *29*, 185–200.
8. Parra, A.; Madrid, R.; Echevarria, D.; del Olmo, S.; Morenilla-Palao, C.; Acosta, M.C.; Gallar, J.; Dhaka, A.; Viana, F.; Belmonte, C. Ocular surface wetness is regulated by TRPM8-dependent cold thermoreceptors of the cornea. *Nat. Med.* **2010**, *16*, 1396–1399. [CrossRef]
9. Avizorex Pharma, S.L. Submits Clinical Trial Application for Its Lead Compound AVX-012 for Dry Eye Syndrome. Press Release. Available online: http://www.pcb.ub.edu/portal/documents/430271/0/Avizorex+press+release.pdf/29c18a21-d884-4939-8927-10d845cb8108 (accessed on 15 December 2020).
10. Aerie Pharmaceuticals Announces Agreement to Acquire Avizorex Pharma, S.L. to Advance Its Dry Eye Program. News Release. Available online: https://investors.aeriepharma.com/news-releases/news-release-details/aerie-pharmaceuticals-announces-agreement-acquire-avizorex (accessed on 18 December 2020).
11. Assessing the Safety and Efficacy of AVX-012 in Subjects with Mild-to-Moderate Dry Eye Syndrome (AVX012CT001). Available online: https://clinicaltrials.gov/ct2/show/NCT03162094 (accessed on 13 December 2020).
12. Watson, H.R.; Rowsell, D.G.; Spring, D.J. Substituted p-menthanecarboxamides and compositions containing them. UK Patent 1,351,761, 4 February 1971.
13. Yin, Y.; Le, S.C.; Hsu, A.L.; Borgnia, M.J.; Yang, H.; Lee, S.-Y. Structural basis of cooling agent and lipid sensing by the cold-activated TRPM8 channel. *Science* **2019**, *363*, eaav9334. [CrossRef]
14. Smith, J.G.; Wright, G.F. The diastereomeric menthyl chlorides obtained from (−) menthol. *J. Org. Chem.* **1952**, *17*, 1116–1121. [CrossRef]
15. Reynolds, M.; Polakis, P. TRP-P8 Active Compounds and Therapeutic Treatment Methods. WO2005/002582A2, 2 July 2004.
16. Beckmann, J.; Dakternieks, D.; Dräger, M.; Duthie, A. New insights into the classic chiral Grignard reagent (1*R*,2*S*,5*R*)-methylmagnesium chloride. *Angew. Chem. Int. Ed.* **2006**, *45*, 6509–6512. [CrossRef] [PubMed]
17. Dillner, D.K. Syntheses of C-1 Axial Derivatives of $_{L}$-Menthol. *Org. Prep. Proced. Int.* **2009**, *41*, 147–152. [CrossRef]
18. COD3000283 Contains the Supplementary Crystallographic Data for the (1S,2S,5R)-Diastereromer, Compound 5. Available online: http://www.crystallography.net/cod/search.html (accessed on 15 December 2020).
19. Dilk, E.; Schöning, A.; Oertling, H.; Gömann, C.; Heinemeyer, H. Herstellung von Menthancarbonaldehyd, Menthancarbonsäure und Folgeprodukten. DE102012202885A1, 5 May 2012.
20. Xu, B.; Tambar, U.K. Remote allylation of unactivated C(sp^3)-H bonds triggered by photogenerated amidyl radicals. *ACS Catal.* **2019**, *9*, 4627–4631. [CrossRef]
21. Spino, C.; Godbout, C.; Beaulieu, C.; Harter, M.; Mwene-Mbeja, T.M.; Boisvert, L. *p*-Menthane-3-carboxaldehyde: A useful chiral auxiliary for the synthesis of chiral quaternary carbons of high enantiomeric purity. *J. Am. Chem. Soc.* **2004**, *126*, 13312–13319. [CrossRef]
22. Dillner, D.K.; Traficante, D.D. Complete ^{1}H and ^{13}C NMR assignments of the epimeric menthane-1-carboxylic acids. *Mag. Res. Chem.* **2007**, *45*, 193–197. [CrossRef] [PubMed]

SUPPLEMENTARY MATERIAL FOR

Synthesis, characterization and HPLC analysis of the (1*S*,2*S*,5*R*)-diastereomer and the enantiomer of the clinical candidate AR-15512

Sergio Rodríguez-Arévalo[a], Eugènia Pujol[a], Sònia Abás[a], Carles Galdeano[b], Carmen Escolano[a] and Santiago Vázquez[a]

[a]*Laboratori de Química Farmacèutica (Unitat Associada al CSIC), Facultat de Farmàcia i Ciències de l'Alimentació, and Institute of Biomedicine (IBUB), Universitat de Barcelona, Av. Joan XXIII 27-31, 08028 Barcelona, Spain*

[b]*Department of Pharmacy and Pharmaceutical Technology and Physical Chemistry, Faculty of Pharmacy and Food Sciences and Institute of Biomedicine, University of Barcelona, Av. Joan XXIII, 27-31, E-08028, Barcelona, Spain*

Table of contents

Figure S1: ^{1}H, ^{13}C, HSQC and COSY, and IR spectra of compound **4**	Page S3
Figure S2: ^{1}H, ^{13}C, HSQC and COSY, and IR spectra of compound **5**	Page S10
Table S1	Page S18
Table S2	Page S19
Table S3	Page S20
Table S4	Page S25
Table S5	Page S26
Figure S3: HPLC chromatograms of AR-15512 and compound **4**	Page S27
Figure S4: HPLC chromatograms of AR-15512 and compound **5**	Page S30

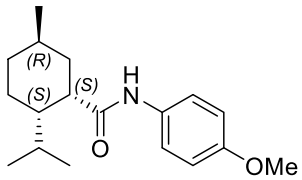

^{1}H (400 MHz, $CDCl_3$)

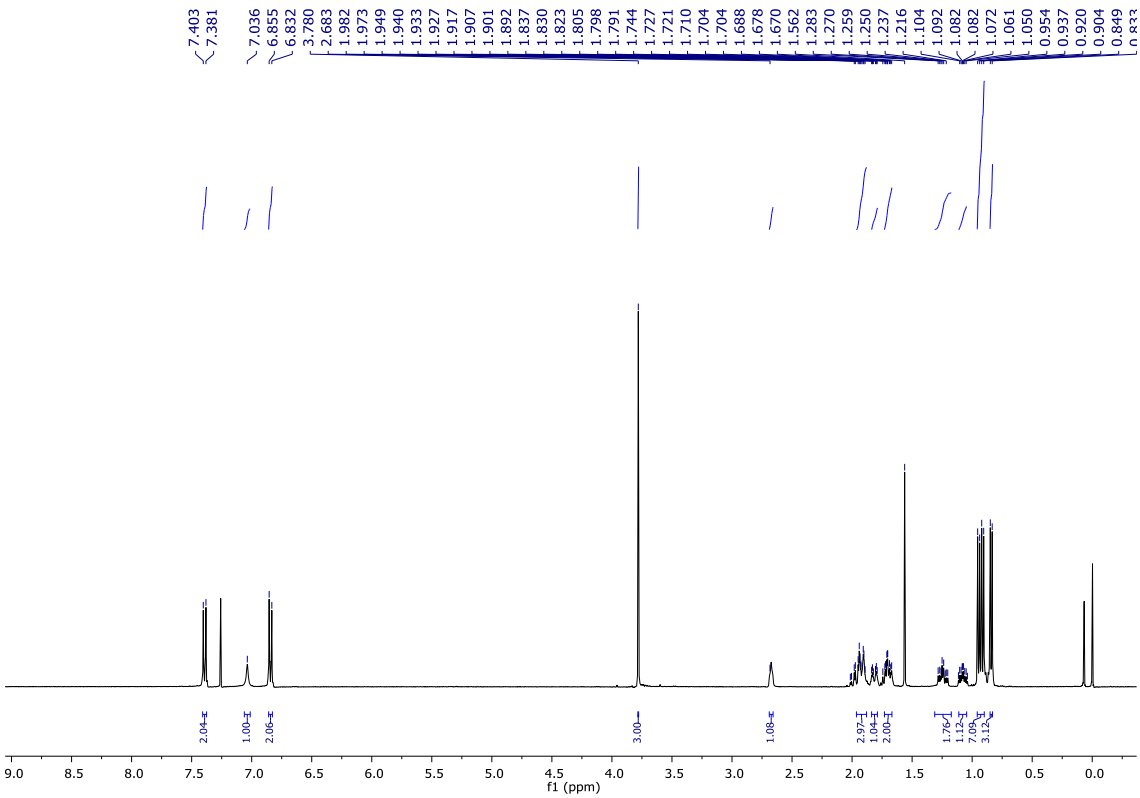

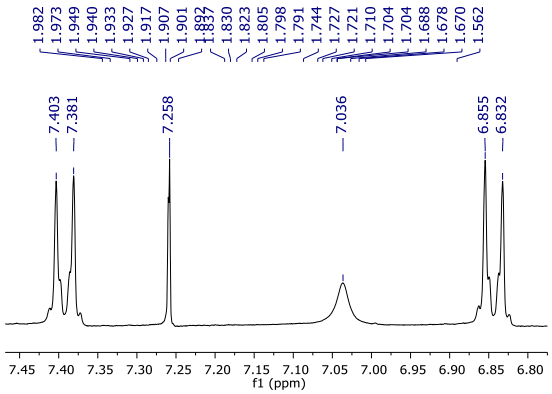

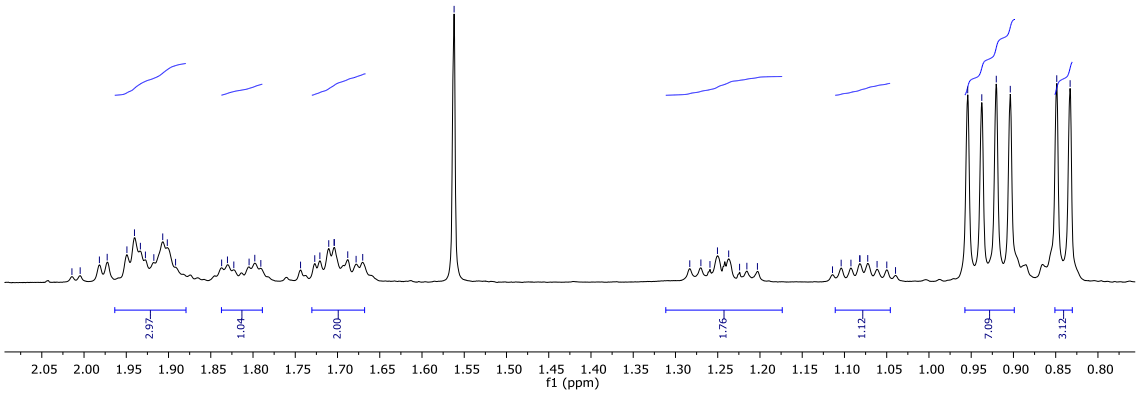

^{13}C (100.6 MHz, $CDCl_3$)

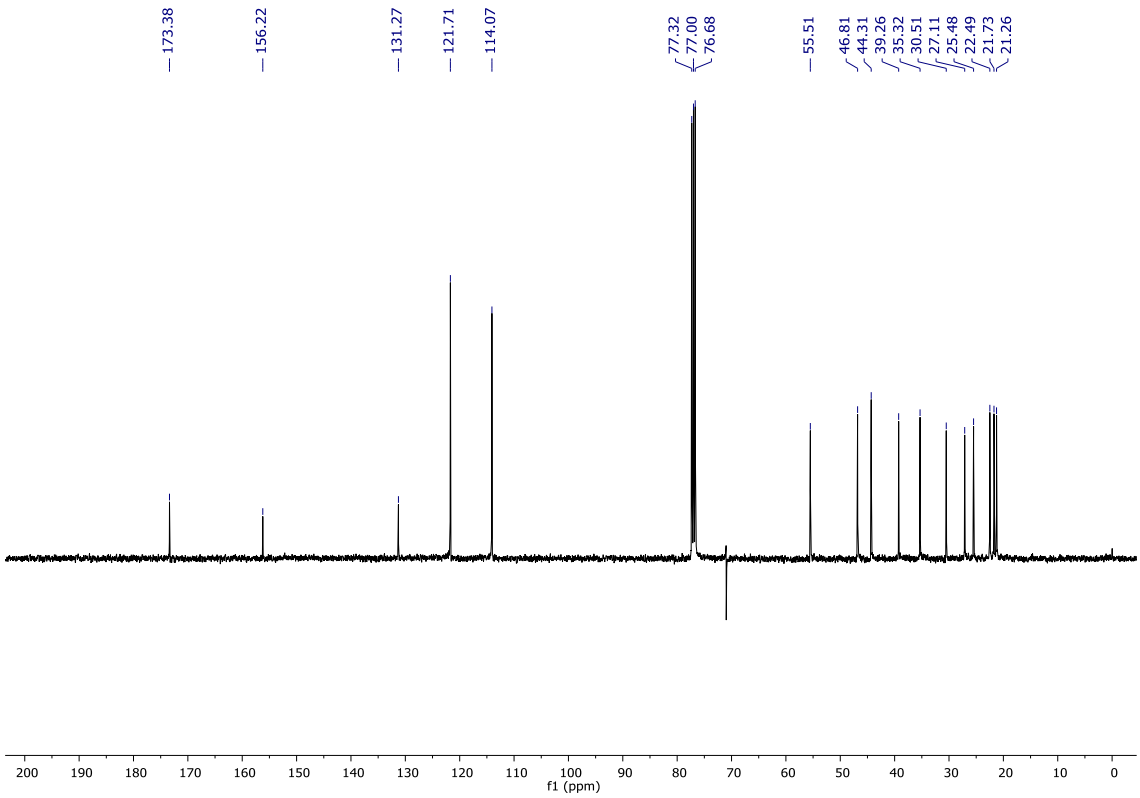

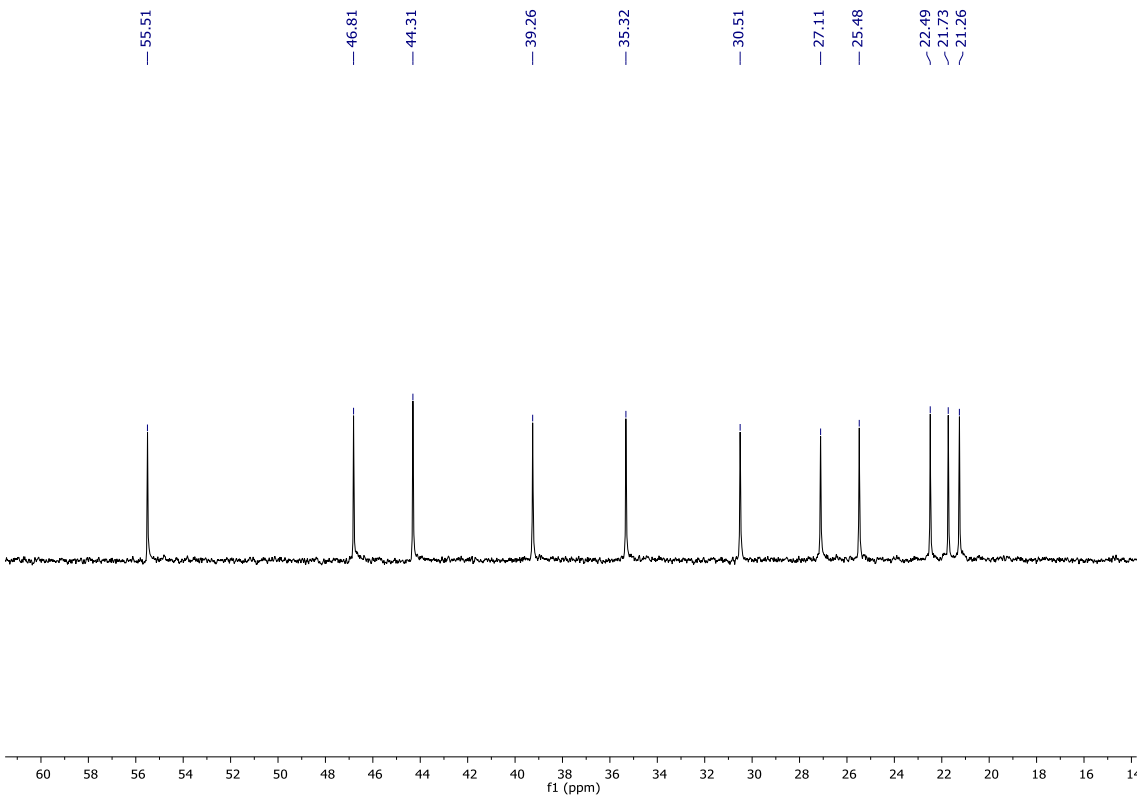

HSQC (400 MHz, $CDCl_3$)

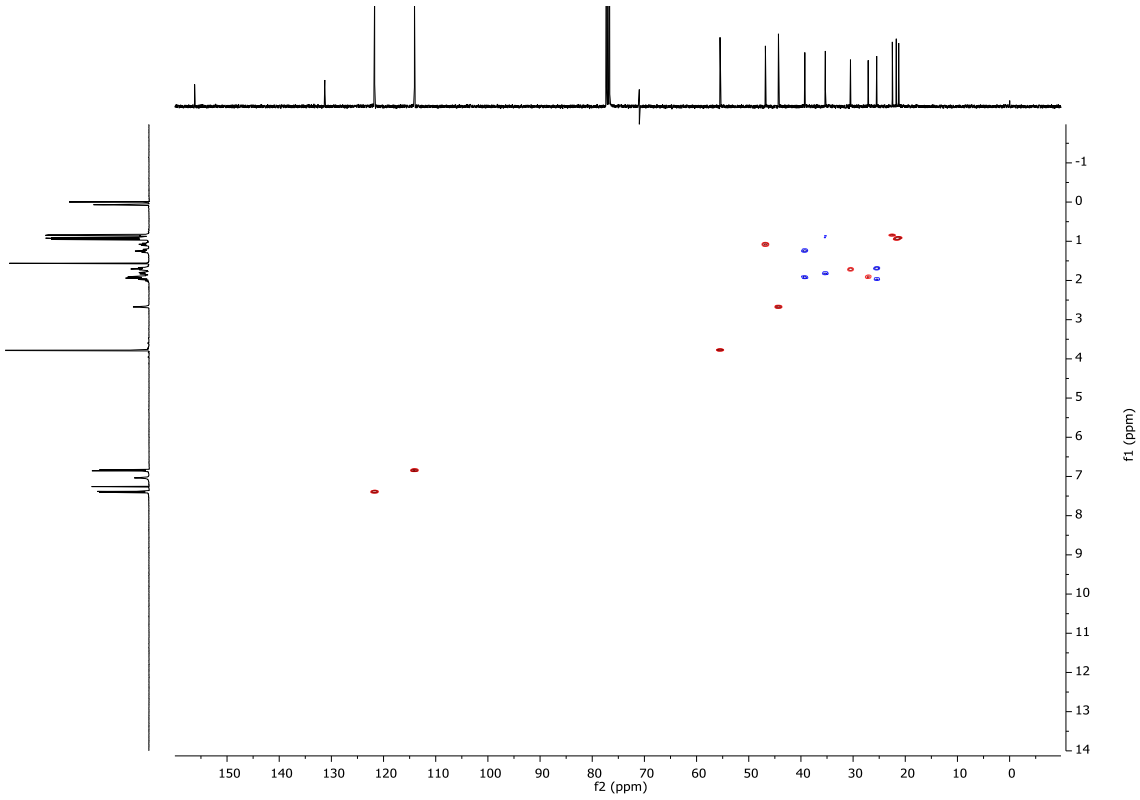

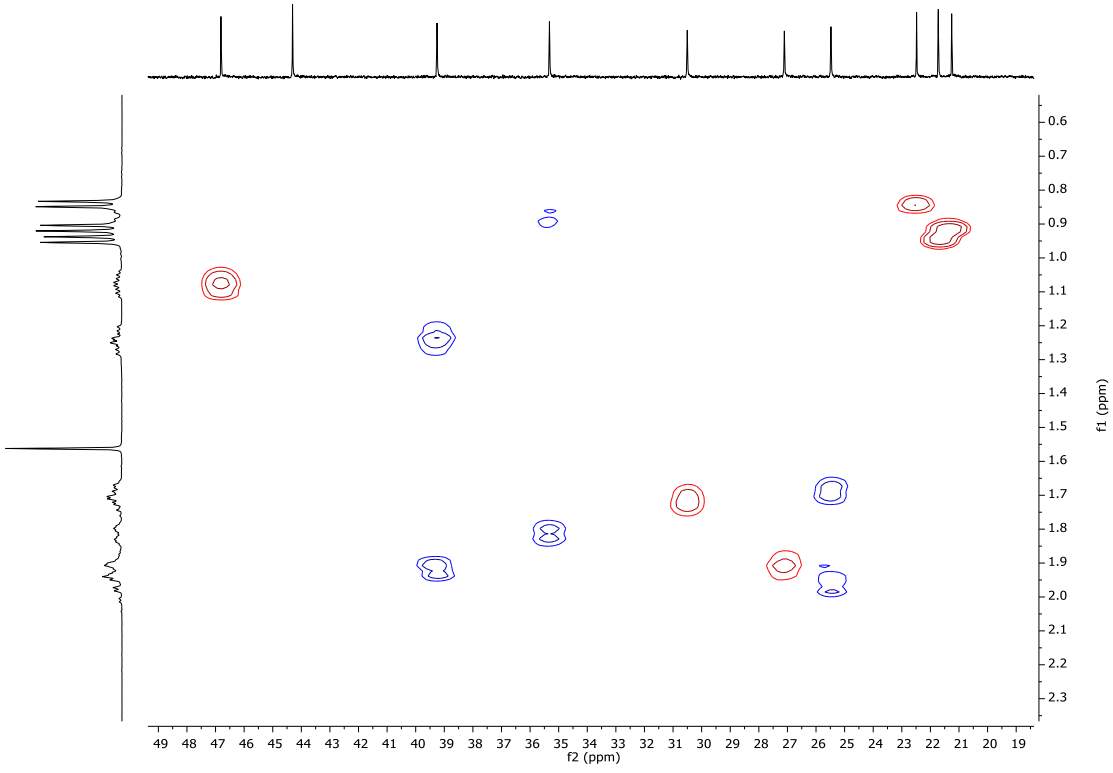

COSY (400 MHz, $CDCl_3$)

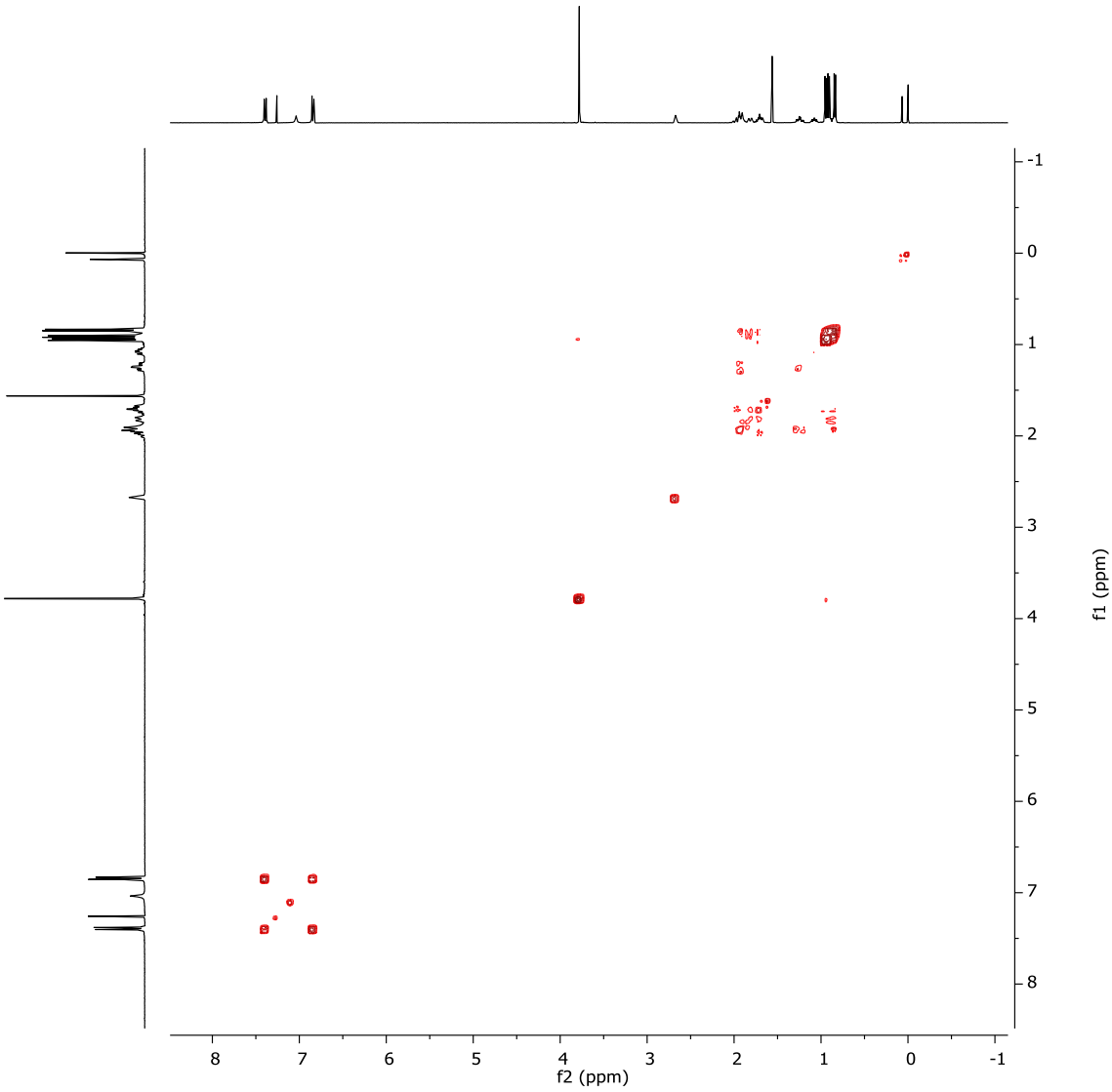

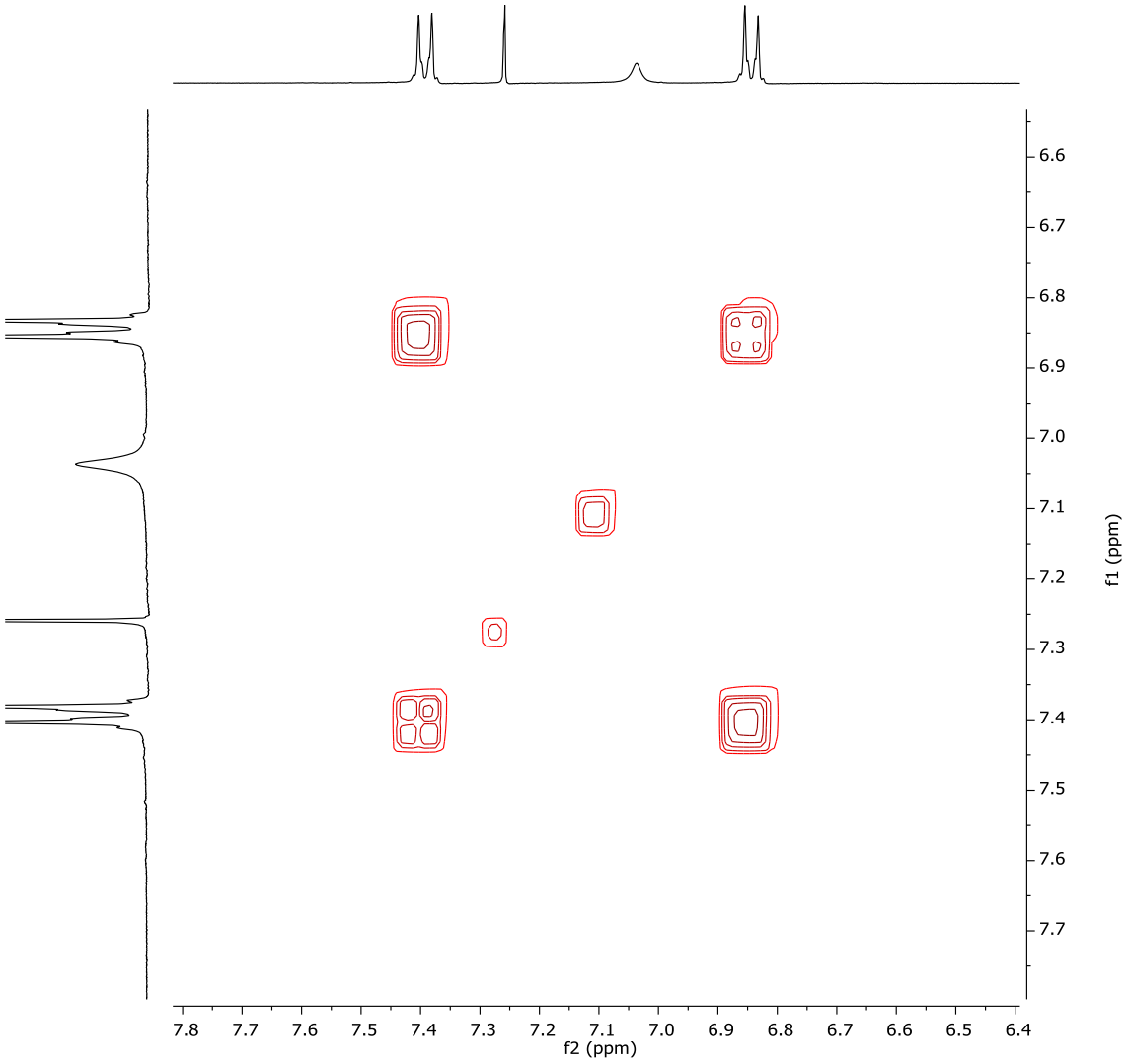
6.6
6.7
6.8
6.9
7.0
7.1
7.2
7.3
7.4
7.5
7.6
7.7
f1 (ppm)
7.8
7.7
7.6
7.5
7.4
7.3
7.2
7.1
7.0
6.9
6.8
6.7
6.6
6.5
6.4
f2 (ppm)

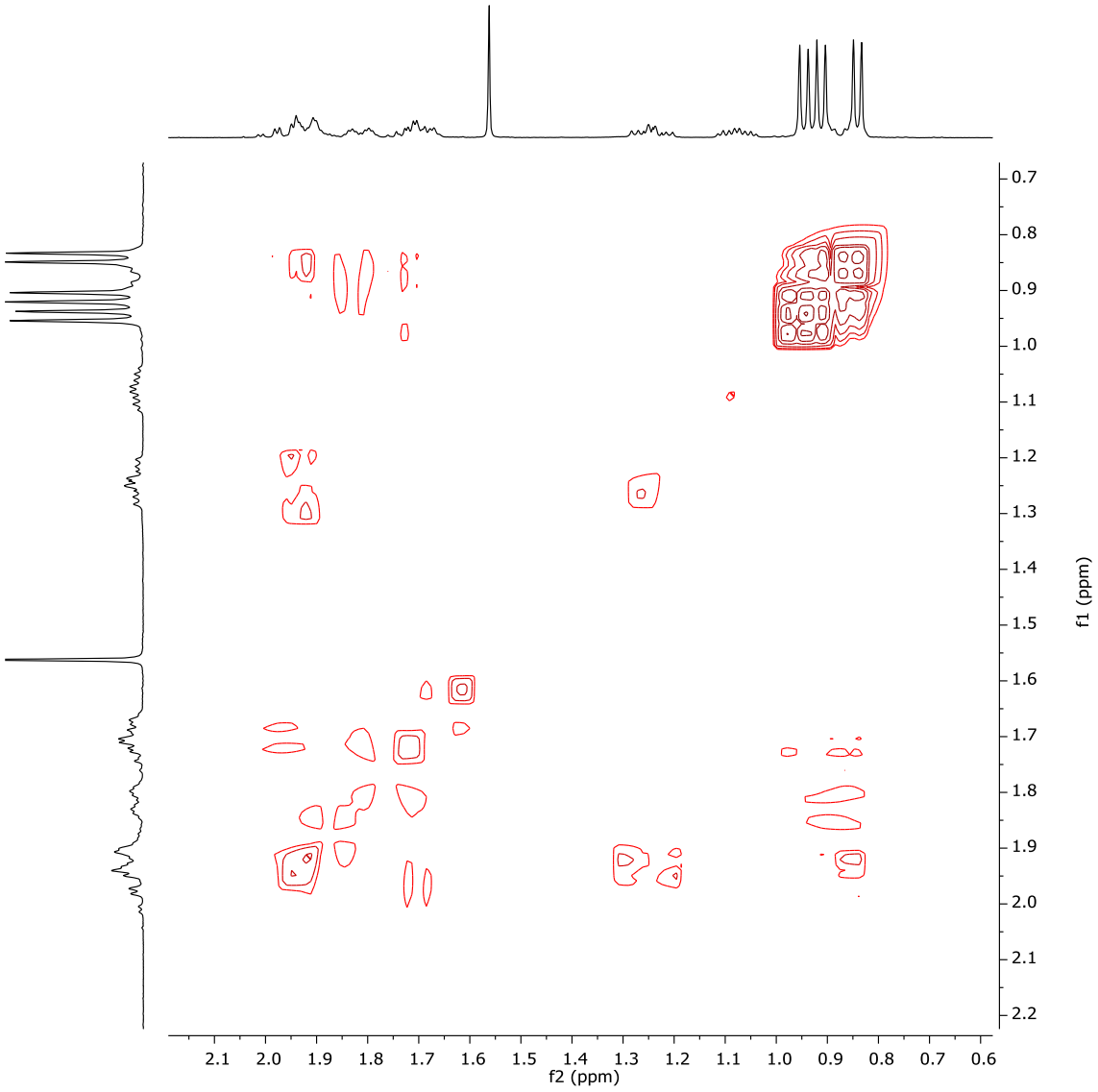
0.7
0.8
0.9
1.0
1.1
1.2
1.3
1.4
1.5
1.6
1.7
1.8
1.9
2.0
2.1
2.2
f1 (ppm)
2.1 2.0 1.9 1.8 1.7 1.6 1.5 1.4 1.3 1.2 1.1 1.0 0.9 0.8 0.7 0.6
f2 (ppm)

IR spectrum

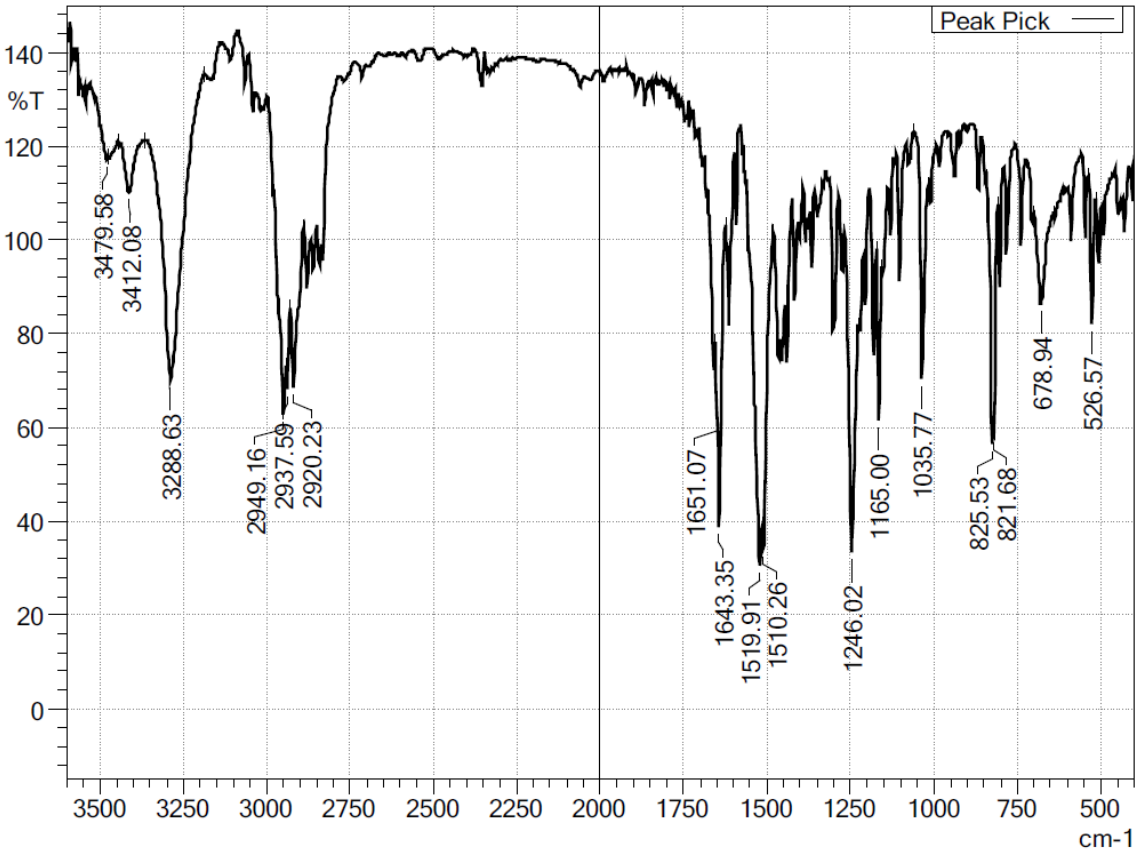

No.	Peak	Intensity	Corr. Intensity	Base (H)	Base (L)	Area	Corr. Area	Area color
1	526.57	82.19	28.92	538.14	514.99	-10.658	246.570	Auto
2	678.94	86.46	19.26	702.09	640.37	124.997	480.292	Auto
3	821.68	58.22	6.93	823.60	808.17	286.005	28.918	Auto
4	825.53	56.33	7.68	844.82	823.60	181.645	-111.872	Auto
5	1035.77	70.27	46.78	1058.92	1016.49	-139.244	606.376	Auto
6	1165.00	61.39	34.97	1172.72	1155.36	323.561	256.670	Auto
7	1246.02	33.26	58.02	1269.16	1224.80	1445.945	1078.110	Auto
8	1510.26	33.97	12.75	1514.12	1481.33	956.741	-7.751	Auto
9	1519.91	30.42	17.46	1554.63	1514.12	1546.766	296.228	Auto
10	1643.35	38.89	33.71	1649.14	1624.06	745.284	327.499	Auto
11	1651.07	62.59	5.80	1654.92	1649.14	184.056	15.567	Auto
12	2920.23	68.49	21.08	2929.87	2889.37	650.521	408.979	Auto
13	2937.59	68.24	8.99	2941.44	2929.87	290.688	51.110	Auto
14	2949.16	62.89	17.99	2978.09	2941.44	658.969	349.963	Auto
15	3288.63	70.06	57.37	3365.78	3186.40	-1256.928	3841.016	Auto
16	3412.08	110.20	10.87	3442.94	3365.78	-1311.649	317.203	Auto
17	3479.58	117.09	1.10	3483.44	3475.73	-136.074	4.329	Auto

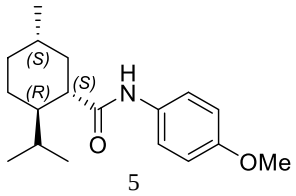

5

^{1}H (400 MHz, $CDCl_3$)

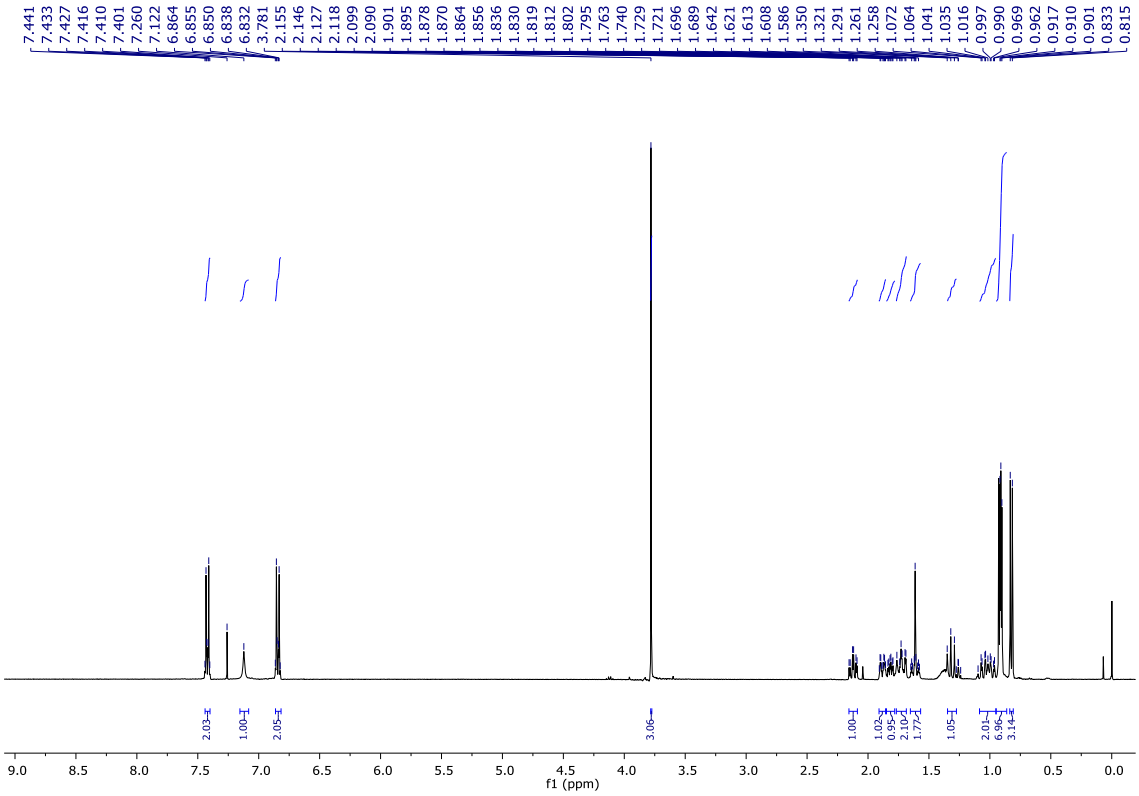

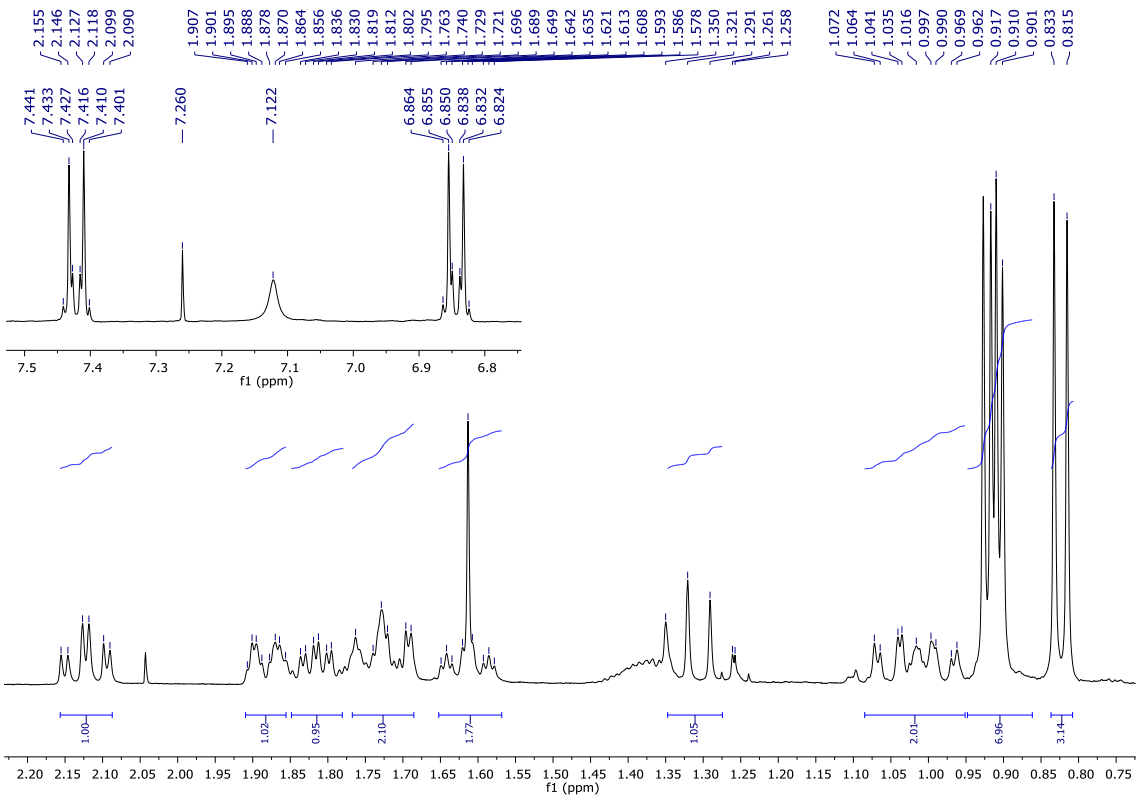

^{13}C (100.6 MHz, $CDCl_3$)

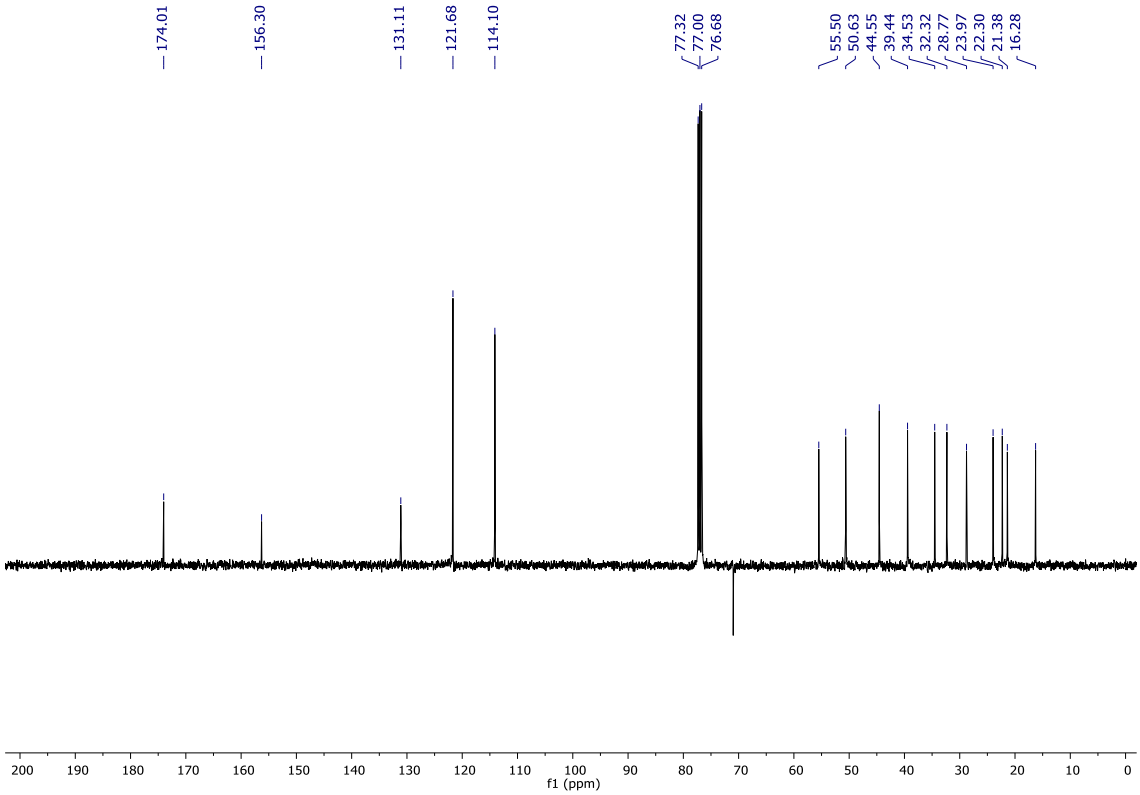

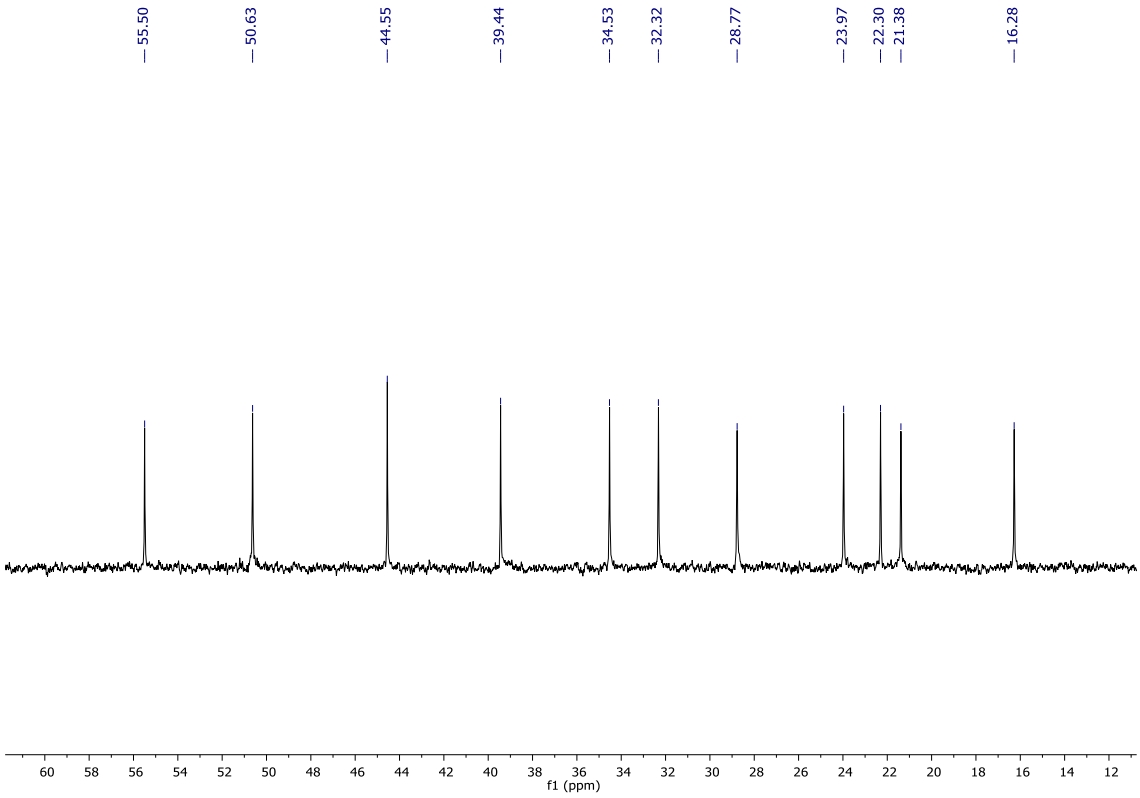

HSQC (400 MHz, $CDCl_3$)

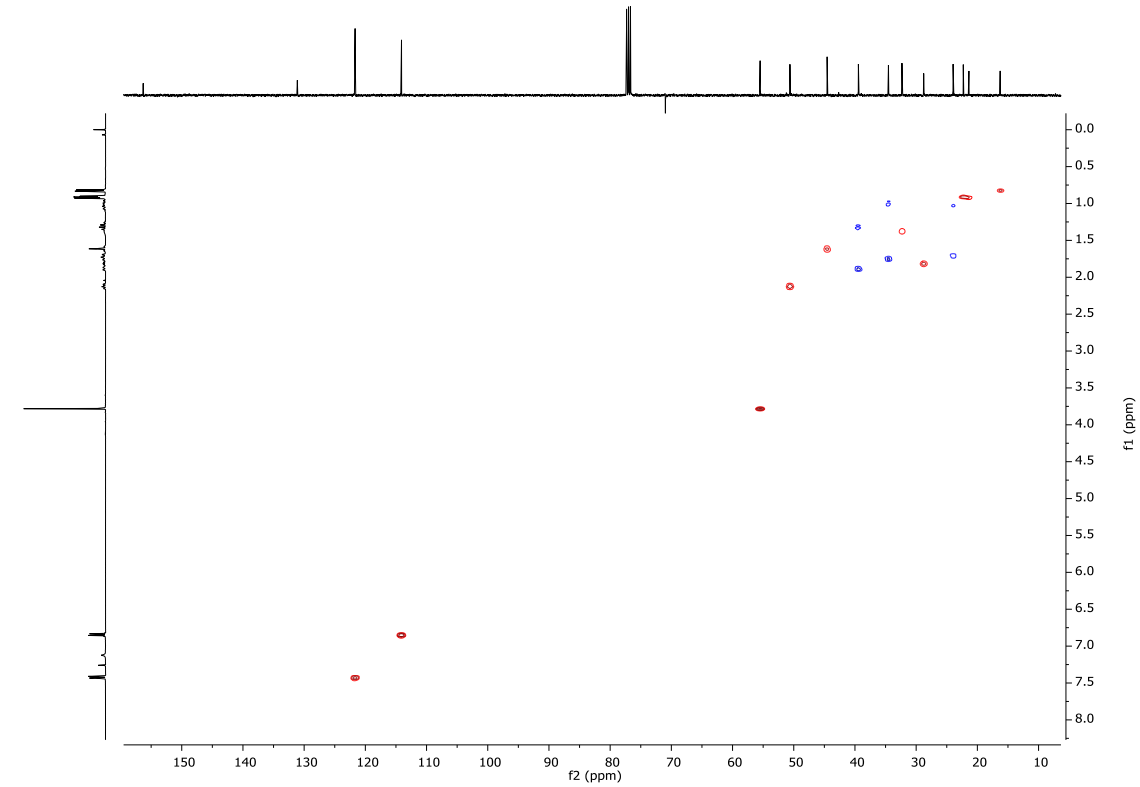

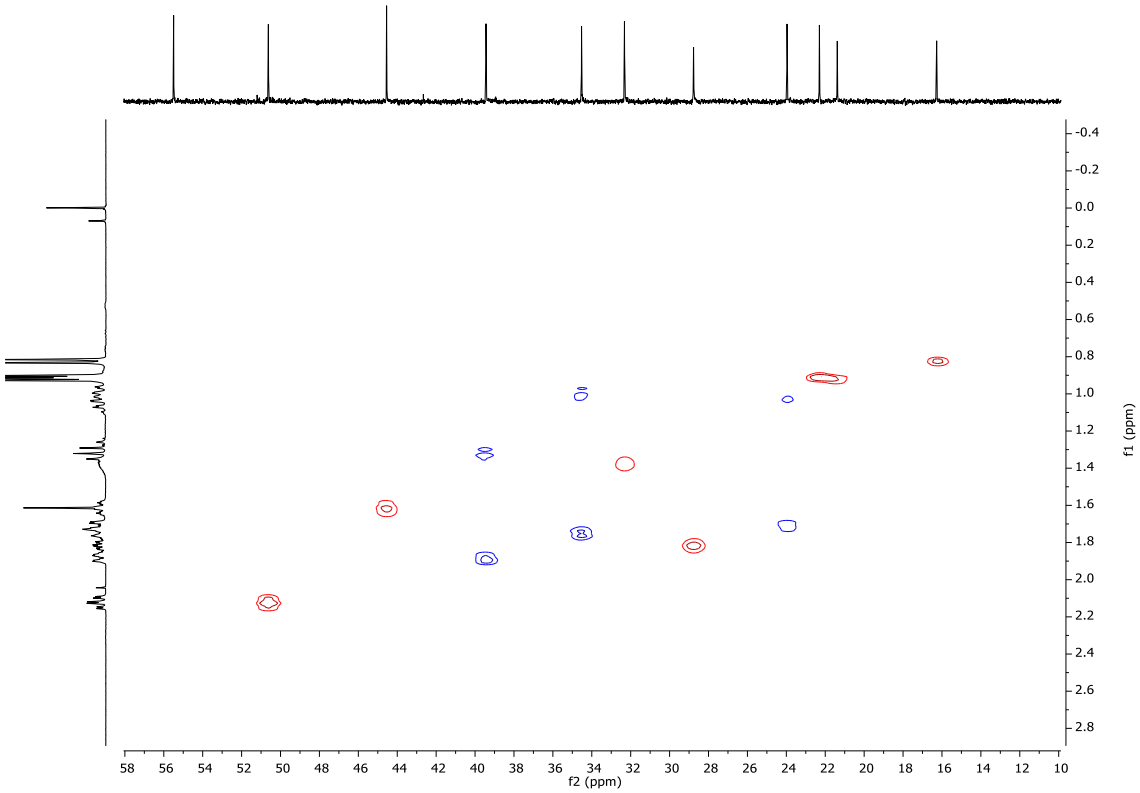

COSY (400 MHz, $CDCl_3$)

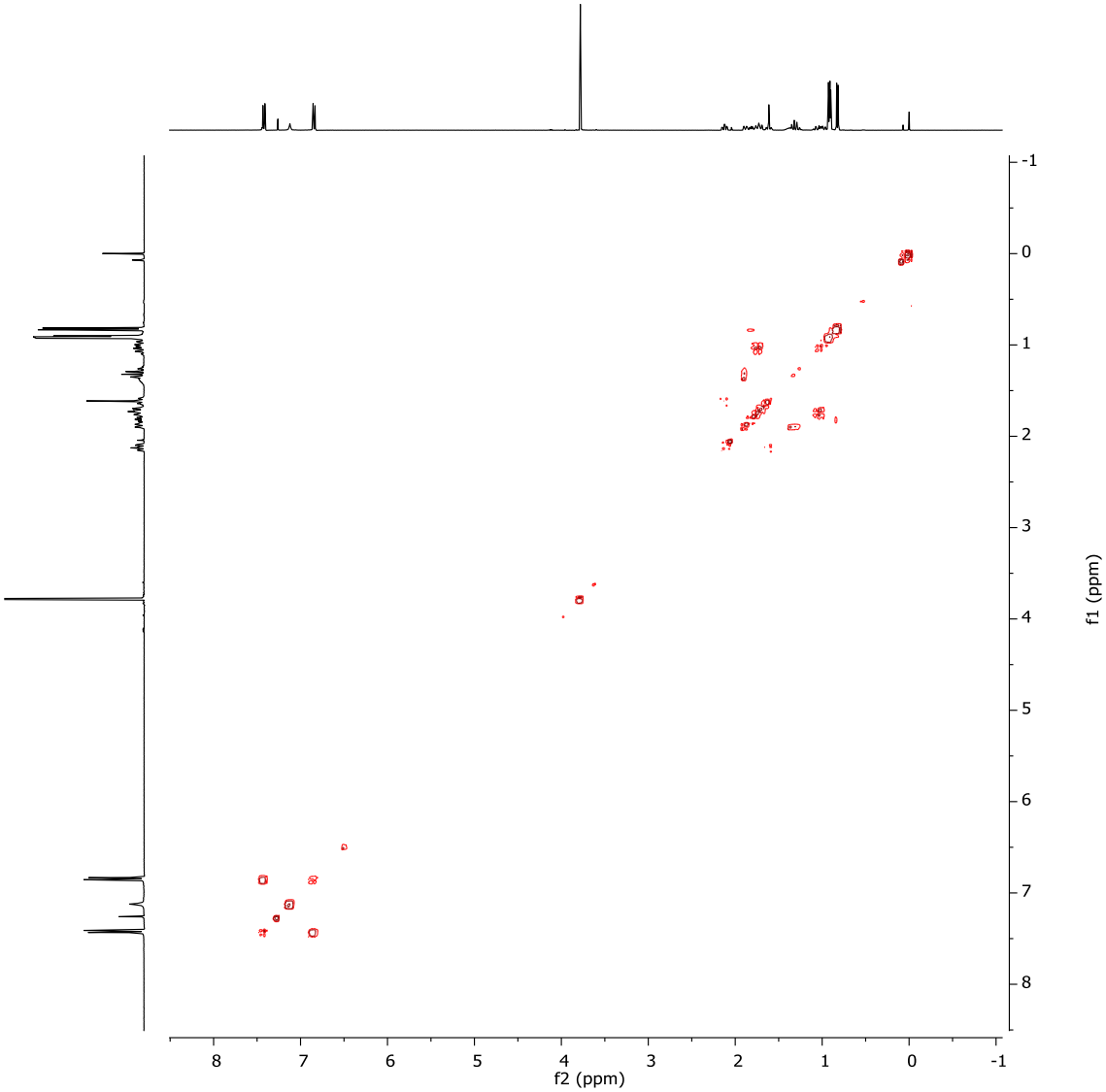

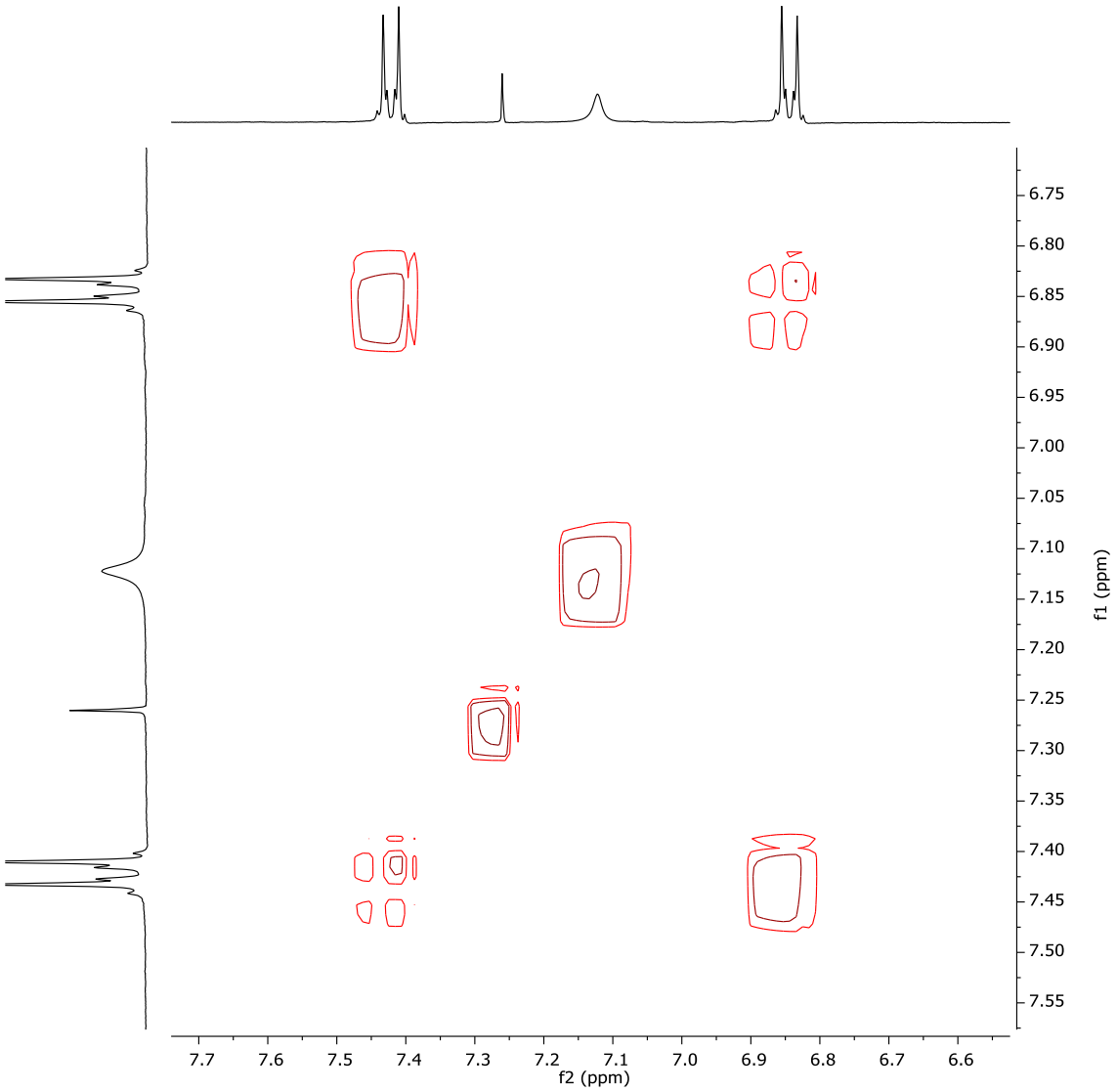
6.75
6.80
6.85
6.90
6.95
7.00
7.05
7.10
7.15
7.20
7.25
7.30
7.35
7.40
7.45
7.50
7.55
f1 (ppm)
7.7
7.6
7.5
7.4
7.3
7.2
7.1
7.0
6.9
6.8
6.7
6.6
f2 (ppm)

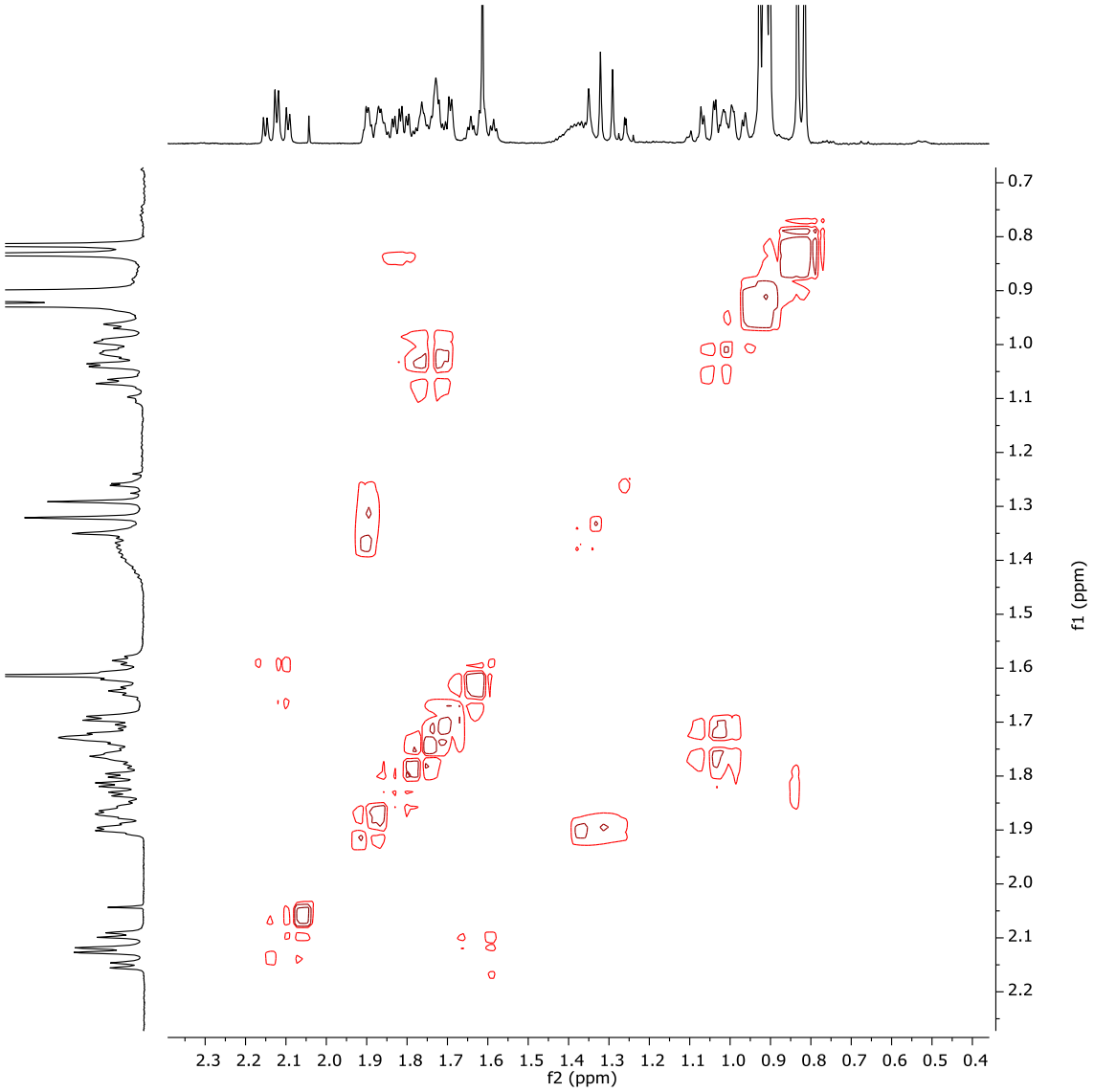
0.7
0.8
0.9
1.0
1.1
1.2
1.3
1.4
1.5
1.6
1.7
1.8
1.9
2.0
2.1
2.2
f1 (ppm)
2.3 2.2 2.1 2.0 1.9 1.8 1.7 1.6 1.5 1.4 1.3 1.2 1.1 1.0 0.9 0.8 0.7 0.6 0.5 0.4
f2 (ppm)

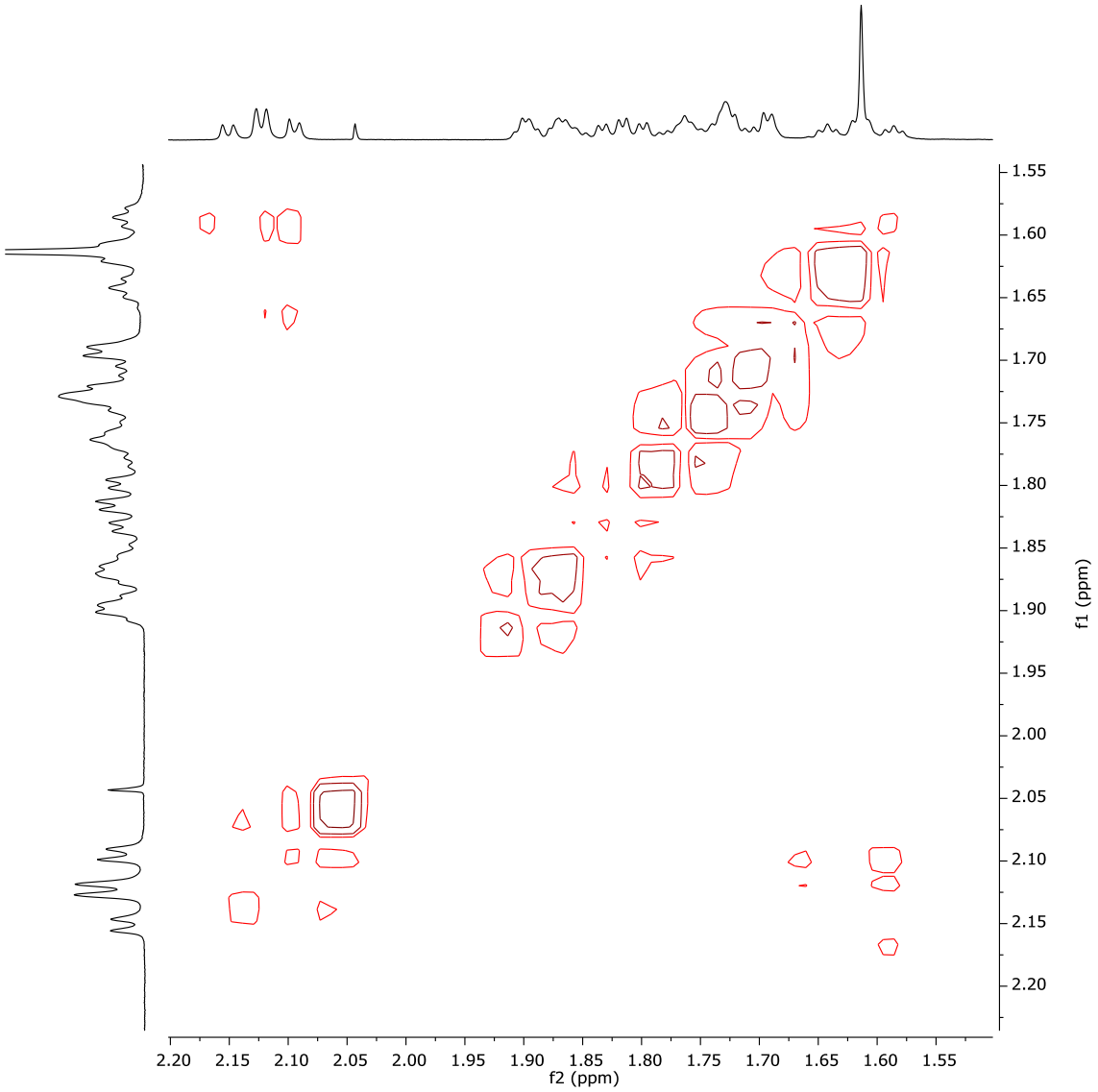
1.55
1.60
1.65
1.70
1.75
1.80
1.85
1.90
1.95
2.00
2.05
2.10
2.15
2.20
f1 (ppm)
2.20 2.15 2.10 2.05 2.00 1.95 1.90 1.85 1.80 1.75 1.70 1.65 1.60 1.55
f2 (ppm)

IR spectrum

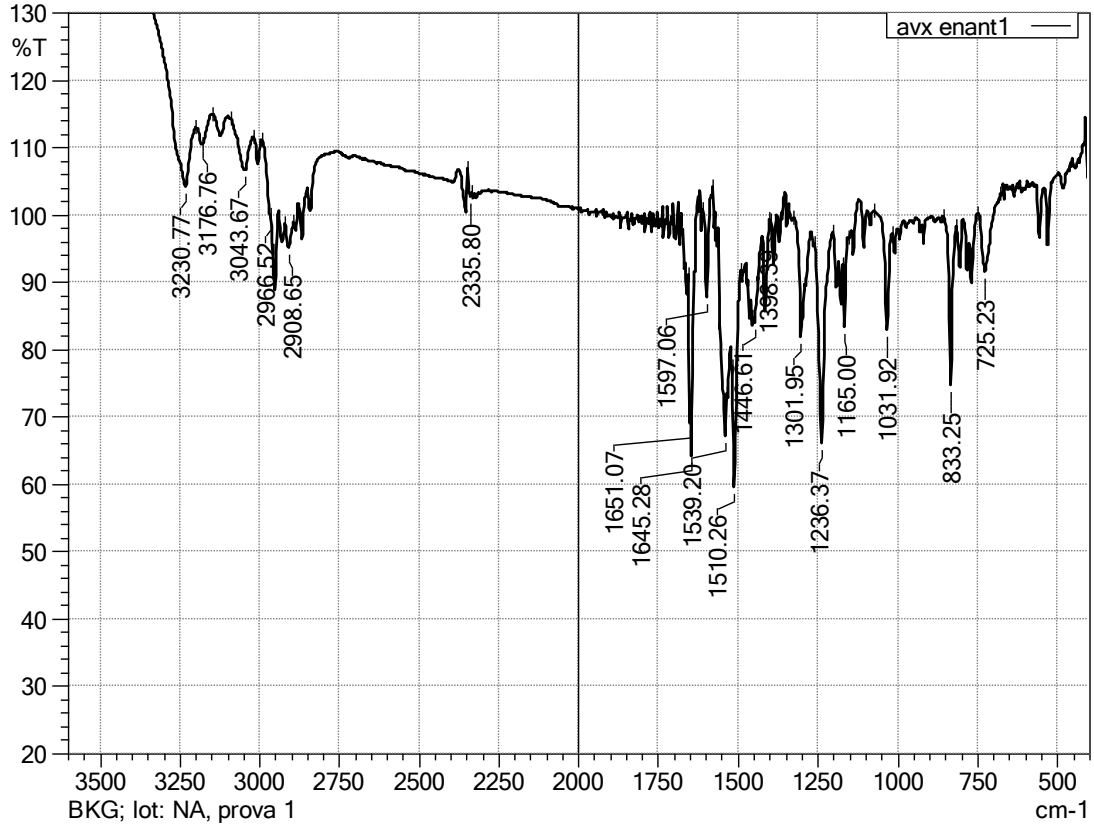

No.	Peak	Intensity	Corr. Intensity	Base (H)	Base (L)	Area	Corr. Area	Area color
1	725.23	91.52	9.66	748.38	677.01	161.357	282.553	Auto
2	833.25	74.61	24.26	856.39	815.89	319.665	278.608	Auto
3	1031.92	82.89	15.13	1074.35	1016.49	252.137	182.864	Auto
4	1165.00	83.30	10.53	1170.79	1153.43	153.352	57.664	Auto
5	1236.37	66.02	30.41	1259.52	1201.65	801.264	603.562	Auto
6	1301.95	81.86	11.01	1325.10	1290.38	286.531	97.526	Auto
7	1398.39	98.84	0.29	1400.32	1396.46	3.900	0.564	Auto
8	1446.61	83.95	3.06	1452.40	1436.97	214.817	25.390	Auto
9	1510.26	59.55	22.06	1517.98	1490.97	662.537	248.654	Auto
10	1539.20	67.14	9.16	1554.63	1533.41	556.720	103.606	Auto
11	1597.06	87.67	14.52	1610.56	1577.77	71.476	152.944	Auto
12	1645.28	64.14	12.70	1649.14	1624.06	350.565	34.900	Auto
13	1651.07	68.93	9.49	1654.92	1649.14	133.541	26.869	Auto
14	2335.80	102.72	1.53	2345.44	2331.94	-46.527	21.211	Auto
15	2908.65	95.17	3.50	2918.30	2891.30	86.666	51.988	Auto
16	2966.52	99.89	0.88	2991.59	2964.59	-169.100	-20.629	Auto
17	3043.67	106.55	5.91	3089.96	3018.60	-717.299	201.286	Auto
18	3176.76	110.37	0.37	3178.69	3145.90	-425.900	-8.787	Auto
19	3230.77	104.17	12.96	3387.00	3197.98	-3922.012	783.082	Auto

Table S1: Crystal data and structure refinement for compound **4**, (1*S*, 2*S*, 5*R*)-diastereoisomer of AR-15512.

Identification code	cu_D29VB58A_0m_a	
Empirical formula	C18 H27 N O2	
Formula weight	289.40	
Temperature	100(2) K	
Wavelength	1.54178 Å	
Crystal system	Orthorhombic	
Space group	P 21 21 21	
Unit cell dimensions	a = 9.1371(2) Å	α= 90°.
	b = 10.3821(3) Å	β= 90°.
	c = 17.4893(4) Å	γ = 90°.
Volume	1659.08(7) $Å^3$	
Z	4	
Density (calculated)	1.159 Mg/m^3	
Absorption coefficient	0.583 mm^{-1}	
F(000)	632	
Crystal size	0.576 x 0.101 x 0.046 mm^3	
Theta range for data collection	5.462 to 59.070°.	
Index ranges	-10<=h<=9, -7<=k<=11, -19<=l<=18	
Reflections collected	8003	
Independent reflections	2370 [R(int) = 0.0219]	
Completeness to theta = 67.679°	79.9 %	
Absorption correction	Semi-empirical from equivalents	
Max. and min. transmission	0.7516 and 0.6145	
Refinement method	Full-matrix least-squares on F^2	
Data / restraints / parameters	2370 / 0 / 194	
Goodness-of-fit on F^2	1.103	
Final R indices [I>2sigma(I)]	R1 = 0.0280, wR2 = 0.0725	
R indices (all data)	R1 = 0.0295, wR2 = 0.0734	
Absolute structure parameter	0.05(7)	
Extinction coefficient	n/a	
Largest diff. peak and hole	0.160 and -0.183 $e.Å^{-3}$	

Table S2: Atomic coordinates (x 10^4) and equivalent isotropic displacement parameters (Å^{2}x 10^3) for cu_D29VB58A_0m_a. U(eq) is defined as one third of the trace of the orthogonalized U^{ij} tensor.

	x	y	z	U(eq)
O(1)	8842(1)	6625(1)	5102(1)	17(1)
O(2)	9061(2)	10230(1)	8006(1)	30(1)
N(1)	6818(2)	7757(2)	5429(1)	17(1)
C(1)	4614(2)	4898(2)	5506(1)	28(1)
C(2)	6154(3)	2931(2)	5385(1)	30(1)
C(3)	6125(2)	4392(2)	5276(1)	19(1)
C(4)	6561(2)	4791(2)	4457(1)	18(1)
C(5)	7966(2)	4141(2)	4182(1)	21(1)
C(6)	8420(2)	4567(2)	3382(1)	23(1)
C(7)	8621(2)	6016(2)	3329(1)	19(1)
C(8)	9097(2)	6434(2)	2534(1)	30(1)
C(9)	7208(2)	6678(2)	3567(1)	19(1)
C(10)	6633(2)	6281(2)	4361(1)	16(1)
C(11)	7542(2)	6896(2)	4989(1)	15(1)
C(12)	7416(2)	8362(2)	6091(1)	16(1)
C(13)	8059(2)	7639(2)	6665(1)	19(1)
C(14)	8612(2)	8221(2)	7316(1)	20(1)
C(15)	8520(2)	9552(2)	7395(1)	20(1)
C(16)	7856(2)	10277(2)	6828(1)	22(1)
C(17)	7306(2)	9687(2)	6180(1)	20(1)
C(18)	9588(3)	9513(2)	8642(1)	34(1)

Table S3: Bond lengths [Å] and angles [°] for cu_D29VB58A_0m_a.

O(1)-C(11)	1.237(2)
O(2)-C(15)	1.372(2)
O(2)-C(18)	1.423(3)
N(1)-C(11)	1.352(2)
N(1)-C(12)	1.426(2)
N(1)-H(1N)	0.8800
C(1)-C(3)	1.530(3)
C(1)-H(1A)	0.9800
C(1)-H(1B)	0.9800
C(1)-H(1C)	0.9800
C(2)-C(3)	1.529(3)
C(2)-H(2A)	0.9800
C(2)-H(2B)	0.9800
C(2)-H(2C)	0.9800
C(3)-C(4)	1.544(3)
C(3)-H(00F)	1.0000
C(4)-C(5)	1.528(3)
C(4)-C(10)	1.557(3)
C(4)-H(4)	1.0000
C(5)-C(6)	1.525(3)
C(5)-H(5A)	0.9900
C(5)-H(5B)	0.9900
C(6)-C(7)	1.518(3)
C(6)-H(6A)	0.9900
C(6)-H(6B)	0.9900
C(7)-C(8)	1.520(3)
C(7)-C(9)	1.521(3)
C(7)-H(7)	1.0000
C(8)-H(8A)	0.9800
C(8)-H(8B)	0.9800
C(8)-H(8C)	0.9800
C(9)-C(10)	1.541(3)

C(9)-H(9A)	0.9900
C(9)-H(9B)	0.9900
C(10)-C(11)	1.517(3)
C(10)-H(10)	1.0000
C(12)-C(13)	1.384(3)
C(12)-C(17)	1.388(3)
C(13)-C(14)	1.385(3)
C(13)-H(13)	0.9500
C(14)-C(15)	1.391(3)
C(14)-H(14)	0.9500
C(15)-C(16)	1.386(3)
C(16)-C(17)	1.383(3)
C(16)-H(16)	0.9500
C(17)-H(17)	0.9500
C(18)-H(18A)	0.9800
C(18)-H(18B)	0.9800
C(18)-H(18C)	0.9800
C(15)-O(2)-C(18)	117.50(16)
C(11)-N(1)-C(12)	124.45(17)
C(11)-N(1)-H(1N)	117.8
C(12)-N(1)-H(1N)	117.8
C(3)-C(1)-H(1A)	109.5
C(3)-C(1)-H(1B)	109.5
H(1A)-C(1)-H(1B)	109.5
C(3)-C(1)-H(1C)	109.5
H(1A)-C(1)-H(1C)	109.5
H(1B)-C(1)-H(1C)	109.5
C(3)-C(2)-H(2A)	109.5
C(3)-C(2)-H(2B)	109.5
H(2A)-C(2)-H(2B)	109.5
C(3)-C(2)-H(2C)	109.5
H(2A)-C(2)-H(2C)	109.5
H(2B)-C(2)-H(2C)	109.5
C(2)-C(3)-C(1)	108.87(18)

C(2)-C(3)-C(4)	112.11(16)
C(1)-C(3)-C(4)	112.64(16)
C(2)-C(3)-H(00F)	107.7
C(1)-C(3)-H(00F)	107.7
C(4)-C(3)-H(00F)	107.7
C(5)-C(4)-C(3)	113.00(16)
C(5)-C(4)-C(10)	111.71(16)
C(3)-C(4)-C(10)	112.14(16)
C(5)-C(4)-H(4)	106.5
C(3)-C(4)-H(4)	106.5
C(10)-C(4)-H(4)	106.5
C(6)-C(5)-C(4)	112.88(16)
C(6)-C(5)-H(5A)	109.0
C(4)-C(5)-H(5A)	109.0
C(6)-C(5)-H(5B)	109.0
C(4)-C(5)-H(5B)	109.0
H(5A)-C(5)-H(5B)	107.8
C(7)-C(6)-C(5)	112.12(16)
C(7)-C(6)-H(6A)	109.2
C(5)-C(6)-H(6A)	109.2
C(7)-C(6)-H(6B)	109.2
C(5)-C(6)-H(6B)	109.2
H(6A)-C(6)-H(6B)	107.9
C(6)-C(7)-C(8)	111.92(18)
C(6)-C(7)-C(9)	109.15(16)
C(8)-C(7)-C(9)	111.37(17)
C(6)-C(7)-H(7)	108.1
C(8)-C(7)-H(7)	108.1
C(9)-C(7)-H(7)	108.1
C(7)-C(8)-H(8A)	109.5
C(7)-C(8)-H(8B)	109.5
H(8A)-C(8)-H(8B)	109.5
C(7)-C(8)-H(8C)	109.5
H(8A)-C(8)-H(8C)	109.5

H(8B)-C(8)-H(8C)	109.5
C(7)-C(9)-C(10)	114.54(16)
C(7)-C(9)-H(9A)	108.6
C(10)-C(9)-H(9A)	108.6
C(7)-C(9)-H(9B)	108.6
C(10)-C(9)-H(9B)	108.6
H(9A)-C(9)-H(9B)	107.6
C(11)-C(10)-C(9)	110.67(15)
C(11)-C(10)-C(4)	111.28(15)
C(9)-C(10)-C(4)	112.15(16)
C(11)-C(10)-H(10)	107.5
C(9)-C(10)-H(10)	107.5
C(4)-C(10)-H(10)	107.5
O(1)-C(11)-N(1)	121.91(17)
O(1)-C(11)-C(10)	123.09(17)
N(1)-C(11)-C(10)	114.99(17)
C(13)-C(12)-C(17)	119.11(18)
C(13)-C(12)-N(1)	120.87(17)
C(17)-C(12)-N(1)	119.98(17)
C(12)-C(13)-C(14)	121.01(18)
C(12)-C(13)-H(13)	119.5
C(14)-C(13)-H(13)	119.5
C(13)-C(14)-C(15)	119.54(19)
C(13)-C(14)-H(14)	120.2
C(15)-C(14)-H(14)	120.2
O(2)-C(15)-C(16)	115.89(17)
O(2)-C(15)-C(14)	124.46(18)
C(16)-C(15)-C(14)	119.65(18)
C(17)-C(16)-C(15)	120.38(18)
C(17)-C(16)-H(16)	119.8
C(15)-C(16)-H(16)	119.8
C(16)-C(17)-C(12)	120.29(19)
C(16)-C(17)-H(17)	119.9
C(12)-C(17)-H(17)	119.9

O(2)-C(18)-H(18A)	109.5
O(2)-C(18)-H(18B)	109.5
H(18A)-C(18)-H(18B)	109.5
O(2)-C(18)-H(18C)	109.5
H(18A)-C(18)-H(18C)	109.5
H(18B)-C(18)-H(18C)	109.5

Symmetry transformations used to generate equivalent atoms:

Table S4: Anisotropic displacement parameters ($Å^2 x\ 10^3$) for cu_D29VB58A_0m_a. The anisotropic displacement factor exponent takes the form: $-2\pi^2[\ h^2\ a^{*2} U^{11} + ...\ + 2\ h\ k\ a^*\ b^*\ U^{12}]$.

	U^{11}	U^{22}	U^{33}	U^{23}	U^{13}	U^{12}
O(1)	13(1)	19(1)	18(1)	0(1)	-1(1)	0(1)
O(2)	39(1)	26(1)	24(1)	-9(1)	-6(1)	-5(1)
N(1)	13(1)	19(1)	19(1)	-2(1)	0(1)	3(1)
C(1)	25(1)	35(1)	22(1)	6(1)	4(1)	-1(1)
C(2)	38(1)	24(1)	27(1)	3(1)	4(1)	-7(1)
C(3)	19(1)	21(1)	18(1)	1(1)	-1(1)	-3(1)
C(4)	18(1)	18(1)	17(1)	-2(1)	-3(1)	-3(1)
C(5)	23(1)	16(1)	24(1)	-2(1)	0(1)	1(1)
C(6)	22(1)	25(1)	22(1)	-7(1)	2(1)	2(1)
C(7)	16(1)	26(1)	15(1)	1(1)	-2(1)	-2(1)
C(8)	28(1)	42(1)	20(1)	3(1)	4(1)	2(1)
C(9)	18(1)	21(1)	17(1)	2(1)	-3(1)	0(1)
C(10)	12(1)	18(1)	18(1)	1(1)	-1(1)	2(1)
C(11)	16(1)	12(1)	15(1)	5(1)	2(1)	-1(1)
C(12)	13(1)	19(1)	17(1)	-1(1)	4(1)	-1(1)
C(13)	19(1)	15(1)	21(1)	-2(1)	3(1)	-2(1)
C(14)	20(1)	22(1)	20(1)	1(1)	0(1)	-1(1)
C(15)	19(1)	23(1)	19(1)	-4(1)	4(1)	-5(1)
C(16)	25(1)	15(1)	26(1)	-4(1)	5(1)	-1(1)
C(17)	18(1)	20(1)	21(1)	1(1)	2(1)	1(1)
C(18)	40(1)	39(1)	24(1)	-6(1)	-7(1)	-7(1)

Table S5: Hydrogen coordinates (x 10^4) and isotropic displacement parameters (Å^2 x 10^3) for cu_D29VB58A_0m_a.

	x	y	z	U(eq)
H(1N)	5917	7958	5298	20
H(1A)	4596	5838	5457	41
H(1B)	4410	4657	6038	41
H(1C)	3869	4521	5171	41
H(2A)	5539	2522	4995	45
H(2B)	5781	2716	5894	45
H(2C)	7162	2620	5335	45
H(00F)	6858	4774	5635	23
H(4)	5761	4483	4113	21
H(5A)	8766	4341	4544	25
H(5B)	7822	3195	4183	25
H(6A)	9348	4136	3242	27
H(6B)	7663	4294	3010	27
H(7)	9404	6272	3698	23
H(8A)	8351	6178	2161	45
H(8B)	10029	6020	2405	45
H(8C)	9216	7371	2523	45
H(9A)	6445	6485	3181	23
H(9B)	7369	7621	3564	23
H(10)	5613	6619	4410	19
H(13)	8121	6730	6611	22
H(14)	9052	7715	7706	25
H(16)	7778	11184	6884	27
H(17)	6850	10191	5794	23
H(18A)	8808	8952	8835	51
H(18B)	9896	10106	9047	51
H(18C)	10424	8985	8482	51

HPLC chromatograms of AR-15512 and compound 4

SAMPLE INFORMATION

Sample Name:	AR-15512
Sample Type:	Unknown
Vial:	1
Injection #:	8
Injection Volume:	10.00 ul
Run Time:	30.00 Minutes

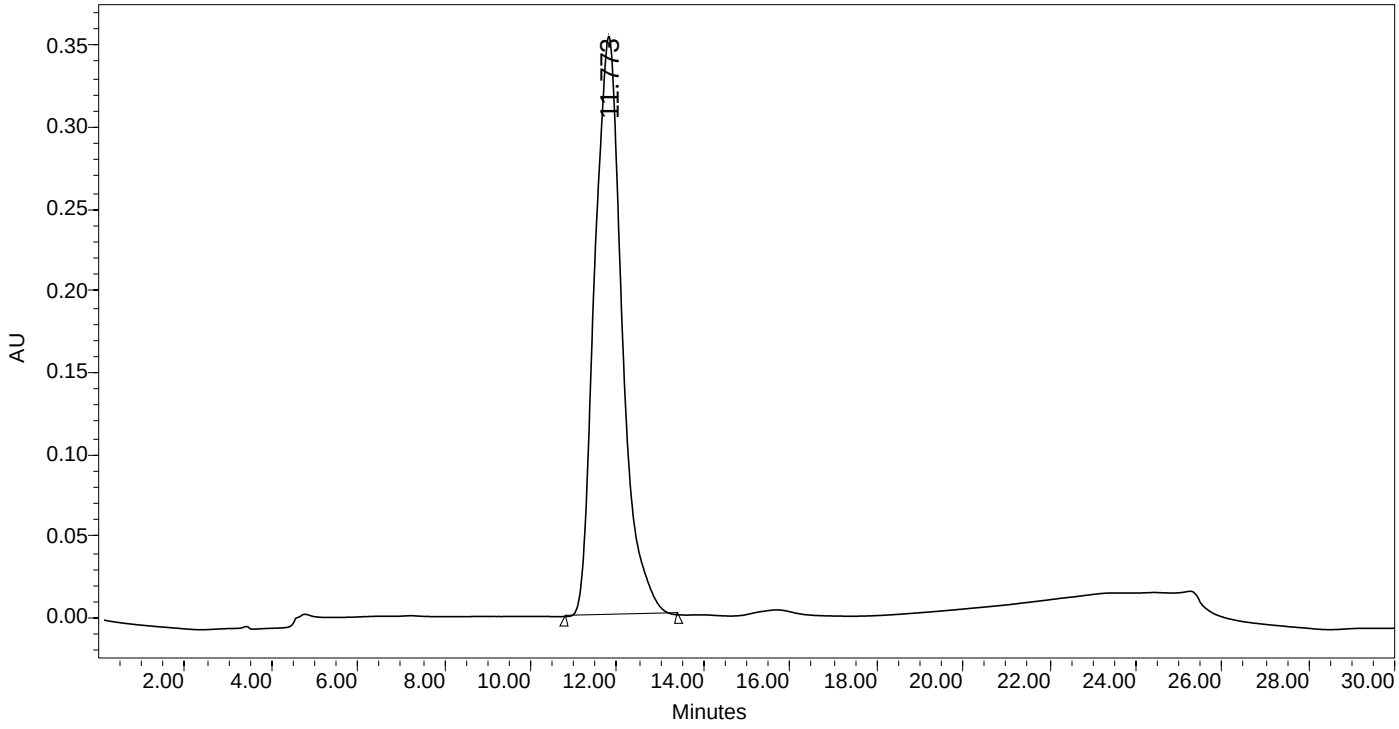

	RT (min)	Area (µV*sec)	% Area	Height (µV)	% Height
1	11.773	15747289	100.00	353932	100.00

SAMPLE INFORMATION

Sample Name:	diastereomer, compound 4
Sample Type:	Unknown
Vial:	1
Injection #:	3
Injection Volume:	10.00 ul
Run Time:	35.00 Minutes

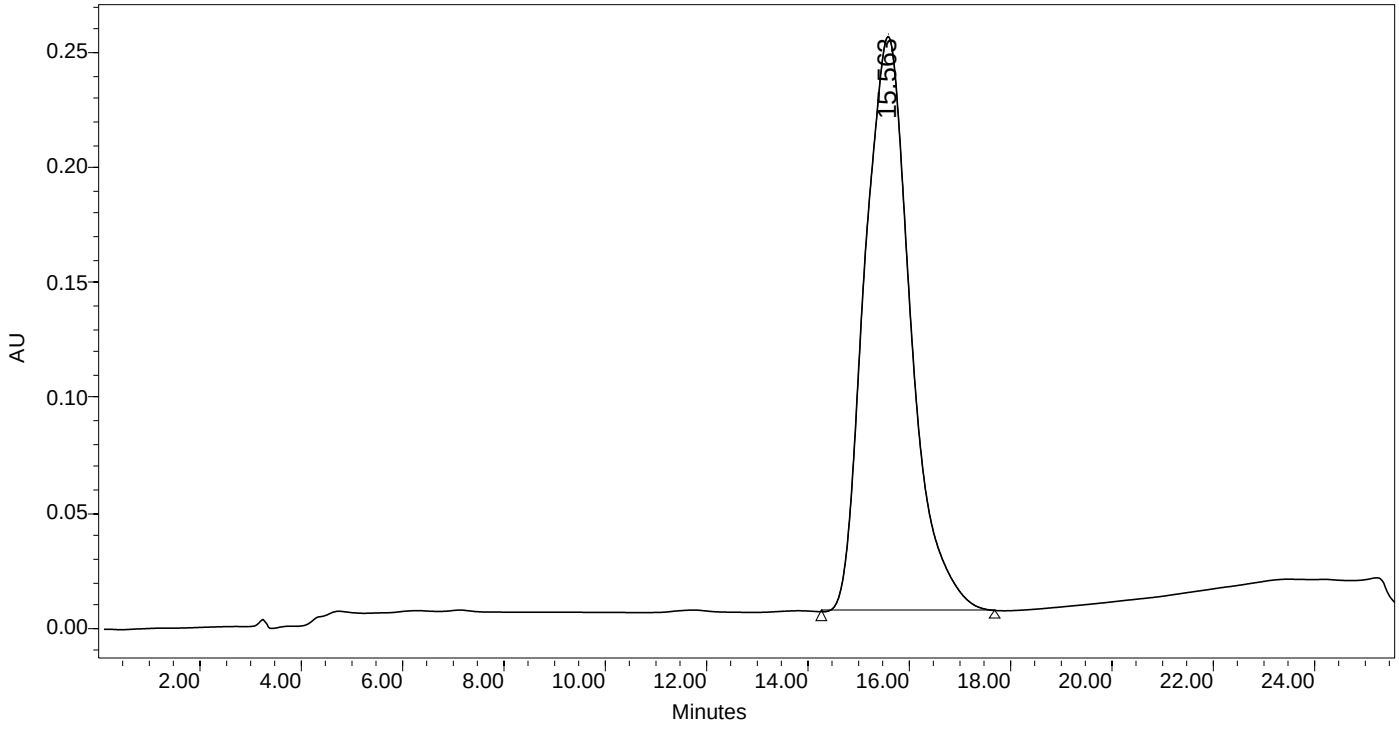

	RT (min)	Area (µV*sec)	% Area	Height (µV)	% Height
1	15.563	15768984	100.00	249674	100.00

SAMPLE INFORMATION

Sample Name:	mixture of AR-15512 and compound 4
Sample Type:	Unknown
Vial:	1
Injection #:	1
Injection Volume:	6.00 ul
Run Time:	35.00 Minutes

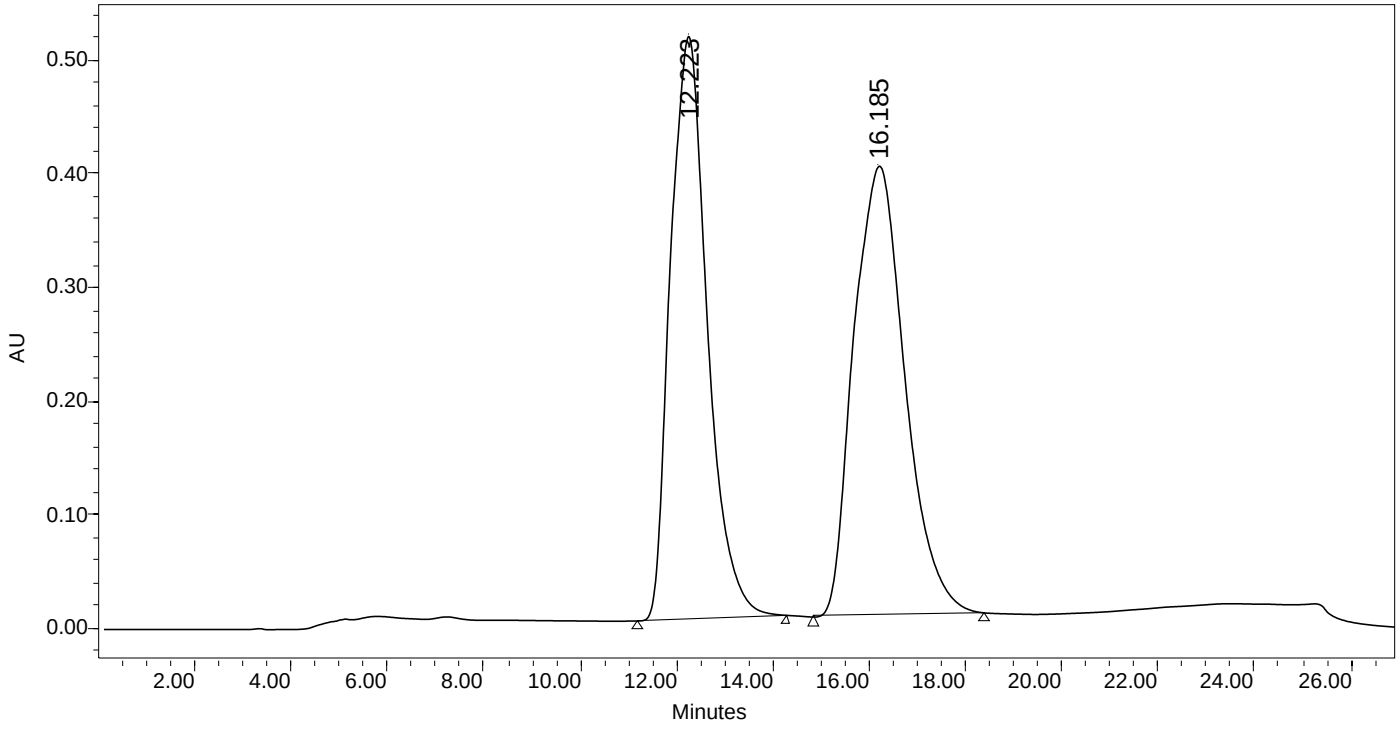

	RT (min)	Area (µV*sec)	% Area	Height (µV)	% Height
1	12.223	27320387	48.25	512990	56.46
2	16.185	29299443	51.75	395629	43.54

HPLC chromatograms of AR-15512 and its enantiomer, compound 5

SAMPLE INFORMATION

Sample Name:	AR-15512 quiral
Sample Type:	Unknown
Vial:	1
Injection #:	4
Injection Volume:	10.00 ul
Run Time:	30.00 Minutes

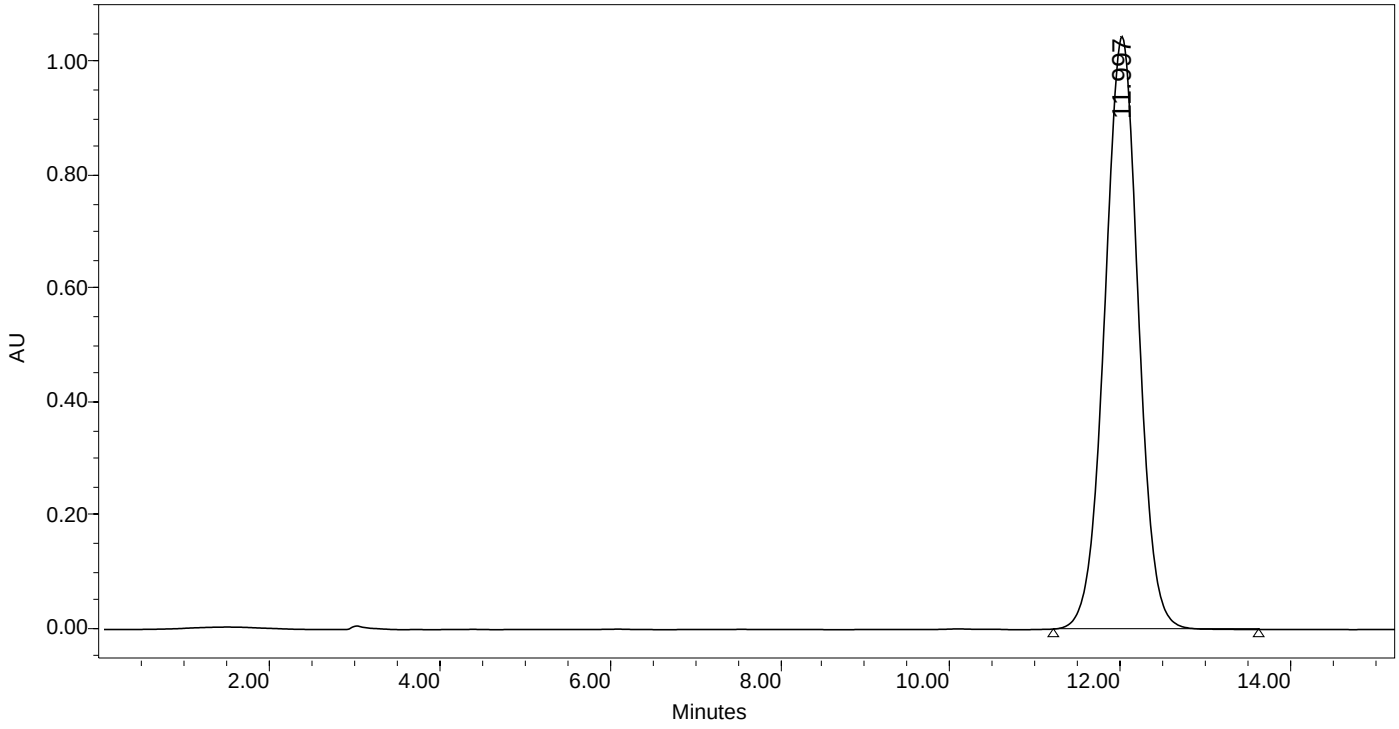

	RT (min)	Area (µV*sec)	% Area	Height (µV)	% Height
1	11.997	28732349	100.00	1046759	100.00

SAMPLE INFORMATION

Sample Name:	enantiomer, compound 5
Sample Type:	Unknown
Vial:	1
Injection #:	2
Injection Volume:	10.00 ul
Run Time:	30.00 Minutes

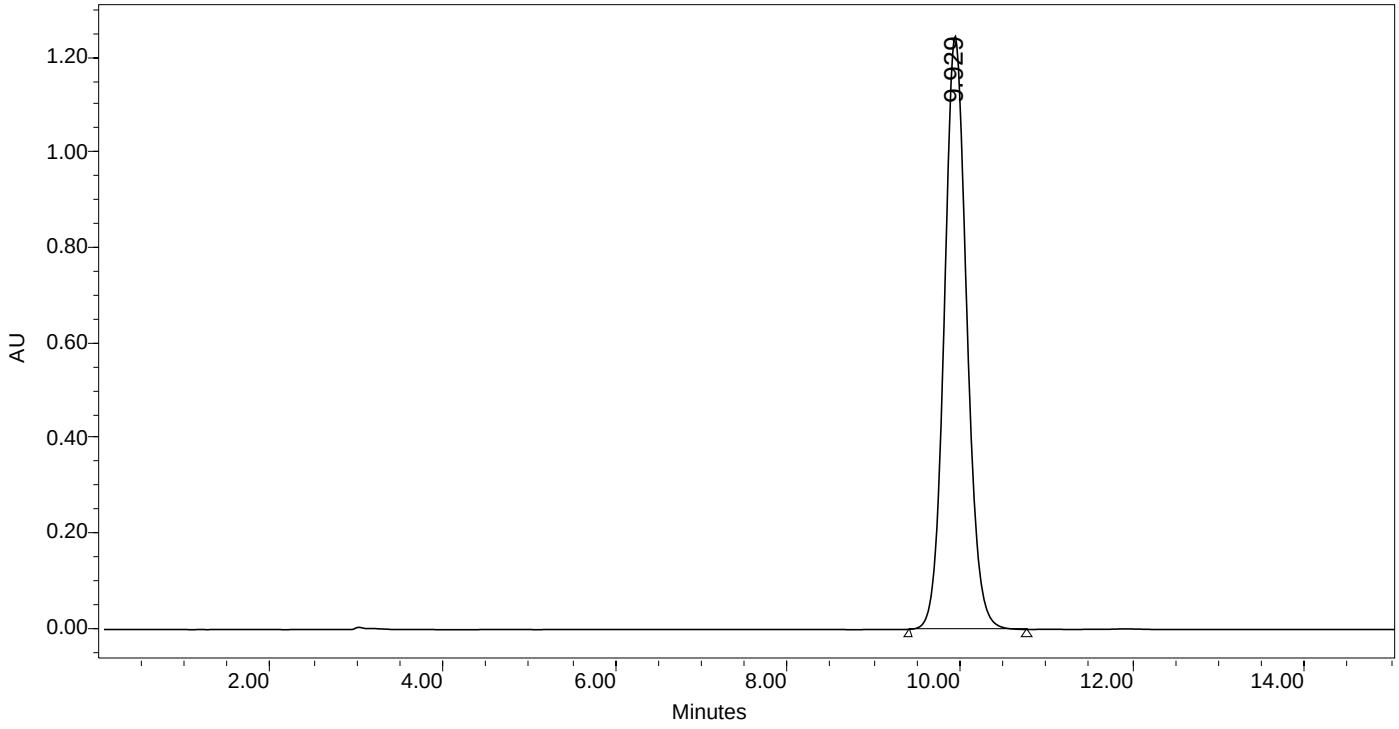

	RT (min)	Area (µV*sec)	% Area	Height (µV)	% Height
1	9.929	22558988	100.00	1245766	100.00

SAMPLE INFORMATION

Sample Name:	Mixture AR-15512 and compound 5
Sample Type:	Unknown
Vial:	1
Injection #:	16
Injection Volume:	10.00 ul
Run Time:	30.00 Minutes

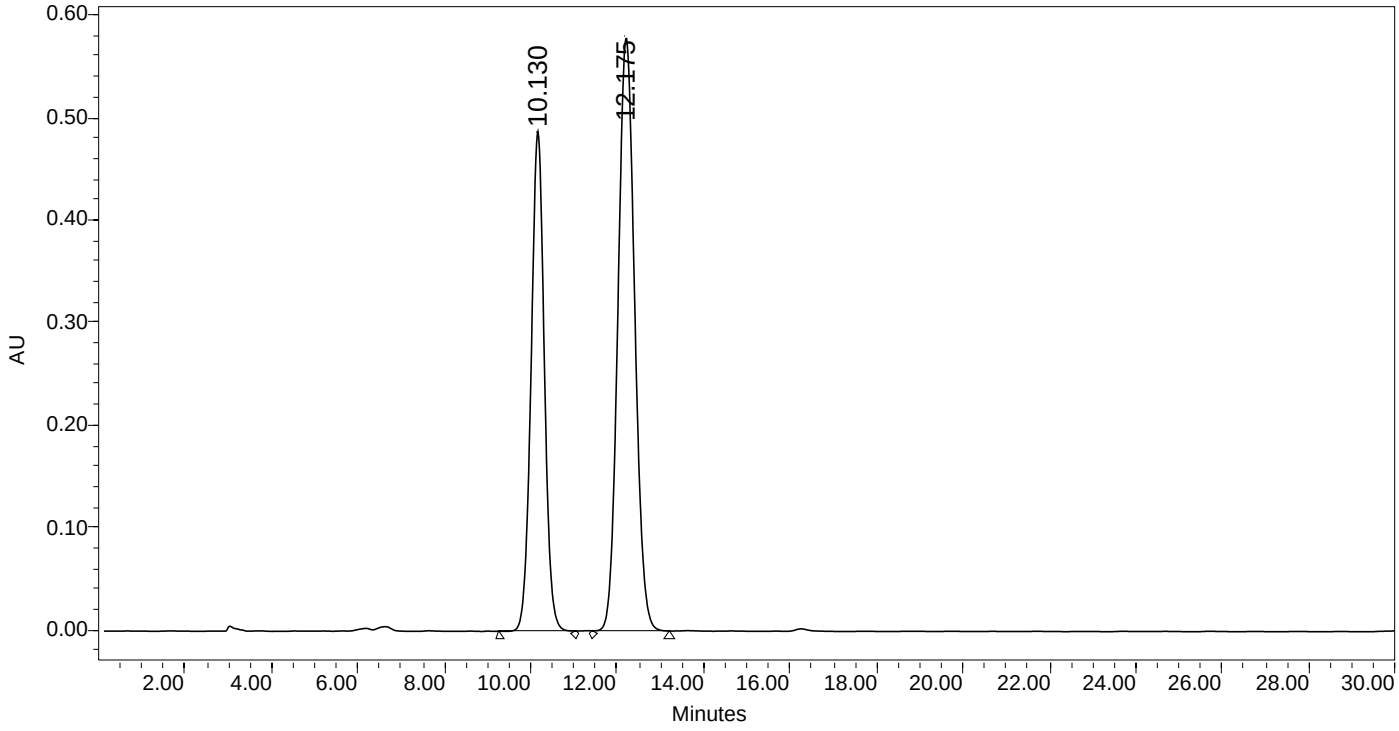

	RT (min)	Area (µV*sec)	% Area	Height (µV)	% Height
1	10.130	10404747	40.00	487679	45.73
2	12.175	15608331	60.00	578793	54.27

SAMPLE INFORMATION

Sample Name:	mixture of enantiomers
Sample Type:	Unknown
Vial:	1
Injection #:	2
Injection Volume:	10.00 ul
Run Time:	30.00 Minutes

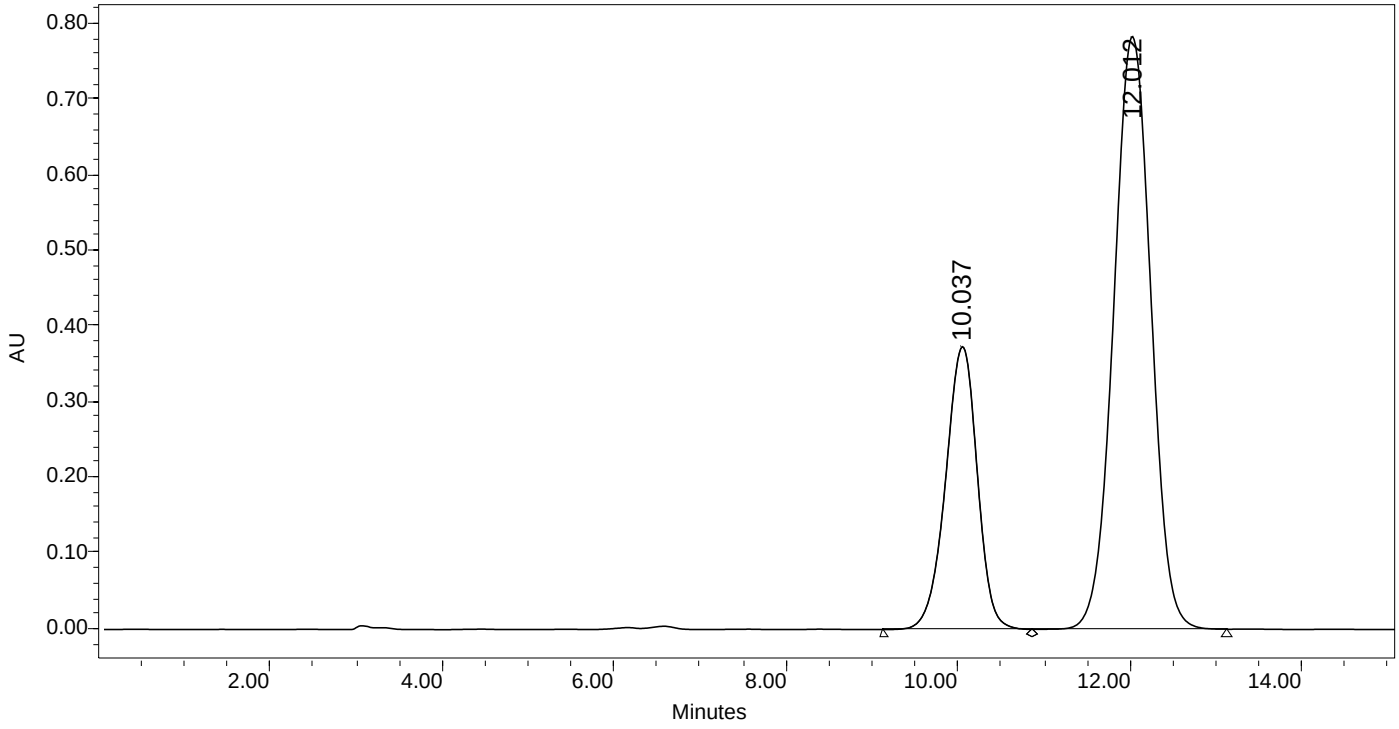

	RT (min)	Area (µV*sec)	% Area	Height (µV)	% Height
1	10.037	9597223	28.93	373760	32.29
2	12.012	23577747	71.07	783586	67.71

Conclusiones

En relación con el objetivo principal de esta Tesis Doctoral enmarcada en el ámbito de la Química Médica, varios compuestos heterocíclicos de diversa naturaleza han sido diseñados, sintetizados y evaluados farmacológicamente.

Las principales conclusiones derivadas de cada capítulo de esta Tesis Doctoral son las siguientes:

Capítulo 2: La reacción de cicloadición [3+2] diastereoselectiva entre PhosMic y derivados y maleimidas *N*-sustituidas, ha dado lugar a una librería de compuestos con núcleo de α-iminofosfonatos bicíclicos. Estos compuestos presentan una elevada afinidad por I_2-IR y selectividad I_2-IR/α_2-AR, siendo la primera familia de ligandos de estos receptores que no contienen un anillo de imidazol o imidazolina. Asimismo, los estudios preliminares de seguridad y metabolismo junto a los efectos farmacológicos observados *in vitro* e *in vivo* demuestran la eficacia de esta familia de compuestos para el estudio del papel terapéutico que pueden tener en enfermedades neurodegenerativas y a largo plazo como una posible nueva aproximación para el tratamiento de dichas enfermedades.

Capítulo 3: La familia con estructura de benzofuranil-2-imidazol preparada, sustituidos de forma diversa, han revelado una buena afinidad I_2-IR y selectividad I_2-IR/α_2-AR. Los resultados de estudios de 3D-QSAR y ADMET *in silico* e *in vitro*, sumado al perfil farmacocinético del compuesto **LSL60101**, abrieron la puerta a los estudios *in vivo*. Además, el tratamiento del modelo murino para la enfermedad de Alzheimer5xFAD con **LSL60101** evidenció efectos beneficiosos en comportamiento y cognición. Por lo consiguiente, todos estos resultados determinan las estructuras a base de benzofuranil-2-imidazol como potenciales compuestos para abordar la terapia de la enfermedad de Alzheimer.

Capítulo 4: Se ha presentado la reacción multicomponente consecutiva (cMCR) con isocianometilfosfonatos que gracias a su combinación con una diamina y una cetona nos ha permitido obtener bis(2-imidazolin-4-il)fosfonatos de manera diastereoselectiva, siendo la primera vez que describe la obtención de bisimidazolinas por cMCR y el primer trabajo sintético de cMCR que emplea isocianofosforados. La reacción transcurre con buenos rendimientos y economía de

átomo, eficiencia y ausencia de disolvente, mediante el uso de horno microondas. Asimismo, desde el punto de vista estereoquímico, se determinó de manera inequívoca la estructura de uno de los compuestos sintetizados por medio del análisis cristalográfico de rayos X.

Capítulo 5: Se diseñaron y sintetizaron compuestos con estructura de 3-alquil-1,8-dibencilxantinas con actividad inhibitoria de la enzima PEPCK-M. Los favorables resultados de los estudios preliminares de ADMET dieron lugar a estudios *in vivo*. El tratamiento diario de dos modelos murinos con xenoinjertos subcutáneos con el compuesto **iPEPCK-2** inhibió el crecimiento tumoral. Por ello, se puede concluir que, dada la actividad antitumoral de estos compuestos, la inhibición de la PEPCK-M como una potencial vía novedosa para la terapia del cáncer.

Capítulo 6: Se describió la síntesis y caracterización completa del enantiómero y del diastereómero en *C*-1 de **AR-15512**, un agonista del receptor TRPM8 en fase clínica 2b como solución oftálmica para el tratamiento del ojo seco. Adicionalmente, se diseñó y desarrolló dos métodos de HPLC para identificar ambos estereoisómeros y diferenciarlos del candidato clínico **AR-15512.**

Anexo: Otras publicaciones

Publicaciones por orden cronológico:

- **Disease-modifying treatment with I_2 imidazoline receptor ligand LSL60101 in an Alzheimer's disease mouse model: A Comparative study with donepezil**. Vasilopoulou, F.; Rodríguez-Arévalo, S.; Bagán, A.; Escolano, C.; Griñán-Ferré, C.; Pallàs, M. *Br. J. Pharmacol*. **2021**, 178, 3017-3033.

- **I_2 imidazoline receptor modulation protects aged SAMP8 mice against cognitive decline by suppressing the calcineurin pathway**. Vasilopoulou, F.; Griñán-Ferré, C.; Rodríguez-Arévalo, S.; Bagán, A.; Abás, S.; Escolano, C.; Pallàs, M. *GeroScience* **2021**, *43*, 965-983.

- **Amelioration of BPSD-Like Phenotype and Cognitive Decline in SAMP8 Mice Model Accompanied by Molecular Changes after Treatment with I_2-Imidazoline Receptor Ligand MCR5.** Vasilopoulou, F.; Bagán, A.; Rodríguez-Arévalo, S.; Escolano, C.; Griñán-Ferré, C.; Pallàs, M. *Pharmaceutics* **2020**,*12*, 475.

- **Phosphoenolpyruvate from Glycolysis and PEPCK Regulate Cancer Cell Fate by Altering Cytosolic Ca^{2+}.** Moreno-Felici, J.; Hyrossova, P.; Aragó, M.; Rodríguez-Arévalo, S.; García-Rovés, P.M.; Escolano, C.; Perales, J.C. *Cells* **2020**, *9*, 18.

- **Study of the behavioral and cognitive improvement induced by novel imidazoline I_2 receptor ligands in SAMP8 mice model.** Griñán-Ferré, C.; Vasilopoulou, F.; Abás, S.; Rodríguez-Arévalo, S.; Bagán, A.; Sureda, F.X.; Pérez, B.; Callado, L.F.; García-Sevilla, J.A.; García-Fuster, J.; Escolano, C.; Pallàs, M. *Neurotherapeutics* **2019**, *16*, 416-431.

Received: 17 December 2020 | Revised: 28 March 2021 | Accepted: 29 March 2021

DOI: 10.1111/bph.15478

RESEARCH PAPER

Disease-modifying treatment with I_2 imidazoline receptor ligand LSL60101 in an Alzheimer's disease mouse model: a comparative study with donepezil

Foteini Vasilopoulou[1] | Sergio Rodríguez-Arévalo[2] | Andrea Bagán[2] | Carmen Escolano[2] | Christian Griñán-Ferré[1] | Mercè Pallàs[1]

[1]Pharmacology Section, Department of Pharmacology, Toxicology and Medicinal Chemistry, Faculty of Pharmacy and Food Sciences, and Institut de Neurociències, University of Barcelona, Barcelona, Spain

[2]Laboratory of Medicinal Chemistry (Associated Unit to CSIC), Department of Pharmacology, Toxicology and Medicinal Chemistry, Faculty of Pharmacy and Food Sciences, and Institute of Biomedicine (IBUB), University of Barcelona, Barcelona, Spain

Correspondence
Christian Griñán-Ferré and Mercè Pallàs, Pharmacology Section, Department of Pharmacology, Toxicology and Medicinal Chemistry, Faculty of Pharmacy and Food Sciences, and Institut de Neurociències, University of Barcelona, Av. Joan XXIII, 27-31, E-08028 Barcelona, Spain.
Email: christian.grinan@ub.edu; pallas@ub.edu

Funding information
Generalitat de Catalunya, Grant/Award Number: 2018FI-B-00227; Universitat de Barcelona, Grant/Award Numbers: UB2018, UB2016; "la Caixa" Foundation, Grant/Award Number: CI18-00002; Agència de Gestió d'Ajuts Universitaris i de Recerca, Grant/Award Number: 2017SGR106; Ministerio de Ciencia e Innovación, Grant/Award Numbers: PID2019-106285RB-I00, PID2019-107991RB-I00

Background and Purpose: The development of effective therapeutic strategies against Alzheimer's disease (AD) remains a challenge. I_2 imidazoline receptor ligands have a neuroprotective role in AD. Moreover, co-treatment of AChE inhibitors with neuroprotective agents have shown better effects on the prevention of dementia. Here, we assessed the potential therapeutic effect of the I_2 ligand, donepezil and their combination in 5XFAD mice.

Experimental Approach: 5XFAD female mice were treated with low doses (1 $mg \cdot kg^{-1} \cdot day^{-1}$) of LSL60101, donepezil and donepezil plus LSL60101, during 4 weeks per os. Novel object recognition, Morris water maze, open field, elevated plus maze and three-chamber tests were used to evaluate the cognitive and behavioural status after treatment. The effects on AD-like pathology were assessed with immunohistochemistry, western blot, ELISA and qPCR.

Key Results: Chronic low-dose treatment with LSL60101 and donepezil reversed cognitive deficits and impaired social behaviour. LSL60101 treatment did not affect anxiety-like behaviour in contrast to donepezil. In the 5XFAD brains, LSL60101 and donepezil/LSL60101 treatments attenuated amyloid-β pathology by decreasing amyloid-β_{40} and amyloid-β_{42} levels, amyloid-β plaque number and tau hyperphosphorylation. These alterations were accompanied by reduced microglia marker Iba-1 levels and increased *Trem2* gene expression. LSL60101 and donepezil decreased glial fibrillary acidic protein (GFAP) astrocytic marker reactivity. However, only LSL60101 and donepezil/LSL60101 treatments significantly increased the synaptic marker levels of post-synaptic density protein 95 and synaptophysin.

Conclusion and Implications: Chronic low-dose treatment with selective I_2- ligands can be an effective treatment for AD and provide insights into combination treatments for symptomatic and disease-modifying drugs.

KEYWORDS
Alzheimer's disease, donepezil, I_2 imidazoline receptors, neuroinflammation, synaptic plasticity, β-amyloid

Abbreviations: AD, Alzheimer's disease; Ccl12, chemokine (C–C motif) ligand 12; GFAP, glial fibrillary acidic protein; I_2, imidazoline-2 receptors; Iba-1, ionized calcium-binding adaptor molecule 1; PSD95, postsynaptic density protein 95; p-Tau, hyperphosphorylated tau; Trem2, triggering receptor expressed on myeloid cells 2.

1 | INTRODUCTION

Alzheimer's disease (AD) is the leading cause of dementia among the elderly and the most common irreversible and uncurable neurodegenerative disorder, clinically characterised by progressive behavioural disturbances and memory loss (Murray et al., 2011). **Amyloid-β** plaques and neurofibrillary tangles, consisting of hyperphosphorylated **tau** (p-Tau), are two major neuropathological AD markers, which lead to synaptic failure (DeTure & Dickson, 2019; Selkoe, 2008; Walsh & Selkoe, 2004). Moreover, the inflammatory response triggered by amyloid-β deposits and tau hyperphosphorylation, among others and mediated by activated microglia and reactive astrocytes has a key role in the progression of AD (Dickson & Rogers, 1992; Meraz Rios et al., 2013). Thus, targeting amyloid-β aggregation, p-Tau and neuroinflammation has been proved so far, the main disease-modifying strategy for treating AD.

However, up to date, only symptomatic treatments, including the **AChE** inhibitors and the **N-methyl-D-aspartate (NMDA)** antagonists, are available for AD therapy. Those drugs showed modest symptomatic benefits on behaviour and cognition, but they did not halt the progression of AD (Grossberg, 2003; Mehta et al., 2012). Among AChE inhibitors, **donepezil** is clinically used for cognitive dysfunction in AD (Giacobini, 2000). Besides its main effects on the enhancement of cholinergic transmission, donepezil has been demonstrated to exert the potential for disease pathway modifications in AD, including attenuation of amyloid-β load and anti-inflammatory properties *in vitro* and *in vivo* (Kim et al., 2014). However, it lacks a curative effect. Therefore identifying new molecular targets for the development of treatments is crucial. In this context, to further enhance the noncholinergic therapeutic effects of donepezil, a combination of donepezil with other neuroprotective agents could provide a novel approach to preserve cognitive function and/or delay AD pathology.

I_2 imidazoline receptors are receiving growing attention due to the neuroprotective effects in the CNS (Bousquet et al., 2020). In the brain, I_2 receptors are found in both neurons and glial cells (Olmos et al., 1994; Regunathan et al., 1993) and their modulation has been associated with neurodegenerative disorders, including AD (Ruiz et al., 1993). Most notably, the density of I_2 receptors was found to increase in AD patients (Garcia-Sevilla et al., 1998). Several lines of evidence provided by our group demonstrated that selective I_2 ligands protected against cognitive impairment and ameliorated AD pathological features related to amyloid precursor protein processing, tau hyperphosphorylation, neuroinflammation and oxidative stress processes, using well-established AD animal models (Abás et al., 2017, 2020; Griñán-Ferré et al., 2019; Vasilopoulou, Griñán-Ferré, et al., 2020). Likewise, **agmatine**, the proposed endogenous ligand for I_2 receptors, prevented cognitive deficits in amyloid-β 1–42 peptide-injected mice and of note, its effect was augmented and attenuated by I_2 agonists and antagonists, respectively (Kotagale et al., 2020). Collectively, this evidence supports the potential therapeutic effect of I_2 ligands in AD.

Among the I_2 ligands, the selective I_2 ligand LSL60101 [2-(2-benzofuranyl)imidazole] (K_i ratio for α_2/I_2 receptors = 286) has been associated with the induction of several central effects, such as acute hyperphagic effects (Menargues et al., 1995) and inhibition of the development of opioid-induced tolerance and potentiation of morphine analgesia (Boronat et al., 1998). Interestingly, LSL60101 was shown to promote neuronal protection mediated by the induction of reactive astrocytes (Casanovas et al., 2000). However, the neuroprotective effect of LSL60101 on AD pathological conditions has not been reported.

In the present *in vivo* study, we explored the I_2 receptor ligand LSL60101 beneficial effects on the behavioural capabilities and cognitive impairments presented in AD, as well as on AD markers, including neuroinflammation, glial reactivity and synaptic plasticity in 5XFAD mice, a widely accepted transgenic mouse model for early-onset AD. Considering that women have a higher risk of dementia and females are under-represented in rodent models of AD, we used 5XFAD females. Additionally, the comparative effect with donepezil, considered a symptomatic AD treatment, was investigated alone and in combination therapy with the I_2 ligand LSL60101 to explore the joint effects of both compounds in ameliorating AD pathology and molecular changes presented by 5XFAD mice.

What is already known

- I_2-receptor modulation by selective I_2 ligands is neuroprotective in the CNS.
- As AChE inhibitors do not modify disease progression new drugs treating AD progression are needed.

What does this study add

- LSL60101, an I_2 ligand, treatment ameliorated cognitive impairments in 5XFAD mice and modified disease progression.
- LSL60101 has greater effects on AD markers and synaptic plasticity than donepezil, even in combination.

What is the clinical significance

- Chronic treatment with I_2 ligands would be a relevant therapeutic disease-modifying strategy against AD.

2 | METHODS

2.1 | Animals

The 5XFAD mouse model is a well-characterised double transgenic amyloid precursor protein/PSEN1 model, which co-expressed five familial AD mutations (JAX MMRRC Stock# 034840). This animal model incorporates AD pathological characteristics, including early

plaque formation and gliosis starting at 2 months, robust cognitive and behavioural deficits such as memory impairment, reduced anxiety and social disturbances starting at 4–5 months and neuronal loss at 6 months (Griñán-Ferré et al., 2018; Landel et al., 2014; Oakley et al., 2006). Thus, at the selected age of 7 months, 5XFAD mice provide a severe AD pathological landscape suitable for evaluating the drug effects.

In the present study, 5XFAD ($n = 47$) and wild-type (WT, $n = 46$) female mice (7 months old) were used to perform behavioural and molecular analyses. Females were used because AD incidence is higher in women and few studies are available. WT animals were randomly divided into WT control (WT Ct) ($n = 11$), WT treated with donepezil (1 mg·kg^{-1}·day^{-1}) (WT Dp) ($n = 12$) and LSL60101 (WT LSL) (1 mg·kg^{-1}·day^{-1}) ($n = 12$),and the cotreatment of donepezil (1 mg·kg^{-1}·day^{-1}) and LSL60101 (1 mg·kg^{-1}·day^{-1}) (WT Dp + LSL). 5XFAD mice were randomly divided into:- 5XFAD control (5XFAD Ct) ($n = 11$), 5XFAD treated with donepezil (1 mg·kg^{-1}·day^{-1}) (5XFAD Dp) ($n = 12$) and LSL60101 (5XFAD LSL) (1 mg·kg^{-1}·day^{-1}) ($n = 12$) and the co-treatment of donepezil (1 mg·kg^{-1}·day^{-1}) and LSL60101 (1 mg·kg^{-1}·day^{-1}) (5XFAD Dp + LSL).

The animals had free access to food and water and were kept under standard temperature conditions (22 ± 2°C) and 12-h light/dark cycles (300/0 lux). Compounds were dissolved in 1.8% (2-hydroxypropyl)-β-cyclodextrin and administered through drinking water. Control groups received water plus 1.8% (2-hydroxypropyl)-β-cyclodextrin during the treatment period. For the drugs administration, dosages were calculated on the basis of average daily water consumption recorded in each cage and they were confirmed by recalculations once a week. Each animal's weight was also recorded once a week during the treatment period and the drug dosages were recalculated when necessary based on the results obtained. The average daily water consumption was 5 ml·day^{-1} for each animal without observing significant differences among the groups. Likewise, the body weight of the control and treated groups did not change significantly during the treatment period (Figure S1). The intervention sample size was chosen following previous studies in our laboratory and using one of the available interactive tools (http://www.biomath.info/power/index.html). Moreover, the animal number mismatch among experimental groups was due to the exclusion of mice by death or ethical reasons according to the final point indicated in the approved protocol.

After 4 weeks of treatment, behavioural and cognitive tests were performed to study the effects of treatment on learning, memory, anxiety behaviour and social interaction (Figure 1a). Mice were also treated during this period and up to their killing (46 days in total). All studies and procedures for the mouse behaviour tests, brain dissection and extractions followed the standard ethical guidelines (European Communities Council Directive 2010/63/EU and Guidelines for the Care and Use of Mammals in Neuroscience and Behavioural Research, National Research Council 2003). Animal studies are reported in compliance with the ARRIVE guidelines (Percie du Sert et al., 2020) and with the recommendations made by the *British Journal of Pharmacology* (Lilley et al., 2020). They were approved by Bioethical Committees from the University of Barcelona and the Government of Catalonia.

2.2 | Behavioural tests

2.2.1 | Novel object recognition test

A modification of the novel object recognition test protocol was performed (Ennaceur & Delacour, 1988). In brief, mice were placed in a 90° two-arm (25 × 20 × 5 cm) black maze, with removable walls for easy cleaning and light intensity in midfield was 30 lux. Before the memory, trial mice were habituated to the apparatus for 10 min for 3 days. On Day 4, the animals were submitted to a 10-min acquisition trial, in which they were allowed to freely explore two identical objects located at the end of each arm (first trial—familiarisation). After 2 h (for short-term memory evaluation) and 24 h (for long-term memory evaluation) from the first trial, the mice were submitted to a 10-min retention trial, in which one of the two identical objects had been replaced by a novel one. The behaviour was recorded and the time that the mice spent exploring the new object (TN) and the old one (TO) was measured manually. Exploration was defined as sniffing or touching the objects with nose and/or forepaws. The discrimination index (DI) was calculated as (TN − TO)/(TN + TO). To avoid object preference biases, objects were alternated; 70% EtOH was used to clean the arms and objects after each trial to eliminate olfactory cues.

2.2.2 | Morris water maze

The Morris water maze test was performed as described previously (Griñan-Ferré et al., 2016) in an open circular pool, filled with water, which temperature was maintained at 22 ± 1°C. The water surface was divided into four quadrants (Q1, Q2, Q3 and Q4) by two principal perpendicular axes and five starting points were set. Four visual clues were placed on the walls of the tank. The animals' swimming paths were recorded and the data were analysed with SMART Version 3.0 software (Panlab, Cornellà, Spain). On Day 1, mice were placed individually into the pool, facing the wall and allowed to swim for 60 s to be habituated to the experimental conditions. On Day 2, a white platform was submerged 1.5 cm below the water level in the middle of the Q1 platform and the acquisition phase took place for 5 days. Each day, the animals were submitted to five trials starting from the positions set in random order. At each trial, mice were allowed to swim for 60 s and, if not able to find the platform within 60 s, were guided to the visible platform. The mice remained for 30 s onto the platform for spatial orientation. There was no resting phase between each trial and the subsequent one; 24 h after the last training, a memory test was performed. For this, the platform was removed from the pool and the mice were tested for 60 s. The distance to the target and the time spent in the platform quadrant (Q1), among other parameters, were measured.

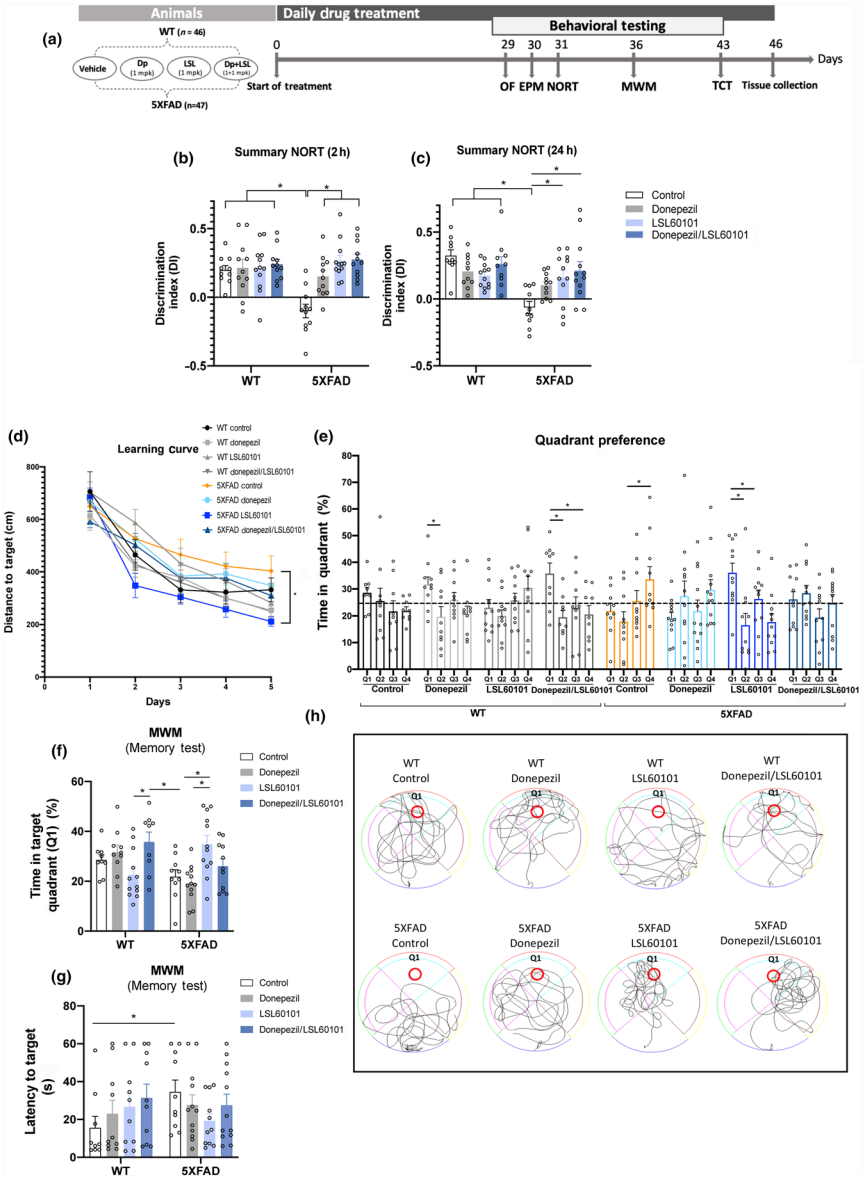

FIGURE 1 Effects of low-dose chronic treatment with I_2- receptor ligand LSL60101, donepezil and coadministration on cognitive status in 5XFAD and WT mice. (a) Scheme of experimental design:- open field (OF), elevated plus maze (EPM), novel object recognition test (NORT), Morris water maze (MWM) and three-chamber test (TCT). Results of NORT:- discrimination index calculated by using exploration time for novel and familiar object in (b) the short-term memory test session (2 h) (WT, $n = 10–12$ per group; 5XFAD $n = 11–12$ per group; two-way ANOVA with Tukey's post hoc analysis showing significant effect of genotype and treatment, with significant interaction) and (c) the long-term memory test session (24 h) (WT, $n = 10–12$ per group; 5XFAD $n = 10–12$ per group; two-way ANOVA with Tukey's post hoc analysis showing significant effect of genotype and treatment, with significant interaction). Results of Morris water maze (MWM): (d) distance to target (platform) (cm) during the training session (WT $n = 10–11$ per group; 5XFAD $n = 10–12$ per group; two-way ANOVA with Tukey's post hoc analysis for each day; Day 5; showing non significant effect of genotype and treatment, with significant interaction). (e) Quadrant preference in the test session as time (%) spent in each quadrant (WT $n = 9–12$ per group; 5XFAD $n = 10–12$ per group; one-way ANOVA with Tukey's post hoc analysis between quadrants for each experimental group). (f) Time (%) spent in platform quadrant in the test session (WT $n = 9–12$ per group; 5XFAD $n = 10–12$ per group; two-way ANOVA with Tukey's post hoc analysis; showing significant effect of genotype and treatment, with significant interaction). (g) Latency to target (platform) (s) in the test session (WT $n = 9–12$ per group; 5XFAD $n = 10–12$ per group; two-way ANOVA with Tukey's post hoc analysis). (h) Representative images of trajectory during memory test. Bars show mean ± SEM; *P <.05

2.2.3 | Open field

Emotional alterations and locomotor activity were evaluated by the open field test using a white plywood apparatus (50 × 50 × 25 cm) as previously described (Archer, 1973; Griñan-Ferré et al., 2016). The apparatus' ground was divided into the centre and peripheral area. Each individual was placed at the centre of the open field and allowed to explore the apparatus for 5 min. The apparatus was cleaned with

70% ethanol after between trials. The behaviour was recorded and later analysed with SMART Version 3.0 software. The locomotor activity of the mice calculated as the sum of total distance travelled in 5 min, the centre stay duration and the number of rearings were evaluated.

2.2.4 | Elevated plus maze

Animals were tested for anxiety-like behaviour by performing the elevated plus maze test, based on a previously described protocol (Walf & Frye, 2007). The elevated plus maze apparatus consisted of two open arms (30 × 5 × 15 cm) and two closed arms (30 × 5 × 15 cm). The mice were placed at the arms' junction and allowed to explore the apparatus for 5 min freely. Elevated plus maze apparatus was cleaned with 70% ethanol between tests. The behaviour was recorded and later analysed with SMART Version 3.0 software. Parameters recorded included the total distance travelled during the 5 min test; the time spent in open arms, closed arms and centre; and the number of rearings.

2.2.5 | Three-chamber test

Three-chamber test evaluated mice social behaviour following a previously described protocol (Companys-Alemany et al., 2020). A box (15 × 15 × 20 cm) divided into three equally dimensioned rooms with openings among them was used. The mice were submitted to 15-min trials. First, each mouse was placed in the centre of the box and allowed to explore the three chambers for 5 min (habituation). The entries to each room were measured manually. Afterwards, an intruder (same sex and age) was placed in a metal cage in one of the rooms and behaviour was recorded for 10 min. The time spent in each room and interacting with the intruder (e.g. sniffing and grooming) was measured manually. The three-chamber test apparatus was cleaned with 70% ethanol between the trials to eliminate olfactory cues.

2.3 | Brain processing

Mice were killed by cervical dislocation 3 days after the behavioural and cognitive tests were completed. The brains were immediately removed from the skulls,and the hippocampi were dissected, frozen and maintained at −80°C. For immunohistochemistry experiments, mice were anaesthetised (ketamine 100 mg·kg^{-1} and xylazine 10 mg·kg^{-1}, i.p.) and then perfused with 4% paraformaldehyde (PFA) diluted in 0.1-M phosphate buffer solution intracardially. Their brains were removed and postfixed in 4% PFA overnight at 4°C. Afterwards, the solutions were changed to PFA + 15% sucrose. Finally, the brains were frozen on powdered dry ice and stored at −80°C until sectioning. All immuno-related procedures involved comply with the editorial on immunoblotting and immunohistochemistry (Alexander et al., 2018).

2.4 | Protein levels determination by western blotting

For protein extraction, hippocampus samples were thawed and mixed in 200-μl lysis buffer (50-mM Tris–HCl pH 7.4, 150-mM NaCl, 5-mM EDTA and 1% Triton X-100) containing phosphatase and protease inhibitor cocktail (Cocktail II, Sigma-Aldrich, St. Louis, MO, USA). Once homogenised, samples were maintained on ice for 30 min. Afterwards, the samples were centrifuged at 10,000× *g* for 30 min at 4°C and the supernatants were collected and maintained at −80°C. Total protein amount was quantified with the method of Bradford as described previously (Bradford, 1976).

For western blot aliquots of 15 μg of hippocampal protein were used. Protein samples were separated by SDS-PAGE (8–16%) and transferred onto PVDF membranes (Millipore, Burlington, MA, USA). Afterwards, membranes were blocked in 5% BSA in 0.1% Tris-buffered saline–Tween 20 (TBS-T) for 1 h at room temperature by overnight incubation at 4°C with the primary antibodies listed in Table S1. Membranes were washed and incubated with secondary antibodies for 1 h at room temperature. Immunoreactive proteins were viewed with a chemiluminescence-based detection kit, following the manufacturer's protocol (ECL Kit; Millipore) and digital images were acquired using a ChemiDoc XRS+ System (Bio-Rad Laboratories, Hercules, CA, USA). Semiquantitative analyses were carried out using Image Lab software (Bio-Rad Laboratories) and results were expressed in arbitrary units (AU), considering control protein levels as 100%. Protein loading was monitored by immunodetection of GAPDH or β-actin. For p-Tau quantification, blots were also normalised by total tau (t-Tau) protein levels.

2.5 | RNA extraction and gene expression determination

Total RNA isolation from hippocampal samples was performed using the TRIzol® reagent according to the manufacturer's instructions (Bioline Reagents, London, UK). The yield, purity and quality of RNA were determined spectrophotometrically with a NanoDrop™ ND-1000 apparatus (Thermo Fisher, Waltham, MA, USA) and an Agilent 2100B Bioanalyzer (Agilent Technologies, Santa Clara, CA, USA). RNA samples with 260/280 ratios and RINs higher than 7.5, respectively, were selected. RT-PCR was performed. Briefly, 2 μg of mRNA was reverse transcribed using a high-capacity cDNA reverse transcription kit (Applied Biosystems, Foster City, CA, USA).

SYBR® Green real-time PCR was performed using a Step One Plus Detection System (Applied Biosystems) with SYBR Green PCR Master Mix (Applied Biosystems). Each reaction mixture contained 6.75 μl of cDNA (with a concentration of 2 μg), 0.75 μl of each primer (with a concentration of 100 nM) and 6.75 μl of SYBR Green PCR Master Mix (2×) (Applied Biosystems).

The data were analysed utilising the comparative cycle threshold (Ct) (ΔΔCt) method, in which the levels of a housekeeping gene are used to normalise differences in sample loading and preparation. The

normalisation of expression levels was performed with β-actin. The primer sequences and TaqMan probes used in this study are presented in Table S2. Each sample was analysed in duplicate and the results represent the *n*-fold difference in the transcript levels among different groups.

2.6 | Amyloid-β levels quantification by ELISA

Amyloid-β_{40} and amyloid-β_{42} protein levels were measured by ELISA with the human amyloid-β_{40} ELISA Kit (Invitrogen, #KHB3481; Thermo Fisher) and human amyloid-β_{42} Ultrasensitive ELISA Kit (Invitrogen, #KHB3441), respectively. The samples were diluted by standard dilution buffer at a percentage of 50% and all procedures followed the manufacturer's instructions.

2.7 | Glial immunohistochemical identification

For immunohistochemical studies, the frozen brains were embedded in OCT Cryostat Embedding Compound (Tissue-Tek, Torrance, CA, USA) and 30-μm-thick brain coronal sections were obtained at −20°C on a cryostat (Leica Microsystems CM 3050S cryostat, Wetzlar, Germany) and kept in a cryoprotectant solution at −20°C until use. Free-floating slices were placed in a 24-well plate and washed with 0.01-M PBS. Next, the free-floating sections were blocked with 0.1-M PBS solution containing 1% BSA and 0.3% Triton X-100 for 20 min at room temperature. Afterwards, slices were washed with PBS 0.01 M two times for 5 min each and were incubated with the primary antibodies listed in Table S1 overnight at 4°C. The primary antibodies were diluted in a 0.1-M PBS solution containing 1% BSA and 0.3% Triton X-100. On the following day, the coronal slices were washed with 0.1-M PBS two times for 5 min each and then incubated with the secondary antibodies listed in Table S1 at room temperature for 1 h. Later, the sections were washed two times for 5 min each with 0.1-M PBS and were incubated with 5-μM Hoechst staining solution (Sigma-Aldrich) for 5 min in the dark at room temperature. After being washed, the slices were mounted using Fluoromount-G (EMS, Hatfield, PA, USA).

2.8 | Amyloid-β plaque histology

Amyloid-β plaques were stained with thioflavin S. Brain coronal sections of 30 μm were obtained (Leica Microsystems CM 3050S cryostat, Wetzlar, Germany) and kept in a cryoprotectant solution at −20°C until use. Free-floating slices were placed in a 24-well plate and washed with 0.01-M PBS for 5 min at room temperature to be rehydrated. Next, the brain sections were washed with 70% ethanol for 1 min, followed by a wash with 80% ethanol for 1 min. The slices were then incubated with 0.3% thioflavin S (Sigma-Aldrich) solution for 15 min at room temperature in the dark. Afterwards, the samples were washed using 80%, 70% and 50% EtOH for 1 min. Three 2-min washes with 0.1-M PBS and the slices were mounted using Fluoromount-G (EMS).

2.9 | Image acquisition and analysis

Image acquisition was performed with a fluorescence laser microscope (Olympus BX51, Hamburg, Germany) using 4×, 10× and 20× objectives, and images were analysed by using ImageJ software (RRID:SCR_003070) as previously described. For quantification of amyloid plaques, similar and comparable histological areas were selected, focusing on the adjacent positioning of the whole cortical area and the hippocampus of the one brain hemisphere. The images were converted to 8-bit greyscale images, thresholded within the linear range and the number of particles (analyse particle function 10-Infinity), as well as the percentage of area covered by thioflavin S (20× objective), was calculated and averaged from two different sections from each animal. Glial fibrillary acidic protein (GFAP) and Iba-1-stained images (10× objective) were acquired, maintaining constant exposure for all samples across single experiments. The fluorescence intensity of the positive cells was measured in hippocampal CA1, CA3 and dentate gyrus areas and quantification was averaged from two to three different sections from each animal.

2.10 | Statistical analysis

The data and statistical analysis comply with the recommendations of the *British Journal of Pharmacology* on experimental design and analysis in pharmacology (Curtis et al., 2018). Group size may vary according to power analysis and expertise of the authors regarding the behavioural tests (Griñan-Ferré et al., 2016; Griñán-Ferré et al., 2018) and statistical analysis was undertaken only for studies where each group size was at least $n = 5$. The blinded analysis was performed for behavioural tests. All data are expressed as the mean ± SEM. Statistical analysis was conducted using GraphPad Prism Version 8 statistical software (RRID:SCR_002798). All data were tested for normal distribution and equal variance. In the cognitive and behavioural studies, means were compared with two-way ANOVA or one-way ANOVA when necessary, followed by Tukey's post hoc tests. In molecular studies, means were compared with two-tailed unpaired Student's *t*-test (WT control vs. 5XFAD control) or one-way ANOVA followed by Tukey's post hoc tests (5XFAD control vs. 5XFAD-treated groups). The post hoc tests were conducted only if F in ANOVA achieved $P < .05$ and there was no significant variance inhomogeneity. Statistical significance was considered when P values were <.05. Statistical outliers were determined with Grubbs' test and, when necessary, were removed.

2.11 | Nomenclature of targets and ligands

Key protein targets and ligands in this article are hyperlinked to corresponding entries in the IUPHAR/BPS Guide to PHARMACOLOGY http://www.guidetopharmacology.org and are permanently archived in the Concise Guide to PHARMACOLOGY 2019/20 (Alexander et al., 2019).

3 | RESULTS

3.1 | I_2 ligand LSL60101 and donepezil improve memory deficits in 5XFAD mice

Short- and long-term working memory were evaluated by novel object recognition test. 7-month-old 5XFAD mice presented robust cognitive deficits compared with WT (Figure 1b,c). LSL60101 treatment resulted in a rapid and sustained recovery of cognitive function by increasing the discrimination index in both 2- and 24-h memory tests (Figure 1b,c). Donepezil enhanced but did not sustain memory function in 5XFAD mice, as a significant increase of the discrimination index was found after 2 h, but not at 24-h memory test (Figure 1b,c). Co-treatment did not improve cognition in comparison with individual treatments (Figure 1b,c). Treatments had no significant effects on WT cognitive performance (Figure 1b,c).

For spatial learning and memory evaluation, the Morris water maze was performed. After 5 days of training, all experimental groups presented curves with progressively shorter path length on consecutive days. Of note, the path length to the platform was significantly decreased in LSL60101-treated 5XFAD mice when compared with 5XFAD controls (Figure 1d). In the probe trial, 5XFAD mice showed a reduced percentage of time spent in the platform quadrant, whereas the mice spent significantly more time in the quadrant opposite to the platform. Moreover, 5XFAD control mice presented increased latency to target compared with WT mice and, overall, a weaker cognitive performance (Figures 1e,g,h and S2). LSL60101 treatment significantly increased the time spent in the platform quadrant in the 5XFAD-treated mice compared with both vehicle and donepezil-treated 5XFAD, whereas LSL60101 treatment had no effect on WTs (Figure 1e,f,h). Neither donepezil nor cotreatment improved 5XFAD mice spatial memory (Figure 1d,e), although WT-treated mice performed better (Figure 1d,f,h). All treatments decreased the path length to the platform, albeit not significantly, due to the different performance of individual mice (Figure S2).

3.2 | I_2 receptor ligand LSL60101 does not affect behavioural and emotional disturbances in 5XFAD mice in contrast to donepezil

We also investigated the effect of the treatments on the 5XFAD and WT mice anxiety-like behaviour by performing the open field and elevated plus maze tests. No differences in locomotor activity were observed among the WT and 5XFAD groups (Figure 2a). 5XFAD mice presented a significant increase in the time spent in the centre of the open field compared with WT mice (Figure 2b). No effect was observed on the WT mice behaviour after treatments. 5XFAD treated with donepezil but not with LSL60101 showed a significant decrease in the time spent in the centre compared with 5XFAD controls, reverting to the WT healthy phenotype (Figure 2b). Co-treatment LSL60101/donepezil displayed the same results that showed donepezil alone in all parameters evaluated (Figure 2b and Table S3).

Similarly, in the elevated plus maze, 5XFAD mice spent significantly more time in the open arms and less in the closed arms in comparison with age-matched WTs (Figure 2d,e). Donepezil had a positive effect by reverting the evaluated 5XFAD elevated plus maze parameters to those shown by WT group (Figure 2d–f and Table S4). I_2 ligand treatment alone did not affect any of the elevated plus maze parameters studied, whereas cotreatment maintained the donepezil values. Treatments did not induce significant changes in elevated plus maze parameters evaluated in WT mice (Table S4).

3.3 | I_2 ligand LSL60101 and donepezil ameliorate social deficits presented by 5XFAD mice

To evaluate the effect of treatments on social behaviour, mice were subjected to the three-chamber test. No differences in the number of entries to each chamber were determined in the habituation phase in any tested group (Figure 2g). On the contrary, mice spent more time in the intruder's chamber during the test phase in all experimental conditions (Figure 2h). When the social interaction was evaluated, 5XFAD mice spent significantly less time interacting with the intruder compared with the WT healthy control (Figure 2i). All treatments improved social impairments in 5XFAD-treated groups by increasing the time of interaction compared with the 5XFAD controls, but only 5XFAD treated with donepezil reached significance (Figure 2i), whereas for LSL60101, $P < .06$ was calculated. WT-treated mice presented no differences compared with WT controls.

3.4 | I_2 ligand LSL60101, but not donepezil, reduces amyloid-β plaques; by contrast, donepezil/LSL60101 attenuates amyloid-β pathology in 5XFAD mice

The number of amyloid plaques in 5XFAD hippocampus and cortex mice was assessed by histochemical staining with thioflavin S. LSL60101 induced a significant decrease in the total number and area (%) covered by the plaques in 5XFAD mice compared with the 5XFAD controls, demonstrating a neuroprotective function of I_2 ligand regarding the senile plaque formation. Treatment with donepezil did not reduce the number of amyloid plaques or area significantly in 5XFAD mice (Figure 3a–c). The protein levels of amyloid-β determined by western blots tended to decrease in all treated groups without reaching significance (Figure 3d,h). Protein concentrations of amyloid-β_{40} and amyloid-β_{42}, determined by ELISA, were significantly higher in 5XFAD in comparison with WT healthy control, whereas treatment with LSL60101 reduced significantly amyloid-β_{40} and amyloid-β_{42} levels. Donepezil did not modify amyloid-β concentration species significantly and combination of donepezil and LSL60101 treatment did not modify the effect of LSL60101 alone (Figure 3e,f). As expected, full-length amyloid precursor protein levels were increased in 5XFAD mice compared with WT mice and treatments did not modify protein expression

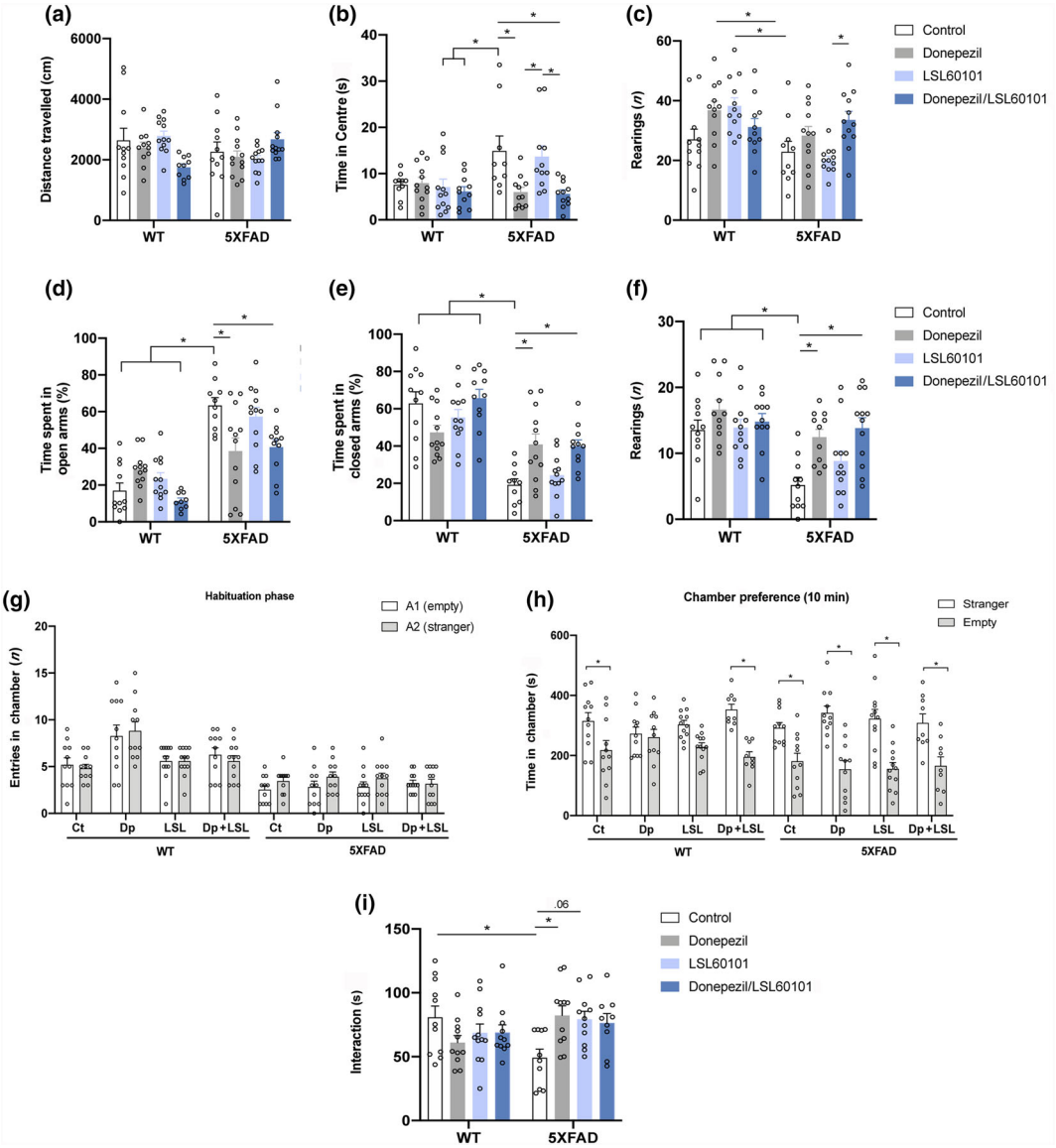

FIGURE 2 Effects of low-dose chronic treatments I_2-IR LSL60101, donepezil and co-administration on behavioural and social status in 5XFAD mice and WT controls. Results of open field :- (a) locomotor activity measured as distance travelled (cm) (WT $n = 10–12$ per group; 5XFAD $n = 11–12$ per group; two-way ANOVA with Tukey's post hoc analysis). (b) Time spent in the centre (s) (WT $n = 10–12$ per group; 5XFAD $n = 9–11$ per group; two-way ANOVA with post hoc analysis showing significant effect of genotype and treatment, with significant interaction). (c) Number of rearings (WT $n = 11–12$ per group; 5XFAD $n = 10–12$ per group; two-way ANOVA with Tukey's post hoc analysis showing significant effect of genotype and treatment, with significant interaction). Results of elevated plus maze (EPM):- (d) time (%) spent in open arms (WT $n = 11–12$ per group; 5XFAD $n = 10–12$ per group; two-way ANOVA with Tukey's post hoc analysis showing significant effect of genotype and treatment, with significant interaction). (e) Time (%) spent in closed arms (WT $n = 11–12$ per group; 5XFAD $n = 10–12$ per group; two-way ANOVA with post hoc analysis showing significant effect of genotype and treatment, with significant interaction). (f) Number of rearings (WT $n = 11–12$ per group; 5XFAD $n = 11–12$ per group; two-way ANOVA with post hoc analysis showing significant effect of genotype and treatment, with significant interaction). Results of three-chamber test (TCT): (g) entries in chambers (A1 and A2) in the habituation phase (n) (WT $n = 11–12$ per group; 5XFAD $n = 11–12$ per group; unpaired Student's t test). (h) Time in chambers (empty and stranger) during the test session (WT $n = 10–11$ per group; 5XFAD $n = 9–11$ per group; unpaired Student's t-test). (i) Time of interaction with intruder (s) in the test session (WT $n = 11–12$ per group; 5XFAD $n = 10–11$ per group two-way ANOVA showing non-significant effect of genotype and treatment, with significant interaction). Bars show mean ± SEM; $^*P < .05$

(Figure 4a,h). Interestingly, alterations in the levels of proteins implicated in the amyloid precursor protein processing showed complementary results in the combination of LSL60101 and donepezil treatment. In this line, the protein levels of C-terminal fragments were found significantly reduced in LSL60101-treated group compared with the 5XFAD controls. LSL60101/donepezil-treated

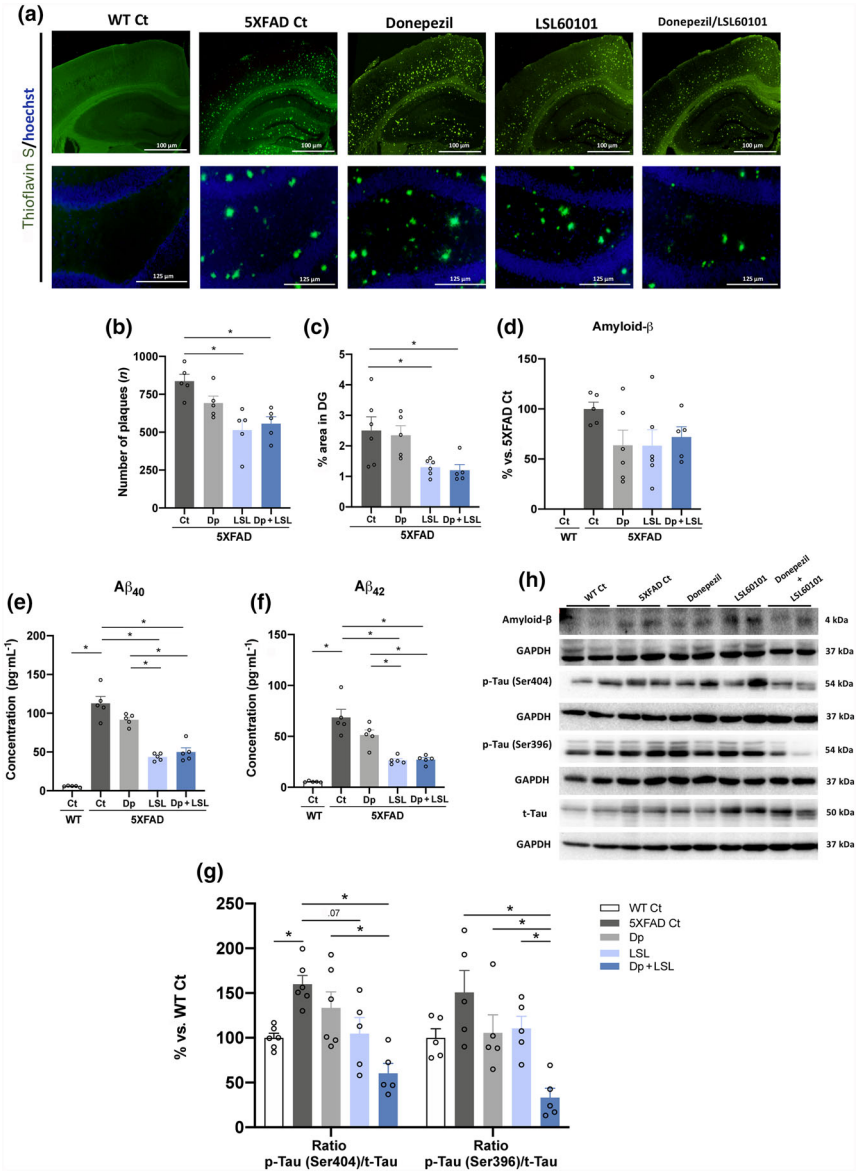

FIGURE 3 Effects of low-dose chronic treatments I_2- receptor ligand LSL60101, donepezil and co-administration on AD markers in 5XFAD mice. (a) Representative images of thioflavin S staining of amyloid plaques and quantification of (b) amyloid plaque number in cortex and hippocampus and (c) area (%) covered by plaques in the dentate gyrus area of the hippocampus in the 5XFAD mice. Data are presented as the mean ± SEM and each dot represents one mouse ($n = 5$ per group); averaged from 2–3 sections from the same brain area per animal. Levels of amyloid-β_{40} and amyloid-β_{42} and representative western blot and quantifications for (d–h) β-amyloid, p-Tau (Ser404) and p-Tau (Ser396) in the hippocampus of 5XFAD mice. Values in bar graphs are adjusted to 100% for protein levels of the control WT or the control 5XFAD. Bars represent mean ± SEM. Student's *t*-test or one-way ANOVA with Tukey's post hoc analysis, $^*P < .05$; $n = 5$–6 per group

group showed a significant decrease in C-terminal fragments compared with monotherapy (Figure 4b,h). The protein levels of phosphorylated amyloid precursor protein at Th668 were decreased significantly only for the combination of donepezil/LSL60101-treated animals (Figure 4c,h). Soluble amyloid precursor protein β levels were found increased in 5XFAD controls compared with WT mice, confirming the amyloid pathology process. Furthermore, a significant decrease in donepezil/LSL60101-treated group was determined (Figure 4d,h). Soluble amyloid precursor protein α levels were found increased after combination treatment when compared with 5XFAD controls or donepezil-treated mice (Figure 4e,h). Regarding the levels of **BACE1 (β-secretase 1)** and **ADAM10**, no significant differences were observed among the 5XFAD groups (Figure 4f–h). However, when the gene expression of enzymes implicated in amyloid degradation was studied, treatments slightly increased gene expression of **insulin-degrading enzyme (IDE)**, whereas **neutral endopeptidase *neprilysin* (*Nep*)** was only reduced in the donepezil and LSL60101 groups (Figure 4i).

3.5 | I_2 ligand LSL60101 and combination with donepezil reduce tau hyperphosphorylation in 5XFAD mice

Tau hyperphosphorylation, another major marker of AD, was evaluated in the hippocampus of the 5XFAD mice. I_2- ligand LSL60101 and the cotreatment donepezil/LSL60101 decreased the tau phosphorylation at the Ser404 and Ser396, diminutions that reached significance for the donepezil/LSL60101-treated 5XFAD mice. Of note, significant differences in p-Tau levels were also found between the donepezil/LSL60101 5XFAD-treated mice and the donepezil or LSL60101-treated ones (Figure 3g,h).

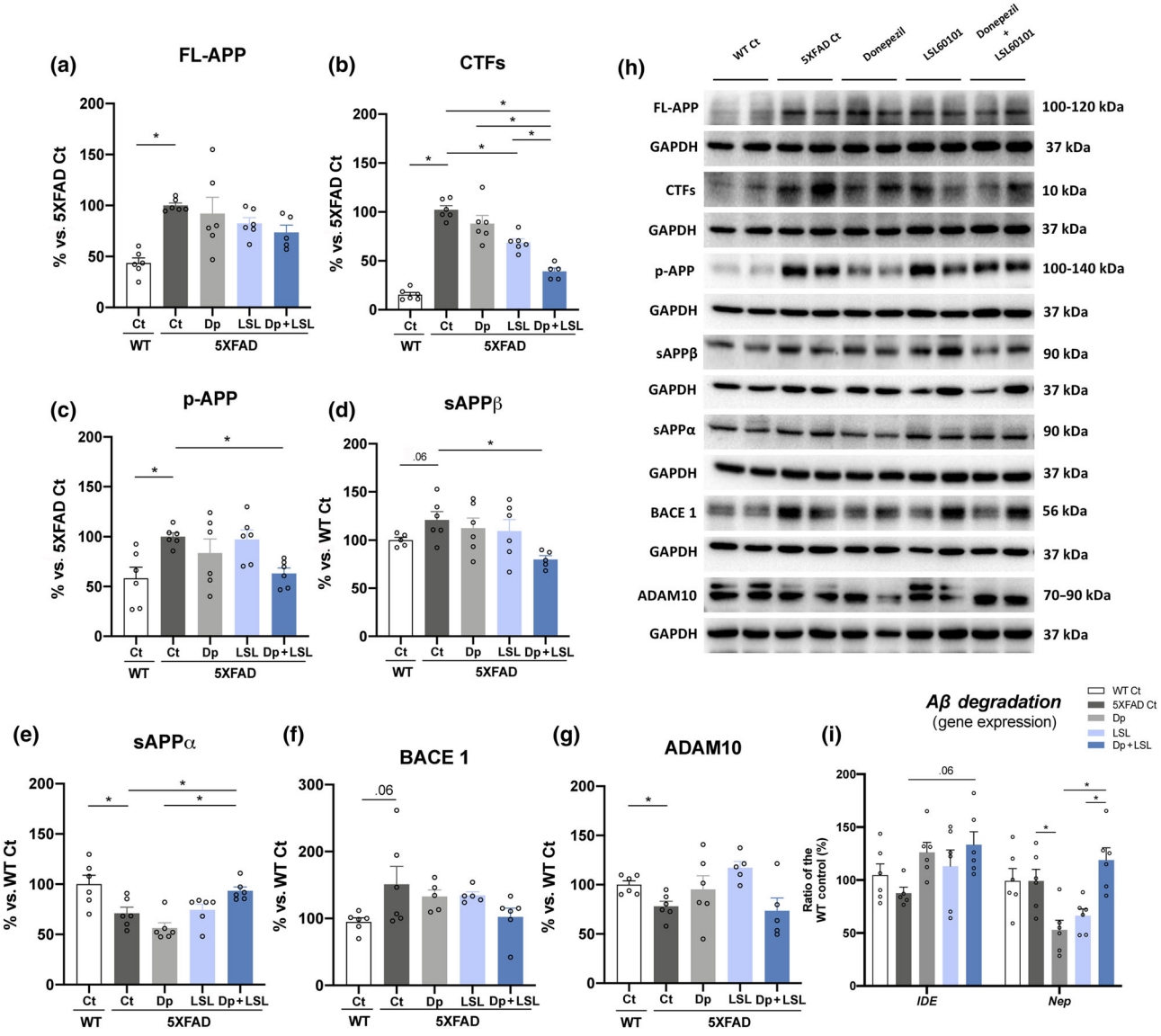

FIGURE 4 Effects of low-dose chronic treatments I_2 receptor ligand LSL60101, donepezil and co-administration on amyloid-β (Aβ) pathology and amyloid precursor protein (APP) processing in 5XFAD mice. Representative western blots and quantifications for (a–h) FL-APP, C-terminal fragments (CTFs), p-APP, sAPPβ, sAPPα, BACE 1 and ADAM10 in the hippocampus of 5XFAD mice. Values in bar graphs are adjusted to 100% for protein levels of the control WT or the control 5XFAD. Representative gene expression in the hippocampus of the 5XFAD mice for *IDE* and *Nep* (i). Gene expression levels were determined by real-time PCR. Values in bar graphs are adjusted to 100% for relative gene expression of the WT control. Bars represent mean ± SEM. Unpaired Student's *t*-test or one-way ANOVA with Tukey's post hoc analysis, $^*P < .05$; $n = 5–6$ per group

3.6 | Effects of LSL60101 on microglia activation and inflammatory marker expression

In the AD brain, the formation of amyloid-β plaques leads to the activation of astrocytes and reactive gliosis. To examine changes in microglia reactivity, ionized calcium-binding adaptor molecule 1 (Iba-1) was determined by immunohistochemistry experiments. Importantly, LSL60101 treatment resulted in a significant decrease in Iba-1 levels in the hippocampus (Figure 5a–d) and in the cortex (Figure S3) of 5XFAD mice, whereas donepezil did not affect Iba-1 immunoreactivity (Figure 5a–d). Donepezil/LSL60101 combination reduced significantly Iba-1 levels in the cortex (Figure S3) and the dentate gyrus area in the hippocampus (Figure 5a–d). The gene expression of different inflammatory mediators was evaluated in the hippocampus of 5XFAD mice. In whole, 5XFAD mice presented an evident exacerbation of inflammatory response compared with WT mice, whereas treatments led to the up-regulation of specific markers studied. No significant changes were determined in **IL-1β (Il-1b)** and **IL-6 (Il-6)** markers in treated groups compared with 5XFAD controls (Figure 5e). However, **chemokine (C–C motif) ligand 12 (Ccl12)** and **IL-18 (Il-18)** genes were found increased in LSL60101 group and donepezil/LSL60101-treated groups compared with 5XFAD controls

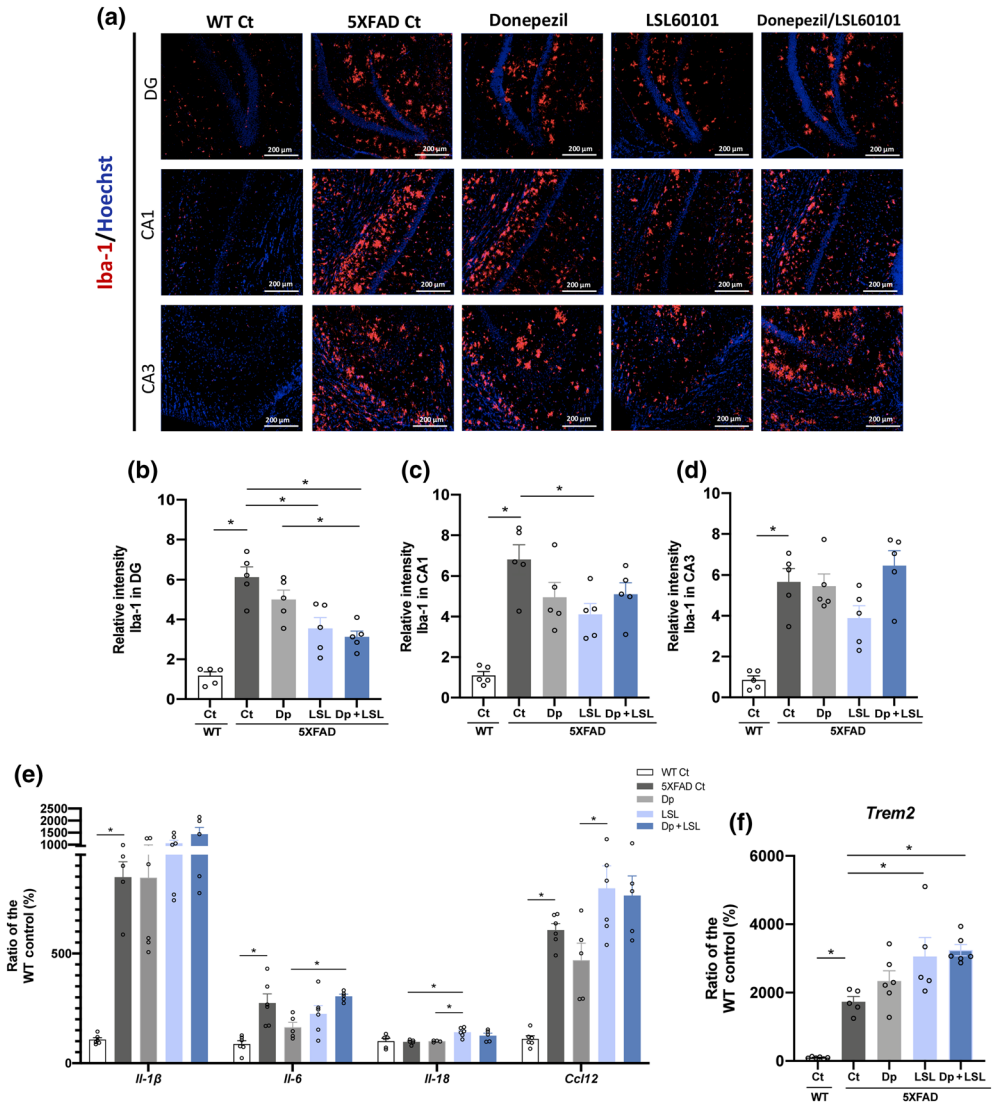

FIGURE 5 Effects of low-dose chronic treatments I_2 receptor ligand LSL60101, donepezil and co-administration on microgliosis and inflammatory markers in 5XFAD mice. (a) Representative images of Iba-1 immunostaining and quantification in (b–d) dentate gyrus (DG), cornu ammonis (CA) 1 and CA3 areas of the hippocampus of the 5XFAD mice. Data are presented as the mean ± SEM of relative fluorescent intensity of the positive cells averaged from 2–3 different sections from the same brain area per animal and each dot represents one mouse ($n = 5$ per group). Representative gene expression in the hippocampus of the 5XFAD mice for (e) *Il-1β*, *Il-6*, *Il-18* and *Ccl12* and (f) *Trem2*. Gene expression levels were determined by real-time PCR. Values in bar graphs are adjusted to 100% for relative gene expression of the WT control. Bars show mean ± SEM. Unpaired Student's *t*-test or one-way ANOVA with Tukey's post hoc analysis, $^*P < .05$; $n = 5–6$ per group

(Figure 5e). Moreover, the gene expression of *triggering receptor expressed on myeloid cells 2* (*Trem2*) was increased significantly after treatment with the I_2 ligand LSL60101 and the combination-treated group (Figure 5f), confirming the results of *Il-18* and *Ccl12*.

3.7 | LSL60101 effects on astroglial activation and synaptic dysfunction

All treatments were able to attenuate astrogliosis in the hippocampus of 5XFAD brains by decreasing GFAP immunoreactivity in dentate gyrus, CA1 and CA3 areas in 5XFAD mice groups in comparison with untreated mice (Figure 6a–d). Similar results were observed in the cortex (Figure S3). Likewise, synaptic plasticity markers were evaluated by western blot. Decreases in the protein levels of postsynaptic density protein 95 (PSD95) and synaptophysin were determined in 5XFAD mice when compared with WT mice (Figure 6e–g). I_2 ligand LSL60101 increased PSD95 levels when compared with 5XFAD control (Figure 6e,g). Synaptophysin levels were found to increase in LSL60101 and donepezil/LSL60101-treated 5XFAD mice, reaching significance only for the combination-treated group. Donepezil treatment was not able to modify these markers significantly (Figure 6f,g).

4 | DISCUSSION

The identification of new targets for AD treatment is required due to the lack of effective treatment. At present, AChE inhibitors are one of the standard therapeutic options clinically available for AD patients, however those treatments provide only symptomatic benefit in AD (Rosini et al., 2014; Sinforiani et al., 2003). Fortunately, the number of disease-modifying drugs targeting AD markers such as **aducanumab (BIIB037)**, which is currently in Phase 3 trials, is increasing (Cummings et al., 2020). Combination therapies of symptomatic and disease-modifying drugs have centred attention due to the multifactorial origin of the disease and most current clinical trials combine donepezil with novel neuroprotective drugs (Frölich et al., 2019). However, it remains a challenge that must be addressed to unveil new strategies

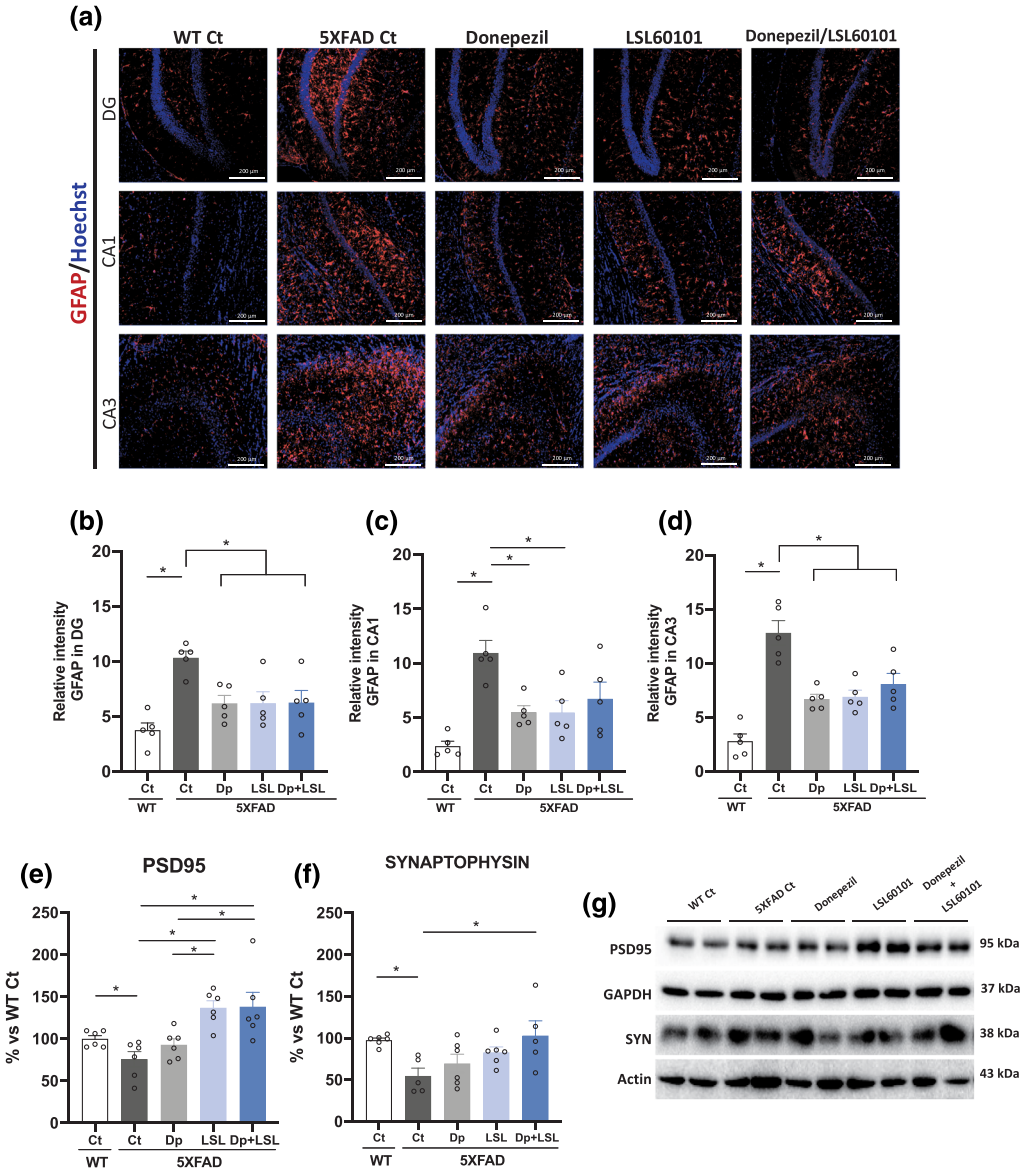

FIGURE 6 Effects of low-dose chronic treatments I_2 receptor ligand LSL60101, donepezil and co-administration on astrogliosis and synaptic plasticity in 5XFAD mice. (a) Representative images of GFAP immunostaining and quantification in (b–d) dentate gyrus (DG), cornu ammonis (CA) 1 and CA3 areas of the hippocampus of the 5XFAD mice. Data are presented as the mean ± SEM of relative fluorescent intensity of the positive cells averaged from 2–3 different sections from the same brain area per animal and each dot represents one mouse ($n = 5$ per group). Representative western blot and quantifications for (e–g) postsynaptic density protein 95 (PSD95) and synaptophysin (SYN) in the hippocampus of 5XFAD mice. Values in bar graphs are adjusted to 100% for protein levels of the control WT. Bars show mean ± SEM. Unpaired Student's *t*-test or one-way ANOVA with Tukey's post hoc analysis, $^*P < .05$; $n = 5$–6 per group

that could be more effective in disease-modifying treatment rather than address symptoms (Schmitt et al., 2004).

Several studies have described the symptomatic effects of donepezil in animal models of dementia and AD, but few *in vivo* studies have evaluated donepezil neuroprotective effects regarding the disease-modifying actions of this compound alone or in combination (Jiangbo & Liyun, 2018; Krishna et al., 2020; Ongnok et al., 2021; Yang et al., 2020). Here, we studied the effect of chronic low doses of an I_2 ligand, donepezil and their combination.

In the light of our studies, we demonstrated for the first time the neuroprotective effects of selective I_2 ligands in the senescence-accelerated mouse prone 8 (SAMP8), a mouse model of late-onset AD (Griñán-Ferré et al., 2019). LSL60101, a selective I_2 ligand, has been shown to induce several biological effects associated with I_2 receptor occupancy and, most importantly, neuroprotective effects in the CNS (Boronat et al., 1998; Casanovas et al., 2000; Menargues et al., 1995; Sánchez-Blázquez et al., 2000). Therefore, it represents a suitable drug candidate to validate this receptor as a target for AD. Here, we

demonstrated the efficacy of chronic low-dose I_2 ligand LSL60101 treatment compared with donepezil by assessing the beneficial outcomes in a model of familial AD.

Cognitive abilities are the essential indicators to unveil pharmacological effects in AD. First, chronic low-dose treatment with the I_2 ligand LSL60101 or donepezil reversed the cognitive deficits presented by 7-month-old 5XFAD mice without affecting WT mice in the novel object recognition test paradigm. However, in the spatial memory test, only LSL60101 showed improvements in memory. Likewise, 5XFAD exhibited improved social behaviour after LSL60101 or donepezil treatment. In agreement with these results, donepezil has been shown to improve social interactions in scopolamine-induced memory impairments in mice (Riedel et al., 2009) and in drug trials for AD (Boada-Rovira et al., 2004). Nevertheless, the beneficial effect of an I_2 ligand treatment on social interaction deficits has not been described previously.

By contrast, I_2 ligand LSL60101 did not modify anxiety-like behaviour, albeit previous studies have shown the *in vivo* anxiolytic and antidepressant-like effects induced by I_2 ligands (Finn et al., 2003; Tonello et al., 2012). Interestingly, the absence of antidepressant effect after treatment with LSL60101 in healthy rats was recently described (Hernández-Hernández et al., 2020), further supporting our results because anxiety-like and depressive-like behaviours are strongly associated, sharing common molecular pathways (Gatt et al., 2009). In contrast, and according to literature (Fitzgerald et al., 2020), chronic treatment with donepezil showed beneficial effects on the anxiety-related disturbances exhibited by 5XFAD mice.

Recently, we reported that the amyloidogenic amyloid precursor protein processing pathway was suppressed in senescence-accelerated mouse prone 8 and 5XFAD mice after treatment with novel I_2 ligands, anticipating the role of I_2 modulation in the amyloid-β biogenesis (Abás et al., 2020;Griñán-Ferré et al., 2019; Vasilopoulou, Griñán-Ferré, et al., 2020). Accordingly, in this study, we demonstrated for the first time that chronic low-dose treatment with I_2 ligand LSL60101 attenuated the amyloid plaque burden in 5XFAD mice. In addition, amyloid-β plaque reduction was accompanied by a decrease in C-terminal fragments, amyloid-β_{40} and amyloid-β_{42} protein levels. Conversely, recently, it was reported that the I_2 ligand BU224 does not ameliorate amyloid-β amyloidosis in 5XFAD mice but improves memory (Mirzaei et al., 2020). In contrast with LSL60101 like molecules, BU224 blocked the memory-enhancing effect of agmatine in memory deficits induced by amyloid-β_{42} in mice (Kotagale et al., 2020). These discrepancies between I_2 ligands can be explained by differences in compound administration conditions, such as dose, time (subchronic vs. chronic) and administration route. Thus, we hypothesise that low doses of LSL60101, as well as chronic treatment, have a clear beneficial effect on amyloid burden because of differential characteristics among I_2 ligands (Garau et al., 2013; Sánchez-Blázquez et al., 2000).

Several studies have demonstrated the effect of donepezil on amyloid-β pathology in AD models, reporting either beneficial changes (Dong et al., 2009; Takada-Takatori et al., 2019) or lack of effect (Ju & Tam, 2020). Here, low-dose donepezil treatment did not induce significant changes either in amyloid-β plaques or in amyloid precursor protein processing in 7-month-old 5XFAD. Of note, co-administration of I_2 LSL60101 and donepezil showed a greater effect on amyloid precursor protein processing than monotherapy. Regarding the amyloid-β degradation, the co-treatment of donepezil/LSL60101 induced an increase in amyloid-β degradation enzyme gene expression in 5XFAD mice, which was not determined in the other treated groups. To sum up, this is the first time an I_2 ligand was shown to effectively reduce the amyloid-β plaques in a mouse model of AD.

The presence of p-Tau, another major AD marker, in the 5XFAD model is supported by previous studies suggesting that tau pathology may be downstream from amyloid-β pathology (Blanchard et al., 2003; Saul et al., 2013). I_2 ligand LSL60101 ameliorated tau pathology in the hippocampus of 5XFAD mice. Interestingly, it was shown recently that chronic treatment with idazoxan, a mixed α_2/I_2 ligand, reduced p-Tau reversing cognitive deficits in AD mice because of its α_2 blockade action (Zhang et al., 2020). In this case, the effect of LSL60101 on tau pathology can be attributed to its I_2 selectivity, more than to the α_2 one. Surprisingly, the p-Tau reduction reached significance in the 5XFAD mice treated with the combination of LSL60101 with donepezil demonstrating, in this case, a putative additive effect of the drugs on tau pathology. Indeed, amelioration of tau pathology has been induced in AD animal models both by donepezil (Yoshiyama et al., 2010) and by I_2 ligand treatments (Griñán-Ferré et al., 2019; Vasilopoulou, Griñán-Ferré, et al., 2020). It is possible that the activation of distinct molecular pathways by the two molecules with different modes of actions resulted in a remarkable p-Tau reduction observed in the donepezil/LSL60101-treated mice group.

It is well established that amyloid-β accumulation jointly with p-Tau increases microglial activation and inflammatory mediators' production in AD brains (Akiyama et al., 2000; Serrano-Pozo et al., 2011; Zhang & Jiang, 2015). On the one hand, chronic low-dose LSL60101 treatment reduced microgliosis in 5XFAD mice in contrast to the standard of care donepezil, explaining the decrease in the amyloid deposition that in turn would lead to a decrease in gliotic response after LSL60101 treatment. On the other hand, inflammatory gene expression increase (*Il-18* and *Ccl12*) was observed after treatment with I_2 ligand LSL60101 and LSL60101/donepezil, but not with donepezil. Interestingly, this was further supported by a significant up-regulation of *Trem2* gene expression determined in the LSL60101-treated mice, further confirming the neuroinflammatory modulation by I_2 ligand LSL60101 (Griñán-Ferré et al., 2019; Hwang et al., 2010; Vasilopoulou, Bagan, et al., 2020). In fact, increased *Trem2* expression has been shown to reprogram microglia responsivity mediating microglial cytokine release, migration and clearance of amyloid-β deposits, ameliorating neuropathological and behavioural deficits of AD mouse models (Lee et al., 2018; Zhao et al., 2018).

It has been described that the I_2 receptors modulate the expression of astrocyte marker GFAP, especially considering their primary location in astrocytes (Olmos et al., 1994; Regunathan et al., 1993, 1999). GFAP diminution was observed *in vivo* and *in vitro* after treatment with selective I_2 ligands (Griñán-Ferré et al., 2019; Siemian et al., 2018; Vasilopoulou, Griñán-Ferré, et al., 2020). In agreement with those results, chronic low-dose treatment with I_2 ligand

LSL60101 attenuated astrogliosis in 5XFAD mice. By contrast, it has been shown that chronic treatment with LSL60101 increased GFAP immunoreactivity (Alemany et al., 1995), resulting in reactive astrogliosis and preventing motoneuron cell death in neonatal rats (Casanovas et al., 2000). However, here, in a neurodegenerative landscape provided by the 5XFAD model, the diminution of GFAP reactivity ran in parallel with the attenuation of the amyloid-β pathology and microglial activation observed after LSL60101 and donepezil treatment, given further support to the beneficial effects of I_2 ligand on mice behaviour. Ultimately, we demonstrated that chronic low-dose treatment with I_2 ligand and donepezil enhanced synaptic plasticity, further supporting the cognitive and behavioural improvement induced by the LSL60101 in 5XFAD mice.

Nevertheless, one limitation of our study was that only female 5XFAD mice were used to establish the protective effect of LSL60101 on AD markers and cognition. It would be of great interest to carry out experiments on male mice once we have demonstrated the disease-modifying effects promoted by LSL60101 in a female mice model of AD.

5 | CONCLUSIONS

Collectively, we report that chronic low-dose treatment with I_2 ligand LSL60101 reversed cognitive deficits in 5XFAD mice, altering AD neuropathological markers, including glial activation and synaptic dysfunction. Strikingly, treatment with I_2 ligand LSL60101 was found to exert greater beneficial effects under the neurodegenerative process caused by amyloid-β pathology than donepezil. However, combination treatment only showed discrete synergistic effects at the molecular level (e.g. tau hyperphosphorylation or synaptic plasticity), suggesting that increased dosage and/or duration of the treatment may be able to produce better effects on both behaviour and AD markers, targeting simultaneously pathological and symptomatic reliefs. In conclusion, our findings demonstrate the therapeutic potential of the I_2 recetor ligands for AD treatment as a disease-modifying single therapy and provide new insights into their efficacy.

ACKNOWLEDGEMENTS

This study was supported by Ministerio de Economía y Competitividad of Spain and FEDER (Ministerio de Ciencia e Innovación; PID2019-107991RB-I00 and PID2019-106285RB-I00) and 2017SGR106 (Agència de Gestió d'Ajuts Universitaris i de Recerca [AGAUR], Catalonia). The project leading to these results has received funding from "la Caixa" Foundation (ID100010434), under Agreement CI18-00002. F.V. thanks the Universitat de Barcelona (UB) for the APIF grant (UB2016); S. R.-A. to Generalitat de Catalunya (2018FI-B-00227); and A.B. for the APIF Grant Institute of Biomedicine (UB2018).

AUTHOR CONTRIBUTIONS

F.V., C.G.-F. and M.P. conceived the study, designed all the experiments and interpreted the data; F.V. and C.G.-F. performed the experiments and data analysis; all authors revised the manuscript draft; S.R.-A., A.B. and C.E. synthesised the compounds tested. F.V., C.G.-F. and M.P. wrote, revised and finalised the manuscript.

CONFLICT OF INTEREST

The authors declare no conflicts of interest.

DECLARATION OF TRANSPARENCY AND SCIENTIFIC RIGOUR

This Declaration acknowledges that this paper adheres to the principles for transparent reporting and scientific rigour of preclinical research as stated in the *BJP* guidelines for Design & Analysis, Immunoblotting and Immunochemistry and Animal Experimentation and as recommended by funding agencies, publishers and other organisations engaged with supporting research.

DATA AVAILABILITY STATEMENT

The data that support the findings of this study are available from the corresponding author upon reasonable request. Some data may not be available because of privacy or ethical restrictions.

ORCID

Foteini Vasilopoulou https://orcid.org/0000-0003-3656-7714
Sergio Rodríguez-Arévalo https://orcid.org/0000-0001-7400-0220
Carmen Escolano https://orcid.org/0000-0002-9117-8239
Christian Griñán-Ferré https://orcid.org/0000-0002-5424-9130
Mercè Pallàs https://orcid.org/0000-0003-3095-4254

REFERENCES

Abás, S., Erdozain, A. M., Keller, B., Rodríguez-Arévalo, S., Callado, L. F., García-Sevilla, J. A., & Escolano, C. (2017). Neuroprotective effects of a structurally new family of high affinity imidazoline I $_2$ receptor ligands. *ACS Chemical Neuroscience*, *8*(4), 737–742. https://doi.org/10.1021/acschemneuro.6b00426

Abás, S., Rodríguez-Arévalo, S., Bagán, A., Griñán-Ferré, C., Vasilopoulou, F., Brocos-Mosquera, I., Muguruza, C., Pérez, B., Molins, E., Luque, F. J., Pérez-Lozano, P., de Jonghe, S., Daelemans, D., Naesens, L., Brea, J., Loza, M. I., Hernández-Hernández, E., García-Sevilla, J. A., García-Fuster, M. J., … Escolano, C. (2020). Bicyclic α-iminophosphonates as high affinity imidazoline I_2 receptor ligands for Alzheimer's disease. *Journal of Medicinal Chemistry*, *63*, 3610–3633. https://doi.org/10.1021/acs.jmedchem.9b02080

Akiyama, H., Barger, S., Barnum, S., Bradt, B., Bauer, J., Cole, G. M., Wyss-Coray, T., Eikelenboom, P., Emmerling, M., Fiebich, B. L., Finch, C. E., Frautschy, S., Griffin, W. S., Hampel, H., Hull, M., Landreth, G., Lue, L., Mrak, R., Mackenzie, I. R., … Wyss-Coray, T. (2000). Inflammation and Alzheimer's disease. *Neurobiology of Aging*, *21*, 383–421. https://doi.org/10.1016/s0197-4580(00)00124-x

Alemany, R., Olmos, G., Escribá, P. V., Menargues, A., Obach, R., & García-Sevilla, J. A. (1995). LSL 60101, a selective ligand for imidazoline I_2 receptors, on glial fibrillary acidic protein concentration. *European Journal of Pharmacology*, *280*, 205–210. https://doi.org/10.1016/0014-2999(95)00214-6

Alexander, S. P. H., Kelly, E., Mathie, A., Peters, J. A., Veale, E. L., Armstrong, J. F., Faccenda, E., Harding, S. D., Pawson, A. J., Sharman, J. L., Southan, C., Buneman, O. P., Cidlowski, J. A., Christopoulos, A., Davenport, A. P., Fabbro, D., Spedding, M., Striessnig, J., Davies, J. A., … Wong, S. S. (2019). The Concise Guide to

PHARMACOLOGY 2019/20: Introduction and other protein targets. *British Journal of Pharmacology*, *176*(Suppl 1), S1–S20. https://doi.org/10.1111/bph.14747 PMID: 31710719; PMCID: PMC6844537

Alexander, S. P., Roberts, R.E., Broughton, B. R., Sobey, C. G., George, C. H., Stanford, S. C., Cirino, G., Docherty, J. R., Giembycz, M. A., Hoyer, D., & Insel, P. A. (2018). Goals and practicalities of immunoblotting and immunohistochemistry: A guide for submission to the British Journal of Pharmacology. *British Journal of Pharmacology*, *175*, 407–411. https://doi.org/10.1111/bph.14112

Archer, J. (1973). Tests for emotionality in rats and mice: A review. *Animal Behaviour*, *21*, 205–235. https://doi.org/10.1016/S0003-3472(73)80065-X

Blanchard, V., Moussaoui, S., Czech, C., Touchet, N., Bonici, B., Planche, M., Canton, T., Jedidi, I., Gohin, M., Wirths, O., Bayer, T. A., Langui, D., Duyckaerts, C., Tremp, G., & Pradier, L. (2003). Time sequence of maturation of dystrophic neurites associated with Aβ deposits in APP/PS1 transgenic mice. *Experimental Neurology*, *184*, 247–263. https://doi.org/10.1016/S0014-4886(03)00252-8

Boada-Rovira, M., Brodaty, H., Cras, P., Baloyannis, S., Emre, M., Zhang, R., Bahra, R., & 322 Study Group. (2004). Efficacy and safety of donepezil in patients with Alzheimer's disease. *Drugs & Aging*, *21*, 43–53. https://doi.org/10.2165/00002512-200421010-00004

Boronat, M. A., Olmos, G., & García-Sevilla, J. A. (1998). Attenuation of tolerance to opioid-induced antinociception and protection against morphine-induced decrease of neurofilament proteins by idazoxan and other I_2-imidazoline ligands. *British Journal of Pharmacology*, *125*, 175–185. https://doi.org/10.1038/sj.bjp.0702031

Bousquet, P., Hudson, A., García-Sevilla, J. A., & Li, J. X. (2020). Imidazoline receptor system: The past, the present, and the future. *Pharmacological Reviews*, *72*, 50–79. https://doi.org/10.1124/pr.118.016311

Bradford, M. M. (1976). A rapid and sensitive method for the quantitation of microgram quantities of protein utilizing the principle of protein-dye binding. *Analytical Biochemistry*, *72*, 248–254. https://doi.org/10.1016/0003-2697(76)90527-3

Casanovas, A., Olmos, G., Ribera, J., Boronat, M. A., Esquerda, J. E., & García-Sevilla, J. A. (2000). Induction of reactive astrocytosis and prevention of motoneuron cell death by the I_2-imidazoline receptor ligand LSL 60101. *British Journal of Pharmacology*, *130*, 1767–1776. https://doi.org/10.1038/sj.bjp.0703485

Companys-Alemany, J., Turcu, A. L., Bellver-Sanchis, A., Loza, M. I., Brea, J. M., Canudas, A. M., Leiva, R., Vázquez, S., Pallàs, M., & Griñán-Ferré, C. (2020). A novel NMDA receptor antagonist protects against cognitive decline presented by senescent mice. *Pharmaceutics*, *12*, 1–17. https://doi.org/10.3390/pharmaceutics12030284

Cummings, J., Lee, G., Ritter, A., Sabbagh, M., & Zhong, K. (2020). Alzheimer's disease drug development pipeline: 2020. *Alzheimer's & Dementia: Translational Research & Clinical Interventions*, *6*, 1–29.

Curtis, M. J., Alexander, S., Cirino, G., Docherty, J. R., George, C. H., Giembycz, M. A., Hoyer, D., Insel, P. A., Izzo, A. A., Ji, Y., MacEwan, D. J., Sobey, C. G., Stanford, S. C., Teixeira, M. M., Wonnacott, S., & Ahluwalia, A. (2018). Experimental design and analysis and their reporting II: Updated and simplified guidance for authors and peer reviewers. *British Journal of Pharmacology*, *175*, 987–993. https://doi.org/10.1111/bph.14153

DeTure, M. A., & Dickson, D. W. (2019). The neuropathological diagnosis of Alzheimer's disease. *Molecular Neurodegeneration*, *14*, 32. https://doi.org/10.1186/s13024-019-0333-5

Dickson, D. W., & Rogers, J. (1992). Neuroimmunology of Alzheimer's disease: A conference report. *Neurobiology of Aging*, *13*, 793–798. https://doi.org/10.1016/0197-4580(92)90104-6

Dong, H., Yuede, C. M., Coughlan, C. A., Murphy, K. M., & Csernansky, J. G. (2009). Effects of donepezil on amyloid-β and synapse density in the Tg2576 mouse model of Alzheimer's disease. *Brain Research*, *1303*, 169–178. https://doi.org/10.1016/j.brainres.2009.09.097

Ennaceur, A., & Delacour, J. (1988). A new one-trial test for neurobiological studies of memory in rats. 1: Behavioral data. *Behavioural Brain Research*, *31*, 47–59.

Finn, D. P., Martí, O., Harbuz, M. S., Vallès, A., Belda, X., Márquez, C., Jessop, D. S., Lalies, M. D., Armario, A., Nutt, D. J., & Hudson, A. L. (2003). Behavioral, neuroendocrine and neurochemical effects of the imidazoline I_2 receptor selective ligand BU224 in naive rats and rats exposed to the stress of the forced swim test. *Psychopharmacology*, *167*, 195–202. https://doi.org/10.1007/s00213-003-1392-3

Fitzgerald, P. J., Hale, P. J., Ghimire, A., & Watson, B. O. (2020). The cholinesterase inhibitor donepezil has antidepressant-like properties in the mouse forced swim test. *Translational Psychiatry*, *10*, 255. https://doi.org/10.1038/s41398-020-00928-w

Frölich, L., Atri, A., Ballard, C., Tariot, P. N., Molinuevo, J. L., Boneva, N., Geist, M. A., Raket, L. L., & Cummings, J. L. (2019). Open-label, multicenter, phase III extension study of idalopirdine as adjunctive to donepezil for the treatment of mild-moderate Alzheimer's disease. *Journal of Alzheimer's Disease*, *67*, 303–313. https://doi.org/10.3233/JAD-180595

Garau, C., Miralles, A., & Garcia-Sevilla, J. A. (2013). Chronic treatment with selective I_2-imidazoline receptor ligands decreases the content of pro-apoptotic markers in rat brain. *Journal of Psychopharmacology*, *27*, 123–134. https://doi.org/10.1177/0269881112450785

Garcia-Sevilla, J., Escriba, P., Walzer, C., Bouras, C., & Guimon, J. (1998). Imidazoline receptor proteins in brains of patients with Alzheimer's disease. *Neuroscience Letters*, *247*, 95–98. https://doi.org/10.1016/S0304-3940(98)00265-1

Gatt, J. M., Nemeroff, C. B., Dobson-Stone, C., Paul, R. H., Bryant, R. A., Schofield, P. R., Gordon, E., Kemp, A. H., & Williams, L. M. (2009). Interactions between BDNF Val66Met polymorphism and early life stress predict brain and arousal pathways to syndromal depression and anxiety. *Molecular Psychiatry*, *14*, 681–695. https://doi.org/10.1038/mp.2008.143

Giacobini, E. (2000). Cholinesterase inhibitors stabilize Alzheimer disease. *Neurochemical Research*, *25*, 1185–1190. https://doi.org/10.1023/A:1007679709322

Griñan-Ferré, C., Palomera-Ávalos, V., Puigoriol-Illamola, D., Camins, A., Porquet, D., Plá, V., Aguado, F., & Pallàs, M. (2016). Behaviour and cognitive changes correlated with hippocampal neuroinflammaging and neuronal markers in female SAMP8, a model of accelerated senescence. *Experimental Gerontology*, *80*, 57–69. https://doi.org/10.1016/j.exger.2016.03.014

Griñán-Ferré, C., Izquierdo, V., Otero, E., Puigoriol-Illamola, D., Corpas, R., Sanfeliu, C., Ortuño-Sahagún, D., & Pallàs, M. (2018). Environmental enrichment improves cognitive deficits, AD hallmarks and epigenetic alterations presented in 5xFAD mouse model. *Frontiers in Cellular Neuroscience*, *12*, 224. https://doi.org/10.3389/fncel.2018.00224

Griñán-Ferré, C., Vasilopoulou, F., Abás, S., Rodríguez-Arévalo, S., Bagán, A., Sureda, F. X., Pérez, B., Callado, L. F., García-Sevilla, J. A., García-Fuster, M. J., Escolano, C., & Pallàs, M. (2019). Behavioral and cognitive improvement induced by novel imidazoline I_2 receptor ligands in female SAMP8 mice. *Neurotherapeutics*, *16*, 416–431. https://doi.org/10.1007/s13311-018-00681-5

Grossberg, G. T. (2003). Cholinesterase inhibitors for the treatment of Alzheimer's disease: Getting on and staying on. *Current Therapeutic Research, Clinical and Experimental*, *64*, 216–235. https://doi.org/10.1016/S0011-393X(03)00059-6

Hernández-Hernández, E., García-Sevilla, J. A., & García-Fuster, M. J. (2020). Exploring the antidepressant-like potential of the selective I_2-imidazoline receptor ligand LSL 60101 in adult male rats. *Pharmacol. Reports*, *73*, 288–295. https://doi.org/10.1007/s43440-020-00148-5

Hwang, J., Hwang, H., Lee, H.-W., & Suk, K. (2010). Microglia signaling as a target of donepezil. *Neuropharmacology*, *58*, 1122–1129. https://doi.org/10.1016/j.neuropharm.2010.02.003

Jiangbo, N., & Liyun, Z. (2018). Effect of donepezil hydrochloride & aerobic exercise training on learning and memory and its mechanism of action in an Alzheimer's disease rat model. *Pakistan Journal of Pharmaceutical Sciences*, *31*, 2897–2901.

Ju, Y., & Tam, K. Y. (2020). 9R, the cholinesterase and amyloid beta aggregation dual inhibitor, as a multifunctional agent to improve cognitive deficit and neuropathology in the triple-transgenic Alzheimer's disease mouse model. *Neuropharmacology*, *181*, 108354. https://doi.org/10.1016/j.neuropharm.2020.108354

Kim, H. G., Moon, M., Choi, J. G., Park, G., Kim, A.-J., Hur, J., Lee, K. T., & Oh, M. S. (2014). Donepezil inhibits the amyloid-beta oligomer-induced microglial activation in vitro and in vivo. *Neurotoxicology*, *40*, 23–32. https://doi.org/10.1016/j.neuro.2013.10.004

Kotagale, N., Dixit, M., Garmelwar, H., Bhondekar, S., Umekar, M., & Taksande, B. (2020). Agmatine reverses memory deficits induced by $A\beta_{1-42}$ peptide in mice: A key role of imidazoline receptors. *Pharmacology, Biochemistry, and Behavior*, *196*, 172976. https://doi.org/10.1016/j.pbb.2020.172976

Krishna, K. V., Saha, R. N., & Dubey, S. K. (2020). Biophysical, biochemical, and behavioral implications of ApoE3 conjugated donepezil nanomedicine in a $A\beta_{1-42}$ induced Alzheimer's disease rat model. *ACS Chemical Neuroscience*, *11*, 4139–4151. https://doi.org/10.1021/acschemneuro.0c00430

Landel, V., Baranger, K., Virard, I., Loriod, B., Khrestchatisky, M., Rivera, S., Benech, P., & Féron, F. (2014). Temporal gene profiling of the 5XFAD transgenic mouse model highlights the importance of microglial activation in Alzheimer's disease. *Molecular Neurodegeneration*, *9*, 33. https://doi.org/10.1186/1750-1326-9-33

Lee, C. Y. D., Daggett, A., Gu, X., Jiang, L. L., Langfelder, P., Li, X., Wang, N., Zhao, Y., Park, C. S., Cooper, Y., Ferando, I., Mody, I., Coppola, G., Xu, H., & Yang, X. W. (2018). Elevated TREM2 gene dosage reprograms microglia responsivity and ameliorates pathological phenotypes in Alzheimer's disease models. *Neuron*, *97*, 1032–1048e5. https://doi.org/10.1016/j.neuron.2018.02.002

Lilley, E., Stanford, S. C., Kendall, D. E., Alexander, S. P. H., Cirino, G., Docherty, J. R., George, C. H., Insel, P. A., Izzo, A. A., Ji, Y., Panettieri, R. A., Sobey, C. G., Stefanska, B., Stephens, G., Teixeira, M., & Ahluwalia, A. (2020). ARRIVE 2.0 and the British Journal of Pharmacology: Updated guidance for 2020. *British Journal of Pharmacology*, *177*, 3611–3616. https://doi.org/10.1111/bph.15178

Mehta, M., Adem, A., & Sabbagh, M. (2012). New acetylcholinesterase inhibitors for Alzheimer's disease. *International Journal of Alzheimer's Disease*, *2012*, 728983.

Menargues, A., Cedó, M., Artiga, O., Obach, R., & García-Sevilla, J. A. (1995). Effects of the I2-imidazoline receptor ligand LSL 60101 on various models of anorexia in rats. *Annals of the New York Academy of Sciences*, *763*, 494–494. https://doi.org/10.1111/j.1749-6632.1995.tb32439.x

Meraz Rios, M. A., Toral-Rios, D., Franco-Bocanegra, D., Villeda-Hernández, J., & Campos-Peña, V. (2013). Inflammatory process in Alzheimer's disease. *Frontiers in Integrative Neuroscience*, *7*, 59.

Mirzaei, N., Mota, B. C., Birch, A. M., Davis, N., Romero-Molina, C., Katsouri, L., Palmer, E. O. C., Golbano, A., Riggall, L. J., Nagy, I., Tyacke, R., Nutt, D. J., & Sastre, M. (2020). Imidazoline ligand BU224 reverses cognitive deficits, reduces microgliosis and enhances synaptic connectivity in a mouse model of Alzheimer's disease. *British Journal of Pharmacology*, *178*, 654–671. https://doi.org/10.1111/bph.15312

Murray, M. E., Graff-Radford, N. R., Ross, O. A., Petersen, R. C., Duara, R., & Dickson, D. W. (2011). Neuropathologically defined subtypes of Alzheimer's disease with distinct clinical characteristics: A retrospective study. *Lancet Neurology*, *10*, 785–796. https://doi.org/10.1016/S1474-4422(11)70156-9

Oakley, H., Cole, S. L., Logan, S., Maus, E., Shao, P., Craft, J., Guillozet-Bongaarts, A., Ohno, M., Disterhoft, J., van Eldik, L., Berry, R., & Vassar, R. (2006). Intraneuronal β-amyloid aggregates, neurodegeneration, and neuron loss in transgenic mice with five familial Alzheimer's disease mutations: Potential factors in amyloid plaque formation. *The Journal of Neuroscience*, *26*, 10129–10140. https://doi.org/10.1523/JNEUROSCI.1202-06.2006

Olmos, G., Alemany, R., Escriba, P. V., & García-Sevilla, J. A. (1994). The effects of chronic imidazoline drug treatment on glial fibrillary acidic protein concentrations in rat brain. *British Journal of Pharmacology*, *111*, 997–1002. https://doi.org/10.1111/j.1476-5381.1994.tb14842.x

Ongnok, B., Khuanjing, T., Chunchai, T., Kerdphoo, S., Jaiwongkam, T., Chattipakorn, N., & Chattipakorn, S. C. (2021). Donepezil provides neuroprotective effects against brain injury and Alzheimer's pathology under conditions of cardiac ischemia/reperfusion injury. *Biochimica et Biophysica Acta - Molecular Basis of Disease*, *1867*, 165975. https://doi.org/10.1016/j.bbadis.2020.165975

Percie du Sert, N., Hurst, V., Ahluwalia, A., Alam, S., Avey, M. T., Baker, M., Browne, W. J., Clark, A., Cuthill, I. C., Dirnagl, U., Emerson, M., Garner, P., Holgate, S. T., Howells, D. W., Karp, N. A., Lazic, S. E., Lidster, K., MacCallum, C. J., Macleod, M., … Würbel, H. (2020). The ARRIVE guidelines 2.0: Updated guidelines for reporting animal research. *PLoS Biology*, *18*(7), e3000410. https://doi.org/10.1371/journal.pbio.3000410

Regunathan, S., Feinstein, D. L., & Reis, D. J. (1993). Expression of non-adrenergic imidazoline sites in rat cerebral cortical astrocytes. *Journal of Neuroscience Research*, *34*, 681–688. https://doi.org/10.1002/jnr.490340611

Regunathan, S., Feinstein, D. L., & Reis, D. J. (1999). Anti-proliferative and anti-inflammatory actions of imidazoline agents: Are imidazoline receptors involved? *Annals of the New York Academy of Sciences*, *881*, 410–419. https://doi.org/10.1111/j.1749-6632.1999.tb09389.x

Riedel, G., Kang, S. H., Choi, D. Y., & Platt, B. (2009). Scopolamine-induced deficits in social memory in mice: Reversal by donepezil. *Behavioural Brain Research*, *204*, 217–225. https://doi.org/10.1016/j.bbr.2009.06.012

Rosini, M., Simoni, E., Minarini, A., & Melchiorre, C. (2014). Multi-target design strategies in the context of Alzheimer's disease: Acetylcholinesterase inhibition and NMDA receptor antagonism as the driving forces. *Neurochemical Research*, *39*, 1914–1923. https://doi.org/10.1007/s11064-014-1250-1

Ruiz, J., Martín, I., Callado, L. F., Meana, J. J., Barturen, F., & García-Sevilla, J. A. (1993). Non-adrenoceptor [^{3}H]idazoxan binding sites (I_2-imidazoline sites) are increased in postmortem brain from patients with Alzheimer's disease. *Neuroscience Letters*, *160*, 109–112. https://doi.org/10.1016/0304-3940(93)90925-B

Sánchez-Blázquez, P., Boronat, M. A., Olmos, G., García-Sevilla, J. A., & Garzón, J. (2000). Activation of I_2-imidazoline receptors enhances supraspinal morphine analgesia in mice: A model to detect agonist and antagonist activities at these receptors. *British Journal of Pharmacology*, *130*, 146–152. https://doi.org/10.1038/sj.bjp.0703294

Saul, A., Sprenger, F., Bayer, T. A., & Wirths, O. (2013). Accelerated tau pathology with synaptic and neuronal loss in a novel triple transgenic mouse model of Alzheimer's disease. *Neurobiology of Aging*, *34*, 2564–2573. https://doi.org/10.1016/j.neurobiolaging.2013.05.003

Schmitt, B., Bernhardt, T., Moeller, H.-J., Heuser, I., & Frölich, L. (2004). Combination therapy in Alzheimer's disease: A review of current evidence. *CNS Drugs*, *18*, 827–844. https://doi.org/10.2165/00023210-200418130-00001

Selkoe, D. J. (2008). Soluble oligomers of the amyloid β-protein impair synaptic plasticity and behavior. *Behavioural Brain Research*, *192*, 106–113. https://doi.org/10.1016/j.bbr.2008.02.016

Serrano-Pozo, A., Frosch, M. P., Masliah, E., & Hyman, B. T. (2011). Neuropathological alterations in Alzheimer disease. *Cold Spring Harbor Perspectives in Medicine*, *1*, a006189.

Siemian, J. N., LaMacchia, Z. M., Spreuer, V., Tian, J., Ignatowski, T. A., Paez, P. M., Zhang, Y., & Li, J. X. (2018). The imidazoline I_2 receptor agonist 2-BFI attenuates hypersensitivity and spinal neuroinflammation in a rat model of neuropathic pain. *Biochemical Pharmacology*, *153*, 260–268. https://doi.org/10.1016/j.bcp.2018.01.032

Sinforiani, E., Banchieri, L. M., Zucchella, C., Bernasconi, L., & Nappi, G. (2003). Cholinesterase inhibitors in Alzheimer's disease: Efficacy in a non-selected population. *Functional Neurology*, *18*, 233–237.

Takada-Takatori, Y., Nakagawa, S., Kimata, R., Nao, Y., Mizukawa, Y., Urushidani, T., Izumi, Y., Akaike, A., Tsuchida, K., & Kume, T. (2019). Donepezil modulates amyloid precursor protein endocytosis and reduction by up-regulation of SNX33 expression in primary cortical neurons. *Scientific Reports*, *9*, 11922. https://doi.org/10.1038/s41598-019-47462-4

Tonello, R., Villarinho, J. G., da Silva Sant'Anna, G., Tamiozzo, L., Machado, P., Trevisan, G., & Rubin, M. A. (2012). The potential antidepressant-like effect of imidazoline I_2 ligand 2-BFI in mice. *Progress in Neuro-Psychopharmacology and Biological Psychiatry*, *37*, 15–21. https://doi.org/10.1016/j.pnpbp.2011.11.005

Vasilopoulou, F., Bagan, A., Rodriguez-Arevalo, S., Escolano, C., Griñán-Ferré, C., & Pallàs, M. (2020). Amelioration of BPSD-like phenotype and cognitive decline in SAMP8 mice model accompanied by molecular changes after treatment with I_2-imidazoline receptor ligand MCR5. *Pharmaceutics*, *12*, 475. https://doi.org/10.3390/pharmaceutics12050475

Vasilopoulou, F., Griñán-Ferré, C., Rodríguez-Arévalo, S., Bagán, A., Abás, S., Escolano, C., & Pallàs, M. (2020). I_2 imidazoline receptor modulation protects aged SAMP8 mice against cognitive decline by suppressing the calcineurin pathway. *GeroScience*, 27–31.

Walf, A. A., & Frye, C. A. (2007). The use of the elevated plus maze as an assay of anxiety-related behavior in rodents. *Nature Protocols*, *2*, 322–328. https://doi.org/10.1038/nprot.2007.44

Walsh, D. M., & Selkoe, D. J. (2004). Oligomers on the brain: The emerging role of soluble protein aggregates in neurodegeneration. *Protein and Peptide Letters*, *11*, 213–228. https://doi.org/10.2174/0929866043407174

Yang, H., Mu, W., Wei, D., Zhang, Y., Duan, Y., Gao, J. X., Gong, X.-Q., Wang, H.-J., Wu, X.-l., Tao, H., & Chang, J. (2020). A novel targeted and high-efficiency nanosystem for combinational therapy for Alzheimer's disease. *Advancement of Science*, *7*, 1–13.

Yoshiyama, Y., Kojima, A., Ishikawa, C., & Arai, K. (2010). Anti-inflammatory action of donepezil ameliorates tau pathology, synaptic loss, and neurodegeneration in a tauopathy mouse model. *Journal of Alzheimer's Disease*, *22*, 295–306. https://doi.org/10.3233/JAD-2010-100681

Zhang, F., Gannon, M., Chen, Y., Yan, S., Zhang, S., Feng, W., Tao, J., Sha, B., Liu, Z., Saito, T., Saido, T., Keene, C. D., Jiao, K., Roberson, E. D., Xu, H., & Wang, Q. (2020). β-Amyloid redirects norepinephrine signaling to activate the pathogenic GSK3β/tau cascade. *Science Translational Medicine*, *12*, eaay6931. https://doi.org/10.1126/scitranslmed.aay6931

Zhang, F., & Jiang, L. (2015). Neuroinflammation in Alzheimer's disease. *Neuropsychiatric Disease and Treatment*, *11*, 243–256. https://doi.org/10.2147/NDT.S75546

Zhao, Y., Wu, X., Li, X., Jiang, L.-L., Gui, X., Liu, Y., Sun, Y., Zhu, B., Piña-Crespo, J. C., Zhang, M., Zhang, N., Chen, X., Bu, G., An, Z., Huang, T. Y., & Xu, H. (2018). TREM2 is a receptor for β-amyloid that mediates microglial function. *Neuron*, *97*, 1023–1031.e7. https://doi.org/10.1016/j.neuron.2018.01.031

SUPPORTING INFORMATION

Additional supporting information may be found online in the Supporting Information section at the end of this article.

How to cite this article: Vasilopoulou, F., Rodríguez-Arévalo, S., Bagán, A., Escolano, C., Griñán-Ferré, C., & Pallàs, M. (2021). Disease-modifying treatment with I_2 imidazoline receptor ligand LSL60101 in an Alzheimer's disease mouse model: a comparative study with donepezil. *British Journal of Pharmacology*, 1–17. https://doi.org/10.1111/bph.15478

GeroScience (2021) 43:965–983
https://doi.org/10.1007/s11357-020-00281-2

ORIGINAL ARTICLE

I_2 imidazoline receptor modulation protects aged SAMP8 mice against cognitive decline by suppressing the calcineurin pathway

Foteini Vasilopoulou · Christian Griñán-Ferré · Sergio Rodríguez-Arévalo · Andrea Bagán · Sònia Abás · Carmen Escolano · Mercè Pallàs

Received: 16 December 2019 / Accepted: 28 September 2020 / Published online: 31 October 2020

Abstract Brain aging and dementia are current problems that must be solved. The levels of imidazoline 2 receptors (I_2-IRs) are increased in the brain in Alzheimer's disease (AD) and other neurodegenerative diseases. We tested the action of the specific and selective I_2-IR ligand B06 in a mouse model of accelerated aging and AD, the senescence-accelerated mouse prone 8 (SAMP8) model. Oral administration of B06 for 4 weeks improved SAMP8 mouse behavior and cognition and reduced AD hallmarks, oxidative stress, and apoptotic and neuroinflammation markers. Likewise, B06 regulated glial excitatory amino acid transporter 2 and *N*-methyl-D aspartate 2A and 2B receptor subunit protein levels. Calcineurin (CaN) is a phosphatase that controls the phosphorylation levels of cAMP response element-binding (CREB), apoptotic mediator BCL-2-associated agonist of cell death (BAD) and GSK3β, among other molecules. Interestingly, B06 was able to reduce the levels of the CaN active form (CaN A). Likewise, CREB phosphorylation, BAD gene expression, and other factors were modified after B06 treatment. Moreover, phosphorylation of a target of CaN, nuclear factor of activated T-cells, cytoplasmic 1 ($NFAT_{C1}$), was increased in B06-treated mice, impeding the transcription of genes related to neuroinflammation and neural plasticity. In summary, this I_2 imidazoline ligand can exert its beneficial effects on age-related conditions by modulating CaN pathway action and affecting several molecular pathways, playing a neuroprotective role in SAMP8 mice.

Keywords I_2 imidazoline receptors · Aging · Behavior · Neuroinflammation · NFAT · Neuroprotection · Alzheimer's disease

Abbreviations

AD	Alzheimer's disease
Aldh2	Aldehyde dehydrogenase 2
APP	Amyloid precursor protein
BAD	BCL-2-Associated agonist of cell death
Bdnf	Brain-derived neurotrophic factor
CaMKII	Calcium calmodulin kinase II
CaN	Calcineurin
CDK5	Cyclin-dependent kinase
cDNA	Complementary DNA
CREB	cAMP response element-binding
Ct	Cycle threshold

Electronic supplementary material The online version of this article (https://doi.org/10.1007/s11357-020-00281-2) contains supplementary material, which is available to authorized users.

F. Vasilopoulou · C. Griñán-Ferré · M. Pallàs (✉)
Pharmacology Section, Department of Pharmacology, Toxicology and Medicinal Chemistry, Faculty of Pharmacy and Food Sciences, and Institute of Neurociencies, University of Barcelona, Av. Joan XXIII, 27-31, E-08028 Barcelona, Spain
e-mail: pallas@ub.edu

S. Rodríguez-Arévalo · A. Bagán · S. Abás · C. Escolano
Laboratory of Medicinal Chemistry (Associated Unit to CSIC), Department of Pharmacology, Toxicology and Medicinal Chemistry, Faculty of Pharmacy and Food Sciences, and Institute of Biomedicine (IBUB), University of Barcelona, Av. Joan XXIII, 27-31, E-08028 Barcelona, Spain

Cxcl-10	C-X-C motif chemokine ligand 10
(EAAT)2	Excitatory amino acid transporter 2
ERK	Extracellular signal-regulated kinase
GAPDH	Glyceraldehyde-3-phosphate dehydrogenase
GFAP	Glial fibrillary acid protein
GSK3β	Glycogen synthase kinase 3β
H_2O_2	Hydrogen peroxide
Hmox 1	Hemoxygenase 1
I_2-IR	Imidazoline 2 receptors
Ide	Insulin-degrading enzyme
Ifn-γ	Interferon gamma
iNOS	Inducible nitric oxide synthase
LTD	Long-term depression
LTP	Long-term potentiation
MAO	Monoamine oxidase
mRNA	Messenger RNA
Nep	Neprilysin
NFATc1	Nuclear factor of activated T-cells, cytoplasmic 1
NMDA	*N*-Methyl-*d*-aspartate
NMDAR	*N*-Methyl-D-aspartate receptor
NORT	Novel object recognition test
Nrf1	Nuclear factor-erythroid 2-related factor 1
OFT	Open field test
OS	Oxidative stress
p-Tau	Hyperphosphorylated tau
PD	Parkinson's disease
PKA	Protein kinase A
PP2B	Phosphatase 2B
PVDF	Polyvinylidene difluoride
ROS	Reactive oxygen species
qPCR	Real-time quantitative PCR
RT-PCR	Reverse transcription-polymerase chain reaction
SAMP8	Senescence-accelerated mouse prone 8
sAPPα	Soluble APP α
sAPPβ	Soluble APP β
SDS-PAGE	Sodium dodecyl sulphate-polyacrylamide gel electrophoresis
SEM	Standard error of the mean
TBS-T	Tween 20 TBS
TBS	Tris-buffered saline
TN	Novel object, new location
Tnf-α	Tumor necrosis factor alpha
TO	Old object, old location
TrkB	Tropomyosin-related kinase B
WB	Western blotting
ΔΔCt	Cycle threshold method

Introduction

Aging has become a problem worldwide, since older people are more prone to developing chronic and degenerative diseases. At the brain level, aging affects several molecular pathways that predispose patients to neurodegeneration, causing dementia, cognitive impairment and degraded quality of life. Among dementias, the most prevalent is Alzheimer's disease (AD) [23]. AD has aroused considerable interest because of its strong influence on quality of life among elderly individuals and because of the limited drugs available to combat cognitive loss and neuropsychiatric symptoms.

β-Amyloid deposition in senile plaques and tau hyperphosphorylation forming neurofibrillary tangles are specific hallmarks of AD [50]. However, there are no successful pharmacological treatments that modify the progression of AD, given that acetylcholinesterase inhibitors and memantine fail to stop the progression of dementia [16, 17]. Apart from the use of approved drugs, several clinical attempts have been made to treat AD progression using various other strategies, such as immunotherapy against β-amyloid and beta-secretase (BACE) inhibitor administration, but the results have been disappointing [15]. These results show that addressing only the "β-amyloid cascade hypothesis" cannot fully control the progression of the disease, and this hypothesis also cannot explain the advanced neuronal damage in AD. Therefore, identifying new pharmacological targets for AD treatment is an active area of research.

In most neurodegenerative processes, including AD, neuroinflammation and oxidative stress (OS) are common traits. It is well-accepted that Ca^{2+} dysfunction is a consequence of homeostatic imbalance in nerve cells that unleashes a string of molecular and cellular processes, including neuroinflammation, OS, changes in neuronal plasticity, differential expression of glutamate and cholinergic receptors, and amyloid pathology [52]. Together, these processes end with cognitive decline and neurodegeneration. Calcineurin (CaN), also known as protein phosphatase 2B, is a Ca^{2+}-dependent Ser/Thr phosphatase that is highly abundant in the brain, appearing at high levels in neurons and low levels in glia in healthy adult animals [31]. CaN is related to long-term potentiation (LTP) and long-term depression (LTD), and dysregulation of CaN has been linked with cognitive loss in an AD mouse model [6, 45]. Of importance, CaN levels and signaling are increased in the

cortex in AD patients [63] and in the contexts of other human neurodegenerative pathologies, including Parkinson's disease (PD) [12], Lewy body aggregation [35] and vascular pathology [44]. Moreover, CaN activity prevents fear memory formation in the amygdala by dephosphorylation and inhibition of downstream kinases, including AKT and extracellular signal-regulated kinase (ERK) [33]. *N*-methyl-D-aspartate receptor (NMDAR) [39, 60] and glycogen synthase kinase 3β (GSK3β) [61] are some of the key actors in central nervous system function that are controlled by the phosphatase activity of CaN, which in turn is controlled by calcium calmodulin kinase II (CaMKII) and intracellular Ca^{2+} levels [7]. Nuclear factor of activated T-cells (NFAT) consists of at least two different components, one with nuclear localization and one that is phosphorylated and localized in the cytoplasm [27]. Furthermore, recently, the CaN pathway has been observed to link astrocytic Ca^{2+} dysregulation to neuroinflammation, glutamate, β-amyloid accumulation and synaptotoxicity [52].

Imidazoline 2 receptors (I_2-IRs) [8] are increased in AD brains [22, 47], and radioactive ligands have been studied as biomarkers for AD and PD progression in patients [58, 62]. There is evidence that I_2-IR ligands reduce neurodegenerative processes, including cognitive decline, neuroinflammation, OS and AD hallmarks, but less is known about the upstream mechanism involved in the beneficial effects of I_2-IR modulation. Thus, the objective of this work was to delineate the molecular mechanisms involved in the neuroprotective effect of I_2-IR modulation in a mouse model of AD linked to the aging process, the senescence-accelerated mouse prone 8 (SAMP8) model. To this end, we used a newly synthesized I_2-IR ligand, diethyl (1*R*S,3a*S*R,6a*S*R)-5-(3-chloro-4-fluorophenyl)-4,6-dioxo-1-phenyl-1,3a,4,5,6,6a-hexahydropyrrolo[3,4-c]pyrrole-1-phosphonate, named B06, which has outstanding affinity and selectivity for I_2-IRs over α_2 adrenoreceptors [3, 18].

The SAMP8 strain is a non-transgenic mouse strain established through phenotypic selection of the AKR/J mouse strain, and is an attractive model with which to study aging processes, especially age-related deterioration of learning and memory, emotional disorders and neurochemical alterations [43, 57]. At approximately 5 months of age, the mice begin to undergo an accelerated process of senescence, and the brain aging manifests as severe cognitive decline and neuroinflammation [4]. It is considered a late-onset AD mouse model characterized by altered amyloid precursor protein (APP) processing and high levels of tau hyperphosphorylation [11, 37]. Moreover, inflammatory and OS markers are present at early ages and during adulthood [24, 25].

Methods

In vivo studies in mice

Twelve-month-old female SAMP8 mice ($n = 23$) (Envigo, Sant Feliu de Codines, Barcelona, Spain) were used to carry out cognitive and molecular analyses. The animals were randomly allocated to two experimental groups: the SAMP8 control group (control) ($n = 12$), which was administered vehicle (2-hydroxypropyl)-β-cyclodextrin 1.8% in drinking water, and the SAMP8 group, which was treated with the I_2-IR ligand B06 (5 mg/kg) ($n = 11$). The animals had free access to food and water and were kept under standard temperature conditions (22 ± 2 °C) and 12 h/12 h light/dark cycles (300 lx/0 lx). B06 (5 mg/kg/day) was diluted in 1.8% (2-hydroxypropyl)-β-cyclodextrin and administered through drinking water. After 4 weeks of treatment, behavioral and cognitive tests, including short- and long-term memory, were performed to study the effects of treatment on learning and memory. Weight and water consumption were controlled each week, and the B06 concentration was adjusted accordingly to reach the optimal dose until euthanasia.

The studies and procedures for the mouse behavior tests, brain dissection and extractions followed the ARRIVE and standard ethical guidelines (European Communities Council Directive 2010/63/EU and Guidelines for the Care and Use of Mammals in Neuroscience and Behavioral Research, National Research Council 2003) and were approved by the bioethical committees of the University of Barcelona and the Government of Catalonia. All efforts were made to minimize the number of animals used and their suffering.

Novel object recognition test (NORT)

Briefly, mice were placed in a 90° two-arm 25-cm-long, 20-cm-high, 5-cm-wide black maze. Before performing the test, the mice were individually habituated to the apparatus for 10-min periods for 3 days. On day 4, the animals were allowed to freely

explore in a 10 min acquisition trial (first trial), for which they were placed in the maze in the presence of two identical objects at the end of each arm (Fig. 1a). After a delay (2 h for short-term memory evaluation and 24 h for long-term evaluation), the animal was allowed to explore the old object and one novel object in each trial (Fig. 1a). The time that the mice spent exploring the novel object (TN) and the time that the mice spent exploring the old object (TO) were measured. A discrimination index (DI) was defined as (TN − TO)/(TN + TO). Exploration of an object was defined as pointing the nose toward the object at a distance ≤2 cm and/or touching it with the nose [5]. Turning or sitting around the object was not considered exploration. To avoid object preference biases, the objects were counterbalanced.

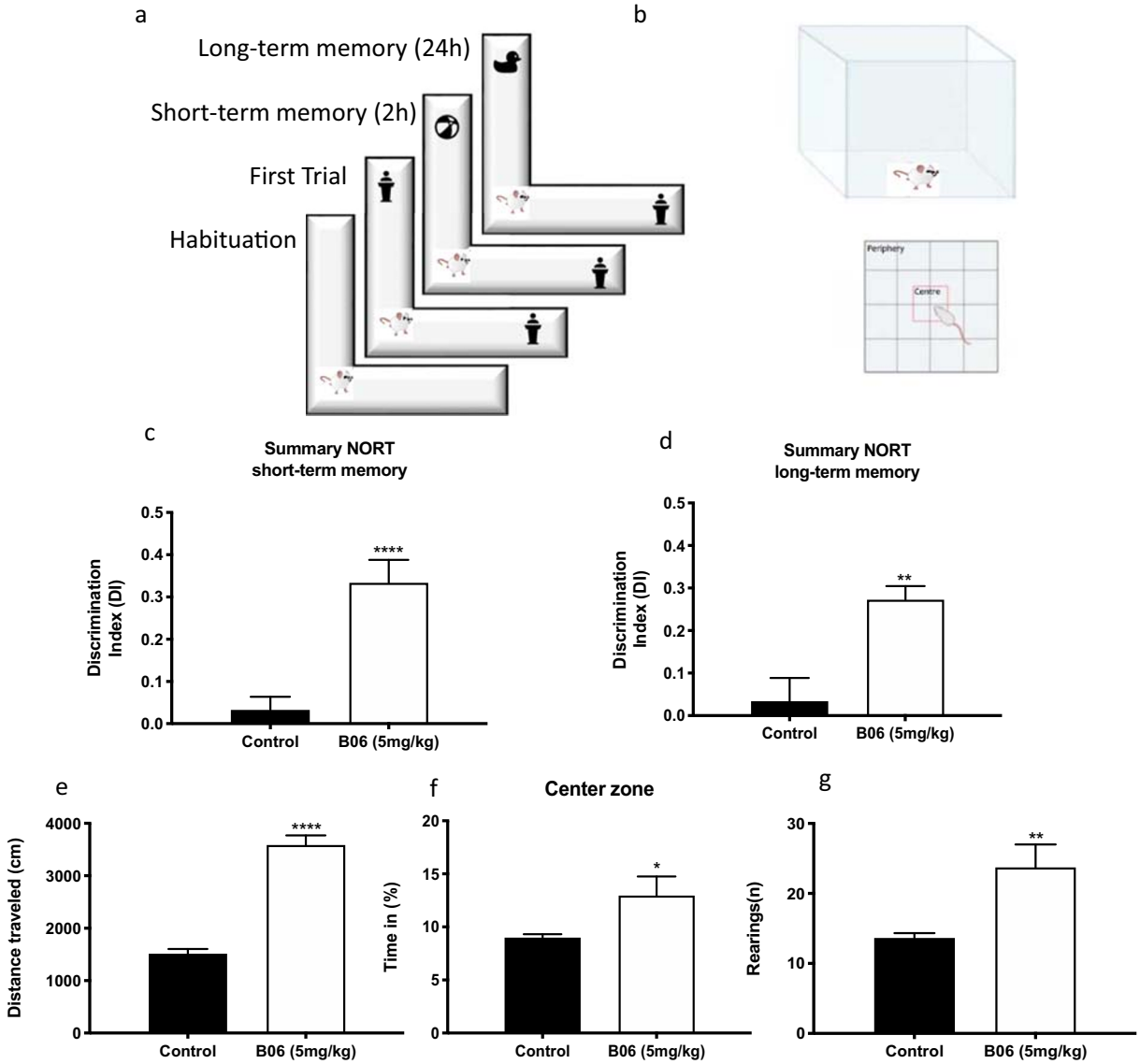

Fig. 1 Scheme for NORT (**a**) and OFT (**b**) experimental paradigms. The I_2-IR ligand improved the novel object recognition abilities [measured as discrimination index, (DI)] in SAMP8 treated with B06 at 5 mg/Kg/day (B06 5 mg/kg) in comparison with the SAMP8 control in both summary short-term memory (**c**) and summary long-term memory (**d**). In the open field test (OFT), 12-month-old SAMP8 treated with B06 at 5 mg/Kg/day (B06 5 mg/kg) presented a significant increase in the distance traveled (**e**), the percentage of time spent in the center zone (**f**) and the number of rearings (**g**). Values represented are mean ± standard error of the mean (SEM); $n = 15$ (control $n = 8$, B06 $n = 7$); $^{*}p < 0.05$; $^{**}p < 0.01$; $^{***}p < 0.001$; $^{****}p < 0.0001$ vs. control

Open field test (OFT)

The open field test (OFT) was performed as previously described [24] (Fig. 1b). Briefly, mice were placed at the center of and allowed to explore a white plywood box (50 × 50 × 25 cm) for 5 min. Behavior was scored with SMART® [Spatial Monitoring and Reporting Tool] version 3.0 software, and each trial was recorded for later analysis. The parameters scored included the center stay duration, number of rearings, number of defecations and distance traveled.

Determination of oxidative stress

Hydrogen peroxide (H_2O_2) was measured as an indicator of OS, and it was quantified using a hydrogen peroxide assay kit (Cat. No. MAK165, Sigma-Aldrich, St. Louis, MO, USA) according to the manufacturer's instructions.

Immunodetection experiments

Brain processing

Three days after the behavioral and cognitive tests, mice were euthanized for protein extraction and RNA and DNA isolation. After euthanasia, the brains were immediately removed from the skulls, and the hippocampi were dissected, frozen and maintained at −80 °C.

For an IHC experiment, mice were anesthetized (ketamine 100 mg/kg and xylazine 10 mg/kg, intraperitoneally) and then perfused intracardially with 4% paraformaldehyde (PFA) diluted in 0.1 M phosphate buffer solution. Their brains were removed and postfixed in 4% PFA overnight at 4 °C. Afterwards, the solutions were changed to PFA + 15% sucrose. Finally, the brains were frozen on powdered dry ice and stored at −80 °C until sectioning.

Protein level determination by western blotting

For subcellular fractionation, 150 μL of buffer A (10 mM HEPES pH 7.9, 10 mM KCl, 0.1 mM EDTA pH 8, 0.1 mM EGTA pH 8, 1 mM DTT, 1 mM PMSF, protease inhibitors) was added to each sample, and the mixtures were incubated on ice for 15 min. Next, the samples were homogenized with a tissue homogenizer, 12.5 μL Igepal 1% was added, and the Eppendorf tubes were vortexed for 15 s. Following 30 s of full-speed centrifugation at 4 °C, the supernatants (cytoplasmic fractions) were collected, 80 μL of buffer C (20 mM HEPES pH 7.9, 0,4 M NaCl, 1 mM EDTA pH 8, 0.1 mM EGTA pH 8, 20% glycerol 1 mM DTT, 1 mM PMSF, protease inhibitors) was added to each pellet, and the pellets were incubated under agitation at 4 °C for 15 min. Subsequently, the samples were centrifuged for 10 min at full speed at 4 °C. The supernatants (nuclear fractions) were collected.

For western blotting (WB), aliquots of 20 μg of hippocampal protein were used. Protein samples from mice were separated by sodium dodecyl sulfate-polyacrylamide gel electrophoresis (SDS-PAGE) (8–12%) and transferred onto polyvinylidene difluoride (PVDF) membranes (Millipore). Afterwards, the membranes were blocked in 5% nonfat milk in 0.1% Tris-buffered saline with Tween 20 (TBS-T) for 1 h at room temperature before being incubated overnight at 4 °C with the primary antibodies listed in Supplementary Table 1.

The membranes were washed and incubated with secondary antibodies for 1 h at room temperature. Immunoreactive proteins were viewed with a chemiluminescence-based detection kit following the manufacturer's protocol (ECL Kit; Millipore, Burlington, MA, USA), and digital images were acquired using a ChemiDoc XRS+ System (Bio-Rad, Hercules, CA, USA). Semiquantitative analyses were carried out using Image Lab software (Bio-Rad), and the results are expressed in arbitrary units (AU), with the control protein levels set as 100%. Protein loading was routinely monitored by immunodetection of glyceraldehyde-3-phosphate dehydrogenase (GAPDH) or β-actin.

Immunofluorescence

Brain coronal sections of 30 μm were obtained (Leica Microsystems CM 3050S cryostat, Wetzlar, Germany) and kept in a cryoprotectant solution at −20 °C until use. Free-floating slices were placed in a 24-well plate and washed with 0.1M PBS. Next, the free-floating sections were blocked with a solution containing 1% (BSA), 0,3% Triton X-100, 0.1M PBS for 20 min at room temperature; washed with PBS 0.1M two times for 5 min each; and incubated with the primary antibodies listed in Supplementary Table 2 overnight at 4 °C. On the following day, the coronal slices were washed with 0.1M PBS 0.1M 2 times for 5 min each and then incubated with the secondary antibodies listed in

Supplementary Table 2 at room temperature for 1 h. Later, the sections were washed two times for 5 min each with 0.1M PBS and were incubated with 5μM Hoechst staining solution (Sigma-Aldrich, St. Louis, MO) for 5 min in the dark at room temperature. Finally, the slices were mounted using Fluoromount-G (EMS, Hatfield, Pennsylvania, USA), and image acquisition was performed with a fluorescence laser microscope (Olympus BX41, Hamburg, Germany) by using x4 and x20 magnification. At least four images from 4 different individuals in each group were analyzed with ImageJ/Fiji software available online from the National Institutes of Health.

RNA extraction and gene expression determination

Total RNA isolation was carried out using TRIzol® reagent according to the manufacturer's instructions. The yield, purity and quality of RNA were determined spectrophotometrically with a NanoDrop™ ND-1000 apparatus (Thermo Scientific, Waltham, MA, USA) and an Agilent 2100B Bioanalyzer (Agilent Technologies, Santa Clara, CA, USA). RNA samples with 260/280 ratios and RNA integrity numbers (RINs) higher than 1.9 and 7.5, respectively, were selected. Reverse transcription-polymerase chain reaction (RT-PCR) was performed. Briefly, 2 μg of messenger RNA (mRNA) was reverse-transcribed using a high-capacity cDNA reverse transcription kit (Applied Biosystems, Foster City, CA, USA).

SYBR® Green real-time PCR was performed on a StepOnePlus Detection System (Applied Biosystems) with SYBR® Green PCR master mix (Applied Biosystems). Each reaction mixture contained 6.75 μL of complementary DNA (cDNA) (with a concentration of 2 μg), 0.75 μL of each primer (with a concentration of 100 nM) and 6.75 μL of SYBR® Green PCR master mix (2×).

TaqMan-based real-time PCR (Applied Biosystems) was also performed in a StepOnePlus Detection System (Applied Biosystems). Each 20 μL TaqMan reaction contained 9 μL of cDNA (25 ng), 1 μL of 20× TaqMan gene expression assay probe and 10 μL of 2× TaqMan universal PCR master mix.

The data were analyzed utilizing the comparative cycle threshold (Ct) (ΔΔCt) method, in which the levels of a housekeeping gene are used to normalize differences in sample loading and preparation. Normalization of expression levels was performed with *β-actin* for SYBR® Green-based real-time PCR and *Gapdh* for TaqMan-based real-time PCR. The primer sequences and TaqMan probes used in this study are presented in Supplementary Table 3. Each sample was analyzed in duplicate, and the results represent the n-fold differences in the transcript levels among different groups.

Statistical analysis

Statistical analysis was conducted using GraphPad Prism version 8 statistical software. The data are expressed as the mean ± standard error of the mean (SEM). Means were compared with two-tailed Student's *t* test. Statistical significance was considered when p values were <0.05. Statistical outliers were determined with Grubbs' test and when necessary were removed from the analyses.

Results

Prevention of memory loss and behavioral impairment in SAMP8 mice after I_2-IR ligand treatment

The NORT demonstrated significant differences between the control and I_2-IR ligand B06 groups in both short- and long-term evaluations. Significantly higher DI values were obtained for the B06-treated mice than for the control mice at 2 h and 24 h after novel object exposure, indicating a neuroprotective action of B06 against the characteristic SAMP8 mouse memory loss (Fig. 1c–d).

In addition, the results regarding locomotor activity, time spent in the center area and number of rearings, as assessed with the OFT paradigm, revealed significant changes in behavior in the B06 group in comparison with the control group (Fig. 1e–g).

AD hallmark modifications in the hippocampi of SAMP8 mice induced by I_2-IR ligand treatment

The levels of key proteins involved in APP processing were evaluated. The I_2-IR ligand B06 promoted significant increases in soluble APPα (sAPPα) levels but clearly tended to decrease soluble APPβ (sAPPβ) levels

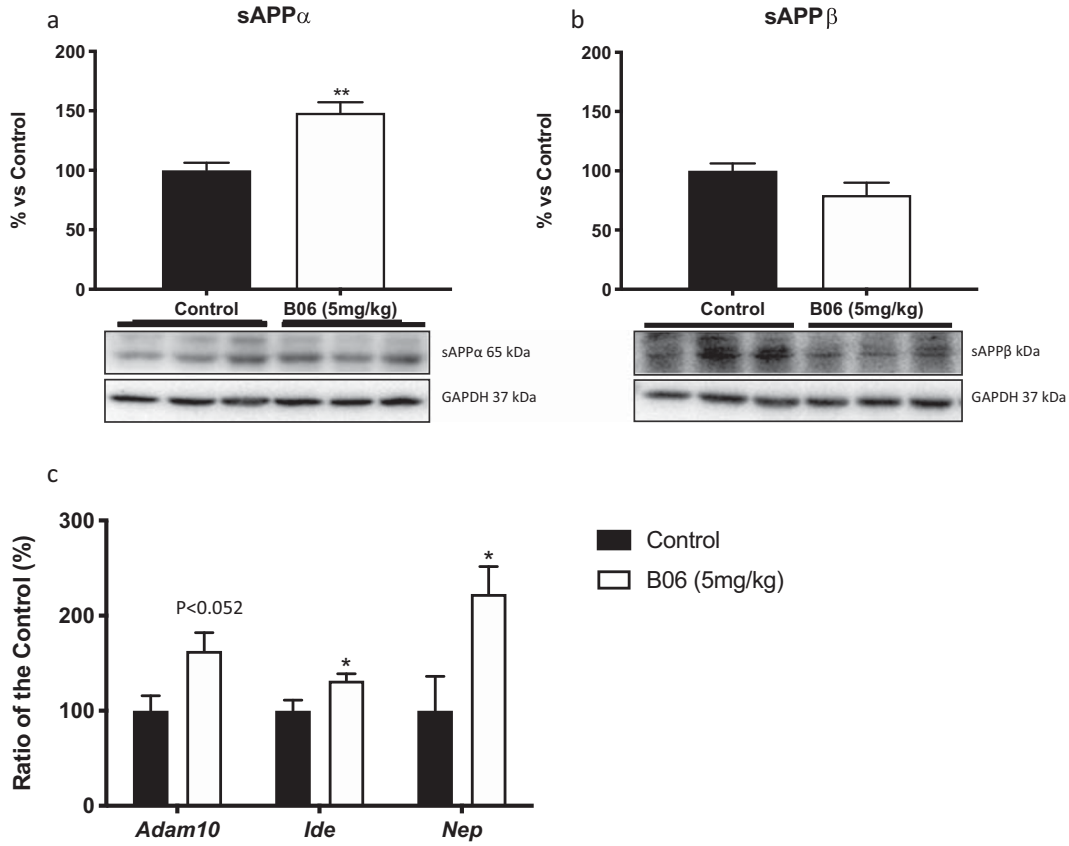

Fig. 2 Treatment with the I_2-IR ligand B06 resulted in significant differences in the amyloid processing and Aβ degradation pathway between the 12-month-old control SAMP8 (Control) and the SAMP8 treated with B06 at 5 mg/Kg/day (B06 5 mg/kg). Representative western blot for sAPPα and sAPPβ protein levels and quantification (**a**, **b**). Values in bar graphs were adjusted to 100% for the protein of control SAMP8 (Control). Representative gene expression for *Adam10*, *Ide* and *Nep* (**c**). Gene expression levels were determined by real-time PCR. Values are the mean ± standard error of the mean (SEM); ($n = 3$–5 animals per group); $^{*}p < 0.05$; $^{**}p < 0.01$ vs. Control

(Fig. 2a–b). Accordingly, the gene expression of *Adam10*, a constitutive α-secretase, increased, indicating a shift to the non-amyloidogenic pathway (Fig. 2c). Moreover, the gene expression of both insulin-degrading enzyme (*Ide*) and neprilysin (*Nep*) was increased after B06 treatment (Fig. 2c).

Tau hyperphosphorylation is a characteristic post-translational modification in aged SAMP8 mice. B06 treatment induced significant decreases in phosphorylation at the Ser404 and Ser396 sites in tau protein (Fig. 3a–b). There are two main kinases implicated in tau hyperphosphorylation: glycogen synthase kinase 3β (GSK3β) and cyclin-dependent kinase 5 (CDK5). GSK3β phosphorylated at Ser9 is the inactive form of the enzyme and is correlated with reduced tau phosphorylation. As expected, the I_2-IR ligand B06 increased p-GSK3β (Ser9) levels, indicating that it reduced kinase activity (Fig. 3c). CDK5 is also activated by phosphorylation, and p25, a coactivator, controls its activity. The results showed that the I_2-IR ligand-treated group presented decreases in the p-CDK5 level and p25/p35 ratio (Fig. 3d–e).

I_2-IR ligand treatment changes synaptic and apoptotic markers in SAMP8 mice

The I_2-IR ligand B06 reduced the protein levels of the NMDA2B receptor, increased those of the form

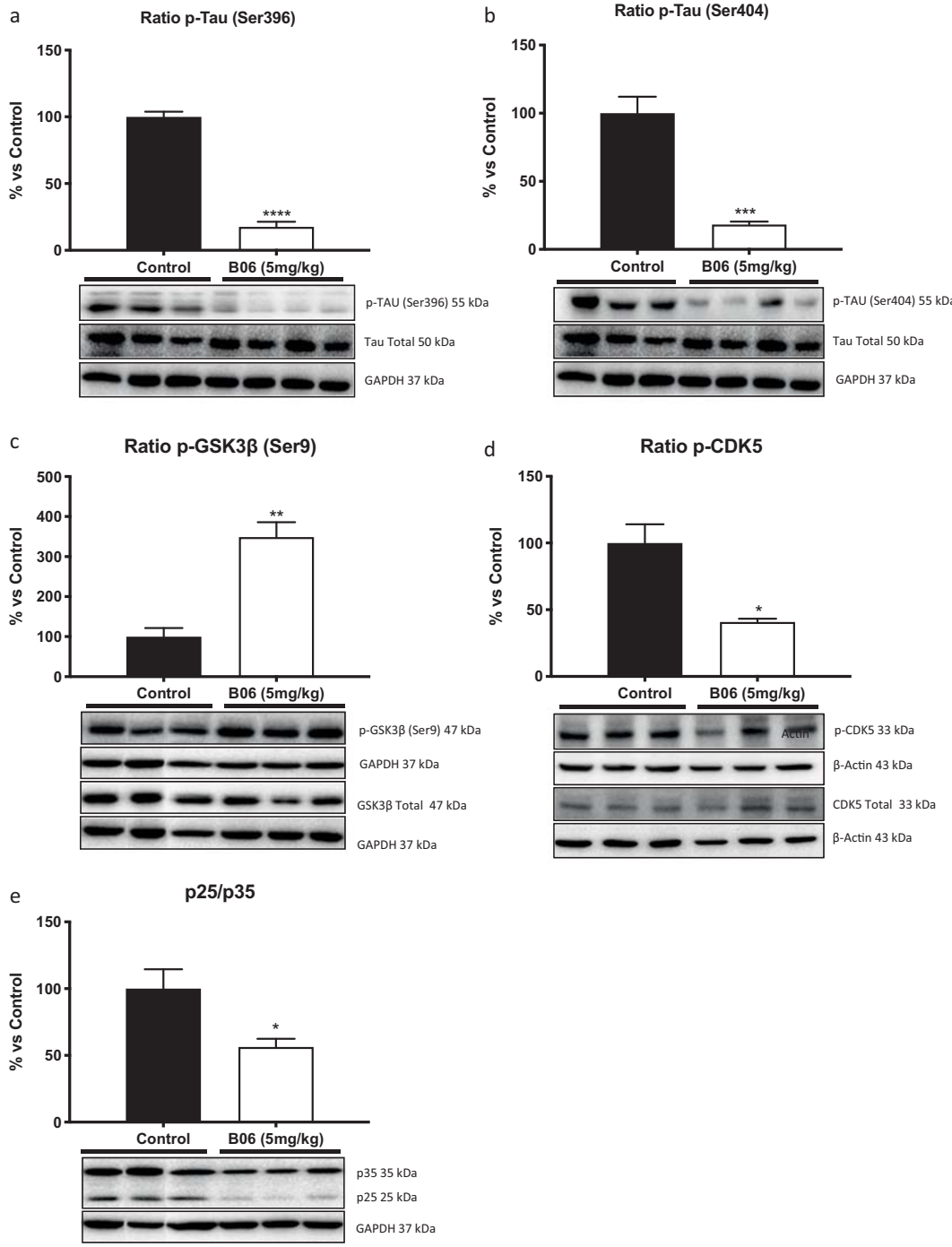

Fig. 3 The I_2-IR treatment mediated a significant decrease in tau phosphorylation and the implicated kinases in 12-month-old SAMP8 treated with B06 at 5 mg/Kg/day (B06 5 mg/kg) when compared to control SAMP8 (Control). Representative western blot for ratio p-Tau (Ser396 and Ser404), ratio p-GSK3β (Ser9), ratio p-CDK5, p25/35 and quantification (**a**–**e**). Values in bar graphs were adjusted to 100% for protein of control SAMP8 (Control). Values are the mean ± Standard error of the mean (SEM); ($n = 3$–5 animals per group); *$p < 0.05$; **$p < 0.01$; ***$p < 0.001$; ****$p < 0.0001$ vs. Control

phosphorylated at Tyr1472 and increased those of the NMDA2A receptor significantly (Fig. 4a–c).

The levels of calcium/calmodulin-dependent protein kinase II (CaMKII), a marker of synaptic plasticity, did not show significant changes, but the levels of the phosphorylated form of cAMP response element-binding protein (CREB) were dramatically increased (Fig. 4d) in the B06 group. Accordingly, the gene expression of the CREB target brain-derived neurotrophic factor (*Bdnf*) was increased in the B06 group (Fig. 4g).

Protein kinase A (PKA) is a master regulator of the activity of CREB, among other transcription factors. B06-treated animals showed increased protein levels of PKA α (the catalytic fragment) (Fig. 4e). We found significant recovery of AKT, also known as protein kinase B, phosphorylation and subsequent activation (Fig. 4f) in the B06 group, indicating a pathway of neuroprotective regulation after B06 treatment.

B-cell lymphoma 2 (BCL-2), Bax, BCL-2-associated agonist of cell death (BAD) and caspase 3 are key factors in apoptotic signaling in neurons. B06 was able to reduce caspase 3 and Bcl-2-like protein 4 (Bax) protein levels; surprisingly, it also reduced BCL-2 protein levels (Fig. 5a–c). An increase in p-BAD was also observed (Fig. 5d); however, in this case, phosphorylation of BAD indicated a lack of capacity to form apoptotic pores by dimerization of BAD, which subsequently weakened the proapoptotic role of this factor. Overall, prevention of apoptotic mechanisms followed treatment with the I_2-IR ligand B06.

Neuroinflammation and oxidative state changes in SAMP8 mice after I_2-IR ligand treatment

A highly significant decrease in GFAP protein levels was observed in the B06 group (Fig. 6a), indicating that astrogliosis and neuroinflammation processes were ameliorated in I_2-IR ligand B06-treated mice. Astrocytes control glutamatergic signaling through glutamate transporters, and B06 was able to enhance the protein levels of excitatory amino acid transporter (EAAT) 2 (Fig. 6b). The expression of proinflammatory cytokines including interleukin 6 (*Il-6*), *Il-18*, *Il-1β*, interferon gamma (*Ifn-γ*), tumor necrosis factor-alpha (*Tnf-α*) and C-X-C motif chemokine ligand 10 (*Cxcl-10*) was decreased after treatment with the I_2-IR ligand B06 (Fig. 6c), and the decrease reached significance for *Il-6*, *Il-18* and *Il-1β*. H_2O_2 levels in the hippocampus were significantly diminished in the B06 mouse group, showing that global redox homeostasis was shifted due to the antioxidant role of the I_2-IR ligand in SAMP8 mice (Fig. 6d). The expression of nuclear factor-erythroid 2-related factor 1 (*Nrf1*), a key gene controlling the oxidative cell environment, was higher in the group treated with the I_2-IR ligand B06 than in the untreated mouse group (Fig. 6e). In addition, the gene expression of antioxidant machinery enzymes such as hemoxygenase 1 (*Hmox 1*) was increased, whereas that of aldehyde dehydrogenase 2 (*Aldh2*) was reduced, indicating that B06 prevented the SAMP8 brain from experiencing an oxidant environment by neutralizing radical oxygen species (ROS) (Fig. 6e). Conversely, a significant increase in the gene expression of inducible nitric oxide synthase (*iNOS*) was found, although this increase could have improved synaptic function (Fig. 6e). Finally, immunostaining quantification of GFAP fluorescence intensity demonstrated that B06 treatment significantly reduced GFAP staining, especially in the dentate gyrus (DG) and CA1 regions (Fig. 6f–m), suggesting a reduction in astrogliosis. Moreover, immunostaining quantification of S100A9 fluorescence intensity showed that B06 treatment reduced S100A9 staining, especially in the CA1 and CA3 regions, but the reductions were not significant (Fig. 6f–m).

I_2-IR ligand treatment modifies CaN/NFAT signaling in the SAMP8 mouse hippocampus

In light of the obtained results, we focused on CaN, an upstream protein with phosphatase activity toward CREB or BAD that plays a role in neurodegeneration. The protein levels of CaN A, the active form, were reduced after treatment with the I_2-IR ligand B06 (Fig. 7a). We also evaluated $NFAT_{C1}$, a different target of CaN. The results showed an increase in the phosphorylated form (Fig. 7b).

As a summary of the results, Fig. 8 shows the molecular alterations related to cognitive improvement as well as the key role of CaN in controlling the cellular response after treatment with the I_2-IR ligand B06.

Discussion

Here, we report that treatment with the I_2-IR ligand B06 in a SAMP8 mouse model, a model of neurodegeneration linked to aging that is considered to assimilate late-onset AD, has beneficial effects via modulation of the CaN pathway. Imidazoline receptors were described in the 1990s, and I_2-IRs are related to neurodegenerative diseases such as AD [22], Huntington's disease [46] and PD [46, 58, 62]. However, the signal transduction pathway for I_2-IR remains elusive [8]. Previous reports have indicated putative roles related to monoamine oxidase (MAO) A or B [36] and intracellular calcium concentration control through NMDA receptors or intracellular calcium stores [28, 67]. We recently demonstrated that ligands for I_2-IRs are able to prevent neurodegeneration by acting on the apoptotic mechanism [2] and decreasing the activity of kinases (CDK5, GSK3β, etc.) [1, 26], leading to the recovery of cognitive capabilities in an AD mouse model [26]. However, the intrinsic mechanisms that induce these changes are not precisely known.

B06 is a new improved I_2-IR ligand with a lower *Ki* for I_2-IR than previous ligands and high selectivity for I_2-IRs over α_2 adrenoceptors [18]. The latter characteristic is of the utmost importance for avoidance of undesirable adverse effects on, for example, the vascular system. We previously reported that administration of B06 to a 5xFAD mouse model, a transgenic representative model of AD, reduces cognitive decline, neuroinflammation, tau hyperphosphorylation and APP processing [18].

In the present work, we demonstrated that the I_2-IR ligand B06 was able to improve cognition and ameliorate anxiety-like behavior in aged SAMP8 mice. Furthermore, we confirmed that on the molecular level, treatment with B06 reduced the exhibition of AD hallmarks such as APP processing and tau hyperphosphorylation, inhibited tau kinase (CDK5 and GSK3β) activation, reduced the gene expression of neuroinflammation markers including *Il-6*, *Il-18* and *Tnf-α*, and decreased OS.

When the apoptotic pathway was studied, decreases in caspase 3, Bax and BCL-2 levels were found. However, there has been a lack of consistency among I_2-IR studies regarding the reduction in apoptotic signaling [21]. Our results are consistent with those of several studies showing that administration of I_2-IR ligands such as 2-BFI and BU224 can reduce apoptotic marker levels in the rat brain cortex [32]. Considering that I_2-IRs have been reported to be involved in key pathways associated with neurodegeneration, we also evaluated several master pathways in B06-treated senescent mice, including those that are under the control of cytosolic calcium, astrocyte activation and synaptic neural plasticity. The localization of I_2-IRs remains elusive, but several studies have reported astrocytes as a major cell type with I_2-IR binding sites [14]. Of note, astrogliosis and activated microglial cells are associated with amyloid processing, indicating that this AD hallmark is a major trigger of gliosis [59]. After B06 treatment, a very significant decrease in the expression of the hippocampal pan-astrocytic reactive marker GFAP indicated strong control of neuroinflammation and a reduction in astrogliosis that in turn could prevent neuronal function loss. Moreover, S100A9, a Ca^{2+}-binding protein with a critical role in modulating the inflammatory response and inducing cytokine release by astrocytes [60], was used as a marker of neuroinflammation mediated by reactive astrocytes. In our study, we found clear reductions in two hippocampal areas, CA1 and CA3, confirming a reduction in the inflammatory state after treatment with B06. Likewise, the expression of the EAAT2 isoform (or Glt 1), a glutamate transporter located predominantly in astrocytes, was increased after treatment with the I_2-IR ligand B06. EAAT2 is implicated in glutamate clearance and has a leading role in the removal of excess glutamate and other potentially toxic mediators [19]. In line with these findings, our previous results for two other I_2-IR ligands [26] showed the same action regarding astrogliosis. However, in contrast, another study on the I_2-IR ligand LSL60101 showed induction of reactive astrocytosis in the facial motor nuclei of neonate rats after short-term treatment [13], suggesting that the effects differ

Fig. 4 Changes in NMDARs, neuronal plasticity and kinase pathways induced by I_2-IR ligand B06 in 12-month-old SAMP8 after treatment at 5 mg/Kg/day (B06 5 mg/kg) in comparison with 12-month-old control SAMP8 (Control). Representative western blot for NMDAR2B, NMDAR2A, ratio p-NMDAR2B (Tyr1472). Ratio p-CREB in nucleus protein levels and quantification (**a**–**d**). Representative western blot for kinases PKA, ratio p-AKT and quantification (**e**, **f**). Values in bar graphs were adjusted to 100% for the protein of control SAMP8 (Control). Representative gene expression for Bdnf (**g**). Gene expression levels were determined by real-time PCR. Values are the mean ± standard error of the mean (SEM); ($n = 3$–5 animals per group); $^{*}p < 0.05$; $^{**}p < 0.01$; $^{***}p < 0.001$ vs. Control

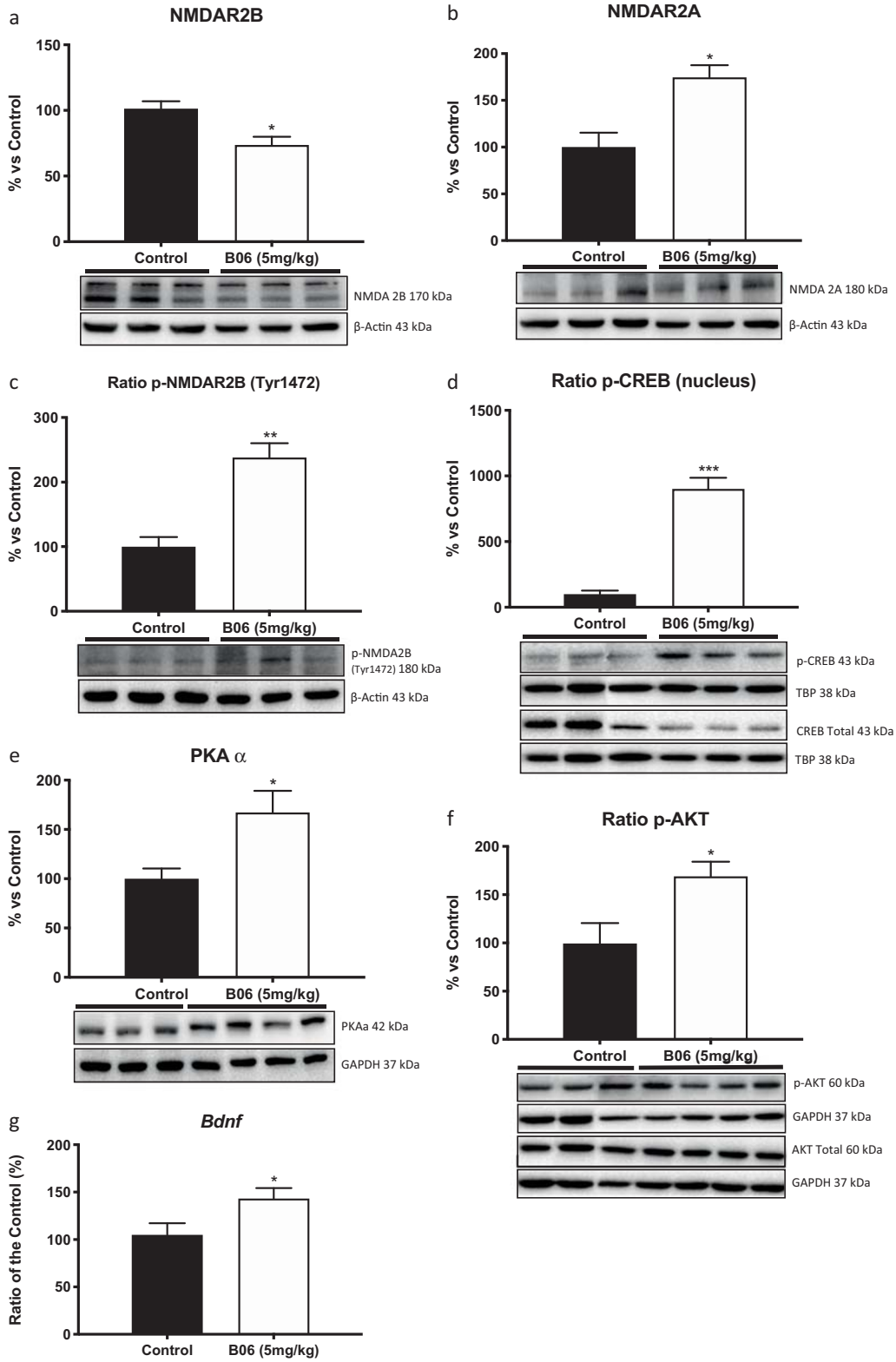
a
NMDAR2B
% vs Control
150
100
50
0
*
Control
B06 (5mg/kg)
NMDA 2B 170 kDa
β-Actin 43 kDa
b
NMDAR2A
% vs Control
200
150
100
50
0
*
Control
B06 (5mg/kg)
NMDA 2A 180 kDa
β-Actin 43 kDa
c
Ratio p-NMDAR2B (Tyr1472)
% vs Control
300
200
100
0
**
Control
B06 (5mg/kg)
p-NMDA2B (Tyr1472) 180 kDa
β-Actin 43 kDa
d
Ratio p-CREB (nucleus)
% vs Control
1500
1000
500
0
***
Control
B06 (5mg/kg)
p-CREB 43 kDa
TBP 38 kDa
CREB Total 43 kDa
TBP 38 kDa
e
PKA α
% vs Control
200
150
100
50
0
*
Control
B06 (5mg/kg)
PKAa 42 kDa
GAPDH 37 kDa
f
Ratio p-AKT
% vs Control
200
150
100
50
0
*
Control
B06 (5mg/kg)
p-AKT 60 kDa
GAPDH 37 kDa
AKT Total 60 kDa
GAPDH 37 kDa
g
Bdnf
Ratio of the Control (%)
200
150
100
50
0
*
Control
B06 (5mg/kg)

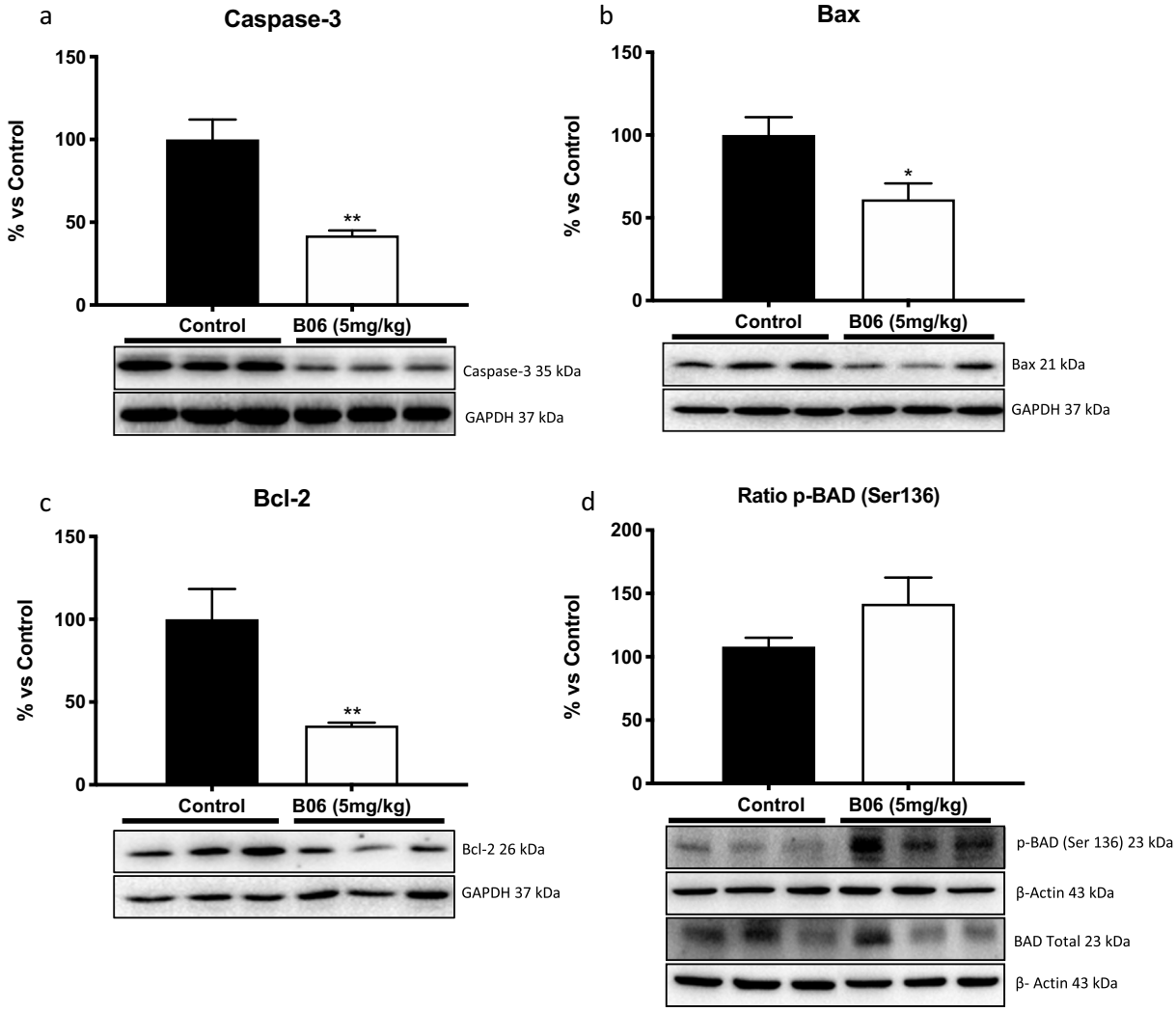

Fig. 5 Treatment with the I_2-IR ligand B06 suppressed apoptosis by inhibiting the implicated apoptotic factors in 12-month-old SAMP8 treated with B06 at 5 mg/Kg/day (B06 5 mg/kg) as compared to control SAMP8 (Control). Representative western blot for caspase-3, Bax, BCL-2, ratio p-BAD (Ser136) and quantification (**a**–**d**). Values in bar graphs were adjusted to 100% for the protein of control SAMP8 (Control). Values are the mean ± standard error of the mean (SEM); ($n = 3$–5 animals per group); *$p < 0.05$; **$p < 0.01$ vs. Control

depending on both the physicochemical properties of the I_2-IR ligand and the experimental model.

Notably, in astrocytes, increased CaN activity can lead to modification of the kinase activity of GSK3β [61]. Calcium entry through NMDA2B receptors enhances the activation of GSK3β through CaN phosphatase activity, and in turn, GSK3β amplifies this phosphatase activity, dephosphorylating CREB [56, 60]. In addition, the interaction of I_2-IR ligands with NMDA receptors has been well described [41, 42]. Thus, our results support the idea that modulation of I_2-IRs by B06 is able to induce changes in

Fig. 6 I_2-IR ligand, B06, attenuated neuroinflammation and OS state in 12-month-old SAMP8 treated mice at 5 mg/Kg/day (B06 5 mg/kg) when compared to the control SAMP8 (Control). Representative western blot for GFAP, GLT-1/EAAT-2 (**a**–**b**). Representative images for GFAP (c) and S100A9 immunostaining (**c**) and quantification for GFAP and S100A9 on the bar chart (**d**–**j**). Representative gene expression for inflammatory markers Il-6, *Il-18*, *Il-1β*, *Ifn-γ*, *Tnf-α* and *Cxcl-10* (**k**) and OS markers *Hmox1*, *iNOS*, *Nrf1* and *Aldh2* (**l**). Quantification of intracellular H_2O_2 (μM) (**m**). Gene expression levels were determined by real-time PCR. Values in bar graphs were adjusted to 100% for the protein of control SAMP8 (Control). DG: dentate gyrus. Scale bar for immunohistochemical images is 200 μm. Values are the mean ± standard error of the mean (SEM); (n = 3–5 animals per group); *$p < 0.05$; ***$p < 0.001$ vs. Control

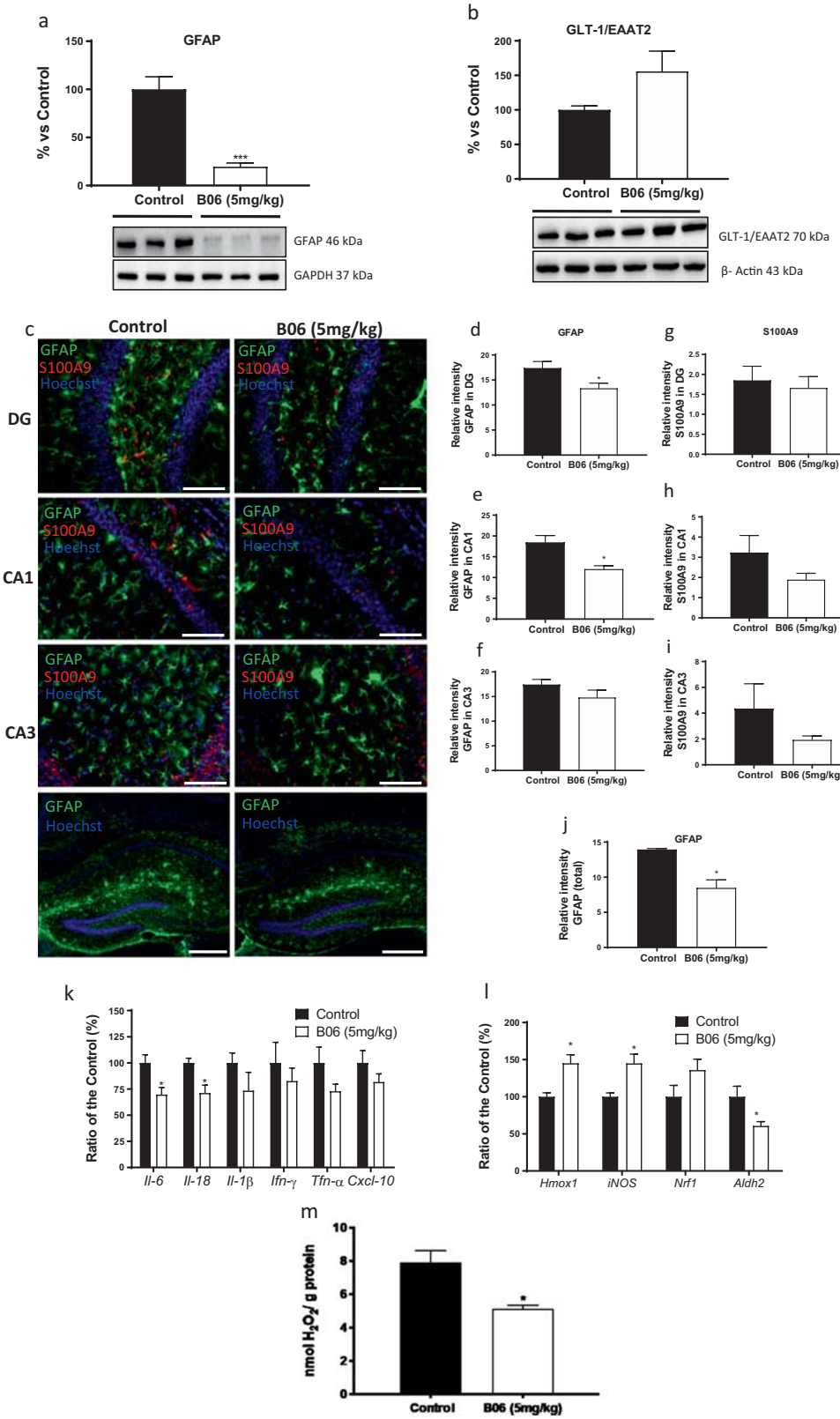
a
GFAP
% vs Control
150
100
50
0
***
Control
B06 (5mg/kg)
GFAP 46 kDa
GAPDH 37 kDa
b
GLT-1/EAAT2
% vs Control
200
150
100
50
0
Control
B06 (5mg/kg)
GLT-1/EAAT2 70 kDa
β- Actin 43 kDa
c
Control
B06 (5mg/kg)
DG
CA1
CA3
GFAP
S100A9
Hoechst
d
GFAP
Relative intensity GFAP in DG
e
Relative intensity GFAP in CA1
f
Relative intensity GFAP in CA3
g
S100A9
Relative intensity S100A9 in DG
h
Relative intensity S100A9 in CA1
i
Relative intensity S100A9 in CA3
j
GFAP
Relative intensity GFAP (total)
k
Ratio of the Control (%)
Control
B06 (5mg/kg)
Il-6
Il-18
Il-1β
Ifn-γ
Tfn-α
Cxcl-10
l
Ratio of the Control (%)
Hmox1
iNOS
Nrf1
Aldh2
m
nmol H2O2/ g protein
Control
B06 (5mg/kg)

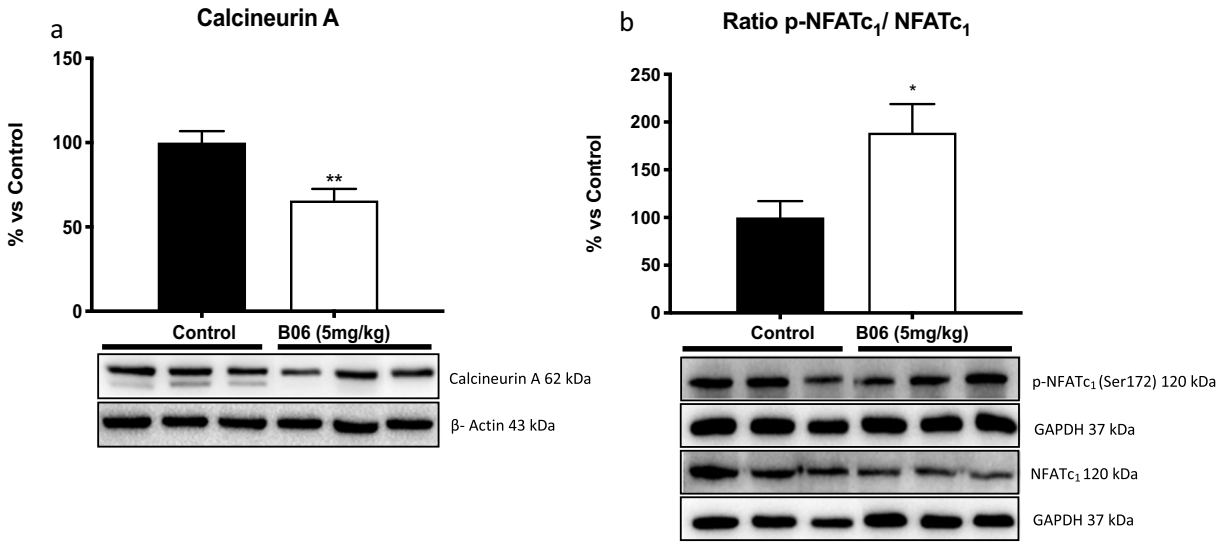

Fig. 7 Modulation of CaN signaling after B06 treatment in 12-month-old SAMP8 treated mice at 5 mg/Kg/day (B06 5 mg/kg). Representative western blot for CaN A, ratio p-NFATc1/NFATc1 and quantification (**a**, **b**). Values in bar graphs were adjusted to 100% for protein of control SAMP8 (Control). Values are the mean ± standard error of the mean (SEM); ($n = 3$–5 animals per group); *$p < 0.05$; **$p < 0.01$ vs. Control

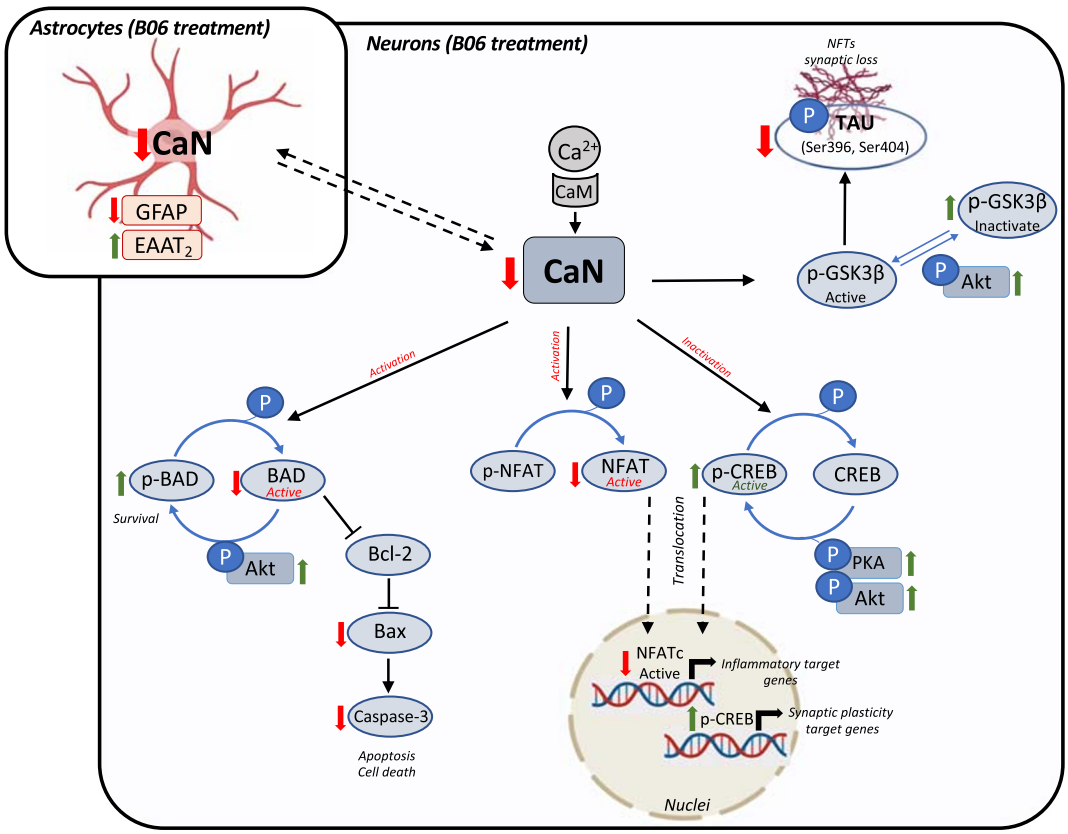

Fig. 8 Graphical abstract showing molecular changes in CaN signaling after treatment with B06

NMDA receptors. We definitively observed changes in NMDA receptor subunit composition and activation. On the one hand, increases in NMDA2A receptor protein levels were observed. On the other hand, decreases in NMDA2B receptor protein levels with increased phosphorylation were observed. These changes are associated with LTP, which may partially explain the improvement in cognition observed in B06-treated SAMP8 mice.

To further elucidate the molecular mechanisms modulated by B06, we examined the negative crosstalk between AKT and GSK3β signaling that participates in synaptic plasticity [9] controlled by CaN phosphatase activity. As mentioned, B06 treatment reduced GSK3β activation by increasing the levels of its inactive form phosphorylated at Ser9, whereas it activated AKT signaling. Because AKT is a recognized pro-survival molecule that participates in neural plasticity, modulation of AKT signaling in animals treated with the I_2-IR ligand B06 likely contributed to the favorable effects on cognition observed in SAMP8 mice [55, 68].

p-CREB controls the expression of genes related to synaptic disruption and LTP, such as *Bdnf* [10]. Neuronal growth and survival require the expression of CREB target genes that control various proteins, including BDNF and its receptor tropomyosin-related kinase B (TrkB) [66]. On the one hand, treatment with the I_2-IR ligand B06 increased nuclear p-CREB levels and increased *Bdnf* gene expression. On the other hand, B06 increased the levels of PKA, which can drive p-CREB nuclear translocation. Of note, PKA acts as a negative modulator of $NFATc_1$, a transcription factor that regulates the transcription of genes that play crucial roles in axonal outgrowth control [51]. Interestingly, I_2-IR ligand treatment induced an increase in $NFATc_1$ phosphorylation in parallel with decreases in *Il-6*, *Ifn-γ* and *Tnf-α* gene expression. $NFATc_1$ and CaN are master regulators that control EAAT2 up- or downregulation [54]. We hypothesize that the observed changes in $NFATc_1$ are responsible for the increase in EAAT2 described above.

$NFATc_1$ is dephosphorylated by CaN, which enables its nuclear translocation. Continuous NFAT activation and nuclear signaling result in neurodegenerative morphological abnormalities, including neuritic dystrophy, dendritic spine loss and modulation of β-amyloid accumulation. Indeed, NFAT activity stimulates the amyloidogenic pathway [29, 53] and its inhibition has been found to significantly reduce β-amyloid plaque formation in an AD mouse model [20]. Therefore, a reduction in nuclear NFAT should have beneficial effects in senescence models, in which overactivation of neurodegenerative pathways is a key cause of cognitive decline [24, 25].

The last finding, closely linked with the findings described above, is the implication of CaN in the beneficial effects of the I_2-IR ligand B06 in SAMP8 mice. CaN is a multicomponent protein in which CaN A has phosphatase activity regulated by calcium levels [48]. Calcium dysregulation can be induced by age-related changes, such as OS and inflammation [19, 45]. Furthermore, inhibition of CaN signaling produces neuroprotection in models of injury and disease [40, 64], reduces neuroinflammation [19] and cognitive impairment [34], and improves synapse function [30]. Consistent with these findings, we hypothesized that in SAMP8 mice, which are characterized by neuroinflammation and OS, an imbalance in calcium levels occurs, activating CaN A and inducing neurodegeneration. Specifically, astrocytic CaN is activated under inflammatory conditions and can, for example, activate GSK3β and inactivate AKT, influencing NMDAR-mediated axonal outgrowth [60]. As stated above, the I_2-IR ligand B06 reduced CaN A protein levels, and accordingly, we found activation of AKT and strong inactivation of GSK3β.

Regarding the OS observations, CaN can be activated after H_2O_2 addition to neuronal cultures [49]. Likewise, the reductions in OS markers after treatment with the I_2-IR ligand B06 could have also contributed to a reduction in CaN activity. These findings correlate with cognitive improvement, increasing neuroprotective signaling and reducing tau hyperphosphorylation. Conversely, CaN A can dephosphorylate tau. However, the balance between tau phosphorylation and dephosphorylation is due to a shift in tau kinase activity [65]. Hyperactivation of the PP1A domain of CaN A results in dephosphorylation of a few transcription factors, including CREB (which blocks CREB translocation to the nucleus) and NFAT (which enables NFAT translocation to the nucleus). In both cases, the reduced synaptic and growth gene transcription necessitates plasticity, and the increased expression of proinflammatory factors participates in neurodegenerative processes. Moreover, hyperactivation of the phosphatase 2B (PP2B) domain increases BAD dephosphorylation, favoring the action of BAD as a proapoptotic factor [38].

In conclusion, the data from our study demonstrate that modulation of I_2-IRs by B06 reduces neuroinflammation, OS and CaN protein levels in SAMP8 mice. The decreases in CaN protein levels can explain the changes in CREB, $NFAT_{c1}$ and BAD phosphorylation levels. In addition, the decreases in CaN levels result in modification of the kinase activity of GSK3β and AKT, among other molecules, leading to reduced tau hyperphosphorylation and preventing cognitive decline in SAMP8 mice. Collectively, our findings provide evidence that the CaN pathway is a critical component of the neuroprotective effects of I_2-IR ligands on SAMP8 model mice, providing insight into several molecular modifications observed after I_2-IR ligand treatment. In the future, deeper knowledge of the role of the I_2-IR signaling cascade in AD will provide new therapeutic targets for cognitive decline and AD.

Acknowledgements We strongly acknowledge the advice of Dr. Andrés G. Fernández (our mentor in the CaixaImpulse 2018 program) for invaluable advice. This study was supported by Ministerio de Economía y Competitividad of Spain and FEDER (PID2019-107991RB-I00, PID2019-106285RB-I00) and 2017SGR106 (AGAUR, Catalonia). The project leading to these results has received funding from "la Caixa" Foundation (ID 100010434), under agreement CI18-00002. F.V. thanks the UB for APIF grant (UB2016); S. R.-A. to Generalitat de Catalunya, (2018FI-B-00227) and A. B. for APIF grant to Institute of Biomedicine (UB2018).

Author contributions CGF, MP and CE contributed to conceptualization and funding acquisition. SA, SRA and AB synthesized and purified B06. CGF and FV performed experiments and formal data analysis. CGF, CE, FV and MP wrote, reviewed and edited the manuscript. All authors read and approved the final version of the manuscript.

Compliance with ethical standards

Declarations Not applicable.

Competing interests The authors have no competing interests to declare.

References

1. Abás S, Estarellas C, Luque FJ, Escolano C. Easy access to (2-imidazolin-4-yl)phosphonates by a microwave assisted multicomponent reaction. Tetrahedron. 2015;71:2872–81. https://doi.org/10.1016/j.tet.2015.03.065.
2. Abás S, Erdozain AM, Keller B, Rodríguez-Arévalo S, Callado LF, García-Sevilla JA, et al. Neuroprotective effects of a structurally new family of high affinity imidazoline I_2 receptors ligands. ACS Chem Neurosci. 2017;8(4):737–42. https://doi.org/10.1021/acschemneuro.6b00426.
3. Abás S, Rodríguez-Arévalo S, Bagán A, Griñán-Ferré C, Vasilopoulou F, Brocos-Mosquera I, et al. Bicyclic α-Iminophosphonates as High Affinity Imidazoline I2 Receptor Ligands for Alzheimer's Disease. J Med Chem. 2020 Apr 9;63(7):3610–3633. https://doi.org/10.1021/acs.jmedchem.9b02080.
4. Akiguchi I, Pallàs M, Budka H, Akiyama H, Ueno M, Han J, et al. SAMP8 mice as a neuropathological model of accelerated brain aging and dementia: Toshio Takeda's legacy and future directions. Neuropathology. 2017;37:293–305. https://doi.org/10.1111/neup.12373.
5. Antunes M, Biala G. The novel object recognition memory: neurobiology, test procedure, and its modifications. Cogn Process. 2012;13:93–110. https://doi.org/10.1007/s10339-011-0430-z.
6. Baumgärtel K, Mansuy IM. Neural functions of CaN in synaptic plasticity and memory. Learn Mem. 2012;19:375–84. https://doi.org/10.1101/lm.027201.112.
7. Bezprozvanny I, Hiesinger PR. The synaptic maintenance problem: membrane recycling, Ca^{2+} homeostasis and late onset degeneration. Mol Neurodegener. 2013;8:23. https://doi.org/10.1186/1750-1326-8-23.
8. Bousquet P, Hudson A, García-Sevilla JA, Li JX. Imidazoline receptors system: the past, the present and the future. Pharmacol Rev. 2020;72:1–30. https://doi.org/10.1124/pr.118.016311.
9. Bradley CA, Peineau S, Taghibiglou C, Nicolas CS, Whitcomb DG, Bortolotto ZA, et al. A pivotal role of GSK3 in synaptic plasticity. Front Mol Neurosci. 2012;5:13. https://doi.org/10.3389/fnmol.2012.00013.
10. Bridi MS, Hawk JD, Chatterjee S, Safe S, Abel T. Pharmacological activators of the NR4A nuclear receptors enhance LTP in a CREB/CBP-dependent manner. Neuropsychopharmacology. 2017;42(6):1243–53. https://doi.org/10.1038/npp.2016.253.
11. Canudas AM, Gutierrez-Cuesta J, Rodríguez MI, Acuña-Castroviejo D, Sureda FX, Camins A, et al. Hyperphosphorylation of microtubule-associated protein tau in senescence-accelerated mouse (SAM). Mech Ageing Dev. 2005;126(12):1300–4.
12. Caraveo G, Auluck PK, Whitesell L, Chung CY, Baru V, Mosharov EV, et al. Calcineurin determines toxic versus beneficial responses to alpha-synuclein. Proc Natl Acad Sci U S A. 2014;111(34):E3544–52. https://doi.org/10.1073/pnas.1413201111.
13. Casanovas A, Olmos G, Ribera J, Boronat MA, Esquerda JE, García-Sevilla JA. Induction of reactive astrocytosis and prevention of motoneuron cell death by the I(2)-imidazoline receptor ligand LSL 60101. Br J Pharmacol. 2000;130(8):1767–76. https://doi.org/10.1038/sj.bjp.0703485.
14. Choi DH, Yun JH, Lee J. Protective effect of the imidazoline I2 receptor agonist 2-BFI on oxidative cytotoxicity in astrocytes. Biochem Biophys Res Commun. 2018;503(4):3011–6. https://doi.org/10.1016/j.bbrc.2018.08.086.

15. Cummings J. Lessons learned from Alzheimer disease: clinical trials with negative outcomes. Clin Transl Sci. 2018;11:147–52. https://doi.org/10.1111/cts.12491.
16. Cummings JL, Morstorf T, Zhong K. Alzheimer's disease drug-development pipeline: few candidates, frequent failures. Alzheimers Res Ther. 2014;6(4):37. https://doi.org/10.1186/alzrt269.
17. Cummings J, Lee G, Ritter A, Zhong K. Alzheimer's disease drug development pipeline: 2018. Alzheimers Dement. 2018;4:195–214. https://doi.org/10.1016/j.trci.2018.03.009.
18. Escolano C, Pallás M, Griñán-Ferré C, Abás S, Callado LF, García-Sevilla JA. Synthetic I_2 imidazoline receptor ligands for prevention or treatment of human brain disorders. WO 2019/121853 A1, June 2019.
19. Furman JL, Norris CM. Calcineurin and glial signaling: neuroinflammation and beyond. J Neuroinflammation. 2014;11:158. https://doi.org/10.1186/s12974-014-0158-7.
20. Furman JL, Sama DM, Gant JC, Beckett TL, Murphy MP, Bachstetter AD, et al. Targeting astrocytes ameliorates neurologic changes in a mouse model of Alzheimer's disease. J Neurosci. 2012;32:16129–40.
21. Garau C, Miralles A, Garcia-Sevilla JA. Chronic treatment with selective I_2-imidazoline receptor ligands decreases the content of pro-apoptotic markers in rat brain. J Psychopharmacol. 2013;27(2):123–34. https://doi.org/10.1177/0269881112450785.
22. García-Sevilla JA, Escribá PV, Walzer C, Bouras C, Guimón J. Imidazoline receptor proteins in brains of patients with Alzheimer's disease. Neurosci Lett. 1998;247:95–8.
23. GBD 2016 Neurology Collaborators. Global, regional, and national burden of neurological disorders, 1990–2016: a systematic analysis for the Global Burden of Disease Study 2016. Lancet Neurol. 2010;18(5):459–80. https://doi.org/10.1016/S1474-4422(18)30499-X.
24. Griñán-Ferré C, Palomera-Avalos V, Puigoriol-Illamola D, Camins A, Porquet D, Plà V, et al. Behaviour and cognitive changes correlated with hippocampal neuroinflammaging and neuronal markers in SAMP8, a model of accelerated senescence. Exp Gerontol. 2016a;80:57–69. https://doi.org/10.1016/j.exger.2016.03.014.
25. Griñán-Ferré C, Puigoriol-Illamola D, Palomera-Ávalos V. Environmental enrichment modified epigenetic mechanisms in SAMP8 mouse hippocampus by reducing oxidative stress and inflammaging and achieving neuroprotection. Front Aging Neurosci. 2016b;8:1–12.
26. Griñán-Ferré C, Vasilopoulou F, Abàs S, Rodríguez-Arévalo S, Bagán A, Sureda FX, et al. Behavioral and cognitive improvement induced by novel imidazoline I2 receptor ligands in female SAMP8 mice. Neurotherapeutics. 2019;16:416–31. https://doi.org/10.1007/s13311-018-00681-5.
27. Horsley V, Pavlath GK. NFAT ubiquitous regulator of cell differentiation and adaptation. J Cell Biol. 2002;156(5):771–4. https://doi.org/10.1083/jcb.200111073.
28. Jiang SX, Zheng RY, Zeng JQ, Li XL, Han Z, Hou ST. Reversible inhibition of intracellular calcium influx through NMDA receptors by imidazoline I(2) receptor antagonists. Eur J Pharmacol. 2010;629(1–3):12–9. https://doi.org/10.1016/j.ejphar.2009.11.063.
29. Jin SM, Cho HJ, Kim YW, Hwang JY, Mook-Jung I. Aβ-induced Ca(2+) influx regulates astrocytic BACE1 expression via calcineurin/NFAT4 signals. Biochem Biophys Res Commun. 2012;425(3):649–55. https://doi.org/10.1016/j.bbrc.2012.07.123.
30. Kim S, Violette CJ, Ziff EB. Reduction of increased calcineurin activity rescues impaired homeostatic synaptic plasticity in presenilin 1 M146V mutant. Neurobiol Aging. 2015;36(12):3239–46. https://doi.org/10.1016/j.neurobiolaging.2015.09.007.
31. Kuno T, Mukai H, Ito A, Chang CD, Kishima K, Saito N, et al. Distinct cellular expression of calcineurin A alpha and A beta in rat brain. J Neurochem. 1992;58:1643–51. https://doi.org/10.1111/j.1471-4159.1992.tb10036.x.
32. Li JX. Imidazoline I_2 receptors: an update. Pharmacol Ther. 2017;178:48–56. https://doi.org/10.1016/j.pharmthera.2017.03.009.
33. Lin CH, Lee CC, Gean PW. Involvement of a CaN cascade in amygdala depotentiation and quenching of fear memory. Mol Pharmacol. 2003;63:44–52. https://doi.org/10.1124/mol.63.1.44.
34. Liu J, Si Z, Li S, Huang Z, He Y, Zhang T, et al. Prevents cognitive impairment by inhibiting reactive astrogliosis in pilocarpine-induced status epilepticus rats. Front Cell Neurosci. 2018;11:428. https://doi.org/10.3389/fncel.2017.00428.
35. Martin ZS, Neugebauer V, Dineley KT, Kayed R, Zhang W, Reese LC, et al. α-Synuclein oligomers oppose long-term potentiation and impair memory through a calcineurin-dependent mechanism: relevance to human synucleopathic diseases. J Neurochem. 2012;120(3):440–52. https://doi.org/10.1111/j.1471-4159.2011.07576.x.
36. McDonald GR, Olivieri A, Ramsat RR, Holt A. On the formation and nature of the imidazoline I2 binding site on human monoamine oxidase-B. Pharmacol Res. 2010;62(6):475–88. https://doi.org/10.1016/j.phrs.2010.09.001.
37. Morley JE, Farr SA, Kumar VB, Armbrecht HJ. The SAMP8 mouse: a model to develop therapeutic interventions for Alzheimer's disease. Curr Pharm Des. 2012;18:1123–30. https://doi.org/10.2174/138161212799315795.
38. Mukherjee A, Morales-Scheihing D, Gonzalez-Romero D, Green K, Taglialatela G, Soto C. CaN inhibition at the clinical phase of prion disease reduces neurodegeneration, improves behavioral alterations and increases animal survival. PLoS Pathog. 2010;6(10):e1001138. https://doi.org/10.1371/journal.ppat.1001138.
39. Mulkey RM, Endo S, Shenolikar S, Malenka RC. Involvement of a calcineurin/inhibitor-1 phosphatase cascade in hippocampal long-term depression. Nature. 1994;369(6480):486–8.
40. O'Donnell JC, Jackson JG, Robinson MB. Transient oxygen/glucose deprivation causes a delayed loss of mitochondria and increases spontaneous calcium signaling in astrocytic processes. J Neurosci. 2016;36:7109–27. https://doi.org/10.1523/JNEUROSCI.4518-15.2016.
41. Olmos G, Ribera J, Garcia-Sevilla JA. Imidazoli(di)ne compounds interact with the phencyclidine site of NMDA receptors in the rat brain. Eur J Pharmacol. 1996;310(2–3):273–6.

42. Olmos G, DeGregorio-Rocasolano N, Paz Regalado M, Gasull T, Assumpcio Boronat M, Trullas R, et al. Protection by imidazol(ine) drugs and agmatine of glutamate-induced neurotoxicity in cultured cerebellar granule cells through blockade of NMDA receptor. Br J Pharmacol. 1999;127(6):1317–26. https://doi.org/10.1038/sj.bjp.0702679.
43. Pallàs M. Senescence-accelerated mice P8: a tool to study brain aging and Alzheimer's disease in a mouse model. ISRN Cell Biol. 2012;2012:1–12. https://doi.org/10.5402/2012/917167.
44. Pleiss MM, Sompol P, Kraner SD, Mohmmad Abdul H, Furman JL, Guttmann RP, et al. Calcineurin proteolysis in astrocytes: implications for impaired synaptic function. Biochim Biophys Acta. 2016;1862(9):1521–32. https://doi.org/10.1016/j.bbadis.2016.05.007.
45. Reese LC, Taglialatela G. A role of calcineurin in Alzheimer's disease. Curr Neuropharmacol. 2011;9(4):685–92. https://doi.org/10.2174/157015911798376316.
46. Reynolds GP, Boulton RM, Pearson SJ, Hudson AL, Nutt DJ. Imidazoline binding sites in Huntington's and Parkinson's disease putamen. Eur J Pharmacol. 1996;301(1-3):R19–21.
47. Ruiz J, Martin I, Callado LF, Meana JJ, Barturen F, Garcia-Sevilla JA. Non-adrenoreceptor [3H]idazoxan binding sites (I2-imidazoline sites) are increased in postmortem brain from patients with Alzheimer's disease. Neurosci Lett. 1993;160:109–12. https://doi.org/10.1016/0304-3940(93)90925-B.
48. Rusnak F, Mertz P. Calcineurin: form and function. Physiol Rev. 2000;80(4):1483–521.
49. Sée V, Loeffler JP. Oxidative stress induces neuronal death by recruiting a protease and phosphatase-gated mechanism. J Biol Chem. 2001;276(37):35049–59. https://doi.org/10.1074/jbc.M104988200.
50. Serrano-Pozo A, Frosch MP, Masliah E, Hyman BT. Neuropathological alterations in Alzheimer disease. Cold Spring Harb Perspect Med. 2011;1(1):a006189. https://doi.org/10.1101/cshperspect.a006189.
51. Sheridan CM, Heist EK, Beals CR, Crabtree GR, Gardner P. 2002 protein kinase A negatively modulates the nuclear accumulation of NF-ATc1 by priming for subsequent phosphorylation by glycogen synthase kinase-3. J Biol Chem. 2002;277(50):48664–76. https://doi.org/10.1074/jbc.M20702920.
52. Sompol P, Norris C. Ca2+, astrocyte activation and calcineurin/NFAT signaling in age-related neurodegenerative diseases. Front Aging Neurosci. 2018;10:199. https://doi.org/10.3389/fnagi.2018.00199.
53. Sompol P, Furman JL, Pleiss MM, Kraner SD, Artiushin IA, Batten SR, Quintero JE, Simmerman LA, Beckett TL, Lovell MA, Murphy MP, Gerhardt GA, Norris CM. Calcineurin/NFAT Signaling in Activated Astrocytes Drives Network Hyperexcitability in Aβ-Bearing Mice. J Neurosci. 2017 37(25):6132–6148. https://doi.org/10.1523/JNEUROSCI.0877-17.2017.
54. Su ZZ, Leszczyniecka M, Kang DC, Sarkar D, Chao W, Volsky DJ, et al. Insights into glutamate transport regulation in human astrocytes: cloning of the promoter for excitatory amino acid transporter 2 (EAAT2). Proc Natl Acad Sci U S A. 2003;100:1955–196. https://doi.org/10.1073/pnas.0136555100.
55. Sun J, Nan G. The extracellular signal-regulated kinase 1/2 pathway in neurological diseases: a potential therapeutic target (review). Int J Mol Med. 2017;39(6):1338–46. https://doi.org/10.3892/ijmm.2017.2962.
56. Szatmari E, Habas A, Yang P, Zheng JJ, Hagg T, Hetman M. A positive feedback loop between glycogen synthase kinase 3beta and protein phosphatase 1 after stimulation of NR2B NMDA receptors in forebrain neurons. J Biol Chem. 2004;280(45):37526–35. https://doi.org/10.1074/jbc.M502699200.
57. Takeda T. Senescence-accelerated mouse (SAM) with special references to neurodegeneration models, SAMP8 and SAMP10 mice. Neurochem Res. 2009;34:639–59. https://doi.org/10.1007/s11064-009-9922-y.
58. Tyacke RJ, Myers JFM, Venkataraman A, Mick I, Turton S, Passchier J, et al. Evaluation of 11C-BU99008, a PET ligand for the imidazoline 2 binding site in human brain. J Nucl Med. 2018;59(10):1597–602. https://doi.org/10.2967/jnumed.118.208009.
59. Vehmas AK, Kawas CH, Stewart WF, Troncoso JC. Immune reactive cells in senile plaques and cognitive decline in Alzheimer's disease. Neurobiol Aging. 2003;24(2):321–31. https://doi.org/10.1016/s0197-4580(02)00090-8.
60. Wang Y, Tang JL, Xu X, Zhou XP, Du J, Wang X, et al. NMDA receptors inhibit axonal outgrowth by inactivating AKT and activating GSK-3β via calcineurin in cultured immature hippocampal neurons. Exp Cell Res. 2018;371(2):389–98. https://doi.org/10.1016/j.yexcr.2018.08.033.
61. Watanabe K, Uemura K, Asada M, Masato M, Akiyama H, Shinohama S, et al. The participation of insulin-like growth factor- binding protein 3 released by astrocytes in the pathology of Alzheimer's disease. Mol Brain. 2015;8:82. https://doi.org/10.1186/s13041-015-0174-2.
62. Wilson H, Dervenoulas G, Pagano G, Tyacke RJ, Polychronis S, Myers J, et al. Imidazoline 2 binding sites reflecting astroglia pathology in Parkinson's disease: an in vivo11C-BU99008 PET study. Brain. 2019;142(10):3116–28. https://doi.org/10.1093/brain/awz260.
63. Wu HY, Hudry E, Hashimoto T, Kuchibhotla K, Rozkalne A, Fan Z, et al. Amyloid beta induces the morphological neurodegenerative triad of spine loss, dendritic simplification, and neuritic dystrophies through calcineurin activation. J Neurosci. 2010;30(7):2636–49. https://doi.org/10.1523/JNEUROSCI.4456-0.
64. Xiong TQ, Chen LM, Tan BH, Guo CY, Li YN, Zhang YF, et al. The effects of calcineurin inhibitor FK506 on actin cytoskeleton, neuronal survival and glial reactions after pilocarpine-induced status epilepticus in mice. Epilepsy Res. 2018;140:138–47. https://doi.org/10.1016/j.eplepsyres.2018.01.007.

65. Yu D, Tong L, Song G, Lin W, Zhang L, Bai W, et al. Tau binds both subunits of CaN, and binding is impaired by calmodulin. Biochim Biophys Acta. 2008;1783:2255–61. https://doi.org/10.1016/j.bbamcr.2008.06.015.
66. Zhang F, Kang Z, Li W, Xiao Z, Zhou X. Roles of brain-derived neurotrophic factor/tropomyosin-related kinase B (BDNF/TrkB) signalling in Alzheimer's disease. J Clin Neurosci. 2012;19(7):946–9. https://doi.org/10.1016/j.jocn.2011.12.022.
67. Zhao H, Jin-Long Y, Susan XJ, Sheng-Tao H, Rong-Yuan Z. Fast, non-competitive and reversible inhibition of NMDA-activated currents by 2-BFI confers neuroprotection. PLoS ONE. 2013;8(5):e64894. https://doi.org/10.1371/journal.pone.0064894.
68. Zhu X, Castellani RJ, Takeda A, Nunomura A, Atwood CS, Perry G, et al. Differential activation of neuronal ERK, JNK/SAPK and p38 in Alzheimer disease: the 'two hit' hypothesis. Mech Ageing Dev. 2001;123:39–46. https://doi.org/10.1016/S0047-6374(01)00342-6.

pharmaceutics

MDPI

Article

Amelioration of BPSD-Like Phenotype and Cognitive Decline in SAMP8 Mice Model Accompanied by Molecular Changes after Treatment with I_2-Imidazoline Receptor Ligand MCR5

Foteini Vasilopoulou [1], Andrea Bagan [2], Sergio Rodriguez-Arevalo [2], Carmen Escolano [2], Christian Griñán-Ferré [1,*,†] and Mercè Pallàs [1,*,†]

[1] Pharmacology Section, Department of Pharmacology, Toxicology and Medicinal Chemistry, Faculty of Pharmacy and Food Sciences, and Institut de Neurociències, University of Barcelona, Av. Joan XXIII, 27-31, E-08028 Barcelona, Spain; ftn.vasilopoulou@gmail.com

[2] Laboratory of Medicinal Chemistry (Associated Unit to CSIC), Department of Pharmacology, Toxicology and Medicinal Chemistry, Faculty of Pharmacy and Food Sciences, and Institute of Biomedicine (IBUB), University of Barcelona, Av. Joan XXIII, 27-31, E-08028 Barcelona, Spain; abaganpo7@alumnes.ub.edu (A.B.); rodriguez.arevalo@ub.edu (S.R.-A.); cescolano@ub.edu (C.E.)

* Correspondence: christian.grinan@ub.edu (C.G.-F.); pallas@ub.edu (M.P.)

† These authors contributed equally to this work.

Received: 24 April 2020; Accepted: 22 May 2020; Published: 23 May 2020

Abstract: Behavioural and psychological symptoms of dementia (BPSD), including fear-anxiety- and depressive-like behaviour, are present in Alzheimer's disease (AD), together with memory decline. I_2-imidazoline receptors (I_2-IRs) have been associated with neuropsychiatric and neurodegenerative disorders, further, I_2-IR ligands have demonstrated a neuroprotective role in the central nervous system (CNS). In this study, we assessed the effect of the I_2-IR ligand MCR5 on both cognitive and non-cognitive symptoms in the Senescence accelerated mice prone 8 (SAMP8) mouse model. Oral administration of I_2-IR ligand MCR5 (5 mg/kg/day for four weeks) in 10-month SAMP8 mice ameliorated both BPSD-like phenotype and cognitive decline by attenuating depressive-like behaviour, reducing fear-anxiety-like behaviour and improving cognitive performance using different tasks. Interaction of I_2-IR ligand MCR5 with serotoninergic system did not account for behavioural or cognitive improvement, although changes in molecular pathways underlying depression and anxiety phenotype were observed. MCR5 increased levels of p-AKT, phosphorylated glycogen synthase kinase 3 β (GSK3β) at Ser9 and phosphorylated mammalian target of rapamycin complex 1 (mTORC1) levels in SAMP8 treated mice compared to SAMP8 control. Moreover, MCR5 treatment altered N-methyl-d-aspartate receptor (NMDA) 2B phosphorylation, and decreased the protein levels of phosphorylated cyclin-dependent kinase 5 (p-CDK5) and dopamine- and cyclic adenosine monophosphate (cAMP)-regulated phosphoprotein of Mr 32 kDa phosphorylated at Thr75 (p-DARPP32), with a parallel increase in protein kinase A (PKA) and p-cAMP response element-binding (pCREB) levels. Consistent with these changes MCR5 attenuated neuroinflammation by decreasing expression of pro-inflammatory markers such as *Tumor necrosis factor-alpha (Tnf-α), Interleukin 1β (Il-1β), Interleukin 6 (Il-6),* and promoted synaptic plasticity by increasing levels of postsynaptic density protein 95 (PSD95) as well as ameliorating tropomyosin-related kinase B (TrkB) and nerve growth factor receptor (NGFR) signalling. Collectively, these results increase the potential of highly selective I_2-IR ligands as therapeutic agents in age-related BPSD and cognitive alterations.

Keywords: I_2-imidazoline receptors; Behavioural and psychological symptoms of dementia (BPSD); brain-derived neurotrophic factor (BDNF); neuroinflammation; age

1. Introduction

Nowadays, the global population of the elderly is increasing in parallel to the diagnosis of neurodegenerative diseases (ND) and psychiatric disorders. Thus, ageing is the main factor associated with ND, such as Alzheimer's disease (AD), which is the leading cause of dementia [1]. So far, the AD research has mainly focused on cognitive impairment and typical AD hallmarks, although no effective treatments are able to reduce or halt the progression of the disease [2].

On the other hand, non-cognitive symptoms are becoming increasingly important due to their prevalence, generating several dysfunctions and representing one of the most troublesome domains of treating dementia [3]. These non-cognitive symptoms that patients suffer, commonly referred to as "Behavioural and psychological symptoms of dementia" (BPSD), mainly include aberrant motor behaviour, hallucinations, aggressive and anxiety behaviour and depression, among others [4]. In AD, the patients present BPSD since the early stages [5], which, as the disease is progressing, tend to increase their frequency. BPSD are the cause of higher morbidity and poor quality of life for patients and caregivers [6]. Approximately between 40% and 60% of AD patients experience anxiety and depressive symptoms [7]. Therefore, these symptoms are associated with cognitive impairment, increasing the risk of persistence for mild cognitive impairment (MCI) and dementia, being both the most common psychiatric syndromes [8,9].

The biogenic monoamine 5-hydroxytryptamine (5-HT), or serotonin, has been tied to cognitive decline and multiple other BPSD domains [10,11], while it is well-known that loss in serotonin transporters and changes in synaptic proteins can fire mechanisms linked to depression by alteration of specific cerebral circuits [12]. Several studies support that the mechanisms underlying the complex manifestations of anxiety and depressive illness involve dysregulation of brain-derived neurotrophic factor (BDNF) [13,14] and N-methyl-d-aspartate receptor (NMDAR) [15], promoting disturbances in cellular signalling and neuronal plasticity. Among cellular pathways affected in the pathophysiology of depression, we can name the mammalian target of rapamycin (mTOR), mitogen-activated protein kinases (MAPK) or glycogen synthase kinase 3 (GSK-3), as discussed.

I_2-Imidazoline receptors (I_2-IRs) have been progressively attracting scientific interest as a promising biological target, which modulation could result in potential therapeutic effects. Several preclinical studies describe I_2-IRs involvement in neurological diseases such as AD, Parkinson's disease (PD) and multiple psychiatric disorders [16–18]. I_2-IRs have been associated with anxiety and depressive behaviours [16,19]. In preclinical models of mood disorders, several I_2-IR ligands exerted beneficial effects on non-cognitive symptoms [20,21]. Interestingly, agmatine, the endogenous I_2-IR ligand [22], has a modulatory effect on anxiety and depression [23,24]. Specifically, those studies that had utilized allegedly α2-selective imidazoline radioligands, i.e., [^{3}H]-clonidine, could be reinterpreted in terms of the increased number of those receptors in depression. Although the molecular identity of the I_2 binding site remains unknown, an I_2 binding site has been reported to be encoded by monoamine oxidase genes (both MAO-A and MAO-B), suggesting a novel explanation for the antidepressant efficacy of idazoxan, a prototypic I_2-IR ligand. We have previously described, MCR5 diethyl [(1-(3-chloro-4-fluorobenzyl)-5,5-dimethyl-4-phenyl-4,5-dihydro-1*H*-imidazol-4-yl]phosphonate] as an I_2-IR highly selective compound over α2-adrenoreceptors and high affinity for the I_2-IR [25], characterized by neuroprotective abilities in models of cognitive decline and AD [26,27].

The senescence-accelerated mouse prone 8 (SAMP8) is an accelerated ageing model, established through phenotypic selection from a common genetic pool of AKR/J-strain of mice [28–30]. Besides the age-related cognitive decline that mainly characterizes the SAMP8 model, this strain also displays anxiety- and depressive-like behaviour in comparison to their senescence-acceleration resistant counterparts, SAMR1 mice [28]. In particular, the SAMP8 mouse presents alterations in the serotoninergic system and BDNF expression, calcium signalling pathways and increased neuroinflammation that lead to the development of BPSD and in particular depressive-like behaviour [31]. Collectively, therefore it is believed that this rodent model is appropriate for studying depressive-like behaviour in an aged population with cognitive impairment.

In the present study, we assessed the cognitive and non-cognitive effects, especially anxiety- and antidepressant-like effects as the main BPSD behaviours of the I_2-IR ligand MCR5 diethyl [(1-(3-chloro-4-fluorobenzyl)-5,5-dimethyl-4-phenyl-4,5-dihydro-1*H*-imidazol-4-yl) phosphonate] in vivo, providing as well that the evidence referred to induced molecular changes that could explain such effects, using the SAMP8 mice model. As aforementioned, MCR5 tested in previous works of our group, presented neuroprotective and analgesic effects, showed promising results in models of brain damage [26] and prevented cognitive decline in SAMP8 aged female mice, including molecular changes associated with age and neurodegenerative processes [27]. Thus, we studied some molecular pathways related to neurodegeneration and neuropsychiatric disorders that are characteristic of age-related behavioural and cognitive abnormalities of SAMP8.

2. Methods

2.1. Animals

SAMR1 (n = 11) and SAMP8 (n = 25) male mice (10-month-old) were used to perform behavioural and molecular analyses. The animals were divided randomly into three groups: SAMR1 Control (SR1-Ct) (n = 11), SAMP8 Control (SP8-Ct) (n = 11) and SAMP8 treated with I_2-IR ligand MCR5 (5 mg/Kg) (SP8-MCR5) (n = 14). Animals had free access to food and water and were kept under standard temperature conditions (22 ± 2 °C) and a 12-h light/dark cycle (300 lux/0 lux). Control groups received water plus vehicle (1.8% 2-hydroxypropyl-β-cyclodextrin). MCR5 (5 mg/Kg/day) was dissolved in vehicle and administered through drinking water for 4 weeks. Water consumption was controlled each week, and I_2-IR ligand concentrations in water were adjusted accordingly to reach the optimal dose (see Figure 1).

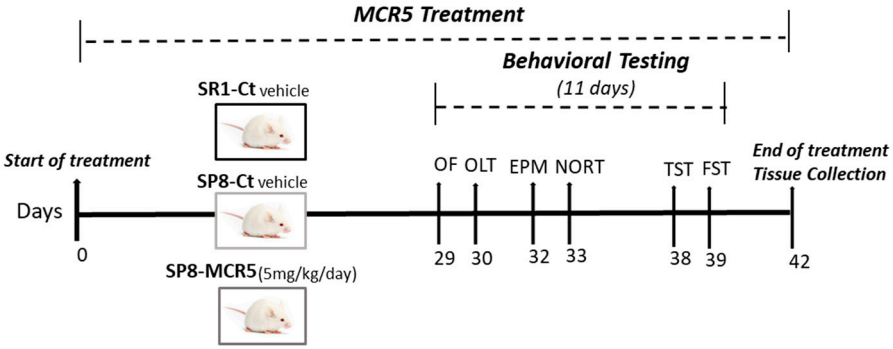

Figure 1. Scheme of experimental design.

All experimental procedures involving animals followed the standard ethical guidelines of European Communities Council Directive 86/609/EEC and by the Institutional Animal Care and Use Committee of the University of Barcelona (670/14/8102, approved at 11/14/2014) and by Generalitat de Catalunya (10291, approved 1/28/2018).

2.2. Evaluation of Anxiety- and Depressive-Like Behaviour as Well as Cognitive Performance

2.2.1. Tail Suspension Test (TST)

Briefly, to evaluate the potential anti-depressant effect of MCR5 in mice. Animals were suspended by their tail leads to an immobile posture using adhesive tape and hung approximately 30 cm above the table. The fragments, 17 cm each, of tape, were cut and an imprint 2 cm, on each fragment, was placed from one end. The task lasts for 6 min, and the duration of immobility was evaluated manually. Passively hanging was considered as immobility. The total time of mobility was subtracted from the 6 min of task time and was declared as the immobility time [32,33].

2.2.2. Forced Swimming Test (FST)

The cylindrical tank (10 cm internal diameter, 50 cm high) filled with water (10 cm height) at 22–25 °C required for mice forced to swim for 6 min. The mice behaviour to avoid the aversive situation was recorded during this time. The session was videotaped, and the time that each mouse remained mobile was entirely analysed. The total time of mobility was subtracted from the 6 min of task time and was called the immobility time. The mice were considered as immobile when they keep floating, doing only those movements necessary to maintain their heads out of the water [34].

2.2.3. Elevated Plus Maze (EPM)

The anxiety-related behaviour was assessed by elevated plus maze (EPM) [35]. The apparatus consisted of two open arms (30 × 5 × 15 cm), and two enclosed arms (30 × 5 × 15 cm) positioned 40 cm above the ground. The junction of four arms formed a central square platform (5 × 5 cm). Each mouse was located on the central platform facing and was allowed to move freely for 5 min. The behaviour parameters evaluated were the number of entries in the open arms and the percentage of time spent in the open and closed arms, among others, scored with SMART® vers.3.0 software. In addition, the anxiety index was calculated as follows: Anxiety Index = 1 − [([Open arm time/Test duration] + [Open arms entries/Total number of entries])/2] [36]. The tests were recorded using a camera attached to the roof and located above the apparatus.

2.2.4. Open Field Test (OFT)

In brief, the OFT was performed using a wall-enclosed area as previously described [37]. The ground was divided into two defined as the centre and peripheral areas. Behaviour was evaluated with SMART® ver.3.0 software, and each test was recorded for later evaluation using a camera located above the apparatus. Mice were located at the centre and allowed to explore the white polywood box (50 × 50 × 25 cm) for 5 min. Then, the animals were returned to their home cages, and the OFT apparatus was cleaned with 70% ethanol (EtOH). The parameters measured included centre time duration, rearings, defecations, and the locomotor activity, calculated as the sum of global distance moved in the arena for 5 min.

2.2.5. Novel Object Recognition Test (NORT)

In brief, mice were located in a 90°, two-arm, 25 × 20 × 5 cm black maze. The walls could be removed for easy cleaning. Before the memory phase, a 3-day-habituation was performed in which the mice were located individually in the apparatus for 10 min. On day 4, the familiarization phase took place, in which the animals were placed in the maze in the presence of two identical, novel objects (A + A) or (B + B) located at the end of each corner arm. During this 10-min acquisition trial, the mice were allowed to explore the two identical objects. After 2 h and 24 h from that trial, the animals were submitted to a 10-min retention trial in which one of the two objects was replaced by a novel object. The behaviour of the mice was recorded during the 2 h and 24 h retention trials using a camera attached to the roof and located above the apparatus. The time spent exploring the new object (TN) and the time spent exploring the old one (TO) were evaluated manually and the discrimination index (DI) was calculated as (TN-TO)/(TN+TO) [38]. To avoid olfactory cues, 70% EtOH was used to clean the arms and objects after test.

2.2.6. Object Location Test (OLT)

The test was performed in a cage (50 × 50 × 25 cm), in which three walls were white except one that was black, and lasted 3 days. On day 1, mice were familiarized to the arena for 10 min. On day 2, two identical objects (A + A) were located in front of the black wall, and the mice were freely allowed to explore both objects for 10 min (Trial 1—training phase). On day 3, after a retention period of 24 h mice were returned to the testing arena for another 10 min (Trial 2—testing phase) with one object moved to

a different position (opposite direction toward the black wall) and were allowed to explore. The trials were recorded, and the object exploration time was measured manually. The time sniffing the object in the old position (PO) and the time exploring the object in the new position (TN) were evaluated. The DI defined as (PN-TO)/(PN+PO) was determined as an indicator of the cognitive performance [39]. For the elimination of olfactory cues, 70% EtOH was used to clean the testing arena after each trial.

2.3. Determination of Transporters, Receptors and Alterations in Molecular Pathways

2.3.1. In Vitro Pharmacology: Binding Assays

The purpose of this study was to test MCR5 in Binding assays by using Eurofins radioligand assays. Briefly, binding for receptors 5-HT1A, 5-HT1B, 5-HT2A, 5-HT2B, ion channel 5-HT3 and 5-HT transporter (SERT) was studied using radioactively labelled ligands specific for each target in human recombinant cell lines (For details see Table S6). MCR5 was tested at 10 μM. MCR5 interaction was calculated as a % inhibition of the binding of a radioactively labelled ligand specific for each target. Percentages were calculated as follow: percent inhibition of control specific binding = 100 − [(measured specific binding/control specific binding) × 100]. Results showing an inhibition or stimulation higher than 50% are considered to represent significant effects of the test compounds.

2.3.2. Tissue Preparation for Biochemical Analysis

Mice were euthanised by cervical dislocation 3 days after the behavioural and cognitive tests were finished. Brains were immediately dissected out from the skull. The hippocampus of each animal was separated, snap frozen in dry ice and kept at −80 °C.

For Western Blot (WB) and immunodetection, hippocampus samples were thawed and mixed in lysis buffer containing phosphatase and protease inhibitors (Cocktail II, Sigma-Aldrich). Once mixed, samples were maintained on ice for 30 min. Samples were centrifugated at 10,000× *g* for 30 min at 4 °C, and the supernatants were collected and saved at −80 °C. Total protein amounts were obtained, and the Bradford method was used to determine protein concentration.

For ELISA evaluation, samples were processed following the instructions provided by the kit manufacturer (Biosensis, Thebarton, Australia). In brief, hippocampus samples were thawed and mixed through sonication at 4 °C in 200 volumes of RIPA buffer (50 mM Tris-HCl, 150 mM NaCl, 1% (*v/v*) NP-40 and 0.5% (*w/v*) sodium deoxycholate, pH = 7.5–8) containing a protease and phosphatase inhibitor cocktail. Once mixed, samples were maintained on ice for 30 min. Sample sonication and cooling with ice were performed. Samples were centrifuged at 14,000× *g* for 30 min at 4 °C, and the supernatants were obtained and maintained at −80 °C. Protein amount was quantified through the Bradford method.

2.3.3. Protein Levels Determination by Western Blot

For WB, aliquots of 15 μg of hippocampal protein were used. Protein samples were isolated by Sodium dodecyl sulphate-Polyacrylamide gel electrophoresis SDS–PAGE (8–15%) and transferred onto PVDF membranes (Millipore, Burlington, MA, USA). The membranes were blocked in 5% non-fat milk or 5% bovine serum albumin (BSA) in Tris-buffered saline (TBS) solution with 0.1% Tween 20 (TBS-T) during 1 h at room temperature. Next, the membranes were incubated overnight at 4 °C containing the primary antibodies listed in Table S1. The antibodies were dissolved in TBS-T with 5% BSA or 5% non-fat milk.

Membranes were cleaned and incubated with the secondary antibodies for 1 h at room temperature. Immunoreactive proteins were detected with a chemiluminescence-based detection kit, following the manufacturer's protocol (ECL Kit, Millipore, Burlington, MA, USA). Digital images were collected using a ChemiDoc XRS+ System (BioRad, Hercules, CA, USA). Semi-quantitative analyses of the band intensities were carried out using ImageLab software (BioRad), and results were expressed in arbitrary

units (AU). Values were normalized to Glyceraldehyde-3-phosphate dehydrogenase (GAPDH) or β-Actin.

2.3.4. Determination of ProBDNF and MBDNF Levels in the Hippocampus

The hippocampal determination of pro-Brain-derived neurotrophic factor (proBDNF) and mature-Brain-derived neurotrophic factor (mBDNF) protein levels was made according the instructions of the ELISA kit (Biosensis, Thebarton, Australia).

2.3.5. RNA Extraction and Gene Expression Determination

RNA isolation from hippocampal samples was performed using the TRIzol® reagent according to the manufacturer's protocols (Bioline Reagent, Memphis, TN, USA). The yield, purity and quality of RNA were determined with a NanoDrop™ND-1000 (Thermo Scientific, Waltham, MA, USA) apparatus and an Agilent 2100B Bioanalyzer (Agilent Technologies, Santa Clara, CA, USA). RNAs with 260/280 ratios and RNA integrity number (RIN) higher than 1.9 and 7.5, respectively, were collected. Reverse Transcription-Polymerase Chain Reaction (RT-PCR) was performed as follows: 2 μg of messenger RNA (mRNA) was reverse-transcribed using the high capacity cDNA reverse transcription kit (Applied Biosystems, Foster City, CA, USA). Real-time quantitative PCR (qPCR) was employed to quantify the mRNA expression of the genes evaluated listed in Table S2.

SYBR® Green real-time PCR was performed using a Step One Plus Detection System (Applied-Biosystems) employing SYBR® Green PCR Master Mix (Applied-Biosystems). Each reaction mixture contained 6.75 μL of complementary DNA (cDNA) (2 μg concentration), 0.75 μL of each primer (100 nM concentration), and 6.75 μL of SYBR® Green PCR Master Mix (2X).

Data were measured using the comparative cycle threshold (Ct) method (ΔΔCt), where the housekeeping gene expression *β-Actin* was used to normalize differences in sample loading and preparation. Each sample was evaluated per duplicate, and the results represent the n-fold difference of the gene expression among groups.

2.4. Data Acquisition and Statistical Analysis

Data are expressed as mean ± standard error of the mean (SEM). Statistical analyses were performed using One-Way analysis of variance (ANOVA) with Tukey's post hoc tests or two-tail Student's t-test if it was necessary through GraphPad Prism ver. 8 for Mac (GraphPad Software, San Diego, CA, USA). Statistical differences were considered significant when values of p were < 0.05. Statistical outliers were discriminated using Grubbs' test and were removed from the analysis.

3. Results

3.1. I_2-IR Ligand MCR5 Reduced Cognitive Loss in SAMP8 Male Mice

NORT and OLT revealed robust impairment in working, and spatial memory in SAMP8 control in comparison with age and sex mated SAMR1 control (Figure 2B–D). Remarkably, after treatment with MCR5, a significant increase in the discrimination index (DI) was obtained both in the NORT short-term memory test (Figure 2B) and the NORT long-term memory test in treated SAMP8 compared to the SAMP8 control group (Figure 2C). Moreover, DI for treated SAMP8 group was closer to DI delivered by SAMR1, indicating a neuroprotective effect for MCR5. Similarly, in OLT, I_2-IR treatment significantly improved spatial memory in treated SAMP8 compared to the SAMP8 control group by increasing the DI, further demonstrating the beneficial effect of MCR5 on cognitive loss associated to age in SAMP8 mice (Figure 2D). The summary data of the NORT and OLT are presented in Supplementary Table S3.

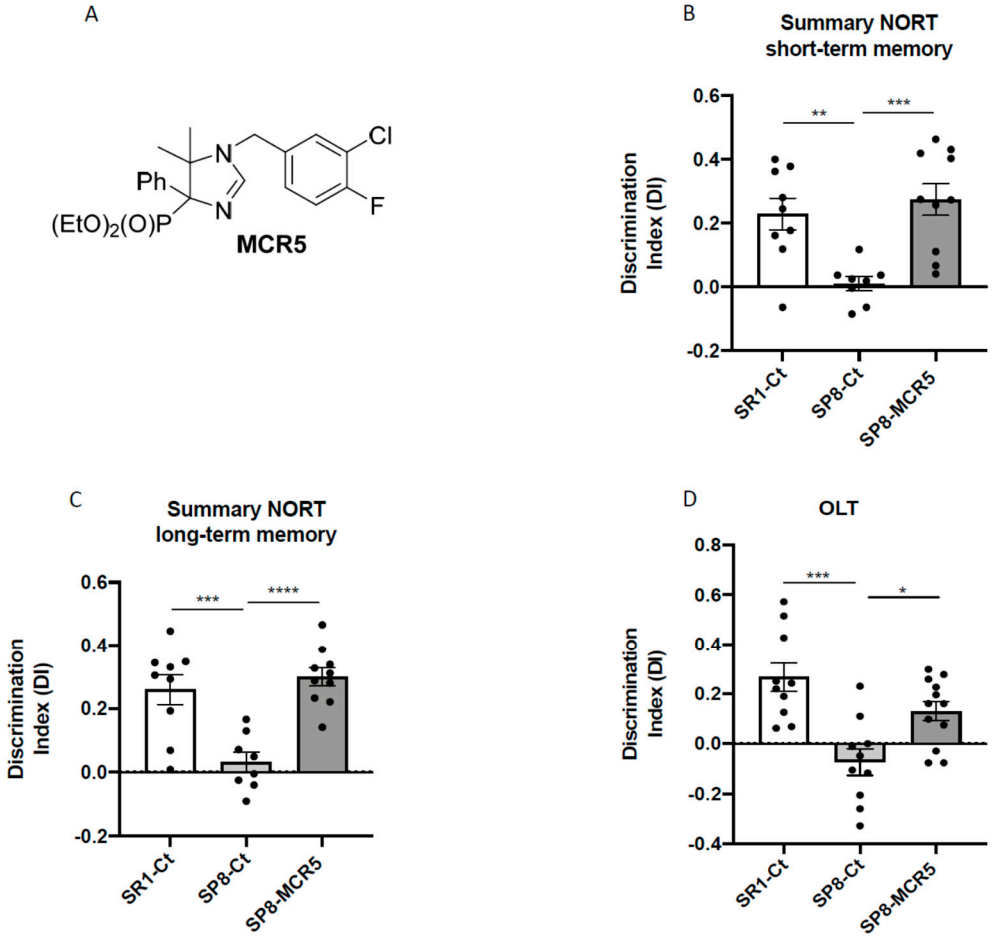

Figure 2. Structure of I_2-IR ligand MCR5 (**A**). Results of Novel object recognition test (NORT), and Object location test (OLT) in male mice at 10-month-old SR1 and SP8 Ct mice groups and SP8 treated with I_2-IR ligand MCR5 (5 mg/Kg) mice group. For NORT: Summary of Discrimination Index (DI) from short-term memory (**B**), and summary of DI from long-term memory (**C**). For OLT: Summary of DI (**D**). Values represented are mean ± Standard error of the mean (SEM); $n = 36$ (SR1-Ct $n = 11$; SP8-Ct $n = 11$; SP8-MCR5 $n = 14$). * $p < 0.05$; ** $p < 0.01$; *** $p < 0.001$; **** $p < 0.0001$.

3.2. I_2-IR Ligand MCR5 Improved Emotional Parameters Associated with Fear- Anxiety- and Depressive-Like Behaviours in SAMP8 Male Mice

To evaluate the anti-depressant like effect of MCR5, we assessed the TST and FST. By one hand, an increase in both immobility and floating time was obtained from the TST and FST respectively between SAMR1 and SAMP8 control groups (Figure 3A–F), corroborating the depressive-like behaviour described in SAMP8 mice. On the other hand, MCR5 treatment induced a significant decrease in time of immobility and/or floating in treated SAMP8 when compared to SAMP8 control. Therefore, in both widely used tests for the study of depression-like behaviour, we were able to observe that MCR5 treatment reversed the depressive-like signs that SAMP8 mice exhibit, driving them to a similar behaviour to SAMR1.

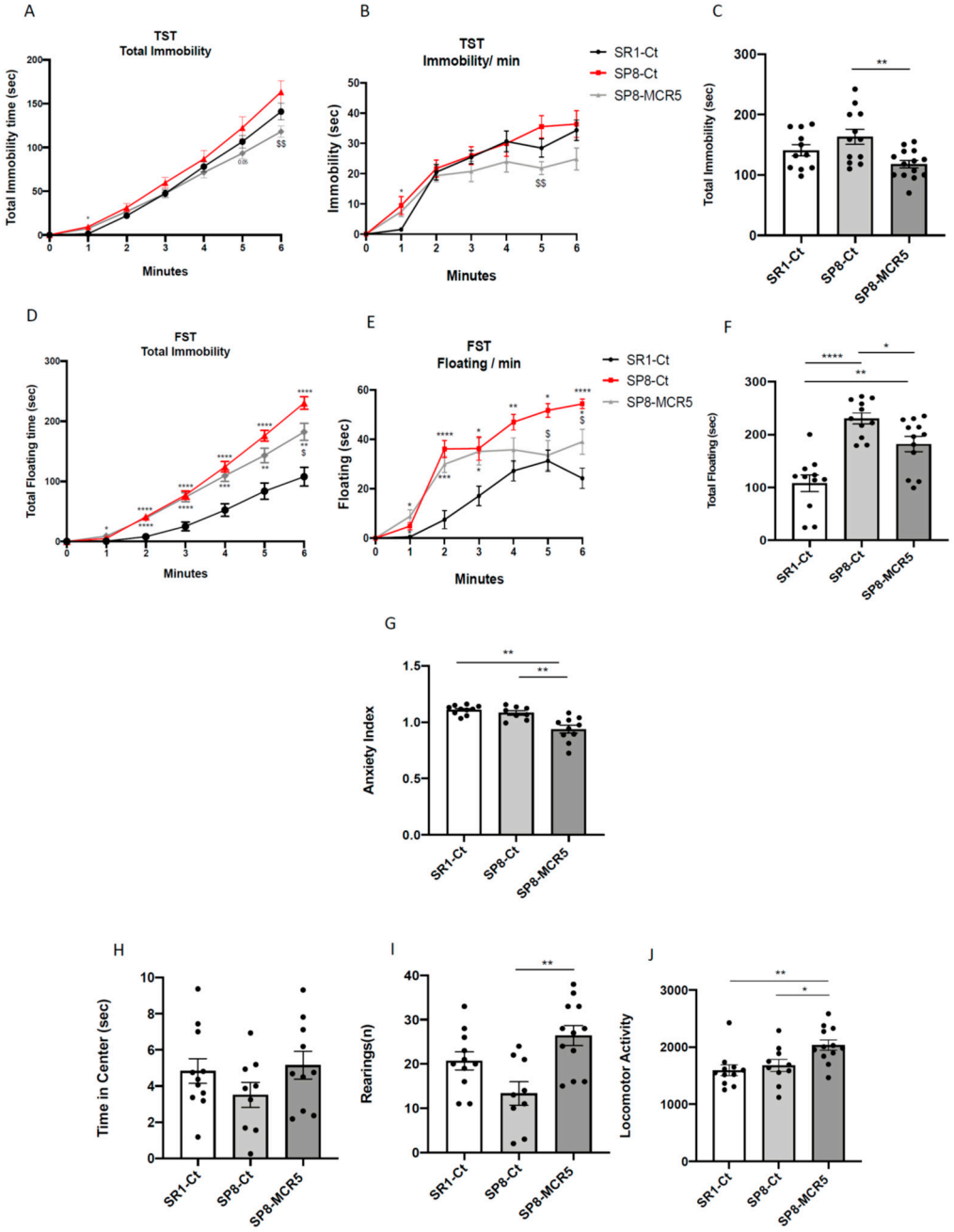

Figure 3. Results of Tail suspension test (TST), Forced swimming test (FST), Elevated plus maze (EPM), and Open field test (OFT) in male mice at 10-month-old SR1 and SP8 Ct mice groups and SP8 treated with I_2-IR ligand MCR5 (5 mg/Kg) mice group. For TST: total immobility curve (**A**), immobility/min (**B**), and total immobility (**C**). For FST: total immobility curve (**D**), floating/min (**E**), and total floating (**F**). For EPM: anxiety index (**G**). For OFT: time in the centre (**H**), rearings (**I**), and locomotor activity (**J**). Values represented are mean ± Standard error of the mean (SEM); n = 36 (SR1-Ct n = 11; SP8-Ct n = 11; SP8-MCR5 n = 14). * $p < 0.05$; ** $p < 0.01$; *** $p < 0.001$; **** $p < 0.0001$.

Behavioural and emotional changes after MCR5 treatment were evaluated by EPM and OFT. Regarding the EPM, although there were found no differences in the anxiety-like phenotype between the SAMR1 control group and SAMP8 control group, MCR5 treatment induced an anxiolytic effect on SAMP8 mice in comparison with both control groups (Figure 3G). Additional parameters measured in the EPM are presented in Supplementary Table S4. The OFT demonstrated that SAMP8 control group exhibited increased fear, presenting decreased time spent in centre as well as vertical activity

or rearings (Figure 3H,I). Strikingly, MCR5 treatment induced an anxiolytic effect on SAMP8 mice in comparison with the SAMP8 control group (Figure 3H,I). Furthermore, according to the results obtained in the OFT paradigm, locomotor activity was improved in SAMP8 treated group (Figure 3J). Additional parameters and statistical scores obtained in the OFT are depicted in Supplementary Table S5. Thus, results obtained in both EPM and OFT demonstrated changes in fear-anxiety-like behaviour and locomotor activity after treatment with MCR5.

3.3. Interaction of I_2-IR Ligand MCR5 with Serotonin Receptors and Transporter

Provided that the serotoninergic system is implicated in depressive behaviour, it was worth paying attention to the effect of MCR5 on serotonin receptors and transporter. Binding studies with 10 μM MCR5 to the 5-HT receptors and 5-HT transporter were performed by Eurofins (https://www.eurofinsdiscoveryservices.com/). The experiment was performed following Eurofins validation Standard Operating Procedure. The compound binding was calculated as a % inhibition of the binding of each radioactively labelled ligand specific for its target. Results indicated that MCR5 did not display a specific capacity to displace specific ligands for 5-HT_{1A}, 5-HT_{1B}, 5-HT_{2A}, 5-HT_{2B}, ion channel 5-HT_3 and 5-HT transporter (Table S6).

Moreover, we studied the gene expression of *5-HT_{1A}*, *5-HT_{1B}* and *5-HT_{2A}* receptors. As described, SAMP8 only presented a significant reduction in gene expression of *5-HT_{1A}* and *5-HT_{2A}* receptors compared to the SAMR1 control group (Figure 4A). Interestingly, treatment with MCR5 was only able to produce slight restoration of *5-HT_{2A}* gene expression in SAMP8 (Figure 4A). Likewise, protein levels of SERT were unchanged between SAMR1 and SAMP8 control groups, and the MCR5 treatment did not alter the transporter's protein levels (Figure 4B,C).

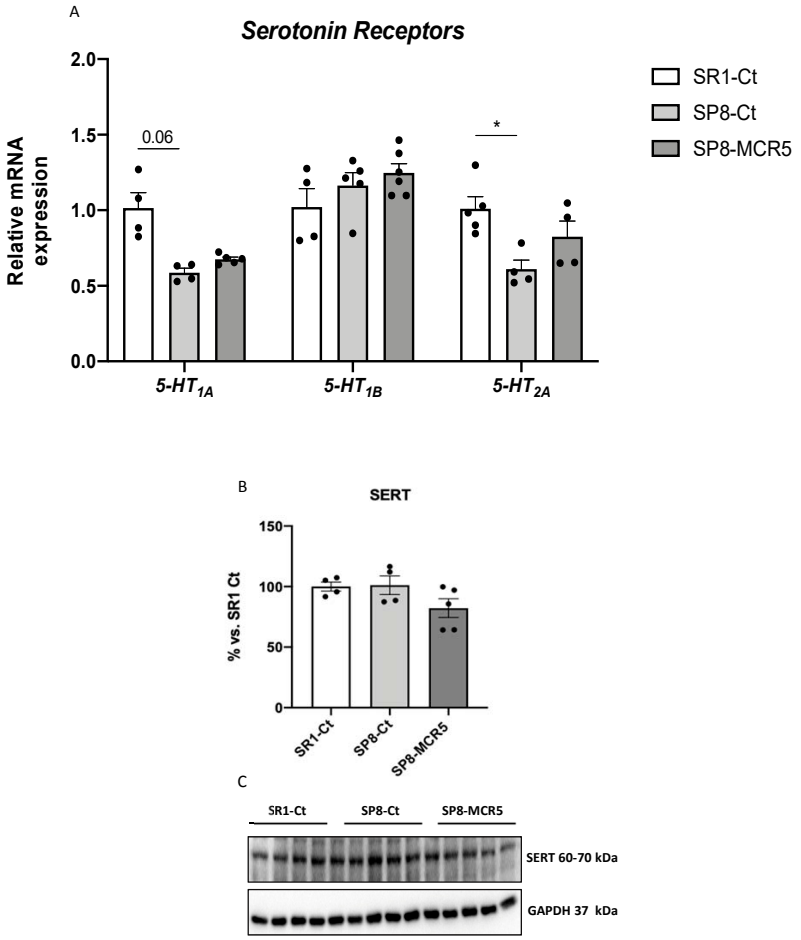

Figure 4. Representative gene expression for *5-HT$_{1A}$*, *5-HT$_{1B}$*, and *5-HT$_{2A}$* (**A**). Representative Western Blot and quantification for SERT (**B**,**C**). Gene expression levels were determined by real-time PCR. Values in bar graphs are adjusted to 100% for protein levels of the control SAMR1 (SR1-Ct). Values are the mean ± Standard error of the mean (SEM); (n = 4–6 for each group). * $p < 0.05$.

3.4. MCR5 Enhanced AKT/mTOR/GSK3β Pathways Promoting a Reduction of Pro-Inflammatory Cytokines in SAMP8 Male Mice

Critical proteins linked to molecular pathways that are altered in the pathology of depression associated with neuronal inflammation were evaluated. WB analysis showed a significant decrease in p-AKT/AKT ratio (protein kinase B) in SAMP8 control in comparison with the SAMR1 control group. MCR5 administration to SAMP8 promoted a significant increase in p-AKT/AKT ratio compared to SAMP8 control (Figure 5A,H). We observed a slight but not significant increase in Phosphatidylinositol 3,4,5-trisphosphate 3-phosphatase (PTEN) protein levels in SAMP8 mice in comparison with SAMR1. Conversely, we found a significant diminution in PTEN levels in SAMP8 treated mice compared to the SAMP8 control group (Figure 5B,H). Accordingly, protein levels of GSK3β phosphorylated in Ser9 (p-GSK3β(Ser9)) were significantly increased after MCR5 treatment in SAMP8 mice. No significant changes between SAMR1 control and SAMP8 control were determined for this kinase (Figure 5C,H). On the other hand, p-mTOR/mTOR ratio was unaltered among the three experimental groups (Figure 5D,I). Interestingly, MCR5 increased in a significant way p-TORC1/TORC1 ratio in SAMP8 treated mice compared to both control groups (Figure 4E,H). Lastly, albeit did not reach significance, a tendency to increase p-p70S6K/p70S6K ratio after I_2-IR ligand treatment compared to both control groups, was observed (Figure 5F,H).

Considering the results obtained on these pathways, we studied pro-inflammatory cytokines markers in the hippocampus of SAMR1 and SAMP8 mice. Significantly increased gene expression of *Il-1β* and *Il-6* in SAMP8 control in comparison with SAMR1 mice was determined, confirming the inflammatory phenotype related to anxiety- and depressive-like behaviours presented by SAMP8 (Figure 5H). A significant reduction of *Tnf-α* gene expression in MCR5 treated SAMP8 mice group compared to both control groups was found (Figure 5I). Lastly, a tendency to reduce *Il-1β* and *Il-6* gene expression in MCR5 treated SAMP8 mice group compared to the SAMP8 control group, restoring levels to those of SAMR1 control strain was found (Figure 5I). Jointly with the decrease in the proinflammatory cytokines, an increase in the anti-inflammatory cytokine ratio, TGF-1β monomer/dimer was induced by MCR5 in SAMP8 treated mice (Figure 5H,G).

3.5. Changes in PKA/CREB and NMDAR/CDK5/DARPP32 Signalling Cascades after Treatment with I_2-IR Ligand MCR5 in SAMP8 Male Mice

A significant increase in PKA protein levels was found after MCR5 treatment in SAMP8 compared to untreated SAMP8 control, which expressed slightly lower levels of the mentioned kinase in comparison with SAMR1 control (Figure 6A,G). Accordingly, we found a diminished p-cAMP response element-binding (CREB)/CREB ratio in SAMP8 mice group compared to SAMR1 mice group, and MCR5 treatment restored the ratio in SAMP8 treated mice to SAMR1 levels (Figure 6B,G). A significant increase in the p-NMDA2B/NMDA2B ratio between the SAMR1 control, and SAMP8 control was observed (Figure 6C,G), and MCR5 increased p-NMDA2B/NMDA2B ratio in treated SAMP8 mice in comparison with the SAMP8 control. Moreover, we determined a significant reduction in the p-CDK5/CDK5 ratio between SAMR1 control and SAMP8 control (Figure 6D,G). Besides, a significant reduction in the p-CDK5/CDK5 ratio in SAMP8 treated mice group in comparison with the SAMP8 control mice was found. Conversely, we found reduced p-DARPP32 (Thr75)/DARPP32 ratio in the SAMR1 control group and SAMP8 treated group compared to the SAMP8 control, being significant only in the SAMP8 treated group (Figure 6E,G). Finally, we found significantly higher levels of ratio p-Erk$_{1/2}$/Erk$_{1/2}$ were determined in SAMP8 control mice when compared to SAMR1 control, whereas MCR5 restored p-Erk$_{1/2}$/Erk$_{1/2}$ to SAMR1 levels (Figure 6F,G).

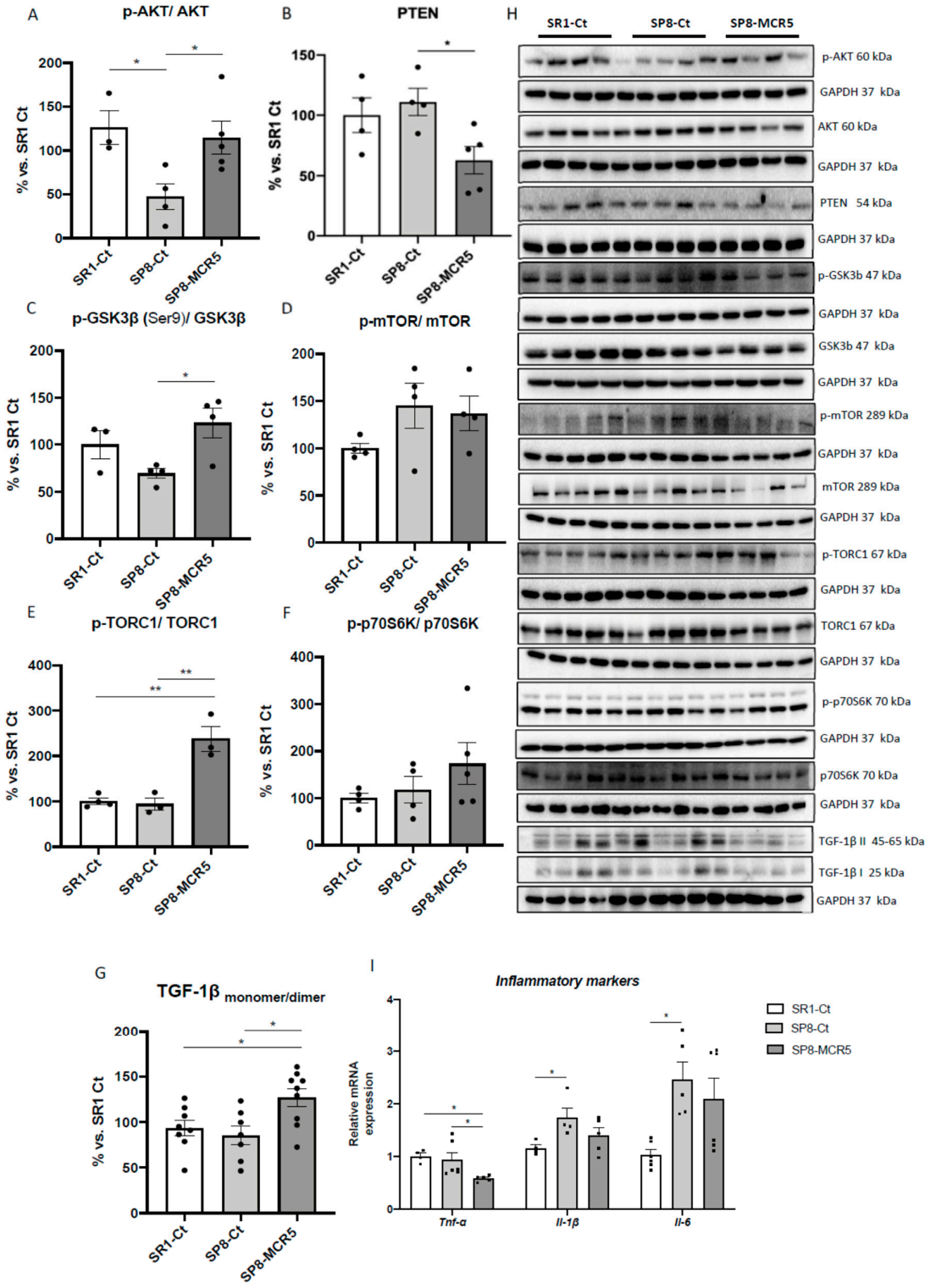

Figure 5. Representative Western blots and quantifications for the ratio of p-AKT/AKT, PTEN, ratio p-GSK3β(Ser9)/GSK3β, ratio p-mTOR/mTOR, ratio p-TORC1/TORC1, p-p70S6K/p70S6K, and TGF-1β monomer/dimer (**A**–**H**). Values in bar graphs are adjusted to 100% for protein levels of the control SAMR1 (SR1-Ct). Representative gene expression for *Tnf-α*, *Il-1β*, and *Il-6* (**I**). Gene expression levels were determined by real-time PCR. Values are the mean ± Standard error of the mean (SEM); (n = 4–6 for each group). * $p < 0.05$; ** $p < 0.01$.

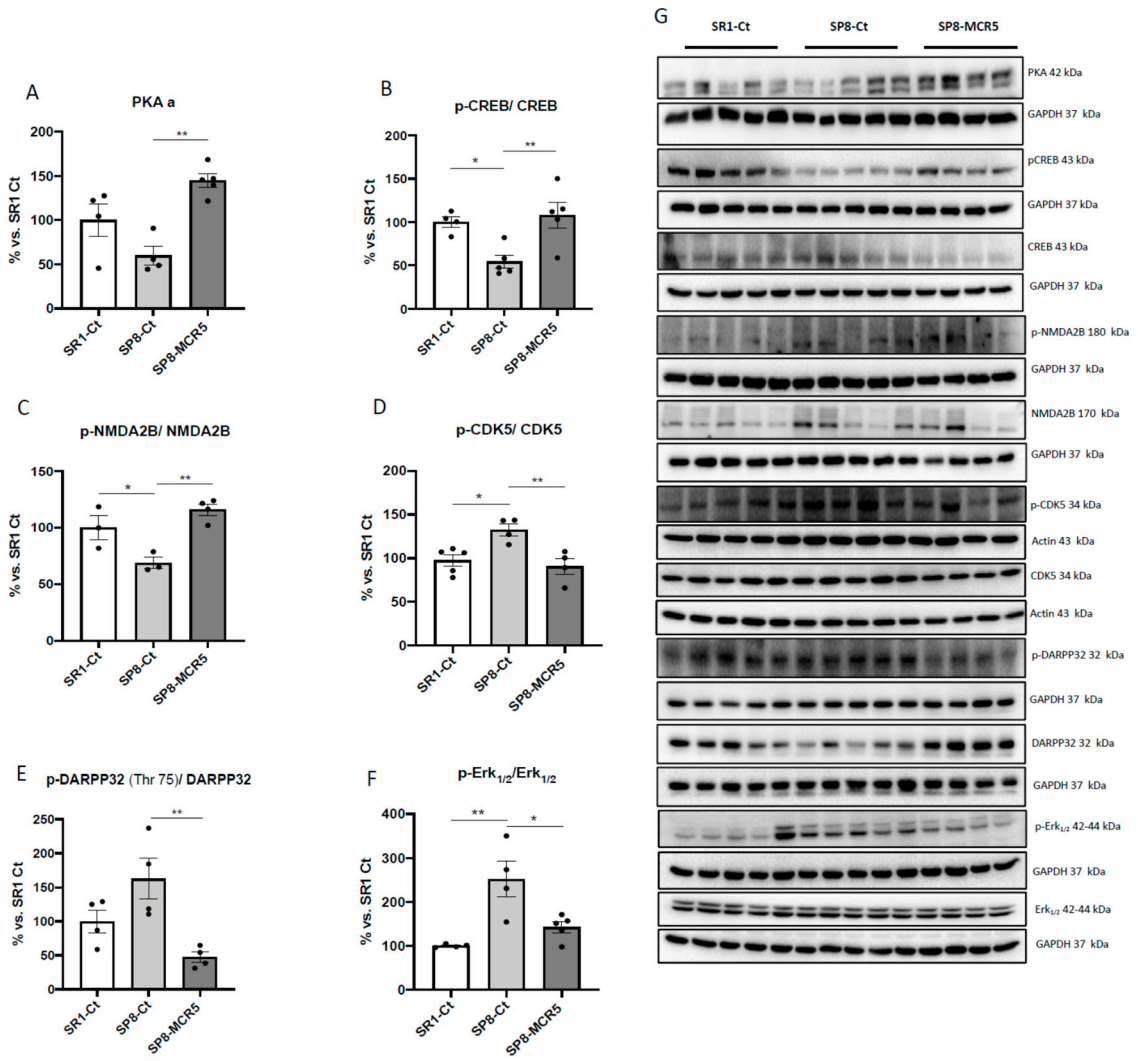

Figure 6. Representative Western blots and quantifications for PKA a, the ratio p-NMDA2B/NMDA2B, ratio p-DARPP32(Thr75)/DARPP32, ratio p-CDK5/CDK5, ratio p-CREB/CREB and p-Erk$_{1/2}$/Erk$_{1/2}$(**A**–**G**). Values in bar graphs are adjusted to 100% for protein levels of the control SAMR1 (SR1-Ct). Values represented are mean ± Standard error of the mean (SEM); (n = 4–6 for each group). * $p < 0.05$; ** $p < 0.01$.

3.6. Effects of I_2-IR Ligand MCR5 on BDNF/TrkB/NGFR(p75) Signalling Pathway after Treatment with MCR5

An increase in proBDNF protein levels in both SAMP8 groups in comparison with the SAMR1 control group is observed, albeit no significant differences were found (Figure 7A). Likewise, no changes in the mBDNF protein levels among experimental groups were found (Figure 7B). Pursuing BDNF molecular pathways, TrkB levels were also evaluated. Ratio TrkB-truncated (TL)/Full Length (FL) was slightly higher in the SAMP8 group compared to the SAMR1 group and was significantly reduced after MCR5 treatment (Figure 7C,F). According to these findings, a significant increase in nerve growth factor receptor (NGFR) protein levels in MCR5 treated SAMP8 in comparison with SAMP8 mice was found. Besides, a significant increase in NGFR protein levels in SAMR1 mice compared to the SAMP8 control was determined (Figure 7D,G). Lastly, we also extend the analysis of the Postsynaptic density 95 (PSD95) protein levels, a synaptic plasticity marker, which is regulated by BDNF/TrkB signalling and AKT/mTOR/GSK3β. Noteworthy, we found higher levels in SAMP8 treated with MCR5 than in control mice groups (Figure 7F,G).

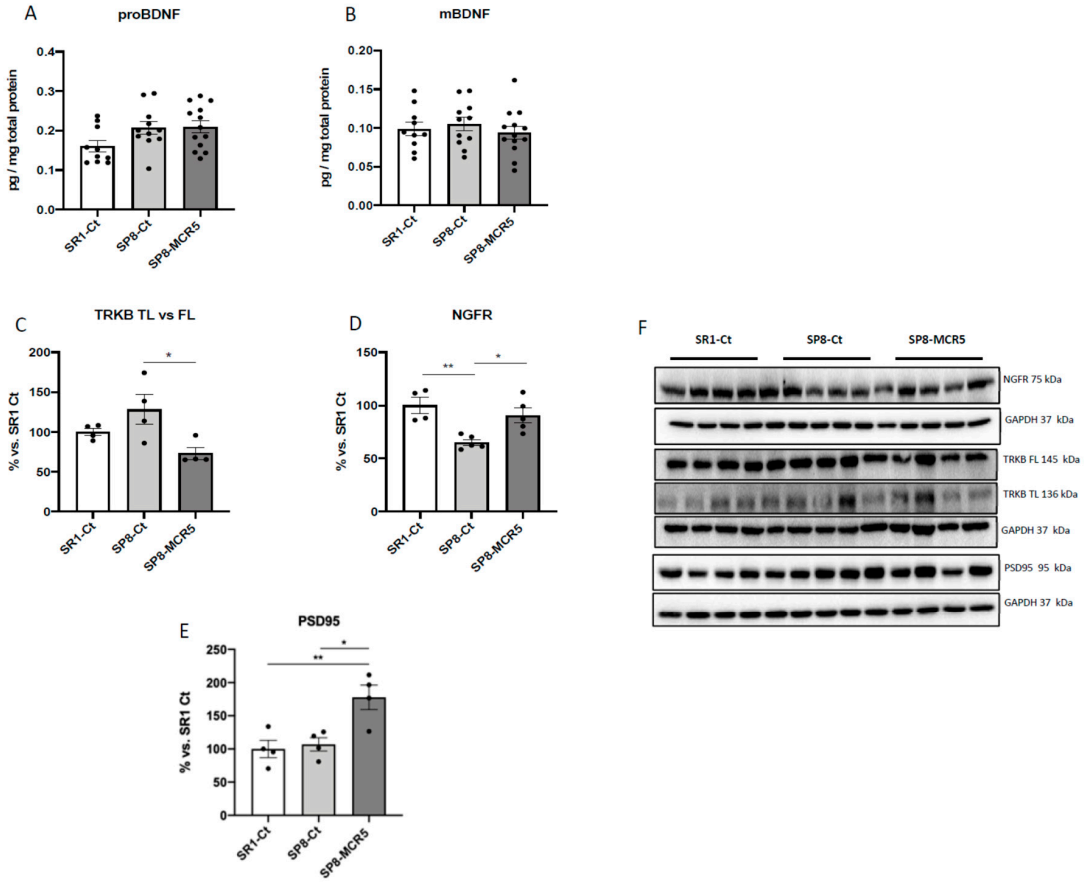

Figure 7. Protein levels of proBDNF (**A**), and mBDNF (**B**). Representative Western Blot and quantifications for ratio TrkB-TL vs. TrkB-FL, NGFR, and PSD95 (**C**–**F**). Values represented are mean ± Standard error of the mean (SEM); (n = 4–13 for each group). * $p < 0.05$; ** $p < 0.01$.

4. Discussion and Conclusions

Besides neurodegeneration, AD has been associated with increased incidents of neuropsychiatric disorders in humans, such as anxiety and depression, among other BPSD. New research has to be performed to face this collateral complication of AD because current therapies for both AD and BPSD are not completely effective and safe. On the one hand, some AD drugs can develop BPSD signs as adverse effects, i.e., memantine. On the other hand, BPSD drugs exacerbate cognitive impairment [7].

As aforementioned, I_2-IR are associated with the pathogenesis of several brain disorders [40,41] and neurodegenerative diseases such as AD [18]. Furthermore, I_2-IR ligand MCR5 demonstrated neuroprotective effects under different interventions and rodent models [26,27,42]. In line with these results, MCR5 treatment improved cognitive decline presented by older SAMP8 male mice, including working and spatial memory by using NORT and OLT, respectively. The behavioural tests applied demonstrated that older SAMP8 presented, in whole, anxiety- and depressive-like behaviours, as well as fearful behaviour, with less locomotion and rears, avoiding the OF centre zone. In the present study, we showed a substantial improvement in BSPD and cognitive performance, demonstrating anti-anxiety- and anti-depressant-like effects after treatment with MCR5 in older SAMP8. Therefore, to our knowledge, this is the first study in which both changes have been demonstrated in AD mice for an I_2-IR ligand.

Those non-cognitive and cognitive modifications promoted by MCR5 were accompanied by changes in some molecular pathways associated with ND process presented in these brain disorders. Previously it has been demonstrated that serotonin receptor densities such as 5-HT_{2A} did not suffer changes with age in SAMR1 compared to SAMP8 mice, whereas SERT increases at 9 months of age [31]. Regarding the serotoninergic system, here, we did not observe any significant change in gene expression of serotonin receptors and SERT protein levels after MCR5 treatment. Additionally, MCR5 did not bind to these membrane structures, allowing discarding an antidepressant effect mediated by inhibition of SERT or by interaction with 5-HT receptors.

It is important to note that, although the dopamine and serotonin pathways are the major targets for neuropsychiatric drugs, new mechanisms have been described, including mechanisms related to the neurodegenerative process presented in AD [43]. Indeed, it is well-demonstrated that I_2-IR neuroprotective effects are mediated by pleiotropic mechanisms.

Accumulating evidence suggests that the pathology of main brain disorders is associated with neuronal inflammation [44,45]. It has been described that AKT/GSK3/mTOR signalling is involved in the immune cell activation, downregulating pro-inflammatory cytokines such as TNF-α, IL-1β, IL-6, and IFN-γ and upregulating the anti-inflammatory cytokines [43,46]. In addition, recent studies have demonstrated that both dopamine and serotonin exert part of their actions by modulating the activity of this pathway [47]. In this study, we reported that the I_2-IR ligand treatment modified levels of AKT/GSK3/mTOR key proteins that might explain in part the reduction in the gene expression of the pro-inflammatory cytokine such as *Tnf-α*, *Il-1β* and *Il-6*. Conjointly with increased pro-inflammatory markers, a deficit of anti-inflammatory markers such as TGF-1β has been reported, contributing to inflammaging and cognitive impairment both in AD and other brain disorders such as depression [48,49]. I_2-IR ligand treatment also increased levels of active TGF-1β. TGF-1β, besides Smad-mediated pathways, activates Smad-independent pathways, including the PIK3/AKT [50], further supporting the alterations observed in this pathway after I_2 -IR treatment.

Phosphorylation of AKT protein has been shown to promote neuroprotection against cell death, increasing cell survival [51]. On the one hand, we found increased levels of p-AKT in treated SAMP8 mice in comparison to the SAMP8 control, reaching the healthy mice group, SAMR1. On the other hand, PTEN a protein that regulates AKT kinase activity was downregulated in SAMP8 treated mice. In line with our findings, fluoxetine upregulates the expression of the p-AKT [52]. Of note, SAMP8 mice showed a higher level of activated GSK3β in comparison with SAMR1 [53,54]. Moreover, some antidepressant drugs or atypical antipsychotics such as lithium regulate GSK3 by inhibiting its activity in the brain [55,56]. Changes in GSK3β activity described in SAMP8 mice reinforces the depressive-like behaviour shown. Interestingly, I_2-IR treatment was able to decrease the GSK3β activity, giving clues for the possible pathway modulated through this receptor rending on anxiety and depression as well as improvement in cognition observed after MCR5 treatment. It can be kept in mind that inhibition of GSK3β may result in a reduction in tau hyperphosphorylation leading to the reduction in neurofibrillary tangles, then neuronal dysfunction accordingly with previous results demonstrating a neuroprotective role for MCR5 [42]. Moreover, dysregulation of mTOR signalling and concretely mTORC1, has been described under chronic restrain stress and administration of escitalopram and paroxetine prevented these changes [57]. Likewise, ketamine has been reported to activate mTOR and downstream constituents such as p70S6K resulting in increased levels of postsynaptic density proteins such as PSD95, GluR1, synapsin I [58]. In this study, we demonstrated that MCR5 treatment significantly increased ratio p-mTORC1 in SAMP8 mice in parallel with an increase in PSD95 levels, which can further explain the improvement of both cognitive and non-cognitive signs presented by SAMP8 mice.

Other signalling cascades altered after MCR5 treatment included NMDAR/CDK5/DARPP32 and PKA/CREB signalling. MCR5 inhibited NMDAR/CDK5/DARPP32 in treated SAMP8. Based on our findings, we suggest that MCR5 might exert anti-depressant-like and neuroprotective effects through this signalling pathway. DARPP32 modulates the dopamine pathway [59] and is, therefore, a key regulator for the pathogenesis of several neuropsychiatric disorders [60]. Here, we found a significant reduction of p-CDK5 and p-DARPP32 (Thr75) in SAMP8 treated with I_2-IR ligand, implicating this pathway in the beneficial role of MCR5 in SAMP8 neuropathology. Moreover, phosphorylation of DARPP-32 in Thr75 by p-CDK5, in turn, inhibits PKA and thereby reduces the efficacy of dopamine signalling [61]. Interestingly, consistent with the reported decreased levels of p-DARPP32 in Thr75, increased PKA levels were determined in SAMP8 mice treated with I_2-IR ligand MCR5. Indeed, we also found that MCR5 treatment induced the activation of the PKA/CREB signalling cascade, increasing protein levels of both PKA and p-CREB. Of interest, several studies demonstrated that activation of PKA/CREB pathway in the hippocampus leads to neuroprotective effects not only by upregulating BDNF protein levels, but also reducing neuroinflammation in several brain disorders such as anxiety, in an early episode of depression and AD [62]. This evidence is coincident with the diminution of pro-inflammatory cytokines such as *Tnf-α*, *Il-1β* and *Il-6* found after MCR5 administration. Given its implication in CREB phosphorylation, we also investigated the levels of p-$Erk_{1/2}$. Surprisingly, its levels were found increased in SAMP8 control mice and significantly decreased in the SAMP8 treated mice. However, increased $ERK_{1/2}$ activation has been reported in socially defeated animals, and $Erk_{1/2}$ mediated increase in inflammatory markers is established [63–65]. In the present study, a reduction of $Erk_{1/2}$ activation induced by MCR5 treatment is also consistent with the decreased pro-inflammatory markers observed.

Given that downregulation of BDNF function has been demonstrated in the brains of patients with neurodegenerative or neuropsychiatric disorders, evaluation of the BDNF levels and TrKB signalling in the hippocampus after MCR5 treatment was relevant [13,14]. Indeed, one cause for the reduced BDNF levels is due to BDNF/TrkB signalling dysfunction mediated by endogenous small molecules, driving to changes associated with the above-mentioned pathways [66,67]. In our hands, MCR5 treatment did not produce any change in proBDNF and mBDNF protein levels. However, MCR5 ameliorated BDNF/TrkB signalling, promoting TrkB-FL protein levels. BDNF also binds to nerve growth factor receptor (NGFR), also known as p75 neurotrophin receptor (p75NTR), albeit with a low-affinity [68,69]. MCR5 was also able to increase the levels of NGFR. These changes, jointly with the increase of the synaptic marker PSD95 levels that was demonstrated in SAMP8 mice after I_2-IR ligand treatment, revealed that MCR5 promoted synaptic function, which is reported impaired in brain disorders.

Altogether, these results demonstrated that MCR5 also plays a neuroprotective role against neurodegeneration induced through pathways associated with anxiety and depression, pointing out an alternative target for slowing down the disease progression (Figure 8).

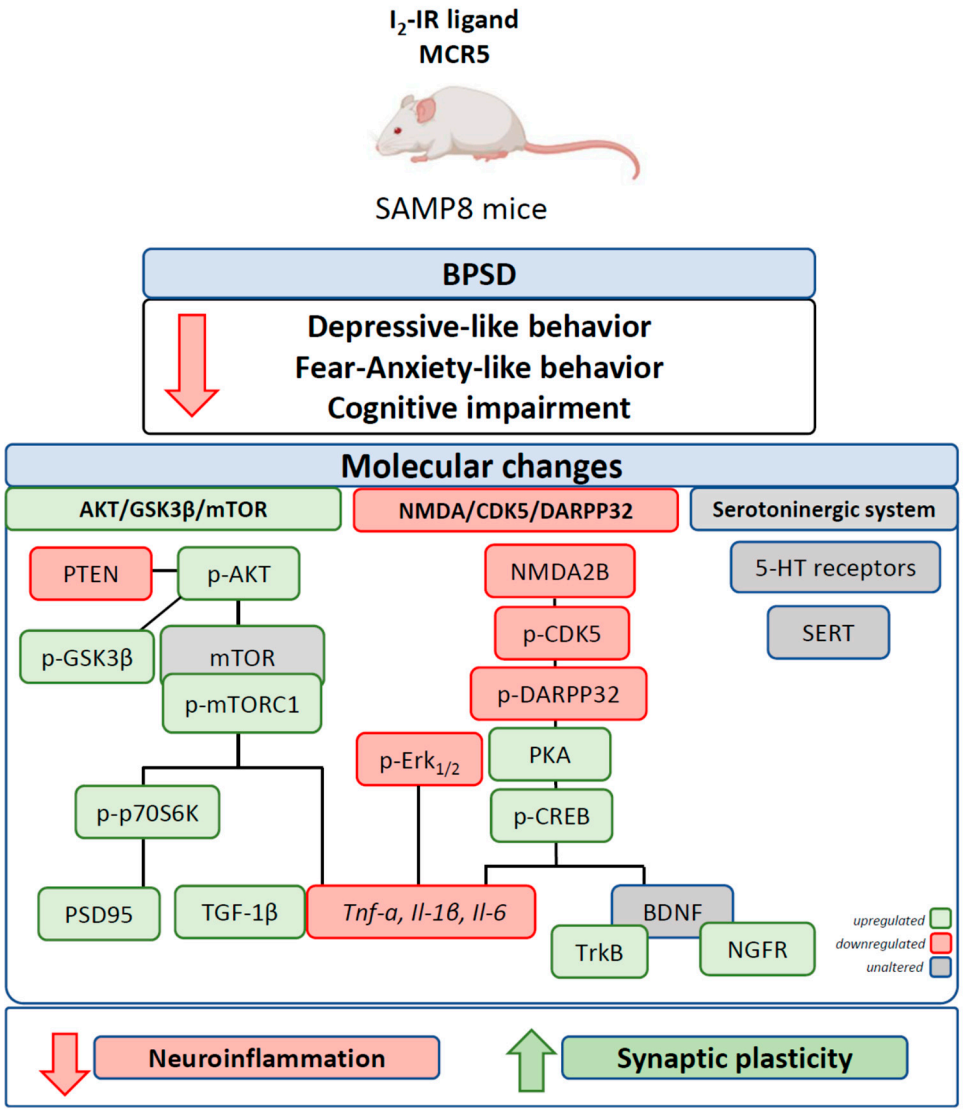

Figure 8. Cartoon illustrating a summary of behavioural, cognitive and molecular effects after MCR5 treatment in SAMP8 mice.

Supplementary Materials: The following are available online at http://www.mdpi.com/1999-4923/12/5/475/s1, Table S1: Antibodies used in Western blot studies, Table S2: Primers and probes used in qPCR studies, Table S3: Results of Novel object recognition test (NORT), and Object location test (OLT) Table S5: Parameters measured in the Open Field Test (OFT), Table S6: In Vitro Pharmacology: Binding Assays for MCR5 (10 μM) to 5-HT receptors and transporter.

Author Contributions: F.V. carried out the experimental intervention, performed behaviour experiments, WB analysis and RT-PCR experiments. C.G.-F., and M.P. analysed the data and drafted the manuscript. A.B. and S.R.-A. synthesized and purified MCR5. C.E. designed and supervised MCR5 synthesis. C.G.-F. and M.P. designed the experiments and supervised the study. F.V., C.G.-F., A.B., S.R.-A., C.E. and M.P. contributed to the writing the manuscript. All authors read and approved the final version of the manuscript.

Funding: This research was funded by the Ministerio de Economía y Competitividad of Spain (SAF2016-33307). The project leading to these results has received funding from "la Caixa" Foundation (ID 100010434) under agreement CI18-00002. C.G.-F., F.V., C.E., S.R.-A., A.B. and M.P. belong to 2017SGR106 (Generalitat de Catalunya). J Financial support was provided for F. V. (University of Barcelona, APIF_2017), S.R.-A. (Generalitat de Catalunya, 2018FI_B_00227), A.B. (Institute of Biomedicine UB_2018).

Conflicts of Interest: The authors claim no financial conflict of interest.

References

1. Cummings, J.L.; Morstorf, T.; Zhong, K. Alzheimer's Disease Drug-Development Pipeline: Few Candidates, Frequent Failures. *Alzheimers. Res. Ther.* **2014**, *6*, 37. [CrossRef] [PubMed]
2. Cummings, J.; Lee, G.; Ritter, A.; Zhong, K. Alzheimer's Disease Drug Development Pipeline: 2018. *Alzheimer's Dement. Transl. Res. Clin. Interv.* **2018**, *4*, 195–214. [CrossRef]
3. Griñan-Ferré, C.; Puigoriol-Illamola, D.; Palomera-ávalos, V.; Pérez-Cáceres, D.; Companys-Alemany, J.; Camins, A.; Ortuño-Sahagún, D.; Teresa Rodrigo, M.; Pallàs, M. Environmental Enrichment Modified Epigenetic Mechanisms in SAMP8 Mouse Hippocampus by Reducing Oxidative Stress and Inflammaging and Achieving Neuroprotection. *Front. Aging Neurosci.* **2016**, *8*. [CrossRef] [PubMed]
4. Cerejeira, J.; Lagarto, L.; Mukaetova-Ladinska, E. Behavioral and Psychological Symptoms of Dementia. *Front. Neurol.* **2012**, *3*, 73. [CrossRef] [PubMed]
5. Reisberg, B.; Borenstein, J.; Salob, S.P.; Ferris, S.H. Behavioral Symptoms in Alzheimer's Disease: Phenomenology and Treatment. *J. Clin. Psychiatry* **1987**, *48* (Suppl. 5), 9–15.
6. Kar, N. Behavioral and Psychological Symptoms of Dementia and Their Management. *Indian J. Psychiatry* **2009**, *51* (Suppl. S1), S77.
7. Kołaczkowski, M.; Mierzejewski, P.; Bienkowski, P.; Wesołowska, A.; Newman-Tancredi, A. Antipsychotic, Antidepressant, and Cognitive-Impairment Properties of Antipsychotics: Rat Profile and Implications for Behavioral and Psychological Symptoms of Dementia. *Naunyn. Schmiedebergs. Arch. Pharmacol.* **2014**, *387*, 545–557. [CrossRef]
8. Leyhe, T.; Reynolds III, C.F.; Melcher, T.; Linnemann, C.; Klöppel, S.; Blennow, K.; Zetterberg, H.; Dubois, B.; Lista, S.; Hampel, H. A Common Challenge in Older Adults: Classification, Overlap, and Therapy of Depression and Dementia. *Alzheimer's Dement.* **2017**, *13*, 59–71. [CrossRef]
9. Mega, M.S.; Cummings, J.L.; Fiorello, T.; Gornbein, J. The Spectrum of Behavioral Changes in Alzheimer's Disease. *Neurology* **1996**, *46*, 130–135. [CrossRef]
10. Dillon, C.; Serrano, C.M.; Castro, D.; Leguizamón, P.P.; Heisecke, S.L.; Taragano, F.E. Behavioral Symptoms Related to Cognitive Impairment. *Neuropsychiatr. Dis. Treat.* **2013**, *9*, 1443. [CrossRef]
11. Lanctôt, K.L.; Herrmann, N.; Mazzotta, P. Role of Serotonin in the Behavioral and Psychological Symptoms of Dementia. *J. Neuropsychiatry Clin. Neurosci.* **2001**, *13*, 5–21. [CrossRef] [PubMed]
12. Lohoff, F.W. Overview of the Genetics of Major Depressive Disorder. *Curr. Psychiatry Rep.* **2010**, *12*, 539–546. [CrossRef] [PubMed]
13. Castrén, E.; Rantamäki, T. The Role of BDNF and Its Receptors in Depression and Antidepressant Drug Action: Reactivation of Developmental Plasticity. *Dev. Neurobiol.* **2010**, *70*, 289–297. [CrossRef] [PubMed]
14. Serafini, G. Neuroplasticity and Major Depression, the Role of Modern Antidepressant Drugs. *World J. Psychiatry* **2012**, *2*, 49. [CrossRef] [PubMed]
15. Autry, A.E.; Adachi, M.; Nosyreva, E.; Na, E.S.; Los, M.F.; Cheng, P.; Kavalali, E.T.; Monteggia, L.M. NMDA Receptor Blockade at Rest Triggers Rapid Behavioural Antidepressant Responses. *Nature* **2011**, *475*, 91–95. [CrossRef] [PubMed]
16. García-Sevilla, J.A.; Escriba, P.V.; Sastre, M.; Walzer, C.; Busquets, X.; Jaquet, G.; Reis, D.J.; Guimon, J. Immunodetection and Quantitation of Imidazoline Receptor Proteins in Platelets of Patients with Major Depression and in Brains of Suicide Victims. *Arch. Gen. Psychiatry* **1996**, *53*, 803–810. [CrossRef]
17. Gargalidis-Moudanos, C.; Pizzinat, N.; Javoy-Agid, F.; Remaury, A.; Parini, A. I2-Imidazoline Binding Sites and Monoamine Oxidase Activity in Human Postmortem Brain from Patients with Parkinson's Disease. *Neurochem. Int.* **1997**, *30*, 31–36. [CrossRef]
18. Ruiz, J.; Martin, I.; Callado, L.F.; Meana, J.J.; Barturen, F.; Garcia-Sevilla, J.A. Non-Adrenoceptor [3H] Idazoxan Binding Sites (I2-Imidazoline Sites) Are Increased in Postmortem Brain from Patients with Alzheimer's Disease. *Neurosci. Lett.* **1993**, *160*, 109–112. [CrossRef]
19. Parini, A.; Moudanos, C.G.; Pizzinat, N.; Lanier, S.M. The Elusive Family of Imidazoline Binding Sites. *Trends Pharmacol. Sci.* **1996**, *17*, 13–16. [CrossRef]
20. Finn, D.P.; Martí, O.; Harbuz, M.S.; Vallès, A.; Belda, X.; Márquez, C.; Jessop, D.S.; Lalies, M.D.; Armario, A.; Nutt, D.J. Behavioral, Neuroendocrine and Neurochemical Effects of the Imidazoline I 2 Receptor Selective Ligand BU224 in Naive Rats and Rats Exposed to the Stress of the Forced Swim Test. *Psychopharmacology* **2003**, *167*, 195–202. [CrossRef]

21. Tonello, R.; Villarinho, J.G.; da Silva Sant'Anna, G.; Tamiozzo, L.; Machado, P.; Trevisan, G.; Martins, M.A.P.; Ferreira, J.; Rubin, M.A. The Potential Antidepressant-like Effect of Imidazoline I2 Ligand 2-BFI in Mice. *Prog. Neuro-Psychopharmacol. Biol. Psychiatry* **2012**, *37*, 15–21. [CrossRef] [PubMed]
22. Li, G.; Regunathan, S.; Barrow, C.J.; Eshraghi, J.; Cooper, R.; Reis, D.J. Agmatine: An Endogenous Clonidine-Displacing Substance in the Brain. *Science (80-)* **1994**, *263*, 966–969. [CrossRef] [PubMed]
23. Aricioglu, F.; Altunbas, H. Is Agmatine an Endogenous Anxiolytic/Antidepressant Agent? *Ann. N. Y. Acad. Sci.* **2003**, *1009*, 136–140. [CrossRef] [PubMed]
24. Head, G.A.; Mayorov, D.N. Imidazoline Receptors, Novel Agents and Therapeutic Potential. *Cardiovasc. Hematol. Agents Med. Chem. (Formerly Curr. Med. Chem. Hematol. Agents)* **2006**, *4*, 17–32. [CrossRef]
25. Abas, S.; Estarellas, C.; Luque, F.J.; Escolano, C. Easy Access to (2-Imidazolin-4-Yl) Phosphonates by a Microwave Assisted Multicomponent Reaction. *Tetrahedron* **2015**, *71*, 2872–2881. [CrossRef]
26. Abás, S.; Erdozain, A.M.; Keller, B.; Rodríguez-Arévalo, S.; Callado, L.F.; García-Sevilla, J.A.; Escolano, C. Neuroprotective Effects of a Structurally New Family of High Affinity Imidazoline I2 Receptor Ligands. *ACS Chem. Neurosci.* **2017**, *8*, 737–742. [CrossRef]
27. Griñán-Ferré, C.; Vasilopoulou, F.; Abás, S.; Rodríguez-Arévalo, S.; Bagán, A.; Sureda, F.X.; Pérez, B.; Callado, L.F.; García-Sevilla, J.A.; García-Fuster, M.J.; et al. Behavioral and Cognitive Improvement Induced by Novel Imidazoline I2 Receptor Ligands in Female SAMP8 Mice. *Neurotherapeutics* **2019**, *16*. [CrossRef]
28. Butterfield, D.A.; Poon, H.F. The Senescence-Accelerated Prone Mouse (SAMP8): A Model of Age-Related Cognitive Decline with Relevance to Alterations of the Gene Expression and Protein Abnormalities in Alzheimer's Disease. *Exp. Gerontol.* **2005**, *40*, 774–783. [CrossRef]
29. Miyamoto, M. Characteristics of Age-Related Behavioral Changes in Senescence-Accelerated Mouse SAMP8 and SAMP10. *Exp. Gerontol.* **1997**, *32*, 139–148. [CrossRef]
30. Pallàs, M. Senescence-Accelerated Mice P8: A Tool to Study Brain Aging and Alzheimer's Disease in a Mouse Model. *ISRN Cell Biol.* **2012**, *2012*, 1–12. [CrossRef]
31. Pérez-Cáceres, D.; Rodrigo, M.T.; Pubill, D.; Camins, A.; Camarasa, J.; Escubedo, E.; Pallàs, M. Depression-like Behavior Is Dependent on Age in Male SAMP8 Mice. *Biogerontology* **2013**, *14*, 165–176. [CrossRef] [PubMed]
32. Steru, L.; Chermat, R.; Thierry, B.; Simon, P. The Tail Suspension Test: A New Method for Screening Antidepressants in Mice. *Psychopharmacology* **1985**, *85*, 367–370. [CrossRef] [PubMed]
33. Can, A.; Dao, D.T.; Terrillion, C.E.; Piantadosi, S.C.; Bhat, S.; Gould, T.D. The Tail Suspension Test. *JoVE (J. Vis. Exp).* **2012**, *59*, e3769. [CrossRef] [PubMed]
34. Porsolt, R.D.; Le Pichon, M.; Jalfre, M. Depression: A New Animal Model Sensitive to Antidepressant Treatments. *Nature* **1977**, *266*, 730–732. [CrossRef] [PubMed]
35. Lister, R.G. The Use of a Plus-Maze to Measure Anxiety in the Mouse. *Psychopharmacology* **1987**, *92*, 180–185. [CrossRef] [PubMed]
36. Cohen, H.; Matar, M.A.; Joseph, Z. Animal Models of Post-traumatic Stress Disorder. *Curr. Protoc. Neurosci.* **2013**, *64*, 9–45. [CrossRef] [PubMed]
37. Archer, J. Tests for Emotionality in Rats and Mice: A Review. *Anim. Behav.* **1973**, *21*, 205–235. [CrossRef]
38. Ennaceur, A.; Delacour, J. A New One-Trial Test for Neurobiological Studies of Memory in Rats. 1: Behavioral Data. *Behav. Brain Res.* **1988**, *31*, 47–59. [CrossRef]
39. Griñán-Ferré, C.; Marsal-García, L.; Bellver-Sanchis, A.; Kondengaden, S.M.; Turga, R.C.; Vázquez, S.; Pallàs, M. Pharmacological Inhibition of G9a/GLP Restores Cognition and Reduces Oxidative Stress, Neuroinflammation and ß-Amyloid Plaques in an Early-Onset Alzheimer's Disease Mouse Model. *Aging* **2019**, *11*. [CrossRef]
40. GARCÍA-SEVILLA, J.A.; Escriba, P.V.; Guimon, J. Imidazoline Receptors and Human Brain Disorders A. *Ann. N. Y. Acad. Sci.* **1999**, *881*, 392–409. [CrossRef]
41. Li, J.-X.; Zhang, Y. Imidazoline I2 Receptors: Target for New Analgesics? *Eur. J. Pharmacol.* **2011**, *658*, 49–56. [CrossRef] [PubMed]
42. Abás, S.; Rodríguez-Arévalo, S.; Bagán, A.; Griñán-Ferré, C.; Vasilopoulou, F.; Brocos-Mosquera, I.; Muguruza, C.; Pérez, B.; Molins, E.; Luque, F.J. Bicyclic α-Iminophosphonates as High Affinity Imidazoline I2 Receptor Ligands for Alzheimer's Disease. *J. Med. Chem.* **2020**, *63*, 3610–3633. [CrossRef] [PubMed]
43. Kitagishi, Y.; Kobayashi, M.; Kikuta, K.; Matsuda, S. Roles of PI3K/AKT/GSK3/MTOR Pathway in Cell Signaling of Mental Illnesses. *Depress. Res. Treat.* **2012**, *2012*, 1–8. [CrossRef]

44. Hashioka, S.; Klegeris, A.; Monji, A.; Kato, T.; Sawada, M.; McGeer, P.L.; Kanba, S. Antidepressants Inhibit Interferon-γ-Induced Microglial Production of IL-6 and Nitric Oxide. *Exp. Neurol.* **2007**, *206*, 33–42. [CrossRef] [PubMed]
45. Knezevic, D.; Verhoeff, N.P.L.G.; Hafizi, S.; Strafella, A.P.; Graff-Guerrero, A.; Rajji, T.; Pollock, B.G.; Houle, S.; Rusjan, P.M.; Mizrahi, R. Imaging Microglial Activation and Amyloid Burden in Amnestic Mild Cognitive Impairment. *J. Cereb. Blood Flow Metab.* **2018**, *38*, 1885–1895. [CrossRef]
46. Haidinger, M.; Poglitsch, M.; Geyeregger, R.; Kasturi, S.; Zeyda, M.; Zlabinger, G.J.; Pulendran, B.; Hörl, W.H.; Säemann, M.D.; Weichhart, T. A Versatile Role of Mammalian Target of Rapamycin in Human Dendritic Cell Function and Differentiation. *J. Immunol.* **2010**, *185*, 3919–3931. [CrossRef]
47. Duman, R.S.; Voleti, B. Signaling Pathways Underlying the Pathophysiology and Treatment of Depression: Novel Mechanisms for Rapid-Acting Agents. *Trends Neurosci.* **2012**, *35*, 47–56. [CrossRef]
48. Caraci, F.; Battaglia, G.; Busceti, C.; Biagioni, F.; Mastroiacovo, F.; Bosco, P.; Drago, F.; Nicoletti, F.; Sortino, M.A.; Copani, A. TGF-B1 Protects against Aβ-Neurotoxicity via the Phosphatidylinositol-3-Kinase Pathway. *Neurobiol. Dis.* **2008**, *30*, 234–242. [CrossRef]
49. Caraci, F.; Spampinato, S.F.; Morgese, M.G.; Tascedda, F.; Salluzzo, M.G.; Giambirtone, M.C.; Caruso, G.; Munafò, A.; Torrisi, S.A.; Leggio, G.M. Neurobiological Links between Depression and AD: The Role of TGF-B1 Signaling as a New Pharmacological Target. *Pharmacol. Res.* **2018**, *130*, 374–384. [CrossRef]
50. Derynck, R.; Zhang, Y.E. Smad-Dependent and Smad-Independent Pathways in TGF-β Family Signalling. *Nature* **2003**, *425*, 577–584. [CrossRef]
51. Dudek, H.; Datta, S.R.; Franke, T.F.; Birnbaum, M.J.; Yao, R.; Cooper, G.M.; Segal, R.A.; Kaplan, D.R.; Greenberg, M.E. Regulation of Neuronal Survival by the Serine-Threonine Protein Kinase Akt. *Science (80-)* **1997**, *275*, 661–665. [CrossRef] [PubMed]
52. David, D.J.; Samuels, B.A.; Rainer, Q.; Wang, J.-W.; Marsteller, D.; Mendez, I.; Drew, M.; Craig, D.A.; Guiard, B.P.; Guilloux, J.-P. Neurogenesis-Dependent and-Independent Effects of Fluoxetine in an Animal Model of Anxiety/Depression. *Neuron* **2009**, *62*, 479–493. [CrossRef] [PubMed]
53. Canudas, A.M.; Gutierrez-Cuesta, J.; Rodríguez, M.I.; Acuña-Castroviejo, D.; Sureda, F.X.; Camins, A.; Pallàs, M. Hyperphosphorylation of Microtubule-Associated Protein Tau in Senescence-Accelerated Mouse (SAM). *Mech. Ageing Dev.* **2005**, *126*, 1300–1304. [CrossRef] [PubMed]
54. Casadesús, G.; Gutierrez-Cuesta, J.; Lee, H.; Jiménez, A.; Tajes, M.; Ortuño-Sahagún, D.; Camins, A.; Smith, M.A.; Pallàs, M. Neuronal Cell Cycle Re-Entry Markers Are Altered in the Senescence Accelerated Mouse P8 (SAMP8). *J. Alzheimer's Dis.* **2012**, *30*, 573–583. [CrossRef]
55. Li, X.; Polter, A. Glycogen Synthase Kinase-3 Is an Intermediate Modulator of Serotonin Neurotransmission. *Front. Mol. Neurosci.* **2011**, *4*, 31.
56. Young, W. Review of Lithium Effects on Brain and Blood. *Cell Transplant.* **2009**, *18*, 951–975. [CrossRef]
57. Seo, M.K.; Choi, C.M.; McIntyre, R.S.; Cho, H.Y.; Lee, C.H.; Mansur, R.B.; Lee, Y.; Lee, J.-H.; Kim, Y.H.; Park, S.W. Effects of Escitalopram and Paroxetine on MTORC1 Signaling in the Rat Hippocampus under Chronic Restraint Stress. *BMC Neurosci.* **2017**, *18*, 39. [CrossRef]
58. Li, N.; Lee, B.; Liu, R.-J.; Banasr, M.; Dwyer, J.M.; Iwata, M.; Li, X.-Y.; Aghajanian, G.; Duman, R.S. MTOR-Dependent Synapse Formation Underlies the Rapid Antidepressant Effects of NMDA Antagonists. *Science (80-)* **2010**, *329*, 959–964. [CrossRef]
59. Fienberg, A.A.; Hiroi, N.; Mermelstein, P.G.; Song, W.-J.; Snyder, G.L.; Nishi, A.; Cheramy, A.; O'callaghan, J.P.; Miller, D.B.; Cole, D.G. DARPP-32: Regulator of the Efficacy of Dopaminergic Neurotransmission. *Science (80-)* **1998**, *281*, 838–842. [CrossRef]
60. Nishi, A.; Shuto, T. Potential for Targeting Dopamine/DARPP-32 Signaling in Neuropsychiatric and Neurodegenerative Disorders. *Expert Opin. Ther. Targets* **2017**, *21*, 259–272. [CrossRef]
61. Nishi, A.; Bibb, J.A.; Matsuyama, S.; Hamada, M.; Higashi, H.; Nairn, A.C.; Greengard, P. Regulation of DARPP-32 Dephosphorylation at PKA-and Cdk5-sites by NMDA and AMPA Receptors: Distinct Roles of Calcineurin and Protein Phosphatase-2A. *J. Neurochem.* **2002**, *81*, 832–841. [CrossRef] [PubMed]
62. Luo, Y.; Kuang, S.; Li, H.; Ran, D.; Yang, J. CAMP/PKA-CREB-BDNF Signaling Pathway in Hippocampus Mediates Cyclooxygenase 2-Induced Learning/Memory Deficits of Rats Subjected to Chronic Unpredictable Mild Stress. *Oncotarget* **2017**, *8*, 35558. [CrossRef] [PubMed]

63. Krishnan, V.; Han, M.-H.; Graham, D.L.; Berton, O.; Renthal, W.; Russo, S.J.; LaPlant, Q.; Graham, A.; Lutter, M.; Lagace, D.C. Molecular Adaptations Underlying Susceptibility and Resistance to Social Defeat in Brain Reward Regions. *Cell* **2007**, *131*, 391–404. [CrossRef] [PubMed]
64. Patki, G.; Solanki, N.; Atrooz, F.; Allam, F.; Salim, S. Depression, Anxiety-like Behavior and Memory Impairment Are Associated with Increased Oxidative Stress and Inflammation in a Rat Model of Social Stress. *Brain Res.* **2013**, *1539*, 73–86. [CrossRef] [PubMed]
65. Shin, J.A.; Lee, K.-E.; Kim, H.-S.; Park, E.-M. Acute Resveratrol Treatment Modulates Multiple Signaling Pathways in the Ischemic Brain. *Neurochem. Res.* **2012**, *37*, 2686–2696. [CrossRef] [PubMed]
66. Greenberg, M.E.; Xu, B.; Lu, B.; Hempstead, B.L. New Insights in the Biology of BDNF Synthesis and Release: Implications in CNS Function. *J. Neurosci.* **2009**, *29*, 12764–12767. [CrossRef]
67. Minichiello, L. TrkB Signalling Pathways in LTP and Learning. *Nat. Rev. Neurosci.* **2009**, *10*, 850–860. [CrossRef]
68. Chao, M.V.; Bothwell, M.A.; Ross, A.H.; Koprowski, H.; Lanahan, A.A.; Buck, C.R.; Sehgal, A. Gene Transfer and Molecular Cloning of the Human NGF Receptor. *Science (80-)* **1986**, *232*, 518–521. [CrossRef]
69. Sandhya, V.K.; Raju, R.; Verma, R.; Advani, J.; Sharma, R.; Radhakrishnan, A.; Nanjappa, V.; Narayana, J.; Somani, B.L.; Mukherjee, K.K. A Network Map of BDNF/TRKB and BDNF/P75NTR Signaling System. *J. Cell Commun. Signal.* **2013**, *7*, 301–307. [CrossRef]

cells

MDPI

Article

Phosphoenolpyruvate from Glycolysis and PEPCK Regulate Cancer Cell Fate by Altering Cytosolic Ca^{2+}

Juan Moreno-Felici [1], Petra Hyroššová [1], Marc Aragó [1], Sergio Rodríguez-Arévalo [2], Pablo M. García-Rovés [1], Carmen Escolano [2] and Jose C. Perales [1,3,*]

[1] Department of Physiological Sciences, School of Medicine, University of Barcelona, Feixa Llarga s/n, 08907 L'Hospitalet del Llobregat, Barcelona, Spain; juanmorenofelici@gmail.com (J.M.-F.); petra.hyrossova@gmail.com (P.H.); marc.arago@gmail.com (M.A.); pgarciaroves@ub.edu (P.M.G.-R.)

[2] Laboratory of Medicinal Chemistry (Associated Unit to CSIC), Faculty of Pharmacy and Food Sciences, and Institute of Biomedicine (IBUB), University of Barcelona, 08028 Barcelona, Spain; sergio6_6@hotmail.com (S.R.-A.); cescolano@ub.edu (C.E.)

[3] IDIBELL, Gran Via de l'Hospitalet 199, 08908 L'Hospitalet de Llobregat, Barcelona, Spain

* Correspondence: jperales@ub.edu; Tel.: +34-934024295; Fax: +34-934024268

Received: 23 November 2019; Accepted: 16 December 2019; Published: 19 December 2019

Abstract: Changes in phosphoenolpyruvate (PEP) concentrations secondary to variations in glucose availability can regulate calcium signaling in T cells as this metabolite potently inhibits the sarcoplasmic reticulum Ca^{2+}/ATPase pump (SERCA). This regulation is critical to assert immune activation in the tumor as T cells and cancer cells compete for available nutrients. We examined here whether cytosolic calcium and the activation of downstream effector pathways important for tumor biology are influenced by the presence of glucose and/or cataplerosis through the phosphoenolpyruvate carboxykinase (PEPCK) pathway, as both are hypothesized to feed the PEP pool. Our data demonstrate that cellular PEP parallels extracellular glucose in two human colon carcinoma cell lines, HCT-116 and SW480. PEP correlated with cytosolic calcium and NFAT activity, together with transcriptional up-regulation of canonical targets PTGS2 and IL6 that was fully prevented by CsA pre-treatment. Similarly, loading the metabolite directly into the cell increased cytosolic calcium and NFAT activity. PEP-stirred cytosolic calcium was also responsible for the calmodulin (CaM) dependent phosphorylation of c-Myc at Ser62, resulting in increased activity, probably through enhanced stabilization of the protein. Protein expression of several c-Myc targets also correlated with PEP levels. Finally, the participation of PEPCK in this axis was interrogated as it should directly contribute to PEP through cataplerosis from TCA cycle intermediates, especially in glucose starvation conditions. Inhibition of PEPCK activity showed the expected regulation of PEP and calcium levels and consequential downstream modulation of NFAT and c-Myc activities. Collectively, these results suggest that glucose and PEPCK can regulate NFAT and c-Myc activities through their influence on the PEP/Ca^{2+} axis, advancing a role for PEP as a second messenger communicating metabolism, calcium cell signaling, and tumor biology.

Keywords: phosphoenolpyruvate carboxykinase (PEPCK); PEPCK-M; PCK2; phosphoenolpyruvate carboxykinase; cancer metabolism; calcium; c-Myc; NFAT; CaMK2G; phosphoenolpyruvate; TCA cycle; cataplerosis; sarcoplasmic reticulum Ca^{2+}/ATPase pump (SERCA)

1. Introduction

Intracellular Ca^{2+} signaling is involved in the coordination of several cellular and physiological processes in normal and tumor cells alike, including bioenergetics, senescence [1], autophagy [2],

apoptosis, cell proliferation, immune evasion, and metastasis [3,4]. The nuclear factor of activated T cells (NFAT) family of transcription factors is one of the key effectors of calcium signals in the control of immune system activation, inflammatory responses [5], angiogenesis, metastasis, and other biological processes [6]. Also, the proto-oncogenes of the Myc family of transcription factors involved in several cellular processes, including cell proliferation [7], and cell growth and metabolism [8–10], have been shown to respond to calcium both transcriptionally and post-transcriptionally upon CaMKIIγ-dependent phosphorylation at Ser62 [11].

Two principal calcium transporters and pumps regulate calcium trafficking between the ER and cytosol, IP_3R, which consists on a Ca^{2+}-permeable ER ion channel, and SERCA, a Ca^{2+}/ATPase pump located in the ER membrane that regulate the return of Ca^{2+} from the cytosol to the ER lumen. SERCA activity is inhibited by oncogenes like Ras, and the antiapoptotic c member BcL-2, and activated by the tumor suppressor p53 [12]. Therefore, with DNA damage or cellular stress, calcium fluxes might determine cellular fate.

SERCA requires ATP to recover Ca^{2+} into the ER lumen, so under low energy conditions, SERCA activity can be compromised. In addition, glycolytic intermediates, such as glucose-6-phosphate (G6P) or phosphoenolpyruvate (PEP), can regulate SERCA activity in the brain [13] and T cells [14], independently of ATP. In T cells, extracellular glucose is key to activating cell proliferation, aerobic glycolysis, and anabolism as T cells mount anti-tumoral responses. Therefore, increased consumption of glucose by CD4 and CD8 T cells translates into raising the pool of PEP, inhibiting SERCA, and increasing cytosolic Ca^{2+} which in turn signals the activation of NFAT. In this context, an increment of PEP produced by overexpression of cytosolic PEPCK (PEPCK-C; PCK1) using retrovirus transduction was sufficient to inhibit SERCA activity and assure T cell activation [14]. However, the physiological role of the endogenous PEPCK pathway was not assessed. Interestingly, ER-stress up-regulates ATF4-dependent transcription of mitochondrial PEPCK (PEPCK-M; PCK2), an isoform of PEPCK commonly found in tumor cells [15]. In the tumor environment, high basal levels of ER stress are commonly found as stromal and cancer cells compete for limited quantities of nutrients [16]. In consequence, we hypothesize that the cataplerotic activity of PEPCK-M fluxing glutamine [17] and/or lactate [18] carbons towards the glycolytic intermediary pool might have a potential role in modulating cytosolic calcium signaling pathways, and hence the metabolic fate of the cell.

2. Materials and Methods

2.1. Cell Culture

Human colon (HCT116 and SW480) carcinoma cell lines were cultured in DMEM supplemented with 10% FBS, 10,000 units/mL penicillin, 10 mg/mL streptomycin, and 2 mM L-glutamine (Biological Industries, Kibbutz Beit-Haemek, Israel) and incubated in a humidified atmosphere of 5% CO_2 at 37 °C. Ionomycin, PMA (phorbol 12-myristate 13-acetate), and Cyclosporin A were purchased from Merk (Darmstadt, Germany).

2.2. RNA Extraction and Quantitative RT-PCR

Transcriptional regulation of targets of NFAT was analyzed by qRT-PCR at 6 h post-treatment. Total RNA was extracted using TRIsure™ reagent. cDNA synthesis mRNA was performed using a high capacity cDNA reverse transcription kit (ThermoFisher Scientific, Waltham, MA USA). cDNA was quantitated using real-time quantitative RT-PCR assays in a 7900HT real-time quantitative RT-PCR system (ThermoFisher Scientific, Waltham, MA USA) using commercial Taqman primers for PTGS2 (Hs00153133-m1), IL6 (Hs00174131_m1), and TBP (Hs99999910_m1). Data analysis was based on the $\Delta\Delta$Ct method.

2.3. Western Blot

Cells were homogenized in RIPA buffer supplemented with protease and phosphatase inhibitors and centrifuged at 15,000× *g* for 15 min at 4 °C. Western blots were performed with 20–30 μg of cell extract. Proteins were separated in 8–12% SDS-PAGE and transferred to an Immobilon

membrane (Merk Millipore, Burlington, MA, USA). Following primary antibodies were used: anti-phospho-Ser62/T58 c-Myc (Santa Cruz, Dallas, TX, USA; sc-377552), anti-c-Myc C-19 (Santa Cruz, Dallas, TX, USA; sc-788), anti-GLS1 (Abcam, Cambridge, UK; ab131554), anti-cSHMT A-2 (Santa Cruz, Dallas, TX, USA; sc-365203), anti-mSHMT F-11 (Santa Cruz, Dallas, TX, USA; sc-390641), anti-HK-2 (Cell Signaling, Danvers, MA, USA; 2867), anti-Glut1 (Santa Cruz, Dallas, TX, USA; sc-277228), anti-LDHA (Santa Cruz, Dallas, TX, USA; sc-137243). All membranes were normalized using mouse monoclonal anti-γ-tubulin antibody (Sigma-Aldrich, Darmstadt, Germany; T-6557). Horseradish peroxidase activity linked to secondary antibody was detected with ECL substrate (Pierce) in a Fujifilm LAS 3000 Intelligent Dark Box IV imaging system (Tokio, Japan).

2.4. Immunofluorescence

SW480 cells plated on coverslips (Ø 15 mm) were washed with PBS and fixed with 4% paraformaldehyde in PBS for 10 min. Cells were blocked in blocking buffer (PBS with 1% NHS, and 0.1% Triton™ X-100) for 2 h and then treated with NFATc2 (A2) and c-Myc (C-19) primary antibodies (Santa Cruz, sc-514929 and sc-788 respectively) overnight at 4 °C. After 3 washes with blocking buffer, cells were incubated with anti-rabbit Alexa Fluor® 555 (Invitrogen, Carlsbad, CA, USA, A28175) or anti-mouse Alexa Fluor® 488 secondary antibodies (Invitrogen, A27039) for 2 h. During this incubation, DAPI was added to stain the nuclei. After washing 3 times with blocking buffer, samples were examined using a confocal laser scanning microscopy ZEISS LSM 880 (Carl Zeiss AG, Oberkochen, Germany) and ZEN 2012 (Zeiss, Oberkochen, Germany) was used to collect digital images.

2.5. Transfection and Luciferase Assays

Cells were transfected using polyethyleneimine (linear polyethyleneimine, Mr 25,000, Sigma-Aldrich, Darmstadt, Germany). The NFAT 3x-Luc plasmid (0.7 μg) and 0.3 μg of pSV40-β-galactosidase control vector (Promega, Madison, WI, USA) were co-transfected into 6-well plates containing 80% confluent cells and then distributed into 24-well plates. Cells were incubated overnight in complete medium before treatment. Luciferase activity was measured in a luminometer (TD 20/20; Turner Designs, San Jose, CA, USA) using the luciferase assay system (Promega). The luciferase values were normalized to β-galactosidase activity using the luminescent β-galactosidase detection kit II (Takara Bio USA, Kusatsu, Japan). pNFATx3-Luc vector was a gift of Mercè Pérez-Riba (Medical and Molecular Genetics Center, IDIBELL, L'Hospitalet del Llobregat, Spain).

2.6. Cytosolic Calcium Measurement

Cells grown up to 80% of confluence in a 96-well plate were washed with PBS and then stained with Fluo-4 according to the manufacturer instructions (Molecular Probes™ Invitrogen, Fluo-4 NW Calcium Assay Kit F36206). Fluorescence measurements were performed using the fluorescence spectrometer POLARstar Omega microplate reader (BMG LABTECH, Ortenberg, Germany).

2.7. Cellular PEP Loading

Cells grown up to 70% of confluence were washed and pre-incubated in sucrose medium (sucrose 250 mM, NaF 10 mM, glucose 10 mM, K_2HPO_4 10 mM; pH 6.0) for 5 min. Then, cells were incubated for 15 min with sucrose medium with the desired PEP concentration.

2.8. PEP Determination Assay

PEP was extracted with perchloric acid (1 M). PEP was determined through an enzymatic assay. The ATP formed during the conversion of PEP to pyruvate by pyruvate kinase was measured using StayBriteTM kit (Highly stable ATP bioluminescence assay kit K791-1000; Biovision, Milipitas, CA, USA). The samples were diluted in the PEP assay buffer (gly-gly 0.1 M; KCl 0.2 M; $MgCl_2$ 1 mM; reconstituted enzyme from StayBrite™ kit 0.1% (*v*/*v*); pH 7). The increment of luminescence was measured with a luminometer (TD 20/20; Turner Designs, San Jose, CA, USA) 2 min after the addition

of pyruvate kinase (to a final concentration of 13.5 U/mL), and the results were normalized by protein content.

2.9. Glycolytic Flux Measurement

Glycolytic flux was determined by measuring the formation of $^{3}H_2O$ from D-[5-^{3}H]-glucose by the enolase step of glycolysis. Briefly, cells were treated with medium containing 1 μCi of D-[5-^{3}H]-glucose/mL for 1 h at 37 °C. After incubation, triplicated 50 μL aliquots of media were transferred to uncapped PCR tubes containing 50 μL of 0.2 N HCl and placed into scintillation vial containing 0.5 mL non-labeled H_2O. The sealed scintillation vials were left 24 h at 37 °C to allow equilibration between $^{3}H_2O$ produced by cells and non-labeled H_2O. PCR tubes were removed and 10 mL of scintillation solution was added into each vial, mixed, and the radioactivity was quantified using a scintillation analyzer. The rate of glycolytic flux was corrected for recovery.

2.10. Glucose Consumption Assay

Glucose consumption was determined by colorimetry assay, based upon two enzymatic reactions, catalyzed by glucose oxidase and peroxidase. The assay was performed by mixing 15 μL of media or standard with 200 μL of reaction buffer prepared as recommended by manufacturer PGO (Sigma-Aldrich, Darmstadt, Germany, P7119). Absorbance was measured at 450 nm after 30 min of incubation at 37 °C. The amount of consumed glucose was obtained by subtracting the final concentration values from the glucose concentration in the original medium. Finally, values were normalized by protein content.

2.11. Lactate Production Assay

Lactate production was determined by the measurement of NADH produced in the reaction catalyzed by lactate dehydrogenase enzyme (LDH). NADH was determined by fluorescence (excitation 340 nm/emission 460 nm). The assay was performed by mixing 10 μL of media or standard with 200 μL of reaction buffer (0.3 M hydrazine sulfate, 0.87 M glycine, 2.5 mM NAD^+, and 0.19 M EDTA at pH 9.5). The background NADH fluorescence was measured and 25 μL of LDH (344 U/mL) was added into each sample. After 20 min of incubation at RT NADH synthesized in LDH, catalyzed reaction was measured and corrected for background. The amount of net lactate production was determined by subtracting lactate measured in the original medium. Finally, values were normalized by protein content.

3. Results

3.1. Glycolytic and Cataplerotic Fluxes towards PEP Cooperate to Regulate Cytosolic Calcium

The influence of glucose metabolism on the intracellular levels of PEP and its correlation with intracellular calcium was studied by measuring both PEP and relative calcium levels at different concentrations of extracellular glucose. As shown in Figure 1, cellular PEP linearly increased when glucose concentration in the media was elevated from 0 to 25 mM, both in HCT116 and SW480 colon carcinoma cells (Figure 1A). Cytosolic Ca^{2+} concentrations, as determined by relative Fluo4 fluorescence mediated by Ca^{2+} binding, correlated with the level of PEP and glucose media concentrations (Figure 1B; correlation statistics in Figure 1C). Loading known concentrations of PEP into cells caused a dose-dependent increase of Ca^{2+} (Figure 1D,E; correlation statistics in Figure 1F), providing further evidence that the glycolytic intermediate PEP can directly mediate changes in Ca^{2+} levels.

Cellular PEP levels are also maintained by the PEPCK-dependent cataplerosis of TCA cycle carbons that contribute to the synthesis of glycolytic intermediates (Hyrossova et al., unpublished), serine/glycine [19] and triglycerides [20,21]. In most tumor models, and specifically in the cellular models utilized in this work, the mitochondrial isoform of PEPCK (PEPCK-M) plays this key role as it is the only isoform of PEPCK expressed [22]. Therefore, we interrogated the implication of PEPCK-

M in the regulation of PEP and Ca^{2+} fluctuations, we measured PEP and Ca^{2+} at various levels of activation of PEPCK-M more specifically using a potent inhibitor of PEPCK-M prepared in our laboratory, iPEPCK-2 [22], in the presence or absence of glucose (Figure 1G). PEPCK-M activity contributed to the PEP/Ca^{2+} axis in both colon carcinoma cell lines in the presence of glucose, as its inhibition effectively reduced cellular PEP concentrations and cytosolic calcium (Figure 1H,I). Glucose starvation was more effective at reducing PEP and Ca^{2+} levels than PEPCK-M inhibition, especially in SW480 cells. In the absence of glucose, the concentration of PEP was found close to the detection limit of our assay in both models but the inhibition of PEPCK-M was effective at further decreasing PEP concentrations (Figure 1H). All these results suggest a role for PEPCK-M in upkeeping the PEP pool, even in the presence of glucose.

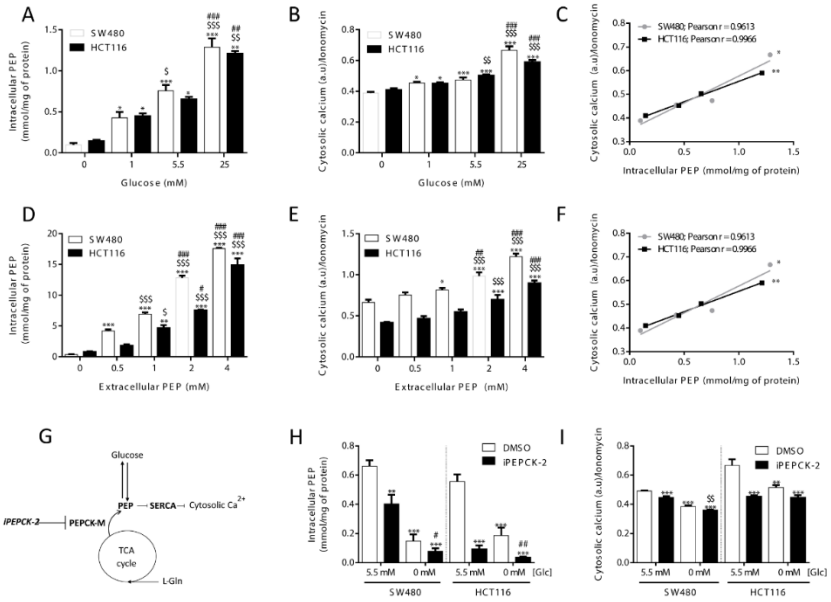

Figure 1. Glucose availability and PEPCK-M regulates cytosolic calcium through PEP. Intracellular levels of (**A**) PEP and (**B**) cytosolic calcium in both HCT116 and SW480 cells cultured on media with different glucose levels (**C**; correlation statistics). Effect of extracellular loading of PEP in both HCT116 and SW480 cells on (**D**) intracellular PEP and (**E**) cytosolic calcium concentrations (**F**; correlation statistics). Drawing depicting calcium regulation by PEP from glucose or cataplerotic sources (**G**). Intracellular levels of PEP (**H**) and cytosolic calcium (**I**) on both HCT116 and SW480 cells submitted to inhibition of the PEPCK pathway with 8.68 μM of IPEPCK-2 or vehicle (DMSO) at either 5.5 or 0 mM concentration of glucose in the media. Data are the mean ± SE, n = 5. One-way ANOVA, with Sidak post-test, $^{*,\$,\#}$ $p < 0.05$, $^{**,\$\$,\#\#}$ $p < 0.01$, $^{***,\$\$\$,\#\#\#}$ $p < 0.001$. Correlation data was analyzed by a Pearson test. * versus 0 mM glucose or 0 mM extracellular PEP (A and B; D and E; D and E), or 5.5 mM Glc, DMSO condition (H and I). $ versus 5.5 mM glucose or 0.5 mM extracellular PEP (A and B; D and E), or glucose 0 mM, DMSO condition. # versus 1 mM glucose or 1 mM PEP (A and B; D and E).

3.2. Intracellular PEP Modulates NFAT Activity and Its Target Genes

To study if the presence of glucose, via modulation of PEP levels, can activate the calcineurin/NFAT cascade, we evaluated the activity of a luciferase reporter vector under the control of a chimeric promoter containing 3 adjacent canonical NFAT binding sites. The model was validated using ionomycin as a positive control of activation of NFAT, and cyclosporin A, to abrogate Ca^{2+} signaling (Figure 2A). With this tool, we analyzed the level of activation of NFAT at various glucose concentrations (Figure 2B) and upon PEP loading (Figure 2C). Increasing extracellular glucose or PEP concentrations produced a similar dose-dependent increase in NFAT activity. Furthermore, NFAT

cellular localization was consistent with its measured activation level as it was preferentially located into the nucleus upon ionomycin treatment or in the presence of glucose and excluded into the cytosol when glucose was absent or calcium signaling inhibited with cyclosporin A (CsA; Figure 2D,E).

Under NFAT activation, its target genes, IL6 and PTGS2, were transcriptionally up-regulated as analyzed by qRT-PCR (Figure 2F–K). Results showed that ionomycin-induced calcium flux significantly increased IL6 and PTGS2 gene transcription (Figure 2F,I). The expression of PTGS2 and IL6 were increased at higher concentrations of glucose (Figure 2G), being highest at 25 mM, and lowest at 0 mM glucose co-treated with CsA (Figure 2G,J). When PEP was loaded onto cells in culture, IL6 and PTGS2 mRNA content augmented in a dose-dependent manner (Figure 2H,K). Finally, CsA was able to abolish the up-regulation of IL6 and PTGS2 caused by PEP, demonstrating calcineurin/NFAT-dependent regulation (Figure 2H,K).

Collectively, these data indicate that NFAT dependent transactivation activity depends on glucose availability and subsequent intracellular changes on the PEP pool.

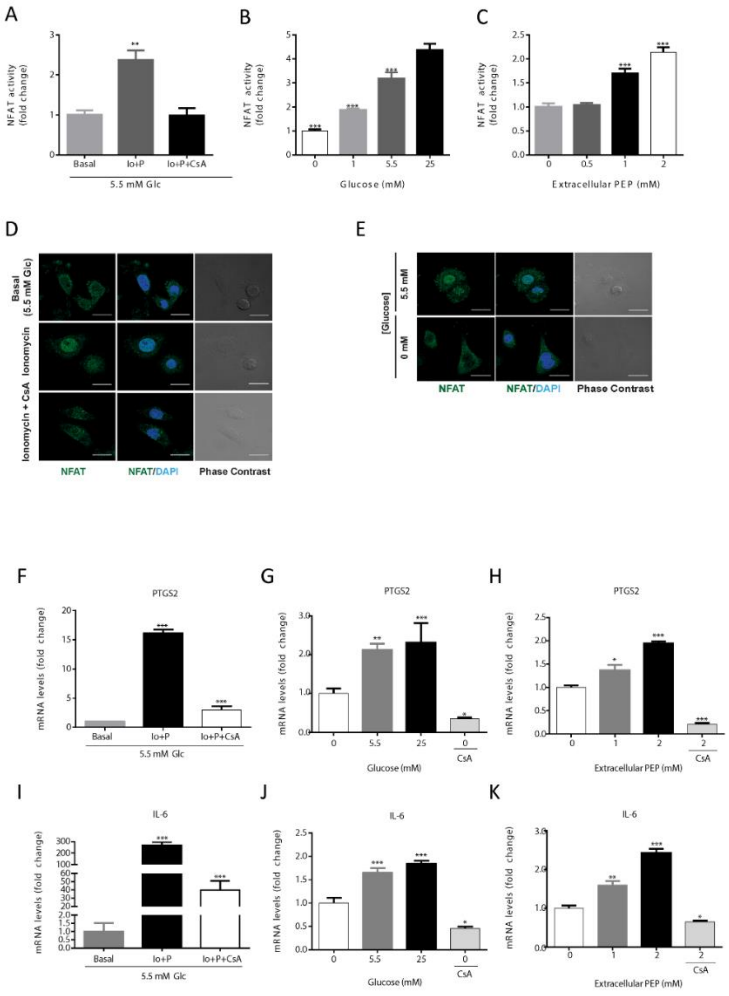

Figure 2. Activation of the NFAT pathway by PEP/calcium. NFAT is activated by ionomycin (1 μM) and inhibited by CsA (1 μM) (**A**). NFAT activity at various glucose concentrations in the culture media (**B**). NFAT activation levels at different extracellular PEP loads (**C**). Direct immunofluorescence for NFATc1 (green) and nuclear associated DAPI (blue) in basal, ionomycin (1 μM) and CsA (1 μM) conditions (**D**). Direct immunofluorescence for NFATc1 (green) and nuclear DAPI (blue) in the presence or absence of glucose in the culture media (**E**). NFAT target genes PTGS2 and IL-6 mRNA levels in the presence of ionomycin (1 μM) or ionomycin plus CsA (1 μM) (**F**,**I**). NFAT target genes PTGS2 and IL-6 mRNA levels at various glucose concentrations in the culture media (**G**,**J**). NFAT target genes PTGS2 and IL-6 mRNA levels at different extracellular PEP loads (**H**,**K**). Data are the

mean ± SE, n = 5. One-way ANOVA, with Sidak post-test, * $p < 0.05$, ** $p < 0.01$, *** $p < 0.001$. * versus basal, 0 mM glucose or 0 mM extracellular PEP (A–C; F–K). Scale bar represents 20 μm.

3.3. Calcium-Dependent Phosphorylation at Ser62 Stabilizes c-Myc

In T cell lymphoma (TCL) c-Myc protein is stabilized by calmodulin (CaM) kinase II gamma (CaMKIIγ) upon phosphorylation at Ser62 [11]. Therefore, we checked the phosphorylation status of c-Myc by Western blot in conditions that altered PEP and calcium pools. Ionomycin-dependent phosphorylation of c-Myc was shown with p-Ser62 specific antibodies (Figure 3A; quantitated in Supplementary Figure S3). Furthermore, phosphorylation was abrogated by pretreatment with KN-93, an inhibitor of calmodulin (Figure 3A; quantitated in Supplementary Figure S3). In addition, we assayed the subcellular localization of total c-Myc (Figure 3B). Total c-Myc increased its nuclear localization with ionomycin. These data suggest that proto-oncogene c-Myc is regulated by calcium signaling in cancer colon carcinoma cells.

As calcium signaling can stabilize the c-Myc protein, and glucose controls cytosolic Ca^{2+} levels through PEP, we next questioned whether the presence of extracellular glucose or PEP at varying concentrations might alter c-Myc phosphorylation and nuclear localization. Partial nuclear exclusion of c-Myc was observed under glucose deprivation (Figure 3C), in agreement with lowered phosphorylation observed under glucose starvation, a reduction that was mimicked by total c-Myc (Figure 3D; quantified in Figure 3E). Similarly, phosphorylated c-Myc was increased after two hours of treatment with PEP (Figure 3F; quantified in Figure 3G).

In addition, we evaluated the effect of glucose and PEP on the expression of c-Myc targets such as glucose transporter (GLUT1), mitochondrial glutaminase (mGLS), and the cytosolic serine hydroxymethyl-transferases (cSHMT; Figure 3H,J; quantitated in Figure 3I,K).

Figure 3

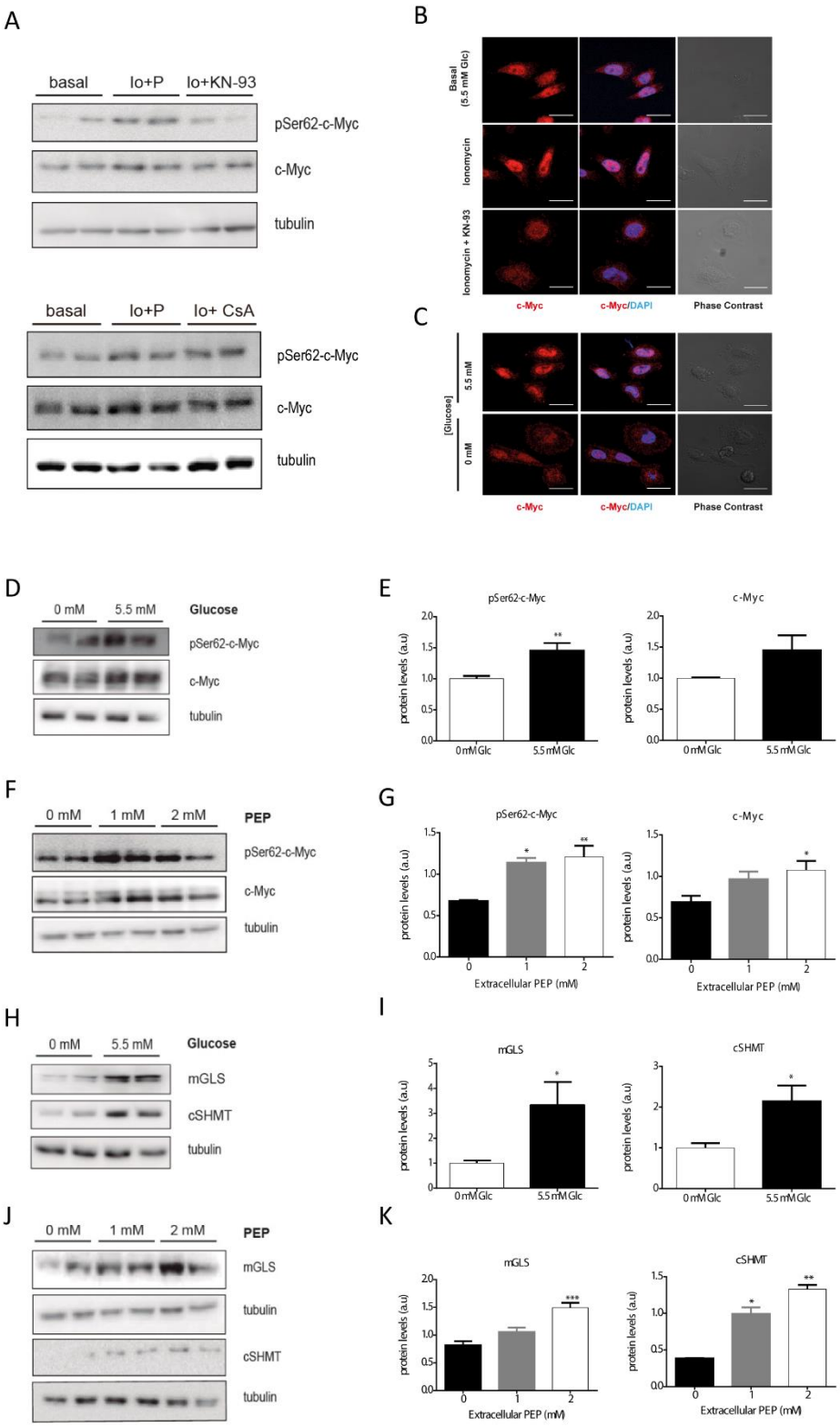

Figure 3. Glucose increases c-Myc phosphorylation at Ser62 in a PEP/Ca^{2+} dependent manner. Analysis of the phosphorylation of c-Myc by Western blot after 2 h in basal media (5.5 mM glucose), ionomycin (Io; 1 μM), ionomycin plus CsA (1 μM), and ionomycin plus KN-93 (5 μM) conditions (**A**). Direct immunofluorescence for c-Myc (red) and DAPI (blue) after 30 min treatment in basal, ionomycin (1 μM) and ionomycin plus KN-93 (5 μM) conditions (**B**). Direct immunofluorescence for

c-Myc (red) and DAPI (blue) in the presence and absence of glucose in the media (**C**). Western blot analysis of the phosphorylation of c-Myc at Ser62 after 2 h in the presence of various concentrations of glucose in the culture media (**D**). Densitometric analysis (**E**) of WB shown in (D). Western blot analysis of the phosphorylation of c-Myc at Ser62 after 15 min treatment with extracellular PEP (**F**). Densitometric analysis (**G**) of WB shown in (F). Western blot analysis of mitochondrial glucosamine (mGLS), and cytosolic serine hydroxymethyltransferase (cSHMT), both described as a c-Myc targets, after 4 h in the presence or absence of glucose in the culture media (**H**). Densitometric analysis (**I**) of WB plotted in (H). Western blot analysis of mitochondrial glucosamine (mGLS), and cytosolic serine hydroxymethyltransferase (cSHMT), both described as c-Myc targets, after 15 min treatment with extracellular PEP (**J**). Densitometric analysis (**K**) of WB shown in (**J**). All experiments were performed in the SW480 cell line. Data are the mean ± SE, n = 4 (for western blot analysis, 2 replicates were loaded in each experiment, and each experiment was independently repeated at least twice). * $p < 0.05$, ** $p < 0.01$, *** $p < 0.001$; versus glucose 0mM or PEP 0 mM. One-way ANOVA, Sidak post-test. Scale bar represents 20 μm.

3.4. PEPCK-M Modulates Calcium Signaling Because of Its Impact on the PEP Pool

As shown in Figure 1, PEPCK-M plays an important role in the maintenance of the PEP pool, even in the presence of glucose. In addition, we have demonstrated that changes in Ca^{2+} produced by different glucose and PEP concentrations lead to activation and nuclear translocation of NFAT. For these reasons, we analyzed PEPCK-M contribution to NFAT activation by measuring NFAT activity and NFAT cellular localization in the presence or absence of a potent PEPCK-M inhibitor previously validated in our laboratory (iPEPCK-2; [22]; Figure 4). A reduction in NFAT activity was observed when PEPCK-M was inhibited in the presence of glucose in SW480 cells (Figure 4A), consistent with reduced NFAT activity found in SW480 and HCT116 cell lines upon glucose depletion. In addition, NFAT activity was always lower after PEPCK-M inhibition, indicating that PEPCK-M might have a major role in maintaining NFAT activity (Figure 4A). As reasoned, NFAT targets PTGS2 and IL6 were similarly down-regulated by conditions that reduced PEP concentrations and concomitant cytosolic calcium signaling, namely IPEPCK-2 treatment or glucose deprivation, with an additive down-regulation found in the case of PTGS2 (Figure 4B). Logically, we found that NFAT nuclear localization was mainly observed in the presence of glucose and DMSO and was decreased when cells were glucose starved, or PEPCK-M was inhibited (Figure 4C).

Our results suggest that NFAT activation is modulated in a glucose- and PEPCK-M-dependent manner. For that reason, we aimed to analyze the protein stabilization of c-Myc and c-Myc target genes in conditions of limited PEPCK-M activity. C-Myc phosphorylation at Ser62 was reduced by IPEPCK-2 or by glucose starvation (Figure 4D; quantified in Figure 4E). Although total c-Myc was reduced in the presence of IPEPCK-2, this effect was not statistically significant. Finally, c-Myc targets, such as mGLS, and cSHMT were negatively regulated by IPEPCK-2 consistent with decreased phosphorylation and nuclear localization of c-Myc in these conditions (Figure 4D; quantified in Figure 4C,E).

Figure 4

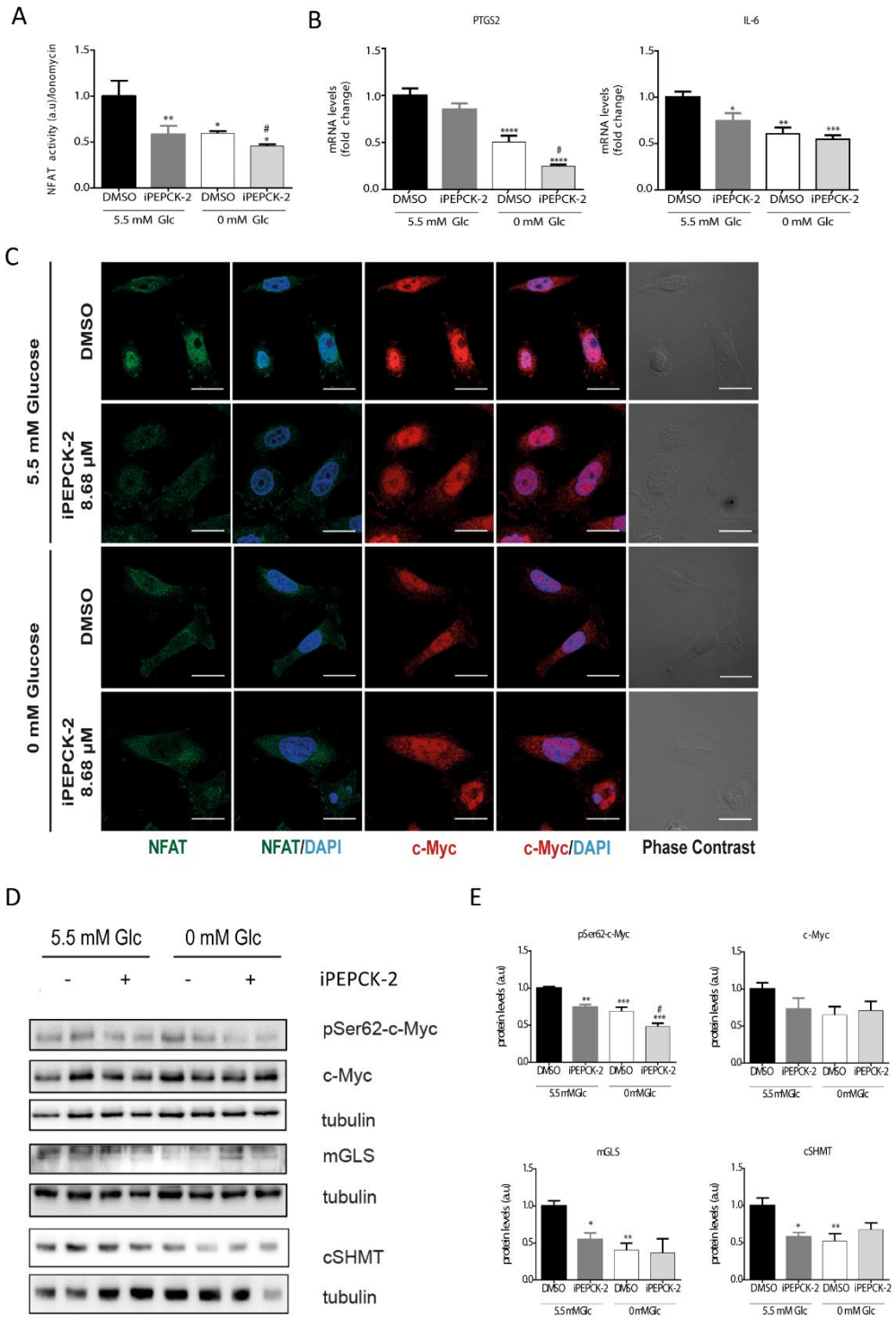

Figure 4. Consequences of PEPCK-M inhibition on the levels of activation of the NFAT and c-Myc pathways. (**A**) NFAT activity in the presence of IPEPCK-2 (8.68 µM) or vehicle (DMSO) in SW480 cells cultured in media with 5.5 mM glucose or the absence of glucose (0 mM). (**B**) PTGS2 and IL6 mRNA expression in the presence of IPEPCK-2 (8.68 µM) or vehicle (DMSO) in SW480 cells cultured in media with 5.5 mM glucose or the absence of glucose (0 mM). (**C**) Direct immunofluorescence for c-Myc (red) and NFAT (green) after 2 h of treatment with DMSO or IPEPCK-2 (8.68 µM), in SW480 cell culture in the presence or absence of glucose. (**D**) Western blot analysis of the phosphorylation status of c-Myc at Ser62, and the activation of several c-Myc target proteins. (**E**) Densitometry of WB shown in (**D**).

Data are the mean ± SE, n = 4 (for Western blot analysis, 2 replicates were loaded in each experiment, and each experiment was independently repeated at least twice). * $p < 0.05$, ** $p < 0.01$, *** $p < 0.001$ versus DMSO/5.5 mM glucose; or $^{\#}$ $p < 0.05$, $^{\#\#}$ $p < 0.01$, $^{\#\#\#}$ $p < 0.001$ versus DMSO/0 mM glucose. One-way ANOVA, Sidak post-test. Scale bar represents 20 μm.

4. Discussion

The Warburg effect, one of the hallmarks of cancer, allows cancer cells to switch their metabolism to aerobic glycolysis with the objective to increase energy production rates while maintaining anabolism [23,24]. Thus, tumor cells fiercely compete for glucose carbons in the tumor microenvironment with the host tissue and infiltrating immune cells. As a consequence, temporary or locally reduced availability of glucose endures responses in these cells which might contribute to the pathological state of the tumor microenvironment. In a paradigmatic case, T-cells exposed to limiting glucose concentrations cannot activate proper anti-tumoral response [24]. The mechanism for this regulated process was found to implicate the glycolytic intermediate PEP, an inhibitor of ER Ca^{2+}-ATP pump SERCA [14]. Therefore, we hypothesized that a similar mechanism would take place in the tumor cell to relay the concentration of glucose and other metabolites in the environment with PEP levels and calcium cell signaling, with consequential gene expression changes that are relevant to tumor biology.

Indeed, our data from two colon carcinoma cell lines confirmed that changes in extracellular glucose concentration exhibited concurrent changes in the levels of PEP and cytosolic calcium. Importantly, changes in intracellular PEP because of direct loading of PEP into the cell or by altering the cataplerotic provision of PEP by the activity of the PEPCK-M pathway using a specific inhibitor, iPEPCK-2, correlated well with changes in calcium levels measured by the surrogate Fluo-4 indicator. Canonical calcium signaling includes calmodulin (CaM) and calcineurin (CaN) pathways, NFAT activation being the most prominent downstream consequence of CaN dependent calcium signaling. Consistently, the NFAT-dependent transcriptional activity of a chimeric luciferase reporter gene was modulated by glucose availability and PEP loading in colon cancer cells, correlating with a predominant localization of NFAT in the nucleus. Also, the inhibition of PEPCK-M exhibited a reduction of NFAT activity and an increase of cytosolic localization of this transcription factor, in accordance with the observed changes in the cytosolic calcium levels. All in all, this suggests that the same mechanisms that impede T-cells from activating anti-tumoral responses in conditions of limited glucose can operate in tumors as the NFAT signaling pathway is reported as a key factor to improve their capacity to effectively compete for these nutrients [16], and in tumor progression and metastasis [25]. Consistently, target genes of NFAT were regulated upon changes in PEP concentrations; cyclooxygenase 2 (PTGS2), an immune-modulator and a negative prognostic factor in colon cancer [26] by promoting tumor progression and metastasis [27]; and IL-6, a cytokine implicated in cancer progression [28], and tumorigenicity [29]. These results suggest that glucose-promoted PEP and/or PEPCK-M activity could have an impact on inflammation, colon cancer progression, and metastasis through the transactivation of PTGS2 and IL6 by the PEP/Ca^{2+}/NFAT signaling pathway.

Part of the Ca^{2+} signaling cascade, calmodulin kinase type II gamma (CaMKIIγ), plays an important role in tumor progression of prostate cancer by activation of AKT in a PI3K-independent manner [30], or in the development of colitis-associated cancer through activation of STAT3 [31]. Importantly, CaMKIIγ binds to c-Myc in a calcium-dependent manner [32] and phosphorylates c-Myc at Ser62 thereby increasing its stability and its half-life [11]. Consistently, c-Myc phosphorylation at Ser62 by ionomycin was inhibited only by KN-93, an inhibitor of CaMKIIγ, and not by cyclosporin A. PEP loading increased c-Myc phosphorylation at Ser62 by CaMKIIγ. These results agree with data reported by Ying Gu and collaborators [11] and suggest that c-Myc protein is regulated by PEP/Ca^{2+} by posttranslational mechanisms, independently of calcineurin/NFAT pathway activation. Other studies indicate that c-Myc can be regulated by NFAT transcriptionally [33]. However, we did not observe regulation of c-Myc transcription after changes in PEP levels (data not shown), suggesting cell-to-cell variability in the transcriptional response to NFAT on c-Myc transcription [34]. Interestingly, our data show that total c-Myc protein levels were lower when glucose was lacking,

pointing to c-Myc stability regulation by calcium. Concurrently with c-Myc phosphorylation rates, several c-Myc targets relevant to metabolism were also regulated by glucose, and this regulation was PEP-dependent. Moreover, nuclear distribution was also observed in the presence of glucose, consistent with the translocation of phosphorylated c-Myc in these situations.

Several c-Myc targets modulated by PEP/Ca^{2+} (i.e., Glut1, LDH-A) are associated with clinical colorectal cancer progression [35] and are also induced by K-Ras, commonly mutated in these cancers. Regulation of other targets such as glutaminase (GLS1) and the cytosolic isoform of serine hydroxymethyltransferase (cSHMT) suggest changes in the metabolic layout in agreement with the Warburg effect phenotype [23,36]. This is consistent with the need for double inhibition of c-Myc and PI3K signaling pathways to reduce glucose uptake and glycolytic flux in lymphoma cell lines [37]. In this setting, glucose uptake could regulate c-Myc activation through PEP and calcium, providing a feedback loop into its own metabolism. Consistently, the inhibition of PEPCK-M reduced the amount of PEP and phosphorylated c-Myc in the presence or absence of glucose, accounting for a regulatory axis that is independent of glucose but can promote glucose metabolism.

In this context, it is plausible to view PEP as a rheostat of either glucose carbon flux or cataplerotic fluxes (i.e., PEPCK-M) from other carbons sources such as glutamine, to "inform" on the availability of biosynthetic precursors of the glycolytic pool, such as serine and glycine, to cope with sustenance and growth at various stages of tumor development. Thus, PEPCK-M could regulate calcium signaling, especially in glucose starved conditions where glucose does not contribute to the PEP pool. PCK2 transcription is controlled by the ER stress pathway, downstream of GNC2-PERK-ATF4 [15]. ER is quasi constitutive in tumors, where glucose is low. Therefore, ER-stress could potentiate the PEP/Ca^{2+} axis in a PEPCK-M dependent manner, especially in conditions of limited nutrients for the cell. In fact, PEPCK-M is able to impact on PEP and calcium levels even in the presence of glucose, especially in HCT116 cells. A metabolomics study on HeLa cells (data not shown) showed that PEPCK-M activity contributed glutamine labeled carbons into PEP only under glucose starvation, suggesting that PEPCK-M might influence PEP levels indirectly, possibly by altering the glycolytic flux in the cell. However, the glycolytic flux measured in HCT116 and SW480 cells with [5-^{3}H]-glucose clearly indicated that glycolysis was unaffected by PEPCK-M inhibition (Supplementary Figure S1). In addition, glucose consumption or lactate production was not altered by PEPCK-M inhibition (Supplementary Figure S2). Altogether, these results indicate that PEPCK-M does not alter PEP levels indirectly through the modulation of glycolysis, and hint for a contribution of PEPCK-M to the maintenance of the PEP pool in the presence of glucose by fluxing glutamine or other anaplerotic carbons from the TCA cycle, at least in certain types of cancer.

To conclude, we propose a model where glucose and PEPCK-M regulate calcium signaling through PEP (Figure 5). Glucose metabolism or cataplerosis from carbons such as glutamine, contribute to maintaining PEP levels, leading to an inhibition of the SERCA pump similarly to T-cells [14]. Cytosolic Ca^{2+} then activates calcineurin (CaN) and calmodulin (CaM) pathways, and in turn, NFAT is translocated into the nucleus, whereas c-Myc is stabilized upon CaMKIIγ phosphorylation at Ser62. NFAT and c-Myc produce activation of expression of several genes implicated in inflammation and metastasis (PTGS2), glucose uptake and glycolysis (Glut1 and HKII), glutamine catabolism (GLS1) and serine and glycine synthesis, and transference of carbons to one-carbon metabolism (cSHMT) that allow for NADPH recycling. This scenario indicates that glucose and PEPCK-M are supporting, through the PEP/Ca^{2+} axis, a proliferative state in tumors, and bring about the importance of this target for cancer metabolism, as exemplified by the efficacy of potent inhibitors of this pathway in pre-clinical studies [22].

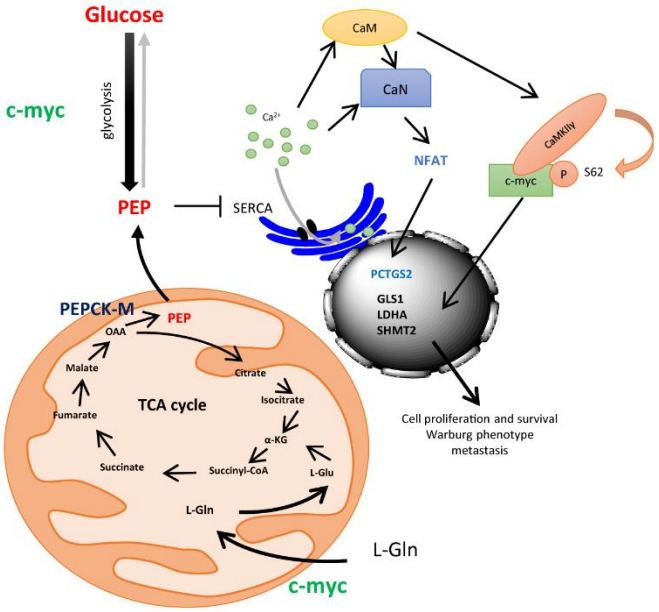

Figure 5. Drawing depicting a model for the integration of ER-stress mediated up-regulation of PEPCK-M and the control of integrative signals downstream of the PEP/Ca^{2+} axis.

Supplementary Materials: The following are available online at www.mdpi.com/xxx/s1, Figure S1: Glycolytic flux was independent of PEPCK-M activity in human colon carcinoma cells, Figure S2: PEPCK-M activity did not alter glucose consumption and lactate production, Figure S3: Quantitation of WB showed at Figure 3A.

Author Contributions: J.M.-F.: performed experiments, collected and analyze data. Wrote the manuscript. P.H.: performed experiments, collected and analyze data, and discussed the preliminary draft and provided feedback on general and specific details of the manuscript. M.A.: performed experiments, collected and analyze data, and discussed the preliminary draft and provided feedback on general and specific details of the manuscript. S.R.-A.: performed experiments, collected and analyze data. P.M.G.-R.: discussed the preliminary draft and provided feedback on general and specific details of the manuscript. C.E.: analyzed data, discussed the preliminary draft and provided feedback on general and specific details of the manuscript. J.C.P.: analyzed data, discussed the preliminary draft and provided feedback on general and specific details of the manuscript. Conceived of the work. Wrote the manuscript. All authors have read and agreed to the published version of the manuscript.

Funding: This work was supported by grants from the Spanish "Ministerio de Economia y Competitividad" (MINECO; BFU2015-66030-R) to JCP and CE, Generalitat de Catalunya (2017SGR106 and 2017SGR204), and the European Union (European Regional Development Fund, FEDER). We are indebted to the "Ministerio de Educación" FPU and the "Ministerio de Economia y Competitividad" (MINECO) FPI for financial support for PH and JMF, respectively, and to the Generalitat de Catalunya FI program for partial financial support for MA and SRA.

Ackonwledge: We acknowledge the skillful technical support by the Scientific and Technical Services at the University of Barcelona, Bellvitge Campus, and to the "Consorci de Serveis Universitaris de Catalunya" (CSUC) for computational facilities.

Conflicts of Interest: The authors declare no conflicts of interest.

References

1. Wiel, C.; Lallet-Daher, H.; Gitenay, D.; Gras, B.; Le Calvé, B.; Augert, A.; Ferrand, M.; Prevarskaya, N.; Simonnet, H.; Vindrieux, D.; et al. Endoplasmic reticulum calcium release through ITPR2 channels leads to mitochondrial calcium accumulation and senescence. *Nat. Commun.* **2014**, *5*, 3792.

2. Rimessi, A.; Bonora, M.; Marchi, S.; Patergnani, S.; Marobbio, C.M.; Lasorsa, F.M.; Pinton, P. Perturbed mitochondrial Ca $^{2+}$ signals as causes or consequences of mitophagy induction. *Autophagy* **2013**, *9*, 1677–1686.
3. Xu, M.; Seas, A.; Kiyani, M.; Ji, K.S.Y.; Bell, H.N. A temporal examination of calcium signaling in cancer-from tumorigenesis, to immune evasion, and metastasis. *Cell Biosci.* **2018**, *8*, 25.
4. Monteith, G.R.; Prevarskaya, N.; Roberts-Thomson, S.J. The calcium–cancer signalling nexus. *Nat. Rev. Cancer* **2017**, *17*, 367–380.
5. Shaw, J.P.; Utz, P.J.; Durand, D.B.; Toole, J.J.; Emmel, E.A.; Crabtree, G.R. Identification of a putative regulator of early T cell activation genes. *Science* **1988**, *241*, 202–5.
6. Pan, M.-G.; Xiong, Y.; Chen, F. NFAT gene family in inflammation and cancer. *Curr. Mol. Med.* **2013**, *13*, 543–54.
7. Dang, C. V c-Myc target genes involved in cell growth, apoptosis, and metabolism. *Mol. Cell. Biol.* **1999**, *19*, 1–11.
8. Goetzman, E.S.; Prochownik, E. V. The Role for Myc in Coordinating Glycolysis, Oxidative Phosphorylation, Glutaminolysis, and Fatty Acid Metabolism in Normal and Neoplastic Tissues. *Front. Endocrinol. (Lausanne).* **2018**, *9*, 129.
9. Wang, R.; Dillon, C.P.; Shi, L.Z.; Milasta, S.; Carter, R.; Finkelstein, D.; McCormick, L.L.; Fitzgerald, P.; Chi, H.; Munger, J.; et al. The transcription factor Myc controls metabolic reprogramming upon T lymphocyte activation. *Immunity* **2011**, *35*, 871–82.
10. Dang, C. V MYC, metabolism, cell growth, and tumorigenesis. *Cold Spring Harb. Perspect. Med.* **2013**, *3*.
11. Gu, Y.; Zhang, J.; Ma, X.; Kim, B.; Wang, H.; Li, J.; Pan, Y.; Xu, Y.; Ding, L.; Yang, L.; et al. Stabilization of the c-Myc Protein by CAMKIIγ Promotes T Cell Lymphoma. *Cancer Cell* **2017**, *32*, 115-128.e7.
12. Bittremieux, M.; Parys, J.B.; Pinton, P.; Bultynck, G. ER functions of oncogenes and tumor suppressors: Modulators of intracellular Ca2 + signaling. *Biochim. Biophys. Acta - Mol. Cell Res.* **2016**, *1863*, 1364–1378.
13. Cole, J.T.; Kean, W.S.; Pollard, H.B.; Verma, A.; Watson, W.D. Glucose-6-phosphate reduces calcium accumulation in rat brain endoplasmic reticulum. *Front. Mol. Neurosci.* **2012**, *5*, 51.
14. Ho, P.-C.; Bihuniak, J.D.; Macintyre, A.N.; Staron, M.; Liu, X.; Amezquita, R.; Tsui, Y.-C.; Cui, G.; Micevic, G.; Perales, J.C.; et al. Phosphoenolpyruvate Is a Metabolic Checkpoint of Anti-tumor T Cell Responses. *Cell* **2015**, *162*, 1217–1228.
15. Méndez-Lucas, A.; Hyroššová, P.; Novellasdemunt, L.; Viñals, F.; Perales, J.C. Mitochondrial phosphoenolpyruvate carboxykinase (PEPCK-M) is a pro-survival, endoplasmic reticulum (ER) stress response gene involved in tumor cell adaptation to nutrient availability. *J. Biol. Chem.* **2014**, *289*, 22090–102.
16. Chang, C.-H.; Qiu, J.; O'Sullivan, D.; Buck, M.D.; Noguchi, T.; Curtis, J.D.; Chen, Q.; Gindin, M.; Gubin, M.M.; van der Windt, G.J.W.; et al. Metabolic Competition in the Tumor Microenvironment Is a Driver of Cancer Progression. *Cell* **2015**, *162*, 1229–41.
17. Vincent, E.E.; Sergushichev, A.; Griss, T.; Gingras, M.C.; Samborska, B.; Ntimbane, T.; Coelho, P.P.; Blagih, J.; Raissi, T.C.; Choinière, L.; et al. Mitochondrial Phosphoenolpyruvate Carboxykinase Regulates Metabolic Adaptation and Enables Glucose-Independent Tumor Growth. *Mol. Cell* **2015**, *60*, 195–207.
18. Alvarez, Z.; Hyrossova, P.; Perales, J.C.; Alcántara, S. Neuronal Progenitor Maintenance Requires Lactate Metabolism and PEPCK-M-Directed Cataplerosis. *Cereb. Cortex* **2016**, *26*, 1046–1058.
19. Balsa-Martinez, E.; Puigserver, P. Cancer Cells Hijack Gluconeogenic Enzymes to Fuel Cell Growth. *Mol. Cell* **2015**, *60*, 509–511.
20. Méndez-Lucas, A.; Duarte, J.A.G.; Sunny, N.E.; Satapati, S.; He, T.; Fu, X.; Bermúdez, J.; Burgess, S.C.;

Perales, J.C. PEPCK-M expression in mouse liver potentiates, not replaces, PEPCK-C mediated gluconeogenesis. *J. Hepatol.* **2013**, *59*, 105–13.

21. Leithner, K.; Triebl, A.; Trötzmüller, M.; Hinteregger, B.; Leko, P.; Wieser, B.I.; Grasmann, G.; Bertsch, A.L.; Züllig, T.; Stacher, E.; et al. The glycerol backbone of phospholipids derives from noncarbohydrate precursors in starved lung cancer cells. *Proc. Natl. Acad. Sci.* **2018**, *115*, 6225–6230.
22. Aragó, M.; Moreno-Felici, J.; Abás, S.; Rodríguez-Arévalo, S.; Hyroššová, P.; Figueras, A.; Viñals, F.; Pérez, B.; Loza, M.I.; Brea, J.; et al. Pharmacology and preclinical validation of a novel anticancer compound targeting PEPCK-M. *Biomed. Pharmacother.* **2020**, *121*, 109601.
23. Vander Heiden, M.G.; Cantley, L.C.; Thompson, C.B. Understanding the Warburg effect: the metabolic requirements of cell proliferation. *Science* **2009**, *324*, 1029–33.
24. Pearce, E.L.; Poffenberger, M.C.; Chang, C.-H.; Jones, R.G. Fueling immunity: insights into metabolism and lymphocyte function. *Science* **2013**, *342*, 1242454.
25. Tie, X.; Han, S.; Meng, L.; Wang, Y.; Wu, A. NFAT1 Is Highly Expressed in, and Regulates the Invasion of, Glioblastoma Multiforme Cells. *PLoS One* **2013**, *8*, e66008.
26. Cetin, M.; Buyukberber, S.; Demir, M.; Sari, I.; Sari, I.; Deniz, K.; Eser, B.; Altuntas, F.; Camcı, C.; Öztürk, A.; et al. Overexpression of cyclooxygenase-2 in multiple myeloma: Association with reduced survival. *Am. J. Hematol.* **2005**, *80*, 169–173.
27. Al-Salihi, M.A.; Terrece Pearman, A.; Doan, T.; Reichert, E.C.; Rosenberg, D.W.; Prescott, S.M.; Stafforini, D.M.; Topham, M.K. Transgenic expression of cyclooxygenase-2 in mouse intestine epithelium is insufficient to initiate tumorigenesis but promotes tumor progression. *Cancer Lett.* **2009**, *273*, 225–32.
28. Nagasaki, T.; Hara, M.; Nakanishi, H.; Takahashi, H.; Sato, M.; Takeyama, H. Interleukin-6 released by colon cancer-associated fibroblasts is critical for tumour angiogenesis: anti-interleukin-6 receptor antibody suppressed angiogenesis and inhibited tumour–stroma interaction. *Br. J. Cancer* **2014**, *110*, 469–478.
29. Lin, J.-T.; Wang, J.-Y.; Chen, M.-K.; Chen, H.-C.; Chang, T.-H.; Su, B.-W.; Chang, P.-J. Colon cancer mesenchymal stem cells modulate the tumorigenicity of colon cancer through interleukin 6. *Exp. Cell Res.* **2013**, *319*, 2216–2229.
30. Rokhlin, O.; Taghiyev, A.F.; Bayer, K.U.; Bumcrot, D.; Kotelianski, V.E.; Glover, R.A.; Cohen, M.B. Calcium/calmodulin-dependent kinase II plays an important role in prostate cancer cell survival. *Cancer Biol. Ther.* **2007**, *6*, 732–742.
31. Ma, X.; Meng, Z.; Jin, L.; Xiao, Z.; Wang, X.; Tsark, W.M.; Ding, L.; Gu, Y.; Zhang, J.; Kim, B.; et al. CAMK2γ in intestinal epithelial cells modulates colitis-associated colorectal carcinogenesis via enhancing STAT3 activation. *Oncogene* **2017**, *36*, 4060–4071.
32. Raffeiner, P.; Schraffl, A.; Schwarz, T.; Röck, R.; Ledolter, K.; Hartl, M.; Konrat, R.; Stefan, E.; Bister, K. Calcium-dependent binding of Myc to calmodulin. *Oncotarget* **2017**, *8*, 3327–3343.
33. Singh, G.; Singh, S.K.; König, A.; Reutlinger, K.; Nye, M.D.; Adhikary, T.; Eilers, M.; Gress, T.M.; Fernandez-Zapico, M.E.; Ellenrieder, V. Sequential Activation of NFAT and c-Myc Transcription Factors Mediates the TGF-β Switch from a Suppressor to a Promoter of Cancer Cell Proliferation. *J. Biol. Chem.* **2010**, *285*, 27241–27250.
34. Mognol, G.P.; de Araujo-Souza, P.S.; Robbs, B.K.; Teixeira, L.K.; Viola, J.P.B. Transcriptional regulation of the *c-Myc* promoter by NFAT1 involves negative and positive NFAT-responsive elements. *Cell Cycle* **2012**, *11*, 1014–1028.
35. Graziano, F.; Ruzzo, A.; Giacomini, E.; Ricciardi, T.; Aprile, G.; Loupakis, F.; Lorenzini, P.; Ongaro, E.; Zoratto, F.; Catalano, V.; et al. Glycolysis gene expression analysis and selective metabolic advantage in the

clinical progression of colorectal cancer. *Pharmacogenomics J.* **2017**, *17*, 258–264.

36. Burns, J.S.; Manda, G. Metabolic Pathways of the Warburg Effect in Health and Disease: Perspectives of Choice, Chain or Chance. *Int. J. Mol. Sci.* **2017**, *18*.
37. Broecker-Preuss, M.; Becher-Boveleth, N.; Bockisch, A.; Dührsen, U.; Müller, S. Regulation of glucose uptake in lymphoma cell lines by c-MYC- and PI3K-dependent signaling pathways and impact of glycolytic pathways on cell viability. *J. Transl. Med.* **2017**, *15*, 158.

Neurotherapeutics (2019) 16:416–431
https://doi.org/10.1007/s13311-018-00681-5

ORIGINAL ARTICLE

Behavioral and Cognitive Improvement Induced by Novel Imidazoline I_2 Receptor Ligands in Female SAMP8 Mice

Christian Griñán-Ferré[1] · Foteini Vasilopoulou[1] · Sònia Abás[2] · Sergio Rodríguez-Arévalo[2] · Andrea Bagán[2] · Francesc X. Sureda[3] · Belén Pérez[4] · Luis F. Callado[5,6] · Jesús A. García-Sevilla[7] · M. Julia García-Fuster[7] · Carmen Escolano[2] · Mercè Pallàs[1]

Published online: 20 November 2018

Abstract

As populations increase their life expectancy, age-related neurodegenerative disorders such as Alzheimer's disease have become more common. I_2-Imidazoline receptors (I_2-IR) are widely distributed in the central nervous system, and dysregulation of I_2-IR in patients with neurodegenerative diseases has been reported, suggesting their implication in cognitive impairment. This evidence indicates that high-affinity selective I_2-IR ligands potentially contribute to the delay of neurodegeneration. *In vivo* studies in the female senescence accelerated mouse-prone 8 mice have shown that treatment with I_2-IR ligands, **MCR5** and **MCR9**, produce beneficial effects in behavior and cognition. Changes in molecular pathways implicated in oxidative stress, inflammation, synaptic plasticity, and apoptotic cell death were also studied. Furthermore, treatments with these I_2-IR ligands diminished the amyloid precursor protein processing pathway and increased Aβ degrading enzymes in the hippocampus of SAMP8 mice. These results collectively demonstrate the neuroprotective role of these new I_2-IR ligands in a mouse model of brain aging through specific pathways and suggest their potential as therapeutic agents in brain disorders and age-related neurodegenerative diseases.

Keywords Imidazoline I_2 receptors · (2-imidazolin-4-yl)phosphonates · Behavior · Cognition · Neurodegeneration · Neuroprotection · Aging

Introduction

Imidazoline receptors (non-adrenergic receptors for imidazolines) [1] have been identified as a promising biological target that deserves further investigation using multidisciplinary approaches to build a comprehensive understanding of their pharmacological possibilities. To date, three main imidazoline receptors, I_1-, I_2- and I_3-IR, have been identified as binding sites that recognize different radiolabeled ligands involving different locations and physiological

Christian Griñán-Ferré and Foteini Vasilopoulou contributed equally to this work.

Electronic supplementary material The online version of this article (https://doi.org/10.1007/s13311-018-00681-5) contains supplementary material, which is available to authorized users.

✉ Mercè Pallàs
pallas@ub.edu

[1] Pharmacology Section, Department of Pharmacology, Toxicology and Medicinal Chemistry, Faculty of Pharmacy and Food Sciences, and Institut de Neurociències, University of Barcelona, Av. Joan XXIII, 27-31, 08028 Barcelona, Spain

[2] Laboratory of Medicinal Chemistry (Associated Unit to CSIC), Department of Pharmacology, Toxicology and Medicinal Chemistry, Faculty of Pharmacy and Food Sciences, and Institute of Biomedicine (IBUB), University of Barcelona, Av. Joan XXIII, 27-31, 08028 Barcelona, Spain

[3] Pharmacology Unit, Faculty of Medicine and Health Sciences, University of Rovira and Virgili, C./St. Llorenç 21, 43201 Reus, Tarragona, Spain

[4] Departament of Pharmacology, Therapeutic and Toxicology, Autonomous University of Barcelona, 08193 Barcelona, Spain

[5] Department of Pharmacology, University of the Basque Country, UPV/EHU, 48940 Leioa, Bizkaia, Spain

[6] Centro de Investigación Biomédica en Red de Salud Mental, CIBERSAM, Leioa, Spain

[7] Laboratory of Neuropharmacology, IUNICS and IdISBa, University of the Balearic Islands (UIB), Cra. Valldemossa km 7.5, 07122 Palma de Mallorca, Spain

functions [2–4]. The pharmacological characterization of I_1-IR is understood the best, and they are used in the antihypertensive drugs moxonidine [5] or rilmenidine [6]. To date, I_2-IR have not been structurally described, although García-Sevilla's group has defined distinct binding proteins corresponding to subgroups of I_2-IR sites [7]. I_2-IR are involved in analgesia [8], glial tumors [9], inflammation [10] and a plethora of brain disorders, such as AD [11, 12], Parkinson's disease (PD) [13], and different psychiatric disorders [14–16]. The efficacy of the analgesic CR4056 in osteoarthritis has advanced this compound in the first-in-class I_2-IR ligand to achieve phase II clinical trials [17]. I_2-IR are widely distributed in the CNS, bind imidazoline-based compounds [18, 19], such as idazoxan or valldemossine [20], and have been associated with the catalytic site of monoamine oxidase enzyme (MAO) [21]. A neuroprotective role for I_2-IR was described through the pharmacological activities observed for their ligands [22]. Idazoxan reduced neuron damage in the hippocampus after global ischemia in the rat brain [23] and agmatine, identified as the endogenous I_2-IR ligand [24], has demonstrated modulatory actions in several neurotransmitters that produce neuroprotection both *in vitro* and in rodent models [25]. The compelling evidence has demonstrated that other selective I_2-IR ligands (Fig. 1) provide benefits such as being neuroprotective against cerebral ischemia *in vivo* [26, 27], inducing beneficial effects in several models of chronic opioid therapy, leading to neuroprotection by direct blocking of *N*-methyl-D-aspartate receptor (NMDA) mediated intracellular [Ca^{2+}] influx [28], or provoking morphological/biochemical changes in astroglia that are neuroprotective after neonatal axotomy [22].

At a cellular level, I_2-IR are situated in the outer membrane of the mitochondria in astrocytes [29], and a direct physiological function of glial I_2-imidazoline preferring sites that regulate the level of the astrocyte marker glial fibrillary acidic protein (*Gfap*) has been proposed [30]. In addition, astrogliosis is a pathophysiological trend in brain neurodegeneration as in AD [31]. The density of I_2-IR is markedly increased in the brains of patients with AD [13], and in gliosis associated with brain injury [32].

The pharmacological characterization of these receptors relies on the discovery of selective I_2-IR ligands devoid of a high affinity for I_1-IR and α_2-adrenoceptors. The reported I_2-IR ligands are structurally restricted, featuring rigid substituted pattern imidazolines, and most of which are not entirely selective and thus interact with α-adrenoceptors [19], which causes side effects [33]. Our chemistry program aimed to find new selective I_2-IR ligands to increase the arsenal of pharmacological tools to exploit the therapeutic potential of I_2-IR in neuroprotection.

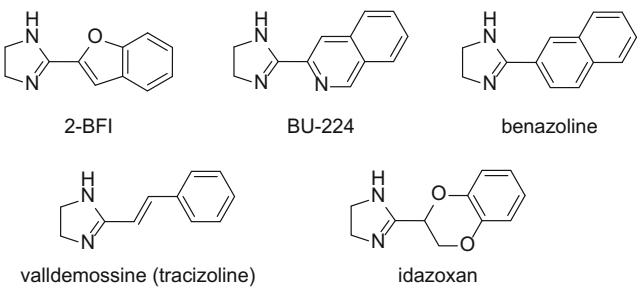

Fig. 1. Representative I_2-IR ligands

We have recently synthesized a series of new chemical scaffolds, 2-imidazolin-4-yl)phosphonates [34], by an isocyanide-based multicomponent reaction under microwave irradiation to avoid using solvents. The experimental synthetic conditions fulfill the principles of green chemistry, giving access to novel compounds with high selectivity and affinity for I_2-IR. Among them, we tested **MCR5** [diethyl (1-(3-chloro-4-fluorobenzyl)-5,5-dimethyl-4-phenyl-4,5-dihydro-1*H*-imidazol-4-yl)phosphonate] in a previous work to demonstrate its neuroprotective and analgesic effects, and it showed promising results in models of brain damage [35]. In particular, mechanisms of neuroprotection related to regulating apoptotic pathways or inhibiting p35 cleavage mediated by this new active compound have been found. In the present work, we explored the behavioral and cognitive status, including molecular changes associated with age and neurodegenerative processes, presented by SAMP8 mice when treated with the new highly selective I_2-IR ligands **MCR5** and **MCR9** [methyl 1-(3-chloro-4-fluorobenzyl)-5,5-dimethyl-4-phenyl-4,5-dihydro-1*H*-imidazole-4-carboxylate] (Fig. 2). SAMP8 is a naturally occurring mouse strain that displays a phenotype of accelerated aging with cognitive decline, as observed in AD, and is widely used as a feasible rodent model of cognitive dysfunction [36]. To the best of our knowledge, this manuscript reports the first study that includes cognitive and behavioral parameters of novel I_2-IR ligands in a well-characterized animal model for studying brain aging and neurodegeneration.

Material and Methods

Synthesis of I_2-IR Ligands MCR5 and MCR9

The compounds were prepared using our previously optimized conditions [34]. I_2-IR p*K*i for **MCR5** and **MCR9** were

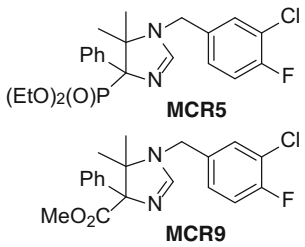

Fig. 2. Structure of I_2-IR ligands **MCR5** and **MCR9**

determined as 9.42±0.16 nM and 8.85±0.21 nM, respectively, showing that both compounds also had high selectivity against α_2 adrenergic receptors (457 and 1862, respectively) [35].

The Blood-Brain Barrier (BBB) Determination Method

The *in vitro* permeability (Pe) of the novel compounds through a lipid extract of the porcine brain was determined using a mixture of PBS/EtOH 70:30. The concentration of drugs was determined using a UV/VIS (250-500 nm) plate reader. Assay validation was carried out by comparing the experimental and reported permeability values of 14 commercial drugs (see supporting information), which provided a good linear correlation: Pe (exp) = 1.003 Pe (lit) – 0.783 (R^2 = 0.93). Using this equation and the limits established by Di et al. [37] for BBB permeation, the following ranges of permeability were established: Pe (10^{-6} cm·s^{-1}) > 5.18 for compounds with high BBB permeation (CNS+); Pe (10^{-6} cm·s^{-1}) < 2.06 for compounds with low BBB permeation (CNS–); and 5.18 > Pe (10^{-6} cm·s^{-1}) > 2.06 for compounds with uncertain BBB permeation (CNS±).

Measurements of Hypothermic Effects

For this study, 25 adult male CD-1 mice (30-40 g) bred in the animal facility at the University of the Balearic Islands were used. Mice were housed in standard cages under defined environmental conditions (22°C, 70% humidity, and a 12-h light/dark cycle, lights on at 8:00 AM) and with free access to a standard diet and tap water. Experimental procedures followed the ARRIVE [38] and standard ethical guidelines (European Communities Council Directive 86/609/EEC and Guidelines for the Care and Use of Mammals in Neuroscience and Behavioral Research, National Research Council 2003) and were approved by the Local Bioethics Committee (UIB-CAIB). All efforts were made to minimize the number of mice used and their suffering.

Mice were handled and weighed by the same person for 2 days so they could habituate to the experimenter before any experimental procedures were initiated. For the acute treatment, mice received a single dose of **MCR9** (20 mg/kg, i.p., n=6) or vehicle (a mixture of equal parts of DMSO and saline, i.p., n=7). For the repeated treatment, mice were treated daily with **MCR9** (20 mg/kg, i.p., n=6) or vehicle (a mixture of equal parts of DMSO and saline, i.p., n=6) for 5 consecutive days. The hypothermic effect of compound **MCR9** was evaluated by measuring rectal temperature before any drug treatment (basal value) and 1 h after drug injection by a rectal probe connected to a digital thermometer (compact LCD thermometer, SA880-1M, RS, Corby, UK). Mice were sacrificed immediately after the last measurement of rectal temperature.

SAMP8 Mouse *In Vivo* Experiments

SAMP8 female mice (n=26) (12 months old) were used to carry out cognitive and molecular analyses. We divided these animals randomly into three groups: SAMP8 Control (n=10) and SAMP8 treated with I_2-IR ligands (**MCR5**, n=8 and **MCR9**, n=8). Animals had free access to food and water and were kept under standard temperature conditions (22 ±2°C) and a 12-h light/dark cycle (300 lux/0 lux). **MCR5** and **MCR9** (5 mg/Kg/day) were dissolved in 1.8% 2-hydroxypropyl-β-cyclodextrin and administered through drinking water for 4 weeks. Water consumption was controlled each week, and I_2-IR ligand concentrations were adjusted accordingly to reach the optimal dose.

Studies and procedures involving mice brain dissection and subcellular fractionation were performed by the ARRIVE [38] and international guidelines for the care and use of laboratory animals (see above) and approved by the Ethics Committee for Animal Experimentation at the University of Barcelona.

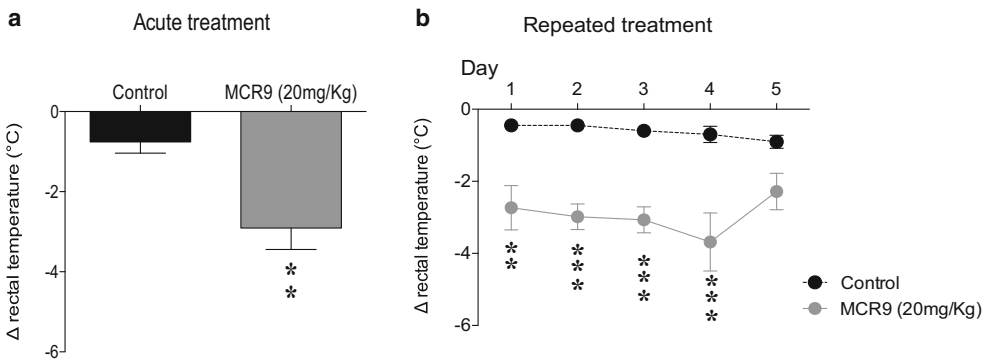

Fig. 3. Acute and repeated measurement of the hypothermic effect of compound **MCR9** in mice. **a** Effect of acute treatment with **MCR9** (20 mg/kg, i.p.) on rectal body temperature in mice. Columns are means ± SEM of the difference (Δ, 1 h - basal value) in body temperature (°C) for **MCR9**-treated mice compared with vehicle-treated **Control** mice. Data were analyzed using Student's t-test. **p<0.01. **b** Effect of repeated (5 days) treatments with **MCR9** (20 mg/kg, i.p., closed circles) on rectal body temperature in mice. Circles are means ± SEM of the difference (Δ, 1 h - basal value) in body temperature (°C) for **MCR9**-treated mice compared with vehicle-treated **Controls**. Data were analyzed using repeated measures ANOVA followed by Sidak's multiple comparison test. **p<0.01, ***p<0.001; (n=6–7 animals per group)

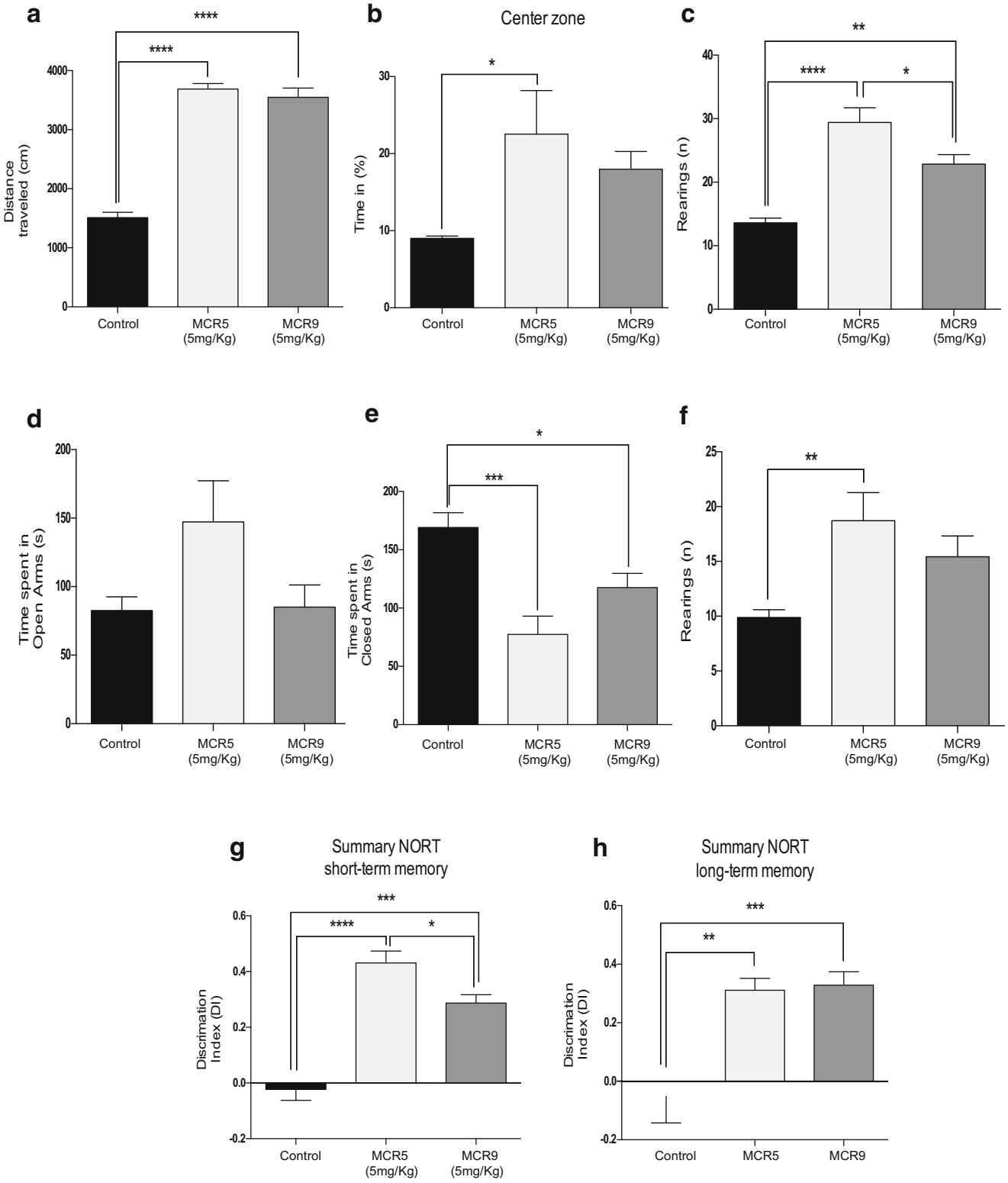

Open Field (OFT), Elevated Plus Maze (EPM), and Novel Object Recognition Test (NORT)

The OFT apparatus was a white polywood box (50x50x25 cm). The floor was divided into two areas defined as center zone and peripheral zone (15 cm between the center zone and the wall). Behavior was scored with SMART® vers. 3.0 software, and each trial was recorded for later analysis using a camera situated above the apparatus. Twenty-six mice (n=8-10 per group) were placed at the center and allowed to explore

◀ **Fig. 4.** Behavioral and cognitive improvement in 12-month-old treated SAMP8 mice with both I_2-IR ligands. **a** A significant increase in the distance traveled in the open field test in the I_2-IR ligand treated groups compared with the **Control** group. **b** A significant increase in the percentage of time in the center zone of the opened field test in the **MCR5** treated group compared with the **Control** group, and no significant difference between the **MCR9** and **Control** groups. **c** A significant increase in the number of total rears of the opened field test among groups. **d** The time spent in the opened arms of the EPM did not differ among groups. **e** A significant increase in the time spent in the closed arms among the **Control** group compared with the treated groups. **f** A significant increase in the number of total rears of the EPM in the **MCR5** group compared with the **Control** group. **g** The results of the NORT in the short-term memory (2 h) revealed a significant increase in both I_2-IR ligand treated groups compared with the **Control** group as well as a significant reduction in the DI of the **MCR9** group compared with **MCR5** group, and (**h**) a significant increase in the DI of the long-term memory (24 h) in both I_2-IR ligand treated groups compared with the **Control** group. Data expressed as means ± SEM (n=8-10 animals per group) and analyzed using one-way ANOVA followed by Tukey's post hoc test for multiple comparisons. *p<0.05, **p<0.01, ***p<0.001 and ****p<0.0001

the box for 5 min. Afterward, the mice were returned to their home cages and the OFT apparatus was cleaned with 70% EtOH. The parameters scored included center staying duration, rears, defecations, and the distance traveled, calculated as the sum of total distance traveled in 5 min.

The EMP apparatus consists of opened arms and closed arms, crossed in the middle perpendicularly to each other, and a central platform (5×5cm) constructed of dark and white plywood (30×5×15 cm). To initiate the test session, 26 mice (n=8-10 per group) were placed on the central platform, facing an open arm, and allowed to explore the apparatus for 5 min. After the 5-min test, mice were returned to their home cages, and the EPM apparatus was cleaned with 70% EtOH and allowed to dry between tests. Behavior was scored with SMART® vers. 3.0 software, and each trial was recorded for later analysis using a camera fixed to the ceiling at a height of 2.1 m and situated above the apparatus. The parameters recorded included time spent on opened arms, time spent on closed arms, time spent in the center zone, rears, defecation and urination.

The NORT protocol employed was a modification of that of Ennaceur and Delacour [39]. In brief, 26 mice (n=8-10 per group) were placed in a 90°, two-arm, 25-cm-long, 20-cm-high, 5-cm-wide black maze. The walls could be removed for easy cleaning. Light intensity in mid-field was 30 lux. Before performing the test, the mice were individually habituated to the apparatus for 10 min for 3 days. On day 4, the animals were submitted to a 10-min acquisition trial (first trial), during which they were placed in the maze in the presence of two identical, novel objects (A+A or B+B) at the end of each arm. A 10-min retention trial (second trial) was carried out 2 h and 24 h later, with one of the two objects changed. During these second trials, mice behavior was recorded with a camera. The time with the new object (TN) and the time with the old object (TO) were measured. A discrimination index (DI) was defined as (TN −TO)/(TN+TO). The maze and the objects were cleaned with 96% EtOH after each test to eliminate olfactory cues.

Brain Processing

Mice were euthanized by cervical dislocation 1 day after the behavioral and cognitive tests finished. Brains were immediately removed from the skull. The hippocampus of each mouse was then isolated and frozen in powdered dry ice. Each hippocampus was maintained at -80°C for further use. Tissue samples were homogenized in lysis buffer containing phosphatase and protease inhibitors (Cocktail II, Sigma-Aldrich). Total protein levels were obtained and the Bradford method was used to determine protein concentration.

Protein Levels Determination by Western Blot (WB)

For WB, aliquots of 15 μg of hippocampal protein were used. Protein samples from 15 mice (n=5 per group) were separated by SDS-PAGE (8-12%) and transferred onto PVDF membranes (Millipore). Afterward, membranes were blocked in 5% non-fat milk in 0.1% Tween20 TBS (TBS-T) for 1 h at room temperature, followed by overnight incubation at 4°C with the primary antibodies listed in Table 1 (Supporting Information). Membranes were washed and incubated with secondary antibodies for 1 h at room temperature. Immunoreactive proteins were viewed with a chemiluminescence-based detection kit, following the manufacturer's protocol (ECL Kit; Millipore) and digital images were acquired using a ChemiDoc XRS+ System (BioRad). Semi-quantitative analyses were carried out using ImageLab software (BioRad), and results were expressed in arbitrary units, considering control protein levels as 100%. Protein loading was routinely monitored by immunodetection of glyceraldehyde-3-phosphate dehydrogenase (GAPDH).

Determination of OS in the Hippocampus

Hydrogen peroxide (H_2O_2) from 12 mice (n=4 per group) was measured in hippocampal tissue protein extracts obtained as described above. It was used as an indicator of OS and was quantified using a hydrogen peroxide assay kit (Sigma-Aldrich, St. Louis, MI) according to the manufacturer's instructions.

RNA Extraction and Gene Expression Determination

Total RNA isolation was carried out using the TRIzol® reagent according to manufacturer's instructions. The yield, purity, and quality of RNA were determined spectrophotometrically with a NanoDrop™ ND-1000 (Thermo Scientific) apparatus and an Agilent 2100B Bioanalyzer (Agilent Technologies). RNAs with 260/280 ratios and RIN higher than 1.9 and 7.5, respectively, were selected. Reverse Transcription-Polymerase Chain Reaction (RT-PCR) was

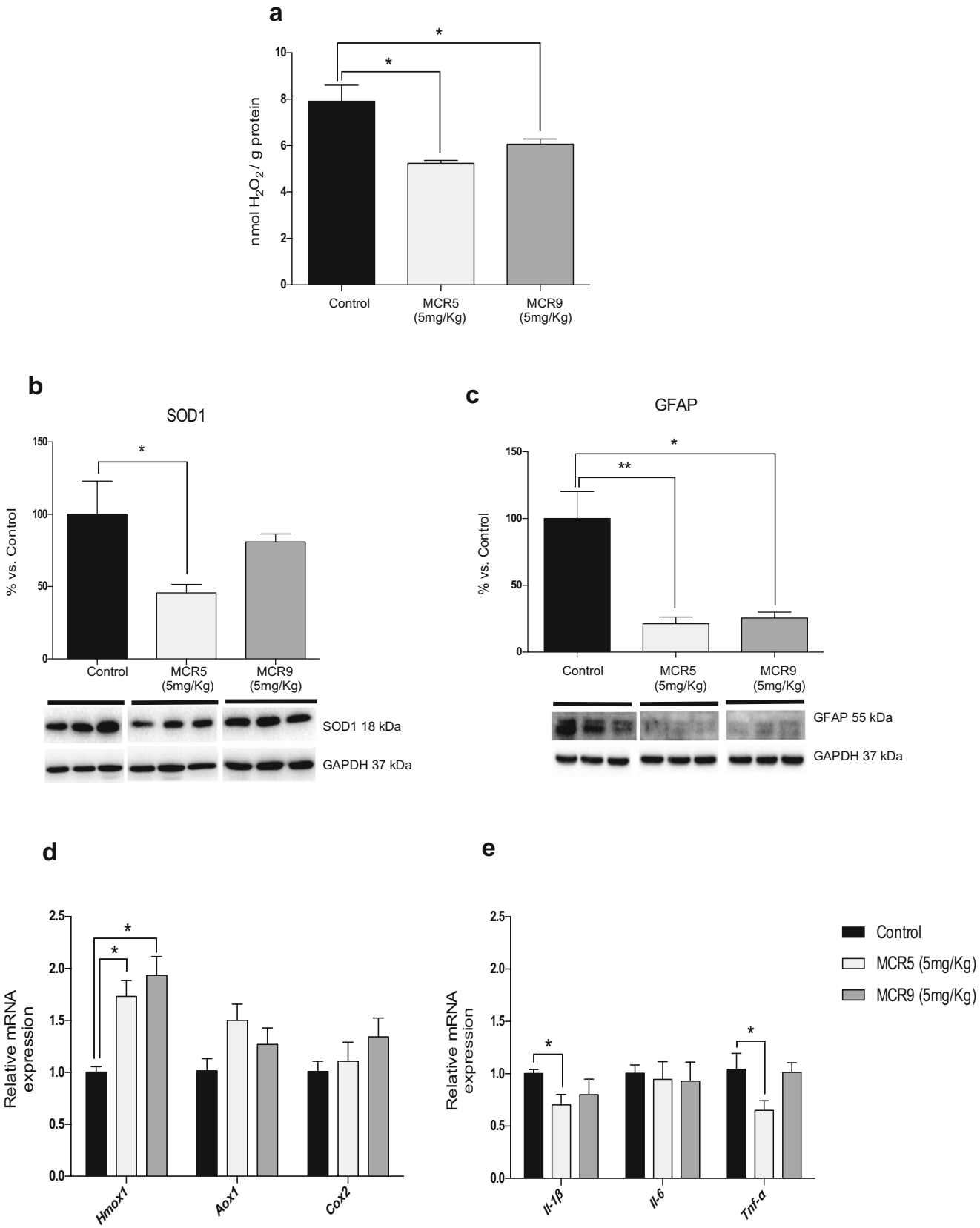
a
nmol H_2O_2 / g protein
Control
MCR5 (5mg/Kg)
MCR9 (5mg/Kg)
b
SOD1
% vs. Control
SOD1 18 kDa
GAPDH 37 kDa
c
GFAP
% vs. Control
GFAP 55 kDa
GAPDH 37 kDa
d
Relative mRNA expression
Hmox1
Aox1
Cox2
e
Relative mRNA expression
Il-1β
Il-6
Tnf-α
Control
MCR5 (5mg/Kg)
MCR9 (5mg/Kg)

◀ **Fig. 5.** Reduced OS and inflammatory markers in 12-month-old treated SAMP8 mice with both I_2-IR ligands. **a** There was a significant reduction in the hydrogen peroxide concentration in both I_2-IR ligand treated groups compared with the **Control** group in homogenates of the hippocampus tissue. **b** A significant reduction in SOD1 protein levels in the **MCR5** group compared with the **Control** group and no difference between the **MCR9** and **Control** groups. **c** A significant reduction in *Gfap* protein levels in the **MCR5** and **MCR9** groups compared with the **Control** group. **d** Gene expression of antioxidant enzymes in the mouse hippocampus. A significant increase in *Hmox1* gene expression, but not for *Aox1* and *Cox2,* among both I_2-IR ligand treated groups and the **Control** group. **e** A significant reduction in gene expression of *Il-1β* and *Tnf-α* in the **MCR5** group compared with the **Control** group, and a tendency for the same genes to reduce in the **MCR9** group. However, *Il-6* gene expression did not differ among groups. Values in bar graphs are adjusted to 100% for protein level of the **Control** group. Gene expression levels were determined by real-time PCR. Data are expressed as means ± SEM (n=4-5 animals per group) and analyzed using one-way ANOVA followed by Tukey's post hoc test for multiple comparisons. *p<0.05

performed as follows: 2 μg of mRNA was reverse-transcribed using the high capacity cDNA reverse transcription kit (Applied Biosystems). Real-time quantitative PCR (qPCR) was employed to quantify the mRNA expression of OS genes heme oxygenase (decycling) 1 (*Hmox1*), aldehyde oxidase 1 (*Aox1*), cyclooxygenase 2 (*Cox2*), inflammatory genes interleukin 6 (*Il-6*), interleukin 1 beta (*Il-1β*), tumor necrosis factor alpha (*Tnf-α*), amyloid processing gene disintegrin, and metalloproteinase domain-containing protein 10 (*Adam10*) and amyloid degradation gene neprilysin (*NEP*). The primers are listed in Table 2 (Supporting Information).

SYBR® Green real-time PCR was performed in a Step One Plus Detection System (Applied-Biosystems) employing SYBR® Green PCR Master Mix (Applied-Biosystems). Each reaction mixture contained 7.5 μL of cDNA (a 2-μg concentration), 0.75 μL of each primer (a 100-nM concentration, each), and 7.5 μL of SYBR® Green PCR Master Mix (2X).

TaqMan-based real-time PCR (Applied Biosystems) was also performed in a Step One Plus Detection System (Applied-Biosystems). Each 20 μL of TaqMan reaction contained 9 μL of cDNA (25 ng), 1 μL 20X probe of TaqMan Gene Expression Assays and 10 μL of 2X TaqMan Universal PCR Master Mix.

Data were analyzed using the comparative cycle threshold (Ct) method (ΔΔCt), where the housekeeping gene level was used to normalize differences in sample loading and preparation. Normalization of expression levels was performed with *actin* for SYBR® green-based real-time PCR results and *Tbp* for TaqMan-based real-time PCR. Each sample (n=4-5 per group) was analyzed in duplicate, and the results represent the n-fold difference of the transcript levels among different groups.

Statistical Analysis

The statistical analyses were conducted using GraphPad Prism ver. 6 statistical software. Data were expressed as the mean ± standard error of the mean (SEM). Means were compared with one-way analysis of variance (ANOVA) and Tukey's post hoc test or two-tailed Student's *t*-test when necessary. Statistical significance was considered when p values were <0.05. Statistical outliers were performed out with Grubbs' test and were removed from the analysis.

Results

BBB Permeation Assay for I_2-IR Ligands MCR5 and MCR9

The tested compounds **MCR5** and **MCR9** had Pe values of 13.5±0.9 and 26.9±1.7, respectively, well above the threshold for high BBB permeation, so they were predicted to be able to cross the BBB and reach their biological target in the CNS. Supplementary information on results analysis can be found in the supporting material (Table 3).

Hypothermic Effects of MCR9 in Mice

Selective I_2-IR ligands induce hypothermia in rodents [4]. In particular, the hypothermic effect of compound **MCR5** in mice was evaluated in a recent study from our research group (results for compound **2c** in ref 35) [35]. Similar to **MCR5**, **MCR9** induced mild hypothermia as assessed by a moderate reduction (-2.3°C) in rectal temperature 1 h after injection at the tested dose of 20 mg/kg in adult CD-1 mice and as compared with vehicle-treated controls (Fig. 3a, day 1). While repeated (5 days) administration (20 mg/kg) revealed persistently the hypothermic effects of **MCR9** from days 1 to 4 (range from -2.3 to -3.2°C), on day 5 no significant change was observed in body temperature (-1.8°C change) as compared with vehicle-treated controls (Fig. 3b).

Beneficial Effects on Behavior and Cognition Induced by MCR5 and MCR9 in SAMP8 Mice

Results obtained in OFT demonstrated that both compounds increased locomotor activity and time spent in the center zone (Fig. 4a and b). Furthermore, a significant increment in the vertical activity, quantified by the number of total rears, was observed in mice treated with **MCR5** or **MCR9** in OFT and the EPM (Fig. 4c and f). EPM data indicated a reduction in anxiety-like behavior by a significant decrease in time spent in closed arms for treated animals compared with controls (Fig. 4e). These results are supported by a preference for opened arms, although not significant, for **MCR5** (Fig. 4d). Moreover, a significant increase in the DI indicates an improved performance in recognition of the new object in the NORT between **MCR5**- and **MCR9**-treated SAMP8 mice compared with the control group. A robust effect in short (2

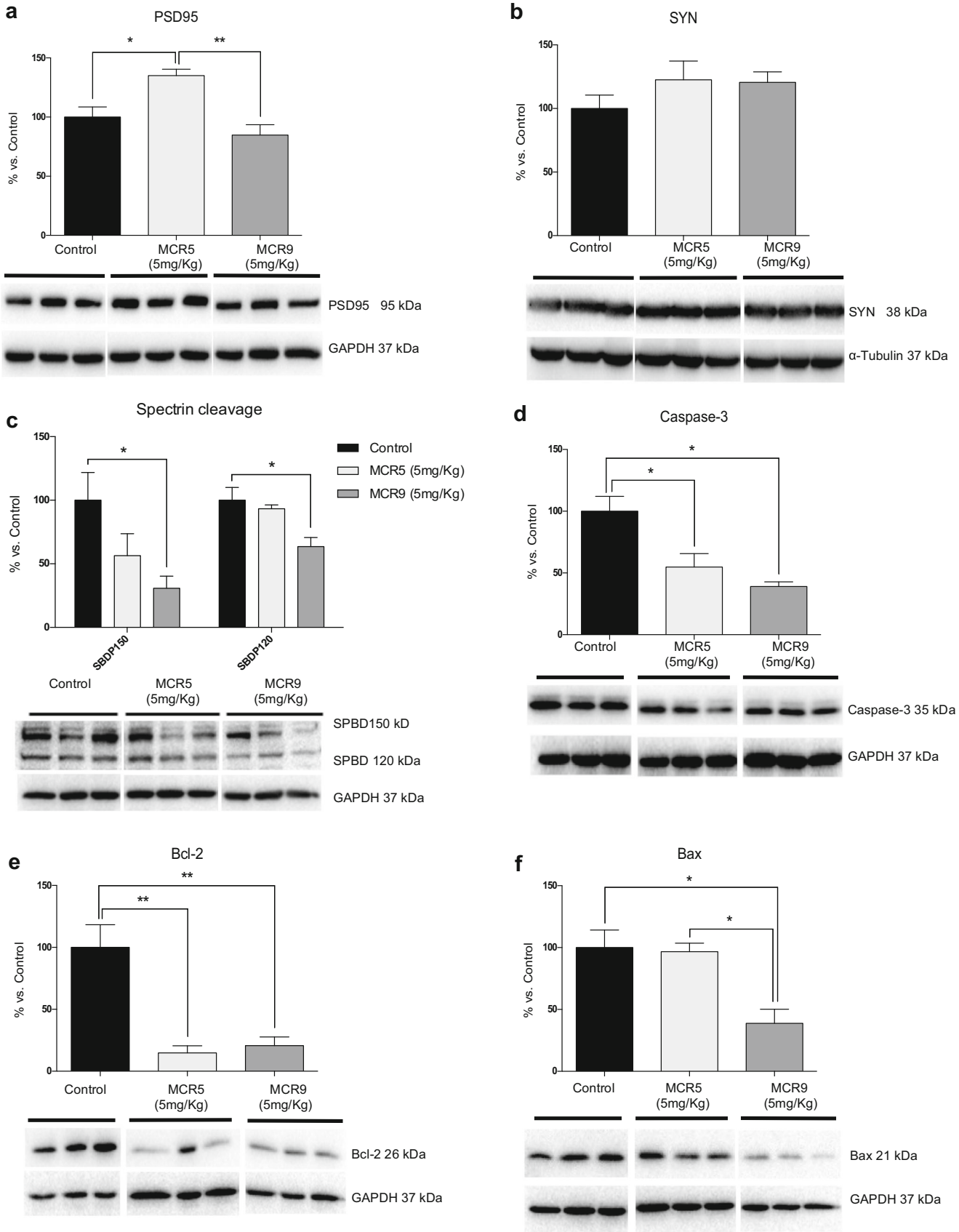
a
PSD95
% vs. Control
Control
MCR5 (5mg/Kg)
MCR9 (5mg/Kg)
PSD95 95 kDa
GAPDH 37 kDa
b
SYN
SYN 38 kDa
α-Tubulin 37 kDa
c
Spectrin cleavage
Control
MCR5 (5mg/Kg)
MCR9 (5mg/Kg)
SBDP150
SBDP120
SPBD150 kD
SPBD 120 kDa
GAPDH 37 kDa
d
Caspase-3
Caspase-3 35 kDa
GAPDH 37 kDa
e
Bcl-2
Bcl-2 26 kDa
GAPDH 37 kDa
f
Bax
Bax 21 kDa
GAPDH 37 kDa

◀ **Fig. 6.** Changes in synaptic markers and apoptotic factors in 12-month-old treated SAMP8 mice with both I_2-IR ligands. **a** A significant increase in PSD95 protein levels in the **MCR5** group compared with the other two groups. **b** A tendency for SYN protein levels to increase in both I_2-IR ligand treated groups compared with the **Control** group. **c** A tendency for a reduction in the spectrin fragment SPBD 150, and a significant reduction in the spectrin fragment SPBD 120 in the **MCR9** group compared with the **Control** group. **d** A significant reduction in Caspase-3 protein levels in both I_2-IR ligand groups compared with the **Control** group. **e** A significant reduction in Bcl-2 protein levels in both I_2-IR ligand groups compared with the **Control** group. **f** A significant reduction in Bax protein levels in the **MCR9** group compared with the other groups. Values in bar graphs are adjusted to 100% for protein level of the **Control** group. Representative WB for each protein in the mouse hippocampus is shown. Data are expressed as means ± SEM (n=5 animals per group) and analyzed using one-way ANOVA followed by Tukey's post hoc test for multiple comparisons. *p<0.05, **p<0.001

h) and long-term (24 h) memory was found for the two tested compounds (Fig. 4g and h).

OS and Inflammatory Markers Reduced by MCR5 and MCR9 in SAMP8 Mice

OS and neuroinflammation are thought to be key risk factors in the development of neurodegeneration. The hydrogen peroxide levels in the hippocampus were significantly reduced in brains of mice treated with either **MCR5** or **MCR9** compared with the control group (Fig. 5a). Of note, superoxide dismutase 1 (SOD1) protein levels in treated mice were reduced by **MCR5** but not by **MCR9** (Fig. 5b). Moreover, *Hmox1* gene expression, an important key enzyme in cellular antioxidant-defense, was also significantly increased with both **MCR5** and **MCR9** (Fig. 5d). Other OS markers, such as *Aox1* or *Cox2*, were not significantly altered (Fig. 5d). Regarding the inflammation markers, no changes were observed in *Il-6* gene expression for tested compounds, but a significant decrease in *Il-1β* and *Tnf-α* for **MCR5** treated SAMP8 mice was found (Fig. 5e). Moreover, a significant diminution in *Gfap* gene expression was determined, reinforcing the prevention of inflammatory processes by **MCR5** and **MCR9** (Fig. 5c).

Changes in Synaptic Markers and Apoptotic Factors Induced by MCR5 and MCR9 in SAMP8 Mice

MCR5, but not **MCR9**, induced an increase in postsynaptic density protein 95 (PSD95) protein levels (Fig. 6a). Protein levels for synaptophysin (SYN), a presynaptic protein, showed a slight increase for both compounds, although it did not reach significance (Fig. 6b). To determine the implication of proteolytic processes in the **MCR5** and **MCR9** compounds, we found reduced levels of calpain (data not shown) with a significant diminution in 150 α-spectrin breakdown fragment (SPBD) (Fig. 6c). Furthermore, **MCR9** and **MCR5** reduced caspase-3 activity in SAMP8 mouse hippocampi, because of the diminution of caspase-3 protein levels and 120 SPBD fragments, which reached significance for **MCR9** (Fig. 6c and d). Moreover, B-cell lymphoma 2 (Bcl-2) levels were diminished, and Bcl-2-associated X (Bax), a key protein in the apoptotic cascade, was reduced by **MCR5** (Fig. 6e and f), supporting a possible implication of I_2-IR in apoptosis processes.

Changes in Mitogen-Activated Protein Kinase (MAPK) Signaling Pathways Reduced Hyperphosphorylation of Tau Induced by MCR5 and MCR9 in SAMP8 Mice

Key proteins associated with molecular pathways disturbed in brain disorders and neurodegeneration were evaluated by WB. Interestingly, **MCR5**, but not **MCR9**, increased the p-AKT/AKT ratio (protein kinase B) (Fig. 7a). Accordingly, higher levels of inactivated glycogen synthase kinase 3 beta (GSK3β), phosphorylated in Ser9, were determined (Fig. 7b). Extracellular signal-regulated kinase (ERK½) inhibition by **MCR5** and **MCR9** was demonstrated by a reduction of the p-ERK½ ratio (Fig. 7c). Furthermore, cyclin-dependent kinases 5 (CDK5) measured by the p-CDK5/CDK5 and p25/p35 ratios were also reduced (Fig. 7d and e). Taking into account the results obtained on kinases CDK5, GSK3β, AKT, and ERK½, we studied Tau hyperphosphorylation levels in the hippocampi of SAMP8 mice. A significant reduction in Tau phosphorylation in treated SAMP8 mice was found, specifically for the Ser404 phosphorylation site, whereas the Ser396 phosphorylation site was reduced without reaching significance (Fig. 7f).

Changes in APP Processing and Aβ Degradation Induced by MCR5 and MCR9 in SAMP8 Mice

We found a significant increase in sAPPα protein levels in **MCR9** treated SAMP8 mice (Fig. 8a) and a significant reduction in sAPPβ protein levels in **MCR5** treated SAMP8 mice (Fig. 8b). Furthermore, a significant increase in gene expression for *Adam10*, an α-secretase that cleaves APP and *NEP*, an Aβ degrading enzyme (Fig. 8c and d), was observed in both treated mice groups compared with that in non-treated animals.

Discussion

I_2-IR are related to several physiological and pathological processes, including those of the CNS, such as pain [8], neuropathic pain [40], seizures [41, 42], and neurodegenerative diseases such as AD [14, 43]. Our lab has a research line on developing new high affinity and selectivity I_2-IR ligands, maintaining the imidazoline scaffold and incorporating

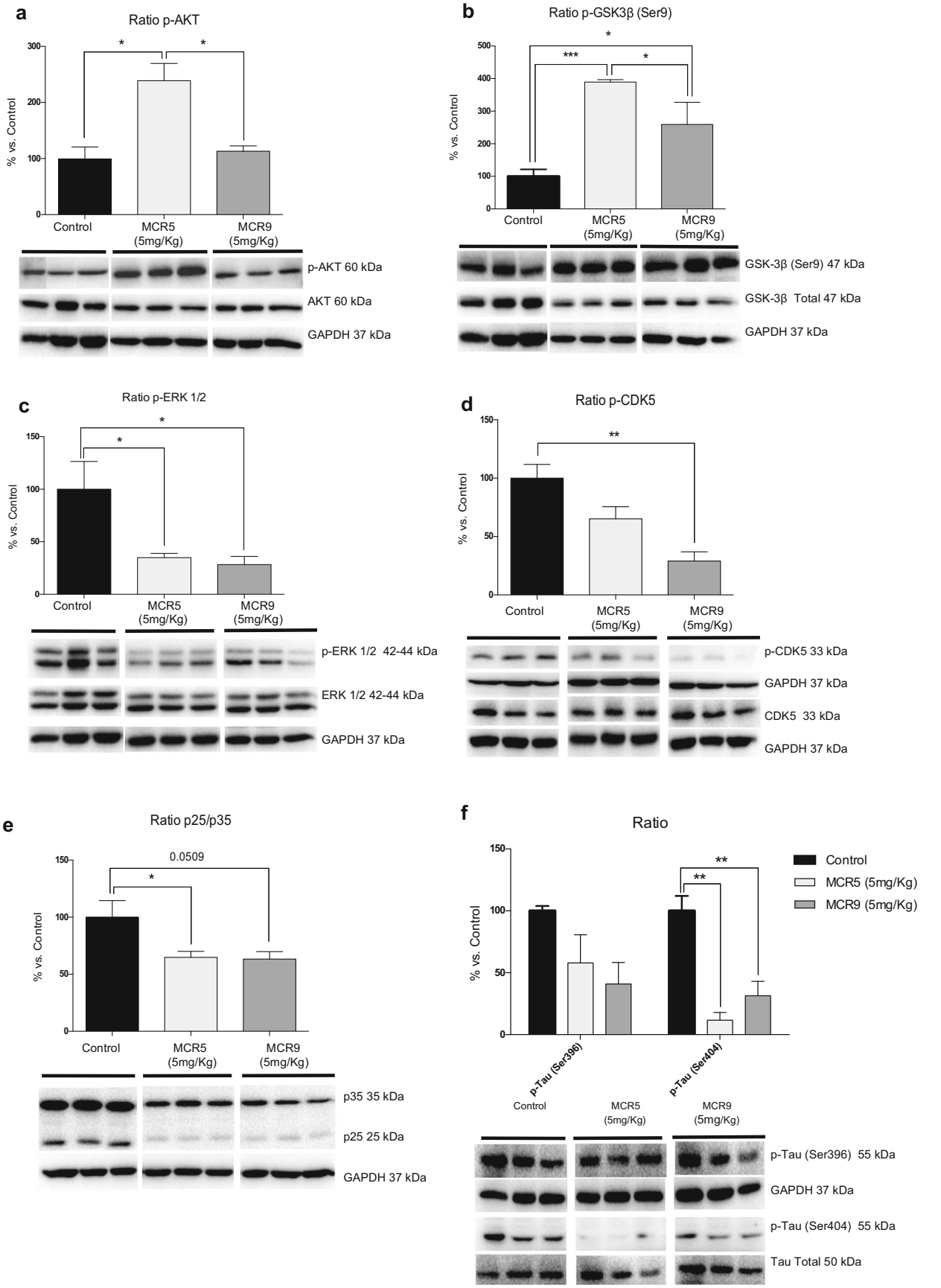
a
Ratio p-AKT
% vs. Control
Control
MCR5 (5mg/Kg)
MCR9 (5mg/Kg)
p-AKT 60 kDa
AKT 60 kDa
GAPDH 37 kDa
b
Ratio p-GSK3β (Ser9)
GSK-3β (Ser9) 47 kDa
GSK-3β Total 47 kDa
GAPDH 37 kDa
c
Ratio p-ERK 1/2
p-ERK 1/2 42-44 kDa
ERK 1/2 42-44 kDa
GAPDH 37 kDa
d
Ratio p-CDK5
p-CDK5 33 kDa
GAPDH 37 kDa
CDK5 33 kDa
GAPDH 37 kDa
e
Ratio p25/p35
0.0509
p35 35 kDa
p25 25 kDa
GAPDH 37 kDa
f
Ratio
Control
MCR5 (5mg/Kg)
MCR9 (5mg/Kg)
p-Tau (Ser396)
p-Tau (Ser404)
p-Tau (Ser396) 55 kDa
GAPDH 37 kDa
p-Tau (Ser404) 55 kDa
Tau Total 50 kDa

◀ **Fig. 7.** Changes in kinase signaling pathways reduced hyperphosphorylation of Tau in 12-month-old SAMP8 mice treated with both I_2-IR ligands. **a** A significant increase in the p-AKT ratio in the **MCR5** group compared with the other two groups. **b** A significant increase in inactive p-GSK3β (Ser9) protein levels in both I_2-IR ligand treated groups compared with the **Control** group. **c** A significant reduction in p-ERK½ in both I_2-IR ligand treated groups compared with the **Control** group. **d** Changes in the p-CDK5/CDK5 ratio induced by **MCR5** and **MCR9** treatment. **e** Changes in the p25/p35 ratio in the **MCR5** and **MCR9** groups compared with the **Control** group. Representative WB are shown. **f** A reduction in p-Tau (Ser396), as well as a significant reduction in p-tau (Ser404) in both I_2-IR ligand treated groups compared with the **Control** group. Values in bar graphs are adjusted to 100% for protein level of the **Control** group. Data are expressed as means ± SEM (n=5 animals per group) and analyzed using one-way ANOVA followed by Tukey's post hoc test for multiple comparisons. *p<0.05, **p<0.01, ***p<0.001

several substituents in the imidazoline ring. Some of these were previously tested for their neuroprotective role [35].

Given the enormous potential of I_2-IR and their implications in brain disorders and neurodegenerative diseases such as AD, we set out to explore whether **MCR5** and **MCR9**, two members of a structurally new family of I_2-IR ligands, might improve the behavioral and cognitive status in SAMP8 model mice. The main chemical structural differences were a phosphonate substituent on the imidazoline ring for **MCR5** in contrast with an ester group for **MCR9** (Fig. 2).

Published results from our lab demonstrated that **MCR5** presented a p*K*i for the I_2-IR of 9.42±0.16 and high selectivity when compared with the α_2 receptor affinity [35]. Likewise, **MCR9** is a high-affinity I_2-IR ligand (p*K*i 8.85±0.21) but with a higher selectivity against α_2 receptors. Both **MCR5** and **MCR9** were predicted to be able to cross the BBB, an important drug characteristic when action is expected in the CNS.

Previous studies have evaluated the effects of selective I_2-IR ligands on inducing hypothermia in rodents [e.g., idazoxan or BU224] [44]. Accordingly, **MCR5** can induce hypothermia in mice, and showed a neuroprotective role in kainate-induced seizures, modifying levels of a Fas-associated protein with death domain (FADD) receptor [35]. While acute **MCR5** (5 and 20 mg/kg) induced mild hypothermia, repeated (20 mg/kg, 5 days) administration of **MCR5** revealed significantly attenuated hypothermic effects from day 2, which indicated the induction of tolerance to the hypothermic effects of the drug [35]. For **MCR9**, repeated (20 mg/kg, 5 days) administration revealed persistent hypothermic effects up to day 4. These results suggest that the slow induction of tolerance to the hypothermic effects caused by **MCR9** might be started following 5 days of drug administration, although a more extended treatment paradigm might be needed for confirmation.

The hypothermic effects exerted by **MCR5** and **MCR9** might be relevant to induce neuroprotection because it was previously proposed for some of the neuroprotective effects induced by the I_2-IR selective ligand idazoxan. Several experiments have ascertained a possible role for hypothermia in mediating neuroprotection. For example, small drops in temperature exerted neuroprotection in cerebral ischemia [45] and are typically used in the clinic to improve the neurological outcome under various pathological conditions (e.g., stroke, brain injury). Although the mechanisms explaining the neuroprotective effects mediated by hypothermia are not well understood, some researchers have suggested that they might be related to the inhibition of glutamate release [46].

SAMP8 mice have been studied as a non-transgenic murine mouse model of accelerated senescence and late-onset AD. These mice exhibit cognitive and emotional disturbances, probably due to the early development of pathological brain hallmarks, such as OS, inflammation, and activation of neuronal death pathways, which mainly affect the cerebral cortex and hippocampus [47, 48]. To date, this rodent model has not been used to test I_2-IR ligands. Thus, this work is the first investigation of the effects of the improvement of cognitive impairment and behavior in this mouse model after treatment with I_2-IR ligands.

Behavioral and cognitive effects were investigated through three well-established tests in SAMP8 mice: the OFT, which is an experiment used to assay general locomotor activity and anxiety in rodents [49]; the EPM, one of the most widely used tests for measuring anxiety-like behavior [50]; and the NORT, as a standard measure of cognition (for short- and long-term memory) [51].

The OFT and EPM parameters indicated a reduction in cognitive impairment through showing improved locomotor activity jointly with an anti-anxiousness effect. Likewise, the NORT results demonstrated an improvement in cognitive and short- and long-term learning capabilities in hippocampal memory processes. Therefore, all the assessed parameters showed robust beneficial effects on cognition and behavior after **MCR5** and **MCR9** treatment in SAMP8 mice.

The results in cognitive and behavioral effects were supported by a cellular and biochemical assessment of characteristic parameters related to cognitive decline and AD. The compelling evidence demonstrated a neuroprotective role for I_2-IR. The neuroprotective role can be related to OS and inflammation [52] by measuring OS indicators and inflammation markers in SAMP8 mouse brain tissue treated with the I_2-IR ligands, **MCR5** and **MCR9**. Results showed significant reduced hydrogen peroxide levels in hippocampal tissue and increased *Hmox1* gene expression in treated **MCR5** and **MCR9** SAMP8 mice, but not in other sensors for OS, such as *Aox1* or *Cox2*. SOD1 protein levels were reduced by **MCR5** but not by **MCR9**. Regarding inflammation markers, no changes were observed in *Il-6* gene expression for tested compounds, but a significant decrease in *Il-1β* and *Tnf-α* for **MCR5** treated SAMP8 mice was

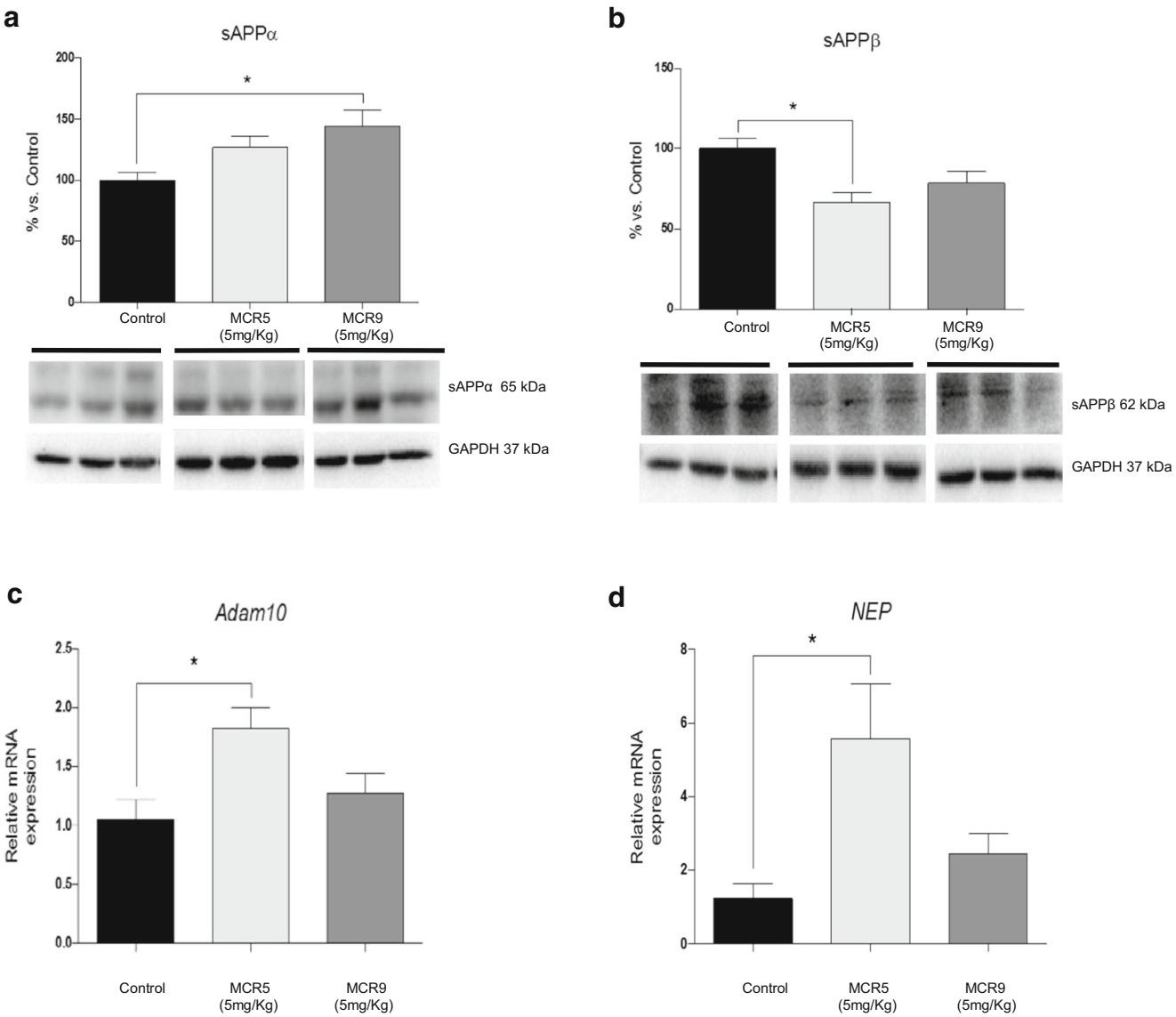

Fig. 8. Changes in APP processing and Aβ degradation enzymes in 12-month-old SAMP8 mice treated with both I_2-IR ligands. Representative WB of the APP and its fragments. **a** A significant increase in sAPPα protein levels in the **MCR9** group compared with the **Control** group, and no significant difference between the **MCR5** and **Control** groups. **b** A significant reduction in sAPPβ protein levels in the **MCR5** group compared with the **Control** group, and no significant difference between the **MCR9** and **Control** groups. **c** A significant increase in *Adam10* gene expression in the **MCR5** group compared with the **Control** group, and no significant difference in the **MCR9** group. **d** A significant increase in *NEP* gene expression in the **MCR5** group compared with the **Control** group, and no significant difference in the **MCR9** group. Values in bar graphs were adjusted to 100% for protein level of the **Control** group. Gene expression levels were determined by real-time PCR. Data are expressed as means ± SEM (n=4-5 animals per group) and analyzed using one-way ANOVA followed by Tukey's post hoc test for multiple comparisons. *p<0.05

found. In addition, reduced astrogliosis was found in treated animals, corroborating a reduced inflammatory environment in hippocampi of **MCR5** and **MCR9** treated SAMP8 mice. Altogether these results showed a relatively weak influence in OS and inflammation mechanisms by I_2-IR ligands in SAMP8 mice [53–57]. However, a role for those two pathological conditions related to I_2-IR ligand interaction cannot be discarded because **MCR5** elicited beneficial effects despite the old age of the SAMP8 mice. Aged SAMP8 mice present lower inflammation and OS due to being at the endpoint of the senescence process [56, 57]. Therefore, it can be challenging to determine drug effects on these processes in aged SAMP8 mice.

MCR5 and **MCR9** effects on key molecular markers for synapsis and apoptosis were studied to unravel the prevention of cognitive decline by I_2-IR ligands in SAMP8 mice, which is characterized by alterations in those processes. In consonance with better cognitive performance, the compounds tested increased synaptic markers such as SYN and PSD95, indicating a neuroprotective role for **MCR5** and **MCR9**.

There are several cellular and molecular pathways related to better synaptic performance, including proteolytic and phosphorylation activities or apoptotic processes. Regarding proteolytic processes, calpain is an intracellular protease that cleaves the CDK5 activator p35 to a p25 fragment**. MCR5** and **MCR9** diminished calpain levels and its activity with a reduced 150 SPBD fragment. Moreover, a significant reduction in p25 protein levels was found in treated SAMP8 mice. A decrease in p25 can also influence CDK5 activity, as implicated in Tau phosphorylation [58, 59]. These results indicate that CDK5 phosphorylation activity should be diminished after I_2-IR ligand treatment, corroborating results obtained previously for **MCR5** in a kainate model of neuronal damage [60].

Caspase 3 mediated apoptosis was also addressed. A significant reduction of caspase 3 activity and diminution of Bax protein were found in **MCR9** treated SAMP8 mice. Because Bax is described as a pro-apoptotic protein, its diminution indicates a possible protective role for I_2-IR ligands in neurons [61]. By contrast, reduced levels of Bcl-2, considered an anti-apoptotic protein, deserve further studies. Several authors have indicated that when Bax is reduced, Bcl-2 is less necessary for blocking Bax dimer to form the mitochondrial pore; in this situation cells reduce the Bcl-2 levels as a control mechanism [62].

An increase in p-AKT was induced by the I_2-IR ligands, whereas a decrease in ERK½ activation was observed. p-AKT inactivated GSK3β, a key kinase involved in the process of Tau hiperphosphorylation, by phosphorylation in Ser9. To this point, **MCR5-** and **MCR9**-treated SAMP8 mice showed an increase of Ser9 phosphorylated GSK3β and reduced Tau hyperphosphorylation.

ERK½ inhibition (that reduction of p42/p44) by **MCR5** and **MCR9** can contribute to the beneficial effect elicited by I_2-IR on synaptic markers and Tau phosphorylation processes. ERK½ belongs to a subfamily of MAPKs and plays diverse roles in the CNS, such as neuronal survival or death, synaptic plasticity, and learning and memory through phosphorylation of regulatory enzymes and kinases [63, 64]. Although crucial for neuronal survival, there is some evidence that prolonged activation of the ERK pathway can induce a deleterious effect to the cell [65, 66]. Interestingly, long-lasting ERK activation in neurons has been demonstrated in neurodegenerative diseases such as AD [67, 68] and PD [69]. Here, the inhibition of this kinase participates in post-translational modifications in cytoskeletal proteins such as Tau, ameliorating the neuronal network functioning, as demonstrated with an increase in synaptic markers.

The relationship among MAPKs, such as ERK½ [70], and PI3K, such as AKT, and imidazoline receptors is well defined [71, 72]. In this respect, it has been described that either ERK or AKT can be associated with the multifunctional *Fas*/*FADD* complex [73, 74]. Apoptosis is an important contributor to neurodegeneration [75], and in this regard, the FADD protein has been suggested as a putative biomarker for pathological processes associated with the course of clinical dementia [76]. It has been reported that total FADD has a central role in promoting apoptosis [77, 78] and its phosphorylation at Ser191/194 mediates non-apoptotic actions such as cell growth and differentiation [79]. In our previous work, we demonstrated that **MCR5** modified FADD phosphorylation (i.e., it increased the p-FADD/FADD ratio) in a kainate-treated rat model [35]. These results could explain the modulation of proteins from the apoptotic pathway mentioned before (e.g., a diminution in caspase 3 activation and significant changes in Bcl-2 and Bax), which seems to favor anti-apoptotic actions mediated through I_2-receptors, and especially by **MCR5**.

Tau hyperphosphorylation is a histological trend in many neurodegenerative diseases characterized by cognitive decline, including AD. Therefore, we studied APP processing pathways. Aberrant APP processing is a hallmark of cognitive decline diseases [80]. To assess the capacity of the tested compounds to modify this pathological hallmark, we evaluated APP fragments, specifically, sAPPα and sAPPβ. Despite neither APP fragment reaching significance in either I_2-IR ligand-treated SAMP8 mice group, we found a clear tendency that indicates the non-amyloidogenic pathway preference. Moreover, sAPPα is described as a neuroprotective, neurotrophic and cell excitable regulator with synaptic plasticity [81]. *Adam10* [82] and *NEP* [83] gene expression were higher in **MCR5** and **MCR9** treated mice groups than in non-treated animals. In sum, I_2-IR ligands foster a diminution in the amyloidogenic pathway and higher degradation of β-amyloid in the SAMP8 mice model.

In conclusion, the effectiveness of the two new I_2-IR ligands in an *in vivo* female model for cognitive decline was demonstrated in this study. SAMP8 model mice are gated to neurodegenerative processes, such as AD, and our research has shown that **MCR5** and **MCR9** can open new therapeutic avenues against these pathological conditions that currently have unmet medical needs. Although different authors have previously indicated the relationship between I_2-IR and cognitive decline, this study is the first experimental evidence that demonstrates the possibility of using this receptor as a target for cognitive impairment. Here, we demonstrate that this strategy could represent a future approach to treating devastating conditions such as AD.

Acknowledgments This study was supported by the Ministerio de Economía y Competitividad of Spain (SAF2016-77703 and SAF2014-55903-R) and the Basque Government (IT616/13). C.G.-F., F.V., F.X.S., C.E. and M.P. belong to 2017SGR106 (AGAUR, Catalonia). J.A.G.-S. is a member emeritus of the Institut d'Estudis Catalans (Barcelona, Catalonia). Financial support was provided for F.V. (University of Barcelona, APIF_2017), S.R.-A. (Generalitat de Catalunya, 2018FI_B_00227) and A.B. (Institute of Biomedicine UB_2018).

Required Author Forms Disclosure forms provided by the authors are available with the online version of this article.

Author Contributions C.G.-F. and F.V. contributed equally. C.G.-F., C.E., L.F.C. and M.P. designed the study. B.P. performed the PAMPA-BBB permeation experiments. C.G.-F. and F.V. carried out the behavior and cognition studies and cellular parameters determination (OS and inflammation markers, synaptic markers and apoptotic factors, and hyperphosphorylation of Tau). J.A.G.-S. and M.J.G.-F. performed the hypothermic studies. S.A., S.R.-A. and A.B. synthesized and purified the I_2-IR ligands. C.G.-F., L.F.C., F.X.S., J.A.G.-S., M.J.G.-F., C.E. and M.P. contributed to writing the manuscript. All authors have read and approved the final version of the manuscript.

Abbreviations AD, Alzheimer's disease; *Adam10*, A disintegrin and metalloproteinase domain-containing protein 10; ANOVA, One-way analysis of variance; APP, Amyloid precursor protein; *Aox1*, Aldehyde oxidase 1; AKT, Protein kinase B; Bcl-2, B-cell lymphoma 2; Bax, Bcl-2-associated X; BBB, Blood-brain barrier; CDK5, Cyclin-dependent kinase 5; CNS, Central nervous system; *Cox2*, Cyclooxygenase 2; Ct, Cycle threshold; DI, Discrimination index; EPM, Elevated plus maze; ERK, Extracellular signal-regulated kinase; GAPDH, Glyceraldehyde-3-phosphate dehydrogenase; FADD, Fas-associated protein with death domain; *Gfap*, Glial fibrillary acidic protein; GSK3β, Glycogen synthase kinase 3 beta; *Hmox1*, Heme oxygenase (decycling) 1; I_2-IR, I_2-Imidazoline receptors; *Il-1β*, Interleukin 1 beta; *Il-6*, Interleukin 6; MAO, Monoamine oxidases; MAPK, Mitogen-activated protein kinase; *NEP*, Neprilysin; NMDA, *N*-methyl-D-aspartate; NORT, Novel object recognition test; OFT, Open field test; OS, Oxidative stress; PCR, Polymerase chain reaction; PD, Parkinson's disease; Pe, Permeability; PI3K, Phosphatidylinositol-4,5-bisphosphate 3-kinase; PSD95, Postsynaptic density protein 95; SAMP8, Senescence accelerated mouse prone 8; SPBD, Spectrin breakdown; SEM, Standard error of the mean; SOD1, Superoxide dismutase 1; SYN, Synaptophysin; TBP, Tata-binding protein; TN, Time with new object; *Tnf-α*, Tumor necrosis factor alpha; TO, Time with old object; WB, Western blot

REFERENCES

1. Bousquet P, Feldman J, Schwarts J. Central cardiovascular effects of alpha-adrenergic drugs: differences between catecholamines and imidazolines. J. Pharmacol. Exp. Ther. 1984;230:232-236.
2. Head GA, Mayorov DN. Imidazoline receptors, novel agents and therapeutic potential. Cardiovasc. Hematol Agents Med. Chem. 2006;4:17-32.
3. Lowry JA, Brown JT. Significance of the imidazoline receptors in toxicology. Clin. Toxicol. 2014;52:454-469.
4. Li, JK. Imidazoline I_2 receptors: An update. Pharmacol. Ther. 2017;178:48-56.
5. Fenton, C, Keating, G M, Lyseng-Williamson KA. Moxonidine: a review of its use in essential hypertension. Drugs 2006;6:477-496.
6. Reid JL. Rilmenidine: A clinical overview. Am. J. Hypertens. 2000;13:106S-111S.
7. Olmos G, Alemany R, Boronat MA, García-Sevilla JA. Pharmacologic and molecular discrimination of I_2-imidazoline receptor subtypes. Ann. N.Y. Acad. Sci. 1999;881:144-160.
8. Li JX, Zhang Y. Imidazoline I2 receptors: target for new analgesics? Eur. J. Pharmacol. 2011;658:49-56.
9. Callado LF, Martín-Gomez JI, Ruiz J, Garibi J, and Meana JJ. Imidazoline I_2 receptors density increases with the malignancy of human gliomas. J. Neurol., Neurosurg. Psychiatry 2004;75: 785-787.
10. Regunathan S, Feinstein DL, Reis DJ. Anti-proliferative and anti-inflammatory actions of imidazoline agents. Are imidazoline receptors involved? Ann. N.Y. Acad. Sci. 1999;881:410-419.
11. Ruíz J, Martín I, Callado LF, Meana JJ, Barturen F, García-Sevilla JA. Non-adrenoreceptor [^{3}H] idazoxan binding sites (I_2-imidazoline sites) are increased in postmortem brain from patients with Alzheimer's disease. Neurosci. Lett. 1993;160:109-112.
12. García-Sevilla JA, Escribá PV, Walzer C, Bouras C, Guimón J. Imidazoline receptor proteins in brains of patients with Alzheimer's disease. Neurosci. Lett. 1998;247:95-98.
13. Gargalidis-Moudanos C, Pizzinat N, Javoy-Agid F, Remaury A, Parini A. I_2-imidazoline binding sites and monoamine oxidase activity in human postmortem brain from patients with Parkinson's disease. Neurochem. Int. 1997;30:31-36.
14. Meana JJ, Barturen, F, Martín I, García-Sevilla JA. Evidence of increased non-adrenoreceptor [^{3}H]idazoxan binding sites in the frontal cortex of depressed suicide victims. Biol. Psychiatry 1993;34:498-501.
15. García-Sevilla JA, Escribá PV, Sastre, et al. Immunodetection and quantitation of imidazoline receptor proteins in platelets of patients with major depression and in brains of suicide victims. Arch. Gen. Psychiatry 1996;53:803-810.
16. Smith KL, Jessop DS, Finn DP. Modulation of stress by imidazoline binding sites: implications for psychiatric disorders. Stress 2009;12: 97-114.
17. Comi E, Lanza M, Ferrari F, Mauri V, Caselli G, Rovati LC. Efficacy of CR4056, a first-in-class imidazoline-2 analgesic drug, in comparison with naproxen in two rat models of osteoarthritis. J. Pain Res. 2017;10:1033-1043.
18. Regunathan S, Reis DJ. Imidazoline receptors and their endogenous ligands. Ann. Rev. Pharmacol. Toxicol. 1996;36:511-544.
19. Dardonville C, Rozas I. Imidazoline binding sites and their ligands: an overview of the different chemical structures. Med. Res. Rev. 2004;24:639-661.
20. Boronat MA, Olmos G, García-Sevilla JA. Attenuation of tolerance to opioid-induced antinociception and protection against morphine-induced decrease of neurofilament proteins by idazoxan and other I_2-imidazoline ligands. Br. J. Pharmacol. 1998;125:175-185.
21. McDonald GR, Olivieri A, Ramsay RR, Holt A. On the formation and nature of the imidazoline I_2 binding site on human monoamine oxidase B. Pharmacol. Res. 2010;62:475-488.
22. Casanovas A, Olmos G, Ribera J, Boronat MA, Esquerda JE, García-Sevilla JA. Induction of reactive astrocytosis and prevention of motoneuron cell death by the I_2-imidazoline receptor ligand LSL 60101. Br. J. Pharmacol. 2000;130:1767-1776.
23. Gustafson I, Westerberg E, Wieloch T. Protection against ischemia-induced neuronal damage by the α_2-adrenoceptor antagonist idazoxan: influence of time of administration and possible mechanisms of action. J. Cereb. Blood Flow Metab. 1990;10:885-894.
24. Qiu WW, Zheng RY. Neuroprotective effects of receptor imidazoline 2 and its endogenous ligand agmatine. Neurosci. Bull. 2006;22:187-191.
25. Gilad GM, Gilad VH. Accelerated functional recovery and neuroprotection by agmatine after spinal cord ischemia in rats. Neurosci. Lett. 2000;296:97-100.
26. Han Z, Xiao MJ, Shao B, Zheng RY, Yang GY, Jin K. Attenuation of ischemia induced rat brain injury by 2-(-2-benzofuranyl)-2-imidazoline, a high selectivity ligand for imidazoline I(2) receptors. Neurol. Res. 2009;31:390-395.
27. Maiese K, Pek L, Berger SB, Reis D J. Reduction in focal cerebral ischemia by agents acting at imidazole receptors. J. Cereb. Blood Flow Metab. 1992;12:53-63.
28. Jiang SX, Zheng RY, Zheng JQ, Li XL, Han Z, Hou ST. Reversible inhibition of intracellular calcium influx through NMDA receptors by imidazoline (I)2 receptor antagonists. Eur. J. Pharmacol. 2010;629:12-19.

29. Ruggiero DA, Regunathan S, Wang H, Milner TA, Reis DJ. Immunocytochemical localization of an imidazoline receptor protein in the central nervous system. Brain Res. 1998;780:270–293.
30. Olmos G, Alemany R, Escriba PV, García-Sevilla JA. The effects of chronic imidazoline drug treatment on glial fibrillary acidic protein concentrations in rat brain. Br. J. Pharmacol. 1994;111:997-1002.
31. Rodríguez-Arellano JJ, Parpura V, Zorec R, Verkhratsky, A. Astrocytes in physiological aging and Alzheimer's disease. Neuroscience 2016;323:170-182.
32. Martín-Gómez JI, Ruíz J, Barrondo S, Callado, LF, Meana JJ. Opposite changes in Imidazoline I_2 receptors and α_2-adrenoceptors density in rat frontal cortex after induced gliosis. Life Sci. 2005;78: 205-209.
33. Sica DA. Alpha 1-adrenergic blockers: current usage considerations. J. Clin. Hypertens. (Greenwich) 2005;7:757-762.
34. Abás S, Estarellas C, Luque FJ, Escolano C. Easy access to (2-imidazolin-4-yl)phosphonates by a microwave assisted multicomponent reaction. Tetrahedron 2015;71:2872-2881.
35. Abás S, Erdozain AM, Keller B et al. Neuroprotrective effects of a structurally new family of high affinity imidazoline I_2 receptors ligands. ACS Chem. Neurosci. 2017;8:737-742.
36. Morley JE, Farr SA, Kumar VB, Armbrecht HJ. The SAMP8 mouse: a model to develop therapeutic interventions for Alzheimer's disease. Curr. Pharm. Des. 2012;18:1123-1130.
37. Di L, Kerns EH, Fan K, McConnell OJ, Carter G. T. High throughput artificial membrane permeability assay for blood-brain barrier. Eur. J. Med. Chem. 2003;38:223–232.
38. McGrath JC, Lilley E. Implementing guidelines on reporting research using animals (ARRIVE etc.): new requirements for publication in BJP. Br. J. Pharmacol. 2015;172:3189-3193.
39. Ennaceur A, Delacour J. A new one-trial test for neurobiological studies of memory in rats. 1: Behavioral data. Behav. Brain Res.1988;31:47-59.
40. Ferrari F, Fiorentino S, Mennuni L, Garofalo P, Letari O, Mandelli S, Giordani A, Lanza M, Caselli G. Analgesic efficacy of CR4056, a novel imidazoline-2 receptor ligand, in rat models of inflammatory and neuropathic pain. 2011;4:111-125.
41. Jackson HC, Ripley TL, Dickinson SL, Nutt DJ. Anticonvulsant activity of the imidazoline 6,7-benzoidazoxan. Epilepsy Res. 1991;9(2):121-126.
42. Min JW, Peng BW, He X, Zhang Y, Li JX. Gender difference in epileptogenic effects of 2-BFI and BU224 in mice. Eur J Pharmacol. 2013;718(1-3):81-86.
43. Keller B, García-Sevilla JA. Immunodetection and subcellular distribution of imidazoline receptor proteins with three antibodies in mouse and human brains: Effects of treatments with I1- and I2-imidazoline drugs. J Psychopharmacol. 2015;29(9):996-1012.
44. Thorn DA, An XF, Zhang Y, Pigini M, Li, JX. Characterization of the hypothermic effects of imidazoline I_2 receptor agonist in rats. Br. J. Pharmacol. 2009;166:1936-1945.
45. Craven JA, Conway EL. Effects of alpha 2-adrenoceptor antagonists and imidazoline 2-receptor ligands on neuronal damage in global ischemia in the rat. Clin. Exp. Pharmacol. Physiol. 1997;24:204-207.
46. Illevich UM, Zornow MH, Choi KT, Scheller M, Strnat MA. Effects of hypothermic metabolic suppression on hippocampal glutamate concentrations after transient global cerebral ischemia. Anesth. Analg. 1994;78:905-911.
47. Takeda T. Senescence-accelerated mouse (SAM) with special references to neurodegeneration models, SAMP8 and SAMP10 mice. Neurochem. Res. 2009;34:639-659.
48. Pallàs M. Senescence-accelerated mice P8: a tool to study brain aging and Alzheimer's disease in a mouse model. ISRN Cell Biol. 2012:1-12.
49. Archer J. Tests for emotionality in rats and mice: A review. Anim. Behav. 1973;21:205-235.
50. Dawson GR, Tricklebank MD. Use of the elevated plus maze in the search for novel anxiolític agents. Trends Pharmacol. Sci. 1995;16: 33-36.
51. Antunes M, Biala G. The novel object recognition memory: neurobiology, test procedure, and its modifications. Cogn. Process. 2012;13:93-110.
52. Gao H-M, Zhou H, Hong JS. Oxidative Stress, Neuroinflammation, and Neurodegeneration. In: Peterson P. K., Toborek M. (Eds) Neuroinflammation and Neurodegeneration, 2014; pp. 81-104, Springer, New York, NY.
53. Fujibayashi Y, Yamamoto S, Waki A, Konishi J, Yonekura Y. Increased mitochondrial DNA deletion in the brain of SAMP8, a mouse model for spontaneous oxidative stress brain. Neurosci. Lett. 1998:254:109-112.
54. Sureda FX, Gutierrez-Cuesta J, Romeu M, Mulero M, Canudas AM, Camins A, Mallol J,Pallàs M. Changes in oxidative stress parameters and neurodegeneration markers in the brain of the senescence-accelerated mice SAMP-8. Exp. Gerontol. 2006;41: 360-367.
55. Gutierrez-Cuesta J, Sureda FX, Romeu M, Canudas AM, Caballero B, Coto-Montes A, Camins A, Pallàs M. Chronic administration of melatonin reduces cerebral injury biomarkers in SAMP8. J. Pineal Res. 2007;42:394-402.
56. Griñán-Ferré C, Palomera-Avalos V, Puigoriol-Illamola D, Camins A, Porquet D, Plà V, Aguado F, Pallàs M. Behaviour and cognitive changes correlated with hippocampal neuroinflammaging and neuronal markers in SAMP8, a model of accelerated senescence. Exp. Gerontol. 2016;80:57-69.
57. Griñan-Ferré C, Puigoriol-Illamola D, Palomera-Ávalos, V. et al. Environmental enrichment modified epigenetic mechanisms in SAMP8 mouse hippocampus by reducing oxidative stress and inflammaging and achieving neuroprotection. Front. Aging Neurosci. 2016;8:1-12.
58. Gao L, Tian S, Gao H, Xu Y. Hypoxia increases Abeta-induced tau phosphorylation by calpain and promotes behavioral consequences in AD transgenic mice. J. Mol. Neurosci. 2013;51:138-147.
59. Kimura T, Ishiguro K, Hisanaga S. Physiological and pathological phosphorylation of tau by Cdk5. Front. Mol. Neurosci. 2014;7:1-10.
60. Keller B, García-Sevilla JA. Regulation of hippocampal Fas receptor and death-inducing signaling complex after kainic acid treatment in mice. Prog. Neuropsychopharmacol. Biol. Psychiatry. 2015;3:63:54-62.
61. Cheng EH, Wei MD, Weiler S, Flavell RA. Mak TW, Lindster T, Korsmeyer SJ. BCL-2, BCL-X(L) sequester BH3 domain-only molecules preventing BAX- and BAK-mediated mitochondrial apoptosis. Mol. Cell. 2001;8:705-711.
62. Martin LJ. Mitochondrial and Cell Death Mechanisms in Neurodegenerative Diseases. Pharmaceuticals. 2010;3:839-915.
63. Sweatt JD. The neuronal MAP kinase cascade: a biochemical signal integration system subserving synaptic plasticity and memory. J Neurochem. 2001;76:1–10.
64. Hardingham GE, Bading H. Synaptic versus extransynaptic NMDA receptor signalling: implications for neurodegenerative disorders. Nat. Rev. Neurosci. 2010;11:682-696.
65. Imajo M, Tsuchiya Y, Nishida E. Regulatory mechanisms and functions of MAP Kinase signalling pathways. IUBMB Life 2006;58: 312-317.
66. Cruz CD, Cruz F. The ERK 1 and 2 pathway in the nervous system: from basic aspects to possible clinical applications in pain and visceral dysfunction. Curr. Neuropharmacol. 2007;5:244-252.
67. Hyman BT, Elvhage TE, Reiter J. Extracellular signal regulated kinases. Localization of protein and mRNA in the human hippocampal formation in Alzheimer's disease. Am. J. Pathol. 1994;144: 565-572.

68. Russo C, Dolcini V, Salis S, Venezia V, Zambrano N, Russo, T, Schettini G. Signal transduction through tyrosine-phosphorylated C-terminal fragments of amyloid precursor protein via an enhanced interaction with Shc/Grb2 adaptor proteins in reactive astrocytes of Alzheimer's disease brain. J. Biol. Chem. 2002; 277: 35282-35288.
69. Kulich SM, Chu CT. Sustained extracellular signal-regulated kinase activation by 6-hydroxydopamine: implications for Parkinson's disease. J. Neurochem. 2001;77:1058-1066.
70. Montolio M, Gregori-Puigjané E, Pineda D, Mestres J, Navarro P. Identification of small molecule inhibitors of amyloid β-induced neuronal apoptosis acting through the imidazoline I(2) receptor. J. Med. Chem. 2012;55(22):9838-46.
71. Zhang F, Ding T, Yu L, Zhong Y, Dai H, Yan M. Dexmedetomidine protects against oxygen-glucose deprivation-induced injury through the I2 imidazoline receptor-PI3K/AKT pathway in rat C6 glioma cells. J Pharm Pharmacol. 2012;64(1):120-7.
72. Xuanfei L, Hao C, Zhujun Y, Yanming L, Jianping. Imidazoline I2 receptor inhibitor idazoxan regulates the progression of hepatic fibrosis via Akt-Nrf2-Smad2/3 signaling pathway. Oncotarget. 2017;8(13):21015-21030.
73. García-Fuster, MJ, Miralles, A, and García-Sevilla, JA. Effects of opiate drugs on Fas-Associated Protein with Death Domain (FADD) and effector caspases in the rat brain: Regulation by the ERK1/2 MAP kinase pathway. Neuropsychopharmacology 2007;32:399-411.
74. Ramos-Miguel A, García-Fuster MJ, Callado LF, La Harpe R, Meana JJ, García-Sevilla JA. Phosphorylation of FADD (Fas-associated death domain protein) at serine 194 is increased in the prefrontal cortex of opiate abusers: relation to mitogen activated protein kinase, phosphoprotein enriched in astrocytes of 15 kDa, and Akt signaling pathways involved in neuroplasticity. Neuroscience 2009;161:23-38.
75. Papaliagkas V, Anogianaki A, Anogianakis G, Ilonidis G. The proteins and the mechanisms of apoptosis: A mini-review of the fundamentals. Hippokratia 2007;11:108-113.
76. Ramos-Miguel A, García-Sevilla JA, Barr A. et al. Decreased cortical FADD protein is associated with clinical dementia and cognitive decline in an elderly community sample. Mol. Neurodegener. 2017;12:26.
77. Chinnaiyan AM, O'Rourke K, Tewari M, Dixit VM. FADD, a novel death domain-containing protein, interacts with the death domain Fas and initiates apoptosis. Cell. 1997;81:505-512.
78. Scott FL, Stec B, Pop C, et al. The Fas-FADD death domain complex structure unravels signalling by receptor clustering. Nature 2009; 457:1019-1022.
79. Alappat EC, Feig C, Boyerinas B. et al. Phosphorylation of FADD at serine 194 by CKIα regulates its nonapoptotic activities. Mol. Cell. 2005;19:321-332.
80. O'Brien RJ, Wong PC. Amyloid precursor protein processing and Alzheimer's disease. Annu. Rev. Neurosci. 2011;34:185-204.
81. Gralle M, Botelho MG, Wouters FS. Neuroprotective secreted amyloid precursor protein acts by disrupting amyloid precursor protein dimers. J. Biol. Chem. 2016; 284:15016-15025.
82. Lichtenthaler SF. Alpha-secretase cleavage of the amyloid precursor protein: proteolysis regulated by signaling pathways and protein trafficking. Curr. Alzheimer Res. 2012;9:165-177.
83. El-Amouri SS, Zhu H, Yu J, Marr R, Verma IM, Kindy MS. Neprilysin: An Enzyme Candidate to Slow the Progression of Alzheimer's Disease. Am. J. Pathol. 2008;172:1342-1354.